Xintan Chang  *Editor*

# Proceedings of the 11th International Mine Ventilation Congress

Proceedings of the 11th International Mine Ventilation Congress

Xintan Chang
Editor

# Proceedings of the 11th International Mine Ventilation Congress

*Editor*
Xintan Chang
Xi'an University of Science and Technology
Xi'an, Shaanxi, China

# Foreword

The main goal of the International Mine Ventilation Congress (IMVC) is to "promote and encourage exchanges among mine ventilation professionals, accelerate the progress of engineering technology in mine ventilation, health and safety." Since 1975, IMVC has presented ten highly successful ventilation conferences, with participants from all major mining countries, including mine managers, mining engineers, practitioners and researchers from universities and research institutions, suppliers, and consulting companies. It is clear that IMVC has become a major forum for exchanging information on best practices, research, and technological advances, and for assessing progresses toward improved mine health and safety through better ventilation. The IMVC has made significant contributions to advance scientific and technological progress in mine ventilation worldwide and to facilitate exchanges and cooperation among all stakeholders.

The 11th IMVC is jointly hosted by Xi'an University of Science and Technology (XUST) and China University of Mining and Technology (CUMT). This is the first time in its 43-year history this Congress comes to China, which would not be possible without the efforts of Profs. Xintan Chang, Shugang Li of XUST assisted by Profs. Deming Wang and Fubao Zhou of CUMT. Professor Chang also Chairs the Organizing Committee overseeing day-to-day administrative activities.

This Congress is also not possible with the support of the mineral industry and other organizations—China Coal Industry Association, Central South University, Beijing University of Science and Technology, Shenhua Group, and universities such as Central South University, Anhui University of Technology, South China University, 500 suppliers and manufacturers, and many associations closely affiliated with coal and metalliferous mining sectors. In addition to his XUST team, Prof. Chang also leads the Editorial Committee, assisted by his two Associate Editor, Profs. Jerry Tien of Monash University and Chalmers of University of New South Wales, both in Australia, and committee members Profs. Shugang Li (XUST) and Deming Wang (CUMT). The Executive Committee, chaired by Mr. Frank Von Glehn (South Africa), and other members have provided valuable advises to the Congress preparation.

With the theme of "Progress in Technology and Management to Promote Health, Safety through Green Mining", main topics of this Congress include ventilation planning and design, mine dusts and dusts control, mine gas extraction and gas management, gas outburst prediction and control, explosion prediction and control, diesel particulate matter measurement and control, mine fire, coal spontaneous combustion problems, occupational health, heating and refrigeration, and mine climatic control, mine fans, auxiliary ventilation, detection, monitoring and automation, mine emergency design and rescue technology, mine safety laws and regulations, mine health and safety education and training. The Organization Committee is gratified by the positive response to the Congress—out of the over 155 abstracts, 89 papers are included in this proceeding, with the authors representing over 20 countries. In addition to technical sessions, the Congress program also includes an opening session, a closing session, a pre-congress workshop with eight topics on issues and solutions, 15 invited speakers with topics addressing current and emerging issues, and four field trips visiting some of China's largest and most efficient modern mining operations.

China is one of the world's leading mineral-producing and mineral-consuming countries; its continued economic growth was the result of a combination of trade and investment, and a strong mineral industry that provides materials and energy. China's mining industry is huge: producing and consuming more than 10 billion tons of mineral products each year from nearly 100,000 enterprises of various mining, processing and equipment manufacturing, and playing a critical role in the development of China as well as global economic growth. The majority of these are underground operations where ventilation is critical to its success.

Due to the advent of mining technological development, shutting down and consolidation of thousands of unsafe and inefficient small-scale operations, as well as enhanced government supervision and enforcement, the mining industry has witnessed an increased mineral production with improved mine safety and efficiency. Mining accidents and fatality rate have been continuously improving, with per 100,000 h rate approaching that of the developed countries. Despite these impressive gains, many issues still remain, especially in mine ventilation and in occupational health and safety.

The professional progresses in mine ventilation over past several decades have been impressive; it is important that we maintain this momentum. In an era of globalization, it is also essential that the Chinese mining community interacts with the world and learn from them. On the other hand, the world community also benefits from a safe and healthy Chinese mining industry. The Congress is pleased to be able to gather hundreds of mining and ventilation engineers, scientists, technical services, mine managers, and health professionals in one place, to provide

an excellent opportunity for our fellow ventilation colleagues overseas to interact with their Chinese counterpart up close, and vice versa. This will no doubt help everybody to further improve mine health and safety through more efficient technologies and better management.

I wish the 11th IMVC a complete success!

Huainan, China                                                                                         Liang Yuan
May 2018

# Preface

Ever since its debut in South Africa in 1975, the International Mine Ventilation Congress (IMVC) has now become the most influential conference worldwide in mine ventilation, safety, and occupational health. For the first time in its history, the 11th IMVC will be held in China, jointly hosted by Xi'an University of Science and Technology (XUST) and China University of Mining and Technology (CUMT). It offers a rare opportunity for the world to explore China's mining industry closely, and for Chinese ventilation professionals to interact with their colleagues outside of China as well.

Like the previous Congresses, such a world event would not be possible without the participation of professionals in the community worldwide. The Organizing Committee received a total of 215 abstracts, out of which 89 papers are selected by the Editorial Committee. The number of domestic abstracts from China reaches 155, or 72% of total abstracts submitted, and the domestic papers eventually selected is 36, or 40.4% of total papers in the Proceedings, far beyond the number of papers authored by Chinese professionals in previous Congresses.

The Proceedings cover a wide range of topics, including ventilation design and planning, diesel exhaust emission and control, dust and methane control, occupational health and safety, mine environment control, mine fire and explosion prevention, coal spontaneous combustion control, emergency handling and mine rescue, etc., giving an indication of the trends and concerns of the industry over the years. Browsing through the Proceedings, mine gases, dusts, coal spontaneous combustion, and occupational health are still the concerns, which reflects the fact that the focus on safety still remains the priority in mine ventilation, while pursuit for a higher standard of occupational health in mines is quite evident.

The 11th IMVC has been enthusiastically embraced by China's mining community with aspirations for memorable success. China is a non-English-speaking country under an Eastern-style working environment, and thus presents great challenges for the preparation of the Congress with English as its working language. I would like to thank the mine ventilation community worldwide for their heartening contributions to the Congress, especially the hosting universities, and members of the Academic Committee, Advisory Committee, and Organizing

Committee for their valuable supports. My sincere thanks also go to the colleagues and individuals for their whole-hearted coordination in program, field trip, and exhibition arrangements; all chairpersons, authors, keynote, and workshop speakers; and volunteers for their irreplaceable efforts. The Proceedings is ready for the Congress now, I would like to single out specifically Profs. Jerry Tien, Duncan Chalmers, Shugang Li, and Deming Wang, as well as all members of the Editorial Board for their highly effective work in Proceedings compiling and editing.

Welcome the 11th IMVC coming to China and wish the best for IMVC's everlasting success.

Xi'an, China                                                                    Xintan Chang
May 2018

# History of IMVC

The first International Mine Ventilation Congress (IMVC) was launched in Johannes-burg, South Africa in 1976, there has been ten IMVC every four years since then, and it has become a popular forum for ventilation practitioners, researchers, equipment manufacturers and suppliers, consultants and government officials all over the world to exchange best practices, explore R&D developments, and launch new products to build a better and a safer industry. It has also served as a useful forum to attract and train future ventilation professionals and mine planning engineers, as well as for mining companies to search for more effective means to improve mine safety.

By any account, China is the largest mining country in the world, with around 100,000 registered underground operations, and ventilation plays a key role to ensure a safe and effective operating environment. It is only fitting that the 11th IMVC is held in China, which is expected to attract in excess of 400 international and domestic delegates from all branches of mining industry, manufacturers, research establishments and universities concerning mine ventilation, occupational health and safety management.

The 11th IMVC is jointly hosted by Xi'an University of Science and Technology and China University of Mining and Technology, and sponsored by China's huge mining industry, equipment manufacturers and the government. Both universities have made significant contributions in mine ventilation and played a leading role in the development of China's natural resources and energy industry.

The International Mine Ventilation Congress

| IMVC | Year | Host City & Country | Chairman of Organizing Committee | Editors of the Proceedings |
|------|------|---------------------|----------------------------------|----------------------------|
| 1st | 1975 | Johannesburg, South Africa | Misi Barcza & John Burrows | R Hemp & F Lancaster |
| 2nd | 1979 | Reno, Nevada, USA | Arthur Baker | P Mousset-Jones |
| 3rd | 1984 | Harrogate, UK | Michael West | M Howes & J Jones |
| 4th | 1988 | Brisbane, Australia | Stewart Gillies | Stewart Gillies |

(continued)

(continued)

| IMVC | Year | Host City & Country | Chairman of Organizing Committee | Editors of the Proceedings |
|------|------|---------------------|----------------------------------|-----------------------------|
| 5th | 1992 | Johannesburg, South Africa | John Burrows | R Hemp |
| 6th | 1997 | Pittsburgh PA, USA | Bob Dalzell | Raja Ramani |
| 7th | 2001 | Krakow, Poland | W Trutwin | S Wasiliewski |
| 8th | 2005 | Brisbane, Australia | Stewart Gillies | Stewart Gillies |
| 9th | 2009 | New Delhi, India | Durga Panigrahi | Durga Panigrahi |
| 10th | 2014 | Sun City, South Africa | Frank von Glehn | Fvon Glehn & Mark Biffi |
| 11th | 2018 | Xi'an, China | Xintan Chang | Xintan Chang |

# Organizer

Professor Xintan Chang of the Executive Committee also serves as the Chairman of the Organizing Committee, along with three vice chairs and 20 other members from the mining industry, academia, and research institutions, both China and overseas to administer day-to-day operations of the Congress.

Editor:

Chief-editor: Prof. Xintan Chang, China

Associate Editors: Prof. Jun Deng, China; Prof. Fubao Zhou, China; Prof. Jerry Tien, USA

Members of Editorial Board:

- Prof. Xintan Chang, China;
- Prof. Jerry Tien, USA;
- Duncan Chalmers, Australia;
- Prof. Shugang Li, China;
- Prof. Deming Wang, China;
- Frank von Glehn, South Africa;
- Prof. Xinquan Zhou, China;
- Prof. Jun Deng, China;
- Prof. Fubao Zhou, China;
- Keith Wallace, USA;
- Prof. Ting-xiang Ren, Australia;
- Dr. Liming Yuan, USA;
- Prof. Kray Luxbacher, USA;
- Prof. Jin Longzhe, China;
- Steve Hardcastle, Canada;
- Prof. Lin Boquan, China;
- Dr. Bharath Belle, Australia;
- Dr. Guang Xu, Australia;
- Dr. Hsin Wei Wu, Australia.

# Contents

# Part I
# Vent System Optimization I

# Mobile Equipment Power Source—Impact on Ventilation Design

Chery Allen[1(✉)] and Jozef Stachulak[2]

[1] Vale Canada Ltd, Ontario Operations, 18 Rink St, Copper Cliff, Toronto, ON P0M1N0, Canada
Cheryl.allen@vale.com
[2] MIRARCO, 935 Ramsey Lake Rd, Sudbury, ON P3E2C6, Canada
jstachulak@mirarco.org

**Abstract.** Many Canadian mines are being developed deeper and further from the shaft to extract ore and at the same time challenged with meeting environmental conditions associated with diesel powered mobile equipment. Over the past few years alternative power sources, such as battery technology, have been gaining momentum as a solution for reducing emissions and minimizing the capital and operating costs of ventilation systems in new and expanding mines. Currently in most areas of Canada, air volume design criteria are based primarily on emissions from the diesel engine which may shift as the mobile equipment power source changes. This paper will address the design parameters that should be considered to assess the opportunities within a mine integrating non-diesel powered mobile equipment; as well as the associated impacts to the ventilation system design.

**Keywords:** Ventilation · Design · Mobile equipment · Air volume
Heat · Diesel · Battery

## 1 Introduction

Mobile mining equipment powered by the diesel engine has proven very valuable and flexible in its use; however, it also has a disadvantage of emitting heat, gaseous substances and diesel particulate matter (DPM). The World Health Organization (WHO) has confirmed that diesel emissions are a known carcinogen [1] resulting in regulations allowing less exposure to contaminants. The requirement to curtail emissions and at the same time realizing a substantial increase in the cost of power and fuel; there is incentive to replace the diesel engine with an alternative power source such as a battery motor.

The debate continues as to the degree of adoption of battery vehicles on surface and underground. As stated by CEO Atsushi Horiba "electric vehicles won't ever make up more than a third of autos worldwide" due to the feasibility of building the scale of infrastructure required to enable battery powered cars [2]. However, change will be required to meet emission targets. "The North American and European markets have the strictest rules when it comes to air quality underground and, given that the European Union recently introduced a new standard on air quality for the industry

(Stage V) which must be adopted by 2019, many mines will be considering whether to upgrade their current fleets (a costly exercise in-itself) or make the switch to battery electric—a technology that will see them much further into the future" [3]. An interim step of retro-fitting an existing fleet with high efficiency diesel particulate filters (DPF) or implementing modern diesel engines (i.e. Tier 4) is also an alternative strategy that could be practical, cost effective and a lower risk solution [4, 5].

Ventilation systems are necessary to dilute and remove contaminants from the mine; however, they are both capital and operating cost intensive. The electric power consumed to operate a mine ventilation system has been reported to be up to 40% of the entire mine's electric power consumption [6], or even higher as measured in typical base metal Canadian mines consuming between 50 and 80% of the site's electrical power demand [7]. Reducing the airflow into a mine will result in a significant drop in power consumption; therefore, the alternative of mine designs employing battery/electric equipment [8] as well as new mine project feasibility studies [9, 10] are underway.

This paper will discuss ventilation design and the impact when diesel powered equipment is replaced and/or integrated with battery powered equipment in stages or in full.

## 1.1 Methodology

A mine design case study of a deep Canadian metal mine will compare the associated volumes, infrastructure and power requirements for: (1) all diesel equipment, (2) hybrid with battery/electric and diesel equipment, (3) all battery/electric equipment based on agreed upon ventilation design criteria.

Figure 1 shows the level layout used in the study analysis with locations and type of equipment considered to be part of a normal production fleet. Table 1 lists the associated equipment power used in the design and analysis for each scenario. As can be seen, the power rating of the battery equipment is less (70%) than that of the equivalent diesel equipment [6].

Table 2 lists the level air volumes required for the mobile equipment selection and Table 3 lists examples of the key input parameters used for climatic calculations for each scenario. The resultant air volumes were based on meeting established reject air temperature criteria.

## 2 Ventilation Design Criteria

A set of design criteria provides a structured approach to meet the many demands of a ventilation design including solutions to ensure a safe work environment, flexibility to meet a Life of Mine Plan, address technical issues related to primary airway systems and mining depth, be robust yet fit-for-purpose, apply appropriate technology and economically responsible. Figure 2 is a graphical description of the ventilation design process. The established criteria should be developed such that it can be used for any mobile equipment power source (i.e. diesel or battery/electric); however, some aspects of the criteria may only apply to a specific type of power source. For example, an
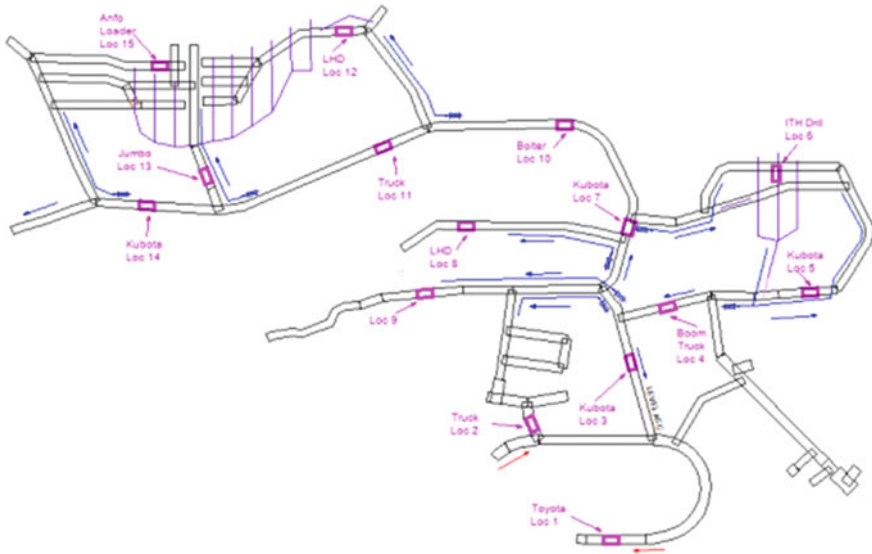
**Fig. 1.** Level plan view showing equipment locations

**Table 1.** Example of engine and motor sizes associated with Fig. 1

|  | Diesel (kW) | Battery/diesel (kW) | Battery (kW) |
|---|---|---|---|
| Personnel carrier | 100 | 100 | 70 |
| Haulage truck | 439 | 307 | 307 |
| Scooptram | 239 | 167 | 167 |
| Boom truck | 172 | 172 | 120 |
| Bolter | 119 | 119 | 84 |

**Table 2.** Air volumes required for each equipment scenario with associated drift velocities

| Equipment | Location | Volume ($m^3$/s) | Velocity (m/s) |
|---|---|---|---|
| Diesel | Main access drift | 94.4 | 3.7 |
|  | Stope access drift | 42.5 | 1.7 |
| Diesel/electric | Main access drift | 84.9 | 3.4 |
|  | Stope access drift | 26 | 1 |
| Electric | Main access drift | 54.7 | 2.2 |
|  | Stope access drift | 16.5 | 0.6 |

electric mine would not necessarily apply a specific air volume based only on equipment power rating as is done for the diesel engine. The criteria should be approved by the appropriate authority and thus create a basis for transparent design that can be audited and pass acceptance hurdles regardless of the design resource(s) [11].

**Table 3.** Example of thermal parameters used for climatic calculations and modeling

| Input data | Value |
|---|---|
| Surface intake temperature | 6 °C DB/WB |
| Virgin rock temperature (VRT) | 4.5–51.1 °C |
| Geothermal gradient | 55 m/°C |
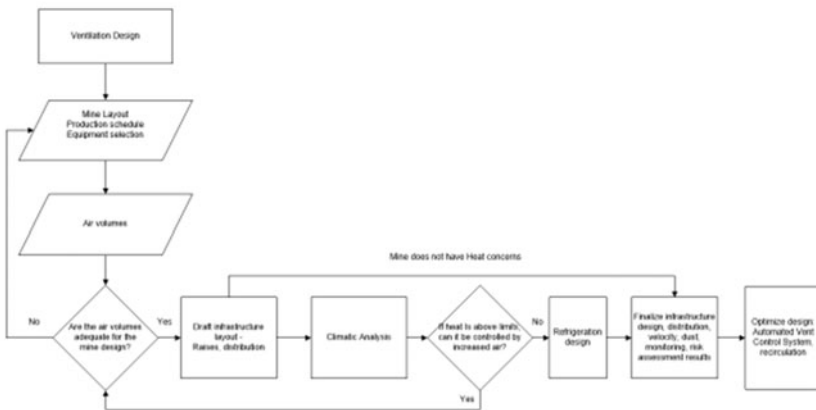


**Fig. 2.** Process flow for a basic ventilation design

The ventilation engineer occupies a somewhat delicate position. While you represent the company's interests, you are also charged with looking out for the working man. The two occasionally come into conflict. Rigorously establishing design parameters can be your best tool to deal with this point [12].

## 2.1   Air Volume

Determining air volume is challenging when integrating the "mine project plan", the "as built" infrastructure, mine expansion potential, and system efficiency declines as the mine ages. For example, if a mine required an additional 25% volume, above the maximum capacity, through existing raises, the increased fan pressure would be 56% and the power would increase by 95% (i.e. existing fan operating at 4.0 kPa/1500 kW would then need to operate at 6.3 kPa/2930 kW).

Figure 3 shows the process of air volume determination for an underground mine indicating the influence of the equipment selection for diesel vs electric/battery. In the case study, it was assumed that diesel engines do not have diesel particulate filters

## Air Volume
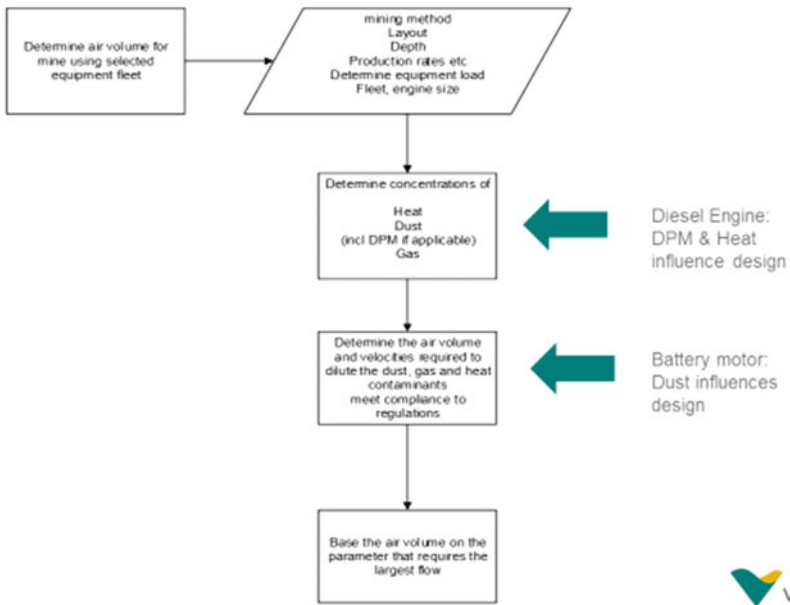


**Fig. 3.** Flow diagram for air volume determination indicating the parameters that influence the air volume calculations

(DPF). The process describes the major steps from information gathering of mining method, depth, geology, equipment fleet; then quantifying the types and concentration of contaminants; determining the air volumes and velocities necessary to meet air quality regulations and other regulations specific to equipment type.

An example of a methodology to determine air volumes applying design criteria for a diesel mine is shown in Table 4 where it provides an initial estimate of the air volume required [13].

An equipment list as shown in Table 5 can be used to quantify the power distribution from mobile equipment in a battery/electric mine, but it is not possible to apply a factor to the equipment power rating, as in a diesel mine, to obtain an initial estimate of the required mine air volume. A more thorough analysis considering blast clearance, dust generation, airway velocity and workplace temperature is required.

### 2.2  Air Velocity

Air velocity is an important criterion for the control of dust, gas, DPM and heat; thus finding the correct balance is necessary as shown in Fig. 4.

Respirable dust concentration decreases by dilution as airflow increases. Large dust particle concentrations increase as air velocity rises due to enhanced pick-up and delayed settling. The optimum velocity is in the range of 1.5–3.25 m/s as shown in Fig. 5.

**Table 4.** Air volume determination using diesel equipment

| Diesel equipment | | | | | | | | |
|---|---|---|---|---|---|---|---|---|
| Activity | Equipment | # of equipment | kW | Total kW | Factor | 0.06 cms/kW | Utilization | CMS required |
| | | | | | **1.2** | | | |
| Level—production | 8 yd scoop | 2 | 242 | 484 | 580.8 | 34.848 | 100% | 34.8 |
| | Personnel carrier | 1 | 100 | 100 | 120 | 7.2 | 40% | 2.9 |
| | ITH | 1 | 76 | 76 | 91.2 | 5.472 | 40% | 2.2 |
| | Anfo loader | 1 | 110 | 110 | 132 | 7.92 | 40% | 3.2 |
| | Kubota | 1 | 37 | 37 | 44.4 | 2.664 | 40% | 1.1 |
| | 30 T truck | 1 | 305 | 305 | 366 | 21.96 | 100% | 22.0 |
| | Bolter | 1 | 119 | 119 | 142.8 | 8.568 | 40% | 3.4 |
| | | | | | | | | 69.5 |
| | Volume/heat aux recirc | 25% factor | | | | | 25% | 17.4 |
| **Production** | | | | **1231** | **1477** | | | **87** |
| Development | 8 yd scoop | 1 | 242 | 242 | 290.4 | 17.424 | 100% | 17.4 |
| | 30 T truck | 1 | 305 | 305 | 366 | 21.96 | 100% | 22.0 |
| | Bolter | 1 | 119 | 119 | 142.8 | 8.568 | 40% | 3.4 |
| | Personnel carrier | 1 | 100 | 100 | 120 | 7.2 | 40% | 2.9 |
| | | | | | | | | 45.7 |
| **Development** | | **4** | | **766** | **919** | | | **46** |
| Activity totals | Production (6 levels adjusted for truck activity) | 6 | | 7386 | 8863 | | | 478 |
| | Development (3 levels) | 3 | | 2298 | 2758 | | | 137 |
| | Development ramp (1 ramp) | 1 | | 766 | 919 | | | 46 |
| | | | | **10450** | **12540** | | | **660** |
| **Subtotal mobile equipment** | | | | **10450** | 12540 | | | **660** |
| | Infrastructure (garages, conveyors) | 1 | | | | | | 47 |
| | **Subtotal infrastructure** | | | | | | | **47** |
| | **Base subtotal** | | | | | | | **707** |
| | Fel 3 design primal leakage factor 15% | | | | | | 0.15 | 106 |
| | **Total fresh air volume** | | | | | | | **813** |

**Table 5.** Equipment summary by mining activity for a battery/electric mine

| Battery equipment | | | | |
|---|---|---|---|---|
| Activity | Equipment | # of equipment | kW | Total kW |
| Level— production | 8 yd scoop | 2 | 169 | 338 |
| | Personnel carrier | 1 | 70 | 70 |
| | ITH | 1 | 53 | 53 |
| | Anfo loader | 1 | 77 | 77 |
| | Kubota | 1 | 26 | 26 |
| | 30 T truck | 1 | 213 | 213 |
| | Bolter | 1 | 83 | 83 |
| **Production** | | 7 | | **860** |
| Development | 8 yd scoop | 1 | 169 | 169 |
| | 30 T truck | 1 | 213 | 213 |
| | Bolter | 1 | 83 | 83 |
| | Personnel carrier | 1 | 70 | 70 |
| **Development** | | 4 | | **535** |
| **Totals** | **Production** | 6 | | 5160 |
| | **Development** | 3 | | 1605 |
| | **Development ramp** | 1 | | 535 |
| | | | | **7300** |
| **Subtotal mobile equipment** | | | | **7300** |
| | Fixed equipment | 1 | | 400 |
| | Fel 3 desiqn primary leakaqe factor 15 % | | | |
| | Total equipment power | | | **7700** |

Recent research, as shown in Fig. 6, shows there is an impact to the body's ability to manage thermal stress dependent on air velocity [14]. It can be seen that the lower air velocity boundary for cooling, due to evaporation, is 0.5 m/s with target conditions at 1.5 m/s.

> The two parameters to focus in a ventilation design are wet-bulb temperature and air velocity when heat issues are expected in the mine design. When air velocity exceeds 0.75 m/s the maximum wet bulb temperature where work efficiency does not deteriorate is about 26°C; an economic temperature range for a relatively young, healthy, acclimatized work force is 26°C to 28.5°C; and temperatures nearing 29°C and above are in a safety factor range which can be dangerous. [12]

## 2.3 Other Criteria

It is beneficial to include criteria that establishes parameters around distribution, control philosophy, economic optimization of airway sizing, temperature limits and risk.

**Temperature criteria** is often based on reject temperatures, which are defined as temperature measured at the last place the air reports before leaving the level or area.
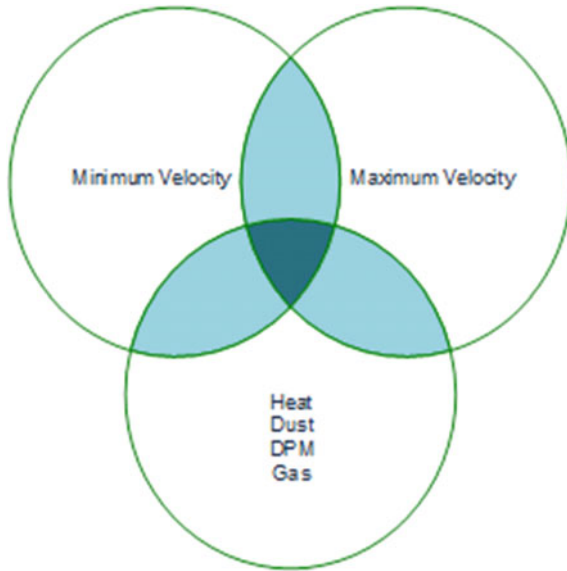
**Fig. 4.** Air velocity balance
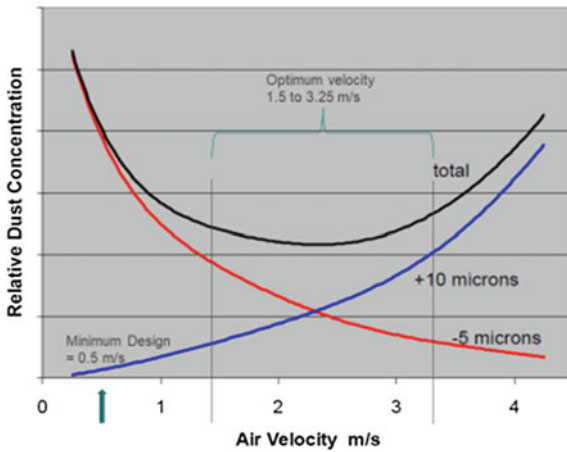


**Fig. 5.** Influence of air velocity on dust particle size [Malcolm McPherson]

**A risk assessment** should be conducted on the complete ventilation design to highlight any critical issues that may be inherent within the design (i.e. a ventilation system can spread the products of combustion just as efficiently as it does life-sustaining oxygen) [12, 15]. The ventilation design should make every effort to
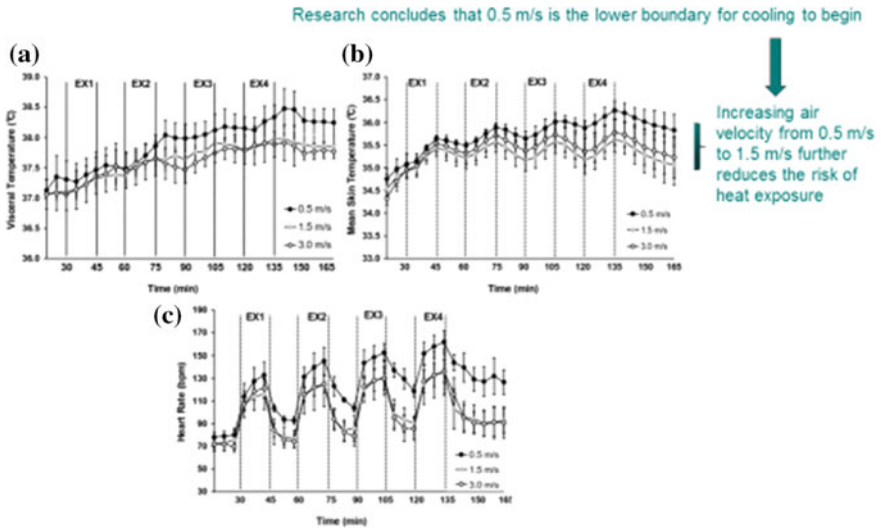
**Fig. 6.** Influence of air velocity on heat stress to the human body [14]

meet the established design criteria; however, it may be necessary to deviate from the criteria and a risk assessment can identify controls that are required to reduce the associated risk.

## 3   Workplace Temperature

Workplace temperatures impact safety and production therefore must be maintained to safe working limits or monitored by a heat management procedure. As found in a 1980s study of heavy work in S. Africa, an increase in temperature from 25 to 29 °C wet bulb relates to a decrease in performance of 14% [16]. Climatic modeling is conducted to predict air temperatures when opening new mining areas and can be used to determine air volumes necessary to control heat. A large component of heat in a mine production area is from mobile equipment and can significantly impact ventilation design in a hot mine, as discussed in Sect. 4.

Heat from the diesel engine is in the form of sensible and latent heat, whereas heat from the battery/electric motor is only in the form of sensible heat. The diesel combustion engine has an overall efficiency about one-third that of the electric motor; and as a result, the diesel engine will generate approximately three times as much heat as the electric motor for the identical mechanical work output. This heat radiates three ways with approximately one-third from the radiator and vehicle body, one-third as heat content in the exhaust gases and the remaining one-third from shaft power (frictional process required for the diesel unit to perform work) [17]. The battery/electric motor is efficient, thus the heat generated is equal to the mechanical work output plus system inefficiency.

# 4   Case Study Results

## 4.1   Comparison Discussion

For all three scenarios in the case study [13, 18] the surface intake air temperature was constant at 6 °C wb/db, drift size was kept constant at 4.9 m × 5.2 m (25.5 m$^2$) with only air volumes being changed between scenarios, as per Table 2, to maintain the same stope and reject temperatures. Air volumes are based on design criteria discussed previously.

**Total heat load**. The single largest contribution toward total heat load is mobile equipment as indicated in Fig. 7; and is worth noting that the heat load balance in the scenario employing all battery/electric equipment is approximately 50% less in comparison with the scenario using all diesel equipment (1380 kW vs. 2982 kW).

**Air velocity** can be both a control for and contributor to hazards. As can be seen in previous Table 2, the air velocities in an all-electric mine fall within the lower recommended range in comparison to the air velocities at the higher limits in a diesel mine. Air velocities that are too high can entrain large dust particles that become airborne; and low air velocity not being able to adequately dilute and remove
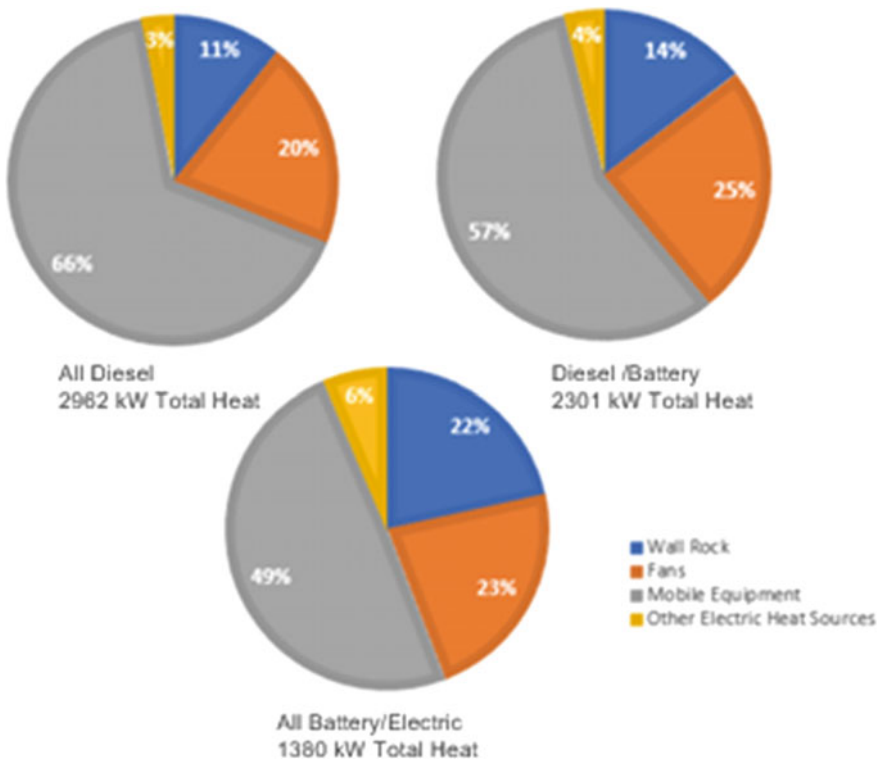


**Fig. 7.** Comparison of heat generation on a typical production level from source contributions per scenario

contaminants. To demonstrate the impact to a ventilation design from changing air volumes and subsequently air velocity, the drift size for all scenarios in the case study was held constant.

## 4.2   Benefits

There are benefits to the underground environment from removing the diesel engine to power mobile equipment. Health benefits come from removal of Diesel Particulate Matter, in engines not fitted with a high efficiency DPF, and additional heat in deep mines. The cost benefits come from the potential for reducing the total air volume which influences sizing of infrastructure and power demand.

**Airway dimension** size is based on the air volume impact to velocity and power required to circulate air throughout the mine. Table 6 compares potential raise size reductions for secondary raises that transfer air between levels and Table 7 compares primary raises. Decreasing air volume through internal secondary raises when comparing an all-diesel mine to an all-electric mine corresponds to a decrease in raise size by 21%, and the potential for a 13% size reduction of a primary raise.

**Table 6.** Comparison of ventilation raise reduction with varying air volume at constant pressure drop within secondary raise systems

|  | Air volume (cms) | Volume reduction | Raise bore diameter (m) | Size reduction |
|---|---|---|---|---|
| Diesel | 94.4 |  | 3.35 |  |
| Diesel → battery | 54.7 | 94.4 → 54.7 42% | 2.65 | 3.35 → 2.65 21% |

**Table 7.** Comparison of ventilation raise reduction with varying air volume at constant pressure drop within primary raise systems

|  | Air volume (cms) | Volume reduction | Raise bore diameter (m) | Size reduction |
|---|---|---|---|---|
| Diesel | 391.7 |  | 5.79 |  |
| Diesel → battery | 269.0 | 94.4 → 54.7 31% | 5.03 | 5.79 → 5.03 13% |

**Energy reduction** is significant when decreasing the air volume due to the cubic relationship between air volume and power. The power comparison in Tables 8 and 9 includes an analysis of auxiliary distribution systems and primary fan systems. In the case study, changing from a diesel mine to a battery mine reduced the power demand on a level by 61%, and by 31% in the primary system. If the duct size was optimized within the auxiliary system to decrease fan pressure, the power reduction on a level will be further increased. The potential monetary savings can be projected by applying the site power cost/kW to the number of active levels and power demand of primary fans.

**Table 8.** Power reduction comparison from air volume changes for secondary air distribution on a level per Table 2

| Equipment type | Level air volume (m³/s) | Volume reduction | Stope access fan power (kW) | Power reduction |
|---|---|---|---|---|
| Diesel | 94.4 | | 134 | 134 → 52 |
| Battery | 54.7 | 94.4 → 54.7 | 52 | |
| | | 42% | | 61% |

**Table 9.** Power reduction comparison from air volume changes from primary fan systems

| Equipment type | Air volume for mine production (m³/s) | Volume reduction | Primary fan power (kW) | Power reduction |
|---|---|---|---|---|
| Diesel | 391.7 | | 1951 | 1951 → 1336 |
| Battery | 269 | 391.7 → 269 | 1336 | |
| | | 31% | | 31% |

**Heating and Cooling**. Energy savings can also be realized from smaller heating and cooling systems due to decreased air volume. Natural gas volumes and cooling power ($MW_R$) requirements will decrease by up to 31% when operating an all battery/electric mine.

## 5   Challenges

There are currently some challenges for full scale implementation of battery-electric vehicles into underground mining operations. "The first is lack of a single charging standard for battery-electric vehicles. Currently, there are a number of different manufacturers all doing different things in regards to charging infrastructure, batteries, chargers and electric current requirements" [19].

Present battery charge life does not match the eight to ten-hour shift requirement; therefore, battery management must also be understood as attention will need to be paid to the design, type and location of charging stations and implications to mine infrastructure (i.e. battery swapping stations with overhead crane requirements). "Charging currently takes about two hours, and switching a battery takes around 10 min. The problem at present is that you pay for the capacity of the battery, so if you need an 8-h battery it is twice the size, weight and price. Then you need another battery on top of that to switch out for charging. This is a trade-off between cost, size and what is possible with today's technology" [3].

Application of this equipment into the mining industry is indispensable for maturing the technology which will then demonstrate success for future business cases.

# 6   Conclusion

The primary role of an underground ventilation system is to provide airflow to dilute and remove contaminants to safe levels where people are required to work or travel. A mine ventilation design can be complicated so a structured approach is beneficial to ensure the design provides a robust and fit-for-purpose system that meets the mining requirements for the mine life. Establishing design parameters can be the best tool to achieve a system that provides a quality work environment and meets the needs of the business.

The battery/electric mine will require a more comprehensive design that considers the impact of velocity on blast clearance, heat and dust levels due to air volume reductions that are possible as a result of zero gaseous and DPM emissions from mobile equipment.

There are benefits to the mine design from replacing diesel engines with battery/electric equipment such as realizing capital cost reductions from smaller raises and fans and operating cost reductions from lower power, natural gas and refrigeration demand. However, there are challenges with the current state of technology associated with equipment maturity, battery management, charging infrastructure, and mine design integration. Fitting current diesel engines with diesel particulate filters could be an interim and cost effective step toward eliminating DPM in underground mines [4, 5] along with introducing alternative powered mobile equipment.

Although there are challenges, mine designs employing zero emission and low heat vehicles are a beneficial tool to sustain mining into the future.

# References

1. Paddock, C.: Diesel Exhaust Fumes Cause Cancer, WHO. https://www.medicalnewstoday.com/articles/246495.php, last accessed 2018/02/01
2. Buckland, K., Horie, M.: Diesel's Death "Overstated," Says Man Whose Gear Found VW Fraud. http://europe.autonews.com/article/20170905/ANE/170909903/diesels-death-overstated-says-man-whose-gear-found-vw-fraud, last accessed 2018/02/01
3. Leonida, C.: Battery Electric: the Death of Diesel Underground? http://www.aramine.com/images/presse/big/086.Batteryelectric—MiningMagazine2017–06.pdf, last accessed 2018/02/01
4. Stachulak, J.S., Allen, C., Hensel, V.: Successful application of a diesel particulate filter system at Vale's Creighton mine. CIM J. **6**(4), 227–232 (2015)
5. Stachulak, J., Conard, B.R., Schnakenberg, G.: Evaluation of Diesel Particulate Filter System at Stobie Mine. Sudbury, Ontario, Canada. http://www.camiro.org/sites/default/files/DEEP/Project_Reports/MasterStobie-ver2—Sept2012.pdf, last accessed 2018/02/01
6. Halim, A., Kerai, M.: Ventilation requirement for 'electric' underground hard rock mines—a conceptual study. In: The Australian Mine Ventilation Conference, Adelaide, pp. 215–220 (2013)
7. Vale company report, unpublished, Sudbury. Ontario (2015)
8. Durnan, M.: Kirkland Lake Gold Pioneering Battery-Powered Mining. North. Ontario Bus., https://www.northernontariobusiness.com/industry-news/mining/kirkland-lake-gold-pioneering-battery-powered-mining-547882, last accessed 2018/02/01

9.  Jamasmie, C.: Canada's Goldcorp to Make Borden an All-Electric Mine, http://www.mining. com/canadas-goldcorp-to-make-borden-an-all-electric-mine, last accessed 2018/02/01
10. Kelly, L.: Going Deep in Sudbury—Northern Ontario Business. https://www.northernonta- riobusiness.com/industry-news/mining/going-deep-in-sudbury-590909, last accessed 2018-/ 02/01
11. Stachulak, J.S.: Ventilation strategy and unique air conditioning at Inco Limited. In: 4th US Mine Ventilation Symposium. Berkeley, California (1989)
12. Marks, J.: Nuts-and-bolts ventilation planning for hardrock mines. In: 4th US Mine Ventilation Symposium. Berkeley, California, pp. 1–61 (1989)
13. Allen C, Stachulak JS.: Ventilation design case studies. In: MDEC's workshop. Toronto, Canada, pp. 37–61 (2016)
14. Hardcastle, S.G., Wright, H.E., Phinney, C.N., Kenny, G.P., Allen, C.: Erosion of the air velocity cooling benefit for workers in the mining industry associated with changing workforce characteristics. In: 23rd World Mining Congress and Expo. Montréal, Québec (2013)
15. Stachulak, J.S.: Inco's design and protection against underground fires. CIM Bull. **87**(984), 58–63 (1994)
16. Vale-Inco's international ventilation workshop. Sudbury, Ontario, Canada (2010)
17. Malcolm, M.: Subsurface Ventilation and Environmental Engineering, 1st edn. Chapman & Hall, London (1993)
18. Allen, C., Stachulak, J.: Mobile equipment and ventilation design. In: CIM MEMO Conference. Sudbury, Ontario, Canada (2016)
19. Electric equipment. http://minewiki.engineering.queensu.ca/mediawiki/index.php/Electric_ equipment, last accessed 2018/02/01

# Pros and Cons of Primary Ventilation Systems and the Need for Critical Spares

Johannes Holtzhausen[✉]

OZ Minerals, First Floor, 162 Greenhill Road, Parkside, SA, Australia
johannes.holtzhausen@ozminirals.com

**Abstract.** Various vendors of primary ventilation systems supply products in the market today and it is sometimes hard to distinguish between what system would best fit my operation. There is no wrong system, just a wrong application of a system and with that the question is laid before you, which system offers what to an operation and how will the operation benefit? We intend to explore the difference between axial, centrifugal and mixed flow fans and the benefits it offers an operation but also the hidden aspects many times not explored. Some of the points that will be touched on will be redundancy through design, fan efficiencies, electrical input power, maintenance requirements and the need for critical spares. We intend to show what the result of poor maintenance of a primary fan installation may lead to and how it could impact on your business. The unavailability of critical spares may have significant impacts on the operation. Too often ventilation controls are chosen for the wrong reason, forgotten about until the day a major fan failure occurs, and then only discovered no contingency plan has been put in place. It is important, even more so for a small operator, to protect the business against unplanned stoppages, which may result in major loss to production and revenue.

**Keywords:** Economics · Redundancy · Performance

## 1 Primary Ventilation Systems

### 1.1 Scoping of a Primary Ventilation System

How do we identify the correct ventilation system for our application, is a question we have heard numerous times in the industry. The answer to the question lies in the hands of the Ventilation Engineer and may only be fully explored if the following points are considered.

#### 1.1.1 Standards and Legal Requirement

Environmental standards and legal requirements vary from state to state in Australia. It is important, no matter where you are operating in the world, to know what the minimum legal requirements are as required by the said government, legislations, regulations and inspectorate. Most companies have internal standards set in line with legislation to safeguard the health and safety of its employees. Establishing the maximum/minimum temperatures, pressures, gas levels and flow rates will lay the foundation for the design of the ventilation network. Finalising the ventilation

management/design standards prior to the design phase will give the engineer a good understanding of minimum guidelines to follow.

### 1.1.2   Mining Method and Production Rate

The mining method and planned production rate play an integral part in the mine ventilation design and drive the air volume required to safely ventilate the mine. The mining method and production rate will directly impact the environmental considerations such as heat, dust, humidity, radiation, fumes and gases. Equipment to be used is an important factor and may require additional considerations. With the use of diesel technology in the underground environment it must be noted that there are various legal requirements depending on the state or country the mine will be operating in. In Australia there are two regularly used guidelines for a mine using diesel-powered mining equipment, which are 0.05 and 0.06 $m^3$/s/kW total engine rated power.

### 1.1.3   Environmental Stressors

Knowing environmental stressors impacting on the underground environment throughout the life of the mine will help plan a ventilation system that includes opportunity for growth and expansion. Some to be considered are historic weather station data for the area, stressors encountered by established mines in the area, surface rock temperature, thermal gradient, effects of auto compression, virgin rock temperature at depth, miniralisation (sulphides, carbonaceous matter), natural gas, heat and types of mine dusts.

### 1.1.4   Life of Mine

Understanding the extend of the ore body and the expected life of mine will allow for a design that is scalable and tailor made throughout the various stages of the mining process. This design could then include high end technology or a simple design to cater for a quick and safe extraction of the ore body. A cheap installation may be the most expensive option over time if total cost of ownership were not considered.

### 1.1.5   Resources

Availability and the access to resources have to be considered. Availability of support and maintenance resources are sometimes overlooked leading to increased operating costs or the lack of regular scheduled maintenance of ventilation systems. Availability natural resources and power supply.

### 1.1.6   Supplier Confidence

The selected supplier or suppliers must have a good track record with the confidence and market share suggesting that they will be around for the life of the installation. It is important to check references and quality, not only of previous installations, but also of continued support services.

## 1.2 Mine Ventilation—Primary Ventilation Fan

There are multiple fan companies competing in all industries for market share offering a wide range of fan technologies. In the mining industry there are three types of fan technology mainly used (Fig. 1).
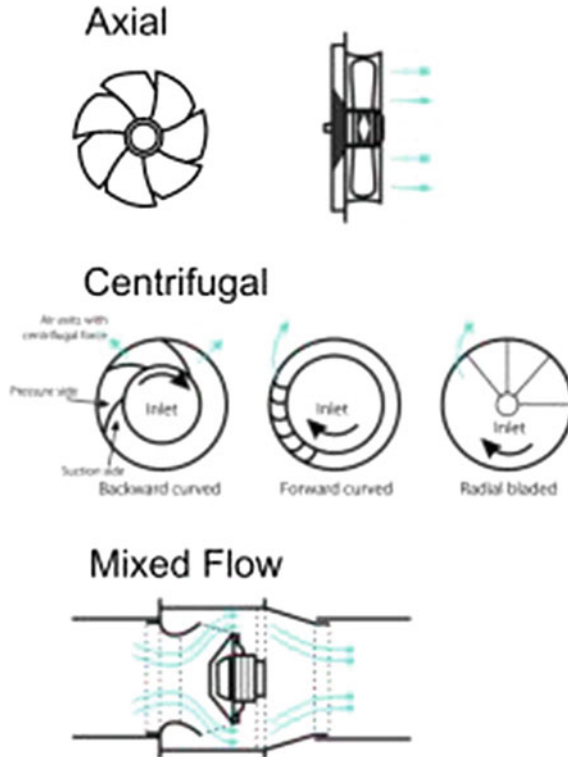


**Fig. 1.** Illustration of fan types

### 1.2.1 Axial Flow Fan

An axial fan serves as a type of compressor increasing the pressure of the air handled by the fan. There are multiple blade designs for axial flow fans and they all force the air to move parallel to the shaft around which the blades rotate. The flow for that reason is axially in and out, linearly, and for that reason the name axial flow fan. Axial flow fans are widely used in the Australian mining sector as primary and booster fan installations. The reasons vary but are largely due to ease of installation (smaller footprint), shallower underground mines not requiring a high pressure fan solution, lower initial capital layout. The long term pro's and con's may be further compared in Table 1.

**Table 1.** Simple fan comparison

| | Purchase cost | Running cost | Characteristics | Noise | Performance efficiency | Ease of maintenance |
|---|---|---|---|---|---|---|
| Axial flow fan | Lowest | High | High flow, low pressure | Higher | Lower | With in line motors it requires the fan to be stopped and the motor to be exposed for maintenance and lubrication. There are designs removing the motor from the fan casing but these are more expensive options and does result in drive shaft and gearbox losses should it be fitted |
| Centrifugal fan | Highest | Low | Low flow, high pressure | Lower noise but due to the frequency is harder to silence | Higher | Motors are external from the fan and maintenance are mostly easier to carry out. Component may be bulkier though and should fan failures occur it could require more heavy lifting |
| Mixed flow fan | Mid range | Mid range | Higher flow than centrifugal, significant static pressure capability | Higher | Claims to be the same or better than centrifugal | With in line motors it requires the fan to be stopped and the motor to be exposed for maintenance and lubrication. There are designs removing the motor from the fan casing but these are more expensive options and does result in drive shaft and gearbox losses should it be fitted |

### 1.2.2   Centrifugal Fan

Centrifugal fans move air radially and the direction of the air moving out the fan is changed. This change in direction of airflow is normally by 90° from the angle of the inflowing airstream. Centrifugal fans can handle higher pressure systems. Centrifugal fans have not been installed as regularly as axial flow fans in Australia mining. This is due to various reasons which differ from project to project but has mostly to do with a

large initial capital layout, shallower mining not requiring high pressure fans and the larger footprint of the installation. In a mine with a extended mine life and at a depth exceeding 1000 m a centrifugal fan total cost of ownership may be much lower. This must not however be accepted as the norm and each project must have a full financial evaluation completed confirming the best solution, not only for cost, but also practical application and use.

### 1.2.3    Mixed Flow Fan

Mixed flow fans maintain the static pressure over the fan and combines axial and radial components to produce a diagonal airflow compressor stage. The exit mean radius is normally greater than the inlet, not unlike a centrifugal fan design, but the airflow exit the fan in an axial rather than a radial direction.

### 1.2.4    Exhaust Versus Forced Primary Ventilation Systems

Exhaust type primary ventilation systems with the fan installed on surface are the most commonly used for Australian underground mines. The reason for this has much to do with cost of installation, maintenance, ease of access and less so with efficiency and performance. There are numerous examples of Exhaust, Forced, Force Exhaust and gated systems in the mining industry and their efficiency has much to do with the application and design requirements.

There are many more factors and considerations to take into account not listed in Table 2 when picking your primary fan solution. At times a combination of solutions applied in various sections of the mine would better serve the operation. Care must be invested in not being locked into a solution as a result of the popular choice but rather that of the right choice for your operation. This choice may only become clear when all aspects of the requirements have been investigated and appropriately considered in the design.

## 1.3    Selecting the Right Solution for the Application

To select the right solution for the application many performance indicators have to be considered. Understanding the various fan technologies and what they may offer the operation is important but these benefits have to be cross-checked against the operational needs. The obvious fit for an application is sometimes not that obvious and rather dictated by time, budget and availability instead of total cost of ownership, reliability, maintenance, environmental impact and scalability. Many engineers are left frustrated with primary fan installations not hitting the mark nor ticking the boxes for the life of mine.

It is also true that much needed resources are wasted on some projects installing solutions that are never to be utilised to its full potential. This is almost always the result of poor planning and over engineering without doing the necessary planning and due diligence checks. Many engineers live by the motto "rather bigger and more than too small and less", this is a frustrating outlook as a fan must deliver the flow and pressure equal to the planning that was done. Should an installation not perform as per the planning it is an indication of both poor planning and design work or the fan manufacturer not meeting the design criteria for the fan installation.

**Table 2.** Simple primary fan force exhaust comparison

| Primary fan—exhaust system | | Primary fan—forced system | |
|---|---|---|---|
| Advantages | Disadvantages | Advantages | Disadvantages |
| Airborne contaminants captured in the return airway circuit | Intake air quality deteriorates as the air flow deeper underground (auto compression) | Better quality air is delivered to the lowest section of the mine | More complex secondary ventilation system required to control contaminants in the circuit |
| Pressure difference allow natural gas to drain into ventilating circuit and be exhausted via the return air circuit | Airborne contaminants accumulate in ventilation circuit as it is carried to the lowest point of return in the mine. Quality of air is poorer in the lower section of the mine | No contact contamination due to diesel, decline, pump station/sump and other infrastructure | Higher contact time and exposure to airborne contaminants as cleanest air is contained to the free system (where no regular work is scheduled) |
| In the case of a fire in the working area the smoke and heat is contained to the ventilation district | Best quality air is not necessarily delivered to the lowest point of the mine where work takes place | No coffin seal required on belt installations | Amount of air heated and cooled not easily controlled |
| Less complex secondary ventilation designs required during mine development | Additional bulk system required to be installed for heating and cooling purposes | Heating and cooling of intake air better controlled | Longer re-entry times after firings |
| Most harmful air containing contaminants isolated in the return air circuit where no continuous daily tasks are planned | | | More complex ventilation systems required for Hi risk areas such as the magazine, fuel bay and oil storage |
| Hi risk areas such as the magazine, fuel bay and oil storage can easily be ventilated directly to return | | | |

## 2  Operations

Ventilation systems are one of the most costly ongoing expenses a mine will pay for; choosing the wrong ventilation system for an operation will be a costly mistake. Ventilation is far too often a hidden cost buried in the operational budget never to be

looked at. There are important points to be considered when choosing a ventilation system for the mine.

## 2.1 Efficiency

The power consumption of the fan will make up the bulk of the running cost of the fan over time. Should the wrong solution be sourced, that is not efficient it may lead to millions of dollars lost over time. Some regional locations in Australia pay a premium for power generation with generators. These generator banks will be impacted as larger generator sets will have to be installed, more fuel will be used which in some locations are flown or shipped in and over time the additional cost may lead to marginal projects closing down.

Table 3 indicates that if a 1400 kW installation is utilised where a 1200 kW installation is required, the consequence will be an A\$525 K annual loss. This cost excludes any additional maintenance and reduction in installation cost.

**Table 3.**  Cost comparison

| Fan size kW input power | Cost kW/h for power | Cost of running fan per annum A\$ | Cost saving per annum A\$ |
|---|---|---|---|
| 1400 | \$ 0.30 | \$ 3,679,200 | 0 |
| 1300 | \$ 0.30 | \$ 3,416,400 | −\$ 262,800 |
| 1200 | \$ 0.30 | \$ 3,153,600 | −\$ 525,600 |
| 1100 | \$ 0.30 | \$ 2,890,800 | −\$ 788,400 |
| 1000 | \$ 0.30 | \$ 2,628,000 | −\$ 1,051,200 |
| 900 | \$ 0.30 | \$ 2,365,200 | −\$ 1,314,000 |

## 2.2 Maintenance

Maintenance remains the heart of a ventilation system to ensure the system will operate efficiently based on its original design. It is unfortunate that this at most operations is not performed to the standard it should be. It has long alluded me why this is the case as it is an asset that comes at a great cost to the operation with continuous impact on the bottom line. The entire operation is reliant on the ventilation system to provide worker health and safety and production without delay due to inadequate ventilation. I know of multiple primary fan failures which have occurred due to poor maintenance.

> Miners at XXX Coal's XXX Colliery have again been forced above ground amid methane level concerns, after a ventilation system cut out at the weekend – the second fan failure in three weeks.

There are so many examples like the one above and one must ask how much a total stoppage of production amount to and is it worth the time saved by not conducting regular fan maintenance? The design of the primary fan is not always maintenance friendly and care must be taken to consider the effort, technical expertise and equipment that will be required to maintain said installation. The manufacturer of the

ventilation system must supply service manuals and train all persons responsible for the continued maintenance of the plant. Engineering drawings and parts lists serve as a great tool when the installations are older and require major work or parts to be replaced.

## 2.3    Redundancy

Redundancy through design may cost a fraction more during the project phase but has the potential to save operations millions of dollars over the life of the asset. Redundancy remain a hard sell during project phase as you spend money countering an action/event most of the times rated as unlikely to happen.

Figure 2 is a good example of how redundancy may be built into a fan design. By having multiple or standby fans it allows underground workings to be adequately ventilated in case of a fan failure or a planned maintenance. When single fan installations are utilised 100% of the ventilating air is lost to the underground workings during stoppages (planned or unplanned) compared to 35–45% in an in parallel fan installation. Other examples are back up power generators, duel feeder cables and the list goes on. By considering redundancy in the system it allows the operation and the maintenance team function normally without interruption. Easy role out cradles allowing quick change over of complete fan units are extremely popular in Australia and widely used.



**Fig. 2.**  Three exhausting fans in parallel with a well-designed bend to minimize shock loss

## 2.4    Environmental Impact

When a mine is situated in the outback some of the points may not be as relevant as to an operation close to a residential community. These points must still be considered as they will impact on the employees on the mine site just as they would in a community.

Noise generated by the plant must be considered together with the effective attenuation thereof. Silencers are often used to control noise but other alternatives may be considered such as noise barriers, damping products, alterations to the outlet of the

fan (facing into the ground and not up in the air), containing within building and positioning away from work areas.

Fallout from underground due to contaminants being carried in the airstream and being rejected into the general atmosphere. In wet mines allot of moisture may be exhausted through the primary ventilation fan.

Impact on the fauna and flora of the area due to temperature differences, contaminants and continuous flow. The footprint of the installation must also be considered.

### 2.5    Critical Spares

Now with critical spares many mine sites fall short, including some of the larger operators. Critical spares are always hard to justify as it is a big expense for a component of the project that will probably never be used. Some fan installations operate for 30 years, when well maintained, without ever needing to use anything other than replacing bearings and fan blades, and applying lubricants during planned maintenance. The selection of critical spares must be done making use of a risk matrix identifying acceptable risk to the organization and putting into place controls where risk is not acceptable. For the risk assessment the true loss must be assessed in conjunction with the risk to health and safety during unplanned fan stoppages.

For smaller operators, risk is quantified in a whole other way as budgets may be smaller and profit margins narrower. There are no right and wrong when it comes to critical spares and it has to be assessed from project to project. Should critical spares not form part of the project scope the engineer must identify the availability and the lead time of high risk items such as: fan blades and impellers, transformer, drive shaft, gearbox, bearings, switch gear, sensors and electrical motors.

### 2.6    Safety

Safety and systems of safety must be included in the design to ensure no harm come to any mine workers. Various safety considerations need to be made such as, railings to prevent falling from height, lock out systems, inspection hatches for easy access, fencing off of the installation and site specific systems and procedures. It is always good to include the members from the engineering team during the design phase of a ventilation system to make sure all aspects relevant to their safety are addressed.

## 3    Conclusion

Unfortunately there is no silver bullet to be applied to ventilation design with multiple factors and project requirements dictating what the perfect solution will be for each project. The perfect solution also rarely remain perfect as a mining operation is dynamic and ever adapting to new information as it becomes available during the life of the operation. The important part for engineers to remember is to make sure all necessary considerations at the time has been capture explaining the logic behind the design. There are many engineering calculations and considerations to be made in the scoping and selecting of the fan but the base of those calculations must be formed from

what is the desired outcome. The engineer employed on site must be the one who take ownership of the design parameters dictating project guidelines, even as a junior engineer a contractor/consultancy must not be relied up on solely. You may design the best system in the world, but if it does not comply to the operations requirements to achieve their production plan and output, it serves no purpose.

## References

1. Pearson, A.: Fan Fails. Mercury, 17 Nov (2016)
2. du Plessis, J.J.L. (ed.): Environmental and Occupational Environment Engineering in Mines, 3rd edn. Mine Ventilation Society of South Africa (2014)

# Controlled Primary Ventilation Recirculation and Re-use with Reconditioning—A Strategy for Deep Mines

Leon van den Berg[1], Katie Manns[1(✉)], and Steven Bluhm[2]

[1] BBE Consulting Australia, Joondalup, WA 6027, Australia
{lvandenberg,kmanns}@bbegroup.com.au
[2] BBE Consulting, Bryanston Sandton, 2146, South Africa
sbluhm@bbe.co.za

**Abstract.** Australian underground mines are inevitably getting deeper particularly where steep dipping ore bodies are involved. The mining depths will eventually extend beyond original mine design horizons at which point the installed ventilation infrastructure will generally not be able to sustain mining needs. The ventilation systems will become strained due to system resistance, higher leakage, auto-compression and rock temperatures. Furthermore, with increasing depth, more trucks will generally be required to sustain production rates. These mines will start to experience local hot zones and areas of flow stagnation along the trucking declines. At this stage, the primary ventilation systems will require upgrades, and this could include ventilation raises [surface and u/g], additional refrigeration capacity and high pressure fans [or booster fans]. These infrastructure upgrades will require significant investment with long project lead times. At depth, the technical feasibility of successfully establishing longer raises also becomes an important consideration. Strategies that employ controlled recirculation of the primary ventilation, with reconditioning, can offer solutions that allow deferral of the new infrastructure. Furthermore, if effective scrubber technology can be developed, primary ventilation upgrades could perhaps be avoided. The reconditioning of primary ventilation is technically feasible and advantageous from a mine cooling perspective. However, the issue that has prevented mines from adopting the technology on a wide spread basis has been gas and respirable particulate management. This paper considers the merits of controlled recirculation, advantages of employing these strategies and scrubbing technologies that should be the subject of further research. The paper also examines how a controlled recirculation strategy could conceptually be implemented in a deep mechanized mine. It is argued that the significant cost associated with primary ventilation upgrades warrants a critical review of controlled recirculation and R + D investment into related technologies.

## 1 Introduction

As mining depths increase, operations inevitably reach a point where the existing primary ventilation infrastructure can no longer support the operation. With increasing depth, the trucking fleets are increased in order to sustain the same production rate over

longer haulage distances. At the same time the available ventilating air reduces due to increased pressure on fans and higher leakage rates. At depth, the mines experience low airflow or even flow stagnation resulting in zones with poor air quality in terms of temperature and contaminant levels. A critical depth is eventually reached at which point the mine has to invest in new primary ventilation infrastructure which may include surface raises, primary fans, booster fans and refrigeration equipment.

In cases where the existing surface ventilation shafts are at maximum capacities, new surface shaft/raise infrastructure would be required. The cost of establishing new surface shafts is a very significant component of any primary ventilation upgrade. These shaft development projects also carry a risk of cost overruns or delays particularly if unexpected geotechnical or groundwater conditions are encountered. These risks can be reduced by following sound design practice, however some residual risk will always remain. It is also worth noting that there is limited raise bore equipment available with the capability of developing large diameter raises at depth. As the demand for this equipment increases, its availability [or lack thereof] could make expansion projects very challenging.

In the context of increasing cost pressures in the mining industry, controlled recirculation with reconditioning is an attractive alternative. These systems can offer solutions allowing deferral of shaft capital or even an alternative to additional surface shafts. The technologies to recondition primary air in terms of heat and nuisance dusts are well established. Research has demonstrated that wet scrubbers that employ ultrafine spray systems can also effectively remove some of the respirable dust fraction and even some gasses if chemical additives are deployed. One of the main barriers to adopting the technology more widely is the perceived risk of recirculation and concern around diesel particulate. These concerns are understandable but given the advanced monitoring and filtering/refrigeration technologies and significant cost benefit that controlled recirculation or re-use with reconditioning could offer, these issues certainly warrant consideration. In the context of this paper. It is important to make a clear distinction between controlled recirculation and controlled re-use of air. Controlled recirculation as discussed in this paper involves purposefully directing a small percentage of exhaust air back into the intake or fresh air system. On the other hand, re-use can be defined as ventilating two distinct mining areas in series by re-using a percentage or all the air from one mining area in another mining area. The recirculation and re-use strategies described in this paper involve the use of reconditioning to improve air quality. This includes cooling the air and scrubbing systems to remove contaminants.

This paper considers the history of controlled recirculation and re-use, some operations currently using recirculation as well as different scrubbing technologies that should be the subject of further research. The paper also examines how a controlled recirculation strategy could conceptually be implemented in deep mechanized mines. It is argued that the significant cost associated with primary ventilation upgrades warrants a critical review of controlled recirculation and possible R + D investment into related technologies.

## 2  History

In the past there have been numerous controlled recirculation schemes applied and many small-scale strategies have been used for the control of dust, methane and heat in collieries. In South Africa, a recirculation scheme was in operation at a deep gold mine [ERPM] in 1948. The use of controlled recirculation [for reducing heating costs] has also been considered in Canada. However, until the early 1980s, controlled recirculation was generally based on small-scale localized systems. There were significant advances in the 1980s with the application of a large-scale recirculation system at Loraine gold mine in South Africa [1], for the efficient distribution of underground cooling in the Homestake gold mine in the United States [2] and a major scheme at the Wearmouth Colliery in the UK [3].

Since then a number of fairly large controlled recirculation and re-use schemes have been successfully implemented and reported in the literature. Two recent examples of operational mines that have implemented such strategies are Palabora Copper Mine [PMC] which is a deep block cave operation in South Africa. Van den Berg et al. [4] describes how PMC used this strategy to recondition the air from the crusher and re-use it for development. PMC were able to utilize this strategy as the crusher exhaust had no significant diesel contaminants, no silica and no radon, and as such only the nuisance dust was required to be controlled. Another current scheme can be found at Vale's Taquari Vasouras potash mine in Brazil. Bluhm et al. [5], describes how Taquari utilize controlled recirculation and refrigeration to relieve the critical shortage of primary ventilation due to limited shaft capacity and to manage heat in production areas. Taquari were able to implement a controlled recirculation and refrigeration scheme because, like PMC, they have minimal diesel contaminants, no radon and no silica concerns.

In all these systems there has been an emphasis on the safety, control and monitoring systems. It goes without saying that this is an essential and integral part of any recirculation and re-use system. But this is a specialized subject on its own and this paper does not examine this aspect in any depth. It is however, covered in the literature, for example, Bluhm et al. [5].

## 3  Opportunities

Although there are many potential applications, two possible types of opportunities for using controlled recirculation are explored here:

- Increasing decline airflow rates
- Ventilating satellite ore bodies

### 3.1  Application to Increase Decline Air Flow Rates

Australian mines are continuingly increasing with depth and most operations employ diesel trucks for material handling. At depth, these mines sometimes employ a so-called hybrid push-pull ventilation system to ensure fresh and in most cases chilled

air is fed directly to working areas on production levels without being contaminated by the primary diesel fleet on the decline. This hybrid push-pull distribution system uses secondary fans in walls and ducting to distribute fresh air to workings directly from surface intake raises. In this type of system, the secondary fans become an integral part of the primary ventilation circuit. The advantages and disadvantages of this hybrid system are described by Derrington [6] and this paper does not explore this particular approach in any detail.

However, where mines apply these types of systems, the airflow used on active levels is not necessarily fully utilized in terms of its ability to dilute contaminants or its ability to absorb heat. The air supplied to the levels using this hybrid approach bypasses the upper sections of the main decline and sometimes only ventilates levels with low contaminant producing activity or even levels temporarily inactive and some of this air will therefore still be relatively 'fresh' when it exhausts to return. A downside of this approach, is that as mines get deeper, the decline is often starved of ventilation due to leakage and airflow allocations to upper levels. In some cases, the decline airflow may even stagnate. This results in sections of the decline experiencing high contaminant concentrations and wet-bulb temperatures. This not only impacts personnel traveling along the decline but also any activity or infrastructure that has to be ventilated from the decline. When the operation reaches this situation, a primary airflow upgrade to increase overall ventilation would be generally required.

The air that is supplied to the levels from the fresh air raise will theoretically have lower contaminant concentrations and temperatures when compared to the decline exhaust. The mixed exhaust air in the return system will consequently be of better quality when compared to the decline sections that encounter low airflow. If this air can be reconditioned and reintroduced into the decline it would increase airflow, reduce contaminant levels and reduce air temperature along the 'critical' decline sections. This could provide a temporary solution for improving decline airflow, allowing the deferral of capital associated with primary surface infrastructure or even replacement thereof, depending on the level of reconditioning achieved.

It is worth noting that some mines already implement a similar philosophy without reconditioning where hybrid ventilation systems are in place. The air supplied to the levels from the fresh air raise is often directed back to the lower decline to be re-used for diluting truck emissions operating on the lower section of the decline. This does not however resolve the air quality issues in the critical section of the decline. The controlled recirculation strategy with reconditioning is being proposed as a possible future solution for this scenario.

## 3.2 Application for Satellite Ore Body

As mining reserves are depleted in the primary ore body, many existing operations identify smaller satellite ore bodies to supplement the production from the primary ore body. These satellite ore bodies are sometimes accessed from the existing decline and may even be shallower than the main ore body. The increased number of active levels associated with this additional ore body will require additional ventilation. In turn, this triggers the need for additional surface ventilation infrastructure. Mines will often consider ventilating this satellite ore body in series with the primary ore body to defer

or avoid capital expenditure. This however will negatively impact the air quality particularly in deep mines that experience high heat loads and leakage rates. Re-use strategies are not uncommon in these types of mines however rarely is any attempt made to recondition the air to improve air quality.

For example, consider a mine with a small satellite marginal ore body away from the primary ore body, this satellite ore body would be too deep to consider developing a decline from surface and so the logical access for this satellite ore body will be from the existing decline. However, the new ore body will often be too far away to easily utilize the existing ventilation infrastructure and, even if it is not, there is often no 'spare' capacity in the primary ventilation system. In this scenario, a series ventilation strategy could be considered in which the air that is used in the satellite ore body is re-conditioned and re-used in the primary ore body by supplementing the decline flow in the primary ore body.

## 4 Modeling

Basic Ventsim Visual models were developed to simulate the possible impact of a controlled recirculation and reconditioning system. The base case model represents a hypothetical but 'typical' deep Australian mine which has reached the limits of its current ventilation infrastructure and which has low airflow on the declines as described above. The base case has been set up as a typical hybrid push-pull parallel system with a fresh air intake raise, a return air exhaust raise and a single decline.

Five production levels were modelled at a depth of 1.5 km with allowance for 7 trucks and 4 loaders (see Fig. 1) [Other design criteria included 20 °C wet bulb surface temperature, 2.5 °C/100 m geothermal gradient, 3 W/m °C rock conductivity and 0.3 rock wetness fraction].

The modelled heat loads included that from auto-compression, diesel equipment, strata and fans. Diesel heat loads and contaminant data were calculated from actual diesel consumption data from an operational mine with similar parameters. The maximum diesel particulate emissions were estimated from US-EPA limits for Tier 2 non-road compression-ignition engines which was based on the average engine loading determined from the actual fuel burn. The CO and NOx concentrations were set at the maximum limits of 1500 and 1000 ppm respectively [Western Australian Mine Regulations 1995 for mines using dilution rates of 0.05 $m^3$/s per kW]. Figure 2 shows how recirculation may be introduced above the reference position.

The base case results (Fig. 3) show the high temperatures and gas concentrations along the critical portion of the decline where low flow is experienced. This will impact personnel traveling along the decline as well as any mining activity that may need to be ventilated from the decline. The following scenarios were also modeled:

- Scenario 1: 120 kg/s recirculation with 3.5 MW spray chamber (Figs. 4 and 5).
- Scenario 2: 120 kg/s recirculation with 3.5 MW spray chamber and high efficiency scrubber stage (Fig. 6).

Scenario 1 illustrates the benefits of utilizing a basic controlled re-circulation system whereby the mine would take a portion of the air out of the exhaust raise and
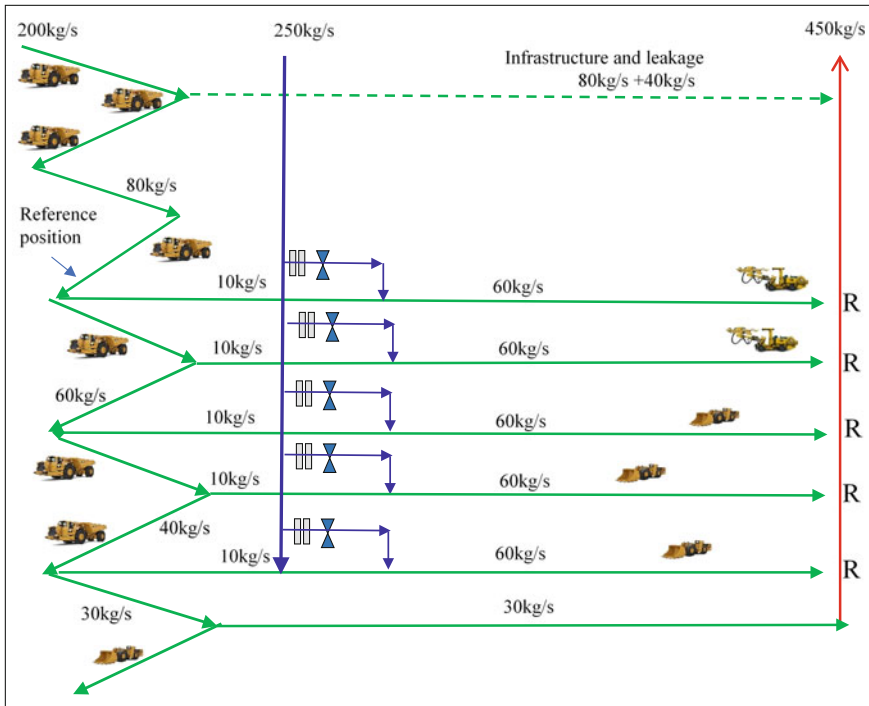
**Fig. 1.** Typical parallel system with hybrid ventilation configuration

re-condition it in a conventional air cooling spray chamber. This would chill the exhaust air and eliminate some respirable dust and possibly some DPM. For the present purposes, it is assumed that the conventional spray chamber [in this study] will have 0% efficiency in eliminating CO and NOx and 15% efficiency at eliminating DPM.

Scenario 2 (Fig. 6) illustrates the benefits of utilizing a custom designed scrubber system in conjunction with the conventional spray chamber (Fig. 9). Bluhm et al. [7], have suggested that the theoretical efficiencies of such a scrubber system could be 25% for CO, 85% for NOx and 80% for DPM.

The base case model (Fig. 3) shows that the temperatures on the decline above the production zone will exceed the recommended operating maximum underground temperature of 32 °C wet bulb (see Fig. 6). The CO and NOx concentrations will also be fairly high at 12 and 8 ppm respectively and the DPM can be expected to be around 115 μg/m$^3$ (see Figs. 7 and 8).

Scenario 2 models show that re-conditioning a portion of exhaust air and re-injecting it at some location above the critical section of decline will be very beneficial. The temperature can be reduced to 26.5 °C wet bulb with modelled reference position CO levels reducing from 12 to 9 ppm and NOx from 8 to 4 ppm and DPM levels from 115 to 64 μg/m$^3$ (Fig. 9).
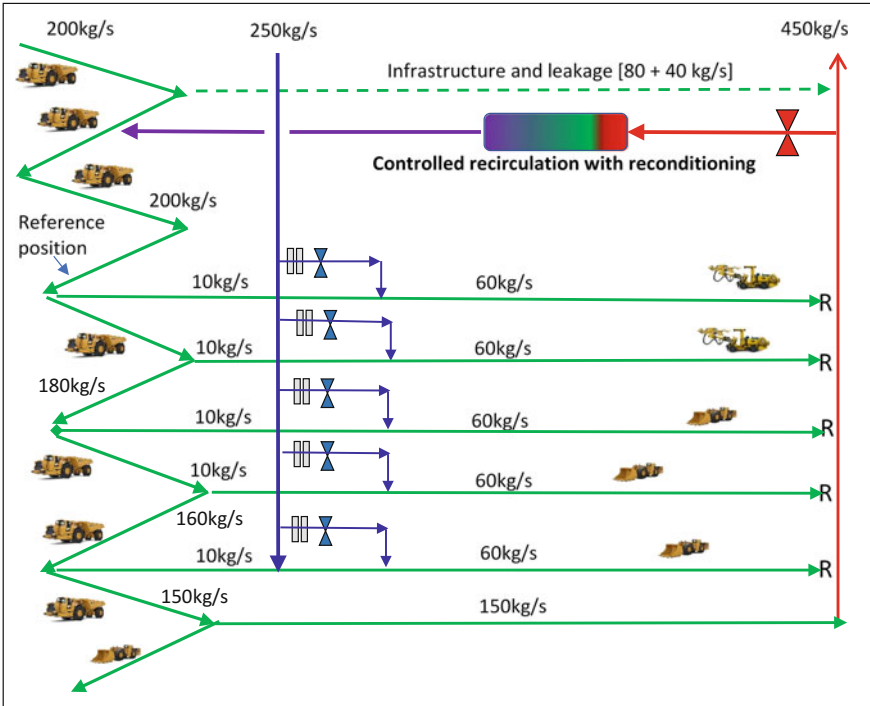
**Fig. 2.** Typical parallel system with hybrid ventilation configuration but including recirculation
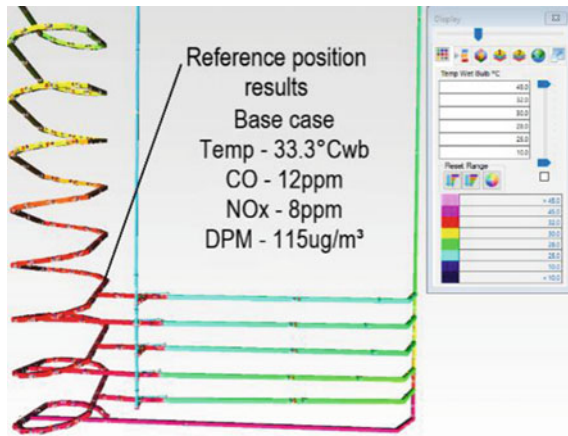


**Fig. 3.** Base case model showing temperature color coding [no recirculation]
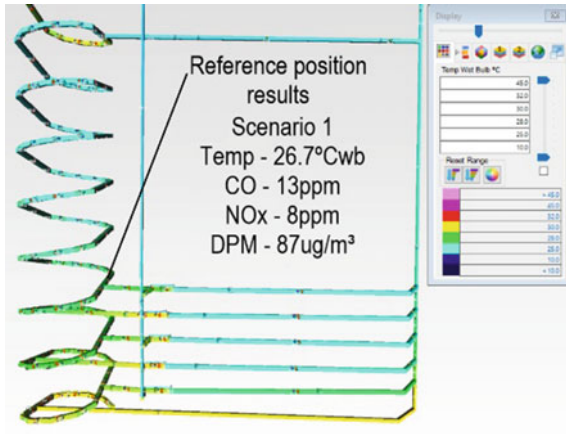
**Fig. 4.** Scenario 1: recirculation with air cooler spray chamber but no special scrubber section [temperature color code]
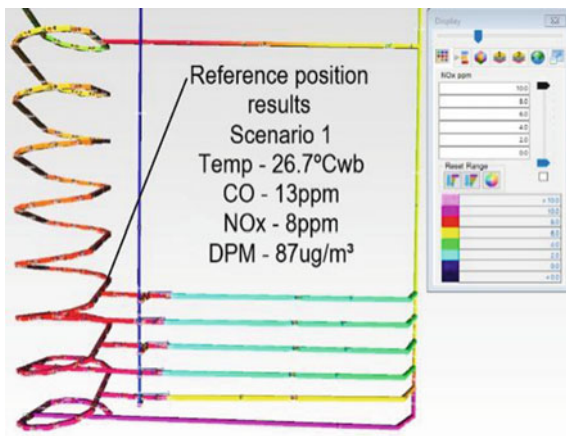


**Fig. 5.** Scenario 1: recirculation with air cooler spray chamber but no special scrubber section [NOx concentration color code]

The system model recirculates 120 kg/s of 450 kg/s, which is only 25% of the overall exhaust quantity. In terms of the re-use strategy described previously, a similar re-use factor of 25% was considered. The models suggest that under the appropriate conditions and with sufficient air supplied at a global level to meet diesel dilution criteria the use of a controlled recirculation and refrigeration scheme does not increase contaminant levels above occupational limits.
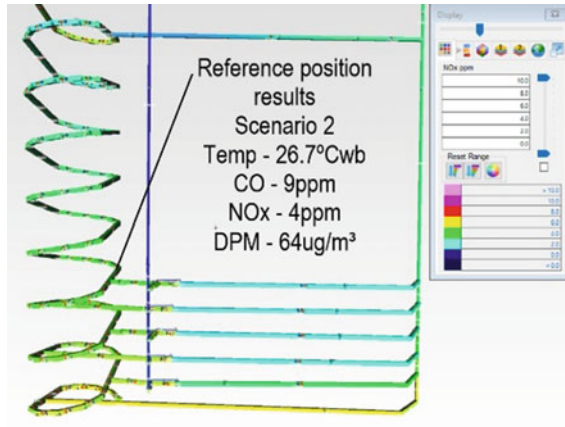
**Fig. 6.** Scenario 2: recirculation with air cooler spray chamber including special scrubber section [NOx concentration color code]
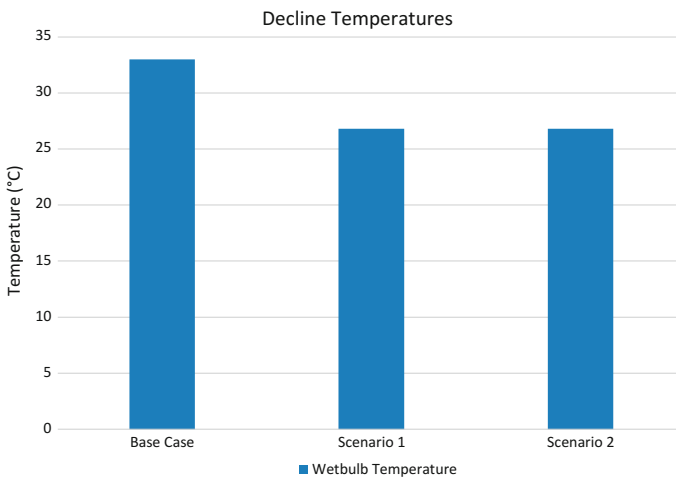


**Fig. 7.** Decline temperature for different scenarios [at reference position]

## 5  Reconditioning Systems

The filtering of dust in underground mines, for recirculation has been considered for many decades and there are numerous papers that detail the theoretical possibilities of the different types of filtration technology and this is only briefly discussed here. There are a number of technologies that could be considered for the bulk filtration of mine exhaust air to capture particulate matter including cyclones, electrostatic precipitators, media filters and wet scrubbers.
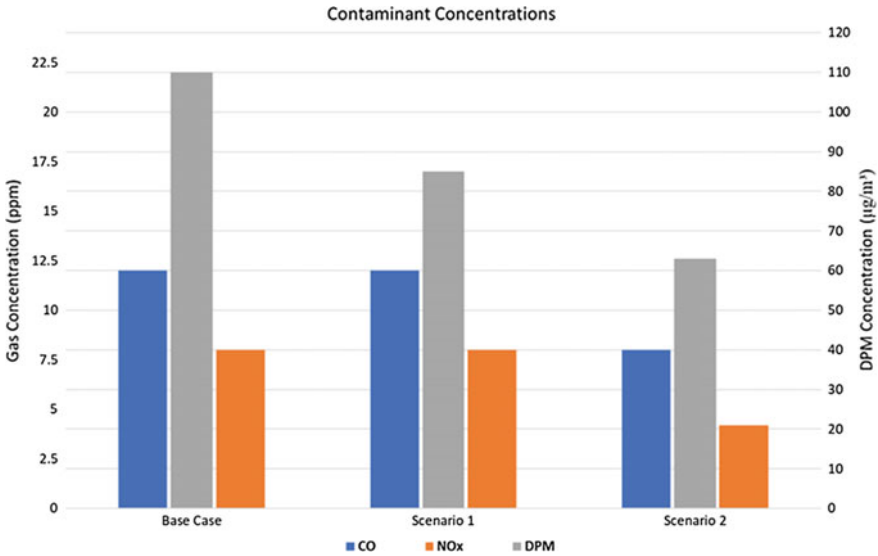
**Fig. 8.** Contaminant concentrations for different scenarios [at reference position]



Conventional cooling spray nozzles        Atomised scrubbing spray nozzles
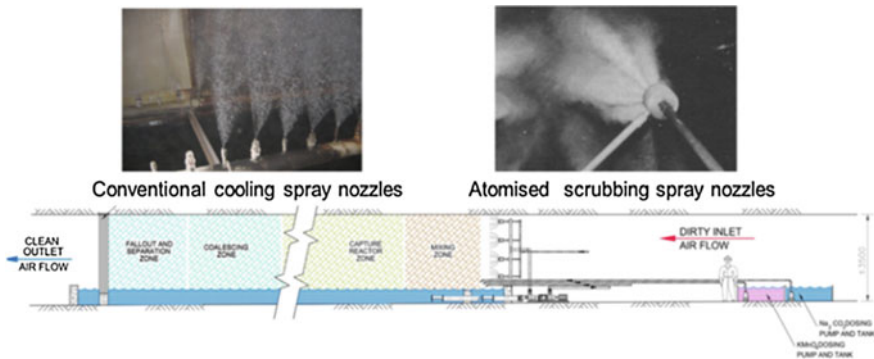
**Fig. 9.** Conceptual layout of spray chamber and scrubber system

Cyclones use inertial forces to separate particulates from the air stream and they are not effective for the smaller particulates. The increased awareness of the harmful nature of ultrafine particles specifically nano-diesel particulates and the inability of cyclones to deal with these means cyclones have limited application. Furthermore, cyclone systems will not be practical for the large bulk air flow rates being considered for recirculation and re-use schemes.

Electrostatic precipitators remove particles from the air using the forces of an induced electrostatic charge. They are highly efficient filtration devices that have a minimal pressure drop and can easily remove fine particulate matter such as dust and smoke from the air stream. However, these systems are very expensive and would require large underground excavations and would use significant power. Again, this

approach will not be practical for the large bulk airflow rates being considered for recirculation and re-use schemes.

Media filters rely on the filters media to collect particles on its surface. The filtered product builds up on the surface and this is then regularly discharged [often with reverse pulse air systems].

Wet scrubbers are low energy scrubbers as they have less pressure loss compared to the other systems. These scrubbers can typically be simple spray chambers or spray towers with or without some form of packing. Due to the low pressure losses this is the most suited technology for controlled recirculation. Wet scrubbers are effective at capturing dust particles and when combined with chilled water also serve to cool the air. These types of hybrid scrubber and cooling systems have been used to recondition air from crusher systems [4].

Bluhm et al. [7], describes the opportunities to enhance wet scrubbers, with ultra-fine water particles and oxidizing chemistry, allowing them to deal with contaminants that are challenging to remove from the air. These include but are not limited to NOx, DPM, respirable dust and even CO to some extent. The inability to scrub these contaminants is often seen as a hurdle to implementing controlled recirculation with bulk re-conditioning. However, it is believed that, through research and development these issues can be addressed. Bluhm et al. [7], suggests examples of how the use of a chemical solution of sodium carbonate, potassium permanganate, ozone and water can be used in scrubbers to enhance oxidation. This paper suggests that contaminants can be effectively removed by a system (see concept in Fig. 8) that incorporates the following features:

- Large direct contact surface area between contaminated air and a chemical/water mix using atomizing nozzles.
- Addition of a strong oxidizing agent to the chemical/water solution.
- Addition of a neutralizing agent to the chemical/water solution.

## 6  Managing Risk

The principal risk that needs to be managed in a controlled recirculation system [or indeed any re-use system] is flammable gas and blast fume clearance. Both these risks can be managed by implementing effective engineering controls. In the case of blast fume clearance, a controlled recirculation system can be shut down prior to blasting commencing and re-started after sufficient time has lapsed for fumes to clear. The use of self-close doors on recirculation fans and automated louvres with safety interlocks can be configured to ensure no recirculation occurs during the period the system is shut down. With satellite ore body applications, both systems can be connected to return using automated louvres. Prior to blasting, louvres could be set to ensure that both ore bodies exhaust directly to return after blasting.

In terms of flammable gas, the risk in mechanized hard rock mines is much lower compared to coal mines. Nevertheless, there is always a risk of flammable gas from strata being encountered. In both the recirculation and re-use scenarios, this can be managed by flammable gas monitoring with interlocks to shut down the system and alarms.

Another issue is exposure to respirable silica dust. The reconditioning system must be specifically and effectively designed to capture respirable dust. This risk needs to be reviewed and assessed in each case but fortunately dust particles are one of the easier contaminants to scrub.

DPM, similarly to the respirable silica dust will require a scrubbing system that effectively captures the respirable fraction. The modeling however indicates that even without capturing DPM, recirculation can yield better conditions by increasing airflow to areas that carry diesel equipment. The additional air assists with the dilution in areas that may have low flows without a recirculation system. Future advances in DPM filter technology and the ability to capture particulates at the source [diesel engine] could negate this issue. Real time monitoring to manage the DPM load in the recirculated air which triggers system flushing when levels exceed pre-set levels can perhaps be considered to manage the risk. The ideal would however be a system that is able to effectively captures these particulates at source.

## 7   Ventilation on Demand [VoD]

Controlled recirculation or re-use strategies with reconditioning could be considered the ultimate VoD strategy. Such a system could react to the mining activity and contaminant levels on a real-time basis by adjusting the percentage of air recirculated/re-used and controlling the process parameters of the reconditioning system.

Combined with real-time underground environment monitoring, this system can therefore be adjusted to ensure that environment levels are maintained within acceptable limits. By doing this, a controlled recirculation/re-use system with reconditioning fully integrated into a VoD strategy has the potential to significantly reduce ventilation power demand and associated costs. Bluhm et al. [7], estimated that power savings for a deep mine recirculating around 30% globally could be huge, based on case studies conducted as a part of the DeepMine research programme in South Africa.

## 8   Enabling Technology

There are a number of emerging enabling technologies that could facilitate the adoption of controlled recirculation or re-use with reconditioning. These include:

- Automation
- DPM filters
- Electrical equipment

### 8.1   Automation

Mines are increasingly looking towards automation and, as a result, communications as well as control systems underground are continuously improving. Furthermore, VoD systems including underground environment monitoring and automated louvres are also being adopted. Access to these technologies becomes an enabler for the proposed

controlled recirculation/re-use systems. These technologies allow effective control of these systems and monitoring of the environment to manage the risk.

## 8.2 DPM Filters

As noted earlier, the ability to filter DPM contaminates effectively in bulk air is yet to be proven. However, advances in DPM technology and a transition to stricter diesel engine emission standards such as Tier 4 or Euro V engines could reduce the levels of DPM from machines. In these cases, the need to have highly efficient DPM filtration of bulk air may not be a constraint.

## 8.3 Electrical Equipment

Although it is argued that the need for ventilation is reduced through the implementation of electrical equipment this is only partially true. Although electrical equipment reduces the amount of diesel contaminants, other contaminants such as dust, blast fumes and more importantly heat [including heat from the electrical equipment] remains a factor in deep mines. It is also a reality that mine ventilation rates are dependent on mining activity and not necessarily just the equipment fleet [diesel or electrical]. Therefore, increased demand from mining activity would still warrant consideration of controlled re-circulation or re-use strategies. The benefit of having a predominantly electric fleet is that diesel exhaust gas and DPM concentrations will be much lower to start with and the need to scrub these contaminants becomes less important. Mines with predominantly electrical equipment and no major silica dust or flammable gas can more readily implement controlled recirculation. The reconditioning system will primarily have to scrub dust and cool the air. This can be readily done using existing spray chamber technology described previously.

## 9 Immediate Applications

Mines with predominately electrical equipment, no respirable dust or silica dust, no flammable gas or radon present would be able to almost immediately follow a strategy with controlled recirculation or re-use. Even mines with diesel equipment that do not have some of the other critical contaminants listed previously, can give serious consideration to controlled recirculation and re-use. Mines that supply sufficient overall airflow to meet diesel dilution criteria would have environment conditions that are well below exposure limits in terms of diesel exhaust pollutants. For example, in mines where airflow is determined by high levels of mining activity rather than diesel dilution, there will generally be more air provided than is needed for diesel dilution only. In these mines, and subject to detailed risk assessment that address blasting and possible emergency events as well as confirming actual contaminant levels underground, may be in a position to implement controlled recirculation and re-use. Indeed, a number of mechanized mines already employ significant re-use factors albeit without reconditioning.

## 10   Case for R + D

The biggest resistance to controlled recirculation relates to the management of critical airborne contaminants. It is suggested that there is a strong case for R + D investment and efforts to be directed into scrubber technology that can better manage these specific contaminants.

The concept of controlled recirculation/re-use with reconditioning is not new. As noted, a number of papers have been written and 'research' has been undertaken over many decades. However, the mining industry has been slow to apply these approaches and invest in R + D to improve scrubber efficiency, prove successful scrubbing of gasses and address the issue of scrubbing diesel particulate matter.

Recent consulting work undertaken by the authors suggest that a primary ventilation upgrade for a deep mine in Australia could cost between AUD$60 million and AUD$90 million. Of this, the cost of the associated surface, underground raises and development of intake and return systems can be up to 40%. Such an upgrade would typically increase overall mine airflow by about 250 m$^3$/s.

In contrast, a basic underground spray chamber and refrigeration system capable of cooling air from 28 to 20 wb and scrubbing dust from the same amount of air underground would be about AUD$20 million and AUD$30 million. This is significantly less than a complete primary upgrade and, although the scrubbing capability needs proving, there is a compelling business case for this approach. Therefore, the authors would urge that there is a very good motivation for R + D investment and effort to be directed towards refining the required bulk scrubbing systems.

## 11   Conclusion

As mechanized mines with trucking fleets deepen, the number of trucks increase and associated diesel exhaust and heat load on the decline also increases. These mines also often experience reduced airflow and even flow stagnation along their declines due to leakage in the upper section of the mines. This leads to localized hot zones and areas of high contaminant concentrations. An effective recirculation strategy with reconditioning technology that effectively captures contaminants could have a huge effect on mine viability. Similarly, a reconditioning system could be used to allow series ventilation related to secondary ore bodies. When considering the significant cost of primary ventilation upgrades it is argued that there is a strong motivation for R + D into supporting scrubber technology.

## References

1. Burton, R.C.: Controlled Recirculation of Mine Ventilation Air, Chamber of Mines Research Organization research report No. 53/84, South Africa (1984)
2. Marks, J.R., Shaffner, L.M.: Controlled recirculation at the Homestake gold mine. In: Proceedings 4th US Mine Ventilation Symposium, Berkeley (1989)

3. Robinson, R., Harrison, T.: Controlled Recirculation of Air at Wearmouth Colliery. The Mining Engineer, England (1987)
4. van den Berg, L., Marx, W., Bezuidenhout, M., Botha, P., Meredith, G.: Refrigeration and cooling system design—a case study. In: Proceedings 6th International Seminar on Deep and High Stress Mining, Perth (2012)
5. Bluhm, S., Funnell, R., de Oliveira, L.: Controlled recirculation and refrigeration at Vale's Taquari Potash Mine. In: The Australian Mine Ventilation Conference, Adelaide (2013)
6. Derrington, A.S.: A critique of the push-pull hybrid ventilation system. In: The Australian Mine Ventilation Conference, Adelaide (2013)
7. Bluhm, S., Funnel, R.: Controlled recirculation of ventilation—why is this not applied more often to save energy? In: 10th International Mine Ventilation Congress, IMVC (2014)

# Research on Ventilation Layout in Jet-Flow Gallery Ventilation System in a Twin-Tunnel Construction

Liu Rong[1,2], Wang Liang[1,2(✉)], Ren Song[1,2], and Zhang Zhen[1,2]

[1] State Key Laboratory for the Coal Mine Disaster Dynamics and Controls, Chongqing University, Chongqing 400044, China
lw38c@cqu.edu.cn

[2] College of Source and Environmental Sciences, Chongqing University, Chongqing 400044, China

**Abstract.** The emergence of the jet-flow gallery ventilation system partially solves the ventilation problem during the construction period of a long tunnel. When employing this system, if ventilation arrangement is unreasonable, contaminated air reversal will likely to occur, which will lead to a hazardous environment in the working area of the tunnel. In this paper, based on numerical simulation research, the velocity distribution in the tunnel was investigated. The distance between the main ventilator and the transverse gallery, velocity in tunnel face, velocity in circulating are studied. Through the research, it has been found that as the distance between the main ventilator and the transverse gallery increases, the velocity in circulating is enhanced, and the velocity in tunnel face decreases, as the reverse flow of the contaminated air will be controlled.

**Keywords:** Jet-Flow gallery ventilation · Reverse flow · Flow velocity

## 1 Introduction

Due to China's rapid economical growth, there also have been corresponding expansion in infrastructure development such as highways, high-speed railroad and many subsurface projects (for example, shopping malls), highways and railroad projects led to the development of thousands miles of tunnels,[1] all of these tunnels must be properly ventilated. Many of these tunnels are getting longer with increased cross-sectional areas and complexity, adding to the challenge and cost of ventilation. Jet-flow gallery ventilation [1] are one of the systems tried in the field, they appeared to provide positive solutions, but also have new challenges.

Fang et al. [1] uses FLUENT to model the diffusion characteristics of toxic and harmful gases in gallery ventilation, and found that this method tends to eliminate "dead zone". Wang [2, 3] simulated TBM construction ventilation using k–e model in

---

[1] Statistics show that by the end of 2016, a total of 15,181 highway tunnels had been put into operation in China with a total length of 14,040 km. Among them, 815 tunnels were longer than 3 km (with a total of 3662.7 km in total length), and 3520 tunnels were 1–3 km in length (6045.5 km in total length) [12].

long diversion tunnels. Toraño [4] studied dust behavior in two auxiliary ventilation systems by Computational Fluid Dynamics (CFD) models. Sasmit [5] uses the commercially available CFD software to analyze air velocity field and methane concentration in different ventilation systems. Li [6] uses CFD software to calculate whether a velocity of 0.15 m/s is suitable for large section tunnels. There are also many scholars studied how to properly ventilate during tunnel operation [7, 8]. Fana [9] focused on smoke backflow of natural ventilation, and explained smoke bifurcation. Zhao [10] searched for smoke movement in the metro tunnel with FDS, and established two models to study critical ventilation velocity. Besides, Cascetta [11] also analyzed smoke pattern of thermal plume behavior using a reduced scale model of a road tunnel.

The success for a jet-flow gallery ventilation system depends on ventilation efficiency and the cost of the system. If the distance between the main ventilator and the transverse gallery is too long, airway resistance will increase as a result and an corresponding increase the cost both in duct material and energy. However, too short a distance will result in contaminated air being re-introduced into the main flow, and subsequently allow the contaminated air to be sent into the tunnel face again by the main ventilator. The purpose of this paper is to study the effect of main ventilator location, airflow velocity, and velocity in the development face area on ventilation efficiency when jet-flow gallery ventilation is used during construction.

## 2 Numerical Modeling and Calculation

The focus of this study is the airflow behavior between the tunnel face and transverse gallery. The model mainly focused two areas near the transverse gallery and near the construction face. The tunnel section is a three-centered arch with a width of 15.32 m and a height of 7.55 m. Due to the constant changing in positions of the main ventilator in the tunnel, overall length of the model will also vary (with lengths of 100, 120, and 150 m). The models are described in detail as follows: The outlet of the air duct is 15 m away from the face, and the distance between the left tunnel and right tunnel is 30 m. The angle between the transverse gallery and the tunnel is 60°, and the diameter of the duct is 1.8 m. The tunnel model is shown in Figs. 1 and 2.

In order to obtain the impact of the distance between the main ventilator and the transverse gallery, velocity in tunnel face, velocity in circulating on the layout of the ventilation, various scenarios were studied, are shown in Table 1.

## 3 Results and Discussion

In order to better observe the velocity vector of the airflow-in tunnel, three survey lines are arranged in the airflow in tunnel. The line positions are located in the center, the left and right side of the tunnel. The height of the line is the same as the height of the duct. Location of the three lines is shown in Fig. 3.
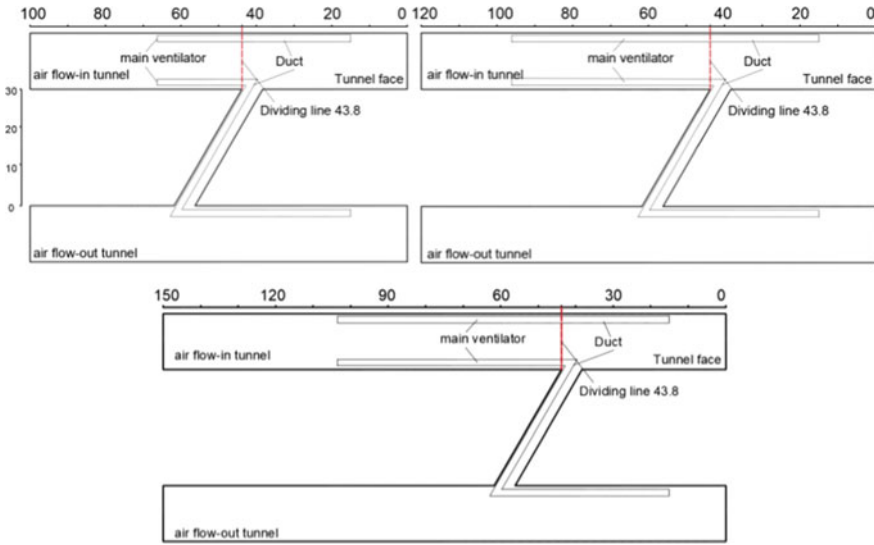
**Fig. 1.** Model floor plan (top view)
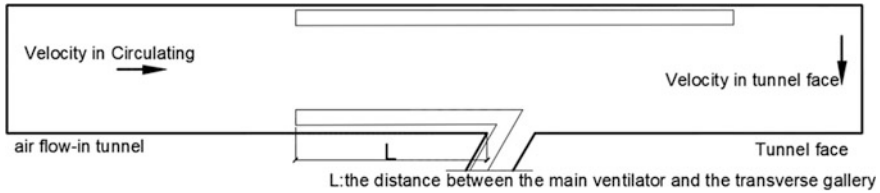


**Fig. 2.** Flow variables in the tunnel (top view)

## 3.1   Comparison on Different Velocities in Circulating Airflow

To investigate whether there is contaminated air entering the main ventilator, we need to observe whether reverse flow present from the fan to the transverse gallery. The velocity spectrums of the three lines are shown in Fig. 4.

From the Fig. 4a, it can be seen that the three lines show a abruptly change at 66.2 m where the main ventilator being installed. When the velocity in circulating is 2.0 m/s, although there is no reverse velocity, the velocity at the main ventilator is basically reduced to 0 m/s. It is a critical state for the occurrence of the reverse flow. When the velocity reaches 3 m/s, there is no reverse velocity in the range of 43.8–80 m. The velocity near the main ventilator reduced because a large amount of fresh air was sucked by the main ventilator and delivered to the face. The difference between Fig. b, c and a is velocity in tunnel face. This leads to different critical velocity. It can be seen that the critical velocity has increased with the increase of the velocity in tunnel face. Because the velocity in tunnel face represents the volume of the main ventilator.

**Table 1.** Calculation parameters

| Main ventilator position | Calculation number | Velocity in tunnel face (m/s) | | Velocity in circulating (m/s) | | | |
|---|---|---|---|---|---|---|---|
| | | Left | Right | | | | |
| 1.5 times of the tunnel diameter | 1.5-NS1 | 0.5 | 0.5 | 1.0 | 1.5 | 2.0 | 3.0 |
| | 1.5-NS2 | 1.0 | 1.0 | 1.5 | 2.0 | 3.0 | 4.0 |
| | 1.5-NS3 | 1.5 | 1.5 | 2.0 | 3.0 | 4.0 | 5.0 |
| 2.0 times of the tunnel diameter | 2.0-NS1 | 0.5 | 0.5 | 1.0 | 1.5 | 2.0 | 3.0 |
| | 2.0-NS2 | 1.0 | 1.0 | 1.5 | 2.0 | 3.0 | 4.0 |
| | 2.0-NS3 | 1.5 | 1.5 | 2.0 | 3.0 | 4.0 | 5.0 |
| 2.5 times of the tunnel diameter | 2.5-NS1 | 0.5 | 0.5 | 1.0 | 1.5 | 2.0 | 3.0 |
| | 2.5-NS2 | 1.0 | 1.0 | 1.5 | 2.0 | 3.0 | 4.0 |
| | 2.5-NS3 | 1.5 | 1.5 | 2.0 | 3.0 | 4.0 | 5.0 |
| 3.0 times of the tunnel diameter | 3.0-NS1 | 0.5 | 0.5 | 1.0 | 1.5 | 2.0 | 3.0 |
| | 3.0-NS2 | 1.0 | 1.0 | 1.5 | 2.0 | 3.0 | 4.0 |
| | 3.0-NS3 | 1.5 | 1.5 | 2.0 | 3.0 | 4.0 | 5.0 |
| 3.5 times of the tunnel diameter | 3.5-NS1 | 0.5 | 0.5 | 1.0 | 1.5 | 2.0 | 3.0 |
| | 3.5-NS2 | 1.0 | 1.0 | 1.5 | 2.0 | 3.0 | 4.0 |
| | 3.5-NS3 | 1.5 | 1.5 | 2.0 | 3.0 | 4.0 | 5.0 |
| 4.0 times of the tunnel diameter | 4.0-NS1 | 0.5 | 0.5 | 1.0 | 1.5 | 2.0 | 3.0 |
| | 4.0-NS2 | 1.0 | 1.0 | 1.5 | 2.0 | 3.0 | 4.0 |
| | 4.0-NS3 | 1.5 | 1.5 | 2.0 | 3.0 | 4.0 | 5.0 |

*Note* 3.0NS1-3.0 means that the distance from the main ventilator to the transverse gallery is 3 times the tunnel diameter, the velocity in tunnel face is 0.5 m/s, and the velocity in circulating is 3.0 m/s
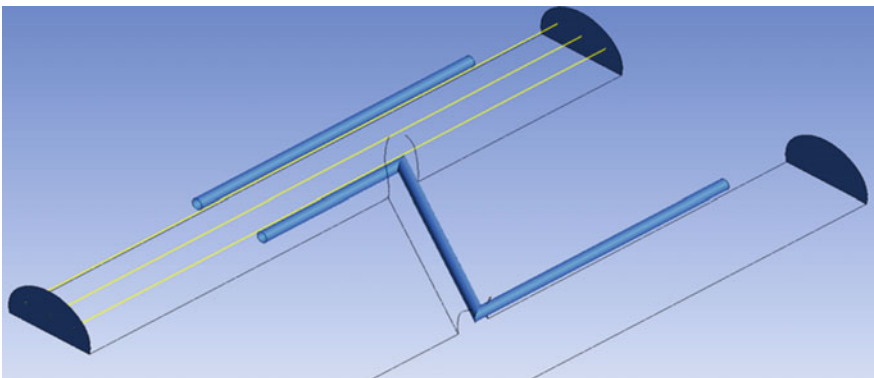


**Fig. 3.** The location of three lines
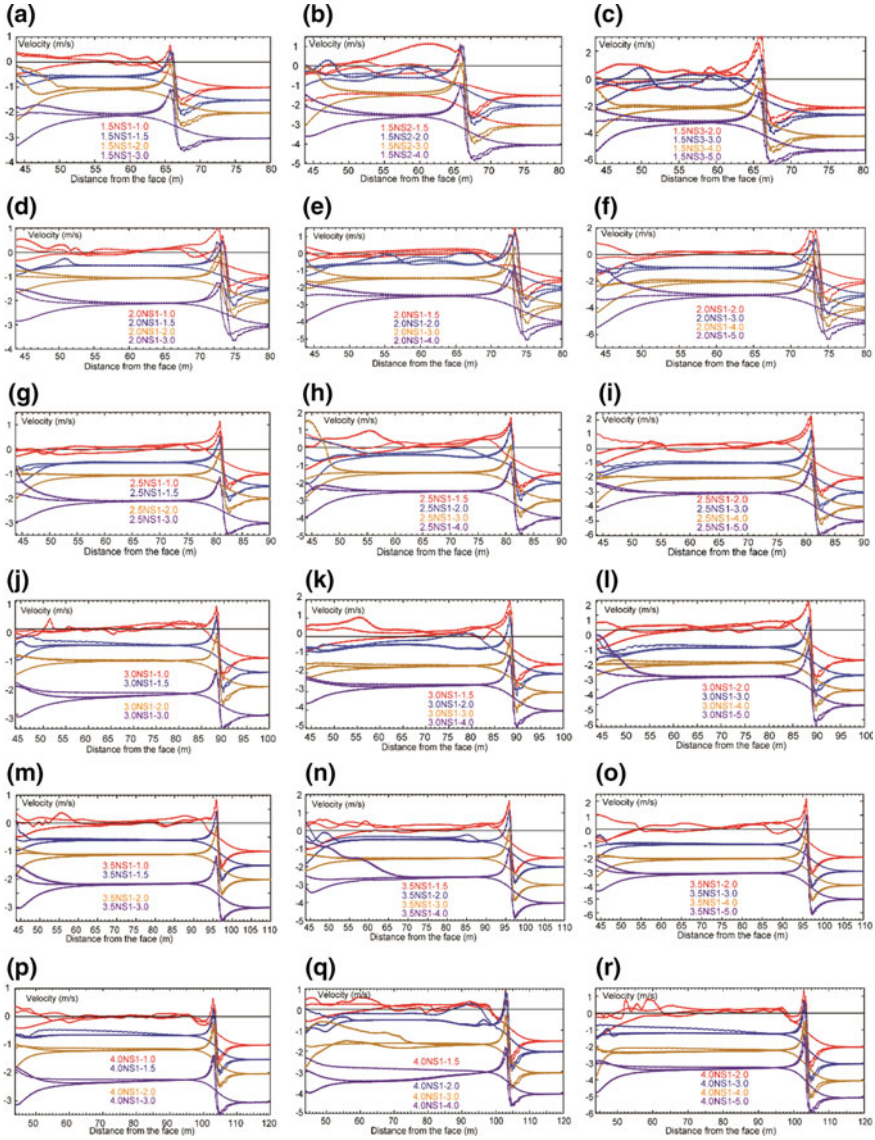
**Fig. 4.** Velocity curve of survey lines

By comparing the calculation results, no matter where the main ventilator is located, trends of the critical velocity change are similar. If the air volume in circulation can satisfy the sum of the suction volumes of the two main ventilators, there will be no reverse velocity. And if the remaining air quantity in the tunnel can meet the minimum velocity requirement, the working area will not be contaminated.

## 3.2   Comparison of Different Main Ventilator Locations

When the velocity around the tunnel face and in circulation are identical, comparison study was conducted using the velocity curves when the main ventilator is assigned to different positions. As can be shown in Fig. 5, as the distance between the main ventilator and the transverse gallery increases, the minimum velocity is increased. The minimum velocity increases means that the probability of the reverse airflow is reduced. Therefore, it can be concluded that as the distance increases, the possibility of reverse wind of the contaminated air gradually decreases.

## 3.3   Comparison of Different Velocities in Tunnel Face

As can be seen from the Fig. 6, with the increase of the velocity in tunnel face, the probability of reverse contaminated air will increase until the backflow occurs.
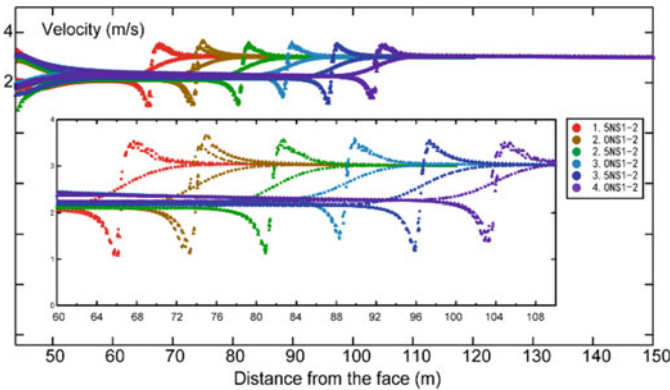


**Fig. 5.**   Comparison of different ventilator positions
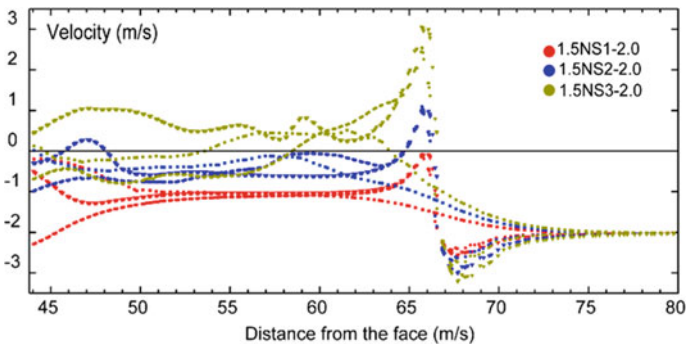


**Fig. 6.**   The impact of tunnel face flow velocity on reverse flow

## 4    Conclusions

Through the numerical study, it was found that there are three control factors for the presence of reverse flow for a tunnel construction period ventilation layout. (1) the distance between the main ventilator and the transverse gallery, (2) velocity in tunnel face, and (3) velocity in circulation. After comparison study, the following conclusions can be drawn: as the distance between the main ventilator and the transverse gallery increases, the velocity in circulating increases, and when the velocity in tunnel face decreases, the reverse flow of the contaminated air will decrease.

## References

1. Fang, Y., Fan, J., Kenneally, B., et al.: Airflow behavior and gas dispersion in the recirculation ventilation system of a twin-tunnel construction. Tunneling Undergr. Space Technol. **58**, 30–39 (2016)
2. Wang, X., Zhang, Z., Zhou, Z., et al.: Numerical simulation of TBM construction ventilation in a long diversion tunnel. Tunneling Undergr. Space Technol. **26**, 560–572 (2011)
3. Liu, Z., Wang, X., Cheng, Z., et al.: Simulation of construction ventilation in deep diversion tunnels. Comput. Fluids **105**, 28–38 (2014)
4. Toraño, J., et al.: Auxiliary ventilation in mining roadways driven with roadheaders: validated CFD modeling of dust behavior. Tunneling Undergr. Space Technol. **26**(1), 201–210 (2011)
5. Sasmito, A.P., et al.: Some approaches to improve ventilation system in underground coal mines environment-A computational fluid dynamic study. Tunneling Undergr. Space Technol. **34**, 82–95 (2013)
6. Li, M., Aminossadati, S.M., Chao, W.: Numerical simulation of air ventilation in super-large underground developments. Tunneling Undergr. Space Technol. **52**, 38–43 (2016)
7. Du, T., et al.: A method for design of smoke control of urban traffic link tunnel (UTLT) using longitudinal ventilation. Tunneling Undergr. Space Technol. **48**, 35–42 (2015)
8. Weng, M.-C., et al.: Study on the critical velocity in a sloping tunnel fire under longitudinal ventilation. Appl. Therm. Eng. **94**, 422–434 (2016)
9. Fan, C.G., Ji, J., Wang, W., et al.: Effects of vertical shaft arrangement on natural ventilation performance during tunnel fires Int. J. Heat Mass Transf. 158–169 (2014)
10. Zhao, S., Liu, F., Wang, F., et al.: A numerical study on smoke movement in a metro tunnel with a non-axisymmetric cross-section. Tunneling Undergr. Space Technol. **73**, 187–202 (2018)
11. Cascetta, F., Musto, M., Rotondo, G.: Innovative experimental reduced scale model of road tunnel equipped with realistic longitudinal ventilation system. Tunneling Undergr. Space Technol. **52**, 85–98 (2016)
12. Zhao, Y., Li, P.: A statistical analysis of China's traffic tunnel development data. Engineering **3**, 3–5 (2018)

# Influence of the Ratio of the Blowing and Sucking Flow on the Wall-Rotating Circulating Airflow in Fully Mechanized Excavation Face

Rong-hua Liu[1,2(✉)], Yong-jun Li[1], Peng-fei Wang[1,2], Wei Shu[1], and Shang-xu Gou[1]

[1] School of Resource, Environment and Safety Engineering, Hunan University of Science and Technology, Xiangtan 411201, Hunan, People's Republic of China
15273285186@163.com

[2] Work Safety Key Lab on Prevention and Control of Gas and Roof Disasters for Southern Coal Mines, Hunan University of Science and Technology, Xiangtan 411201, Hunan, People's Republic of China

**Abstract.** This paper is to examine the influence of the ratio of blowing and exhausting flow on the wall-rotating circulating airflow in a fully mechanized excavation face using Fluent under different arrangement. The results show that the wall-rotating circulating airflow can effectively control dust diffusion in a fully mechanized working face, improve dust scrubber performance to reduce dust concentration at the driver and the rear of the tunnel. When the ratio is less than 0.9, the wall-blown airflow can control the dust-bearing airflow well up to 5 m from the working face, preventing dust from spreading to the driver's area and its rear roadway, and the dust control performance is the best when this ratio is at 0.8.

**Keywords:** Fully mechanized excavation face · Coanda cyclone ventilation Ratio of blowing and sucking flow · Numerical simulation

## 1 Introduction

At present, the dust concentration of many coal mines is exceeding the standard, which seriously endangering the health of the workers in the underground work [1–3]. In order to reduce the dust concentration in the fully mechanized working face, some mines use the wall circulation wind mode, and use the dust blower to purify the dust-containing airflow to the rear-row roadway, and obtain good dustproof effect. In order to evaluate the working environment and ventilation effect of the fully mechanized face under the action of the wall-rotating wind, to improve the ventilation efficiency and optimize the ventilation parameters, it is necessary to study the wind speed distribution and the dust concentration distribution in the fully mechanized excavation face [4]. In this paper, the numerical simulation of fully mechanized digging roadway

with CFD is carried out to analyze the characteristics of wind flow and the movement of dust under the condition of different blowing-suction flow ratio.

## 2   Physical Model and Boundary Conditions

### 2.1   Physical Model

According to the site investigation, a rectangular roadway with a length of 30 m, a width of 4.5 m and a height of 3.2 m was established, the outlet of the pressure air cylinder is 5 m from the end of the working face, the diameter of the blower is 800 mm, and the central axis of the blower is 2.7 m high from the ground. The second half of the press-in hair dryer is an accessory hair dryer. The accessory hair dryer is provided with a radial slit air outlet of length 1.6 m and a width of 0.03 m at 5 m each, a total of three outlet air outlets. The diameter of the suction tube is 800 mm, the center of the front suction outlet is 1.6 m from the ground and 3 m from the driving head, which is located on the body of the boring machine; the transport belt is located under the suction tube and is the transport belt transfer point at 15 m from the heading head. The model sets 0.6, 0.7, 0.8, 0.9, 1.0, 1.2 total of six sets of blowing and suction flow ratio, in the simulation, the exhaust volume is set to 250 m$^3$/min unchanged, and the blowing rate is changed by changing the pressure air volume. In the coordinate system x is the roadway width direction, y is the height direction, z is the roadway heading direction, as shown in Fig. 1.
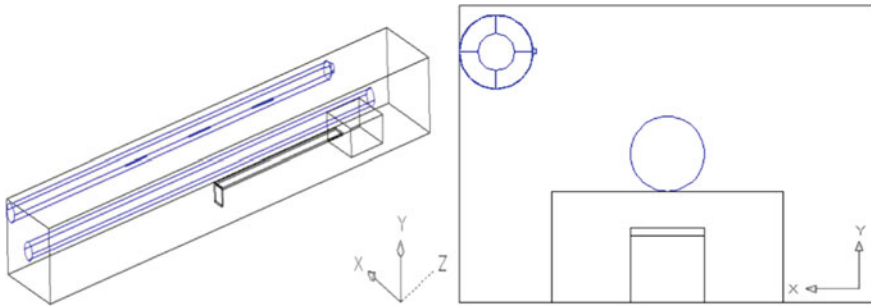


**Fig. 1.**  Physical model of Coanda swirling ventilation

The model adopts the Coanda swirling pressure pumping mixed ventilation, and the fresh air enters the roadway from the end outlet and the strip gap through the pressure air tube respectively, after the dust is diluted through the face of the head, one part of the dust-bearing airflow is drawn from the suction tube, and the other part of the dust air from the suction tube and the tunnel between the discharge, as shown in Fig. 2.

By using gambit, the mesh of the model is divided into the grid, the interval size of the mesh is 1.5 and divided into the grid, as shown in Fig. 3.
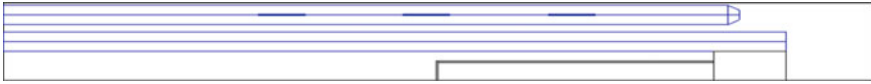
**Fig. 2.** The main view of the wall-rotating circulation wind in fully mechanized excavation face
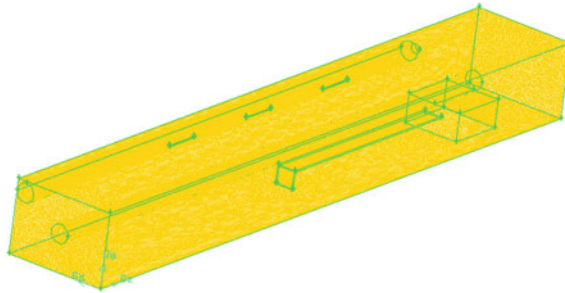


**Fig. 3.** Physical model grid division

## 2.2 Boundary Conditions

The physical model in gambit is imported into fluent, and the boundary conditions and particle source parameters are set, the specific conditions are shown in Table 1.

**Table 1.** Boundary condition and particle source parameter setting

| Project | Parameters | Setting |
|---|---|---|
| Title (centered) | Entrance boundary | Velocity inlet |
| | Export boundary | Outflow |
| | Hydraulic diameter | 0.80 m |
| | Turbulent intensity | 3.22% |
| | Wall motion | Stationary wall |
| Particle source | Injection type | Surface |
| | Material | High volatile coal |
| | Diameter distribution | Rosin-Rammler |
| | Min. diameter | 1 μm |
| | Mean diameter | 12.5 μm |
| | Max. diameter | 60 μm |
| | Spread parameter | 1.77 |
| | Total flow rate | 1.5 g/s |

## 3   Mathematical Background

A discrete phase model based on Euler-Lagrangian method is used to study the airflow characteristics and dust concentration distribution in the roadway, in which the dust particles are discrete phase and the air is continuous phase [5–8]. This paper assumes that the airflow is incompressible and steady fluid and ignores heat transfer, on the basis of this, we adopt two-path model, the gas phase control equation is as follows [5–7]:

Continuity equation:

$$\frac{\partial u_i}{\partial x_i} = 0 \tag{1}$$

Equation of the momentum:

$$\frac{\partial}{\partial x_j}\left(\rho u_i u_j\right) = -\frac{\partial p}{\partial x_i} + \frac{\partial \tau_{ij}}{\partial x_j} + \rho g_i \tag{2}$$

Formula, $p$ is static pressure; $\partial \tau_{ij}$ is stress tensor; $g_i$ is the force of gravity in the direction of $i$.

Solid phase Control equation:

$$\frac{du_p}{dt} = F_D\left(u - u_p\right) + \frac{g\left(\rho_p - \rho\right)}{\rho_p} + F_S \tag{3}$$

Formula, $F_D$ is Mass drag force of granular unit, following forms:

$$F_D = \frac{18\mu}{\rho_p d_p^2} \cdot \frac{C_D Re_p}{24} \tag{4}$$

## 4   Numerical Simulation Results and Analysis

### 4.1   Flow Field of Airflow

Simulation results of airflow flow field under the action of wall-rotating flow wind in fully mechanized excavation face is as shown in Figs. 4 and 5.

Figure 4 is the velocity vector of the horizontal plane at the respiration belt height (y = 1.6 m) in the tunneling roadway. As you can see from Fig. 4, the smaller the suction flow ratio, the smaller the wind speed of drainage face, at this time, suction airflow dominated the exhaust, driving machine driver before the dust-bearing airflow can be effectively controlled, so that the dust generated from the driving surface from the suction outlet all sucked into the exhaust tube; with the increase of blowing capacity, the volume of hair is increasing, which leads to the air flowing out from the pressure cylinder, after the dust is swept through the face, some of them are sucked by the exhaust tube directly, there is also a part of the dust airflow spread to the rear of the
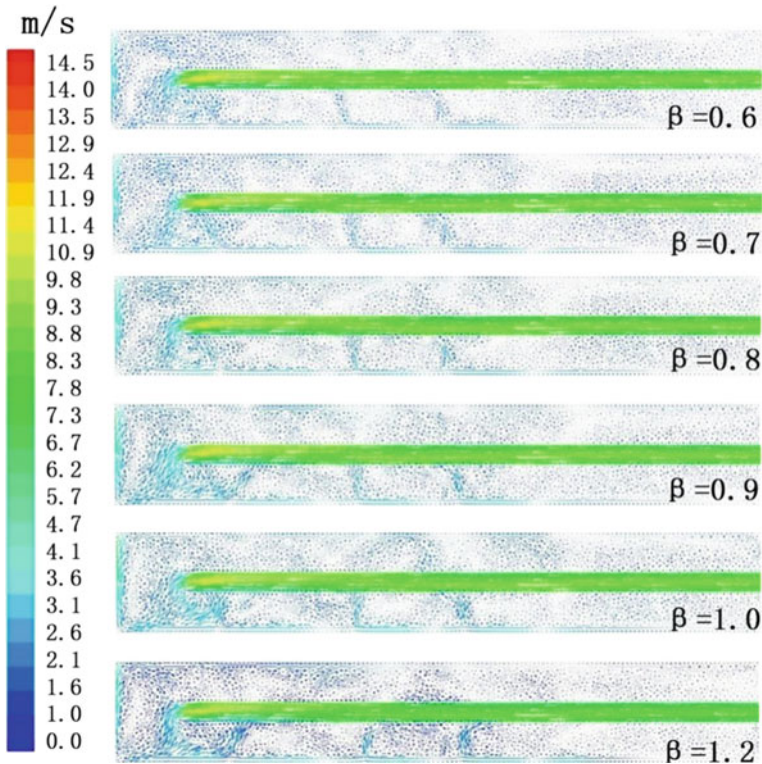
**Fig. 4.** The velocity vector distribution diagram of different blowing and sucking flow rate in y = 1.6 m section

suction outlet, into the driving machine driver work area, the tunnel appeared in the backflow. As can be seen in the figure, when the suction flow ratio is greater than 0.9, the backflow over the driver's work area into the tunnel area behind the roadheader, resulting in a drop in the suction tuyere effect.

Figure 5 is an integrated map of radial wind velocity vector which is wind speed on the x and y plane) and axial wind velocity in the cross section which is z direction of the tunneling roadway. As you can see from the picture, due to the impact of the roadheader fuselage, although the shape of the rotating wind curtain has changed in the driver of the Roadheader, a radial air curtain can still be formed in the whole tunnel section, which is combined with the fuselage of the roadheader to block the dust flow in the heading surface and prevent the dust from working face from spreading to the tunnel rear. When the suction flow ratio is less than 0.7, the radial wind speed of the section is small, the anti-jamming ability of the wind curtain is poor, and the effect of the air curtain plugging is affected. With the increase of the ratio of blowing and absorbing flow, the radial wind velocity on the section is more and more strong, and the anti-jamming ability of the air curtain is stronger and better. However, when the ratio of blowing and sucking is increased to 0.9, the direction of axial wind velocity in the
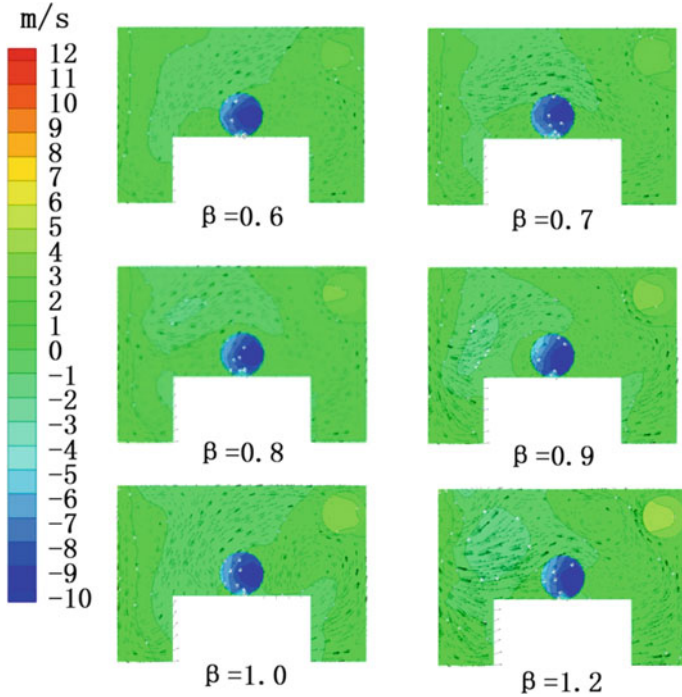
**Fig. 5.** Velocity vector and Z-direction velocity cloud of different blowing and suction flow in Z = 24.5 m section

section is changed and negative, that is, the axial wind velocity of the air flow is changed from the point heading face to the rear of the roadway. It shows that the air curtain has a loophole in the tunnel section, and the dust of the working face is diffused into the driver work area.

Combined Figs. 4 and 5 simulation results, when the suction flow ratio is around 0.8, the radial air curtain formed at the driver of the driving machine in the tunnel has strong anti-interference ability. It also ensures that the axial wind velocity of the radial air curtain is uniformly inward in the direction of the roadway, forming a complete radial wind curtain. Plugging the dust air in the working face to prevent the dust from spreading outward.

## 4.2   Dust Concentration Distribution

Figure 6 is the concentration distribution of dust in the roadway under the action of the wall-rotating flow wind in the fully mechanized working face. A numerical simulation result section of a dust concentration at a certain distance from the positive direction of x axis and z-axis of the roadway, along the x-axis positive direction is 0.2, 1.5, 2.8, 4.1, 1.5 m is the position of the driving driver; along the z-axis positive direction is 15, 18, 21, 23, 25, 26.5, 28, 29.5, 25 m is the position of the driving driver.
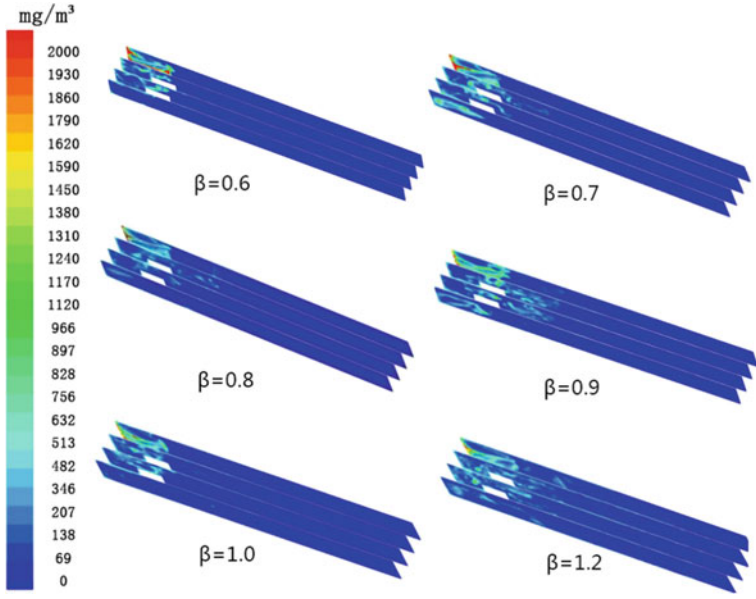
(a) x direction
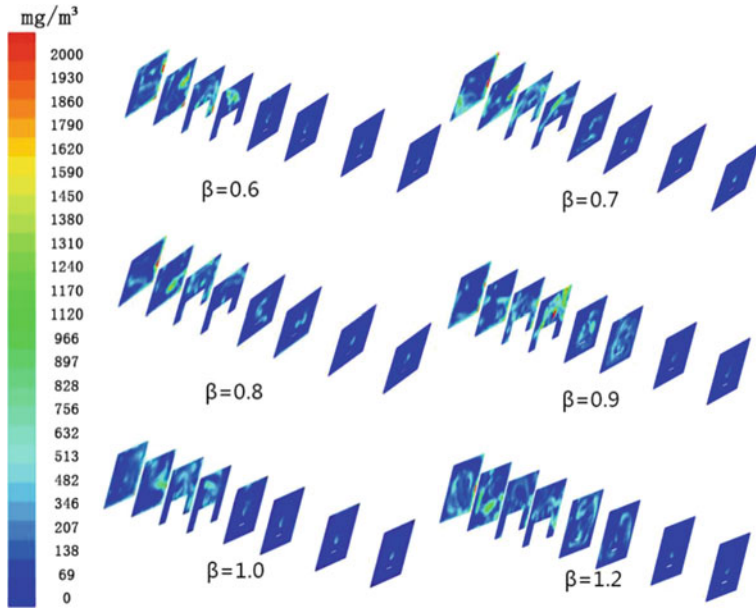


(b) z direction

**Fig. 6.** Overall change trend of dust concentration in different directions along roadway

Figure 6 shows, with the increase of airflow ratio, the general trend is that the diffusion distance of dust in roadway is getting farther and further, which shows that the efficiency of suction outlet of exhaust tube is getting lower. Especially when the suction flow ratio reaches 0.9, the dust control effect of the wind curtain drops significantly, and the dust concentration on the roadway section of the driving machine driver is increased sharply, it shows that the dust control wind curtain in front of the driver is damaged, and the dust-isolating wind curtain is broken, and with the further increase of the blowing and sucking flow ratio, the loopholes of the dust control wind curtain are more and more big, the dust control effect is worse [9, 10]. When the suction flow ratio is less than 0.7, the driver section of the dust concentration is still high, is due to the dust control wind screen radial wind speed is too small, the wind curtain's anti-interference ability is weaker, the dust of the heading face is spread to the driver working face area under the action of various disturbed airflow, which leads to the increase of dust concentration in the driver's office.

Synthesis of the above simulation results and analysis, the ratio of blowing and sucking flow is an important factor affecting the effect of the wind control of the wall spinning in fully mechanized working face, and the suction flow ratio is too large or too small, are not conducive to control the dust diffusion in the working face and improve the dust collection effect [11–13]. The results show that when the suction flow ratio is around 0.8 the wind control dust with the wall rotation in the fully mechanized working face is the best.

## 5   Conclusion

(1) In the roadway of the fully mechanized working face, the wind-blown wind curtain is formed and the dust-bearing airflow in the working face is blocked to prevent the dust from spreading outward.

(2) The suction flow ratio has a great effect on the effect of the wall-rotating air control dust. The suction flow ratio is too large, the rotating wind screen has a loophole, which reduces the effect of suction tuyere, the suction flow ratio is too small, the wind speed is too small, the anti-interference ability is weak, the dust-isolating effect is poor.

(3) When the suction flow ratio is less than 0.9, the wall-blown circulation wind can better control the dust-containing airflow in the head 5 m of the working face, and prevent the dust from spreading to the driver's working area and its rear roadway. When the suction flow ratio is around 0.8, the best dust control effect can be obtained by the wall-rotating circulation wind.

## References

1. Cheng, W.F.: Numerical simulation of fully mechanized working face of rotary air curtain suction dust control flow. J. China Coal Soc. **36**(8), 1342–1348 (2011, Aug)
2. Liu, R.F.: Study on the dust distribution law in the working face of the pressed ventilation. J. China Coal Soc. **27**(3), 233–236 (2002, June)
3. Liu, R.F.: Study on the dust distribution law in the working face of the pressed ventilation. J. China Coal Soc. **27**(3), 233–236 (2002, June)
4. Luo, W.F.: Numerical simulation of air flow characteristics and dust concentration in fully mechanized mining face. Res Min. Eng. **28**(4), 18–22 (2013, Dec)
5. Hui, F.Z.: A Self-Study Manual for FLUENT14 Flow Field Analysis. People's post and Telecommunications Press, Bei Jing (2014)
6. Junjie, F.Z.: FLUENT Engineering Technology and Example Analysis: All 2 Volumes. China Water Conservancy and Hydropower Press, Bei Jing (2013)
7. Deming, F.W.: Mine Ventilation and Safety. China University of Mining and Technology press, Xu Zhou (2007)
8. Jiang, Z.F.: Parameter optimization of long pressure short pumping ventilation system in roadways in rock roadway. Coal Sci. Technol. **43**(1), 54–58 (2015, Jan)
9. Zhang, Y.F.: The effect of the wall air duct on the ventilation and dust removal in the heading face. Saf. Coal Min. **28**(12), 161–163 (2017, Jan)
10. Liu, R.F.: A new type of cyclone air curtain air exhaust hood numerical simulation study. Environ. Eng. **27**(4), 68–72 (2009, Aug)
11. Hu, F.F.: Study on the law of dust migration in fully mechanized mining flour based on CFD numerical simulation. China Coal **38**(6), 94–98 (2012, June)
12. Wang, F.F.: Computational Fluid Dynamics Analysis. Tsinghua University Press, Beijing (2004)
13. Zhen, G.F.: Using rosin rammler distribution function to study the distribution of coal particle size. J. Taiyuan Univ. Technol. **37**(3), 317–319 (2006, May)

# Part II
# Vent System Optimization II

# Calculating Shock Losses in Mine Ventilation Networks

Mikhail Semin[(✉)] and Andrey Shalimov

Mining Institute Ural Branch Russian Academy of Sciences, 78A Sibirskaya St.,
Perm, Russia 614007
mishkasemin@gmail.com

**Abstract.** In this paper, we investigate the relative contribution of shock losses to the total pressure drop in a mine ventilation network. It is shown that for a specific class of mines it is necessary to consider the shock losses of mine airway junctions. This class includes mines with large airway cross-sectional areas and extended work areas. A comparative analysis of existing literature on methods to calculate shock losses is conducted using ventilation system with parallel airways. Existing methods are compared with the results of 3D numerical simulation of airflow through junctions. Several existing methods for shock loss calculation incorrectly assume airways being symmetrical with uniform airflow distribution of airflow in parallel airways This symmetry is physically incorrect, and asymmetric methods is identified to more accurately calculate shock losses underground.

**Keywords:** Mine ventilation · Air distribution · Shock loss · Airway junction
Airway split · Numerical simulation

## 1 Introduction

Modern mining operations with large production and quick advances result in rapid expansion and increased complication of mine ventilation system. Calculation of air distribution becomes more complicated or almost impossible without numerical modeling. Calculating mine ventilation networks are becoming increasingly important considering an increasingly complicated ventilation system.

The efficiency of computational model is determined at least by two factors:

1. Speed of the model construction.
2. Accuracy of forecasting made by the model.

The first factor assumes decrease of the total time spent on development of accurate working model using data from ventilation surveys. The second factor means stable accuracy of the model predictions when air distribution in mine is changed. Computational model of ventilation network based on one set of experimental data achieved for one ventilation mode, should give adequate forecast of air flows for other possible ventilation modes.

Usually, formulation of mine ventilation network models is based on the first and the second laws of Kirchoff. In this example, airflow distribution in mine ventilation

network can be found by solving nonlinear equations with unknown airflows and pressure drops in each mine airway [1].

Mine ventilation network including only straight airway resistances (or Atkinson resistances) may result in less accurate result when airflow distribution varied sufficiently comparing to the initial state. Mainly, it is concerned with the influence of shock losses at bends and junctions of mine airways, changes in its' cross-sectional area etc. [2, 3]. Decrease of accuracy occurs even when shock losses are considered using equivalent length approach [3]. It is concerned with sufficiently different functional relation between pressure loss and airflow in case of straight airways and in case of bends and junctions [2, 4]. Therefore, when the airflow distribution in mine is changed, there is disproportional pressure response in straight airways, in bends and junctions.

It leads to more complicated redistribution of airflows in mine ventilation network after changing the ventilation mode. These redistributed airflows and pressure losses does not satisfy the former system of equations representing the first and the second laws of Kirchoff with only Atkinson resistances determined from ventilation survey at one specified ventilation mode. One can observe it particularly during the main fan reversal [2].

## 2    Estimation of the Relative Contribution of the Shock Losses

The relative contribution of shock losses depends on airway cross-sectional areas, air velocity magnitudes, air inlet angles at junctions etc. The relative contribution of the shock losses depends on the specific features of the mine.

A simple estimation of the shock losses contribution can be made using the following criteria:

$$K = \frac{P_S}{P_S + P_A},\tag{1}$$

where $P_S$ is total pressure drop across an airflow path due to shock losses and $P_A$ is the total pressure drop across the same airflow path in straights airways (due to Atkinson resistance).

The value of the criteria (1) also depends on the specific features of the mine. It's primarily reflected in the properties of the airflow path, which is different for each specific mine. The simplest way to estimate the average properties of the airflow path is to use integral characteristics of a mine or of a district—average cross section area S and perimeter P, remoteness of work areas L, total airflow Q etc. These characteristics allow us to consider two simplified idealized districts of a mine corresponding to two commonly used ventilation layouts: (a) U-tube ventilation district and (b) through-flow ventilation district (see Fig. 1).

We assume that intake and return airways have infinite number of equally-spaced air connections with each other. Junction angle for each air connection is 90°. Resistances of air connections are determined in such a way as to divide the flow into equal
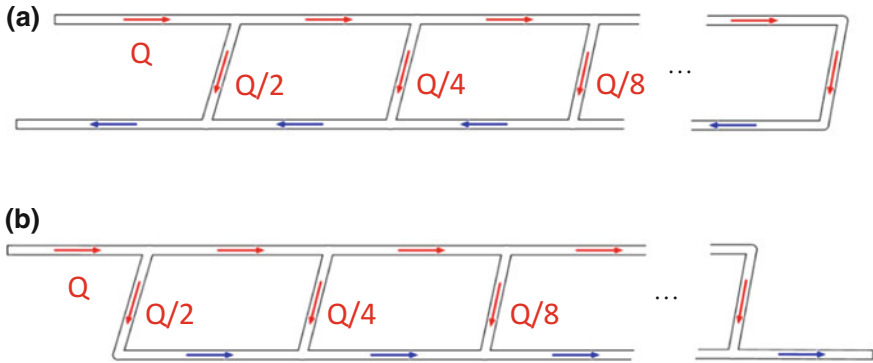
**Fig. 1.** Two simplified districts of a mine corresponding to two ventilation layouts: U-tube ventilation district (**a**) and through-flow ventilation district (**b**)

parts. The total airflow through the district is Q. The length of each airways is L. Cross-sectional area of each airways is S and cross-sectional perimeter is P.

The districts may be chosen in a variety of ways: with other proportions of the airflows in connections, other junction angles, additional parallel intake and return airways etc. But in this paper, we pay our attention to this simple case.

In this case the pressures $P_A$ and $P_S$ are determined as follows:

$$P_A = 1.64 \frac{\alpha PL}{S^3} Q^2, \tag{2}$$

$$P_S = 4.1 \frac{\rho Q^2}{S^2}. \tag{3}$$

Here $\alpha = 0.5\rho f$ is the coefficient of air resistance, kg/m$^3$; $\rho$ is air density, kg/m$^3$, f is roughness coefficient [3].

Calculation of pressure $P_A$ is based on the Darcy equation, while calculation of the shock losses $P_S$ is accomplished using empirical formula for right-angled junctions given by Mokhirev [4].

The criteria (1) takes on values from 0 to 1 and represents relative fraction of the shock losses in total pressure drop across the airflow path. Figure 2 shows isogram of the criteria in case of airways with circular cross section $P = \sqrt{4\pi S}$ and coefficient of air resistance $\alpha = 0.007$ kg/m$^3$. The value of $\alpha$ corresponds to arc wall steel lining. The zones corresponding to different types of mines are also shown in Fig. 2.

As follows from Fig. 2, there is a class of mines with sufficiently great relative fraction of shock losses (more than 20%). This class includes mines with large cross-sectional areas of airways and small remoteness of work areas. It is recommended to take into account shock losses when calculating air distribution in this class of mines.
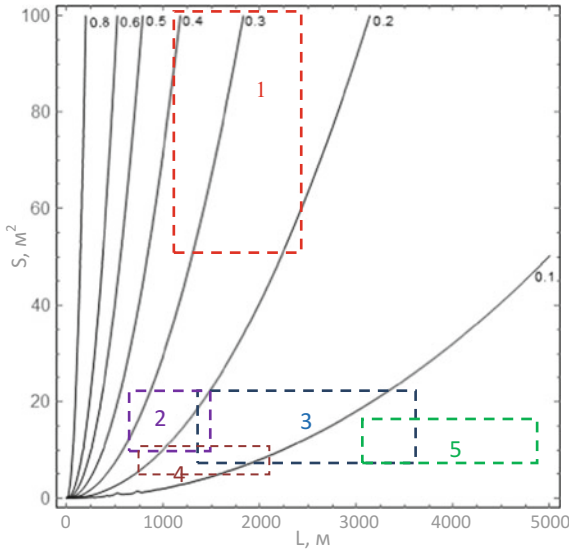
**Fig. 2.** Isogram of criteria (1), relative fraction of the shock losses from different types of mines: 1—gypsum mine of "Gypsum Knauf Novomoskovsk", 2—diamond mines of "Alrosa" company, 3—head rock mines of "Norilsk Nickel" company, 4—oil mines of "Lukoil" company, 5—potash mines of "Uralkali" and "Belaruskali" companies

## 3    Methods for Shock Loss Calculation

Nowadays, a number of methods for calculating pressure differential produced by the shock loss at junctions are described in the literature. The simplest method is the equivalent length method [3, 6]. According to it, shock losses are considered as an additional term $R_S$ in air resistance of the branch:

$$R_S = \frac{\rho X}{2S^2},\qquad(4)$$

where $X$ is empirical coefficient (shock loss factor), which depends on the type of airways junction.

According to [3], shock losses resistance $R_S$ should be assigned to the side inflow branches and to the all outflow branches. The specific value X can be determined with the help of tables and nomographs summarizing complex experimental studies [3, 5, 6].

The similar method was introduced in the seminal work on mine ventilation in the USSR [7]. The values of coefficient X are presented in case of right-angled splits and junctions of three airways. At that, shock loss resistances are recommended to include only for side branches. Thus, straight airflow has not any additional resistances. Physically it is not correct. Described methods, which are based on formula (4), give results sufficiently different from results of 3D numerical modeling and experimental study of airflow [8].

More complex approach to shock losses modeling is presented in [4, 9]. The monograph [4] contains a number of empirical functions of shock loss calculation in right-angled junctions of three airways. Additional air resistances are included both in inlet and outlet branches.

The monograph [9] presents a universal method for calculating shock losses in T-junctions in case of any angle between the branches.

Shock loss at splits:

$$P_{Si} = X \frac{\rho}{2} \left( V_i^2 - 2V_1 V_i \cos \delta_1 + V_1^2 \right) \quad i = 2, 3. \tag{5}$$

Shock loss at junctions:

$$P_{Si} = X \frac{\rho}{2} \left( V_i^2 - 2V_3 \left( \frac{Q_1}{Q_3} V_1 \cos \delta_1 + \frac{Q_2}{Q_3} V_2 \cos \delta_2 \right) + V_3^2 \right), \\ i = 1, 2. \tag{6}$$

Here X is empirical friction coefficient, which varies from 1 (smooth concrete lining) to 2 (rough walls without lining), $V_i$ is the average velocity in i-th branch, $\delta_i$ is the angle between i-th branch and horizontal axis (see Fig. 3).
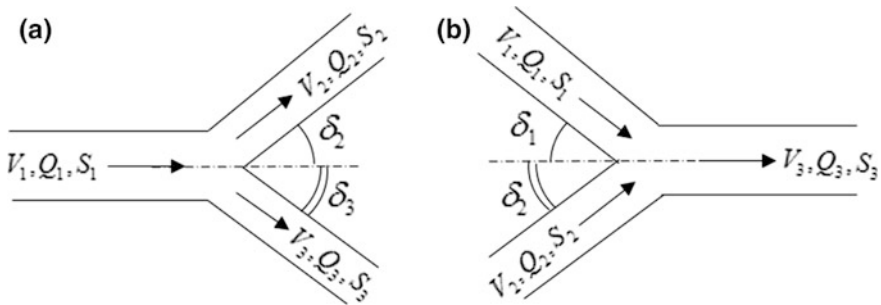


Fig. 3. T-junctions: **a** airflow split and **b** airflow junction

The above-mentioned studies are devoted to bends and junctions of maximum three branches. Study on shock loss in junctions of an arbitrary number of branches was conducted in paper [10]. An analytical formula for shock loss determination was derived as a generalization of Borda–Carnot equation.

$$P_{Si} = \sum_j \frac{Q_i Q_j}{Q_\Sigma^2} \frac{\rho (V_i - V_j)^2}{2}. \tag{7}$$

Here $Q_\Sigma$ is total airflow through the junction, index "i" is referred to the outlet branches, while index "j" is referred to the inlet branches. Number of inlet and outlet branches may be selected in an arbitrary way.

Derivation of the formula (7) assumes several simplifications:

1. Energy loss due to airflow turn is not considered.
2. Variable friction factor is not considered.
3. Pressure loss $P_{Si}$ is a part of air resistances of outlet branches, while inlet branches have no summands corresponding to the shock loss.

The influence of shock loss factor was also carefully studied in hydraulics. The handbook [11] offers a number of models and methods to calculate shock losses (or minor losses) in pipe networks. The methods for calculation shock losses are formulated in general terms and can be applied for any fluids. The friction factor, which has a great importance in mine airways, is sufficiently smaller in smooth pipes, therefore the accuracy of these methods can be low in case of rough walls without lining when blasting technique is used.

In the present paper authors attempted to combine existing methods (5)—(7) of shock loss calculation. The 1D mathematical model of airflow junction with arbitrary physical and geometry properties was formulated according to 1D conservation laws and experimental data. The following expression for shock loss was derived

$$
\begin{aligned}
P_{Sij} = {} & X \sum_s \frac{Q_s}{Q_\Sigma} \frac{\rho(V_s - V_j)^2}{2} + X \sum_j \frac{Q_s}{Q_\Sigma} \frac{\rho(V_i^2 - V_s^2)}{2} \\
& + X \sum_j \frac{Q_s}{Q_\Sigma} \rho(V_i - V_s) + 2X \sum_j \frac{Q_s}{Q_\Sigma} \rho V_s V_j \sin^2(\delta_{sj}/2).
\end{aligned}
\tag{8}
$$

Here X is friction coefficient; $P_{Sij}$ is pressure drop due to the shock loss between i-th inlet branch and j-th outlet branch, Pa; $Q_s$ is the volume airflow in s-th branch, $m^3$/s; $V_s$ is the average velocity in s-th branch, m/s; $\rho$ is air density, kg/$m^3$; $\delta_{sj}$ is the angle between s-th inlet stream and j-th outlet stream, °; indices "i" and "s" are referred to inlet branches, while index "j" is referred to outlet branches.

Formula (8) was implemented numerically using mesh current method for calculation of air distribution in mine ventilation networks in software application "AeroSet" [12].

## 4  Comparative Study of Existing Methods

The comparative study of existing methods is conducted in the context of solving air distribution problem for the following system of mine airways (see Fig. 4). This system consists of four branches and clearly demonstrates the shock loss influence on air distribution in parallel branches.

It is assumed that all branches have the similar physical and geometry properties: length L, cross-sectional area S and perimeter P, air resistance coefficient α. Air moves from the left to the right due to depression of a fan.

The classical approach of solving air distribution problem using only straight airway resistances in Kirchhoff's circuit laws results in the wrong solution with equal airflows in the branches No. 2 and No. 3. At that, results of 3D numerical simulation of
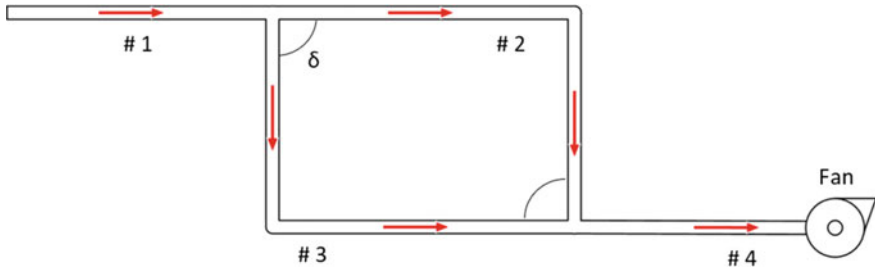
**Fig. 4.** System of mine airways

steady-state turbulent airflow in ANSYS CFX show that the airflows in two parallel branches are sufficiently different. The discrepancy between airflows strongly depends on angle $\delta$ of junction and coefficient of air resistance $\alpha$.

Figure 5 shows the results of 3D numerical simulations using the following parameters of the problem: $L = 50$ m, $S = 7$ m$^2$, $P = 8$ m, $V_1 = 2$ m/s. Coefficient of air resistance $\alpha$ takes on the values from 0.005 (concrete lined airways) to 0.05 (unlined airways when blasting technique is used). Angle $\delta$ of junction varies from 20° to 120°. As the result, the ratio between airflows in parallel branches varies in a wide range. In case of $\delta = 90°$ it ranges from 1.5 to 3 (see Fig. 5). The greater airflow is observed in the branch No. 2. This fact has the following explanation. At the airflow split, shock loss of the straight flow is much lesser than shock loss of the flow in side branch. While shock losses at airway junction are roughly the same for straight flow and side flow.
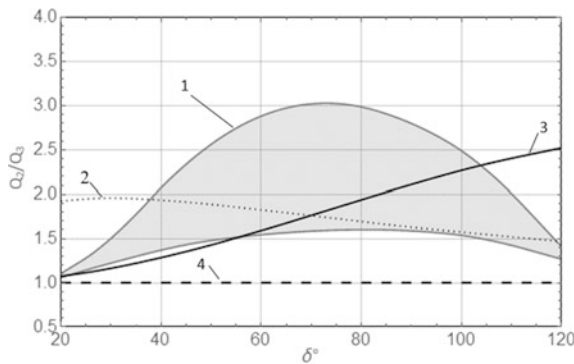


**Fig. 5.** The ratio between airflows in parallel branches as a function of junction angle $\delta$: 1—results of 3D numerical simulation in ANSYS CFX for values of wall roughness in the interval [0.005, 0.05], 2—hydraulic method, described in [11], 3—model proposed by authors, 4—a class of symmetric shock losses methods proposed by McPherson [3], Mokhirev [4], Kharev [9], Kazakov [10]

When airflow in the system is reversed, the situation changes dramatically. The new reversal airflow ratio in the parallel branches become reciprocal to the old value. This example shows principal asymmetry of shock losses in relation to the change of airflow direction.

Figure 5 also shows the ratios between parallel airflows calculated using methods, which were described above. Most methods predict the equal airflow distribution in parallel airways. These methods can be ranged in a class of symmetric shock losses in relation to airflow reversal.

Asymmetric air distribution in parallel airways was achieved by means of two methods—hydraulic method [11] and method (8) proposed by the authors. These two methods both correspond to the results of 3D simulation on qualitative level, but in terms of quantity each method has its own limitations.

The results of 3D simulation show the following scenario of airflow ratio change. At first, the airflow ratio grows up with the increasing of junction angle δ from 20° to 75°. It is caused by increasing of shock loss in side branch flow at the split of parallel airways. At that, shock loss of the straight flow at the split remains the same relatively small value. When the junction angle δ becomes greater than 75°, decreasing tendency of the airflow ratio is observed. It is concerned primarily with the increasing influence of shock loss at the junction of parallel airways. The air stream from the side branch No. 2 enters the junction at a high angle >75°. It leads to formation of a large stagnant wake in the branch No. 4 right after the junction, which is energetically unfavourable and leads to decrease of airflow in the branch No. 2.

Hydraulic method of calculation shock losses [11] predicts only decreasing of airflow ratio, while proposed model (8) describes only the process of airflow ratio growth.

Considering high inaccuracy of experimental data used for creating mathematical models of mine ventilation networks, quantitative deviations of the methods [11] and (8) are not crucial. Usually, the mine is designed in such a way that airflow turns by the angles lesser than 90°. From this point of view, the physical process of airflow ratio growth on parallel airways is more important.

It should be added that method (8) is universal and applicable for arbitrary airway junctions, when the hydraulic method consists of many formulae, which are applicable only for specific splits or junctions and hardly suitable for implementation in mine ventilation network models.

## References

1. Kruglov, Y.V., Levin, L.Y., Zaitsev, A.V.: Calculation method for the unsteady air supply in mine ventilation networks. J. Min. Sci. **5**(47), 651–659 (2011)
2. Levin, L.Y., Semin, M.A., Klukin, Y.A.: Experimental study of change in air distribution on potash mines during revers of main fan installation. Bulletin of PNRPU. Geology. Oil Gas Eng. Min. **4**(17), 89–97 (2015)
3. McPherson, M.J.: Subsurface Ventilation and Environmental Engineering. Chapman and Hall, London (1993)

4. Mokhirev, N.N., Radko, V.V.: Engineering calculations of shaft ventilation. Construction. Reconstruction. Exploitation. Moscow, LLC "Nedra Business Center" (2007)
5. ASHRAE Handbook, Fundamentals Volume. American Society of Heating, Refrigerating and Air-Conditioning Engineers, Inc. (2017)
6. Prosser, B.S., Wallace, K.G.: Practical values of friction factors. In: Proceedings of the 8th US Mine Ventilation Symposium (1999)
7. Skochinsky, A., Komarov, V.: Mine Ventilation. Moscow, "Mir" Publishers (1969)
8. Jade, R.K., Sastry, B.S.: Prediction of shock loss at splits in mine airways—a computational and experimental assessment. In: Proceedings of the 10th US/North American Mine Ventilation Symposium (2004)
9. Kharev, A.A.: Shock Losses in Mine Ventilation Networks. Moscow, "Ugletekhizdat" Publishers (1954)
10. Kazakov, B.P., Shalimov A.V., Stukalov, V.A. Modeling of the air resistances at airway junctions. Min. J. **12** (2009)
11. Idelchik, I.E.: Handbook of Hydraulic Resistance, 4th Edition Revised and Augmented. Begell House, Moscow (2008)
12. "AeroSet" Software Application. http://aeroset.net/en/

# A Preliminary Experimental Investigation of the Airflow Resistance of an Evolving Cave in a Block/Panel Cave Mine

S. Sreekumar Ajitha[1], R. Bhargava[1], Y. Pan[1], A. Jha[1],
P. Tukkaraja[1(✉)], K. Shahbazi[1], K. Katzenstein[1], and D. Loring[2]

[1] South Dakota School of Mines and Technology, Rapid City, SD, USA
PT@sdsmt.edu
[2] Freeport-McMoRan Inc., Phoenix, USA

**Abstract.** Block caving is an underground mining method, which uses gravity to exploit the mineral deposits that are too deep for conventional open-pit mining and is generally used to extract massive low-grade deposits. Design of ventilation systems for block caving mines is a relatively challenging task. Apart from the commonly used traditional ventilation design software packages, Computational Fluid Dynamics (CFD) techniques are also commonly used to understand the complex behavior of air/gas flow through the system. However, this study uses a laboratory scale (1:100) model set-up to investigate the ventilation characteristics of a block/panel cave mine, and the changes in the system caused by changing cave characteristics such as porosity and permeability (flow paths). This paper presents a preliminary study of an on-going project, the challenges faced while working on the experimental model, and the methods by which these issues were dealt with; the future study of this project will address the effect of changing cave characteristics on the ventilation system.

**Keywords:** Block caving · Scale model · Ventilation

## 1 Introduction

Block caving is a bulk mining method used for large, fractured, and deep-seated orebodies. This method is gaining popularity as it is an alternative to surface mining for extracting deep seated mineral deposits. Panel cave mining is a variation of block caving, where the orebody is divided up into panels and bulk extraction of material through induced caving as in block caving, but production moves sequentially along the length of the orebody.

A simple illustration of a block cave mine is shown in Fig. 1. The ore body is undermined using undercut drifts, which causes it to progressively collapse under its own weight. The broken ore is then collected at drawpoints and is transported to the surface via production drifts. The major concerns associated with ventilation in such mines are the quantification of influx of harmful gases (such as radon) from the caved zone, and the estimation of airflow requirements under changing cave characteristics. Hence, to design an effective ventilation system to ensure a safe working environment,

quantification these two parameters is critical. In order to quantify these parameters (gas emissions and the airflow requirements), understanding of the cave characteristics such as cave porosity and airflow resistance (permeability) is essential.
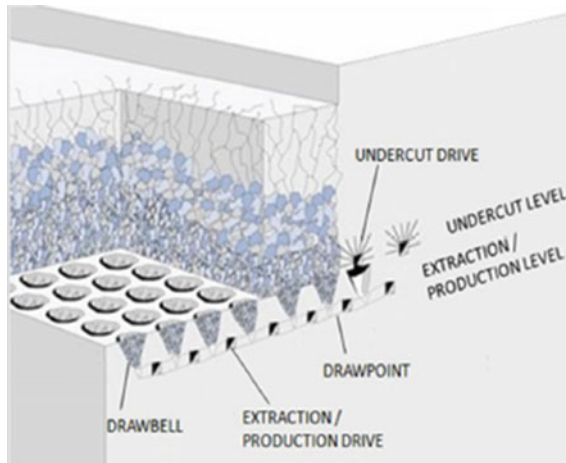


**Fig. 1.** Schematic representation of a typical block cave mine (after Sainsbury et al. [1])

Generally, CFD techniques [2–4] and Particle Flow Codes (PFC) [5] are used for this purpose, and some researchers have used physical scale models to study the fines migration in the cave [6]. However, this study utilizes a physical scale model (1:100 scale) to study the cave characteristics in a typical block/panel cave mine. This paper details the preliminary investigations performed using this model, describes the challenges associated with it, and presents the analysis of the results obtained from the model. Furthermore, it also discusses the experiments performed using a simpler model which was used to study the feasibility of experimenting on the bigger model.

## 2　Experimental Model

### 2.1　Construction

As can be seen from Fig. 2, our experimental model was made of wood, with the windows made using plexiglass. It has 9 production drifts (2 inches in diameter), 8 undercut outlet drifts (2 inches in diameter), 3 undercut inlet drifts (1inch in diameter), and 94 drawbells. The model has a hard roof, which has a duct (8 inches) connected to an exhaust fan. This exhaust fan was used to simulate the exhaust ventilation system from a real world mine scenario designed to pull radon/gases out of the caves. The model is connected to a fan. For the duration of the preliminary experiments, the undercut outlets and the production outlets were closed. Therefore, the air entered into the cave through the production and undercut inlets and exited through the exhaust duct on the roof.

**Fig. 2.** Experimental model (1:100 scale)

The measurements taken from the model include the static head near the fan, velocity and velocity pressure near the entrance to the model, and the static pressure difference between the production inlet and exhaust. Pitot tube, hot wire anemometer, and air flowmeter are used for these measurements.

An AutoCAD model (Fig. 3) was created based on the experimental setup, and it will be utilized for comparing the future CFD simulation results with the experimental results.

## 2.2 Investigation of the Effects of Undercut Inlet and Exhaust Fan

Three different scenarios were investigated under two different conditions (empty and filled) in each scenario. In the first scenario the production inlets were opened, while both the production and undercut inlets were opened in the second scenario, with the exhaust fan turned off in both scenarios. The third scenario was similar to the first except the exhaust fan was turned on.

Tables 1, 2 and 3 provide the experimental data from the measurements and include the fan static head, the static pressure difference, the velocity pressure difference, total pressure difference, and the air quantities. Figure 4 shows the cave characteristic curves for each scenario. From these curves, it was observed that the difference in the total pressure was directly proportional to the quantity raised to the power of 1.8; and the slopes of these curves provide the airflow resistance values for each case.

(a) Front View          (b) Top View

(c) Isometric View
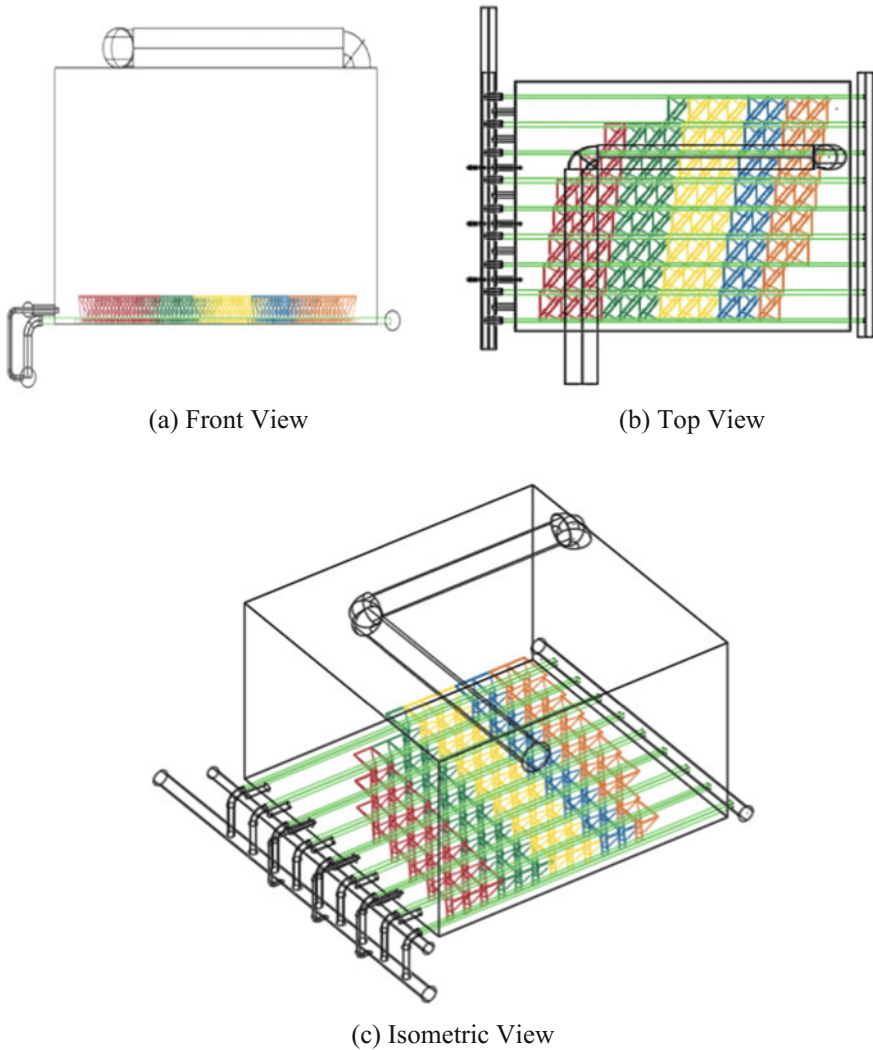
**Fig. 3.** AutoCAD illustration of the experimental model

As can be identified from the graph, the cave's airflow resistance decreases when the undercut inlets are opened, and the exhaust fan was turned on. This was due to the fact that when the undercut inlets were opened, there was an addition of a parallel path for the airflow through the cave; and when the exhaust fan was turned on, a suction effect was created at the outlet by the fan.

**Table 1.**  Three layers of material with no exhaust fan or undercut inlet

| Inlet vel. Pr (Pa) | Inlet quantity (m³/s) | Outlet quantity (m³/s) | Outlet velocity pressure (Pa) | Delta Vp (Pa) | Delta Vs (Pa) | Delta Tp (Pa) | Average quantity (m³/s) |
|---|---|---|---|---|---|---|---|
| 5 | 0.02 | 0.02 | 0.23 | 4.74 | 3 | 7.74 | 0.02 |
| 18 | 0.04 | 0.04 | 0.94 | 17.95 | 5 | 22.95 | 0.04 |
| 54 | 0.08 | 0.07 | 2.46 | 52.94 | 10 | 62.94 | 0.07 |
| 83 | 0.09 | 0.08 | 3.60 | 79.39 | 14 | 93.39 | 0.09 |
| 105 | 0.11 | 0.09 | 4.79 | 99.90 | 16 | 115.90 | 0.10 |
| 125 | 0.12 | 0.10 | 5.86 | 119.19 | 18 | 137.19 | 0.11 |

**Table 2.**  Three layers of material with undercut inlet only

| Inlet vel. Pr (Pa) | Inlet quantity (m³/s) | Outlet quantity (m³/s) | Outlet velocity pressure (Pa) | Delta Vp (Pa) | Delta Vs (Pa) | Delta Tp (Pa) | Average quantity (m³/s) |
|---|---|---|---|---|---|---|---|
| 5 | 0.02 | 0.02 | 0.23 | 4.84 | 3 | 7.84 | 0.02 |
| 18 | 0.05 | 0.04 | 0.94 | 18.09 | 4 | 22.09 | 0.04 |
| 56 | 0.08 | 0.07 | 2.46 | 54.09 | 6 | 60.09 | 0.08 |
| 86 | 0.10 | 0.08 | 3.60 | 83.61 | 8 | 91.61 | 0.09 |
| 108 | 0.11 | 0.09 | 4.79 | 104.78 | 7 | 111.78 | 0.10 |
| 130 | 0.12 | 0.10 | 5.86 | 122.64 | 8 | 130.64 | 0.11 |

**Table 3.**  Three layers of material with exhaust fan only

| Inlet vel. Pr (Pa) | Inlet quantity (m³/s) | Outlet quantity (m³/s) | Outlet velocity pressure (Pa) | Delta Vp (Pa) | Delta Vs (Pa) | Delta Tp (Pa) | Average quantity (m³/s) |
|---|---|---|---|---|---|---|---|
| 11 | 0.04 | 0.03 | 0.60 | 10.6 | 5 | 15.6 | 0.03 |
| 27 | 0.06 | 0.05 | 1.26 | 25.9 | 6 | 31.9 | 0.05 |
| 64 | 0.08 | 0.08 | 3.24 | 61.3 | 11 | 72.3 | 0.08 |
| 91 | 0.10 | 0.09 | 4.29 | 87.6 | 14 | 101.6 | 0.09 |
| 117 | 0.11 | 0.10 | 5.22 | 110.7 | 16 | 126.7 | 0.10 |
| 134 | 0.12 | 0.11 | 6.94 | 126.8 | 19 | 145.8 | 0.12 |
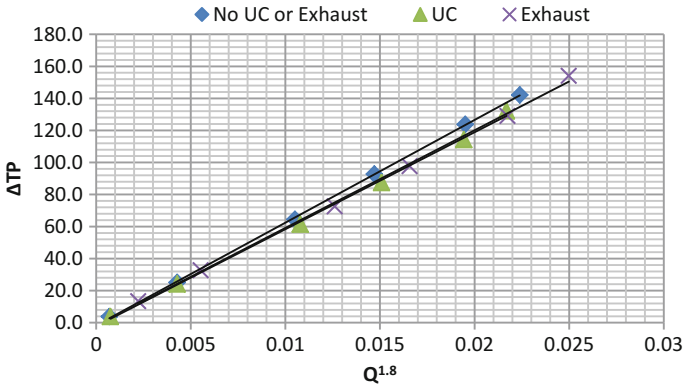
**Fig. 4.** Cave characteristics under different conditions

## 3 Challenges Associated with the Model

As can be expected from a model of such large dimensions and complex structure, there were a considerable number of problems associated with running the experiments on it. One of the major challenges had been finding a suitable material to simulate the broken rock mass within the cave.

The main criteria for choosing the materials were the following:

- It needs to be available in varying sizes to simulate the different levels of fragmentation observed in the different zones within the cave (namely, in situ, primary, and secondary fragmentation).
- It needs to light enough so that a large amount of the material may be safely and effectively loaded at the same time into the model.
- The material needs to be solid enough that it can cause a significant amount of resistance to the airflow.
- And most importantly, the cost of the materials must not be very high.

The Figs. 5, 6 and 7 show the different materials that were used for this purpose. The hollow plastic balls were light, and available in a variety of sizes, but they were too expensive to be used to fill the whole model.

Balloons were used next, since they are light and cheap, but they were not able to provide a significant resistance to the airflow within the model.

Finally, empty packaging boxes were considered to simulate the broken rock mass. The boxes were light, available in different sizes, provided some resistance to the airflow, and very considerably cheaper than the plastic balls. They were also easier to load into the model as compared to the balls and balloons. The only major issue with the boxes was its inability to block the drawpoints, as the smallest size boxes available were $4 \times 4 \times 4$ inches. To overcome this problem, it was decided to use a combination of boxes and balls to simulate the broken rock mass. The balls would form the first layer, while the boxes would form the higher layers, thereby causing resistance to the airflow coming up from the production drifts and into the caved zone.

**Fig. 5.** Plastic balls of different dimensions were used to fill the model



**Fig. 6.** Balloons of varying sizes were used to simulate the broken rock mass



**Fig. 7.** Empty boxes of different sizes used to simulate broken rock mass

During the initial fabrication of the model, the research team had decided to use a soft roof (made using a tarp) to simulate the cave top. However, this led to many problems during the experiments, the most prominent of which was the expansion of the tarp due to the pressure generated within the cave. Due to this volume expansion, the measured pressure drop of the system became unreliable. Therefore, the team decided to use a hard roof (made from wood) for the model. This made the readings from the model more reliable and was helpful in setting up an exhaust system right on top of the cave.

Another challenge that was associated with the model was choosing the liquid used to create the smoke to identify the airflow patterns. A few other options were investigated, such as using colored smoke, but most of these methods had the side-effect of leaving a residue inside the model after use. Also, since the model is hard to clean, and made of wood, it is susceptible to rot if exposed to a high level of moisture. Therefore, the chosen liquid needs to be such that it does not leave a residue within the model, as well as does not have high moisture content. The smoke must also be easily noticeable, so that the airflow patterns can be visualized. For this purpose, industrial strength fog juice was purchased, and then diluted so that it would not leave any glycerin residue on the walls or the drifts of the model.

## 4    Smaller Model with Simpler Arrangement

Due to some of the challenges mentioned above, the following model was fabricated as a test set-up to study the feasibility of the model on an even smaller scale. The setup is shown in Fig. 8. The dimensions of the box are approximately 22 ¼ × 25 ¼ × 46 ½ inches. The model consists of one production inlet, one exhaust outlet, and one undercut inlet.



**Fig. 8.** Smaller model experimental setup

The main purposes of the smaller model were:

- To investigate if there will be any significant pressure drop across the cave if the porosity of the cave changes.

- To study the effect of the undercut ventilation on the cave airflow resistance.

Plastic balls were used to fill the model, and measurements were taken after filling the model with one layer of balls (1.5-in. dia.), and then by filling the model with three layers of balls (1.5, 2, 2.75 in. dia.). The measurements were also taken with and without the undercut drift being operated (Figs. 9, 10 and 11).
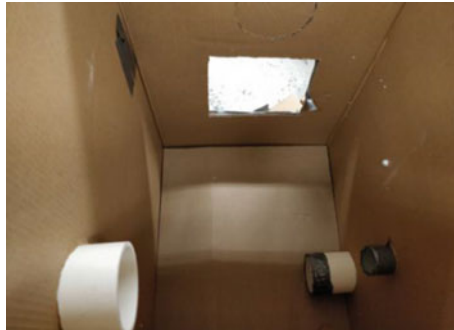


**Fig. 9.** Inside view of the smaller model



**Fig. 10.** Model filled with one layer of balls (1.5-inch dia.)

The data obtained from the experiments are given below (Tables 4, 5, 6 and 7):

Graphs were plotted with pressure drop on the y-axis and quantity raised to the power of 1.8 on the x-axis; they are shown in Figs. 12 and 13.

From the above graphs, the following inferences can be made:

- The airflow resistance of the cave was significantly lowered when the undercut was in operation.
- The addition of two more layers of plastic balls had increased the cave airflow resistance significantly.

**Fig. 11.** Model filled with three layers of balls (1.5, 2, 2.75 inches in diameter)

**Table 4.** One layer of material with undercut

| Static P (Pa) | Vel. Pr (Pa) | Vel. (m/s) | Quantity (m³/s) | Pressure drop (Pa) | $Q^{1.8}$ |
|---|---|---|---|---|---|
| 95 | 13 | 4.66 | 0.04 | 93 | 0.003 |
| 246 | 38 | 7.96 | 0.06 | 239 | 0.007 |
| 345 | 67 | 10.57 | 0.09 | 342 | 0.012 |
| 397 | 86 | 11.97 | 0.10 | 386 | 0.015 |

**Table 5.** One layer of material without undercut

| Static P (Pa) | Vel. Pr (Pa) | Vel. (m/s) | Quantity (m³/s) | Pressure drop (Pa) | $Q^{1.8}$ |
|---|---|---|---|---|---|
| 117 | 12 | 4.47 | 0.04 | 116 | 0.003 |
| 239 | 37 | 7.85 | 0.06 | 234 | 0.007 |
| 374 | 63 | 10.25 | 0.08 | 369 | 0.011 |
| 437 | 75 | 11.18 | 0.09 | 431 | 0.013 |

**Table 6.** Three layers of material with undercut

| Static P (Pa) | Vel. Pr (Pa) | Vel. (m/s) | Quantity (m³/s) | Pressure drop (Pa) | $Q^{1.8}$ |
|---|---|---|---|---|---|
| 104 | 15 | 5.00 | 0.04 | 102 | 0.003 |
| 240 | 35 | 7.64 | 0.06 | 237 | 0.007 |
| 370 | 64 | 10.33 | 0.08 | 363 | 0.012 |
| 433 | 75 | 11.18 | 0.09 | 428 | 0.013 |

With these observations, similar experiments can be conducted in the larger experimental model to identify the true extent of the change in airflow resistance caused by changing specific cave parameters.

**Table 7.** Three layers of material without undercut

| Static P (Pa) | Vel. Pr (Pa) | Vel. (m/s) | Quantity (m³/s) | Pressure drop (Pa) | $Q^{1.8}$ |
|---|---|---|---|---|---|
| 168 | 12 | 4.47 | 0.04 | 166 | 0.003 |
| 318 | 28 | 6.83 | 0.06 | 315 | 0.005 |
| 437 | 38 | 7.96 | 0.06 | 431 | 0.007 |
| 496 | 47 | 8.85 | 0.07 | 492 | 0.009 |
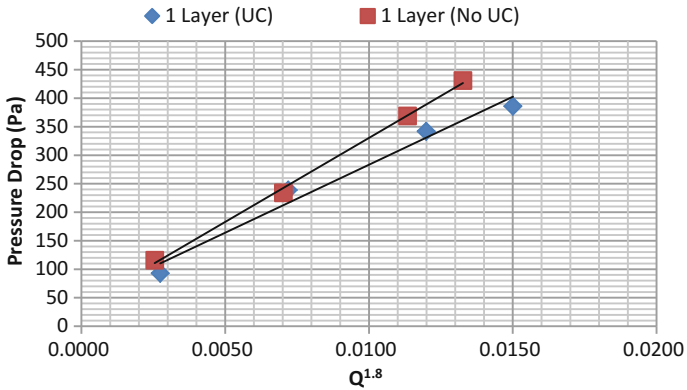


**Fig. 12.** Cave characteristics for one layer of plastic balls
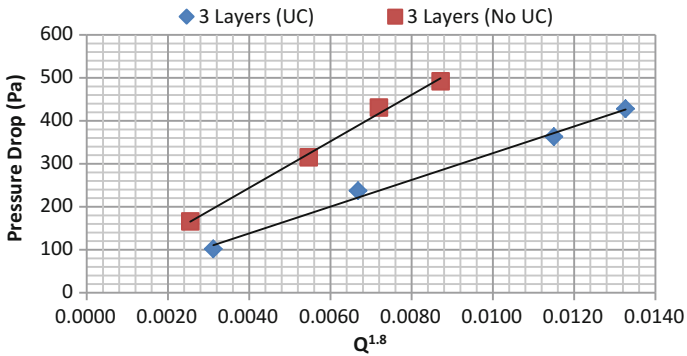


**Fig. 13.** Cave characteristics for three layers of plastic balls

## 5   Conclusions

As discussed in this paper, a 1:100 scale model was developed to study the ventilation aspects of a block/panel cave mine. The experiments that have been carried out using this model have shown the importance of the undercut drifts and the exhaust fan in

reducing the airflow resistance within the cave. This paper has also discussed in detail about some of the major challenges associated with building and experimenting on the model, which can be a helpful guide to other researchers who are attempting to build similar scale models. Further experiments conducted utilizing this model will be very helpful in obtaining the detail knowledge of the cave characteristics within a block/panel cave mine, which could be used in designing efficient ventilation systems.

# References

1. Salisbury, B.L., Sainsbury, D.P., Pierce, M.E.: A historical review of the development of numerical cave propagation simulations. In: Proceedings of the 2nd International FLAC/DEM Symposium on Numerical Modelling (2011)
2. Ajayi, K., Tukkaraja, P., Shahbazi, K., Katzenstein, K., Loring, D.: Computaional fluid dynamic study of radon gas migration in block caving mines. In: 15 the North American Mine Ventilation Symposium, Virginia (2015)
3. Baysal, A., Erogul, D., Ajayi, K., Tukkaraja, P., Shahbazi, K., Katzenstein, K., Loring, D.: Effect of the air gap associated with cave evolution on cave resistance. In: 15th North American Mine Ventilation Symposium
4. Erogul, D., Baysal, A., Ajayi, K., Tukkaraja, P., Shahbazi, K., Katzenstein, K., Loring, D.: Prediction of airflow resistance of a mature panel cave. In: 16th North American Ventilation Symposium
5. Board, M., Pierce, M.E.: A review of recent experience in modeling of caving. In: Proceedings of the International Workshop on Numerical Modeling for Underground Mine Excavation Design
6. Armijo, F., Irribarra, S., Castro, R.: Experimental study of fines migration for caving mines. In: 3rd International Symposium on Block and Sublevel Caving, pp. 356–361

# An Investigation of the Effects of Particle Size, Porosity, and Cave Size on the Airflow Resistance of a Block/Panel Cave

Y. Pan[1(✉)], R. Bhargava[1], A. Jha[1], P. Tukkaraja[1], K. Shahbazi[1],
K. Katzenstein[1], and D. Loring[2]

[1] South Dakota School of Mines and Technology, Rapid City, SD 57701, USA
Yong.Pan@mines.sdsmt.edu
[2] Freeport-McMoRan Inc, Phoenix, USA

**Abstract.** Block/panel caving is a preferred underground mining method for extracting deep seated, low-grade mineral deposits due to its high production rates and low mining costs. In a typical block/panel cave mine, cave zone or cave column is an important part of mine ventilation system, although traditional mine ventilation practices fail to estimate its airflow resistance due to the dynamic nature of caving process. In this study, a combination of flow through porous media and VENTSIM modeling approaches were used first to estimate the airflow resistance of a conduit/column filled with hollow plastic balls and then to predict the airflow resistance of a cave zone/cave column. This study also investigates the effects of broken rock size (particle size), porosity, and cave height and volume on the airflow resistance of a cave zone/cave column in a typical block/panel cave mine using a lab scale physical model.

**Keywords:** Block caving · Mine ventilation · Airflow resistance

## 1 Introduction

Block/panel caving is a popular underground mining method due to its low cost and high productivity. The cave zone in a block/panel mine is an important part of the mine ventilation system, however, traditional mine ventilation practices fail to estimate and assign reasonable attributes to the cave zone branches in the mine ventilation network model. Airflow patterns observed [3] in a cave zone are different from a typical drift/tunnel where the airflow is normally turbulent in nature. However, the phenomenon of airflow behavior through a typical cave zone is not well understood; previous Computational Fluid Dynamics (CFD) studies suggest that it could be a transitional flow.

Inaccurate estimation of air pressure and airflow requirements leads to leakage problems, and higher ventilation costs or accumulation of higher concentrations of harmful gases, for example, radon in the production drifts. The proactive radon control measures that are in practice at a panel cave mine are [1, 2]: (1) negative pressure on

the cave—either regulators or fans connecting the broken ore of the cave to an isolated main exhaust drift; (2) isolation of the cave—bulk heading of all intake air sources to the caved ore.

Air blast is another issue in a block cave mine—sudden drop of rock from the yield zone creates high pressure in the air gap region and causes air to pass through cave zone and into production drifts, which is another threat to the safety of mine workers. Hence, prediction of cave zone airflow resistance is very important, however, it is difficult to predict due to the dynamic nature of the caving process, the characteristics of a cave (dimension of cave zone, broken rock size, and porosity) change during the cave evolution. Some of these changes may increase the cave airflow resistance while others may decrease it. This study considers different porous media columns to investigate airflow through a cave zone. The porous media columns are various sizes of test columns, which are filled with different sizes of particles, different porosity, and different lengths.

Airflow resistance is one of the most important attributes that should be assigned to network branches for designing an effective ventilation system. The factors that affect the cave airflow resistance are particle size (broken rock sizes), column height, cave area, and cave porosity. This study develops a relationship between these parameters and the cave airflow resistance by using Grey Relational Analysis (GRA) to examine the relative effect of each parameter on the airflow resistance of a cave zone column. The GRA will rank the parameters based on their relative effect on the predicted variable, in this case, airflow resistance. Using this information, the parameter which has highest influence can be adjusted to reduce the cave airflow resistance.

This study also develops a simple VENTSIM model to investigate the characteristics of a propagating cave and to compare its results with the CFD simulation results [3, 4].

## 2 Experimental Procedure

Different parameters were considered for porous media experiments—four different sizes of particles (hallow plastic balls): 2.54, 3.81, 5.08 and 6.98 cm in diameter; three different sizes of test columns (tubes): 15.24, 20.32 and 25.4 cm in diameter; five pressure taps at 30.48 cm apart along a test column to measure static pressure differences at different depths. The taps were made of 5 mm diameter tube and extended into the test column about 1 cm from the inside wall to avoid wall effect on pressure measurements.

For all the cases, average column porosity was measured by filling the tube with water four times. Three plastic sheets were used to check the water spillage during the experiment.

A variable speed fan was used to supply air into the tube; the airflow rates were measured using a hot wire anemometer having a range of $0.2 \sim 20$ m/s. Air velocity measurements were taken at the outlet of the tube at multiple points as shown in Fig. 1. The internal circle of a tube was divided into two equal areas, eight positions were chosen for each area and a total 16 positions were selected as velocity test points. Six iron wire meshes were prepared to prevent plastic balls going out of a tube. In each set

of the measurements, multiple symmetrical readings were recorded and the average velocity was calculated from the readings. The airflow rates were calculated by multiplying the mean air velocity with the internal cross-section area of the tube.
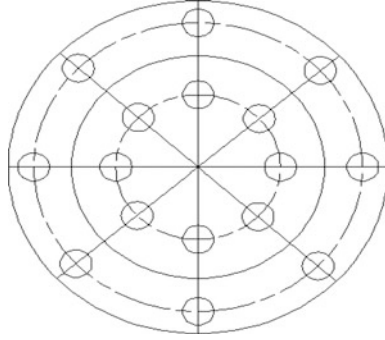


**Fig. 1.** Airflow velocity measurement positions at the outlet of the porous media



**Fig. 2.** An experimental model setup

Static pressure drops between the pressure taps was measured using an airflow meter with a pressure range of ±4000 Pa. Figure 2 shows the experimental setup with porous media and fan setup.

## 3   Results and Analysis

From the experimental data shown in Table 1, the relation between the pressure drop and the quantity was developed as given in Eq. 1.

$$\Delta P = R \cdot Q^{1.8} \tag{1}$$

**Table 1.**  Experimental data

| No. | Tube dia. (cm) | Ball size (cm) | Length (cm) | Porosity (%) | Resistance ($Ns^2/m^8$) |
|-----|------|------|------|------|------|
| 1 | 20.32 | 2.54 | 30.48 | 40.43 | 57,541 |
| 2 | 20.32 | 3.81 | 30.48 | 43.12 | 36,603 |
| 3 | 20.32 | 5.08 | 30.48 | 44.74 | 24,263 |
| 4 | 20.32 | 6.985 | 30.48 | 49.59 | 9923 |
| 5 | 20.32 | 2.54 | 60.96 | 40.40 | 1,12,652 |
| 6 | 20.32 | 3.81 | 60.96 | 43.83 | 52,035 |
| 7 | 20.32 | 5.08 | 60.96 | 45.47 | 40,264 |
| 8 | 20.32 | 6.985 | 60.96 | 47.81 | 29,400 |
| 9 | 20.32 | 2.54 | 91.44 | 40.96 | 2,25,145 |
| 10 | 20.32 | 3.81 | 91.44 | 44.39 | 88,423 |
| 11 | 20.32 | 5.08 | 91.44 | 45.68 | 54,297 |
| 12 | 20.32 | 6.985 | 91.44 | 48.51 | 40,121 |
| 13 | 15.24 | 2.54 | 30.48 | 42.64 | 1,35,897 |
| 14 | 15.24 | 3.81 | 30.48 | 44.55 | 8,44,55 |
| 15 | 15.24 | 5.08 | 30.48 | 46.24 | 75,685 |
| 16 | 15.24 | 2.54 | 60.96 | 42.84 | 3,12,026 |
| 17 | 15.24 | 3.81 | 60.96 | 44.31 | 1,43,422 |
| 18 | 15.24 | 5.08 | 60.96 | 46.66 | 1,20,047 |
| 19 | 15.24 | 2.54 | 91.44 | 42.46 | 5,24,466 |
| 20 | 15.24 | 3.81 | 91.44 | 44.78 | 2,56,021 |
| 21 | 15.24 | 5.08 | 91.44 | 45.86 | 1,87,440 |
| 22 | 25.4 | 2.54 | 30.48 | 38.65 | 26,720 |
| 23 | 25.4 | 3.81 | 30.481 | 40.97 | 13,286 |
| 24 | 25.4 | 5.08 | 30.48 | 43.76 | 9190 |
| 25 | 25.4 | 6.985 | 30.481 | 46.86 | 5364 |
| 26 | 25.4 | 2.54 | 60.96 | 39.59 | 53,404 |
| 27 | 25.4 | 3.81 | 60.96 | 41.12 | 28,737 |
| 28 | 25.4 | 5.08 | 60.96 | 43.25 | 17,619 |
| 29 | 25.4 | 6.985 | 60.96 | 47.44 | 10,542 |
| 30 | 25.4 | 2.54 | 91.44 | 39.45 | 78,426 |
| 31 | 25.4 | 3.81 | 91.44 | 41.46 | 38,441 |
| 32 | 25.4 | 5.08 | 91.44 | 43.58 | 24,750 |
| 33 | 25.4 | 6.985 | 91.44 | 47.33 | 15,316 |

where

P    is the pressure drop in Pa;
Q    is the airflow rate in $m^3/s$;
R    is the airflow resistance in $Ns^2/m^8$

## 3.1    Relationship Analysis

Multiple regression analysis was performed to develop a relationship between tube diameter, ball size, length, porosity and the airflow resistance. The nonlinear relationship obtained from the analysis is given in Eq. 2.

$$R = 10^{9.034 - 0.05\, D_{ball} + 0.008\, L - 0.096\, A - 0.06\, P} \tag{2}$$

where

R    is the airflow resistance, $Ns^2/m^8$;
D    is the particle diameter, cm;
L    is the length, cm;
A    is the area (tube dia), cm;
P    is the porosity, %

From Table 2, $R^2$ is larger than 0.8, meaning the regression is reliable. From the equation it can be easily observed that the airflow resistance increases with the increase of length and decreases with the increase of porosity, area dimension, and particle size. If the cave zone is regarded as a large porous media column, during the cave development stage, cave footprint (area) increases with the addition of new draw bell connections to the cave, this decreases the cave zone airflow resistance; during the cave evolution the increase in cave height increases the cave airflow resistance; as the broken rock material flows through the cave, due to comminution and grinding, the decrease in broken rock size decreases the cave airflow resistance; when the porosity of broken rock region decreases, the cave zone airflow resistance increases. It is also clear from the equation that these four parameters significantly affect the cave airflow resistance.

**Table 2.** Regression statistics

| Multiple R | 0.99 |
|---|---|
| R square | 0.98 |

## 3.2    Parameter Effect Analysis

Multiple attributes decision making (MADM) method aims to select the best from the existing alternatives by considering multiple attributes which are frequently in conflict with each other. Grey relational analysis (GRA) is an important part of grey system theory, which is suitable for solving problems with complicated interrelationships between multiple factors and variables [5].

There are four main steps involved in the GRA as shown in Fig. 3. The first step is translating the performance of all alternatives into a comparability sequence. This step is called grey relational generating. After which, a reference sequence is defined. Then the grey relational coefficient between all comparability sequences and the reference sequence is calculated. Finally, based on these grey coefficients, the grey relational grade between the reference sequence and every comparability sequences is calculated.
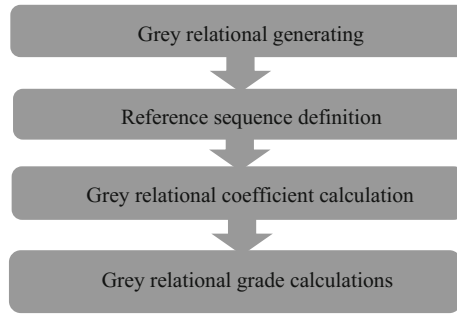
**Fig. 3.** Procedures for GRA

If a comparability sequence translated from an alternative has the highest grey relational grade between a reference sequence and itself, that alternative will be the best choice.

**Grey Relational Generating**. The processing of performance values for every alternative into comparability sequence analogous to normalization is called grey relational generating in GRA.

If there are m alternatives and n attributes, the ith alternative can be expressed as $Y_i = (y_{i1}, y_{i2}, \ldots, y_{ij}, \ldots, y_{in})$, where $y_{ij}$ is the performance value of attribute j of alternative i. The term $Y_i$ can be translated into the comparability sequence $X_i = (x_{i1}, x_{i2}, \ldots, x_{ij}, \ldots, x_{in})$ by using Eqs. 3, 4, and 5.

$$x_{ij} = \frac{y_{ij} - Min\{y_{ij}, i = 1, 2 \ldots, m\}}{Max\{y_{ij}, i = 1, 2, \ldots m\} - Min\{y_{ij}, i = 1, 2 \ldots m\}} \quad for\ i = 1, 2, \ldots, n \quad (3)$$

$$x_{ij} = \frac{Max\{y_{ij}, i = 1, 2, \ldots, m\} - y_{ij}}{Max\{y_{ij}, i = 1, 2, \ldots, m\} - Min\{y_{ij}, i = 1, 2, \ldots m\}} \quad (4)$$
$$for\ i = 1, 2 \ldots, m\ j = 1, 2, \ldots n$$

$$x_{ij} = 1 - \frac{\left|y_{ij} - y_j^*\right|}{Max\{Max\{y_{ij}, i = 1, 2 \ldots, m\} - y_{ij}^*, y_{ij}^* - Min\{y_{ij}, i = 1, 2, \ldots, m\}\}} \quad (5)$$
$$for\ i = 1, 2, \ldots, m \quad j = 1, 2, \ldots n$$

Equation 3 is used for the larger the more influential attributes; Eq. 4 is used for the smaller the more influential attributes; and Eq. 5 is used for the closer to the desired value $y_j^*$ the better. Cave airflow resistance and length can be analyzed by Eq. 3 whereas ball size, area, and porosity can be analyzed by Eq. 4.

**Reference Sequence Definition**. After the grey relational generating process, all values are scaled to $0 \sim 1$. The reference sequence $X_0$ as $(x_{01}, x_{02}, \ldots, x_{0j}, \ldots, x_{0n})$, is defined and then the aim is to find the alternative comparability sequence that is closed to the reference sequence.

**Grey Relational Coefficient Calculation**. Grey relational coefficient is used for determining how close $x_{ij}$ is to $x_{0j}$. The larger the grey relational coefficient is, the closer the $x_{ij}$ and $x_{0j}$ are. The grey relational coefficient can be calculated by Eq. 6.

$$\gamma(x_{oj}, x_{ij}) = \frac{\Delta_{\min} + \varsigma \Delta_{\max}}{\Delta_{ij} + \varsigma \Delta_{\max}} \quad for\ i = 1,\ 2,\ \ldots, m \quad j = 1,\ 2,\ \ldots\ n \tag{6}$$

$\gamma(x_{0j}, x_{ij})$ is the grey relational coefficient between $x_{ij}$ and $x_{oj}$, and $\Delta_{ij} = |x_{0j} - x_{ij}|$, $\Delta_{\min} = Min\{\Delta_{ij}, i = 1, 2, \ldots\ m;\quad j = 1,\ 2,\ \ldots\ n\}, \Delta_{\max} = Max\{\Delta_{ij}, i = 1, 2, \ldots, m;\quad j = 1, 2, \ldots n\}, \varsigma$ is the distinguishing coefficient, $\varsigma \in [0,\ 1]$ normally $\varsigma = 0.5$.

**Grey Relational Grade Calculation**. After calculating the entire grey relational coefficient $\gamma(x_{0j}, x_{ij})$, the grey relational grade can then be calculated using Eq. 7.

$$\Gamma(X_0, X_i) = \frac{1}{n} \sum_{1}^{n} \gamma(x_{0j}, x_{ij})\ for\ i = 1,\ 2, \ldots\ m \tag{7}$$

The relative influences of four parameters of tube area, balls size, length, and porosity on airflow resistance were carefully calculated, and the results were shown in Table 3.

**Table 3.** Grey relational grades and weights

|               | Area dimension | Ball size | Length | Porosity |
|---------------|----------------|-----------|--------|----------|
| Average grade | 0.68           | 0.60      | 0.64   | 0.62     |
| Weight        | 0.27           | 0.24      | 0.25   | 0.24     |

Based on grey relational grade value, the sequence of factors in the decreasing order of influence on airflow resistance is area dimension, length, porosity, and ball size.

## 4   VENTSIM Analysis

VENTSIM is a popular underground mine ventilation simulation software package commonly used to solve simple one-dimensional ventilation network problems. Broken rock particles cannot be simulated in VENTSIM, however, broken rock zone can be simulated by assigning appropriate airflow resistance values to the network braches as shown in Fig. 4 (different colors represent different zones in the cave); and the air gap in the cave can be simulated in the similar fashion. These resistances were obtained from the experimental study.

A resistance of 100,000 $Ns^2/m^8$ was assigned to cave zone columns; 300,000, and 1,000,000 $Ns^2/m^8$ were assigned to draw bells columns, and yield zones respectively.

As shown in Fig. 4, from the first row of draw bells to the 5th row of draw bells (from left to the right), the air passes from the production drifts into the cave zone
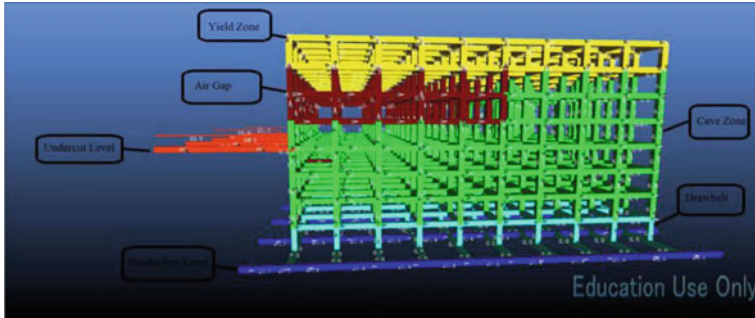
**Fig. 4.** VENTSIM model

whereas after 6th row of draw bells airflows from cave zone to production drifts. Similar observations were made from the CFD simulation studies [2, 3].

Cave characteristic curve was generated (Fig. 5) from the calculate pressure drops across the cave under different assumed airflow resistance values for airgap zone as 1; 10; 100; 1000; 10,000 to 100,000 $Ns^2/m^8$; the extreme (100,000 $Ns^2/m^8$) resistance value simulates the cave scenario of no air gap zone.
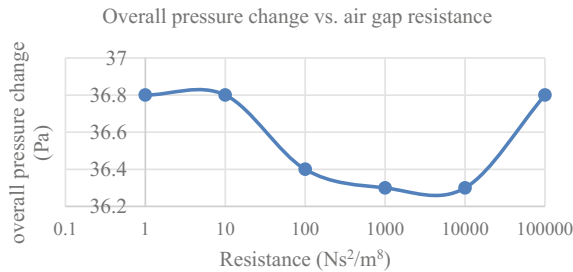


**Fig. 5.** Overall pressure change over air gap resistance

Change in air gap resistance has little influence on overall pressure change. As the resistance increases the overall pressure change reduces except at 100,000 $Ns^2/m^8$. The maximum effect of air gap on the overall pressure change is about 1.3%. An increase of air gap resistance will decrease overall pressure change to some extent and then it will increase with the increase in resistance. However, the difference in change in pressure drop with respect air gap height is not very significant. Similar observations were made from the CFD simulation studies [2, 3].

Radon flow simulation was performed with a fixed radon concentration of cave zone and draw bell zone was set to 1000 Bq/l. Figure 6 shows the radon concentrations in the production drifts. As can be seen from the figure, radon concentration increases along the airflow direction (from left to right). Radon concentration is higher near
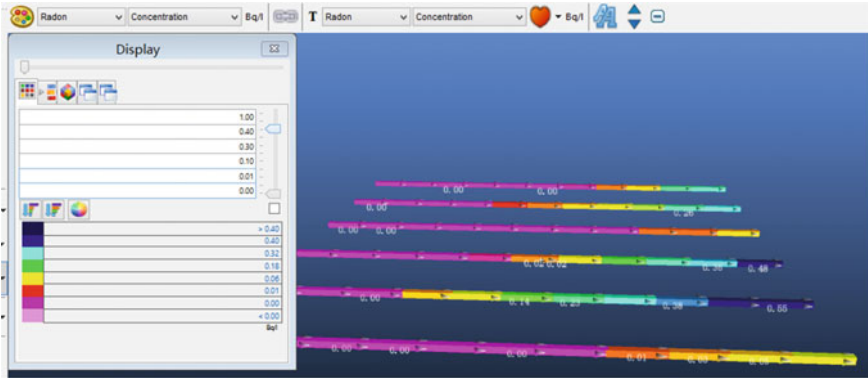
**Fig. 6.** Radon concentration distribution in production drifts

outlets and lower near the inlet in all the production drifts. Similar observations were made from the CFD simulation studies [2, 3].

## 5    Conclusions

A nonlinear mathematical relationship was developed between the cave airflow resistance and the influenced parameters such as particle size, porosity, length, and area dimension of porous media. It was observed that airflow resistance increases with the increase of the length and decreases with the increase of area dimension, porosity, and particle size. Grey relational analysis reveals that the area dimension of the cave (porous media) is the major contributing factor followed by length and porosity to the variation in the cave airflow resistance value whereas the particle size has the lowest contribution.

The airflow patterns through production drifts and the cave zone observed from the simple one-dimensional VENTSIM modeling confirms the observations made from the CFD simulation studies. The influence of the change of air gap resistance on the overall pressure change was observed to be about 1.3% which was not very significant. Radon concentration increases along the direction of airflow in the production drifts; radon concentrations were observed to be relatively higher at the production drift outlets compared to the inlet concentrations.

## References

1. Loring, D.M., Nelson, B.V: Transition of the henderson mine ventilation system to the new lower levels. In: 11th US/North American Mine Ventilation Symposium, pp. 41–45 (2006)
2. Erogul, D. Baysal, A., Ajayi, K.M., Tukkaraja, P., Shahbazi, K., Katzenstein, K., Loring, D.: Effect of the air gap associated with cave evolution on cave resistance. In: 15th North American Mine Ventilation Symposium, pp. 193–199 (2015)

3. Erogul, D., Ajayi, K.M., Tukkaraja, P., Shahbazi, K., Katzenstein, K., Loring, D.: Evaluation of cave airflow resistance associated with multiple air gap geometries during cave evolution. In: 16th North American Mine Ventilation Symposium, vol. 14, pp. 9–15 (2017)
4. Baysal, A., Ajayi, K.M., Tukkaraja, P., Shahbazi, K., Katzenstein, K., Loring, D.: Prediction of airflow resistance of a mature panel cave. In: 16th North American Mine Ventilation Symposium, vol. 14, pp. 27–34 (2017)
5. Kuo, Y., Yang, T., Huang, G.-W.: The use of grey relational analysis in solving multiple attributes decision-making problems. Comput. Ind. Eng. **55**, 80–93 (2008)
6. Oh, J., Bahaaddini, M., Sharifzadeh, M., Chen, Z.: Evaluation of air blast parameters in block cave mining using particle flow code. In: Int. J. Min. Reclam. Environ. 1–15 (2017)

# Selecting the Best Development Face Ventilation Scheme Using G1-Coefficient of Variation Method

Zhou Zhiyong[1], Mehmet Kizil[2], Chen Zhongwei[2,3(✉)],
and Chen Jianhong[1]

[1] School of Resources and Safety Engineering, Central South University,
Changsha 410083, China
[2] School of Mechanical and Mining Engineering, The University of Queensland,
St Lucia, QLD 4072, Australia
csuzzy@126.com
[3] State Key Laboratory for GeoMechanics and Deep Underground Engineering,
China University of Mining and Technology, Xuzhou 221116, China

**Abstract.** The current popular methods for decision making and project opti-
misation in mine ventilation contain a number of deficiencies as they are solely
based on either subjective knowledge or objective information. This paper
presents a new approach to rank the alternatives using G1-coefficient of varia-
tion method. The focus of this approach is to use combination weighing, which
is able to compensate for the deficiencies in index single weighing method. In
the case study, an evaluation index system was established to determine the
evaluation value of each ventilation mode to select the best development face
ventilation mode. The result shows that the proposed approach is able to rank
the alternative development face ventilation mode reasonably, the combination
weighing method had the advantages of using both subjective and objective
weighing methods by taking into consideration of both the experience and
practical knowledge, and any possible changes in a scenario. This approach
provides a more reasonable and reliable procedure to analyze and evaluate
different ventilation modes.

**Keywords:** Development face ventilation · G1 method · Coefficient of
variation method · Comprehensive evaluation · Optimization

## 1 Introduction

Underground mining is conducted in relatively small spaces, it is faced with many
safety threats in the mining process, among which dust contamination is a common
issue for mine operators [1, 2]. Dust hazard seriously affects mine production safety
and workers' health [1–3]. Furthermore, with the depletion of shallow mineral
resources, deep mining is the inevitable trend. One of the outstanding problems during
deep mining is high temperature. So, for an underground mine, good ventilation is the
key for a safe production environment [4–7]. In single heading development, proper
ventilation is essential [2]. Development face ventilation is critical as it can impede

mine production [8], and to ensure the health and safety of the development crew. Thus, it is essential to comprehensively evaluate the different development face ventilation schemes for the optimal design for an efficient system. In the past, ventilation planning was done based on designers' knowledge and experiences by weighing all pros and cons, and choosing among many alternatives [9]. Thus, a method based on the Multi-Attribute Decision Making (MADM) theory is recommended to evaluate or assess the mine ventilation system [6]. MADM methods consist of numerous different techniques in selecting the best alternatives, which include Fuzzy AHP, Grey Relational Analysis, Artificial Neural Network, Genetic Algorithms, etc.

## 2 State of the Art

A review of the literature reveals that the MADM techniques have been used for a variety of applications in decision making and project optimisation for mine ventilation systems. Mirhedayatian et al. [9] used the Fuzzy AHP for selecting the best tunnel ventilation system. Cheng et al. [4] used the Fuzzy AHP method to establish the reliability allocation model for the mine ventilation systems design. Sa et al. [10] used the grey system theory to optimize the ventilation system of a mine. Wu [11] put forward an improved grey correlative method for risk assessment on mine ventilation system. Cheng and Yang [6] used the Rough Set theory to assist the selection of best ventilation indices and the Support Vector Machine to classify the risk ranks for the mine ventilation system. Based on a BP neural network approach, Wang [12] set up an evaluating model for mine ventilation system reliability. Karacan [13] used reservoir models and artificial neural networks for optimizing ventilation air requirements in development mining of coal seams. Kozyrev and Osintseva, Deng and Liu, Shriwas and Calizaya, Zhang, Lowndes et al. [14–18] applied Genetic Algorithms for the optimisation of mine ventilation system. The stated methods work to an extent in evaluating and optimum selection of mining ventilation systems, but all have some deficiencies. For example, the Grey Relational Analysis method is mainly used for conditions where system information is incomplete or undefined, and cannot reflect the evaluated object's absolute level. Artificial Neural Network does not have the unified metrics, which requires normalization with the membership function, making a complicated calculation process. Also, with such method, the effect of the subjective factor is difficult to measure. In addition, the Fuzzy Comprehensive Evaluation cannot solve the problem of repetition caused by the correlation of system index. The determination of the membership function is also rather subjective with the Fuzzy Comprehensive Evaluation method.

The purpose of this paper is to further improve the evaluation process, to remedy the deficiencies of evaluation index single weight determining method, and making use of both expert's experience and knowledge and new changes of objective conditions. By considering the advantages of the subjective and objective weight determining methods, this paper comprehensively uses both types of methods to arrive the combination weight determination. The paper uses a combination of the G1 [19] method (subjective), and the coefficient of variation method (objective). Taking this into consideration, the paper is able to construct an optimum evaluation model for

development face ventilation systems based on the combination weight determining. The model was also used in a case study.

## 3 Methodology

### 3.1 Data Standardization

Based on the mathematics piecewise function thought, indices' original data are made standardized with a dimensionless process [20]:

$$P_i = \frac{|A_i - m(A)|}{\max A - \min A} \tag{1}$$

where $P_i$ is the dimensionless value of $A_i$, $\max A$ is the maximum value of index $A$, and $\min A$ is the minimum value of index $A$. When $A$ is a positive index, $m(A) = \min A$; when $A$ is a negative index, $m(A) = \max A$; $A_i$ is the $i$th specific value of index $A$.

The Formula (1) is interpreted as: for index $A$, the dimensionless value presents the relative distance between the deviation between the $i$th value and the worst value, and the deviation between the maximum value and the minimum value. A bigger relative distance means a bigger $P_i$ (the dimensionless value of $A_i$), which is in direct proportion to optimum.

### 3.2 Index Combination Weight Determining

Subjective weight determining mainly makes use of the experience and wisdom of experts. Experience is the knowledge recognized from the past event afterwards. Once determined, it is rarely changed. Though such method is mature and has been commonly used in many applications, it lacks objectiveness. Similarly, objective weight determining is dynamic, reflecting in that index weight are related with index value, but also shows a lack of expert experience and knowledge [20]. By combining the G1 method and the Coefficient of Variation method, a combination weight determining method was created that has the advantages of both subjective weight determining and objective weight determining.

**Subjective Weight Determining with the G1 Method**. The G1 method is a subjective weight determining method [19], where the index weight is determined by first sequencing the index importance and then followed by estimating the relative degree of importance between the adjacent sequenced indices. It is upgraded from the AHP method, and has resolved the disadvantages of the previous large and complex calculations and the required consistency checks.

(1) *Index sequencing*

$$X_1 > X_2 > \cdots > X_k \quad k = 1, 2, \ldots, m$$

where ">" refers to the index on the left has more importance than the index on the right.

$$r_k = \omega_{k-1}^s / \omega_k^s \quad k = m, m-1, \ldots, 3, 2$$

Where $r_k$ refers to the relative importance degree between adjacent indexes, $\omega_k^s$ is the $k$th index weight with G1 method.

(2) *Index weight calculation*

$$\omega_k^s = \left(1 + \sum_{k=2}^m \prod_{i=k}^m r_i\right)^{-1} \tag{2}$$

$$\omega_{k-1}^s = r_k \omega_k^s \tag{3}$$

**Objective Weight Determining with the Coefficient of Variation Method**. The Coefficient of Variation method [20] is an objective weight determining method that directly processes the index data with mathematics to calculate the index weight. It is able to achieve the index dynamic weight determining through a full consideration of the relative variation between each indices and the reduction of the interferences from the subjective factors.

(1) *Index Coefficient of Variation*

$$V_k = \sigma_k / \overline{X}_k \quad k = 1, 2, \ldots, m \tag{4}$$

where $V_k$ is the coefficient of variation of the $k$th index, $\sigma_k$ is the standard deviation of the $k$th index, and $\overline{X}_k$ is the arithmetic mean value of the $k$th index.

(2) *Index weight*

$$\omega_k^0 = \frac{V_k}{\sum_{k=1}^m V_k} \quad k = 1, 2, \ldots, m \tag{5}$$

where $\omega_k^0$ is the $k$th index weight with Coefficient of Variation method.

**Index Combination Weight**. Index combination weight is defined as the linear combination of the two weights mentioned from above, the expression [20] is

$$\omega_k^{s0} = \beta \omega_k^s + (1 - \beta) \omega_k^0 \quad k = 1, 2, \ldots, m \tag{6}$$

where $\beta$ is the percentage of subjective weight in combination weight and $\omega_k^{s0}$ is the combination weight of the $K$th index.

Optimal value of $\beta$ is calculated with the mathematical optimization problem inspirations, to achieve the optimal combination of the two weight. The objective function is built based on the rational of getting the minimum value of the quadratic sum with two deviations. In this case, one is the deviation between combination weight value and the weight value with G1 method, the other is the deviation between combination weight value and the weight value with Coefficient of Variation method. The expression is as following:

$$\min y = \sum_{k=1}^{m} \left[ \left( \omega_k^{s0} - \omega_k^s \right)^2 + \left( \omega_k^{0s} - \omega_k^0 \right)^2 \right] \tag{7}$$

The process involves the substitute of Formula (6) into Formula (7), take derivative with respect to $\beta$, set its first-derivative value as 0, solve the equation, and get the optimal value of $\beta$ (0.5). In the final, the optimal combination weight of the $k$th index is

$$\omega_k^{s0} = 0.5\omega_k^s + 0.5\omega_k^0 \tag{8}$$

The denotation of Formula (8) is that the index combination weight has its optimal value when subjective weight and objective weight account for 50 and 50%, respectively. If the calculated combination weight is equal to the subjective weight and the objective weight, we can infer that both the subjective weight determining method and the objective weight determining method have the same cognition for index importance. Otherwise, the combination weight is the combined result of subjective weight and objective weight.

## 3.3  Optimum Evaluation Model of the Development Face Ventilation Method Based on Combination Weight

**Definition of Mathematical Evaluation Function**. Based on the notion of mathematical function, evaluation value of the ventilation method can be defined as dependent variable, and the evaluation index can be defined as independent variable. With certain mathematical models, multi-index comprehensive evaluation issue is transferred to determine the indexes' comprehensive evaluation values. In this case, values of indexes are fitted into matrix $P = (p_1, p_2, \ldots, p_m)^T$, in which vector $p_i = (p_{i1}, p_{i2}, \ldots, p_{ij}), 1 \leq i \leq j$, represents the vector value of the $i$th index from the first project to the $j$th project. Index value matrix can be shown as

$$\begin{pmatrix} p_{11} & p_{12} & \cdots & p_{1j} \\ p_{21} & p_{22} & \cdots & p_{2j} \\ \cdots & \cdots & \cdots & \cdots \\ p_{m1} & p_{m2} & \cdots & p_{mj} \end{pmatrix}$$

$\omega_k^{s0} = (\omega_1, \omega_2, \ldots, \omega_m)$ is the independent variable coefficient (index weight) vector.

The $i$th project has its comprehensive evaluation expression:

$$P_i = f\left( \omega_k^{s0}, p_{1i}, \ldots, p_{mi} \right) \quad 1 \leq i \leq j \tag{9}$$

**Building the Optimum Evaluation Model**. As the evaluation indexes are independent with each other, and the index weight value is consistent with this kind of index. The independent variable coefficient has apparent effect on the dependent variable in a linear function, and the dependent variables have a linear compensation effect. As a result, the optimum evaluation model [19] was constructed as

$$P_i = \omega_1^{s0} p_{1i} + \omega_2^{s0} p_{2i} + \cdots + \omega_m^{s0} p_{mi} = \sum_{k=1}^{m} \omega_k^{s0} p_{ki} \qquad (10)$$

where $P_i$ is the comprehensive evaluation value of the $i$th method with a data range of [0, 1]. The value of $P_i$ has direct proportion to optimum.

Formula (10) explains that the evaluation value of the ventilation method is equal to the sum of the product of each index values and their weight. Accordingly, Fig. 1 illustrates the overall structure of the proposed approach in this paper for obtaining the final comprehensive evaluation values of alternatives. In the following section, this method will be used to design a ventilation system for a field case.

```
┌─────────────────────────────────────────┐
│   Step 1 - data dimensionless processing │
└─────────────────────────────────────────┘
                    │
                    ▼
┌─────────────────────────────────────────┐
│ Step 2 – calculate index layered weight  │
│            with G1 method                 │
└─────────────────────────────────────────┘
                    │
                    ▼
┌─────────────────────────────────────────┐
│ Step 3 – calculate index weight with      │
│       Coefficient of Variation method     │
└─────────────────────────────────────────┘
                    │
                    ▼
┌─────────────────────────────────────────┐
│ Step 4 – calculate index combination      │
│                weight                     │
└─────────────────────────────────────────┘
                    │
                    ▼
┌─────────────────────────────────────────┐
│ Step 5 – calculate comprehensive          │
│  evaluation value of each ventilation     │
│                method                     │
└─────────────────────────────────────────┘
                    │
                    ▼
┌─────────────────────────────────────────┐
│ Step 6 – final ranking of alternatives by │
│     comprehensive evaluation value        │
└─────────────────────────────────────────┘
```
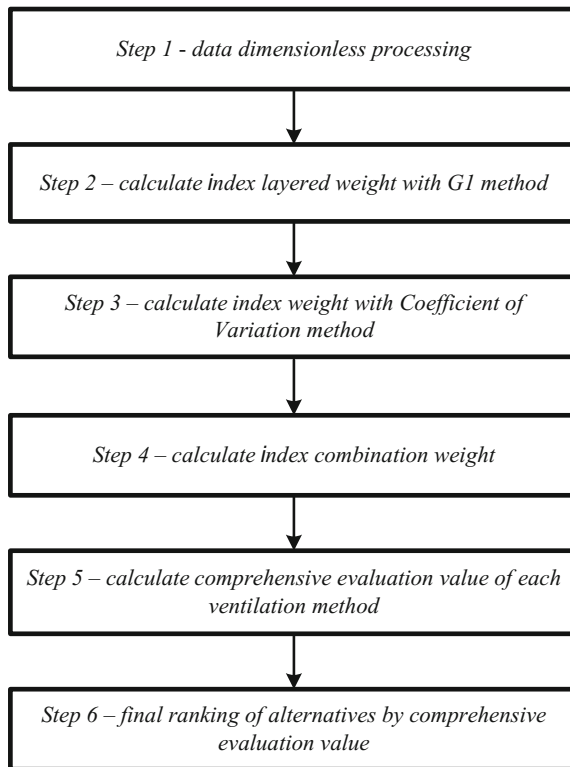
**Fig. 1.** Overall structure of the proposed approach for alternative prioritization in G1-coefficient of variation

## 4 Result Analysis and Discussion

There is a large copper polymetallic mine located at high altitude area. As the mine has severe dust pollution, an optimal design for the development face ventilation mode is planned to take in place to improve the working face environment and to ensure

occupational health and safety of underground workers. The high altitude creates extreme low oxygen and low pressured working environment, which evidently decreases both the worker's and equipment's working efficiency in comparison to a lower altitude area. Moreover, the single ventilation mode can easily form an anoxic area with the negative pressure, which threatens worker's life. Thus, this mine's unique character of the high altitude drives the requirement of a compound ventilation mode.

The inspected options for the ventilation mode are as follows: A1—short-range pressing—long-range absorption (front pressing—back absorption) (Fig. 2c), A2—short-range pressing—long-range absorption (front absorption—back pressing) (Fig. 2d), A3—long-range pressing—short-range absorption (front pressing—back absorption) (Fig. 2a), A4—long-range pressing—short-range absorption (front absorption—back pressing) (Fig. 2b), and A5—long-range pressing—long-range absorption (front absorption—back pressing) (Fig. 2e).



(a) long-range pressing - short-range absorption (front pressing - back absorption)

(b) long-range pressing - short-range absorption (front absorption - back pressing)

(c) short-range pressing - long-range absorption (front pressing - back absorption)

(d) short-range pressing - long-range absorption (front absorption - back pressing)

(e) long-range pressing - long-range absorption (front absorption - back pressing)

**Fig. 2.** The inspected options for the ventilation mode

The evaluation index selection principle is to use as few indexes as possible to reflect the most important and comprehensive information. Decisions on adapting the appropriate ventilation mode can be made through an evaluation in the areas of

technical feasibility, economic rationality, and safety reliability. The hierarchy of the decision-making problem is illustrated in Fig. 3. The criteria and sub-criteria for this problem are listed in Table 1 [21]:
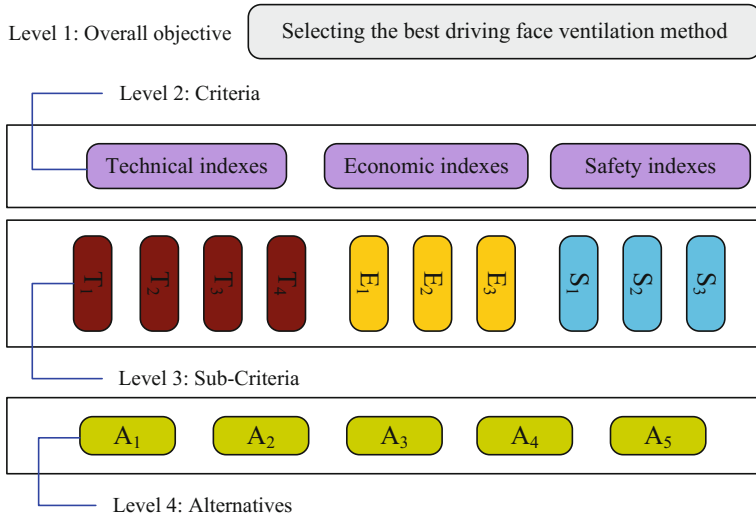


**Fig. 3.** Hierarchical structure of selecting the best development face ventilation mode

**Table 1.** The criteria layer and sub-criteria layer for decisions on appropriate ventilation mode

| Serial number | Criteria layer | Sub-criteria layer |
|---|---|---|
| 1 | Technical indexes (T) | Total air volume of development face ($T_1$) |
| 2 | | Total ventilation resistance of development face ($T_2$) |
| 3 | | Supply-demand ratio of air volume ($T_3$) |
| 4 | | Available air-flow rate ($T_4$) |
| 5 | Economic indexes (E) | Fan power ($E_1$) |
| 6 | | Fan efficiency ($E_2$) |
| 7 | | Exterior leakage ($E_3$) |
| 8 | Safety indexes (S) | Fan stability ($S_1$) |
| 9 | | Airflow stability ($S_2$) |
| 10 | | Oxygen content of air ($S_3$) |

It should be noted that total ventilation resistance of development face, fan power, and exterior leakage are negative indexes, while the others are all positive indexes. Moreover, when exhaust ventilation is applied, the high altitude environment can easily lead to the appearance of negative pressure and an anoxic phenomenon. Consequently, the oxygen level of the air is selected as a key factor for our safety indexes [21].

With all the criteria ready in place, the proposed method is now practiced for selecting the best development face ventilation mode. Evaluation index values for each ventilation mode are shown in Table 2. The values of S1 and S2 were obtained from expert's advice.

**Table 2.** Evaluation index values of each ventilation mode

| Sub-criteria layer | $A_1$ | $A_2$ | $A_3$ | $A_4$ | $A_5$ |
|---|---|---|---|---|---|
| $T_1$ (m$^3$/s) | 84.64 | 85.94 | 87.56 | 88.76 | 90.98 |
| $T_2$ (N · s$^2$/m$^4$) | 13.5 | 13.83 | 14.18 | 15.01 | 15.96 |
| $T_3$ | 0.95 | 0.97 | 0.99 | 1.02 | 1.05 |
| $T_4$ | 0.862 | 0.853 | 0.879 | 0.871 | 0.84 |
| $E_1$ (KW) | 12 | 14 | 16 | 19 | 23 |
| $E_2$ | 0.87 | 0.85 | 0.89 | 0.86 | 0.84 |
| $E_3$ (%) | 2.7 | 2.9 | 2.8 | 3.1 | 3.3 |
| $S_1$ | 9.1 | 8.9 | 9.2 | 9 | 8.8 |
| $S_2$ | 9.2 | 9.3 | 9.4 | 9.4 | 9.5 |
| $S_3$ (%) | 21.1 | 21.2 | 21.6 | 21.4 | 21.3 |

## 4.1   Data Dimensionless Processing

With the use of Formula (1), the original data of all indexes from Table 2 were transformed into their dimensionless values, showed in Table 3.

**Table 3.** Dimensionless values of evaluation index

| Sub-criteria layer | $A_1$ | $A_2$ | $A_3$ | $A_4$ | $A_5$ |
|---|---|---|---|---|---|
| $T_1$ | 0.000 | 0.205 | 0.461 | 0.650 | 1.000 |
| $T_2$ | 1.000 | 0.866 | 0.724 | 0.386 | 0.000 |
| $T_3$ | 0.000 | 0.200 | 0.400 | 0.700 | 1.000 |
| $T_4$ | 0.564 | 0.333 | 1.000 | 0.795 | 0.000 |
| $E_1$ | 1.000 | 0.818 | 0.636 | 0.364 | 0.000 |
| $E_2$ | 0.600 | 0.200 | 1.000 | 0.400 | 0.000 |
| $E_3$ | 1.000 | 0.667 | 0.833 | 0.333 | 0.000 |
| $S_1$ | 0.750 | 0.250 | 1.000 | 0.500 | 0.000 |
| $S_2$ | 0.000 | 0.333 | 0.667 | 0.667 | 1.000 |
| $S_3$ | 0.000 | 0.200 | 1.000 | 0.600 | 0.400 |

## 4.2   Index Weight Determining with G1 Method

**Criteria layer weight determining**. According to the experts, the sequence of the three criteria layers (Technical indexes, Economic indexes and Safety indexes) and the rational assignment for the relative degree of importance between the three criteria layers are determined. These are respectively determined as

$$T > S > E$$

$$r_2 = W_T/W_S = 1.8; r_3 = W_S/W_E = 1.8$$

Substituting $r_2 = 1.8; r_3 = 1.8$ into Formula (2) and the weight ($W_E$) of criteria layer E can be derived, it is

$$\omega_3 = \left(1 + \sum_{k=2}^{3} \prod_{i=k}^{3} r_i\right)^{-1} = 0.1656$$

Substituting $\omega_3 = 0.1656$ into Formula (3) and the weight ($W_S$) of criteria layer S can be derived, which is

$$\omega_2 = r_3\omega_3 = 0.2981$$

Then, the weight ($W_T$) of criteria layer T can be derived, which is

$$\omega_1 = 1 - \omega_2 - \omega_2 = 0.5363$$

And the weight vector is

$$(W_T, W_E, W_S) = (0.5363, 0.1656, 0.2981)$$

**Sub-criteria layer weight determining**. According to the experts, the sequence of the four sub-criteria layers of T (technical indexes) criteria layer and the rational assignments for relative degree of importance between the sequenced adjacent layers are determined. These are

$$W_{T_1} = W_{T_3} > W_{T_4} > W_{T_2}$$

$$W_{T_1}/W_{T_3} = 1; W_{T_3}/W_{T_4} = 1.9; W_{T_4}/W_{T_2} = 1.7$$

Substituting the rational assignments into Formula (2) and the weight ($W_{T_2}$) of sub-criteria layer $T_2$ can be derived. Substituting the weight of $T_2$ into Formula (3) and the weight ($W_{T_4}$) of sub-criteria layer $T_4$ can be derived. Similarly, the weights of other sub-criteria layers $T_3$ and $T_1$ can be derived. Finally, the weight vector of the four sub-criteria layers under criteria layer T is determined as

$$(W_{T_1}, W_{T_2}, W_{T_3}, W_{T_4}) = (0.3526, 0.1092, 0.3526, 0.1856)$$

Correspondingly, the sequences of the sub-criteria layers under criteria layer E and layer S, and the rational assignments for relative degree of importance between the sequenced adjacent layers can be determined. These are

$$W_{E_2} > W_{E_1} > W_{E_3}$$

$$W_{E_2}/W_{E_1} = 1.8; W_{E_1}/W_{E_3} = 1.7$$

$$W_{S_3} > W_{S_1} > W_{S_2}$$

$$W_{S_3}/W_{S_1} = 2.6; W_{S_1}/W_{S_2} = 1.7$$

And the weight vector is

$$(W_{E_1}, W_{E_2}, W_{E_3}) = (0.2951, 0.5313, 0.1736)$$

$$(W_{S_1}, W_{S_2}, W_{S_3}) = (0.2387, 0.1404, 0.6209)$$

**Index Weight on Overall Objective**. Using the results from (1) and (2), the weight of T1 on T, and the weight of T on overall objective can now be calculated. Finally, the weight of index T1 on overall objective can be derived as

$$W_{T_1}^s = W_{T_1} * W_T = 0.1891$$

With this procedure, the weights of the other indexes on overall objective can be determined. The results are shown in Table 4.

**Table 4.** Combination weight of indexes

| CL | SCL | W-G1 | CV | W-CV | CW | CW-CL |
|----|-----|------|----|------|----|-------|
| $T$ | $T_1$ | 0.1891 | 0.8392 | 0.1081 | 0.1486 | 0.4683 |
|    | $T_2$ | 0.0586 | 0.6782 | 0.0873 | 0.0730 | |
|    | $T_3$ | 0.1891 | 0.8641 | 0.1113 | 0.1502 | |
|    | $T_4$ | 0.0995 | 0.7261 | 0.0935 | 0.0965 | |
| $E$ | $E_1$ | 0.0489 | 0.6975 | 0.0898 | 0.0694 | 0.2297 |
|    | $E_2$ | 0.088 | 0.8743 | 0.1126 | 0.1003 | |
|    | $E_3$ | 0.0287 | 0.7083 | 0.0912 | 0.0600 | |
| $S$ | $S_1$ | 0.0712 | 0.7906 | 0.1018 | 0.0865 | 0.3020 |
|    | $S_2$ | 0.0419 | 0.7126 | 0.0918 | 0.0668 | |
|    | $S_3$ | 0.185 | 0.8743 | 0.1126 | 0.1487 | |

*Note* CL stands for criteria layer; *SCL* for sub-criteria layer; *W-G1* for weight with G1 method; *CV* for coefficient of variation; *W-CV* for weight with coefficient of variation; *CW* for combination weight; and *CW-CL* for combination weight of criteria layer

### 4.3   Index Weight Determining with Coefficient of Variation Method

**Index coefficient of variation**. With the dimensionless values of the indexes shown in Table 3, the arithmetic mean value and the standard deviation of each index can be obtained. When substituting the results into Formula (4), the coefficient of variation of each index can be determined. The results are shown in Table 4.

**Index weight determining**. When substituting the coefficient of variation values from Table 4 into Formula (5), the weight of each index can be obtained. The results are also shown in Table 4.

## 4.4 Index Combination Weight Determining

The combination weight of each index can be determined by Formula (8), with results shown in Table 4. It is important to understand the combination weight of each criteria layer is the sum of combination weight of each sub-criteria layer under the layer.

## 4.5 Final Ranking of Alternatives by Comprehensive Evaluation Value

The comprehensive evaluation value is obtained through substituting the dimensionless values in Table 3 and the combination weight in Table 4 into Formula (10). The results are shown in Table 5.

**Table 5.** Final evaluation value and ranking of alternatives

| Alternatives | Evaluation value of T-index | Rank by T | Evaluation value of E-index | Rank by E | Evaluation value of S-index | Rank by S | Comprehensive evaluation value | Final rank |
|---|---|---|---|---|---|---|---|---|
| $A_1$ | 0.1274 | 5 | 0.1896 | 2 | 0.0649 | 5 | 0.3819 | 4 |
| $A_2$ | 0.1559 | 4 | 0.1168 | 3 | 0.0736 | 4 | 0.3464 | 5 |
| $A_3$ | 0.2778 | 3 | 0.1945 | 1 | 0.2797 | 1 | 0.7520 | 1 |
| $A_4$ | 0.3066 | 1 | 0.0854 | 4 | 0.1770 | 2 | 0.5690 | 2 |
| $A_5$ | 0.2988 | 2 | 0.0000 | 5 | 0.1263 | 3 | 0.4251 | 3 |

The evaluation values are shown in Fig. 4. The following results are established: (1) A4 (long-range pressing—short-range absorption (front absorption—back pressing)) has the maximum evaluation score when ranking only by technical indices; (2) A3 (long-range pressing—short-range absorption (front pressing—back absorption)) has the maximum evaluation score when ranking by both economic indexes and safety indexes; (3) The comprehensive evaluation score of A3 (long-range pressing—short-range absorption (front pressing—back absorption)) is evidently higher than others and can be chosen as the optimal ventilation mode, and A4 (long-range pressing—short-range absorption (front absorption—back pressing)) has the second-maximum comprehensive evaluation score and can be considered as an alternative ventilation mode.

The field experiments were conducted to verify the effectiveness of the preferred ventilation mode. The result showed that there was a significant reduction of the dust concentration in 0–300 s, and the dust in the development roadway can be almost completely discharged within 1200 s, at this time the dust mass concentration remained at 0.5 mg/m$^3$ or less. Compared with other options, the ventilation mode of long-range pressing—short-range absorption (front pressing—back absorption) is more efficient, while it is more obvious for reducing the concentration of dust.
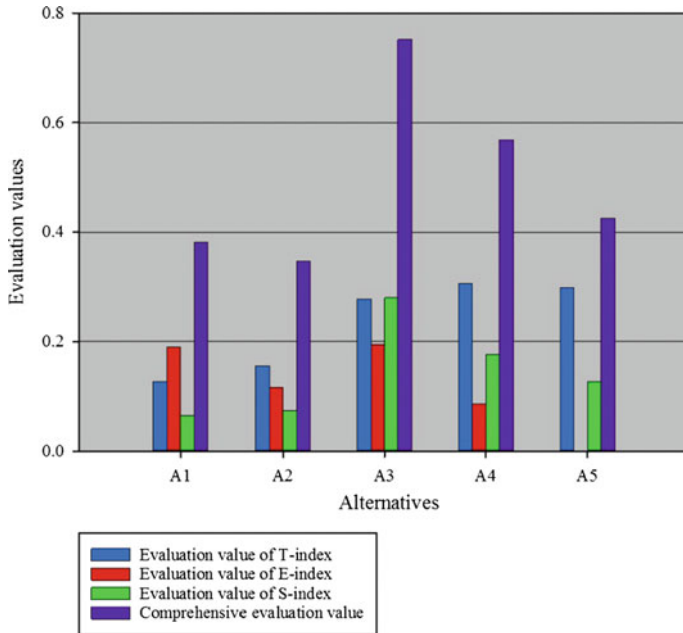
**Fig. 4.** Bar graph of evaluation scores for alternatives

## 5    Conclusions

To comprehensively evaluate the different development face ventilation arrangement for the optimal choice, a novel method for calculating the comprehensive evaluation value of alternatives was introduced to select the best ventilation scheme for a development face. By considering the advantages of the subjective and objective weight determining methods, this study used the above mentioned two methods to establish the optimum evaluation model of development face ventilation mode. The conclusions were obtained as follows.

(1)  According to the weight calculation results, the technical index was determined with the highest weight, the safety index weight was the second, and the economic index weight was the lowest. This shows that the effective and sufficient air supply is the most important at the development face, followed by the stability and quality of air supply, while the economic indexes are not the main factors of ventilation mode selection.

(2)  The comprehensive evaluation value of the optimal ventilation mode is the highest, but not every criteria layer index's evaluation value of the final choice is the highest, the evaluation value of one criterion layer index is even in the medium level. Therefore, the optimal choice of ventilation mode is determined by the comprehensive evaluation of all the indexes, it doesn't compare each index of the inspected options respectively.

(3) The case study considered in this paper verified that the proposed approach is able to rank the alternative development face ventilation mode reasonably. It compensates for the disadvantages of the index single weight determining method, for it considers the experience and wisdom of experts and can reflect the new changes of objective conditions.

This study provides a more direct method for analyzing and evaluating different ventilation modes, which can meet the demands for optimization of development face ventilation modes in mine. However, the evaluation indexes in this study apply to metal mine. Further study is needed to establish the evaluation indexes for other type mine.

# References

1. Ren, T., Wang, Z.W., Graeme, C.: CFD modelling of ventilation and dust flow behaviour above an underground bin and the design of an innovative dust mitigation system. Tunn. Undergr. Space Technol. **41**, 241–254 (2014)
2. Zhang, G., Li, L.X., Ji, H.G., Xiao, K.R., Yin, G.G., Song, L.: In situ investigation of gaseous pollution in the ramp of an underground gold mine. Indoor Built Environ. **23**(2), 293–298 (2014)
3. Farshid, G.S., Abdulrahman, B., Farhad, F.: Application of local exhaust ventilation system and integrated collectors for control of air pollutants in mining company. Ind. Health **50**, 450–457 (2012)
4. Cheng, J., Zhou, F., Yang, S.: A reliability allocation model and application in designing a mine ventilation system. Iran. J. Sci. Technol. Trans. Civil Eng. **38**(C1), 61–73 (2014)
5. Jundika, C.K., Agus, P.S., Arun, S.M.: CFD simulation of methane dispersion and innovative methane management in underground mining faces. Appl. Math. Model. **38**, 3467–3484 (2014)
6. Cheng, J.W., Yang, S.Q.: Data mining applications in evaluating mine ventilation system. Saf. Sci. **50**, 918–922 (2012)
7. Maleki, B., Mozaffari, E.: A comparative study of the iterative numerical methods used in mine ventilation networks. Int. J. Adv. Comput. Sci. Appl. **7**(6), 356–362 (2016)
8. Bascompta, M., Castanon, A.M., Sanmiquel, L., Oliva, J.: A GIS-based approach: influence of the ventilation layout to the environmental conditions in an underground mine. J. Environ. Manage. **182**, 525–530 (2016)
9. Mirhedayatian, M., Jelodar, M.J., Adnani, S., Akbarnejad, M., Saen, R.F.: A new approach for prioritization in fuzzy AHP with an application for selecting the best tunnel ventilation system. Int. J. Adv. Manufact. Technol. **68**, 2589–2599 (2013)
10. Sa, Z.Y., Wang, Y., Zhang, H.N., Song, H., Li, F.: Optimization of mine ventilation system based on grey system theory. In: 7th International Symposium on Safety Science and Technology, pp. 1683–1687. Hangzhou, China (2010)
11. Wu, L.Y., Yang, Y.Z.: Improved grey correlative method for risk assessment on mine ventilation system. In: 4th International Conference on Mechanical and Electrical Technology, pp. 2629–2633. Kuala Lumpur, Malaysia (2012)

12. Wang, H.: Study on reliability theory and method for mine ventilation system based on artificial neural network. Dissertation, Liaoning Technical University, Fuxing (2004) (in Chinese)
13. Karacan, C.Ö.: Development and application of reservoir models and artificial neural networks for optimizing ventilation air requirements in development mining of coal seams. Int. J. Coal Geol. **72**, 221–239 (2007)
14. Kozyrev, S.A., Osintseva, A.V.: Optimizing arrangement of air distribution controllers in mine ventilation system. J. Min. Sci. **48**(5), 896–903 (2012)
15. Deng, L.J., Liu, J.: New approach for ventilation network graph drawing based on Sugiyama method and GA-SA algorithm. Comput. Model. New Technol. **18**(8), 45–49 (2014)
16. Shriwas, M., Calizaya, F.: Application of genetic algorithms for solving multiple fan ventilation networks. In: Application of Computers and Operations Research in the Mineral Industry—Proceedings of the 37th International Symposium, pp. 488–498. Alaska, America (2015)
17. Zhang, M.: The research of speed control system based on intelligent PID controller to mine local ventilator. In: 2011 Second International Conference on Mechanic Automation and Control Engineering, pp. 858–861. Hohhot, China (2011)
18. Lowndes, I.S., Fogarty, T., Yang, Z.Y.: The application of genetic algorithms to optimise the performance of a mine ventilation network: the influence of coding method and population size. Soft. Comput. **9**, 493–506 (2005)
19. Guo, Y.J.: Comprehensive Evaluation Theory and Method. Science Press, Beijing (2002). (in Chinese)
20. Zhuang, P., Li, Y.X.: Appraisement model and empirical study of enterprise investment risk based on G1-coefficient of variation.Soft. Science **25**(10), 107–112 (2011). (in Chinese)
21. Gong, J., Hu, N.L., Cui, X., Wang, X.D.: Optimization of drifting ventilation method for high-altitude mine. Sci. Technol. Rev. **33**(4), 56–60 (2015). (in Chinese)

# Optimization of Ventilation System in Wongawilli Mining Face with a Continuous Miner

Du Tao[(⊠)]

Taiyuan Research Institute of CCTEG, Taiyuan City, Shanxi 030006, China
Dutao0350@163.com

**Abstract.** The ventilation system at the Wongawilli mining face using a continuous miner was introduced. A complete air pressure ventilation system was not formed in the existing ventilation system. The working face needs large air volume, but the air velocity in the roadway is low, and consequently the dust cannot be effectively controlled. A return airway for recovery area in construction area is proposed in this paper. At the same time, auxiliary fan was used to strengthen the air supply to the working face to optimize the ventilation system. The ventilation system was analyzed using minimum weighted relative error method, which further showed that the ventilation method using full pressure in mine combined with the auxiliary fan in the working face was the optimal ventilation method.

**Keywords:** Continuous miner · Wongawilli · Boundary coal mining
Ventilation system · Minimum weighted relative error method

## 1 Introduction

The Wongawilli mining using continuous miner mining method was first originated in Australia, which has the advantages of combined mining and development, fast coal mining, less initial equipment investment, and strong mobility and high mechanization, safety and high efficiency in boundary coal mining and irregular block mining. This method has been adopted in many mining areas in Shanxi, Shaanxi, and Inner Mongolia in the past 30 years. However, due to the limitation of stopping conditions, it is generally difficult to establish a complete ventilation system in the working face under the mining process conditions, and the stability of the air flow in the working face is poor, which is likely to cause potential safety hazards [1]. Therefore, analyzing and optimizing the supporting ventilation system for the process is of great significance for ensuring the safe and efficient production of the working face.

## 2   Ventilation Method for the Continuous Miner Wongawilli Mining Face

As continuous miner 'Wongawilli' mining process is mostly used for mining boundary coal, the shape of the working face is extremely irregular, and it is also unavoidable to be adjacent to the old empty area. Consequently, the mining roadway is arranged irregularly, resulting in ventilation system is complicated and easy to leak into the adjacent old empty areas. At the same time, the ventilation system of working surface is vulnerable to poisonous and harmful gases in the old empty areas. Therefore, the large amount of air distribution, low wind speed, poor system stability, and high dust concentration are the basic characteristics of the ventilation of "Wangi Willy" mining method.

The mining of 24206 corner or boundary coal in the Pingshuo No. 2 mine employs the continuous coal miner Wongawilli mining process, arranged according to the shape characteristics of the segment and the existing roadway [2, 3]. Local fans are used for ventilation during tunneling of all branch roadways and stopping branch roadway prior to cutting through. Figure 1 shows the ventilation system.
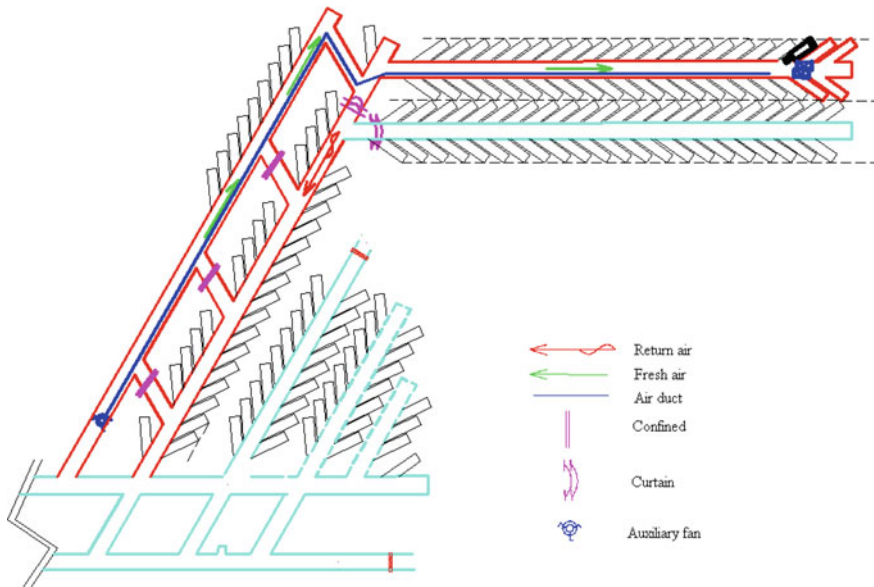


Fig. 1.   Ventilation system of Wongawilli mining face

## 3   Optimization of Ventilation System

The above mentioned ventilation system has poor ventilation conditions, and the inlet and return air lanes are juxtaposed and the air leakage is large. The working face is diffused ventilation during stopping, in particular, fresh airflow flushes the working

face and then enters the return air lane where stopping is performed. The working staff in the working face is in return air. The air quality is poor, and the dust concentration is high, causing great harm to people and causing a lot of hidden dangers. Therefore, scientific and rational optimization of the ventilation system can ensure safe and efficient production.

In order to avoid the ventilation air methane of working face flow through the work lanes and improve the working environment quality, a return air passage can be constructed in the stopping area, and the connection lanes can be reasonably arranged according to the actual conditions of the working surface to reduce the influence of the roof falling from the gob area on the return air passage [4]. This can ensure the smooth return air passage, but also to facilitate the operation of the equipment such as the shuttle car; on the other hand, the working surface has many ventilation facilities, large air leakage, poor system reliability, weak disaster resistance, so the local fan can be used to strengthen the supply of wind to working face [5]. Figure 2 shows the ventilation system optimization.

The application features and advantages and disadvantages of the above three ventilation system schemes are not the same. See Table 1 for details.

## 4 Analysis of Ventilation System

The above two optimization schemes have certain advantages over the original scheme, but both have their own advantages and disadvantages. Therefore, further comprehensive analysis is needed to determine the safe, reliable and economically reasonable ventilation system. Use the length of each lane and the 100 m wind resistance $R100 = 0.072 \ N^2$ s/m 8 to calculate the wind resistance of each roadway. The total air intake is 18 $m^3$/s. Calculate the ventilation resistance of the above three solutions respectively. The results are 11.2, 18.6, 9.5 Pa respectively. This shows that the third ventilation system scheme has the least resistance of ventilation network and is more economical and reasonable [6].

Whether the ventilation system is rational or not depends on whether it can provide stable and reliable air flow to the target site and whether it is easy to manage, that is, it depends on the ventilation network and the ventilation structure [7]. The analysis of the above ventilation system is shown in Table 2.

In order to ensure the scientificity of the optimization scheme, minimum weighted relative error method is used for further analysis.
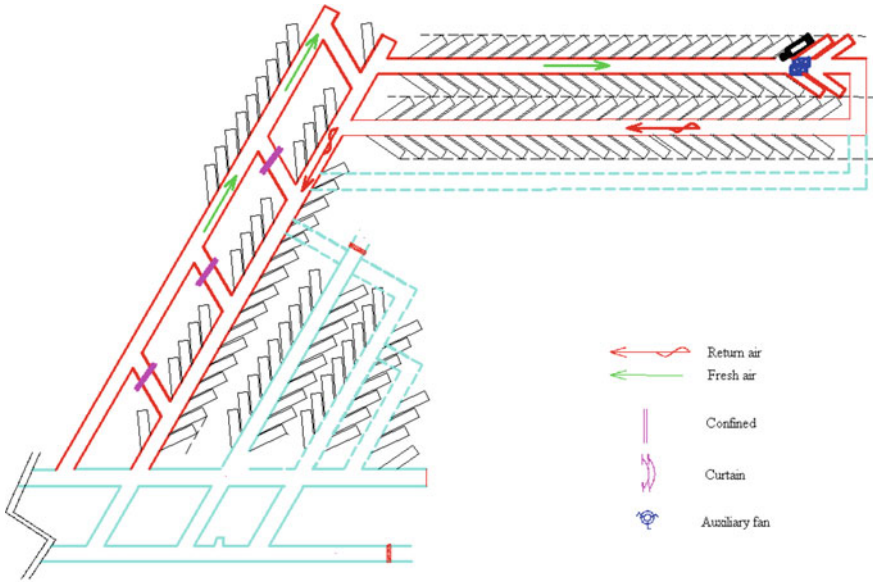
(II) Ventilation with total pressure
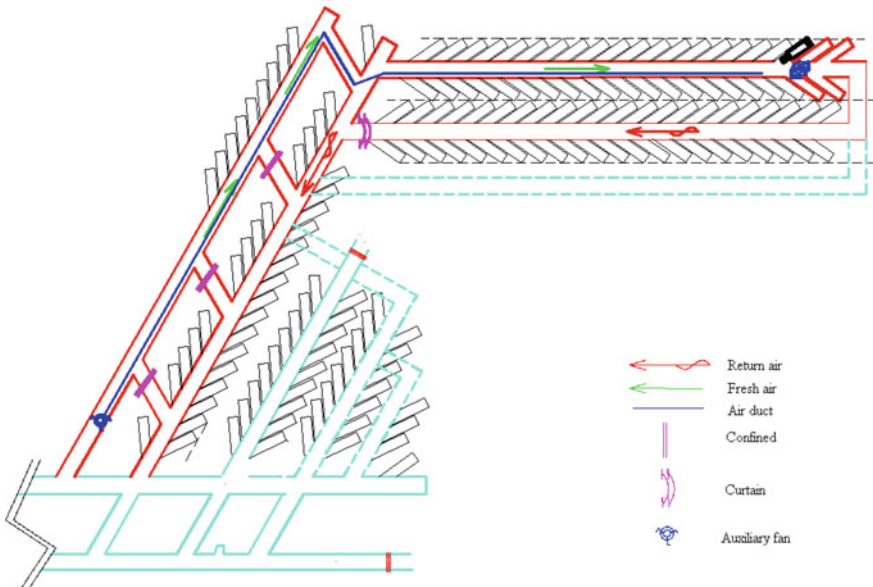


(III) Ventilation system of local fan combined with total pressure

**Fig. 2.** Ventilation system optimization

**Table 1.** Scheme comparison

| Item | S. no. | Ventilation method | Feature | Weakness |
|---|---|---|---|---|
| Before optimization | I | Original ventilation system | The main and auxiliary transportation roadway in the section are the inlet and return air lanes; the stopping working face uses the local fan to supply the air; the ventilation air methane on the flushing working face is returned to the return roadway through the stopping branch roadway | The working face relies on the local fan to supply the air, and the reliability is poor; the operating environment is of poor quality |
| Optimized | II | Full pressure ventilation system | Dig the area boundary air return passage, and the branch road and the return air passage are connected when the working face is stopping to form a complete wind pressure ventilation system, and the ventilation is performed by using the mine air flow | Ventilation facilities are many; ventilation management is difficult; ventilation facilities interfere with the transport of coal shuttles; it is impossible to achieve pressurized ventilation and is vulnerable to poisonous and harmful gases in old empty areas |
| | III | Auxiliary fan and full pressure mixed ventilation system | Dig the area boundary air return passageway, the branch road and the return air passage pass through when the working face is stopping, thus forming a complete-air-pressure ventilation system, using the mine air flow for ventilation, installing a local fan in the inlet roadway of working face to strengthen the air supply for the working face | Equipment is too much; management is complex |

**Table 2.** Analysis of ventilation systems

| S. no. | Index | Schemes | | |
|---|---|---|---|---|
| | | I | II | III |
| 1 | Confined/unit | 3 | 3 | 3 |
| 2 | Curtain/unit | 2 | 0 | 1 |
| 3 | Auxiliary fan/unit | 2 | 0 | 1 |
| 4 | Ventilation network | Easy | Complex | Easy |
| 5 | Work amount (m) | 0 | 30 | 30 |
| 6 | Air volume of face | Unstable | Unstable | Stable |

### 4.1   Indices of Ventilation System

The ventilation system of Wongawilli mining is characterized by large air leakage, unstable air volume, difficult ventilation management, poor ventilation quality of the working surface, etc. The evaluation indicators of the ventilation system should fully reflect these characteristics, and each indicator should have independent physical meanings, consistent with the principles of science, measurability, comparability and conciseness. Hence, the main criteria for determining the ventilation system are five items, namely, ventilation facilities, local ventilators, ventilation networks, ventilation quality of working face, and engineering quantities. According to the degree of importance of each index to the ventilation system program, the weights of each index obtained using the "relative importance sequence matrix method" are 6, 4, 8, 10, and 3, respectively.

### 4.2   Optimization Step for Minimum Weighted Relative Error Method

This method converts indicators of different natures and different factors to non-dimensional quantities to calculate relative deviation values δ ij (i is the index of the scheme; j is each scheme). The weights of each index are evaluated comprehensively to determine the optimal plan. The specific evaluation procedure is as follows:

(1) **Develop a ventilation system plan**
(2) **Calculate or determine the index values for each scheme**

$$f_i = \left| f_{i1}, f_{i2}, \ldots f_{ij}, \ldots, f_{in} \right| \tag{1}$$

(3) **Determine the standard index value**

$$f_i^0 = f_{i\max} \text{或} f_{i\min} \tag{2}$$

(4) **Calculate the relative deviation of each index**

$$\delta_{ij} = \frac{\left| f_i^0 - f_{ij} \right|}{f_i^0} \tag{3}$$

(5) **Relative deviation matrix** It's constituted by the relative deviation values calculated according to the indicators of each scheme.

$$|\delta ij| = \begin{bmatrix} \delta_{11} & \delta_{12} & \dots & \delta_{1i} & \dots & \delta_{1n} \\ \delta_{21} & \delta_{22} & \dots & \delta_{2j} & \dots & \delta_{2n} \\ \vdots & \vdots & \dots & \vdots & \dots & \vdots \\ \delta_{m1} & \delta_{m2} & \dots & \delta_{mj} & \dots & \delta_{mn} \end{bmatrix} \tag{4}$$

(6) **Calculate the comprehensive evaluation index**

$$K_j = \frac{1}{W_a} \sqrt{\sum_{i=1}^{m} (\delta_{ij} W_i)^2} \tag{5}$$

$$W_a = \frac{\sum_{i=1}^{m} W_i}{m} \tag{6}$$

(7) **Determine the optimal solution for the ventilation system**. The corresponding scheme with the smallest comprehensive evaluation value is the optimal one.

In the above formula, i—the number of the indicator, j—serial number of the program, fij—Index value, $\delta_{ij}$—Relative deviations of indicators, Wi—The weight of the indicator, Wa—The average weight.

## 4.3 Analysis and Evaluation of Ventilation System

The indicators and standard value of various indicators of above three types of ventilation program are shown in Table 3.

Table 3. Evaluation indexes and standards of ventilation system

| S. no. | Index | Value | | | Standard value |
|---|---|---|---|---|---|
| | | I | II | III | |
| 1 | Ventilation facilities/unit | 5 | 3 | 4 | 2 |
| 2 | Auxiliary fan/unit | 2 | 0 | 1 | 0 |
| 3 | Ventilation network | 10 | 4 | 10 | 10 |
| 4 | Work amount (m) | 0 | 30 | 30 | 0 |
| 5 | Air volume of face | 2 | 5 | 10 | 10 |

Calculation of the ratings of each indicator is shown in Table 4. The comprehensive evaluation index of each program is Wa = 6.2, K1 = 1.52, K2 = 1.47, K3 = 1.02. The optimal scheme is minimum weighted relative error method. So the third scheme is the optimal scheme for ventilation system of room and pillar mining. The analysis result is consistent with the on-site application results. The working surface of the scheme is the full wind pressure of the mine combined with local ventilation. Stable air flow is

provided at where local fan is installed. Local fans can supply large amount of air, which can ensure air requirement of each site; at the same time, the ventilation system has strong resistance to disasters. Once the local fan stops, personnel can quickly withdraw to the main and auxiliary roadways.

**Table 4.** Assessed value of the ventilation system

| Index | Weight | Evaluated value $(\delta_{ij}W_i)^2$ | | |
|---|---|---|---|---|
| | | I | II | III |
| Ventilation facilities/unit | 6 | 0 | 36 | 36 |
| Auxiliary fan/unit | 4 | 16 | 0 | 4 |
| Ventilation network | 8 | 0 | 23.04 | 0 |
| Work amount (m) | 3 | 9 | 0 | 0 |
| Air volume of face | 10 | 64 | 25 | 0 |
| $\frac{1}{W_a}\sqrt{\sum_{i=1}^{m}(\delta_{ij}W_i)^2}$ | | 1.52 | 1.47 | 1.02 |

## 5  Conclusion

The mining face of 24206 boundary coal mining of Pingshuo No. 2 mine in the timely adjustment of the ventilation system in the mining process, using full wind pressure combined with local fan, not only to meet the wind requirement of working face, but also prevent intrusion of poisonous and harmful gases in the adjacent open space to ensure safe stopping of the working face.

a. In order to ensure the stability of air flow of working face in the boundary coal Wongawilli mining process with the continuous miner, the ventilation system with full wind pressure of the coal mine combined with auxiliary fans for enhanced ventilation shall be adopted.
b. In order to ensure the air volume at where the lauxiliary fan is installed, the cross connection lanes of the preparation lanes for the inbound and outbound wind shall be temporarily sealed, as shall meet the requirements of easy installation, reusability, strictness, and no leakage.
c. Minimum weighted relative error method comprehensively considers the influencing factors of the ventilation system, and the evaluation results are consistent with the actual conditions, providing theoretical support for the optimization of the ventilation system.
d. There are many structures and facilities in the ventilation system of Wongawilli mining method with the continuous miner, and management should be strengthened to ensure safe production.

# References

1. Guoshu, Z.: Ventilation Safety. China University of Mining and Technology Press, Xuzhou (2007)
2. Zhi-fa, L., Jian-ming, S., Jin, P., et al.: Application of Wongawilli coal mining method in Shendong mining area. Coal Sci. Technol. **30**, 11–14 (2002)
3. Jian-wu, Y.: Analysis on shortwall mechanized Wangeviry mining method applied to Datong mine area. Coal Sci. Technol. **10**(4), 23–25 (2005)
4. Yunxi, T.: Mine Ventilation System Optimization. Coal Industry Press, Beijing (1992)
5. Run-qiu, L., Shi-liang, S., Xin, P.: Summarization of safety assessment methods for mine ventilation system. China Saf. Sci. J. **18**(1), 112–118 (2008)
6. Yun-zhen, T., Chun-hua, L., Zhen-yi, L., et al.: Ventilation systems of room and pillar mining method. J. China Coal Soc. **26**(1), 67–70 (2001)
7. Ji-bo, L., De-qing, M., Yong-guo, S., et al.: Comprehensive prevention and control of CO release from small coal mine under negative pressure ventilation. Saf. Coal Mines **33**(8), 25–27 (2002)

# Ventilation-on-Demand System in Pulang Copper Mine

Qi-fa Ge[1,2(✉)], Wei-gen Zhu[2], Wei-guo Zhang[2], Qing-gang Chen[2], and Zhuo-ming Yang[2]

[1] University of Science and Technology, Beijing, China
geqf@enfi.com.cn
[2] China ENFI Engineering Corporation, Beijing, China

**Abstract.** A Ventilation-on-Demand (VOD) system can provide the required fresh air to a specific area underground at will, based on the balance between intake air supply and demand. The system consists of three parts, a monitor system (MS), the ventilation system (VS) and a VOD control system. MS is responsible of monitoring the microclimate environment of VS, number of personnel, number of vehicles, regulators and other essential variables to ensure quality and quantity of air underground. This paper introduced the mine VOD system in Pulang Copper Mine, used the three-dimensional ventilation simulation Ventsim Visual™ software to simulate various scenarios of this mine. Simulation results show that a significant energy can be saved by using a VOD system.

**Keywords:** VOD · Microclimate environment monitoring · Fan frequency control · Energy saving

## 1 Introduction

After years of mining, near-surface resources have been quickly depleting. A significant number of mining operations have exceeded 1500 m from surface. With the increase of mining intensity and mining depth, to deliver adequate amount of intake air for deep underground workings have become increasingly challenging. Ventilation and refrigeration also consumes a significant amount of electricity, averaging 30–40% of the total mine power required, and even reaching 50% in some cases. This would help an operation to significantly improve it energy efficiency. To counter increasing energy consumption due to increased mining depth, VOD has been proposed in several overseas operations with varying degree of success. This system has shown to improve the underground operating environment while significantly reduce ventilation energy consumption.

## 2   VOD System

VOD system is mainly composed of remote control ventilation equipment, surface communication system, equipment and personnel positioning system. VOD system can provide required fresh air at specific locations and improve mine ventilation efficiency. The VOD communication platform diagram is shown in Fig. 1.
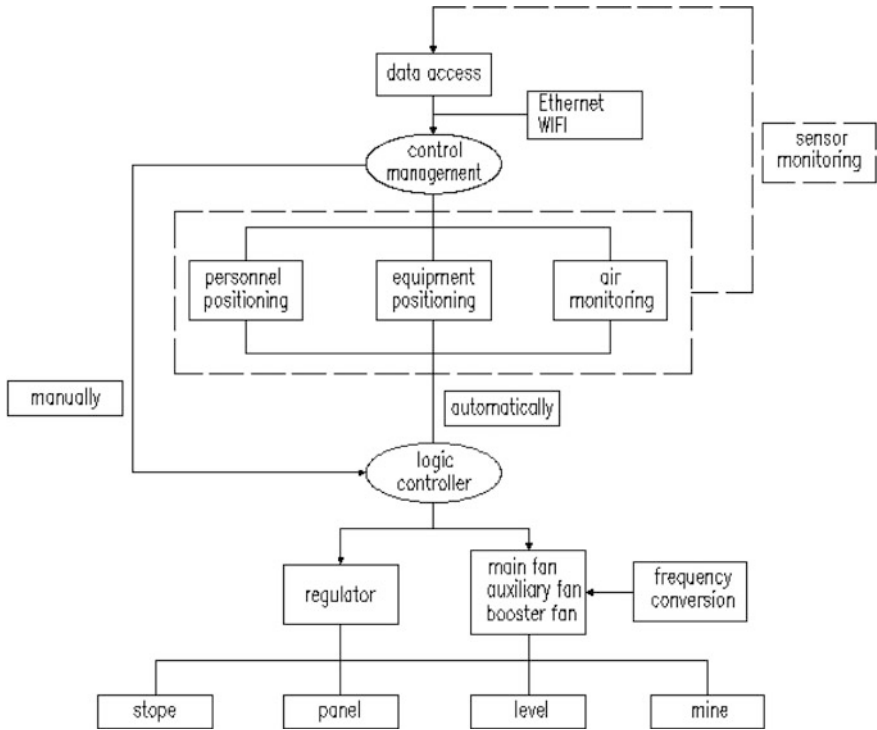


**Fig. 1.** Communication platform diagram

Various sensors are installed in underground main airways, tunnels and chambers to achieve the real-time monitoring airflow, fan frequency and power consumption, and other atmospheric parameters such as temperature, humidity, air velocity, and $NO_2$, $O_2$, CO concentration.

Personnel and vehicles underground are equipped with identification cards. VOD can recognize accurate location of all workers and vehicles through a decentralized communication base station (with the function of unlimited communication and positioning).

Collected data was transmitted to the surface VOD control system through the underground communication system. The three-dimensional ventilation simulation

software can perform automatic simulation based on real-time data, calculate and update required air quantity of all areas. By comparing the difference between actual air quantity and required air quantity, VOD system can adjust and control the fan and regulator remotely in real time, so as to meet safety requirements underground.

## 3    VOD System Design in Pulang Copper Mine

Pulang Copper Mine designs an integrated digital network communication system. Using the communication feature, the System can integrate underground personnel and equipment location, toxic and hazardous gas concentration data and fan operation.

### 3.1    Ventilation System

Pulang Copper Mine uses block caving method with a production of 12.5 million t/a.

Fresh air enters the mine from 3850 m Intake Adit, 3600 m Intake Adit, 3660 m adit and 3720 m Adit. Airflow is distributed by auxiliary fans underground, and return air is exhausted to the surface through the 3700 m Exhaust Adit, South Exhaust Shaft and 3540 m Belt Conveying Adit.

According to ventilation requirements at Pulang, the ventilation system consists of three stations as shown in Table 1.

**Table 1.** Multistage station layout of Pulang copper mine

| Station no. | Location | Operation mode | Design air quantity (m³/s) | | High altitude pressure (Pa) | |
|---|---|---|---|---|---|---|
| | | | Early | Later | Early | Later |
| I | 3850 m intake adit | Forced | 250 | 260 | 663 | 621 |
| I | 3600 m intake adit | Forced | 255 | 260 | 1221 | 1150 |
| II | Return air raise crosscut in 3700 m exhaust level | Exhausted | 25–35 | 25–35 | 350–600 | 350–600 |
| III | 3700 m exhaust adit | Exhausted | 250 | 300 | 1160 | 1847 |
| III | South exhaust air shaft | Exhausted | 380 | 330 | 805 | 1190 |

Pulang copper mine ventilation system schematic diagram is shown in Fig. 2.

### 3.2    VOD System

**VOD Criterion**. According to Pulang's production plan, the mining process is divided into four work areas (Table 2).

Condition 1, between 15: 00 and 16: 00 with air quantity of 650 m³/s;

Condition 2, two time periods [17: 00—22: 00] and [09: 00—14: 00] with an average air quantity of 560 m³/s.

Condition 3, between 01: 00—06: 00, with air quantity of 450 m³/s;
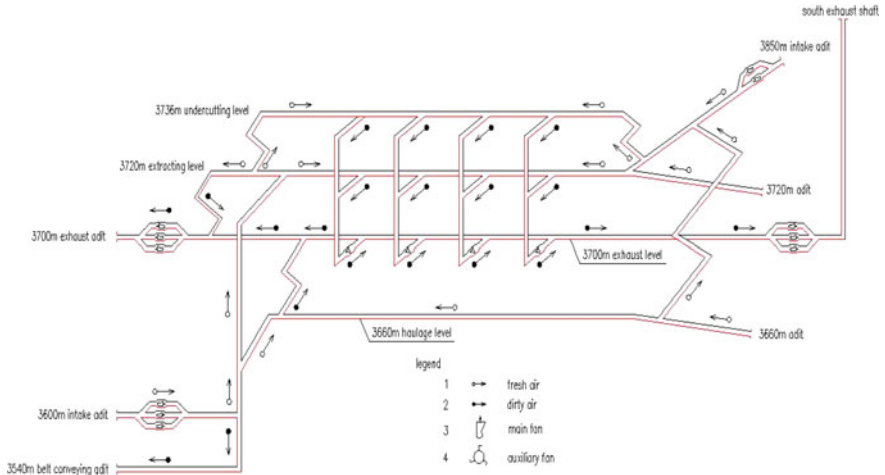
**Fig. 2.** Ventilation system schematic diagram of Pulang copper mine

**Table 2.** Work conditions at main levels

| Main level | Work condition 1 (full load) 650 m³/s | Work condition 2 (normal load) 560 m³/s | Work condition 3 (moderate load) 450 m³/s | Work condition 4 (light load) 300 m³/s |
|---|---|---|---|---|
| 3736 m | 3 undercutting faces | 2 undercutting faces | 1 undercutting faces | 1 undercutting faces |
|  | 2 excavating faces | 1 excavating faces | 1 excavated faces | 1 undercutting blasting faces |
|  | 1 mucking faces | 1 mucking faces | 1 mucking faces | 1 excavating blasting faces |
| 3720 m | 16 extracting faces 2 secondary crushing faces 2 drilling faces 1 mucking faces | 16 extracting faces 2 drilling faces 1 mucking faces | 12 extracting faces 1 drilling faces 1 mucking faces | 6 extracting faces 1 blasting faces |
| 3660 m | 6 trains working | 6 trains working | 4 trains working | 1 train working or maintaining |
| Proportion | 8% (2 h) | 50% (12 h) | 25% (6 h) | 17% (4 h) |

Condition 4, two time periods [23: 00—24: 00] and [07: 00—08: 00], with an average air flow of 300 m³/s.

Work conditions for the entire day are shown in Fig. 3.

**Equipment and Personnel Positioning and identification**. Staff are equipped with identification cards in the underground. Through the communication base station (wireless communication and positioning function) at every level, System can
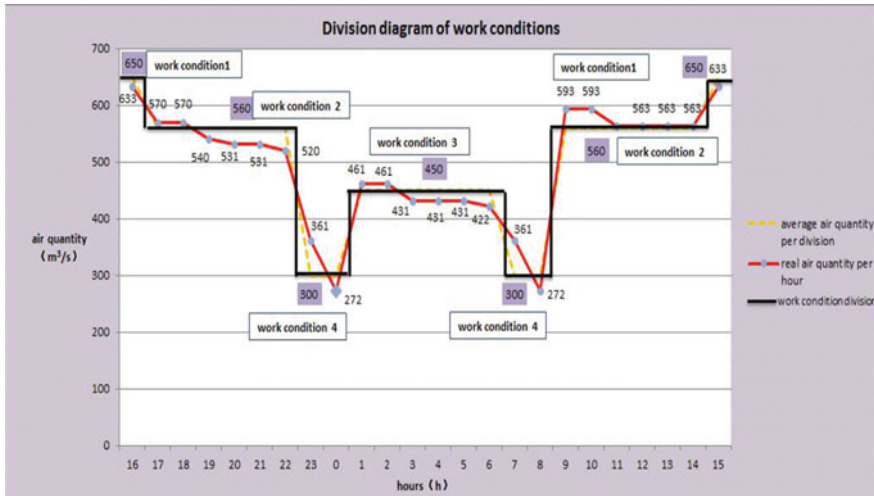
**Fig. 3.** Division diagram of work conditions in Pulang copper mine

accurately record the time of workers entering or leaving the mine, and display current workers ID number and whereabouts underground in real time. Through the positioning system, managers will have information on the number of workers on duty, as well as monitor the real-time movement of personnel underground.

The underground wireless communication system is developed based on the mine personnel positioning system, communication station both have the function of personnel positioning and wireless communication. Once the staff positioning platform has been built, the mine will achieve wireless communication by directly purchasing wireless handheld platform and wireless vehicular platform.

**Equipment Monitoring**. Pulang copper's mine monitoring system consists of sensors, monitoring substation, switch and surface monitoring central station. According to the Pulang copper mine condition, the main gases are carbon monoxide, nitrogen dioxide. In particular areas, sensors of air velocity, pressure and fan switch need to be installed.

Signal is transferred to monitoring substations by sensors, which then send the electrical signal to switch in CAN bus. After receiving, switch can send it to surface monitoring center station by the optical cable. Surface monitoring center station can achieve comprehensive monitoring of the underground production environment and raise the alarm timely.

**Adjustable Regulators and Mine Fan**. Under the VOD system in Pulang Copper Mine, VOD system can directly realize remote automatic control management and ensure timely and accurate adjustment by monitoring the parameters such as the air quantity, pressure and regulators like automatic air doors, adjustable air doors and adjustable air window.

(1)  Main adjustable regulators

Regulators (Table 3) in Pulang copper mine are designed to be controlled remotely.

**Table 3.**  Main adjustable regulators

| No. | Air quantity (m³/s) | Regulator type | Installation location | Quantity |
|---|---|---|---|---|
| 1 | 0.1 | Automatic air door | Crosscut of storehouse for Blasting and Explosive Materials in 3720 m level | 1 |
| 2 | 5.6 | Automatic air door | Maintenance chamber for trackless equipment at 3720 m level | 1 |
| 3 | 1.8 | Automatic air door | Maintenance chamber for trackless equipment at 3720 m level | 1 |
| 4 | 2.6 | Adjustable air door | Crosscut of elevator raise at 3720 m level | 1 |
| 5 | 6.9 | Adjustable air door | Crosscut of elevator raise at 3660 m level | 2 |
| 6 | 2.6 | Adjustable air door | Crosscut of elevator raise at 3660 m level | 1 |
| 7 | 4.8 | Adjustable air door | Crosscut of intake raise at 3660 m level | 1 |
| 8 | 16.5 | Adjustable air window | Crosscut of exhaust raise at crushing station | 1 |
| 9 | 46.8 | Adjustable air window | Ramp at 3660 m level | 1 |

(2)  Variable-frequency Fan

Fans in Pulang copper mine are designed to be variable-frequency.

(1)  Variable-frequency booster fan

According to the actual situation of the Pulang Copper Mine, the booster fan is mainly used for the dead end to remove the gas and dust.

In many mines, booster fan has to be moved frequently, which can cause remote control operation problems and huge energy waste. According to the VOD system of Pulang Copper Mine, A VOD intelligent control box with mechanical & electrical integration is being researched. The control box integrates all the electrical components of on-site control box and low-pressure plate. It can be installed on the booster fan and move together, as well as be remotely controlled according to temperature and humidity conditions.

(2)  Variable-frequency main fan and auxiliary fan

Main fan and auxiliary fan air quantity intelligent adjustment is based on the mine total air quantity changes of 4 work conditions (Table 2). Fan layout can be seen in Table 1.

VOD systems mainly monitors the pressure, air velocity and start-stop state of the main fan and auxiliary fan. It analyses the monitoring data from the underground and then gives the order. The air quantity is adjusted mainly by frequency controlling.

### 3.3     Pulang Copper Mine VOD System Energy Saving Analysis

According to the VOD system design in Pulang Copper Mine, this paper simulated all work conditions of the mine with 3D ventilation simulation software Ventsim Visual$^{TM}$. Ventilation model is shown in Fig. 4, and frequency settings of fans are shown in Table 4.
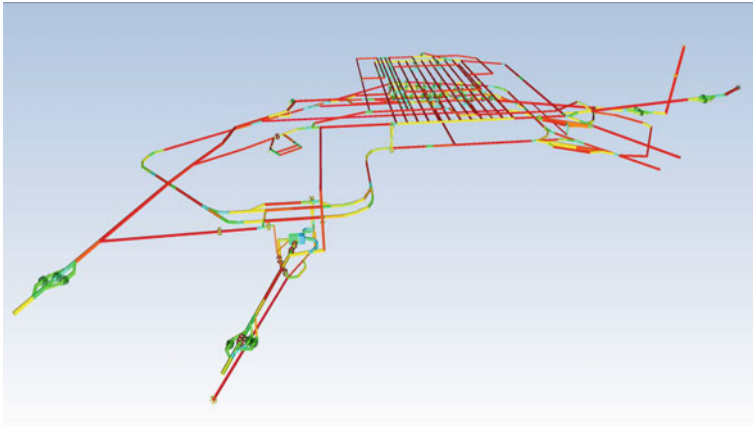


**Fig. 4.** Three-dimensional ventilation simulation software Ventsim VisualTM ventilation model

Fan output power decreases under the frequency control, which means energy conservation. Power cost of fan is set as 0.1 US dollars/kwh, and the annual simulation power costs of four work conditions are shown in Table 5.

As seen from the above table, on the basis of providing sufficient air flow for different work conditions under VOD system, the annual power cost of fans gradually reduces with the air quantity declining. If the Pulang copper mine takes a fixed air quantity annually of 650 m$^3$/s, the mine's annual power cost is 2,152,190 dollars, while the cost is 979,072 dollars under VOD system, saving 1,173,118 dollars, 54.5% less.

**Table 4.**  Fan frequency conversion scheme

| Station no. | Specification | Blade angle | Work condition 1 (full load) 650 m³/s | | Work condition 2 (normal load) 560 m³/s | | Work condition 3 (moderate load) 450 m³/s | | Work condition 4 (light load) 300 m³/s | |
|---|---|---|---|---|---|---|---|---|---|---|
| | | | Speed (%) | Quantity (m³/s) | Speed (%) | Quantity (m³/s) | Speed (%) | Quantity (m³/s) | Speed (%) | Quantity (m³/s) |
| I (3850 m intake adit) | K40-8-№26 | 29 | 100 | 261.9 | 85 | 227.2 | 75 | 195.1 | 45 | 121.3 |
| I (3600 m exhaust adit) | K45-6-№20 | 40 | 100 | 259.6 | 75 | 203.7 | 60 | 161.0 | 35 | 101.2 |
| II (crosscut of return air raise in 3700 m exhaust level) | K40-6-№15 | 29 | 80–100 | 25–35 | 70–80 | 25–30 | 50–60 | 15–20 | 35–40 | 10–20 |
| III (3700 m exhaust adit) | K45-6-№20 | 35 | 100 | 263.2 | 90 | 230.7 | 65 | 170.0 | 45 | 112.6 |
| III (South exhaust shaft) | K40-8-№26 | 29 | 96 | 361.9 | 85 | 309.1 | 70 | 253.5 | 45 | 160.1 |

**Table 5.** Annual power cost of Pulang copper mine ventilation network

| Economic indicators | Work condition 1 | Work condition 2 | Work condition 3 | Work condition 4 | Total |
|---|---|---|---|---|---|
| Annual power cost ($) | 2,152,190 | 1,253,128 | 610,520 | 162,960 | |
| Time proportion (%) | 8 | 50 | 25 | 17 | 100 |
| Each work condition annual power ($) | 172,175 | 626,564 | 152,630 | 27,703 | 979,072 |

## 4    Conclusion

This paper analyzed the ventilation problems faced in deep mines in the world, and introduced the development, composition and function of VOD system. VOD system in Pulang copper mine was designed and divided into four work conditions. This paper simulated all work conditions by using three-dimensional ventilation simulation software Ventsim Visual$^{TM}$. The results show that the VOD system has obvious energy-saving effect on mine energy consumption.

## References

1. Liu, J., Xie, X.P.: Principle of energy savings of multi-fan and multistage fan station ventilation system. Nonferrous Met. **5**, 71–74 (2010). (In Chinese)
2. Zhang, G.J., Zhang, F.M., Hou, Y.F.: Research for intelligent control system of local ventilator in mine. Colliery Mech. Electr. Technol. **2**, 7–12 (2010). (In Chinese)
3. Wang, T.T.: Frequency conversion technology and its application in main fan of mine. Coal **19**(3), 43–45 (2010). (In Chinese)
4. Jia, A.M.: Remote monitoring and energy saving research of multistage fan station ventilation. Met. Mine **6**, 113–119 (2012). (In Chinese)
5. Jia, A.M., Huang, S.Y.: Application of remote monitoring technology in Cangshan Iron mine. Mod. Min. **7**, 75–78 (2012). (In Chinese)
6. Xie, X.P., Han, M.H.: Research on informationization and intellectualization of mine ventilation. Yunnan Metall. **41**(5), 1–7 (2012). (In Chinese)
7. Wu, H.L., Wang, P., Pan, J.Y., Wang, L.S.: Study on underground VOD intelligent ventilation technology of metal mine. Met. Mine **6**, 123–127 (2014). (In Chinese)
8. Allen, C., Keen, B: Ventilation on demand (VOD) project—vale Inco ltd. Coleman Mine. In: Proceedings of the 12th U.S./North American Mine Ventilation Symposium, pp. 45–49, Nevada, June 2008
9. Bartsch, E., Laine, M., Anderson, M.: The application and implementation of optimized mine ventilation on demand (OMVOD) at the Xstrata Nickel Rim South Mine, In: Proceedings of the 13th U.S./North American Mine Ventilation Symposium, pp. 41–44, Ontario, June 2010

10. O'Connor, D.: Ventilation on demand (VOD) auxiliary fan project—vale inco limited, Creighton mine. In: Proceedings of the 12th U.S./North American Mine Ventilation Symposium, pp. 41–44. Nevada (2008)
11. Gillies, A.D., Wu, H.W., Tuffs, N., Sartor, T.: Development of a real time airflow monitoring and control system. In: Ganguli, R., Bandopadhyay, S. (eds.) Proceedings of the 10th U.S. Mine Ventilation Symposium, pp. 145–155. Balkema, Netherlands (2004)
12. Wu, H.W., Gillies, A.D.S.: Real-time airflow monitoring and control within the mine production system. In: Gillies, A.D.S (ed.) Proceedings of the 8th International Mine Ventilation Congress, pp. 383–389. AusIMM, Melbourne (2004)
13. Mutama, K.R., Meyer, M.A.: Remote monitoring and automation of a large mine ventilation network. In: Proceedings of the 11th U.S./North American Mine Ventilation Symposium, pp. 67–74. Taylor and Francis Group Plc. (2006)
14. Hardcastle, S.G, Kocsis, C., O'Connor, D. Justifying ventilation—on—demand in a Canadian mine and the need for process based simulations. In: Proceedings of the 11th U.S./North American Mine Ventilation Symposium, pp. 15–27. Taylor and Francis Group Plc. (2006)
15. Wallace, K.G. Optimization of the Red Lake mine ventilation system. In: Proceedings of the 11th U.S./North American Mine Ventilation Symposium, pp. 61–66. Taylor and Francis Group Plc. (2006)
16. Li, G., Kocsis, C., Hardcastle, S.G.: 3D CANVENT—a three dimensional mine ventilation modeling package. Natural Resources Canada (2008)
17. du Plessis, J.J.L., Marx, W.M.: Main fan energy management. In: Proceedings of the 12th U.S./North American Mine Ventilation Symposium, pp. 441–446. Wallace (2008)
18. Luo, H.Z.: Design of intelligent ventilation control system for mine driving face. Mech. Res. Appl. **5**, 164–165 (2015). (In Chinese)
19. Wang, W.C., Qiao, W., Li, G., Tian, C.: Application of mine intelligent partial ventilation system in Huhewusu coal mine. Saf. Coal Min. **43**(6), 114–116 (2012). (In Chinese)
20. Lu, X.M.: Study status and development orientation of mine ventilation intelligent technology. Coal Sci. Technol. **44**(7), 47–52 (2016). (In Chinese)
21. Guo, N.Q., Hu, M.Z.: The 3D simulation model of mine ventilation network. Min. Metall. **18**(3), 79–83 (2009). (In Chinese)

# Part III
# Mine Dusts and Control I

# Evaluation of Gravimetric Sampler Bias, Effect on Measured Concentration, and Proposal for the Use of Harmonised Performance Based Dust Sampler for Exposure Assessment

B. Belle[1,2(✉)]

[1] Anglo American Coal, Brisbane City, Australia
Bharath.Belle@angloamerican.com
[2] UNSW, Sydney, Australia

**Abstract.** The last three years has brought about alarming news of re-identification of coal worker's pneumoconiosis (CWP) or 'black lung" in Australia after reporting nearly being absent for over five decades. While, the CWP statistics in South Africa (SA) are unverifiable, but certainly CWP has not been eliminated. These events have re-kindled the need for better understanding of the dust monitoring, performance of sampling devices, and compliance determination. Over the last half century, gravimetric sampling has been the fundamental means for dust exposure monitoring using recognised respirable size-selective standards. In both South Africa and Australia, the gravimetric sampling technique in coal mines has been followed since 1988 and 1983 respectively using samplers of original Higgins-Dewell (HD) type design. This paper provides the evaluation results of currently used South African and Australian gravimetric samplers compared against the original UK SIMPEDS 'true reference' sampler. The results consistently suggested that the South African and Australian cyclones do not conform to the required size selective curve or even the 'true' reference sampler. The results show that the currently used SA and Australian samplers showed a $D_{50}$ sampling bias as high as 59 and 47% respectively against the size-selective curve. Similarly, under the controlled laboratory coal dust test conditions measuring the same coal mine dust level in a chamber, the South African, Australian and UK standard SIMPEDS sampler were 7.87, 9.79 and 6.71 $mg/m^3$ respectively, which aligned with the sampling bias. The differences can in part be attributed to the 'un-auditable' inherent design and manufacturing quality, or unverifiable data on size-selective sampling curve. This finding has significant implications towards exposure data collected over the last 25 years and their subsequent use in the arrival of the dose-response curves. Therefore, it is strongly recommended that the harmonised use of 'true reference' SIMPEDS cyclone that meets the ISO (1995) criteria uniformly across the industry would benefit the exposure assessment and compliance determination.

**Keywords:** Dust · Respirable · Sampling

# 1   Introduction

Respirable dust sampling is pivotal in estimating the 'dose' of individual worker exposure to dust and in deriving quantitative respiratory disease risks in epidemiological studies. Based on the past epidemiological knowledge [1], it has been established that the respirable dust particle size distribution is critical due to its potential health effects and quantifying the risks. Respirable dust refers to particles that settle deep within the lungs that are not ejected by exhaling, coughing, or expulsion by mucus. Since these particles are not collected with 100% efficiency by the lungs, respirable dust is defined in terms of size-selective sampling efficiency curves. This had led to internationally recognised respirable size-selective sampling [2] widely known as the British Medical Research Council (BMRC) definition of the respirable dust fraction or Johannesburg curve with a median aerodynamic diameter of 5 µm collected with a 50% efficiency (D50). In reality, these size-selective curves represent lung penetration of dust particles that dust sampling instruments attempt to replicate. The International standards organization (ISO) in 1995 recommended [3] that the definition of respirable dust follow the theoretical convention described by Soderholm [4, 5] with a D50 of 4 µm. An international collaboration [3, 6–8] for sampling harmonisation has led to the agreement on the definitions of health-related aerosol fractions in the work-place, defined as the inhalable, thoracic and respirable curve. Figure 1 summarises the BMRC and ISO size-selective curves for dust sampling in mines [3, 9]. It is important to note that it is not only a difference in the D50 value but an entire size-selective curve. The new respirable size-selective curve is different from previous definitions used in the United States, South Africa, Australia and Europe and truly rep-resents an international harmonization of the definition of respirable dust.
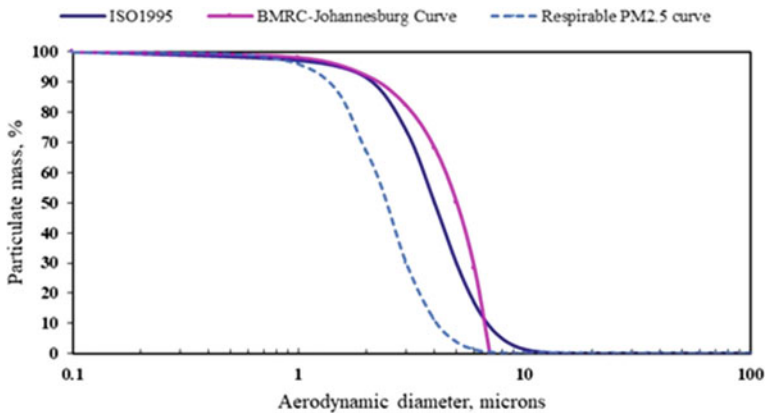


**Fig. 1.**  Respirable dust size-selective sampling curves

Therefore, for any personal exposure monitoring, the chosen respirable dust sampling device should achieve the theoretical sampling definition criterion as closely as possible to minimize bias using the D50 performance criteria at the recommended flow

rates. Due to the complex nature of sampler performance evaluations and their differences, regulatory bodies have dealt with this aspect by decreeing one specific sampling device, (i.e., Mining Research Establishment (MRE) horizontal plate elutriator, Dorr-Oliver cyclone, HD cyclone), as the reference sampler of choice. What is important herein is whatever sampler is used for exposure measurement, they are to be referenced to epidemiological health effects data to derive any meaningful benefits.

Formerly, sampling conventions corresponded more to some device than to a health-related issues. For example, the BMRC respirable aerosol convention adopted in 1959 at the Johannesburg Pneumoconiosis Conference [1] fitted the efficiency of the MRE 113A horizontal elutriator. The US law declared that the "respirable aerosol fraction" was the fraction of dust collected by a specific sampler. The ISO (1995) harmonisation curve resulted in the standardisation of health-related aerosol fractions independently from the samplers used. Today, compliance samplers should conform to the ISO1995 respirable curve. As a result, there were modifications and operation specifications of the samplers which required samplers to be tested in ideal conditions to yield their sampling efficiency curve and their performance expressed by bias maps. While there may be differing views on the choice of sampler to be used in the industry, the use of D50 as a selection criteria is the only widely used and accepted criteria for dust sampler selection, in conjunction with the comparative laboratory concentration tests under controlled calm air conditions.

## 2 Basics of Personal Dust Samplers

The primary purpose of personal respirable dust sampling is to characterize (with regard to mass and size) the quality of the ambient air to evaluate a miner's dust exposure. The mass of respirable dust inhaled can be determined by sampling. The measurement of dust in mines is usually carried out using various gravimetric sampling instruments. For personal coal mine dust sampling, the dust sampler or cyclone is normally mounted on the upper chest, close to the collarbone within the breathing zone [10]. The breathing zone is the space around the worker's face from where the breath is taken, and is generally accepted to extend no more than 30 cm from the mouth. Gravimetric dust monitoring involves sampling a known volume of ambient air through a filter. The filters are weighed before and after exposure to determine the mass of particles. The collected dust sample is expressed as mass of dust (mg) per cubic meter ($m^3$) of air.

With the acceptance of a defined gravimetric based size-selective sampling, various types of dust samplers called 'cyclones' were developed and used in mines worldwide since the 1960s [9]. Cyclones are named for the rotation of air within its chamber that separates and selects dust particles of interest from ambient airborne dust. The cyclone functions on the basis of a centrifugal force principle, i.e., the rapid circulation of sampled air separates particles according to their aerodynamic diameter.

In a cyclone, non-respirable particles are forced to the periphery of the airstream, impact the cyclone wall, and collect in a grit pot, while particles less than a specified size remain in the centre of the air stream and deposit onto a pre-weighted filter medium. The size fraction sampled is very sensitive to type of cyclone used, flow rate,

and variations in flow rate. Various commercially available cyclones can approximate specified size-selective curves when correctly designed and operated at a certain flow rate. Any minor deviation from the recommended flow rate would lead to differences in measured dust results. For example, a small change in flow rate of HD type UK Casella cyclone from 1.9 to 2.2 Lpm can result in differences of up to 20% in measured dust values [11, 12]. Both South Africa and Australia have adopted the new size-selective curve with change in HD type sampler flow rates from 1.9 to 2.2 Lpm. Therefore, there may be a need for amendment to the exposure limits to incorporate the measurement differences due to change in sampling flow rates. The impact of this change is not linear because while higher flow rates result in more air volume sampled, the dust is of smaller mean particle size, and differences between flow rates will depend of the particle size distribution sampled.

With the advent of the internationally accepted respirable size-selective curves, research studies have com-pared various dust samplers available for use in mines. What is obvious from the various studies [13–16] is that there are significant differences in measured dust levels from different samplers measuring the same aerosol. The reasons affecting the performance of these different dust samplers can be attributed to inherent cyclone design, air velocity, and direction of airflow, humidity, sampler inlet size, geometry, orientation, aerosol particle size, aerosol density differences, electrical charge, particle bounce properties, and conductive properties of cy-clones. Globally, over the last 6 decades, various size-selective conventions have been used, as well as various types of personal gravimetric samplers being used by mines. Until recently, Feb 2016, in the USA, the Dorr-Oliver 10 mm nylon cyclone [17–19] was the widely used sampler operated at 2.0 Lpm across the entire U.S. coal mining industry. On the other hand, most of the European countries (including UK) use the HD type cyclone [15, 20–26]. The latest real-time continuous personal dust monitor (CPDM), PDM3700 uses a HD cyclone operated at 2.2 Lpm and manufactured by MESA Laboratories (USA).

The UK HD plastic cyclone or also called the UK SIMPEDS (Safety in Mines Personal Equipment for Dust Sampling) is used as a reference sampler operating at a flow rate of 2.2 Lpm which has been characterized previously [27]. The SIMPEDS or Casella cyclone sampler of the generic HD type is recommended for use in the UK for optimal agreement with the respirable convention.

Currently, these HD cyclones are referred to by commercial names such as Casella, SKC, MESA (formerly BGI). For all cyclone performance evaluation purposes, HSE uses Casella SIMPEDS plastic sampler as a 'true reference' sampler. Some of these HD type cyclones are metal as well as the plastic type. It is possible that different laboratories recommend different flow rates for the same cyclone.

Another laboratory study [15] investigated various cyclone models at a flow rate of 2.1 Lpm and observed that D50, increased with increasing inner diameter of the vortex tube or surface properties of cyclone material. What this would mean is that one supplier, for example, Supplier D of a metal or plastic HD cyclone vortex tube with an inner diameter of 3.12 mm would result in higher $D_{50}$ of 5.32 μm than the Supplier A of an HD plastic cyclone with a vortex tube with an inner diameter of 3.02 mm $D_{50}$ of 4.54 μm, a difference in $D_{50}$ of 0.7 μm. The laboratory results and a study by Lidén and Kenney [28] provide the explanation on the differences (of up to twice as large) increased measured dust concentrations by supplier D cyclones when compared with

the Supplier A plastic cyclones. It is certain that manufacturer modifications such as blacking, tapering of the vortex tube inlet, and gasket type do influence the cyclone penetration curves.

## 2.1   History of South African Gravimetric Samplers a Subsection Sample

The original Department of Mineral and Energy Affairs (DME) document [29] titled "Guidelines for the Gravimetric Sampling of Respirable Airborne Dust Concentrations in Coal Mines" for risk assessment in terms of the occupational diseases in mines and works Act (1973) do not refer to specific dust sampler for use in South African mines. However, a note on the instruments acceptable as gravimetric samplers [30] documents few samplers as meeting the following criteria:

- The particle size distribution of the dust on the filter in the test instrument must comply with the 'Johannesburg Curve' for respirable dust, i.e., particle aerodynamic diameter of less than 7 μm.
- The coefficient of correlation must be 0.9 for the linear regression line against MRE 113A gravimetric dust sampler.
- The standard error of estimate must not exceed 10% of the mean sample mass.
- A calibration curve is required for deviations of approximately greater than 10% from the reference curve.

However, the approved sampling cyclones suggested during the 1980s were HD type SKC and Casella cyclones with relevant filters and sampling pumps to be operated at 1.9 Lpm. There has also been a reference to a Dorr-Oliver cyclone used in conjunction with COMSA (Chamber of Mines South Africa) inhalable dust sampler used in gold mines that were initially operated at 1.0 Lpm and then changed to be operated at 1.85 Lpm [31] or rounded off to 1.9 Lpm to align with the UK SIMPEDS sampler. Another technical note [32], documents the use of Gilian GX-37 cyclone, GX-35 cyclone and the Gilian GX-R25 mm cyclone operated at 1.9 Lpm for use in South African mines. However, the evaluations were done merely on mass concentration comparison basis (<5% measured difference) and no information on size-selective curves were available.

Although, original gravimetric sampler lists included various traditional cyclone manufacturer trade names such as Casella and SKC, their use at mines has disappeared from the exposure monitoring regime completely. Currently, in South Africa it is noted that almost all of the sampling is carried out using locally manufacturer "plastic type HD (Envirocon model GX1)" cyclone without any published knowledge of its size-selective performance as required by the original criteria [30]. The reason for the use of this particular cyclone head or the operating specifications such as flow rate of 1.9 or 2.2 Lpm could not be established. Interestingly, South Africa was the first country in the world to switch over to the new size-selective curve [12] and no amendments to the OEL to coal dust or silica dust have been made.

- A French study [16] of fifteen respirable aerosol samplers had studied the South African 25 mm GX1 cyclone had noted that the cyclones when operated at 1.9 and 2.5 Lpm flow rate, they conform to BMRC and ISO (1995) respirable curve with a

D50 of 5.81 and 4.21 μm respectively. Despite the above, author is not aware of any regulatory guidance on operating these South African manufactured cyclones used for exposure monitoring.

- A HSE size selection characteristic study [33] noted that the locally manufactured South African cyclones were very similar in its performance to the HD type SIMPEDS cyclone. The HSE tests were carried out at 1.8, 2.0 and 2.3 Lpm with a resulting D50 of 5.9, 5 and 4.6 μm. There were no size-selective data for the SA cyclone that were readily available from the HSE [35] to calculate the bias maps. However, without specific testing at a flow rate of 2.2 Lpm, recommendation of HSE was accepted to operate the SA cyclone operate at a flow rate of 2.2 Lpm to emulate ISO (1995) curve. The HD type SA cyclones have operated at a flow rate of 2.2 Lpm since 1997 [36].

## 2.2    History of Australian Gravimetric Samplers

Since the adoption of gravimetric sampling in Australia in 1983, both the plastic and aluminum HD cyclones have been used and operated at 1.9 Lpm. As per AS2985 [37], Australian dust sampling followed the BMRC [1] with a zero efficiency for particles of 7 μm. The AS2985 recommended dust sampling devices included the BCIRA (British Cast Iron Research Association), HD cyclones and SIMPED cyclones. However, AS2985 [38, 39] made amendments to the definition of the respirable dust aligned with the ISO (1995) definition and cyclones were recommended to be operated at 2.2 Lpm flow rate. Currently, further investigations have indicated that almost all of the sampling in some mining regions is carried out using a specific manufacturer, "plastic type HD" cyclone without any reference knowledge of its size-selective performance. The reason for the selection of this particular supplier of cyclones could not be established other than ease of its availability. In addition, conformity of the currently available SKC cyclone or Casella cyclone test evaluation reports that are used in Australia are not readily available. New South Wales (NSW) amended the occupational exposure limits (OEL) when they switched over to the new size-selective curve however, Queensland OEL limits were not changed. In the absence of publicly available original field evaluation data, the switch-over to the newly adopted curve has resulted in confusions over the validity of dust limits between the two states.

As a general observation, other than slight design modifications, the currently available various cyclone particle separators are essentially of the same design as the original cyclone, described by Higgins and Dewell [20], as used by and manufactured for the British Cast Iron Research Association. The UK SIMPEDS sampler, Australian sampler and the South African (37 mm GX1) are shown in Fig. 2. The air inlet configuration of the SA cyclone sampler is different to the MESA (formerly BGI), Casella and SKC cyclone samplers. It comprises a tangential slot entry rather than the tubular entry found on the other cyclones. The SA cyclone sampler is a sealed unit and so the vortex finder is permanently attached to the cyclone elutriator.

In the absence of the original HSE data on South African GX1 cyclone tests [33], the author was able to contact and obtain the raw test results carried out on SA samplers in 1996–97 from the French laboratory [34] that recommended the sampler to be
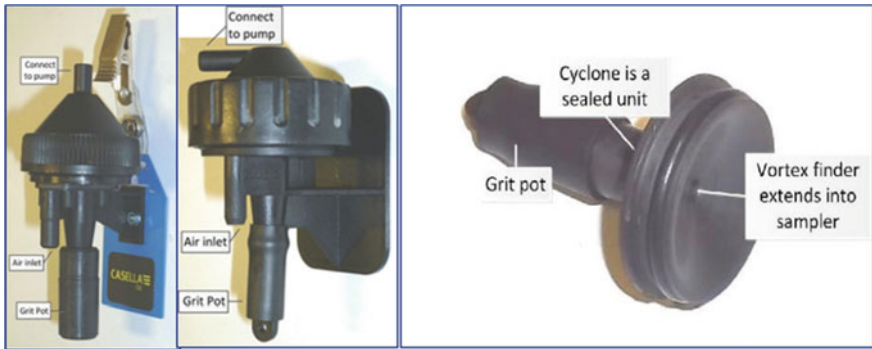
**Fig. 2.** HD test samplers: SIMPEDS cyclone (left); Australian cyclone (AS) (middle) and South African cyclone (SA) (right)

operated at 2.5 Lpm. Figure 3 shows the penetration efficiency of the cyclones for different flow rates using the French cyclone size characterisation tests.
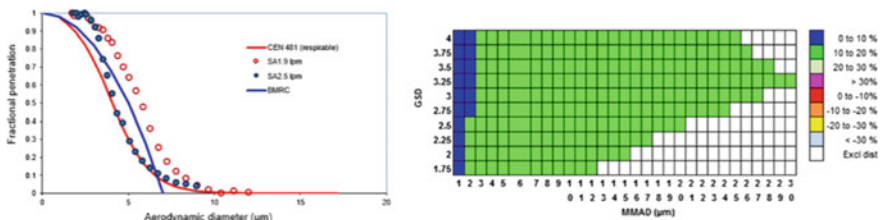


**Fig. 3.** Fractional penetration of particles through South African GX1 gravimetric sampler and Bias map for 2.5 Lpm flow rate (using 1996 French test data)

From the fractional penetration efficiency and bias map at 2.5 Lpm for the HD type sampler (25 mm), it is noted that at 1.9 Lpm the cyclone largely oversamples both BMRC and ISO 1995 respirable aerosol fraction. The French study recommended that the SA cyclone operate at 2.5 Lpm to satisfy the requirement with a $D_{50}$ of 4 µm. The French study data noted that SA cyclone didn't perform to Johannesburg curve at 1.9 Lpm nor the new ISO curve when operated at 2.2 Lpm. These conflicting French and UK studies necessitated the review of penetration efficiency tests of South African cyclones for operations. In addition, the service providers or research laboratories both in Australia and South Africa could not demonstrate the exposure monitoring indeed meets the required respirable dust sampling specification [3].

## 2.3 Cyclone Sampling Efficiency and Dust Concentration Tests

The cyclone sampling efficiency and dust concentration tests are very complex and require sophisticated laboratory test chambers, which are scarce with handful of expertise on operational monitoring experience. Currently, there are very few such

facilities available globally such as in UK, France, Sweden and USA. Therefore, in the absence of such quality facilities in Australia and South Africa, tests were carried out independently at the Health and Safety Executive (HSE) in UK. Tests were carried out to determine the penetration characteristics of a total of 12 plastic cyclone samplers, 3 South African cyclones, 3 used Australian cyclones from three different mines, 3 new Australian samplers, and 3 UK SIMPEDS sampler [40]. The HSE tests are standard cyclone sampling efficiency tests conducted in triplicate. For all comparison purposes, the UK SIMPEDS Casella plastic cyclone is considered as a 'true reference sampler' by the HSE. This is based on the previously well-established research study [27] and the evaluation standard set forth by the HSE to the mining industry. The design of the sampler test system is based on that described by Kenny and Lidén [41] used for the measurement of polydisperse aerosol penetration through cyclone samplers inside a calm air chamber and is not discussed here. The approach requires measurements of the aerodynamic size distribution of an aerosol penetrating through the cyclone sampler under test and that of the aerosol challenging it. The two size distributions are compared to obtain the penetration characteristics of the cyclone sampler. The experimental cyclone efficiency and dust concentration test set-up is shown in Fig. 4. The laboratory had confirmed that all test cyclone flow rate, before and after each test, were found to be within 2% of the target value of 2.2 Lpm.



**Fig. 4.** Cyclone sampler efficiency testing (left) and dust concentration test set up [40]

## 2.4    Data Analysis and Calculation of Sampler Bias for Test Aerosol

All the data associated with the evaluations in this study were obtained from the independently commissioned study at the HSE laboratories. The particle size, and cyclone penetration for the reference SIMPEDS plastic cyclone and test cyclone sampler were measured as a fraction of the reference aerosol. Using the measured size data, fractional penetration efficiency was plotted to determine the $D_{50}$ from the fitted curves for each of the test and reference cyclones. The measured performance data for each cyclone sampler was assessed against the respirable target convention defined in BS EN 481(1993) [42]. For evaluation purposes, the bias values were calculated for the respirable aerosol size distribution range of 1–30 μm mass median aerodynamic

diameter (MMAD) with geometric standard deviation (GSD) range of 1.75–4.0 (step of 0.25) as specified using bias map approach in BS EN 13205-2:2014 [43]. Using the calculated bias values, a two-dimensional diagram (bias map) showing the GSD and MMAD on the axes, and points of equal bias joined to form contours are drawn. In this paper, the average of all the repeat tests for each of the gravimetric samplers were calculated and bias maps are produced for the identical calm test chamber conditions for test cyclones. For any aerosol size distribution A, the bias in the sampled concentration is defined in Workplace exposure—Assessment of sampler performance for measurement of airborne particle concentrations [42] as:

$$\Delta i = \Delta i(D_A, \sigma_A) = \frac{cC_i - C_{std}}{C_{std}} \tag{1}$$

where:

$C_{std}$     is the concentration that would be sampled by a sampler that perfectly follows the sampling convention and is a function of the sampled aerosol size distribution, $A$;

$c$     is the correction factor stated either in the manufacturer's instructions for use or in the relevant measuring procedure; No other correction factor may be applied to the sampled concentrations. If no correction factor is stated, c is assigned a value of 1,00.

$C_i$     is the mean sampled relative concentration and is a function of the sampled aerosol size distribution, $A$;

$D_A$     is the mass median aerodynamic diameter of the sampled aerosol, $A$;

$\Delta i$     is the bias or relative error in the aerosol concentration measured using the candidate sampler, for aerosol size distribution A, and

$\sigma_A$     is the geometric standard deviation (GSD) of the sampled aerosol, $A$.

Similarly, for the sampler flow rate of 2.2 Lpm, the fractional mass sampled (FMS) from a test aerosol with lognormal size distribution (aerodynamic mass median diameter, MMAD, and geometric standard deviation [GSD], $\sigma_g$) will be a function of [28] the size distribution parameters and the flow rate, Q, and is evaluated as an integral over all aerodynamic particle sizes, $D_{ae}$,

$$\text{FMS}(MMAD, \sigma_g, Q) = corr \int_0^\infty eff(D_{ae}, Q) f(D_{ae}, MMAD, \sigma_g) dD_{ae} \tag{2}$$

where:

$eff(D_{ae}, Q)$     the sampler efficiency curve, including measured or assumed aspiration losses.

$F(D_{ae}\ MMAD, \sigma_g)$     the mass distribution density function of an aerosol with parameters MMAD and $\sigma_g$

$corr$     a correction factor used to overcome sampler bias.

The sampler bias is then calculated [28] for each aerosol size distribution selected, and each flow rate (in this study at 2.2 Lpm), by comparing the numerically modelled FMS values to what would have been obtained by an ideal sampler perfectly following a sampling convention,

$$bias(MMAD, \sigma_g, Q) = 100 \frac{FMS_{SAMPLER} - FMS_{IDEAL}}{FMS_{IDEAL}} \qquad (3)$$

## 2.5    Results and Discussions

Table 1 shows the measured particle size at which 50% of the particles penetrated for all test cyclones ($D_{50}$) for each test, along with the percentage deviation, Bias $D_{50}$, from the $D_{50}$ of 4 μm given in BS EN 481 [42]. Figure 5 shows the average fractional penetration curve for the three South African, six Australian (3 used and 3 new) and three SIMPEDS gravimetric samplers, all operated at 2.2 Lpm flow rate. The plot also highlights the ISO (1995) respirable convention [3, 42] for comparison.

**Table 1.** Summary statistics of measured D50 of SIMPEDS, Australian and South African samplers

| Gravimetric sampler | Test-1 | | Test -2 | | Test-3 | | Average | | SD | CV |
|---|---|---|---|---|---|---|---|---|---|---|
| | $D_{50}$ (μm) | % Bias $D_{50}$ | $D_{50}$ (μm) | % Bias $D_{50}$ | $D_{50}$ (μm) | % Bias $D_{50}$ | $D_{50}$ (μm) | % Bias $D_{50}$ | μm | |
| SA1 | 5.51 | 37.75 | 5.36 | 34.00 | 5.33 | 33.25 | 5.40 | 35.00 | 0.096 | 1.79 |
| SA2 | 5.87 | 46.75 | 5.68 | 42.00 | 5.82 | 45.50 | 5.79 | 44.75 | 0.098 | 1.70 |
| SA3 | 4.62 | 15.50 | 4.68 | 17.00 | 4.61 | 15.25 | 4.64 | 15.92 | 0.038 | 0.82 |
| AS1[a] | 5.80 | 45.00 | 5.48 | 37.00 | 5.64 | 41.00 | 5.64 | 41.00 | 0.160 | 2.84 |
| AS2[a] | 6.13 | 53.25 | 6.36 | 59.00 | 6.10 | 52.50 | 6.20 | 54.92 | 0.142 | 2.30 |
| AS3[a] | 6.20 | 55.00 | 5.85 | 46.25 | 6.00 | 50.00 | 6.02 | 50.42 | 0.176 | 2.92 |
| AS1[b] | 5.70 | 42.50 | 5.42 | 35.50 | 5.42 | 35.50 | 5.51 | 37.83 | 0.162 | 2.93 |
| AS2[b] | 6.28 | 57.00 | 6.14 | 53.50 | 6.04 | 51.00 | 6.15 | 53.83 | 0.121 | 1.96 |
| AS3[b] | 5.67 | 41.75 | 5.65 | 41.25 | 5.71 | 42.75 | 5.68 | 41.92 | 0.031 | 0.54 |
| SIMPEDS1 | 4.40 | 10.00 | 4.36 | 9.00 | 4.31 | 7.75 | 4.36 | 8.92 | 0.045 | 1.04 |
| SIMPEDS2 | 4.39 | 9.75 | 4.33 | 8.25 | 4.28 | 7.00 | 4.33 | 8.33 | 0.055 | 1.27 |
| SIMPEDS3 | 4.18 | 4.50 | 4.18 | 4.50 | 4.12 | 3.00 | 4.16 | 4.00 | 0.035 | 0.83 |

[a]Used Australian samplers from different mine sites, [b]New Australian sampler

From Table 1, it is noted that the $D_{50}$ value for South African, Australian and the SIMPEDS samplers were 5.28, 5.95 and 4.28 μm respectively. From the tabulated results, it can be clearly seen that cyclone samplers SA1 and SA2 exhibited a higher positive sampling bias (>35%) compared to the respirable convention [3, 42] for theoretical aerosols with mass median aerodynamic diameters 1–30 μm and geometric standard deviations 1.75–4. They would therefore be expected to overestimate
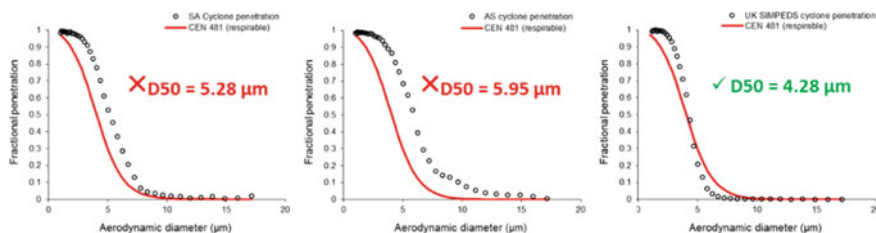
**Fig. 5.** Fractional penetration average of particles through South African (left), Australian (middle) and UK SIMPEDS cyclone (Right) gravimetric samplers as a function of aerodynamic particle diameter [40]

measurements of the respirable dust in the field. However, SA3 sampler exhibited unusually lower bias of <20%, but demonstrated significant variations from the other two in terms of sampling performance. The reason for the higher $D_{50}$ cut-point and high bias for SA1 and SA2 is not clear as the cyclone specifications are not readily available. Laboratory inspections concluded that there was an observed difference in the air inlet slot dimension for SA2 which appeared to be wider than SA1 and SA3 whose dimensions appeared similar. It was noticed that the SA1 sampler had been extensively used as there were signs of wear to the body. Whether these observations were the cause of the differences in sampling performance is speculative, but it suggests a potential variation in manufacturing tolerance. On the other hand, the measured $D_{50}$ of the Australian gravimetric sampler (both new and used) was up to 59% higher (AS2 in Test2) than the target value of 4 µm.

From the Table 1 and Fig. 5 it is noted that the measured $D_{50}$ for the South African samplers was considerably higher than the target value of 4 µm i.e. between 33 and 47% higher, except for SA3 sampler with a $D_{50}$ of 4.64 µm for 3 repeat tests. Similarly, measured $D_{50}$ for the Australian (used and new) cyclones was considerably higher than the target value of 4 µm, i.e. between 35 and 59% higher. In contrast, the measured $D_{50}$ for the 'true reference' UK SIMPEDS plastic cyclone was much closer to the target value i.e. 3–10% higher with an average $D_{50}$ of 4.28 µm. It is also interesting to note that there are differences in individual Australian and South African cyclone samplers or larger scatter in terms of measured $D_{50}$ values given by a higher coefficient of variation (RSD) in Table 1. Similarly, what is a critical finding from the penetration plots (Fig. 5) is that both the South African and Australian samplers have a tail of the penetration graph that extends much further into the larger particle sizes than the reference SIMPEDS UK 'true' cyclone samplers (i.e. the penetration approaches zero at about 8 µm for the SIMPEDS and >15 µm for the South African and Australian cyclones respectively).

Figure 6 shows the bias maps of gravimetric samplers. Both the South African and Australian gravimetric samplers exhibited a high sampling bias, giving a positive bias often greater than 30% higher than the respirable convention. They would therefore be expected to overestimate measurements of the respirable concentration of airborne dust in the workplace.
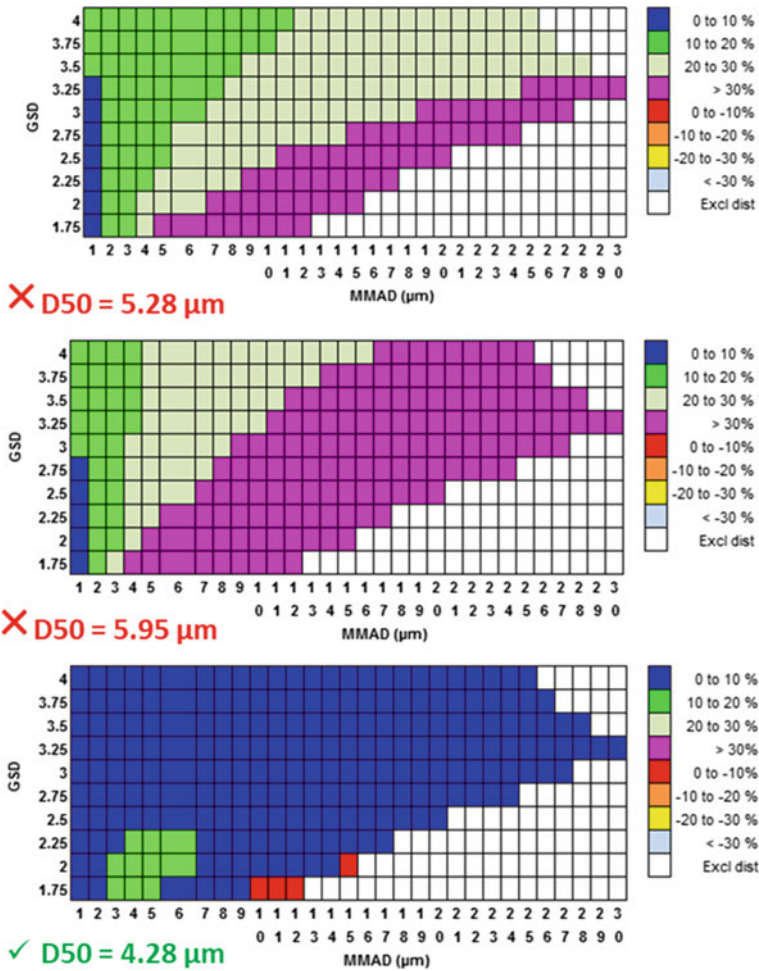
**Fig. 6.** Bias map of gravimetric samplers (South Africa-Top); Australian Sampler (Middle) and SIMPEDS sampler (Bottom) for various dust

These independent laboratory results with higher $D_{50}$ values and bias have reinforced the conclusions that the current South African and Australian gravimetric samplers significantly overestimated the measured respirable dust levels based on size analyses during field measurements [44]. Regardless of the attributable reasons for the non-conformance to the respirable size-selective curve [3], both the current South African and Australian cyclones must be discontinued their use in their current design and use.

## 2.6 Measured CYCLONE Dust Concentrations

Table 2 and Fig. 7 shows the dust levels measured by each gravimetric test sampler when exposed to an airborne coal dust cloud in the HSE laboratory test chamber. The samples of each SIMPEDS and Australian cyclone sampler gave consistent measurements of the dust concentration, given by a coefficient of variation (CV) value of less than 5% between samplers for each repeat test. However, the SA cyclone showed a significant variation in performance between samplers illustrated by a RSD of 13.3, 19.2 and 21.5% for each test. This supports the variation in $D_{50}$ between the three SA cyclone samplers shown in Table 1. The ratio of SA cyclone sampler dust levels to average SIMPEDS cyclone sampler dust levels increased in the order SA3 (0.99), SA1 (1.13), SA2 (1.40). This is consistent with the increase in $D_{50}$ values shown in Table 1 with only SA3 sampler closely matching the SIMPEDS sampler. The ratio of Australian cyclone dust measurement to SIMPEDS cyclone dust measurement is

**Table 2.** Summary of measured dust levels under controlled coal dust tests

| Test# | #1 | | | | #2 | | | | #3 | | | |
|---|---|---|---|---|---|---|---|---|---|---|---|---|
| Sampler | mg/m$^3$ | Avg. | SD | CV | mg/m$^3$ | Avg. | SD | CV | mg/m$^3$ | Avg. | SD | CV |
| SA1[a] | 8.4 | | | | 7.2 | | | | 7.0 | | | |
| SA2[a] | 10.2 | 8.9 | 1.1 | 13.3 | 9.0 | 7.5 | 1.4 | 19.1 | 8.7 | 7.1 | 1.5 | 21.5 |
| SA3[a] | 8.03 | | | | 6.2 | | | | 5.7 | | | |
| AS1[b] | 10.7 | | | | 9.0 | | | | 9.0 | | | |
| AS2[b] | 11.5 | 10.9 | 0.5 | 4.6 | 9.7 | 9.2 | 0.4 | 4.6 | 9.6 | 9.2 | 0.39 | 4.25 |
| AS3[b] | 10.6 | | | | 8.9 | | | | 8.9 | | | |
| RC1[c] | 7.4 | | | | 6.4 | | | | 6.4 | | | |
| RC2[c] | 7.7 | 7.5 | 0.2 | 3.3 | 6.1 | 6.3 | 0.2 | 3.1 | 6.2 | 6.2 | 0.15 | 2.48 |
| RC3[c] | 7.3 | | | | 6.5 | | | | 6.1 | | | |

[a]South African HD sampler, [b]Australian HD sampler, [c]UK SIMPEDS sampler
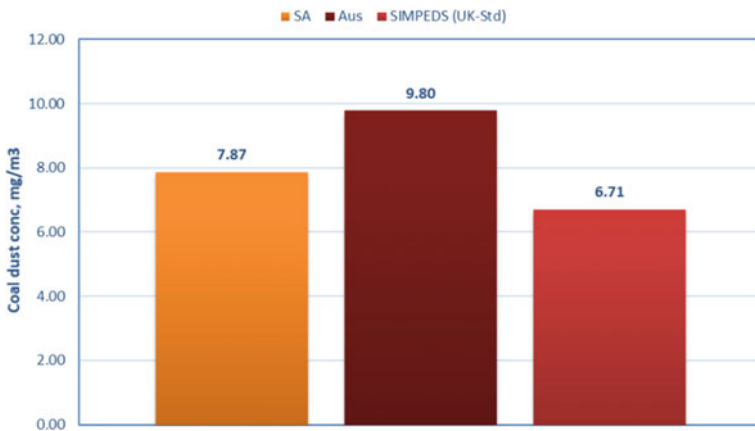


**Fig. 7.** Measured average dust levels under controlled test conditions [40]

consistently around 1.41–1.53, i.e. the Australian cyclone sampler measured approximately 40–50% higher dust levels than the reference SIMPEDS cyclone sampler. This is consistent with the higher value of $D_{50}$ measured previously for all three used and new Australian cyclones.

From the laboratory controlled concentration test results it was noted that the measured dust levels of gravimetric samplers are significantly different when operated at the same sampler flow rates. The average measured dust levels for the South African, Australian and the UK SIMPEDS samplers for the sampling period were 7.87, 9.79 and 6.71 mg/m$^3$ respectively. Using the linear regression of the data, it can be inferred that there is a positive 'concentration measurement bias' in respirable dust levels for Australian and South African samplers by 46 and 26% respectively. From an operational perspective, the implications of this findings are significant when compliance and epidemiological determinations are made.

# 3    Conclusions

This paper summarises comparative cyclone penetration efficiency and dust concentration results evaluated under controlled conditions between the South African, Australian and the 'reference true' SIMPEDS UK reference sampler operated in accordance with the respirable size-selective curve [3] at a flow rate of 2.2 Lpm. The following conclusions can be drawn from the sampler evaluations:

- The measured $D_{50}$ for the 'true reference' UK SIMPEDS standard plastic cyclone was 4.28 µm. This was within 3–10% of the ISO target MMAD of 4 µm and aligned to the bias map criteria.
- In contrast, particle penetration efficiency results shown that the $D_{50}$ value for South African and the Australian samplers were 5.28, and 5.95 µm respectively. The South African samplers exhibited a higher positive sampling bias, than the target value of 4 µm, i.e. between 33 and 47% higher, except for SA3 sampler with a $D_{50}$ of 4.64 µm for 3 tests. Similarly, measured $D_{50}$ for the Australian (used and new) cyclone samplers was considerably higher than the target value of 4 µm, i.e. between 35 and 59% higher.
- Based on the particle size penetration plots, both the South African and Australian penetration graphs have tails into larger particle sizes than the reference sampler or the ISO criteria.
- Calculated average bias map using the sampling efficiency data, show that both the South African and Australian gravimetric samplers exhibited a high positive sampling bias, often greater than 30% higher than the respirable convention. They would therefore be expected to overestimate measurements of the respirable dust levels in the workplace.
- An independent concentration measurement of dust aerosol showed that the average measured dust levels for the South African, Australian and the UK SIMPEDS samplers for the sampling period were 7.87, 9.79 and 6.71 mg/m$^3$ respectively. Based on the laboratory controlled concentration test conditions, it can be inferred that there is a 'concentration measurement bias' in respirable dust levels for

Australian and South African samplers by 46 and 26% respectively. From an operational perspective, the implications of this findings are significant when compliance and epidemiological determinations are made.

In summary, an independent laboratory data and their analyses with higher $D_{50}$ values and bias have rein-forced the conclusions that the current South African and Australian gravimetric sampler results significantly overestimated the true respirable dust levels. It is acknowledged that the manufacturing challenges of samplers, design variations, inlet geometry variations of samplers, sampler material type, and some discrepancies in evaluation methodology difficulties in particle-size dependent efficiency measurement are well understood by the aerosol professionals. However, these are known variables and should not be the reason in over or underestimation of the personal exposure results which may show to cause significant non-compliance. This also con-tributes to the loss of confidence in the exposure data that ultimately gets used in deriving dose-response relationships. This situation can be avoided by following the path of single SIMPEDS sampler in the South African and Australian industry. This was the approach used in the USA and in fact current continuous personal dust monitors (CPDMs), also commercially known as PDM3700, contain a correction factor to reference their results to the Coal Mine Dust Personal Sampling Unit used since 1969. The benefits of harmonised use of a single true standard sampler would enable greater understanding of exposure data derived worldwide or within the mining industry. Regardless of the attributable reasons for the non-conformance to the size-selective curve, both the current South African and Australian cyclones must be discontinued from use in their current design. The study has demonstrated that it is critical to ensure the samplers used at the mining operations by the third-party service providers or research laboratories for exposure monitoring indeed demonstrate and meets the respirable dust size-selective performance criteria and quality. Hopefully the findings in this paper will assist in ensuring the selection and use of the samplers and more importantly, result in the implementation of the harmonised use of prescribed dust sampler for use in the global mining industry. This paper and the work contained herein is an effort to improve the exposure monitoring and improve engineering controls in workplaces.

# References

1. Orenstein, A.J.: Proceedings of the 1959 Pneumoconiosis Conference, Johannesburg. Churchill, London, UK (1960)
2. BMRC: British Medical Research Council Report, UK (1952)

3. International Standards Organization (ISO): Air Quality: Particle Size Fraction Definitions for Health-Related Sampling. International Organization for Standardization, Geneva, Switzerland ISO 7708:1995 (1995)
4. Soderholm, S.C.: Proposed international conventions for particle size-selective sampling. Ann. Occup. Hyg. **33**(3), 301–320 (1989)
5. Soderholm, S.C.: Why change ACGIH's definition of respirable dust. Appl. Occup. Environ. Hyg. **6**(4), 248–250 (1991)
6. American Conference of Governmental Industrial Hygienists (ACGIH): Particle Size-Selective Sampling in the Workplace. ACGIH, Cincinnati, OH, USA (1985)
7. American Conference of Governmental Industrial Hygienists (ACGIH): Particle size-selective sampling for particulate air contaminants. In: Vincent, J.H. (ed.) ACGIH, Cincinnati, OH, USA (1999)
8. Comite´ Europe´en de Normalisation (CEN): Workplace Atmospheres: Size Fraction Definitions for Measurement of Airborne Particles in the Workplace. European Standard EN 481:1993E, CEN, European Committee for Standardization, rue de Stassart 36, B-1050, Brussels, Belgium (1993)
9. NIOSH: Criteria for a Recommended Standard: Occupational Exposure to Respirable Coal Mine Dust, DHHS (NIOSH) Publication Number 95–106 (1995)
10. Health and Safety Executive (HSE): MDHS 14/3 General Methods for Sampling and Gravimetric Analysis of Respirable and Inhalable Dust, Methods for the Determination of Hazard Substances. HSE Books, London (2000)
11. Kenny, L., Bristow, S., Ogden, T.: Strategy and Time table for the Adoption of the CEN/ISO Sampling Conventions in the UK. AIHCE, Philadelphia (1996)
12. Belle, B.: International harmonisation sampling curve (ISO/CEN/ACGIH): background and its influence on dust measurement and exposure assessment in South African mining industry. J. Mine Vent. Soc. S Afr. **2004**, 56–58 (2004)
13. Lidén, G., Kenny, L.C.: Comparison of measured respirable dust sampler penetration curves with sampling conventions. Ann. Occup. Hyg. **35**, 485–504 (1991)
14. Kenny, L.C., Gussman, R.A.: Characterization and modelling of a family of cyclone aerosol pre-separators. J. Aerosol Sci. **28**, 677–688 (1997)
15. Gudmundsson, A., Lidén, G.: Determination of cyclone model variability using a time-of-flight instrument. Aerosol Sci. Technol. **28**(3), 197–214 (1998)
16. Görner, P., Wrobel, R., Micka, V., Skoda, V., Denis, J., Fabries, J.: Study of fifteen respirable aerosol samplers used in occupational hygiene. Ann. Occup. Hyg. **45**(1), 43–54 (2001)
17. Jacobsen, M., Lamonica, J.A.: Personal Respirable Dust Sampler. Department of the Interior, Bureau of Mines, Washington DC, IC8458 (1969)
18. Lippmann, M., Harris, W.B.: Size-selective sampler for estimating respirable dust concentrations. Health Phys. **8**, 155–163 (1962)
19. Caplan, K.J., Doemeny, L.J., Sorensen, S.D.: Performance characteristics of the 10 mm cyclone respirable mass sampler. Am. Ind. Hyg. Assoc. J. **38**(2), 83–95 (1977)
20. Higgins, R.I., Dewell, P.: A gravimteric size-selecting personal sampler. In: Davies, C.N. (ed.) Inhaled Particles and Vapours II, pp. 575–586. Pergamon Press, Oxford (1967)
21. Harris, G.W., Maguire, B.A.: A gravimetric dust sampling instrument (SIMPEDS): preliminary results. Ann. Occup. Hyg. **11**, 195–201 (1968)
22. Maguire, B.A., Barker, D., Badel, D.A.: SIMPEDS 70: an improved version of the SIMPEDS personal gravimetric sampling instrument. In: Walton, W.H. (ed.) Inhaled Particles III, pp. 1053–1056. Unwin, Old Woking (1971)
23. Maguire, B.A., Barker, D., Wake, D.: Size-selection characteristic of the cyclone used in the SIMPEDS 70 MK2 gravimetric dust sampler. Staub **33**(3), 95–98 (1973)

24. Gwatkin, G., Ogden, T.L.: The SIMPEDS Respirable Dust Sampler-Side-by-Side Comparison with The 113A, Colliery Guardian (1979)
25. Ogden, T.L., Barker, D., Clayton, M.P.: Flow-dependence of the Casella respirable-dust cyclone. Ann. Occup. Hyg. **27**, 261–271 (1983)
26. Blackford, D.B., Harris, G.W., Revell, G.: The reduction of dust losses within the cassette of the SIMPEDS personal dust sampler. Ann. Occup. Hyg. **29**(2), 169–180 (1985)
27. Maynard, A.D., Kenny, L.C.: Performance assessment of three personal cyclone models, using an aerodynamic particle sizer. J. Aerosol Sci. **26**(4), 671–684 (1995)
28. Lidén, G., Kenny, L.C.: Optimisation of the performance of existing respirable dust samplers. App. Occup. Environ. Hyg. **8**, 386–391 (1993)
29. DME (Department of Mineral and Energy Affairs (DME) document): Guidelines for the Gravimetric Sampling of Respirable Airborne Dust Concentrations in Coal Mines, 1st edn, p. 16. GME 16/3/2/3/2, South Africa
30. Grabe, F.H.: Instruments Acceptable as Gravimetric Samplers, AQS 96, AQS 2/17, COM Air Quality Research, South Africa, p. 3 (1988)
31. Schroder, H.H.E.: A Note on Dust Measurements in Coal Mines, p. 8. South Africa (1982)
32. Lamprecht, A., Rowe, D.: Note on the Evaluation and Approval of Gravimetric Sampling Instruments: Gilian GX-37 Cyclone, Gilian GX-25 Cyclone and the Gilian GX-R25 mm Cyclone Versus the GME Reference Instrument MRE 113A, GME 16/3/2/8, p. 15. South Africa (1991)
33. Kenny, L., Baldwin, P.E.J., Maynard, A.D.: Respirable Dust Sampling at Very High Concentrations. HSE, UK (1998)
34. Görner, P.: Personal Communications. France (2017)
35. Kenny, L.: Personal Communications. UK (2016)
36. Belle, B., Du Plessis, J.J.L.: Summary Report on Underground Mechanical Miner Environmental Control. CSIR-Miningtek, SIMRAC, ESH 98-0249, South Africa (1998)
37. AS 2985-1987: Workplace Atmospheres-Method for Sampling and Gravimetric Determination of Respirable Dust, September 1987
38. AS 2985-2004: Workplace Atmospheres-method for Sampling and Gravimetric Determination of respirable Dust (2004)
39. AS 2985-2009: Workplace Atmospheres-method for Sampling and Gravimetric Determination of Respirable Dust (2009)
40. HSE: Testing the Performance of Personal Cyclone Samplers, CBRU/2016/093. In: Thorpe, A. (ed.) Internal Confidential Report, UK, p. 29 (2016)
41. Kenny, L.C., Liden, G.: A technique for assessing size selective dust samplers using the APS and polydisperse test aerosols. J. Aerosol Sci. **22**, 91–100 (1991)
42. BS EN 481: Workplace Atmospheres: Size Fraction Definitions for Measurement of Airborne Particles in the Workplace. Comité Européen de Normalisation (CEN) standard EN 481 (1993)
43. BS EN 13205-2: Workplace Exposure—Assessment of Sampler Performance for Measurement of Airborne Particle Concentrations. Part 2: Laboratory Performance Test Based on Determination of Sampling Efficiency (2014)
44. Belle, B.: Pairwise evaluation of PDM3700 and traditional gravimetric sampler for personal dust exposure assessment. In: Mine Ventilation Conference, Brisbane, 28–30 Aug 2017, Australia, AusIMM Publication Series No 4/2017, ISBN 978-1-925100-61-7 (2017)

# Design of Auxiliary Ventilation System for Effective Dust Dispersion in Underground Coal Mine Development Heading—A Computational Simulation Approach

Devi Prasad Mishra[(✉)], Aashish Sahu, and Durga Charan Panigrahi

Department of Mining Engineering, Indian Institute of Technology (Indian School of Mines), Dhanbad 826004, India
devi_agl@yahoo.com, aashishsahu6@gmail.com,
dc_panigrahi@yahoo.co.in

**Abstract.** The fine dust particles produced during production poses serious health hazard to the miners and decreases mine productivity. Hence, effective dispersion of dust to a safer level is of paramount significance. This paper presents monitoring of dust concentration using Grimm Aerosol Spectrometer (Model 1.108) and establishes a best combination of auxiliary ventilation parameters for effective dust dispersion in continuous miner development heading. Three-dimensional numerical simulations using CFD software ANSYS-Fluent 14.0 were conducted using actual mine data to study the effects of various auxiliary ventilation parameters on dust dispersion. The k-ε turbulence model was used for simulations. The important auxiliary ventilation parameters such as air velocity, ventilation duct diameter, height of duct from mine floor and setback distance of duct opening from mine face were varied in the ranges of 3–7 m/s, 0.6–1 m, 2–3 m and 5–8 m, respectively. The forcing auxiliary ventilation system was considered in this study which helped in better understanding of dust dispersion under varied scenarios and identifying parameters affecting dust dispersion in development heading. It also established a best suitable combination of auxiliary ventilation parameters for effective dust dispersion and alleviating the dust problem in a continuous miner development heading.

**Keywords:** Dust dispersion · Coal mine · Development heading
Auxiliary ventilation · CFD simulation

## 1   Introduction

The coal dust generated during underground coal production causes difficulty in efficient working, serious health problems to the miners and potential coal dust explosion hazard. Hence maintaining dust concentration below the permissible limit in underground coal mines is of paramount importance. As per the Directorate General of Mines Safety (DGMS), India Guidelines [1], the permissible limit for airborne respirable dust concentration in mine atmosphere is 3 mg/m$^3$ when the free silica content of the dust is 5% or less.

The dust problems in underground coal mines are increasing day-by-day with increase in mine mechanization and production. A large amount of coal dust is produced especially when the mine development heading is excavated by continuous miner. This necessitates proper dust control management through various methods and strategies to ensure safe working environment in underground coal mines. Water spraying is widely practiced to minimize the dust concentration in mine atmosphere, nevertheless it increases humidity of mine environment and requires large quantity of water. Under such condition, adequate ventilation is preferred for effective dust management at mine faces.

Researchers have numerically investigated the airflow behavior and dust dispersion in underground mine face considering different auxiliary ventilation parameters. Niu et al. [2] observed that the dust concentration in development headings can be reduced by increasing air velocity and the concentration varies significantly near mine face (within 7 m). Kurnia et al. [3] found that application of brattice causes better dust control at mine face among various dust dispersion methods. Torrano et al. [4] concluded that dust control in underground mining roadway advanced by road header can be achieved by increasing airflow velocity, reducing setback distance from the face and modifying ventilation duct height from the floor. Tariq et al. [5] numerically evaluated the effect of line brattice length with respect to brattice distance from the wall on airflow rate reaching the mine face. Kurnia et al. [6] found that the dust dispersion behavior in underground mine face is mainly affected by brattice blockage and setback distance. They observed that full blockage offers better dust dispersion as compared to the half blockage and quarter blockage, and shorter setback distance offers better dust control. Mishra et al. [7] concluded that ventilation plays a significant role on methane dispersion in tailgate of a retreating longwall mine panel.

## 2 Methodology

The present study focuses on dust monitoring and numerical simulations on effects of different auxiliary ventilation parameters on dust dispersion behavior in underground development heading under various scenarios. Three-dimensional computational simulations using k-ε turbulence model were performed to investigate the effects of air velocity in duct, duct diameter, setback distance and height of duct on dust dispersion.

### 2.1 Study Area

The dust concentration, airflow rate and dimensions of a continuous miner development heading of Jhanjra Project Colliery of Eastern Coalfield Ltd (ECL) were used for the simulations. Jhanjra Project Colliery is situated in Jhanjra Tehsil of Burdwan district of West Bengal, India (Fig. 1). The colliery has been categorized as Degree I gassy mine as per the Indian Coal Mines Regulations [8]. It is a fully mechanized mine and the largest coal producing underground mine of ECL with annual production of 3.50 MT. Coal is mined from this colliery both by bord & pillar and longwall mining methods. Exhaust ventilation system is used in the mine.
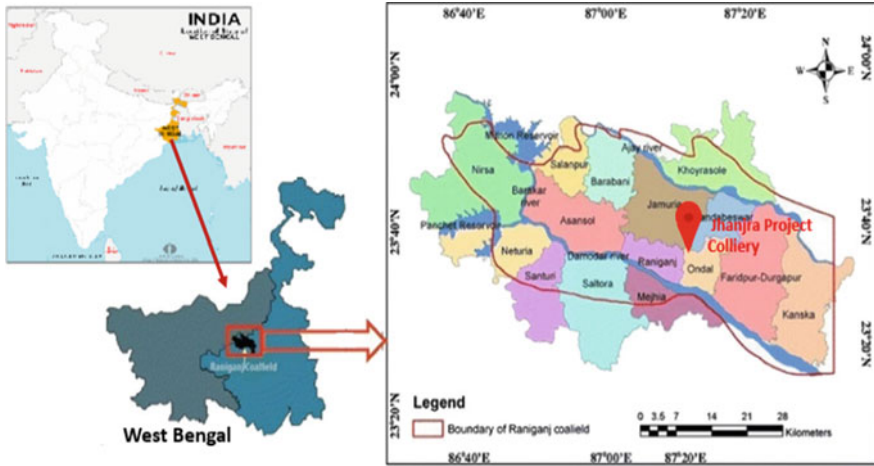
**Fig. 1.** Location of Jhanjra project colliery

## 2.2 Dust Monitoring in Development Heading

The dust monitoring in bord & pillar development heading with a continuous miner in conjunction with shuttle cars was done using a 16 channel Grimm Aerosol Spectrometer (Model 1.108). The spectrometer works on light scattering principle and measures the dust concentration in 16 size ranges varying from >0.23 to >20 μm in μg/m$^3$. The dust monitoring data stored in the instrument can be transferred to computer through USB-data cable for analysis using Grimm windows software according to EN 481 [9].

Dust monitoring was conducted 6 m away from the mining face during coal cutting by a continuous miner. The average dust concentration data in 16 different sizes and variation of dust concentration with time are shows in Fig. 2. The total (>0.23 μm) and respirable (<5 μm) dust concentrations were measured 52.3 and 26.74 mg/m$^3$, respectively, which are much higher than the legally required dust concentration. This suggests that measures for dust dispersion in the heading to a safer level are necessary.
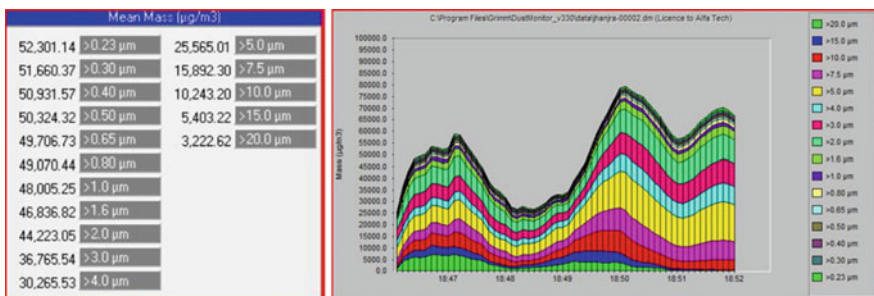


**Fig. 2.** Average dust concentration of different particle sizes and variation of dust concentration with time measured in continuous miner development heading

## 2.3 Numerical Simulations

### 2.3.1 Computational Domain Formulation

Three-dimensional numerical simulations of dust dispersion in underground development heading were performed using ANSYS Fluent 14.0 software. The computational domain of rectangular shaped development heading was created considering the height (H), width (W) and length (L) as 4, 6 and 15 m, respectively. The geometry was meshed with approximately 1.2 million tetrahedron cells (Fig. 3).
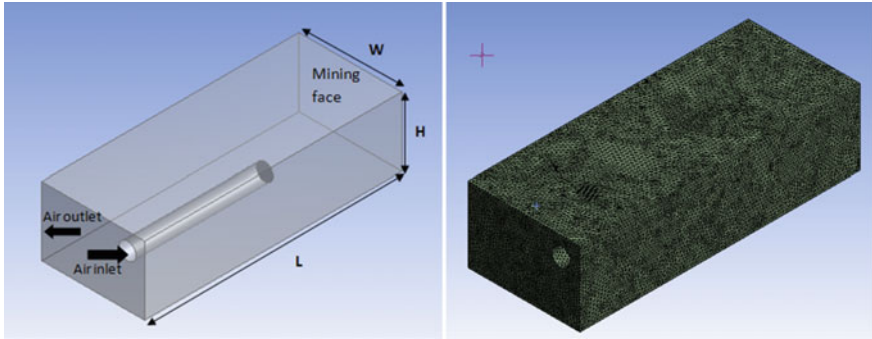


**Fig. 3.** Geometry of the computational domain of dimensions: H = 4, W = 6 and L = 15 and the meshed geometry of underground development heading

The rate of dust generation from mining face by a continuous miner was assumed to be constant. Dust movement was considered utilizing discrete phase model (DPM) [2]. The gravity effect was considered in simulations as dust particles settle down due to gravity. The standard k−ε turbulence model comprising two equations for solving the turbulent kinetic energy was selected for the simulations [6, 10].

### 2.3.2 Boundary Conditions

The boundary conditions of numerical simulations are summarized in Table 1. The total dust flow rate generated from mine face was calculated using the following formula [3]:

$$\text{Total flow rate} = \text{c.v. A} \, \text{kg/s} \tag{1}$$

where c is the dust concentration $(kg/m^3)$, v is the air velocity (m/s) and A is the cross sectional area of development heading $(m^2)$. The air velocity at the inlet of development heading was measured 2.5 m/s and at the outlet the stream-wise gradient of temperature was set to zero and pressure was considered standard atmospheric pressure [2, 3].

The auxiliary ventilation parameters were varied under four scenarios as summarized in Table 2.

**Table 1.** Boundary conditions of the CFD modelling

| Parameter | Value |
|---|---|
| Injection type | Surface (mine face) |
| Coal dust density (kg/m$^3$) | 1400 |
| Material | Coal-mv$^a$ |
| Diameter distribution | Rosin–Rammler |
| Dust particle diameter range (m) | $0.23 \times 10^{-6}$–$1 \times 10^{-4}$ |
| Spread parameter | 2.78 |
| Air velocity at development heading inlet (m/s) | 2.5 |
| Total dust flow rate (kg/s) | 0.00314 |
| Auxiliary fan diameter (m) | 1 |
| Height of development heading (m) | 4 |
| Length of development heading (m) | 15 |
| Width of development heading (m) | 6 |

$^a$*mv* medium volatile

**Table 2.** Combinations of auxiliary ventilation parameters in different scenarios

| Case | Variation | Combinations of parameters |
|---|---|---|
| Case 1: Effect of air velocity | 3–7 m/s at 1 m/s intervals | Duct diameter = 1 m, setback distance = 7 m and duct height = 3 m |
| Case 2: Effect of duct diameter | 0.6, 0.7, 0.8 and 1 m | Air velocity = 7 m/s, setback distance = 7 m and duct height = 3 m |
| Case 3: Effect of setback distance of duct | 5 to 8 m at 1 m intervals | Air velocity = 7 m/s, duct diameter = 1 m and duct height = 3 m |
| Case 3: Effect of duct height from floor | 2, 2.25, 2.5 and 3 m | Air velocity = 7 m/s, duct diameter = 1 m and setback distance = 7 m |

## 3    Results and Discussion

### 3.1    Effect of Air Velocity

The effect of air velocity on dust dispersion in development heading was investigated by varying the air velocity in ventilation duct in the range of 3–7 m/s at 1 m/s intervals and keeping other parameters constant (Case 1 in Table 2). Figures 4 and 5 illustrate the contours of air velocity and dust concentration respectively at 2 m intervals from the mine face at various air velocities. The contours show that the dust concentration in heading varies according to the variation of air velocity. From Fig. 4, it can be observed that the dead or air stagnation zones are formed at corners of the heading, especially near the corner diagonally opposite to the ventilation duct. These dead zones are marked with accumulation of higher dust concentrations (Fig. 5).

The variations of average dust concentration in the heading at 0.5 m intervals from mine face at different air velocities are shown in Fig. 6. Generally, dust concentration in the heading followed a decreasing trend with increase in air velocity and distance

**Fig. 4.** Air velocity contours in development heading at 2 m intervals from mine face at different air velocities **a** 3 m/s, **b** 4 m/s, **c** 5 m/s, **d** 6 m/s and **e** 7 m/s



**Fig. 5.** Contours of dust concentration in development heading at 2 m intervals from mine face at different air velocities **a** 3 m/s, **b** 4 m/s, **c** 5 m/s, **d** 6 m/s and **e** 7 m/s

from the mine face due to greater dust dispersion. A distinct variation in dust concentration in the heading with variation of air velocity was observed up to a distance of 2 m from the mine face, thereafter, the variation became less significant and more or less stabilized, which can be noticed from the overlapping of the graphs.

The average dust concentrations obtained from simulations at 1 m away from the mining face were estimated to be 221, 194, 159, 112 and 83 mg/m$^3$, respectively at air velocity 3, 4, 5, 6 and 7 m/s. The concentrations at 2 m from the face considerably reduced to 85, 75, 67, 71 and 64 mg/m$^3$ at the respective air velocities. Thereafter, the

**Fig. 6.** Variation of average dust concentration in development heading at 0.5 m intervals from mine face at different air velocities

dust concentration along the heading more or less stabilized. A sudden rise in dust concentration was observed between 6 and 8 m away from mine face because of recirculation of air near the discharge end of the duct placed at 7 m from the face. The actual dust generation in continuous miner heading was so high (52.3 mg/m$^3$ measured at 6 m from the face) that it could be reduced to a level of 58, 57, 132, 65 and 47 mg/m$^3$ at 6 m distance from mine face at air velocity 3, 4, 5, 6 and 7 m/s respectively. This validates the simulation results as the dust concentration measured in the mine at 6 m distance from the face was 52.3 mg/m$^3$. The dust concentration in the heading was found to be minimum at 7 m/s air velocity, nevertheless the difference between the dust concentrations estimated at 6–7 m/s air velocities was found to be less. Therefore, it is preferable to maintain the air velocity in duct between 6 and 7 m/s.

## 3.2    Effect of Ventilation Duct Diameter

The effect of ventilation duct diameter on dust dispersion behavior in development heading was studied at different duct diameters, viz. 0.6, 0.7, 0.8 and 1 m and keeping other parameters constant (Case 2 in Table 2). The objective was to find out if the optimum duct diameter will cause better dust dispersion in the heading. Figures 7 and 8 illustrate the contours of air velocity and dust concentration at 2 m intervals along the development heading for different ventilation duct diameters. Figure 7 clearly shows that the dead zones formed near the diagonally opposite corners of ventilation duct diminish gradually with increase in duct diameter at a constant air velocity of 7 m/s. This is due to increase in airflow rate with increase in duct diameter at a constant air velocity. Figure 8 shows that the dust concentration is minimum near the roof corner (duct discharge end) and maximum at the dead zones in case of all the tested duct diameters.

The variations of average dust concentration in the heading at 0.5 m intervals from mine face at different ventilation duct diameters are shown in Fig. 9. From the figure it is evident that the dust concentration decreases with increase in duct diameter for a
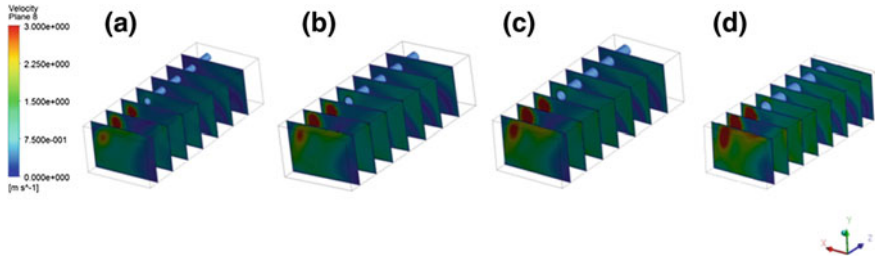
**Fig. 7.** Air velocity contours in development heading at 2 m intervals from mine face at different ventilation duct diameters **a** 0.6 m, **b** 0.7 m, **c** 0.8 m and **d** 1 m
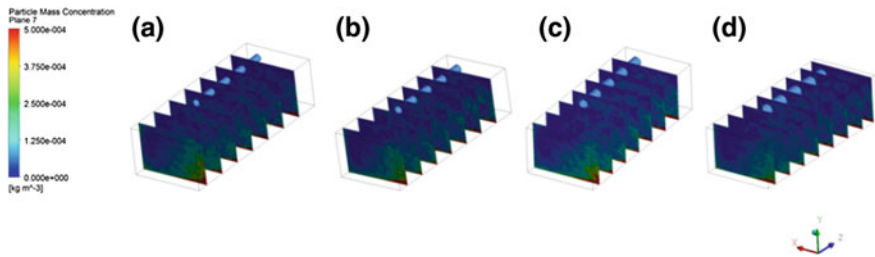


**Fig. 8.** Contours of dust concentration in development heading at 2 m intervals from mine face at different ventilation duct diameters **a** 0.6 m, **b** 0.7 m, **c** 0.8 m and **d** 1 m diameters
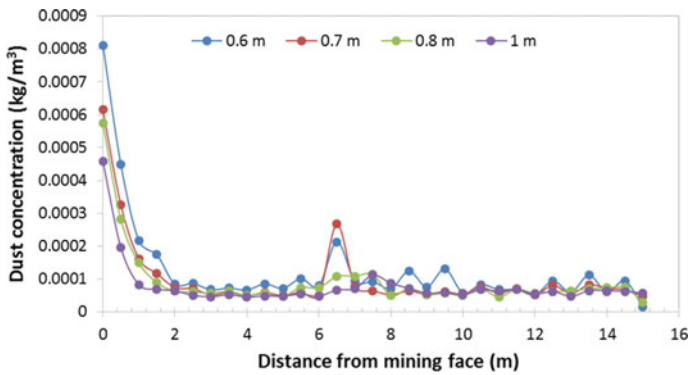


**Fig. 9.** Variation of average dust concentration in development heading at 0.5 m intervals from the mine face at different duct diameters

particular air velocity due to delivery of larger air quantity. Therefore, the average dust concentration along the development heading was found to be minimum at largest duct diameter of 1 m and maximum with smallest diameter of 0.6 m. While the average dust concentrations at 1 m distance from mine face were measured 216, 161, 149 and 83 mg/m$^3$ respectively at duct diameters 0.6, 0.7, 0.8 and 1 m, the concentrations at

2 m from the face measured 84, 73, 64 and 62 mg/m$^3$ at the respective duct diameters. Thereafter, the dust concentration nearly stabilized throughout the heading, except a sudden rise in dust concentration noticed at 6.5 m away from the face especially with small duct diameters 0.6 and 0.7 m due to recirculation of air near the discharge end of duct. Since, 1 m diameter ventilation duct resulted in greater dust dispersion, it is preferable to use the same for auxiliary ventilation of development heading.

### 3.3  Effect of Setback Distance

In order to examine the effect of setback distance of duct on dust dispersion and find out the optimum setback distance for better dust dispersion in development heading, the setback distance from mine face was varied from 5 to 8 m at 1 m intervals, while keeping other parameters constant as presented in Table 2 (Case 3). Figures 10 and 11 illustrate the contours of air velocity and dust concentration respectively at 2 m intervals from the mine face at different setback distances. These contours clearly show that the increase in setback distance in the studied range resulted gradual decrease in dead zone formed opposite to the ventilation duct and in turn decreased the dust concentration.
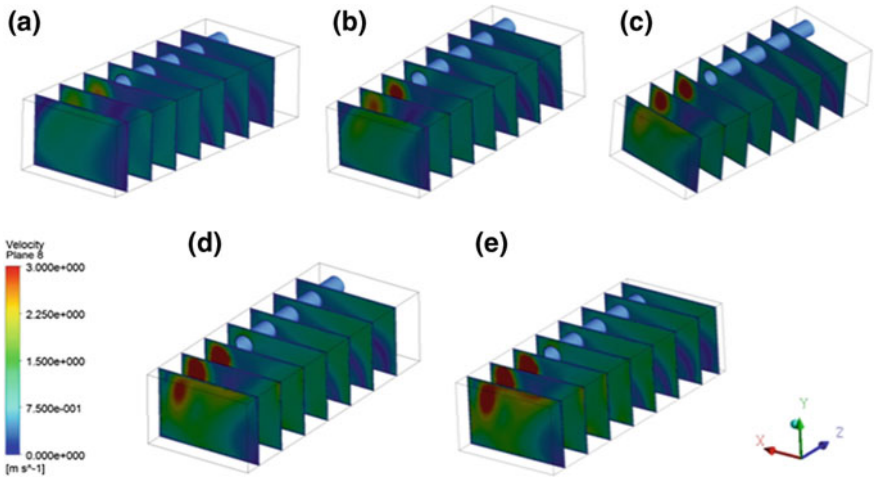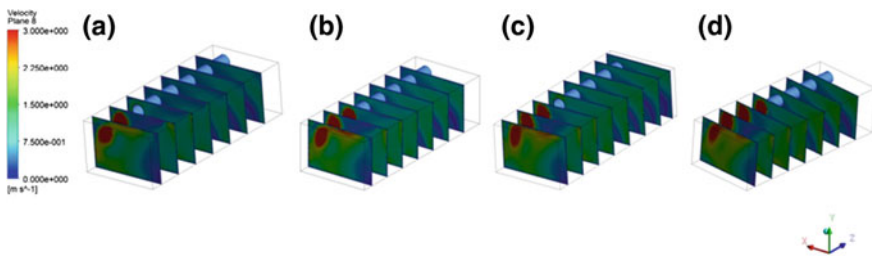


**Fig. 10.** Air velocity contours in development heading at 2 m intervals from mine face at different setback distance **a** 5 m, **b** 6 m, **c** 7 m and **d** 8 m
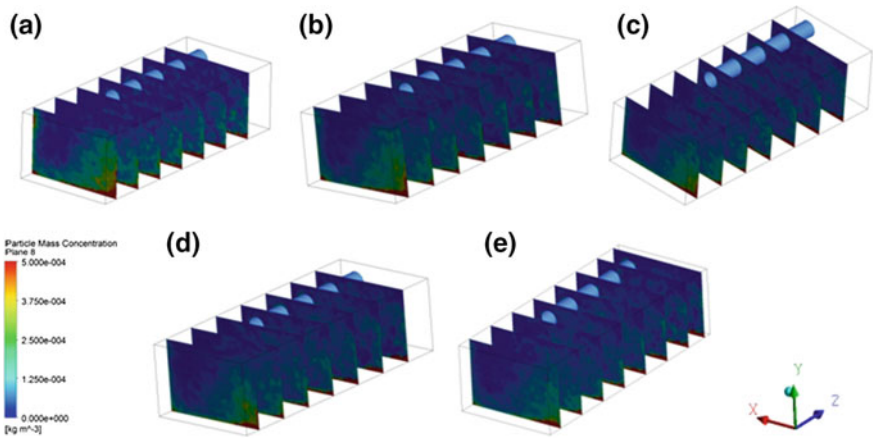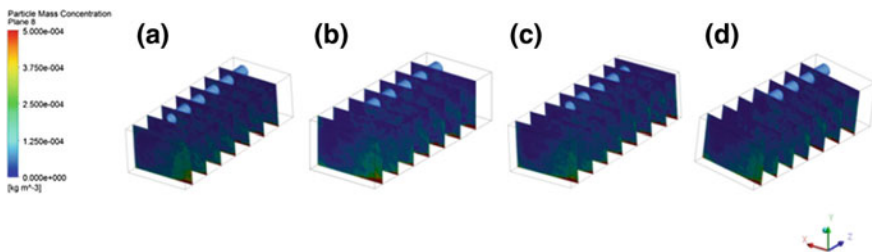


**Fig. 11.** Contours of dust concentration in development heading at 2 m intervals from mine face at different setback distance **a** 5 m, **b** 6 m, **c** 7 m and **d** 8 m

The variations of average dust concentration in development heading at 0.5 m intervals from the mine face at different setback distances have been presented in Fig. 12. Generally the dust concentration in heading up to 5 m from the face decreased with increase in setback distance. Thereafter, the variation in dust concentration was found to be uneven and it did not follow any distinctive trend with variation of setback distance. The average dust concentrations at 2 m away from the face were measured 59, 59, 64 and 45 mg/m$^3$ at setback distance of 5, 6, 7 and 8 m respectively. Generally, better dust dispersion was achieved at setback distance of 7 and 8 m with negligible difference in results between them. Therefore, it is preferable to maintain the setback distance of duct from mine face between 7 and 8 m.
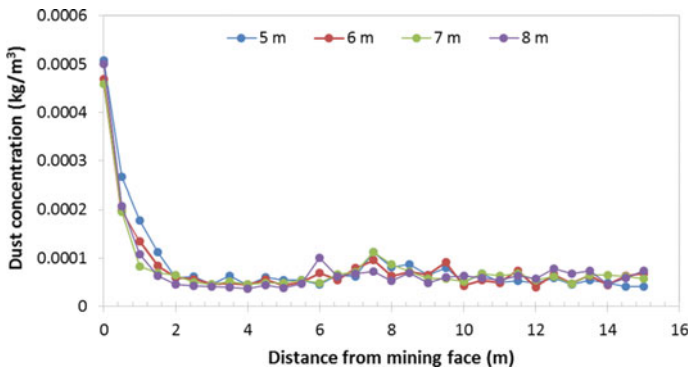


**Fig. 12.** Variation of average dust concentration in development heading at 0.5 m intervals from the mine face at different setback distance

### 3.4    Effect of Duct Height

The effect of duct height from mine floor on dust dispersion in development heading was examined at 2, 2.25, 2.5 and 3 m heights from the floor keeping other parameters constant (Case 4 in Table 2). The objective was to find out the optimum duct height for better dust dispersion from continuous miner heading. Figures 13 and 14 illustrate the contours of air velocity and dust concentration respectively at 2 m intervals from the mine face with different duct heights from mine floor. Figure 14 clearly shows that among all the tested duct heights, 2.25 m height causes greater dust dispersion and reduced the dust concentration in heading to a minimum.

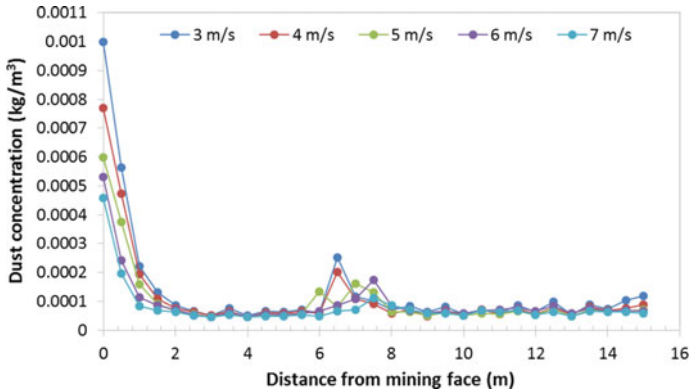Figure 15 shows the variations of average dust concentration in development heading at 0.5 m intervals from mine face at different duct heights. The results show that the dust concentration steadily decreased up to 5.5 m distance from mine face in case of all the duct heights. Subsequently, dust concentration in the heading fluctuated with all duct heights except 2.25 m, at which the concentration fairly stabilizes along the heading. Among all, 2.25 m duct height resulted maximum dust dispersion in the heading. As a result, the average dust concentration significantly reduced to its minimum value of 32 mg/m$^3$ and 5 mg/m$^3$ at 1 m and 15 m respectively from mine face.
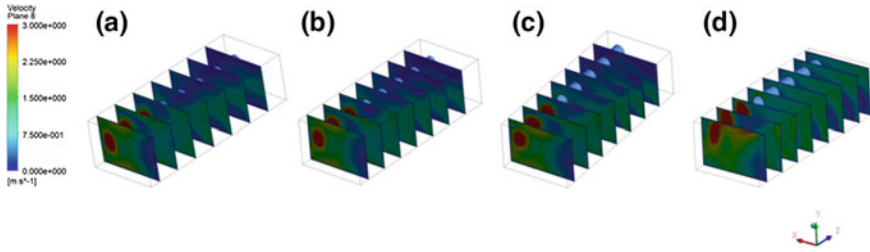
**Fig. 13.** Air velocity contours in development heading at 2 m intervals from mine face at different heights of duct from mine floor **a** 2 m, **b** 2.25 m, **c** 2.5 m and **d** 3 m
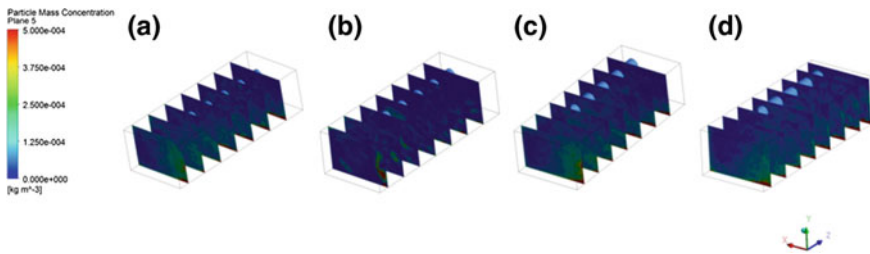


**Fig. 14.** Contours of dust concentration in development heading at 2 m intervals from mine face at different heights of duct from mine floor **a** 2 m, **b** 2.25 m, **c** 2.5 m and **d** 3 m
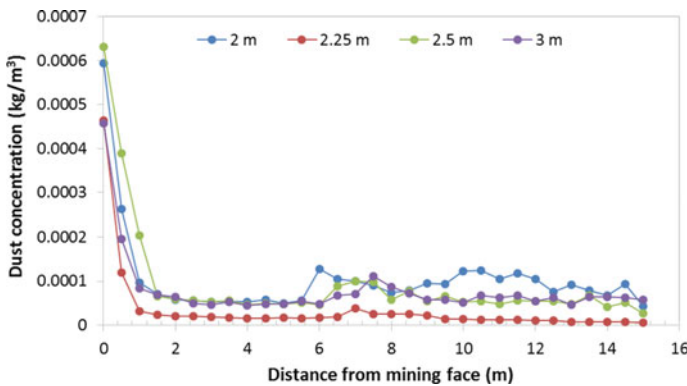


**Fig. 15.** Variation of average dust concentration in development heading at 0.5 m intervals from mine face at different duct heights from mine floor

This suggests that duct height from floor is the significant auxiliary ventilation parameter and duct height of 2.25 m found to be most suitable for effective dust dispersion in continuous miner development heading.

## 4   Conclusions

In this study, the dust concentration in continuous miner development heading was measured using Grimm Aerosol Spectrometer (Model 1.108). The total and respirable dust (<5 μm) concentrations at 6 m distance from mining face were measured 52.3 and 26.74 mg/m$^3$, respectively. Also, the effects of various auxiliary ventilation parameters on dust dispersion behavior in development heading were numerically examined under various scenarios. The conclusions drawn from the present study are outlined below:

1. The dust concentration in development heading decreases with increase in air velocity and distance from the mine face due to greater dust dispersion effect of higher air velocity. Dust concentration in the heading was found to be minimum at 7 m/s air velocity.
2. Increase in ventilation duct diameter from 0.6 to 1 m caused greater dust dispersion and reduced the dust concentration along the heading at a constant air velocity.
3. Generally the dust concentration in heading decreased with increase in setback distance up to 5 m from the mine face. The dust concentration was found to be relatively low at setback distances of 7 and 8 m.
4. Height of duct from mine floor was found to be the most significant auxiliary ventilation parameter. Maximum dust dispersion was achieved at a duct height of 2.25 m, which significantly reduced the dust concentration in heading to a minimum level of 32 and 5 mg/m$^3$ at 1 and 15 m distance respectively from mine face.
5. The best suitable combination of auxiliary ventilation parameters for effective dust dispersion in mine development heading is: air velocity-7 m/s, duct diameter-1 m, setback distance-7 to 8 m and height of duct from mine floor-2.25 m.

## References

1. DGMS Circular (Circular tech. 5). Lovely Prakashan Dhanbad, India (1987)
2. Niu, W., Jiang, Z.G., Tian, D.M.: Numerical simulation of the factors influencing dust in drilling tunnels: its application. Min. Sci. Technol. (China) **21**, 11–15 (2011)
3. Kurnia, J.C., Sasmito, A.P., Mujumdar, A.S.: Dust dispersion and management in underground mining faces. Int. J. Min. Sci. Technol. **24**, 39–44 (2014)
4. Torano, J., Torno, S., Menendez, M., Gent, M.: Auxiliary ventilation in mining roadways driven with roadheaders: validated CFD modeling of dust behavior. Tunn. Undergr. Space Technol. **26**, 201–210 (2011)
5. Tariq, F., Bekir, G.: Evaluation of line brattice length in an empty heading to improve airflow rate at the face using CFD. Int. J. Min. Sci. Technol. **27**, 253–259 (2017)
6. Kurnia, J.C., Sasmito, A.P., Hassani Ferri, P., Mujumdar, A.S.: Introduction and evaluation of a novel hybrid brattice for improved dust control in underground mining faces: a computational study. Int. J. Min. Sci. Technol. **25**, 537–543 (2015)

7. Mishra, D.P., Kumar, P., Panigrahi, D.C.: Dispersion of methane in tailgate of a retreating longwall mine: a computational fluid dynamics study. Environ. Earth Sci. **75**, 475 (2016)
8. The Coal Mines Regulations, India (CMR) (2017)
9. Grimm Aerosol Spectrometer manual
10. Zhou, G., Zhang, Q., Bai, R., Fan, T., Wang, G.: The diffusion behavior law of respirable dust at fully mechanized caving face in coal mine: CFD numerical simulation and engineering application. Process Saf. Environ. Prot. **106**, 117–128 (2017)

# Coping with Diffuse Dust Emissions in Mining by Fibrous Filters with Trickling Water Cleaning

Federico Marangoni[1,2] and Gernot Krammer[2(✉)]

[1] Università di Bologna, Via Zamboni 33, 40126 Bologna, Italy
[2] Graz, University of Technology, Inffeldgasse 13, 8010 Graz, Austria
`krammer@tugraz.at`

**Abstract.** In underground mining operation, air is contaminated with fine dusts that can be removed by filtration effectively. Filter cleaning is envisioned to prolong filter media lifetime and to ensure uninterrupted operation requiring little maintenance. For cake filtration, reverse airflow or pulse flow, or filter shaking are widely used. But for depth bed filtration which is needed to meet more stringent emission requirement, continuous filter cleaning is generally not practical. The concept of continuous liquid rinsing of depth filter media is proposed and preliminary studies are performed. These laboratory studies on single vertical fibers include hydrodynamic tests of water along various filter fibers as well as cleaning with different sample dusts. All tested fibers have hydrophobic properties that result in the formation of clamshell droplets with moderate particle removal success. Small, plate-like particles are particularly difficult to remove. Comparative tests with oil that forms a homogeneous film provide excellent particle removal.

**Keywords:** Dust filtration · Fiber cleaning · Water rinsing

## 1 Introduction

During mining dust emissions are omnipresent, causing major problems for miners and equipment. In underground mining and other confined spaces, emitted dusts are usually resolved by a well-designed ventilation system where contaminated air (dusts but also other exhaust fumes and hazardous gases) is diluted by fresh air or reconditioned locally. An effective ventilation system is a challenge as mining faces where most dusts are generated are constantly advancing. Anyhow, once the dusty air is diluted by the ventilation system, thus lowering dust concentration (below the threshold of set emission limits) and no specific dust removal system is needed. But, in case that there are excessive dusts in the airflow and reconditioning is necessary, dust removal is paramount since in confined spaces dust concentration in terms of occupational exposure needs to be as low as 1 mg/m$^3$ or less [1] up to 2.5 mg/m$^3$ [2]. But these limits are still two orders of magnitude higher than generally required limits, i.e., below 50 µg/m$^3$ [3].

Generally, cake filtration is at its lower application limit and depth filtration need to be used when aiming towards emission limits [3]. Since these filters need to be replaced regularly, i.e., when the filter capacity is reached and the pressure loss across the filter rises, and servicing these filters underground is particularly cumbersome. Liquid water sprays are used to suppress dust formation and distribution [4, 5]. This is quite efficient to tackle point sources but once dust is already distributed in the air, a large volume of airflow with water spray are needed for effective dust suppression. This will generate large amount of slurry that needs to be collected and treated before discharge or reuse [3].

Generally, air filters exhibit complex structures where many single fibers are entangled forming a felt with a regular woven structure embedded for mechanical support. These support fibers are made up of numerous aligned single fibers. Inside the filter, voids are in irregular shapes. Due to the inertia of dust particles, dust-laden airflow do not strictly follow the regular airflow path as it flows through the complex filter structure. Instead, dusty airflow hit fibers and most dust particles deposit on the filter, i.e., they are removed from or bounce back to air stream, or into the air stream [6]. Rather open filter structures—significantly larger openings than the particle size— guarantee low pressure loss across the filter that reduces the likelihood of particles to come in contact with filter fiber surfaces and being trapped on filter surface. The void fraction of the filter is a measure of the depth filter's capacity [7]. Increasing filter thickness results in a better separation efficiency, higher filter capacity but also in slightly higher flow resistance, i.e., higher pressure loss.

To increase a dust filter life, filter cleaning is essential, periodically either on-line, i.e., without interruption of mining operation, or off-line where the filter is either dismounted for cleaning or filter elements subjecting to cleaning sealed off from others [3]. To ensure truly continuous filter operation, continuous filter cleaning is needed which can be achieved by shaking the filters and thus separating the already deposited filter cake removed from the filter, or rinsing the filter with water where the deposited particles are washed off and the rest of the filter is treated afterwards. These cleaning measures—shaking or water rinsing—as well as other measures like reverse pulsing or counter airflow are initiated only periodically and/or sequentially to not reduce overall performance. Shaking, counter airflow or reverse pulsing liberate the deposited filter cake and it must be ensured that these particles (or cake scales) have the necessary time to settle and form a sediment which can be removed from the filter unit [8].

## 1.1 Concept of In-line Water Rinsing

The concept of in-line water rinsing does not target the entire filter at once because airflow might be interrupted by a continuous and dense water curtain (generally provided during liquid off-line cleaning). Instead, the liquid needs to be present only spatially leaving sufficient voids open where the gas can pass through.

For successful filter cleaning by liquid rinsing, liquid droplets need to be present. This liquid may be provided either by condensation of constituents in the gas phase, i.e., mist formation or by injection of liquid droplets into the gas stream upstream the filter [9, 10]. Of course, these liquid droplets can be provided directly onto the filter by trickling mode [11]. Anyhow, these droplets may adhere to the filter fibers as the gas

moves through the filter. Generally, this is a dangerous and often unwanted situation since this liquid phase together with the solid particles may form deposits on the filter and the pressure drop rises quickly and a continuation of filter operation is not possible [10]. This is particularly common when the liquid droplets are present only temporarily and these slurry droplets dry up. Thus, it is paramount that these droplets not only get in contact with the contaminating solid particles, but that these solid particles give up their connection with the fibers in favor of liquid phase. Moreover, these "loaded" droplets must be collected separately, i.e., separated from the fiber structure and not re-entrained into the gas phase [12].

Unless droplets are re-entrained by the gas flow, the fiber structure may serve as a guiding structure for the loaded droplet movement [13], which, of course, requires, that these droplets are not pinned stably on the fiber but will flow along the single fibers as well as across more complex filter fiber assemblies. Generally, filter fibers are oriented arbitrarily and sometimes also interlinked and thus these droplets need to be capable to overcome crossings as well as upward bending. If droplet movement is predominantly relying on gravity, a critical minimum droplet size must be exceeded to ensure droplet movement along the fiber and to allow at least temporary discharge from the fiber. Clearly impinging loaded water droplets, that disintegrate on impact can cause particle re-entrainment in the gas phase and shall be avoided. Moreover, also re-entrained droplets need to be avoided as they contaminate the clean gas.

### 1.2 Scope

Different material systems, i.e., fiber material, and disperse dust particles and liquid droplets are investigated experimentally. Single fibers are covered with fine dust particles and liquid droplets are created and carefully placed on the vertically oriented fibers where they move along by gravity. The situation is optically followed by a high-speed camera to determine the external shape, i.e., size and the flow velocity of droplets. Pictures are taken from the fibers before and after rinsing, respectively, by optical microscopy to determine the cleaning capacity qualitatively [11].

## 2 Material and Experiment

Four different fiber materials are investigated with different diameters and geometries, i.e., PTFE, P84 Polyimide, stainless steel and polyester. The geometry of the cross-section as well as the dimensions are given in Table 1. SEM pictures of the original fibers are shown in Fig. 1.

Five different types of dusts are used and are listed in Table 2 together with their characteristic diameters x50 and x90. SEM pictures are shown in Fig. 2.

Two different liquids are used, i.e., double distilled water and lubrication oil with a dynamic viscosity of 0.695 Pa·s. Table 3 highlights the systems that are actually investigated.

For the preparation of a dusted fiber, a single fiber is taken and submerged in the respective particle heap. Afterwards it is carefully pulled out longitudinally and mildly shaken to remove loosely adhering particles. Fibers are investigated visually by an

**Table 1.**  Characteristic dimensions of fibers

| Fiber material | Geometry | Diameter/length × width (μm) |
|---|---|---|
| PTFE dtex 110 | Rectangular | 237 × 20 |
| P84 Polyimide | Trilobite | 20 |
| Stainless steel | Circular | 350 |
| Polyester | Circular | 35 |
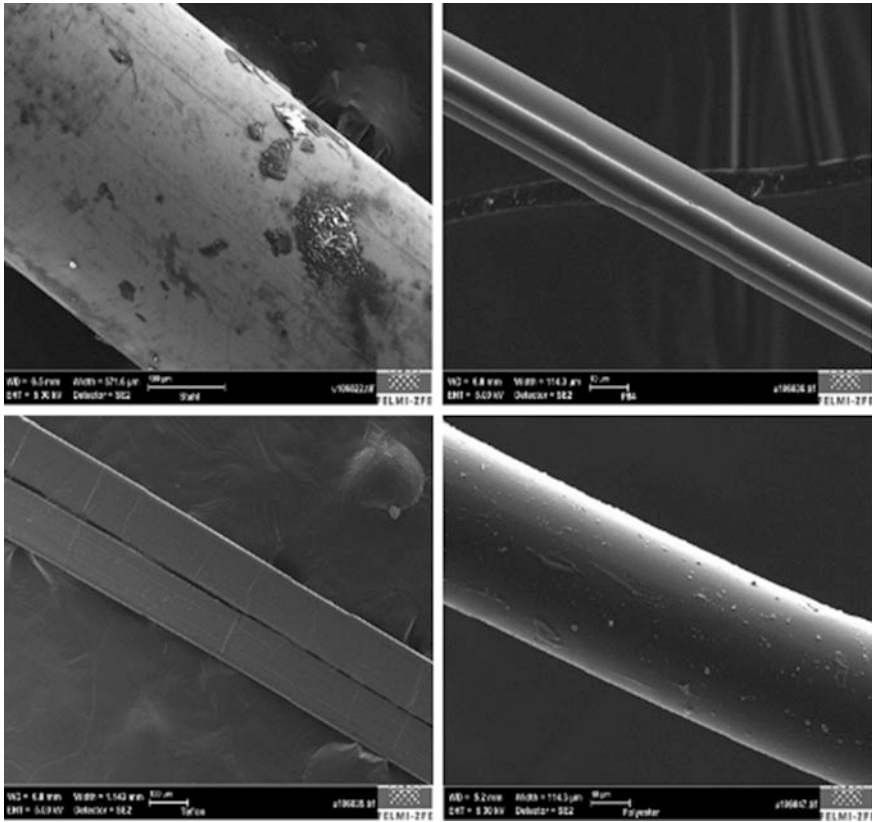


**Fig. 1.**  Fibers—upper left: steel, upper right: P84, lower left: Teflon, lower right: polyester

**Table 2.**  Characteristic data of the dust material

| Particle material | X50 (μm) | X90 (μm) |
|---|---|---|
| Graphite | 70 | 157 |
| PEEK | 21 | 42 |
| Talcum | 10 | 37 |
| Quartz | 16 | 44 |
| Limestone | 36 | 193 |
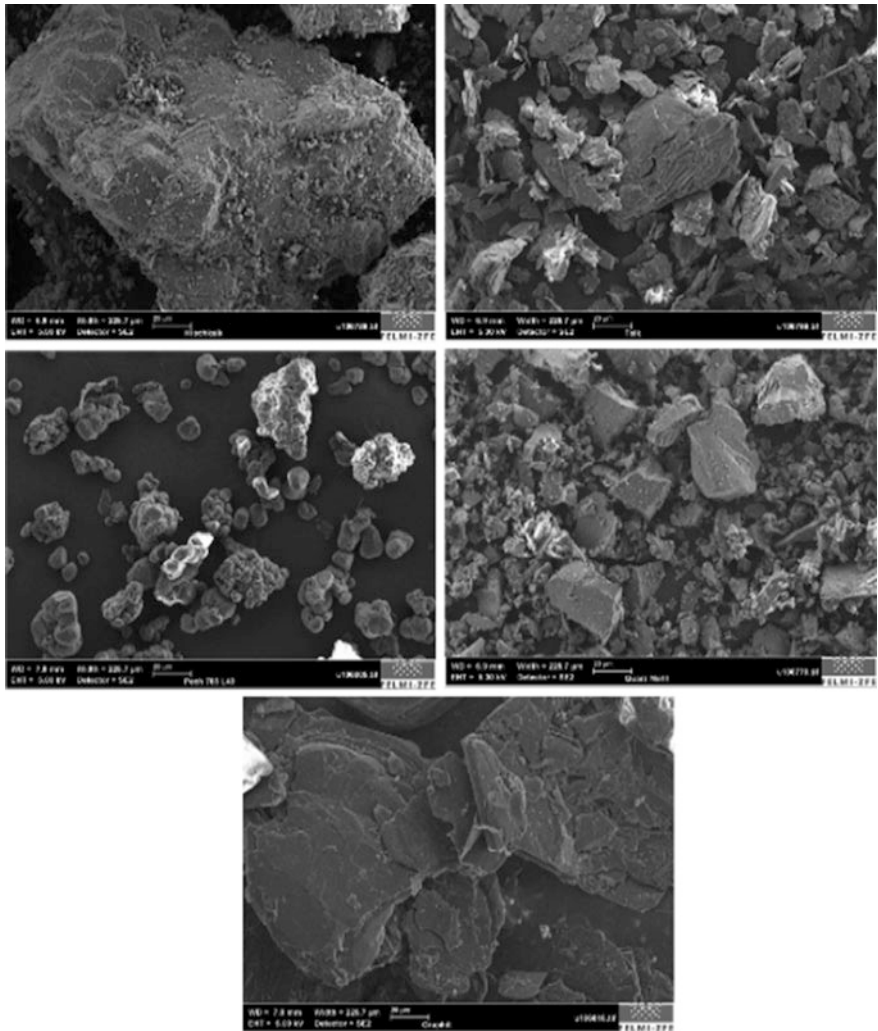
**Fig. 2.** SEM pictures of the particles (upper left: limestone, upper right: Talcum, middle left: Peek, middle right: quartz, lower: graphite (bar is always 20 μm)

optical microscope to obtain a qualitative impression of the particle density on the fiber. For liquid droplet rinsing tests, the end of the fiber, not covered with particles, is carefully fed through a liquid funnel. Both ends of the fiber are fixed and the fiber is straightened vertically. Generally, the liquid droplets are placed on the fiber through differently sized funnels, syringe or pipettes, which are filled by an automatic dosing system or a predefined volume is provided manually. During some of the test, the liquid droplets are directly placed on the fiber by a syringe.

The size of the droplets depends predominately on the kind of liquid and on the opening size of the funnel or syringe, respectively. The number of droplets per time is

**Table 3.** Investigated systems with respect to particle type, filter type and liquid, i.e., oil or water, respectively

|  | FIBER | | | |
|---|---|---|---|---|
| Particle | PTFE (110 dtex) | Stainless steel | P84 | Polyester |
| Limestone | Oil and Water | | Oil and Water | Water |
| Quartz | | Oil and Water | | Water |
| Talcum | Oil and Water | | Water | |
| PEEK | Oil and Water | | Water | Water |
| Graphite | | Water | Water | Water |

decided by the quantity of liquid provided. An optical system, i.e., high-speed camera (300 Hz) is placed perpendicular to the vertical fiber with continuous illumination as backlight. A schema of the set-up is depicted in Fig. 3. The tips of the syringe and funnels are all cut normal to the axis with different circular diameters resulting in different mean diameters as given in Table 4. For the larger discharge openings, two different classes of particles are formed, generally in a strict succession with a larger droplet sometimes immediately followed by a smaller (secondary) one. For the smaller discharge openings, only the smaller class is present. Some of the droplets loose contact with the fiber quickly whereas others adhere to the fiber and move along the fiber until they are discharged into the liquid collection reservoir. The window of camera observation is kept constant and the droplet images are present in 2D only. In a simplistic way the geometry of each droplet is captured two times by two diameters, i.e., maximum
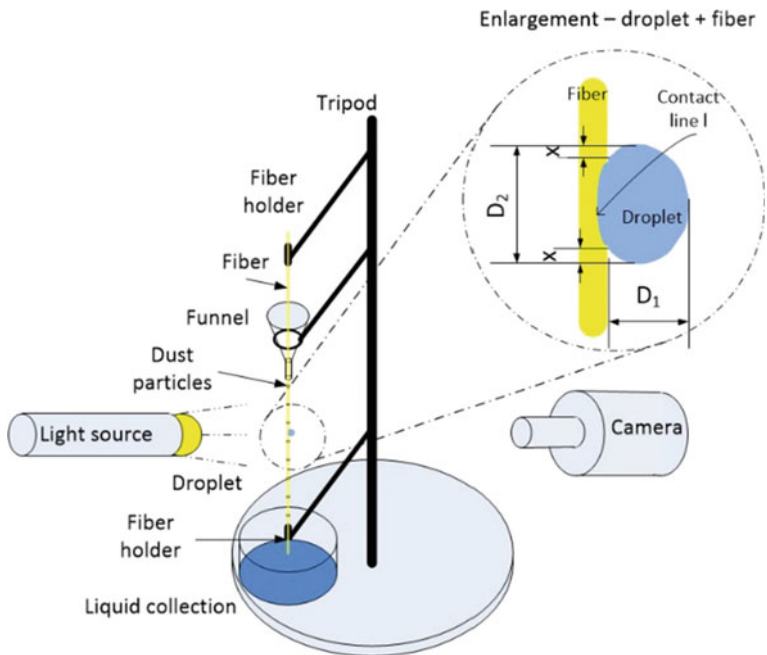


**Fig. 3.** Experimental setup for dust removal from a vertical filter fiber by liquid droplets

**Table 4.** Liquid discharge opening, mean water droplet volume, and calculated circular droplet diameter

|  | Exit Diameter (mm) | Mean droplet volume (mm$^3$) | $D_1$ (mm) | $D_2$ (mm) |
|---|---|---|---|---|
| Pipette | 0.2 | 7.4 ± 1.4 | 2.3 | 2.6 |
| Pipette | 1 | 12.5 ± 2.5 | 2.6 | 3.1 |
| Funnel | 3 | 58.2 ± 13.8 | 4.2 | 7.8 |
|  |  | 13.4 ± 11.1 | 1.2 | 3.3 |
| Funnel | 5 | 88 ± 14.6 | 5.2 | 6.4 |
|  |  | 3.7 ± 2.4 | 1.2 | 2.2 |
| Syringe | 2.2 | 45.5 | 4.43 |  |

horizontal and vertical ones, respectively, which are shown schematically in the enlargement of Fig. 3. Arithmetic mean diameters are calculated from the two images resembling respective mean diameters of a prolate spheroid with two equivalent horizontal diameters and one long vertical diameter. With these diameters the droplet volume is calculated. Based on this a volume, the diameter of the equivalent sphere is determined which is given in Table 4. These results suggest an almost linear increase of the droplet volume with the diameter of the opening of the liquid discharge unit.

The velocity of the droplet is calculated by measuring the vertical distance of two droplet images in consecutive frames, i.e., at a set image sequence rate.

## 3   Results and Discussion

### 3.1   Hydrodynamics

The correlation between water droplet velocity and volume as a function of the fiber type is depicted in Fig. 4. The results are quite similar among PTFE and P84 fibers whereas for the stainless steel fiber the velocity is markedly lower. The difference whether the fiber is dusted or clean is investigated for PTFE dtex 110 only. The velocity appears to be slightly higher for a clean fiber as compared with the dusted one. As expected the velocity increases rapidly as the droplet volume increase but seems to arrive at a steady-state level for larger droplets. Clearly, fibers not exceeding a critical size tend to adhere to the fiber without moving. (The droplet velocity as observed here is around one order of magnitude lower than the respective free falling drop velocity.)

Whether a droplet is moving along a fiber and if so, at which velocity can be calculated through a force balance acting on such a droplet. The most relevant forces are gravity, drag and interaction force between the droplet and the fiber whereas acceleration and buoyancy forces are generally negligible.

The force balance is given by

$$F_g - F_D - F_i = 0 \tag{1}$$

The interaction force, also termed restoring force due to surface tension on the contact line [14], between the droplet and the fiber shall be expressed by the contact
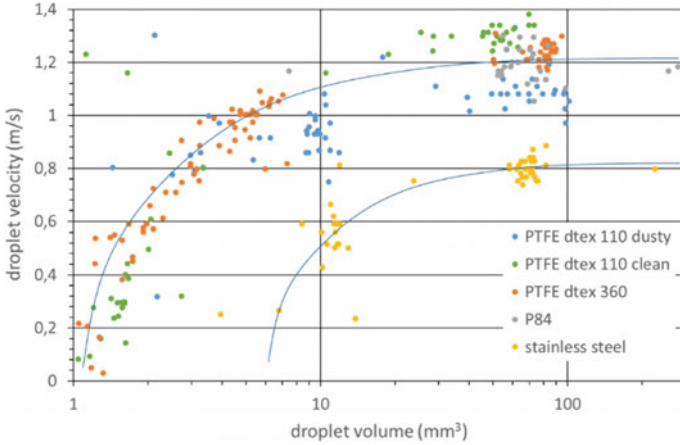
**Fig. 4.** Water droplet velocity on clean fibers versus droplet volume for different fiber materials. (Solid lines denote manual trend lines for stainless steel and others, respectively)

length l (also termed penetration curve length or pinning triple line) times the surface tension of the liquid (for water $\sigma = 0.072$ N/m). Thereby the specific contact situation is lumped into the contact length l.

$$F_i = l \cdot \sigma \tag{2}$$

Whether a droplet slides along the fiber as a film or carries out a rotational movement, could not be determined optically though it can be estimated by calculation of the Bond number [15]. Droplets that exhibit hydrophobic behavior tend to favor a rolling movement [16]. A clarification of the mode of movement is however relevant: When a sliding film meets dust particles, the particles may be lifted (and thus detached) from the surface or they are overflown. Once overflown, these particles may be detached and fully immersed in the liquid film, slide along the surface together with the film (same or different speed), or stay put without movement. Droplets that move along a surface by rotational movement may also pick up dust particles on their surface. Dust particles that are immersed in the liquid can be estimated by the so called Bond number [17].

$$Bo \equiv \frac{m \cdot g}{l \cdot \sigma} \tag{3}$$

where m denotes the mass of the particles and l and $\sigma$ the perimeter of the surface of the particle and the surface tension of the liquid, respectively. Since the Bond number is well below one for these dust particles, it is to be expected that the particles are not immersed in the liquid body but stay on the surface. Clearly, the capacity of particle uptake is smaller in this case compared with the situation where the particles penetrate the liquid surface and are collected inside the droplet.

Dependent upon the fiber diameter, droplet volume, contact angle and surface tension the droplet can assume different conformations on a fiber, i.e., complete wetting, clamshell, symmetric barrel or asymmetric barrel shape. Also, the surface roughness of the fiber has an influence on the type of conformation [18–20]. If the contact angle is low, the liquid is wetting the fiber fully and no droplets form. Thus, a continuous liquid film is formed that flows along the fiber. At a larger contact angle droplets form denoting partial wetting situation which is also termed (hydro)phobic behavior, and in case of a contact angle above 150° also super(hydro)phobic behavior.

The contact length l is a space curve, which is difficult to be estimated from the existing 2D images. For a barrel-shape droplet configuration the contact line is basically two times the circumference of the fiber.

A barrel shape configuration is observed when the Laplace contact angle is low and the droplet is big in comparison to the fiber diameter. Here the pairing of water and fiber is hydrophobic, clam-shell configuration is to be expected particularly since the difference between the vertical elongation ($D_2$) and its horizontal distance ($D_1$) is generally below 20% [19] justifying the approximation of the droplet as a sphere. In Fig. 5 the calculated contact length is plotted over the experimentally determined diameter $D_2$.
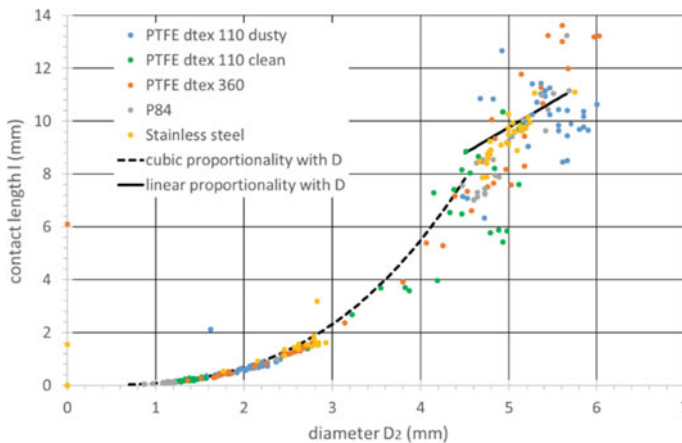


**Fig. 5.** Calculated contact length l over water droplet diameter $D_2$

Irrespective of the size, geometry and type of fiber the data collapse in a master curve. Clearly, the major fraction of the contact line of larger droplets (with respect to the fiber diameter) is present along fiber axis. This explains the linear proportionality between the contact length and the fiber diameter $D_2$ with a proportionality factor of almost two, which is mathematically expressed in the equation below and graphically shown in Fig. 5. On the other hand, the contact length of smaller, clamshell droplets correlates with the droplet volume as depicted in Fig. 5, which is the consequence of how the contact line is calculated from the force balance. The geometric profile of this contact line is however not accessible. Between these two regimes, i.e., $D_{crit,small}$ and $D_{crit,large}$ a transition zone might be present.

$$
\begin{aligned}
D_{crit,large} &< D_2 < D_{2,disloge} \quad l \approx 2 \cdot (1 - 2 \cdot x) \cdot D_2 \\
D_{2,min} &< D_2 < D_{crit,small} \quad l \propto D_2^3
\end{aligned}
\tag{4}
$$

where x expresses the receding length due to hydrophobicity (see also insert in Fig. 3). [From the fit x was determined as 12 μm which is a value plausible given the diameter of the smallest fiber investigated, i.e., P84 (see Table 1)].

Clearly, particles will potentially only be removed where the droplet is on contact with the dusted fiber. For a barrel-shape droplets, the entire circumference of the fiber is cleaned at once whereas for clamshell droplets only streaks are subject of cleaning and also only temporarily since between successive droplets there is always a gap. For a perfectly vertically oriented and homogeneous fiber, the position of droplets is arbitrary with the potential that the entire fiber is subject for cleaning. However, generally the situation is much more inhomogeneous in terms of orientation, droplet deposition and fiber surface homogeneity. Thus, preferential pathways of these droplets are expected which is visually observed even for the laboratory set-up.

## 3.2   Cleaning Performance

The cleaning performance of the fibers is difficult to access: The appearance of the dusted fiber before and after cleaning is compared qualitatively by optical observation (see e.g. Fig. 6) and the performance is rated by classes 1 (excellent) to 5 (no cleaning at all). The results are listed for water and oil in Table 5. The parameters are type of fiber, particle type, and quantity of liquid used.
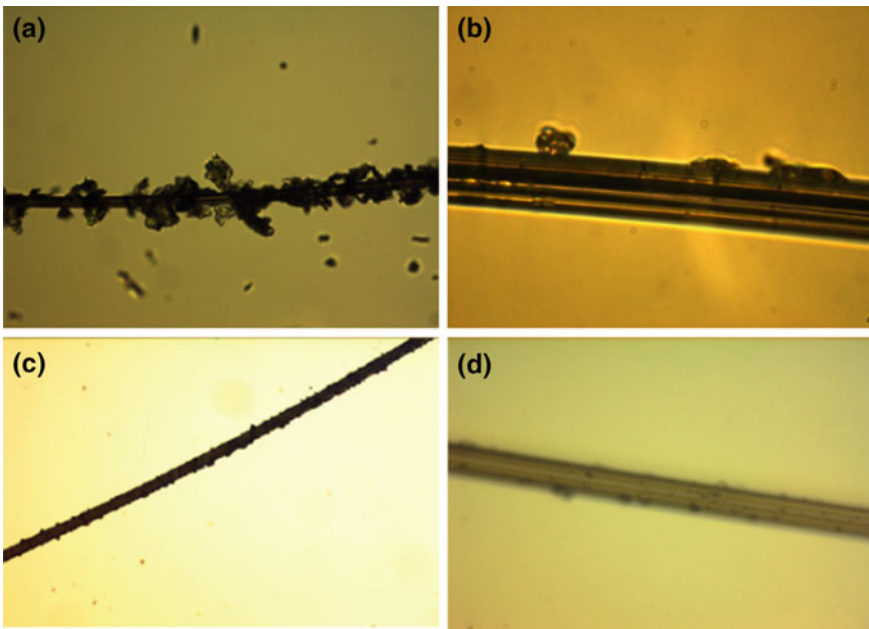


**Fig. 6.** Talcum (upper) and limestone (lower) of dusted (**a**) and cleaned (**b**) P84 fibers

**Table 5.** Qualitative cleaning efficiency (class 1: very good, class 2: good, class 3: medium, class 4: poor) for different fibers, particle material and quantity of water (upper table) and oil (lower table)

| No. | Fiber | Particle | $H_2O$ clean. (mL) | Class |
|---|---|---|---|---|
| 1 | PTFE | Lime | 0.343 | 3 |
| 2 | PTFE | | 1.914 | 1 |
| 3 | PTFE | Peek | 0.049 | 3 |
| 4 | PTFE | | 0.5 | 2 |
| 5 | PTFE | Talcum | 0.035 | 4 |
| 6 | PTFE | | 0.464 | 4 |
| 7 | SS | Graph | 0,0 h | 1 |
| 8 | SS | | 1.32 | 1 |
| 9 | SS | Quartz | 0.028 | 2 |
| 10 | P84 | Graph | 0.528 | 1 |
| 11 | P84 | Peek | 0.176 | 1 |
| 12 | P84 | Talcum | 0.792 | 2 |
| 13 | P84 | Lime | 1.056 | 2 |
| 14 | Polyester | Lime | 1.5 | 3 |
| 15 | Polyester | | 5 | 2 |
| 16 | Polyester | Peek | 2 | 1 |
| 17 | Polyester | | 5 | 1 |
| 18 | Polyester | Quartz | 2 | 3 |
| 19 | Polyester | | 5 | 2 |
| 20 | Polyester | Graph | 2 | 2 |
| 21 | Polyester | | 5 | 1 |
| 22 | PTFE | Lime | 1 | 1 |
| 23 | PTFE | Talcum | 1 | 1 |
| 24 | PTFE | Peek | 1 | 1 |
| 25 | SS | Quartz | 1 | 2 |
| 26 | P84 | Lime | 1 | 1 |

A comparison of the cleaning performance between oil and water as the cleaning fluid shows that oil is substantially more suitable to remove particles than water, which can be attributed to the hydrophobicity of water whereas oil is perfectly wetting.

As expected smaller particles (Peek, Talcum, Quartz) are more difficult to remove from the fibers. Graphite, which is rather coarse, exhibits good removal properties. But the cleaning performance of limestone which is also coarser than the other powders remains ambiguous indicating that other parameters may be relevant as well. Talcum, which is particularly fine and has plate-like shape, is most difficult to remove.

Moreover, the quantity of cleaning liquid is also relevant for particle removal: If the amount of liquid is too small, cleaning efficiency is poor but after a critical threshold is met, further liquid rinsing has little to no effect in terms of better cleaning. This indicates that some particles cannot be removed from the fibers at all.

## 4　Conclusions

The system—fiber, particle type, size and shape and the type of fluid—has a big influence on the cleaning performance. For practical applications, a wetting fluid shall be selected for particle removal. The droplet diameter needs to be around two orders of magnitude larger than the fiber diameters conventionally used for depth filter media to ensure droplet movement along gravity. While these large droplets provide additional surface area for particle removal, they also block gas flow and contribute to an augmented pressure drop. The tests were performed at single vertical fibers; in practice, however, filter media consist of numerous, often entangled, fibers where the droplets may accumulates on crossing before they can overcome such an obstacle or they must even detach when fibers reorient upwards. When using a liquid for filter cleaning, a suspension is created that needs to be collected and may need downstream handling adding to process complexity. When using liquid for filter cleaning, this liquid may evaporate and change the gas composition, e.g., in case of water, relative humidity is increased or droplets may be entrained into the gas stream. As expected liquid rinsing of fibers results in particle removal and thus it is a viable cleaning concept.

## References

1. Criteria for a recommended standard—Occupational Exposure to Respirable Coal Mine Dust, US Department of Health and Human Services (NIOSH) 95–106, Cincinnati, Ohio, US, Sept. 1995
2. Work Health and Safety (Mines) Regulation 2014, New South Wales, Australia, NSW legislation website 2014, no. 799 (version 12.12.2014)
3. Sparks, T., Chase, G.: Filters and Filtration Handbook, 6th edn. Elsevier, NY (2016)
4. Prostanski, D.: J. Sust. Min. **12**(2), 29–34 (2013)
5. Wang, H., Wang, C., Wang, D.: Pow. Techn. **320**, 498–510 (2017)
6. Löffler, F., Dietrich, H., Flatt, W.: Dust Collection with Bag Filters and Envelope Filters. Friedr. Vieweg & Sohn, Braunschweig, Germany (1988)
7. Purchas, D.B., Sutherland, K.: Handbook of Filter Media. Elsevier, Oxford (2002)
8. Leith, D., First, M.W., Feldman, H.: J. of Air Pollution Control Association **27**(7), 636–642 (1977)
9. Azis, N.I., Johnston, A.J., Craft, T.: Min. Sci. Technol. **8**, 177–188 (1989)
10. Peukert, W., Wadenpohl, C.: Powder Technol. **118**, 136–148 (2001)
11. Marangoni, F.: Filter cleaning with liquid droplets. Master Thesis, University of Bologna, Italy (2017)
12. Charvet, A., Gonthier, Y., Bernis, A., Gonze, E.: Chem. Engng Res. Design **86**, 569–576 (2008)
13. Kampa, D., Wurster, S., Buzengeiger, J., Meyer, J., Kasper, G.: Int. J. Multiph. Flow **58**, 313–324 (2014)
14. Mullins, B.J., Braddock, R.D., Agranovski, I.E.: Math. Comp. Sim. **81**, 1257–1271 (2011)
15. Suzuki, S., Nakajima, A., Sakai, M., et al.: Chem. Lett. **37**(1), 58–59 (2008)

16. Mahadevan, L., Pomeau, Y.: Phys. Fluids **11**, 2449 (1999)
17. Zlokarnik, M.: Scale-Up—Modellübertragung in der Verfahrenstechnik. Wiley-VCH, Weinheim, Germany (2000)
18. Gac, J.M., Gradon, L.: Colloids and surfaces A: Physicochem. Eng. Aspects **414**, 259–266 (2012)
19. McHale, G., Newton, M.I.: Colloids Surf., A **206**, 79–86 (2002)
20. Carroll, B.J.: Langmuir **2**, 248–250 (1986)

# Review of Real-Time Respirable Dust Survey Findings in Australian Coal Mines

Hsin Wei Wu[(✉)] and Stewart Gillies

Gillies Wu Mining Technology Pty Ltd, Brisbane, Australia
`hsinwei@minserve.com.au`

**Abstract.** Over the last 12 years, more than 20 real-time respirable dust surveys have been undertaken at various longwall and development faces in eight Australian underground coal mines by the authors. A number of the surveys were done in a series to monitor the improvements of dust conditions from various dust control devices or strategies applied in these mines or to evaluate the effectiveness of these devices. These real-time respirable dust surveys were conducted using state of art real-time Personal Dust Monitors (PDMs), a prototype of a continuous personal dust monitor (CPDM) recently introduced in US coal mines by the 2014 US MSHA final dust rules. The PDM was introduced into the Australian coal mining industry through an ACARP funded research project to evaluate the real-time PDM for personal respirable dust evaluation use particularly in engineering studies. This paper attempts to review the findings from these surveys undertaken in Australian coal mines. They provide guidance for performing effective, efficient and practical way real-time respirable dust surveys in an engineering study in the future. This is especially important due to the recent progressing incidences of Coal Workers Pneumoconiosis (CWP) in the Australian coal mining industry.

**Keywords:** Real-time respirable dust survey · Personal dust monitor (PDM)
Coal workers pneumoconiosis (CWP)

## 1 Introduction

Dust on longwall production faces has always been an issue of concern for production, safety and the health of workers in the underground coal mining industry in Australia and globally. Longwall personnel can be exposed to harmful dust from multiple dust sources including, but not necessary limited to, intake roadways, outbye conveyor belts, crusher/beam stage loaders (BSL), shearers, longwall face support shields (or chocks) advances and dust resulting from falling mined-out areas (such as gob or goaf) or over pressurization of the mined out areas.

Production from longwall mining in Australia has increased remarkably over the last two decades. The Table 1 shows some of the monthly and annual production records in various publication sources [1–6].

With the increase in coal production due to the advancement in longwall equipment technology and methodology, dust loads have also increased and this has resulted in an increase in personnel dust exposure levels. Increased production has also meant that

**Table 1.** Australian longwall production records published over the years

| Monthly production records | | | Annual production records | | |
|---|---|---|---|---|---|
| Year | Mine | Tonnage | Year | Mine | Tonnage |
| 2000 | Oaky Creek | 772,029 | 2005 | Beltana | 7,627,644 |
| 2005 | Beltana | 955,049 | 2009 | Newlands North | 8,318,421 |
| 2009 | Newlands North | 961,891 | 2015 | Grasstree | 10,000,000 |
| 2009 | Oaky North | 1,146,721 | 2015 | Narrabri[a] | 10,000,000 |
| 2015 | Grasstree | 1,200,537 | | | |

[a]Was projected by ICN report, July 2015

more dust is being produced and controlling both respirable and inhalable dust continue to present the greatest ongoing challenge for the coal mining industry.

In Australia this increased dust exposure level for underground coal workers can be directly attributed to the increase in coal production and the continued development of medium and thick seam mines, which allow the installation of bigger and more productive longwall equipment. Dust control mitigation processes vary from mine to mine, with each individual mine having a dust mitigation setup that is effective for that particular mine operation.

Since May 2015 more than 20 new CWP cases have been reported in the Queensland coal mining industry, with most in underground operations and one case from a surface operation. A review of the respiratory component of the Coal Mine Workers' Health Scheme in Queensland is recently undertaken as the first step of a five-point action plan to tackle the issue.

CWP has been a major concern in the U.S. over the last few years despite recorded conformance to exposure level legislation. This has led to issues on the validity and suitability of dust control strategies and the dust sampling methodologies currently utilized in Australia and the U.S. The U.S. MSHA has recently reduced the shift averaged permissible exposure limit for respirable coal dust from 2.0 to 1.5 mg/m$^3$. Starting February 2016, MSHA requires the use of Continuous Personal Dust Monitors (CPDM) to measure real-time respirable dust exposure under certain circumstances.

Real-time respirable dust sampling techniques have particular application for determining high source locations, efficiency of engineering means of suppression and other approaches to handle the problem. This paper gives an overview of case studies where real-time respirable dust monitoring was utilized to optimize dust control strategies at various Australian and US mines. The use of real-time respirable dust monitoring is able to provide mine operators with a comprehensive dust production signature of their operations hence allowing the implementation of more efficient controls at individual dust sources.

Statutory dust measurements in underground Australian coal mines were conducted mainly by Safety in Mines Testing and Research Station (SIMTARS) and Coal Services that rely on Australian Standards AS 2985 for respirable size dust particles, and AS 3640 for inhalable size dust particles. The majority of dust sampling to date has been with cyclone separation and collection of the sized particles for weighing, generally over the period of a full shift.

Although the above statutory method provides an accurate measurement for the total dust exposure for the period sampled, it does not always accurately reflect the source, quantity and timing of respirable dust entering the longwall face from different sources. This presents difficulties in determining the relative effectiveness of the different control technologies in use.

## 2    Review of Dust Controls and Monitoring

National Institute for Occupational Safety and Health (NIOSH) research [7] indicates that there are at least six individual dust sources on an average longwall production face. NIOSH Studies indicated that longwall shearers and chocks are the main dust sources on longwall faces, representing up to 80% of the total dust make. As the longwall shearer travels along the face, a significant portion of dust occurs in the crushing zone around the pick tips of the cutting drum. Generally the leading drum cuts the full drum height and generates the majority of the dust, while the trailing drum produces less dust due to the less coal being cut, concurrently as longwall supports (shields or chocks) are lowered and advanced. Crushed coal and/or rock can fall from the top of the chock canopy directly into the face airflow. Most of this dust becomes airborne, and quickly disperses into the walkways.

Dust generated due to face spalling ahead of the shearer is a major problem particularly for thick seam longwall faces. Dust can also be lifted up from the Armored Face Conveyor (AFC) by ventilation air when the direction of coal transport is against the direction of the airflow. Dust can be generated at all the conveyor transfer points along the intake airways. The movement of any outbye equipment can also cause significant quantities of dust to be raised into the atmosphere. A portion of dust can also be produced following roof caving behind the chocks and/or sudden gob falls. A significant part of this gob dust can be pushed onto the face as the leaked airflow returns to the face along the face support line.

### 2.1    Longwall Dust Controls

The mining industry's pursuit to achieve statutory dust levels worldwide has produced a number of methods for longwall dust control over the decades. These dust control methods include ventilation controls, water sprays mounted on shearer drums, deep coal cutting, modified cutting sequences, shearer clearer, dust extraction drum, water infusion, use of scrubbers at stage loader/belt transfer points and other methods. The majority of the dust control techniques have been developed in the USA, UK and some other western countries and their application is more suited to low to medium coal seam heights up to 3.0 m. Longwall management has been partially successful in controlling operators dust exposure levels by adopting a combination of the above dust control techniques.

The two main dust control approaches generally adopted by the industry are administrative and engineering. Administrative controls or work practices are designed to minimize the exposure of individual workers by positioning them in the work area in such a way as to limit the time they are exposed to a particular dust source [8]. Work

practices can be effective in protecting some individuals only if they are followed properly and consistently, and if the environmental exposure remains constant and predictable. Unfortunately, this is not the characteristic of longwall mining in general. Furthermore, the potential for frequent change of location can make it very difficult to identify sources of dust exposure. Engineering controls aim to lower the levels of respirable dust in the mine atmosphere by either reducing dust generation or by suppression, dilution, or capturing and containing the dust. These control measures are usually designed for application to particular conditions. Some are restricted to one operation while others are more general in nature.

A typical dust control design on a longwall includes the basic use of sprays as the first point of control. The sprays used vary considerably from mine to mine. However, a typical spray setup would include solid or hollow cone sprays for the BSL discharge and crusher with various water pressures and flow rates. The number and positioning of sprays will vary from mine to mine. The shearer will have a series of drum sprays dependent on the drum type, usually supplied by the manufacturer. Some mining operations utilize a "shearer clearer" which consists of a series of up to 10 sprays dependent on desired configuration. These sprays are usually in a solid cone configuration. For shield generated dust, solid cone sprays are positioned in the support canopy. In most cases the aim of dust mitigation has not been the total suppression of the coal dust, but to reduce the respirable dust from the vicinity of the mine workers.

Face ventilation has always been the primary means to dilute and remove airborne dust by increasing face air quantities. Some mines modify the behavior of the ventilation by employing ventilation curtains and brattice wings to reduce the amount of air going past the Main Gate (MG) chocks, over pressurizing the gob and returning somewhere further along the face with contamination. Longwall face ventilation quantities in Australian mines range typically from 40 $m^3$/s up to over 100 $m^3$/s depending upon the production and gas dilution requirements.

Examples of engineering dust controls currently utilized in Queensland coal mines as reported recently [9] are

- automation and remote equipment operation (offering the opportunity to remove the operator from the source of the dust)
- ventilation controls (providing clean air through the mine)
- enclosure of dust sources (for example, dust curtains around certain equipment)
- use of water sprays and other wetting agents to suppress dust (including at the cutting face and on conveyor belts)
- use of scrubbers and dust extraction drums
- modified cutting sequences
- enclosed air-conditioned (filtered) and positive pressure cabins on mobile equipment such as trucks, shovels and dozers, and
- maintenance of roadways through grading, watering and the application of salt granules to prevent the accumulation of dust.

While the development of longwall mining has led to high productivity records, the consequent production of high amounts of airborne dust has placed even more stringent demands on dust controls. Extensive studies have shown that high dust exposures on longwall mining operations are mainly due to:

- Inadequate air volume and velocity;
- Insufficient water quantity and pressure;
- Poorly designed external water spray systems;
- Lack of dust control at the stage loader and crusher;
- Dust generated during support movement; and
- Cutting sequences that position face workers downwind of the cutting machine.

## 2.2  Dust Monitoring

The current personal dust monitoring regime in Australia provides the mine tested result with a single figure for shift average respirable dust exposure levels for five samples taken over a minimum of 4 h during a production shift. The majority of dust sampling to date has been carried out with cyclone separation and collection of the sized particles for weighing, generally over the period of a full shift. Although this method provides an accurate measurement for the total dust exposure for the period sampled, it does not always accurately reflect the source, quantity and timing of respirable dust entering the longwall from different sources, hence presents difficulties in determining the relative effectiveness of the different control technologies in use. Tests based on this methodology also have a number of limitations including reduced information from the results and the large number of invalid samples due to over-exposure to dust levels.

Since 1st February 2016, US mine operators have been required to use the CPDM to sample for respirable coal mine dust on working sections of underground coal mines and other areas. In addition, the CPDM must be used to sample air for all Part 90 miners (miners who have evidence of Black Lung), and may be used for sampling at surface mines if approved. From on 1st August 2016 (24 months after the effective date) concentration limits for respirable coal mine dust will be reduced. The overall respirable dust standard in coal mines is reduced from 2.0 to 1.5 $mg/m^3$ of air. The standard for Part 90 miners and for air used to ventilate places where miners work is being reduced from 1.0 to 0.5 $mg/m^3$ of air.

The CPDM is a belt-wearable, computerized device that measures and displays the real-time, accumulated and full-shift exposure to respirable coal mine dust as shown in the Fig. 1. Reporting dust concentrations in real-time empowers miners and operators to take immediate action to avoid excessive airborne dust levels that can injure miners' lungs. Unlike the samples from existing dust sampling devices that require several days to collect, ship and process, the CPDM's measurement of respirable dust provides more immediate, full-shift exposure data. This device, which represents a major improvement in respirable dust sampling technology, was approved for use by both MSHA and NIOSH.

Real-time respirable dust sampling technique has particular application for determining high source locations, efficiency of engineering means of suppression and other approaches to handling the problem. The following sections give an overview of case studies where real-time respirable dust monitoring was utilized to optimize dust control strategies at various Australian mines. They also attempt to review and summarize the findings from these real-time respirable dust surveys undertaken in Australian coal mines. They provide consideration and guidance for performing future real-time

**Fig. 1.** MSHA respirable dust rule—phase II continuous personal dust monitor

respirable dust surveys for engineering studies in an effective, efficient and practical way. This is especially important due to the recent incidences of CWP in the Australian coal mining industry.

These real-time respirable dust surveys were conducted using state of art real-time PDMs which is the prototype of the CPDM as recently introduced to US coal mines by the 2014 US MSHA final dust rules. The PDM was originally developed to measure respirable coal mine dust mass to provide accurate exposure data at the end of a work shift. Additionally, the new monitor continuously displays near real-time dust exposure data during the shift. The PDM uses a tapered-element oscillating microbalance (TEOM) to measure the mass of dust deposited on a filter and continually displays the cumulative exposure concentration data.

The accuracy and precision of the PDM has been determined by comparison to gravimetric filter samplers in the laboratory and in four US coal mines. Laboratory results with different coal types and size distributions showed that there is a 95% confidence that the individual PDM measurements were within ±25% of the reference measurements. Mine test results indicate that data taken with adjacent PDM and reference samplers are indistinguishable.

The PDM was first introduced into the Australian coal mining industry through an ACARP funded research project to evaluate the real-time PDM for personal respirable dust evaluation use particularly in engineering studies.

## 3   Real Time Respirable Dust Surveys and Findings

Over the last 12 years, 24 real-time respirable dust surveys have been undertaken at eight Australian underground coal mines with about 135 series of PDM measurements in their production and development faces. A number of examples are given in the following sections to illustrate real-time dust monitoring in Australian coal mines to

identify dust sources and to optimize duct controls. Results from dust monitoring using real-time PDM instruments are shown from two Australian coal mines with a particular emphasis given to the longwall dust sources and controls in place. Dust control strategies utilized are also described.

## 3.1    Sources of Dust Generation

Mine A is a gassy longwall mine with seam and extraction thickness of about 4.0 m, typical longwall panels were 200 m wide using 114 two-leg chock shields and 2.8–3.8 km panel lengths. Ventilation air quantities at longwall production faces were ranging from 70 to 90 m$^3$/s. The longwall panel has a number of potential dust sources. A detailed survey is able to assist in evaluating the contribution of each component dust source, show the contribution from a number of major sources and the cumulative dust level faced by a miner at different points throughout the panel. The particular longwall panel ran from Chock No 1 at the MG to Chock No 114 at the Tail Gate (TG) with four operators, namely MG operator, MG Shearer operator, TG Shearer operator and Chock operator. For conformity of approach a number of reading sequences were taken just inbye the MG at Chock No 8 or just outbye the TG at Chock No 110. Dust readings for a number of measurements sequences are set down and average values calculated.

Tests were also carried out to monitor the dust suppression efficiency of sprays in the BSL and at the belt transfer point where the longwall belt and the main trunk belt met. For the BSL test, one PDM was placed outbye of BSL, the second PDM was placed on top of the BSL inbye of the spray and the third PDM further inbye of the BSL at Chock No 8. During the test, BSL sprays were on initially and then disconnected for about 30 min and then reconnected again.

The results showed that with the water sprays off dust concentration levels downstream of the BSL were dramatically increased to more than 1.0 mg/m$^3$ while the dust concentration level upstream of BSL remained constant (0.2–0.3 mg/m$^3$) with little variations. It was found that the fluctuations in dust levels measured by the PDM upstream of the BSL correlated well with whether there is coal loaded on the moving conveyor belt or not. When there is no coal on the belt the dust levels upstream of the BSL were measured at around 0.2 mg/m$^3$. It is possible to draw a horizontal line as shown in Fig. 2 to indicate whether there is coal on the belt or not.

In undertaking longwall studies it is important to maintain consistency with measurement conditions along the face activities. Figure 3 examines studies undertaken over the majority of a shift. The shearer position data was downloaded from the mine monitoring system. A cutting sequence took on average slightly less than one hour. It can be seen in the figure that seven cutting cycles occurred across the 7-h study time period with good regularity. One early period of 45 min of cutting was lost to belt structure removal. Measurements were carried out at longwall face positions monitoring the dust levels experienced by shearer and chock operators in a unidirectional mining cutting sequence. Results of these tests for various operator position combinations are analyzed and summarized as shown Table 2.

Figure 3 also illustrates monitoring dust make across the length of a shearer when cutting from MG to TG and then back to MG between 15:30 and 16:17 as shown by the shearer position data downloaded from the mine monitoring system. One PDM unit

**LW BSL Dust Suppression PDM Measurements**
**(5 Mins Rolling Average)**
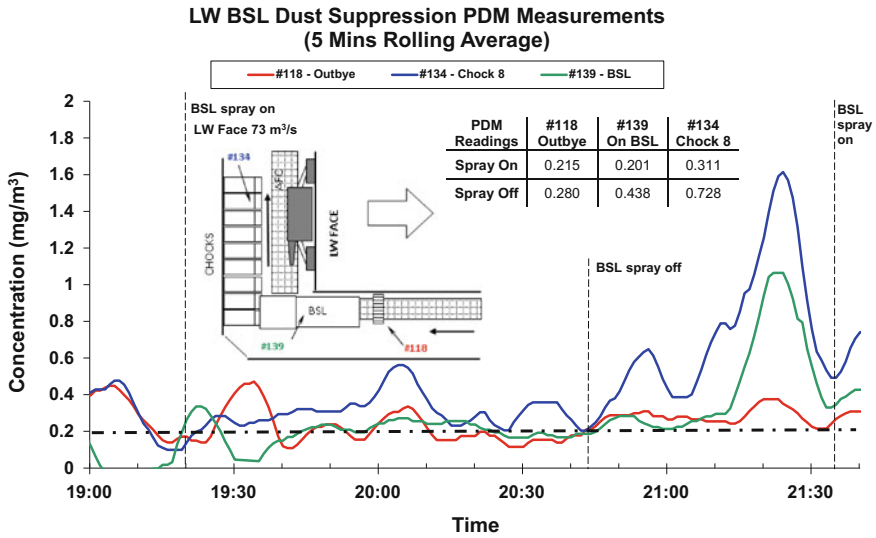


**Fig. 2.** Real-time PDM dust readings across a Longwall BSL with sprays on and off

**LW Face PDM Measurements**
**(5 minutes rolling average)**
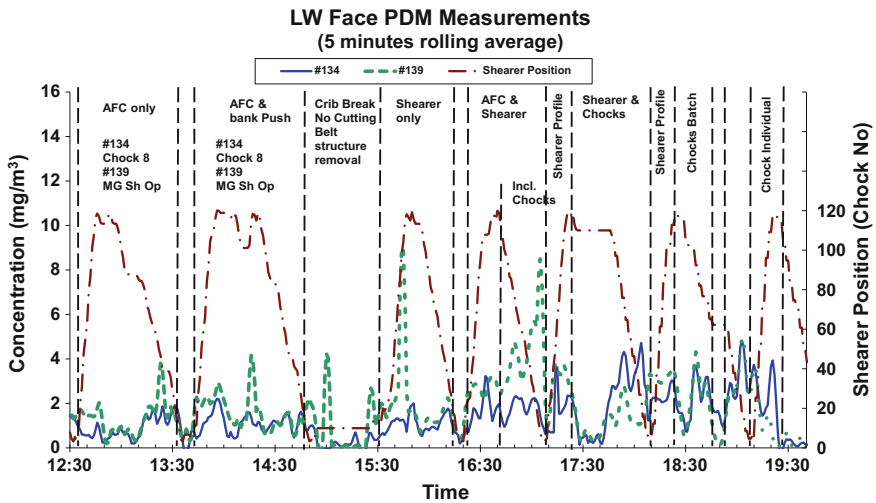


**Fig. 3.** Real-time dust surveys with shearer positions and dust levels

(#134) was worn by a person who shadowed the MG shearer operator for a cutting cycle during unidirectional cutting with average dust level of 1.05 mg/m³ recorded. The other PDM unit (#139) was worn shadowing the TG operator with average dust level of 2.09 mg/m³ over the same period. The results showed an increase (1.04 mg/m³) in dust exposure faced by the TG operator over the MG operator. The

**Table 2.** Dust readings across different sources within a longwall panel

| Test no. | Check #8 | MG operator | TG operator | Check operator | Inbye chock operator | Chock #10 | Comments |
|---|---|---|---|---|---|---|---|
| 1 | | 1.00 | 1.12 | | | | Shadowing operators |
| 2 | | 1.11 | | 1.52 | | | Shadowing operators |
| 3 | | | | | | 3.90 | Fixed position test |
| 4 | | 1.53 | | | | 4.57 | Shearer clearer off |
| 5 | | 1.58 | | | | 4.65 | Shearer clearer off |
| 6 | 0.89 | 1.29 | | | | | AFC dust only |
| 7 | 1.12 | 1.62 | | | | | AFC and bank push dust |
| 8 | 1.64 | | | | 4.26 | | AFC, shearer & chock dust |
| 9 | | 1.51 | | | 3.18 | | Shearer & chock dust |
| 10 | | | 1.53 | | | | Outside air stream (5 min ave.) |
| 11 | | | 1.47 | | | | Outside air stream (30 min ave.) |
| Average | 1.22 | 1.38 | 1.37 | 1.52 | 3.72 | 4.37 | |

unusual anomalous "bump" in the PDM 139 result trace at about 15:45 is put down to a significant face-slabbing fall which was very obvious to those nearby.

## 3.2    Effectiveness of Dust Control Devices

Mine B is a gassy longwall mine as well with mining heights ranging 4.1–4.5 m. Typical longwall panels are 250 m wide using 151 two-leg large and heavy chock shields and about 2.5–4.0 km long with twin heading gate roads. Over a period of five years, eight series of real-time dust surveys at Mine B's longwall faces to assess the baseline dust situations and to optimize the effectiveness of various dust controls were implemented.

Performance audit of the BSL Dust Scrubber for respirable dust reduction has been undertaken. The first part of the surveys evaluated the scrubber operating normally for a period of extensive face cutting with the scrubber sprays alternatively off and on. A second part of the surveys was undertaken with the aim to monitor dust along the face with the scrubber on and compare with a similar situation with the scrubber off. Face coal cutting activity and shearer position on the face was recorded during both tests.

The BSL dust scrubber survey was undertaken in consecutive tests with the scrubber water sprays off and on. With an air quantity of 36.7 $m^3$/s flowing through the BSL, it is possible to calculate the dust make from the BSL and crusher. Results were evaluated depending on whether face cutting was occurring or not. The results

demonstrated that the overall average filtration efficiency of the BSL dust scrubber is about 47% with mining active or not active. However, when mining was active, the dust filtration efficiency of the scrubber is reduced to about 21%. When mining is not active, the filtration efficiency of the scrubber is increased to about 78%.

Higher level of efficiency occurred when the scrubber was not "working hard". This indicates that with active mining the scrubber was overloaded and a lesser proportion of the dust is impacted or captured by water droplets. It is clear that the dust scrubber performs effectively at low dust loads but not as effectively at higher loads. It was recommended that consideration be given to using two independent scrubber units with one drawing air from the crusher and the other from under the hood at the outbye BSL end where coal passes onto the panel conveyor belt (Fig. 4).



**Fig. 4.** BSL Dust Scrubber performance test PDM results
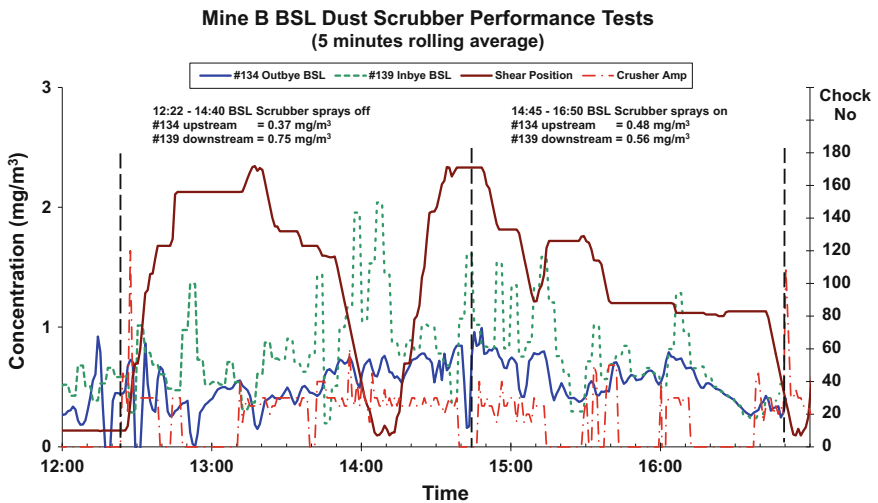
Several real-time longwall dust surveys were conducted at Mine B to evaluate the dust situations with various dust controls implemented over the years. The Table 3 gives dust levels at various manning positions in the longwall production area recorded. During the initial longwall dust survey (Baseline—Standard), standard dust controls and strategies were implemented. The results from the survey formed the baseline data.

In the next two series of dust surveys undertaken about four and 12 months after the initial surveys, improved dust controls and strategies were applied. Improved and additional dust controls and strategies which contributed lower dust levels at various longwall positions in the second series of the dust surveys were as follows:

1. Improved face air quantity,
2. New finer shearer sprays (50%) installed,
3. New sails installed on the top of MG Drive,
4. Good housekeeping—washing away loose coal on platoons in the face walkway.

**Table 3.** Summary of three survey series of dust results at various manning positions

| Average dust levels (mg/m$^3$) | Face Q (m$^3$/s) | Outbye Level | MG Chock #8 | MG shearer operator |
|---|---|---|---|---|
| Baseline—standard | 63.4 | 0.28 | 2.54[a] | 1.91 |
| Improved condition 1 | 71.2 | 0.30 | 1.16 | 1.33 |
| Improved condition 2 | 70.5 | 0.30 | 0.62 | 0.91 |

[a]Unusual local high dust level experienced was a direct result of additional dust created by strata stress loaded MG chocks (No 1 to 5) advancements

Further improved and additional dust controls and strategies resulting in lower dust levels at various longwall positions in the third series of surveys were as follows:

1. Full finer shearer sprays installation completed.
2. Water Mist Venturi system installed at Chock #6 with three sprays in the front at 45° and one at the back with 10° to the face line.

### 3.3   Summary of Findings from Real Time Dust Surveys

As mentioned earlier, over the last 12 years, 24 real-time respirable dust surveys have been undertaken at eight Australian underground coal mines with about 135 series of PDM measurements in their production and development faces. More than 80 series of real-time PDM measurements have been undertaken in seven Australian longwall mines in 12 separate longwall panels. Some longwall panels had up to three real-time PDM surveys done during their production periods for various purposes such as baseline dust surveys, evaluations of dust controls, strategies and new shearer cutting method on dust levels. The Tables 4 and 5 show summary of panel dimension, ventilation and production details of these longwall panels during the real-time PDM surveys. In brief,

1. Except for two panels were in Highwall longwall mines, the rest were in traditional longwall mines with multiple heading Mains and two or three gate roads.
2. Seven panels used Homotropal belt arrangement and five had Antitropal belt arrangements.
3. Eight panels had dedicated intakes from back panel shafts or bleeder roads.
4. Eight panels utilized the Uni-Directional (Uni-Di) shearer cutting method. However, one of these switched to the Bi-Directional (Bi-Di) shearer cutting during its second series of real-time PDM surveys. The rest of panels used the Bi-Di cutting. Cutting web depths of these panels were either 850 mm or 1000 mm.
5. Panel widths were ranging from 200 to 300 m and the mining heights were from 2.7 m to 4.3 m high with panel lengths ranging from 1890 to 3770 m.
6. Panel ventilation pressures varied from 300 to 1450 Pa. Total panel air quantities were in the range of 46–138 m$^3$/s with face air quantities varied from 34 to 77 m$^3$/s.

Table 6 gives a summary of the real-time PDM survey results and purposes of these surveys in the 12 Australian longwall panels. PDM measurements were classified into

**Table 4.** Summary of ventilation arrangements and roadway dimensions

| Mine LW | Panel ventilation | | | Roadway | | Beltway | Comments |
|---------|-------------------|---|---|---------|---|---------|----------|
| | Pressure (Pa) | Total Q (m³/s) | Face Q (m³/s) | Width (m) | Height (m) | | |
| A1 | 1350 | 75 | 37 | 5.2 | 3.2 | Antitropal | Bleeder road |
| A2 | 1450 | 90 | 65 | 5.2 | 3.2 | | return |
| B1 | 300 | 126 | 48 | 5.4 | 3.4 | Homotropal | Back shaft intake |
| B2A | 450 | 80 | 47 | 5.3 | 3.2 | Homotropal | Bleeder road |
| B2B | 500 | 81 | 58 | 5.3 | 3.2 | | intake |
| B3A | 1100 | 113 | 64 | 5.4 | 3.4 | Homotropal | Back shaft intake |
| B3B | 850 | 103 | 71 | 5.4 | 3.4 | | |
| B3C | 420 | 95 | 71 | 5.4 | 3.4 | | |
| B4 | 1200 | 110 | 77 | 5.4 | 3.4 | Antitropal | Back shaft intake |
| C1 | 1000 | 90 | 55 | 5.4 | 3.5 | Homotropal | Highwall LW |
| C2 | 1000 | 90 | 60 | 5.4 | 3.5 | | panel |
| D1A | 1210 | 85 | 50 | 5.3 | 2.7 | Homotropal | 3 Hdgs; back shaft |
| D1B | 1160 | 85 | 56 | 5.3 | 2.7 | | intake |
| D2 | 950 | 92 | 58 | 5.3 | 2.7 | Homotropal | 3 Hdgs; back shaft intake |
| D3A | 1260 | 138 | 34 | 5.3 | 2.7 | Homotropal | 3 Hdgs; back shaft |
| D3B | 1260 | 138 | 34 | 5.3 | 2.7 | | intake |
| E | 330 | 46 | 40 | 5.4 | 2.7 | Antitropal | Highwall LW panel |
| F | 1000 | 77 | 45 | 4.8 | 3.3 | Homotropal | Back boreholes intake |
| G | 600 | 87 | 75 | 5.4 | 2.9 | Antitropal | Bleeder road return |

various manning or positional categories along the LW face area namely, outbye or background, BSL/Crusher, MG Chock (support) or AFC, Shearer MG side (or operator's position), Shearer TG side (or operator's position), Cock operator and TG Chock positions.

As expected the average dust levels of manning or positional locations in these longwall panels are progressively increasing as locations move further inbye of the longwall face areas. The following gives a summary of findings from the Table 6. As limited date available at Chock operator and TG Chock positions, no further analysis is done in these two positions.

**Outbye, BSL/Crusher and MG Chock Positions**. Outbye or background of longwall panel dust levels were ranging from 0.10 to 0.37 mg/m³ with an average of 0.24 mg/m³. Some of the lower outbye dust levels were found in the longwall panels with separate or dedicated fresh air intakes such as back panel shafts. An average of 13% reduction in outbye dust levels can be found with such panel intake arrangements. Longwall panels with Homotropal belt arrangements for their belt roads also have

**Table 5.** Summary of LW production face details

| Mine LW | Face height (m) | Panel width (m) | Cutting method | Web depth (mm) | Panel length (m) | Face position (m) | Face Q ($m^3$/s) |
|---|---|---|---|---|---|---|---|
| A1 | 4.0 | 205 | Uni-Di | 1000 | 2590 | 2190 | 37 |
| A2 | | | | | 2490 | 2090 | 65 |
| B1 | 4.3 | 300 | Uni-Di | 850 | 2550 | 850 | 48 |
| B2A | 3.4 | 300 | Uni-Di | 850 | 1890 | 1650 | 47 |
| B2B | | | | | 1890 | 1350 | 58 |
| B3A | 4.3 | 300 | Uni-Di | 850 | 3180 | 2950 | 64 |
| B3B | | | | | 3180 | 2650 | 71 |
| B3C | | | | | 3180 | 950 | 71 |
| B4 | 4.3 | 300 | Uni-Di | 850 | 3300 | 2550 | 77 |
| C1 | 4.2 | 205 | Uni-Di | 850 | 2450 | 1150 | 55 |
| C2 | | | | | 2450 | 950 | 60 |
| D1A | 2.7 | 300 | Uni-Di | 1000 | 2420 | 760 | 50 |
| D1B | | | | | 2420 | 560 | 56 |
| D2 | 2.7 | 300 | Uni-Di | 1000 | 3620 | 1150 | 58 |
| D3A | 2.7 | 300 | Uni-Di | 1000 | 3770 | 3350 | 34 |
| D3B | | | Bi-Di | | 3770 | 3350 | 34 |
| E | 2.9 | 264 | Bi-Di | 1000 | 3350 | 3100 | 40 |
| F | 3.2 | 275 | Bi-Di | 1000 | 3000 | 2600 | 45 |
| G | 2.9 | 200 | Bi-Di | 1000 | 3530 | 820 | 75 |

lower outbye dust levels with an average of 16% reduction of outbye dust levels could found with Homotropal belt when compared with Antitropal belt panels.

Dust levels at BSL/Crusher were between 0.24 and 0.66 mg/m$^3$ with an average dust level of 0.47 mg/m$^3$. Longwall panels with Homotropal belt arrangements also have lower dust levels at BSL/Crusher with the difference about 30% found between Homotropal and Antitropal belt panels.

Average dust level found in the MG Chock position (or AFC dust source) was about 0.91 mg/m$^3$ with a range from 0.36 to 1.91 mg/m$^3$ of dust levels measured. Interesting, longwall production panels more than halfway through their overall panel lengths have shown much lower dust levels (about 50–100% reductions) in all these positions when compared with panels still had more than 50% of the overall panel lengths. Panels with Uni-Di cutting also have lower dust levels in BSL/Crusher and MG Chock positions when compared with the panels with Bi-Di cutting.

**Shearer MG and TG Positions**. Average dust levels at shearer MG and TG positions are 1.40 and 2.06 mg/m$^3$ respectively. Further analyses of the effects of various panel geometry, production and ventilation parameters on shearer MG and TG positions reveal the following findings as shown in Table 7.

Based on Table 7, it was found that

**Table 6.** Summary of PDM survey results for the 14 Australian LW panels

| Mine LW | Outbye | BSL crusher | MG Chock/AFC | Shearer MG | Shearer TG | Chock operator | TG Chock | Comments |
|---|---|---|---|---|---|---|---|---|
| A1 | 0.23 | 0.45 | 1.22 | 1.38 | 1.37 | 1.52 | 4.37 | Baseline |
| A2 | 0.19 | 0.55 | 1.07 | 1.77 | 2.52 | 3.43 | 6.68 | Baseline |
| B1 | 0.10 | 0.24 | 0.82 | 1.12 | 1.43 | | | Baseline |
| B2A | 0.37 | 0.54 | 0.85 | 1.41 | | | | BSL, Baseline |
| B2B | 0.28 | 0.45 | 1.33 | 1.61 | 1.70 | 1.47 | | Baseline, Bi-di Trial |
| B3A | 0.28 | 0.48 | 0.71 | 1.91 | 2.18 | | | Baseline |
| B3B | 0.23 | 0.38 | 0.74 | 1.33 | | | | Improvements I |
| B3C | 0.22 | 0.30 | 0.62 | 0.94 | | | | Improvements II |
| B4 | 0.33 | 0.54 | | 1.27 | | | | Baseline |
| C1 | 0.25 | 0.47 | 0.68 | 0.75 | 0.88 | | | Baseline |
| C2 | | | | 0.76 | 1.02 | 1.57 | 2.88 | Shearer scrubber |
| D1A | 0.18 | | 0.61 | 1.41 | | | | Baseline |
| D1B | 0.16 | | 0.36 | 1.04 | | | | Improvements |
| D2 | 0.26 | | 0.54 | 1.12 | | | | Radial drums |
| D3A | 0.19 | | 1.57 | 2.39 | | | | Baseline |
| D3B | 0.19 | | 1.91 | | 8.69* | | | Bi-di cutting trial |
| E | 0.29 | 0.52 | | 1.98 | 5.21 | 2.97 | | Baseline |
| F | 0.25 | 0.50 | 0.68 | 1.67 | 2.24 | 2.80 | 4.42 | Baseline |
| G | 0.28 | 0.66 | | | | | | Baseline |
| Average | 0.24 | 0.47 | 0.91 | 1.40 | 2.06 | 2.29 | 4.59 | |

**Table 7.**

| Panel parameters | Average dust level (mg/m$^3$) | |
|---|---|---|
| | Shearer MG | Shearer TG |
| Panels still had more than half of panel lengths | 1.70 | 2.83 |
| Panels still had less than half of panel lengths | 0.89 | 0.83 |
| *Dust level reduction percentage (%)* | 90 | 240 |
| Cutting web depth—1000 mm | 1.59 | 2.83 |
| Cutting web depth—850 mm | 1.23 | 1.44 |
| *Dust level reduction percentage (%)* | 29 | 97 |
| Face mining heights more than 4.0 m | 1.58 | 3.05 |
| Face mining heights less than 4.0 m | 1.25 | 1.57 |
| *Dust level reduction percentage (%)* | 26 | 95 |
| Panel width less than 250 m | 1.48 | 2.55 |
| Panel width more than 250 m | 1.17 | 1.45 |
| *Dust level reduction percentage (%)* | 27 | 76 |
| Panel with Bi-Di cutting method | 1.82 | 3.72 |
| Panels with Uni-Di cutting method | 1.35 | 1.59 |
| *Dust level reduction percentage (%)* | 35 | 135 |

- Newer longwall production panels with more than 50% of their overall panel lengths remaining have higher dust levels in shearer MG and TG positions which are almost two to three times higher than those panels with less than 50% of their overall panel lengths left.
- Panels with cutting web depth of 850 mm have dust levels of 29 and 97% reduction correspondingly at the shearer MG and TG positions as well when compared with the panels with 1000 mm web depth.
- A similar relationship in dust level reductions (26 and 95%) in these two shearer positions is observed in panels with lower than 4 m face mining heights when compared with the panels with more than 4 m face heights.
- Similarly, panels with less than 250 m panel width have dust levels of 27 and 76% reduction correspondingly at the shearer MG and TG positions as well when compared with the panels with more than 250 m wide.
- Panels with Uni-Di cutting also have lower dust levels (35 and 135% less) at shearer MG and TG positions when compared with the panels with Bi-Di cutting. In fact, average dust level of panels with Uni-Di cutting at shearer TG is less than half of panels using Bi-Di cutting.

It should be noted that these findings are only looking at the particular influence of one individual parameter have on the dust levels along some longwall face positions. Full comprehensive analysis of these parameters in various combinations should be undertaken in order to have better or broad understandings of their combined effects on the dust levels along some longwall face positions in these longwall panels.

## 4   Conclusions and Recommendations

Two case studies of real-time dust monitoring in Australian longwall mines were summarized and presented. This is with particular emphases on the real-time dust monitoring as an engineering tool that can effectively and efficiently assess impacts of dust controls and/or strategies implemented at mines. Statuary shift-averaged monitoring will still have its roles to identify whether there is a dust issue or not at this stage but it will not be able to assist the optimisation of dust mitigation controls and strategies in a practical way.

Some preliminary findings on the influences of panel geometry, production and ventilation parameters have on the dust levels along longwall face positions in 12 Australian longwall panels based on real-time dust survey results were discussed. It was found that separate or dedicated fresh air intakes and Homotropal belt arrangements could provide lower outbye or background dust levels for the longwall production faces. Longwall panels with production faces in their second half of overall panel lengths, shallower cutting web depth, lower face mining heights, narrower longwall panel widths and Uni-Di cutting method could all contribute to lower dust levels at some manning or positional locations along the longwall production faces. Further detailed analyses of these parameters and their combined influences on the dust levels along selected longwall face positions in these longwall panels are recommended.

Australian longwall mining experience has indicated that the efficiency of some of the existing dust control methods reduces significantly in thick coal seams and under high production environments. As the current trend in the industry is to substantially increase the face production levels and to extract more thick coal seams, there is an urgent need for detailed investigation of various dust control options and development of appropriate dust management strategies. Findings from this paper provide some basic consideration and guidance for performing any future real-time respirable dust surveys for engineering studies in an effective, efficient and practical way. This is especially important due to the recent emerging incidences of CWP in the Australian coal mining industry.

## References

1. Erisk: http://www.erisk.net/erisk7/article/324612/oaky_creek_sets_australian_rec-ord_pro-ducing_772_029_tonnes_of_coal (1999). Last accessed 26 July 2016
2. Coal Age: http://www.coalage.com/news/suppliers-news/243-newlands-longwall-sets-new-australian-annual-production-record.html#.Vw2-2fl95QI (2005). Last accessed 26 July 2016
3. Coal Age: http://www.coalage.com/news/suppliers-news/243-newlands-longwall-sets-new-australian-annual-production-record.html#.Vw2-2fl95QI (2009). Last accessed 26 July 2016
4. International Coal News: http://www.internationalcoalnews.com/storyView.asp?-storyID=1037796&section=News&sectionsource=s46&aspdsc=yes (2009). Last accessed 26 July 2016

5. International Coal News: http://www.internationalcoalnews.com/storyview.asp?-storyID= 826953408&section=News&sectionsource=s46&Highlight=longwall&aspdsc=yes    (2015). Last accessed 26 July 2016
6. World    Coal:    http://www.worldcoal.com/mining/22122015/Anglo-Americans-Grasstree- achieves-national-record-for-underground-coal-production-3331  (2015). Last  accessed  26 July 2016
7. Colinet, J., Rider, J., Listak, J., Organiscak, J. and Wolfe, A.: Best Practices for Dust Control in Coal Mining, Information Circular 9517, January 2010, Department Of Health And Human Services Centers for Disease Control and Prevention National Institute for Occupational Safety and Health (2010)
8. Mine Safety and Health Administration (MSHA): US Department of Labor, Practical Ways to Reduce Exposure to Coal Dust in Longwall Mining—A Toolbox (1999)
9. Queensland Parliament: Black Lung White lies, Inquiry into the re-identification of Coal Workers. In: Pneumoconiosis in Queensland, Report No. 2, 55th Parliament Coal Workers' Pneumoconiosis Select Committee, May 2017 (2017)

# Explosive Testing of Rock Dust Dispersibility for Coal Dust Explosion Prevention

Jürgen F. Brune[(✉)] and Richard C. Gilmore

Colorado School of Mines, Golden, CO 80401, USA
jbrune@mines.edu

**Abstract.** Limestone rock dust is used in many coal mines to inertize coal dust and prevent mine explosions. Since rock dusting creates a nuisance to workers downwind from the dust application, suppliers are offering wet and foam-applied rock dust products. Researchers at the Colorado School of Mines have constructed a full-size explosion test drift where they can generate controlled explosions at defined wind speeds of 30–50 m/s, the minimum wind speed that can entrain coal dust and propagate coal dust explosions. Initial results with different wet-applied, that then dried rock dust products suggest that explosive forces break-up clumps of the rock dust, but this wet-applied dust does not disperse as easily as dry-applied dust. Also, hydrophobized rock dust and dust meeting German specifications disperses more readily.

**Keywords:** Coal · Dust explosions · Rock dusting

## 1 Introduction

Underground coal mines in the United States commonly use dry rock dust to inertize coal dust and prevent coal dust explosions. The 2010 explosion of the Upper Big Branch mine that killed 29 miners was the worst mining accident in the US in almost 40 years. The investigation of this accident revealed that the operator did not have sufficient rock dust concentration throughout the mine to prevent and suppress a coal dust explosion [1].

Following the Upper Big Branch explosion, researchers from the National Institute for Occupational Safety and Health (NIOSH) have identified deficiencies in rock dusting practices and in the sampling methods used to document adequate rock dust concentration [2]. The U.S. Mine Safety and Health Administration (MSHA) [3] issued an alert to mine operators to verify that the rock dust used meets the size criteria set forth in 30 CFR §75.2 [4], i.e. 100% passing 20-mesh (0.84 mm) sieve and 70% passing 200-mesh (74 μm) sieve.

Continuous application of rock dust to mine floor, ribs and roof creates nuisance dust downwind that can prevent or hinder other work in the mine. While rock dust is typically applied continuously using trickle dusters in mining section returns, outbye mine workings are dusted periodically during shift changes or off-shift hours. Dust is re-applied every few days or, in less dusty airways after longer intervals. This periodic application of rock dust in the mining cycle can lead to thin layers of coal dust accumulating on top of inert rock dust. Sapko et al. [5] showed that a 0.24 mm thin

layer of coal dust on top of 100% rock dust is sufficient to propagate a coal dust explosion. In addition, wetting and drying of rock dust may cause rock dust to agglomerate or cake, which prevents dispersal of the rock dust by explosion forces making it ineffective at quenching an explosion.

To solve some of these problems associated with the dust application and caking problem, rock dust manufacturers have developed several alternative solutions, including:

1. Wet-applied rock dust that does not create a nuisance downwind during application. Manufacturers claim that, after drying, this dust has the same air entrainment characteristics as dry-applied dust.
2. Foam-applied dust with similar characteristics as wet-applied dust.
3. Hydrophobized rock dust designed not to agglomerate as it dries after getting wet.

Based on laboratory-scale explosion tests [6], it appears that the addition of anti-caking compounds or hydrophobizing improves the dispersibility of conventional rock dust that have been exposed to moisture; however, the dispersibility of rock dusts with various hydrophobic additives in an actual mining environment in not known.

Mine safety regulations in Germany [7] specify the allowable shape of the rock dust's size distribution curve. That curve must be "well-graded" with approximately equal amounts in size fractions ranging from $10^{-1}$ mm down to about $10^{-4}$ mm. If the rock dust does not comply with this well-graded size distribution, hydrophobizing agents must be added. There is a maximum limit of 0.3% on any water-soluble components such as calcium hydroxide and salts. In addition, moisture must be below 0.5%.

## 2   Test Drift and Experimental Design

Researchers at the Colorado School of Mines have developed an underground explosion test drift to determine the entrainability of various alternative rock dust products during specifically designed and repeatable blast waves.

Figure 1 shows the explosion test drift in the Colorado School of Mines Edgar Experimental Mine. The dead-end drift is about 60 m long and has a cross section 3 m wide and 2.7 m high. The vertical posts hold pencil probes to record the static explosion pressures while the red streamers help visualize the explosive pressure wave in high-speed camera images.

Figure 2 shows a plan view of the experimental layout. Controlled explosions are set off near the dead end (left side) of the test drift by stringing two curtains of detonating cord. Sensors marked in red are bi-directional pressure sensors that detect the total and static explosion pressures to calculate the dynamic pressure. Locations marked with black dots indicate piezo-type static pencil probes and total pressure sensors.

The blast curtains are fired in two consecutive blasts delayed by 67 ms using programmable, precision delay detonators. The 67 ms delay was chosen so that the first detonation wave, its reflection, the second wave and its reflection occur at equal time intervals. The wave tempering zone marked in Fig. 2 serves to equalize the individual

**Fig. 1.** Edgar Mine dust explosion test drift
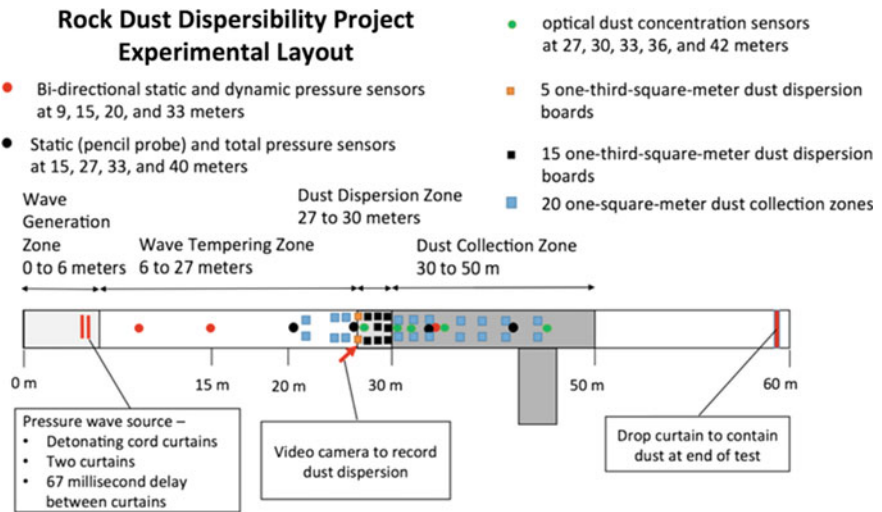


**Fig. 2.** Plan view of the experimental layout in the explosion test drift

blast and reflection peaks and form a continuous blast wave. The lengths of the detonating cord are varied to generate a weak, medium and strong blast wave. The sizes of the blast waves were designed to generate wind velocities of 30–50 m/s. Nagy [8] found that the weakest coal dust explosions can propagate with air speeds of 50 m/s while Cybulski [9] measured speeds as low as 30 m/s. Researchers deemed it critical to evaluate rock dust dispersibility at similar air speeds. If rock dust can disperse at the slow air speed associated with a weak coal dust explosion, it will surely disperse at the higher air speed associated with a strong explosion.

The desired pressure wave to emulate a weak coal dust or methane-air explosion has a static pressure of about 14–21 kPa, an associated dynamic (velocity) pressure of about 0.7–1.4 kPa, and a corresponding air speed of about 30–50 m/s. Researchers consider this a "light blast of air" as specified in U.S. regulation 30 C.F.R. § 75.2 [4] that defines the physical properties of rock dust to be used in U.S. coal mines to inertize coal dust and prevent explosions. Table 1 shows the design blast wave data in comparison.

**Table 1.** Blast wave data

| Blast size | Curtain 1 det. cord, 0 ms delay (m) | Curtain 2 det. cord, 67 ms delay (m) | Static pressure, kPa | Dynamic pressure, kPa | Wind velocity, m/s |
|---|---|---|---|---|---|
| Weak | 27 | 24 | 17–20 | 0.7–1.4 | 30–45 |
| Medium | 42 | 27 | 24–27 | 1.4–2.0 | 45–60 |
| Strong | 54 | 36 | 31–34 | 2.0–2.7 | 60–69 |

Pressures and wind velocities recorded in the dispersion zone, see Fig. 2

To generate the desired pressure wave, researchers designed a net-like lattice of detonating cord that explodes near the closed end of the tunnel, shown in Fig. 3. To produce a static pressure wave of 0.7–1.4 kPa at a distance of 15–30 m in a 3 m by 2.7 m drift requires a 0.27 kg PETN charge [10] or about 52 m of typical detonating cord with a core load of 5.3 g/m. The design pressure waves are highly reproducible, with pressures recorded from consecutive blasts differing by less than 1%.



**Fig. 3.** Detonation cord lattice for a medium-sized blast

## 3   Preparation of Rock Dust for Testing

Researchers prepared rock dust products in three different ways, dry-applied, wet-applied then left to dry, and foam-applied, then left to dry. Dust was placed on 60 × 60 cm acrylic boards placed in the dispersion zone. Figure 4 shows the placement of dry rock dust on the dispersion boards.
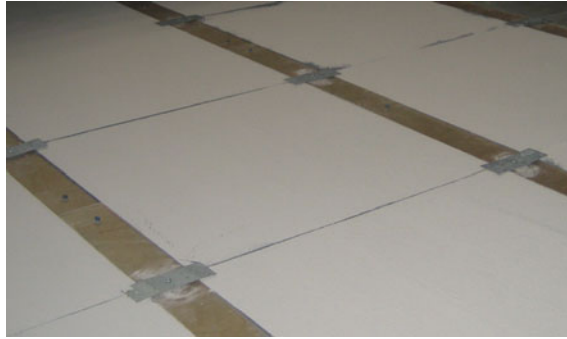
**Fig. 4.** Dry rock dust placed on dispersion boards

Each board was prepared with a dust load of 500 g and boards weighed before and after each blast to determine the amount of dust scoured up. Following each test, the airborne dust was allowed to settle for at least 24 h, then collected from 1 m$^2$ marked areas using a hand brush and dust pan to determine the amount of dust deposited. Samples were sifted through a 20-mesh (0.84 mm) sieve to eliminate larger rock particles that might affect the weight of the dust collected. After collecting the dust samples, the test area was washed down with a high-pressure washer to remove all loose rocks and dust, and allowed to completely dry to prepare a clean drift for the next test.

During the test, static and total blast pressures were recorded to ensure consistency from test to test. Light obscuration dust density probes were used to provide relative, comparative measurements of dust density. Finally, each test was recorded with several video cameras providing up to 240 frames per second.

A minimal amount of natural dust exists in the mine, however, researchers conducted a test without any rock dust applied to determine the natural amount of dust deposited on the floor and walls of the test area to eliminate bias from the rock dust experiments.

## 4 Experimental Results

Researchers performed 36 tests by the end of 2017, with the program scheduled to continue through 2018. Research findings can be summarized as follows:

1. The explosion test facility generates wind blasts that are consistent and repeatable from test to test. Figure 5 demonstrates the repeatability comparing dry-applied, conventional rock dust scouring and deposition data from Blasts 31, 32 and 34. Blasts 31 and 32 show nearly identical results for "medium" blasts, while Blast 34 is a "strong" blast.
2. Hydrophobized, dry-applied rock dust also disperses slightly more readily than conventional rock dust. This is shown in Fig. 6. Blast 32 with conventional rock dust is compared to blasts 14 through 17 with hydrophobic dust. Scouring amounts
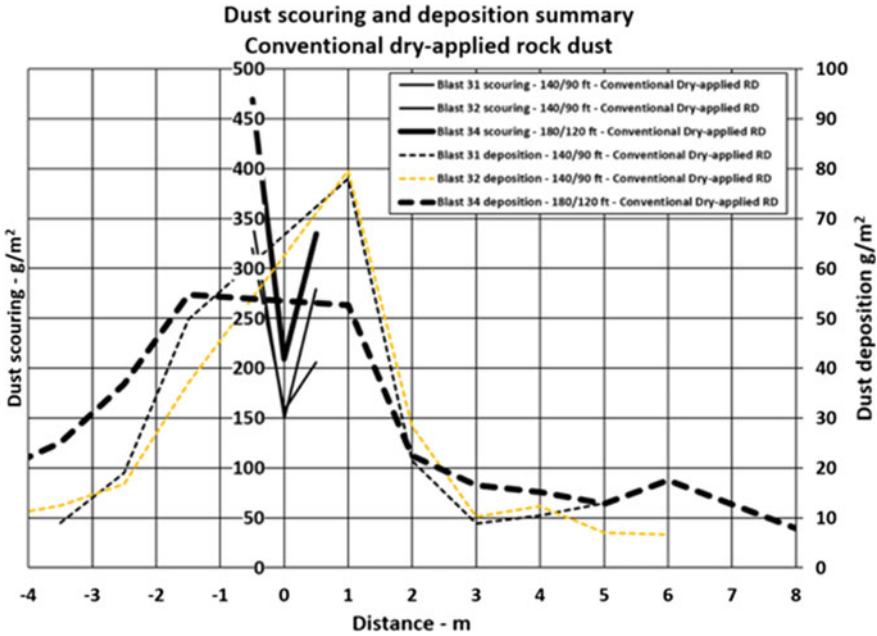
**Fig. 5.** Comparison of dust scouring and deposition data from several blast tests with conventional, dry-applied rock dust
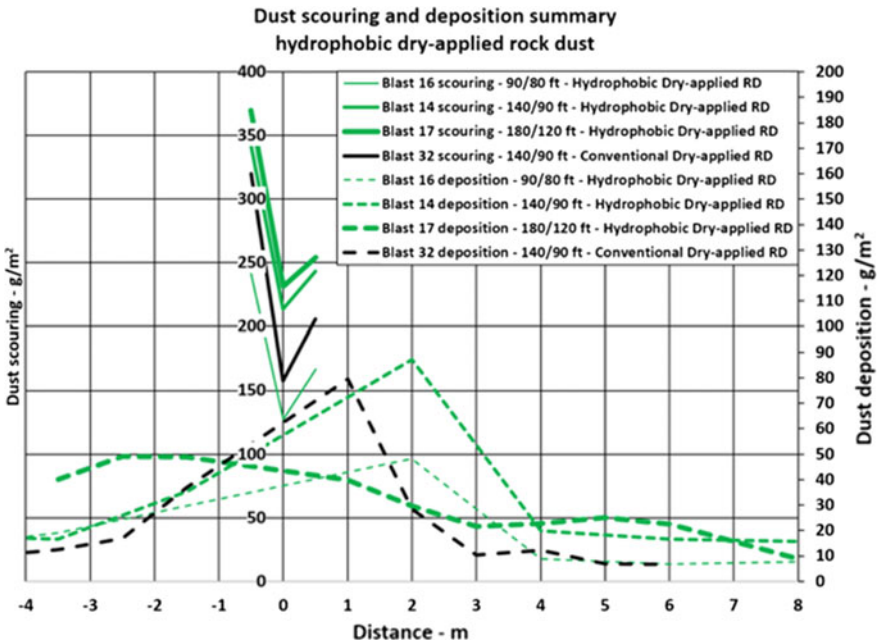


**Fig. 6.** Comparison of hydrophobized, dry-applied rock dust to U.S. conventional rock dust

are generally higher for the hydrophobic dust while deposition data are generally higher, though not consistently so. Researchers note that the deposition from Blasts 14 exceeds that of similar sized Blast 32.

3. German specification, dry-applied rock dust appears to disperse more readily than U.S. specification, conventional rock dust. This is shown in Fig. 7, where Blasts 23 and 24 show considerably more scouring and deposition compared to Blast 32. Blast 20 was performed without any dust to document the effects of dust deposition of natural dust dislodged from the dry, cleaned walls and floor of the test facility. This finding was also confirmed with data from light obscuration dust sensors.
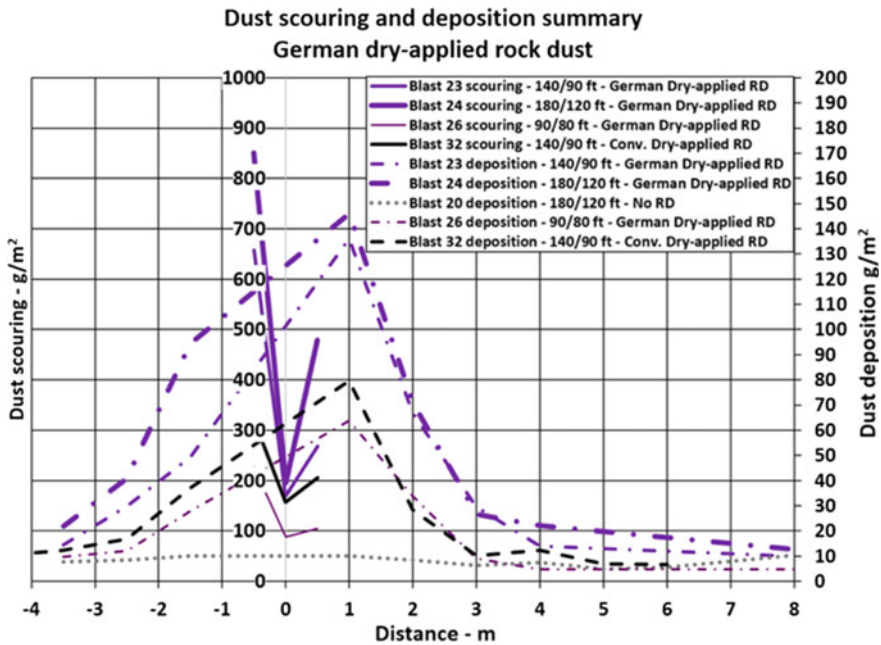


**Fig. 7.** Comparison of conventional, dry-applied rock dust with German specification dust

4. The deposition of large Blast 17 is lower in the outbye deposition area (distance from center of dust placement boards > 0) but much higher in the inbye area. This is an indication that the hydrophobic dust remains airborne much longer than the conventional dust. More hydrophobic dust is pulled back towards the dead-end of the test drift by the "suckback" air draft following the explosion.

5. Both wet- and foam-applied dust alternatives do not appear to perform as well as dry-applied products. Although it is too early for a final conclusion, researchers observed that both wet- and foam-applied products are scoured up in larger chunks that do not readily disintegrate into the original, fine dust particles that are essential to inertize coal dust and prevent it from exploding. Figure 8 shows a series of images from scouring of dry-applied conventional rock dust where dust particles are

smoothly entrained into the air. Figure 9 shows images from wet-applied dust that then dried. In these images, chunks of agglomerated dust larger than 1 cm are visible. Although these chunks quickly disintegrate into smaller pieces, these pieces are still larger than 1 mm. Such chunks are too large to provide effective inertization and shielding to quench coal dust explosions and prevent them from propagating. Initial analysis indicates that only about 40% of the collected dust will pass a 20-mesh (0.84 mm) sieve. This would violate the U.S. regulation 30 CFR §75.2 [4] that requires 100% of the dust to pass a 20-mesh sieve. Researchers are conducting additional tests to confirm this finding. These tests will include particle size analyses of the dust deposited from wet- and foam-applied tests.

**Fig. 8.** Scouring of dry-applied, dry rock dust

**Fig. 9.** Scouring of wet-applied, then dried rock dust. The images center and right clearly show chunks of agglomerated dust

## 5   Summary and Conclusions

Researchers at the Colorado School of Mines compared the entrainability of dry, powdered, conventional rock dust to two alternative rock dust products, including a hydrophobized rock dust and limestone dust meeting specifications set forth by the mining authorities in Germany. Both alternative products were found to disperse slightly more readily as conventional dust when applied dry. Both products also meet U.S. rock dust specifications and are expected to perform well in inertizing coal dust.

All three dust products were also tested when applied wet and conventional dust was tested when applied as a foam. After drying, the wet- and foam-applied products did not perform as well as dry-applied dust. During the explosion, the dust flew off in larger chunks. Initially, these chunks were several centimeters in size but later broke apart into smaller pieces. However, the smaller pieces no longer meet U.S. rock dust specifications, as much less than 100% could pass through a 20-mesh (0.84 mm) sieve.

Further testing will be required to confirm the findings. Researchers plan to conduct scaled explosion tests to determine whether wet- and foam-applied dust products are capable of quenching a coal dust explosion.

# References

1. Page, N.G., Watkins, T.R., Caudill, D.R., Cripps, J.F., Godsey, C.J., Maggard, A.D., Moore, A.D., Morley, T.A., Phillipson, S.E., Sherer, H.E., Steffey, D.A.: Mine safety and health administration, coal mine safety and health. Report of Investigation—Fatal Underground Mine Explosion 5 Apr 5, 2010, Arlington VA, Dec 2011 (2011)
2. Harris, M.L., Weiss, E.S., Man, C.K., Harteis, S.P., Goodman, G.V., Sapko, M.J.: Rock dusting considerations in underground coal mines. In: Hardcastle, S., McKinnon, D.L. (eds.) Proceedings of the 13th U.S./North American Mine Ventilation Symposium, Sudbury, Ontario, Canada, pp. 267–271, 13–16 June 2010. MIRARCO—Mining Innovation, Sudbury (2010)
3. Stricklin, K.: Mine safety and health administration program information bulletin ("PIB"), pp. 11–50. http://www.msha.gov/regs/complian/PIB/2011/pib11-50.asp. Last accessed 1 Sept 2015
4. United States Code of Federal Regulations, Part 75, U.S. Government Printing Office (2018)
5. Sapko, M.J., Weiss, E.S., Watson, R.W.: Explosibility of float coal dust distributed over a coal-rock dust substratum. In: Proceedings of the 22nd International Conference of Safety in Mines Research Institutes 1987, pp. 459–468. China Coal Industry Publishing House, Beijing, 1987
6. Landesoberbergamt NW, Germany: Prüfbestimmungen des Landesoberbergamts Nordrhein-Westfalen für Gesteinstaub gem. § 224 BVOSt, 20 Feb 1970 (German State Mining Authority, North-Rhine Westphalia, Testing Regulations for Stone Dust, 20 Feb 1970)
7. Perera, I., Sapko, M., Harris, M.L., Zlochower, I., Weiss, E.S.: Design and development of a dust dispersion chamber to quantify the dispersibility of rock dust. J. Loss Prev. Process Ind. **39**, 7–16 (2016)
8. Nagy, J.: The Explosion Hazard in Mining, Mine Safety and Health Administration. U.S. Department of Labor, IR 1119, 69 pp (1981)
9. Cybulski, W.G.: Coal dust explosions and their suppression (trans. from Polish). National Center for Scientific, Technical and Economic Information, Warsaw, Poland (available as TT73- 54001 from National Technical Information Service. U.S. Dept. of Commerce, Springfield. VA 22161. USA) (1975)
10. Smith, A., Sapko, M.: Detonation wave propagation in underground mine entries. J. Mine Vent. Soc. S. Afr., 20–25 (2005)

# CFD Modelling of Ventilation, Dust and Gas Flow Dispersion Patterns on a Longwall Face

Ting Ren[1](✉) and Zhongwei Wang[2]

[1] Faculty of Engineering and Information Sciences, Centre of Infrastructure Protection and Mining Safety, University of Wollongong, Wollongong, Australia
tren@uow.edu.au
[2] College of Safety Science and Engineering, Xi'an University of Science and Technology, Xian, China

**Abstract.** Modern underground longwall mines are using large volume of ventilating airflow to maintain a working environment on longwall face and development heading. The design and effective management of ventilation flow on a longwall face is critical to the safety and productivity of the working place with due consideration of dust mitigation and gas emission dispersion. CFD models are developed to provide a better understanding of the ventilation airflow patterns on a typical longwall face extracting a medium-high seam. Results from the CFD models provide a clear visualization of airflow patterns as it enters from the maingate to the longwall, then passes the shearer along the face, before returning to the tailgate. Local recirculation and turbulence zones can be clearly identified where dust contamination and gas accumulation hazards could exist. Ventilation pressure drops along the face could also be estimated with the shearer and chock advance at different locations. Gas emission and dust generation from different sources on the longwall are modelled and their dispersion patterns predicted as the shearer cuts from tailgate to maingate. The use of wing brattices and curtains at different locations (maingate, maingate goaf entry and tailgate) and its effect on dust and gas dispersion are modelled to provide improved control and risk management on the longwall.

**Keywords:** Mine ventilation · Longwall mining · CFD · Dust dispersion

## 1 Introduction

Underground coal mine ventilation plays the most critical role in maintaining a safe and comfortable working environment for miners. A variety of longwall ventilation systems are being used in Australian underground coal mines with the consideration of mine gas emission, fugitive dust and climate control such as heat and humidity. Almost all mines use a combination of shaft and/or drift access for personnel, materials and ventilation. Figure 1 shows a typical Australian longwall mine and its ventilation system. Most longwall panels use "U" ventilation arrangement with two gateroad headings development (Hdg) and between $5 \sim 11$ mains headings depending on ventilation, transport and storage requirements. A longwall panel would normally have two gateroads for intake fresh air (maingate or MG) and one gateroad (the travel road

of previous panel) for return air (tailgate or TG). In a development panel, a heading is used as an intake roadway or travel road (TR) and the other heading is used as the return roadway or belt road (BR) through which the panel belt is located for transport. Under certain mining conditions when high gas emissions are expected during longwall mining, a three-gateroad system will be used to allow high volume of ventilation to be provided to development headings and longwall face.
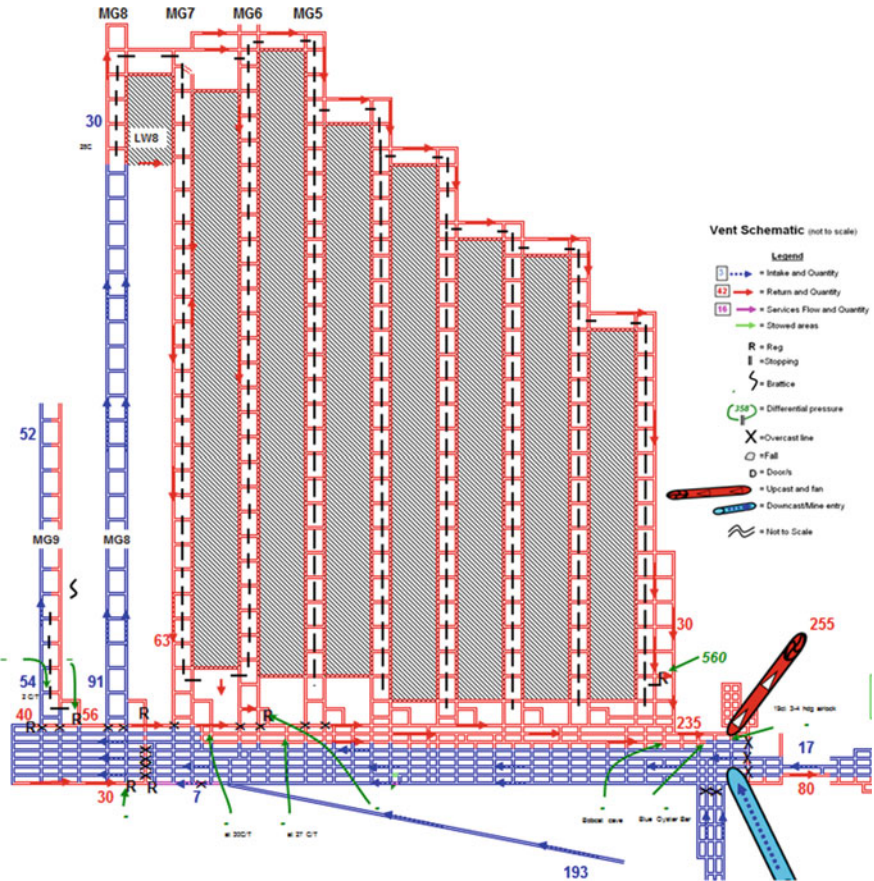


**Fig. 1.** A typical Australian Longwall mine and its ventilation system

Ventilation flow patterns at these working places such as development heading and longwall face can be complicated due to the presence of equipment, machine and human activities, ventilation control devices (VCD) and various moving objects. A sound knowledge of the airflow characteristics is of critical importance to the occupational health and safety of mine workers. A ventilation officer or engineer must ensure that the ventilation air that is breathed in must not be contaminated to

sub-standard or dangerous conditions if hazardous gases or particles produced in the course of operations are not controlled, safely extracted or mitigated to harmless levels.

Generally, dust exposure levels are significantly higher on longwall faces than in other mining environments. This problem becomes more severe at high production levels, at operations employing bi-di cutting and in thick seam conditions. The respirable dust flow behaviour in a longwall face is complicated due to the nature of longwall mining. The generation, dispersion and transport of airborne dust is primarily controlled by the spatial velocity and the flow pattern of the ventilation air. Furthermore the emission of mine gas such as methane from the longwall face and goaf areas presents a serious hazard of gas explosion in the event of a potential frictional ignition.

To understand dust flow behavior and gas dispersion under the harsh longwall mining condition and to assess the effectiveness of different dust and gas control techniques, numerical modelling has become a essential approach to assist laboratory experiments and field studies. CFD simulation has emerged as a powerful predictive and design tool in almost every branch of fluid dynamics and engineering field. CFD studies on airflow patterns within the headings of underground coal mines under various ventilation scenarios have been conducted by many researchers worldwide including but not limited to Hargreaves and Lowndes [1], Toraño et al. [7, 8]. Ren and Balusu [3, 4] investigated both the airflow and dust flow behaviour at typical longwall faces using CFD longwall models. Xu et al. [10] conducted CFD studies to investigate the impact of ventilation controls on airflow inside a mine, and simulated the use of tracer gas for ventilation damage detection. Wang and Ren also conducted a range of CFD modelling studies of airflow and dust behavior in underground coal mines [9] (2014).

More recently, Xu et al. [11] conducted a comprehensive review of the use of CFD modelling approach in mining engineering.

This paper aims to provide an overview of CFD simulation studies of longwall ventilation patterns, dust and gas flow dynamics along the longwall face, aiming at providing some new insights and guidance for the operators.

## 2  Development of Longwall CFD Model

To simulate the three dimensional phenomenon of airflow, respirable dust and gas dispersion on the longwall face, CFD longwall models can be developed based on specific longwall conditions. Key parameters to be considered include longwall geometry, major longwall equipment, longwall ventilation systems, and most importantly gas and dust generation sources and associated control measures. As the longwall geometry can be complicated when considering key features of longwall equipment, CAD models for these equipment can be imported into the CFD platform such as ANSYS Workbench for geometry cleanup and meshing of the CFD model. Figure 2 shows a typical CFD longwall model for an Australian longwall mine.

Using the base-case CFD models, initial simulations were conducted to generate the base flow patterns. Depending upon site conditions, CFD models can be used to simulate face ventilation characteristics with airflow rates varying between 30 and 110 m³/s for Australian longwalls. Base CFD models results have to be validated
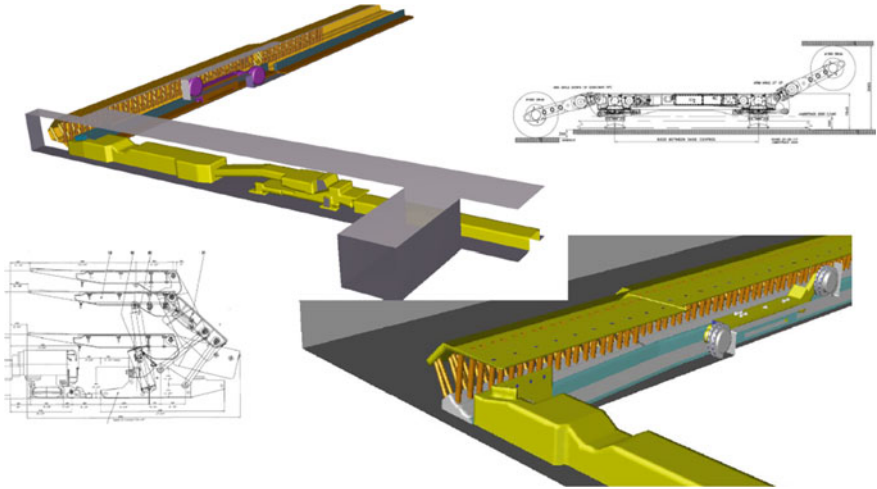
**Fig. 2.** Development of a longwall CFD model

against ventilation velocity values measured on site, which can then be used for parametric investigations of various controls and mitigation strategies for gas and dust.

## 3   LW Ventilation Flow Patterns

As the ventilation flow reaches the longwall, it will mostly travel along the longwall face, and eventually report to the tailgate (return roadway). The airflow dynamics of the ventilation dictates the work environment, as well as the dilution and mitigation of gas emissions and dust contaminations as a result of mining activities. Figure 3 shows the face ventilation flow distribution patterns for a 4.5 m thick seam longwall face with a ventilation volume of 55 m$^3$/s. The majority of the airflow (40 m$^3$/s) is provided via the last open cut-through and a small portion (15 m$^3$/s) comes from the belt road.

On entering the maingate (MG), airflow velocities increase significantly in walkway areas due to the presence of beam stage loader (BLS) and other equipment. As expected, the main stream ventilation will enter the face with high momentum, firstly impacting on the chocks near the maingate, and then turning towards the face. A zone of recirculation can also be seen around the corner between the face and the maingate. From these results it can be observed that airflow velocities are almost evenly distributed ahead of the shearer at around 3 m/s, and then increase up to around 3.5 m/s between the shearer and the face chock legs area due to the presence of shearer obstruction. The airflow is then 'forced' back to the face side as a result of chocks advancement.

In general, it can be observed from that the main stream of the face airflow starts to converge towards the walkway immediately on impact with the shearer body. Airflow diversion near the upwind corner of the shearer body can be clearly seen in Fig. 3. As intake air travels past the shearer body, the velocity distribution across the face changes

(a) ventilation velocity contour



(b) Ventilation velocity vectors



(c) Ventilation velocity vectors around the cutting shearer drum
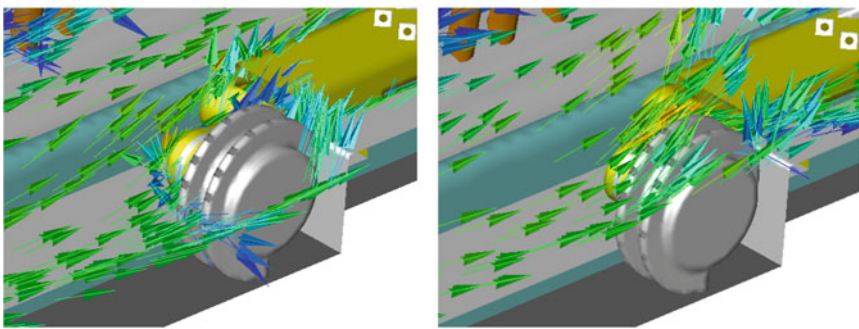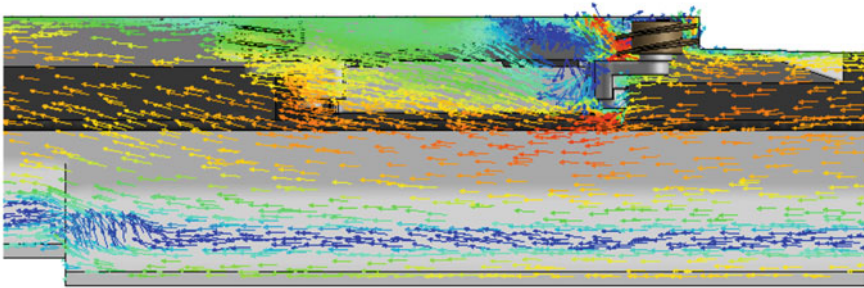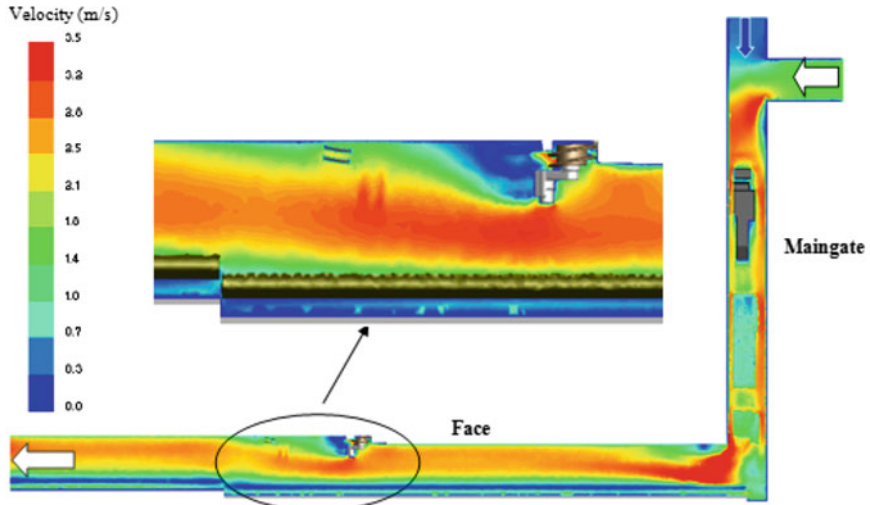
**Fig. 3.**  CFD modelling of ventilation flow pattern along a longwall face

significantly with velocity values across different zones ranging from 0 to 3.5 m/s. Results also show that the air velocity behind the chock legs area is fairly small in the range of 0.1–1.0 m/s. Simulation results also show a significant ventilation blind-spot

behind the maingate cutting drum where gas accumulation could exist. Figure 3c shows the distribution of flow vectors around the shearer drums when the drums are rotating at a speed of 35 rpm. The impact of drum rotation on regional airflow patterns can be observed. It is also noticed that the rotating direction of the drums affects the velocity distribution to some extent.

The validation of model results with field measured data is an essential part in numerical simulation. Face velocity survey data from the longwall face was used to calibrate and validate CFD base model. This normally involved a series of steps, e.g., comparison between the results of the base-case models and field measure data, and slight adjustments in the CFD models where necessary, mostly for the obstruction area of cut-coal in the models.

As stated previously, the major concern on longwall face is the respirable dust particles that can travel with the airflow and be breathed into face workers' lungs. Present knowledge of respirable dust flow behaviour indicates that these fine particles will exhibit similar aerodynamics patterns to other gases such as air. Therefore, the respirable dust behaviour was modelled by a single phase model (in which the dust particles do not interact with the continuous phase, i.e., do not change the airflow) in these CFD models. It is to be noted that modelling of total dust flow behaviour requires two-phase flow, in which dust particles interact with airflow and may alter the primary airflow.

## 4 Respirable Dust Dispersion

To investigate the dispersion behavior of respirable dust on the longwall face, 'respirable dust particles' were released from several positions in different simulations. The dust release locations in various CFD models stand for the common dust sources on a longwall face. Figure 4 shows the dispersion patterns of respirable dust released at



(a) Dust release from the cutting drum and face spalling



(b) Dust release from longwall chock movement
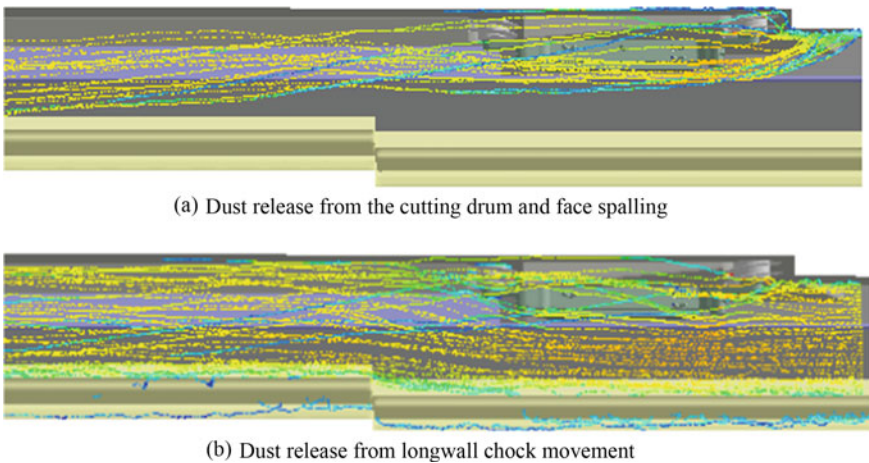
**Fig. 4.** Respirable dust dispersion from different dust sources on the longwall

different locations: face spalling ahead of the cutting drum and chock movement ahead of the shearer. And that figure shows the dust dispersion characteristics without operation of dust control measures. It is found that the location of dust generation and local airflow patterns determine the respirable dust flow behavior in a large extent. Dust generated from the cutting drum/coal spalling and chock movement can lead to significant airflow contaminations if effective mitigation strategies cannot be implemented.

Dust generated at crusher/stage loader is a major source of contamination of the intake ventilation. Dust particles will mix with the primary ventilation flow and travel along the entire length of the longwall face, contributing to the dust exposure of all the face personnel. In addition, high dust generation during maingate cut-out is also a major problem due to high air velocities at the maingate corner. Intake dust contamination remains a major issue in a number of longwall mines.

Air curtains are commonly used near the stage loader area of the longwall face in an effort to separate the contaminated air from fresh air. The objective here is to divert the fresh air onto the walkway on the face whilst pushing the contaminated flow to the inside of the face away from the face operators. To study the effect of curtains near the stage loader on the dispersion of dust particles, CFD modelling studies were carried out with different combinations of curtain designs, as shown in Fig. 5.

Figure 5b shows the results when air curtains 3 and 6 are used. Results show that under normal ventilation, the dust follows the mainstream ventilation and traverses directly towards the walkway area of the face, indicating high dust exposure levels for the face operators. When curtains 3–6 were in operation, most of the particles were directed towards the inside boundary of the longwall face, and stayed away from the walkway area. This curtain combination seems to be effective in reducing the intake dust exposure levels of the operators near the maingate area and in reducing dust pick-up during maingate cut-out or face sumping operations.

## 5  Gas Emission and Dispersion

A major function of the ventilation system is to dilute gas levels below statutory limit. To ensure safety and productivity, gas monitors are normally placed at the upper TG corner, in the TG and on the tailgate side of shearer body. However, it is noted that the highest gas level along face might not be able to be detected by placing monitors at these positions. For instance, more gas will be released during shearer cutting coal from face, therefore, the gas concentration around the drums might be significantly higher than the results reported by monitors installed away from the drums. Using the CFD modelling approach, the dynamics of methane flow and distribution patterns along the entire face can be better understood.

Figure 6 shows the gas dispersion patterns along the face when the shearer is cutting in different directions. In all cases, the residual seam gas content is assumed to be 4 $m^3$/t and methane is liberated from the cutting drums, the longwall face, AFC and the goaf area behind the longwall chocks.

As the flow enters the face, methane distribution changes significantly along the face and within the goaf region. The impact of flow separation on methane distribution can be clearly seen, e.g., the methane level is slightly higher in the recirculation zone of

Curtain 5

Curtain 2

Curtain 1

Curtain 6

Curtain 3

Curtain 4

(c) Options of air curtain orientation

Dust flow pattern without air curtains

Dust flow pattern with air curtains (3 & 6) near stage loader

(d) Intake dust dispersion patterns without and with air curtains
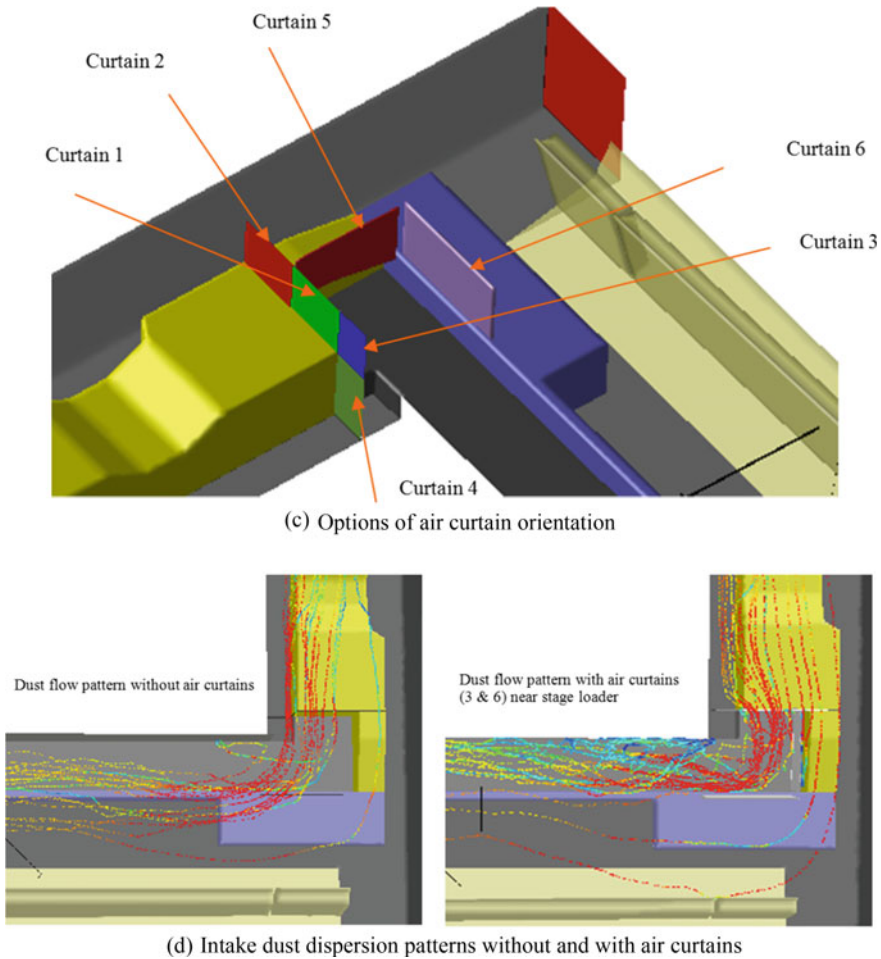
**Fig. 5.** Intake dust flow dispersion patterns without and with air curtains

face entry which is caused by flow separation. It is worth noting that this effect vanishes gradually as the shearer moves towards the TG and starts to appear as the shearer moves from the TG to the MG. The methane distribution in the immediate goaf varies greatly according to shearer cutting positions, in particular at the return end of face. The methane distribution at the MG side of goaf is similar among the six scenarios modelled, this is mainly because the dilution of leaked airflow to the goaf on MG side. At the middle and TG side of the goaf, methane starts to accumulate due to the sluggish airflow within that region. It is observed that methane distribution in the goaf is affected by the shearer position. Due to increased air ingress to the goaf at the shearer position, methane is flushed to the deep goaf as the shearer cuts coal from face middle to the TG. And this can be more clearly observed when the shearer is close to the TG. It is also noted that we can identify the source of methane causing accumulation at face end from Fig. 6, i.e. at the inner TG corner where flow circulates, methane is mainly from the

(a) Gas dispersion along the longwall face- shear cutting from MG to TG

(b) Gas dispersion along the longwall face- shear cutting from TG to MG
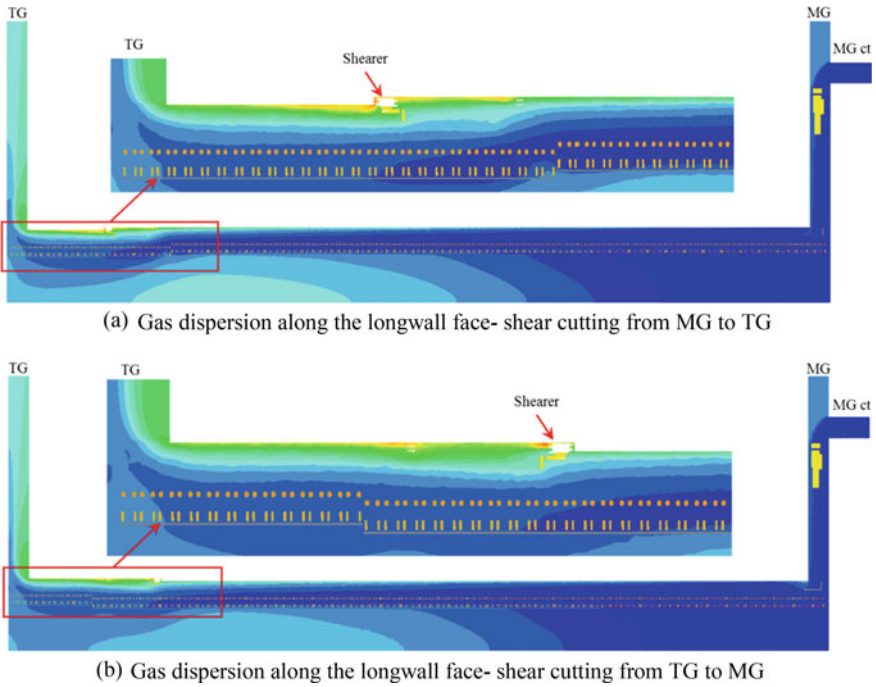
**Fig. 6.** Gas dispersion along the longwall face

longwall face; whilst at the upper TG corner, methane is dominantly emitted from the goaf and adjacent seams.

The 1% methane concentration iso-surface distribution around the shearer is shown in Fig. 7. It can be observed that the methane concentration is significantly higher
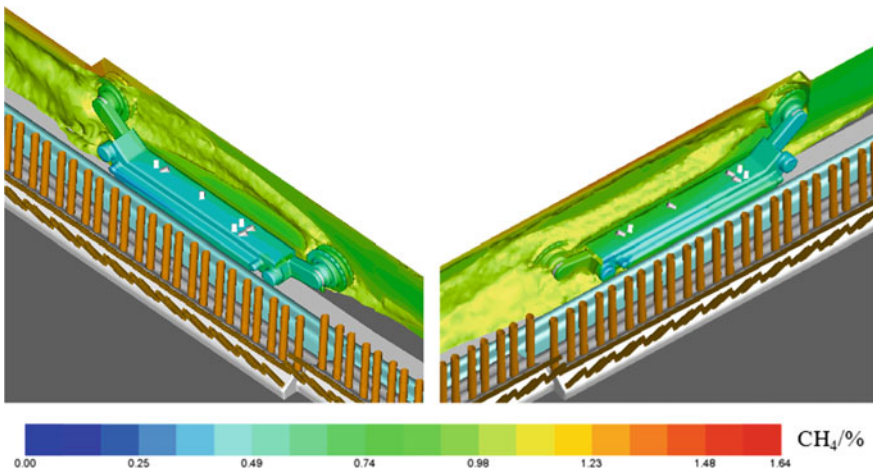


**Fig. 7.** Methane concentration distribution around the shearer when cutting in different directions

around the TG drum than it around the MG drum in either the MG-TG pass or the TG-MG pass.

## 6 Summary

The management and optimization of longwall face ventilation is critical to the safety and productivity of modern longwall mines. A sound knowledge of airflow dynamics is essential for ventilation officer (VO) or engineer to ensure sufficient ventilation is delivered to the working space with appropriate control and mitigation strategies for dust and gas management.

CFD models were developed in this study to better understand the flow dynamics and contaminant dispersion patterns within typical longwall faces. These models can be adopted on the basis of specific mining conditions to study face ventilation dynamics and dispersion characteristics of dust particles and fugitive gas emissions from different sources on the longwall. These studies can include simple ventilation management practices such as the use of air curtains or brattice, the development of effective dust control measures such as water sprays or dust scrubbers, and gas dispersion and accumulation controls. Outcomes from these CFD modelling studies can offer improved knowledge and insight into the flow dynamics on the longwall face and consequently provide useful input into the management of ventilation and occupational health and safety in underground coalmines.

## References

1. Hargreaves, D.M., Lowndes, I.S.: The computational modelling of the ventilation flows within a rapid development drivage. Tunn. Undergr. Space Technol. **22**, 150–160 (2007)
2. Kissell, F.N.: Handbook for Methane Control in Mining, p. 61. US Department of Health and Human Services, CDC/NIOSH Office of Mine Safety and Health Research (2006)
3. Ren, T., Balusu, R.: Innovative CFD modelling to improve dust control in longwalls. In: Aziz, N. (ed.) Proceedings Eighth Underground Coal Operators' Conference, pp. 137–142. The Australasian Institute of Mining and Metallurgy, Illawarra Branch (2008)
4. Ren, T., Balusu, R.: The use of CFD modelling as a tool for solving mining health and safety problems. In: Aziz, N., Nemcik, J. (eds.) Proceedings 10th Underground Coal Operators' Conference, pp. 339–349. The Australasian Institute of Mining and Metallurgy, Illawarra Branch (2010)
5. Ren, T., Wang, Z.: Computational fluid dynamics modelling of respirable dust and gas behaviour on a longwall face. In: Australian Mine Ventilation Conference, pp. 191–200. Australasian Institute of Mining and Metallurgy, Australia (2013)
6. Ren, T., Wang, Z., Cooper, G.: CFD modelling of ventilation and dust flow behaviour above an underground bin and the design of an innovative dust mitigation system. Tunn. Undergr. Space Technol. **41**(1), 241–254 (2014)

7.  Toraño, J., Torno, S., Menéndez, M., Gent, M.: Auxiliary ventilation in mining roadways driven with roadheaders: validated CFD modelling of dust behaviour. Tunn. Undergr. Space Technol. **26**, 201–210 (2011)
8.  Toraño, J., Torno, S., Menéndez, M., Gent, M., Velasco, J.: Models of methane behaviour in auxiliary ventilation of underground coal mining. Int. J. Coal Geol. **80**, 35–43 (2009)
9.  Wang, Z., Ren, T.: Investigation of airflow and respirable dust flow behaviour above an underground bin. Powder Technol. **250**, 103–114 (2013)
10. Xu, G., Luxbacher, K.D., Ragab, S., Schafrik, S.: Development of a remote analysis method for underground ventilation systems using tracer gas and CFD in a simplified laboratory apparatus. Tunn. Undergr. Space Technol. **33**, 1–11 (2013)
11. Xu, G., Luxbacher, K.D., Ragab, S., Xu, J., Ding, X.: Computational fluid dynamics applied to mining engineering: a review. Int. J. Min. Reclam. Environ. **31**, 251–275 (2017)

# Part IV
# Mine Dusts and Control II

# Study of the Effect of Drilling Bite Depth and Bit Wear Condition on Drilling Specific Energy and Dust Generation During Bolt-Hole Drilling

Yi Luo[1], Hua Jiang[1,2(✉)], and Mingming Li[1]

[1] West Virginia University, Morgantown, WV, USA
hujiang@mix.wvu.edu
[2] College of Safety Science and Engineering, Xi'an University of Science and Technology, Xi'an, Shaanxi, China

**Abstract.** The respirable dust generated during bolt-hole drilling can present serious health problems to the miners involved in roof drilling operations. The amount of respirable dust generated mainly depends on the rock strength and the way of drilling is conducted. Previous research indicate that a higher drilling bite depth is preferable for the reduction of respirable dust. In this research, the effects of drilling bite depth and bit wear on drilling specific energy and respirable dust generation have been investigated through laboratory experiments. The relationships among drilling specific energy, respirable dust and drilling bite depth were established. The influence of bit wear on drilling specific energy and respirable dust were also accounted. The results have shown a significant reduction in respirable dust amount, as well as a reduction in specific energy when drilling under larger bite depths properly determined for the type of rock. It was found that the use of worn bit can decrease the energy efficiency and generating more respirable dusts than drilling with new bit. The findings from this research has demonstrated the feasibility of using drilling control technique as a proactive approach for dust control and productivity improvement.

**Keywords:** Roof drilling · Energy efficiency · Respirable dust
Bit wear · Bite depth

## 1 Introduction

The drilling operation in roof bolting process, especially in hard rocks, generates a large amount of respirable coal and quartz dusts. The respirable dust (size < 10 μm) generated during the bolt-hole drilling can present serious health problems to the miners involved in roof bolting operations as well as other activities. Several researches have been conducted on evaluating the respirable dust hazard associated with roof bolting process. Joy et al. [1] has assessed the dust hazard during the roof bolting process by roof bolter with an on-board vacuum dust collection system, especially respirable quartz hazard. It confirmed that roof bolting dust contains enormous high content of respirable quartz dust. Besides the vacuum dust collection system commonly

mounted on the roof bolters, several roof bolter dust control technologies for reducing the dust exposure of underground roof bolter operators have been developed, such as canopy air curtain, drilling bit sleeve and mist drilling technique [2, 3].

Based on our previous research, the respirable dust generated during drilling depends not only on rock formation but also drilling control [4, 5]. The studies found that many of the drilling parameters such as thrust, torque, specific energy, noise dose, etc. are strongly related to the drilling bite depth (i.e., the penetration depth per bit revolution). The most important finding is that the specific energy, the total energy to break one unit volume of rock decreases exponentially as the bite depth increases. As the respirable dust is a result of excessive breakage of rock, it is anticipated that to achieve a rationally high drilling bite depth could greatly reduce the respirable dust from the drilling process. Drill bit wear condition, another critical factor influencing drilling efficiency was rarely studied in terms of quantified energy consumption and dust generation characteristics.

In this study, drilling experiments with different bite depths and bit wear conditions were conducted. The drilling feedback data as well as the generated dust samples were collected. The specific energy and the amount of respirable dust was evaluated regarding to different drilling control and bit wear scenarios. Based on the experiments, drilling control algorithm can be developed to reduce specific energy and respirable dust while ensuring drilling safety and productivity.

## 2 Laboratory Drilling Experiments

Laboratory drilling tests were conducted and the test setup is shown in Fig. 1. The tests were designed to cover a full range of bite depth based on the bit design, drilling safety, and available drilling power. The drilling system can be set at different penetration and rotation rates to achieve the preset bite depth for each test. The drilling safety check is to prevent excessive thrust placed on the drill steel to cause its bending failure [4]. As a long hole is drilled in hard rock, the maximum allowable thrust on a long drill steel becomes a critical limiting factor for achieving the desirable bite depth. After drilling each hole, the cuttings and dust particles deposited in different stages of the vacuum dust collection system have been collected for further size analysis.

Thirty-seven testing holes have been drilled on a concrete block with the bite depth ranging from 0.109 to 0.752 cm/revolution. The drilling parameters and feedback data are shown in Table 1. All the drilling tests were conducted using a 3.493 cm tungsten carbide drag bit that is widely used in the underground coal mines for drilling roof bolt holes. The first 12 tests were designed to evaluate the bit wear effect on drilling energy consumption and dust production. A new bit was used for the first test and it was used continuously until it was substantially worn out after test 9, and the final bit weight loss is 31.44 g. For this bit, it will be regarded as worn out condition when the weight loss is over 30 g (14.2% of new bit weight). A noticeable bit wear was observed after drilling test 5. So drilling tests 5–9 were regarded as drilling with worn bits in the analysis. For test 10, 11 and 12, three worn bits with weight loss of 1.62, 25.31 and 27.54 g used in the previous drilling tests were used, respectively. For the rest of the tests, a new drill bit was used for each hole to avoid the influence of bit wear.
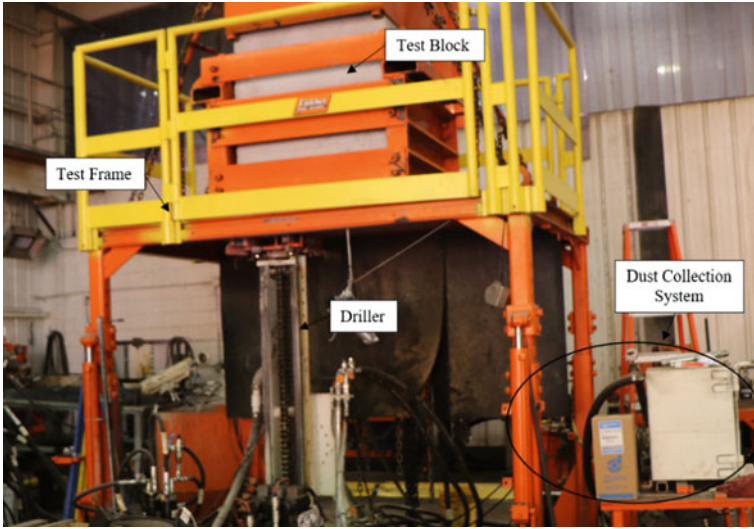
**Fig. 1.** Experiment setup of the drilling study

## 3   Experiment Results and Data Analysis

Dust samples were collected after the drilling of each hole and the size distribution (on a volume basis) were analyzed using a CILAS model 1190 particle size analyzer. The results of the respirable dust percentage were presented in Table 1. It should be noted that for tests 19, 20 and 23, the drilling failed as the bits encountered the steel rope in the concrete block. For the three tests, dust samples were not collected but the drilling data before the failure were still collected.

### 3.1   Drilling Specific Energy Relationship with Different Bite Depths and Bit Wear Conditions

The total drilling power at the bit ($P_c$) can be calculated as the summation of the powers for torque ($T$) and for thrust ($W$), respectively as shown in Eq. 1. In the equation, $R$ and $v$ are the rotation rate (in revolutions/min) and the penetration rate (in cm/s), respectively.

$$P_c = \frac{2\pi \cdot T \cdot R}{60} + W \cdot v \qquad (1)$$

The energy expended can be expressed in terms of the specific energy, which is widely used in the drilling literature for the evaluation of the drilling condition and bit selection [6]. The drilling specific energy is the amount of energy consumed to break a unit volume of rock and is determined by dividing the amount of input energy by the rock volume drilled [7]. Therefore, specific energy is an indicator to evaluate drilling efficiency, a lower drilling specific energy indicate a higher drilling efficiency because

**Table 1.** Summary of drilling parameters, energy consumption and respirable dust generation

| No. | Bit condition or weight loss, g | Pre-set bite depth | Achieved | | | Thrust, N | Torque, N cm | Specific energy, N/cm$^2$ | Res. dust Pct., % |
| | | | Bite depth | $v$ | $R$ | | | | |
| | | cm/rev | cm/rev | cm/s | rev/min | | | | |
| 1 | Bit #1 | 0.152 | 0.168 | 0.84 | 299 | 5305.4 | 7953.7 | 19,464.6 | 23.5 |
| 2 | Bit #1 | 0.102 | 0.118 | 0.86 | 434 | 5304.4 | 9399.0 | 32,528.2 | 49.8 |
| 3 | Bit #1 | 0.091 | 0.109 | 0.82 | 454 | 5463.6 | 9407.6 | 35,437.6 | 31.4 |
| 4 | Bit #1 | 0.122 | 0.128 | 1.08 | 507 | 6504.8 | 10,210.3 | 32,842.1 | 27.4 |
| 5 | Bit #1 | 0.152 | 0.120 | 1.04 | 522 | 7007.2 | 10,858.7 | 37,222.1 | 30.1 |
| 6 | Bit #1 | 0.396 | 0.234 | 2.02 | 517 | 8568.2 | 11,261.2 | 20,024.6 | 39.4 |
| 7 | Bit #1 | 0.427 | 0.183 | 1.53 | 500 | 8791.8 | 10,592.6 | 23,976.1 | 29.4 |
| 8 | Bit #1 | 0.457 | 0.185 | 1.54 | 499 | 8722.0 | 10,081.4 | 22,649.8 | 27.5 |
| 9 | Bit #1 | 0.406 | 0.199 | 1.00 | 301 | 8711.7 | 7659.9 | 16,185.3 | 29.6 |
| 10 | 1.62 | 0.213 | 0.205 | 1.70 | 497 | 5779.1 | 9155.8 | 18,478.4 | 25.3 |
| 11 | 25.31 | 0.213 | 0.150 | 1.24 | 497 | 8734.9 | 10,099.4 | 27,775.3 | 27.3 |
| 12 | 27.54 | 0.213 | 0.131 | 1.09 | 500 | 8743.3 | 9841.1 | 31,065.3 | 42.0 |
| 13 | New | 0.122 | 0.152 | 1.17 | 462 | 4634.5 | 8453.8 | 22,856.5 | 25.9 |
| 14 | New | 0.152 | 0.171 | 1.12 | 392 | 4892.7 | 9296.5 | 22,320.1 | 22.5 |
| 15 | New | 0.183 | 0.204 | 1.60 | 470 | 4880.3 | 8502.3 | 17,166.7 | 23.4 |
| 16 | New | 0.213 | 0.212 | 1.77 | 502 | 5686.3 | 8713.6 | 17,033.0 | 32.2 |
| 17 | New | 0.218 | 0.235 | 1.60 | 409 | 5371.1 | 9520.4 | 16,767.2 | 22.2 |
| 18 | New | 0.244 | 0.241 | 2.02 | 503 | 5436.4 | 8656.7 | 14,911.7 | 22.8 |
| 19 | New | 0.244 | 0.252 | 2.10 | 500 | 6853.2 | 9322.9 | 15,400.2 | |
| 20 | New | 0.244 | 0.256 | 2.14 | 503 | 6006.1 | 8872.2 | 14,444.8 | |
| 21 | New | 0.244 | 0.258 | 2.11 | 491 | 5546.0 | 9071.3 | 14,614.7 | 21.6 |
| 22 | New | 0.274 | 0.276 | 2.30 | 501 | 6621.7 | 9329.4 | 14,099.9 | 23.3 |
| 23 | New | 0.274 | 0.287 | 2.39 | 501 | 5912.5 | 9193.3 | 13,358.1 | |
| 24 | New | 0.290 | 0.287 | 2.03 | 425 | 5595.6 | 9509.7 | 13,782.9 | 20.4 |
| 25 | New | 0.305 | 0.293 | 2.51 | 515 | 5994.0 | 9530.0 | 13,557.5 | 21.4 |
| 26 | New | 0.305 | 0.308 | 2.62 | 510 | 6007.6 | 9559.6 | 12,962.9 | 20.7 |
| 27 | New | 0.366 | 0.391 | 3.28 | 503 | 7107.9 | 9965.2 | 10,781.5 | 20.8 |
| 28 | New | 0.406 | 0.393 | 2.97 | 453 | 6646.9 | 8529.2 | 9212.4 | 21.0 |
| 29 | New | 0.457 | 0.415 | 3.05 | 441 | 7190.8 | 10,072.4 | 10,297.9 | 17.1 |
| 30 | New | 0.427 | 0.435 | 3.66 | 504 | 7298.0 | 9932.8 | 9706.6 | 20.6 |
| 31 | New | 0.427 | 0.445 | 3.70 | 499 | 7712.0 | 9982.9 | 9576.0 | 19.7 |
| 32 | New | 0.488 | 0.539 | 4.11 | 458 | 7923.0 | 11,387.5 | 9064.0 | 20.8 |
| 33 | New | 0.533 | 0.551 | 3.66 | 398 | 8357.0 | 10,105.3 | 7959.0 | 19.5 |
| 34 | New | 0.579 | 0.588 | 4.95 | 505 | 9567.7 | 11,143.5 | 8283.9 | 20.6 |
| 35 | New | 0.610 | 0.642 | 4.27 | 399 | 9452.3 | 10,450.1 | 7203.1 | 20.2 |
| 36 | New | 0.762 | 0.732 | 5.21 | 427 | 12,325.5 | 11,268.0 | 7030.0 | 20.0 |
| 37 | New | 0.686 | 0.752 | 4.98 | 397 | 10,902.3 | 11,272.6 | 6768.8 | 20.7 |

less energy is used to drill a same volume of rock. The specific energy for rotary drilling can be expressed mathematically in terms of drilling bite depth ($b$), penetration rate, torque and thrust, as shown in Eq. 2 in which $A_b$ is the borehole cross-sectional area, in cm$^2$.

$$\epsilon = \frac{P_c}{A_b \cdot v} = \frac{2\pi T}{A_b \cdot b} + \frac{W}{A_b} \tag{2}$$

The drilling specific energy for tests with different bite depths and bit wear conditions were calculated and plotted in Fig. 2. From the new bit drilling results, a good exponentially decreasing trend is observed between specific energy and drilling bite depth. A sharp decrease in specific energy occurs when the bite depth is smaller than 0.3 cm/rev with a maximum 64% reduction in specific energy in comparison to the initial specific energy of about 37,222 N/cm$^2$ at the bite depth of 0.12 cm/rev. For bite depth range beyond 0.3 cm/rev, an additional 18% reduction in specific energy is realized to the minimum value of 6768 N/cm$^2$.
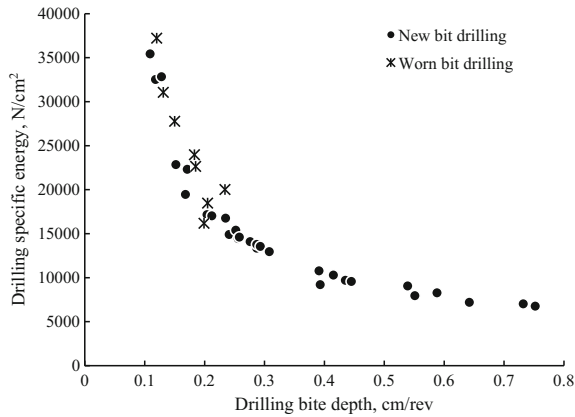


**Fig. 2.** The drilling specific energy with different bite depths and bit wear conditions

The similar trend can be found for drilling with worn bits in Fig. 2 despite of varying bit wear conditions. By comparing the specific energy for a similar bite depth with a new bit drilling, it is found that the drilling specific energy expended by a worn bit is higher than a new bit drilling with the same drilling bite depth. Apparently, more energy is wasted on overcoming the friction force, generating noise and heat when drilling is conducted with a worn bit.

## 3.2 Influences of Bite Depths and Bit Wear on Respirable Dust

Respirable dust is of primary concern as it can penetrates into and deposit in the alveolar region of the lung that gradually hinders the lung's function. Therefore, the feasibility and effectiveness for proper drilling control to reduce respirable dust are

evaluated using the experimental drilling data. Figure 3 shows the percentage of respirable dust in the collected cutting samples for the performed drilling tests. When new drill bits are used, the cutting contains about 31.4% respirable dust when the drilling was conducted with bite depth of 0.11 cm/rev. Significant reduction in the percent of respirable dust is observed as the drilling bite depth increases to about 0.30 cm/rev. When the bite depth is higher than 0.30 cm/rev, the percentage of respirable dust levels of around 20%. It can be easily explained by the fact that less over-breakage of rock (higher energy efficiency and less respirable dust) when drilling is conducted with higher bite depth. Figure 3 also shows that the respirable dust produced by drilling with worn bits is much more than that by new bits for the same drilling control. Such additional amount respirable dust is caused by additional friction area at the wear flat area on the worn bit.
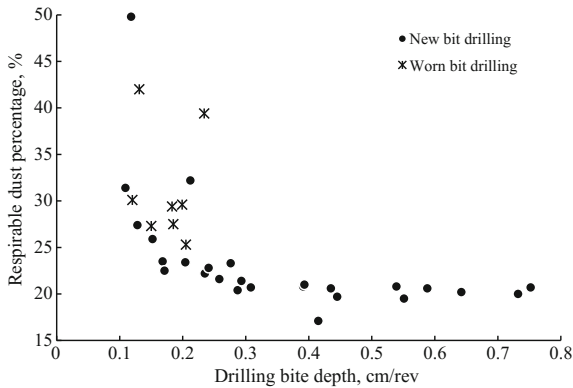


**Fig. 3.** The respirable dust generation with different bite depths and bit wear conditions

## 4   Discussion

The drilling specific energy and respirable dust generation data indicate that a better drilling efficiency with less respirable dust production can be achieved at higher drilling bite depth. It should be noted that the majority of the fine dust is produced by the frictional grinding action between the dill bit and the rock. A higher bite depth can reduce the total contact area for drilling a bolt hole of a specified length, therefore, less respirable dust to be generated by grinding over this area. In addition, the rock fragmentation in rotary drilling is a two-stage process: the crack initiation and crack propagation. The depth of the crack initiation point is proportional to the bite depth [8]. Therefore, a larger drilling bite depth yields more larger fragments. Therefore, to break the same volume of rock, a higher drilling bite depth results in lower drilling specific energy so that less energy is wasted on over-breaking the rock for less fine cutting particles.

Figure 4 shows that a good increasing relationship existed between the drilling specific energy and the percent of respirable dust, especially for the drilling tests performed with new dill bits. For the tests drilled with worn bits, it is hard to observe any pattern other than they generated significantly higher amount of respirable dust than those drilling tests with new bits. The drilling specific energy is also in a higher range indicating lower energy efficiency. These relationships confirm with previous analysis that when drilling with a higher drilling efficiency, less respirable dust will be generated.
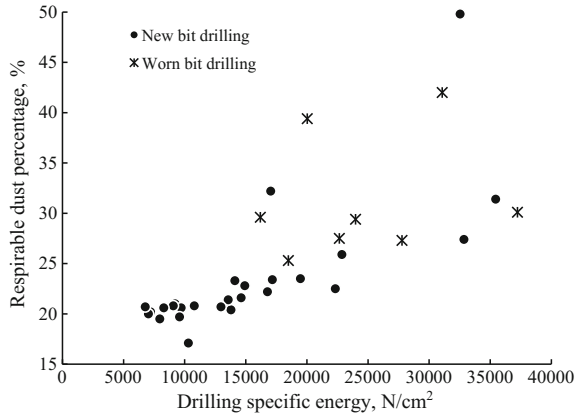


**Fig. 4.** The relationship between drilling specific energy with respirable dust generation

In the drilling process, the input energy is mainly consumed by overcoming the rock strength and interface friction. As shown in Table 1, for drilling with worn bits, the drilling system is often unable to achieve the pre-set bite depth. A higher thrust is required to achieve the intended bite depth and consequently results in a larger friction force. In such case, a smaller portion of the total energy is actually used for cutting the rock while the major part of the energy is consumed by frictional grinding action. Therefore, the use of an excessively worn bit can lower the energy efficiency and waste more drilling energy on producing respirable dust, noise and heat.

## 5    Conclusions

A proactive dust control method for reducing the respirable dust generated through proper control of the drilling process in roof bolting operations has been proposed. The feasibility and the effectiveness of the approach has been proven by theoretical and experimental studies. Based on the studies, the drilling bite depth and bit wear condition are the two key factors affecting the dust generation characteristics and energy consumption. The results have shown a significant reduction in respirable dust amount, as well as a reduction in specific energy when drilling under larger bite depths. It was found that the use of worn bit can decrease the energy efficiency and generating more

respirable dusts than drilling with new bit. Therefore, by achieving a low specific energy with a proper drilling bite depth, while avoiding using excessively worn bits, significant reduction of quartz-rich respirable dust from its generation source could be achieved.

The advantages of this proposed proactive approach is that it not only reduces the specific energy, respirable dust, noise dose and bit wear but also can improve drilling productivity when drilling is properly controlled based on the rock to be drilled. Future research is to develop a feed-back drilling control algorithm for the roof bolter machine to determine and apply the rational drilling parameters based on the roof strength.

# References

1. Joy, G.J., Listak, J.M., Beck, T.W.: Respirable quartz hazards associated with coal mine roof bolter dust. In: Proceedings of the 13th U.S./North American Mine Ventilation Symposium, pp. 59–64 (2010)
2. Listak, J.M., Beck, T.W.: Development of a canopy air curtain to reduce roof bolters' dust exposure. Min. Eng. **64**(7), 72–79 (2012)
3. Beck, T.W.: Evaluations of bit sleeve and twisted-body bit designs for controlling roof bolter dust. Min. Eng. **67**(2), 34–40 (2015)
4. Luo, Y., Qiu, B., Li, M.M.: Reducing drilling noise in roof bolting operation through rationalized drilling. In: 23rd World Mining Congress, Montreal, Canada (2013)
5. Jiang, H., Luo, Y., Li, M.M.: Experimental study on effects of drilling parameters on respirable dust production during roof bolting operations. J. Occup. Environ. Hyg. **15**(2), 143–151 (2018)
6. Rabia, H.: Specific energy as a criterion for bit selection. J. Petrol. Technol. **37**(7), 1225–1229 (1985)
7. Teale, R.: The concept of specific energy in rock drilling. Int. J. Rock Mech. Min. Sci. Geomech. Abstr. **2**(1), 57–73 (1964)
8. Hareland, G., Yan, W., Nygaard, R., Wise, J.L.: Cutting efficiency of a single PDC cutter on hard rock. J. Can. Pet. Technol. **48**(6), 1–6 (2009)

# Applications of Water Infusion for Dust Control in Underground Coal Mines—A Critical Review

Ting Ren[1(✉)], Jian Zhang[2], and Jianping Wei[2]

[1] School of Civil, Mining & Environmental Engineering, University of Wollongong, Wollongong, Australia
tren@uow.edu.au
[2] School of Safety Science and Engineering, Henan Polytechnic University, Jiaozuo 454000, China

**Abstract.** Coal mine dust continues to be a health and safety issue in underground coal operations. Water infusion method was developed and widely applied in European coal mines for dust control, and is now a common practice in most Chinese coal mines. This method typically involves the injection of water into the coal seam usually ahead of mining to increase its moisture content and therefore reduce dust generation during mining. Field practices indicated that it was possible to inject 9–15 l of water into 1 $m^3$ of coal and increase its moisture content by approximately 1% with a respirable dust reduction of 40–65% during mining. A limited scale of water infusion trials was conducted in Appin and West Cliff collieries of Australia in late 1980s; a 30–50% reduction of dust levels was reported. With the availability of other dust control methods such as water spraying systems, water infusion method has not been considered as a viable means for dust mitigation in modern mines and as such it has not been utilised in Australian underground mines. The increase in production output and the deployment of more powerful equipment for coal cutting and transport, intensive SIS and UIS gas drainage practices mean that workers could be exposed to more dust contaminations. Whilst the mine operators are committed to suppress and dilute airborne dust particles using these passive measures, there is a need to critically examine and subsequently develop this proactive dust control technology for practical applications in Australian coal mines. The paper provides a critical review of the water infusion technologies in view of its technological advances and practical application limitations. The key parameters influencing the effect of water infusion on dust control are identified and discussed, particularly coal moisture content. The use of gas drainage boreholes as secondary water infusion holes is discussed.

**Keywords:** Coal mine dust · Water infusion · Dust control · Underground coal mines

# 1 Introduction

Coal mine dust has long been a health and safety issue in underground coal mines [1–4]. Coal workers' pneumoconiosis (CWP) is one of a range of mine dust lung diseases (MDLD) caused by long-term exposure to mine dust. To date various techniques such as water spray, scrubber, and water infusion have been developed to mitigate dust generation during longwall cutting. Among these methods water infusion is an important one and the only one technique attempting to reduce dust generation proactively. Water infusion is the process of injecting water with or without surfactant under a certain pressure into the coal seam ahead of working face. The liquid infuses into the seam along coal seam cleats and fractures and penetrates a considerable distance from the hole radially.

Water infusion techniques have been recognized and widely practiced for many years in European mining as an effective means of dust control. Belgium has utilized water infusion techniques for many years and Belgian experience suggested 13 l water per cubic metre coal was able to bring down the respirable dust produced during mining by 65% [5]. In the northern coalfields of France it was the routine dust control technique for 89% of the coal produced [6]. Mining regulations in Germany required water infusion where possible, and over 50% of their longwalls are infused [7–9]. The German experience indicated that at least ten litres water was required to infuse one cubic metre coal to suppress dust. Later on trials were conducted in several coal seams in US during 1970s–1980s and it was found water infusion was a promising and cost effective dust mitigation technique [10–13]. For water infusion to be effective, the US experience indicated that the quantities of water would have to approach 0.5–1% of coal volume [7]. In Australia, a limited scale of water infusion trials was conducted in Appin and West Cliff collieries in late 1980s; a 30–50% reduction of dust levels was reported [14]. In China water infusion trials were conducted in about ten coalfields during 1953–1974 and it was indicated water infusion can lead to dust reduction during mining ranged from 30 to 50% and coalbed moisture content was increased by one percent in weight after infusion [10].

With the availability of other dust control methods such as water spraying systems, water infusion method has not been considered as a viable means for dust mitigation in modern mines and as such it has not been utilised in Australian underground mines. The increase in production output and the deployment of more powerful equipment for coal cutting and transport, intensive gas drainage practices mean that workers could be exposed to more dust contaminations. As of 2 March 2018, there are 66 confirmed cases of MDLD among current and former Queensland mine workers, according to the Department of Natural Resources, Mines and Energy (DNRME), QLD Government, Australia. The re-emergence of CWP in Australia is causing serious concerns at all levels from the government regulating bodies to the mine operators. Whilst the mine operators are committed to suppress and dilute airborne dust particles using these passive measures, these confirmed CWP cases in Australia demonstrated the insufficiency of these passive measures for respirable dust control and the need to critically examine and subsequently develop this proactive dust control technology for practical applications in Australian coal mines. The paper provides a critical review of the water

infusion technologies in view of its technological advances and practical application limitations. To provide more insights, mechanism of water flow in coal cleats and role of surfactant in the process is discussed. The key parameters influencing the effect of water infusion on dust control are identified and discussed. The use of gas drainage boreholes as secondary water infusion holes is briefly discussed. Lastly practical limitations of water infusion are also discussed.

## 2 Basics of Water Infusion

To date, according to European and US experience, three water infusion methods have been developed, namely infusion from face, infusion from advance gateroad, and remote infusion as depicted in Fig. 1 [7, 12, 13, 15]. In Fig. 1a, horizontal holes are drilled into the face to a depth of about the daily advance ($\sim$3 m) of the panel (shallow infusion). Under some circumstances, holes are drilled to about 12 m (deep infusion). The spacing of these holes is approximately 1.5–2 times the length of the holes. In Fig. 1b, water is injected into coal seam from pre-drilled holes in coal ribs from
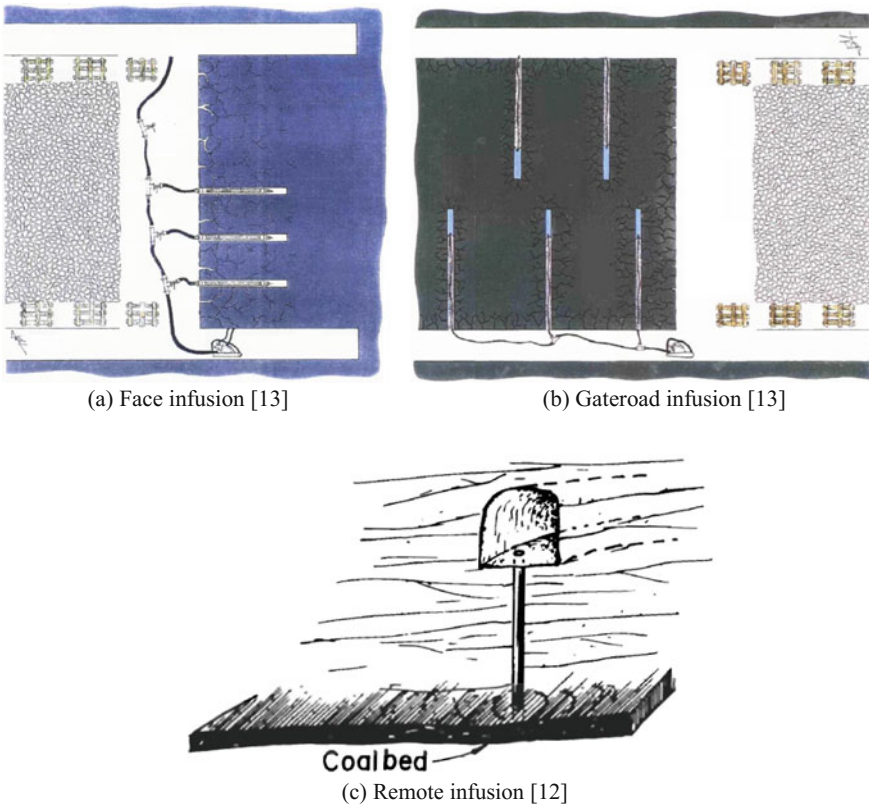


(a) Face infusion [13]        (b) Gateroad infusion [13]

(c) Remote infusion [12]

**Fig. 1.** Illustrations of various coal seam infusion methods

gateroads. Hole depth ranges from 18 to 36 m and the sealed depth ranges from 14 to 18 m. The third method is known as remote infusion or infusion from outside of the mined coal seam, as shown in Fig. 1c. If there is a roadway above the panel being mined, holes are drilled downward from this roadway into the panel and infused continuously. Face infusion has serious operational limitations in that it requires large numbers of holes to be drilled and infused in one shift otherwise production shift can be delayed. Remote infusion requires more expensive and difficult drills and this method is not widely used [11]. Drilling and infusion from gateroad shows promise by solving operational problems. Completion of the infusion process of a hole is determined by regular inspections of water seepage on both sides of the panel. However, seepage may be difficult to find at the ribs because mining induced fractures parallel to the rib will prevent water from migrating to the entry. Water may be observed at all places along the ribs and seeping from the panel near the floor. Another sign that the infusion process may be complete is a drop in infusion pressure, accompanied by an increase in flow rate, which usually indicates that the water has reached the rib or is short-circuiting along the path of the least resistance.

## 3   Mechanism of Water Flow in Coal Cleats

Coal seams are naturally fractured and can be characterised as being made of fractures and matrix (solid coal). As depicted in Fig. 2, coal is a collection of matrix blocks and fractures, where the fractures can be classified into three orthogonal classes: face cleats, butt cleats and bedding plies, in terms of their direction and connectedness [16]. Generally there are at least two sets of vertical fractures that intersect at right angles to form an interconnected network throughout the coalbed. These two fracture systems are known as face and butt cleats. Face cleats are composed of well-developed, extensive, roughly planar fractures which run parallel to each other, and butt cleats are also roughly planar but are neither as well-developed nor as continuous as face cleats [17]. The matrix block plays no part in the infusion process. Although it contains an interconnected pore system, these openings, which are about 5–10 m in diameter, are too small to permit water to pass [11]. Therefore, infusion of water into coalbed is confined in the cleat system only.

  Coal seam cleat system plays an important role in water infusion in coal seam. If the difference between the face and butt cleat is marginal (i.e. where a coal seam is friable), water tends to migrate uniformly in all directions from the centre of the panel, and infusion is circular in a planar view as shown in Fig. 3a. When the face cleat is significantly more prominent, water migrates faster along the face cleat and the infusion zone tends to be elliptical (i.e. where a coal seam is blocky). If the face cleat is perpendicular to the mining face, water runs faster parallel to mining advancing direction as shown in Fig. 3b. If the face cleat is parallel to the mining face, water runs faster towards to two ribs of longwall panel as shown in Fig. 3c.

  During water infusion, the motion of water into coal cleats is driven by the impetus pressure of water injection $P_w$, the capillary force $P_c$, and the molecular diffusion [18]. Flow resistance pressure $P_r$ and gas pressure $P_g$ also play roles in water flow in coal cleats but they can be ignored where water infusion pressure is large. Molecular
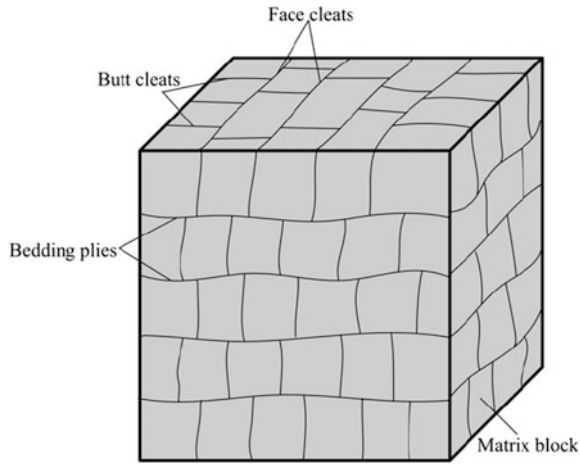
**Fig. 2.** A representative structure of coal lump [16]



(a) Marginal difference between face and butt cleat



(b) Face cleat perpendicular to the mining face



(c) Face cleat parallel to the mining face
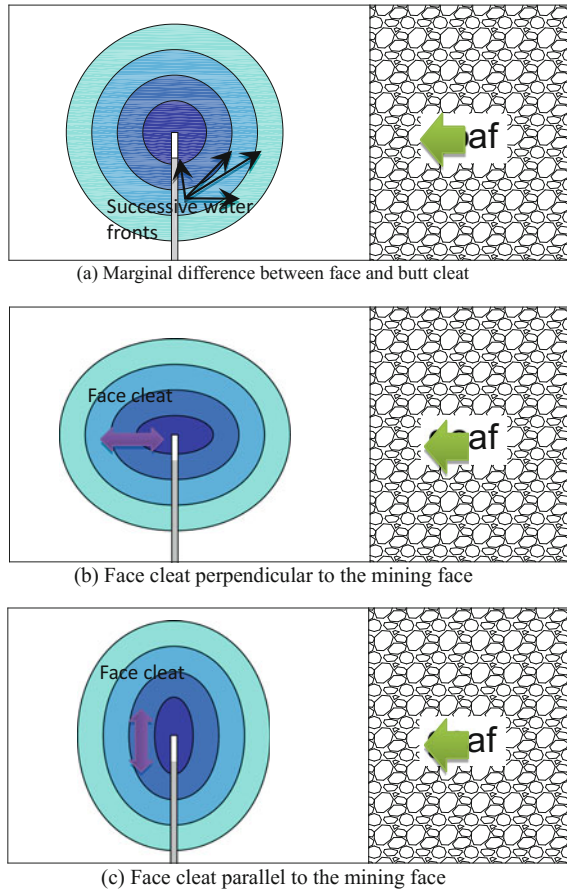
**Fig. 3.** Schematic relations between seam cleat systems and infusion zones

diffusion can be also ignored because the diffusion process is very slow. If the cross-sectional shape of the coal cleat is circular and the effect of gravity can be ignored, the force analysis for water movement in the coal cleat can be illustrated in Fig. 4, where only horizontal movement is considered. During infusion, the movement of water into coal cleats is driven by the differential pressure from injection, capillary force, flow resistance, and gas. The flow is usually laminar. According to the flow equation of Hagen-Poiseuille [19], the rate of water movement is calculated by the following equation:
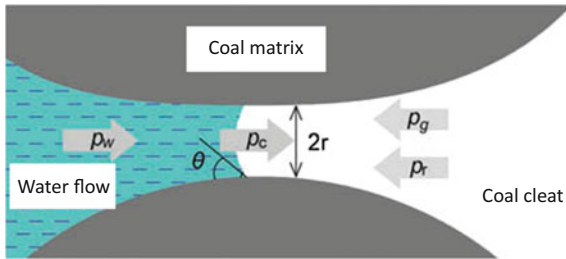


**Fig. 4.** A schematic view of water movement in coal pore system [18]

$$\frac{dl}{dt} = \frac{\sum P \cdot r^2}{8\eta l} \tag{1}$$

where $\sum P$ is the total differential pressure between two ends of the l-length coal cleat, $\sum P = P_w + P_c - P_r - P_g$, Pa; $\eta$ is the dynamic viscosity coefficient of water (Pa · s); $r$ is the radius of the coal pore (m).

The capillary force pressure $P_c$ can be calculated:

$$P_c = \frac{2 \cdot \gamma \cdot \cos \theta}{r} \tag{2}$$

where $\gamma$ is the surface tension of water (mN/m) and $\theta$ is the contact angle at the coal–water interface (°). Take Eq. 2 into Eq. 1, which yields the following equation:

$$\frac{dl}{dt} = \left( P_w - P_g + \frac{2 \cdot \gamma \cdot \cos \theta}{r} \right) \cdot \frac{r^2}{8\eta l} \tag{3}$$

Equation 3 shows that the rate of water movement in coal cleats decreases rapidly with the decrease of the diameter of coal cleat. It is therefore more time consuming for water to permeate into smaller coal cleats.

## 4    The Role of Surfactant

As discussed in Eq. 3, the capillary pressure $P_c$ mainly depends on $\gamma \cdot \cos \theta$. The purpose of the involvement of surfactant (i.e. the wetting agent) is to increase capillary pressure in coal cleats. The magnitude of such increment can be assessed by a rising factor [18]. The capillary force rising factor $F_C$ can be defined as the ratio of $\gamma_s \cdot \cos \theta_s$ of water with the wetting agent to the $\gamma_w \cdot \cos \theta_w$ of water without wetting agent as the following:

$$F_C = \frac{\gamma_s \cdot \cos \theta_s}{\gamma_w \cdot \cos \theta_w} \tag{4}$$

where $\gamma_s$ and $\gamma_w$ (mN/m) are the surface tensions of the water with and without surfactant respectively. $\theta_s$ and $\theta_w$ are the contact angles of water-coal interface with and without surfactant respectively. Greater $F_C$ denotes faster water movement and better wetting effects on coal seam. The wetting agent is able to reduce the contact angle at the coal–water interface and also the surface tension of water, as shown in Fig. 5.



(a) with wetting agent            (b) without wetting agent
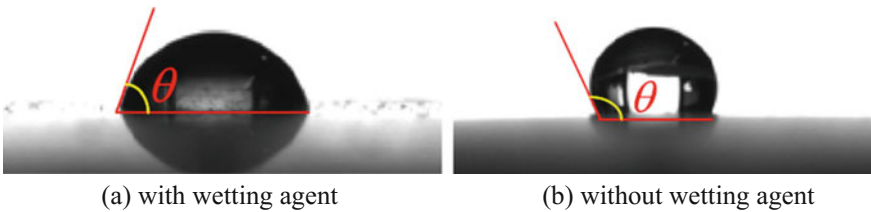
**Fig. 5.**  Examples of water-coal interface contact angle with(out) wetting agent [21]

Li et al. [18] investigated wettability (surface tensions, contact angles, and capillary imbibition) of the wetting agents lauryl dodecyl sulfate (SDS, $C_{12}H_{25}SO_4Na$), sodium dodecyl benzene sulfonate (LAS, $C_{18}H_{29}SO_3Na$), sodium dioctyl sulfosuccinate (AOT, $C_{20}H_{37}NaO_7S$), and SDS compounded with five additives on a coal-seam sample in the laboratory. It was found a compound wetting agent made of 0.1 wt% SDS + 0.05 wt% NaAc was optimal for the wettability enhancement of a China long flame coal. Crawford and Mainwaring [20] studied the influence of surfactant (sodium dodecyl sulphate-SDS, cetyl trimethyl ammonium bromide-CTAB and Teric G12A8) adsorption on the surface characterisation of three Australian coals. It was reported that adsorption of surfactants did not increase the surface hydrophobicity for the lowest rank coal, however appreciable changes in contact angle were measured as the rank of the coal increased. Li et al. [21] studied wetting performance of three different ranks of coal dust sample (anthracite, bituminous and lignite) and it was found the wetting performance was poor for the coal with higher volatile content. The wetting behaviours of coal dust could be greatly improved by adding two surfactants (SDS and sodium carboxymethyl cellulose) and SDS was reported to be a better choice and 0.2%

concentrations were recommended during coal dust suppression applications. Zhang [22] tested surface tensions of water containing different surfactants including quick T, SDS, JFC-S, and AEO-9, respectively and their contact angles at surfaces of two coals were also determined. A compound wetting agent (0.1% quick T + 0.04% AEO-9 + 0.04%CaCl$_2$) was reported to decrease contact angle below 10° in 15 s. It was also found under a same pressure more water containing wetting agent can be injected into coal seam than pure water [22].

## 5   Key Parameters

The effectiveness of water infusion is a function of the amount of water the coal seam accepts (its infusibility), which depends on a variety of factors as summarised in Fig. 6. These factors mainly include: (a) coalbed characterisation, which determines the original conditions of the coal seam; (b) extraction method, which determines the pattern of fissuring and fracturing in the coalbed; (c) drilling process, which determines
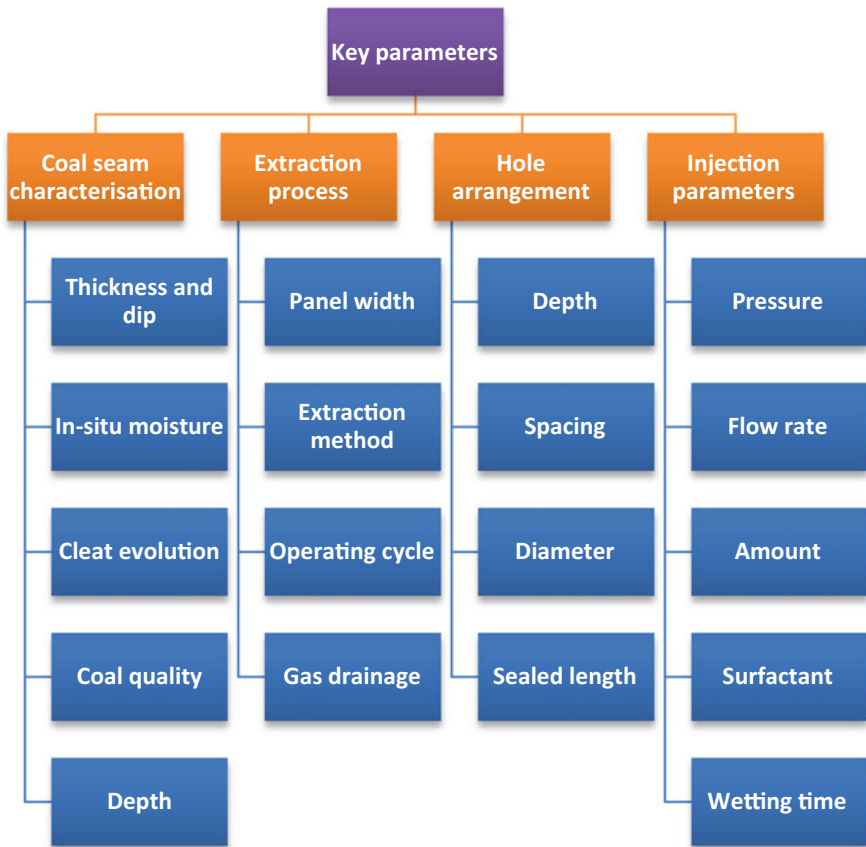


**Fig. 6.** A hierarchy of key factors of water infusion

the performance of water infusion if a coal seam is proven to be suitable to be infused; and (d) infusion parameters, which are used to carry out an infusion operation. It is possible to establish the injectability of a seam from injectability curves revealing the relationship between the three main parameters involved, i.e. water pressure, flow-rate and amount. The injectability curves are obtained either by measuring the amount of water entering the block at a given point per unit of time, at a given pressure and under the particular conditions present in the environment, or by measuring the pressure necessary to obtain a specific flowrate at different depths [13].

## 6   Use of Gas Drainage Boreholes

It was indicated that the cost of infusion is directly proportional to the number of infusion holes needed [7]. A major part of the cost of water infusion is from borehole drilling and sealing process. Gas drainage of coal seam prior to extraction is a routine practice for most gassy coal mines. After gas drainage, coal seam is very likely to become drier as a result of free moisture being depleted from coal cleat system. To reduce the cost arising from drilling and dust generation after gas drainage, the possibility of using pre-drilled gas drainage boreholes to inject water for dust control was investigated. Hu et al. [23] designed a water injection system through the inseam gas drainage boreholes to control dust arising from the coal cutting at longwall face in Yangquan coalfield, China. It was discussed when the gas drainage boreholes entered the areas affected by abutment pressure, gas drainage pipeline was detached and water injection started. As shown in Figure 7, if water infusion starts in the stress concentration zone (post peak of abutment pressure) where mining induced cracks are not developed, it would be difficult to completely wet the coal seam; while if water injection starts very close to working face, it may results in short circuiting of water flow. It was demonstrated that under the influence of abutment pressure, water injection
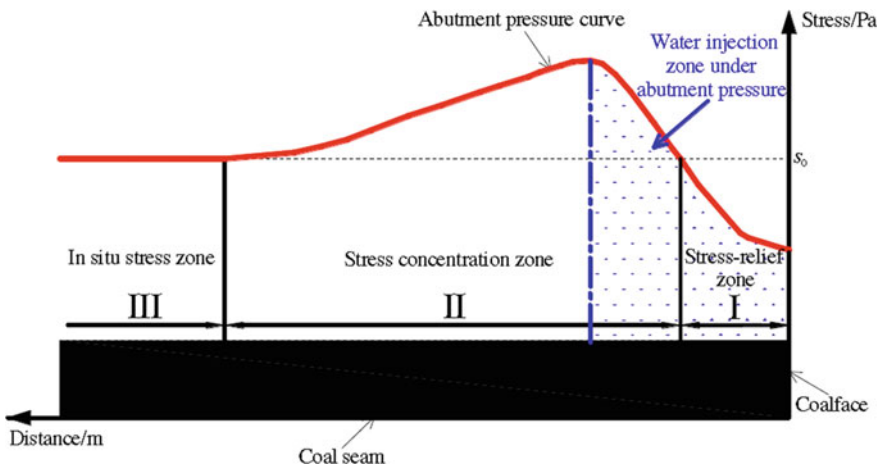


**Fig. 7.** Stress redistribution ahead of working face [23]

through inseam gas drainage boreholes was able to decrease the dust level at working face and it had marginal influence on gas drainage due to end of service expectancy of gas drainage borehole. Wang and Yuan [24] also reported approximately 50% dust reduction by water infusion (40 m ahead working face) through in seam gas drainage boreholes in another China coal mine. Even though not many trials of water infusion using gas drainage borehole can be found, it does show some promise by considerably reducing cost from secondary drilling operation.

## 7   Conclusion

Water infusion is an old yet effective dust mitigation measure in some coal seams. Due to operational difficulty and deployment of many passive dust mitigation devices, water infusion method has not been considered as a viable means for dust mitigation in Australian underground mines. The re-emergence of CWP in Australia may demonstrate the insufficiency of these passive measures to bring respirable dust to a safe level and therefore there is a need to critically examine and subsequently develop this proactive dust control technology for practical applications in Australian coal mines. The paper provides a critical review of the water infusion technologies in view of its technological advances and practical application limitations. To date mainly three infusion methods, namely face infusion, gateroad infusion and remote infusion, have been developed and utilised in Europe, US, and China. The mechanistic understanding of water flow in coal seam is investigated. It is found water is confined flow in big cleats and fractures rather than small pores. Water flow in coal cleats is driven by a net force of impetus pressure of water injection, capillary force, flow resistance pressure and gas pressure. Key parameters of water infusion are identified and briefly discussed. These key contributors can be summarised into four categories: (a) coalbed characterisation; (b) extraction method; (c) drilling arrangement; (d) infusion parameters. The use of pre-drilled gas drainage boreholes as subsequent water injection holes is also discussed. It indeed shows prospects in reducing operational cost but clearly it needs more research and demonstrations. Lastly the practical limitations of water infusion are revealed. Although water infusion is a worthwhile alternative dust control technique, it may not work for all longwall operations or it has to be supplemented with passive controls.

## References

1. Ren, T.X., Plush, B., Aziz, N.: Dust controls and monitoring practices on Australian longwalls. Procedia Eng. **26**, 1417–1429 (2011)
2. Ji, Y., Ren, T., Wynne, P., Wan, Z., Ma, Z., Wang, Z.: A comparative study of dust control practices in Chinese and Australian longwall coal mines. Int. J. Min. Sci. Technol. **26**(2), 199–208 (2016)
3. Sapko, M.J., Cashdollar, K.L., Green, G.M.: Coal dust particle size survey of US mines. J. Loss Prev. Process Ind. **20**(4), 616–620 (2007)

4. Organiscak, J.A., Page, S.J.: Airborne dust liberation during coal crushing. Coal Prep. **21**(5–6), 423–453 (2000)
5. Neels, P.V., Deguildre,G.: General remarks on advance remote infusion of water in a Campine Colliery. In: Proceedings of the Conference on Technical Measures of Dust Prevention and Suppression in Mines, Luxemburg (1972)
6. Ducrocq, D.: Low-pressure water infusion. In: Proceedings of the Conference on Technical Measures of Dust Prevention and Suppression in Mines, Luxembourg (1972)
7. McClelland, J.J., Organiscak, J.A., Jankowski, R.A., Pothini, B.R.: Water infusion for coal mine dust control: three case studies. Bureau of Mines, Pittsburgh (1987)
8. Becker, H.: Seam infusion in high-speed workings. In: Proceedings of the Conference on Technical Measures of Dust Prevention and Suppression in Mines, Luxemburg, I (1972)
9. Heising, C., Becker, H.: Dust control in longwall workings. In: Proceedings of the 2nd US Mine Ventilation Congress, pp. 603–611 (1980)
10. Cervik, J., Sainato, A., Baker, E.: Water Infusion: An Effective and Economical Longwall Dust Control. US Department of the Interior, Bureau of Mines, USA (1983)
11. Cervik, J., Sainato, A., Deul, M.: Water Infusion of Coalbeds for Methane and Dust Control. Department of the Interior, Bureau of Mines, USA (1977)
12. Cervik, J., Sainato, A., Deul, M.: Water Infusion of Coalbeds for Methane and Dust Control [17 refs]. Bureau of Mines, Pittsburgh Mining and Safety Research Center, Pittsburgh (1977)
13. Martinez Fidalgo, M., Álvarez-Santullano, L.: Current Status of Water Infusion as a System of Dust Control in Spanish, French and German Mines. Instituto Nacional de Silicosis, Spain (1994)
14. Hewitt, A., Lama, R.D.: Research on dust control for high production longwall mining in Australia. In: Baafi, E.Y. (ed.) 21st Century Higher Production Coal Mining Systems, Wollongong, (1988)
15. Charbonnier, J.: Technical measures of dust prevention and suppression in coal-mines. vol. 1. Series on Industrial Health and Medicine (1966)
16. Wang, K., Zang, J., Wang, G., Zhou, A.: Anisotropic permeability evolution of coal with effective stress variation and gas sorption: model development and analysis. Int. J. Coal Geol. **130**, 53–65 (2014)
17. Seidle, J.P., Jeansonne, M.W., Erickson, D.J.: Application of matchstick geometry to stress dependent permeability in coals. In: SPE Rocky Mountain Regional Meeting. Society of Petroleum Engineers, Richardson (1992)
18. Li, J., Zhou, F., Liu, H.: The selection and application of a compound wetting agent to the coal seam water infusion for dust control. Int. J. Coal Prep. Utilization **36**(4), 192–206 (2016)
19. Gao, S.Q., Liu, H.P.: Capillary Mechanics. Science Press, Beijing (2010)
20. Crawford, R.J., Mainwaring, D.E.: The influence of surfactant adsorption on the surface characterisation of Australian coals. Fuel **80**(3), 313–320 (2001)
21. Li, Q., Lin, B., Zhao, S., Dai, H.: Surface physical properties and its effects on the wetting behaviours of respirable coal mine dust. Powder Technol. **233**, 137–145 (2013)
22. Zhang, W.: Experimental study on compound wetting agent of dust prevention and water injection for coal seam. Master thesis, Anhui University Of Science & Technology (2015)
23. Hu, G., Xu, J., Ren, T., Dong, Y., Qin, W., Shan, Z.: Field investigation of using water injection through inseam gas drainage boreholes to control coal dust from the longwall face during the influence of abutment pressure. Int. J. Min. Reclam. Environ. **30**(1), 48–63 (2016)
24. Wang, J., Yuan, G.: Study on using gas drainage hole water injection dust suppression technology. Sci. Technol. Eng. **13**(27), 8111–8114 (2013)
25. CFhiew, Pittsbutgh Coalbed: Methane and Dust Control by Water Infusion. Report of Investigations. 764011, p. 972

26. Liu, X., Li, Z., Zhang, X., Yu, H., Wang, P.: Application of affusion in coal for dust control. Procedia Eng. **26**, 902–908 (2011)
27. Jia, Z.: Research on the Dust Control Technology with Dynamic Pressure Water Injectionon Fully Mechanized Caving Face. Taiyuan University of Technology, Taiyuan (2012)
28. Wang, L.: Study of Qinan Mine 10114 Working Face Coal Seam Water Injection Effect. Anhui University of Science & Technology, Huainan (2013)
29. Guo, H.: Research on Water Infusion in Qipanjing Coal Seam. Kunming University of Science and Technology, Kunming (2014)
30. Liu, Z.: The Research on Water Infusion Parameters and Construction Technology for Longwall Top Coal Caving Face Used for Tang'an no. 3 Coal. Taiyuan University of Technology, Taiyuan (2010)
31. Frid, V.: Electromagnetic radiation method water-infusion control in rockburst-prone strata. J. Appl. Geophys. **43**(1), 5–13 (2000)
32. Aguado, M.B.D., González Nicieza, C.: Control and prevention of gas outbursts in coal mines, Riosa–Olloniego coalfield, Spain. Int. J. Coal Geol. **69**(4), 253–266 (2007)
33. Jiang, J., Cheng, Y., Mou, J., Jin, K., Cui, J.: Effect of water invasion on outburst predictive index of low rank coals in dalong mine. PLoS One **10**(7), e0132355 (2015)

# The Current State of Chinese Coal Mining Dust Hazard and Prevention

Zhai Xiaowei[✉], Hou Qinyuan, Han Jinzi, and Wang Jiaojiao

College of Safety Science and Engineering, Xi'an
University of Science and Technology, Xi'an 710054, China
zhaixw@xust.edu.cn

**Abstract.** In order to realize the severity of dust hazard in Chinese underground coal mines, improve the efficiency of dust control and reduce the incidence of pneumoconiosis, the authors counted Chinese occupational disease report in recent years. The production process of dust in the coal mining process is analyzed. The mechanism for the coal dust to harm the human body is identified. The theory and technology research in the field of dust prevention and control of occupational disease hazard are reviewed. The important achievements, China's laws and regulations for preventing and controlling black lung problems are introduced. The government's policy, laws and regulations, enterprise management, theory and technology innovation have played important roles for the significant development of China's mining coal mine dust prevention and control of occupational disease hazards.

**Keywords:** Coal mining · Dust hazard · Pneumoconiosis · Dust prevention and control

## 1 Introduction

Currently about 95% of China's coal production is from the underground mining with widespread geological conditions. Due to complex mining condition, relatively low management and technical levels, not well educated work force and insufficient attention to dust prevention and control, the pneumoconiosis disease in coal mining industry is relatively serious [1]. As of the end of 2016, a total of 924,603 cases of occupational diseases has been reported in China that includes 831,246 cases of pneumoconiosis, accounting for 90% of occupational diseases, and coal workers pneumoconiosis (CWP) or silicosis accounted for more than 90% of the total number of pneumoconiosis. A total of 27,992 new cases of pneumoconiosis were reported in 2016 (an increase of 1911 cases from that in 2015) accounting for 88.06% of the total number of occupational disease reported in the same year. Among the different industries, the largest three numbers of occupations of occupational disease cases are still in coal, non-ferrous metals and mining ancillary activities as shown in Fig. 1. In the 27,992 new cases of pneumoconiosis, 95.49% are the coal workers pneumoconiosis (CWP) while silicosis are 16,658 cases and 10,072 cases, respectively, and 46.69% cases is distributed in the coal industry [2].
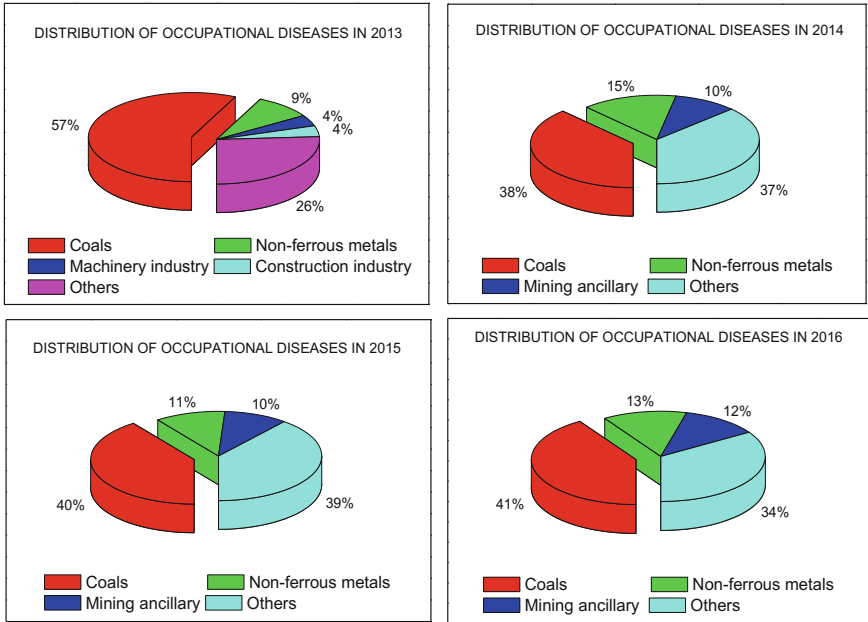
**Fig. 1.** Occupational diseases distribution in the past four years

Pneumoconiosis is still the China's most serious occupational disease, and the coal industry is the main pathogenesis of pneumoconiosis. Pneumoconiosis cases, according to a report in 2010–2016, pneumoconiosis cases caused by well versed in coal mining industry accounted for more than 50% of all reported cases of pneumoconiosis. The situation of dust coal mining production is much serious, and seriously affects the coal industry's sustainable development [3]. Statistics of newly-issued occupational cases in the country are shown in Table 1.

**Table 1.** Statistics of newly-issued occupational cases in China

| Year | New career/ases | New pneumoconiosis/cases | New pneumoconiosis of coal industry/cases | The proportion of new pneumoconiosis cases in coal industry accounted for it of the national/% |
|------|-----------------|--------------------------|-------------------------------------------|--------------------------------------------------------------------------------------------------|
| 2010 | 27,240 | 23,812 | 13,968 | 58.65 |
| 2011 | 29,879 | 26,401 | 15,421 | 58.41 |
| 2012 | 27,420 | 24,206 | 13,399 | 55.35 |
| 2013 | 26,393 | 23,152 | 15,078 | 65.12 |
| 2014 | 29,972 | 26,873 | 11,396 | 42.41 |
| 2015 | 29,180 | 26,081 | 11,625 | 44.57 |
| 2016 | 31,789 | 27,992 | 13,070 | 46.69 |

## 2    Coal Mine Dust Source

Dust is referred to the solid particles suspended in the air. There are many names for dust, such as dust, smoke, powder, etc. [4]. According to the international organization for standardization, suspended solids with particle size of less than 75 μ is defined as dust.

There are so many ways to classify the dust, commonly based on the nature, particle diameter, free silica content in dust. According to the chemical properties and composition of dust content, dust can be divided into three classes: inorganic dust, organic dust and mixed dust. Based on particle size, dust can be divided into coarse dust, fine dust, micro dust and ultramicro dust. According to the aerodynamic diameter, the dust can be divided into non-inhalable dust, inhalable dust and respirable dust, in which the respiratory dust is most harmful to the human body [5].

No matter how to classify, dust is natural enemies to the human health in the coal mining industry and a major cause for a variety of diseases. The dust is formed in the process of production in which solid particles float in the air for a long time. As coal mine production scale and strength's increasing, the amount of dust is in subsequently increasing. At the same time, the surface of dust can also often absorb the harmful gas or other liquid material to become the carrier of other hazardous substances. The mine dust pollutes the underground work environment, and affect the mine workers' health of body and mind. A variety of ore-bearing rock particles produced in the mine production is called mine dust. Due to different free silica content in the mine dust, coal dust could be divided into silicon dust, coal dust and cement dust, etc. Silicon dust mainly comes from various production process including rock (or half coal rock) drilling, blasting, loading, the gangue cart, transportation, self-closed guniting build by laying bricks or stones, roadway supporting and underground ventilation, and so on; Coal dust mainly comes from the production process including overburden of coal, drilling, blasting, loading, crushing, transportation and soon on; Cement dust mainly comes from the shotcrete operation in roadway construction, brick laying, roadway support, repair and maintenance of ground facilities etc.

## 3    Mining Coal Mine Dust Hazards

### 3.1    Dust Hazard Pathway

The source of dust determines the opportunity and approach of dust exposure to the human body. In coal mining process, the roadway development, roadway support, coal cutting, coal transportation, transfer and so on, these major production technology and the link will generate dust. The dust moves into the body of the coal mine workers through the respiratory tract, eyes, skin and so on, among which, respiratory tract is the main pathway [6, 7]. The dust inhaled in the human respiratory tract, the vast majority of which is exhaled. Because of the absence of resistance, the inhalation of dust particles will move into the gas exchange area of the respiratory bronchioles and alveolar ducts and alveolar after inhaled into trachea and main bronchi, and

bronchioles, and in the process of entering, the side effects produces, which affects gas exchange function (as shown in Fig. 2).
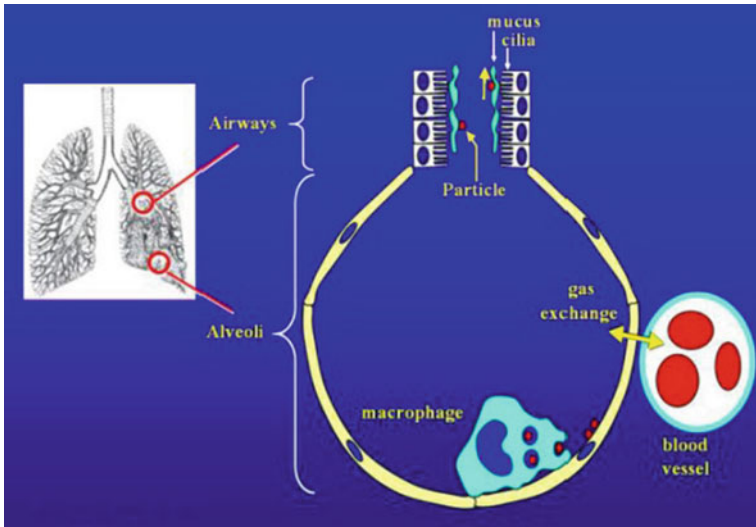


**Fig. 2.** The function process of dust inhaling into respiratory diagram

After the inhalable dust is inhaled into respiratory tract, it will deposit in the respiratory tract primarily through impact, gravity sedimentation, dispersion (also called Brownian motion), electrostatic deposition, interception. Only a small portion of the inhalable dust can enter the alveolar area. All these sedimentation is related to size, density and air velocity through airway of dust. Air turbulence in the airway will also affect the settlement form and efficiency to a great extent. The dust deposited in the respiratory tract will be cleared by the body through a variety of ways.

### 3.2    The Harm of Dust to Coal Workers

All dust is harmful to the human body but different features especially the chemical properties of dust may cause different damages. The damage caused by dust on human body is various, particularly to the respiratory system [8].

(1) Effects on the respiratory system
    The biggest impact of dust to the human body is to the respiratory system, including pneumoconiosis, dust composure, organic dust-induced lung lesions, respiratory tumors and respiratory inflammation and other diseases.
    Pneumoconiosis is one of the most influential and serious diseases in the production of occupational diseases in coal mines. It is a systemic disease mainly caused by lung fibrosis due to long-term inhalation of dust. Long-term inhalation of different kinds of dust can lead to different types of pneumoconiosis or lung

disease, in election coal mine mainly manifested in coal, lung, silicosis and coal silicosis, as shown in Fig. 3.
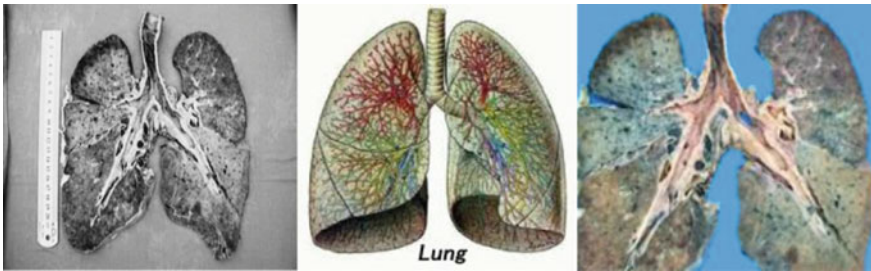


**Fig. 3.** Pneumoconiosis patients' chest radiographs

(2) Local action

Dust acts on respiratory tract mucous membrane, at early time, its function hyperfunction can be caused, submucosal blood capillary dilates, congests, mucus gland's secretion increases to prevent more dust; mucosal mast lesions is formed for a long time, because of a lack of mucosal epithelial cell nutrition, atrophic lesions is caused, respiratory protection against function declines. Skin contacts with dust for a long time will lead obstructive sebaceous adenitis, acne, folliculitis, pyoderma.

(3) The poisoning effect

Dust containing soluble toxic substances (such as lead, arsenic, and manganese) can quickly dissolves. When such substances are absorbed by the respiratory tract mucosa, acute poisoning symptoms would appear according to the subsidence's toxicity.

## 4   Present Situation and Problems of Dust Control in Coal Mines

### 4.1   Current Situation of Dust Control

**Regulations of dust prevention and control**. China's existing dust prevention and control laws, regulations and procedures are divided into 3 large levels. The first level has the national law of the "People's Republic of China Mine Safety Law" and the "Occupational Disease Prevention Law". The second level is "Coal Mine Safety Code" while the third is related to the coal industry technical standards. As early as in 1987, the state council issued "The pneumoconiosis disease prevention and control regulations of the People's Republic of China". On October 27, 2001, China enacted "The occupational disease prevention law of the People's Republic of China", which is the legal basis of dust prevention and control in coal mines.

In addition, China's Administration of Production Safety issued "The Workplace Occupational Health Supervision and Management Regulations" "Unit of Choose and Employ Persons the Occupational Health Supervision and Management Measures", "Measures for Supervision and Administration of 'Three Concurrent' of Occupational Disease Protection Facilities in Construction Projects" "Regulations on Prevention and Control of Occupational Hazards in Coal Mine Workplaces". In the revised "Coal Mine Safety Code", the content of prevention and control of occupational disease hazards are increased. It is well versed in coal dust from the occupational protection facilities design, construction and acceptance and mine mining process of dust prevention and control. The coal industry shale abide the provisions of the whole process of occupational health surveillance.

For dust hazard in coal production, China promulgated the "Technical specification of comprehensive dust control measures for underground coal mines" "Technical specification of high-pressure spraying for the working and heading face in mines". "Technical specification of comprehensive dust control measures for underground coal mine" stipulates the general requirements of dust prevention and control technology of coal mine underground working place, dust control, prevention and isolation of coal dust explosion and dust detection method.

In terms of individual protective dust, "Provision standard for personal protective equipment of coal mine occupational safety and health" was enacted, which stipulates distribution cycle of the occupational-disease-inductive individual protective equipment for different type of work.

For individual protection, China promulgated the "Provision standard for personal protective equipment of coal mine occupational safety and health". The issue cycle of individual protective articles for different occupational diseases was stipulated.

**Theory of dust prevention and control**. The dust problem of coal industry is very complicated while the related research is very extensive. Great attention has been given to the dust prevention and control in mine working faces for a long time in the world. A lot of research has been done in this field.

Since 1930s, research has been performed to study the law of dust movement. The former Soviet Union's scholar O o squaw conducted a series of studies on the relationship between the velocity of airflow and the movement of dust, and determined the necessary conditions for dust to flow [9]. Since the 1950s, the United States, Japan and other countries have done research on the dispersion characteristics of dust in mine airflow in terms of the concentrations of airborne and respirable dusts, the velocity of airflow and the distribution of dust particle size. Mathematic models for predicting dust concentration and settling in mine wind roadway have been developed. Guided the development of wind and dust shunt technology, so that the underground dust prevention technology has taken a step forward [10–13]. In recent years, many scholars use computer simulation software to simulate the movement and trajectory of mine dust so that the dust migration mechanism under different conditions can be understood and the theory is constantly improving [14–19].

At present in China, the studies of the airflow movement and the dust trajectory using 1-D or 2-D flow mathematical model have been conducted. However, 3-D computer simulation technique has been less applied and the understanding of dust distribution and migration is still not systematic and comprehensive enough. In

addition, the relationship between wind speed and dust migration rule is studied. Some other parameters, such as the technical conditions of coal mining and the humidity and temperature, are not sufficiently considered.

**Technology of dust prevention and control**. With the development of the theory of dust prevention, the technology of dust prevention and control has been developing. It shows that any kind of dust-prevention technology is very difficult to reduce the dust to the "Coal Mine Safety Code" stipulated in the scope. Therefore, according to the specific dust production site, the nature of dust and production technology, such as the implementation of comprehensive treatment. At present, the coal mines in China have gradually used the dust-proof technology in the pre-mining stage, during the mining process and dust generation. The main dust control technologies are classified into pre-mining water injection, ventilation dilution, dust capturing, water spraying to remove dust, air curtain dust separation, chemical additives and personal protection devices (PPD) [20–24].

The PPD's are the last resort for protecting coal miners and play a pivotal role [25]. At present, the PPDs are in the forms of self-suction dust masks, filter-type air supply dust masks and pneumatic helmets and so on. The high efficiency of PPDs is one of the important technical measures to solve the coal mine dust harm to the miners' physical health.

## 4.2   Current Problems

**Lack of government attention**. In 2010, China issued a notice on the division of responsibilities of the Occupational Health Supervision Department, which made a clear division of responsibilities between the Ministry of Health, the General Administration of Safety, the Human Resources Social Security Department and the ACFTU. However, the risk of occupational diseases is not clear, and the contradiction between the serious shortage of supervision power and the large number of occupational disease cases is still outstanding. There is not a good understanding in many local governments about the importance and urgency of the prevention and treatment of occupational diseases. The investment on occupational disease prevention and control is insufficient.

**The main responsibility of coal mine enterprises is not put into place**. The main responsibility for prevention and control of occupational diseases in coal enterprises is not fulfilled. Some enterprises do not carry out the construction project "three simultaneous" work of the occupational disease prevention facilities according to law, the occupational Disease Hazard Project Declaration, the work place occupational disease risk factor Periodic examination, the occupation health guardianship and the occupational health training and so on implementation is ineffective.

**Legal construction needs to be perfected**. The construction of occupational disease legal system in China started late, and many regulations and standards were constantly modified to meet the new situation. At present, the legal system of dust hazard and occupational disease prevention is not perfect, some laws and regulations are not operable, and the implementation is easy to cause the uncoordinated between departments. Some areas of the law still exist ineffective, unclear powers and responsibilities, lack of supervision, the ability to coordinate the implementation of poor, low level of legislation and other factors.

**Dust control technical equipment behind**. With the continuous progress of science and technology, many new dust-proof technologies have matured abroad and have been widely used in the underground. But the development of mine dust-proof technology is slow, most of mine still adopt conventional dustproof measure. Some coal enterprises lack of capital investment, can not introduce advanced dust-proof equipment, leading to China's election coal mining technology equipment overall lag behind.

# 5    Development Trend of Dust Prevention and Control in Coal Mine

Occupational safety and health is the important matter of the people's life and property safety and physical health. It is the symbol of economic and social coordinated healthy development. It is the party and government's high responsibility to protect the people interests. On December 26, 2016, the State Council issued the "National Occupational disease Prevention and Control program (2016–2020)", adhere to the goal-oriented and problem-oriented, highlighting the prevention and control of occupational disease hazards of strategic, systematic, guiding, operational, the overall work objectives for 2020 and 10 quantifiable specific indicators of work were identified. At the same time, it also points out the development trend of dust prevention and control in coal mine, insists on the innovation of theory and technology and supervision and management mechanism, and strengthens the source management.

(1)  Theory and technology innovation refers to the use of new technology, equipment, new process equipment and transformation of coal mining. The development of dust prevention and control in election coal mine in China needs not only the support of theory but also the guarantee of technology, only by strengthening the theory and technological innovation can we improve the technological level of election coal mining, improve the working environment of miners and reduce the occurrence of pneumoconiosis.

(2)  Innovation of supervision and management mechanism. On the one hand, State Administration of Work Safety should conscientiously carry out the supervision and management functions of occupational disease hazards in workplaces, increase the supervision of occupational diseases, and urge enterprises to fulfill the legal responsibility of occupational disease prevention. On the other hand, the coal enterprises conscientiously implement the main responsibility of occupational disease prevention and control, safety management must be in charge of occupational health, the establishment of occupational hazards prevention and control responsibility system, and the implementation of occupational disease prevention and control responsibility.

# References

1. Zhang, Q.: Present situation, problems and countermeasures of coal industry layout and structure in China. China Econ. Trade Herald **14**, 20–21 (2005)
2. Wang, C.: Bulletin on Occupational Disease Prevention and Control in the 2016. State Administration of Work Safety, 28 Dec 2017
3. Li, Y.: Theory and Technology of Mine Dust Prevention and Control. China Coal Industry Publishing House, Beijing (2015)
4. Yang, S.: Theory and Technology of Dust Control. China University of Mining and Technology Press, Xuzhou (2007)
5. Nie, B., Li, X., Yang, T.: Distribution of PM2. 5 dust during mining operation in coal workface. J. China Coal Soc. **38**(01), 33–37 (2013)
6. China Coal Industry Labor Protection Science and Technology Society Organization: Prevention and Control Technology of Mine Dust. China Coal Industry Publishing House, Xuzhou (2007)
7. Xu, M., Chen, X.: Theory and Technology of Occupational Hazard Prevention and Control. China University of Mining and Technology press, Xuzhou (2016)
8. Petrova, E.: Occupational diseases. Epidemiological trends of the occupational dust diseases, prevention and early diagnosis. Scr. Sci. Med. **41**(1), 103 (2009)
9. Cui, X., Cheng, J., Li, H., et al.: Discussion on prevention and control of coal dust in fully mechanized mining face. Coal **13**(4), 55–55 (2004)
10. Li, Y.: Study on Control of Dust at Driving Fully Mechanized Face Based on Air Curtain Technology. Liaoning Technology University, Jinzhou (2010)
11. Sasaki, K., Widiatmojo, A., Widodo, N.P., et al.: Numerical simulation on diffusion phenomena in mine airways by using a method of discrete tracer movements. In: U.S. North American Mine Ventilation Symposium (2008)
12. Zhang D.: Study on Regularity of Coal Dust Transport and Dust Treatment Technologies in Coal Conveyer Roadway. Liaoning Technology University, Jinzhou (2010)
13. Song, M.: New technology of coal dust control in foreign countries. Labour Prot. **10**, 40–41 (2001)
14. Liu, X.: Study on Dust Transport Laws and Spray System of Mechanized Excavation Face of Heyang Company. Xi'an University of Science and Technology, Xi'an (2015)
15. Jiang, Z., Chen, J., Wang, J., et al.: Numerical simulation of dust movement regularities in belt conveyer roadway. J. China Coal Soc. **37**(4), 659–663 (2012)
16. Li, Y., Liu, J.: Numerical simulation of dust control using air curtain based on gas-solid two-phase flow. J. Liaoning Tech. Univ. (Nat. Sci.) **31**(05), 765–769 (2012)
17. Wang, P., Liu, R., Gui, Z., et al.: Theoretical research on atomization characteristics and dust suppression efficiency of air-water spray in underground coal mine. J. China Coal Soc. **41**(09), 2256–2262 (2016)
18. Wada, K., Tanaka, H., Suyama, T., et al.: Numerical simulation of dust aggregate collisions. I. Compression and disruption of two-dimensional aggregates. Astrophys. J. **661**(1), 320–333 (2007)
19. Guo, S., Wu, B., Li, D.: Simulating test and study of dust control by air curtain. Min. Saf. Environ. Prot. **32**(1), 11–12 (2005)
20. Wang, H., Jiang, Z., Huang, L., et al.: Experimental research on pressing air-absorption air volumeratio in FPNA ventilation for excavation roadways. J. Liaoning Tech. Univ. (Nat. Sci.) **30**(2), 168–171 (2011)

21. Li, R., Guo, S., Xu, X., et al.: Practice and application of comprehensive dustproof technology in fully mechanized excavation face. Min. Saf. Environ. Prot. **32**(5), 64–65 (2005)
22. Guo, S., Gong, X., Liu, K., et al.: Application of dust removal technique by sectional hole-packing water infusion fully mechanized heading face. Min. Saf. Environ. Prot. **36**(s1), 54–57 (2009)
23. Wang, H., Zhang, H.: Test and application of air curtain in mine. J. China Coal Soc. **31**(5), 615–617 (2006)
24. Zhang, J.: Present situation and countermeasures analysis of underground dust prevention and control. Jiangxi Coal Sci. Technol. **3**, 74–75 (2015)
25. Bacchim Neto, F.A., Aff, A., Mascarenhas, Y.M., et al.: Efficiency of personal dosimetry methods in vascular interventional radiology. Phys. Med. Eur. J. Med. Phys. **37**, 58–67 (2017)

# Numerical Study on Mine Dust Capture Using Nano-Droplet Flow from Wet Steam Condensation

An-wen Zhao, Song Guo[(✉)], Shu-xin Chen, Shang Gao,
Xue-bin Chen, and Chen-chen Li

School of Chemical Engineering, Nanjing University of Science
and Technology, Nanjing 210094, China
`guosong@njust.edu.cn`

**Abstract.** Hazards of mine dust, especially ultrafine dusts, are well known for causing pneumoconiosis such as tuberculosis and lung cancer, which can seriously affect the occupational health of mine workers. Besides, it can also aggravate the mechanical wear, shortening the lifespan of precision instruments, and can also trigger fire and explosions, Although the microscale mine dust can be captured using existing fine spray dust removal technology, removing nano-size dusts are still a challenge. This paper explores the possibility of removing nano-size coal dusts using high velocity through a supersonic nozzle In this work, in term of the condensation phenomenon of wet steam with large-velocity flow in supersonic nozzle, the removal scheme of colliding nanoscale dust with nano-droplets will be designed, and the nucleation and growth from water molecular condensation will be also simulated by using commercial computational fluid dynamics software. By defining the physical properties and motion state of nano-droplets at the nozzle outlet as initial boundary condition, the trajectory, phase transition of evaporation of nano-droplets with large-velocity jet flow will be analyzed. Based on the results of this study this paper discusses the technical feasibility of capturing mine nanoscale dust particles with nano-droplets flow from wet steam condensation.

**Keywords:** Wet steam · Phase transition · Droplet motion · Dust capturing
Numerical simulation

## 1 Introduction

In mining, transport, stacking and minerals handling/processing, large amount of dusts are often generated [1, 2]. Long term inhalation of high concentrations of inhalable mine dusts could lead to pneumoconiosis which seriously affects the health of workers [3]. Meanwhile, dust explosion could occur when airborne dust accumulates to a certain concentration and ignited by sparks or a fire source, threatening the safety of miners as well as impacting production [4]. All coal mining countries in the world have had extensive studies and taken measures to control mine dusts [5, 6]. The most common control measures are water sprays [7], the development of atomization technology has been able to successfully capture mine particles with an aerodynamic

diameter of 5–10 μm [8]. However, there are still drawbacks in existing fine spray dust removal technology [9, 10]: added moisture could decrease BTU values while leading to secondary water pollution.

Nano-dust capture technology is developed to further improve the effectiveness of capturing suspended dust particles. Computational fluid dynamics (CFD) is employed as the computational platform in the design process. Dust removal is accomplished through the use of wet stream from a supersonic nozzle with high-speed flow where nano-scale dust particles colliding with nano-droplets. Technical feasibility of capturing nanoscale mine dust particles will be discussed.

## 2    Simulating the Condensation of Wet Steam in Supersonic Flows

### 2.1    Governing Equations

The flow characteristics of the vapor phase at high-speed expansion are described by three conservation partial differential equations [11], including a continuity equation, a momentum equation and an energy equation, defined as Eqs. (1)–(3):

$$\frac{\partial \rho_v}{\partial t} + \frac{\partial}{\partial x_j}(\rho_v u_j) = S_1 \tag{1}$$

$$\frac{\partial}{\partial t}(\rho_v u_i) + \frac{\partial}{\partial x_j}(\rho_v u_j u_i) = -\frac{\partial P}{\partial x_i} + \frac{\partial}{\partial x_j}\left[\mu\left(\frac{\partial u_j}{\partial x_i} + \frac{\partial u_i}{\partial x_j} - \frac{2}{3}\delta_{ij}\frac{\partial u_i}{\partial x_i}\right)\right] \\ + \frac{\partial}{\partial x_j}\left(-\rho_v \overline{u_i u_j}\right) + S_2 \tag{2}$$

$$\frac{\partial}{\partial t}(\rho_v E) + \frac{\partial}{\partial x_j}(\rho_v u_j E + u_j P) = \frac{\partial}{\partial x_j}\left(\lambda_v \frac{\partial T_v}{\partial x_j} + u_i \tau_{eff}\right) + S_3 \tag{3}$$

where $\rho_v$, $P$ and $E$ represent the vapor density, pressure and total energy, respectively. $\lambda_v$ is the thermal conductivity coefficient of the vapor phase. $S_1$, $S_2$ and $S_3$ will be introduced into the conservation equations of the vapor phase as the source term of the condensation phase transition.

Two additional transport equations are employed to describe the phase transition process during the condensation of the wet steam [12]:

$$\frac{\partial(\rho y_d)}{\partial t} + \frac{\partial}{\partial x_j}(\rho u_j y_d) = S_4 \tag{4}$$

$$\frac{\partial(\rho N_d)}{\partial t} + \frac{\partial}{\partial x_j}(\rho N_d u_j) = J\rho \tag{5}$$

where $y_d$ and $N_d$ represent the mass fraction of the condensed droplets and the number density of the droplets per unit volume, respectively. $J$ is the nucleation rate, and the

source $S_4$ describes the mass generation rate due to condensation. $\rho$ denotes the mixture density of the wet steam, which can be related to the vapor density by the following equation:

$$\rho = \frac{\rho_v}{(1 - y_d)} \tag{6}$$

Additionally, to accurately describe the flow characteristics of droplets phase, an auxiliary expression about droplet radius parameter is needed, which can be presented as follows:

$$r_d = \sqrt[3]{3y_d/(4\pi\rho_d N_d)} \tag{7}$$

where $r_d$ and $\rho_d$ represent the droplet radius and density.

All of the source terms in the above conservation partial differential equations can be defined by the following formulas [13]:

$$S_1 = -S_4 = -\Gamma \tag{8}$$

$$S_2 = -\Gamma u \tag{9}$$

$$S_3 = \Gamma\left(h_{fg} - H\right) \tag{10}$$

$$\Gamma = \frac{4}{3}\pi r_c^3 \rho_d J + 4\pi r_d^2 \rho_d N_d \frac{dr_d}{dt} \tag{11}$$

where $dr_d/dt$ denotes the growth rate of the droplets and $h_{fg}$ denotes the latent heat of the wet steam. $\Gamma$ is the condensation mass of unit steam volume per unit time.

Where the Kelvin-Helmholtz critical droplet radius, $r_c$, denotes the critical radius of stable water molecule clusters in the wet steam flow field, which can be defined as follows:

$$r_c = \frac{2\sigma}{\rho_d R T_v \ln(S)} \tag{12}$$

where $R$ is the gas constant, $\sigma$ is the surface tension of droplet. $S$ is the super-saturation ratio defined as the ratio of vapor pressure to the equilibrium saturation pressure.

## 2.2 Condensation Model

The nucleation rate, $J$, can be calculated by the classical nucleation theory (CNT) which corrected for non-isothermal effects [14], which predicts the nucleation process of the water vapor as follows:

$$J = \theta \frac{q_c \rho_v^2}{\rho_d} \sqrt{\frac{2\sigma}{\pi m_v^3}} \exp\left(-\frac{4\pi r_c^2 \sigma}{3k_B T_v}\right) \tag{13}$$

where $q_c$ is the condensation coefficient (in the present calculation $q_c = 1.0$), $m_v$ is molecular mass of the vapor phase, $k_B$ is the Boltzmann's constant. The coefficient, $\theta$, is the non-isothermal correction factor proposed by Kantrowitz [14], which is given by the following relation:

$$\theta = \left[ 1 + 2\frac{\gamma - 1}{\gamma + 1}\frac{h_{fg}}{RT_v}\left(\frac{h_{fg}}{RT_v} - \frac{1}{2}\right) \right]^{-1} \tag{14}$$

where $\gamma$ is the specific heat ratio.

The growth rate, $dr_d/dt$, of droplets due to the condensation is calculated by Gyarmathy's correction model, which is given by the following relation [15]:

$$\frac{dr_d}{dt} = \frac{\lambda_v}{\rho_d}\frac{1}{(1 + 3.18Kn)}\frac{r_d - r_c}{r_d^2}\frac{\Delta T}{h_{fg}} \tag{15}$$

where $Kn$ is the Knudsen number.

## 2.3 Comparison of Simulation and Experiments

The conservation Eqs. (1)–(3) of vapor phase are directly solved in ANSYS FLUENT. The conservation Eqs. (4)–(7) of droplets phase, the Eqs. (8)–(11) of additional source term, and the Eqs. (13)–(15) of condensation nucleation and droplet growth are performed by the User-Defined Function (UDFs) and User-Defined Scalar (UDS) interface.

For the verification of the numerical model established above, the experiments of the Moore nozzle flows for low inlet pressure was chosen [16]. The geometry of nozzle B used by Moore et al. [16] is illustrated in Fig. 1. Because the nozzle is symmetric about the x-axis, only half of the nozzle is simulated in order to reduce the computational time. Moore et al. experiments [16] deliver a set of data for inlet boundary conditions: total pressure and total temperature are $P_0 = 25$ kPa, $T_0 = 357.6$ K, respectively. Additionally, the grid density is one of the key factor determining the accuracy of the numerical simulation, here, a quadrilateral mesh with 66,225 cells was performed to guarantee a grid independent solution.

Figure 2 shows the comparison between present solution and experimental data of the pressure ratio and droplet radius. It can be seen that the final numerical result is in excellent agreement with the experiment for the supersonic nozzle. The static pressure decreases along the nozzle centerline and experiences a sudden increase when the non-equilibrium condensation happens, and the phenomenon is known as "condensation shock". Due to release of large amount of latent heat in condensation process, the temperature increases of both vapor phase and droplet phase result in a sudden increase in static pressure. Comparing with the experimental data given at a single position, the 0.004 μ deviation of the droplet radius is observed.

The comparison results demonstrate that the numerical model can accurately simulate the condensation process of the wet steam in the supersonic nozzle.
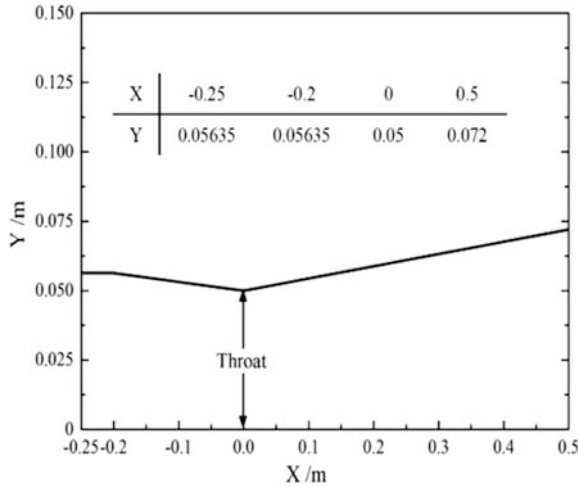
Fig. 1. Geometry of the nozzle B used by Moore et al. [16]
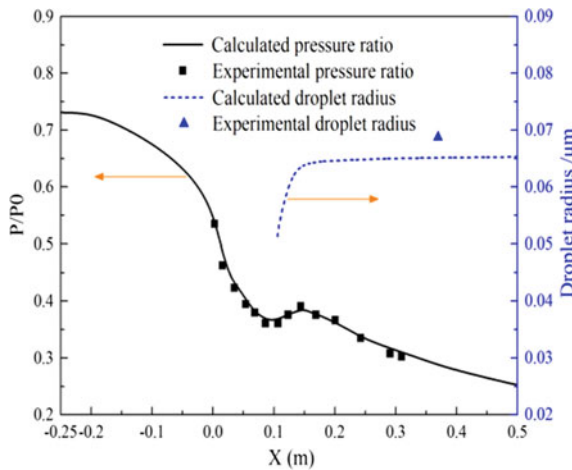


Fig. 2. Comparison between present solution and experimental data for the pressure ratio and droplet radius

## 3 Exploring the Motion and Evaporation of Condensed Droplets in Supersonic Jet Flow Field

### 3.1 Droplet Motion Equation

In the gaseous-droplets two-phase flow model, the momentum exchange between the two phases and the trajectory of the droplet are described by establishing the motion equation of the droplet, and which is calculated in the Lagrangian reference frame [17].

This force balance equates the droplet inertia with the drag force acting on the droplet [18], and can be defined as:

$$\frac{du_d}{dt} = \frac{18\mu}{\rho_d d_d^2} \frac{Re_d}{24} C_D(u - u_d) + \frac{g(\rho_d - \rho)}{\rho_d} \tag{16}$$

where $u_d$ and $d_d$ represent the droplet velocity and diameter, respectively. $Re_d$ is the relative Reynolds number of the droplet, which can be defined as follows:

$$Re_d = \frac{\rho d_d |u_d - u|}{\mu} \tag{17}$$

Here, $C_D$ denotes the drag coefficient which is often used to characterize the force interaction between the droplet and the surrounding gas flow. To improve the accuracy of prediction of the drag coefficient during the droplet movement in supersonic flow field, and based on a review of current literature in the field of drag coefficient for compressible flows, the drag model in the existing computational fluid dynamics code will be updated using the drag expression proposed by Henderson [19] for computing the drag coefficient in supersonic flow situation. The drag coefficient $C_D$ is a function of the relative Reynold number $Re_d$ and it can be defined as follows:

$$C_D = \begin{cases} 24\left(Re_d + \left(\frac{\gamma}{2}\right)^{0.5} Ma_d\left\{4.33 + \left(\frac{3.65 - 1.53T_d/T}{1 + 0.353T_d/T}\right)\right. \\ \left. \exp\left[-0.247\left(\frac{2}{\gamma}\right)^{0.5}\frac{Re_d}{Ma_d}\right]\right\}\right)^{-1} + \exp\left(-\frac{0.5Ma_d}{\sqrt{Re_d}}\right) \\ \left[\frac{4.5 + 0.38\left(0.03Re_d + 0.48\sqrt{Re_d}\right)}{1 + 0.03Re_d + 0.48\sqrt{Re_d}} + 0.1Ma_d^2 + 0.2Ma_d^8\right] \\ + 0.6\left(\frac{\gamma}{2}\right)^{0.5}Ma_d\left[1 - \exp\left(-\frac{Ma_d}{Re_d}\right)\right] \quad (Ma_d \leq 1) \end{cases}$$

$$C_D = \begin{cases} \dfrac{0.9 + \frac{0.34}{Ma_d^2} + 1.86\left(\frac{Ma_d}{Re_d}\right)^{0.5}\left[2 + \frac{4}{\gamma Ma_d^2} + 1.058\frac{1}{Ma_d}\left(\frac{2T_d}{\gamma T}\right)^{0.5} - \frac{4}{\gamma^2 Ma_d^4}\right]}{1 + 1.86\left(\frac{Ma_d}{Re_d}\right)^{0.5}} \\ \hspace{10cm} (Ma_d \geq 1.75) \end{cases}$$

$$C_D(Ma_d, Re_d) = \begin{cases} C_D(1.0, Re_d) + (4/3)(Ma_d - 1)[C_D(1.75, Re_d) - C_D(1.0, Re_d)] \\ \hspace{6cm} (1.0 < Ma_d < 1.75) \end{cases} \tag{18}$$

where $Ma_d$ denotes the Mach number of droplet.

### 3.2 Evaporation Laws for Heat and Mass Transfer

In the gaseous-droplets two-phase phase transition model, it is necessary to establish the expressions of the heat and mass transfer between vapor phase and droplet phase in order to describe the evaporation process of the single droplet. The droplet temperature is calculated in term of a heat balance that relates the sensible heat change in the droplet to the convective and latent heat transfer between the droplet and the vapor phase, and the droplet temperature can be defined by the following formulas [20]:

$$m_d C_{pd} \frac{dT_d}{dt} = hA_d(T_v - T_d) - \frac{dm_d}{dt}h_{fg} + A_d \varepsilon_d \sigma_{sb}\left(\theta_R^4 - T_d^4\right) \tag{19}$$

where $C_{pd}$ denotes droplet heat capacity. $dm_d/dt$ denotes the rate of evaporation, $A_d$, $\varepsilon_d$ and $\sigma_{sb}$ represent the droplet surface area, emissivity and Stefan-Boltzmann constant, respectively. $h$ is the convective heat transfer coefficient calculated by following formulas:

$$h = \frac{Nu\lambda_v}{d_d} \tag{20}$$

$$Nu = 2 + 0.6\mathrm{Re}_d^{0.5}\mathrm{Pr}^{1/3} \tag{21}$$

where Pr is the Prandtl number of the gas phase.

The following expression proposed by Miller et al. [21] and Sazhin [22] will be adopted to describe the evaporation rate of droplet:

$$\frac{dm_d}{dt} = k_c A_d \rho_v \ln(1 + B_m) \tag{22}$$

where $m_d$ denotes single droplet mass, $k_c$ is the mass transfer coefficient. $B_m$ is the Spalding mass number.

### 3.3 Geometry and Boundary Conditions

To study the trajectory and evaporation process of single droplet in the supersonic jet flow field, the supersonic jet flow field cross-section of two-dimensional rectangular plate was adopted as the gas phase flow field calculation domain, which consists of one flow inlet face and three flow outlet faces. The entire open space calculation domain is symmetric about the y-axis, with a dimension of 0.75 m × 5 m. There is a supersonic flow inlet at the far left of the flow inlet face, and the inlet size remains the same as the outlet radius of the Moore nozzle [16] mentioned above.

The supersonic inflow consists of four components: nitrogen, oxygen, water vapor and condensed droplet with extremely small radius, and water vapor is saturated among them. The boundary conditions of supersonic inflow are shown in Table 1, the data in the table is derived from the calculated value of flow parameters after the wet steam was condensed. The remaining boundary conditions will be set as pressure inlet or outlet: gauge pressure is 0 Pa, total temperature is 300 K. Additionally, the specific heat capacity of the gaseous components used in this numerical calculation, which is described through the piecewise polynomial given by NIST [23], and the density is described by the ideal gas formula.

**Table 1.** The boundary conditions of supersonic inflow

| Boundary parameters | Value |
|---|---|
| Inlet gas Mach number | 1.48 |
| Inlet gas temperature (K) | 271 |
| Inlet static pressure (Pa) | 5839.95 |
| Oxygen mass fraction | 0.23 |
| Water vapor mass fraction | 0.042 |
| Injection droplet velocity (m/s) | 619.94 |
| Injection droplet temperature (K) | 271 |
| Injection droplet diameter (m) | 1.31e–07 |

### 3.4    Results and Discussion

There is a large relative velocity between the front face of the supersonic gas flow and the surrounding contact gas when the supersonic mixed gas flow jet into the open space, and resulting in the interaction among the fluids in the contact region and forming a shock wave. The distribution of the characteristic parameters of the jet flow field will be changed because of the shock wave. Figure 3 shows the contour distribution of velocity and temperature parameters of the supersonic jet flow field, it can be seen that the entire jet flow field presents a large velocity gradient due to the influence of aerodynamic drag, shock wave compression and fluid viscosity effect. Meanwhile, the temperature of the high-speed gas flow and the surrounding gas are significantly increased due to the heating effect of shock wave on the compressible fluid medium, and eventually forming a temperature field with certain gradient. There will be a higher temperature of this region where the shock wave compression become stronger.
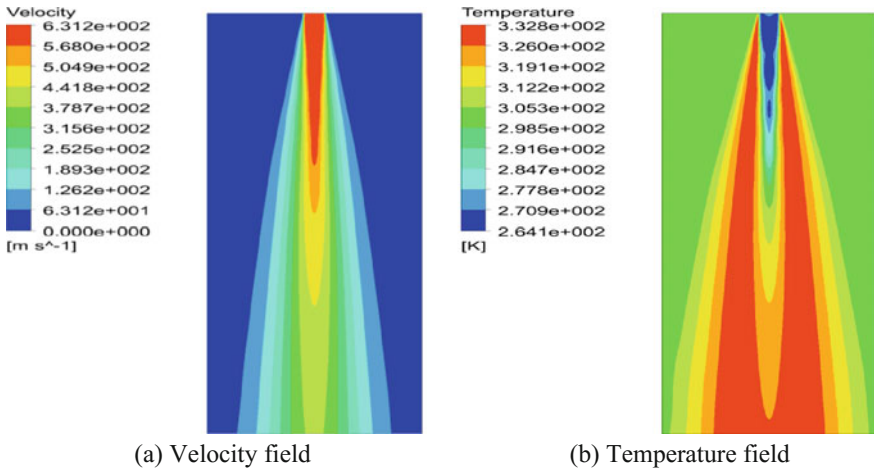


(a) Velocity field            (b) Temperature field

**Fig. 3.**  Contour distribution of characteristic parameters of supersonic jet flow field

Furthermore, the calculation results of the gaseous flow field will be used as the initial solution of the droplet movement, the trajectory and evaporation process of condensed droplet will be calculated by steady method. The droplet is injected from the position of $x = 0$ m, $x = 0.02$ m, $x = 0.04$ m and $x = 0.06$ m in the inlet cross-section of supersonic inflow, and quantitatively evaluation the technical feasibility of capturing nanoscale mine dust particles with nano-droplets flow from wet steam condensation in term of numerical calculation results.

The temperature of the jet flow field will be increased due to the compression and heating of the shock wave, and it will result in the re-evaporation phenomenon of the condensed droplet with high-speed. The relation between the penetration depth and the residence time after a single droplet inject into the supersonic jet flow field from the four different positions mentioned above are shown in Fig. 4. It can be clearly seen that the condensed droplet nearer the central region of the supersonic inflow inlet (i.e. the nozzle outlet), the penetration depth is greater and the residence time is also longer in the supersonic jet flow field. Correspondingly, the penetration depth and the residence time of the condensed droplet injected into the supersonic jet flow field from the position of $x = 0$ m are 1.72 m and 2.75 ms, respectively; the penetration depth of the condensed droplet injected from the position of $x = 0.02$ m is 1.35 m and the residence time is 2.19 ms; the penetration depth of the condensed droplet injected from the position of $x = 0.04$ m is 0.79 m and the residence time is 1.29 ms; the penetration depth of the condensed droplet injected from the position of $x = 0.06$ m is 0.17 m and the residence time is 0.28 ms.

## 3.5 Influence of Particle Diameter on Droplet Trajectory and Evaporation Process

The diameter of condensed droplet produced by the rapid expansion of steam will increase when the total temperature is unchanged, the total pressure is increased of wet steam at the nozzle inlet [24]. Therefore, the influence of particle diameter parameters on the trajectory and evaporation process of condensed droplet in supersonic jet flow field will be further studied by setting the initial droplet diameter to $d_0 = 0.131$ μm, $d_1 = 0.231$ μm, $d_2 = 0.331$ μm, $d_3 = 0.431$ μm and $d_4 = 0.531$ μm, respectively.

Figure 5 shows the trend of penetration depth and residence time of injected droplet which varies with the particle diameter in different positions. It can be seen that the movement distance and time required for the condensed droplet complete the evaporation process in the supersonic jet flow field are gradually increasing as the particle diameter increased, that is, both the penetration depth and the residence time of the droplet are gradually increasing. The penetration depth of the injected droplet at the position of $x = 0$ m in the supersonic inlet cross-section is increased by 5.81%, and the residence time is increased by 6.91% when the particle diameter increases from 0.131
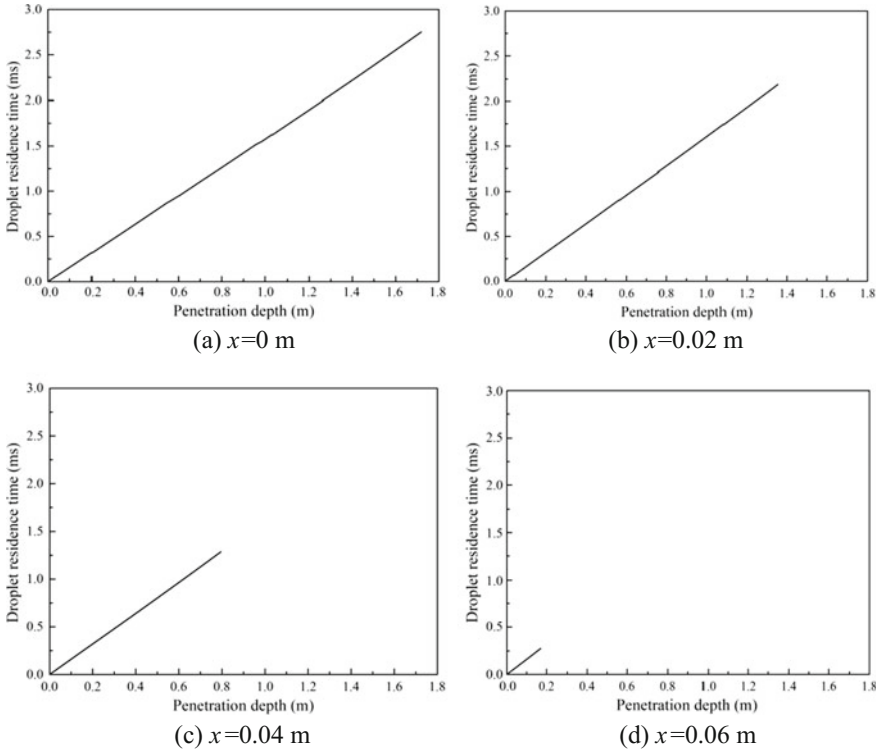
**Fig. 4.** The relation between penetration depth and residence time of injected droplet in different positions

to 0.531 µm. Similarly, the penetration depth of the injected droplet at the position of $x = 0.02$ m is increased by 8.89% and the residence time is increased by 9.13%; the penetration depth of the injected droplet at the position of $x = 0.04$ m is increased by 18.99% and the residence time is increased by 18.60%; the penetration depth of the injected droplet at the position of $x = 0.06$ m is increased by 47.37% and the residence time is increased by 53.57%.
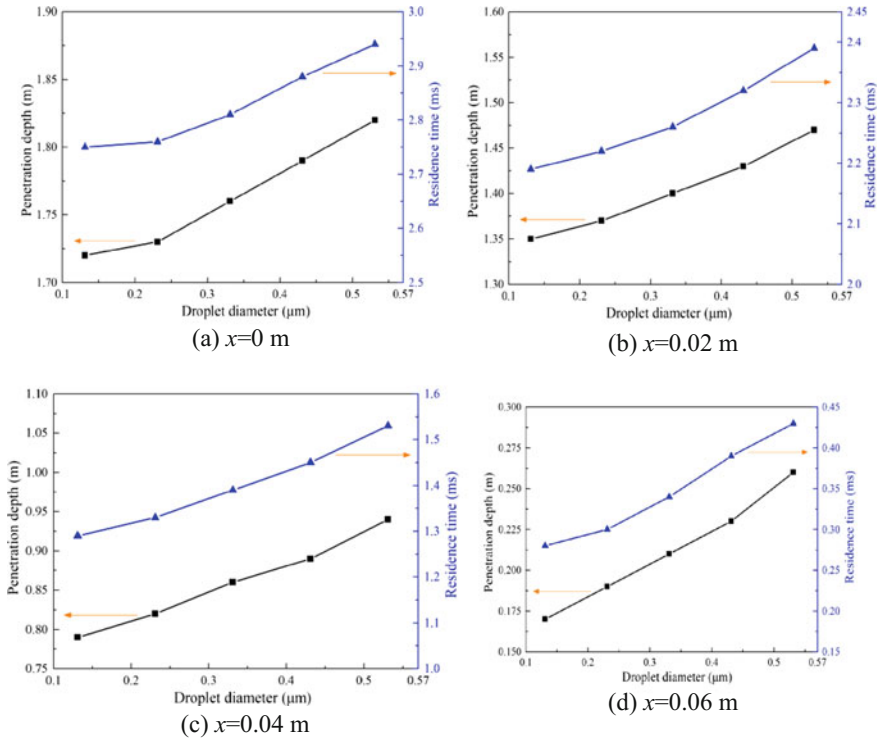
**Fig. 5.** The trend of penetration depth and residence time of injected droplet which varies with the particle diameter in different positions

## 4   Conclusion

(1)  The numerical calculation of wet steam condensation flow in this work indicates: the rapid expansion of gas flow can lead to steam condensation and generate condensed droplet in the size of hundred nanometers when wet steam flows through the supersonic nozzle under the certain inlet boundary conditions.

(2)  The numerical calculation results of gaseous-droplet two-phase supersonic jet flow field indicates: a higher temperature gradient will be appeared in the jet flow field due to the compression and heating effect of the shock wave, and there will be a higher temperature of this region where the shock wave compression become stronger. The increase of ambient gas flow temperature results in the re-evaporation phenomenon of the condensed droplet with high-speed.

(3)  Under the inflow conditions: Mach number is 1.48, temperature is 271 K and diameter of condensed droplet is 0.131 µm, the maximum penetration depth of single droplet in supersonic jet flow field is 1.72 m and the longest residence time is 2.75 ms. It shows that the condensed droplet can collide with the ultrafine dust which is dispersed in the environment within a certain spatial range of the nozzle

outlet flow field, thus the nanoscale mine dust can be captured. In other words, it is theoretically feasible to capture nanoscale mine dust using nano-droplet flow from wet steam condensation.

(4) The penetration depth and residence time of the droplets in the supersonic jet flow field are gradually increasing as the particle diameter increased from 0.131 to 0.531 μm. Among the droplets, the evaporation characteristic parameter variations of the injected droplet at the position of $x = 0.06$ m in the supersonic inlet cross-section are most obvious, the penetration depth and residence time are increased by 47.37 and 53.57%, respectively. It shows that the increasing of the condensed droplet diameter is benefit to improve the penetration effect of the droplet in the supersonic jet flow field.

# References

1. Wang, H.T., Wang, C., Wang, D.M.: The influence of forced ventilation airflow on water spray for dust suppression on heading face in underground coal mine. Powder Technol. **320**, 498–510 (2017)

2. Wang, H.T., Zhang, L., Wang, D.M., He, X.X.: Experimental investigation on the wettability of respirable coal dust based on infrared spectroscopy and contact angle analysis. Adv. Powder Technol. **28**, 3130–3139 (2017)

3. David, J.B., Cara, N.H., Laney, A.S.: Engineering controls are the most protective means of controlling respirable coal mine dust. Lancet Respir. Med. **5**(5), 18–19 (2017)

4. Zheng, Y.P., Feng, C.G., Jing, G.X., Qian, X.M., Li, X.J., Liu, Z.Y., Huang, P.: A statistical analysis of coal mine accidents caused by coal dust explosions in China. J. Loss Prev. Process Ind. **22**(4), 528–532 (2009)

5. Lu, X.X., Zhu, H.Q., Wang, D.M.: Investigation on the new design of foaming device used for dust suppression in underground coal mines. Powder Technol. **315**, 270–275 (2017)

6. Jiang, H.X., Du, C.L., Dong, J.H.: Investigation of rock cutting dust formation and suppression using water jets during mining. Powder Technol. **307**(1), 99–108 (2017)

7. Dariusz, P.: Use of air-and-water spraying systems for improving dust control in mines. J. Sustain. Min. **12**(2), 29–34 (2013)

8. Mei, W.T., Peter, C.R.: Effects of spray surfactant and particle charge on respirable coal dust capture. Saf. Health Work **8**(3), 296–305 (2017)

9. Cheng, W.M., Nie, W., Zhou, G., Zuo, Q.M.: Study of dust suppression by atomized water from high-pressure sprays in mines. J. China Univ. Min. Technol. **40**(2), 185–189 (2011)

10. Xie, Y.S., Fan, G.X., Dai, J.W., Song, X.B.: New respirable dust suppression systems for coal mines. J. China Univ. Min. Technol. **17**(3), 321–325 (2007)

11. Yang, Y., Walther, J.H., Yan, Y.Y., Wen, C.: CFD modeling of condensation process of water vapor in supersonic flows. Appl. Therm. Eng. **115**(25), 1357–1362 (2017)

12. Ding, H.B., Wang, C., Chen, C.: Non-equilibrium condensation of water vapor in sonic nozzle. Appl. Therm. Eng. **71**(1), 324–334 (2014)

13. Cao, X.W., Yang, W.: Numerical simulation of binary-gas condensation characteristics in supersonic nozzles. J. Nat. Gas Sci. Eng. **25**, 197–206 (2015)

14. Keisari, S.J., Shams, M.: Shape optimization of nucleating wet-steam flow nozzle. Appl. Therm. Eng. **103**(25), 812–820 (2016)

15. Avetissian, A.R., Philippov, G.A., Zaichik, L.I.: Effects of turbulence and inlet moisture on two-phase spontaneously condensing flows in transonic nozzles. Int. J. Heat Mass Transf. **51** (18), 4195–4203 (2008)

16. Moore, M.J., Sieverding, C.H.: Two-phase steam flow in turbines and separators: theory, instrumentation, engineering. Hemisphere Publishing Corperation, Washington (1976)

17. Gu, Y.L., Ozel, A., Sundaresan, S.: A modified cohesion model for CFD–DEM simulations of fluidization. Powder Technol. **296**, 17–28 (2016)

18. Chen, X.Z., Wang, J.W.: A comparison of two-fluid model, dense discrete particle model and CFD-DEM method for modeling impinging gas–solid flows. Powder Technol. **254**, 94–102 (2014)

19. Henderson, C.B.: Drag coefficients of spheres in continuum and rarefied flows. J. AIAA **14** (6), 707–708 (1976)

20. Sazhin, S.S.: Modelling of fuel droplet heating and evaporation: recent results and unsolved problems. J. Fuel **196**(15), 69–101 (2017)

21. Miller, R.S., Harstada, K., Bellana, J.: Evaluation of equilibrium and non-equilibrium evaporation models for many-droplet gas-liquid flow simulations. Int. J. Multiph. Flow **24** (6), 1025–1055 (1998)

22. Sazhin, S.S.: Advanced models of fuel droplet heating and evaporation. Prog. Energy Combust. Sci. **32**(2), 162–214 (2006)

23. Dombrovsky, L.A., Sazhin, S.S.: A simplified non-isothermal model for droplet heating and evaporation. Int. Commun. Heat Mass Transfer **30**(6), 787–796 (2003)

24. Noori, S.M.A., Kouhikamadi, R., Atashkari, K.: Two-fluid model for simulation of supersonic flow of wet steam within high-pressure nozzles. Int. J. Therm. Sci. **96**, 173–182 (2015)

# Numerical Simulation of the Dust Movement Rule at a Fully Mechanized Mining Face in Liangshuijing Coal Mine

Jian-guo Wang[1,2(✉)], Fei-wen Qi[1,2], Ya-ru Zhe[1,2],
and Ya-ping Zhang[2,3]

[1] College of Safety Science and Engineering, Xi'an University
of Science and Technology, Xi'an 710054, China
wjglll8@l26.com
[2] Key Laboratory of Western Mine Exploitation and Hazard Prevention
of the Ministry of Education, Xi'an 710054, China
[3] School of Energy Engineering, Xi'an University of Science
and Technology, Xi'an 710054, China

**Abstract.** In order to study the movement pattern of dust generated during support advancing and shearer cutting at # 42,112 fully mechanized mining face in Liangshuijing Coal Mine, a mathematical and physical model were established and the simulation based on gas-solid two-phase flow interaction was carried out. The results show that the airflow velocity shows the "small-large-small" pattern when the airflow enters the mining face, and the flow rate and turbulence intensity reach the maximum in the vicinity of the shearer and a low value area in the sidewalk space. Some of the dusts generated by shield support advancing moves with the airflow, dust particles will settle to different locations of the roadway floor due to different particle sizes. The maximum dust concentration produced by shearer cutting is near the front and rear cutting drums, and about 10 m behind the rear drum close to the side of the coal rib, where the diffusivity is small, as the dust group moves backwards, the range of dust particles continues to expand until it covers the entire working face, correspondingly, the concentration of dust decreases.

**Keywords:** Fully mechanized mining face · Dust movement rule
Dust control · Numerical simulation

## 1 Introduction

With the development of underground coal mining technology, the fully mechanized mining technology has become an important means to mine thick coal seams, however, the use of large machines also increases the amount of dust generated in work places. According to measurement data, dust concentration will reach 8000 mg/m$^3$ without dust prevention and control measurement, which seriously pollutes the underground work place and impact miner's health [1]. Evidently, high concentration dusts have caused severe harm to workers in mining-related industries. Figure 1 shows the cumulative numbers of occupational disease cases and pneumoconiosis cases in China

in the period of 2005–2014. As shown in Fig. 1, the number of pneumoconiosis patients is increasing. In addition, the working space of mechanized mining of thick seam are larger and more complex, further increasing the complexity of diffusion and movement of dust-laden airflow and the difficulty of dust prevention and control in the field.
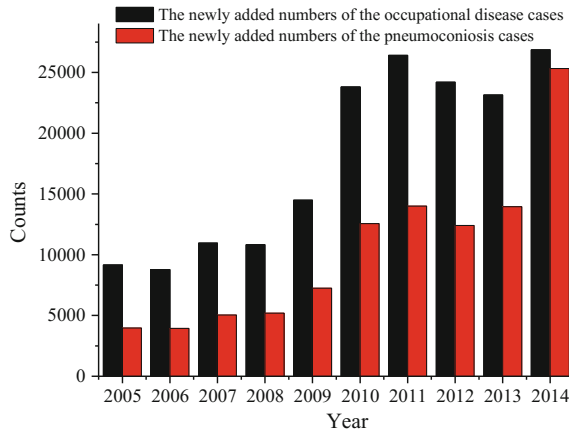


**Fig. 1.** The cumulative numbers of the occupational disease cases and pneumoconiosis cases

The law of dust movement at fully mechanized coal mining face has been mainly studied by experiment and numerical simulation. Because its low-cost, high-efficiency, numerical simulation has been widely used in dust control planning. Patankar and Joseph used large-eddy simulation to simulate airflow, and described the motion of dust particles using the Lagrange method, and also analyzed the spatial distribution of the coal dust and the airflow field under different stokes values [2]. Jiang et al. established a gas-solid two-phase flow model to study dust generation mechanism and diffusion rules in coal mine chambers, working face and heading face, and contrasted the law of dust distribution and the optimal dust removal velocity under different conditions and locations in the process of supporting advancing and shearer cutting [3–6]. Yang derived differential equations describing the particle motion by analyzing the stress state of the dust particles in the flow field of the working face and obtained the motion characteristics of dust particles in both vertical and horizontal directions and the motion track of dust particles [7]. Zuo obtained the difference of the air-dust transport rules between fully mechanized mining faces with large mining height and the general one, and designed a dust removal nozzle used at the large mining faces with large height [8]. Tan et al. studied the relationship between wind speed, drum speed when shearer cutting coal, slider speed and the dust concentration in the working face through the simulation [9]. Zhou et al. using numerical simulation studied the diffusion behavior of respiratory dust from fully mechanized coal cutting, and designed a method to prevent and control respiratory dust in fully mechanized mining face [10].

In summary, although some researchers have established models based on gas-solid two-phase flow interactions, dust distribution law at the fully mechanized mining face has been simulated. However, most of these studies only examined dust distribution under specific conditions. In this paper, the numerical simulation method was used to study the movement dust generated during support advancing and shearer cutting coal at 42,112 fully mechanized mining face in Liangshuijing coal mine. Study results are expected to provide clues for dust prevention and/or control.

## 2   Mathematical Model

### 2.1   Mathematical Model of Airflow

Dust particles in working face is complicated. Currently, there are two approaches for the numerical simulation of multiphase flow: Euler-Lagrange approach and Euler-Euler approach. The Lagrangian discrete phase model follows the Euler-Lagrange approach where the fluid phase is treated as a continuum medium by solving the Navier-Stokes equations, while the dispersed phase is solved by tracking a large number of particles through the calculated flow field. The dispersed phase can exchange momentum, mass, and energy with the continuum phase.

The airflow in the fully mechanized face satisfies the law of mass conservation, Newton's second law and the law of conservation of energy and other physical principles. The airflow is treated as incompressible fluid, and the control equation is of conservation form:

$$\frac{\partial \rho}{\partial t} + \nabla \cdot (\rho \boldsymbol{V}) = 0$$

$$\frac{\partial(\rho \boldsymbol{u})}{\partial t} + \nabla \cdot (\rho \boldsymbol{u} \boldsymbol{V}) = -\nabla P + \rho \boldsymbol{f}$$

$$\rho \frac{d\left(e + V^2/2\right)}{dt} = \rho \boldsymbol{f} \cdot \boldsymbol{V} - \nabla(\rho E \boldsymbol{V}) - \nabla(\boldsymbol{V}\boldsymbol{\Gamma}) + \rho \dot{q}$$

where $\rho$ is the air density (kg/m³); t is time (s); $\boldsymbol{V}$ is the air velocity vector; $\nabla p$ is the fluid pressure gradient (Pa/m); $\boldsymbol{f}$ is the body force vector; e is the internal mass of unit mass fluid (J); and E is the energy from the source term (J). $\boldsymbol{\Gamma}$ is surface stress; $\dot{q}$ is unit mass volume heating rate.

Two-equation turbulence models allow the determination of both turbulent length and time scale by solving two separate transport equations. The standard $k - \varepsilon$ model is a model based on model transport equations for the turbulence kinetic energy (k) and its dissipation rate ($\varepsilon$) [11]:

$$\frac{\partial}{\partial t}(\rho k) + \frac{\partial}{\partial x_i}(\rho k u_i) = \frac{\partial}{\partial x_j}\left[\left(\mu + \frac{\mu_t}{\sigma_k}\right)\frac{\partial k}{\partial x_j}\right] + G_k + G_b - \rho\varepsilon - Y_M + S_k$$

$$\frac{\partial}{\partial t}(\rho \varepsilon) + \frac{\partial}{\partial x_i}(\rho \varepsilon u_i) = \frac{\partial}{\partial x_j}\left[\left(\mu + \frac{\mu_t}{\sigma_\varepsilon}\right)\frac{\partial \varepsilon}{\partial x_j}\right]$$
$$+ C_{1\varepsilon}\frac{\varepsilon}{k}(G_k + C_{3\varepsilon}G_b) - C_{2\varepsilon}\rho\frac{\varepsilon^2}{k} + S_\varepsilon$$

In these equations, $G_k$ represents the generation of turbulence kinetic energy due to the mean velocity gradients; $G_b$ is the generation of turbulence kinetic energy due to buoyancy; $Y_M$ represents the contribution of the fluctuating dilatation in compressible turbulence to the overall dissipation rate; $C_{1\varepsilon}$, $C_{2\varepsilon}$ and $C_{3\varepsilon}$ are constants; $\sigma_k$ and $\sigma_\varepsilon$ are the turbulent Prandtl numbers for k and ε; $S_k$ and $S_\varepsilon$ are source terms.

## 2.2 Mathematical Model of Discrete Phase

ANSYS Fluent predicts the track of a discrete phase particle by integrating the force balance on the particle, which is written in a Lagrangian reference frame. This force balance equates the particle inertia with the forces acting on the particle, and can be written as:

$$\frac{d u_p}{dt} = F_D(u - u_p) + \frac{g(\rho_p - \rho)}{\rho_p} + F$$

where $F$ is an additional acceleration term, $F_D(u - u_p)$ is the drag force per unit particle mass and:

$$F_D = \frac{18\mu}{\rho_p d_p^2} \cdot \frac{C_D Re}{24}$$

Here, $u$ is the fluid phase velocity; $u_p$ is the particle velocity; $\mu$ is the molecular viscosity of the fluid; $\rho$ is the fluid density; $\rho_p$ is the density of the particle, and $d_p$ is the particle diameter. $Re$ is the relative Reynolds Number and $C_D$ is drag coefficient, there are defined as:

$$Re = \frac{\rho d_p |u_p - u|}{\mu}$$

$$C_D = a_1 + \frac{a_2}{Re} + \frac{a_3}{Re^2}$$

where $a_1$, $a_2$ and $a_3$ are constants that apply over several ranges of Re given by Morsi and Alexander [12].

Particles are subjected to many forces during the course of their movement. Except the combined force of gravity and buoyancy force, incorporating additional forces in the particle force balance that can be important under special circumstances, these forces include pressure gradient forces, "virtual mass" forces, Saffman lift forces, and

Brownian forces. The virtual mass and pressure gradient forces are not important when the density of the fluid is much lower than the density of the particles as is the case for liquid/solid particles in gaseous flows. Due to the particle size and the weak interaction force between particles, the air and dust move under isothermal conditions. Therefore, only the fluid's drag force is considered in the calculation, followed by gravity and buoyancy.

## 3  Geometrical Model and Boundary Conditions

### 3.1  Geometrical Model

The situation of on-site fully mechanized coal mining face of LiangShuiJing Mine is very complex. It is necessary to simplify the geometric model and built in an 1:1 size scale by SolidWorks. Figure 2 shows the Geometric model of a fully mechanized mining face, consists of four parts: outer contour, support, shearer, and base of support. The outer contour is a cuboid with its length, width and height of 65.0, 5.0, and 3.0 m, respectively. The entire space of fully mechanized coal mining face contains 43 hydraulic supports, the width and height of the support base are 3.1 and 0.8 m, respectively. The length, width, and height of the shearer main body are 6.0, 1.5, and 1.2 m. The length of rocker arm is 1.8 m. The diameter and thickness of drum are 1.2 and 0.5 m, the first drum of shearer is placed at 27 m away from the side of air inlet.
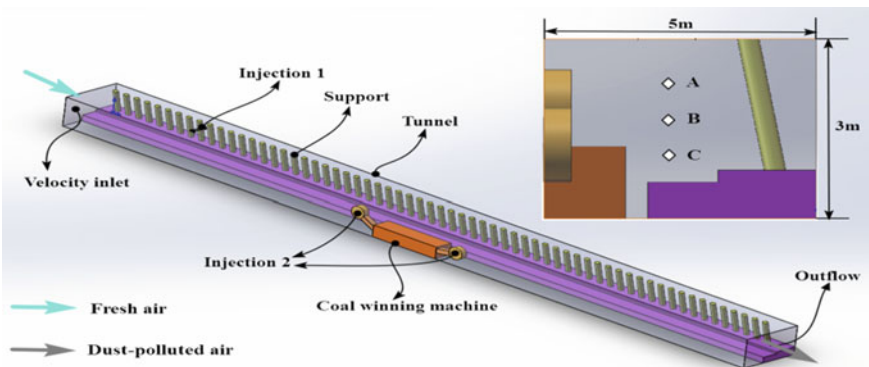


**Fig. 2.**  Geometric model of fully mechanized coal mining face

The file in ".x_t" format is generated to import the ICEM–CFD after the geometric model is constructed by SolidWorks. The quality of grid is higher than 0.4 to meet the solution requirement. Figure 3 shows the mesh of the Geometric model. Then the file in ".msh" format is imported to Fluent, convert the mesh to polyhedral grid to reduce the quantity of cell.
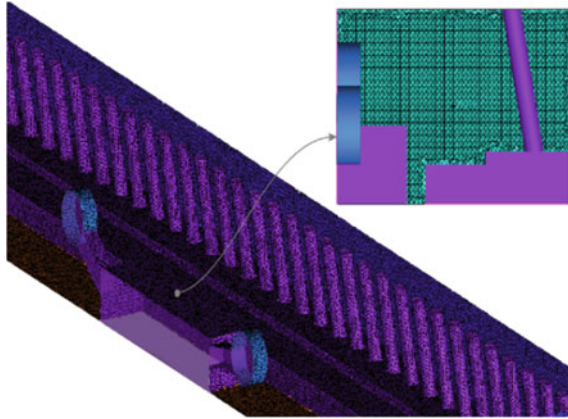
**Fig. 3.** Mesh of the geometric model

## 3.2 Boundary Condition and Solution Control Setting

The dust of a fully mechanized mining face is mainly generated by shearer cutting and support advancing, setting the drum of shearer and support advancing as surface injection source of dust, the sizes of dust of two dust sources follow the Rosin–Rammer distribution [13], and the main parameters are listed in Tables 1 and 2.

**Table 1.** Major parameters setting of discrete phase

| Item | Shearer cutting | Support advancing |
|---|---|---|
| Min diameter (m) | 1e−06 | 1e−06 |
| Max diameter (m) | 0.0002 | 0.0002 |
| Mean diameter (m) | 1e−04 | 1e−04 |
| Mass flow rate (kg/s) | 0.03 | 0.02 |
| Turbulent dispersion | Stochastic tracking | Stochastic tracking |
| Drag law | Spherical | Spherical |
| Diameter distribution | Rosin-Rammler | Rosin-Rammler |

**Table 2.** Major parameters setting of boundary condition

| Name | Type | Setting |
|---|---|---|
| General | Solver type | Pressure-based |
| | Time | Steady |
| Velocity inlet | Velocity inlet | 1.5 m/s |
| | Turbulent intensity | 3.04% |
| | Hydraulic diameter | 3.2 m |
| Air | Density | 1.225 g/l |
| Solution methods | Scheme | SIMPLEC |
| Viscous model | k-epsilon | Standard |
| Outflow | Flow rate weighting | 1 |
| Coal—hv | Density | 1400 kg/m$^3$ |
| DPM | Interaction with continuous phase | On |
| Tunnel and equipment | Wall | No slip |

# 4   Result and Discussion

## 4.1   Analysis of Airflow Field

The movement and diffusion of dusts in coal mining face are affected by many factors, of which has the most obvious effect on it. The migration law of air flow field helps understand the law of dust diffusion. Figure 4 shows the air velocity magnitude along the floor direction. As shown in Fig. 4, the airflow enters the working face from the left of the model at 1.5 m/s, it increases to 1.75 m/s when it reaches roadway, which is affected by the equipment such as hydraulic support and cable trench, while the air velocity near the pillar decreases. In area far away from the shearer, air velocity changes little in the roadway. It is easy to observe from the contours of velocity that the air velocity 1 m from the floor is affected most by the support, and this effect decreases at 1.5 m, but increased again at 2 m from, showing the overall trend of "small-large-small". When the air passes through the shearer, it is affected by the equipment and the roadway cross section is reduced, resulting in the flow velocity suddenly increasing to more than 2 m/s. It is also seen from Fig. 4 that the air in the working face has transverse flow and flows towards the sidewalk direction. Behind the shearer, the air flow becomes gradually stable, but the high-speed flow area was still formed near the coal wall, from the hydraulic support to the coal wall showing gradually increasing trend.

Figure 5 shows the air velocity magnitude at 3, 2, 1 and 0.5 m away from the coal rib along the direction of gravity. It can be seen from Fig. 5 that the air velocity still shows the pattern of "small-large-small" along the airflow direction. In the shearer position the air is affected by the change of the flow cross-section and the disturbance of the drum, and produces the longitudinal airflow towards the roof, which generates a high-speed flow area near the roof and the wind speed is as high as 2.5 m/s. Because of the sudden increase of space in the downwind direction of the shearer, the air velocity begins to decrease and drops to 2 m/s and below in the area of 10–20 m behind the shearer. However, because the air flowing at high speed creates a low pressure zone

(A) 1m from the floor

(B) 1.5m from the floor



(C) 2m from the floor

**Fig. 4.** Air velocity magnitude along the floor direction



(A) 3m away from the coal wall

(B) 2m away from the coal wall

(C) 1.5m away from the coal wall

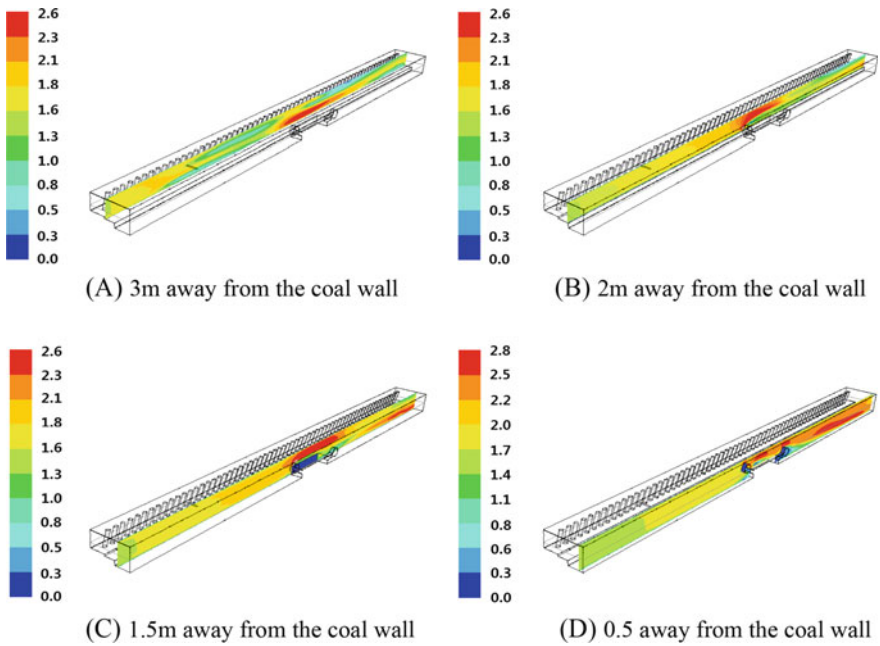(D) 0.5 away from the coal wall
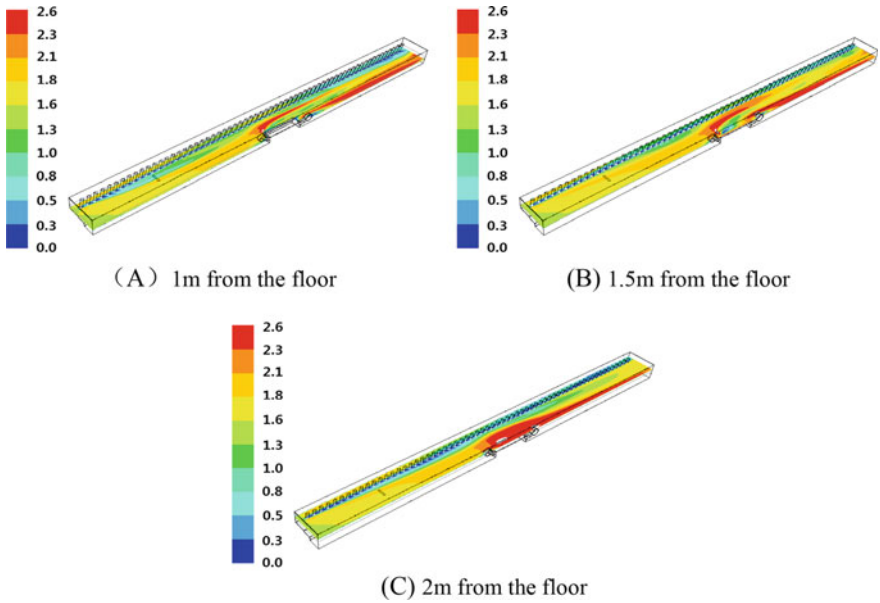
**Fig. 5.** Air velocity magnitude along the direction of gravity

below the drum of the shearer, the wind flow starts to approach the coal wall and forms a high-speed airflow, which decreases along the direction of flow.

Measure points are arranged every 5 m along airflow at the height of 1, 1.5, 2 m in the roadway of the 42,112 fully mechanized mining face. Figure 6 shows the distribution of air velocity along airflow. It is seen from Fig. 6 that there is difference between the measured and the calculation air velocity, but the distribution of the air velocity in the entire working face presents the same tendency. In addition, the direction and the size of the air flow is rather complicated due to the complicated wake and vortex behind the disturbance of the wind passing through the body of shearer and the drum, which lead to the value of the calculated air velocity after the working face 40 m is oscillating, while the measured value changes little.



(A) Numerical simulation          (B) Measured air velocity
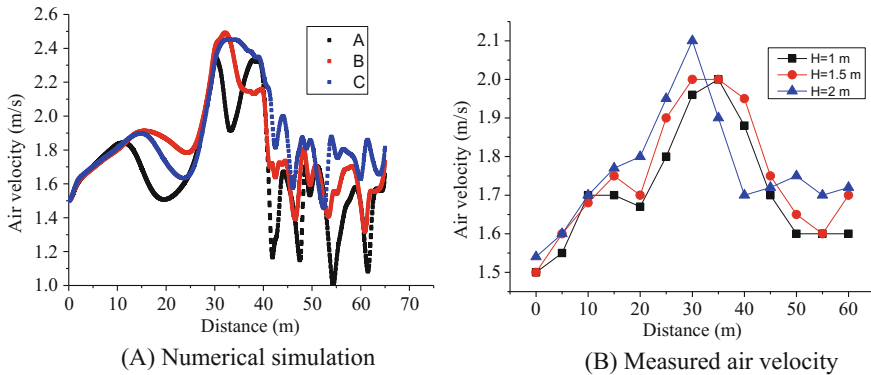
**Fig. 6.** Air velocity magnitude along air flow

## 4.2 The Rule of Dust Movement

Figure 7 illustrates the pathline of dust from different dust sources. As shown in Fig. 7a, when support advancing, the dust is released from the upper surface of the model, and the dust is injected from surface. It can be seen that dust particles of different particle sizes show completely different movement rules. Under the effect of gravity and airflow field, particles with smaller particle sizes flow along the air toward the shearer. After passing through the shearer, the particles begin to diffuse toward the hydraulic support and the dust concentration gradually decreases.

As shown in Fig. 7b, the dust is released from the drum of the shearer when cutting coal. Due to the increase of the velocity of the gas flow field, the dust particles gather together to bypass the shearer to the rear and the phenomenon of dust deposition and diffusion are not obvious. Because the low pressure area below the rear drum causes dust particles with air to flow toward the side close to the coal wall, as the roadway section behind the drum increases, the air velocity gradually decreases, and the dust with a large particle size gradually deposits, while the smaller particle size with the air continue to move, so the dust concentration in the entire roadway reduced and in the position from the shearer 10 m began to diffuse to the direction of the hydraulic support.

**Fig. 7.** Path line distribution of dust from different dust sources

When moving the support and cutting coal at the same time, the dust generated by the support advancing moves backwards to the position of the front drum of the shearer, and part of the dust flies with the air toward the direction of the hydrauli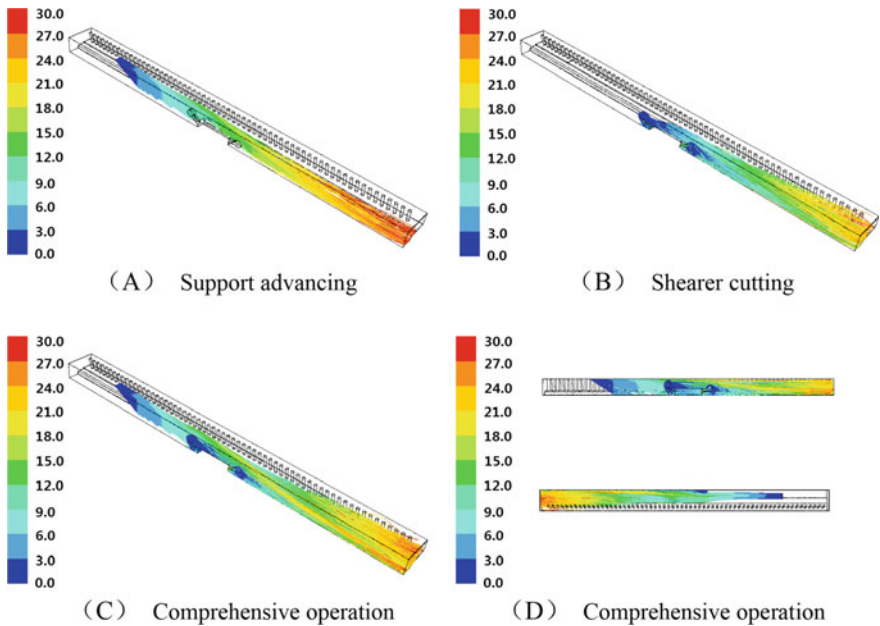c support, and the rest of the dust is mixed with dust from coal cutting moving to the rear of shearer. As can be seen from Fig. 7c, the concentration of dust at the rear of the shearer is significantly reduced at 10 m, and the dust starts to move to the rear of the hydraulic support and the support.

The law of dust movement in working face is characterized by its concentration and distribution. Figure 8 shows the distribution of dust concentration on the plane 1, 1.5 and 2 m away from the floor. It can be seen that the dust concentration is the highest and the distribution range is also the largest at a distance of 1 m from the floor. This is due to the fact that a large amount of dust deposits gradually in the direction of gravity after moving with the wind. So that the lower plane shows a higher dust concentration. Except for the dust generated by support advancing at 2 m from the floor, dust generated from coal cutting has little effect on the upper space. Due to the longitudinal airflow generated at the shearer, part of the dust moves upwards, but quickly moves to the lower space.

The time of dust particles floating in the air is related to the dust particle size. Figure 9 shows the stay time of dust particles with different particle sizes in the plane of 1, 1.5 and 2 m away from the floor. It can see that in the space above the roadway, the dust particles with a diameter larger than 100 μm settle quickly, and as the particle size decreases, the suspension time also gradually prolongs. This conclusion is consistent with the actual result.
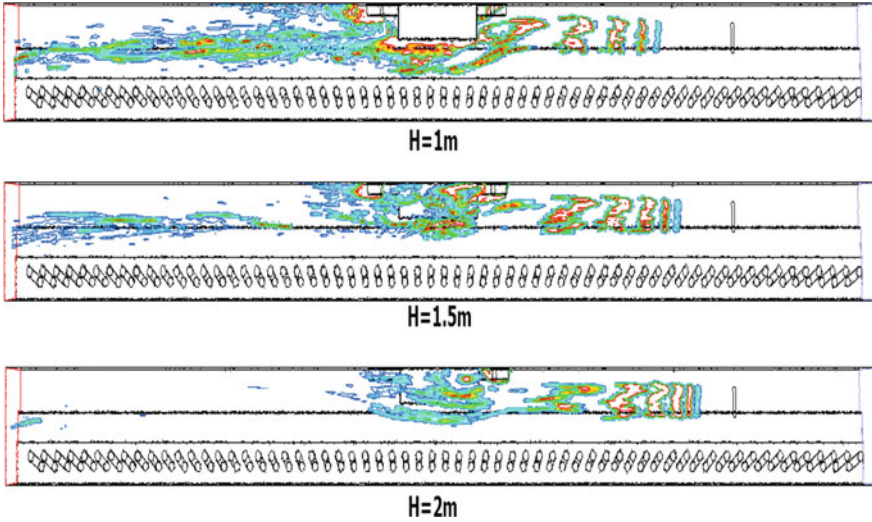
**Fig. 8.** Distribution of dust concentration
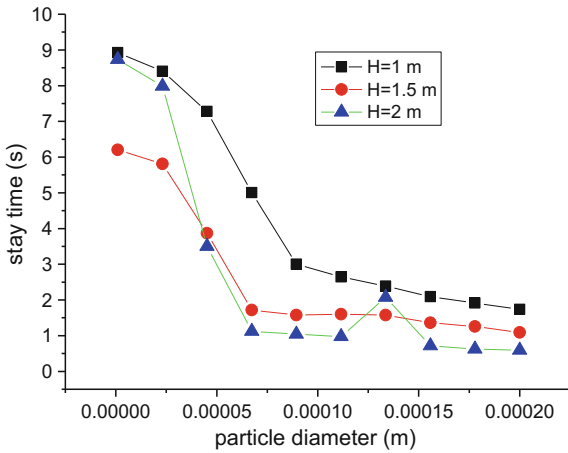


**Fig. 9.** Residence time of dust particles with different particle sizes (need to make change the term on the vertical axis)

## 5   Conclusions

(1) The airflow speed shows the "small-large-small" pattern when the airflow enters the mining face, and the airflow rate and turbulence intensity reach the maximum in the vicinity of the shearer.

(2) The large size dust generated by support advancing will gradually settle when moving with air flow, while the small size dust will spread to the roadway after bypassing the coal mining machine.

(3) The dust generated by shearer cutting has the highest concentration at the drum position, and moves mainly along the side of the coal wall. It begins to diffuse into the roadway about 10 m behind the shearer.

(4) The rate of dust deposition is mainly determined by gravity and the drag force of air, which results in a significantly higher dust concentration in the lower part of the working face than in the upper part.

# References

1. Wang, Y.: Research on numerical simulation of respirable dust distribution rule in fully mechanized mining face. Xi'an University of Science and Technology, Xi'an (2016)
2. Patankar, N.A., Joseph, D.D.: Modeling and numerical simulation of particulate flows by the Eulerian-Lagrangian approach. Int. J. Multiph. Flow **27**(10), 1659–1684 (2001)
3. Chen, Jushi, Jiang, Zhong-an, Yang, Bin, et al.: Numerical simulation of spatial distribution of dust concentration in broken chamber. J. China Coal Soc. **37**(11), 1865–1870 (2012)
4. Liu, Y., Jiang, Z., Cai, W., et al.: Numerical simulation of dust movement in fully mechanized caving face. J. Beijing Univ. Sci. Technol. **29**(4), 351–353 (2007)
5. Wang, H., Jiang, Z., Du, C., et al.: Field measurement and numerical simulation of the volume fraction distribution of fully mechanized roadway dust. J. Liaoning Tech. Univ. **30**(3), 345–348 (2011)
6. Jiang, Z., Zhang, Z., Tan, C., et al.: Optimization of wind speed for ventilation and dust removal of fully mechanized caving face based on numerical simulation. Coal Sci. Technol. **42**(10), 75–78 (2014)
7. Yang, S.: Discussion on dynamic model of dust particle movement in coal faces. J. Shanxi Min. Inst. **12**(3), 250–258 (1994)
8. Zuo, Q.: Diffusion law and dust control techniques of large mining height fully- mechanized face. China University of Mining and Technology, Beijing (2014)
9. Tan, C., Jiang, Z., Chen, J., et al.: Numerical simulation of influencing factors on dust movement during coal cutting at fully mechanized working face. J. Beijing Univ. Sci. Technol. **36**(6), 716–721 (2014)
10. Zhou, G., Zhang, Q., Bai, R., et al.: The diffusion behavior law of respirable dust at fully mechanized caving face in coal mine: CFD numerical simulation and engineering application. Process Saf. Environ. Prot. **106**, 117–128 (2017)
11. Launder, B.E., Spalding, D.B.: Lectures in mathematical models of turbulence. Academic Press, London (1972)
12. Morsi, S.A., Alexander, A.J.: An investigation of particle trajectories in two-phase flow systems. J. Fluid Mech. **55**(2), 193–208 (2006)
13. Zhang, L., Wang, X., Zhang, Z.: Numerical simulation and analysis of particle size distribution of coal dust in fully mechanized face. Coal Mine Modernization **2**, 138–140 (2017)

# Part V
# Methane and Methane Control I

# New Method for Ventilation Methane Content Monitoring

Janusz Kruczkowski and Piotr Ostrogórski[✉]

Strata Mechanics Research Institute of the Polish Academy
of Sciences, 27 Reymonta Street, 30-059 Cracow, Poland
`ostrogorski@img-pan.krakow.pl`

**Abstract.** In this article, the results of experiment measurements were presented. Methane content was measured using newly designed, innovative measuring instruments. The devices make measurements simultaneously and quasi-point. The instruments are prepared to measure methane concentration and air velocity in deep coal mines. The article describes both the handheld and stationary instruments. The method of making measurements and using the measuring instruments was discussed and explained. Measurements were made in a region of a longwall ventilated by means of a U-type ventilation system in normal excavation conditions. The gathered data were compared with the standard acquisition data from the sensors of the mine's telemetry system.

**Keywords:** Mine ventilation · Ventilation methane content measurement
Methane concentration · Anemometer · Methanoanemometer

## 1 Introduction

Measuring methane volumetric flow rate is one of the fundamental problems to be solved in measuring airflow in underground coal mine headings. This is due to the fact that safety must be ensured for those working in areas where methane is present. Keeping miners safe is, in other words, ensuring the safety of coal exploitation and transport to the surface. Measuring the air volumetric flow rate is one of the most difficult problems in mining aerology. Measuring methane volumetric flow rate is a wider problem and so it is even harder to determine. As in any measurement, the aim is to obtain a result with the smallest possible measurement uncertainty. The search for new measurement methods is possible thanks to sensor technologies being developed and new electronic circuits emerging all the time. The Strata Mechanics Research Institute of the Polish Academy of Sciences has been conducting research into measuring volumetric flow rate of air in mines and trying to find new solutions for many years [1]. Vane anemometer sensors and thermos-anemometer sensors for air flow velocity designed at the institute are used for this purpose.

Figure 1 shows a stationary measuring system consisting of spatially laid out integrated sensors of methane flow rate and concentration. The system is used to analyse the distributions of air velocity and methane concentration fields in cross-sections of mine headings [2]. The measuring unit shown in Fig. 1 was fitted in a

longwall. The measuring system shown here obtained valuable data regarding the characteristics of air flow in underground mines. Unfortunately, this kind of measuring instruments cannot be used for routine measurements during mining because they have to be fitted in the heading's cross-section. Their presence there may impede the transit of personnel or machinery.



**Fig. 1.** Measuring system to analyse the distributions of air velocity and methane concentration fields

To ensure safe mining operation, the currently used methods of determining methane flow rate require two separate measurements—of the air volumetric flow rate and of the average concentration of methane in the cross-section of the heading [3]. The measurements are taken at different times and places, which means that the result cannot be obtained in real time. To calculate air flow rate, the value of average velocity at the cross-section and the area of this cross section must be determined [4]. The average velocity is assessed by means of the continuous traverse method using a handheld anemometer. Stationary anemometers are very rarely used for this purpose. The cross-section's area is calculated by means of the geometric method using a tape measure. Methane concentration is most commonly calculated on the basis of time-averaged measurement results from a stationary methanometer (for one shift, week or even month). The pipette sample collection method is also used. The methods of measuring methane flow rate presented here carry the risk of making a number of errors, through the human and instrument errors. It must also be remembered that the responsibility for a reliable measurement does not lie with one person, sometimes an indefinite number of people are responsible. It is also difficult to carry out a reliable uncertainty analysis for such measurements because it is impossible to use or properly calculate the values of all its components.

## 2   The SOM2303 Methanoanemometer

In order to measure methane flow rate during mining, a portable methane flow rate measuring instrument was developed. The SOM 2303 methanoanemometer is an entirely new solution in portable measuring systems [5]. It consists of two separate devices: the SOM 2303 m and the SOM 2303 recorder as shown in Fig. 2. The meter contains two connected measuring sensors. A pellistor methane concentration sensor is attached to the upper surface of the vane anemometer sensor's casing. The inlet to the concentration sensor's measurement chamber is situated inside the vane sensor's casing [6]. The recorder is used to read and archive measurement results. The two devices communicate via radio frequency 868 MHz. The idea of the measurement is based on the possibility of making simultaneous local measurements of air velocity and methane concentration. Using the method in which the operator moves the meter in the plane of the heading's cross-section, which is analogous to the hand-held anemometer-based continuous traverse, measurement data from many points of the plane are obtained. As the frequency of measuring both parameters does not vary and equals 1 Hz, the number of obtained data from the points on the plane which form the path (trajectory) of the meter's motion depends only on the duration of the measurement. To calculate methane flow rate, the surface area of the heading's cross-section must be known. This information must be entered by means of a keyboard placed in the recorder after traversing is complete. The measured methane flow rate is the product of the cross-section's area and averaged values of local velocities and local concentrations. In order to carry out the measurement process correctly, a special extension arm must be used to guarantee that the meter remains in the right position while traversing Fig. 2.



**Fig. 2.**  SOM 2303 hand-held methanoanemometer

**Main technical parameters**.

| Velocity sensor | |
|---|---|
| Flow rate measuring range | $\pm(0.16 \div 15.0$ m/s) |
| Flow rate measuring error | $\pm(0.5\%$ rdg $+ 0.02$ m/s) |
| Methane concentration sensor | |
| Methane concentration measuring sub-ranges | $0 \div 100\%$ LEL; $5 \div 100\%$ V/V |
| Methane concentrations measuring error | 0.1% for the $0 \div 2\%$ V/V range |
| $T_{90}$ response time | <3 s |
| Measurement frequency | 1 Hz |
| Heading's cross-section's area | 99.9 m$^2$ |
| Measuring data memory | 240 h of continuous recording |
| Approval intrinsically safe | ATEX I M1 Ex ia I Ma |

## 3    MPM Stationary Methanoanemometer

Figure 3 shows a stationary measuring instrument used to determine methane flow rate in a mine heading. This device can make continuous measurements of ventilation methane e.g. in a region of a longwall [7]. The idea of the measurement is similar to that described above. The measurement is made on the basis of synchronically obtained data from methane concentration sensors and from the anemometer sensor. The calculations are made for the cross-section of the heading measured at the site of fitting the device; the area is entered into the device's memory. An important feature of the MPM methanoanemometer is its additional, external methane concentration sensor. The data from both sensors analysed together increase measurement accuracy in the situation when the field of methane concentrations in the cross-section where the methanoanemometer is fitted is not homogenous [8]. It is also important that this solution allows emergency states of any one of the sensors to be detected quickly.
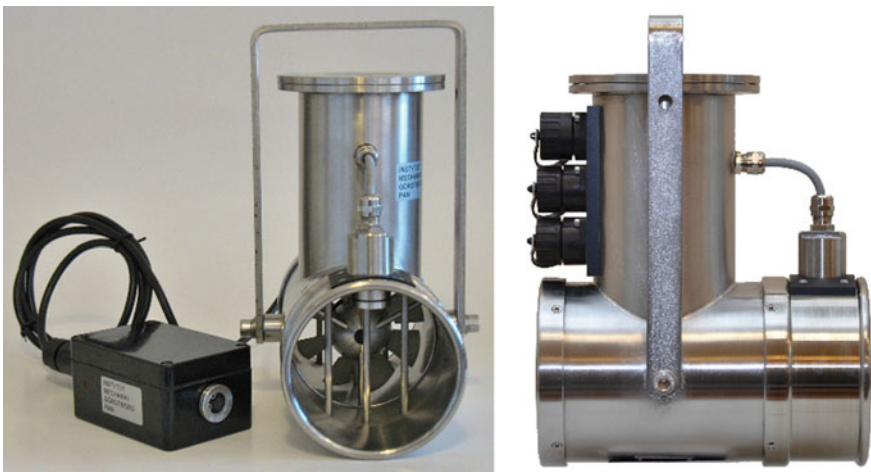


**Fig. 3.** MPM stationary methanoanemometer. The main measuring unit and an additional methane concentration sensor module

The metrological characteristics of the instrument are the same as the SOM 2303 methanoanemometer's. The instrument is compatible with the mine's automatic telemetric systems. The photograph does not show the data and emergency state alert monitor.

## 4    Comparative Ventilation Methane Measurements

The experiment was carried out in a coal mine where most longwalls are classified as category 4—the highest methane hazard category in Polish law. A longwall with high methane content was chosen in order to ensure a small relative quantization error. This is an important aspect in the context of comparing the data obtained from mine gasometry measuring devices with the measurements taken by the MPM and SOM2303 instruments.

Figure 4 shows a part of the longwall where experiment measurements were taken.
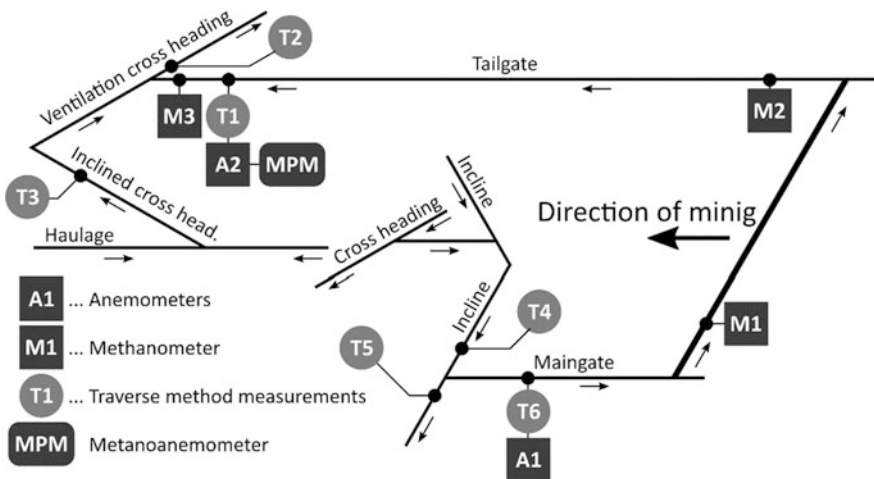


**Fig. 4.** Layout of measurement sensors and traverse places

The longwall was ventilated using a U-type system with upper corner reblowing. Methane drainage was used as a preventive measure. The following were fitted in the tailgate: a 1000 mm diameter ventilation tube, a 300 mm diameter methane drainage pipe, and the top-suspended monorail track. The tailgate and the maingate were 500 m in length. The measurement experiment was being carried out during the whole mining shift. Figure 4 shows the layout of significant sensors of the mine's telemetric system. The points at which hand measurements with the SOM 2303 methanoanemometer were made are marked with a circle with the letter 'T' in the middle. The stationary MPM methanoanemometer was situated at the exit of the longwall at the end of the maingate —before the emergency stopping.

Immediately before the experiment the methane sensors and the anemometer sensors in the MPM and SOM 2303 methanoanemometers were calibrated. Air velocity calibration took place in a wind tunnel of an accredited laboratory. Stationary anemometers labelled with symbols A1 and A2 and stationary methanometers M1, M2, M3, which are part of the mine's telemetric system, were used in the measurements.

The M3 methanometer was placed approximately 12 m from the intersection of the tailgate and the ventilation cross heading. The A2 stationary anemometer was placed approximately 20 m away. The MPM methanoanemometer was placed in the same cross-section. The A1 stationary anemometer was fitted in the maingate, approximately 15 m away from the intersection with the incline. The M1 methanometer was placed approx. 5 m away from the intersection with the maingate. The M2 methanometer was placed in the tailgate approx. 5 m from the intersection with the longwall. The A1 and A2 anemometers were vane anemometers and the M1–M3 methanometers had catalytic and thermoconductometric pellistor methane concentration sensors.

The comparative measurements of methane flow rate were made on the exit from the longwall region in the area of the intersection of the tailgate with the ventilation and inclined cross headings and at the entry into the region near the intersection of the maingate with the incline. The measurement spots are labelled with symbols T1–T6. In order to make these measurements, the SOM 2303 hand-held methanoanemometer was used. During the measurements the air flow in the longwall region was steady and no adjustments were made in the ventilation system.

Figure 5 also shows the geometric data of the heading's cross-section dimensions as well as the positions of the measuring sensors in the place where the MPM methanoanemometer was fitted. The position of the M3 methanometer, which was shifted relative to the cross-section's place by approx. 8 m in the direction of the intersection, is also marked. The methanoanemometer and the A2 anemometer were mounted on fixed extension arms which kept them clear of the side wall. An additional methane concentration sensor of the MPM methanoanemometer was fitted on the right side wall at the height of 1.32 m. The tailgate was equipped with the ŁP10/V32 arch support.
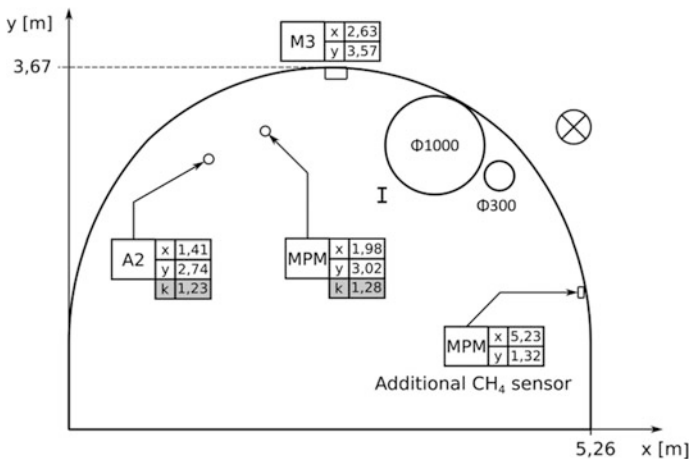


**Fig. 5.** Positions of measuring sensors and technical equipment elements in the tailgate's cross-section

## 5   Results

The first stage of result analysis was determining the correction factors. These factors are used to obtain average velocity for a given cross-section from the air velocity measured by a stationary instrument. For the MPM methanoanemometer, the correction factor k1 was calculated at k1 = 1.28. The A2 anemometer's factor was $k_2 = 1.23$, calculated by the mine's ventilation division's crew and used in the mine's operations.

Figure 6 shows the record of the results from the MPM methanoanemometer. Recording time was 4 h 22 min.
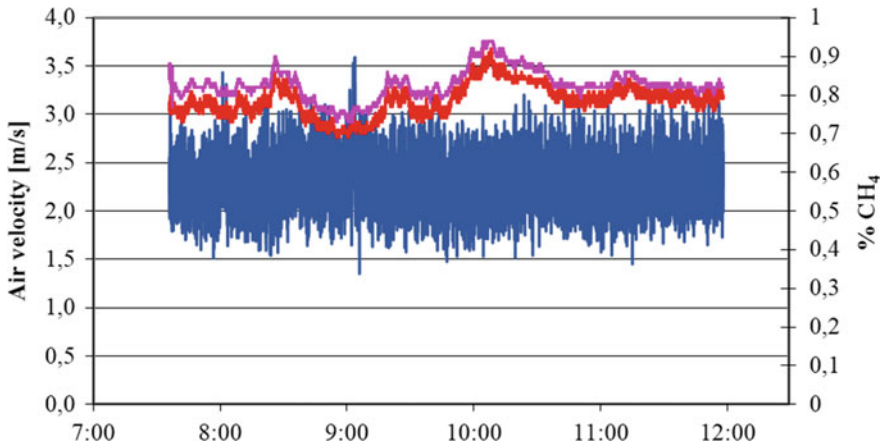


**Fig. 6.** Air velocity and methane concentration recorded by the MPM methanoanemometer

Big fluctuations characteristic of flows in mine headings can be seen on the record of air velocity changes. Apart from small local variations, the methane concentration sensors recorded long-term variations connected with a continuous miner working in the longwall. The amplitude of these variations was 0.22% V/V $CH_4$. A difference in methane concentration can be seen between the MPM sensors. The additional methane sensor fitted on the side wall initially measured greater values than the internal sensor. As the recording progressed, this difference gradually decreased.

An averaged methane flow rate was determined on the basis of the obtained data. Table 1 shows the results of the measurements and the methane flow rate calculated on the basis of the data from the internal concentration sensor. Table 2 shows analogous results, however the rate is calculated for the additional methane sensor. The flow rate values differ as a result of the differences between measured average methane concentrations of 0.79 and 0.83% respectively.

**Table 1.**   Measurement results from the MPM methanoanemometer in the tailgate

| Average local velocity (m/s) | Average local $CH_4$ concentration (%) | Cross-section's area (m²) | K1 correction factor | Averaged methane flow rate (m³/min) |
|---|---|---|---|---|
| 2.28 | 0.79 | 15.40 | 1.28 | 21.30 |

Data from the internal methane concentration sensor

**Table 2.** Measurement results from the MPM methanoanemometer in the tailgate

| Average local velocity (m/s) | Average local $CH_4$ concentration (%) | Cross-section's area ($m^2$) | K1 correction factor | Averaged methane flow rate ($m^3$/min) |
|---|---|---|---|---|
| 2.28 | 0.83 | 15.40 | 1.28 | 22.38 |

Data from the additional methane concentration sensor

Figure 7 shows the records from the mine telemetry system's methanometer and anemometer. The resolution of the methane concentration record was 0.1% $CH_4$, the result of which is that information regarding the tendency of concentration variations during the mining shift is not available.

The measurement resolution in this case is greater compared to the MPM methanoanemometer's record. The indicated methane concentration is constant for the most part of measurement taking, which is not accurate.
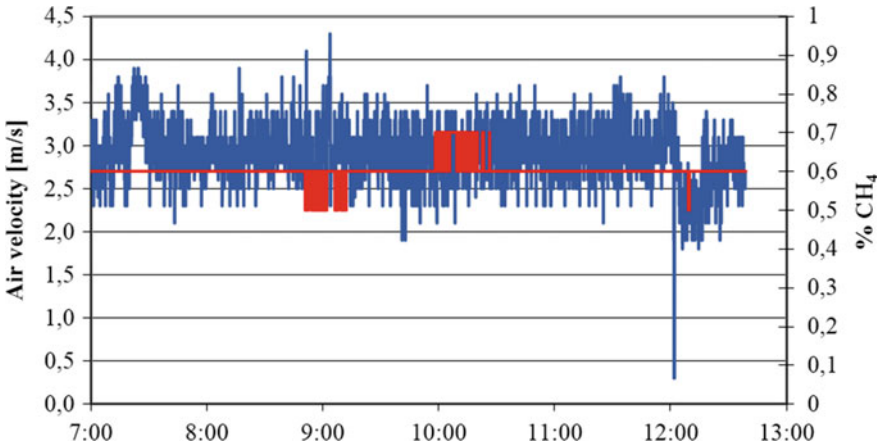


**Fig. 7.** Methane velocity and concentration recorded by the A2 anemometer and the M3 methanometer

Figure 8 shows the recorded distributions of methane concentration and air velocity fields in the tailgate's cross-section. The recording was carried out where stationary sensors labelled as T1 were fitted (Fig. 4). A vertical traverse of 4 min 39 s was performed.

The graph in Fig. 8 shows variations of air velocity and methane concentration on the anemometer's trajectory. Small variations of methane concentration, smaller than 0.1% $CH_4$, can be seen. The fluctuations shown as peaks reflect the vertical motion of the instrument. The slow-varying component reflects the horizontal motion, i.e. the gradual displacement from one side wall to the other.
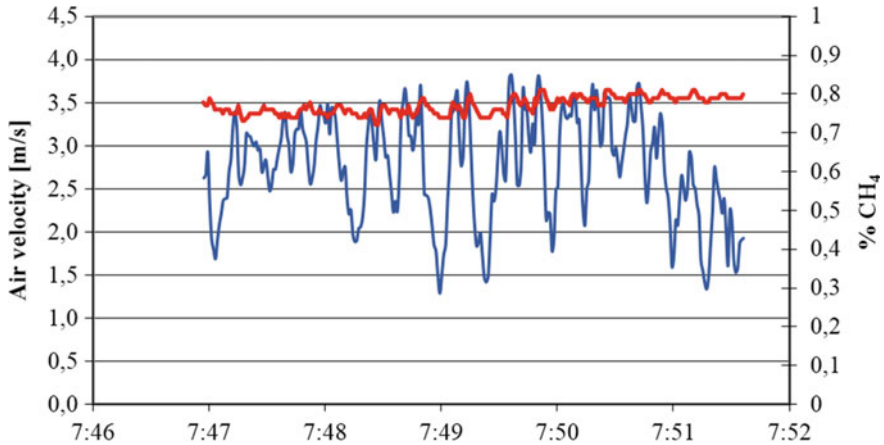
**Fig. 8.** Recording the traverse with a hand-held methanoanemometer. The tailgate

Table 3 shows the comparison of the data obtained using the SOM3203 methanoanemometer and those by the ventilation division's crew using the standard method in Polish mining industry. The data presented in Table 3 were obtained for the duration of one shift.

**Table 3.** Tailgate measurement results

| Flow rate measuring method | Average velocity in heading's cross-section (m/s) | Average CH$_4$ concentration in heading's cross-section (%) | Cross-section's area (m$^2$) | Methane flow rate (m$^3$/min) |
|---|---|---|---|---|
| 1 | 2.76 | 0.77 | 15.40 | 19.64 |
| 2 | 2.70 | 0.60 | 14.80 | 14.39 |

It can be seen that the methane concentration and cross-section's area measurements are different in the two methods (Table 3). Because both sensors of the MPM methanoanemometer indicated average values of 0.8% of methane concentration for the duration of the experiment, and the value of methane concentration measured by the SOM 2303 methanoanemometer was 0.77%, these results must be considered accurate. It seems too unlikely for the M3 methanometer situated at the highest level in the heading's cross-section to indicate concentration values as much as 0.2% smaller than those from other sensors. To determine the cross-section's area for the hand-held methanoanemometer, a method was used which consisted in making a series of measurements of the arch support's geometry and then adjusting the actual geometry with the ŁP10/V32 arch support model using a CAD programme. Also, the cross-sections of the instruments fitted in the heading's cross-sections were subtracted. The above facts justify the claim that the measurement obtained using the SOM 2303 methanoanemometer is a more reliable measurement. Because the methane

concentrations recorded at the langwall's inlet by the M1 methanometer are very close to 0%, the result of calculated methane flow rate at the outlet is assumed to be the value of ventilation methane content of the longwall. An attempt was also made to estimate the balance of methane flow rates at the tailgate outlet node (measurement points T1, T2, T3) and at the maingate inlet node (measurement points T4, T5, T6). It is shown in Table 4.

**Table 4.** Results of measurement by traverse methods

| Measurement place | Average velocity in heading's cross-section (m/s) | Average $CH_4$ concentration in heading's cross-section (%) | Cross-section's area ($m^2$) | Methane flow rate ($m^3$/min) |
|---|---|---|---|---|
| T1 | 2.76 | 0.77 | 15.40 | 19.64 |
| T2 | 3.97 | 0.62 | 16.40 | 24.22 |
| T3 | 1.12 | 0.10 | 15.34 | 1.03 |
| T4 | 3.71 | 0.01 | 15.50 | 0.35 |
| T5 | 2.27 | 0.02 | 11.02 | 0.30 |
| T6 | 2.24 | 0.02 | 14.32 | 0.38 |

The results labelled T1, T2 and T3 refer to the exit node and T4, T5 and T6 to the entry node. After balancing the values obtained for the exit node a difference of flow rate of 3.55 $m^3$/min $CH_4$ can be noticed. However, it must be remembered that the methane flow rate measurement is an indirect measurement, where each component measurement contributes its measurement uncertainty to the final result. When calculating the flow rate from the flow rate balance we obtain another indirect element in the measurement connected with the difference of flow rates.

## 6    Summary

The SOM 2303 methanoanemometer is an innovative, professional instrument which sets new standards in measuring methane flow rate. The solutions used significantly reduce the measurement uncertainty and also make it possible to obtain the results immediately. They take into account the actual distributions of air velocity and methane concentration fields. Very good metrological characteristics must also be noted. Similarly, the stationary MPM methanoanemometer with an external methane concentration sensor module is a new type of measuring instrument which can be used to continuously monitor ventilation methane content in mine headings. Using a second sensor, which can be fitted in a different place than the main device, reduces the uncertainty of determining the flow rate and increases the instrument's functionality. As the experiment measurements in the longwall region showed, when an appropriate place is chosen to install the device and the correction factor for the anemometric sensor is determined appropriately, the results of the measurements obtained from MPM methanoanemometers are very similar to those obtained using the continuous traverse method with SOM 2303 methanoanemometers.

In the course of making the measurements, discrepancies were found between the obtained data and the data at the mine's disposal. Similar situations occurred on many occasions when experiment measurements were being carried out in mines as part of research conducted by the Institute's staff. This means that the ventilation division's crew often do not know the real values of such parameters as air flow rate or methane flow rate. Even if they react appropriately to changes in their values, there is an increased probability of a disaster. As a consequence of not knowing the real measurement data, any subsequent reasons of mining disasters are more difficult to explain or are explained wrongly.

The above remarks constitute a reason for continuing the efforts in order to work out reliable procedures of measuring ventilation methane. The procedures and guidelines for assessing and fighting methane hazard in coal mines which have been in use for years should be reassessed using cutting-edge metrological solutions such as the SOM 2303, MPM, multi-point systems to measure methane concentration and air flow velocity distributions. Knowing the most realistic measure possible of the amount of methane in the air in the mine's ventilation system is important not only for the safety of mining operations. Methane is one of greenhouse gases, whose emission is subject to greater and greater restrictions, including financial ones. Proving the actual measure of emission may very soon become of utmost importance to business owners.

## References

1. Dziurzyński, W., Kruczkowski, J.: Variability of the volumetric air flow rate in a mine fan channel for various damper positions. Arch. Min. Sci. **56** (2011)
2. Krach, A.: Zmienność pola prędkości i strumienia objętości powietrza w wyrobiskach kopalń głębinowych. Archives of Mining Sciences, Kraków (2006)
3. Dziurzyński, W., Kruczkowski, J., Wasilewski, S.: Nowoczesna metoda badania przepływu powietrza i metanu w wyrobisku kopalni. Nowe spojrzenie na wybrane zagrożenia naturalne w kopalniach. Presented at the, Katowice (2012)
4. Kruczkowski, J.: Wyznaczanie metanowości wentylacyjnej przy wykorzystaniu nowej techniki pomiarowej. In: Materiały 7 Szkoły Aerologii Górniczej, pp. 71–82. Instytut Eksploatacji Złóż (2013)
5. Kruczkowski, J., Ostrogórski, P.: Metanoanemometr SOM 2303. In: Nowoczesne metody zwalczania zagrożeń aerologicznych w podziemnych wyrobiskach górniczych, pp. 117–127. Główny Instytut Górnictwa (2015)
6. Kruczkowski, J., Ostrogórski, P.: Urządzenie do pomiaru prędkości przepływu powietrza i stężenia metanu w wyrobisku kopalni. Trans. Strata Mech. Res. Inst. **15** (2013)
7. Kruczkowski, J., Krawczyk, J., Ostrogórski, P.: Laboratory investigations of stationary methane anemometer. Arch. Min. Sci. **62**, 893–909 (2017)
8. Kruczkowski, J.: Rozkład stężeń metanu w wyrobiskach przyścianowych. In: Zagrożenia aerologiczne w kopalniach węgla kamiennego - profilaktyka, zwalczanie, modelowanie, monitoring. Główny Instytut Górnictwa (2013)

# Model Experiment and Numerical Simulation for the Heading Face Methane Behavior

Masahiro Inoue[1](✉), Bing-rui Li[2], and Takumi Hyoudou[1]

[1] Kyushu University, Fukuoka, Japan
`inoue@mine.kyushu-u.ac.jp`
[2] Shandong University of Science and Technology,
Qingdao, People's Republic of China

**Abstract.** Local ventilation using a fan and duct at a heading face is one of the most important ventilation practices in underground mining operations, there have been many studies on this topic. Almost all the researches are assuming that the ventilation system is operating under normal circumstance. But this is not always true, the ventilation system does stop suddenly due to unforeseeable reasons. It is essential that methane emissions and concentration at the heading face in case of sudden ventilation stops be understood. were examined by model experiments and computer simulations. The followings were found for the ventilation stop incident. The heading face will be dangerous by the methane gas increase within 10 min if ventilation stops. Methane concentration in a downward heading face decreases only 15% relatively compared with the horizontal condition. Methane will accumulate in short time, and become extremely high risk in an upward heading faces. The methane concentration decreases to some degree if the gas is sucked by an air mover.

**Keywords:** Ventilation stopping · Methane · Heading face · Model experiment

## 1 Introduction

It is usual in coal mines that dangerous combustible gas emits into the underground openings. Nevertheless, safety is secured as long as proper ventilation is maintained. Local ventilation using a fan and ducts at a heading face is one of the most important ventilation practices in mines, so that there are many studies [1] on the topic. However, almost all the researches are focused on the condition that the ventilation system is working normally. Though it is seldom, the ventilation system stops suddenly by some reason. Therefore, methane concentration at the heading face when ventilation stops were need to be examined. The main purpose of the present research is to know the methane gas behavior at the heading face when the local ventilation stops by sudden power shut down. However it is apparent that some alternative ventilation system is required to maintain the safety of the heading face when the fan stops. Though the flow rate is small, an air mover using compressed air can work even in the electric shutdown. The availability of the small ventilation system as a countermeasures for such a situation was also examined.

One of the authors has already published research work on the methane distribution at a heading in a mine [2] using actual size roadway model [3]. It is suitable to use small scaled model experiment to examine gas behavior by different types of ventilation arrangement [4]. Computer simulation can be a useful tool to examine gas behavior using alternative method in the experiment. The reason is not only for the convenience but also for the safety to conduct the research as methane is explosive. Therefore, methane concentration at the heading face when ventilation stops were examined by model experiments and computer simulations.

## 2  Model for the Experiment

A series of experiment by using a small scale roadway model was conducted. The model used in the experiment is 15 cm height, 15 cm width and 75 cm length as shown in Fig. 1. The supposed actual roadway (prototype) is 2.4 m height, 2.4 m width and 12 m length that means the scale factor is 16. The data about the size and flow rate and so on related to the actual size roadway is called with prototype here after to distinguish from the data related to the model. Figure 2 shows the picture of the model roadway. The head part of the roadway is equipped with a punch metal plate that act as a heading face from which methane gas emits. There are 6 heat conduction type sensors mounted on the center line of the roadway roof. The distances from the heading face to the sensors CH 1, 2, 3, 4, 5 and 6 are 3, 9, 19.5, 34.5, 49.5 and 64.5 cm respectively. The distances are corresponded to 0.5, 1.5, 3.0, 5.5, 8.0 and 10 m in the prototype.

Five different ventilation systems shown in Table 1 were conducted successively. The experiment of exhausting ventilation and forcing ventilation were also conducted to compare with either no ventilation or little ventilation (air mover). Here the "Duct end position" means the distance between the face and the outlet or inlet of the ventilation duct. The duct was placed just below the roof corner of the roadway. Methane flow rate from the mining face is assumed to be 0.6 $m^3$/min in model which makes the methane concentration near the heading to be 0.3% assuming complete mixing with the 200 $m^3$/min of air from the ventilation duct. Experiment using helium was conducted prior to the experiment instead of methane for safety reason. The duct diameter is 3.6 cm as opposed to 0.6 m for the prototype.
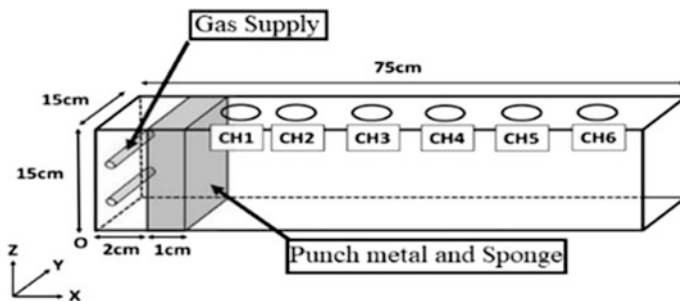


**Fig. 1.** Schematic view of the roadway model
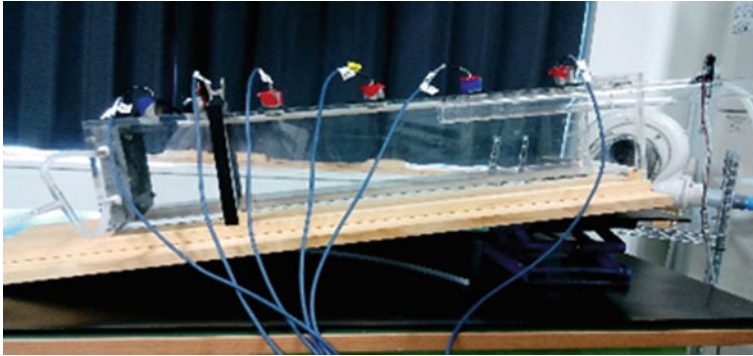
**Fig. 2.** Photo of the roadway model

**Table 1.** Ventilation condition in the experiment

| Ventilation condition | Prototype (supposed) | | | Model (experiment) | | | | |
|---|---|---|---|---|---|---|---|---|
| | | | | | Methane | | Helium | |
| | Duct end position (m) | Gas flow (m³/min) | Air flow (m³/min) | Duct end position (cm) | Gas flow (L/min) | Air flow (L/min) | Gas flow (L/min) | Air flow (L/min) |
| Exhausting 7 m | 7 | 0.6 | 200 | 43 | 0.6 | 195 | 0.8 | 274 |
| Exhausting 2 m | 2 | 0.6 | 200 | 13 | 0.6 | 195 | 0.8 | 274 |
| Forcing 7 m | 7 | 0.6 | 200 | 43 | 0.6 | 195 | 0.8 | 274 |
| No vent. | * | 0.6 | 0 | * | 0.6 | 0 | 0.8 | 0 |
| Small vent. | 1 | 0.6 | 4 | 6 | 0.6 | 4 | 0.8 | 5 |

# 3    Similarity of the Experiment

The similarity low derived from Froude number was used in the experiment. The flow of model and the flow of prototype become similar when the ratio of forces on the flow is the same.

Froude number (Fr) is defined as,

$$Fr = Fi/Fg = \rho \, L^2 V^2 / (\Delta\rho \, L^3 g)$$

where,

$$Fi : \text{Inertia force} = M \, \alpha = \rho \, L^3 (LT^{-2}) = \rho \, L^2 (LT^{-1})^2 = \rho L^2 V^2,$$

Fg: Buoyancy force = $Mg = \Delta\rho L^3 g$,
$\rho$: density, L: characteristic length, V: velocity, $\Delta\rho$: difference of density,
g: gravity and $\alpha$: acceleration.

As, the gravity g is same for both model and prototype,

$$Fr = \rho \, V^2/(\Delta\rho \, L)$$

When m is for model, p is for prototype,

$$Fr = \rho_m V_m^2/(\Delta\rho_m L_m) = \rho_p V_p^2/(\Delta\rho_p L_p)$$

Then, the velocity of the model is defined as follows.

$$V_m/V_p = \sqrt{\{(\rho_p/\rho_m) \cdot (\Delta\rho_m/\Delta\rho_p) \cdot (L_m/L_p)\}} \tag{1}$$

In this experiment $L_m = 0.15$, $L_p = 2.4$ then $L_m/L_p = 1/16$

1. In case that methane is used for the model experiment, following relations are derived from Eq. (1).

$$V_m/V_p = \sqrt{\{(1) \cdot (1) \cdot (1/16)\}}$$

$$V_m = 0.25 \cdot V_p$$

The flow rate of $Q_m$ for the model is defines as follows.

$$Q_m = V_m \cdot L_m^2 = 0.25 \cdot V_p \cdot (L_p/16)^2 = 0.000977 \cdot V_p \cdot L_p^2 = 0.000977 \cdot Q_p$$

Also, time for the model is defined.

$$T_m = L_m/V_m = (L_p/16)/(0.25 \cdot V_p) = 1/4 \cdot L_p/V_p = 0.25 \, T_p$$

The model experiment is continued 6 min for each ventilation condition. It should be noticed that the time 1 min in model corresponds to 4 min in prototype.

2. In case that helium is used for the model experiment instead of methane, special attention is required. The effect of air is thought to be more dominant than emitted gas, it is better to set $\rho_p = \rho_{air}$, $\rho_m = \rho_{air}$. Then,

$$V_m/V_p = \sqrt{\{(1) \cdot (1.3 - 0.18)/(1.3 - 0.72) \cdot (1/16)\}}.$$

$$V_m = 0.35 \cdot V_p$$

The flow rate of helium and time is defined as follows.

$$Q_m = V_m \cdot L_m^2 = 0.00137 \cdot V_p \cdot L_p^2 = 0.00137 \cdot Q_p$$

$$T_m = L_m/V_m = 0.179 \cdot L_p/V_p = 0.179 \cdot T_p$$

The calculated data according to the above similarity used for the model experiment are also listed in Table 1.

## 4    Computer Simulation

FDS (Fire Dynamics Simulator) is used in the computer simulation. FDS is a fire simulation code developed by National Institute of Standards and Technology (NIST), US Department of Commerce, and is provided as an open source program. It is mainly used for predicting behavior such as smoke, temperature, carbon monoxide when fire occurs. The Simulation model used in this research is shown in Figs. 3 and 4. Calculation region = 85 × 19 × 20 (cm). Number of cells = 28 × 19 × 40 + 71 × 19 20 = 48,260. Calculation time is 1800 s for every simulation of methane and helium. About 5–6 days were required to calculate for each simulation by using CPU CORE i7.
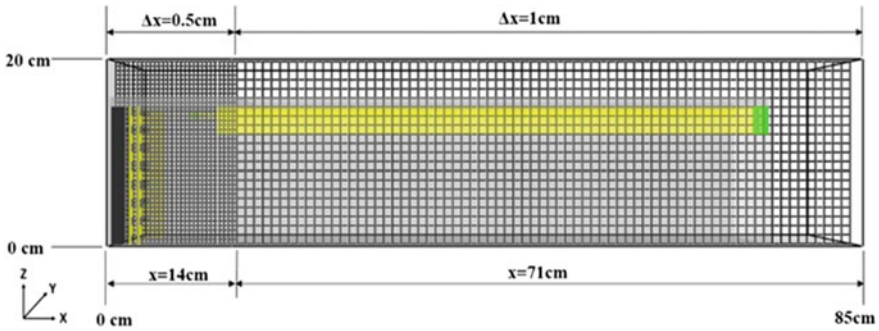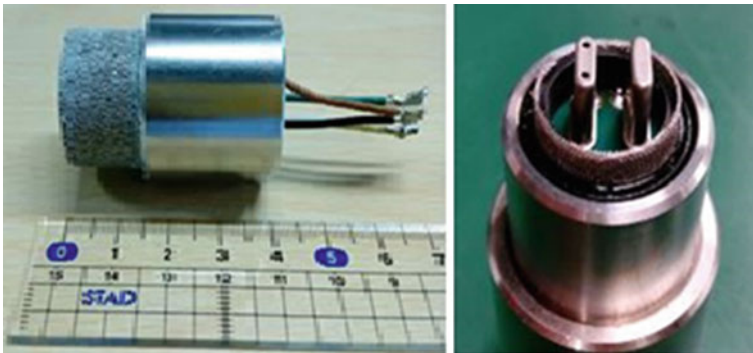


**Fig. 3.** Computer simulation model



**Fig. 4.** Sensors; outside and inside

# 5 Result

## 5.1 Conditions of the Experiments

The heat conduction gas sensors used in the experiments were manufactured by New Cosmos Electric Co., Ltd. The heating element has a maximum diameter of 30 mm and a length of 40 mm (Fig. 4). Gas is detected when it enters into the small aperture of the sensor element. It was found that there is a slight discrepancy between actual and measured gas concentrations when the aperture is set upside or downside; this will be explained later.

Though the behavior of methane changes considerably depending on ventilation arrangement and airway inclination. Three different experiments with various inclination angles were conducted: horizontal, 10° downward heading and 10° upward heading. In addition, the effect of sensor aperture direction and the helium usage instead of methane was also examined as well (Table 2). Five different ventilation arrangements shown in Table 1 were conducted in the experiments.

**Table 2.** Gas, inclination angle and sensor condition in the experiments

| Experiment no | Gases | Inclination | Sensors aperture |
|---|---|---|---|
| 1 | Methane | Horizontal | Upside |
| 2 | Methane | Downward | Upside |
| 3 | Methane | Upward | Upside |
| 4 | Methane | Horizontal | Downside |
| 5 | Methane | Downward | Downside |
| 6 | Methane | Upward | Downside |
| 7 | Helium | Horizontal | Downside |
| 8 | Helium | Downward | Downside |
| 9 | Helium | Upward | Downside |

The ventilation arrangement and experiment results are shown in Fig. 5. The gas behavior of "Exhausting 7 m" then "Exhausting 2 m", "Forcing 7 m", "No ventilation" and finally "Small ventilation" were conducted successively.

## 5.2 Horizontal Roadway

Results of methane emission patterns at the face under five different ventilation arrangements in a horizontal airway with sensors aperture placed upside (Fig. 6, experiment 1) and downside (Fig. 7, experiment 4). Both methane emission patterns were similar, but gas concentration is 20% lower when the aperture is upside than when it is placed downside. The difference in gas concentration caused by the aperture direction is the same as that in the other experiments when the roadways are inclined.
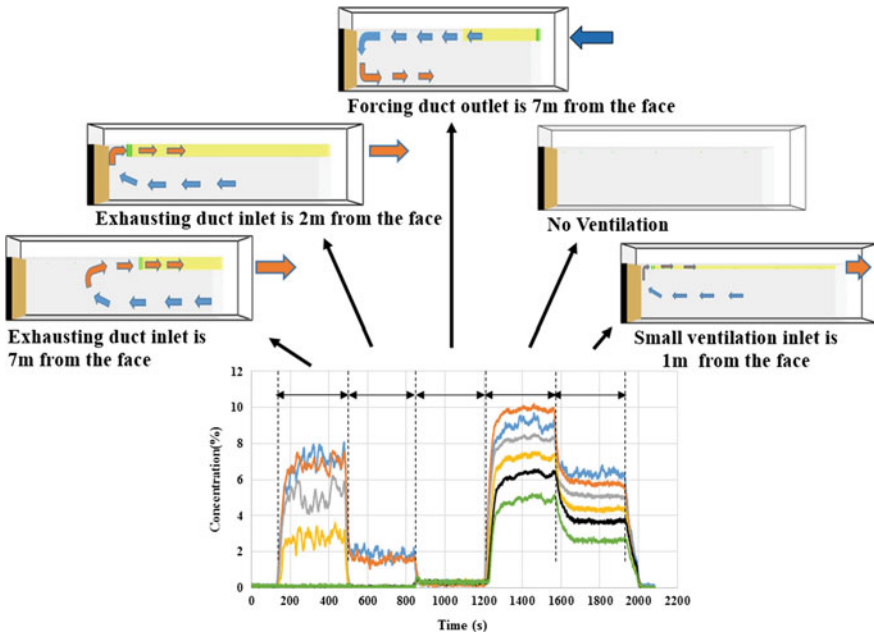
**Fig. 5.** The ventilation conditions and an example of the experiment results
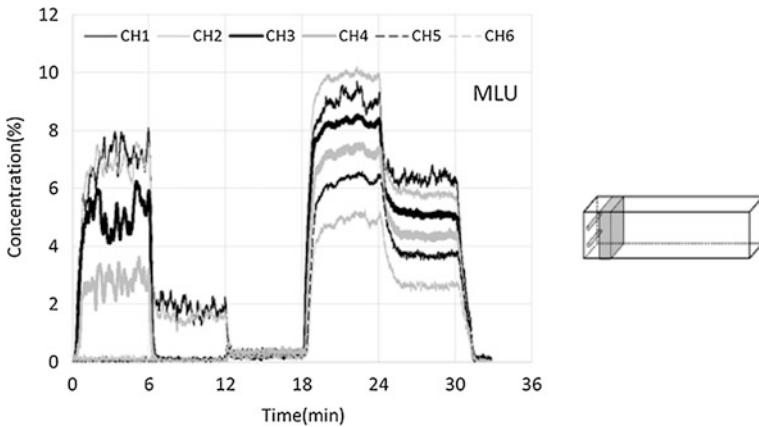


**Fig. 6.** Gas concentration in the horizontal roadway when sensors aperture were upside
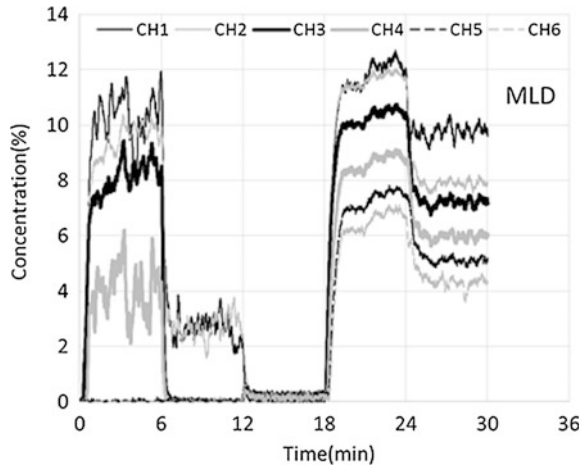
**Fig. 7.** Gas concentration in the horizontal roadway when sensors aperture were downside

In the case of "Exhausting 7 m", in the area of CH 1–CH 3, that is in the area within 3 m from the heading face in prototype, the gas concentration is more than 5%, and is in the explosive range of methane. Even in the case of "Exhausting 2 m", in the area of CH 1 and CH 2, that is in the area within 1.5 m from the face in prototype, the gas concentration is more than 1.5%. The gas concentration in the roadway should be 0.3% if the intake air (195 l/min) and the emitted gas (0.6 l/min) are completely mixed. In the case of "Forcing 7 m" the gas concentration is actually less than 0.5% in all places. Experiment show that the "exhausting" ventilation is not capable of adequately ventilate the heading at all.

In the case of "No ventilation" the gas concentration is shown to be more than 5% in 2 min in all areas. One minute in the model is equivalent to 4 min in prototype, then it means the gas concentration increases more than 5% in the area within 10 m from the face in 8 min in the prototype. It should be pointed out that the gas concentration reaches dangerous levels in a very short time if ventilation stops.

"Small ventilation" using compressed air like air mover can work even in electric shutdown. However, the gas concentration is more than 5% in the area within 3 m from the heading face when the air flow of is 4 m³/min by small ventilation. It needs more than 8 m³/min to prevent the place entering the explosive range.

The methane gas behavior under the same condition by the computer simulation is shown in Fig. 8. The gas concentration obtained by the simulation shows the concentration between the previous two experimental results shown in Figs. 6 and 7.
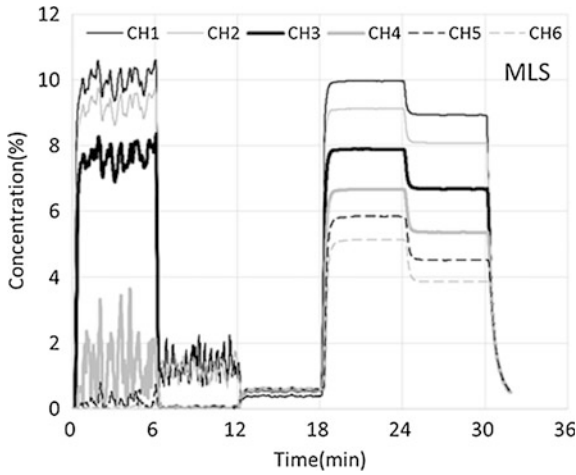
**Fig. 8.**  Gas concentration in the horizontal roadway by computer simulation

## 5.3   Downward Roadway

The methane gas behavior at heading face when the roadway is downward and the sensors aperture were downside (experiment 5) is shown Fig. 9. In the case of "Exhausting 7 m", in the area within 3 m from the heading face in the prototype, the gas concentration is more than 5%. Even in the case of "Exhausting 2 m", in the area within 1.5 m from the heading face in the prototype, the gas concentration is also more than 1.5%. In the case of "Forcing 7 m" the gas concentration is less than 0.5%. In the case of "No vent." the gas concentration is more than 3% in 2 min in the area within 10 m from the heading face. The gas concentration is about 2% lower than that of the horizontal roadway because the lighter gas as methane than air can flow out from the downward inclined roadway.
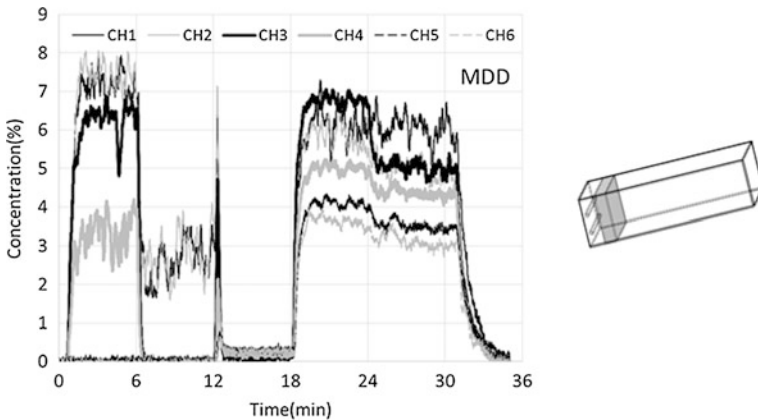


**Fig. 9.**  Gas concentration in the downward roadway when sensor aperture is downside

In the case of "Small ventilation" the gas concentration is more than 5% in the area within 3 m from the heading face. The gas concentration obtained by the computer simulation shows the same trend in the experiment. It tends to be thought that methane gas is easily discharged by the buoyancy from downward heading faces. However, methane concentration decreases only by about 15% relatively compared with the horizontal condition.

## 5.4   Upward Roadway

The methane gas behavior at heading face when the roadway is upward and the sensors aperture were downside (experiment 6) is shown Fig. 10. In the case of "Exhausting 7 m", the area where the concentration is more than 5% extends to 5 m from the heading face. Maximum concentration is considerably higher than that of the previous condition.
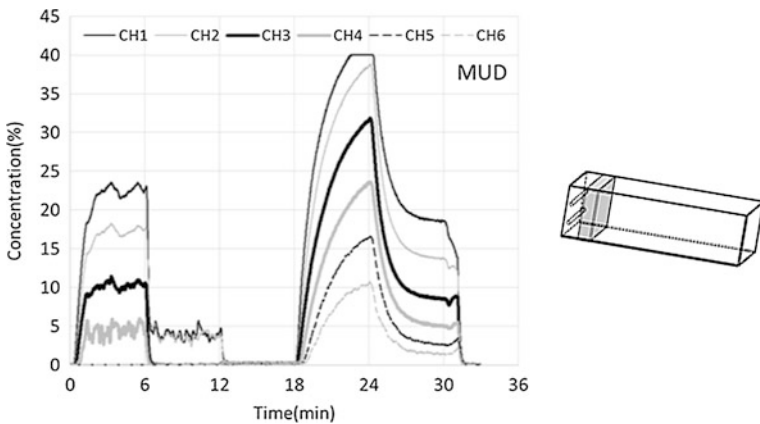


**Fig. 10.**  Gas concentration in the upward roadway when sensors aperture were upside

Even in the case of "Exhausting 2 m", the gas concentration also increased to more than 4% in the area within 1.5 m from the heading face. In the case of "Forcing 7 m" the gas concentration is less than 0.5%.

In the case of "No vent." the gas concentration increased up to 40% in 5 min and is still increasing at the heading face. The roadway inclined and the light gas is difficult to flow out from the heading face, "ventilation stop" is very dangerous situation. In the case of "Small ventilation" the concentration decreases, however, the effect is too small to improve the dangerous situation. The gas concentration obtained by the computer simulation shows the same trend in the experiment.

## 5.5    Helium in Horizontal Roadway

There is a risk of gas explosion when using methane for the experiment. Helium gas was used for the experiment to check the safety of the experiment and to know the preliminary concentration. The helium gas behavior at heading face when the roadway is horizontal and the sensors aperture were downside (experiment 7) is shown in Fig. 11. The results of computer simulation for the same condition is shown in Fig. 12. The computer simulation shows good agreement with that by the experiment. The good agreement is also seen for the inclined roadway conditions. The concentration by helium gas is relatively 20% higher than that for the methane experiment.
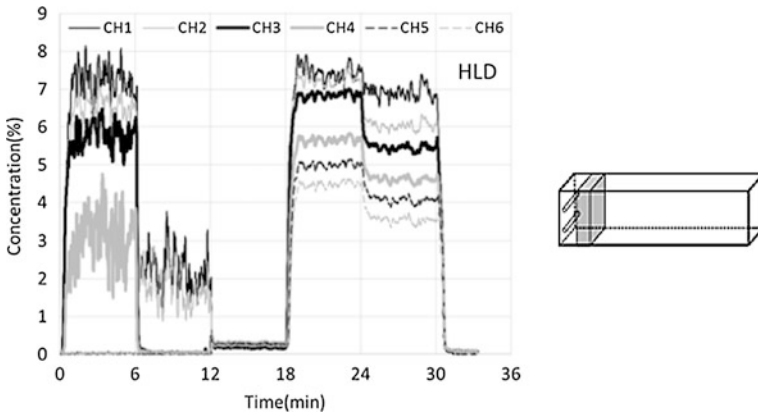


**Fig. 11.** Helium gas concentration in the horizontal roadway when sensors aperture were downside
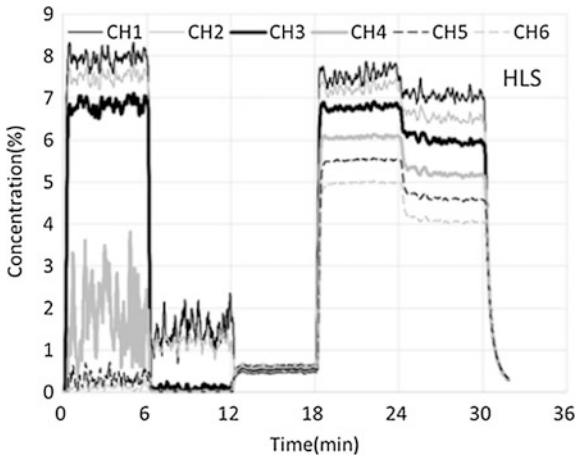


**Fig. 12.**  Helium gas concentration in the horizontal roadway by computer simulation

# 6   Conclusion

A series of experiments using a small scale face model and computer simulations were conducted to know the methane gas behavior at the heading face when the local ventilation stops by sudden electric shut down. The followings were found for the ventilation stop incident.

(1) It will be dangerous within 10 min if ventilation stops. Prompt measure is necessary.
(2) Methane gas accumulates in a short time, become extremely dangerous at upward headings.
(3) Although limited, methane concentration will decrease slightly if an air mover is available when ventilation stops.
(4) Methane is thought to be diluted easily downward headings due buoyancy effect. but experiment/simulation shows the mixing effect is modest, with concentration, decreasing only by 15% compared to horizontal airways.
(5) Even if helium is used instead of methane, reasonable results are obtained.
(6) If a proper model can be made, the computer simulation can reproduce the experiment result well.

The model roadway length is limited to 75 cm from the face for the safety reason. It might affect the results in some degree which tends to let the gas easier to flow away from inside.

# References

1. Moloney, K., Lowndes, I., Hargrave, G.: Analysis of flow patterns in drivages with auxiliary ventilation. Trans. Inst. Min. Metall. **108**, A17–A26 (1999)
2. Nakayama, S., Ichinose, M., Uchino, K., Inoue, M.: Scale tests, in-situ measurements and simulation of methane gas distribution at heading faces. In: Proceedings of the 8th US Mine Ventilation Congress, pp. 187–192. Rolla, USA (1999)
3. Tomita, S., Uchino, K., Inoue, M.: Methane concentration at heading faces with auxiliary ventilation. In: Proceedings of the 8th US Mine Ventilation Congress, pp. 187–192. Rolla, USA (1999)
4. Uchino, K., Inoue, M.: Auxiliary ventilation at heading faces by a fan. In: Proceedings of the 6th International Mine Ventilation Congress, vol. 68, pp. 211–234, 493–496. Pittsburgh, USA (1997)

# Methods of Methane Control
# in Polish Coal Mines

Nikodem Szlązak, Dariusz Obracaj[(✉)], and Justyna Swolkień

AGH University of Science and Technology, al. Mickiewicza 30,
30-059 Kraków, Poland
obracaj@agh.edu.pl

**Abstract.** The state of methane control in Polish coal mines is presented in this paper. The ventilation systems of longwall panels are discussed. The necessity of methane drainage usage is emphasised. Those methods should be adapted with respect to the panel ventilation system. The effectiveness of methane drainage relating to using both the methane drainage method and the panel ventilation system, has been described. The principles of methane drainage planning are formulated, as well as practical guidance is given. It should contribute to effective methane drainage in the conditions of Polish coal mines. It is proposed to choose the ventilation and methane drainage systems for longwall panel depending on the predicted methane emission.

**Keywords:** Multi-Seam mining · Methane control · Methane drainage

## 1   Introduction

The main sources of methane are coal seams because it is autochthonous gas and it is closely related to the coalification process of coal beds in late Carboniferous times. Methane content in the coal seams depends on numerous factors; mainly on the presence or lack of impermeable sediments in overburden that allow or not on degasification and migration of methane into surrounding rocks, where it has been trapped in the pore spaces and structures of methane-bearing strata.

Polish collieries extract coal bed primarily in the Upper Silesian Coal Basin (USCB), which is characterized by a diversity of coalbed methane occurrences and various methane content in coal seams lying in different parts of the basin. Gas contents in the multi-seams vary greatly, both vertically and horizontally. Generally, methane quantities in coal increase with depth with the most gas-rich interval occurring between 500 and 1100 m below the ground. Methane contents in the coal seams range between 0.01 and 1.00 $m^3$/t coal daf in the shallower strata and up to 20 $m^3$/t coal daf in coal seams at the depth 1200 m below the ground surface at the south part of the USCB. The average methane content in coal seams of gassy mines in the south of the USCB is around 10 $m^3$/t coal daf.

Hence, there is a very large range of methane content in coal seams of multi-seam mining in Poland. There are coal seams without impermeable overburden containing only trace amounts of methane. But, there are also coal seams with high methane contents underneath the overlying impermeable thick siltstone or claystone layers.

Conducting mining operations in coal seams with high methane content without using special measures to control methane (ventilation, methane drainage) could be impossible. The control of methane emission also depends on other co-occurring natural threats (*spontaneous fires and heat stress*) for which used preventive actions eliminate methane hazard prevention [1–3].

Safety in mines excavating coal seams with high methane content depends on the correct estimation of methane hazard, drawn up predictions of methane release, conducted observations, methane control as well as undertaken prevention measures.

Predictive methane action includes identification and control methods of methane emission as well as the means of combating the explosive accumulation of methane in workings.

## 2   State of Methane Hazard in Polish Hard Coal Mines

Methane in coal seams constitutes a serious threat to safety in underground coal mines. Geological conditions of methane occurrence in coal seams, as well as the low permeability of Polish coal, without mining exploitation, cause the low methane release. The amount of methane released is closely related with the range of conducted mining works; actual exploitation as well as excavation in site construction [4, 5].

During the past five years there have been 19 accidents connected with ignitions or explosions of methane; resulting in 6 miners losing their lives, 15 were seriously injured, and 20 were slightly wounded. These events occurred in longwall panels using U as well as Y ventilation systems (Table 1). Methane ignition was one of the main reasons for the 5 accidents in 2016 in the Polish mining industry. One of the miners lost his life in one of these accidents (Murcki-Staszic Colliery—Operation Staszic) [6].

In Poland in 2016, coal extraction amounted to 70.4 million tonnes (according to the Industrial Development Agency). During coal production, about 933.8 million $m^3$ of methane was emitted (total methane emission) thus meaning 1771.7 $m^3CH_4$/min (including 1122.65 $m^3CH_4$/min was emitted along with the ventilation air). The mines with the highest total methane emission in 2016 are as follows: Budryk Colliery—277.82 $m^3CH_4$/min, Pniówek Colliery—197.25 $m^3CH_4$/min and Borynia-Zofiowka-Jastrzebie Colliery—189.68 $m^3CH_4$/min. In years 2012–2016 relative methane emission oscillated between 10.5 and 13.3 $m^3CH_4$/t [6, 7].

Table 2 presents the development of methane emission in Polish coal mines in years 2006–2016 [6, 7] and the amount of methane captured by the drainage system and utilised. The increase of methane emissions, despite the decline of coal output, has been observed in recent years. That tendency is caused by the higher methane content of the coal seams as well as increased mining of methane prone coal seams.

Table 3 presents the methane emission from hard coal mines and the methane drainage efficiency in 2016. The average methane drainage efficiency in 2016 was approximately 36.6%, and the average methane utilisation was equal to 57%. What follows is that the past three years have seen a decrease in effective methane utilisation by almost 10.8%.

**Table 1.** List of events related to methane ignition in Polish hard coal mines in the years 2013–2016 [6]

| Coal Mine | Year | Cause of an accident |
|---|---|---|
| Murcki-Staszic—O. Staszic | 2013 | Methane ignition from sparks resulting from cutting a strong roof layer by a shearer |
| Murcki-Staszic—O. Staszic | 2013 | Methane ignition from the friction of the conveyor elements to sandstone blocks under the shearer |
| Rydultowy—Anna | 2013 | Methane ignition from sparks resulting from cutting a strong roof layer by a shearer |
| Knurow-Szczyglowice—O. Szczyglowice | 2013 | Methane ignition from sparks resulting from cutting a strong roof layer by a shearer |
| Sosnica-Makoszowy—O. Sosnica | 2013 | The appearance of an open fire |
| Sośnica-Makoszowy—O. Sosnica | 2013 | Local heating of cracked coal in the fence and sparking caused by the caving of strong roof rocks |
| Borynia-Zofiowka-Jastrzebie—O. Zofiowka | 2013 | Methane ignition from sparks resulting from cutting a strong roof layer by a shearer |
| Chwalowice | 2014 | The cause of methane ignition was conducting blasting works in the area of the intersection with the longwall face to force the caving of roof rocks |
| Budryk | 2014 | Sparks created as a result of cutting a strong roof layer by a roadheader |
| Bielszowice | 2014 | Sparks created as a result of a cutting strong roof layer by a roadheader |
| Myslowice-Wesola—O. Wesola | 2014 | The commission appointed by the President of the State Mining Authority found that the cause of methane ignition was endogenous fire |
| Sosnica | 2015 | Methane ignition and fire occurred in the area of the intersection of a tailgate roadway n108 with the face n108 in the 408/4 seam, at the level of 950 m |
| Myslowice-Wesola—O. Wesola | 2015 | A dangerous event took place in the 01Aw longwall Face in the start-up phase, in seam 510, at the level of 665 m |
| Rydultowy-Anna | 2015 | The fire occurred in the roadway7a-E1, behind the line of the VIII-E1 longwall face in seam 703/1, level 1067 m |
| Ruda—O. Halemba | 2016 | Sparks created during the cut strong rock by a shearer in the fault zone |
| Krupinski | 2016 | Sparks created during the cut strong rock by a shearer in the fault zone |
| Murcki-Staszic—O. Staszic | 2016 | Igniting methane by sparks created during the cut strong rock prone to sparking by a roadheader |
| ZG Brzeszcze | 2016 | Igniting methane by sparks created during the cut strong rock prone to sparking by a roadheader |
| Murcki-Staszic—O. Staszic | 2016 | The appearance of an open fire on the upcast shaft bottom due to the ignition of the considerable volume of methane flowing from the suddenly unseal area |

**Table 2.** The balance of methane emissions in Polish hard coal mining for the last 5 years [6, 7]

| Methane emission | Year | | | | | | | | | |
|---|---|---|---|---|---|---|---|---|---|---|
| | 2007 | 2008 | 2009 | 2010 | 2011 | 2012 | 2013 | 2014 | 2015 | 2016 |
| Total methane emissions, million m³/year | 878.9 | 880.9 | 855.7 | 834.9 | 828.8 | 828.2 | 847.8 | 891.1 | 933.0 | 933.8 |
| Ventilation air methane, million m³/year | 610.1 | 606.7 | 595.9 | 579.0 | 578.6 | 561.5 | 581.7 | 570.1 | 594.0 | 591.7 |
| Methane obtained from the drainage system, million m³/year | 268.8 | 274.2 | 259.8 | 255.9 | 250.2 | 266.7 | 276.6 | 321.0 | 339.0 | 342.1 |
| Amount of utilized methane, million m³/year | 165.7 | 156.5 | 159.5 | 161.1 | 166.3 | 178.6 | 187.7 | 211.4 | 197.1 | 195.0 |
| Methane emission to the atmosphere, million m³/year (*line 2 + line 3-line 4*) | 713.2 | 724.4 | 690.7 | 673.8 | 662.5 | 649.6 | 660.1 | 679.7 | 735.9 | 738.8 |
| Coal output, million tonnes | 87.4 | 83.6 | 77.3 | 76.1 | 75.5 | 79.2 | 76.5 | 72.5 | 72.2 | 70.4 |

In the coming years of exploitation in Polish mines, it is expected that the methane emission will remain at a similar level. This will make the methane hazard still dominant in coal mines in Poland. Safe exploitation will be ensured only if the predictive methane action will be properly selected. The selection of methane prevention is closely related to longwall ventilation systems. The ventilation system should be dependent on predicted gas emission and chosen at the design stage.

## 3   Longwall Ventilation Systems

In Polish coal mines, the retreat longwall system is commonly used. It allows getting high output concentration at relatively low investment outlays. The exploitation system requires the appropriate selection of a longwall panel ventilation system.

In Polish hard coal mines, there is still a mistaken belief that the system of ventilation depends on the development of longwall operations in the coal deposit and the progress of development works as well as operating variables related to the coal output, direction of haulage, transport of materials, power supply, etc. In fact, the choice of ventilation system should be determined by the condition of predicted aerological threats in mines (gas emanation from strata, gas and rock outbursts, spontaneous fires, heat stress) and should take place at the stage of design development works. The decisive factor should be the coexistence of methane emission with the threat of endogenous fires and temperature risk.

**Table 3.** Methane emission in hard coal mines and the drainage efficiency in year 2016 [1]

| Coal Mine | Methane emission | | | | | | Drainage efficiency (%) |
| | Methane drainage system | | Ventilation air methane | | Total | | |
| | m³CH₄/min | mln m³CH₄/year | m³CH₄/min | mln m³CH₄/year | m³CH₄/min | mln m³CH₄/year | |
|---|---|---|---|---|---|---|---|
| Ruda—O. Bielszowice | 6.05 | 3.19 | 27.4 | 14.44 | 33.45 | 17.63 | 18.09 |
| Ruda—O. Halemba | 3.57 | 1.88 | 26.3 | 13.86 | 29.86 | 15.74 | 11.94 |
| Ruda—O. Pokoj | – | – | 2.66 | 1.4 | 2.66 | 1.4 | – |
| ROW—O. Jankowice | 11.95 | 6.3 | 37.78 | 19.91 | 49.73 | 26.21 | 24.04 |
| ROW—O. Chwalowice | 7.29 | 3.84 | 18.59 | 9.8 | 25.88 | 13.64 | 28.15 |
| ROW—O. Marcel | 10.95 | 5.77 | 28.38 | 14.96 | 39.33 | 20.73 | 27.83 |
| ROW—O. Rydultowy | 16.41 | 8.65 | 33.51 | 17.66 | 49.92 | 26.31 | 32.88 |
| Budryk | 130.73 | 68.9 | 147.09 | 77.52 | 277.82 | 146.42 | 47.06 |
| Knurow-Szczyglowice | 54 | 28.46 | 55.37 | 29.18 | 109.37 | 57.64 | 49.38 |
| Sosnica | 15.81 | 8.33 | 40.83 | 21.52 | 56.64 | 29.85 | 27.91 |
| Makoszowy | – | – | 0.78 | 0.41 | 0.78 | 0.41 | – |
| Boleslaw Smialy | – | – | 3.52 | 1.85 | 3.52 | 1.85 | – |
| Brzeszcze | 52.52 | 27.68 | 94.91 | 50.02 | 147.43 | 77.7 | 35.62 |
| Silesia | 34.49 | 18.18 | 37.8 | 19.92 | 72.29 | 38.1 | 47.72 |
| Murcki-Staszic | 27.68 | 14.59 | 54.57 | 28.76 | 82.25 | 43.35 | 33.66 |
| Myslowice-Wesola | 42.75 | 22.53 | 115.8 | 61.03 | 158.55 | 83.56 | 26.96 |
| Wujek | 20.68 | 10.9 | 22.6 | 11.91 | 43.28 | 22.81 | 47.79 |
| Wieczorek | – | – | 38.95 | 20.53 | 38.95 | 20.53 | – |
| Boze Dary | – | – | 3.4 | 1.79 | 3.4 | 1.79 | – |
| Anna | – | – | 3.36 | 1.77 | 3.36 | 1.77 | – |
| Brzeszcze-Wschod | – | – | 17.42 | 9.18 | 17.42 | 9.18 | – |

**Table 3.** (*continued*)

| Coal Mine | Methane emission | | | | | | Drainage efficiency (%) |
|---|---|---|---|---|---|---|---|
| | Methane drainage system | | Ventilation air methane | | Total | | |
| | $m^3CH_4/$ min | mln m$^3$CH$_4$/year | $m^3CH_4/$ min | mln m$^3$CH$_4$/year | $m^3CH_4/$ min | mln m$^3$CH$_4$/year | |
| Borynia-Zofiowka-Jastrzebie | 60.36 | 31.81 | 129.33 | 68.16 | 189.68 | 99.97 | 31.82 |
| Pniowek | 64.51 | 34 | 132.74 | 69.96 | 197.25 | 103.96 | 32.7 |
| Krupinski | 89.31 | 47.07 | 52.88 | 27.87 | 142.19 | 74.94 | 62.81 |
| **Total** | **649.06** | **342.08** | **1122.65** | **591.68** | **1771.71** | **933.76** | – |

The most frequently used ventilation systems for retreat longwall panels at the moment are (Fig. 1):

– a U ventilation system,
– a U ventilation system with parallel return roadway,
– a Y ventilation system:
  • return side ventilation system,
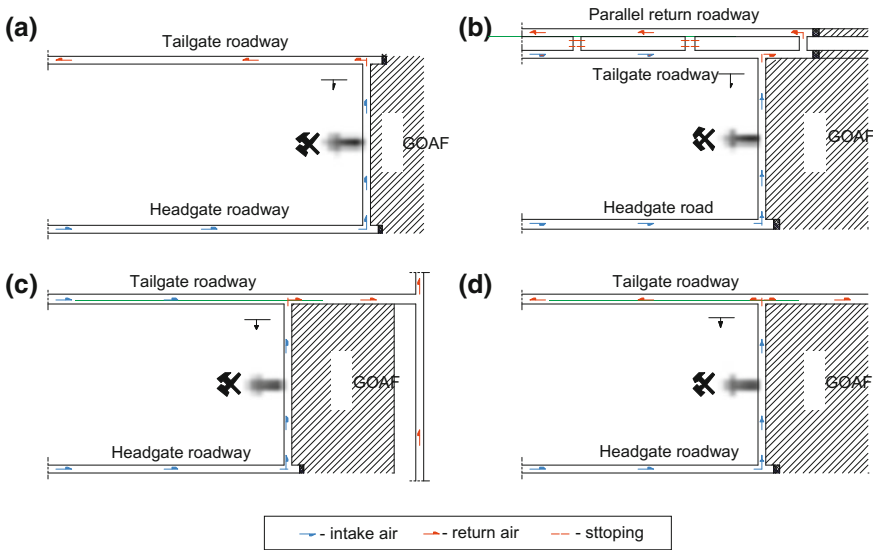  • with return air distribution in two directions (bleeder system).



**Fig. 1.** The most popular panel ventilation systems in Polish hard coal mines: **a** U ventilation system, **b** U ventilation system with parallel return roadway, **c** Y—return side ventilation system, and **d** Y—with return air distribution in two directions (bleeder system) [4, 11]

The paper presents mainly used ventilation systems and the principles of their selection depending on natural threats.

In Polish gassy mines, a number of preventive measures are used to conduct safe longwall mining. Among them. one can mention intensive ventilation, methane drainage, methane monitoring and the use of additional ventilation devices [4, 5, 8].

Intensive ventilation is conducted in order to dilute methane emitted to workings so that its concentration drops to the level required by the mining regulations aimed at guaranteeing work safety. However, such ventilation is often either insufficient to ensure planned mining parameters or impossible to be employed without additional preventive measures. Therefore, methane drainage is implemented in coal mines either before or during mining activities [1–3, 7, 9]. Geological properties (porosity. permeability. reservoir pressure. diffusivity) of coal seams. Coalbed methane content and low desorption of Polish coal seams results in low gas emission without disturbing the structure of strata. Therefore, the amount of released methane is closely connected with

the range and scale of mining activities, both during the development stage and during mining proper [10].

The U ventilation system for retreating longwall panels limits the control of methane emission due to the lack of possibilities of effective methane drainage [4, 5, 8, 11–13]. Especially difficult is methane controlling in low height faces because of difficulties in supplying the required airflow in the face.

The system effectively limits the progress of coal spontaneous combustion. It ensures limited airflow through goaf and lowers the spontaneous fire only in the case of proper longwall face advance rate. The complicated tectonics of seams and geological disturbances might cause problems in obtaining the extraction advance that minimises fire risk. In the case of spontaneous fire in goaf of longwall panel, this system reduces the possibilities of its elimination. In the case when there is serious methane hazard with limited face advance rate and spontaneous combustion of coal occurs, this system makes it difficult to effectively combat with co-occurring threats.

It is necessary to apply additional solutions and ventilation devices that do not completely bring the expected results. An example is the use of an additional force ductline in the tailgate road which supplies fresh air to the tail gate of the face. The fresh air flowing out of the ductline should dilute the methane in the zone of the tail gate. This solution should be used when operating low-height panels, when there is no possibility of increasing the airflow in the face. However, it was widely used for all panels and assumed in technical projects. The correct approach is to calculate the required airflow in the face and to carry out such regulation in the ventilation network so that this airflow is ensured. The use of ductlines with fresh air should be treated as an additional, not as the main protection against methane emission in the zone of the face outlet.

It happens that methane emission to the airways during exploitation is significantly higher than estimated in the technical project. Therefore, the replacing classic U system with parallel return roadway is necessary but generates additional costs (second return roadway).

The U ventilation system in Polish coal mining is generally used in longwall panels classified under categories of I and II of methane hazard (Polish classification of methane hazard in coal mines); while categories of III and IV and high methane emission require its use in combination with effective methane drainage [4, 14].

The Y ventilation system (various types) is used to control methane in longwall panels with high methane emission. The system is appropriate for either gassy or non-gassy longwall panels, or panels with or without high spontaneous combustion risk coal. Also, these longwall panels achieve the record level of advance rates and coal output

The Y return side ventilation system is used for panels in low thickness seams with high methane emission. It allows to move methane concentration towards goaf from longwall face. Intake air is supplied by two roadways (headgate road and tailgate road). After the longwall face is ventilated, the gasses are mixed with fresh air and removed to the return airway. The Y ventilation system with return air distribution in two directions (bleeder system) is convenient for longwall panels of low and medium thickness of coal seams [8].

The U ventilation system with parallel return roadway is used in conditions of very high predicted methane emission. Intake air is supplied to the longwall face through two roadways: the headgate roadway and the interior tailgate roadway, and return air flows through the second (upperlying) tailgate road sometimes termed the exterior return roadway. The main advantage of this system is the possibility of extra airflow supply which affects the limit of methane concentrations, possibility of controlling airflow in the longwall and convenience in draining methane of over- and underlying coal seams.

## 4    Systems of Longwall Methane Drainage

Methane drainage of strata with multiple coal seams is the most effective method of controlling methane emission to longwall face. The method that has proved the most efficient is draining methane from surrounding coal seams and goaf of longwall and transporting it to the surface through pipelines, using the negative pressure from drainage station pumps. Although this method ensures the desired parametres of ventilation, it imposes certain requirements concerning the development works in gassy coal seams.

There are two methods of methane drainage in so far applied technologies. The first method involves drilling cross-measure boreholes, called methane boreholes, from the roadways to the de-stressed zone at roof or at floor layers of a developed seam. The location and parametres of the boreholes depend on the exploitation and ventilation system of the longwall panel.

The second method involves drilling drainage heading in overworked or under-worked seams, therefore it is called the overlying or underlying drainage method.

In order to implement methane drainage in adjacent (overlying and underlying) coal seams, it is necessary to determine the boundaries of the desorption zone created by exploiting the longwall. Drainage boreholes should be positioned in the de-stressed zone without overlapping with the goaf area [12]. Under the geological conditions prevalent in Poland, accurate results of calculating the slope angles of drainage boreholes are presented in Fig. 2.

The location of drilled boreholes is dependent on the exploitation and ventilation systems of longwalls. The results of drainage efficiency in longwall workings with different variation of ventilation systems were presented in publications [4, 11, 15].

The concluded analysis [4, 13] has shown that the highest efficiency of methane drainage has been achieved by means of the U ventilation system with the parallel return roadway and classic U system with the overlying drainage gallery. When a typical Y system of ventilation is implemented, the air-tightness of boreholes drilled from the tailgate roadway behind the longwall front diminishes over time. It is caused by the progressing degradation of the tailgate roadway and the fact that casing pipes are placed in the immediate proximity of the goaf. By contrast, parallel return roadways leave a coal pillar between them, which makes it possible to achieve enduring air-tightness of casing pipes, resulting in a mixture of gases with higher methane concentration.
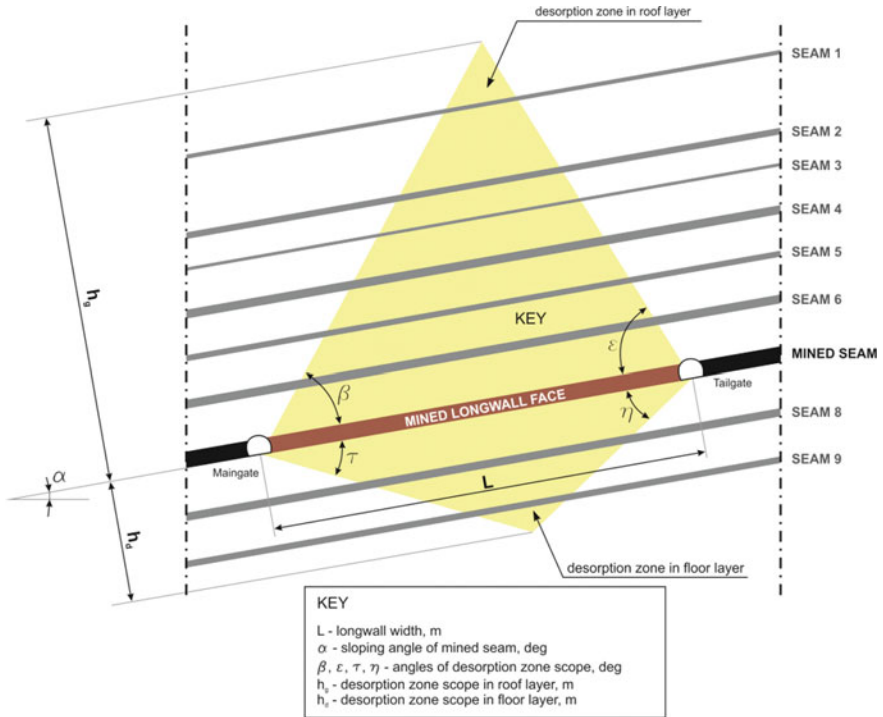
**Fig. 2.** Determining the methane desorption zone during mining a longwall based on work by G. Flügge'a [4, 11]

Table 4 presents the average efficiency of methane drainage in the last 10 years in Polish coal mines depending on overall methane emission at longwall panel.

**Table 4.** The average efficiency of methane drainage of longwalls for different ventilation and methane drainage systems in the last 10 years

| Longwall ventilation system | Overall methane emission around longwall mining panel, $m^3CH_4/min$ | | | | | | | | | Average drainage efficiency (%) |
|---|---|---|---|---|---|---|---|---|---|---|
| | <10 | 10–20 | 20–30 | 30–40 | 40–50 | 50–60 | 60–70 | 70–80 | >80 | |
| U ventilation system | 38.5 | 39.0 | 40.6 | **38.3** | **48.8** | **64.0** | x | x | x | 41.2 |
| Y ventilation system | 33.8 | 43.7 | 52.4 | 56.1 | 49.9 | **46.2** | **57.9** | x | x | 48.7 |
| U ventilation system with a parallel return roadway | x | x | 58.0 | 60.1 | 62.2 | 64.2 | 64.5 | 68.3 | 71.5 | 63.9 |
| U ventilation system with drainage heading | 49.0 | 58.6 | 60.2 | 62.6 | 68.4 | 64.7 | 68.6 | 68.8 | 76.0 | 63.4 |

x—means that this type of drainage system was not used in the cretin range of overall methane emission

The average methane drainage efficiency in the last 10 years was 54%. The lowest methane drainage efficiency of 41% was obtained in panels with a U system. The highest average methane drainage efficiency, which was equal to 63%, was obtained in longwalls with U a ventilation system with a parallel tailgate roadway and an overlying drainage heading. In longwalls ventilated with a Y system, methane drainage efficiency amounted to 49%.

In Table 4 the bold values presents the efficiency of methane drainage, which do not provide safe work conditions due to high methane emission. Regarding the efficiency of methane drainage that has been obtained, the ventilation air methane (VAM) in longwall panels with a U ventilation system should not exceed 15 m$^3$CH$_4$/min.

## 5  Recommendations for Exploitation Design Process Having Regards to "Aerological Threats"

Planning of a specific coal extraction should be a multiple stage process and executed in the right order with respect to the security of all mining operations. Figure 3 presents the algorithm of exploitation design. It consist of (see Fig. 3):

- A preliminary identification of threats—assessment made on the basis of specific natural conditions and mining works carried out so far in the area.
- Preparation of a conceptual design of the exploitation—selection of an exploitation system, technical equipment, technology and a production plan.
- A detailed diagnosis of hazards—it is the preparation of the forecast concerning the threat development, taking into account the results of the first phase of identification, conditions of preliminary project and design of a hazard monitoring system (kind and location of sensors, safety systems, etc.).
- Revisions of design intents—following the verification of conceptual design criteria with threat forecasts and monitoring the project after making the necessary changes.
- Planning of preventive works to reduce different threats—including corrected design assumptions and the dominant threat.
- Preparation of the technical project—following the verification of design assumptions with plans of preventive works after making the necessary changes.

This planning mode tends to eliminate or at least reduce the unpredictability that usually results in financial loss or even dangerous accidents.

In the case of methane emission, a great role in designing of a coal-seam panels development is played by the possibility of methane drainage using. The project must take into account other occurring hazards (see Fig. 3), the general safety of works and cost optimization. The pre-design analysis should be conducted taking into consideration a range of different issues, such as:

- natural conditions (e.g. structure of the strata, parameters of the coal seam).
- forecasting the level of identified threats for the exploitation period (methane emission, spontaneous fires).
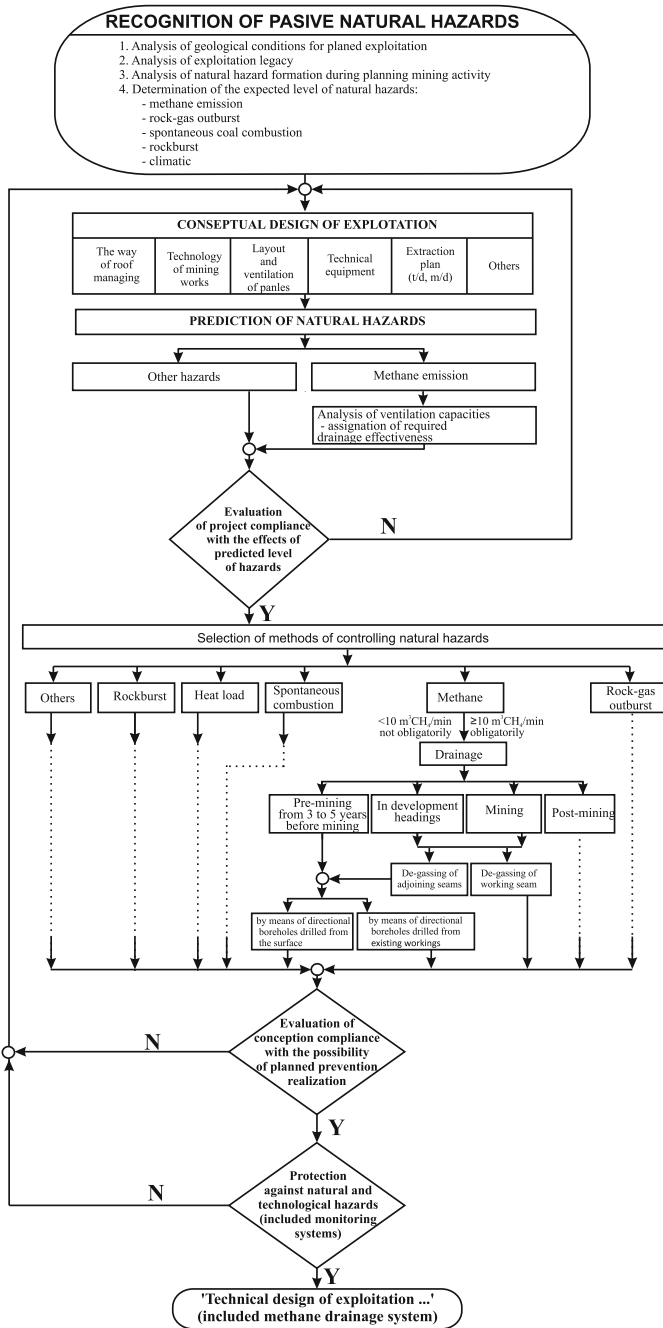
**RECOGNITION OF PASIVE NATURAL HAZARDS**

1. Analysis of geological conditions for planed exploitation
2. Analysis of exploitation legacy
3. Analysis of natural hazard formation during planning mining activity
4. Determination of the expected level of natural hazards:
   - methane emission
   - rock-gas outburst
   - spontaneous coal combustion
   - rockburst
   - climatic

**CONSEPTUAL DESIGN OF EXPLOTATION**

| The way of roof managing | Technology of mining works | Layout and ventilation of panles | Technical equipment | Extraction plan (t/d, m/d) | Others |

**PREDICTION OF NATURAL HAZARDS**

Other hazards

Methane emission

Analysis of ventilation capacities
- assignation of required drainage effectiveness

Evaluation of project compliance with the effects of predicted level of hazards

N

Y

Selection of methods of controlling natural hazards

Others | Rockburst | Heat load | Spontaneous combustion | Methane | Rock-gas outburst

<10 m³CH₄/min not obligatorily | ≥10 m³CH₄/min obligatorily

Drainage

Pre-mining from 3 to 5 years before mining | In development headings | Mining | Post-mining

De-gassing of adjoining seams | De-gassing of working seam

by means of directional boreholes drilled from the surface | by means of directional boreholes drilled from existing workings

Evaluation of conception compliance with the possibility of planned prevention realization

N

Y

Protection against natural and technological hazards (included monitoring systems)

N

Y

'Technical design of exploitation ...' (included methane drainage system)

**Fig. 3.** Drainage in the algorithm of the exploitation design

– the impact of human factors on reducing the level of threats (e.g. at the stage of identifying and forecasting the level of threats, designing exploitation and preventive works).
– the technical and technological level of conducted works (e.g. modernity and the quality of machinery and equipment, mine excavation support, mining system).
– planning the recognition of the actual level of threats present during face advance (e.g. the method of control and system monitoring of the mining area in terms of equipment and parameters of dangerous factors).
– predictability of dangerous events (e.g. rock bursts, spontaneous fires, explosions).

Guidelines on planned coal exploitation, taking into account the methane hazard, may be specified as follows:

• Before starting the design process of exploitation in new coal seams, the level of natural hazards, that save as the basis for a conceptual design, should be identified.
• The conceptual design for a coal seam's extraction or its parts classified under category II of methane hazard must include the prediction of the methane emission rate that determines the selection of the ventilation system and the development of guidance on the prevention of methane hazard.
• The technical project should contain the further detailed prediction of methane emission rate together with the possible ventilation solutions to combat the hazard.
• The longwall workings with overall methane emission estimated to be greater than $10 \text{ m}^3 \text{CH}_4/\text{min}$ should be equipped with methane drainage systems. Methane drainage of the longwall workings can be conducted if the predicted overall methane emission rate is lower than $10 \text{ m}^3 \text{CH}_4/\text{min}$—depending on the mining and geological conditions.

To effectively fight methane hazard and successfully conduct methane drainage, one of four ventilation systems may be applied. The principle of proper choice of methane drainage and ventilation systems can be indicated on the basis of the results presented in Table 4:

– a U ventilation system with the predicted overall methane emission rate up to $25 \text{ m}^3 \text{CH}_4/\text{min}$,
– a Y ventilation system with the predicted overall methane emission rate up to $50 \text{ m}^3 \text{CH}_4/\text{min}$,
– a U ventilation system with a parallel return roadway with the predicted overall methane emission rate exceeding $25 \text{ m}^3 \text{CH}_4/\text{min}$,
– a U ventilation system with a drainage heading with the predicted overall methane emission rate exceeding $25 \text{ m}^3 \text{CH}_4/\text{min}$.

A system with a methane drainage heading can be used if above the mined coal seam there is one non-balanced seam and it is situated at a distance corresponding to 5 times the thickness of the mined seam (however, not less than 12 m above the mined one). In other cases, it is considered not to be appropriate to use this system.

The selection of parameters and location of the cross-measure boreholes should be dependent on the chosen longwall ventilation system, predicted methane emission and determined methane degasification zone, also termed the "desorption" zone.

A methane drainage project should include:

– calculations of the required pressure in boreholes,
– dimensioning of the installation together with the selection of regulatory elements (adjustable gates),
– the selection of the monitoring and controlling system of the gas mixture flow in the methane drainage network.

Every time after the identification of the required quantity of methane captured in new ventilation areas. a mine methane drainage network should be tested in regard to its methane-capture capability. The needed value of the gas pressure (negative pressure) is required to generate any desired flow rate of gas mixture (methane-air mixture) and the required pressure (negative pressure) in one borehole or in all boreholes fitted with packers.

## 6   Conclusions

Methane emission in Polish mines has been growing for several years due to the share of the number of gassy coal seams in the exploitation of coal deposits. However, it is expected that the level of methane emission will be maintained at a similar level in the following years. Therefore, methane emission will still be the dominant threat in Polish hard coal mining.

Before starting the design process of exploitation in new coal seams, the level of natural threats (rock burst, spontaneous fire, methane release, climatic conditions), that save as the basis for a conceptual design, should be identified. The conceptual design for a coal seam's extraction or its parts with methane content above 4.5 $m^3$/t coal daf, must include the prediction of the methane emission rate, that determines the selection of the ventilation system and development of guidance on the prevention of methane hazard.

Design and planning of longwall panels in Polish coal mines should contain the further detailed prediction of methane emission rate together with the possible ventilation solutions to combat the danger of methane explosion. Therefore, it is suggested that the longwall panels with overall methane emission rate estimated to be greater than 10 $m^3CH_4$/min should be equipped with methane drainage systems. Depending on the mining and geological conditions, methane drainage of the longwall panels may be conducted if the predicted gas emission rate is lower than 10 $m^3CH_4$/min.

To effectively control of methane and successfully conduct methane drainage, one of four ventilation systems may be applied in Polish mine conditions, according to the following conditions:

– a U ventilation system with the predicted overall methane emission rate up to 25 $m^3CH_4$/min,
– a Y ventilation system with the predicted overall methane emission rate up to 50 $m^3CH_4$/min,
– a U ventilation system with a parallel return roadway with the predicted overall methane emission rate exceeding 25 $m^3CH_4$/min

– a U ventilation system with drainage heading with the predicted overall methane emission rate exceeding 25 m$^3$CH$_4$/min.

Methane drainage by means of the U ventilation system with an overlying drainage heading can be used if above the mined coal seam there is thin one (not intended to be explored). The vertical distance between the worked seam and the drainage heading should not be less than the fivefold thickness of the worked seam and not less than 12 m. In other cases, the application of this method is no longer economically justified.

## References

1. Roszkowski, J., Szlązak, J., Szlązak, N.: Methane hazard in coal mines and its control. In: Proceedings of The 1th School of Mine Ventilation [Polish Mine Ventilation Conference]. Krakow, 10–13 October 1999. Publisher, Centrum Elektryfikacji i Automatyzacji Gornictwa EMAG., Katowice, Poland (1999) (Polish text)
2. Szlązak, N., Borowski, M., Obracaj, D., Swolkień, J., Korzec, M.: Comparison of methane drainage methods used in polish coal mine. Arch. Min. Sci. **59**(3), 655–675 (2014)
3. Szlązak, N., Korzec, M.: Zagrożenie metanowe oraz jego profilaktyka w aspekcie wykorzystania metanu w polskich kopalniach węgla kamiennego [Methane hazard and its prevention in aspects of the use of methane in Polish coal mines]. AGH J. Min. Geoeng. **34** (3/1), 163–174 (2010) (Krakow, Poland) (Polish text)
4. Szlązak, N., Borowski, M., Obracaj, D., Swolkień, J., Korzec M.: Odmetanowanie górotworu w kopalniach węgla kamiennego [Methane drainage in coal mines]. AGH University of Science and Technology Press, Krakow, Poland (2015) (Polish book)
5. Szlązak, N., Borowski, M., Obracaj, D., Swolkień, J., Korzec, M.: Metoda oznaczania metanonośności w pokładach węgla kamiennego [Method for determination of methane content in coal seams]. AGH University of Science and Technology Press, Krakow, Poland (2011) (Polish book)
6. SMA: Stan bezpieczeństwa i higieny pracy w górnictwie w latach 2010–2016. [Health and safety at work in Polish mining industry in 2010–2016]. Reports of the State Mining Authority SMA [Wyzszy Urzad Gorniczy], BIP 2010–2016, Katowice, Poland (2010–2016) (Polish text)
7. CMI: Raporty roczne o stanie podstawowych zagrożeń naturalnych i technicznych w górnictwie węgla kamiennego [Annual reports on the status of basic natural and technical hazards in hard coal mining]. Reports of Central Mining Institute (CMI). Katowice, Poland (2007–2016) (Polish text)
8. Szlązak, N., Borowski, M., Obracaj, D.: Kierunki zmian w systemach przewietrzania ścian eksploatacyjnych z uwagi na zwalczanie zagrożeń wentylacyjnych. Mineral Resources Management, vol. 24, issue ½ (2008) (Polish text)
9. Filipecki, J., Janowicz, E., Malina Z.: Efficient methods of methane drainage in rock masses of the coal mines "Brzeszcze-Silesia" Ruch I "Brzeszcze". In: Proceedings of the 4th School of Mine Ventilation [Polish Mine Ventilation Conference]. Krakow, 10–13 October 2006. Publisher, Centrum Elektryfikacji i Automatyzacji Gornictwa EMAG (2006) (Polish text)

10. Krause, E., Lukowicz, K.: Methane drainage in Polish hard coal mines achievements and perspectives. In: Proceedings of The 11th International Scientific and Technical Conference "Rockbursts 2004"—New solutions in the field of preventing rockbursts and methane hazards, pp. 8–10. November 2004, Ustron, Poland (2004) (Polish text)
11. Szlązak, N., Borowski, M., Obracaj, D., Swolkień, J., Korzec, M.: Selected issues related to methane hazard in hard coal mines. In: Szlązak N. (ed.) AGH University of Science and Technology Press, Krakow, Poland (2014)
12. Szlązak, N., Obracaj, D., Swolkień, J.: Methane drainage from roof strata using an overlying drainage gallery. Int. J. Coal Geol. **136**, 99–115 (2014)
13. Szlązak, N., Obracaj, D., Swolkień, J.: Possibilities of increasing the effectiveness of mining methane drainage in conditions of low permeability of coal seams. J. Energy Power Eng. **8** (7), 1167–1176 (2014)
14. Szlązak, N., Szlązak, J.: Dobór systemu przewietrzania ściany w aspekcie występujących zagrożeń naturalnych [Selection of a longwall panel's ventilation system in the aspect of natural hazards]. WUG a monthly published by the State Mining Authority, issue 9, pp. 17–22 (2001) (Polish text)
15. Szlązak, N., Obracaj, D., Borowski, M., Korzec, M., Swolkień, J.: Effectiveness of coal mine methane drainage in Polish mines. In: Proceedings of the Twenty-ninth Annual International Pittsburgh Coal Conference: Coal—Energy. Environment and Sustainable Development, Pittsburgh, USA, 15–18 October 2012 (2012)

# The Development of Coal Mine Drainage Monitoring System Based on DSP and PC

Xiaojuan Shi[(✉)], Dalong Nie, and Gaoyang Wang

School of Mechanical Engineering, Xi'an University of Science
and Technology, Xi'an 710054, China
xiaoshi0705@hotmail.com

**Abstract.** In order to solve at the problems of intensive labor, lower reliability and weak emergency ability associated with the current mine drainage system, combining with master PC, using DSP2812 as its control core, a master-slave mode mine drainage monitoring system has been developed. The hardware and software systems for modules of signal conditioning, water pump motor driving and communication of slave DSP2812 control system are modularly designed. The monitoring software interface of master PC is designed in VC++ programming language. Finally all functions of this monitoring system are validated through the experiment. This monitoring system can realize the function of real-time monitoring, display and alarm for water sump level, water pump outlet pressure, drainage pipeline flow and motor temperature. This monitoring system can control the start and stop of pump according to the variation of water sump level, and attain the aim of mine automatic drainage and real-time monitoring.

**Keywords:** Digital signal processor (DSP) · Coal mine drainage
Remote monitoring · Master-slave structure · PC interface

## 1 Introduction

For the safety of underground coal mines, the mine drainage system plays a very important role [1]. Its main task is timely and reliably to drain the mine waste water to the ground surface. The operation safety and reliability of drainage system is crucial to the production and other aspects of the mine [2]. At present, domestic and overseas coal mine enterprises commonly use three kinds of underground drainage methods. The first one is based on relay manual control mode [3]. In this mode, the pump start-stop and switching are all done manually. Staff based on past experiences to determine the rationality of some important parameters such as water level, water inflow and so on. This system has poor ability to handle emergency conditions and to implement automation, consequently supervision and control of the drainage system are not guaranteed. The safety and reliability of coal mine production and operation are greatly decreased. The second one is AT89C52 single-chip control system [4, 5] which has a lower data processing speed. The third one is PLC plus frequency converter control mode [6, 7]. This system starts and stops pump by controlling the AC motor and

basically implement function unattended. However, control algorithms is not attached with this system. Since the drainage system is rather complicated, the current monitoring system is unable to fully meet the practical production requirement and needs further improvement. In this paper, a mine drainage monitoring system based on DSP2812 is designed. It collects system signals by sensors such as liquid level, pressure and temperature, etc. It can monitor operating status of various equipment and water level information in real time. The characteristic parameters such as water level, motor temperature, water inflow can be transmitted to monitoring center and used as a reliable basis for starting and stopping the pump to ensure safe and efficient coal mine production.

## 2 Drainage System Overall Structure Design and Working Principle

The drainage system consists of three pump groups, three drainage lines, DSP2812 processor and monitoring sensors. Each pump group includes the main drainage pump, starting motor, jet pump, solenoid valve and so on. A liquid level sensor monitors the water sump level in real time and collects the water level signals as the main basis for starting and stopping the pump. When the water level reaches the preset warning level, the DSP2812 will output control signals to turn on the solenoid valve coil and to start the jet pump, then the main drainage pump will be in a vacuum state. When the pump inlet negative pressure reaches the system preset value monitored by the negative pressure sensor, the pump motor will start and the jet pump will be closed at the same time. When the pressure sensor detects that the outlet pressure reaches the system preset value, the outlet drainage gate valve will be open. When the water level drops below the safe level during the drainage process, the gate valve should be closed to prevent the pipeline "water hammer" from impacting the pump and shut off the pump motor at the same time. The control block diagram of the drainage system is shown in Fig. 1.
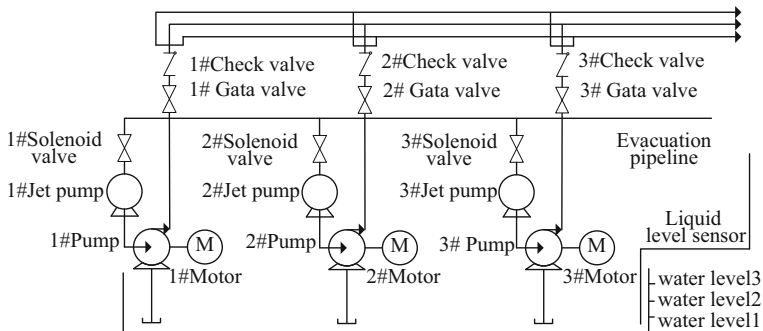


**Fig. 1.** Drainage system block diagram

## 3   Drainage Monitoring System Design

The design of this drainage monitoring system is based on DSP2812. This monitoring system has automatic control and overrun and fault alarm function. Its structure belongs to the master-slave structure type. The mast station system is upper PC monitoring system. The slave station system mainly consists of DSP2812 processor, a variety of monitoring sensors, analogue and digital input module, digital output module, the main drainage pump, jet pump, drain gate valve, solenoid valve, power supply and other parts. Drainage monitoring system block diagram is shown in Fig. 2.
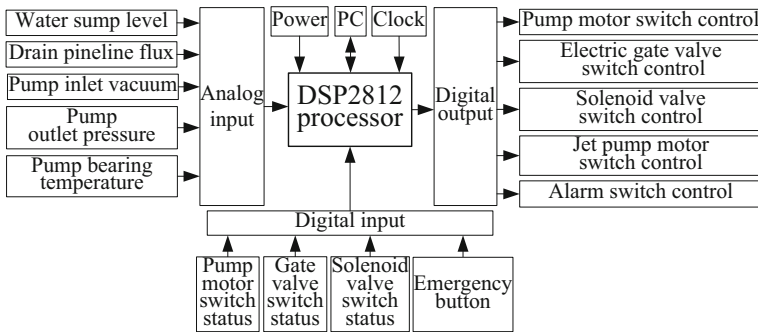


**Fig. 2.** Drainage monitoring system overall structure

The water level signal, the pump inlet negative pressure signal, motor bearing temperature signal and the drainage pipe flow signal collected by monitoring sensor are input to the A/D acquisition module through the signal conditioning circuit. These analogue signals are transmitted to the master computer through the internal A/D conversion module of DSP2812 processor. By comparing the conversion results with the master computer system settings, when signals such as water level exceeds the set value, sound and light alarm device will be triggered and the appropriate control will be sent through digital output module in real time. The variation trend of the various monitoring parameters can be presented in the PC monitoring interface in the form of curves.

### 3.1   Monitoring System Hardware Design

**Microprocessor**. DSP2812 is selected as the processor for this monitoring system. The frequency of this processor is up to 150 MHz. It has many useful resources integrated in the chip such as Flash, RAM memory resources, two serial communication interface (SCI), numerous serial peripheral interface (SPI), 12 bits with 16 conversion channels of ADC conversion module. The ADC module corresponds with event manager EVA/EVB and can be set to cascade mode to sample in sequence. Sampling two-way water level signal, one-way flow signal, four-way temperature signal, four-way inlet

negative pressure signal, four-way outlet pressure signal, the conversion results of these fifteen-way signals are automatically restored in corresponding result register (ADCRESULT0-14). The processor has 56 controllable GPIO ports. Among these GPIO ports, GPIOG4/F4 (transmission) and GPIOG5/F5 (reception) are set as special function ports. They are used as SCI communication interface to facilitate the control of external devices and to reduce the difficulty of the peripheral circuits design.

**Signal conditioning circuit**. After collecting the signals of water level, flow rate, temperature, pressure and etc., the sensor will output a relatively weak 4–20 mA current signal. If this weak current signal is directly performed A/D conversion, the conversion result will be small and the conversion accuracy could be low. Therefore, the 4–20 mA current signal output from the sensor is firstly converted into 0.3 V voltage signal via I/V switching circuit and then is magnified ten-fold via operational amplifier circuit. Finally 3 V output voltage is sent to A/D acquisition section. The series resistance R6 can increase the input impedance. The series diode D1 and D2 can constitute the limiter circuit to make sure that the input signal will be limited to a
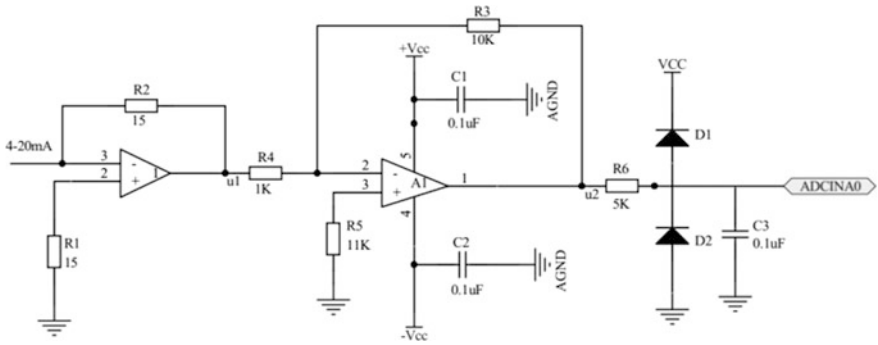


**Fig. 3.** Signal conditioning circuit schematic diagram

section between 0 and 3 V. Signal conditioning circuit is shown in Fig. 3.

The specific calculation step is as follows:

$$u_1 = -IR_2 = -0.02 \times 15 = -0.3 \text{ V} \tag{1}$$

$$u_2 = -((R_3/R_4) \times u_1) = -(10 \times (-0.3)) = 3 \text{ V} \tag{2}$$

**Serial communication**. The long-range communication adopts RS485 communication mode between the upper PC and the lower processor DSP2812. Because the master computer PC port is RS232 communication interface port, it can not realize long-distance data transmission. Through using RS232/485 converter to change the upper computer 232 electrical level into 485 electrical level, only a pair of shielded twisted pair are needed to complete communication. The maximum transmission distance of RS-485 is up to 1500 m. Since a typical coal mine has a long transmission

distance, 485 repeaters are added to establish communication nodes so as to realize remote communication [8]. In the same way, DSP2812 system has 232 port and also need RS232/485 converter to realize remote communication between PC and DSP
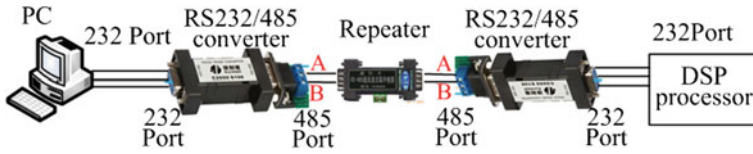


**Fig. 4.** Communication mode between PC and DSP system

control system. The master-slave double-computer communication mode diagram is shown in Fig. 4.

**Starting and stopping control of water pump motor**. The system output control object is the water pump, it can not be directly driven with the DSP pin. The relay power supply is 12 V, while the maximum power supply of the DSP2812 and I/O port output electric level are up to 3 V. In order to prevent the invasion of voltage higher than 3 V and the resulting damage of DSP, the output pulse control signal of DSP need through the photocoupling circuit. In relay control circuit design, the photoelectric coupler adopts TLP521 to realize the electrical isolation between input and output. The output of the control signal is connected to the input coil of the relay. When the input signal of the GPIO port is in low electric level, there will be current in the input coil and the relay will be pulled in. At the same time, the touch spot of contactor will be closed and drive the pump motor to run. When the input signal is high, there is no current in the coil. The relay will be disconnected and the contactor will be closed. So the pump motor and power supply will be disconnected to prevent it from being started. Pump motor driving circuit is shown in Fig. 5.
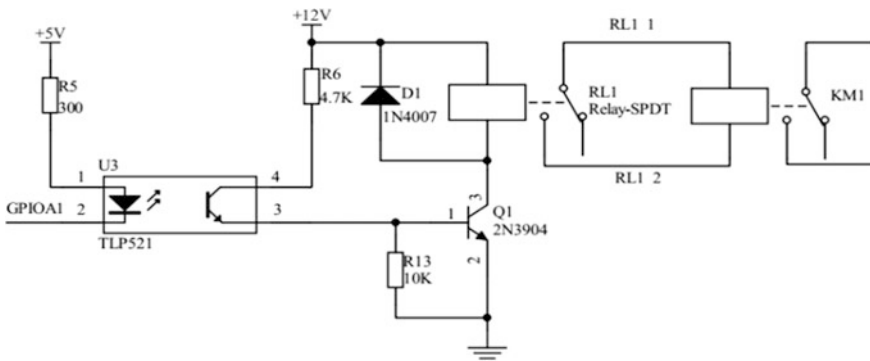


**Fig. 5.** Pump motor drive circuit schematic diagram

## 3.2 Monitoring System Software Design

**DSP software design**. The design of DSP system program adopts CCS6.0 software as the development platform and adopts C language as the program development tool. According to the water level information collected by the sensor, the main program of this system is designed to judge whether the alarming water level and the alarming grade of water level are reached. Then control the start and stop of water pump and make sure the number of operational water pump. Using modular design idea, the DSP system program is divided into the following four modules such as data acquisition module, LCD display module, output control module, control mode selection module. The main program flow chart of the system and start-stop control flow chart of the single water pump are respectively shown in Figs. 6 and 7.
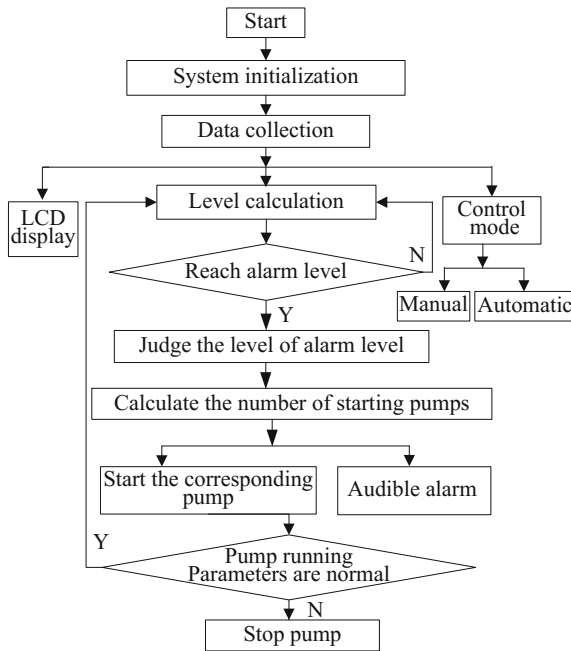


**Fig. 6.** The main program flow chart

**PC software design**. The PC monitoring interface is developed in VC++. The interface mainly consists of four parts: the user login part, display part, sound and light alarm part and the data query part.

(1) The user login part. This part gives the system operators different operating authority and management scope. The behavior of reading and writing, maintenance, implementation and other activities is controlled for operators by different operating rights of login operators.
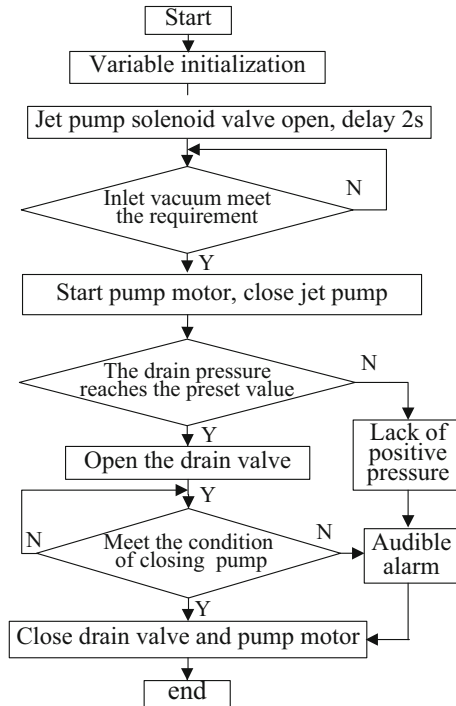
**Fig. 7.** Start and stop of single pump flow chart

(2) Display part. Through PC monitor screen, many information are shown such as the running status of each water pump, the vacuum degree at the water pump suction, the water pump outlet pressure, the drain pipe flow, the motor temperature, the display system control mode and communication status.

(3) Sound and light alarm part. This part can show specific information on this alarm system. When the water pump fails, the cause of the fault can be displayed. Thus the maintenance personnel can effectively handle the fault and ensure the drainage system is safe and reliable.

(4) The Data query part. This part can check the serial number, start and stop time, running time of water pump. It can also inquire water level change trend curve and fault alarm record.

## 4    Experimental Verification

Under the existing condition of the laboratory, a single pump start-stop control experiment platform is set up for drainage monitoring system. The experiment platform is shown in Fig. 8. The main equipment include a 0.75 kW centrifugal water pump, two water tanks ($V = 0.5 \times 0.5 \times 0.5$ m$^3$), an inlet valve, a drain valve, a water level sensor, a flux sensor, a pressure sensor, a temperature sensor, three digital display

instruments and the control circuit based on DSP2812. The installation schematic of the drainage system is shown in Fig. 9. The symbols of L, T, P and F represents the system water level signal, the motor bearing temperature signal, the water pump outlet pressure signal and the drain line flux signal, respectively.



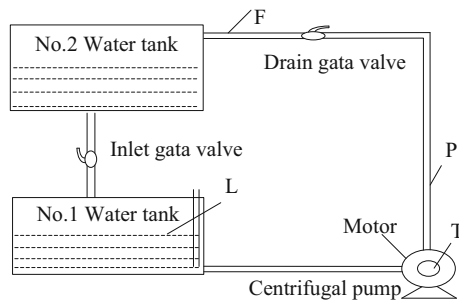**Fig. 8.** Drainage system experimental platform



**Fig. 9.** System installation schematic

In Fig. 9, water tanks No.1 and No.2 represent sump and discharge, respectively. Before starting the water pump, the water level of No.2 water tank is above the limit level of 0.4 cm and the water level in water tank 1 is below the safety water level of 0.2 m. Opening the inlet valve, the water level of No.2 tank would steadily flow to tank 1. At this time, as the pump has not started, the rate of water input is faster than the rate of water output for No.1 tank. Thus water tank 1 will rise. The system will monitor the water level signal of No.1 tank in real-time. When the water level of No.1 tank reaches the upper limit of the preset value of 0.2 m, the motor will be started and drive the water pump for drainage. When outlet pressure is detected to 0.6 Mpa, the drain valve will be opened to drain away water. When the water level drops below the safe water level of 0.2 m, the pump motor is turned off.

The design of this drainage monitoring interface is shown in Fig. 10. 1# pump starting button is green in the picture, it indicates that the 1# pump starts normally and is draining. In Fig. 10, from the operation of pump1#, the water level shows a kind of

downward trend. The outlet pressure is maintained at 0.5 Mpa, the bearing temperature is maintained at about 37 °C and the pine line flux is stabilized at 2L/min. When the water level is below safety level of 0.2 m, the water pump motor will be turned off. The data of monitoring interface indicates that the water pump can start normally. It also indicates that the pressure, the flux and other parameters can be shown normally. Through continuous 24 h normal running, the reliability and stability of the drainage monitoring system are verified.
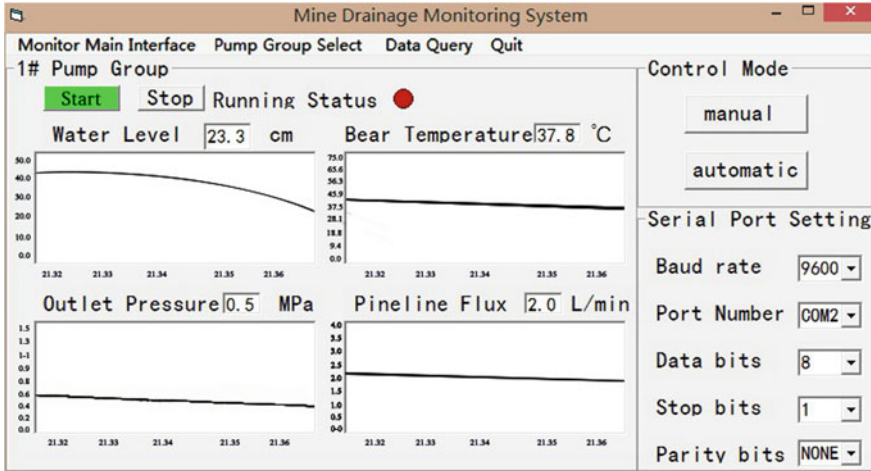


**Fig. 10.** Drainage monitoring interface

## 5    Conclusion

This design adopts DSP control system to replace the traditional PLC control. DSP controller has the advantages of good stability, high precision and rapid processing speed. It can obviously improve the working efficiency of monitoring system. The human-computer interface is designed in VC++. This interface includes useful functions such as online real-time monitoring and display of water level information, monitoring the motor temperature to prevent motor overheating, fault warning of device, historical data query and other function to make the staffs operate easily.

## References

1. Jie, Y.: Design and analysis of mine drainage automatic monitoring system. Sci. Technol. Innov. Appl. **18**, 112 (2016)
2. Li, J.: Drainage Monitoring System. Inf. Technol. **34**(11), 224–226 (2013)
3. Liu, Y.: Research and design of remote monitoring and control system for automatic drainage in coal mine. J. Coal Sci. Technol. **40**(3), 77–80 (2014)
4. XIAO, F.: Monitoring system of mine water level. J. Coal Chem. Ind. **40**(4), 133–137 (2017)

5. Fan, Z.: Design of mine drainage automatic control system. J. Ind. Saf. Environ. Prot. **43**(7), 38–70 (2017)
6. Lu, D.: Discussion on monitoring and control system of mine main drainage based on PLC. Inf. Technol. **13**, 114–116 (2014)
7. Ma, H., Xu, J.: Design of remote monitoring and control system for mine water storehouse based on PLC. Adv. Mater. Res. **457–458**, 1595–1601 (2012)
8. Sun, L.: TMS302F2812 principle and C language program development. Tsinghua University Press, Beijing (2010)

# Study on Online Detection Method of Methane Gas in Coal Mine Based on TDLAS Technology

Jun Deng[1,2], Wei-Le Chen[1(✉)], Wei-Feng Wang[1], Yuan He[1], and Bao-Long Zhang[1]

[1] College of Safety Science and Engineering, Xi'an University of Science and Technology, Xi'an 710054, China
450365218@99.com
[2] Shaanxi Key Laboratory of Prevention and Control of Coal Fire, Xi'an University of Science and Technology, Xi'an 710054, China

**Abstract.** Tunable diode laser absorption spectroscopy (TDLAS) provides a reliable method for detection of methane in coal mine. To study the influence of temperature and pressure on methane concentration detection, 1653.7 nm was selected as the center wavelength of methane according to the HITRAN database (explain what is this database), and then methane online detection system was designed using long path reflection structure detection technology combined with wavelength modulation and harmonic. The standard methane concentrations of 50.0, 99.8 and 200.0 ppm were adopted to study the influence of different temperature and pressure on the methane concentration within the range of −5 to 50 °C and 0–75 kPa. The results indicated that with the increase of temperature, methane concentration gradually decreased at the same pressure. Simultaneously, with the increase of pressure, the methane concentration also gradually decreased at the same temperature. Based on the above results, the temperature and pressure effects of different concentrations were combined to obtain the correction formula. The feasibility of the formula was verified by correcting the methane concentration at different temperatures and pressures. The corrected maximum relative error was 2%, which greatly improves the measurement accuracy and enables the system to meet the needs of methane detection during coal mine production.

**Keywords:** TDLAS · Temperature · Pressure · Methane concentration

## 1 Introduction

Nowadays, more than half of the coal mines in China are classified as high-gas or gas outburst categories. The main component of mine gas is methane, accounting for about 83–89%, which is one of the major factors in coal mine accidents [1–3]. Therefore, it is essential to study methane real-time rapid monitoring for safety production in coal mine. Luo et al. [4] adopted the differential absorption technology to design an infrared methane concentration detection system to monitor gas concentration in coal mine, with the measurement error less than 2%. Feng et al. [5] designed the infrared methane

wireless sensor detection system with an average absolute error at 0.091%. Ni et al. [6] designed the optical fiber methane gas detection system using distributed feedback (DFB) laser wavelength scanning technology with the accuracy of 0.05%.

Tunable Semiconductor Laser Absorption Spectroscopy (TDLAS) mainly employs the narrow line width and wavelength tuning of DFB laser to realize a single absorption spectrum line scanning and measuring, which has many advantages, such as fast, highly efficient, high sensitivity, and high measurement accuracy, and most importantly, it can simultaneously monitor a variety of gases, which is the development direction of gas detection technology [7–9]. However, the temperature and pressure are unstable to cause the change of spectrum width and amplitude of the gas in actual mine environment, leading to deviation of measured gas concentration values. Therefore, it is necessary to correct the temperature and pressure. Shu et al. [10] analyzed the effect of temperature on the line intensity and the relationship between the second harmonic signal and temperature to obtain correction formula. Zhang et al. [11] analyzed the second harmonic peak change to derived correction formula with the temperature of 25–250 °C, the pressure of 0–100 kPa. Zhang et al. [12] studied the $O_2$ concentration of different temperature between 300 and 900 K, and the two algorithms containing correction formula and theoretical formula was used to correct and compare on temperature. Therefore, the change of temperature and pressure will result in changes in the amplitude and line width of absorption lines, which inevitably lead to errors in measurement results. Although many researches have been found to study on the project, there has been few relevant literatures about the correction of temperature and pressure on online monitoring of methane in coal mine.

Based on the TDLAS technology, combined with wavelength modulation and second harmonic detection technology, 1653.7 nm was chosen as the central wavelength of methane according to HITRAN database [13, 14]. Standard methane concentrations of 50.0, 99.8, and 200.0 ppm were selected. Further methane concentration was measured at −5 to 50 °C and 0–75 kPa to get the uncorrected value and actual error value under different pressure and different temperature. The correction formula was obtained by fitting the data. Comparing with uncorrected and correction experimental results, we found that the maximum relative error was reduced by 16%, which indicated that the correction formula could restrain the measurement error caused by the temperature and pressure. It verifies that the system can meet the requirement of on-line detection of methane in coal mine.

## 2 TDLAS Technology Principle

TDLAS mainly changes working temperature and current of tunable diode laser to transform the line width and wavelength of laser, further distinguish the absorption spectrum lines of single or several distance molecules. The single absorption spectrum line of the measured gas information can be obtained at each scanning period. The interference factors, such as the background spectrum line of the measured gas are excluded, which can improve monitoring precision and realize high sensitivity online measurement of gas.

According to the law of Lambert–Beer [15, 16], when a monochromatic laser passes through the gas medium, the change of laser intensity can be expressed by Eq. (1):

$$T_v = \left(\frac{I}{I_0}\right)_v = \exp(CK_vL) \tag{1}$$

where $I$ and $I_0$ are the transmission intensity and initial intensity of the laser, mW; $K_v$ is the absorption coefficient when the frequency is $v$, cm$^{-1}$; $C$ is the gas concentration (molecular number in $T_v$ unit volume), cm$^{-3}$ atm$^{-1}$; $L$ is the optical path length of the absorbing pool, cm.

$K_v$ can be calculated by using Eqs. (2) and (3):

$$Kv = P\sum_{J=1}^{K} X_j \sum_{i=1}^{N_j} S_{i,j}(T)\phi_{i,j} \tag{2}$$

$$\int_{v}^{+\infty} \Phi_{i,j}(v - v_0)d_v = 1 \tag{3}$$

where $P$ is the pressure of the gas, atm; $S(T)$ is the spectral line intensity of the certain temperature T; cm$^{-2}$ atm$^{-1}$; $\Phi(v, v_0)$ is a linear function of the gas absorption spectrum line, cm, which is related to the temperature, the total pressure, and the content of the gas components; $v$ and $v_c$ are the spectral line frequency and center frequency of the gas absorption spectrum line, cm$^{-1}$.

Through the Eqs. (1)–(3), $C$ can be described by using Eq. (4) [17–19]:

$$C = \frac{-\ln(\frac{I}{I_0})}{S(T)\phi(v)PL} \tag{4}$$

## 3  Experimental Device and Process

The experimental system of methane concentration measurement is illustrated in Fig. 1. It mainly includes AFG3052C arbitrary waveform generator, temperature current control panel, DFB laser, and GW-1020D long path gas absorption pool. Standard methane concentrations of 50.0, 99.8 and 200.0 ppm were used as target detection gases. The heating device was programmed constant temperature and humidity box (SE TH-Z-042L), and the pressure device is that a valve connected to the outlet pipe was adopted to control the gas pressure.
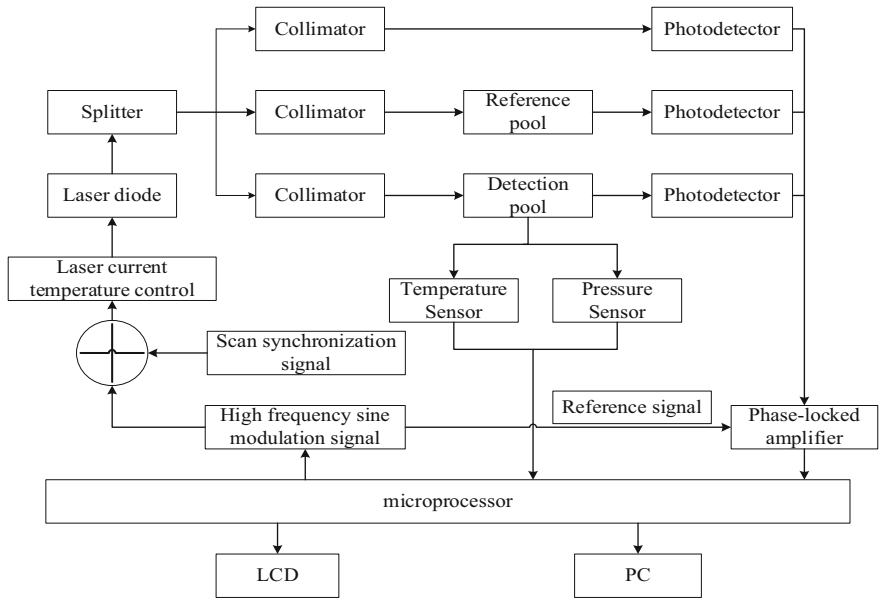
**Fig. 1.** Experimental system of methane concentration measurement

The central frequency of the laser diode is located near 1653.7 nm by temperature roughing, system microprocessor generates high frequency sinusoidal modulation signal and scanning synchronization signal required by the TDLAS system through the control signal generator. The scanning synchronization signal is a low-frequency saw tooth wave, which is used to adjust the injection wavelength of the laser and realize the comprehensive scanning of the gas absorption spectrum line.

The high frequency sinusoidal modulation signal is used to extract gas concentration information that contained in the gas absorption spectrum line to reduce the influence of background noise. These two kinds of signals are superimposed to drive the laser, then generate the laser which can scan the wavelength near the absorption peak of the gas. The laser is divided into 3 path, path 1: The laser directly enters a photodetector through a collimator, system detects the intensity of the laser and then judges the current state of the laser; path 2: The laser enters a photodetector through a built-in reference pool filled with a specific gas, the system will compare the value of the optical path detection and the concentration of the specific gas in real time, then the laser driving parameters are dynamically adjusted to prevent the drift of the system; path 3: The laser will enter the photodetector through the detection pool, the preamplifier amplifies the electrical signal that outputs in the photodetector, then the harmonic detection is carried out by the phase locked amplifier. The microprocessor makes the second harmonic signal accomplishing AD transition then transmits it to the upper computer for subsequent processing and analysis.

The experimental system of temperature and pressure correction measurement is shown in Fig. 1.

# 4   Results and Analysis

## 4.1   Influence and Correction of Temperature and Pressure

To investigate the influence of temperature and pressure on the methane concentration, standard methane concentrations of 50.0, 99.8, 200.0 ppm were adopted to make a comparison. Setting a temperature between −5 and 50 °C in the programmable constant temperature and humidity box (every 5 °C is an interval), and then the pressure was changed from 0 to 75 kPa (each 5 kPa is a gear). The effect of pressure on methane measurement concentration was studied at the same temperature. Simultaneously, the influence of temperature on methane measurement concentration was investigated with the same pressure. Furthermore, Measurement system will keep at least 30 min under constant temperature or pressure until the value of gas concentration no longer changed in the host computer, the value was recorded.

The methane concentration curves at the different temperature and pressure are showed in Fig. 2. The overall impact of the temperature and pressure on measurement concentration was basically the same. So the effect of temperature and pressure can be normalized, respectively.
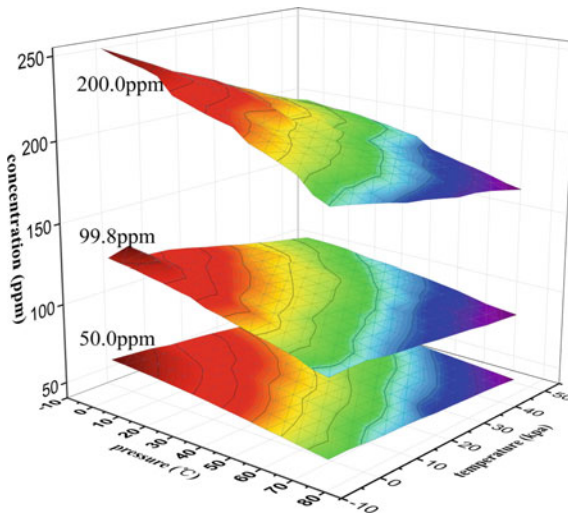


**Fig. 2.**   The methane concentration curves at the different temperature and pressure

The temperature effect normalized curve was obtained by the ratio for measured concentration corresponding to −5 °C and other temperatures at the different pressures and standard concentration, respectively, are depicted in Figs. 3, 4 and 5. The way which obtained the pressure effect normalized curves at the different temperature and standard concentration were same as it are illustrated in Figs. 6, 7 and 8. The tendency of temperature and pressure at the three kinds of concentrations were basically the same. Therefore, the temperature and pressure of the three concentrations can be fused, respectively.
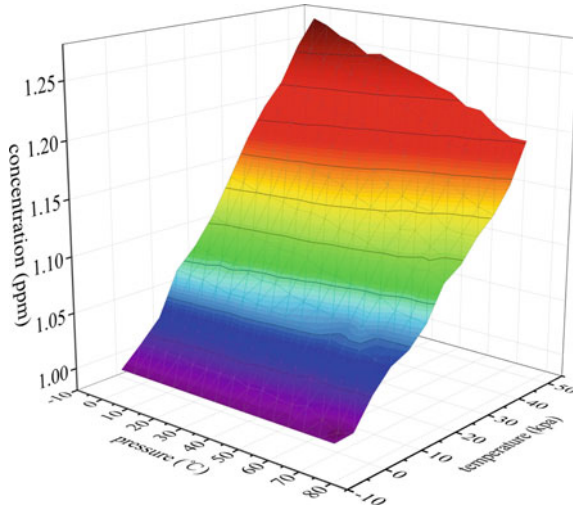
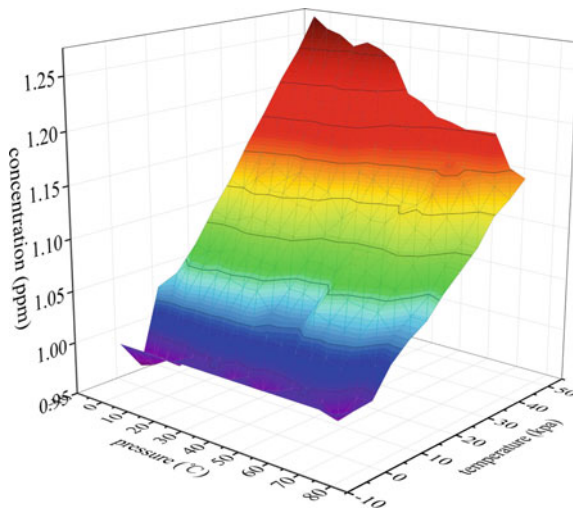**Fig. 3.** 50 ppm temperature influence normalized curve



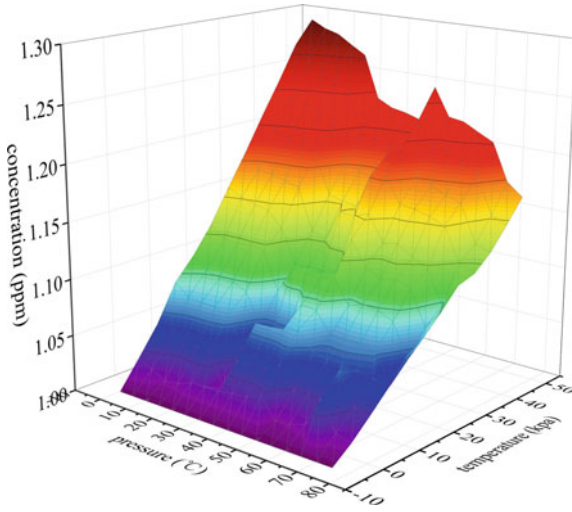**Fig. 4.** 99.8 ppm temperature influence normalized curve

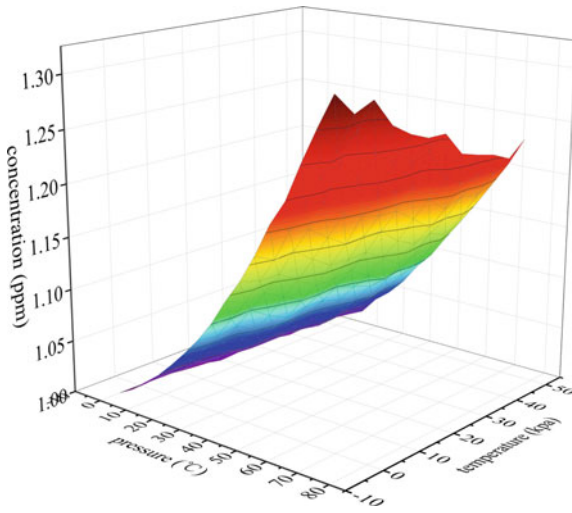**Fig. 5.** 200 ppm temperature influence normalized curve



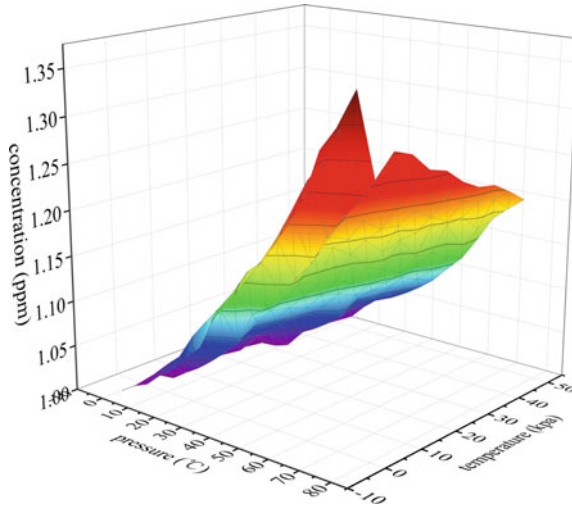**Fig. 6.** 50 ppm pressure influence normalized curve

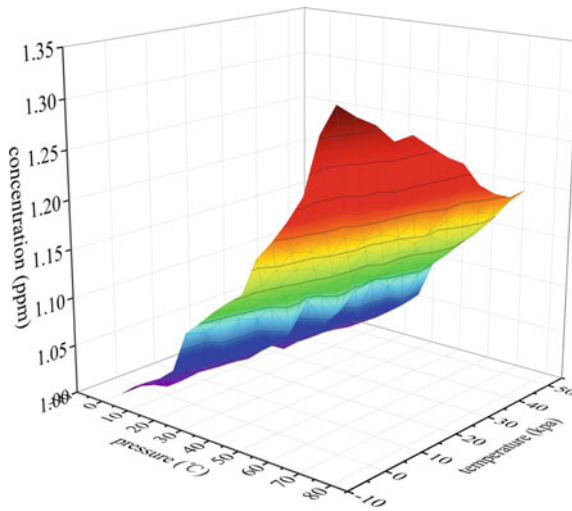**Fig. 7.** 99.80 ppm pressure influence normalized curve



**Fig. 8.** 200 ppm pressure influence normalized curve

Figure 9 shows the average deviations of methane concentration influenced by pressure in. It is worthy noting that the impact of pressure on methane measurement concentration was coincident (?). Therefore, the three average deviation curves were averaging to obtain average value. The fitting curve of average value is shown in Fig. 10. The average deviation obtained from normalization processing data was very small that three bits of data after partial decimal point were missing as a result, resulting in fitting inaccurate. Accordingly, the final average value was expanded 1000 times to fit, the formula of the methane measured concentration with the pressure can be obtained.
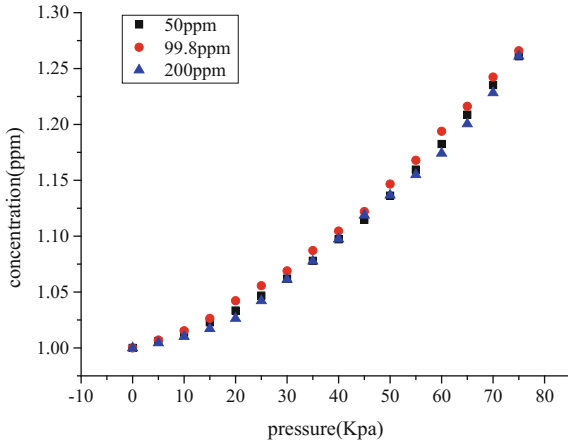
**Fig. 9.** Average deviation of methane concentration influenced by pressure



**Fig. 10.** The fitting curve of average value at different pressure

$$Y = A_1X^2 + A_2X + A_3 \tag{5}$$

Among them, the correlation coefficient $R^2 = 0.999$, $A_1 = -0.029$, $A_2 = -1.334$, and $A_3 = 2.325$, which shows that the equation has high correlation within the range of 0–75 kPa.

The average deviations of methane concentration influenced by temperature are demonstrated in Fig. 11. The influence of temperature on the measured values was consistent at three standard concentrations. Therefore, the three average deviation curves were averaging to obtain average value. The fitting curve of average value is shown in Fig. 12. And then expanding 1000 times of it, the formula of methane measurement concentration with temperature is obtained.

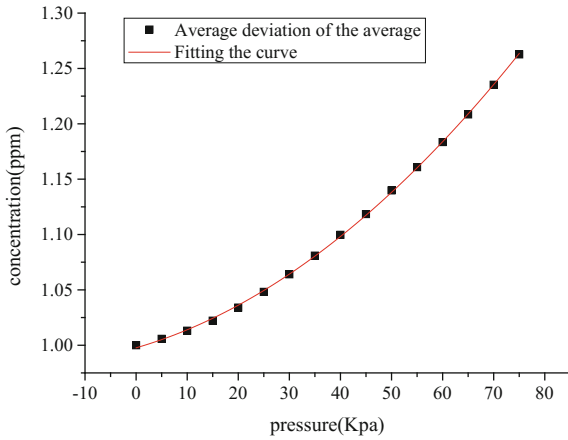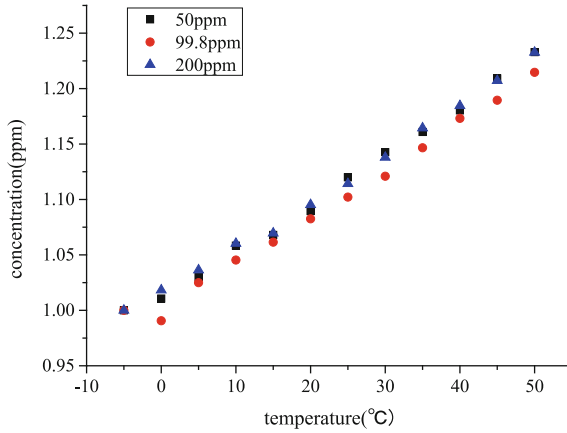**Fig. 11.** The average deviation of methane concentration influenced by temperature
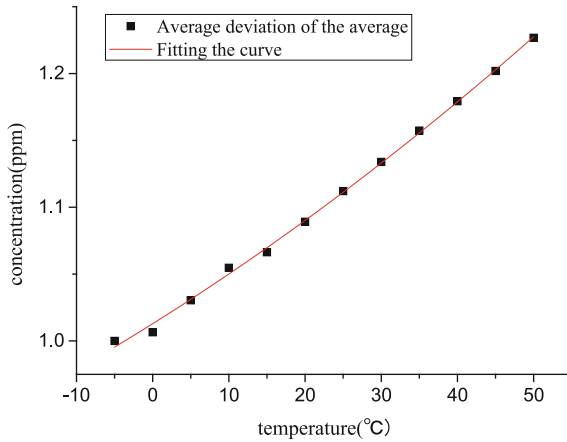


**Fig. 12.** The fitting curve of average value at different temperature

$$Y = B_1X^2 + B_2X + B_3 \tag{6}$$

Among them, the correlation coefficient $R^2 = 0.998$, $B_1 = -0.014$, $B_2 = -3.572$ and $B_3 = 99.17$, which shows that the equation has good correlation within the range of $-5$ to 50 °C.

## 4.2 Data Correction

The above experimental data showed that temperature and pressure had great influence on the methane concentration. Therefore, the temperature and pressure must be modified to ensure the accuracy of the measurement results. The measured concentration at

25 °C and 0 kPa was the zero point value of the standard concentration. The modified formula can be expressed by using Eq. (7):

$$V = v \cdot ((1 - At) \cdot (1 - Ap)) \tag{7}$$

where At and Ap is the temperature and pressure fitting function, respectively; v and V are the result of the uncorrected and corrected concentration measurement, respectively.

To verify the feasibility of the formula, the temperature and pressure of standard methane concentrations for 50.0, 99.8, and 200.0 ppm were used as a constant, and brought it into Eqs. (5)–(7). The corrected methane measured concentration under different temperature and pressure can be obtained. Comparing uncorrected methane measured concentration with corrected value, as shown in Figs. 13, 14 and 15. It can be found that the corrected methane concentration fluctuated in the smaller range of the zero point value, and didn't change much with the change of temperature and pressure.
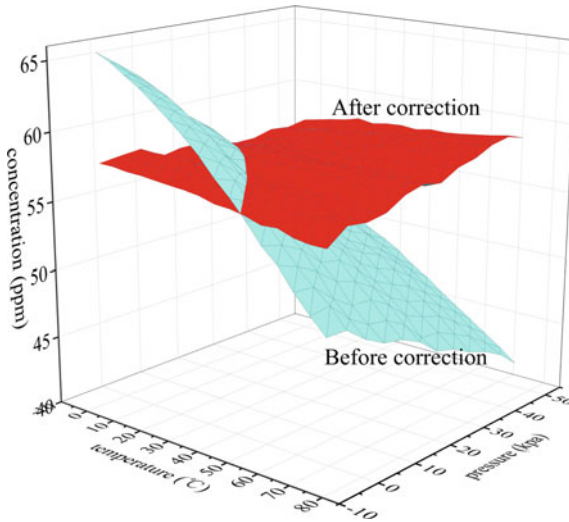


**Fig. 13.** Concentration contrast figure of 50 ppm

The part values of the uncorrected and corrected methane concentration are listed in Table 1, which mainly included the concentration value for temperature of 0, 20, and 45 °C, and the pressure of 15 and 50 kPa. The maximum relative error of the methane measurement before correction could reach 18%, which was unacceptable. Through the correction on the temperature and pressure, the maximum relative error of the system reduced to 2%. It decreased the interference to the concentration caused by the change of the temperature and pressure, and improved the measurement accuracy of the gas concentration.
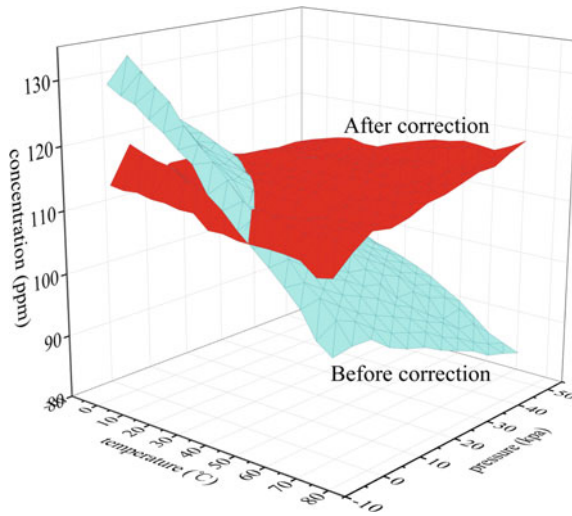
**Fig. 14.** Concentration contrast figure of 99.8 ppm
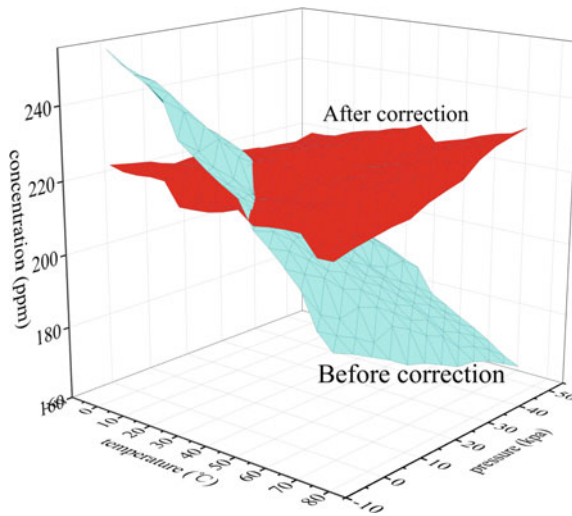


**Fig. 15.** Concentration contrast figure of 200 ppm

**Table 1.** The part values of the uncorrected and corrected methane concentration

| Concentration (ppm) | Temperature (°C) | Pressure (Kpa) | Pre-corrected measurement value (ppm) | Zero value (ppm) | Relative error (%) | Corrected measurement value (ppm) | Relative error (%) |
|---|---|---|---|---|---|---|---|
| 50 | 0 | 15 | 62.664 | 57.398 | 9.175 | 57.823 | 0.740 |
| | 0 | 50 | 55.74 | 57.398 | −2.889 | 57.149 | −0.434 |
| | 20 | 15 | 57.746 | 57.398 | 0.606 | 57.851 | 0.790 |
| | 20 | 50 | 51.946 | 57.398 | −9.499 | 57.824 | 0.742 |
| | 45 | 15 | 51.53 | 57.398 | −10.223 | 57.573 | 0.305 |
| | 45 | 50 | 46.998 | 57.398 | −18.119 | 58.345 | 1.649 |
| 99.8 | 0 | 15 | 127.494 | 114.825 | 11.033 | 117.644 | 2.455 |
| | 0 | 50 | 110.817 | 114.825 | −3.491 | 113.618 | −1.051 |
| | 20 | 15 | 113.424 | 114.825 | −1.220 | 113.631 | −1.040 |
| | 20 | 50 | 101.346 | 114.825 | −11.739 | 112.813 | −1.752 |
| | 45 | 15 | 102.78 | 114.825 | −10.490 | 114.834 | 0.008 |
| | 45 | 50 | 94.217 | 114.825 | −17.947 | 116.964 | 1.862 |
| 200 | 0 | 15 | 244.334 | 220.946 | 10.585 | 225.457 | 2.042 |
| | 0 | 50 | 214.516 | 220.946 | −2.910 | 219.938 | −0.456 |
| | 20 | 15 | 222.094 | 220.946 | 0.520 | 222.499 | 0.703 |
| | 20 | 50 | 199.75 | 220.946 | −9.593 | 222.352 | 0.636 |
| | 45 | 15 | 198.924 | 220.946 | −9.967 | 222.253 | 0.592 |
| | 45 | 50 | 180.546 | 220.946 | −18.285 | 224.135 | 1.443 |

## 5 Conclusions

In this paper, the feasibility of using TDLAS technology to measure the methane in the mine is demonstrated. The temperature condition is −5 to 50 °C and the pressure is 0–75 kPa. In this case, the wavelength modulation technique is used to measure the methane concentration. The effects of temperature and pressure on the measurement of methane concentration are analyzed and revised, and the main conclusions are shown as follows:

(1) Under the conditions of 50, 99.8, 200 ppm, the measurements of methane concentration are basically the same when considering the effects of temperature and pressure, which is proved that the influence of temperature and pressure on the measurement concentration of methane is consistent under different concentrations.
(2) In the same pressure, when the temperature elevated gradually, the methane measurement concentration increased gradually. In the same temperature, when the pressure grew up, the Methane Measurement concentration increased gradually.
(3) According to the above results, a corresponding empirical formula was obtained. By correcting the methane concentration under different concentration and temperature, the maximum relative error before and after correction was 18 and 2%, respectively, which indicated that error after correction was reduced by 16% compared with that before correction, the measurement accuracy of the system was greatly improved. These results provide reliability and feasibility for the application of TDLAS technology in mine coal gas monitoring.

## References

1. He, Y., Zhang, Y., Kan, R., et al.: Study on mash gas monitoring with distributed multipoint fiber optic sensors system in coal mine. In: Photonics and optoelectronics (SOPO), 2012 symposium on. IEEE, pp. 1–4 (2012)
2. Pan, Y.M., Deng, Y.H., Zhang, Q.Z., et al.: Dynamic prediction of gas emission based on wavelet neural network toolbox. J. Coal Sci. Eng. (China) **19**(2), 174–181 (2013)
3. Wang, S., Zhou, F., Kang, J., et al.: A heat transfer model of high-temperature nitrogen injection into a methane drainage borehole. J. Nat. Gas Sci. Eng. **24**, 449–456 (2015)
4. Luo, D.F., Yang, J.H., Zhong, C.G.: Detection technology of methane gas concentration based on infrared absorption spectrum. Spectrosc. Spectral Anal. **31**(2), 384–386 (2011). (China)
5. Feng, G.L., Lu, C.D.: Design and implementation of wireless sensor detection system on infrared methane gas. Comput. Measur. Control **21**(1), 80–81 + 88 (2013)
6. Ni, J., Chang, J., Liu, T., et al.: Fiber methane gas sensor and its application in methane outburst prediction in coal mine. In: Optical fiber sensors conference, 2008. APOS'08. 1st Asia-Pacific. IEEE, pp. 1–4 (2008)
7. Jiang, J., Ma, G., Song, H., et al.: Tracing methane dissolved in transformer oil by tunable diode laser absorption spectrum. IEEE Trans. Dielectr. Electr. Insul. **23**(6), 3435–3442 (2016)

8.  Ma, G., Zhao, S., Jiang, J., et al.: Tracing acetylene dissolved in transformer oil by tunable diode laser absorption spectrum. Sci. Rep. **7**(1), 14961 (2017)
9.  Chen, J., Li, C., Zhou, M., et al.: Measurement of $CO_2$ concentration at high-temperature based on tunable diode laser absorption spectroscopy. Infrared Phys. Technol. **80**, 131–137 (2017)
10. Shu, X.W., Zang, Y.J., Kan, R.F., et al.: An investigation of temperature compensation of HCL gas online monitoring based on TDLAS method. Spectrosc. Spectral Anal. **30**(5), 1352–1356 (2010). (In Chinese)
11. Zhang, Z.F., Zou, D.B., Chen, W.L., et al.: Temperature influence in the TDLAS detection of escaping ammonia. Opto-Electron. Eng. **41**(6), 32–37 (2014). (In Chinese)
12. Zhang, Z.R., Wu, B., Xia, H., et al.: Study on the temperature modified method for monitoring gas concentrations with tunable diode laser absorption spectroscopy, **62**(23), 183–189 (2013) (in Chinese)
13. Gordon, I.E., Rothman, L.S., Hill, C., et al.: The HITRAN2016 molecular spectroscopic database. J. Quant. Spectrosc. Radiat. Transf. **203**, 3–69 (2017)
14. Qi, R.B., He, S.K., Li, X.T., et al.: Simulation of TDLAS direct absorption based on HITRAN database. Spectrosc. Spectral Anal. **35**(1), 172–177 (2015)
15. Claps, R., Englich, F.V., Leleux, D.P., et al.: Ammonia detection by use of near-infrared diode-laser-based overtone spectroscopy. Appl. Opt. **40**(24), 4387–4394 (2001)
16. Zhimin, P., Yanjun, D., Lu, C., et al.: Calibration-free wavelength modulated TDLAS under high absorbance conditions. Opt. Express **19**(23), 23104–23110 (2011)
17. De Tommasi, E., Castrillo, A., Casa, G., et al.: An efficient approximation for a wavelength-modulated 2nd harmonic lineshape from a Voigt absorption profile. J. Quant. Spectrosc. Radiat. Transf. **109**(1), 168–175 (2008)
18. Farooq, A., Jeffries, J.B., Hanson, R.K.: Sensitive detection of temperature behind reflected shock waves using wavelength modulation spectroscopy of $CO_2$ near 2.7 μm. Appl. Phys. B **96**(1), 161–173 (2009)
19. Kluczynski, P., Axner, O.: Theoretical description based on Fourier analysis of wavelength-modulation spectrometry in terms of analytical and background signals. Appl. Opt. **38**(27), 5803–5815 (1999)

# Part VI
# Methane and Methane Control II

# Experimental and Simulation Investigation of $N_2$ Enhanced Gas Drainage in Low Permeable Coal Seam

Jia Lin[✉], Ting Ren, Patrick Booth, and Jan Nemcik

School of Civil, Mining and Environmental Engineering, University of
Wollongong, Wollongong, NSW 2500, Australia
jl562@uowmail.edu.au

**Abstract.** The performance of pre-gas drainage in low permeable seams
especially in $CO_2$ abundant coal seams is not satisfied. Due to the high affinity
between coal and $CO_2$, much more time is required for gas drainage work to
reduce the coal seam gas content below the threshold limit value, thus impacting
the scheduled mining activities. In this study, $N_2$ injection to enhance gas
drainage efficiency was investigated in $CO_2$-rich coal seams. Laboratory tests of
$N_2$ enhanced gas drainage were carried out under different permeability con-
ditions. A triaxial permeability test rig equipped with a back pressure regulator
was used to conduct the test. The variation of gas composition, gas outlet flow
rate, $N_2$ flushing efficiency, and permeability variation were analyzed. A binary
gas migration model was developed to illustrate gas migration in laboratory
scale and this model was imported to COMSOL Multiphysics. The simulation
results were matched well with the laboratory results. Based on the test results, a
two-stage flushing mechanism was obtained. In the first stage, free phase coal
seam gas accounted for the large percentage and this stage last for a shorter time.
In the second stage, desorption time governed the flushing efficiency and
desorbed gas was the primary gas. Through these laboratory experiments and
simulations, we concluded that $N_2$ injection could significantly decrease coal
seam $CO_2$ content level and increase gas drainage efficiency.

**Keywords:** Outburst · Coal mining · Gas content · $N_2$ enhanced gas drainage
ECBM

## 1 Introduction

Gas pre-drainage is one of the most effective methods to control coal and gas outburst
in the mining industry [1]. However, the gas drainage performance is poor in low
permeability coal seams or where the gas composition is abundant in $CO_2$. From
previous studies [2, 3], the coal sorption capacity of $CO_2$ is almost two times larger
than $CH_4$ and in low rank coal seams, this difference is even larger, sometimes reaching
10 times [4, 5]. As a result, it takes much longer time to reduce the gas content below
the threshold limit value (TLV). Moreover, the outburst induced by $CO_2$ is more severe
than $CH_4$. Based on the last fatal outburst that occurred in Australia, at Westcliff
Colliery on 25th January 1994, the Coal Mining Inspectorate and Engineering Branch

of the New South Wales Department of Mineral Resources issued a regulation precluding conventional mining where gas contents were above TLV, and also requiring coal seam gas content testing before mining. Typically, for the pure methane coal seam, the maximum gas content is 8 $m^3/t$ and for the pure $CO_2$ coal seam, this value is 5 $m^3/t$. Based on the regulation, the TLV varies depending on gas composition. In $CO_2$ abundant areas, the TLV is generally much lower and gas drainage is more difficult [6–8].

In the coalbed methane production industry, another type of gas injection can significantly improve gas production and this technology is termed as enhanced coalbed methane recovery (ECBM) [9–11]. Usually, the injected gas is carbon dioxide ($CO_2$), nitrogen ($N_2$) or flue gas. Several field trials and laboratory tests have been done and demonstrate that $N_2$ injection can stimulate coal seam gas production and increase coal seam permeability [12]. Inspired from ECBM technology, enhanced methane drainage by injecting other gases is investigated by several researchers. Thakur proposed the idea of $N_2$-flooding in relation to coal mine gas drainage in low permeability (<1mD) environments but no detailed investigations were provided. Simulation investigation [13] and field trial [14] of $N_2$ injection to enhance coal seam methane drainage were conducted by Packham. The reservoir pressure, composition of the gases produced and flow rate were recorded and analyzed. The results revealed that accelerated methane drainage rates were achieved by $N_2$ injection. Compressed air (consisting of 78% $N_2$ and 21% $O_2$) was used by Fang et al. [15] in a field trial study to improve methane drainage efficiency. The results showed that flue gas injection could also improve methane drainage.

Enhanced gas drainage by $N_2$ injection in low permeability coal seams is not well investigated, especially in $CO_2$ abundant seams. The mechanism of $N_2$ injection to enhance gas drainage is still not clear. In this study, laboratory experiments of $N_2$ flushing coal seam gas were conducted by using a coal sample collected from a gassy coal mine in the Bulli coal seam, Sydney Basin. Based on the test results, a binary gas migration model was built to explain the process of $N_2$ flushing coal seam gas and $N_2$-ECBM.

## 2    Experimental

### 2.1    Sample Preparation and Test Method

Coal lumps were collected from development headings of a coal mine located in the Bulli seam, Sydney Basin in Australia. The gas content in this coal mine is very high with typical virgin gas content levels in the order of 15 $m^3/t$. Another difference from typical coal seams is that the gas composition ($CO_2$ and $CH_4$) is generally in excess of 80% $CO_2$. Due to the higher affinity between coal and $CO_2$, usually it takes a much longer time to reduce the gas content below the TLV. The coal lumps were immediately wrapped by plastics bags underground and transported to the Mining Laboratory in University of Wollongong. Lumps were then processed through concreting, drilling, cutting and milling, as shown in Fig. 1. Standard coal cylinders (length by diameter 110 mm × 54 mm) were obtained for testing. During the samples preparation process,
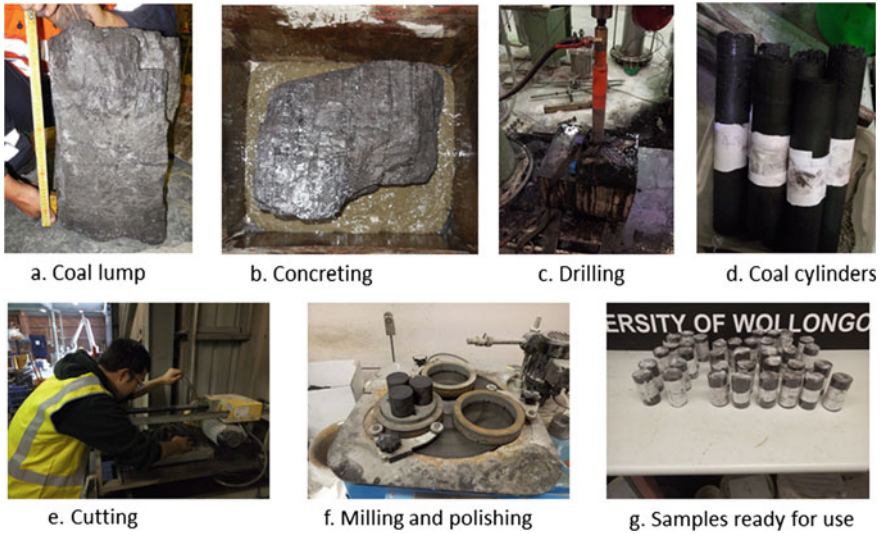
Fig. 1. Sample preparation process

the coal small chips from the same coal lump were collected for proximate analysis and adsorption tests. The test results are summarized in Table 1 and details can be found in our previous study [16, 17].

Table 1. Proximate analysis and Langmuir constants of Bulli coals

| $M_{ad}$ (wt%) | $A_d$ (wt%) | $V_{daf}$ (wt%) | $FC_{ad}$ (wt%) | Langmuir volume $V_L$(m³/t) | | Langmuir pressure $P_L$ (MPa) | |
|---|---|---|---|---|---|---|---|
| | | | | $CO_2$ | $N_2$ | $CO_2$ | $N_2$ |
| 1.17 | 17.46 | 22.98 | 62.74 | 31.45 | 12.37 | 0.91 | 18.3 |

$M_{ad}$ Moisture on air-dry basis; $A_d$ Ash on a dry basis; $V_{daf}$ Volatile matter on dry ash free basis; $FC_{ad}$ Fixed carbon on air-dry basis

A triaxial testing rig equipped with a manual back pressure regulator was used for the test. Heat-shrink tubing was used to protect the coal specimen from the oil inside of the cell which was used for providing the confining pressure. Gas pressure transducers were installed at the gas inlet area and the outlet area. Confining pressure was provided by a hydraulic pump (ranging 0–20 MPa) and its pressure could be controlled manually. The confining pressure was monitored by the pressure transducer. Two flow meters with different ranges were connected to the outlet gas pipeline. One was 0–100 ml/min and the other was 0–500 ml/min. The testing rig is shown in Fig. 2.

Before the $N_2$ flushing test, the permeability of the coal specimen was measured using $CO_2$. For the permeability measurement, the following testing conditions were applied: The gas injection pressure was 4 MPa, confining pressure 5 MPa and the
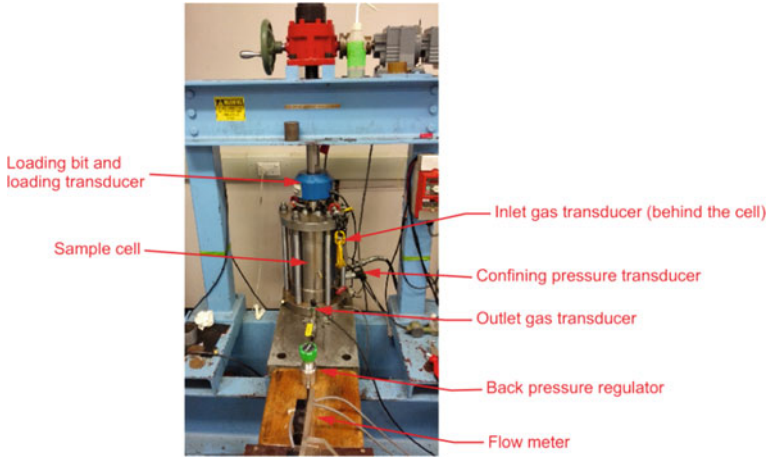
**Fig. 2.** Triaxial rig for $N_2$ flushing test

value of back pressure regulator was adjusted to 3 MPa, which meant the outlet gas pressure was 3 MPa. In this way, we mimicked the reservoir pressure. Based on the field data from the coal mine and the isotherm tests that had been done in our laboratory, 4 MPa was suitable for the test. For the calculation of the permeability of the specimen, the following equation was used:

$$k = \frac{2Q_a P_a \mu L}{A\left(P_1^2 - P_2^2\right)} \tag{1}$$

where $k$ is the permeability (mD), $Q_a$ volumetric rate of flow (cm$^3$/s) at the reference pressure, $P_a$ reference pressure (Pa), $\mu$ fluid viscosity (cp), $L$ core specimen length (cm), $A$ cross-section area of the core specimen (cm$^2$), $P_1$ inlet gas pressure (Pa), $P_2$ outlet gas pressure (Pa).

Before the $N_2$ flushing test, $CO_2$ adsorption equilibrium was reached. From the inlet gas pipeline, $CO_2$ was injected into the sample cell and the coal specimen was soaked with $CO_2$ for five days (Due to the time limitation, we regarded after five days saturation, the equilibrium was reached.). Meanwhile, the back pressure regulator was kept for 3 MPa and flow meters were monitoring the gas flow during this process. After the $CO_2$ saturation, $N_2$ injection replaced $CO_2$ at the inlet of the test rig and the $N_2$ injection pressure was kept constant at 4 MPa.

To evaluate the flushing effects, the gas composition of the gas flow was another key parameter. In our tests, a gas bag was used to collect the gas samples when the gas flew out of the flow meter and a syringe was used for the micro-gas chromatograph (Agilent Micro-GC 490 series) as shown in Fig. 3.

The gas composition changed significantly at the beginning of the test, so we collected gas samples as often as possible. Typically, the frequency of sampling depended on the outlet gas flow rate. If this value is too small, it takes longer time to collect enough volume of gas for Micro-GC analysis. To avoid the errors that occurred

**Fig. 3.** Gas sampling bag (left) and Micro-GC (right)

during gas composition analysis, each gas sample went through the Micro-GC twice. For each run of the Micro-GC, 15 ml of gas sample was required. If the results of the two repeated analysis were unchanged significantly, we regarded the results were reliable and used the averaged value as the final result.

## 2.2 Experimental Results

The performance of $N_2$ flushing is calculated if the gas flow rate and gas composition are obtained. From the isotherm of the coal sample, the relationship between gas pressure and gas content is known. In the test, the total volume of coal seam gas is known, including the free phase gas and sorption phase gas inside of the cell. During the whole test, gas flow rates were recorded at real time and the gas compositions were analyzed as frequently as possible. In this part, we analyzed the performance mainly from gas flow rate and gas composition aspects.

Figure 4a shows the gas composition variations with respect to time. It can be seen that this value changes sharply in the first 700 min and then till the test terminated, the changes are not significant. Specifically, from the test start to 681 min, the $CO_2$ percentage drops from 100 to 5.56%. Small changes are occurred from 681 to 4851 min, only drops from 5.56 to 1.34%. It is noticed that pure $CO_2$ is monitored in the initial 70 min, which means $N_2$ does not reach the outlet pipeline and the $N_2$ breakthrough time is 70 min. From the $N_2/CO_2$ % aspect, this ratio increases in the first 3000 min and after that fluctuates between 60 and 80.

Figure 4b shows the gas flow rate against time. Total gas flow rates are monitored by the flow meter at the outlet pipeline and by using the gas composition results, $N_2$ flow rate and $CO_2$ flow rate are calculated. From Fig. 5, it can be seen that pure $N_2$ flow rate has similar trends with the total gas flow rate and pure $CO_2$ flow rate is much smaller than the total gas flow. The gas flow increases first, and reaches the peak. After that it decreases and in the end, its value stays stable. Specifically, from the test beginning to the time of 741 min, the flow rate increases sharply, reaching the maximum flow rate 94.45 ml/min. From 741 to 3500 min, the flow rate drops to 28 ml/min and at the end of the test, the flow rate is 24 ml/min. It is also noticed that in the first
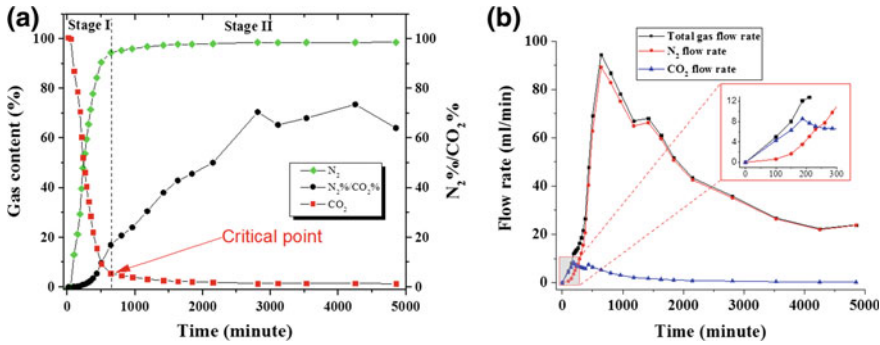
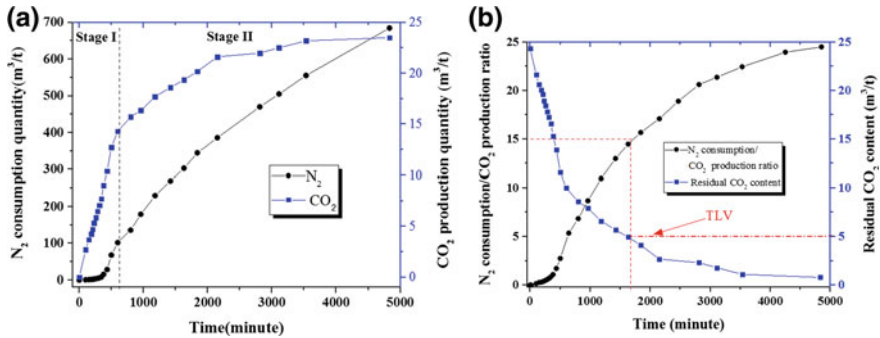**Fig. 4.** Gas composition variations against time (**a**) and gas flow rate variations against time (**b**)



**Fig. 5.** $N_2$ consumption quantity, $CO_2$ production quantity at different time (**a**) and variations of $N_2$ consumption/$CO_2$ production ratio, residual $CO_2$ content (**b**)

200 min, the pure $CO_2$ flow rate exceeds the $N_2$ flow rate even though most of the time during the test $N_2$ flow rate is much higher than the $CO_2$ flow rate.

Figure 4 demonstrates that both gas composition and gas flow rates show two different stages during the test. Moreover, the duration time of each stage in both figures is quite close and we define a critical point (in Fig. 4, the critical points are 681 and 741 min respectively.).

The pure $N_2$ flow rate and pure $CO_2$ flow rate are obtained and then the total cumulative volume of $CO_2$ and $N_2$ is calculated (here refers to $N_2$ consumption quantity and $CO_2$ production quantity). Figure 5a shows the variation of the $N_2$ consumption and $CO_2$ production with respect to time. It can be seen that the $N_2$ consumption shows linearly? For $CO_2$ production curve, its value increases linearly in the first stage and quite stable at the end of the test.

The total gas volume inside of the sample is 25.2 $m^3$/t when the gas pressure is 4 MPa based on the isotherm test. The residual gas content and the ratio of $N_2$ consumption/$CO_2$ production is calculated, as shown in Fig. 5b. From this test, it can be seen that it takes 1600 min to reduce the gas content below 5 $m^3$/t which is defined by the TLV.

## 3    Discussion

It is widely accepted that coal seams are a dual-porosity system: cleat porosity and matrix porosity. The former porosity mainly contributes to the gas migration and Darcy flow occurs in the cleat porosity system. Due to the existence of the two porosity systems, coal seam gas is mainly stored in the coal seam as two different phases: free phase state and sorption phase state. Figure 4 demonstrates that both of the gas composition and gas flow rate change remarkably in the two stages, which mean the N$_2$ flushing mechanism in these two stages, are different. During the N$_2$ injection process, the total gas pressure in the cleat system ($P_f = P_{f1} + P_{f2}$) is kept constant. With continuous injection, N$_2$ partial pressure in the cleat system ($P_{f2}$) increases, and CO$_2$ partial pressure ($P_{f1}$) falls, which means that the original free phase CO$_2$ molecules in the cleat system are flushed out. As a result, in the first stage, the CO$_2$ percentage shows a linear decrease with the N$_2$ injection. Once the CO$_2$ concentration in the cleat system decreases, a CO$_2$ concentration difference forms between the matrix and cleat ($P_{f1} < P_{m1}$). The concentration difference between matrix and cleat enables free CO$_2$ in the matrix pore space to flow to the cleat. As a result, the partial pressure of CO$_2$ in the matrix pore space decreases and adsorbed CO$_2$ desorbs. In the first stage, both of the original free phase CO$_2$ and the desorbed CO$_2$ is replaced while free phase CO$_2$ is the primary production. The first stage ends when most of the free phase state CO$_2$ is flushed out. Therefore, in the second stage, mainly desorbed CO$_2$ is replaced and the CO$_2$ desorption rate becomes the key constraint. In other words, CO$_2$ desorption rate governs the flushing efficiency. In summary, Stage-I: both the original free phase CO$_2$ and sorption phase CO$_2$ that exists in the coal seam is flushed out and the free phase gas accounts a large percentage; Stage-II: only sorption phase CO$_2$ is flushed out and the diffusion rate of CO$_2$ governs the flushing performance.

### 3.1    Permeability Variation

Figure 6 shows the coal specimen permeability variation against the experimental time. It can be seen that permeability experienced the following trajectory: increasing sharply, slightly decrease and then stable. In the test (initial permeability 0.3 mD), the permeability increased significantly in the first 800 min of the test, the maximum value reaching at 9 mD, and then from 800 to 1200 min, the permeability curve shows a dropping trend. From 1200 min until the test terminated, the value was stable at 6 mD. Comparing with the initial permeability, the final permeability increased approximately one order of magnitude.

From previous studies, it is widely accepted that coal seam permeability is governed primarily by two factors: effective stress and sorption-induced matrix swelling. During the CBM production process, with the depletion of coal seam gas (the confining pressure induced by the overburden is regarded constant), the confining pressure shows an increase trend. As a result, the coal seam permeability decreases. But from the sorption-induced strain aspect, the depletion of CBM pressure leading desorption of coal seam gas causes the coal matrix shrinkage and contributes to the coal seam permeability. These two effects govern the coal seam permeability and the coal
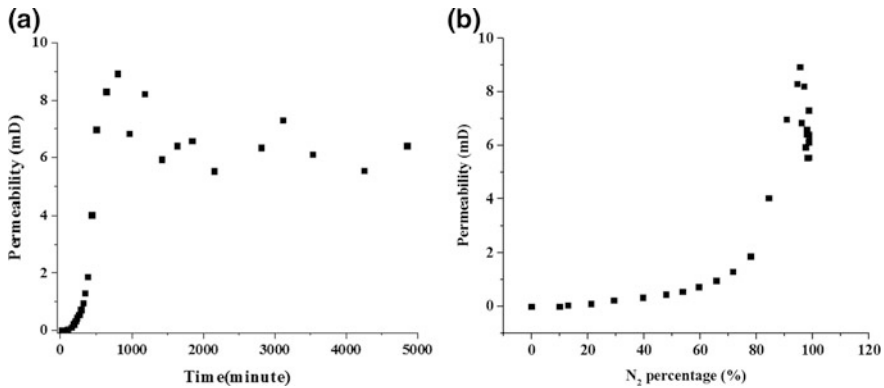
**Fig. 6.** Permeability variations (**a**) evolution during test (**b**) with respect to $N_2$ percentage

seam evolution is complicated. In the $N_2$ flushing coal seam gas process, different situation occurs compared with the traditional CBM production: the gas pressure inside coal seam increase or keeps constant rather than decrease, which means the coal seam effective stress will not contribute to the permeability decrease. The sorption induced coal matrix swelling by $CO_2$ is much larger than that induced by $N_2$ adsorption. The permeability variation of $N_2$ flushing coal seam gas test becomes easy to understand. As described in the previous section, the original free phase $CO_2$ is flushed out first. With the decrease of the partial pressure in the cleat, desorption process occurs, which induces the coal matrix shrinkage and coal permeability increase. But the injected $N_2$ keeps the effective stress at a constant value (the confining pressure is 5 MPa all the time). The permeability in the test shows an increase trend due to the effects of $CO_2$ desorption induced coal matrix shrinkage and $N_2$ adsorption induced coal matrix swelling. But the effect induced by $N_2$ is much smaller than that induced by $CO_2$. In the end of the test, equilibrium is reached and the permeability becomes gradually constant.

## 3.2 Binary Gas Migration Model

Based on the coal seam dual-porosity system and the gas migration laws (Darcy flow and Fick diffusion law), a binary gas migration model is developed to illustrate the $N_2$ flushing-coal-seam-gas process. It is widely accepted that coal seams are dual porosity systems, consisting both cleat porosity (fracture porosity) and matrix porosity. Cleat porosity governs the coal seam permeability and matrix porosity is the gas primary storage area where coal seam gas exists as in an adsorption phase state, as shown in Fig. 7. Darcy flow law can be used to explain the free phase gas migration mechanism and Fick diffusion law to explain coal seam gas exchange between cleat porosity and matrix porosity. These laws are the fundamental theory of nitrogen injection enhanced gas drainage model. The coal seam permeability is one important parameter in coalbed methane production and underground coal mines gas management. Previous researchers have proven that the permeability evolution is controlled by the effective stress and the sorption-induced matrix volume changes. In the CBM production
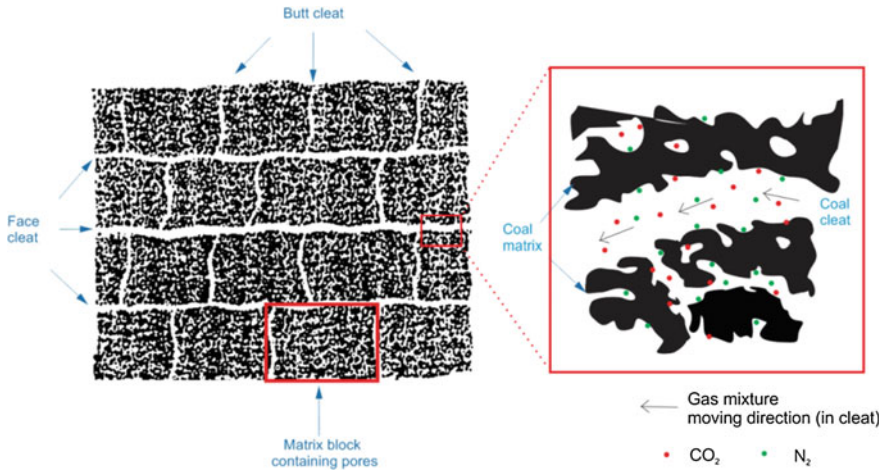
**Fig. 7.** Dual porosity model of coal seam and gas migration process in the coal seams

process, with coal seam gas depletion, effective stress is decreasing and the cleat aperture decreases. As a result, the coal seam permeability decreases. Desorption of coal seam gas induces coal matrix shrinkage and the cleat aperture expand. This will increase the coal seam permeability. In the enhanced gas drainage process, the gas pressure is kept constant due to the injected gas. Hence the effect of effective stress changes can be neglected. Sorption-induced matrix strain needs to be considered. In this model, two types of gas ($N_2$ and coal seam gas) were analyzed separately (the detailed derivation of the model can be found in our previous research).

## 4 Numerical Simulation

In this section, numerical simulations are conducted by COMSOL Multiphysics. As mentioned in the previous study, all the governing equations are written into the PDE module. In this study, we are aiming to simulate from laboratory scale, hence geometry of a coal specimen is built to conduct the simulation. In the $N_2$ enhanced gas drainage test, the gas composition and the residual $CO_2$ content with respect to time are the two parameters to evaluate the performance. In order to make comparisons with laboratory tests, cleat pressures were recorded, including $N_2$ pressure and $CO_2$ pressure (in this study referring to $P_{f1}$ and $P_{f2}$). Based on the gas pressure law, we can use gas pressure ratio to represent gas composition. The $CO_2$ matrix pressure ($P_{m1}$) is used to calculate the residual $CO_2$ content, based on the extended Langmuir model. Figure 8 shows the contour of $CO_2$ and $N_2$ content in the matrix system at different time. It can be seen that $CO_2$ content decreases with the test going. In the simulations, $N_2$ is injected at the top of the specimen, so $CO_2$ residual pressure increases from top to bottom. Opposite trends are observed for the $N_2$ content and it shows an increasing trend with the test going. $N_2$ content is higher at the top of the model than that in the bottom.

Figure 8b shows the gas composition variations and $CO_2$ residual content with respect to time. It can be seen that simulation results match the experiment results well. However, in the first 600 min, deviations are obvious. The experiment data is offset from the simulation data. Specifically, the $CO_2$ percentage during this period is lower in the simulations and the $N_2$ percentage is higher than the experiment data. In the simulation model, the $N_2$ is directly applied at the top of the specimen while in the experiment test, an inlet void exists and free phase gas is contained in this volume. In the laboratory tests, $CO_2$ existing in this void volume was first diluted by the injected $N_2$ and then migrated through coal specimen. This process was neglected in the simulation. From the overall trends, simulation results can well match experiment results and similar changing trends are observed in both experiment results and simulation results. From the simulation results, it can be seen that the binary gas migration model can accurately describe the $N_2$ flushing process.
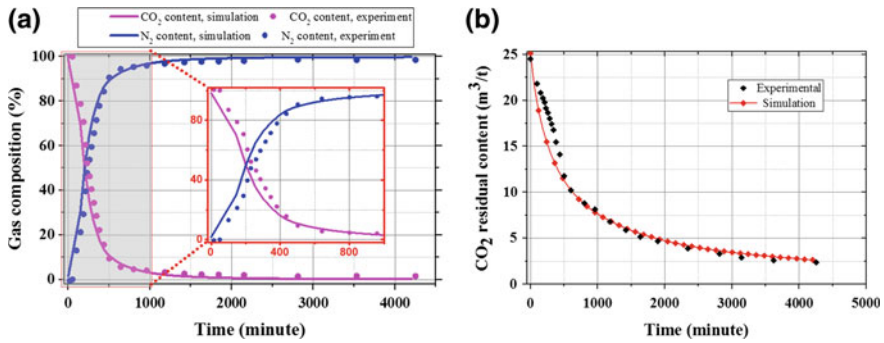


**Fig. 8.** Comparison of **a** Gas compositions **b** $CO_2$ residual content between experiment and simulation

## 5   Conclusions

In this paper, $N_2$ flushing coal seam gas test was conducted and the flushing effect and efficiency were evaluated from different aspects. The tests demonstrate that $N_2$ injection can significantly improve $CO_2$ drainage efficiency. This technology can be considered for use in underground coal mines especially in the low permeability coal seams to improve gas drainage efficiency. A model of binary gas migration in coal seams is developed. Compared with the laboratory test results, it is validated that this model can be used to accurately illustrate the gas migration during $N_2$ enhanced gas drainage process. The follow conclusions are drawn.

- During the $N_2$ flushing process, both free phase $CO_2$ in the cleat system and desorbed $CO_2$ was flushed out. A two-stage flushing process was observed from the gas composition and gas flow rate analysis. In the first stage, both free phase $CO_2$ and desorbed $CO_2$ was flushed out, with the original free $CO_2$ being dominant. Partial pressure difference for $CO_2$ was created between cleat and matrix, thus

leading to the slow desorption of adsorbed $CO_2$ in coal matrix; in the second stage, desorbed $CO_2$ became the dominant product however its flow rate was governed by desorption rate. The duration of the first stage was shorter than that of the second stage, mainly due to the slow $CO_2$ desorption process as compared with the free phase gas displacement in the coal sample.

- The binary gas migration model can be used to illustrate the gas migration during the $N_2$ enhanced gas drainage process. Compared the gas composition and the $CO_2$ residual content with the laboratory tests, it can be observed that the simulation results match the laboratory results well.
- The use of $N_2$ flushing coal seam gas to enhance gas drainage can be an attractive option for significantly improving gas drainage efficiency. This technology can be considered for application in hard-to-drain coal seams especially with significant high $CO_2$ composition.

# References

1. Packham, R., Cinar, Y., Moreby, R.: Application of enhanced gas recovery to coal mine gas drainage systems (2009)
2. Moore, T.A.: Coalbed methane: a review. Int. J. Coal Geol. **101**, 36–81 (2012)
3. White, C.M., Smith, D.H., Jones, K.L., Goodman, A.L., Jikich, S.A., LaCount, R.B., DuBose, S.B., Ozdemir, E., Morsi, B.I., Schroeder, K.T.: Sequestration of carbon dioxide in coal with enhanced coalbed methane recovery: a review. Energy Fuels **19**, 659–724 (2005)
4. Busch, A., Gensterblum, Y.: CBM and $CO_2$-ECBM related sorption processes in coal: a review. Int. J. Coal Geol. **87**, 49–71 (2011)
5. Ranathunga, A.S., Perera, M.S.A., Ranjith, P.G., Rathnaweera, T.D., Zhang, X.G.: Effect of coal rank on $CO_2$ adsorption induced coal matrix swelling with different $CO_2$ properties and reservoir depths. Energy Fuels **31**, 5297–5305 (2017)
6. Lama, R.D., Bodziony, J.: Management of outburst in underground coal mines. Int. J. Coal Geol. **35**, 83–115 (1998)
7. Harvey, C., Singh, R.: A review of fatal outburst incidents in the Bulli seam (1998)
8. Aziz, N., Black, D., Ren, T.: Keynote paper mine gas drainage and outburst control in Australian underground coal mines. Procedia Eng. **26**, 84–92 (2011)
9. Vishal, V., Singh, T.N., Ranjith, P.G.: Influence of sorption time in $CO_2$-ECBM process in Indian coals using coupled numerical simulation. Fuel **139**, 51–58 (2015)
10. Wong, S., Law, D., Deng, X., Robinson, J., Kadatz, B., Gunter, W.D., Jianping, Y., Sanli, F., Zhiqiang, F.: Enhanced coalbed methane and $CO_2$ storage in anthracitic coals—micro-pilot test at South Qinshui, Shanxi, China. Int. J. Greenh. Gas Control **1**, 215–222 (2007)
11. Pini, R., Ottiger, S., Storti, G., Mazzotti, M.: Pure and competitive adsorption of $CO_2$, $CH_4$ and $N_2$ on coal for ECBM. Energy Procedia **1**, 1705–1710 (2009)

12. Mohanty, M.M., Pal, B.K.: Sorption behavior of coal for implication in coal bed methane an overview. Int. J. Min. Sci. Technol. **27**, 307–314 (2017)
13. Packham, R., Cinar, Y., Moreby, R.: Simulation of an enhanced gas recovery field trial for coal mine gas management. Int. J. Coal Geol. **85**, 247–256 (2011)
14. Packham, R., Connell, L., Cinar, Y., Moreby, R.: Observations from an enhanced gas recovery field trial for coal mine gas management. Int. J. Coal Geol. **100**, 82–92 (2012)
15. Fang, Z., Li, X., Wang, G.G.X.: A gas mixture enhanced coalbed methane recovery technology applied to underground coal mines. J. Min. Sci. **49**, 106–117 (2013)
16. Lin, J., Ren, T., Wang, G., Booth, P., Nemcik, J.: Experimental study of the adsorption-induced coal matrix swelling and its impact on ECBM. J. Earth Sci. **28**, 917–925 (2017)
17. Lin, J., Ren, T., Wang, G., Booth, P., Nemcik, J.: Experimental investigation of $N_2$ injection to enhance gas drainage in $CO_2$-rich low permeable seam. Fuel **215**, 665–674 (2018)

# Safe Extraction of Methane and Power Generation in a Gold Mine in South Africa

J. J. L. du Plessis[1] and M. van der Bank[2(✉)]

[1] University of Pretoria, Pretoria, South Africa
[2] Beatrix Gold Mine, Welkom, South Africa
`Marthinus.vanderBank@sibanyegold.co.za`

**Abstract.** The Beatrix Gold Mine is a deep level gold mine in the Free State Province of South Africa with the highest known methane emission rate in the country. Methane is emitted from underground sources intersected during mining operations and is liberated into the general mine atmosphere. The total methane emission rate from underground sources in the mine is at the order of 1600 l/s whilst the 1 and 2 Shaft Complex of the mine emits approximately 1000 l/s of methane gas. The mine has a history of gas accumulations that has led to a number of underground mine explosions. Following the last explosion in 2001 a number of recommendations followed the investigation. Two of these were to consider the extraction of the underground mine methane to render the mine atmosphere safe and the declaration of hazardous locations which require special operating procedures. A number of such workplaces have been declared at the South section of the mine. Methane gas is furthermore a potent greenhouse gas of which the contribution to global warming and climate change is twenty one times higher than that of carbon dioxide as per original project design document with United Nations Framework Convention on Climate Change (UNFCCC). To reduce its inherent danger of being an explosive gas and to mitigate its global warming impact a carbon credit project under the Clean Development Mechanism (CDM) of the Kyoto Protocol has been developed and implemented to capture and destroy the Beatrix mine methane. The mine has designed and constructed an extraction and power generation systems to capture and extract currently 220 l/s of the methane gas emitted in the 1 and 2 Shaft Complex of the mine. The average concentration (% methane per volume) of the gas intersected at source is 85% methane with negligible concentrations of other hydrocarbons and water associated with it. The mine contracted the services of Group Five to do the design and construction of the flare and ancillary equipment on surface and Agrekko as the power generation rental generators. Promethium Carbon was contracted to assist with the carbon related aspects, approval framework and administration of the project. A number of design, safety and construction challenges were faced to effectively extract and transport the gas to the surface of the mine as these emitters are approximately 3600 m away from the mine shaft at a depth of 860 m. Further considerations were the requirements for the type of column to use to transport the methane gas, the pressure loss the methane gas and a pumping system to extract the gas to the surface. The system operates under negative vacuum provided by two blowers on surface delivering it to a flare capable of burning off 450 l/s of methane gas. The one main area of challenge after construction that appeared was the migration of the methane gas through geological features such as faults and

dykes into other workings where the gas was not initially captured through migration of the methane gas. A secondary sealing program was planned and successfully executed during 2016. In this paper a number of benefits for the mine are discussed. This include but are not limited to the removal of approximately 55% of the total volume of methane gas from the general body of the air in the geographical areas of the mine where the methane gas is emitted into the atmosphere and by reducing the risk of methane related incidents. A further benefit of this project is the mitigation of the global warming impact of the methane gas and the reduction of the mine's carbon footprint by approximately 40%. This project could also assist in alleviating the energy shortage experienced within South Africa by means of ultimately generation of 4 MW of electrical power. Currently with the stabilised flow the generation harvest approximately 1.2 MW. The chamber constructed during the secondary sealing phase are in process of building up into almost a 1,000,000 m$^3$ reservoir.

# 1   Introduction

Beatrix Gold Mine situated in a methane rich area in the Free State Province of South Africa is owned by Gold Fields. The highly explosive methane gas is unlocked into the atmosphere during the course of normal mining operations, and diluted with the ventilation air to below its explosion limits and then released into the atmosphere through its ventilation shafts. Methane gas is therefore a major underground safety hazard in addition to the fact that it is a potent greenhouse gas.

It was decided to capture the methane released by the mine's South section being the area with the most active methane sources whilst also having the highest methane emission rate. The challenge was to capture approximately 50% of the gas released in this area and to transport it over a distance of 3600 m underground at a depth of 866 m, up a vertical shaft to the site selected where the methane gas is flared.

Considerations were the methods to transport the methane gas, the pressure loss over the system, the safety systems to address the risk factors involved in the transport of the methane gas as well as a pumping system to extract the gas to the surface.

Gas monitoring systems were installed at strategic positions along the underground methane gas extraction pipeline with its principle of operation to monitor the quality of the methane gas being extracted. All information from this monitoring system is transmitted control room at the main flare as well as to the mine's central control room.

# 2   Description of Beatrix Gold Mine

Beatrix Gold Mine is situated in the Free State Province of South Africa near the town of Theunissen and 40 km south of the city of Welkom. It is 280 km from Johannesburg. The mine consists of three mining sections being the North, South and West sections.

The North and South Sections operate from the main complex of the mine and consist of three operating shafts which supply the downcast ventilation air. The number 2B ventilation shaft is situated at the west of Number 2 Shaft with its primary purpose

to supply ventilation to the South section. Two upcast shafts, one of which is a brattice shaft remove the used air from the mine.

The West section, which is 17 km north of the main complex of the mine, operates from the Number 4 Shaft system which has two downcast shafts from surface to 5 level and a single sub vertical shaft from 5 level to shaft bottom. The upcast facility consists of a sub vertical up cast shaft from 21 to 5 level and from 5 level the No. 1B ventilation shaft which extends to surface.

The mean rock breaking depth of No's 1 and 2 Shafts is 866.6 m, No. 3 Shaft 1091 m and No. 4 Shaft 2036 m. The virgin rock temperature varies from 33.4 °C at No's 1 and 2 Shafts to 49.6 °C at No. 4 Shaft. Production from stoping and development amounts to approximately 225,000 tons per month for the three sections of the mine. The total airflow quantity circulating through the mine is 1826 kg/s.

The mine utilizes 60 MW of refrigeration to maintain acceptable environmental conditions at its West and North sections respectively to counter the effects of the high rock temperatures encountered as a result of the depth at which mining operations take place.

## 3 Methane History

The gold mining area in the Free State was and is associated with methane emissions with Beatrix Gold Mine having the highest methane emission rate of the mines in operation today. The methane is associated with deep seated sources within geological features such as faults, fissures and dykes, unlocked during normal mining operations and released into the atmosphere where it acts as a potent greenhouse gas. Methane is a major safety hazard underground and notwithstanding continuous efforts to keep methane levels under control, methane explosions have occurred in numerous mines in the region which includes Beatrix Gold Mine.

The underground methane emission rate at the mine is at the order of 1600 l/s of which about 1000 l/s is emitted at the South section, 100 l/s at the North section and 500 l/s at the West section. The concentration of the methane being emitted varies between 82% up to as high as 90%. The concentrations of other hydrocarbons are negligible to the extent where it is not even considered.

The mine has a well executed methane management system to control this risk and to protect its employees against its inherent dangers.

## 4 Registration of the Project

Methane gas is a potent greenhouse gas of which the contribution to global warming and climate change is twenty one times higher than that of carbon dioxide. To reduce its inherent danger of being an explosive gas and to mitigate its global warming impact a carbon credit project under the Clean Development Mechanism (CDM) of the Kyoto Protocol has been developed and submitted for registration to capture and utilize the mine methane.

To mitigate this environmental impact of the mining activity with respect to greenhouse gas emissions, the mine entered into an agreement with a project development firm, Promethium Carbon, to design a project that aims to mitigate the global warming effects of the methane released by the mine.

A Project Design Document (PDD) has been submitted to the Clean Development Mechanism (CDM) Executive Board, with the title "The Capture and Utilisation of Methane at the Gold Fields' owned Beatrix Mine in South Africa". The project was approved in October 2008 by the United Nations Framework Convention on Climate Change (UNFCCC) focus on the capture and extraction of approximately 400 l/s of methane gas at the Beatrix South section.

The project has two phases, the first being the capturing and piping of the methane to surface where it is flared. The second phase will be the installation and operation of an electrical power generation plant with any excess methane being flared. In this paper the activities associated with the first phase is discussed.

# 5   Planning the Gas Reticulation System

Due to the geographic nature of the mining operations and the associated methane intersections, it is not possible to capture all the methane gas. It was therefore decided to target specific working areas where high methane emission rates are being experienced.

The target area where the methane is captured is situated towards the western boundary of the South section where the highest rate of methane emission takes place.

When planning the methane reticulation system, various issues had to be considered namely.

## 5.1   The Gas Reticulation Route

Various flare and associated power generation site selection options were considered to ensure that all the required needs would be met.

The depth at which the methane gas is captured varies between 830 and 866 m below surface. The main methane gas reticulation column has been designed and constructed 16 Level being the lowest level of the South section at 866 m below surface.

A number of route considerations were investigated. The first consideration was to capture the methane gas and to transport it along 16 Level to the No. 2B ventilation shaft which is situated in close proximity to the area where the methane gas is being captured. The methane gas pipeline column then had to be installed in the shaft and then transported across the surface to the selected site. This option, however, was decided against for two main reasons being that the methane gas pipeline had to cross a national road and it also had to detour around the mine's slimes dams which would have resulted in a pipeline length of more than 5000 m on surface.

The second consideration was to carry the methane gas pipeline along 16 level towards No. 1 Shaft to a position of approximately 400 m before reaching the shaft. A 300 mm diameter hole would then be drilled from surface to 16 Level, and lined for

transporting the methane gas. The concern in this regard was that ground movement in the hole could affect the lining and subsequent uncontrolled leakage of the methane gas. The cost of such a hole was also excessive and as such this option was not pursued any further. It was finally decided to carry the methane pipeline along 16 Level to the No. 1 Shaft and install it in the shaft from where it was installed across a relatively short distance to the selected site for flaring and power generation. In Fig. 1 the position of the pipeline is shown.
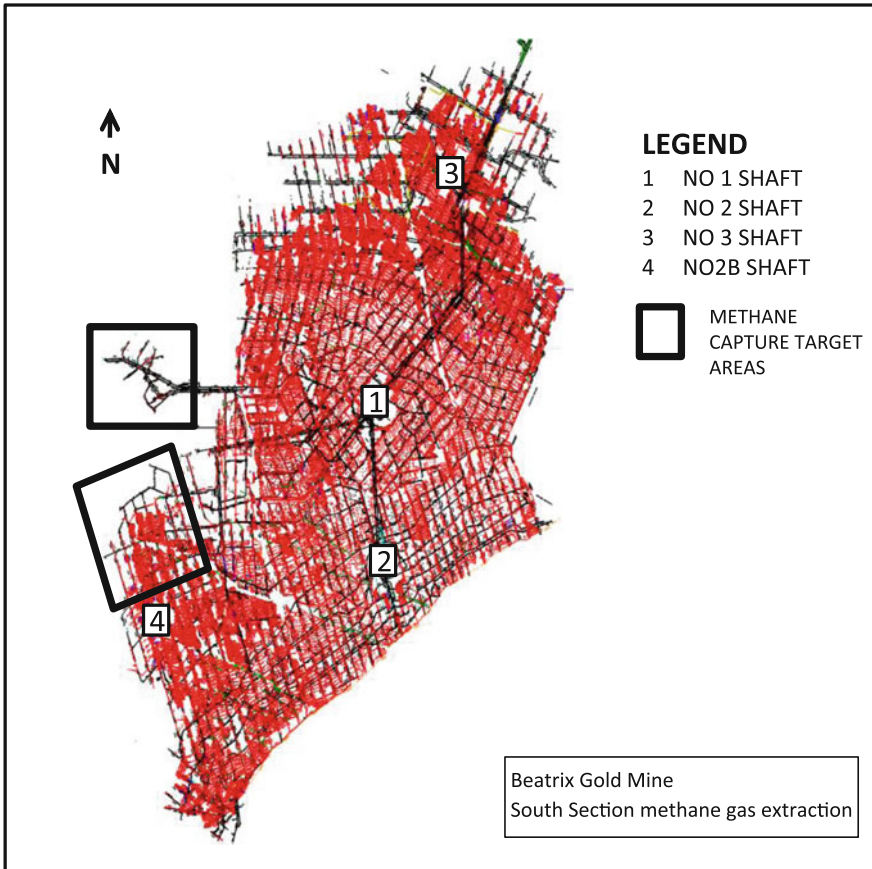


**Fig. 1.** Plan view of the underground workings of the North and South sections showing the areas at which the methane gas is captured

## 5.2 Pipe Selection for the Methane Gas Reticulation System

The methane gas is captured at various localities and fed into the main reticulation pipeline. An ideal gas transport velocity of 11 m/s was used when calculations were performed to determine the required pipe sizes for the reticulation system.

The underground methane gas reticulation system has various branches feeding into the main system consisting of pipe sizes ranging from 110 mm diameter up to the final size of 250 mm diameter. A 450 mm diameter steel pipeline has been installed in the No 1 Shaft and on surface. The final pressure loss calculated across the reticulation system is 25 kilopascals.

The initial pipe selection for the methane drainage system was galvanised pipes with standard flanges. It was realised, however, that selection of the wrong type of gasket could yield numerous leakages. Further investigation into a suitable type of pipe was done and the final selection was made on titanium reinforced PVC (tPVC) pipes. These antistatic pipes are joined by making use of sleeves with o-rings and splines to secure it into position. These pipes are also impact and fire resistant and are capable of handling both high positive and negative pressures making it suitable for this type of application.

## 5.3    Safety Considerations

The safety of mine employees is of utmost importance and therefore care was taken to ensure the safe operation of the methane extraction system. The whole underground system operates under negative pressure whilst the methane gas concentration in the pipeline will not be allowed to be below 40%. It is anticipated that the average gas concentration could be maintained between 70 and 80%.

The system is equipped with flame arrestors both at the main flare as well as one flame arrestor underground. Shut off valves are installed oat each of the methane gas monitoring stations. The status of the methane gas extraction system is monitored on a full time basis by means of six main gas monitoring systems installed along the length of the underground pipeline.

## 5.4    Peer Review

A peer review was done on the underground design and installation of the underground methane gas extraction system. This review which was done as a due diligence and safety issues exercise was facilitated out by a professional engineering company with a proven record of expertise in this field of work. A number of recommendations were made which the mine had to carry out prior to the commissioning of the underground extraction and flaring project. The recommendations made by the peer review group included the following:

- Perform a hazardous area classification of the underground extraction system
- Perform physical audit of all ignition sources along the route
- Carry out a flexibility analysis on the piping design to address pipeline issues such as expansion, support systems, connection and stiffness.
- Implement earthing plan to prevent build up of static electricity
- Carry out leak detection after installation and any modification to the piping.

# 6 Capturing the Methane Gas at Source

The incidence of methane gas intersections varies between drill holes in the rock face to methane seeping through cracks and in some instances geological features and anomalies particularly in stopes.

Two methods to capture the methane are being utilised which can be described as methane capture at source or capturing methane through the construction of methane chambers encapsulating worked out areas by means of explosion resistant seals.

Capturing the methane at source is done through connecting methane sources directly into the methane extraction pipeline in areas where drill holes were drilled into the methane fissures as part of prospect and cover drilling processes. These are directly connected to the methane extraction column as part of the methane capture process. No special holes were drilled in an attempt to locate methane sources for capturing as there is an abundance of methane sources present which were intersected during the course of normal mining operations.

Three worked-out mining areas with numerous methane sources, collectively emitting at the order of 400 l/s of methane gas into the mine atmosphere, were identified to be sealed by means of explosion resistant seals to create methane chambers. These chambers are treated as three individual methane gas sources and are as such connected the methane gas extraction system.

# 7 The Monitoring System

Six main monitoring stations as well as six sub monitoring systems were installed along the extraction system. This system monitors both the quality and quantity of the methane being extracted and all information is relayed to the mine's main control room.

The methane gas travelling in the pipeline is sampled using infrared and chemical gas sensing equipment. The methane purity is calculated by using mathematical algorithms after passing through a drying process to remove the moisture. Pressure and flow measuring equipment in conjunction with a sampling pump is used to ensure that a constant sample is applied at the sensors. Other features of the monitoring system are measuring the gas velocities using flow bars and differential pressure sensors as well as monitoring the temperature of the methane gas and process pressure.

# 8 Conclusion

The project idea was initiated towards the end of 2006, but a number of hurdles had to be overcome mainly as a result of all the approval processes within Gold Fields era at that time and at the CDM secretariat, detailed planning requirements and the financing of the project.

The project will assist in reducing the methane risk in reducing the release of methane into the underground atmosphere at the South Section by 49%. This reduction in the release of methane into the mine's underground atmosphere is a significant

contribution towards maintaining conditions conducive to the safety of the employees of Beatrix Gold Mine.

This project has further benefits in terms of reducing the carbon emissions created as a result of the release of methane gas into the atmosphere. The carbon footprint of the mine was reduced by approximately 41% which is important in terms of the mine's contribution towards reducing global carbon emissions and is in line with Sibanye Stillwater's strategic objective of being the Global Leader in Sustainable Gold Mining.

# References

## Book

1. McPherson, M.J.: Subsurface ventilation and environmental engineering, pp. 436–454. Chapman and Hall, London

## Report

1. **CEAN DEVELOPMENT MECHANISM PROJECT DESIGN DOCUMENT FORM (CDM-PDD)** "The Capture and Utilisation of Methane at the Goldfields' owned Beatrix Mine in South Africa" Published on the Web site of the UNFCCC

# Leveraging Coal Mine Methane/Ventilation Air Methane for Improving Ventilation Standards in Indian Underground Coal Mines and to Reduce Its Carbon Footprints

Satish K. Sinha[1(✉)] and D. C. Panigrahi[2]

[1] Continuing Education, Indian Institute of Technology (ISM), Dhanbad, India
pce@iitism.ac.in; sinhasatish@hotmail.com
[2] Department of Mining Engineering, Indian Institute of Technology (ISM),
Dhanbad, India
dc_panigrahi@yahoo.com

**Abstract.** In underground coal mines, regular make of gas i.e. methane build-up is no surprise particularly in workings of Degree II/III coal seams. Historically, we have had some sordid past and rightly so have reasons to perceive it as a potential threat of mine explosions. Indian Coal Mines Regulations provisions on concerns of dilution of mine air with fresh air sucked from surface atmosphere and eventually venting it (primarily methane and other greenhouse gases) back to surface in order to ensure mines safety. In India, the practice of ventilation is not the bleeder type where safety is doubly ensured. Rather, at places, it has been found to be a case of inadequate ventilation in goaf and other abandoned areas of underground mines that not only adds to ventilation problems but also render a condition conducive to occurrence of fire and explosions. In this paper an attempt has been made to change the perspective of coal mine operators entirely in contrast to traditional practices. A coal mine is a source of revenue not only by coal but mine water, mine gases and the country rock can as well be thought of as resource commodities. This paradigm shift in approach would convert the conventional mining threats of inflammable gas explosion into a commercial proposition. India has over hundreds of gassy mines of which around twenty (20) coal mines have been categorized as highly gassy (Degree III). A study has been made and estimate done about the loss of business opportunity in terms of unaccounted release of coal mine methane and more importantly Ventilation Air Methane (VAM). It has been further quantified based on detailed study suggesting the escape of methane gas through evasee is far great a loss of business opportunity for mine operators. Two detailed cases on CMM and VAM would be an interesting read for mine operators to continue coal mining with sustainability. This would also help them evolve from mere miners to Earth entrepreneurs.

**Keywords:** CMM · VAM · GHG · Sustainability · Carbon-footprint
Additionality

# 1    Introduction

Coal—the backbone of India's energy matrix and the predominant fuel for future. India aims at producing more than 1 billion tonne of coal annually by 2020–21 to meet its envisaged energy demand. In this backdrop, a paradigm shift is contemplated from dominating scenario of surface mining to underground operations in view of growing concerns about land, environment and inhabitants'.

Large scale underground mining of coal renders opportunity to cater to country's demand. However, with every increase in coal production, a corresponding increase in release of methane ($CH_4$) gas adsorbed therein its lattices are inevitable. Methane gas gets formed due to anaerobic decomposition of plant/organic materials in its coalification process. Methane, though physiologically a harmless gas by itself, is highly inflammable and explosive particularly in underground mining conditions.

Underground (UG) mining conditions become explosive when methane percentage ranges from 5–15% is present in general body of mine air. To render it safe, fresh air is flushed, and gas-laden air is ventilated out of the mine reducing the methane content at working areas. An estimated 1 billion $m^3$/year of methane gas is vented to Earth's atmosphere from over 300 coal mines operating in India.

Methane as a potent greenhouse gas, 21–23 times more harmful than $CO_2$—the greenhouse gas considered for global warming. The safety threat of methane in coal mines can now be easily viewed as a staple opportunity towards reducing carbon footprints.

An average estimate of methane release out of a single coal mine through its return air way has also been worked out towards assessing VAM potentialities.

India with around 370 billion tonne (Bt) of estimated coal reserves and production of over 650 Million tonne of coal ranks among the top three coal producing countries in the world after China and USA. The larger pie of coal production in India comes from opencast mining and less than 15% are contributed from underground coal mines which is quite in contrast to China. Country's population of operating UG coal mines is around 340 mostly small in size, producing less than 1 million tonne per year (Mty). More than 5% of these UG mines are highly gassy seams of degree III (i.e. >10 $m^3$) of methane liberated per tonne of coal output) located in various coalfields of India. The usual mining practice is to vent excessive make of methane [termed as Coal Mine Methane (CMM)/Ventilation Air Methane (VAM)] from UG coal faces to the atmosphere, rendering mine atmosphere safe to continue with mining operations.

Currently, due to an increased emphasis on reduction of emission of greenhouse gases (GHGs) causing global warming, leveraging CMM/VAM an important mining by-product can be seen as green initiative towards preventing its emissions to atmosphere causing global warming effect [1].

In each of the potentially gassy UG coal mines, CMM/VAM emission is estimated to be 5–15 million cubic meter (Mm$^3$) per annum, which are even more for large size highly productive (>3 Mty) mines. The make of methane gas has also found to be increasing with rank of coal being mined. Thus, CMM/VAM can be seen as a potential area towards reducing carbon footprints and moving for sustainability under the overall guidelines of United Nations Framework Convention on Climate Change (UNFCCC).

The paper also illustrates VAM plants operating world-wide producing electrical energy, thereby saving in emissions of GHGs in terms of $CO_2$ (equivalent) and explores opportunities of applying similar techno-commercial approach in Indian gassy coal mines. That would help keep planet Earth protected from global warming effect as well [2].

## 2 Potential for Coal Mine Methane in India

India currently ranks sixth in coal mine methane (CMM) emissions (estimated to be 1 billion $m^3$ per year). About three quarters of the domestic electricity is generally coal-fired emitting $CO_2$—the global warming gas. In India, more surface mines have been developed due to the occurrence of country's vast resources at shallow depth and in view of growing coal demand. However, the industry is compelled to undergo a shift towards underground mining [1].

Based on the rate of methane emission, Indian coal mines regulations specify a 3-tier classification. Table 1 refers to distribution of coal mines as per its gassiness:

**Table 1.** Classification of UG coal mines in India based on methane emission

| Class | % of emission | $m^3$/t of coal produced | Number of mines |
|---|---|---|---|
| Degree I | >0.01 | <1.00 | 220 |
| Degree II | >1.00 | <10.0 | 100 |
| Degree III | | >10.0 | 20 |
| **Total** | | | **340** |

### 2.1 Abandoned Mine Methane (AMM)

Only 5% of abandoned mines in India are considered gassy which can be a source of energy tapping as Abandoned Mine Methane (AMM).

### 2.2 Coal Bed Methane/Coal Mine Methane

The Directorate General of Hydrocarbons (DGH), Govt. of India (GoI) estimates that deposits in 44 major coal and lignite fields in 12 states of India covering an area of 35,440 $km^2$ contain 3.4 trillion $m^3$ of CBM depending on the rank of the coal, depth of burial and geotectonic settings of the basins. In Jharia Coalfield of Jharkhand state, the gas content is estimated to be between 7.3 and 23.8 $m^3$ per tonne of coal within the depth range of 150–1200 m. Analyses indicate that methane content increases with rank of coal and with every 100 m increase in depth, an associated increase of 1.3 $m^3$ in methane content is possible [3] (Fig. 1).

### 2.3 Ventilation Air Methane (VAM)

In UG coal mining, adequate precautions are taken against methane gas emission at the working coal faces because of its potential to explode. Mine ventilation conditions are

**Fig. 1.** A CBM plant in operation at Monidih, Jharia Coalfields, Dhanbad, India

improved by circulating fresh air, thereby making methane content in the general body of the mine air diluted to harmless percentage and finally sucked out of the mine to surface via main return air way. Thus, a danger free mine environment is rendered.

In India, in around 340 coal mines, mine ventilation fans run continuously non-stop $24 \times 7$, exhausting methane-laiden mine-air to the atmosphere, contributing to global warming.

An estimate of amount of methane gas escaping from a semi-mechanized UG coal mine (Degree II) of moderate size (0.1 Mty coal). The percentage of methane at the mine exit is considered to be 0.3% in return air (Directorate General of Mines Safety (DGMS)—the mines' safety regulators in India permits up to 0.75% of methane in the general body of return air). Fan at the mine is PV-200 operating $24 \times 7$ delivering 80–100 $m^3$/sec of air.

**Estimation of VAM**:

- Quantity of air at the mine exit: $100 \times 3600$ $m^3$/hour, or $100 \times 3600 \times 24 \times 365$ $m^3$/year
- Amount of Methane liberated: $0.3\% \times 100 \times 3600 \times 24 \times 365$ $m^3$/year, or 9,460,800 $m^3$/year of methane (as return air contains 0.3% methane), $0.717 \times 9,460,800$ kg/year of methane (Density of $CH_4$ being 0.717 kg/$m^3$)

6783.3 tonne/year of methane 156,018 tonne/year of $CO_2$ equivalent (GwP of 1 $CH_4 \equiv 23$ units; 156,018 tonne/year of $CO_2$ equivalent (GwP of 1 $CH_4 \equiv 23$ units of $CO_2$)

- Savings in Carbon footprints/year: 156,018 REC (Renewable Energy Certificate) may be earned for reducing C-footprints and towards sustainability.

If this quantity of methane is saved without letting it being emitted to the atmosphere by routing it to the GENSET (a gas-fired generator for power generation), the gas not only will generate electricity, but also will convert $CH_4$ into $CO_2$ instead, reducing its global warming potential by 21–23 times. Later this $CO_2$ can be further sequestrated to improve carbon productivity and reducing company's carbon footprints.

Economic viability of the VAM Plant needs to be worked out depending upon the quality and quantity of methane gas available.

Around 60–70% of total mine methane is ventilation air methane (VAM) and it accounts for 5–8% of total global methane release. VAM power plants are in operation producing in the range of 200 MW at over 20 mine locations across the globe.

It is worth mentioning here that in Illawara Coalfields, NSW, Australia, VAM plant of 5 MW is operating successfully with 250,000 m$^3$ of air/hour (70 m$^3$/sec) (0.9% methane), reducing 250,000 tonne of $CO^2$ equivalent per year. An initial investment of AUD30 million and technology from Ms. Vocscidizer is in place.

## 3 Ongoing and Proposed CBM/CMM Projects in India

### 3.1 CMM Projects

Current activities include a 19.22 million USD pilot or demonstration project of the United Nations Development Program (UNDP), the Global Environmental Facility (GEF), and the Indian Ministry of Coal (MoC), entitled "Coal Bed Methane Recovery & Commercial Utilization." The project seeks to demonstrate the commercial feasibility of utilizing recovered methane gas, during and after coal extraction. This project is being jointly implemented by Central Mine Planning & Design Institute Limited (CMPDI) and Bharat Coking Coal Limited (BCCL) [both subsidiaries of Coal India Limited (CIL)] in Jharia Coalfields.

**Status of Ongoing CMM projects**. The present status of the project is as follows:

(a) Recovery of CBM/CMM from one well commenced since May 2008 and from four bore wells at Monidih site;
(b) Power generation by gas-fired plant commenced on 27th June 2008 at Monidih Mine site. Generated power is being supplied to Monidih Colony for lighting and domestic usage. Broad parameters of the CMM operation plant are:

- Power generation = 2 × 250 kW Cummins engine gas-fired GENSET;
- Liberated methane concentration ∼94% (approx.);
- Generation of 500 kW electric power from CMM saves emission around 4294 tonne of $CO_2$ equivalent per year; had it been producing by conventional means

and additionally it consumes 5400 m$^3$ of methane/day i.e. 32,504 tonne of $CO^2$ equivalent per year cumulating to 36,798 tonne of $CO^2$ equivalent annually;

- Till recently, the plant worked well, however, there have been reports of wells getting dried up of methane affecting the CMM plant operation and efficiency to a greater extent.

**CBM Project Opportunities**. The Directorate General of Hydrocarbons, the lead organization for CBM development in India, has been working closely with the Ministry of Coal to scope out additional CBM prospective blocks for future round of bidding. In this context, eight CBM blocks in the coalfields of Ib-Valley, Talcher, Satpura, Godavari-Valley, Rajmahal, Singrauli, and Wardha-Valley and Northern Coalfields of the country have been identified. Drilling of core holes to generate CBM-related data in these identified blocks will be implemented.

- Methane content of CMM differs widely from one mine to another and even within one particular project. Even within one coal mine, gas quality fluctuations occur daily or even more frequently. However, modern utilization equipment is designed to deal with different methane concentrations and can adapt to fluctuations of methane concentration. If CMM is distributed via pipeline, as is the practice in some countries, fluctuations are less likely to occur because the pipeline acts as a mixing and storage tank. In addition, in many countries which may become hosts to the flexible mechanism projects, standard gas drainage protocols are employed. This results in sub-optimum production of gas with fluctuating concentrations.
- Recently a coal block of 25 sq. km has been delineated in Jharia Coalfield comprising Jarma, Kapuria and Monidih coal block for possible extraction of methane. Also, a methane drainage plant in Monidin Longwall mine in 16 Top Seam promises erection of a 2 MW plant with an input of 4 cum of air methane mixture with 60% methane as its feed. An investment of Rs. 360 million has been planned in Jharia coalfields to tap Coal Mine Methane from the working mine. This is a joint initiative by CSIRO, Australia, CMPDI and BCCL from Coal India Ltd.
- An area of 57 sq. km has been earmarked by India CBM/CMM clearing house, CMPDI in Kali-Pahari in Nirsa block located in Raniganj coalfield is currently engaged in generating data set from pilot holes that would be guiding to set up a new CMM based power plant therein [3].

**Other CMM Project Opportunities**. There are other CMM Project opportunities scoped out other Jharia and Raniganj Coalfields which are:

- Moher Sub-Basin, Singrauli Coalfield, Madhya Pradesh and Uttar Pradesh and
- Korba Coalfield, Chhattisgarh State, India.

**VAM on Indian Soil**. The hurdle in VAM is the low concentration of methane obtained in its main return of the mine [4]. At Monidih, district return of a mine shows methane concentration range of 0.9–1%. However, it reduces to 0.1% methane in main return through an evasee.

A model of VAM plant that has received first prize in Safety Conclave in Coal India is reproduced below (Fig. 2).

**Fig. 2.** A VAM plant model displayed in a safety conclave of Coal India Ltd.

## 4 Subject Perception

Coal Mines Regulations 2017 has been enacted since November 2017 and one separate Chapter XVI is devoted to "*Extraction of Methane from Working Coal Mines or Abandoned Coal Mines*" The safety directorate of Mines Safety in India (DGMS) shall administer the safety aspects of it and mine operators are under obligation to abide by its provisions as owner/agent/manager. This may be viewed as a reinforcement to mine owners' claim over CMM and of course have laid responsibility over them for its gainful exploitation.

Authors think that in order to promote projects like CMM/VAM, a few provisions like "Additionality" of erstwhile CDM (Clean Development Mechanism) still useful and may be considered for adoption. To render financial support to such environmental friendly projects that would help reduce carbon footprints, a guideline of "Additionality" is being re-proposed [5]. If the project stands through its sub-points, it may be worthwhile promoting. The provisions of "Additionality" are briefly summarized as follows (Table 2).

The need for conservation and utilization of methane gas has assumed tremendous importance in the global as well as national coal mining sectors, triggered by the environmental degradation like global warming and emission of greenhouse gases [6]. The sustainable development, conservation and efficient use of earth resources are imperative for holistic growth of mankind.

**Table 2.** "Additionality" criteria for CMM/VAM projects

| Barrier type | The project may be considered for "Additional" if…. | Examples |
|---|---|---|
| Investment barrier | The project has a higher life-cycle cost per kWh compared to the technology in the baseline. The project developer cannot access financing at a reasonable cost or in an appropriate currency | Discounted costs per kWh of a CMM/VAM, wind plant is higher than a coal fired plant and there is no higher feed-in tariff for renewables to offset these higher costs. Banks are unwilling to lend such unconventional projects |
| Technological barrier | The project technology is not well known and investors/lenders are unwilling to finance the project. The project technology is not yet well developed and may even be a prototype | VAM, Tidal and wave power technology is not well established and considered risky investments |
| Barrier due to prevailing practice | The project technology may be known but is proposed for a new application. The project deploys a well-established technology which is not yet common in the region or country | Venting of methane from coal mines is an accepted and required practice. Capturing and utilizing coal mine methane requires convincing coal mine operators to establish a new practice |
| Other barriers | Assorted policy or legal barriers can create resistance to the adoption or financing of projects | Subsidies for kerosene for diesel fuel in rural areas may prevent the adoption of solar photovoltaic or micro-hydro for lighting and small-scale electricity needs |

## 5   Conclusion

Methane in coal mines, though physiologically harmless by itself, has always drawn attention because of it being highly inflammable that could cause explosions. Presence of methane in gassy coal seams is a safety hazard. In UG coal mining, adequate precautions are constantly observed against methane emission at the working coal faces because of its potential to form an explosive mixture with air.

The mining companies are facing this challenge historically to avert such risks on health and safety of the work-personnel. Even from opencast coal benches, methane gases are liberated into atmosphere adding to greenhouse effect. All out efforts have to be made by the companies to tap the gas before, during and even after mining to render the mine and the surface atmosphere safe. These environmental/health risks can now be transformed into opportunities utilizing the tapped gas in CBM/CMM/VAM plants for generation of electrical energy, thereby saving in emissions of GHGs.

Our regulators, financers and technologically developed countries need to assist mining companies by encouraging initiatives undertaken by mine entrepreneurs' development of practical and legislative frameworks.

# References

1. Sinha, S.K.: Carbon market. Coal Min. Technol. Manag. **13**(1), 11–14 (2008)
2. http://www.methanetomarket.org. Last accessed 18 Feb 2018
3. CMPDI (Event Host): Summary of India's potential for CMM/CBM market & Ongoing and proposed CBM/ CMM Projects in India. Briefing Book, India CMM/CBM Clearinghouse Kick-off Event, Nov, pp. 12–15, 16–18 and its subsequent workshops conducted by India CBM/CMM clearing house, CMPDI, Ranchi
4. AHGE: Challenging misconceptions surrounding coal mine methane. E-Coal, WCI Publication 67, 6–7 Jan (2009)
5. US EPA Homepage. http://www.epa.gov. Last accessed 18 Feb 2018
6. www.unfccc.int. Last accessed 18 Feb 2018

# Influence of Pressure Changes on Gas Distribution in Longwall Gobs

Stanisław Wasilewski[✉]

The Strata Mechanics Research Institute of the Polish Academy of Science,
Kraków, Poland
stanwas@agh.edu.pl

**Abstract.** The mining systems used in the Polish mining industry, longwall system with caving, cause the formation of the gob, where it acts like a "sink" where gases tend to accumulate. The statistics of disasters in recent years in Polish hard coal mines show that most of the events took place or were initiated just in the gob of longwalls with cave-in. It is known from the mining practice that the barometric pressure and its disturbances (known as, "breathing of the gob") can have a significant effect on the ventilation conditions of the underground mines, and in particular on the gas distribution in the gob of the longwalls and the sealed off spaces. The existing solutions with regards to methane and fire hazards being developed in the gob are imprecise and the space inside the gob is practically uncontrolled and poorly recognizable in terms of gas concentration distribution and phenomena occurring in the gob. The paper presents a method of monitoring gases in the mine automatic gasometry system, which enables mine management to monitor, implement control measures in gob areas and examine its effectiveness in real time. To illustrate the potential of the proposed solution, examples of the change in the distribution of gases in the gob as a result of air pressure changes are presented.

**Keywords:** Gas measuring in mine · Monitoring gases in gob of longwalls
Hazards in gob of longwalls mined

## 1 Introduction

In recent years, the threat of explosion in longwall gobs is the most serious gas hazard, often being the cause of recent mining disasters. In practice, it is suspected that the initiation of ignition in gobs may be due to fires in fissures, spontaneous heating sources or self-falling, sparkling compact roof rocks forming a debris.

The influence of barometric pressure changes on the migration of gob gases is known in mining practice as the so-called "breathing of the gob". These phenomena were the subject of model studies [4, 7] and were recorded in the conditions of an underground mine [8, 9]. Recently they have also been the subject of research in the USA and their results have been presented [5, 6] in June at the 16th North American Mine Ventilation Symposium, in Colorado USA. For many years, in conditions of

Polish mines recordings of pressure changes have been done with signaling and warning by means of banners and announcements "Caution: atmospheric pressure drop".

Until now, it is assumed that only atmospheric pressure drops are dangerous because they can cause the outflow of the gob gases into the longwall or adjacent workings, or the outflow of fire gases from the sealed off fire areas. If it is assumed that the initial may be located somewhere in the gob, it cannot be excluded that also a rapid or long-lasting increase in pressure may constitute a danger causing the migration of gases in the gob [12]. The creation of an explosive atmosphere in the vicinity of a fire source or spontaneous heating, which also may lead to ignition or explosion in the gob.

Experimental investigations of gases distribution in the gob were conducted in the Czech mines [1] by taking periodic samples of gases which were subjected to chromatographic analysis in the laboratory. Worldwide solutions are known for monitoring and control of the gob gases [2] in terms of fire hazard based on the so-called "tube bundle system", which are used effectively in mines in Australia, USA, India and China. These systems consist of chromatographic analysis on the surface, air samples taken from the gob and sealed off spaces with the use of a central pump and tube systems. However, due to the size and structure of Polish ventilation networks, it is technically impossible to transfer this solution directly to the conditions of Polish mines.

The currently used in the Polish mining industry methods of chemical analysis of gas samples in the mine laboratory, taken for early detection of endogenous fires, do not guarantee a direct control of processes occurring in the gob for risk assessment. It causes that it is also uncertain whether the scope of preventive measures applied to eliminate the ignition hazard in the gob is properly selected. This fact was the basis for undertaking work to develop new methods and measurement tools enabling continuous control of parameters of the air in the gob.

In 2006–2007, an integrated gob sensor ZCZ was developed to measure the concentration of $CH_4$, $O_2$ gases, by means of which the parameters of gob gases were recorded in the monitoring system [3]. Continuing this research direction within the research project carried out in Strata Mechanics Research Institute of the Polish Academy of Sciences, in the years 2008–2011, the range of the gob. Sensor was extended by the measurement of the concentration of gases $CH_4$, $O_2$, $CO$, $CO_2$ [11]. This new approach to the control of the gob required a number of studies and experiments. They showed that it could not be used in conditions of routine mining operations, due to the difficulties of maintaining of sensors in hard conditions and problems with calibration of inaccessible sensors.

Taking advantage of the experience gained, a solution has been [12] based on the automatic sampling of gas from the gob instead of immersing the integrated the gob sensor in the of gob. Based on this idea, an integrated gob sensor ZCZ-MP has been developed, with an automatic sampling system for the sampling of gases from gob together with the measurement of the concentration of gob gases and their registration in the monitoring system. The system automatically sucks in a sample of gases from the orifices with hoses in the pneumatic system, and the measurement of the gas concentration is carried out by means of sensors in the measuring station installed in the working outside the gob.

The adopted solutions allowed for long-term observations to record changes in distribution of gas concentration also as a result of changes in air pressure, what will be presented in this paper.

## 2  Development of a Solution for the Measurement of the Gob Gases in the Monitoring System

### 2.1  Integrated Gob Sensor ZCZ

For the current control and monitoring of gas concentration in the gob, an integrated gob sensor ZCZ was developed [11] in the form of a tube probe (Fig. 1) with drilled holes for free internal migration of the gob gases inside the probe. Inside the probe sensors ($CH_4$, $O_2$, $CO$, $CO_2$) were placed for automatic measurement of gas concentration in the gob and their automatic recording in the monitoring system.
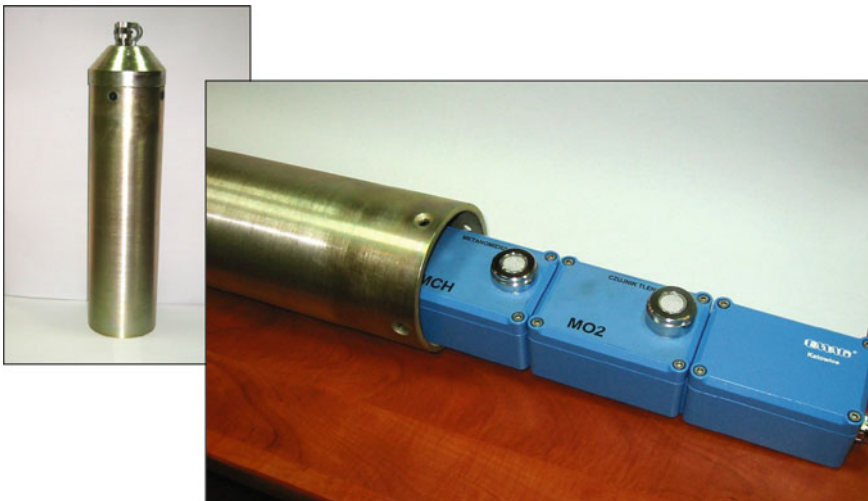


**Fig. 1.**  Integrated gob detector with a set of sensors

In order to control the gas concentration in the gob of longwalls mined with cave-in, a pipeline made of perforated pipes was used, which was laid on the floor of controlled gob, in which an integrated gob sensor (a probe) was placed. As the front of the longwall advanced, the probe with integrated gob sensor remained deeper and deeper in the gob.

In the course of the research carried out with the use of sensors placed in the gob, many valuable records were obtained for identifying the hazard in the gob [11]. Many difficulties were also observed in maintaining continuity of measurement lines with sensors in the gob, failure rate of gas sensors due to flooding of lines and electronic circuits and lack of access to sensors for calibration purposes.

Therefore, it was considered that such a solution could only be useful in experimental conditions but could not be applied in operational conditions.

## 2.2 Integrated Gob Sensor ZCZ-MP

Based on previous experience, a solution was proposed of an integrated gob sensor ZCZ-MP (Fig. 2), with an automatic system of gas sampling from the gob together with measurement of the concentration of the gases $CH_4$, $O_2$, CO, $CO_2$ and their registration in the monitoring system [12]. The metrological parameters of the measurement of gas concentration in the gob are the same as in Table 1. The important difference is that the gas samples are automatically sucked into the measurement chamber by means of a measuring line (hoses) and the measurement systems (sensors) for measuring the concentration of the gob gases are placed in the station outside the gob.



**Fig. 2.** Integrated gob sensor ZCZ-MP, with automatic gas sampling system from the gob

**Table 1.** Metrological parameters of gas sensors

| Parameter | Measuring range | Measuring error |
|---|---|---|
| Methane concentration | 0÷100% $CH_4$ | 0.1% $CH_4$ in the range of 0÷5% $CH_4$, 3% $CH_4$ in the range of 0÷100% $CH_4$ |
| Oxygen concentration | 0÷25% $O_2$ | ± 0.5% $O_2$ |
| Carbon monoxide concentration | 0÷1000 ppm CO | 3 ppm in the range of 0÷200 ppm CO, 25 ppm in the range of 0÷1000 ppm CO |
| Carbon dioxide concentration | 0÷5% $CO_2$ | ± 0.1% $CO_2$ |

# 3  Study of the Gas Concentration in the Gob of Longwall 420 Seam 418 in the Wesoła Mine

The observation of gases in the gob was conducted in the longwall 420 in seam 418B at level 665 m horizon in the Wesoła mine mined by a longitudinal system with roof cave-in and ventilated with a "U" system along the coal body. The research was carried out for three months of the longwall's advancing, in an monitoring system, recording the concentrations of gob gases ($CH_4$, $O_2$, CO, $CO_2$) using an integrated ZCZ-MP sensor [11]. In addition, gas concentration and air velocity sensors in the area, as shown in Fig. 3, have been used to record air parameters in the area of examination.
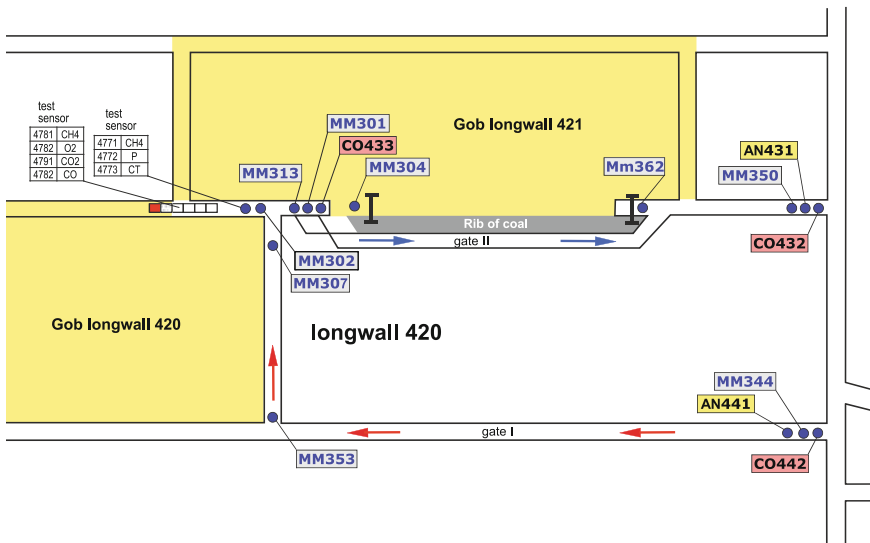


**Fig. 3.** Distribution of sensors in the longwall 420 seam 418B during the examination period

Interesting courses of gas concentration in the gob were recorded during the test period 26.10–4.11, which is shown in Fig. 4. The influence of absolute pressure recorded in the test area on changes of both methane and oxygen concentration in the gob is clearly visible. At the same time, it should be stated that the methane concentration in the gob was negatively correlated with air pressure, while the oxygen concentration was positively correlated with air pressure. The courses of changes in methane and oxygen concentration clearly indicate changes in the distribution of these gases in the gob as a result of the displacement of gob gases as a result of the so-called "breathing of the gob".
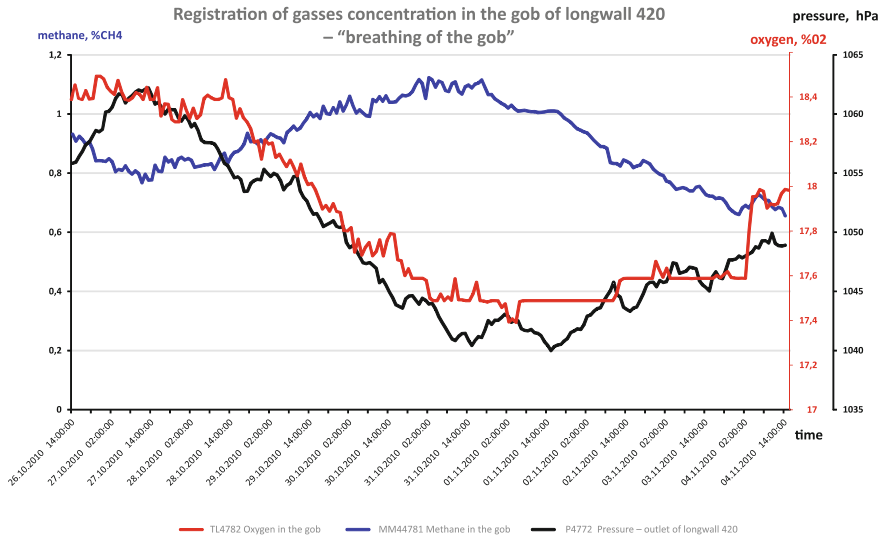
**Fig. 4.** Courses of gas concentration in the gob and absolute pressure recorded in the area of longwall 420 during the tests period 26.10–4.11

## 4   Tests in the Gob of Longwall F-1 in Seam 406/1 in the Zofiówka Mine

The area of longwall F-1, in seam 406/1, in the Zofiówka mine was chosen as the place of long-term observation of the gas concentration in the gob. The advance of longwall F-1 was conducted in the conditions of the fourth methane hazard category and methane and rocks outburst hazard. The longwall F-1 was system mined by a longitudinal system with roof cave-in and ventilated with a "U" system along the coal body.

The tests in the longwall F-1 in the Zofiówka mine were carried out by automatically taking gas samples from the gob using the integrated gob sensor ZCZ-MP and recording data in the monitoring system [9].

During the exploitation of the tail gate F-1 in seam 406/1, its isolation was carried out behind the longwall (Fig. 5) by means of barriers (so-called constructional stoppings), made on the basis of chemical foams or mineral binders. These barriers were built at a distance of 3÷4 m behind the line of the longwall's cave-in. In sequent barriers, measuring pipes were installed at a distance of about 50 m, to which sequent lines of the chromatographic hoses were connected. The ends of the hoses were led to the measuring system of the integrated gob sensor ZCZ-MP integrated to the monitoring system. As the front of the longwall was advancing the ends of subsequent measuring lines remained deeper and deeper in the space of the gob. Simultaneously, parameters of circulating air and barometric pressure in the area of longwall F-1 were recorded in the mine monitoring system [12].

During the study period of the composition of gas samples taken from the gob and changes in absolute pressure in the area of the longwall were recorded (Figs. 6 and 7).
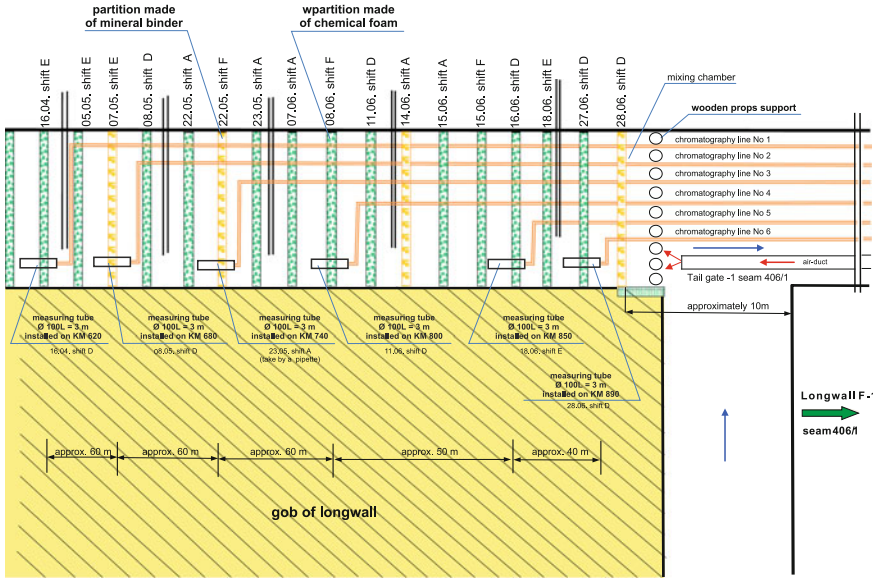
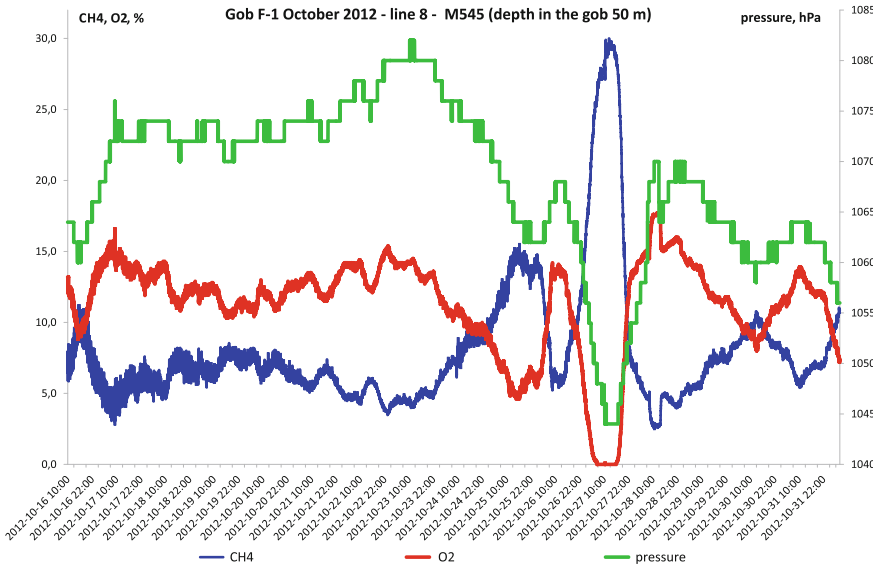**Fig. 5.**  Diagram of installation of measuring tubes and partitions in the top gate F-1 seam 406/1



**Fig. 6.**  Monthly recording of gas composition in the gob and pressure in the monitoring system
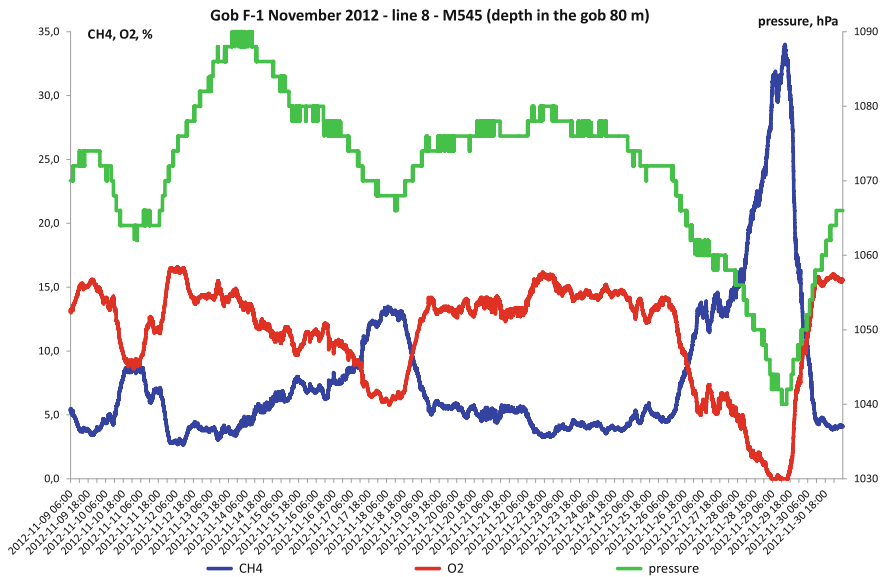
**Fig. 7.** Monthly recording of gas composition in the gob and pressure in the monitoring system

A strong influence of absolute pressure changes on gas concentrations in the gob was observed. These changes confirm by the so-called "breathing of the gob", which has been known from mining practice. Pressure changes were negatively correlated with changes in methane concentration, and the pressure drop caused an increase in methane concentration and were positively correlated with changes in oxygen concentration and the pressure drop caused a decrease in oxygen concentration. Such strong changes in oxygen concentration may have resulted from the driving out of oxygen by methane and the sorption of methane on coal, but also from low-temperature carbon oxidation reactions.

After the completion of mining operation in the area of the liquidated longwall F-1 and after its sealing off, gas measurements were continued in the gob and were still monitored. Figure 8 shows the changes in gases concentrations in the gob recorded in the monitoring system with a distinct effect of "breathing of the gob" due to changes in absolute pressure.

## 5   Summary

- The gob of longwalls in methane areas (especially in those of categories III and IV of methane hazard) are filled with air-methane mixture, where the concentration of methane and oxygen depends on the distance from the line of the roof cave-in, barometric pressure, gassiness, air volume and its velocity in the longwall.
- The research has shown new possibilities of monitoring of areas endangered by fires, through a direct observation of processes occurring in the gob. The research and long-term observations for the monitoring of methane and fire hazards in the
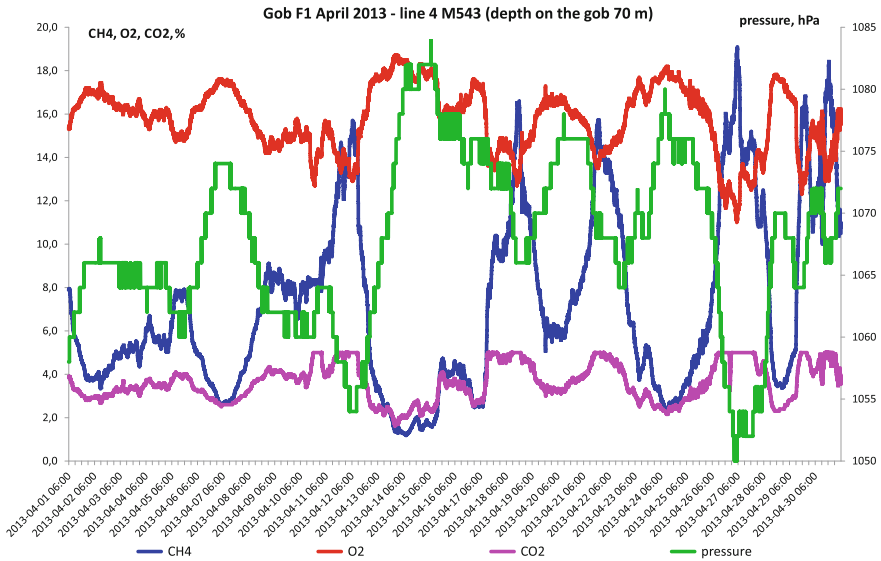
**Fig. 8.** Monthly recording of gas composition in the gob in monitoring system during liquidation of the longwall

gob by a continuous measurement of gob gases in an monitoring system have confirmed that this method can be considered as a new method supplementary to the methods early detection of fires in gob.

- The new solution of the integrated gob sensor ZCZ-MP with the automatic system of gas sampling from the gob together with the measurement of the concentration of gob gases $CH_4$, $O_2$, $CO$, $CO_2$ and registration in the monitoring system seems to be effective and reasonable to investigate the gas concentrations in the gob under operating conditions.
- The long-term observations conducted have confirmed the influence of barometric pressure changes on the migration of the gob gases, which in mining practice is known as the so-called "breathing of the gob".

# References

1. Adamus, A.: Selected measures to suppress spontaneous combustion in Ostrava-Karvina Mines. Current problems in combating mining hazards. In: Scientific and technical conference entitled "Current problems in combating mining hazards". Brenna (2011)
2. Brady, D., Harrison, P., Bell, S.: The need for a tube bundle system for an effective mine gas monitoring system. In: Proceedings of the 9th International Ventilation Congress, pp. 907–916. New Delhi, India (2009)

3. Cimr, A., Wasilewski, S., Przystolik, A.: Possibilities of atmospheric condition assessment in the gob with the use of automatic methanometry. In: Proceedings of the 4th School of Mining Aerology, pp. 509–518. Cracow (2006)

4. Krach, A.: The influence of barometric pressure changes on the concentration of methane in the air currents flowing out of the longwall's area with adjacent gobs—mathematical model and calculation algorithm. Arch. Min. Sci. **49**(1), 43–54 (2004)

5. Krog, R.B., Heasley, K.A.: Longwall emissions during falling atmospheric pressures and the sample frequency required to detect them. In: Proceedings of the 16th North American Mine Ventilation Symposium Colorado School of Mines Golden, pp. 14-1–14-9. Colorado, USA, 17–22 June 2017

6. Lolon, S., Brune, J.F., Bogin, G.E., Grubb, J.W., Juganda, A.: Understanding gob outgassing associated with pressure disturbances in longwall mine. In: Proceedings of the 16th North American Mine Ventilation Symposium Colorado School of Mines Golden, pp. 14-17–14-27. Colorado, USA, 17–22 June 2017

12. Strategic Project Report: Task 3, Development of principles for measurement and testing of mine air parameters for the evaluation of methane and fire hazards in underground hard coal mines. In: Strategic Project "Improvement of Mine Safety". IMG-PAN, Kraków, June 2013 (not published)

11. The Development Project Report R09 0004 04 (N524): Research on gas concentrations distribution in the longwalls mined with cave-in in relation to the risk of spontaneous combustion and methane explosions in gob. IMG-PAN, Kraków (2011) (not published)

7. Trutwin, W.: Influence of ventilation conditions on methane concentration in mine workings. Mining **11**(2) (1973)

8. Wasilewski, S.: Transient states of air parameters caused by disasters and disturbances in the mine's ventilation network. In: Dissertations and Monographs, no. 2, pp. 5–258. EMAG Publishing House (2005)

9. Wasilewski, S., Araszczuk, D.: Operational tests and tests of wireless sensors of the extended automatic gasometry system in the conditions of JSW S. A. mines. In: Improvement of work safety in mines. Theory and practice, pp. 273–296. Gliwice (2014)

10. Wasilewski, S.: Influence of barometric pressure changes on ventilation conditions. In: Deep Mines, Archives of Mining Sciences, vol. 59, issue 3, pp. 621–639. Kraków (2014)

# Using Stress Relief Ratio to Delineate Optimal Methane Drainage Zone in Longwall Goaf

Qingdong Qu[(✉)], Hua Guo, and Andy Wilkins

The Commonwealth Scientific and Industrial Research Organisation (CSIRO),
Brisbane, QLD 4069, Australia
qingdong.qu@csiro.au

**Abstract.** Underground longwall mining in multi-seam gassy conditions induces a large volume of methane emissions, which not only presents a threat to mining safety but also contributes significantly to greenhouse gas emissions. Effective methane extraction from the longwall is the most effective way to control gas emissions. However, this requires a clear delineation of optimal methane drainage zone within the longwall goaf where consistently high flow and high purity methane can be captured. This paper presents a numerical-modelling based method to delineate the 3D distribution of the optimal methane drainage zone. A factor, named Stress Relief Ratio (SRR), is found to be well correlated with known fracture patterns particularly the "O" shaped fracture zone. The SRR has enabled the delineation of the Annual Overlying Zone for longwalls where comprehensive field investigations are not available.

**Keywords:** Annular de-stressing zone · Stress relief ratio · Gas drainage

## 1 Introduction

Underground longwall coal mining leads to stress relief and creates new fractures in the surrounding strata, which can induce large methane emissions from adjacent coal seams. If not controlled, the released methane will migrate into the mine workings, significantly hindering coal production and threating mining safety. However, methane is also a significant source of energy. Any coal mine methane not captured and used is released into the atmosphere, which not only results in greenhouse gas emissions, but also becomes a wasted energy resource. It is estimated that coal mines represent approximately 8% of the world's anthropogenic methane emissions [1].

Integrating coal production and methane extraction into a co-extraction system has become a modern method in underground coal mining, particularly in low permeability multi-seam environment [2, 3]. The integrated extraction system regards methane as an energy resource for extraction and utilisation. To maximise the efficiency of this co-extraction system, drainage gas flow needs to be high, consistent and exceeding desired methane purity (generally greater than 30%).

In the co-extraction system, methane extraction is primarily implemented in the longwall panel, taking advantage of the stress relief effect of mining on adjacent coal seams. Boreholes, drilled either from the ground surface or underground roadways, are

commonly used to drain gas. To achieve a consistently high gas flow, drainage boreholes need to be targeted at the zone where permeability is relatively high [2, 4, 5]. In the longwall goaf, high permeability zone refers to where strata fractures are created by mining. However, quantitative characterization of such a zone in the entire longwall goaf has been a challenge due to the complex and dynamic nature of strata behaviours response to mining. A reliable but simple characterization method of the high permeability zone in the goaf and a clear delineation of the 3D extent of the zone are desirable for methane drainage planning and design.

## 2   Mining Induced Overburden Fractures and Methane Migration

A typical cross-section through a longwall goaf is shown in Fig. 1. When the longwall advances, the immediate roof deforms and collapses, which further induces shearing, delamination, separation and dilation in the overburden strata. The lower part of the overburden strata of the goaf that break into irregular shapes of various sizes is characterised as the caved zone (as shown in Fig. 1). Above the caved zone, the strata which break into blocks but still at least partially held intact are often called the fractured zone. Further up, the strata which deform like a continuous medium and do not generally have cracks cutting through the strata are called the continuous deformation zone [6]. Coal seams situated within the caved and fractured zone are the major sources of gas emissions that contribute to longwall ventilation gas makes [5]. Vertical permeability in these two zones is significantly higher than the top continuous deformation zone.
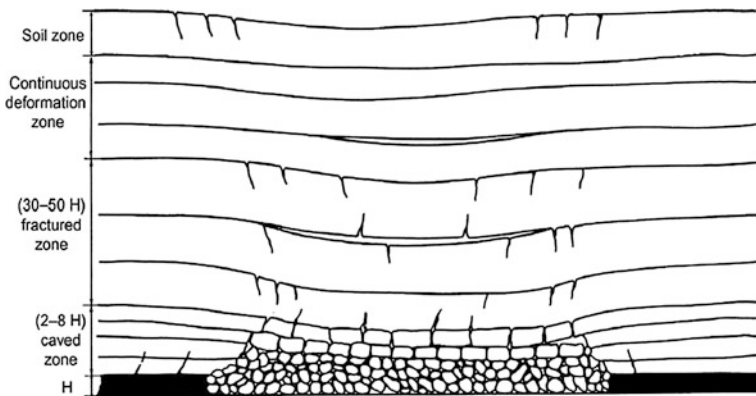


**Fig. 1.** A conceptual model of overburden deformation in response to mining [6]

In a plan section of the caved and fractured zone, the mining induced fractures exhibits an "O" shaped zone [7], as shown in Fig. 2. This model was developed from laboratory experiments by characterising the ratios of strata delamination. Because of

the high void volume maintained in the "O" shaped fracture zone, the zone is characterised as the methane accumulation zone. The zone has formed the basic 2D principle for gas drainage borehole placement in the longwall goaf, and has been adopted successfully in many coal mines [8].
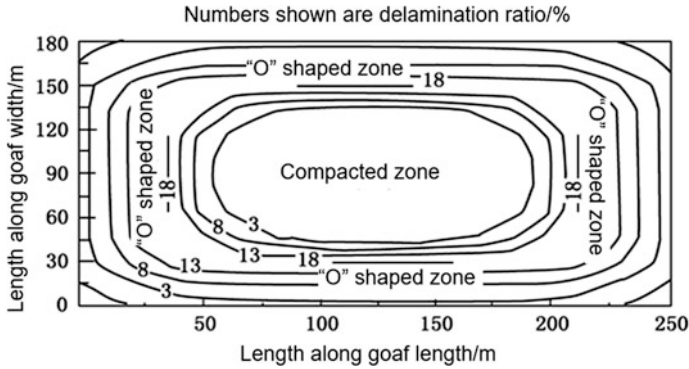


Numbers shown are delamination ratio/%

**Fig. 2.** "O" shaped fracture zone in a plan section [8]

Our previous studies on mining induced strata behaviours have found that strata fractures, permeability and stress changes are correlated [2, 5]. Where strata are largely de-stressed, mining induced fractures are developed and permeability are increased. Therefore, the fractured methane rich zone should be able to be quantified and delineated by a factor associated with stress relief.

This paper presents a numerical-modelling based method that enables a clear and quantitative characterisation of the overburden fracture zone in longwall goaf for methane drainability assessment. CSIRO's unique computer code COSFLOW was employed to conduct the modelling study.

## 3    The 3D Numerical Model

### 3.1    Site Condition

The 3D numerical modelling study was based on an underground longwall panel of a coal mine in China. The working seam of the study panel (17171(1)) is #11-2 seam, which is about 700–750 m below the ground surface, 1.7 m thick on average, and dips at about 7°. The panel was designed to be 205 m wide and 760 m long. It was mined by a retreat longwall mining method with full seam extraction. The mining plan of the 17171(1) panel and its surroundings is shown Fig. 3. Prior to the study panel, there were about six panels around had been mined out.

The working seam is overlain by two gassy coal seams, seam #13-1 at a distance of about 70 m and Seam #17-2 at a distance of about 180 m. The #13-1 seam is of high risk of coal-gas outburst due to higher gas pressure and gas content.
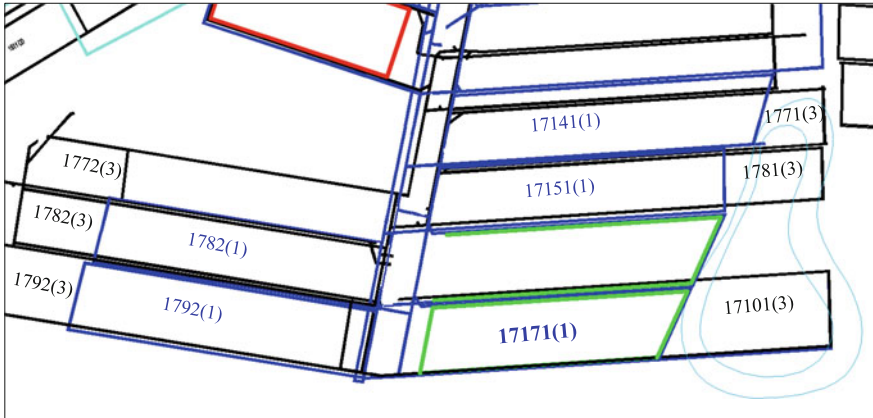
**Fig. 3.** Plan view of the panel

## 3.2 The Computer Code

The numerical modelling was conducted using CSIRO's computer code COSFLOW which is a three dimensional finite element code. The code can simulate both mechanical and coupled strata deformation and fluid flows and can be run in parallel on many computers to save computing times for coupled simulations. In addition, COS-FLOW can incorporate 3D geological models into its model construction.

Compared to other commercial software used in underground engineering, a unique feature of COSFLOW is that it incorporates the Cosserat theory in its description of load-deformation behaviour. Such a method makes COSFLOW very suitable for the simulation of layered rocks and ensures the simulation will not overestimate the deformation for large joint slip and rock layer bending. More information about the mechanical model of COSFLOW can be found in Guo et al. [9].

## 3.3 Model Construction

To better reflect the actual longwall stratigraphy, a 3D geological model was first built based on data of a total of 37 boreholes collected from the coal mine and the stratigraphic sections were analysed (Fig. 4). In order to improve simulation efficiency, the stratigraphic section was then further simplified (Fig. 5) according to strata thickness, strength and other associated properties. After that, the interfaces of the simplified strata were extracted from the 3D geology model and incorporated into COSFLOW.

The constructed 3D COSFLOW model is 3400 m long, 2500 m wide and 1125 m high, with 1,624,430 elements and 1,636,240 nodes (Fig. 6). The initial vertical stress set in the model was proportional to the overburden weight. The major and minor principal horizontal stresses were set to be 1.18 and 0.58 times of the vertical stress respectively, according to the in-site stress measurement at the mine. The mechanical properties of the rock units were determined based on the measurement data provided by the mine as well as those used in other models conducted by CSIRO [2] for the same mining district.
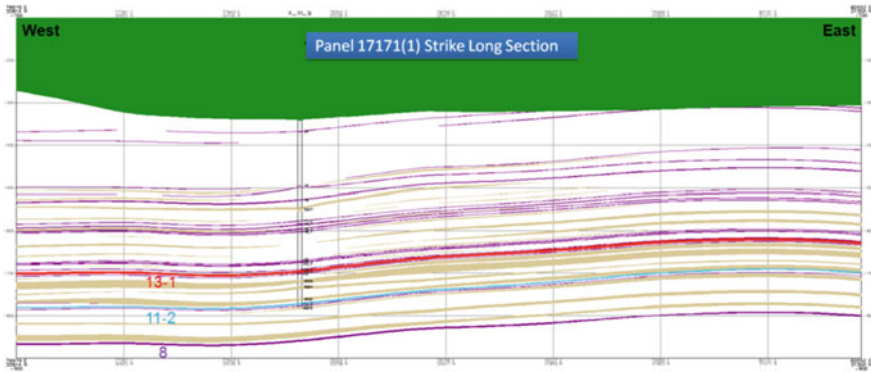
**Fig. 4.** 3D geological model based for COSFLOW model construction

## 4  Using Stress Relief Ratio to Characterise the "O" Shaped Fracture Zone

### 4.1  Definition of the Stress Relief Ratio

As discussed in Sect. 2, the "O" shaped zone is characterised by delamination ratio in the overburden strata which is a direct consequence of strata stress relief in the vertical direction. Therefore, delineation of the "O" shaped fracture zone can be performed by quantitative characterisation of the vertical stress relief.

Figure 7 shows the general understanding on vertical stress redistribution about a longwall goaf [6]. The vertical stress relief pattern is clear from such general understanding. In the mined out area, the vertical stresses are negligibly small immediately behind the face and near the rib side, but increase with distance from the face and the rib side into the goaf. The vertical stress eventually stabilises with the compaction of broken strata in the goaf.

The value of stress relief in a particular point of the longwall goaf can be obtained from the numerical modelling or lab experiments. However, such type of quantification is not sufficient to delineate the 3D extent of the zone in the entire longwall goaf and to assess methane drainability of a coal seam at various mining depth. For example, it is sufficient to say a coal seam at a depth of 300 m is drainable if vertical stress is reduced by 5 MPa (2.5 MPa remaining) but not sufficient for a coal seam at a depth of 800 m (17 MPa remaining). A better quantitative characterisation of the de-stressed zone in the longwall goaf is essential.

A factor named the Stress Relief Ratio (SRR) has been defined by the authors [2] for better quantify the stress relief in the longwall goaf, as shown in Eq. (1). It represents the ratio of stress reduction during or after mining to the in situ stress.
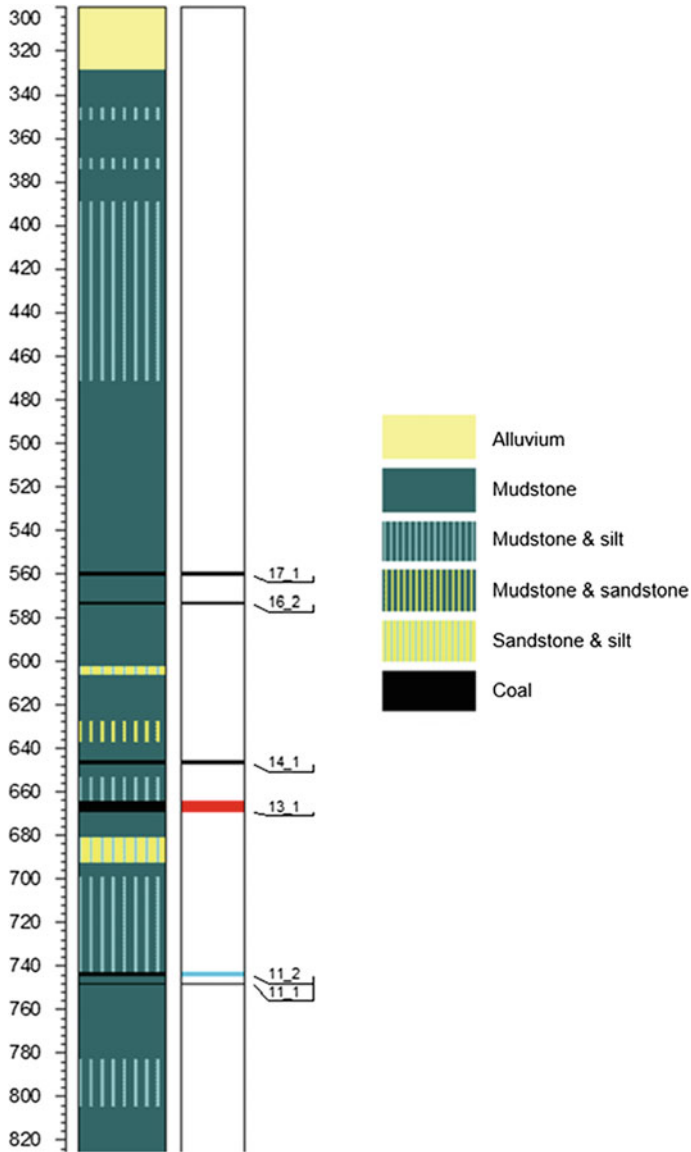
**Fig. 5.** Simplified stratigraphy of the study panel

$$r = 1 - \frac{\sigma_z}{\sigma_{z0}} \tag{1}$$

where r is the stress relief ratio; $\sigma_z$ is the vertical stress during or after mining; $\sigma_{z0}$ is the in situ vertical stress before mining.
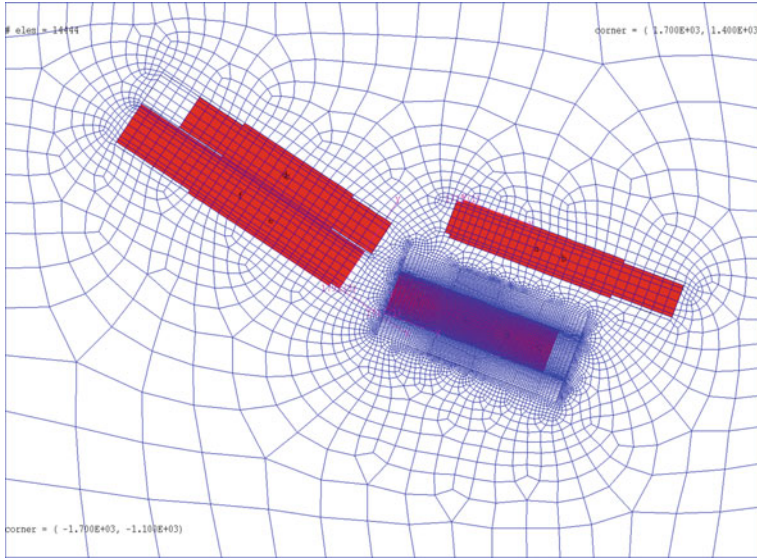
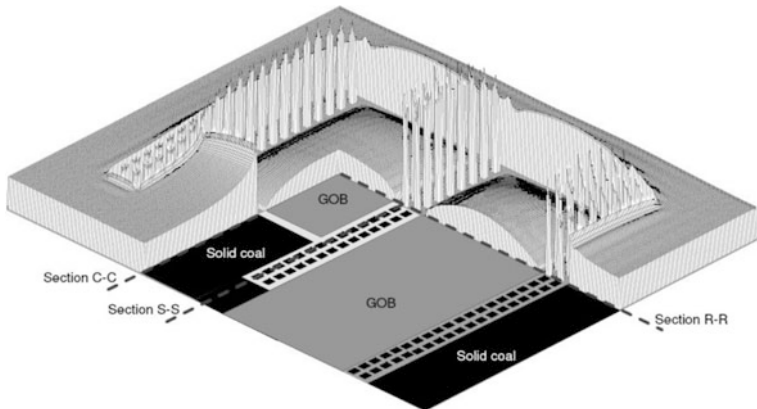**Fig. 6.** The constructed COSFLOW model and mesh



**Fig. 7.** Vertical stress distribution about a longwall panel [6]

## 4.2   Distribution Pattern of SRR

Figure 8 shows the distribution of SRR on the 13-1 seam level in the 17171(1)
longwall goaf. Clearly it can be seen that the pattern of the SRR distribution match very
well with that of the "O" shaped fracture zone as illustrated in Fig. 2.

In addition to the pattern, the SRR also enables further quantitative information
about the "O"-shaped fracture zone which is critical for placement of methane drainage
boreholes. If assuming the "O" shaped fracture zone having a SRR value of over 0.6,
i.e. more than 60% of the vertical stress is reduced, the "O" shaped fracture zone at the
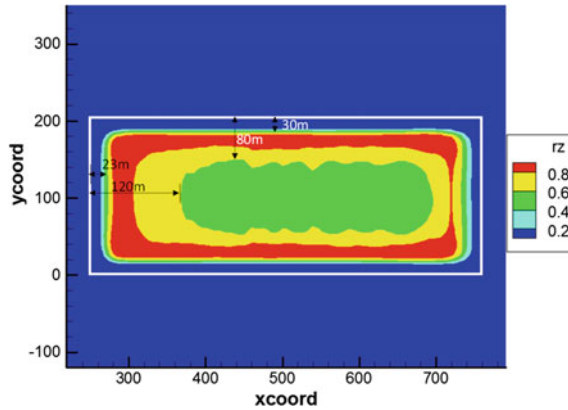
**Fig. 8.** SRR distribution on the level of 13-1 seam

13-1 seam level is located within 23–120 m from the longwall face, and 30–80 m from the side boundary (Fig. 8), respectively. These numbers are very useful to assess the drainability of the 13-1 seam, and predict the extent of fast gas desorption zone and the angle of de-gassed zone. The information is not only important to predict gas extraction capacity of the seam under the co-extraction system but also critical to the evaluation of the effectiveness of reducing outburst risks of this seam.

### 4.3 3D Distribution of SRR

Figure 9 shows the SRR distribution on various sections cutting through the longwall goaf. The SRR distribution clearly reflects the evolution of the "O" shaped fracture zone in the 3D dimension. Obviously, the de-stressed zone is extending up from the immediate roof. On the cross section 20 m behind the longwall face, the highly de-stressed zone (SRR $\geq$ 0.8) extends to about 40 m above the working seam. In another 20 m, the highly de-stressed zone already exceeds the 13-1 seam level which is about 70 m above the working seam (Fig. 9a). The extension angle is about 75° in the direction of panel width. When the mining face is 200 m past, the distribution pattern of the stress relief zone changed dramatically. The vertical stress in the central goaf is largely recovered while the two edge zones remain highly de-stressed. Such evolution pattern of the stress relief in the overburden strata exhibits an "O" shaped zone in the plan view (Fig. 9d).

Comparing the "O" shaped zone on the immediate roof level (Fig. 9d) and that on the 13-1 seam level (Fig. 8), it is observed that the area of the "O" shaped zone reduces with the level above the working seam. This feature also needs to be taken into consideration in the planning and design of methane drainage.
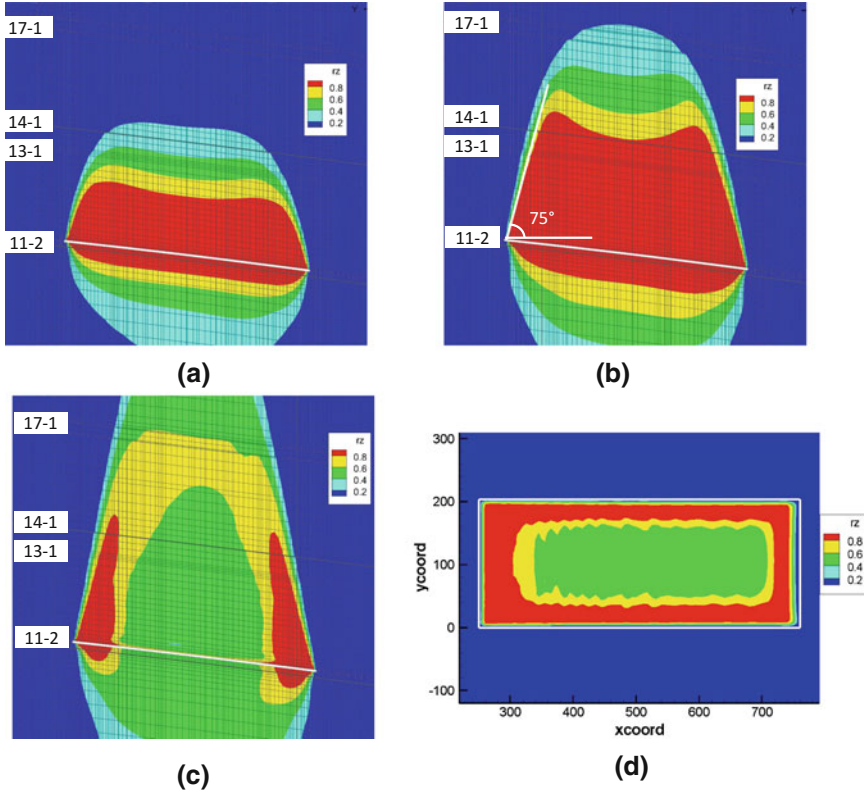
**Fig. 9.** 3D distribution of SRR. **a** 20 m behind the longwall face; **b** 40 m behind the longwall face; **c** 200 m behind the longwall face; **d** plan section on the immediate roof level

## 5 Delineation of Annular Overlying Zone for Optimal Methane Drainage Using SRR

Gas flow with constantly high flowrate and high methane concentration relies on two main factors: high methane desorption rate and high permeability between the coal seams and the drainage boreholes. To achieve effective methane extraction, a 3D delineation of the optimal methane drainage zone with the two factors is desirable.

By analysing a series of data including field pore pressure measurements, gas drainage experience, gas pressure tests and other related gas lab tests as well as comprehensive numerical modelling results, Guo et al. [2] delineated an annular overlying zone (AOZ) in the longwall goaf from where methane extraction can achieve consistently high flowrate and high methane purity. The defined AOZ presents an annular-shape along the perimeter of the longwall goaf over a certain height above the mining seam. The SRR, also developed from that research, was an important factor to the delimitation of the AOZ.

Based on SRR, the upper and side boundaries of AOZ for the study panel 17171(1) can be easily delineated, as shown in Fig. 10. The lower boundary is defined by CFD simulations as it needs to take into consideration of methane purity. The defined AOZ had successfully guided the design and trial of goaf gas drainage with large diameter surface wells [10].
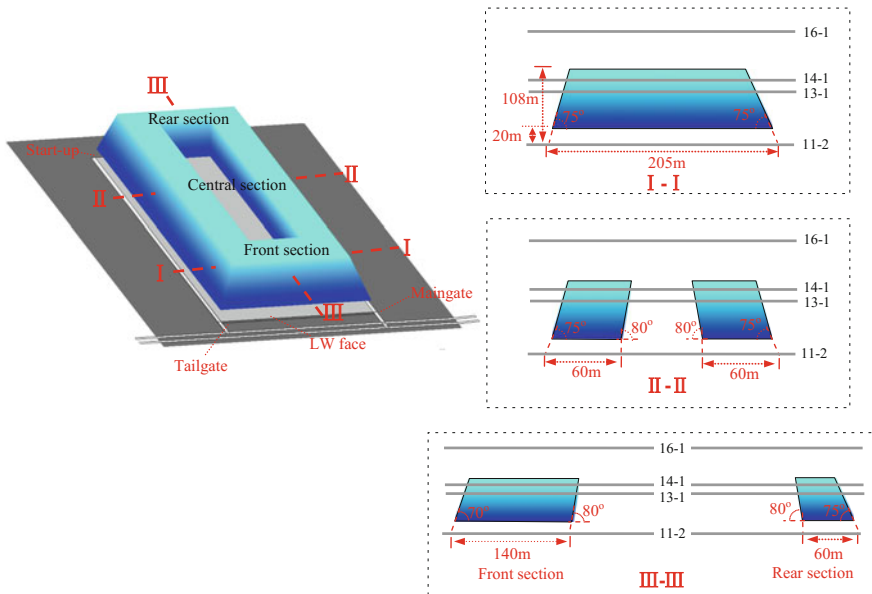


**Fig. 10.** The SRR enabled delineation of the annular overlying zone for the study panel 17171 (1) [10]

The AOZ was also successfully used at a coal mine in Australia, which had led to an innovative gas drainage system. The system, using underground horizontal boreholes to consistently capture methane from the front section of the AOZ, had not only improved coal production and mining safety but also significantly reduced ventilation methane emissions [11]. These applications demonstrate that the AOZ, as mainly defined by SRR, is an effective tool to guide the design of longwall methane drainage.

## 6   Conclusions

Longwall gas drainage design in multi-seam conditions requires an effective characterisation of mining induced overburden behaviours so as to properly delineate the optimal methane drainage zone. Previous understanding of mining induced fracture distribution patterns such as the "O" shaped fracture zone has provided basic 2D principles for methane drainage design. To maximise methane drainage efficiency,

delineation of the 3D optimal methane drainage zone in the longwall goaf as well as a simple and reliable delineation method are desirable.

A numerical-modelling based approach is successfully developed in this paper. A factor named stress relief ratio (SRR) is defined, and is found that its distribution pattern well matches the known fracture patterns such as the "O" shaped fracture zone. This proves the feasibility of using this factor to simply delineate the methane rich zone in the longwall goaf. The SRR has enabled the delineation of the optimal methane drainage zone—Annual Overlying Zone—for longwall where comprehensive field investigations are not available.

# References

1. Karacan, C.Ö., Ruiz, F.A., Cotè, M., Phipps, S.: Coal mine methane: a review of capture and utilization practices with benefits to mining safety and to greenhouse gas reduction. Int. J. Coal Geol. **86**, 121–156 (2011)
2. Guo, H., Yuan, L., Shen, B., Qu, Q., Xue, J.: Mining-induced strata stress changes, fractures and gas flow dynamics in multi-seam longwall mining. Int. J. Rock Mech. Min. Sci. **54**, 129–139 (2012)
3. Yuan, L.: Fundamental of gas drainage in de-stressed coal seams and technological system of integrated extraction of coal and gas. J. China Coal Soc. **34**(1), 1–8 (2009)
4. Qu, Q., Guo, H., Loney, M.: Analysis of longwall goaf gas drainage trials with surface directional boreholes. Int. J. Coal Geol. **156**, 59–73 (2016)
5. Qu, Q., Xu, J., Wu, R., Qin, W., Hu, G.: Three-zone characterisation of coupled strata and gas behaviour in multi-seam mining. Int. J. Rock Mech. Min. Sci. **78**, 91–98 (2015)
6. Peng, S.: Longwall Mining, 2nd edn. West Virginia University, West Virginia (2006)
7. Qian, M., Xu, J.: A study of mining induced "O" shaped fracture zone in overburden. J. China Coal Soc. **23**(5), 466–499 (1998)
8. Xu, J., Qian, M.: Trial of gas drainage from overburden remote coal seams using surface wells. J. China Univ. Min. Technol. **29**(1), 78–81 (2000)
9. Guo, H., Adhikary, D.P., Craig, M.S.: Simulation of mine inflow and gas emission during longwall mining. Rock Mech. Rock Eng. **42**(1), 25–51 (2008)
10. Guo, H., Yuan, L., Liang, Y., Qu, Q., Xue, S., Xie, J.: Co-extraction of coal and methane. Can. Inst. Min. Metall. Pet. J. **6**(1), 5–14 (2015)
11. Guo, H., Todhunter, C., Qu, Q., Kerr, H., Qin, J.: An innovative drainage system for coal mine methane capture optimisation and abatement maximisation. In: Proceedings of Coal Operators' Conference, University of Wollongong, 11–12 Feb 2016, pp. 390–403 (2016)

# Theoretical Model for Micro-flow of Gas in Coal Mine Goaf and the Influence of Viscosity on Pressure Gradient

Wen Jiang[1], Shi-qiang Chen[2,3(✉)], and Hai-qiao Wang[3]

[1] School of Resource, Environment and Safety Engineering, Hunan University of Science and Technology, Xiangtan 411201, Hunan, P. R. of China
[2] Work Safety Key Lab on Prevention and Control of Gas and Roof Disasters for Southern Goal Mines, Hunan University of Science and Technology, Xiangtan 411201, Hunan, P. R. of China
152-7327-9290zunyichsq@l63.com
[3] Hunan Provincial Engineering Techniques Research Centre of Mine Ventilation & Dedusting Equipment, Hunan University of Science and Technology, Xiangtan 411201, Hunan, P. R. of China

**Abstract.** In order to simplify a complex structure of goaf in a coal mine, a new flow region of porous media is presented and established. It consists of eight spheres, one smaller sphere and their empty cavities in cube with double diameters of spheres. Being equal to porosity of the flow region, the minimum flow unit is constructed with this region cutting. Applying Navier-Stocks equations, it is deduced that a one-dimension flow model of this unit is based by one assumption of section-averaged velocity. Numerical calculations have also been conducted using MATLAB, and the viscosity coefficient influenced on pressure gradient, and obtained the quantitative relationship between viscosity coefficient and pressure gradient in four flow stages are discussed. By using the method of weighted length ratio, the influence of the viscosity coefficient on the pressure gradient of the minimum flow unit can be obtained. The flow models of porous media would provide a theoretical reference for the prevention of coal spontaneous combustion in goaf.

**Keywords:** Goaf · Minimum flow unit · Seepage velocity · Navier-Stocks equations · Numerical calculations

## 1 Introduction

About 56% of China's coal reserves are susceptible to spontaneous combustion. The direct and indirect economic losses caused by spontaneous combustion are nearly 10 billion RMB every year [1]. Especially in the fully mechanized coal mining, where the

coal and rock mass is badly broken, the amount of coal remaining in goaf is large and the gas leakage can be significant, often leading to coal spontaneous combustion in this region. A large number of studies have shown that the spontaneous combustion of coal in goaf is closely related to the distribution of leakage flow. Therefore, it is essential to study the law of gas flow in the goaf.

In numerical simulation, the flow of gas in the goaf is calculated by using software such as Fluent and CM, and some visual conclusions are obtained [2–5]. The distribution of gas concentration was analyzed using the energy location and tracer technique by Ren, three zones of spontaneous combustion oxidation in the goaf area using air leakage law [6]. Yu examined the pressure distribution in the goaf using 3-D display for a "U" and "U + I" ventilation system [7]. Wang analyzed the impact of different permeability on leakage flow field quantitatively under various support conditions [8]. Researches have shown that gas flow in the goaf have small numerical values, micro scales and low intensity, a microflow. Moreover, Peng studied the effect of high temperature heat source on the gas micro flow field in goaf, and Luo studied Simulation on effects of microflow air in goaf on changing pressure differences, and Li obtained a critical pressure gradient at both ends of the mining area affecting the microflow in the goaf [9–11]. The existing results are mainly quantified by macro porosity, large scale seepage coefficient and pressure gradient, but the discussion on the gas microflow and its model in goaf is not thorough and systematic. In order to resolve those problems, this paper uses the theory of fluid mechanics and Navier-Stocks equations, and deduce that a one-dimension flow model of this unit based on one assumption of section-averaged velocities. In MATLAB, the influence of viscosity coefficient on pressure gradient should be numerically calculated in order to obtain the quantitative relationship between viscosity coefficient and pressure gradient in four flowing stage. By using the method of weighted length ratio, the influence of the viscosity coefficient on the pressure gradient of the minimum flow unit could be obtained.

## 2 Porous Medium System and Microflow in Goaf

### 2.1 System Geometry and Minimum Flow Unit

For a cube with a length of $2d$, it can accommodate eight spheres with diameters of $d$ exactly. Its most loose arrangement is that the spheres tangent to each other, the side of the sphere and the cube; the porosity of the cube containing eight spheres is $1 - \pi/6$, or about 0.47640122. Then, a small sphere with the diameter of $(\sqrt{3} - 1)d$ is sandwiched among eight large spheres with diameters of $d$ *each*, and that is equal to a hemisphere with diameters of $(\sqrt{3} - 1)d$ clipped among four large spheres with diameters of $d$, as is shown in Fig. 1, and the porosity of the model is 0.373795.

To simplify of the next discussion, the minimum flow unit of that object needs to be established. Cutting the cube along the $X$, $Y$ and $Z$ axes in Cartesian coordinate system, and dividing the cube into eight cubes evenly and every small cube consists of a large sphere and four small 1/8 spheres, its porosity is 0.3736960, which is equal to the
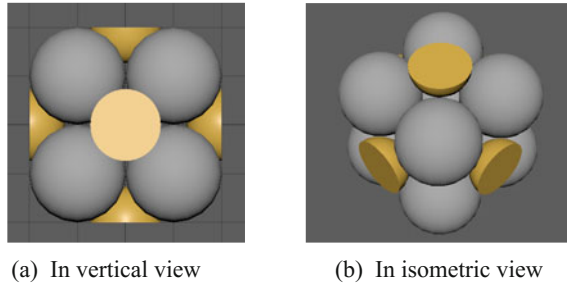
(a) In vertical view        (b) In isometric view

**Fig. 1.** Sketch of microflow system

porosity of this system. Therefore, it could be studied that the flow of fluid in a minimum flow unit. The minimum flow unit has the same porosity as the study object and has a complete flow cycle, as is shown in the Fig. 2.



(a) In isometric view        (b) In projective view
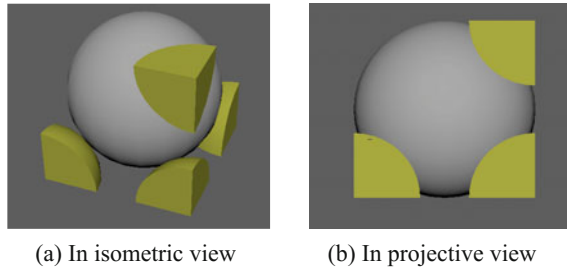
**Fig. 2.** Sketch of the minimum flowing unit

In $Z$ axis, starting from $z = 0$, the cross-sectional area of this unit is

$$A_0 = d^2 - 0.25\pi d^2 \left[ \left( \sqrt{3} - 1 \right) \big/ 2 \right]^2.$$

In the condition of $0 \leq z < (\sqrt{3} - 1)0.5d$, as $z$ increases, this cross-sectional area is equal to the square section area, which the side length is $d$ minus the area of a small semicircle and two large semicircle which the diameters changes with $z$, namely,

$$A_{z1} = d^2 - \frac{1}{4}\pi \left[ \frac{1}{4} \left( \sqrt{3} - 1 \right)^2 d^2 - z^2 \right] - \left[ \left( \frac{d}{2} \right)^2 - \left( \frac{d}{2} - z \right)^2 \right] \pi \qquad (1)$$

when $(\sqrt{3} - 1)0.5d < z \leq 0.5d$,   $A_{z2} = d^2 - \left[ (\frac{d}{2})^2 - (\frac{d}{2} - z)^2 \right] \pi \qquad (2)$

$$\text{when } 0.5d < z \le (1.5 - 0.5\sqrt{3})d, \quad A_{z3} = d^2 - \left[(\frac{d}{2})^2 - (z - \frac{d}{2})^2\right]\pi \qquad (3)$$

$$\text{when } (1.5 - 0.5\sqrt{3})d < z \le d,$$
$$A_{z4} = d^2 - \left[(\frac{d}{2})^2 - (z - \frac{d}{2})^2\right]\pi - \frac{3}{4}\left[\frac{1}{4}\left(\sqrt{3} - 1\right)^2 d^2 - (d - z)^2\right] \qquad (4)$$

Obviously, this flow in the minimum unit is periodically flowing.

## 2.2   Micro-flow Model of the Minimum Flow Unit

In order to discuss the seepage equation of the object model, the seepage velocity in the minimum flow unit shown in the Fig. 2 should be represented by the velocity of the centroid $z$. This study can be generalized to a one-dimensional flow question along the Z direction, and the movement of incompressible fluid conforms to Navier-Stocks Equations,

$$\frac{\partial u_z}{\partial t} + u_x\frac{\partial u_z}{\partial x} + u_y\frac{\partial u_z}{\partial y} + u_z\frac{\partial u_z}{\partial z} = f_z - \frac{1}{\rho}\frac{\partial p}{\partial z} + v\nabla^2 u_z \qquad (5)$$

The flow of this study is a steady flow and the minimum flow unit is only subjected to pressure and viscous force along the $z$-axis, therefore, $\partial u_z/\partial t = 0$, $f_z = 0$. So the formula becomes,

$$u_x\frac{\partial u_z}{\partial x} + u_y\frac{\partial u_z}{\partial y} + u_z\frac{\partial u_z}{\partial z} = -\frac{1}{\rho}\frac{\partial p}{\partial z} + v\nabla^2 u_z \qquad (6)$$

The left part of the equation represents the inertial force. The first item, on the right side of the equation, represents the pressure loss item, and the second term means viscous force. The motion expression of a fluid in a minimum flow unit can be obtained by integrating the minimum unit of flow in the equation separately. The flow of the minimum flow unit can be divided into 4 stages according to different relationship between the cross-sectional area and $z$. Among them, if the sectional relation satisfies the Eq. (1), call it the first flow stage; by analogy, the cross-sectional relation is referred to as the second flow phase, the third flow phase and the fourth flow stages.

# 3   Four Stages of Microflow Model and Numerical Calculations

## 3.1   Model Establishment of the First Flowing Stage

Setting the average flow velocity of the section along the $z$ axis at $u_0$ in the center of the minimum flow unit and the cross-sectional area of the fluid at $A_0$ along Z axis, the average velocity of cross section at $z$ point is $u_{z1}$, the cross-sectional area of the fluid is $A_{z1}$. Using the continuity equation, $A_0 u_0 = A_{z1}u_{z1}$ shown in Fig. 2, when $z = 0$, the

cross sectional area of fluid is $A_0 = d^2 - 0.25\pi d^2 \left[ \left( \sqrt{3} - 1 \right)/2 \right]^2$; the cross sectional area is variable with $z$ is

$$A_{z1} = d^2 - \frac{1}{4}\pi \left[ \frac{1}{4} \left( \sqrt{3} - 1 \right)^2 d^2 - z^2 \right] - \left[ \left( \frac{d}{2} \right)^2 - \left( \frac{d}{2} - z \right)^2 \right] \pi.$$

So, the average velocity of the cross section at $z$ is,

$$u_{z1} = u_0 \frac{d^2 - \frac{1}{16}\pi d^2 \left( \sqrt{3} - 1 \right)^2}{d^2 - \frac{1}{4}\pi \left[ \frac{1}{4} \left( \sqrt{3} - 1 \right)^2 d^2 - z^2 \right] - \left[ \left( \frac{d}{2} \right)^2 - \left( \frac{d}{2} - z \right)^2 \right] \pi} \tag{7}$$

Therefore, the migration acceleration along the Z-axis is,

$$\frac{\partial u_{z1}}{\partial z} = u_0 \frac{\left[ d^2 - \frac{1}{16}\pi d^2 \left( \sqrt{3} - 1 \right)^2 \right] \left[ \frac{5\pi z}{2} - d\pi \right]}{\left\{ d^2 - \frac{1}{4}\pi \left[ \frac{1}{4} \left( \sqrt{3} - 1 \right)^2 d^2 - z^2 \right] - \left[ \left( \frac{d}{2} \right)^2 - \left( \frac{d}{2} - z \right)^2 \right] \pi \right\}^2} \tag{8}$$

Substituting Eq. (7) into Eq. (8), it is obtained,

$$u_{z1} \frac{\partial u_{z1}}{\partial z} = u_0^2 d^4 \frac{\left[ 1 - \frac{1}{16} \left( \sqrt{3} - 1 \right)^2 \pi \right]^2 \left( d\pi - \frac{5}{2}\pi z \right)}{\left\{ d^2 - \frac{1}{4}\pi \left[ \frac{1}{4} \left( \sqrt{3} - 1 \right)^2 d^2 - z^2 \right] - \left[ \left( \frac{d}{2} \right)^2 - \left( \frac{d}{2} - z \right)^2 \right] \pi \right\}^3} \tag{9}$$

$$\frac{\partial^2 u_{z1}}{\partial z^2} = -\frac{5\pi u_0}{2} \frac{d^2 - \frac{1}{16}\pi d^2 \left( \sqrt{3} - 1 \right)^2}{\left\{ \{ d^2 - \frac{1}{4}\pi \left[ \frac{1}{4} \left( \sqrt{3} - 1 \right)^2 d^2 - z^2 \right] - \left[ \left( \frac{d}{2} \right)^2 - \left( \frac{d}{2} - z \right)^2 \right] \pi \}^2 \right\}}$$
$$+ 2u_0 \frac{\left[ d^2 - \frac{1}{16}\pi d^2 \left( \sqrt{3} - 1 \right)^2 \right] \left[ \left( d\pi - \frac{5}{2}\pi z \right)^2 \right]}{\left\{ \{ d^2 - \frac{1}{4}\pi \left[ \frac{1}{4} \left( \sqrt{3} - 1 \right)^2 d^2 - z^2 \right] - \left[ \left( \frac{d}{2} \right)^2 - \left( \frac{d}{2} - z \right)^2 \right] \pi \}^2 \right\}} \tag{10}$$

At this point, the inertia force and viscous force at $z$ point are obtained in Z direction. For the actual flow can only occur in the pore part, in order to get the force of the entire cube unit in Z direction, the forces of fluid system in the pore portion are supposed to be averaged to the entire passage. Setting the volume of the cube $V_0$ and the volume of the passage part $V_z$, according to the concept of the average, it can be concluded:

$$\overline{u_z} = \iiint_{V_z} u_z dV \quad \overline{u_z \frac{\partial u_z}{\partial z}} = \iiint_{V_z} u_z \frac{\partial u_z}{\partial z} dV \quad \overline{\frac{\partial^2 u_z}{\partial z^2}} = \iiint_{V_z} \frac{\partial^2 u_z}{\partial z^2} dV \tag{11}$$

Substituting Eqs. (1) and (7) into Eq. (11),

$$\overline{u_{z1}} = \iiint\limits_{V_{z1}} u_{z1}dV = \frac{\int u_{z1}A_{z1}dz}{\int A_{z1}dz} = \frac{\int_0^{0.5(\sqrt{3}-1)d} u_{z1}A_{z1}dz}{\int_0^{0.5(\sqrt{3}-1)d} A_{z1}dz} \tag{12}$$

Among them, the volume of the flowing part is $V_{z1} = \int_0^{0.5(\sqrt{3}-1)d} A_{z1}dz$, therefore, $\overline{u_z} = 1.80691u_0$.

Substituted Eqs. (1) and (9) into Eq. (11),

$$\overline{u_{z1}\frac{\partial u_{z1}}{\partial z}} = 11.3633\frac{u_0^2}{d} \tag{13}$$

Substituted Eqs. (1) and (10) into Eq. (11),

$$\overline{\frac{\partial^2 u_{z1}}{\partial z^2}} = 7.799927\frac{u_0}{d^2} \tag{14}$$

In addition, it is necessary to determine the inertia forces and viscous forces in the $X$ and $Y$ directions, which are known by symmetry,

$$\frac{\partial u_z}{\partial x} = \frac{\partial u_z}{\partial y}, \quad \overline{u_x\frac{\partial u_z}{\partial x}} = \overline{u_y\frac{\partial u_z}{\partial y}} \quad \frac{\partial^2 u_z}{\partial x^2} = \frac{\partial^2 u_z}{\partial y^2}, \quad \overline{\frac{\partial^2 u_z}{\partial x^2}} = \overline{\frac{\partial^2 u_z}{\partial y^2}} \tag{15}$$

As the water flows from the hole to the throat or from the throat to the hole, the streamline is constantly shrinking or enlarging, and the boundary layer separates and forms a vortex near the spherical surface. Therefore, it is difficult to obtain the distribution function of the velocity gradient along the $X$-axis and $Y$-axis direction and it is hard to derive the inertia force and viscous force in $X$ and $Y$ direction by direct theory derivation. However, it is known from the symmetry that the inertia force and the viscous force in the direction of the $Z$ axis are related to the force in the direction of the $X$ and $Y$ axis [12].

Assuming $u_x/u_z = tg\theta$, therefore, $u_x \cdot \partial u_z/\partial x = tg\theta \cdot u_z \cdot \partial u_z/\partial x$. According to the same dimensions,

$$u_x\frac{\partial u_z}{\partial x} \propto u_z\frac{\partial u_z}{\partial z} \propto u_0^2 \quad \overline{u_x\frac{\partial u_z}{\partial x}} = \beta_1\overline{u_z\frac{\partial u_z}{\partial z}} \propto u_0^2 \tag{16}$$

In the same way

$$\frac{\partial^2 u_z}{\partial x^2} \propto \frac{\partial^2 u_z}{\partial z^2} \propto u_0 \quad \overline{\frac{\partial^2 u_z}{\partial x^2}} = \alpha_1\overline{\frac{\partial^2 u_z}{\partial z^2}} \propto u_0 \quad \overline{\frac{\partial^2 u_z}{\partial y^2}} = \alpha_2\overline{\frac{\partial^2 u_z}{\partial z^2}} \propto u_0 \tag{17}$$

Assuming $\alpha' = \alpha_1 + \alpha_2$, $\beta' = \beta_1 + \beta_2$, then the left part of the equation can be expressed as,

$$\overline{u_x \frac{\partial u_x}{\partial x} + u_y \frac{\partial u_x}{\partial y} + u_z \frac{\partial u_x}{\partial z}} = (1+\beta') \overline{u_z \frac{\partial u_z}{\partial z}} = (1+\beta') \frac{11.36322}{d} u_0^2 \tag{18}$$

The viscous force term in the left part of the equation can be expressed as,

$$\overline{v\left(\frac{\partial^2 u_x}{\partial x^2} + \frac{\partial^2 u_x}{\partial y^2} + \frac{\partial^2 u_x}{\partial z^2}\right)} = v(1+\alpha')\overline{\frac{\partial^2 u_x}{\partial x^2}} = v(1+\alpha')\frac{7.79992 u_0}{d^2} \tag{19}$$

According to

$$u_x \frac{\partial u_z}{\partial x} + u_y \frac{\partial u_z}{\partial y} + u_z \frac{\partial u_z}{\partial z} = -\frac{1}{\rho}\frac{\partial p}{\partial z} + v\nabla^2 u_z \tag{20}$$

$$\frac{1}{\rho}\frac{\partial p}{\partial z} = v\nabla^2 u_z - (u_x \frac{\partial u_z}{\partial x} + u_y \frac{\partial u_z}{\partial y} + u_z \frac{\partial u_z}{\partial z}) \tag{21}$$

$$\frac{\partial p}{\partial z} = \mu\nabla^2 u_z - \rho(u_x \frac{\partial u_z}{\partial x} + u_y \frac{\partial u_z}{\partial y} + u_z \frac{\partial u_z}{\partial z}) \tag{22}$$

Setting the left hand of the above formula as $J$, $J$ represents the pressure loss in per unit length of the flow model. Substituting the above relations into the formula, the equation can be obtained,

$$J = (1+\beta')(11.3632/gd)\rho u_0^2 - \mu(1+\alpha')(7.7999 u_0/gd^2) \tag{23}$$

In addition, according to the preceding derivation process, it is $\overline{u_z} = 1.8069 u_0$. That is to say: the average velocity of the cross section is about 1.8069 times the velocity of the flowing passage.

Assuming $A = -7.7992\mu(1+\alpha')/gd^2$ and $B = 11.36322(1+\beta')\rho/gd$, thus, $J = Au_0 + Bu_0^2$.

$$dp = \frac{\partial p}{\partial x}dx + \frac{\partial p}{\partial y}dy + \frac{\partial p}{\partial z}dz \tag{24}$$

$$dx = u_x dt, \quad dy = u_y dt, \quad dz = u_z dt$$
$$u_x = tg\theta_1 u_z, \quad u_y = tg\theta_2 u_z \tag{25}$$

Substituted Eq. (25) into Eq. (24),

$$dp = \frac{\partial p}{\partial x}tg\theta_1 u_z dt + \frac{\partial p}{\partial y}tg\theta_2 u_z dt + \frac{\partial p}{\partial z}u_z dt = u_z dt\left(\frac{\partial p}{\partial x}tg\theta_1 + \frac{\partial p}{\partial y}tg\theta_2 + \frac{\partial p}{\partial z}\right) \tag{26}$$

Due to the direction of the initial velocity $u_0$ is consistent with the z-axis, the pressure caused by wind speed is mainly applied to the $Z$ axis and affects the flow in the z-axis direction, additionally $tg\theta_1 \approx tg\theta_2 \ll 1$. Therefore, it could be ignored that the

pressure loss in the $X$ and $Y$ direction, and it could be only considered that the pressure loss on the $z$-axis of the mainstream direction,

$$J = 7.7999\mu u_0 d^{-2} - 11.3632\rho u_0^2 d^{-1} \tag{27}$$

Generally, it is assumed that the diameter of the sphere and the initial velocity should be all constants in Eq. (27). Moreover, dynamic viscosity $\mu$ and air density $\rho$ are two variables that influence pressure loss $J$.

The assignments of Eq. (27) could be $d$ with 5 mm and $u_0$ with 1 m/s; on the other hand, the temperature effects on the dynamic viscosity $\mu$ and air density $\rho$. Therefore, the next problem is discussed that the relationship of $J$ with $\mu$ and $\rho$ is on the conditions of different temperatures. It is set that the temperatures are 20, 30, 40, 50 and 60 °C, respectively; in addition, these values of the temperature should be applied in the formulas of the pressure loss with the kinematic viscosity, diameter, density and initial velocity on the conditions of the second, third and forth flowing stages. The calculations are shown in Fig. 3. In Fig. 3, it is shown that the increase of the kinematic viscosity is varied with the pressure loss from −5 to −4.4 Pa/m. It is displayed that the part of the kinematic pressure transforms into the static pressure on account of the sectional area decreasing with the $z$ increasing.



(a) the first flow stage          (b) the second flow stage

(c) the third flow stage          (d) the forth flowing stage

**Fig. 3.** The effects of $v$ on $J$ in the four flowing stages
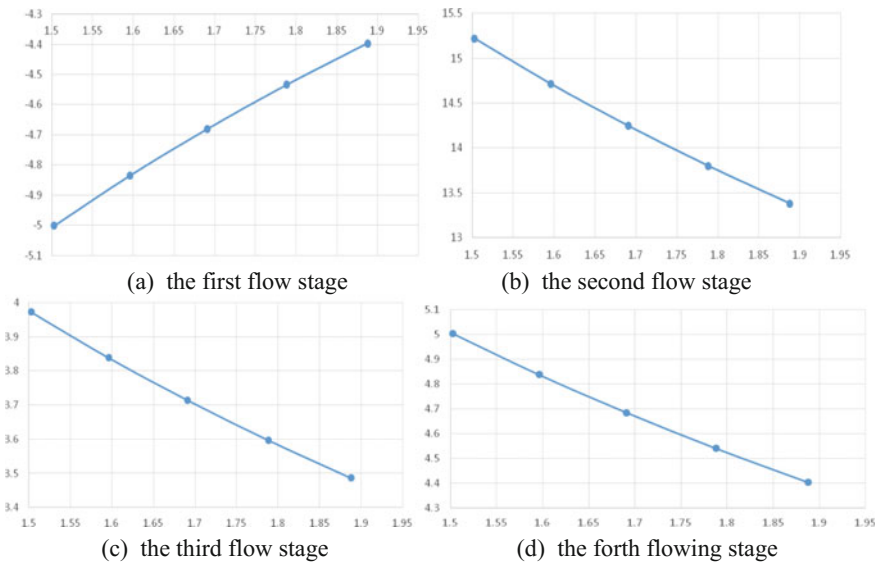
Notes: in Figs. 3 and 4, the horizontal axis is $v \times 10^{-5}$, and $v$ is the kinematic viscosity of 1 m$^2$/s; the vertical axis is $J$, and its unit is Pa/m. In Fig. 4, the cyan line represents the first flowing stage, and the orange, gray and yellow lines represent the second, third and forth stages, respectively; the red line represents the total pressure loss.
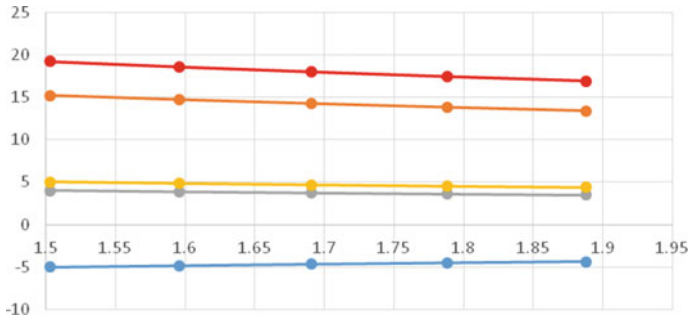
**Fig. 4.** Comparing effects of $v$ on $J$ in the different flowing stages with total loss

## 3.2 The Second Flowing Stage

$$J = -74.0546\mu u_0 d^{-2} + 94.4830\rho u_0^2 d^{-1} \tag{28}$$

## 3.3 The Third Flowing Stage

$$J = -74.0546\mu u_0 d^{-2} + 24.8264\rho u_0^2 d^{-1} \tag{29}$$

## 3.4 The Fourth Flowing Stage

$$J = 8.3909\mu u_0 d^{-2} + 11.3171\rho u_0^2 d^{-1} \tag{30}$$

## 3.5 The Influence of Viscosity on Pressure Loss

Comparing Eqs. (27), (28), (29) and (30), the above four flowing stages could be denoted as $J = Au_0 + Bu_0^2$, this formula is similar to the Forchheimer Law [13]. As shown in Fig. 2, the length of the first flowing stage multiplies with the pressure loss shown in Fig. 3a, and the count contributes for the total pressure loss. Similarly, the counts of the second, third and forth stages, respectively, as shown in Fig. 3b–d, contribute to the total pressure. Results are shown in Fig. 4.

When the initial values are equal to those in the first flowing stage, the calculations of total pressure loss are shown in Fig. 4, where the total pressure loss increases varies with the increasing gas viscosity because of the increasing temperatures is clearly displayed.

# 4    Conclusions

(1) In flowing gas, the pressure loss and initial velocity are satisfied with the quadratic relation presented by Forchheimer.
(2) The dynamic viscosity and density of the gas change as the temperature changes, and both variables affect the pressure loss in the minimum flowing unit.
(3) The total pressure loss of this unit decreases with the increase of the kinematic viscosity.

# References

1. Mai, Q.: Research on Coal Spontaneous Combustion Characteristic of Fully Mechanized Caving Mining Face. Xi'an University of Science and Technology, Xi'an (2013)
2. Gao, K.: Numerical simulation of the influence of working face air leakage on gob gas flow laws. Saf. Coal Mines **43**(07), 8–11 (2012)
3. Lei Yanjie, F.: Study on air leakage flow field and gas distribution in goaf with U ventilation. Coal **23**(11), 30–32 (2014)
4. Gao, J.: Numerical simulation for airflow and gas distribution regulation in the goaf of mechanized working face. J. Saf. Environ. **13**(02), 164–168 (2013)
5. Li, M.: Research on the Law of Air Leakage in Goaf of Gob-Side Entry Retaining with Y-Type Ventilation System on Feng Huang Shan Coal. Taiyuan University of Technology, Taiyuan (2012)
6. Ren, Q.: Similar simulation of air leakage law in goaf with Y-shape ventilation system. China Coal **38**(03), 98–101 (2012)
7. Yu, Z.: Experimental study on the goaf flow field of the "U + I" type ventilation system for a comprehensive mechanized mining face. Int. J. Min. Sci. Technol. **25**(06), 1003–1010 (2015)
8. Wang, H.: Research on Numerical Simulation of Air Flow Distribution in Gob. Henan Polytechnic University, Jiaozuo (2010)
9. Peng, Y.: The Simulation on effects of micro-flow air in goaf from heat source with high temperature. Coal **08**(26), 5–9 (2017)
10. Luo, C.: Simulation on effects of micro-flow air in goaf on changing pressure differences. J. Heilongjiang Univ. Sci. Technol. **26**(01), 1–4 (2016)
11. Li, Y.: Study on critical pressure gradient and width of spontaneous combustion zone of goaf on working facee. Zhongzhou Coal **38**(11), 1–5 (2016)
12. Irmay, S.F.: Solutions of the non-linear diffusion equation with a gravity term in hydrology. Int. Assoc. Sci. Hydrol. **4**(2), 478–499 (1966)
13. Ergun, S.: Fluid flow through randomly packed columns and fluidized beds. Ind. Eng. Chem. **41**(6), 1179–1184 (1949)

# Part VII
# Mine Explosions

# A Practical Comparison of Active and Passive Explosion Barrier

Arend Spaeth[1(✉)] and Bharath Belle[2]

[1] ExploSpot Systems (Pty) Ltd, Pretoria 0081, South Africa
arend.spaeth@explospot.com
[2] Anglo American Coal, Brisbane 4001, Australia
bharath.belle@angloamerican.com

**Abstract.** Methane gas and coal dust explosions are a constant risk hazard during coal mining. Various mitigation controls are used today. The primary differentiation will be controls to either prevent an explosion or to stop an explosion once it has ignited. Common explosion controls will be active or passive explosion barriers. These barriers will be incorporated either in legislation or a mine's Code of Practice. Both types of barriers have been tested according to accepted protocols. These protocols would attend to the requirement of a barrier to stop an explosion. The protocol will however not attend to the aspects concerning practicality, efficiency, maintainability, lifecycle costs and most importantly reliability and damage control. This paper will discuss aspects concerning the implementation and maintenance of active and passive barriers. The paper will furthermore outline the difference in function, thereby highlighting the difference in reliability and damage control.

**Keywords:** Active explosion barrier · Passive explosion barrier
Explosion mitigating control

## 1   Introduction

Methane gas and coal dust explosions have been ever present in the process of coal mining operation. The first explosions reported explosions can be dated back to the 19th century. More recently (2017) fatalities were reported in the Ukraine, Russia and China. The risk of a methane gas and/or a coal dust explosion is still present in coal mining operation.

Over the years a number of methods have been investigated and developed to either prevent or suppress a coal mine explosion. Figure 1 depicts the currently accepted categorization of explosion mitigation controls. The focus is and should remain the prevention of an event leading to methane gas or coal dust explosion. In this case, a mine would typically address aspects such as diluting the methane concentration in the atmosphere by adequately ventilating the area, using water spray to mitigate coal dust at the cutting face or utilizing flameproof or intrinsically safe equipment to mitigate the source of an ignition. Although the 100% prevention of an energy source and combustible atmosphere to spark an explosion remains the obvious goal, it is currently still accepted that it is not possible to fully prevent an explosion in a coal mining operation.

One of the reasons is e.g. the continuous increase of mechanised and automated cutting of coal. As a result, mines look towards means to suppress an explosion in the case it should occur. In this case a mine would investigate the use of constructive or reactive measures. These mitigating controls are, according to Michelis [1], categorized into "explosion stopping", "special structure" or "explosion barriers". The constructive measures such as "explosion stopping" and "special structure" are physical, purpose-built walls or shelters. The explosion barriers on the other hand are equipment introduced into an area that only react once the event of an explosion occurs. The explosion barriers are in turn separated into passive barriers and active barriers. The meaning of passive and active in this case relate to the use of an external power source. Passive barriers therefore do not require a source of energy to detect an explosion but are activated by the pressure wave that leads any explosion. Active barriers are equipment that require a source of energy to detect an explosion. Unlike the passive barrier they are then however independent of the physical dimension of an explosion and will rather react based on the logic and mechanism that has been set for this particular device.
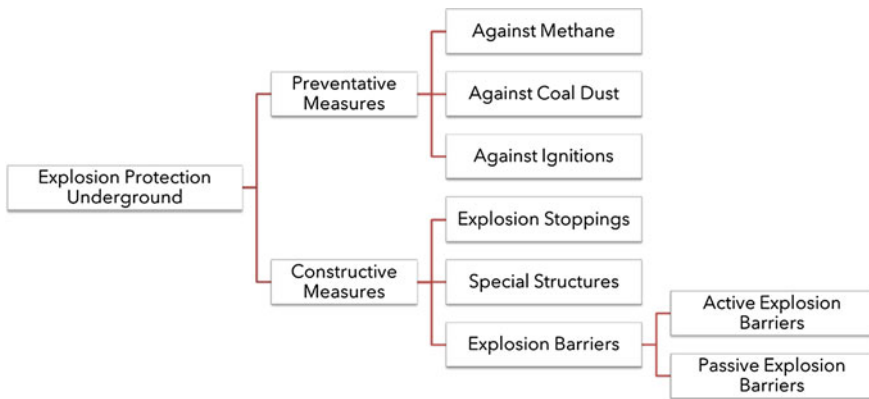


**Fig. 1.** Current categorization of mitigating controls

As an example, the NSW Department of Minerals Resources has created a guideline to support the development, implementation and assessment of underground explosion suppression systems [2]. The document describes the elements to be reviewed, when analyzing which type of suppression barrier to be utilized (Fig. 2). According to the guideline, the explosion suppression management system should be integrated into the mine safety system. The key components listed in this document are: design, purchasing/construction, installation, maintenance and operation. These components have been adopted in this paper as a reference to compare common explosion barriers.
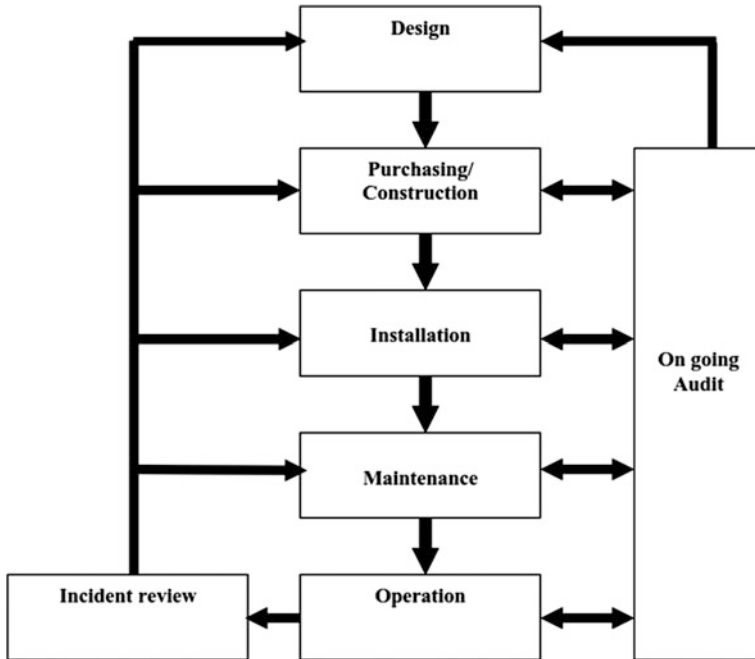
**Fig. 2.** Coal dust explosion prevention and suppression system—element [2]

## 2 Design

The purpose of the design of a suppression barrier is to suppress an explosion as quickly and effectively as possible. Factors to take account of when designing an explosion barrier could be:

1. Taking account of the assumed strength of an explosion (kPa)
2. Distance from cutting face (m)
3. Obstacles within the area e.g. ventilation ducting
4. General requirements of the explosion barrier. e.g. power supply.

The possible strength of an explosion is of particular interest when considering passive explosion barriers. According to du Plesssis and Vassard [3] an explosion could be categorized into "weak", "medium" "strong" or a "supplement" explosion. The description used does not refer to the amount of damage that could be caused, but rather reflects the flame speed and pressure of an explosion. According to du Plessis [4] a standard explosion would be comparable to a $36 \text{ m}^2$ volume of 9% methane/air creating a wind pressure of approx. 25 kPa. A test gallery would then have 6 kg of coal dust on shelves for 10 m. Additionally 138 kg of coal dust would be distributed on the floor for a distance of 140 m. A strong explosion would be considered to be similar to the standard explosion but using 25% more (192 kg opposed to 144 kg for a standard explosion) coal dust. The dynamic pressure would then increase to approx. 50 kPa.

A weak explosion would be comparable to the standard explosion but using a 200 J igniter to activate the methane gas explosion. This results in an explosion of approx. 15 kPa dynamic pressure. The passive barriers commonly used are amongst others: concentrated stone dust barriers and distributed stone dust barriers, concentrated water barriers and distributed water barriers. The same research reported (amongst others) that all passive barriers have been proven effective. The basic working function of any passive barrier is based on enough wind pressure (dynamic pressure) to activate the control. An active explosion barrier in turn is stated to be independent of the strength of an explosion [5]. These systems depend on detection electronics and trigger a suppression reaction based on the occurrence of an explosion. Due to the calibration of an active explosion barrier, there is no risk of an explosion being too slow or too fast. An explosion being too slow (flame speed) would mean that an active barrier is being triggered due to the detection of an explosion and then discharging the suppression agent prior the flame reaching that barrier. An explosion being too fast would, on the other hand cause, the barrier to discharge only once the explosion has passed the barrier. This would cause such a system to be inefficient. Multiple tests such as described by du Plessis and Spaeth [6] and du Plessis and Spaeth [7] have proven the effectiveness of active explosion suppression systems. The tests describe the effectiveness of the active explosion barrier at distances between 5 and 90 m from the explosion source. The flame speeds that were measured at the active barrier vary from 57 to 173 m/s. Up to today it was not possible to determine the maximum flame speed that might pass an active barrier (manufactured by ExploSpot Systems Pty Ltd.).

The property of an active explosion barrier to be independent of the dynamic pressure of an explosion enables a mine to use the barrier even at the closest possible distance to cutting face. The closest possible position of an active barrier is at approx. 7 m mounted on a continuous miner. These active barriers are so called machine mounted systems and have been used in underground coal mining operations since 2001. The closest possible location of a passive barrier as recommended by the Department of Minerals and Energy (DME) of South Africa is 60 m from a coal face. Similar legislation is available for New South Wales in Australia. The UK Health and Safety Executive however states the closest distance from the first passive barrier to the cutting face may be 70 m [8]. The implementation distance from the face is also recognized as one of the greatest shortcomings of a passive barrier [9]. A schematic of a functional implementation area is depicted in Fig. 3. The implementation area directly reflects the "harmful" area of a mining operation.
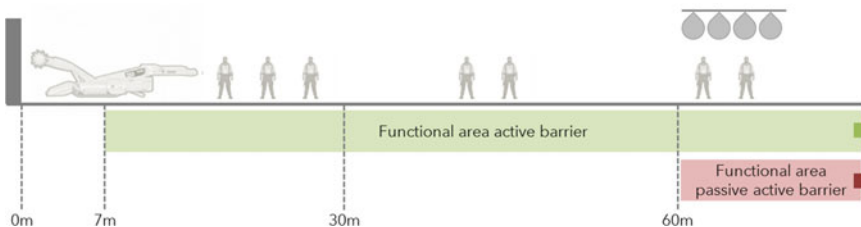


**Fig. 3.** Functional area of active and passive barriers (based on South African Code of Practice)

The roadway will typically have multiple obstacles. These might be, amongst others, a conveyor or ventilation ducting. These obstacles create a dynamic environment for any explosion suppression system. Dynamic in this case refers to a challenge within the barrier design. An obstacle might cause a gap in the barrier development and permit a flame to escape the barrier. A good example is a conveyor. The space between the belts as well as the space between the return belt and the floor might be a locations where it is difficult to ensure full coverage of the inerting or suppression powder. The mine's risk assessment might result in additional passive barriers being deployed along the conveyor. In the case of an active barrier, the suppression outlet should be extended into the "shadow zones". Experiments conducted and as described by Spaeth et al. [5] show, that the active barrier must effectively close all gaps within a roadway. Figure 4 shows examples of how the different barriers can be designed to cope with obstacles within the roadway.



**Fig. 4.** Examples of a passive (left) and an active (right) barrier configuration to ensure obstacle coverage

The design of an explosion barrier should also incorporate general requirements specific to their nature. To name an example, active barriers require a continuous source of power. This source of power will depend on the environment they are located in. Current active barriers can be supplied by either an external power supply or a battery. While the external power supply will limit the barrier to be placed within the physical limits of the power source, a battery-operated barrier can be placed freely at whatever location is applicable. This requirement does not apply to passive barriers. An example of a general requirement specific to passive barriers might be the space requirement (or occupied) within the roadway. Whereas an active barrier only occupies 1 m$^3$ (for a 2.4 m $\times$ 7 m) roadway section, a passive barrier will occupy a much larger area. In the case of a comparable section and assuming a primary barrier is made up of 4 sub-barriers with a stonedust density of 1.2 kg/m$^3$, one hundred (100) 6 kg bags would be required for each sub-barrier. This in turn results in a occupied space of at least 6.7 m$^3$ per sub-barrier. This factor is especially worth noting when considering the available space for moving machinery.

## 3   Purchasing/Construction

Procurement is a dominant factor when evaluating any equipment to be used in an operation environment. In the case of equipment used in a mining environment it would be ideal to determine the costs based on the lifecycle of mine. The cost of a single component e.g. one stone dust bag or one active barrier cannot be generalized. The cost may vary according to country, a mine or a mining company. It should be assumed that a single passive barrier costs a fraction of one active barrier. The passive barrier comprises of stone dust and some sort of container (e.g. bag with hook). In some cases, a barrier could also include a support to fasten the barrier to the roof (e.g. water trough). An active barrier will however be a configuration of sensors, suppression canisters, piping, nozzles, controller and power supply. This agent may vary according to a country's legislation and mine's Code of Practice. In most cases, as in South Africa, China, Australia, Monoammonium Phosphate (more commonly known as MAP or ABC powder) will be used. Although the price of a single active barrier is much higher, the number of systems to be used within a mining operation will be much lower than in the case of a passive barrier. This assumption is based on the fact, that active barriers are reusable. An active barrier is furthermore mobile. It is also possible to move an active barrier as the cutting operation progresses. An active barrier in its design will be able to be used at a variable distance from the cutting face. As the barrier is not reliant on the strength of an explosion (weak, standard or strong) it could be initially placed at e.g. a distance of 15 m from the cutting face. As the cutting operation progresses, the distance to the face will increase. Once the distance to the cutting face becomes too great (according to a particular mine's Code of Practice or risk management system), the active barrier can be moved forward to be located at 15 m again.

## 4   Installation

The installation of any barrier will be based on the design performed in advance. This should result in addressing installation issues such as adequate preparation, the placement, amount (both for containers and powder or suppression agent) and the proper fastening of the equipment. In this process it should be ensured that adequate attention is given to faultless implementation of the design and transparent possibilities of commissioning a barrier.

The preparation would typically address issues such as how and where to fasten a barrier. Bagged barriers would typically be suspended from the roof. As per the HSE "Bagged stonedust barrier" specification, a seam height exceeding 3.5 m will require multiple layers of bags. In some cases, a structure will need to be prepared to suspend the passive barriers. Similarly, an active barrier will need to be fastened to a support structure. The support structure needs to be prepared in advance. The support structure should also allow the barrier to be relocated. Figure 5 presents a few solutions of barriers being implemented in South Africa, China and Australia. In most cases passive barriers will be suspended from the roof. Active barriers may be fastened to the ground, roof or any other structure in place that can support the load. Whereas an active barrier will be considered as one unit, passive barriers will be distributed over an area. The

weight distribution would hence affect the placement. Continuing the example of a 2.4 m × 7 m roadway section and assuming the same requirements as used in Chap. 3 "Design", the total weight of a passive barrier will be 2.41 t spread over a distance of 120 m (assuming a barrier as described in the HSE "Bagged stonedust barrier" Code of Practice [8]. The same roadway section would require 130 kg of suppression powder when using an ExploSpot active barrier [5]. The active barrier will weigh 1.6 t. All connections (hydraulic and electrical) are based on the "poka yoke" principal (from the Japanese for inadvertent error prevention). Thereby ensuring unique and fault free connection and interfaces. Ensuring the design is implemented unmistakably.



**Fig. 5.** Clockwise from top left to bottom right: water trough (China), active explosion barrier (South Africa), BatBag (South Africa and Australia NSW), active roadway barrier (China)

Once the installation has been completed, a barrier needs to be commissioned. The commissioning procedure ensures the installation conforms to the design and operation. Passive barriers will be commissioned using primary visual inspection methods. Some passive barriers such as the stonedust barrier bag have implemented visual guidance in regard to the bag and its content. By means of a red line the inspector will be able to determine whether the bag was roughly filled with the appropriate amount of stonedust. As the bag is transparent, the inspector will also be able to visually inspect the color and the composition of the bags content. By pressing the bag, he will be able to establish whether the content still roughly complies to the Code of Practice in regards to clogging. Active barriers will also be commissioned by means of visual inspection. The barrier will be inspected in regards to obvious physical damage and by

monitoring the controller's display. The display will indicate any electronic or pressure error that effect the barriers performance. The controller will monitor the health and sanity of the active barrier in real time. Therefore, ensuring immediate identification of an error (see Fig. 6).



**Fig. 6.** Error indication and commissioning of passive and active barriers

## 5   Maintenance

Maintenance is of extreme importance in regard to the proper and full functionality of an explosion barrier [2]. If a barrier is not maintained according the Code of Practice or manufacturer's requirements, the risk of an explosion passing a barrier unsuppressed increases to an extent whereby it might be the same as not having a barrier at all. As part of Cain's recommendation [9] the maintenance of explosion barriers should be part of any Code of Practice or Standard Operating Procedure. In practice, the maintenance of a barrier will vary according to type. Bagged barriers might need to be inspected in regard to the number of available bags per barrier. The water content of each water trough within such a barrier might need to be inspected and refilled. Amongst others, each barrier component would need to undergo a visual and under certain circumstances haptic inspection. The active barrier would similarly need to undergo a visual inspection. Here the inspection would, similarly to the commissioning, include a mechanical and an electronic inspection. The mechanical inspection would cover aspects such as "obvious physical damage" and clogging of the nozzles. The electronic inspection as part of the maintenance would include analysis of a controller's user interface. Any sort of visual inspection, regardless of the type being active or passive) is done on-site. Hence the inspector would need to physically go on-site to investigate

the general state of a barrier. Having an electronic interface enables active barriers to communicate with surrounding personnel. Even though they might not have had adequate training to analyze a fault on an active barrier, these interfaces will use basic symbols (typical to a country, culture or other safety) that any mining staff will associate with a certain type of situation. Newer active barriers also provide the possibility of reporting to service dashboards such as the "ExploSpot Maintenance Cloud" [10] (see Fig. 8). These dashboards do not substitute routine maintenance, but rather provide information to have for more efficient and timely maintenance. Using a dashboard, the maintenance personnel would have a clear indication of any part that may be faulty. Hence providing the team e.g. with the correct spare-part prior to inspecting the faulty barrier. This in turn will lower the lead time for the barrier to be fully functional again. These kinds of support tools do however require a basic communication infrastructure. These might not always be in place at the site of an active barrier (Figs. 7 and 8).



**Fig. 7.** Peripheral display indicating health state or operational status

The release mechanism of common active barriers is based on the discharge of pressurized container. Most legislation requires any kind of pressurized container to be serviced once every 12 months. Legislative requirements such as the service of pressurized containers, contribute to the individual barrier type maintenance plan.

## 6   Operation

The operation refers to the actual performance of a barrier in the case of an explosion. It is expected of an explosion barrier to stop and suppress an explosion according to the design set out in the above. Although the operation is often divided into "active" and "passive", practice will rather indicate a difference in regard to the motion of an explosion barrier. Passive barriers have always been regarded to have a particle motion
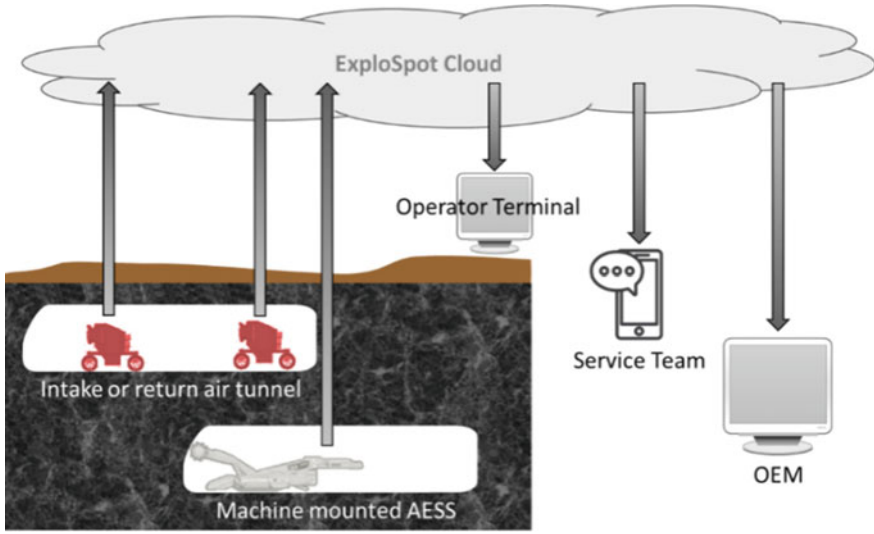
**Fig. 8.** Schematic function of a maintenance support dashboard

in the same direction as the explosion. Active barriers, especially the machine mounted barriers, have always been considered to counter the explosion force. Therefore, the particle motion would be considered to be as a "confrontational motion" or "stopping motion". This also being the reason why active barriers have been considered to stop an explosion at the operator's position [11]. In 1999, the on-board Continuous Miner operator's position was at the rear end of the machine. Developments have however also gone in the direction of using the same concept as passive barriers to merely releasing inerting material into the roadway and hence reacting the way as a passive barrier [12]. These barriers have the same obvious disadvantages as a passive barrier regarding size, placement and safety area. They do however enable the implementation of mechanisms to enhance the commissioning and maintenance aspects as discussed above (Fig. 9).

Unlike passive barriers that cannot be reused, active barriers are designed in such a way as to allow the reuse of most of the components. However, some components are subject to flameproof or intrinsic safe regulations that might not allow the reuse of these components. One manufacturer of a confrontational barrier, has reported that an ExploSpot machine mounted barrier has been in use for up to six years in one of the South African mines [13]. During this time span multiple maintenance runs (pressure canister overhaul) have been conducted to comply to legislation.
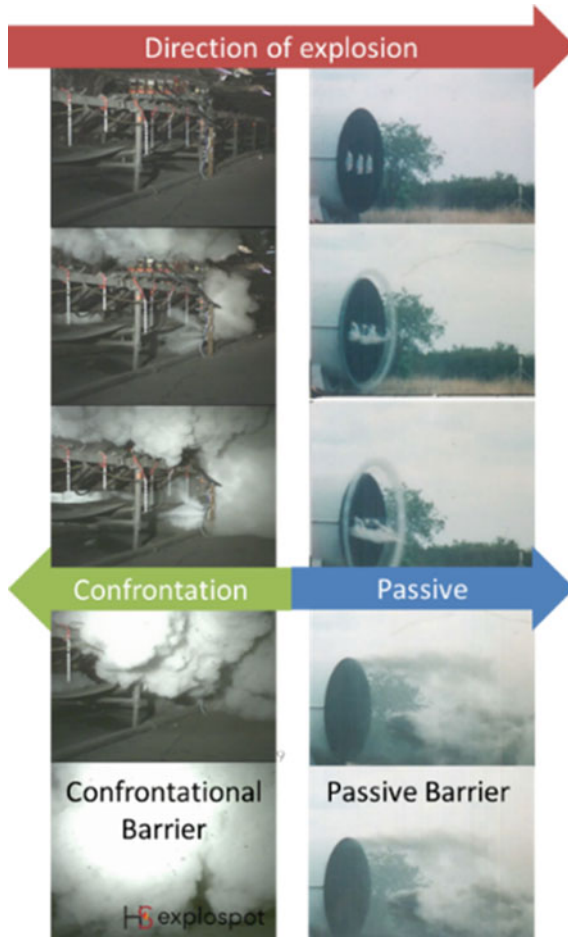
**Fig. 9.** Example of methodology in regard to the suppression motion

## 7  Conclusion

It is generally accepted that both principals of confrontational and passive barriers have been proven to work within the specifications that they have been designed for. In regard to safety, a few differences have however been identified when reviewing the barriers in an operation environment.

1. The categorization of explosion barriers should be revisited when discussing constructive explosion mitigating controls. As to the performance, there are drastic differences between a passive motion of material or a confrontational motion of material. Thereby rather reflecting the effective safe area than the means of activation. This would enable a risk management system to further scale down the high-risk area. A more risk orientated category for explosion barriers would refer to

a confrontational barriers and passive barrier (as a characterization of the function). This category would enable the stopping and suppression of a methane gas and/or coal dust explosion within a few meters (confrontational barrier). A passive barriers (including those that might use an electronic triggering system) can only be implemented at a far distance and although suppressing the explosion within the boundary of barrier, create a fatal zone of some hundred meters (depending on the passive barrier design).

2. The space claim of confrontational barriers is far less than the passive barriers. Due to the dynamic design possibilities of this type of barrier, these barriers can be placed outside the working (moving machinery) area.
3. The cost of a single passive barrier unit is far less than a single active barrier. Practical implementation however shows that the total cost within a 2000 m gate-road will be greater when using passive barriers rather than using an active barrier. As per analysis done by Humphreys et al. [14].
4. The installation of a passive barrier allows the installer to divert from the design of the barrier. This is not possible for confrontational barriers, as they are built on a principal whereby the barrier is susceptible to a wrong installation.
5. A confrontational barrier is far more robust than a passive barrier. Due to the function of passive barrier (low/medium pressure rupture) it will not withstand even minor shock. The confrontational barrier does per specification need to withstand strong outside forces. This however does not mean that it will withstand all influences generated by underground machinery.
6. The current and future possibilities of an active barrier to interface with an inspector, operator or maintenance team is vast. All current implementations ensure a safety orientated interface, allowing the mine to clearly incorporate an active barrier into their Code of Practice or safety procedure.
7. The design of a confrontational barrier is easy implement. The adaptation to a new environment is easy implement.

# References

1. Michelis, J.: Preventative and Constructive Explosion Protection Against Coal Dust and Methane Explosions in Underground Coal Mining. EuropEx Edition 16 (1991)
2. MDG 3006 MRT5: Guideline for Coal Dust Explosion Prevention and Suppression. Mine Safety Operations Division, New South Wales, Australia (2001)
3. du Plessis, J.J.L., Vassard, P.S.: SIMRAC Research Report. Increase the Use of the Stonedust Bagged Barrier Enhancing Its Application for Different Conditions. COL 446. South Africa (1999)
4. du Plessis, J.J.L., Brandt, M.P., Vassard, P.S.: SIMRAC Research Report. Assessment of Explosion Barriers. COL 010. South Africa (1995)
5. Spaeth, A., Belle, B., Phillips, H.: Introducing a new age of highly effective, automatic explosion suppression barriers. In: Australian Mine Ventilation Conference, Brisbane, Australia (2017)
6. du Plessis, J.J.L., Spaeth, H.: Active barrier performance preventing methane explosion propagation. In: 14th Coal Operators' Conference, Wollongong, Australia (2014)

7. du Plessis, J.J.L., Spaeth, H.: Kloppersbos Report EC 2001-0347. Development and Testing of an On-Board Active Suppression System for Continuous Miners in Medium Seam Mining Conditions (2001)
8. Health and Safety Executive. Bagged Stonedust Barriers. Tech. N.p., United Kingdom
9. Cain, P.: The Use of Stone Dust to Control Coal Dust Explosions: A Review of International Practice, Underground Coal Mine Safety Research Collaboration (2003)
10. Spaeth, A., du Plessis, J.J.L.: Utilizing smart active explosion suppression systems to support dynamic risk environments in underground coal mining. In: 16th North American Mine Ventilation Symposium, Colorado, USA (2017)
11. du Plessis, J.J.L., Smith, G.L.: Control strategies for coal dust and methane explosions in underground coal mines: current South African research and development initiatives. J. S. Afr. Inst. Min. Metall. (1999)
12. Humphreys, D., Collecutt, G., Greenwood, J., O'Beirne, T.: The impact of facility construction and scale on the characteristics of experimental coal dust explosions. In: Australian Mine Ventilation Conference, Sydney, Australia (2015)
13. ExploSpot Systems Pty Ltd. Company Quality Management Documentation. South Africa (2018)
14. Humphreys, D., Greenwood, J., Proud, D., Collecutt, G.: Active Explosion Barriers, Final Report on ACARP Project C7028, Australia (1999)

# A Fundamental Study of High-Speed Methane-Air Deflagrations Across Simulated Gob Walls and Sphere Beds

Claire Strebinger, Gregory Bogin$^{(\boxtimes)}$, and Jürgen Brune

Colorado School of Mines, Golden, CO 80401, USA
gbogin@mines.edu

**Abstract.** Detailed knowledge of flame propagation and pressure generation from methane-air deflagrations with and without obstacles is necessary to understand and help mitigate methane gas explosions in longwall coal mines. Experiments were performed in a quartz flow reactor investigating the effects of confinement, void spacing, and gob geometry on methane flame dynamics using a simulated gob of glass spheres. Results show ignition from a confined space increased flame propagation velocity over 5000% and peak pressure 1300%. A 3.8 cm high simulated gob wall (73% void space) further enhanced flame speed 14% and peak pressure approximately 50%. Decreasing void spacing of a sphere bed from 96 to 89% increased flame speeds 2–4% and pressures 15–35%. Results demonstrate that mine layout and gob characteristics can have a significant impact on the propagation and severity of a methane gas explosion. Experiments from this study will aid in providing a comprehensive understanding of the factors contributing to methane explosion enhancement in longwall coal mines.

**Keywords:** Methane combustion · Longwall coal mining · Flame propagation Overpressure

## 1 Introduction

Explosive gas zones of methane-air mixtures are known to exist in longwall coal mines and can migrate towards the longwall face, posing a fatal risk to nearby workers [1]. This is evidenced by the Willow Creek Mine explosion in 2000, killing 2 and injuring 8 miners, in addition to the methane explosion at the Upper Big Branch (UBB) mine in 2010 resulting in the fatality of 29 miners [1–3]. In the report of the Willow Creek Mine explosion, some of the pressure waves from the explosions entrained dust, reversed airflow in the mine, and even threw a miner causing rib injuries [2]. Predicted pressures from UBB mine explosion were upwards of 170 kPa and reflected pressure waves of almost 720 kPa, with flames estimated to have traveled at 450 m/s [3]. Pressure waves of these magnitudes can be harmful to mine workers, mine structures, and equipment. For example, an unprotected person has a 50% chance of rupturing their eardrum at pressures above 100 kPa and a 50% chance of lunch damage at pressures near 210 kPa [4]. Additionally, overpressures between 56 and 490 kPa can severely deform a concrete wall of thickness 240–370 mm [5]. These examples help

demonstrate the need for developing a comprehensive understanding of the resulting methane flame and pressure wave propagation from these explosions in order to develop stronger prevention and mitigation strategies and improve miner safety.

Researchers at the Colorado School of Mines (CSM) are developing a coupled 3-D, computational fluid dynamics (CFD), combustion model to simulate large-scale methane gas explosions in longwall coal mines to provide insight into potential danger on miners and guidance in developing new mitigation strategies [6–9]. Evidence from previous longwall coal mine explosions have shown explosions may occur on EGZ fringes, near the gob, longwall face, and tailgate corner [1–3] which agrees with predicted EGZ locations and movement using CFD modeling [7, 8]. Preliminary research performed by Fig et al. [9, 10] shows methane flame enhancement across a rock gob as depicted in Fig. 1. However, there are many varying parameters including rock size, void size, rock material, and porosity. To gain a stronger understanding of the effect of these gob parameters on methane flame propagation, researchers conducted a series of studies by simulating different gob parameters using solid spheres arranged in different geometries [11]. The major advantage of using spheres is they remove any differences in results due to surface topology and they can easily be arranged in different geometries, allowing researchers to simulate a variety of gob and mine parameters and use results to validate a combustion model being developed at CSM. Results from these studies show methane flame propagation was sensitive to ignition location and the amount of confinement, void spacing, and gob geometry [12]. However, previous studies did not investigate the coupling effects of the methane flame and pressure waves, which is an important aspect of longwall coal mine explosions [2, 3]. This manuscript aims to provide additional insight of the coupling between methane flame and pressure wave propagation by performing key experiments using glass spheres arranged in different geometries to simulate gob parameters leading to enhanced methane-air explosions. In the future, these experiments will be used to validate the combustion model [9, 11] which will be incorporated into a mine-scale CFD ventilation model and used to perform studies on large-scale methane gas explosions in longwall coal mines.



**Fig. 1.** Left—Image of Western U.S. Longwall void [13]. Right—Image of simulated gob used by CSM researchers

## 2    Background

Previous research has shown methane flame enhancement and pressure enhancement across obstacles due to turbulent mixing and accelerated combustion rates [10–17]. Chapman and Wheeler [10] performed a fundamental study of flame acceleration across obstacles, finding that upstream of the obstacle the flame is slightly retarded and then accelerates across the obstacle. They also found that the greatest increase in flame speed was when the restriction reduced the effective diameter of the reactor by half (or a blockage ratio, BR, of 0.5) and that multiple restrictions continued to enhance flame speed [10]. Though Chapman and Wheeler did not take pressure data, Moen et al. recorded pressure data with 0, 1, and multiple obstacles and found a similar trend; i.e. increasing the number of obstacles increased the overpressure [14]. Moen et al. also found that for a single obstacle at the same location, as the BR increases from 0.16 to 0.5, the overpressure increases almost 2-fold [14]. Ciccarelli et al. performed a study using layers of beads across the entire bottom of a horizontal reactor [15]. They found that for a fixed bead layer, reducing the gap height (or blockage ratio) above the bead layer resulted in shorter deflagration-to-detonation run-up distances [15], which agrees with obstacle studies performed by other researchers [10, 14]. However, due to varying experimental setups, ignition locations, and fuels used in these studies it is difficult to compare experiments to fully validate the combustion model being developed at CSM.

## 3    Experimental Setup and Procedure

Since there are safety concerns of performing methane gas explosions in a real longwall coal mine, experiments in both laboratory-scale and large-scale explosion reactors with diameters ranging from 5 to 71 cm and lengths of 43 cm to 6.1 m were performed. This allows researchers to (1) safely perform experiments necessary for understanding methane flame dynamics and (2) understand fundamentally how methane flame parameters such as flame front propagation velocity and pressure may change as a function of scale. Understanding the scalability of methane flames helps researchers to validate on-going CFD combustion models. These models will be incorporated into a mine-scale, ventilation CFD model to simulate large-scale methane gas explosions to help build stronger prevention and mitigation strategies for improved worker safety.

The experiments presented in this manuscript were performed in a 12.5 cm outer diameter, 1.5 m long horizontal cylindrical quartz flow reactor as shown in Fig. 2. The setup and procedure of this reactor has been previous described by Strebinger et al. [12]. In summary, methane and zero-grade air are well-mixed before flowing into the quartz reactor for 5 min (3 fill volumes), after which the mixture settles for 40 s insuring stagnant conditions. The mixture is then ignited using a capacitive discharge spark ignition system providing a 60 mJ electric spark. Flame front propagation velocities are recorded by custom-made ion sensors and the pressure is recorded by a Kistler© 4260 piezoresistive pressure transducer on the closed end of the reactor. Each experimental set consists of 5 runs; flame front propagation velocities are the average of a set and error bars represent the standard deviation of the mean. All experiments were performed using a methane-air mixture stoichiometry of $9.5 \pm 0.3\%$ by volume.

Experiments are performed at 293 K and 83 kPa, which are ambient atmospheric conditions for Golden, CO—elevation 1730 m above sea level.
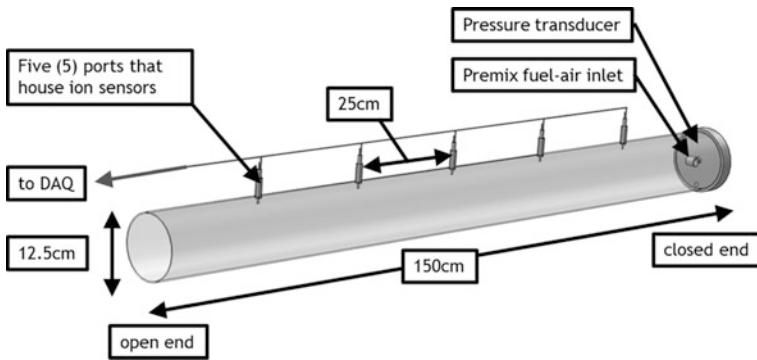


**Fig. 2.** Schematic of laboratory scale experimental horizontal quartz flame reactor

### 3.1 Experimental Parameters

Previous research [12] has shown that for a longwall mine application, methane flames are sensitive to ignition location, simulated gob geometry, and the amount of void space. Therefore researchers have focused on key experiments to investigate these parameters as described below.

#### Ignition Location

The methane-air mixture was either ignited 11 cm from the open end of the reactor (open-end ignition) or 11 cm from the closed end of the reactor (closed-end ignition). An open-end ignition (OEI) is analogous to a methane flame propagating from the tailgate towards the entries. Closed-end ignition (CEI) is similar to a methane explosion from a confined space such as an explosion originating from in or around the gob and propagating towards the longwall face.

#### Simulated Gob Geometry

Glass spheres were arranged in different geometries to help simulate different gob parameters. The main advantages of using glass is that is has thermal properties similar to rock, spheres are simple to model for combustion model validation, and spheres remove any differences in results due to surface topology. It is important to note that the glass spheres are not meant to represent a longwall gob, but are used as a research tool to understand the impact of gob parameters (e.g. porosity, void spacing, size of rocks, height and width, etc.) on explosion propagation.

Two types of simulated gob geometries were used: glass spheres oriented in a wall geometry (Fig. 3) and a simulated gob bed (Fig. 4). The wall geometry consists of 6.35 mm diameter glass spheres arranged in a wall using a non-reacting wire mesh. As the height of the wall increases, the amount of void space decreases, allowing researchers to investigate the effects of void spacing. The simulated gob bed consists of

1 cm diameter glass spheres. Researchers changed the length and height of the simulated gob bed to help simulate how a methane flame may propagate across a longer pile of rock instead of a single obstacle.
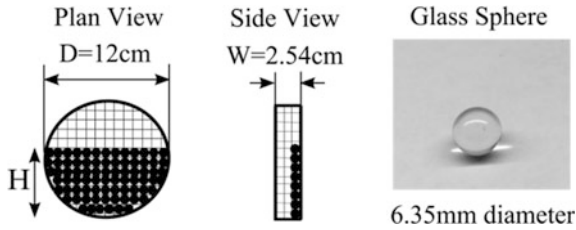


**Fig. 3.** Schematic of simulated gob wall geometry used in this study and image of glass sphere used in this geometry
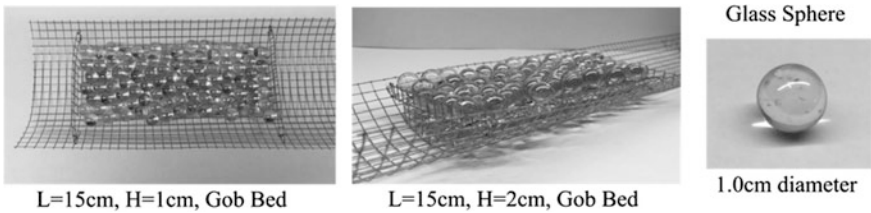


**Fig. 4.** Images of glass sphere and examples of simulated gob beds used in this study

## 4    Results and Discussion

In the first set of experiments, researchers investigated how void spacing of a single simulated gob wall impacts methane flame propagation for both an open-end ignition and closed-end ignition. Figure 5 shows the results of an open-end ignition when the simulated gob wall is located at 37 cm from the open end and the void space decreases from 73% (H = 3.8 cm) to 13% (H = 9.8 cm). Results show that the simulated gob wall with 73% void space (H = 3.8 cm) had no significant effect on methane flame front propagation velocity. However, when the void spacing was decreased to 13% (H = 9.8 cm) there is an enhancement of methane flame front propagation velocity across the obstacle. This is due to the fact that the amount of void space the flame is able to propagation through decreases. Therefore the flame accelerates to maintain the same amount of mass flow rate.

A closed-end ignition is an ignition from a confined space, which results in a pressure wave that increases fluid motion ahead of the flame thereby accelerating the flame to speeds almost 50 times an open-end ignition as shown in Figs. 6 and 7. Although the 3.8 cm tall simulated gob wall (73% void space) did not have a significant impact on an open-end ignition, it greatly accelerated the flame for a closed-end ignition. This is because a closed-end ignition results in a turbulent flame that when
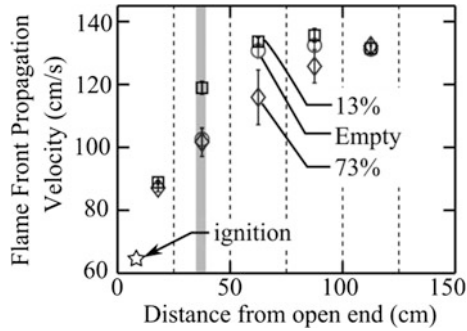
**Fig. 5.** Impact of amount of void space on methane flame front propagation velocity for ignition 11 cm from the open end. Simulated Gob: 6.35 mm diameter spheres in a wall geometry, L = 6.35 mm, Void space = 73% (H = 3.8 cm) or 13% (H = 9.8 cm). Location = 37 cm. Shaded bar represents simulated gob location. Dotted lines represent flame detector locations. $CH_4$ = 9.5 ± 0.3%. Operating conditions 293 K, 83 kPa. Standard deviation range (5 runs): 0–8%. $E_{ign}$ = 60 mJ
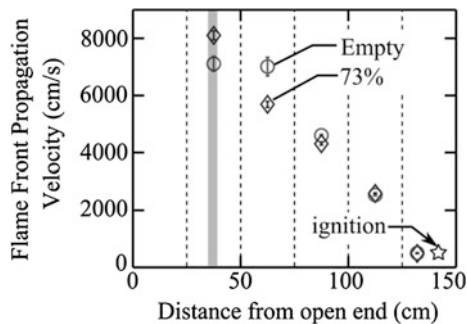


**Fig. 6.** Impact of simulated gob wall on methane flame front propagation velocity for ignition 11 cm from the closed end. Simulated Gob: 6.35 mm diameter spheres in a wall geometry, L = 6.35 mm, Void space = 73% (H = 3.8 cm). Location = 37 cm. Shaded bar represents simulated gob location. Dotted lines represent flame detector locations. $CH_4$ = 9.5 ± 0.3%. Operating conditions 293 K, 83 kPa. Standard deviation range (5 runs): 1–4%. $E_{ign}$ = 60 mJ

passing over an obstacle wall results in flow separation as shown in Fig. 8. This flow separation is important because it forms eddies on the downstream side of the wall, which increases temperatures and fluid motion promoting flame acceleration, agreeing with observations made by other researchers [10, 14]. For an open-end ignition the pressure rise does not significantly affect the unburned mixture upstream of the flame. Thus, when the flame passes over the obstacle wall, the flame continues to burn radially and tangentially as shown in Fig. 8.

In addition to accelerating the methane flame across the simulated gob wall, the 3.8 cm high gob wall (73% void space) also increased the overall pressure rise of the explosion as shown in Fig. 7. The first pressure peak in Fig. 7 corresponds to the initial
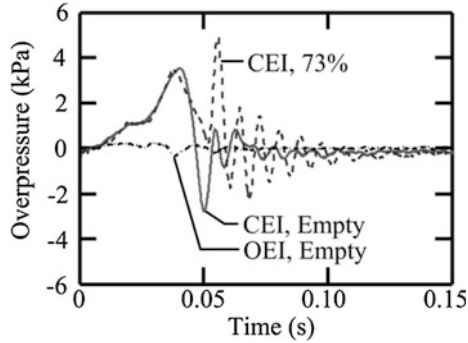
**Fig. 7.** Pressure-time history of an open-end ignition with no gob (empty), a closed-end ignition with no gob (empty), and closed-end ignition with a simulated gob wall (void space 73%). Simulated Gob: 6.35 mm diameter spheres in a wall geometry, L = 6.35 mm, Void space = 73% (H = 3.8 cm). Location = 37 cm. OEI Open Tube $P_{max}$ = 0.25 kPa. CEI Open Tube $P_{max}$ = 3.49 ± 0.05 kPa, $P_{min}$ = −2.57 ± 0.22 kPa. CEI Wall $P_{max}$ = 5.20 ± 0.22 kPa, $P_{min}$ = −2.61 ± 0.18 kPa $CH_4$ = 9.5 ± 0.3%. Operating conditions 293 K, 83 kPa. $E_{ign}$ = 60 mJ
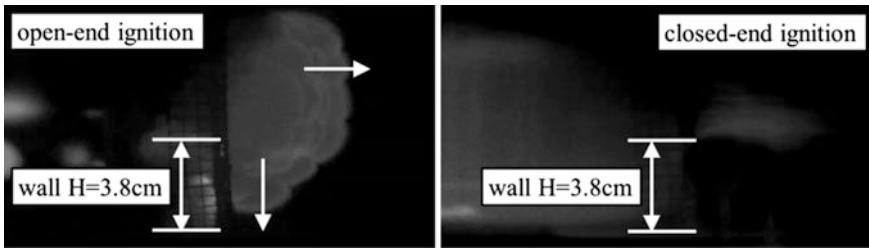


**Fig. 8.** Left: Image of methane flame propagating across a simulated gob wall for an open-end ignition. Right: Image of methane flame propagating across a simulated gob wall for an open-end ignition. Simulated gob wall, L = 6.35 mm, Void space = 73% (H = 3.8 cm). Location 37 cm. $CH_4$ = 9.5 ± 0.3%. Operating conditions 293 K, 83 kPa

kernel expansion of the flame before the onset of venting and the second peak is correlated to the increase in combustion rates after the onset of venting, which agrees well with literature [18]. After these first two peaks, the simulated gob wall increases the pressure in the reactor and sustains pressure oscillations while residual methane-air mixture is burned even though the main flame front has exited the reactor. These results help demonstrate that obstacles can increase the peak overpressure, sustain larger pressure oscillations, increases secondary burn duration and percentage of burned methane-air mixture, therefore increasing the total heat release during an explosion. This is important because large overpressures can knock out ventilations controls, damage mine equipment, and cause harm to workers [1–3]. Additionally, the large positive and negative pressure oscillations induced by the obstacle wall may entrain air, which in a real mine situation, could sustain a methane fire or reverse airflow. Therefore, it is important to have a full understanding of both the peak overpressure

and magnitude of pressure oscillations of a methane gas explosion in order to accurately predict these hazards.

Although the single obstacle wall provided key insight into the mechanisms of methane flame enhancement, there may also be instances in a longwall coal mine where there are large void spaces and piles of rock rubble of varying height and length. In order to understand how these conditions affect methane flame propagation, researchers arranged spheres in a simulated gob bed shown in Fig. 4. In the next set of experiments shown in Fig. 9, the simulated gob bed was 1 layer tall (1 cm in height, 96% void space) and 30 cm long and tested at different distances from the ignition source. Results show that when the simulated gob bed is near to the ignition location there is flame acceleration across the bed, but further from the ignition source, the simulated gob bed had no significant impact on the flame front propagation velocity. This is because during the flame kernel development there is a small pressure rise, as shown in Fig. 7, which may help promote fluid motion through the spheres in the gob bed. In turn, this fluid motion promotes flame acceleration across the gob bed in a feed-back loop also described by other researchers studying flames through porous media [16]. When the simulated gob bed is moved further from ignition, this effect is less pronounced.
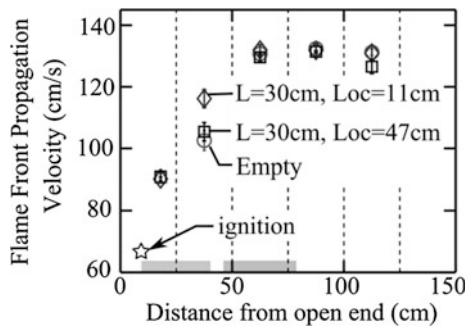


**Fig. 9.** Impact of simulated gob bed location on methane flame front propagation velocity for ignition 11 cm from the open end. Simulated Gob: 1 cm diameter sphere bed, L = 30 cm. Location = 11 cm, 47 cm from the open end, Void space = 96%. Shaded bars represents simulated gob location. Dotted lines represent flame detector locations. $CH_4$ = 9.5 ± 0.3%. Operating conditions 293 K, 83 kPa. Standard deviation range (5 runs): 0–6%. $E_{ign}$ = 60 mJ

In comparison, when the ignition location was moved to the closed end of the reactor, Fig. 10, the simulated gob bed greatly impacts the flame at both locations. Further from the ignition location, when the simulated gob bed was located 11 cm from the open end, it slightly retarded the methane flame upstream of the gob due to pressure resistance from the obstacle. However, when moved closed to the closed end of the reactor, the methane flame was greatly accelerated by the simulated gob bed. This is because the pressure wave ahead of the flame promotes fluid motion in the simulated gob bed and as the flame passes over the simulated gob bed, a turbulent boundary layer is formed as shown in Fig. 11. This turbulent boundary layer increases even more fluid

motion and increases combustion rates, which continue to accelerate the flame. Downstream of the simulated gob bed, flow separation can be seen and the flame front resulting from the turbulent boundary layer is actually ahead flame at the top of the reactor, where the ion sensors record methane flame front propagation velocity. This means that the flame front is actually moving faster than speeds shown in Fig. 10. These results are extremely important because in most experimental setups there is little to no optical access which means there may be a difference in recorded flame speeds and the actual location of the flame front. Measurements of the flame front at different radial positions at each fixed axial position via new techniques are currently underway. This method will allow discretization of the flame front propagation velocities radially as it interacts with the obstacles providing more accurate velocities and enhanced understanding of the turbulent interaction of the fluid flow and flame front.
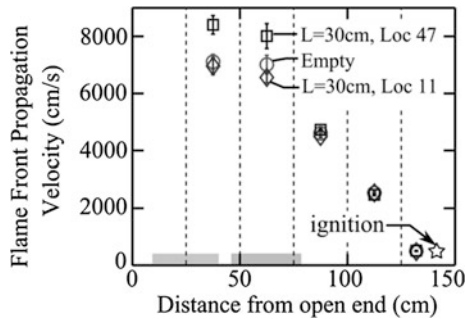


**Fig. 10.** Impact of simulated gob bed location on methane flame front propagation velocity for ignition 11 cm from the closed end. Simulated Gob: 1 cm diameter sphere bed, L = 30 cm. Location = 11 cm, 47 cm from the open end, Void space = 96%. Shaded bars represents simulated gob location. Dotted lines represent flame detector locations. $CH_4 = 9.5 \pm 0.3\%$. Operating conditions 293 K, 83 kPa. Standard deviation range (5 runs): 0–5%. $E_{ign} = 60$ mJ

Experiments were also performed investigating the effects of changing the length and height of the simulated gob bed and the results of these studies are summarized in Table 1. Results show that increasing the length of the simulated gob bed increased the maximum flame front propagation velocity and slightly increased the average peak maximum and minimum pressure recorded. These agree with theory since the flame must maintain mass flow through a longer void space. Additionally, as the height of the simulated gob bed increased from 1 to 2 cm, the void space decreased from 96 to 89%, which increased methane flame speeds approximately 2–4%. For the 30 cm long gob bed maximum peak pressures increased 15% and for the 15 cm long gob bed maximum peak pressures increased 35%. The average peak pressure for the 15 cm long, 2 cm high (89% void space) gob bed was larger than the 30 cm long, 2 cm high (89% void space) gob bed even though the methane flame front propagation velocity was higher for the longer gob. This demonstrates that there is a competing effect of flame acceleration across the gob and pressure resistance of the gob, which will be further explored in future work. Finally, it is interesting to note that the simulated gob beds of
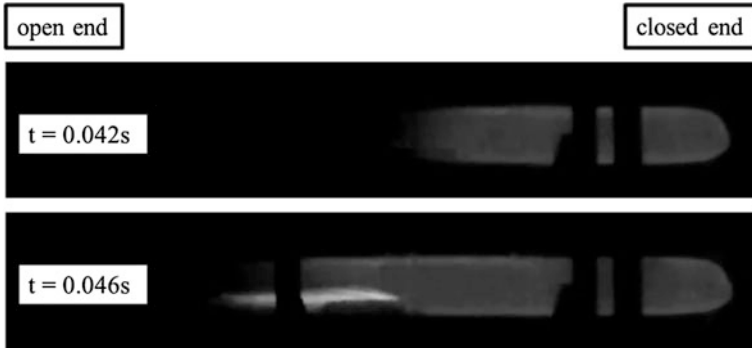
**Fig. 11.** Image of the methane flame before (t = 0.042 s) it encounters a simulated gob bed 15 cm in length and 2 cm in height (Void space = 89%) and image of methane flame as it interacts (t = 0.046 s) with the simulated gob bed during a closed-end ignition (flame moves from right to left). Ignition 11 cm from the closed end. $CH_4 = 9.5 \pm 0.3\%$. Operating conditions 293 K, 83 kPa

height 2 cm (89% void space) produced flame speeds and peak overpressures greater than the simulated gob wall of height 3.8 cm (73% void space). This is important for combustion model validation because it shows that induced turbulence due to a longer obstacle may lead to more violent explosions which agrees with previous researchers who have also noted that flames passing through a porous media can accelerate flames "as effectively as in rough tubes, or in tubes with periodical obstacles" [16].

**Table 1.** Table summarizing the maximum flame front propagation velocity, maximum pressure, and minimum pressure recorded for the closed-end ignition experiments with and without a simulated gob

| Simulated gob conditions | Maximum flame front propagation velocity (cm/s) | Maximum overpressure (kPa) | Minimum overpressure (kPa) |
|---|---|---|---|
| Open | 7100 ± 260 | 3.49 ± 0.05 | −2.57 ± 0.22 |
| Wall H = 3.8 cm, L = 6.35 mm | 8100 ± 158 | 5.20 ± 0.22 | −2.61 ± 0.18 |
| Bed L = 15 cm, H = 1 cm | 7900 ± 153 | 4.56 ± 0.25 | −3.14 ± 0.50 |
| Bed L = 30 cm, H = 1 cm | 8400 ± 325 | 4.79 ± 0.32 | −3.61 ± 0.39 |
| Bed L = 15 cm, H = 2 cm | 8200 ± 289 | 6.23 ± 0.39 | −5.74 ± 0.20 |
| Bed L = 30 cm, H = 2 cm | 8600 ± 281 | 5.52 ± 0.43 | −5.50 ± 0.52 |

In addition to further accelerating the flame, increasing the height of the simulated gob also increases the magnitude of the pressure waves resonating in the reactor as

shown in Fig. 12. This is important because large oscillations in pressure can entrain air. In a real longwall coal mine this could sustain a methane flame and promote flame acceleration. Additionally, these oscillations may lead to reverse airflow in a mine and could damage ventilation controls, increasing the explosion risk.
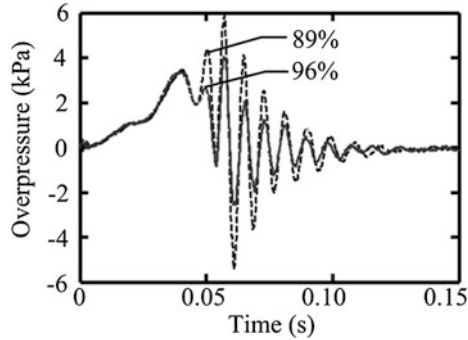


**Fig. 12.** Impact of void spacing on pressure-time history of a closed-end ignition. Ignition 11 cm from closed end. Simulated Gob: 1 cm diameter sphere bed, L = 15 cm, Void spacing 96% (H = 1 cm) or Void space 89% (H = 2 cm). Location = 62 cm from open end. Bed H = 1 cm $P_{max}$ = 4.56 ± 0.25 kPa, $P_{min}$ = −3.14 ± 0.50 kPa. Bed H = 2 cm $P_{max}$ = 6.23 ± 0.39 kPa, $P_{min}$ = −5.74 ± 0.20 kPa $CH_4$ = 9.5 ± 0.3%. Operating conditions 293 K, 83 kPa. $E_{ign}$ = 60 mJ

## 5    Conclusions

In conclusion, researchers have performed a series of experiments investigating the effects of ignition location, void spacing, and simulated gob geometry of methane gas explosion dynamics. Results have shown that ignition from a confined space results in greater overpressures that induced fluid motion ahead of the flame leading to faster flame propagation speeds. Additionally, methane gas explosions in confined spaces are more significantly affected by nearby obstacles. Decreased void spacing and increased gob bed lengths and heights increase methane flame propagation velocity and peak overpressure in addition to sustaining large pressure oscillations. These results are important for longwall coal mining because they show that small changes such as the topology of the walls, movement of the shields and shearer, and location of corridors can significantly affect methane flame and pressure wave propagation.

In the future, the experiments in this manuscript will be used to help validate a CFD, combustion model in order to gain further insight into the dominating mechanisms enhancing methane explosions. Experiments will also be repeated with different size rock rubble of varying material and surface topology. Previous research has shown that small changes to surface roughness of the simulated gob can greatly increase nearby mixing in unburned gases resulting in more complete methane combustion and flame enhancement [17]. Finally, the coupled, 3-D model will be used to identify explosive gas zone locations and model large-scale methane gas explosions. Results

will be used to further understand methane gas explosions in longwall coal mines in order to build stronger prevention and mitigation strategies for improved miner safety.

# References

1. Brune, J.: The methane-air explosion hazard within coal mine gobs. In: SME Transcript 334 (2013)
2. McKinney, R., Crocco, W., Tortorea, J.S., Wirth, G.J., Weaver, C.A., Urosek, J.E., Beiter, D.A., Stephan, C.R.: Report of Investigation, Underground Coal Mine Explosions, July 31–August 1, 2000. Willow Creek mine, MSHA ID No. 42–02113, Plateau Mining Corporation, Helper, Carbon County, Utah (2001)
3. Upper Big Branch Mine Accident Scenario Video, MSHA ID No. 46-08436. https://www.msha.gov/dataeports/reports/Upper%20Big%20Branch%20MineSouth%2C%20Performance%20Coal%20Company. Last accessed 2018/2/1
4. Institute of Medicine: Gulf War and Health: Volume 9: Long-Term Effects of Blast Exposures. The National Academies, Washington, DC (2014)
5. Zhang, Q., Ma, Q.J.: Dynamic pressure induced by a methane-air explosion in a coal mine. Process Saf. Environ. Prot. **93**, 233–239 (2015)
6. Marts, J., Gilmore, R., Brune, J., Bogin, G., Grubb, J., Saki, S.: Dynamic gob response and reservoir properties for active longwall coal mines. SME Min. Eng. J. 41–48 (2014)
7. Juganda, A., Brune, J.F., Bogin Jr., G.E., Grubb, J.W., Lolon, S.A.: CFD modeling of longwall tailgate ventilation conditions. In: 16th North American Mine Ventilation, Golden, CO (2017)
8. Lolon, S.A., Brune, J.F., Bogin Jr., G.E., Grubb, J.W., Juganda, A.: Understanding gob outgassing associated with pressure disturbances in longwall mine. In: 16th North American Mine Ventilation Symposium, Golden, CO (2017)
9. Fig, M., Bogin Jr., G.E., Brune, J.F., Grubb, J.W.: Experimental and numerical investigation of methane ignition and flame propagation in cylindrical tubes ranging from 5 to 71 cm—Part I: effects of scaling from laboratory to large-scale field studies. J. Loss Prev. Process Ind. **41**, 241–251 (2016)
10. Chapman, W., Wheeler, R.: The propagation of flame in mixtures of methane and air. Part IV. The effect of restrictions in the path of the flame. J. Chem. Soc. (129), 2139–2147 (1926)
11. Fig, M, Strebinger, C, Bogin Jr., G.E., Brune, J.F.: The impact of rock pile location on the propagation of methane flames in simulated and experimental flame reactors. In: SME Annual Conference and Exhibit, Minneapolis, MN (2018)
12. Strebinger, C., Fig, M., Bogin Jr., G.E., Brune, J.F., Grubb, J.W.: Effect of simulated gob conditions on the burning velocity of premixed methane-air combustion. In: SME Annual Conference and Exhibit, Denver, CO (2017)
13. Worrall, D., Wachel, E., Ozbay, U., Munoz, D., Grubb, J.W.: Computational fluid dynamic modeling of sealed longwall gob in underground coal mine. In: 14th United States/North American Mine Ventilation Symposium, University of Utah, Salt Lake City, pp. 135–145 (2012)

14. Moen, I., Lee, J., Hjertager, B., Fuhre, K., Eckhoff, R.: Pressure development due to turbulent flame propagation in large-scale methane-air explosions. Combust. Flame **47**, 31–52 (1982)
15. Ciccarelli, G., Hlouschko, S., Johansen, C., Karnesky, J., Shepherd, J.: The study of geometric effects on the explosion front propagation in a horizontal channel with a layer of spherical beads. Proc. Combust. Inst. **32**, 2299–2306 (2009)
16. Babkin, V.S., Korzhavin, A.A., Bunev, V.A.: Propagation of premixed gaseous explosion flames in porous media. Combust. Flame **87**, 182–190 (1991)
17. Strebinger, C., Fig, M., Pardonner, D., Treffner, B., Bogin Jr., G.E., Brune, J.F.: Investigation on the overpressure produced by high-speed methane gas deflagrations in confined spaces. In: SME Annual Conference and Exhibit, Minneapolis, MN (2018)
18. Cooper, M.G., Fairweather, M., Tite, J.P.: On the mechanisms of pressure generation in vented explosions. Combust. Flame **65**, 1–14 (1986)

# The Research on Explosion Tendency Analysis Method for Sealed Fire Area in Coal Mine Based on Coward Explosive Triangle

Baiwei Lei[(✉)], Bing Wu, and Xiaolin Ma

China University of Mining and Technology, Beijing 10083, P.R. China
710562538@qq.com

**Abstract.** When a coal mine fire occurs, the changing trend analysis of explosion hazard is very important to prevent secondary disasters. Nowadays, rescuers need to use various methods to analyze the explosiveness changing trend in the sealed area of a coal mine and reasons for such events, which goes against the requirements for developing explosion control measures in coal mine rapidly. Based on the Coward Triangle, this paper has established a new analysis chart and explosion tendency analysis for the changing trend of explosion hazard, which include the timeline (horizontal axis) versus explosion hazard and amount of deviation (double vertical axis). After careful comparison with other methods, results have shown that using the new method could not only effectively analyze the changing trend of explosion hazard, it could also more accurately characterize the changing trend of various gas compositions, thus providing guidance for developing rescue measures. In the end, the method is introduced which provides rough prediction for when this event might occur and time available for safe escaping in case of an explosion.

**Keywords:** Mine fire · Gas explosiveness · Coward explosive triangle diagram
Explosion tendency analysis

## 1 Introduction

Coal mine is a confined space where a large amount of methane may be emitted from coal seams and sealed area due to pressure difference. When a coal mine fire happens, the rescuers must always assume the possibility of a methane explosion in sealed fire area. In general, the explosion limits of methane ranges between 5 and 15%, but these limits are not stationary and would vary depending on temperature and oxygen concentration. For example, when the temperature rises to 700 °C (1292 °F), the explosion limits of methane will range between 3.25 and 18.75% [1]. Not only would the high temperatures would expand methane explosion range, combustion products could also reduce the lower explosion limit of methane, and increase the upper explosive limit as well.

In addition, there will be inevitable errors in gas sampling because critical areas behind seals may not be accessible and there may be questionable results due to sampling errors as well. Making decisions based on inadequate number of samples and/or inaccurate sampling results can have significant consequences.

As a result, the changing trend analysis of explosion hazard must be carefully analyzed using actual cases if coal mine fire rescue operations [2].

## 2    Literature Review

In addition to coal, there are also other combustible materials underground such as wood, rubber and lubricants. When coal mine fire happens, various combustible gases will be generated in underground fire area, includes $CH_4$, $H_2$, $CO$, $C_2H_2$, $C_2H_4$, $C_2H_6$, $C_3H_8$, $C_3H_6$, etc. [3]. There have been numerous studies from different countries on explosion risk evaluation in sealed coal mine fire zones based on Le Chatelier's Principle, and a variety of evaluation diagrams for explosion hazards. Coward and Jones had introduced a quick and easy method to assess explosion hazards in sealed fire zones by drawing an explosive triangle called "Howard Explosive Triangle", but the original model only considered three kinds of combustible gases, $CH_4$, $CO$ and $H_2$, and it couldn't support continuous evaluation for gas components [4]. Oxygen concentration in mixed gases is one of the determinants of combustion and flame spreading, so Zabetaksi et al. proposed to quickly determine the explosiveness based on the comparison of oxygen concentration in mixed gases and minimum combustion-supporting oxygen concentration, known as the U.S. explosive triangle [5]. The method could support continues monitoring for gas components to judge the explosion trend in sealed fire area, although it doesn't have the ability to predict possible timeline. Since different proportions of the mixed gases will lead to changes of the mixed gas explosion limits, Greuer made the explosive assessment of mixed gas more convenient by dividing the mixed gas into a number of single mixed gases [6]. Yamao also studied the explosiveness of mixed gas [7]; Cheng revised the explosive triangle of mixed gases [8].

By the explosive triangle deformation of mixed gases, Ellicott drew on multiple measured gas data at different times from the same station in one graph to assess the explosive trend of combustible gas [9]; Kukuczka discussed the explosiveness of mixed gas by using a fixed explosive triangle diagram to determine the explosiveness of various of mixture gas, which not only considered the explosiveness of various combustible gases, but also considered the inhibition effects of inert mixture gas to inhibit explosion, such as $N_2$, $CO_2$ [10]. Based on Coward explosive triangle, Hughes and Raybould (1960) developed the analysis method of the Time related explosibility trends graph which set the time as x-axis and the combustible gas concentration as y-axis. The graph could show the changing curves of upper critical value, lower critical value and gas state.

When concentrations of various gases in sealed fire area only increased or decreased with time, using U.S. explosive triangle, Ellicott square-chart model and Kukuczka diagram could effectively analyze the explosion trend. However, due to the influence of fire zone breathing phenomena and fire pressure, the gas components sampling in fixed sampling points fluctuates with different sampling time. On this occasion, it couldn't reflect the explosion risk completely and accurately by using the three methods above. Although the Time related explosiveness trends graph could analyze the changes of explosion trends effectively, but it could not explain whether the inert gases injection or the gases dilution is the reason for the combustible gases

production, which means it could not decide the factors leading to changes of explosion trends.

In order to solve the problem, this paper established a new explosiveness trend analysis chart to analyze the explosiveness variation tendency, which sets the timeline as horizontal axis, the explosion hazard and deviation degree as double vertical axis.

## 3 Explaining Coward Explosive Triangle

### 3.1 Movement Principles of State Point in Coward Explosive Triangle

The Coward explosive triangle is a method to determine explosiveness of combustible gas by analyzing the relations between combustible gas concentration and oxygen concentration. In order to explain the Coward explosive triangle more accurately, it needs to analyze the moving path of the state point that corresponds to different gas component concentration. It divides mixed gases into three classes, the combustible gas, oxygen and inert gases, according to how gas components concentration in sealed fire area are classified into three causes:

a. Air leakage of the sealed fire area or unseal the sealed fire area, the increase of air leads to higher oxygen concentration;
b. Gas emission from coal seam and combustible gases produced by combustion leads to the increase in combustible gas components;
c. Increment in surplus $N_2$ produced by combustion oxygen consumption or artificially inject inert gas to put out fire leads to the increase in inert gas components.

Assume the various gases released to the gas mixture in the sealed fire area could be adequately mixed in very short time without any chemical reactions, set the initial point of gas components in sealed fire area as Point 1 in the Coward explosive triangle (as shown in Fig. 1) with coordinate $(x_1, y_1)$, $x_1\%$ refers to the volume concentration that the combustible gases occupied the mixed gases, $y_1\%$ refers to the volume concentration that the oxygen occupied the mixed gases.
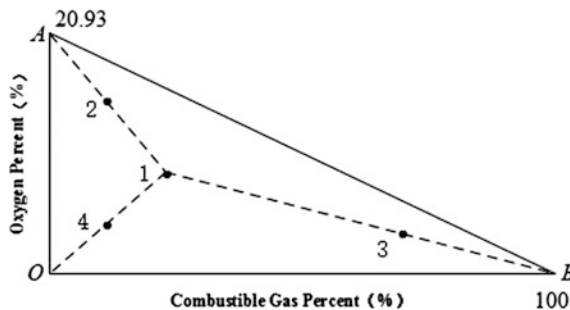


**Fig. 1.** The explosive triangle of mixed gases

a. Only inject air into the mixed gases

Assume injecting m parts of air to unit volume (100 parts) of original mixed gases, the volume concentration of combustible gases after the mixture becomes x%, and the volume concentration of oxygen becomes y%, so its coordinate in the explosive triangle becomes Point 2 (x, y), and based on dilution relation of gases, the gas volume concentration relation between Point 2 and Point 1 could be concluded as:

$$\begin{cases} x = \frac{x_1}{100+m} \times 100 \\ y = \frac{y_1 + m \times 0.2093}{100+m} \times 100 \end{cases} \tag{1}$$

The oxygen volume concentration is:

$$y = \frac{y_1 - 20.93}{x_1} x + 20.93 \tag{2}$$

From formula (2), it could be concluded that when only inject air to mixed gases, the position of Point 2 lies on the line between Point 1 and Point A, which means when only inject air to mixed gases, the initial Point 1 will move along the line to Point A as Fig. 1 shows.

b. Inject combustible gases into mixed gases

Assume injecting m parts of combustible gases to unit volume (100 parts) of original mixed gases, the volume concentration of combustible gases after the mixture becomes x%, and the volume concentration of oxygen becomes y%, so its coordinate in the explosive triangle becomes Point 3 (x, y). Since the ratio of oxygen and inert gases before and after the mixture remains unchanged, the oxygen volume concentration after mixture could be concluded as:

$$y = (100 - x) \frac{y_1}{100 - x_1} \tag{3}$$

From formula (3), it could be concluded that when only inject combustible gases into mixed gases, the position of Point 3 lies on the line between Point 1 and Point B, which means when only inject combustible gases to mixed gases, the initial Point 1 will move along the line to Point B as Fig. 1 shows.

c. Inject inert gases into mixed gases

Assume injecting m parts of inert gases to unit volume (100 parts) of original mixed gases, the volume concentration of combustible gases after the mixture becomes x%, and the volume concentration of oxygen becomes y%, so its coordinate in the explosive triangle becomes Point 4 (x, y). Since the ratio of oxygen and combustible gases before and after the mixture in the unit volume remains unchanged, the conclusions could be drawn as:

$$\frac{y_1}{x_1} = \frac{(100+m)y}{(100+m)x} \tag{4}$$

The oxygen volume concentration after mixture is:

$$y = \frac{y_1}{x_1}x \tag{5}$$

From formula (5), it could be concluded that when only inject combustible inert gases into mixed gases, the position of Point 4 lies on the line between Point 1 and original point, which means when only inject inert gases to mixed gases, the initial Point 1 will move along the line to original point as shown in Fig. 1.

## 3.2 Area Separation of Coward Explosive

Based on the movement principles analysis of the state points, which correspond to different gas component concentration, and gas explosion limits, the mixed gases explosive triangle could be divided into following four areas (as shown in Fig. 2):
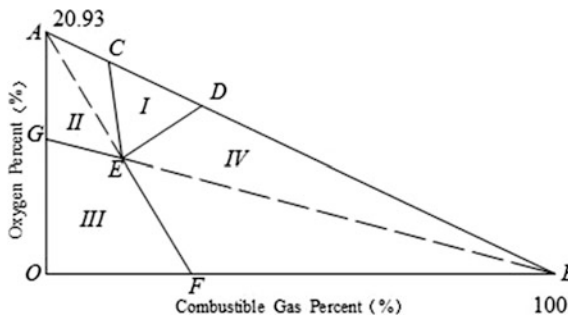


**Fig. 2.** The regional division of explosive triangle of mixed gases

a. Region CDE is the explosion area, area I, explosion will occur if there is any ignition source;

b. Region DBFE is the insufficient oxygen area, area II, where mixed gas has potential risks of explosion. There are sufficient combustible gases in this area, so it will become explosion area if $O_2$ increases;

c. Region EFOG is the safe area, area III, which will not become explosion area if $O_2$ or combustible gases increase unilaterally;

d. Region ACEG is insufficient combustible gas area, area IV, which will become explosion area if combustible gases increases.

## 4    Determination of Mixed Gas Explosive Triangle

To construct mixed gas explosive triangle (as shown in Fig. 2), firstly we need to determine the explosion limit of mixed combustible gases, and then use Le Chatelier's Principle to solve explosive limits of a variety of mixed combustible gases. The mathematical expressions are as follows [11]:

$$V_L = 100/\left(\sum P_i/L_i\right) \tag{6}$$

$$V_u = 100/\left(\sum P_i/U_i\right) \tag{7}$$

where

$V_L, V_U$    the upper and lower explosive limit of mixed combustible gas, %;
$P_i$    volume fraction that combustible gas has in overall combustible gases respectively,%;
$L_i$    lower explosive limit of combustible gas respectively, %;
$U_i$    upper explosive limit of combustible gas respectively, %.

Different combustible gases have different explosive limits, and the effectiveness of explosion suppression for different inert gas to different combustible is also not the same (as shown in Tables 1 and 2). One can look up Tables 1 and 2, and then substitute the data into Eqs. (8)–(10) to calculate the coordinates of Nose Point (Point E) of mixed gas explosive triangle.

**Table 1.** Vertices of explosive triangles (%) [12, 13]

| Gas | Flammable limits | | Nose limits ($N_2$ as inert gas) | | Nose limits ($CO_2$ as inert gas) | |
|---|---|---|---|---|---|---|
| | Lower | Upper | Gas | Oxygen | Gas | Oxygen |
| Methane ($CH_4$) | 5.00 | 14.00 | 5.17 | 9.86 | 5.93 | 12.64 |
| Hydrogen ($H_2$) | 4.00 | 74.20 | 4.20 | 5.11 | 5.19 | 8.47 |
| Carbon monoxide (CO) | 12.50 | 74.20 | 13.06 | 5.15 | 15.67 | 8.00 |
| Ethylene ($C_2H_4$) | 2.75 | 28.60 | 2.88 | 6.09 | 3.52 | 9.47 |
| Ethane ($C_2H_6$) | 3.00 | 12.50 | 3.12 | 8.40 | 3.68 | 11.53 |
| Propene ($C_3H_6$) | 2.00 | 20.51 | 2.09 | 6.28 | 2.56 | 9.69 |
| Propane ($C_3H_8$) | 2.12 | 20.49 | 2.22 | 6.34 | 2.71 | 9.75 |
| Acetylene ($C_2H_2$) | 2.50 | 80.00 | 2.63 | 5.07 | 3.27 | 8.52 |

The calculation expression about combustible content at the Nose Point ($C_N$):

$$C_N = \frac{N_2}{N_2 + CO_2}\left[\frac{100}{\sum (P_i/n_{1,i})}\right] + \frac{CO_2}{N_2 + CO_2}\left[\frac{100}{\sum (P_i/n_{2,i})}\right] \tag{8}$$

**Table 2.** Inert rations [14]

| Gas | Inert ration (m$^3$ of nitrogen per m$^3$ of combustible gas) | Inert ration (m$^3$ of carbon dioxide per m$^3$ of combustible gas) |
|---|---|---|
| Methane (CH$_4$) | 9.23 | 5.69 |
| Hydrogen (H$_2$) | 16.98 | 10.46 |
| Carbon monoxide (CO) | 4.77 | 2.94 |
| Ethylene (C$_2$H$_4$) | 23.59 | 14.54 |
| Ethane (C$_2$H$_6$) | 18.18 | 11.20 |
| Propene (C$_3$H$_6$) | 32.39 | 19.96 |
| Propane (C$_3$H$_8$) | 30.35 | 18.71 |
| Acetylene (C$_2$H$_2$) | 27.81 | 17.14 |

where, $n_{1,i}$ is nose limit for gas, i, in air and excess nitrogen, could be acquired by looking up the third column in Table 1; $n_{2,i}$ is the nose limit for gas, i, in air and excessive carbon dioxide, could be acquired by looking up the fifth column in Table 1.

The calculation expression about excess insert at the nose point ($L_N$):

$$L_N = \frac{N_2}{N_2 + CO_2}\left[\frac{\sum P_i V_{1,i}}{\sum (P_i/n_{1,i})}\right] + \frac{CO_2}{N_2 + CO_2}\left[\frac{\sum P_i V_{2,i}}{\sum (P_i/n_{2,i})}\right] \tag{9}$$

where, $V_{1,i}$ is volume of nitrogen required to render unit volume of gas, i, extinctive, it could be acquired by looking up the first column in Table 2. $V_{2,i}$ is volume of carbon dioxide required to render unit volume of gas, i, extinctive, it could be acquired by looking up the second column in Table 2.

The calculation expression about oxygen content at the Nose Point ($O_N$)

$$O_N = 0.2093(100 - C_n - L_n) \tag{10}$$

So, the coordinate of critical point are as follows:

$$C(V_L, -20.93V_L + 20.93) \qquad D(V_U, -20.93V_U + 20.93),$$

$$E(C_N, O_N) \qquad F(-20.93C_N/(O_N - 20.93), 0)$$

## 5 The Explosive Trend Graph

Generally the gas components in sealed fire zones would change gradually, so once the gas composition shows a continuously changing tendency to explosiveness, it is necessary to take measures immediately to prevent explosive accidents. From the analysis in Chap. 3, the changing path of mixed components state point in the explosive triangle is fixed if the gas mixing ratio remains unchanged. So the explosiveness trends of sealed fire zone gas can be assessed by monitoring relation of the shortest path between monitored state point to the explosive triangle. Set timeline as horizontal axis and the

shortest distance from state point to explosion area as ordinate axis, the explosive trend diagram is drawn and such diagram can conveniently assess the explosiveness in the sealed fire zones. The specific practices are as follows:

Define time as the horizontal axis, the shortest distance to enter or escape from the explosive area, R, as the ordinate axis. When the state point locates inside the explosive area, R represents the shortest distance to flee from the explosive area (a positive value), and when the state point locates outside the explosive area, R represents the opposite number of the distance to enter into the explosive area. In order to express the deviation angle of state point within relevant quadrant, define the deviation degree as S to acquire the moving trace of state point in different quadrants. The value of R and S in different areas are defined as follow:

a. If Point $X_1$ locates inside the explosive area, when injecting air into the enclosed area, $X_1$ moves along the straight line direction of $X_1A$. When injecting combustible air into the enclosed area, $X_1$ moves along the straight line direction of $X_1B$. So drawing two straight line from $X_1$ to A and B respectively which intersects the straight line CE at Point H, DE line at Point I. Take $R = \min(|X_1H|, |X_1I|)$ as the distance that the state point flee from the explosive area, plot it in red. Assume that $\angle X_1ED = \alpha_1$, $\angle CED = \beta_1$ so the calculation expression about deviation degree S refers to: $S = 90 \times \alpha_1/\beta_1$, which is shown as Fig. 3a.

b. If Point $X_2$ locates in area of insufficient combustible gases area, when adding combustible gas into the enclosed zone, X = moves along the straight line direction of $X_2B$ which is the shortest path the state point goes into the explosive area. So draw the straight line from $X_2$ to B which intersects the straight line EC at Point H. Then get $R = -|X_2H|$, plot it in blue. Assume that $\angle X_2EC = \alpha_2$, $\angle GEC = \beta_2$, so the calculation expression about deviation degree S refers to: $S = 90 \times \alpha_2/\beta_2$, which is shown as Fig. 3b.

c. If Point $X_3$ locates in the safe area, whatever kind of gases to inject into the enclosed area, it will not go to the explosive area directly. Define $R = -|X_3E|$, plot it in green. Assume that $\angle X_3EG = \alpha_3$, $\angle FEG = \beta_3$, so the calculation expression about deviation degree S refers to: $S = 90 \times \alpha_3/\beta_3$, which is shown as Fig. 3c.

d. If Point $X_4$ locates in area of insufficient oxygen area, when inject air to the enclosed area, $X_4$ moves along the straight line direction of $X_4A$ which is the shortest path the state point goes into the explosive area. So draw the straight line from $X_4$ to A which intersects the straight line ED at Point I. Then get $R = -|X_4I|$, plot it in yellow. Assume that $\angle X_4EF = \alpha_4$, $\angle FED = \beta_4$, so the calculation expression about deviation degree S refers to: $S = 90 \times \alpha_4/\beta_4$, which is shown as Fig. 3d.

## 6 Application Example

After fire occurred in the working seam of China's Shanxi Tunliu coal mine, and the fire direct extinguishing had failed, the rescuers effectively closed the fire area. Having taken a series of extinguishment measures to the sealed fire area, the preliminary judgment was the fire had extinguished so that they determined to unseal the fire area.
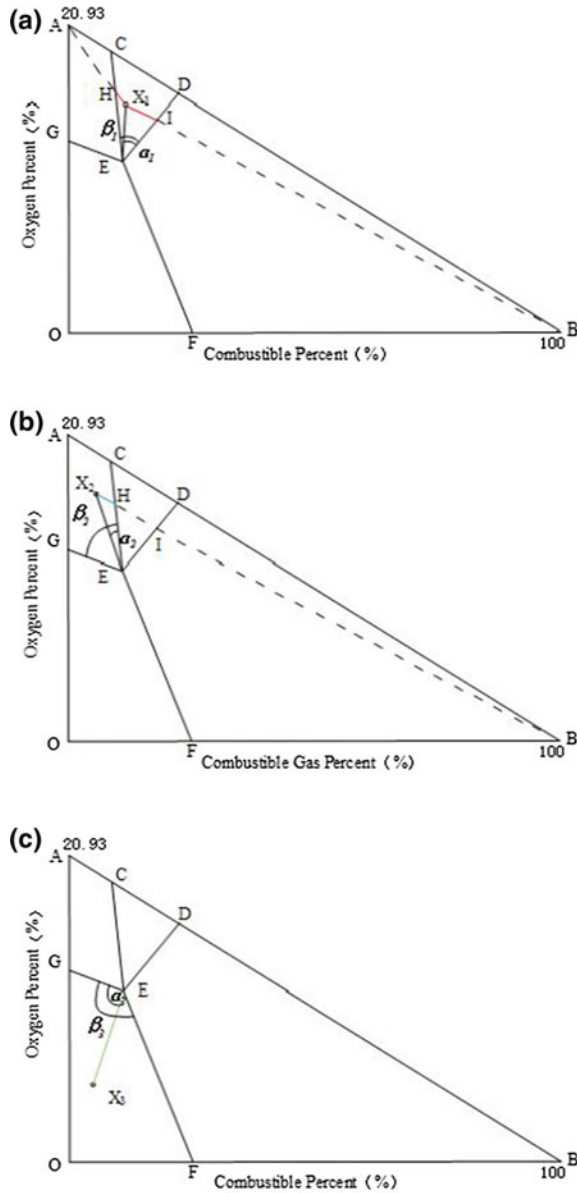
**Fig. 3.  a–d** The explosion risk (R) and deviation degree (S) in area I–area IV

Before the unsealing actions, aerobic observation method, a method used to verify whether there is ignition by continuously inhaling oxygen into the fire zone, was used to verify whether the fire area is in the extinguishing state. The specific implementations of the method are as follows: supplied air to the sealed fire area by opening the surface drilling that linked with the fire zone (keep the oxygen concentration
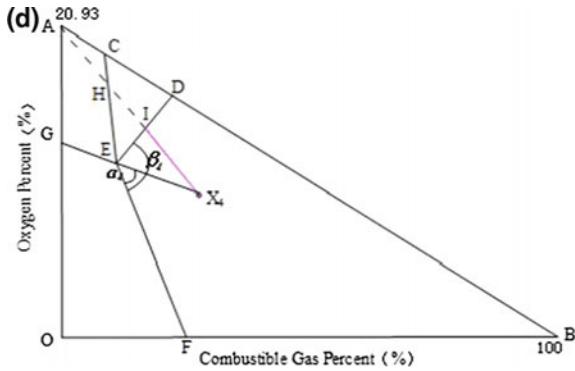
**Fig. 3.** (*continued*)

below 12%), then using the beam tube monitoring systems to continually monitor the gases concentration of $O_2$, $CH_4$ and CO, and observed if there existed re-ignition phenomenon. The most important precautionary measures during aerobic observation period is preventing the occurrence of explosion in sealed fire area, so it needed to real-time analyze the explosive trend of the fire area during the whole aerobic observation period.

During the aerobic observation period, the changing trend of concentration of $O_2$, $CH_4$ were shown as Figs. 4 and 5 separately, then using Ellicott explosion quartet figure (Fig. 6), USBM Explosiveness Diagram (Fig. 7), Time related explosiveness trends graph (Fig. 8) and time-series explosive trend chart (Fig. 9) respectively to continuously monitor the explosion trend in the sealed fire zone, with which we could draw the following diagrams.

Through Figs. 4 and 5, we could see that due to the change of atmospheric pressure, the breathing phenomenon enhanced and the concentration of $O_2$, $CH_4$ fluctuated correspondingly. With the alternative variations between the increasing and decreasing trend of gas concentration in the sealed fire zone, the explosion trend curves, based on
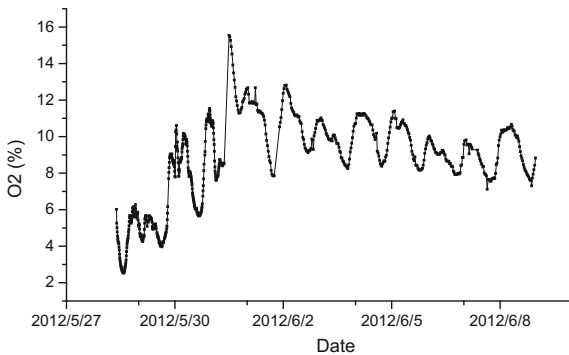


**Fig. 4.** The changing curve of oxygen concentration during aerobic observation period
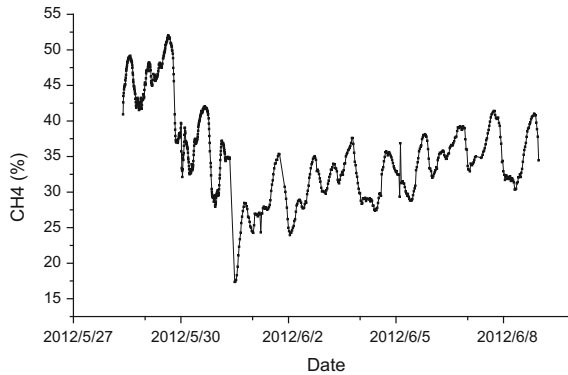
**Fig. 5.** The changing curve of methane concentration during aerobic observation period



**Fig. 6.** Ellicott's diagram

Ellicott explosion quartet figure (Fig. 6), USBM Explosibility Diagram (Fig. 7) and time-series explosive trend chart (Fig. 8) separately, had fluctuated repeatedly and were interweaved together, which covered the analysis integrity of explosiveness changing trend in fire zone. On the other side, though Time related explosiveness trends graph (Fig. 9), it could not be effectively analyzed that the reason for changes of combustible gases components is the inert gases infection or the air dilution. With the help of explosion trends analysis which is newly established in this paper to process the collected data, it could effectively require that the explosion risks in sealed fire area increases gradually in the first phase, and then decreases stably, which all locates in the insufficient combustible gas area of Coward explosive triangle. Then, the rescuers could get air dilution is the reasons for combustible gases changes by analyzing the deviation degree (S).

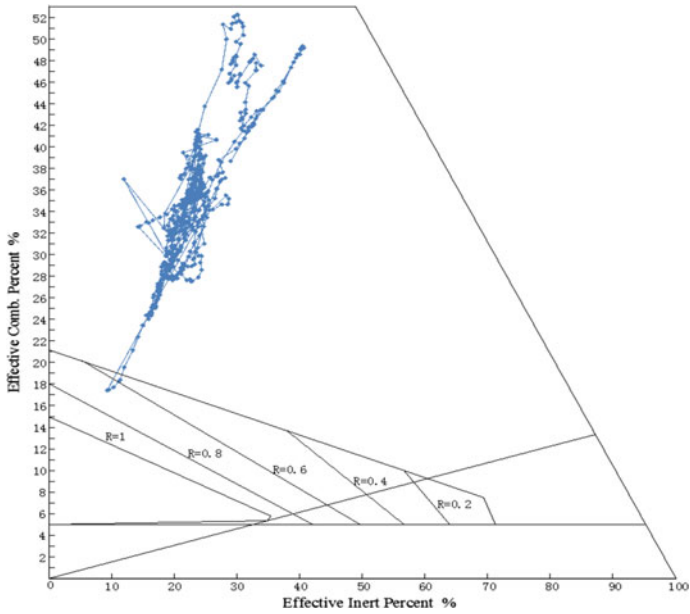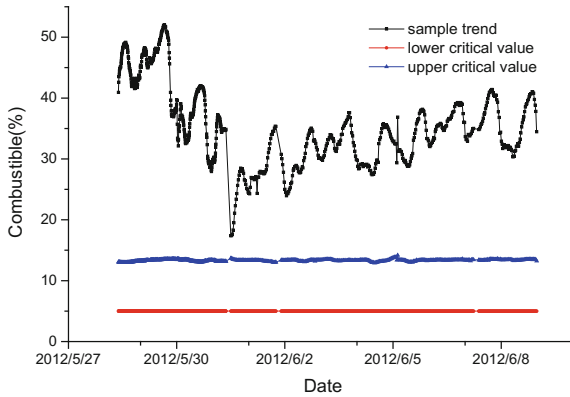**Fig. 7.** USBM explosibility



**Fig. 8.** Time related explosiveness trends

## 7   Prediction of Explosion Risks in Sealed Fire Area

In the highly gaseous coal mines, there exists an explosion risk period in the fire area's sealing and unsealing stage separately. So prediction about when the explosion risks would begin and disappear has important significance to develop the rescue measures.
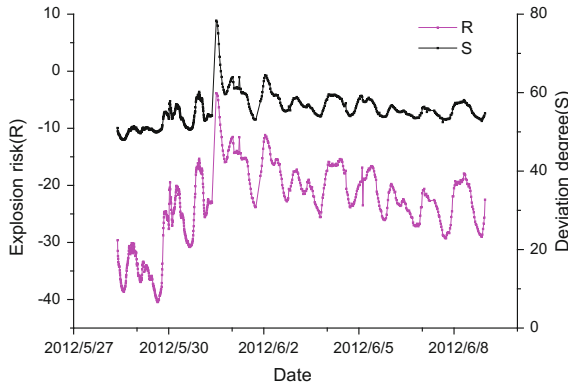
**Fig. 9.** The continuous analysis chart of explosion risk (R)

## 7.1 Explosion Condition

Explosion would only occur when the following three conditions are satisfied at the same time:

a. Existence of gases or other combustible gases which reach a certain concentration;
b. Existence of sufficient oxygen;
c. Existence of the temperature high enough to ignite combustible gases.

When the sealed fire area environment meet the first and second condition, the fire area would have the explosion risks. Therefore, we could predict the explosion risks by analyzing the gases components concentration in the sealed fire zone.

## 7.2 Gas Concentration Prediction and Explosiveness Analysis

Assume that the volume of the enclosed fire zone is certain as $Vm^3$, and the gases are incompressible, various gases in the sealed fire area can be adequately mixed in a very short time, without any chemical reactions. According to the law of conservation of gas quality, when certain amount of gas flows into the fire zone, there will be equal amount of gas flowing out of the fire zone at the same time. In the enclosed space, given the concentration of $N_2$ is $C_1$, $CO_2$ is $C_2$, $O_2$ is $C_3$, $CH_4$ is $C_4$, so the other combustible gas is $L_i$ (i = 1, 2, …, n). The air flow rate flowing into the fire zone is $Q_0$, $N_2$ flow rate is $Q_1$, $CO_2$ flow rate is $Q_2$, $CH_4$ flow rate is $Q_3$, so the air flow rate that outflows the fire zone is $Q_4 = Q_0 + Q_1 + Q_2 + Q_3$. The function of components concentration of various gas which has changed with time can be expressed as follows:

The concentration of $N_2$ changes with time:

$$V dC_1 = (0.78Q_0 + Q_1 + VC_1 - \frac{0.78Q_0 + Q_1 + VC_1}{(Q_0 + Q_1 + Q_2 + Q_3) + V} Q_4) dt_1 \qquad (11)$$

The concentration of $CO_2$ changes with time:

$$VdC_2 = (0.0003Q_0 + Q_2 + VC_2 - \frac{0.0003Q_0 + Q_2 + VC_2}{(Q_0 + Q_1 + Q_2 + Q_3) + V}Q_4)dt_2 \qquad (12)$$

The concentration of $O_2$ changes with time:

$$VdC_3 = (0.21Q_0 + VC_3 - \frac{0.21Q_0 + VC_3}{(Q_0 + Q_1 + Q_2 + Q_3) + V}Q_4)dt_3 \qquad (13)$$

The concentration of $CH_4$ changes with time:

$$VdC_4 = (Q_3 + VC_4 - \frac{Q_3 + VC_4}{(Q_0 + Q_1 + Q_2 + Q_3) + V}Q_4)dt_4 \qquad (14)$$

The concentration of other combustible gases changes with time:

$$VdL_i = (VL_i - \frac{VL_i}{(Q_0 + Q_1 + Q_2 + Q_3) + V}Q_4)dt_{Li} \qquad (15)$$

Assume the initial time t = 0, concentration of $N_2$ is $C_{10}$, $CO_2$ is $C_{20}$, $O_2$ is $C_{30}$, $CH_4$ is $C_{40}$, and other combustible gas is $L_{i0}$ (i = 1, 2, …, n), which can be substituted to Eqs. (11)–(15) for solving differential equations, and results are as follows:

$$C_1 = \frac{0.79Q_0 + Q_1}{Q_4} + \left(C_{10} - \frac{0.79Q_0 + Q_1}{Q_4}\right)e^{-\frac{Q_4}{V}t_1} \qquad (16)$$

$$C_2 = \frac{0.0003Q_0 + Q_2}{Q_4} + \left(C_{20} - \frac{0.0003Q_0 + Q_2}{Q_4}\right)e^{-\frac{Q_4}{V}t_2} \qquad (17)$$

$$C_3 = \frac{0.21Q_0}{Q_4} + \left(C_{30} - \frac{0.21Q_0}{Q_4}\right)e^{-\frac{Q_4}{V}t_3} \qquad (18)$$

$$C_4 = \frac{Q_3}{Q_4} + \left(C_{40} - \frac{Q_3}{Q_4}\right)e^{-\frac{Q_4}{V}t_4} \qquad (19)$$

$$L_i = L_{i0}e^{-\frac{Q_4}{V}t} \qquad (20)$$

Above all, through the Eqs. (16)–(20), if given the volume of sealed fire zone, components and its initial concentration of mixed gases, the air-leakage rate, the amount of inert gas injection and the emission quantity of $CH_4$, the changes of gas components concentration which changed with time could be calculated.

During the analysis of explosion risks of sealed fire area, firstly the rescuers should set the total computing time and discretize the time in units of per minute. Then use Eqs. (16)–(20) to calculate the gas concentration at different time points. At last, make use of the explosiveness tendency analysis method to judge the explosion risk in

Chap. 5. If there is long enough total computing time, the explosiveness tendency analysis chart could display clearly the occurrence and disappearance time point of the explosion risks in sealed fire area.

## 8    Conclusions

Through analysis of the Coward Explosive Triangle, this paper constructs a new analysis chart to asset the explosion risks of mixed gas in sealed fire area. By means of analyzing a practical case, it shows that compared with the former methods, the new method introduced is more convenient and effective in not only analyzing explosion risks changing trends, but also in reflecting the air components changing trends, which give great helps to develop rescue measures.

Based on the new method in this paper to analyze the explosion risk tendency in sealed fire area, it could theoretically predict the time when explosion risks might exist in the fire zone and the time needed to escape from the explosion area. However, since the fire area in underground coal mines are usually quire large, the variation tendency of gas components concentration from a single sampling point could not reflect the actual gas component concentration for the entire fire area, so the method introduced here could only provide a rough ide for the explosion risk in sealed fire area.

## References

1. Owen, G.: Combustion Theory. Science Press, China (1983)
2. Zhou, X., Wu, B.: Theory of Mine Fire Rescues and Applications. Coal Mining Industry Press, China (1996)
3. Timko, R.J., Derick, R.L.: Methods to Determine the Status of Mine Atmospheres—An Overview. National Institute for Occupational Safety and Health Publications, The United States (2006)
4. Coward, H.F., Jones, G.W.: Limits of Flammability of Gases and Vapors. U.S. Bureau of Mines, Bulletin 503. US Government Printing Office, The United States (1952)
5. Zabetaksi, M.G., Stahl, R.W., Watson, H.A.: Determining the Explosibility of Mine Atmospheres. U.S. Bureau of Mines. Bulletin IC7901, The United States (1959)
6. Greuer, R.E.: Study of Mine Fire Fighting Using Inert Gases. USBM Contract Report No. S0231075, The United States (1974)
7. Yamao, S.: Study on explosibility determination of complex gas mixtures. Min. Secur. **30**, 561–575 (1984)
8. Cheng, J.W., Luo, Y.: Modified explosive diagram for determining gas-mixture explosibility. J. Loss Prev. Process Ind. **26**(4), 714–722 (2013)
9. Ellicott, C.W: Assessment of the explosibility of gas mixtures and monitoring of sample-time trends. In: Proceedings of the Symposium Ignitions, Explosions & Fires, pp. 1–20. Australasian Inst Mining and Metallurgy, Wollongong (1981)
10. Kukuczka, M.: A new method for determining explosibility of complex gas mixtures. Mechanizacja I Automatuzacja Górnictwa **164**(11), 36–39 (1982)
11. McPherson, M.J.: Subsurface Ventilation and Environmental Engineering. Chapman & Hall, London United Kingdom (1993)

12. Walter, M.: Haessler Fire: Fundamentals and Control. Marcel Dekker Inc., New York, USA (1989)
13. Yu, Q.X.: Prevention of Coal Mine Methane. China University of Mining and Technology Press, Xuzhou, China (1992)
14. Cheng, J.W., Luo, Y.: Improved Coward explosive triangle for determining explosibility of mixture gas. Process Saf. Environ. Prot. **89**(2), 89–94 (2011)

# Lessons Learnt from Bhatdee Coal Mine Explosion Disaster in India Using Root Cause Analysis Technique

R. M. Bhattcharjee[(✉)], A. K. Dash, and D. C. Panigrahi

Indian Institute of Technology (ISM), Dhanbad 826004, India
rmbhattacharjee@yahoo.com

**Abstract.** Mining remains one of the most hazardous professions worldwide and underground coal mines are specifically notorious for their high rate of accident. In this study, an overview of disasters in Indian coal mines is presented with their identified causes. One of the deadliest causes of such disasters in India is explosion. Out of the total 60 disasters in Indian coal mines since 1901, 24 were caused only due to explosion, taking 1198 precious lives (the number was 2223 in §1 Introduction, please verify). During the last decade, there had been two explosion disasters killing 64 persons. The repeated occurrence of mine explosions, often in a similar manner, is the loud unfinished legacy of mining accidents and their occurrence in the 21st century is unforgivable and warrant a strong call for action to settle down this problem. In this paper one recent coal mine explosion disaster, namely, Bhatdee coal mine disaster in 2006, has been analyzed, where deficiencies in various safety barriers failed to prevent the accident from occurring and then subsequent failure of defenses to prevent this accident scenario from unfolding and to mitigate its consequences. Here the authors emphasized on the identification of the deficiencies pertaining to organizational factor, work environment and task environment and failed defences that allowed some mine hazards into an accident and then into a "disaster". This case study provides an opportunity to demonstrate the concept of root cause analysis that help to describe the accident phenomena. The authors also introduced the safety principle of defense-in-depth, which is the basis for regulations in support of accident prevention and coordinating actions on all levels, organizational, environmental, technical, and regulatory, to improve overall safety in mines.

**Keywords:** Coal mine · Disaster · Explosion · Accident investigation
Root cause analysis

## 1 Introduction

Mining industry remains one of the most risky occupations worldwide, especially underground coal mines for their high rates of accident. History of coal mining is marred by disasters causing huge loss of human lives. Indian coal mining industry had experienced about 60 disasters (10 or more fatalities per accident) resulting in more than 2223 fatalities since 1901, the year of enactment of first mine safety legislation in

India. Out of 60 disasters 24 are due to explosion. Though all these disasters had been inquired into, and recommendations made for prevention of recurrence of similar accidents, the scenario did not change much.

In last sixteen years (i.e. 2000–2016), 64 precious human lives were lost due to two explosion disasters [1]. The most recent one was Anjan Hill Coal Mine disaster which occurred on 6th May, 2010 claiming lives of 14 persons, and before that Bhatdee Coal Mine disaster which occurred in 2006 lost 50 precious lives [1]. In fact, 2010 was a dreaded year in the history of coal mining with four coal mine disasters in four different countries due to explosions, namely, Upper Big Branch Mine disaster, USA (29 fatalities) [2–4]; Raspadskaya Mine disaster, Russia (90 fatalities) [5]; Pike River Mine Disaster, New Zealand (29 fatalities) [5–9] and Anjan Hill Mine disaster, India (14 fatalities) [1]. Soma coal mine disaster, Turkey also claimed 301 precious lives in 2014 [10]. Such workplace disasters indicate layers of serious weaknesses in the system.

A systematic in-depth analysis of accidents helps to identify not only its primary cause, but also the root causes at the system level whose combination leads to the accident [11, 12]. An effective accident investigation identifies all possible accident causation pathways containing all root causes, and thereby helps in providing suitable recommendations for preventing recurrence of similar accidents. If all the key lessons are communicated properly to the whole industry and appropriate changes are made accordingly in the existing system, or additional controls/preventive measures are incorporated, recurrence of similar events may be prevented or, at least, the rate of occurrences and/or consequences may be reduced.

The Bhatdee Coal Mine Disaster in India took place in 2006 giving a big shock to the entire country as 50 coal mine workers died due to an explosion underground. The accident was investigated by different agencies including the Court of Inquiry, Government of India. But the question remains, "what we have learnt from the accident?" It has been 12 years since the accident, has there been any real improvement across the industry in relation to the explosion hazards based on the recommendations of the investigations? Similar disasters occurred in the past with similar recommendations produced from investigations. But, the vulnerability of the underground coal mines in India with regards to explosion hazards remained unchanged, which is still an issue of major concern. One of the primary reasons for such repetitions of similar accident is failure to learn from the past. Perhaps the root cause of the accidents could not be identified and the recommendations are not adequate to effectively address those causes. The Bhatdee Coal Mine disaster has been critically analyzed in this paper to identify the root causes of the accident and existing gaps in explosion hazard management system, and thereby making suitable recommendations to prevent recurrence of such disasters.

## 2  Disaster Case Study

In this section, analysis of Bhatdee coal mine disaster, an explosion involving methane followed by coal dust explosions has been completed. Purpose of this case study is twofold: (1) to provide specifics on mining accidents beyond the statistical perspective, and (2) to identify the root causes along with the all possible or probable causes with

in-depth analysis of safety barriers and lesson learnt. Explosions in mines, whether due to methane emission, coal dust or both, are the most common causes of large number of fatalities in coal mining accidents. Their repeated nature of occurrences, often in a similar manner, both in India and overseas, are a clear sign of the failure of the mining industry and the regulatory system to heed the lessons of the past and adopt a robust approach to reduce and/or eliminate these type of accidents/disasters, or at least lessen their deadly consequences.

The following sections described efforts made to analyze Bhatdee Coal Mine Explosion Disaster as a case study to identify the gaps and lessons. The case is analyzed using the Root Cause Analysis (RCA) techniques like a 5-why or Accident Causation Tree to identify root causes and compared them with causes identified by other inquiries per statutory requirement. This analysis is done to highlight what we have learnt from the accidents and what not? To give a clear view about the disasters, brief description and identified causes are provided as per published reports. Then a gap analysis is conducted to identify the gaps in the current investigation outcome and the failures to learn from the past.

## 2.1  Disaster Case Study: The 2006 Bhatdee Coal Mine Disaster

**Brief Description**. In Bhatdee coal mine, Mohuda bottom seam (1.6–2.2 m) and Mohuda top seam (3.65 m) were being depillared through 17 Incline and 14 Incline, respectively. The seams were dipping at 1 in 3 and were of Degree III in gassiness. Due to sluggish ventilation of the workings in bye 5 dip and inrush of methane in high concentration from the un-stowed goaf, caused layering of methane extending up to face of 1st dip slice off 17 ½ Level and other areas. While the electrical helper was examining or repairing the drill without disconnecting power supply to the drill, it was suspected that the open spark in the drill caused ignition/explosion of methane present in the face area. The flame caused by ignition/explosion of methane travelled towards higher side of the panel where there was explosive mixture of methane and air in a ratio within the explosion range. Methane explosion stirred up the coal dust, and the explosion was converted into a severe coal dust explosion killing all 50 people present underground.

**Identified Causes**. As per the accident inquiry, the explosion was caused by the combination of following reasons:

1. Production and accumulation of the methane gas
2. Inflammable gases were not detected
3. Flame safety lamps were not provided and properly maintained
4. Methane detector was not available at workplace
5. Less Than Adequate (LTA) ventilation
6. Supply of electricity to the drill was not disconnected at the time of adjustment/repairing leading to open sparking
7. Presence of coal dust in mine airways.

**Gap Analysis of Bhatdee Investigation**. As per inquiry, identified causes of the accident like presence of inflammable gases, sparking due to short circuit and LTA gas monitoring, etc. were the direct causes of the explosion. But indirect causes or root

causes leading to direct causes were not identified. The following questions would have helped in identifying the root causes leading to this accident:

1. How and why a single electrical helper was allowed to work alone?
2. Whether or not, adequate supervision was provided.
3. Why he (electrical helper) failed to identify the associated hazards of repairing the drill machine without disconnecting the power?
4. Was that a regular practice in that mine?
5. What was the level of skill, competency and experience of the electrical helper?
6. Whether or not, there was any documented procedure for that job (repairing of electrical equipment in underground).
7. Whether or not, task condition like pressure from higher authority, work pressure led to such unsafe act.
8. Was there any isolation or interlocking system of power transmission underground with methane detectors.
9. Why the presence of gas could not be detected at early stages?
10. How there was buildup of methane in the workings?
11. Why the potential methane accumulation in the goaf was not identified?
12. Why there was huge void in the goaf?
13. Whether such void was normal or usual?
14. Whether there was adequate arrangement for stowing?
15. Whether sand supply was adequate?
16. Was there any continuous and reliable gas monitoring system in that mine?
17. Was there any procedure for gas monitoring?
18. Whether or not, proper gas monitoring resources were provided.
19. Whether or not, proper stone dusting was being done in the mine.
20. Whether or not, proper stone dust sampling was being done in the mine.
21. Was there any standard stone dusting procedure?
22. Was there any standard stone dust sampling procedure?
23. Was there any stone dust barrier?
24. Whether or not risk assessment of explosion hazard was conducted in the mine.
25. Whether or not, there was any history of similar incident in that mine.

Based on the why analysis, an Accident Causation Tree of developed to identify the root causes of the accident and presented in Fig. 1.

A comparison between the causes identified by the statutory inquiry and the possible/potential causes identified through application of RCA technique reveals that

- As per the statutory inquiry, identified causes of the accident are (1) production and accumulation of the methane gas in that seam, (2) presence of inflammable gases were not detected, (3) flame safety lamps were not provided and maintained, (4) the automatic local methane detector was not maintained in workplace, (5) Less Than Adequate (LTA) ventilation, (6) the electric supply to the drill was not disconnected at the time of adjustment due to which sparking occurred, (7) presence of coal dust in the mine.
- The above mentioned causes are the failures or direct causes of the accident. However, the possible/potential causes identified by using RCA technique are
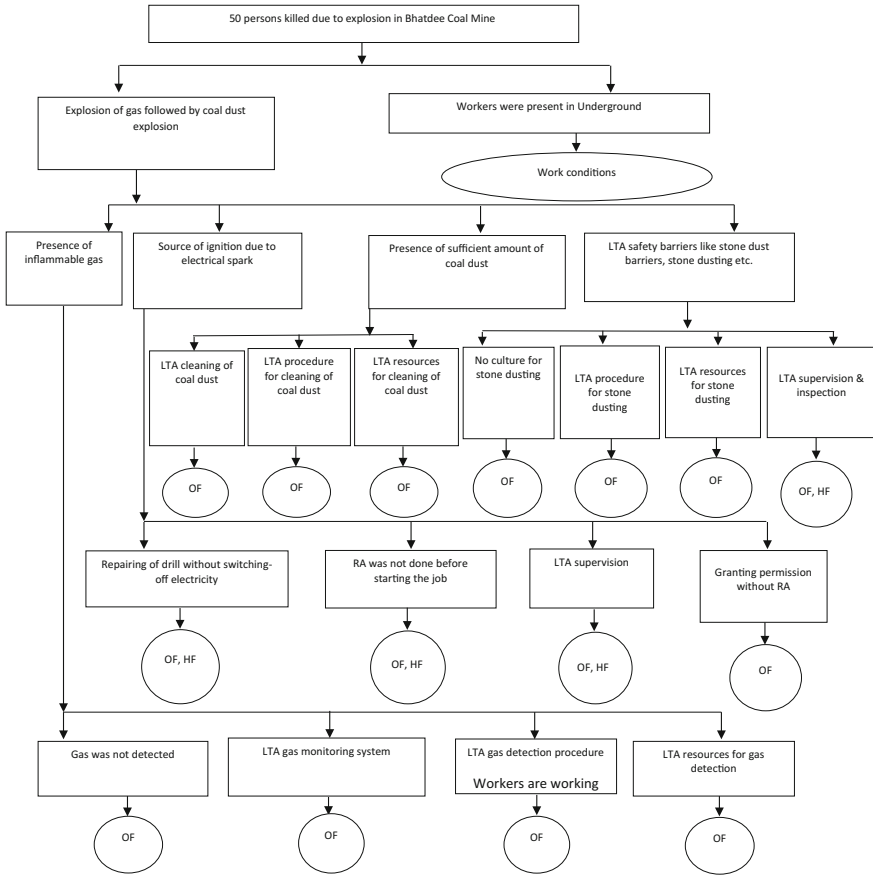
**Fig. 1.** Accident causation tree of Bhatdee coal mine disaster

(1) Lack of pre-drainage methane operation in highly gassy coal seams (Degree III), and large void in the goaf due to lack of resources (sand) for stowing, this is a gap in policy requiring the use of sand stowing, resulted in the accumulation of large quantity of methane in the goaf;

(2) Inadequate ventilation due to lacking properly built ventilation stoppings, and a lack of supervision, damage of ventilation stopping because of poor blasting practices, these resulted in inadequate ventilation resulting in accumulation of methane at high concentration and formation of methane layer in the working places; and

(3) LTA hand held gas detection and continuous and reliable real-time gas monitoring procedure and system led to failure in detecting accumulation of inflammable gas beyond threshold limit, which led to failure to take mitigating measures to dilute methane, resulting in methane build up to explosive range

(4) Lack of effective interlocking system with local methane detector and electricity supply failed to ensure disconnection of supply in the event of accumulation of methane beyond stipulated value; and

(5) Poor working practice, conducting maintenance work in underground without de-energising the equipment that generated spark, a probable source of ignition that caused the explosion,

(6) LTA procedure and resources for controlling coal dust accumulation in underground workings; LTA stone dusting due to lack of resources, dusting procedure and management supervision, which led to a condition susceptible to coal dust explosion,

(7) Methane explosion led to coal dust explosion, which was not contained due to LTA stone dusting and dust barriers,

(8) Failure to withdraw persons from underground due to a lack of hazard recognition, accumulation of methane due to lack of resources, procedure and organization for gas monitoring; and there was also a lack of systematic emergency response system.

## 3    Defense-in-Depth and Lessons Learnt

The different causes identified through the root cause analysis techniques used in this study to investigate into the accident are summarized below:

A. Direct cause of the accident was open sparking, gas explosion, coal dust explosion.

B. The immediate causes or failed defenses were LTA gas monitoring system, LTA stone dusting and stone dust barrier, and LTA supervision.

C. But there were other reasons failed defenses: LTA supervision, accumulation of inflammable gas in the mine, accumulation of large amount of coal dust, LTA stone dusting and barrier, etc. and over-emphasis on production over safety, absence of proper safe work procedure, lack of adequate resources to deal with fire and explosion hazards, etc.

D. In addition, there were human failures like such as: a lack of training in recognizing hazardous conditions, Risk Assessment (RA) procedures.

E. Other organizational factors: Less than adequate (LTA) operating procedure and resources to deal with mine fire and explosion, such as a shortage of gas monitoring system, adequate and effective cleaning of coal dust and stone dusting requirement, lack of risk assessment procedure, culture of denial of existing/potential hazard and normalizing abnormal situation without proper verification.

The above accident analysis through root cause analysis techniques helps in identifying suitable corrective actions against all causal factors. It is expected that implementation of the above recommendations will reduce number of major accidents.

Further analyses of the above accident case study show that the root causes of the accident can be attributed to one or more of the following basic factors [13, 14]:

i. *Culture of denial*: Poor safety culture of pushing for extra production without considering safety, lacking proper hazard identification and risk assessment procedure.
ii. *Ineffective supervision*: Management failure resulting in a shortage of inspectors and key operators, ineffective safety organization, absence of proper reporting system, etc.
iii. *Standard Operating Procedure (SOP)*: Lack of adequate and effective Standard Operating Procedure (SOP) for electrical maintenance in an underground mine.
iv. *Less Than Adequate (LTA) gas monitoring system*: LTA gas monitoring system or regular gas monitoring procedure.
v. *Culture of risk assessment*: LTA risk assessment before any safety-critical jobs.

Despite a number of accidents due to lack of proper risk assessment, the industry has not learnt from them. Mine workers must be trained to recognize the importance of a risk assessment conducted before, during and after every safety critical job is performed regardless of production pressures. Now it is made mandatory in our law [15] and management system also [15].

## 4   Conclusion

This accident clearly showed the importance of a risk-based safety management system through PHMP and SOP and a risk assessment culture before any safety-critical operations. Continuous gas detection in mines is one of the essential requirements for preventing accidents because of potential gas explosions and mine fires. Though the causes identified were common sense and had been repeatedly pointed out in the past, the coal mining industry did not take any lessons from it. Identification of the root causes along with all possible causes through proper accident investigation is needed to prevent the repetition of similar types of incidents/accidents/disasters from happening in future. The lessons learnt will not be effective, had the causes identified by not been acted upon. From the analysis, it shows that the accident in Indian mines is mainly due to the insufficient attention paid to regulations and too many human errors [13, 14, 16]. Identify and assess operational risks systematically before, during and after every routine or non-routine jobs to ensure that safe method and/or practice (SOP) have been followed. Most importantly, poor safety culture such as taking unnecessary risks, culture of denial, normalization of abnormal conditions, etc. must all be completely avoided.

## References

1. DGMS: Directorate General of Mines Safety. The Accident Investigation Report. Dhanbad, India (2016)
2. Davitt McAteer, J. and Associates: Upper Big Branch-The April 5, 2010, Explosion: A Failure of Basic Coal Mine Safety Practices. Report to the Governor, the Governor's Independent Investigation Panel (2011)

3. MSHA: Coal Mine Safety and Health. 2011. Report of Investigation-Fatal Underground Mine Explosion, April 5 (2010)
4. US NRC: Safety Culture Communicator. Case Study 4: April 2010 Upper Big Branch Mine Explosion- 29 Lives Lost, Washington D.C. (2012)
5. MSIA Report: Discussion Paper Safety of Persons in Proximity to Underground Coal Mine Openings, Mine Safety Institute of Australia Pty Ltd., Australia (2014)
6. Macfie, R.: Tragedy at Pike River Mine. AwaPress, Wellington, New Zealand (2013)
7. Bell, S.: Pike river royal commission outcomes. In: 13th Coal Operators' Conference, University of Wollongong, The Australasian Institute of Mining and Metallurgy & Mine Managers Association of Australia, pp. 240–247 (2013)
8. PRRC: Royal Commission on the Pike River Coal Mine tragedy. Wellington, New Zealand (2012)
9. NZ Police: Operation pike website. https://www.police.govt.nz/operation_pike/videos_photos
10. Report of the Soma Coal Mine Disaster Information Report. Greenpeace.org, Turkey (2014)
11. Abdolhamidzadeh, B., Hassan, C.R.C., Hamid, M.D., FarrokhMehr, S., Badri, N., Rashtchian, D.: Anatomy of a domino accident: roots, triggers and lessons learnt. Process Saf. Environ. Prot. **90**, 424–429 (2012)
12. Livingston, A.D., Jackson, G., Priestley, K.: Root Causes Analysis: Literature Review. Contract Research Report 325/2001, HSE Books (2001)
13. Dash, A.K., Bhattacharjee, R.M., Paul, P.S.: Lessons learned from indian inundation disasters: an analysis of case studies. Int. J. Disaster Risk Reduction **20**, 93–102 (2016)
14. Dash, A.K., Bhattacharjee, R.M., Paul, P.S.: Gap analysis of accident investigation methodology in the indian mining industry—an application of swiss cheese model and 5-why model. IAMURE Int. J. Ecol. Conserv. **15**(1), 1–27 (2015)
15. The Coal Mine Regulations (2017)
16. Kletz, T.A.: Hazop and Hazan: Identifying and Assessing Process Industry Hazards, 4th edn. Taylor & Francis, Philadelphia (1999)

# An Overview of Airflow Catastrophe Induced by Methane Draft Pressure in Coal Mine Roadways

Kai Wang[1,2,3(✉)], Lei Li[2], Aitao Zhou[2], Zeqi Wu[2], and Shan Li[2]

[1] Beijing Key Laboratory for Precise Mining of Intergrown Energy and Resources, China University of Mining and Technology, Beijing 10083, China
Safety226@l26.com
[2] School of Resource and Safety Engineering, China University of Mining and Technology, Beijing 10083, China
[3] Hebei State Key Laboratory of Mine Disaster Prevention, North China Institute of Science and Technology, Beijing 101601, China

**Abstract.** The densities of airflow will be changed by the influx of high-concentration gas, and methane draft pressure will be formed in roadways with height differences. The existence of methane draft pressure may also cause air volume reduction, airflow stagnation and even lead to airflow reversal in some roadways of ventilation networks, resulting in airflow disorder. In recent years, a number of achievements have been made in studies on airflow induced by methane draft pressure with different roadway conditions; however, currently available literature fails to provide a summary study on airflow catastrophes induced by methane draft pressure. Therefore, this paper introduces the definition of methane draft pressure, its influences on ventilation networks, experimental and simulation research, and influence factors and prevention measures of airflow disorder induced by methane draft pressure. It is concluded that methane draft pressure is an important area for future studies on airflow disorder in roadways to cover.

**Keywords:** Methane draft pressure · Airflow disorder · Summary study

## 1 Introduction

During coal and gas outbursts, the formation of destructive shock waves and gas flow may lead to airflow reversal. High-pressure gas flow follows the reverse airflow and enters the intake airflow roadway, resulting in gas accumulation. After the disappearance of the impact's dynamic effect, methane draft pressure will lead to further airflow disorder.

Several notable scholars have analyzed the influence of gas flow on mine ventilation networks [1, 2]: Li [3] studied the theory of turbulent diffusion and the theory of longitudinal dispersion, and on the basis of this, the propagation laws of pollutants in roadways were analyzed. Based on the dispersion diffusion equation and ventilation network theory, Lu et al. [4] calculated the distribution of harmful gas concentration in ventilation systems and analyzed the propagation characteristics of harmful gas in

ventilation systems. Wei [5] established equations for the migration and diffusion regularities of abnormal gas emissions through a theoretical analysis. A similar experimental model was established to simulate gas migration. Nie et al. [6] found that the velocity of gas shows a power exponent after its outburst. Mathematical equations describing gas migration in a tunnel were established based on the hydrodynamic theory. Computational fluid dynamics software FLUENT was used to simulate gas concentration variations during outbursts. Scholars studied the laws of gas migration and diffusion in roadways to lay the foundation for analyzing the influences of methane draft pressure on mine ventilation systems.

Zhang and Tang [7] analyzed the reversal of mine airflow after a coal and gas outburst in a coal mine in Shuijiang, Chongqing, finding that it was difficult for the airflow to be recovered for a long period after the outburst. Though they put forward the concept of methane draft pressure, few scholars studied it in the following ten years. In 2010, methane draft pressure gradually became a focus, with more scholars beginning to study the phenomenon by 2012. Zhou [8] divided the influence of coal and gas outbursts on mine ventilation systems into two stages: first, instant airflow disorder is caused by the impact dynamic effect. When shockwave overpressure exceeds the roadway resistance of a particular tunnel, airflow is reversed. Second, methane draft pressure induces mine airflow. Scholars then studied the influence of methane draft pressure on ventilation systems, achieving positive results and suggesting the necessity of summarizing research on airflow disorder induced by methane draft pressure.

## 2   Formation of Methane Draft Pressure

Methane draft pressure is caused by the different densities and heights of roadways. Due to the fact that the density of gas is lower than that of air, the densities of airflow are changed by the influx of high-concentration gases, and methane draft pressure is formed in roadways with height differences. At present, domestic scholars have studied the formation of methane draft pressure and determined a formula for calculating it.

Zhang and Tang [7] proved the existence of methane draft pressure in mine ventilation systems both theoretically and practically. Methane draft pressure is the increment of natural draft pressure that results from coal and gas outbursts in mines. The different pressures are caused by the different densities of gas and air. According to the theory of natural ventilation, the approximate calculation of methane draft pressure is derived from:

$$h_{CH_4} = Z(r_0 - r) \tag{1}$$

where Z is the elevation difference between the two ends of the roadway with high-concentration gas flow (m), $r_0$ is the average air bulk density of the inlet fully-pressured air of the outburst roadway (N/m$^3$), and r is the average air bulk density of the outlet fully-pressured air of the outburst roadway (N/m$^3$).

Li [9] analyzed that the formation of methane draft pressure is similar to that of natural draft pressure, which is caused by density and height difference. However,

while the density difference of natural wind pressure is caused by the difference in air temperature between the intake air shaft and the return air shaft, the influence of temperature change on gas density is not considered when methane draft pressure is formed. For efficient analysis, the bit pressure difference of each branch is defined as methane draft pressure. Thus, we can not only calculate the methane draft pressure of a ventilation circuit, but also regard methane draft pressure and mechanical pressure as the ventilation power of roadways, which makes the ventilation network calculation program simple. The formula for calculating methane draft pressure is given as:

$$h_{M_i} = (\bar{\rho}_i - \rho_a)[z_i(0) - z_i(L_i)]g \tag{2}$$

where $h_{M_i}$ is the methane draft pressure of branch i (Pa), $\bar{\rho}_i$ is the average density of branch i (kg/m$^3$), $\rho_a$ is the air density of the surface atmosphere (kg/m$^3$), $z_i(0)$ is the elevation of the beginning node of branch i (m), and $z_i(L_i)$ is the elevation of the last node of branch i (m).

Scholars use the concept of methane draft pressure to analyze the phenomenon of airflow disorder, and the formula for calculating methane draft pressure provides the basis for theoretical derivation.

## 3 Influence of Methane Draft Pressure on Ventilation Systems

Methane draft pressure may change the direction of airflow, which will affect the ventilation system. Because methane draft pressure is related to the height differences of roadways, it will have varying influences on upward-ventilated roadways versus downward-ventilated roadways.

Li et al. [10] analyzed the change in gas pressure during coal and gas outbursts and the influence of methane draft pressure on ventilation systems by using the NC2.0 simulation system. The results indicate that the outburst pressure after a gas outburst is the main factor leading to airflow change, propagating flow by the pressure wave. The gas outburst increases the air volume in the return airway and decreases air volume in the intake airflow roadway at the same time, sometimes leading to backflow. Wang and Wu [11] analyzed the phenomenon of airflow stagnation caused by gas accumulation at the top of district raises and simulated the process of airflow stagnation. The numerical simulation results show that the phenomenon of airflow stagnation is caused by methane draft pressure coming from the opposite direction of normal ventilation in inclined entry roadways. Methane draft pressure is the main reason for airflow stagnation. Li [9] simulated and analyzed the influence of gas flow on airflow in parallel upward-ventilated roadways and in parallel downward-ventilated roadways. As can be seen by comparing the laws of gas migration in upward-ventilated roadways and downward-ventilated roadways, gas flow can lead to easy reversal of the main branch airflow direction and result in a large amount of gas in lateral branches. It can also expand the range of outburst disasters in downward-ventilated roadways. Because of the existence of negative gas pressure in downward-ventilated roadways, the airflow of the main branches is reduced and is thereby not conducive to discharging gas.

Therefore, methane draft pressure will cause airflow reduction, airflow stagnation and even airflow reversal in some roadways. Because of the different ventilation circuits, methane draft pressure has varying influences on airflow. The ventilation circuits should be evaluated when the influences of methane draft pressure on ventilation networks are analyzed.

# 4 Study of Mechanisms of Airflow Disorder Induced by Methane Draft Pressure

Airflow is generally disordered in roadways. The process of gas migration is a superposition of disorder and diffusion. Mechanisms of airflow disorder induced by methane draft pressure need to be studied because of the interaction between gas and airflow in roadways.

## 4.1 Theoretical Analysis

The theoretical analysis of airflow disorder induced by methane draft pressure lays the foundation for follow-up study. According to the formula for methane draft pressure, Li [9] determined that methane draft pressure is proportional to roadways with height differences and to the gas concentration in the roadway airflow. The larger the height difference is, the larger the methane draft pressure is. The higher the gas concentration is, the larger the methane draft pressure is. When the methane draft pressure is generated in upward-ventilated roadways, the direction of methane draft pressure is the same as that of the ventilation system, which boosts the airflow. When the methane draft pressure is generated in downward-ventilated roadways, the direction of methane draft pressure is opposite to that of the ventilation system and acts as resistance to airflow.

Zhou [8] carried out static theoretical analysis and dynamic theoretical analysis on airflow reversal of the lateral branches induced by methane draft pressure in upward-ventilated roadways. The results of the static theoretical analysis show that the reversal of the airflow of the lateral branches is independent of the resistance of the lateral branches. The dynamic theoretical analysis shows that airflow reversal of the lateral branches is related to their length and the initial wind speed in upward-ventilated roadways, and the length of the roadway is an important factor that affects the magnitude of resistance of the roadway. The limitation of static analysis is that the dynamics of airflow is not considered and the inertia of airflow is neglected. Wu [12] studied the critical conditions of gas countercurrents in downward-ventilated roadways. The relationship between critical wind speed and height difference of the lateral branches was derived theoretically using Archimedes number, which considers differences in fluid density. The critical condition formula for airflow reversal of lateral branches was obtained:

$$\frac{(\rho_a - \bar{\rho})h}{v_l^2} = K \tag{3}$$

where $\rho_a$ is air density (kg/m$^3$), $\bar{\rho}$ is the average density of initial gas flow in gas branches [determined by the initial gas concentration of gas branches (kg/m$^3$)], $v_l$ is the initial speed of lateral branches (m/s), and K is a constant related to acceleration of gravity and roadway resistance.

The above theoretical analysis is used to judge the conditions of airflow reversal of lateral branches induced by methane draft pressure and to provide a theoretical basis for preventing airflow reversal of the lateral branches, as well as to judge the critical wind speed of airflow reversal of lateral roadways with different elevations. However, the relationship between the critical wind speed and the differences in initial density of the two branches should be further verified in future research.

## 4.2 Experiment and Simulation Analysis

Wu [12] set up an experimental platform for the study of methane draft pressure, and a ventilation network model for simulating various forms of roadway ventilation was created. The influence of methane draft pressure on airflow in upward-ventilated roadways and downward-ventilated roadways was studied using the ventilation network model. Zhou et al. [13] established a one-dimensional unsteady flow differential equation and dispersion model of gas concentration for a single roadway. Through the combination of the balance law of node air volume and circuit wind pressure in the theory of ventilation networks, the network model of unsteady flow and the joint model of gas concentration were obtained, and their solution method was put forward and realized through a computer program.

In order to calculate the unsteady mine ventilation network model, Li [9] improved the original VNT program by using Visual C++ 6. The modules of original data input, operation and output were retained, the optimization part of the wind network was deleted, and the unsteady network calculation was added. The program simulated gas outbursts in a simple ventilation network and the influencing factors of airflow inversion in different roadways were analyzed. The essence of airflow disorder induced by methane draft pressure was expounded. Wu [12] improved upon the unsteady program, including the initial air volume accuracy, friction coefficient selection in roadways with adjustment facilities and the boundary conditions chosen in calculation of gas transport. Considering the changes in roadway resistance by regulating facilities and simulating the process of gas emission, models of roadway resistance and input interface of basic parameters of gas emission were added to the unsteady ventilation network calculation program. The improved program was compared with the original program through a simple parallel tunnel operator. The field examples of gas accumulation caused by the stagnation of wind and flow were simulated, and the effects of gas pressure on airflow stagnation were obtained. A schematic diagram of a sample network in provided in Fig. 1.

Li et al. [14] used the equations for vertical dispersion to describe the unsteady propagation of migration and the diffusion of exogenous gas in mine roadways. The numerical simulation model of the one-dimensional finite element method was established. Analysis of the propagation progress of exogenous gas in ventilation roadways was done by a computer simulation system.
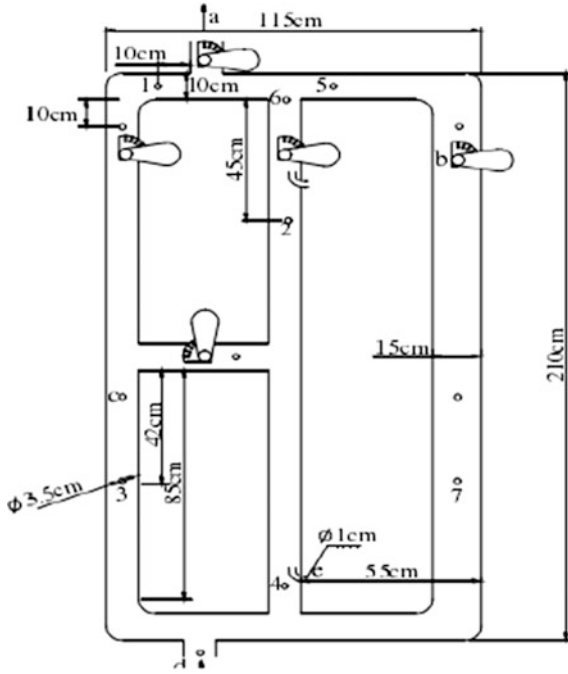
**Fig. 1.** The schematic diagram of the experimental device [12]

The model of mine ventilation networks can accurately analyze the airflow of mine ventilation networks induced by methane draft pressure. However, the unsteady ventilation network calculation program shown in Fig. 2 above is based on the one-dimensional unsteady flow model without considering the compression of roadway
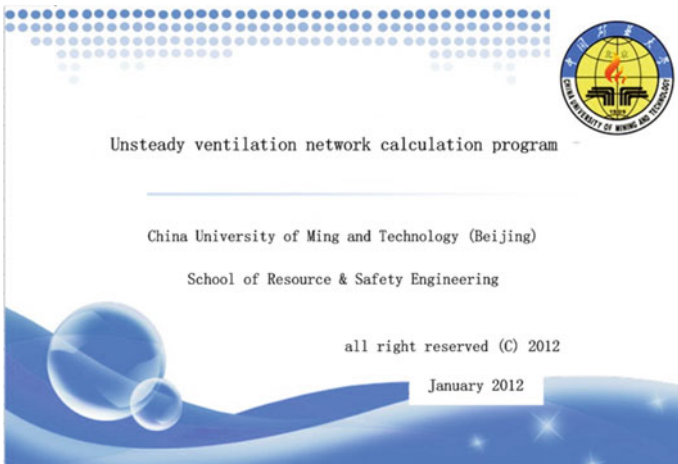


**Fig. 2.** Main interface of the unsteady ventilation network calculation program [9]

airflow, the changes in roadway temperature, the section changes of roadway cross-sections, and gas sources. It is necessary to pay attention to the applicable conditions of the unsteady ventilation network calculation program when the program is used to analyze changes in roadway airflow.

## 5 Influential Factors and Prevention Measures for Airflow Disorder Induced by Methane Draft Pressure

The effects of methane draft pressure on mine airflow are influenced by factors such as the magnitude of methane draft pressure, fan pressure and roadway resistance. In view of this, the measures to prevent airflow disorder induced by methane draft pressure can be analyzed respectively from the magnitude of methane draft pressure, fan pressure and roadway resistance.

### 5.1 Magnitude of Methane Draft Pressure

The existence of methane draft pressure is equivalent to installing an auxiliary fan in the roadway, and the ventilation power is always bottom-up. The greater the methane draft pressure, the easier the airflow disorder. Roadways in areas with outburst danger should be mined carefully to prevent gas accumulation.

Zhou [8] used an unsteady ventilation network calculation program to accumulate the influence of methane draft pressure on the main downward-ventilated branches by setting gas concentrations of 10, 50 and 100%. The results show that the greater the initial methane draft pressure, the greater the possibility of airflow reversal of gas branches. In order to change the initial gas pressure, Wu [12] changed the different elevations of roadways by adjusting the inclination angle of the experimental device. The influences of methane draft pressure on parallel upward-ventilated roadways and parallel downward-ventilated roadways were analyzed, respectively. The experimental results show that when the inclination angle of the roadway is large, the initial gas pressure generated by gas accumulation is larger, and airflow of the lateral roadways can be reversed easily. The changes in airflow and the laws of gas migration are obviously affected. When the inclination angle of the roadway is small, the stability of airflow can be maintained easily, the laws of gas migration are relatively simple and the time of airflow and gas recovery is shorter.

In order to analyze the influences of gas pressure on wind flow, Li [9] altered the initial gas pressure by setting the initial gas concentration of the branches, and simulated the changes in airflow of lateral branches in upward-ventilated roadways and downward-ventilated roadways. The simulation results (see Fig. 3) show that the higher the gas concentration, the greater the gas pressure and the greater the possibility of airflow reversal of lateral branches in upward-ventilated roadways. Therefore, high-concentration gas should be prevented from entering roadways with height differences.
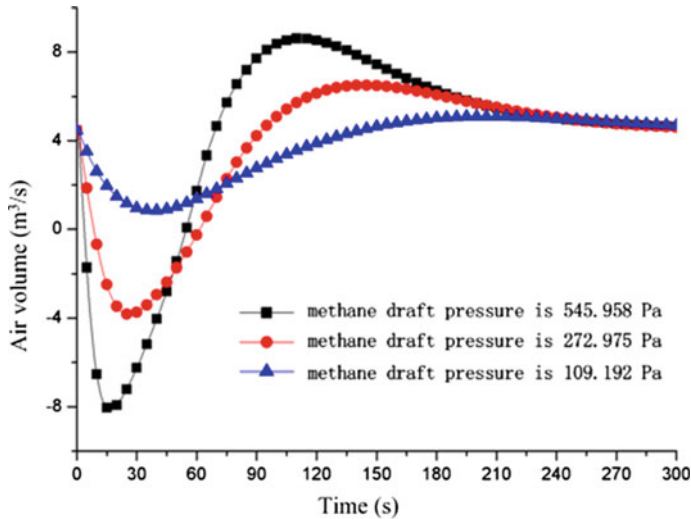
**Fig. 3.** The air volume of lateral branch changes over time under different methane draft pressures in upward-ventilated roadways [9]

## 5.2  Fan Pressure

The phenomenon of airflow disorder is weakened with increasing fan pressure. When the fan pressure is increased to a certain magnitude, the reversal phenomenon can be prevented. It is of positive significance to maintain the stability of mine airflow.

A parallel roadway network model was established by Wu and Chen [15]. A control equation set for air velocities based on the one-dimensional incompressible unsteady differential equation was listed according to this model, and the influence of fan pressure on airflow reversal of the lateral branches induced by methane draft pressure was analyzed. The calculation results show that increasing the fan pressure could reduce the impact of gas flow pressure on airflow, and larger fan pressure could prevent airflow reversals. The increase in fan pressure could increase the original air velocity in the roadway. However, it could not significantly improve the change rate of air velocity. Zhou [8] studied the effects of main fan pressure on airflow disorder of lateral roadways by adding fans with different performance curves to the unsteady mine ventilation network calculation program. The experiment's results show a strong relationship between whether the airflow is reversed and the magnitude of main fan pressure. In order to effectively prevent airflow reversal of the lateral roadways, the normal operation of the main fan must be guaranteed.

Li [9] altered the characteristics of the fan in the unsteady calculation program to simulate the influence of fan pressure on airflow reversal of the lateral branches in upward-ventilated roadways. The simulation results (see Fig. 4) show that the magnitude of main fan pressure has a great influence on airflow, and the smaller the main fan pressure is, the more easily the airflow is reversed. Increasing fan pressure appropriately can prevent airflow reversal.
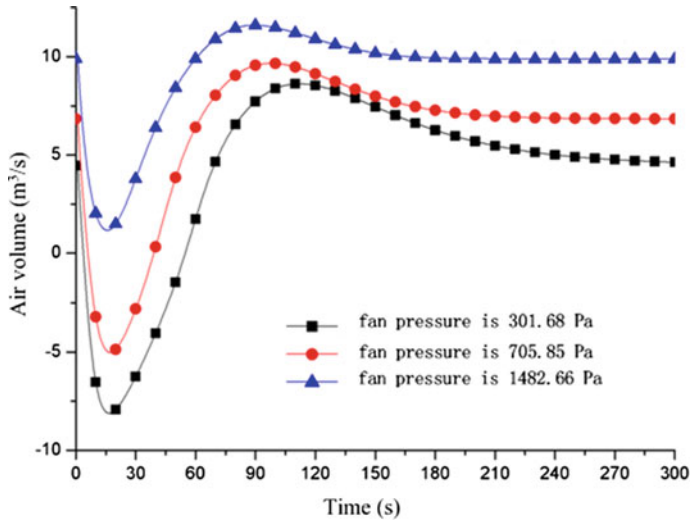
**Fig. 4.** The air volume of lateral branch changes over time under different fan pressures in upward-ventilated roadways [9]

Wu [12] set up an experimental gas-accumulation device and studied the influence of different fan pressures on airflow disorder induced by methane draft pressure in upward and downward-ventilated roadways (see Fig. 1). The experiment's results show that increasing fan pressure can weaken reversal phenomena and reduce the effect of methane draft pressure on mine airflow, which will help airflow recover to the normal level as soon as possible. When the fan pressure is increased to a certain magnitude, the reversal phenomenon can be prevented. Therefore, the normal operation of the main mine fan should always be maintained. In the event of a mine disaster, the wind pressure of the main fan can be properly increased to prevent airflow reversal, thus preventing the expansion of the disaster.

## 5.3 Roadway Resistance

In an actual mine ventilation system, the resistance will be changed with the mining of additional roadways. The changes in roadway resistance will affect ventilation systems and the stability of airflow directly.

Wu [12] set up an experimental inclined roadway gas-accumulation device and studied the influence of lateral branch resistance and gas branch resistance on airflow disorder induced by gas flow. The experiment's results show that the larger the resistance of lateral branches, the smaller the variation range of wind speed, the smaller the resistance of gas branches, and the easier the airflow reversal of the lateral branches.

Wang et al. [16] studied the influences of roadway resistance on airflow disorder by building a similar experimental model of parallel downward-ventilated roadways. The experiment's results show that gas flow pressure can cause complex airflow changes in parallel downward-ventilation roadways and lead to methane and airflow reversals in

the roadways. A vibration model was developed based on a simplification of the experimental system. The vibration model can explain the effects of roadway resistance on the dampening force of the vibration. Both the experiment and model results indicate that the resistance increase of the tilted roadway or the lateral roadway can weaken the airflow. Analysis of the methane movement in the experimental system indicates that for the tilted roadway and the lateral roadway, a resistance increase in one roadway is helpful for the airflow stability but harmful for its own gas discharge.

Li [9] used an unsteady mine ventilation network calculation program to analyze the influence of the resistance of gas branches on lateral roadways. The calculation results show that airflow reversal of the lateral branches is related to the resistance of the main branch, and that the smaller the resistance of the main branch, the more easily the airflow of lateral branches will be reversed (see Fig. 5). Thus, increasing the roadway resistance of the gas branch can prevent airflow reversal of the lateral branches and ensure airflow stability during coal and gas outbursts.
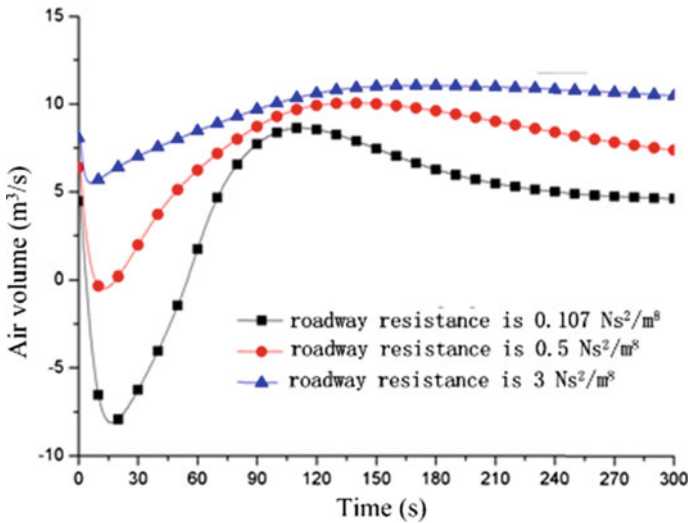


**Fig. 5.** The air volume of lateral branch changes over time under different resistances in upward-ventilated roadways [9]

## 6   Conclusions

In summary, methane draft pressure will result in airflow reduction, airflow stagnation and even airflow reversal in some roadways of ventilation systems. Because of different ventilation methods, methane draft pressure has different influences on airflow. The effects of methane draft pressure on mine airflow is influenced by factors such as the magnitude of methane draft pressure, fan pressure and roadway resistance. Research on

methane draft pressure can provide a theoretical basis for preventing airflow catastrophes. It is concluded that methane draft pressure is an important research area in the study of roadway airflow.

# References

1. Wang, K., et al.: Experimental study of high concentrations of coal mine methane behavior in downward ventilated tilted roadways. J. Wind Eng. Ind. Aerodyn. **158**, 69–80 (2016)
2. Zhou, A., Wang, K.: A transient model for airflow stabilization induced by gas accumulations in a mine ventilation network. J. Loss Prev. Process Ind. **47**, 104–109 (2017)
3. Li, E.L.: Experimental study on diffusion and diffusion of roadway disorder. J. Northeast. Univ. (Natural Science) **3**, 65–69 (1989)
4. Lu, G.L., Li, C.S., Xin, S.: Study on the law of concentration harmful gas spreading in ventilation networks. J. Shandong Univ. Sci. Technol. (Natural Science) **19**(2), 120–122 (2000)
5. Wei, S.Y.: Gas Migration Regularities and Influential Regions of Abnormal Gas Emission. China University of Ming and Technology, Beijing (2013)
6. Nie, B.S., Wang, Y., Dai, L.C., Yang, C.L.: Numerical simulation of gas concentration in roadway after coal and gas outburst. In: Proceedings of 2010 (Shenyang) International Colloquium on Safety Science and Technology (2010)
7. Zhang, R.S., Tang, J.D.: Inquiring into the influence of mine gas on the stability of airflow. Min. Saf. Environ. Prot. **5**, 31–33 (1997)
8. Zhou, A.T.: Research on Propagation Characteristics of Shock Wave and Gas Flow From Gas Outburst and Induced Catastrophic Law of Mine Airflow. China University of Ming and Technology, Beijing (2012)
9. Li, S.: Study of Dynamic Influence on Mine Ventilation Network by Gas Flow After Mine And Gas Outburst. China University of Ming and Technology, Beijing (2012)
10. Li, Z.X., Wang, T.M., Wang, S.Y., Wang, Y.D.: Simulation study of ventilation system disaster evolution in coal and gas outburst mine. J. China Coal Soc. **42**(4), 929–934 (2017)
11. Wang, Y., Wu, Z.Q.: Analysis of airflow stagnation caused by the gas accumulation at the top of district raise. Inner Mongolia Coal Econ. **5**, 120–121 (2017)
12. Wu, Z.Q.: The Study on Methane Accumulation Induced Airflow Disorder in Tilted Roadways. China University of Ming and Technology, Beijing (2017)
13. Zhou, A.T., Wang, K., Wu, Z.Q., Li, S.: Research on airflow catastrophic law induced by gas pressure in mine. J. China Univ. Ming Technol. **43**(6), 1011–1018 (2014)
14. Li, Z.X., Wang, T.M., Jia, J.Z.: Numerical simulation of migration and diffusion of exogenous gas in mine roadways. J. China Univ. Ming Technol. **42**(5), 731–735 (2013)
15. Wu, Z.Q., Chen, Z.: Impact of different fan pressures on airflow reversal induced by gas pressure. Min. Saf. Environ. Prot. **43**(2), 22–25 (2016)
16. Wang, K., Wu, Z.Q., Zhou, A.T., Feng, S.: Study on gas flow pressure caused airflow disorder in parallel downward ventilated roadways. J. Min. Sci. Technol. (1) (2016)

# Part VIII
# DPM

# Review of Diesel Particulate Matter Control Methods in Underground Mines

Ping Chang[(✉)] and Guang Xu

Department of Mining Engineering and Metallurgical Engineering, Western Australian School of Mines, Curtin University, Kalgoorlie 6430, Australia
`ping.chang@postgrad.curtin.edu.au`

**Abstract.** Diesel-powered equipment is widely used in the mining industry due to its superb performance, cost-effectiveness, efficiency as well as durability. However, there is a potential for miners in underground mines to be overexposed to high concentrations of diesel particulate matter (DPM) with the increasing use of diesel engines. In 2012, the International Agency for Research on Cancer (IARC) classified DPM as a carcinogen to humans (group 1) based on sufficient evidence from animal and epidemiological studies. Regulations and control methods have been developed to minimize DPM health hazard in underground mines. This paper firstly reviewed the health effects of DPM on humans based on related animal and epidemiological studies. Findings indicated that both short- and long-term exposure to high concentrations of DPM have adverse impacts (acute irritation, asthma, cough, light-headedness, lung cancer, etc.) on humans, and a recommended limit of DPM concentration ($0.1 \text{ mg/m}^3$, measured as element carbon) should be established to help reduce miners' risk of lung cancer. The effects of DPM control methods were also evaluated, which include source controls and exposure controls. Finally, an optimum DPM controlling strategy was obtained to lower DPM concentrations and provide a safe and healthy working environment for miners.

**Keywords:** Diesel particulate matter (DPM) · Underground mines
Lung cancer · Control methods

## 1 Introduction

The mining industry has been using the diesel-powered equipment extensively since the 1960s due to superb power performance, cost effectiveness, efficiency as well as durability. Compared to gasoline equipment, diesel-powered equipment emits less carbon dioxide and nitrogen oxide [1], but emits much more particulate matters. The wide utilization of diesel engines in confined spaces (underground mines) puts the underground miners under the threat of diesel particulate matter (DPM) exposure. Working in confined areas underground, miners can be over-exposed to DPM exhaust, which is much higher than for workers in other industries. It was reported that the DPM concentration in underground mines can be at least 100 times higher than that measured in other environments where the use of diesel engines is also common [2, 3].

In the past three decades, a great number of animal and epidemiological studies have shown that both long- and short-term exposure to DPM can cause adverse health effects. In 1998, the National Institute for Occupational Health and Safety (NOISH) in the US suggested that DPM had potential carcinogenic effects on humans [4]. In 1989, the International Agency for Research on Cancer (IARC), a part of the World Health Organization (WHO), classified DPM as a probable carcinogen to humans (group 2A) based on sufficient evidence of animal studies and limited evidence of epidemiologic studies [5]. In 2012, based on further evidence in epidemiologic studies, the IARC reclassified DPM as a carcinogenic to humans (group 1). In addition, short-term DPM exposure is linked with acute irritation, asthma, cough, light-headedness etc. For this reason, health issues as a result of DPM exposure have drawn much attention from both the public and governments.

To minimize the health hazards caused by DPM exposure, the DPM concentration needs to be maintained below an acceptable level. Many countries set the DPM concentration limit or standard for mining industries. In order to maintain the DPM levels under the recommendation standard, two main control approaches are commonly used, source controls and exposure controls. Source controls deals with the elimination of DPM before it is emitted outside the diesel engine, which include engine design improvement, engine maintenance and the use of alternative fuel. Exposure control tries to contain DPM exhaust after it is ejected to the working environment. These are mainly achieved through dilution using adequate ventilation, the use of after treatments (DPM filter) and protective equipment.

The aim of this article is to provide an overview of the performance of different DPM control methods in underground mines, and then recommend an efficient and economic DPM control strategy to the mining industry. The paper firstly illustrates the DPM characteristics and the potential health effects on humans by both long-term and short-term DPM exposure. Then, several DPM controlling methods are evaluated in this article. Finally, an optimum DPM controlling strategy is obtained to lower DPM concentrations and provide a safe and healthy working environment for miners based on the summary of the current DPM control technology.

## 2    Characteristics of DPM

### 2.1    Composition of DPM

DPM is produced by the incomplete combustion of fuel in the diesel engine. It is a complex mixture with thousands of components in it [6]. The particulate components mainly consists of elemental carbon (EC), organic carbon (OC), adsorbed condensed hydrocarbons, and sulphate, although its composition is highly variable [7]. EC is the main component of DPM, which can range from about 30–90% of DPM. Commonly, around 30% of DPM is composed of unburned oil and fuel. Other components include condensed inorganic oxides (sulphate), water and ash (contains trace metals) [8].

The range of size distribution of DPM varies. The diameter of DPM ranges from 5 nm to 10 μm. However, more than 90% of the number of the particles are less than 1 μm [9]. It was reported that the filtering capacity of the human nose would be very

low when particles' sizes are less than 0.5 μm [10, 11]. With the ultra-fine characteristics, DPM is able to penetrate the respiratory tract and deposit in the deepest ranges of lungs.

## 2.2 Health Effects

In recent years, a great number of animals and epidemiological studies have been carried out to evaluate the potential health effects of DPM exposure. Many studies have demonstrated the positive association between long-term DPM exposure and the risk of lung cancer.

In 1986, NIOSH published the report "Evaluation of the Potential Health Effects of Occupational Exposure to Diesel Exhaust in Underground Coal Mines". This report included a series of animal studies and epidemiological studies with regard to health effects of long-term DPM exposure. In 1988, NIOSH further analysed the data in the 1986 report and concluded that long-term exposure to high concentrations (over 4 mg/m$^3$) of diesel exhaust could significantly increase the risk of lung tumour for tested animals. However, only limited epidemiological studies [12, 13] cited in the report illustrated that the lung cancer mortality of the railroad workers increased after long-term exposure to DPM emissions. Based on these studies, NIOSH determined that DPM had potential carcinogenic effects on humans [4]. In 1988, IARC also evaluated the health effects of DPM exposure. Similar to the NIOSH recommendation, IARC classified the DPM as a probable carcinogen to humans (group 2A). The review mainly evaluated more than ten cohort studies related to different occupations (railroad workers, drivers, miners) and case-control studies related to various diseases (lung cancer, bladder cancer etc.). However, the association of long-term DPM exposure and the incidence of lung cancer could not be identified due to limited evidence of epidemiological studies. In 2012, IARC conducted another review following the first review in 1988. A major result of this review was that DPM was reclassified to carcinogenic to humans (group 1), and this evaluation was published in a report in 2013 [14]. Sufficient animal and limited epidemiological studies reviewed in the previous report [5] provided the evidence to support the probable carcinogenicity of DPM. In the latest report [14], new evidence for the association between lung cancer and DPM exposure have been provided by epidemiological studies. Two studies cited in the report in particular, an occupational cohorts study [15] and a case-control study [16], provided powerful evidence for the association between lung cancer and long-term DPM exposure.

In addition, short-term or acute exposure to DPM exhaust results in some non-cancer health effects, such as acute irritation, asthma, cough and light-headedness [17–20]. This is especially the case for asthma patients and sensitive groups, who are more easily affected by the DPM exposure.

From the studies above, both long- and short-term DPM exposures are associated with adverse health effects on human. This is particularly the case for long-term DPM exposure, which has potential carcinogenic effects on humans. For these reasons, health issues associated with exposure to DPM are receiving substantial attention from the public, government agencies, and academia.

## 2.3    Standard Limit for DPM

To minimize the DPM hazard on miners, many countries have set limits or passed regulation to control DPM levels for underground mines based on the available studies. Germany set the DPM limit for underground non-coal mines and other surface workplaces at 0.3 and 0.1 mg/m$^3$, respectively [21]. In Canada, most provinces use 1.5 mg per m$^3$ (DPM measured as RCD) as their exposure standard. The Canada Centre for Mineral and Energy Technology (CANMET) finally lowered the standard to 0.75 mg/m$^3$ [22]. The US Mine Safety and Health Administration (MSHA) recommended 0.16 mg/m$^3$ (DPM measured as TC) as a limit for the underground metal/nonmetal mines [23]. In Australia, the Australian Institute of Occupational Hygienists (AIOH) has recommended an 8-h time weighted average (TWA) exposure limit of 0.1 mg/m$^3$ (measured as elemental carbon, EC) [24].

# 3    DPM Controls

Currently, two main approaches have been used to control DPM emissions for the mining industries. One is called source controls, which control the DPM before it is emitted from the diesel engine. The other one is called exposure controls, which control the DPM after it is emitted to the working area.

## 3.1    Source Controls

The source controls mainly include engine maintenance, engine design improvement and using biodiesel.

**Engine maintenance and design improvement**. Reducing the source of DPM should be the first consideration when controlling the DPM level. Diesel exhaust emission is the main source of DPM and diesel engine design is a vital factor affecting the diesel emission rate. Improving the diesel design contributes to the reduction of DPM emissions, which includes improving the combustion chamber design, improving the pump injection systems, increasing the number of intake valves and higher fuel injection pressures [25, 26]. It was reported that the improvements to engine design can reduce as much as 90% of the DPM emissions [25]. However, this method may need to change the current engine's structure, even the whole powertrain system, which is costly and time-consuming and it is impossible to make a technological breakthrough in a short time.

Regular engine maintenance is another method to keep the DPM emission at a low level. A poor condition diesel engine can generate much more DPM than a good one. McGinn [27] has studied the relationship between diesel engine maintenance and exhaust emissions. The results showed that good maintenance of the diesel engine could significantly minimize the DPM emission from the diesel engine. Moreover, he developed a procedure and guidelines for engine maintenance. Another report by NIOSH [28] also indicated the importance of diesel engine maintenance for the DPM emission controls. Several diesel engine servicing procedures have been recommended for the mining industries, which include preventing dust from entering the engine,

maintaining the efficiency of charge compression systems, cooling systems, external exhaust gas recirculation systems, fuel delivery and injection systems, and filtration systems. Due to its low cost and easy implementation, regular diesel engine maintenance can be the first step for DPM emissions control.

**Fuel**. Fuel is another main influencing factor in DPM generation. An appropriate fuel plays a vital factor in the performance of the diesel engine. The sulphur content of the fuel has significant impact on the DPM emissions. Low sulphur diesel fuel usually generates less DPM emissions. It was reported that the use of low-sulphur fuel and lubricant reduced the engine particulate emissions by 30% [25]. The use of alcohol-diesel also contributes to the reduction of DPM emissions [1].

Biodiesel is another proper choice to replace petroleum diesel. Generally, the use of biodiesel results in an apparent reduction in the DPM emission [7, 28–32]. Compared with petroleum diesel, biodiesel contains less aromatics and sulphur but has higher oxygen content. Howell and Weber [29] conducted a study to compare the performance between biodiesel and normal diesel. The results showed that the use of biodiesel results in a 50% DPM reduction in the lab test and 55% time weighted DPM reduction in the field test. NIOSH has conducted a series test to evaluate the effects of several different kinds of biodiesel on the DPM emission by underground diesel mining equipment [32]. The results showed a 30–66% reduction in the total particulate matter when using biodiesel. Bugarski et al. conducted a study to evaluate the effects of biodiesel on DPM size and mass concentration in an underground mine. The results suggested that the total and peak concentration of DPM decreases with an increase of the fraction of biodiesel blend. In Bugarski's other study [28], he reported a 47% DPM reduction by using FAME biodiesel compared with normal diesel. Behçet et al. [31] studied the performance of two biodiesel-diesel fuel blends which were produced from animal fats. The results showed a 15.95 and 10.02% particulate matter reduction for the FOB20 and CFB20 biodiesel, respectively. Lutz et al. [33] compared three different fuels: low-sulphur diesel, biodiesel/diesel blend (B75) and natural gas/diesel blend (GD) in a simulated pilot study. The result showed that both B75 and GD resulted in a DPM reduction. The use of GD fuel resulted in reduction exposure for each set of analyzed data in this study. Ashraful et al. [34] investigated the impact of different percentages of biodiesel on the DPM emissions under different engine loads. The results showed a significant reduction in EC, OC and TC emission when using PB10 and PB20 biodiesel compared with diesel fuel. The EC reduction for PB10 and PB20 varied from 0.75 to 18% and 11.36 to 23.46% for different engine speeds, respectively. Lutz [35] compared personal DPM exposure by using diesel fuel and 75% biodiesel blend (B75); a 22% reduction in respirable DPM was observed by using B75. However, some researchers demonstrated an increase of $NO_x$ emission when using biodiesel [28, 30, 32, 36].

## 3.2 Exposure Controls

The exposure controls mainly include ventilation and the use of aftertreatment devices. Other approaches, such as environmental cabs and personal protective equipment (PPE), are also used to protect the miners from the DPM exposure.

**Aftertreatment Devices**. Aftertreatment devices have the capability to remove pollutant from the exhaust gases before they are emitted to the environment. Aftertreatment devices mainly include diesel oxidation catalytic converters (DOCC), diesel oxidation catalysts (DOC), reusable ceramic filters (RCF), diesel particulate filters (DPF), disposable diesel exhaust filters (DDEF), and ceramic particulate filters (CPF) [6, 7, 25].

A number of researchers illustrated that the filters can reduce diesel particulate emissions effectively. Haney et al. [25] reported that DOCC can reduce DPM emissions by 50%; particulate control systems have a range of 60–90% removal efficiencies by using DPF. Bugarski [37] conducted a compared test between DPF and DOC. The results showed that both DPF and DOC result in a reduction of EC in the diesel exhaust. NIOSH studied the effectiveness of DPF, DFE and DOC on the DPM reduction [7]. The results showed that the efficiencies of different DPF ranged from 81 to 87% in the DPM mass reduction; the DFE's efficiency is more than 80%. However, these filters could only reduce about 40% of the mass concentration when the engine was operated under the highest workload. The United States Environmental Protection Agency (U.S. EPA) and the California Air Resources Board (CARB) have tested several DOC products. The results showed that the reduction in CO and HC were 40 and 50%, respectively; the reduction in total DPM emissions varied from 20 to 35% [28].

Although aftertreatment devices are increasingly used for controlling the DPM levels for underground mines, they still have many disadvantages. The performance of a number of devices is critically dependent on the engine type, because chemical reactions in filters rely on a certain range of temperature [28]. Some DPFs, like disposable paper filters, should be changed frequently. The disposable paper filters should be discarded after being used for 2 or 3 shifts [25]. In addition, one field test which was conducted by Bugarski et al. [38] showed that the DPM concentration was still over the limit even after using filters in the confined zone.

**Ventilation**. The main and widely used method for DPM control in underground mines is ventilation. Ventilation is important in a confined area (underground mine), because it carries fresh air to the working area and dilutes the DPM concentration. It was reported that the DPM concentration decreases with increasing air flow quantities [25]. A good mine ventilation system should be designed to meet the minimum legislative requirement in the areas where the diesel-powered devices are being used.

To control the DPM effectively, it is important to know the required quantity of airflow to dilute the DPM concentration. In the US, MASH has developed a "particulate index (PI)" to calculate the required quantity of air to reduce the DPM emission of a diesel engine to 1 mg/m$^3$ [39]. It is calculated that the amount of ventilation air quantity is 10 (1/0.1) times the PI number to dilute the DPM level to the standard of 0.1 mg/m$^3$. In Australia, the minimum ventilation requirements for the underground mine is based on the power of a diesel engine, which is 0.06 m$^3$/s per kW; the ventilation requirements in China, Chile and South Africa are similar to that of Australia, with 0.067, 0.063 and 0.063 per kW, respectively; in Canada, the ventilation requirement varies from 0.045 to 0.092 m$^3$/s per kW by province [40]. It is easy to maintain the DPM level under the standard when a single diesel device is working underground. However, it becomes difficult when many diesel devices are working

together, because the minimum air flow quantity is the sum of the required air quantity for each diesel device [25]. This may require impractical amounts of air to maintain the DPM level below the limit. In addition, sufficient quantities of fresh air must be used to dilute the DPM exhaust. In fact, the air gets contaminated as it flows in the tunnel, and cannot dilute the DPM effectively at the workface. Because of the opening sizes in underground tunnels, it is difficult to separate the fresh air from the exhaust air [26]. For these reasons, how to use the ventilation efficiently to reduce the DPM concentration needs to be studied further.

**Other Exposure Controls**. Environmental cabs and PPE (respirator filter media or mask) are effective methods to prevent miners from DPM exposure. Environmental cabs, also called enclosed cabins, are usually used by miners to avoid harmful noise. When installed with filtration systems in the cabin, it could also prevent the miners from DPM exposure [26, 28]. Noll et al. [41] reported that the efficiency of a properly functioning enclosed cabin can be more than 90% at capturing DPM. For some high DPM exposure occupation, like diesel engine operators, wearing a proper respirator filter mask can largely reduce the DPM inhaled. Burton et al. [42] reported that a proper mask was over 94% efficient in DPM filtering. Those two methods can only prevent miners from DPM exposure and cannot reduce the DPM level in the working area.

## 4  Summary

In reviewing the literature, it was found that DPM emission has been a threat to underground miners. Numerous epidemiological and animal studies associated the long-term DPM exposure with a high risk of lung cancer. As mining industries increase the utilization of diesel equipment, many countries and agencies have set standard limits of DPM for underground mining industries. Based on the available information, an 8-h TWA DPM exposure standard of 0.1 mg/m$^3$ (measured as submicron EC) is recommended for underground mining industries.

Both the source controls and exposure controls have been discussed in this paper. At present, ventilation is still the primary way to control DPM emission, but how to use the ventilation efficiently to reduce the DPM concentration needs to be studied further. Other approaches are also used for the DPM control. The current paper found that only a single control strategy is not enough to control the DPM effectively. For most cases, the combination of controls seems to be the best way to control the DPM level. Is it possible to find a way (other than ventilation) to reduce the DPM after emission? For example, by using water mist with added surfactant to suppress the DPM. This will be studied in future research.

## References

1. Neeft, J.P., Makkee, M., Moulijn, J.A.: Diesel particulate emission control. Fuel Process. Technol. **47**(1), 1–69 (1996)
2. Noll, J., Mischler, S., Schnakenberg, G., Bugarski, A., Mutmansky, J., Ramani, R.: Measuring diesel particulate matter in underground mines using sub micron elemental

carbon as a surrogate. In: Proceedings for the 11th US North American Mine Ventilation Symposium, State College, PA, pp. 105–110. Taylor & Francis, UK (2006)

3.  Birch, M.E., Noll, J.D.: Submicrometer elemental carbon as a selective measure of diesel particulate matter in coal mines. J. Environ. Monit. **6**(10), 799–806 (2004)

4.  NIOHS: Carcinogenic Effect of Exposure to Diesel Exhaust, Current Intelligence Bulletin 50, U.S. (1988)

5.  IARC: Diesel and Gasoline Engine Exhausts and Some Nitroarenes, vol. 46 (1989)

6.  Zheng, Y.: Diesel Particulate Matter Dispersion Analysis in Underground Metal/Nonmetal Mines Using Computational Fluid Dynamics. Mining Engineering, Missouri University of Science and Technology, USA (2011)

7.  Mischler, S.E., Colinet, J.F.: Controlling and monitoring diesel emissions in underground mines in the United States. In: Mine Ventilation: Proceedings of the Ninth International Mine Ventilation Congress, New Delhi, India, pp. 879–888 (2009)

8.  HEI: Research Directions to Improve Estimates of Human Exposure and Risk from Diesel Exhaust. A Special Report of the Institute's Diesel Epidemiology Working Group, Health Effects Institute, USA (2002)

9.  Kittelson, D., Watts, W., Johnson, J.: Diesel Aerosol Sampling Methodology–CRC E-43. Final Report, Coordinating Research Council (2002)

10. US.EPA: Health Assessment Document for Diesel Engine Exhaust. National Center for Environmental Assessment (2002)

11. Schwab, J.A., Zenkel, M.: Filtration of particulates in the human nose. Laryngoscope **108**(1), 120–124 (1998)

12. Garshick, E., Schenker, M.B., Muñoz, A., Segal, M., Smith, T.J., Woskie, S.R., Hammond, S.K., Speizer, F.E.: A case-control study of lung cancer and diesel exhaust exposure in railroad workers. Am. Rev. Respir. Dis. **135**(6), 1242–1248 (1987)

13. Garshick, E., Schenker, M.B., Muñoz, A., Segal, M., Smith, T.J., Woskie, S.R., Hammond, S.K., Speizer, F.E.: A retrospective cohort study of lung cancer and diesel exhaust exposure in railroad workers. Am. J. Respir. Crit. Care Med. **137**(4), 820–825 (1988)

14. IARC: Diesel and Gasoline Engine Exhausts and Some Nitroarenes, vol. 105 (2013)

15. Attfield, M.D., Schleiff, P.L., Lubin, J.H., Blair, A., Stewart, P.A., Vermeulen, R., Coble, J. B., Silverman, D.T.: The diesel exhaust in miners study: a cohort mortality study with emphasis on lung cancer. J. Natl. Cancer Inst. **104**(11), 869–883 (2012)

16. Silverman, D.T., Samanic, C.M., Lubin, J.H., Blair, A.E., Stewart, P.A., Vermeulen, R., Coble, J.B., Rothman, N., Schleiff, P.L., Travis, W.D.: The diesel exhaust in miners study: a nested case–control study of lung cancer and diesel exhaust. J. Natl. Cancer Inst. **104**(11), 855–868 (2012)

17. Rudell, B., Ledin, M.C., Hammarstr, U., Stjernberg, N., Lundbäck, B., Sandström, T.: Effects of symptoms and lung function in humans experimentally exposed to diesel exhaust. Occup. Environ. Med. **53**(10), 658–662 (1996)

18. Salvi, S.S., Nordenhall, C., Blomberg, A., Rudell, B., Pourazar, J., Kelly, F.J., Wilson, S., Sandstrom, T., Holgate, S.T., Frew, A.J.: Acute exposure to diesel exhaust increases IL-8 and GRO-α production in healthy human airways. Am. J. Respir. Crit. Care Med. **161**(2), 550–557 (2000)

19. Nordenhäll, C., Pourazar, J., Ledin, M., Levin, J.-O., Sandström, T., Ädelroth, E.: Diesel exhaust enhances airway responsiveness in asthmatic subjects. Eur. Respir. J. **17**(5), 909–915 (2001)

20. Mills, N.L., Törnqvist, H., Gonzalez, M.C., Vink, E., Robinson, S.D., Söderberg, S., Boon, N.A., Donaldson, K., Sandström, T., Blomberg, A.: Ischemic and thrombotic effects of dilute diesel-exhaust inhalation in men with coronary heart disease. N. Engl. J. Med. **357**(11), 1075–1082 (2007)

21. AIOH: Diesel Particulate Matter and Occupational Health Issues. AIOH Exposure Standards Committee (2013)
22. Cantrell, B.K., Watts Jr., W.F.: Diesel exhaust aerosol: review of occupational exposure. Appl. Occup. Environ. Hyg. **12**(12), 1019–1027 (1997)
23. MSHA: 30 CFR 57 Diesel Particulate Matter Exposure of Underground Metal & Non Metal Miners, Federal Register, pp. 28924–29012 (2006)
24. DMP: Management of diesel emissions in Western Australia mining operations. In: Resources Safety. Department of Mines and Petroleum, Western Australia, p. 37 (2013)
25. Robert, G.P.S., Haney, A., Waytulonis, Robert W.: An overview of diesel particulate exposures and control technology in the U.S. mining industry. Appl. Occup. Environ. Hyg. **12**(12), 6 (1997)
26. Turner, S.: Diesel particulate exposure and control in western australia underground mines. http://www.gastech.com.au/files/dpm/Diesel%20Particulate%20Report%202006.pdf (2007)
27. McGinn, S.: The Relationship Between Diesel Engine Maintenance and Exhaust Emissions. Final Report (2000)
28. Bugarski, A.D., Cauda, E.G., Janisko, S.J., Mischler, S.E., Noll, J.D.: Diesel Aerosols and Gases in Underground Mines: Guide to Exposure Assessment and Control. Department of Health and Human Services, Public Health Service, Center for Disease Control and Prevention, National Institute for Occupational Safety and Health, Office of Mine Safety and Health Research (2011)
29. Howell, S., Weber, A.: Biodiesel use in underground metal and non-metal mines. Dieselnet site. http://www.dieselnet.com (1997)
30. Bugarski, A.D., Cauda, E.G., Janisko, S.J., Hummer, J.A., Patts, L.D.: Aerosols emitted in underground mine air by diesel engine fueled with biodiesel. J. Air Waste Manage. Assoc. **60**(2), 237–244 (2010)
31. Behçet, R., Oktay, H., Çakmak, A., Aydin, H.: Comparison of exhaust emissions of biodiesel–diesel fuel blends produced from animal fats. Renew. Sustain. Energy Rev. **46**, 157–165 (2015)
32. Bugarski, A.D., Hummer, J., Mischler, S.E., Noll, J.D., Patts, L.D., Schnakenberg, G.: Effectiveness of Selected Diesel Particulate Matter Control Technologies for Underground Mining Applications: Isolated Zone Study, 2004 (2007)
33. Lutz, E.A., Reed, R.J., Lee, V.S., Burgess, J.L.: Occupational exposures to emissions from combustion of diesel and alternative fuels in underground mining—a simulated pilot study. J. Occup. Environ. Hyg. **12**(3), 18–25 (2015)
34. Ashraful, A., Masjuki, H., Kalam, M.: Particulate matter, carbon emissions and elemental compositions from a diesel engine exhaust fuelled with diesel–biodiesel blends. Atmos. Environ. **120**, 463–474 (2015)
35. Lutz, E.A., Reed, R.J., Lee, V.S.T., Burgess, J.L.: Comparison of personal diesel and biodiesel exhaust exposures in an underground mine. J. Occup. Environ. Hyg. (just-accepted) (2017)
36. Liu, Y.Y., Lin, T.C., Wang, Y.J., Ho, W.-L.: Carbonyl compounds and toxicity assessments of emissions from a diesel engine running on biodiesels. J. Air Waste Manage. Assoc. **59**(2), 163–171 (2009)
37. Bugarski, A., Schnakenberg, G., Noll, J., Mischler, S., Patts, L., Hummer, J., Vanderslice, S., Crum, M., Anderson, R.: The Effectiveness of Selected Technologies in Controlling Diesel Emissions in an Underground Mine—Isolated Zone Study at Stillwater Mining Company's Nye Mine, Draft Report. NIOSH, Pittsburgh Research Laboratory (2004)
38. Bugarski, A., Mischler, S., Noll, J., Schnakenberg, G., Crum, M., Anderson, R.: An Evaluation of the Effects of Diesel Particulate Filter Systems on Air Quality and Personal

Exposure of Miners at Stillwater Mine Case Study: Production Zone. Report to M/NM Diesel Partnership, April 1 (2004)

39. MSHA: 30 CFR 7 Mineral Resources, Federal Register (2014)
40. Gangal, M.: Summary of worldwide underground mine diesel regulations. In: Proceedings of the 18th MDEC Conference, Toronto, Ontario (2012)
41. Noll, J., Cecala, A., Organiscak, J.: The effectiveness of several enclosed cab filters and systems for reducing diesel particulate matter. Transactions **330**, 408 (2011)
42. Burton, K.A., Whitelaw, J.L., Jones, A.L., Davies, B.: Efficiency of respirator filter media against diesel particulate matter: a comparison study using two diesel particulate sources. Ann. Occup. Hyg. **60**(6), 771–779 (2016)

# US Diesel Regulations: A Model for All Coal Mines

Pramod Thakur[(✉)]

ESMS LLC, West Virginia University, Morgantown, WV 26505, USA
pramodthakur@frontier.com

**Abstract.** Diesel engines were introduced in US coal mines 50 years ago and their numbers have steadily increased to more than 5000. The driving force behind this phenomenal growth is the mine safety and productivity. The paper reviews US and other international standards in general but discusses the latest West Virginia diesel regulations in particular. The author served on the WV Diesel Commission for 18 years and wrote the most advanced regulations for diesel exhaust control. All diesel exhausts are controlled including the diesel particulate matter to achieve a concentration of 0.12 mg/m$^3$. An integrated approach that requires clean engines, ultra-low sulfur fuel, a catalytic converter and a filtration system is advocated and demonstrated to achieve the highest standards. Replacement of trolley wire haulage by diesel equipment has improved both safety and productivity in many US coal mines.

**Keywords:** Diesel exhaust control · Diesel particulate matter (DPM)
World standards for DPM · Integrated control of exhaust · Clean engines and fuel · Catalytic converter · Diesel soot filters · Mathematical models of diesel exhaust dilution · West virginia diesel regulations

## 1 Introduction

Diesel engines were introduced in US coal mines nearly 50 years ago and their numbers have increased to more than 5000 by now. They are replacing the old trolley wire haulage that had open conductors in mine airways. Frequent electrical sparks created a clear and present danger for methane-air ignitions. Battery haulage was safer but not very efficient. Diesel equipment incorporate both safety and reliability for high coal production. It eliminates shock, fire and explosion hazards from trolley wires and cabled shuttle cars. An additional advantage of diesel equipment use is improved ventilation in the face area. Currently the trolley wire haulage roads are restricted for air velocity at 1.25 m/s. This restriction is imposed to safe-guard against rapid spreading of fire in the track entry. With diesel haulage there are no such restrictions and air quantities can be maximized at the face to improve safety and health of miners. Diesel exhaust, however, contains some substances that can be potentially harmful to human health at uncontrolled, high exposure levels.

Around 1997, US Government took serious steps to minimize the emissions and the states of West Virginia and Pennsylvania further refined the Federal regulations to create a set of regulations that can serve as model for the coal industry of USA and the world.

## 2    Health Hazards of Diesel Particulate Matter (DPM)

Table 1 shows the major components of diesel exhaust. Threshold limit values (TLVs) for all gaseous components of diesel exhaust have been established by the American Conference of Governmental Industrial Hygienists (ACGIH) and are incorporated into Federal Mine Safety and Health Administration (MSHA) regulations. Such incorporations are done only after careful examination of their technical and economic feasibility. Many field studies confirm that meeting these TLVs for gaseous components of diesel exhaust has not been a problem in coal or other mines [1, 2].

**Table 1.** Major components of diesel engine exhaust

| Diesel exhaust | | | | | |
| --- | --- | --- | --- | --- | --- |
| Carbon dioxide | Carbon monoxide | Nitrogen oxides | Unburnt hydrocarbons | Sulfur oxides | Particulate matter (DPM) |

The National Institute of Occupational Safety and Health (NIOSH) has identified DPM as a potential human carcinogen, but in-mine experience over the past fifty years does not provide any epidemiological evidence for such risks. A past study in Australian coal mines, many of which are partially dieselized, determined that the standardized mortality ratio (SMR) for lung cancer in a large cohort of miners was only 78% of that in the general population [3]. A similar study in highly dieselized German potash mines (with no confounders, such as, silica, radon, arsenic, etc.) found similar results for the incidence of lung cancer [4]. Thus, DPM at prevailing concentration levels, does not appear to create any additional health risks. Apart from the lack of substantial epidemiological data, another difficulty in establishing any personal exposure limit (PEL) in the coal mines is the lack of instruments that can accurately measure the DPM concentrations. Previous experience with the coal mine dust PEL also dictates that any PEL for DPM must be based on gravimetric measurements.

In non-coal mines, the combustible fraction of respirable dust can provide a good measure of DPM, but this obviously will not work in mines where combustible minerals are being mined. The elemental carbon technique that differentiates between the fraction of elemental and organic carbons in coal dust and DPM cannot be utilized universally because neither the composition of the coal mine dust nor that of DPM is always the same. Many other techniques, such as carbon isotope ratio analysis, Raman Spectroscopy, and electron spin resonance, also suffer from a similar shortcoming. The size cut-off-based instruments measure everything in mine air below a certain size (0.8 or 1.0 μm). This can be a useful instrument if there was a TLV for all submicron dust particles in the mine atmosphere but is useless if it is used to measure DPM only.

Table 2 shows the major components of DPM. It is generally believed that the polynuclear hydrocarbons attached to solid carbon particles are the potential carcinogens in DPM, but their TLVs are yet to be established. Under these circumstances, the most prudent option is to minimize the concentration of DPM in mine air using state-of-the-art technology and introduce diesel engines in all underground coal mines to improve safety by removing ignition, fire, explosion and tripping hazards related to the use of trolley wire and other electrical cabled equipment. West Virginia and Pennsylvania have achieved a DPM concentration of 0.12 mg/m$^3$ with the innovations discussed here.

**Table 2.**  Major components of diesel particulate matter

| DPM | | | |
|---|---|---|---|
| Solid carbon | Liquid and solid hydrocarbons Includes polynuclear aromatic hydrocarbons (PAH) | Sulfates | Moisture |

## 3   DPM Standards

In spite of the uncertainties discussed earlier, many countries have set a standard for ambient DPM. Table 3 shows the details.

In other countries where they do not have a DPM standard yet, they specify a minimum quantity of ventilation air to dilute the diesel exhaust. Table 4 shows some of them.

**Table 3.**  Current DPM standards

| Country | DPM level (mg/m$^3$) | Analytical technique |
|---|---|---|
| Canada (metal mines) | 1.5 | Combustible respirable dust |
| Germany | 0.2 | Total carbon by NIOSH 5040 method. Sample collected gravimetrically |
| U.S.A. (metal mines) | 0.16 | Total carbon by NIOSH 5040 method. Sample collected gravimetrically |
| U.S.A. (coal mines) | Limits DPM emission | Gravimetric measurement |
| a. Light duty outby engines < 5 gm/h | | |
| b. Heavy duty outby engines < 2.5 gm/h | | |
| c. Heavy duty permissible engines < 2.5 gm/h | | |
| U.S.A. states | | |
| a. West Virginia | 0.12 | Integrated system and ventilation |
| b. Pennsylvania | 0.12 | Integrated system and ventilation |

**Table 4.** Ventilation air for diesel engines

| Country | Ventilation requirement (m$^3$/kw) (CFM/BHP) | |
|---|---|---|
| Australia | 3–3.6 | (80–96) |
| Canada (coal mines) | 2.8–5.6 | (75–150) |
| South Africa | 3.58 | (95) |
| United Kingdom (old) | 5.30 | (140) |

It is, however, assumed that these ventilation quantities will not only dilute the gases in diesel exhaust to safe levels but will also dilute the DPM to a safe level. Better methods to control DPM will be discussed next.

## 4   Diesel Exhaust Control Strategy

Thakur [5] and Schnackenberg [6] advocated separately an integrated approach to minimize diesel exhaust emissions. It consists of the following:

1. Reduce DPM generation.
   a. Clean engines.
   b. Clean fuel.

2. Collect/combust generated DPM.
   a. A catalytic converter.
   b. A soot-filter on most engines.

3. Dilute DPM.
   Adequate ventilation for all approved equipment to dilute DPM to safe levels.

4. Monitor DPM emissions.
   Engine performance needs checked pre-deployment and post-deployment on a periodic basis.

5. Maintenance.
   Proper maintenance of diesel equipment is a must.

6. Training of mechanics and operators.
   The operators and mechanics of diesel equipment must be properly trained, preferably by the equipment manufacturers.

   These steps will be discussed in detail next.

### 4.1   Clean Engines

Specific DPM emissions of an engine define how clean the engine is. Prior to 2000, most approved engines had a high specific emission ranging from 0.105 to 0.4 gm/kwh.

In 2001, the Mine Safety and Health Administration (MSHA) created a new standard for DPM emissions [7]:

| | |
|---|---|
| Light duty outby engines | <5 gm/h. (approx. 0.13 gm/kwh) |
| Heavy duty outby engines | <2.5 gm/h. (approx. 0.03 gm/kwh) |
| Heavy duty permissible engines | <2.5 gm/h. (approx. 0.35 gm/kwh) |

It, indirectly, required a very good filtration system.

Simultaneously the states of Pennsylvania and West Virginia in USA also developed their own criterion for DPM. They agreed on a maximum DPM concentration, on dilution by the name plate air, at 0.12 mg/m$^3$. In response to these regulations, many clean engines were developed by manufacturers that had a specific DPM emission of 0.05–0.06 gm/kwh. Mercedes Benz, Deutz and Cummins were the first to develop clean engines. It was mainly achieved by electronic ignition and turbo charging. All engines needed a MSHA 7E approval number. This required that the engines (with exhaust emission control and conditioning system) must be tested in a certified laboratory by the ISO 8178-1, 8-mode test. The net DPM emission shall not exceed 0.12 mg/m$^3$ when diluted with the MSHA name plate ventilation quantity. The latter is the highest air quantity needed to dilute all gaseous emissions to the statutory limits. The 8-mode test protocol is shown in Table 5.

A typical output of 8-mode test is shown in Table 6.

**Table 5.** 8-Mode Test of ISO 8178-1

| Mode | Engine speed | Percent load (%) | Weight factor |
|---|---|---|---|
| 1 | Rated rpm | 100 | 0.15 |
| 2 | Rated rpm | 75 | 0.15 |
| 3 | Rated rpm | 50 | 0.15 |
| 4 | Rated rpm | 10 | 0.10 |
| 5 | Intermediate[a] | 100 | 0.10 |
| 6 | Intermediate[a] | 75 | 0.10 |
| 7 | Intermediate[a] | 50 | 0.10 |
| 8 | Idle | – | 0.15 |

[a]This usually corresponds to the maximum torque

## 4.2   Clean Fuel

Traditionally all diesel fuels used in coal mines complied with ASTM D975 defined standard for D$_2$ fuel. It had a sulfur content of 500 ppm (by weight), aromatic contents less than 35% and a cetane number of 40–48. Since sulfate typically constitutes 50–60% of the DPM by weight, reduction in sulfur content of fuel was paramount. Fortunately, now the ultra-low sulfur fuel with only 15 ppm sulfur is generally available and is required for coal mine use in many states of USA. This was also the guideline issued by the US Environmental Protection Agency. The flash point for the fuel shall not be less than 125 °F.

**Table 6.** 8-Mode test for a typical diesel engine

| Manufacturer: ABC Company | | | | | | | | |
|---|---|---|---|---|---|---|---|---|
| Serial Name: AB 123–45 | | | | | | | | |
| KW 90 at 2200 rpm | | | | | | | | |
| Test Engineer: John Doe | | | | | | | | |
| Fuel: Carbon, 87%; H, 12.9%; S, 0.06% (by mass) | | | | | | | | |
| Specific gravity: 0.84 | | | | | | | | |
| Air/Fuel Ratio (wt.): 14.46 | | | | | | | | |
| Mode | 1 | 2 | 3 | 4 | 5 | 6 | 7 | 8 |
| Speed (rpm) | 2200 | 2200 | 2200 | 2200 | 1400 | 1400 | 1400 | 600 |
| Torque (NM) | 391 | 299 | 198 | 39 | 470 | 352 | 235 | 0.0 |
| Corrected NO (ppm) | 417 | 339 | 281 | 157 | 594 | 536 | 444 | 171 |
| Corrected $NO_2$ (ppm) | 6.3 | 21.6 | 21.8 | 30.4 | 14.1 | 6.2 | 12.6 | 19.2 |
| Corrected CO (ppm) | 61.5 | 50.7 | 66.3 | 175.5 | 104.7[a] | 87 | 95.9 | 106.2 |
| Corrected $CO_2$ (vol.%) | 6.62 | 5.26 | 4.40 | 2.40 | 6.19 | 7.39 | 5.91 | 1.36 |
| Ventilation, CFM (NO based) | 5167 | 4004 | 2798 | 1090 | 4259 | 3159 | 2271 | 266 |
| Ventilation, CFM ($NO_2$ based) | 389 | 1277 | 1082 | 1051 | 605 | 183 | 321 | 149 |
| Ventilation, CFM (CO based) | 380 | 299 | 329 | 607 | 374 | 266 | 245 | 82 |
| Ventilation, CFM ($CO_2$ based) | 4163 | 3106 | 2187 | 801 | 2934 | 2177 | 164 | 108 |
| Maximum ventilation rate, CFM | 5167 | | | | | | | |
| Maximum ventilation rate rounded, CFM | 5500 (156 m³/min) | | | | | | | |
| CFM/hp. | 46 (1.73 m³/kw/min) | | | | | | | |
| CO emission | 0.5 g/kwh | | | | | | | |
| NOX emission | 3.96 g/kwh | | | | | | | |
| HC emission | 0.044 g/kwh | | | | | | | |
| Particulate emission | 0.09 g/kwh. = 4.385 g/h. (Ave) | | | | | | | |
| [b]Particulate index: | 2580 CFM (73 m³/min) | | | | | | | |
| Particulate index rounded | 3000 CFM or (25 CFM/hp.) | | | | | | | |

[a]This CO level is used to calculate the efficiency of CO control
[b]Required ventilation to dilute DPM to 1 mg/m³

## 4.3  Catalytic Converter (Also Called Diesel Oxidation Catalyst)

It is a device that is placed next to the engine to oxidize gaseous components of diesel exhaust. It also reduces DPM concentration by 20–25%. It has thus become an integral part of all diesel equipment approved for underground use. Table 7 shows the characteristics of a well-designed catalytic converter.

The core of a catalytic converter is an open channel ceramic monolith or a metallic honeycomb substrate that provides support to the catalyst. Cordierite ($2MgO–2Al_2O_3–5SiO_2$) is the most popular ceramic material used for the substrate. It has many good characteristics, such as, high surface area, large open frontal area, low heat capacity, low thermal expansion coefficient and good mechanical strength [7].

**Table 7.** Characteristics of a well-designed catalytic converter

| CO | Reduced by 80 to 95% |
|---|---|
| HC | Reduced by 85 to 90% |
| DPM | Reduced by 25 to 35% |
| Odor control | Very good |
| Influence on engine | Low pressure drop, no fuel penalty |
| Reliability | Very good |
| Durability | $\geq 5000$ h |

Metallic substrates are made of metal, silica, iron, chromium and aluminum alloys. They have higher surface areas and low pressure drop but are more expensive. Both types of substrates are coated with catalysts formulated with noble metals, such as, platinum, palladium and rhodium. The catalyst application is a two-step process. The first step is a wash-coat of aluminum, silica, titanium, cerium and other compounds. In the second step the noble metal catalysts are impregnated on to the wash-coat.

The catalytic converter oxidizes all gases such as, CO, NO and HC to $CO_2$, $NO_2$ and water. The catalysts need to have a temperature above 300 °C for efficient performance. This is the reason they are installed next to the engine. The catalytic converter usually lasts a long time. Five thousand hours of life is common when ultra-low sulfur fuel is used. It is always designed to match the engine exhaust without creating too much back pressure. The current cost varies from $5000 to $10,000 depending on the size of the equipment. The surface of the catalytic converter is always coated with insulating material to keep the surface temperature below 302 °F. For permissible engines, they are water-jacketed.

## 4.4  Diesel Particulate Filters

To collect the DPM and further oxidize the diesel exhaust components (in some cases), a diesel particulate filter is used on most diesel equipment except for very small engines working in outby areas that do not need it to meet legal requirements.

DPM filters can be broadly classified as (a) low temperature filters and (b) high temperature filters depending on the design.

The low temperature filters are suitable for non-permissible heavy-duty diesel equipment working outby in a mine or permissible working in the face areas, such as shuttle cars, front-end loaders. The high temperature filters have a universal appeal and it can be found on all diesel equipment except those that are permissible equipment. The latter can work safely even if the mine air contains 1% methane by volume. This is a legal limit for methane in all US coal mines. The diesel particulate filter must reduce CO concentration to the tailpipe to less than 100 ppm.

**Low Temperature Filters**. These are basically designed to collect DPM and cool the exhaust to a safe level. Figure 1 shows a schematic of a permissible filtration system.

The hot exhaust from the engine goes to a water-jacketed catalytic converter. Next it goes through either a water bath where gases mix with water (as shown) or a water
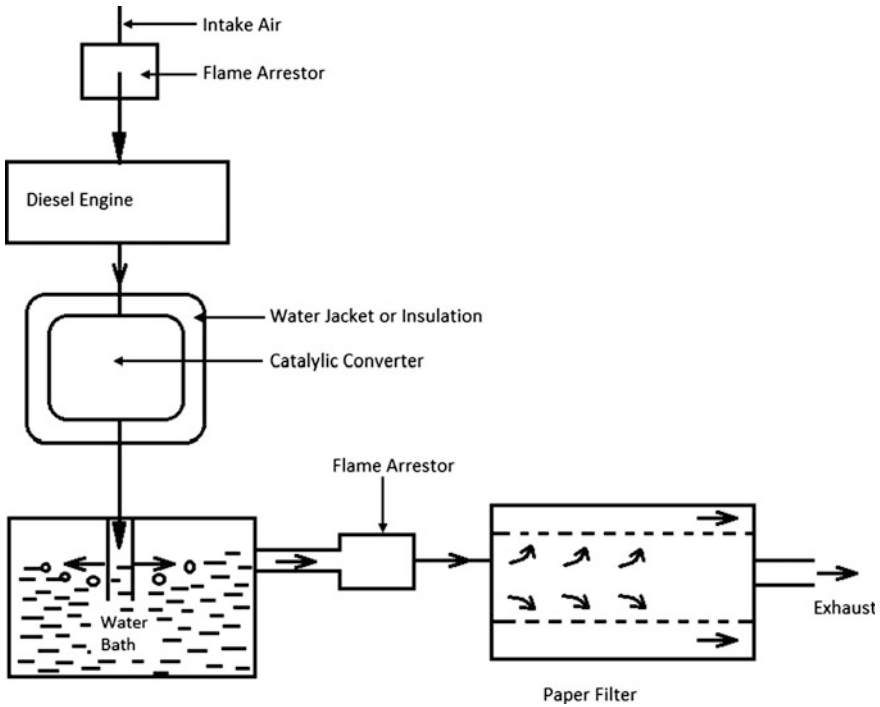
**Fig. 1.** A schematic for a permissible filtration system

cooler without mixing with water that only cools the exhaust. The cooled gas goes through a flame arrestor before it enters the filtration housing. Mostly disposable paper or synthetic paper is used for DPM collection. The filter has to be replaced periodically to keep the intake air pressure generally below 3.5 kPa.

The efficiency of the filtration system varies over a large range but most of them have 90–95% efficiency. Synthetic paper filter is thermally resistant and hence preferred but it is more expensive than the ordinary paper filter.

**High Temperature Filtration System**. They are a bigger version of the catalytic converter but similar in principle. The exhaust gases pass through a filtration system made of a ceramic or silica body that are coated with catalytic metals such as platinum, rhodium and palladium. They require that exhaust temperature be maintained above 350 °C for a short duration each shift for proper operation. They are ideally suited for heavy duty diesel equipment working outby but may not be suitable for light duty equipment for they cannot raise the exhaust temperature high enough for the filter to regenerate. Gradual soot buildup in the filtration system often reduces the efficiency and increases the pressure drop across the unit. In most cases, it is desirable to remove the filtration system and regenerate (burn all soot) in an external regenerating kiln. A spare is needed for continuous operation of the equipment. WV regulations require a minimum collection efficiency of 75%.

### 4.5   Diesel Exhaust Dilution

As discussed earlier, the "name plate ventilation" required by MSHA is sufficient to dilute all gases in diesel exhaust to statutory limits. Federal statutory limits for gases and West Virginia state limits are shown in Table 8.

**Table 8.**   U.S. federal and West Virginia TLV for exhaust gases

| Gas | Federal limit level (ppm) | West Virginia limit (ppm) |
|-----|---------------------------|---------------------------|
| CO | 50 | 35 |
| NO | 25 | 25 |
| $NO_2$ | 5 | 3 |

Corrective actions are required by Federal laws when the gas concentration reaches 50% of limit values but the West Virginia state requires corrective action taken at 75% of the TLV.

A single engine working in an air split requires the "name plate air" but for multiple units the ventilating air required is the sum of the "name plate air" for each diesel unit. The actual air quantities needed in the following situations are mathematically analyzed by Thakur [8, 9] to confirm that MSHA and state requirements are, in fact, larger than what is actually needed and provide additional safety.

1. Single stationary engine in an airway.
2. Single moving engine in an airway.
3. Multiple engines (2–3) in a circuit (such as shuttle cars).
4. Multiple engines (10–100 or so) working in a large mine.

Reference must be made to original work [8, 9] for details but main conclusions are as follows:

1. Static dilution by name plate air provide 50 to 100% additional air than what is actually needed. Air turbulence dissipates gas concentration in addition to dilution by ventilation.
2. Effective ventilation can be larger than "static dilution" for a moving engine, if it moves against the air current.

$$\text{Effective ventilation} = A(u \pm v) \tag{1}$$

Where
A    is the cross-sectional area,
u    is the engine velocity,
v    is the air velocity,
+    sign is when engine moves against the air current,
−    sign is when engine moves in the same direction.

3. Operating a diesel engine in a roadway with zero relative velocity should be avoided. Also, running an engine in a blind heading in the stationary mode must be avoided. Re-breathing of exhaust causes an exponential rise in CO concentration.

4. With three shuttle cars moving in a circuit, the law requires 3 times name plate ventilation air for one unit. Mathematical calculations show actual air needed to be only at 1.6 times the name plate air. It, again, confirms the safety in legal requirements.

5. Computer models developed for diesel exhaust dilution in a network of airways with multiple engines yield results in close agreement with observed values. Program codes in Fortran IV [8] and C ++ [9] are available in published literature.

## 4.6    Diesel Equipment Maintenance and Training of Personnel

The maintenance and training requirements stated in WV Diesel Regulations (Title 196) are one of the best in the coal industry. The following is an excerpt from that.

**Maintenance Plan**. Following is a break-down of the maintenance plan that will be utilized by a mine to insure compliance with the W.V. Diesel Regulations (Title 196). Pre-op means pre-operational in this text.

(a)  All maintenance, repair and diagnostic testing of diesel-powered equipment will be performed by mechanics qualified under
     Section 196-1-24.

(b)  The maintenance of all equipment will begin with the operator's pre-op check list which will be maintained on each piece of diesel-powered equipment until the next 100-h maintenance is performed at which time the old pre-opt check list book will be discarded and a new pre-opt record will begin. By maintaining the pre-op check list on the diesel equipment the qualified mechanic, who is to perform the 100-h maintenance, will be able to read over this document and define problem areas with this particular piece of equipment. This practice will allow the qualified mechanic to have an understanding of problem areas of each particular piece of equipment.

(c)  The 100-h maintenance required by Section 196-1-19 will be performed by a mechanic who has been qualified under Section 196-1-24 of this Act.

   1. The 100-h maintenance intervals will be tracked by a tag system. This tag system will require the qualified mechanic to check the hours of operation at the end of the required maintenance and add 100 h to the actual hours of operation. The qualified mechanic will then insert this number on the tag and attach it to the piece of diesel powered equipment at a conspicuous place in the operator's compartment. This will allow the equipment operator easy reference as to when the next 100-h maintenance will need to be scheduled. We believe this tracking system will insure compliance of Sect. 196-1-19.

   2. A copy of the 100-h check list is attached to this Appendix as "100-h Required Maintenance Check List".

   3. The qualified mechanic will perform all checks and necessary repairs required by Sect. 196-1-19. All repairs of diesel-powered equipment will be recorded in the Diesel-Powered Equipment Maintenance and Repair Book.

4. If the on-board diagnostics controls show that maintenance and or repair is needed prior to the next 100-h maintenance interval a qualified mechanic will perform the necessary maintenance and record the same in the Diesel Powered-Equipment Maintenance and Repair Book.

5. All maintenance and repair of any diesel-powered equipment will be entered in the Diesel-Powered Equipment Maintenance and Repair Book which will be kept on file at the mine as required by Section 196-1-17.

(d) The record keeping at the mine will consist of:

1. Pre-op Check List.
2. 100-h Maintenance Check List.
3. Baseline Sampling Form.
4. 100-h CO Emissions Form.
5. The Diesel-Powered Equipment Repair and Maintenance Form.
6. All forms and check list will be made into book form and kept at the mine site as required by Section 196-1-17.

**Training of Diesel Equipment Operators and Mechanics**. It is ideal for would-be diesel mechanics to train in the schools offered by manufacturers. It is typically a seven-day short course. Diesel instructors are certified by the state and they hold classes at all mines to train diesel operators. It is an eight to sixteen hours-long course where all aspects of safe operation of diesel equipment are thoroughly explained.

So far nearly 1500 diesel-powered equipment have been approved for use in West Virginia underground coal mines. It is hoped that their numbers will multiply and result in gradual replacement of all trolley wire equipment in all coal mines. Besides West Virginia, many other states have formulated diesel laws/regulations to supplement federal laws. Pennsylvania diesel laws are very similar to West Virginia diesel regulations. It is hoped that other states without diesel regulations can use West Virginia diesel regulations as a model to write their own. In fact, these regulations can be a model for global coal industry.

# References

1. Johnson, J.H.: An Overview of Monitoring and Control Methods for Diesel Pollutants in Underground Coal Mines Using Diesel Equipment, CIB Bulletin, pp. 73–87 (1980)
2. Reinbold, E.O.: Ambient pollutant concentration in two underground mines using diesel equipment. Min. Eng. **33**(1), 57–67 (1981)
3. Christie, D.G.S., Brown, A.M., Taylor, R.J., et al.: Mortality in New South Wales coal industry. Med. J. Aust. **163**, 19–21 (1995)
4. Saverin, R., Dahmann, D.: Diesel exhaust and lung cancer mortality in German potash mines. The Health Effects Institute Diesel Workshop, Atlanta, Georgia, USA, March 7–9 (1999)
5. Thakur, P.C., Patts, L.D.: An integrated approach to control diesel particulate matter in underground coal mines. In: Jerry, T. (ed.) The 8th U.S. Mine Ventilation Symposium, pp. 273–279 (1998)
6. Schnackenberg, G.H.: Estimate of technically feasible DPM levels in underground metal and non-metal mines. In: Mining Engineering, pp. 45–51 (2001)

7. Diesel Net: In Diesel Net Technology Guide, 1997, 2000 and 2002, http://www.dieselnet.com
8. Thakur, P.C.: Computer-aided analysis of diesel exhaust contamination of mine ventilation systems. Ph.D. Thesis, The Pennsylvania State University, pp. 223 (1974)
9. Thakur, P.C.: Advanced mine ventilation. Elsevier Publishing, (2018, in press)

# Diesel Exhaust and Diesel Particulate Matter (DPM) in Underground M of India

M. R. Sagesh Kumar[1(✉)], A. K. Dash[2], R. M. Bhattcharjee[2], and
D. C. Panigrahi[2]

[1] Directorate General of Mines Safety, Dhanbad 826001, India
sageshl23@rediffmail.com
[2] Indian Institute of Technology (ISM), Dhanbad 826004, India

**Abstract.** The deployment of diesel-powered equipment in underground mines worldwide has increased exponentially over the last few decades. This extensive deployment is associated with serious health and safety hazards due to exposure of miner to toxic gases and diesel particulate matter (DPM) from the exhausts of this equipment. As early as 1988, the National Institute for Occupational Safety and Health (NIOSH) issued a report which stated that diesel exhaust as a whole is a suspected occupational carcinogen. In June, 2012, the International Agency for Cancer Research (IARC) classified diesel exhaust including DPM as a known human carcinogen (Group 1) based on sufficient evidence that this exposure is associated with an increased risk for lung cancer. Also, a positive association, with limited evidence, of an increased risk of bladder cancer was found. The mining industry in India is poised for quantum jump in production of minerals using different level of mechanisation in underground including diesel-powered equipment. Across the globe numerous studies were conducted to identify the health impacts due to diesel exhaust; however, no comprehensive study has been done in Indian mines. It is expected that the extent of the problem will be quite significant in the near future. Further it is important to develop guidelines for controlling the emissions, dilution, monitoring and mitigation of such toxic gases and DPM to help the industry in introducing such technologies safely. In this paper the authors have made an effort to map the exposure of diesel exhaust and DPM in some of the highly mechanised underground metalliferous mines in India and to suggest a draft national standard on the basis of exposure limits set by countries having similar working environment. The authors in this paper have also thrown light into the established control measures for mitigation of the health hazards due to diesel exhaust gases and DPM.

**Keywords:** Diesel-powered equipment · Exhaust gases · Diesel particulate matter · Health effects · Guidelines for controlling emissions

## 1 Introduction

Mining have been considered as one of the primary or basic industries of early civilization and the importance of this industry continued unaltered ever since. Various technological evolutions in mechanising different mining activities took place since the

man first used hand held tools made of flint and bone for excavation. Diesel powered trackless equipment for mining operations was one of such introductions of modern technology in the mining industry. The diesel powered trackless equipment were first introduced to underground mines in the early 1940s [1] and since then, the use of diesel equipment has grown in numbers and size due to its ease of used and flexibility in operation. These equipment were initially introduced in India during early 1990s and they have become indispensible for improving production and productivity in underground mines. Some of the metalliferous mines in India are now completely mechanised with trackless mining equipment and this has significantly contributed to the improved performance in safety and productivity.

However, use of these diesel-powered machines contributed a new type of hazard for work place environment. The various toxic gases like $CO$, $CO_2$, $NO$, $NO_2$, $SO_2$, aldehydes etc., from the exhausts of machines pose serious health hazards to the miners exposed to such mine atmosphere.

In addition to the diesel exhaust gases, the most critical component in the exhaust is Diesel Particulate Matter (DPM). In the confined spaces of underground mines the potential for miners to get overexposed to DPM and other noxious gases is more compared to other industries. In the United States, National Institute for Occupational Health and Safety (NOISH) in 1988 recommended that DPM had potential carcinogenic effects on humans on the basis of a series of animal and epidemiologic studies [2]. In 1989, International Agency for Research on Cancer (IARC), a part of the World Health Organization (WHO), published a monograph which classified DPM as a probable carcinogen to humans (group 2A) [3]. A number of animal studies have been conducted, which showed that long-term exposure to DPM has the potential to cause lungtumours.

There are also many epidemiological studies on humans that have suggested the association between health effects and long-term DPM exposure [4]. These studies concluded that long-term exposure to high concentrations of DPM could increase the lung cancer risk. In addition, many studies showed that short-term or acute exposure to DPM could also induce negative health effects, such as acute irritation, asthma, cough, light-headedness. In 2012, based on sufficient evidence of animal and epidemiological studies, IARC classified DPM as carcinogenicto humans (Group 1). For these reasons, health issues associated with DPM exposure are receiving substantial attention from the public, government agencies and academia. In order to minimize DPM health hazards, the DPM concentration should be maintained below an acceptable standard. Germany, Canada, Australia and the USA have already set their limit or standard for DPM exposure for mining industries. However no such study was conducted in India and a national standard in exposure limits of DPM is also awaited. A recommended exposure limit of DPM for underground mining industry in India was also suggested based on a summary of the published literature and regulation in different countries.

## 2   History of Use of Diesel-Powered Equipment in Underground Mines

From the introduction of diesel-powered equipment in early 1940s, the use of such equipment in underground mines has increased exponentially over the last several decades. In the United States approximately 150 pieces of diesel equipment were used in underground coal mines in 1974 and by 2014 that number approached 3000 units (This number appears low, there were 3120 pieces in US coal mines in 1996 and this number exceeded 5000 in 2017, according to Pramod Thakur) [5]. A similar trend was seen in underground metal/non-metal mines and by 2014, there were over 7800 units operating in underground metal/non-metal mines in the United States [5]. Diesel-powered trackless mining was initially implemented in India during early 1990s and since then, major non-coal underground mines are deploying diesel- powered trackless equipment extensively. Currently about 400 diesel-powered equipment have been deployed in non-coal mines in India. However, the deployment of diesel operated trackless equipment in Indian underground coal mines are limited to shuttle cars and service trucks in a few longwall faces.

### 2.1   Types of Diesel-Powered Trackless Equipment in India

Diesel-powered trackless equipment can be broadly categorized into either light duty or heavy duty equipment. Light duty equipment consists of those equipment which are not used in regular production cycles like drills, bolters, MPVs, crane tucks, lube trucks, personell carriers, etc. Whereas, heavy duty equipment are LPDTs (dumpers), LHDs (loaders), dozers, etc. involved in ore, waste or fill handling jobs. Generally, light duty equipment accounts for about 35–40% of the total population and loaders are about 30–35% and dumpers are 25–30%.

Apart from this in Indian coal mines about 30 diesel-powered trackless equipment, mostly of flat bed loader, coal haulers and multi-utility vehicles, etc. were used (Table 1).

**Table 1.** Deployment of diesel powered trackless equipment in India (year 2017)

| Sl. no | Type | Nos (Approx) | % of total equipment |
|--------|------|--------------|----------------------|
| 1 | Loader (LHDs) | 115 | 31.5 |
| 2 | Dumpers (LPDTs) | 115 | 31.5 |
| 3 | Drills, bolters and service equipment | 135 | 37 |

## 3   Components of Diesel Exhaust

Diesel emissions area complicated mixture of chemicals and particulates. They can be broadly categorized into a particulate phase and a gas/vapour phase, where each contains both organic and inorganic components. The particulate phase of diesel exhaust includes clusters of respirable particles (i.e. sizesthatcan be inhaled into the

lungs) composed mainly of carbon and are termed "diesel particulate matter". A variety of chemicals are contained within or adsorbed onto the diesel particulate matter, which has the potential to affect the toxicity of the particulate. The major constituents of the gas/vapour phase include carbon monoxide (CO), oxides of nitrogen (NOx), sulphur dioxide ($SO_2$), aldehydes and many polycyclic aromatic hydrocarbons (PAHs). The gas phase is composed of many of the urban hazardous air pollutants, such as acetaldehyde, acrolein, benzene, 1, 3-butadiene, formaldehyde and polycyclic aromatic hydrocarbons [2, 5] (Fig. 1).
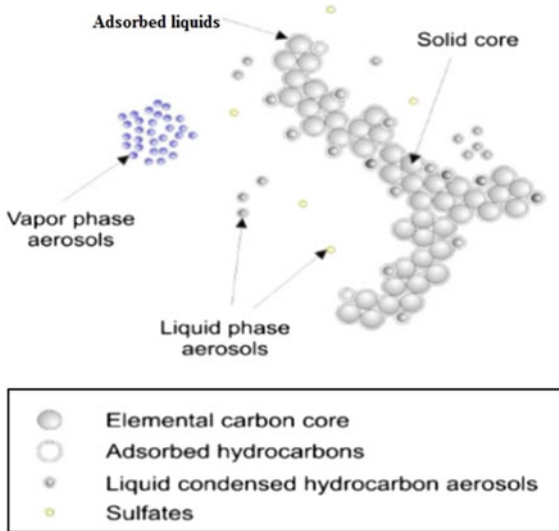


**Fig. 1.** Components of diesel exhaust

## 3.1    Understanding DPM

DPM is a component of diesel exhausts consists of soot particles made up primarily of carbon, ash, metallic abrasion particles, sulfates and silicates. Diesel soot particles have a solid core consisting of elemental carbon, with other substances attached to the surface, including organic carbon compounds known as aromatic hydrocarbons. The high surface area to volume ratios of the core particles of DPM mean they absorb significant quantities of hydrocarbons originating from the un-burnt fuel, lubricating oils and compounds formed during the combustion cycle. More than 1800 compounds have been identified, including polycyclic aromatic hydrocarbons, condensed liquid hydrocarbons, metals and sulphate compounds [7]. DPM is a sub-micron aerosol having more than 90% of the particles' diameters below 1 mm and it is a respirable particulate matter, which is more likely to penetrate the deepest part of the lung, where oxygen enters the blood stream. This causes concerns, because in this region of the lung, the body has fewer means of removing hazardous particles which attach to the

lung tissue [8]. Another consequence of the small size means that DPM is not easily removed from the air stream. Unlike mineral dust, it will not settle to the ground easily under gravity. Once it is airborne, a portion of DPM will likely remain airborne all the way to the mine exhaust. This means that DPM not only affects the workplace where it is produced, it also contaminates workplaces downwind. This is why control of DPM at the source is so important [7].

## 4    Health Effects of Diesel Exhaust/DPM

This extensive use of diesel-powered equipment created the potential for exposure of underground miners to particulate matter and gaseous emissions from this equipment. Such exposure poses a serious problem to the mining industry worldwide as this exhaust gases and DPM have severe health impacts on the miners exposed to them. Also, the inadequate ventilation and confined spaces of underground mines flare up the potential to overexpose the miner to DPM and other noxious gases. Available animal and epidemiological studies have shown that both short-term and long-term exposure to DPM could pose a risk to health. Short-term exposure to high concentrations of Diesel Exhaust (DE)/DPM can cause headache, dizziness, and irritation of the eye, nose and throat severe enough to distract or disable miners and other workers. Prolonged DE/DPM exposure can increase the risk of cardiovascular, cardiopulmonary and respiratory disease and lung cancer. Some of the compounds found in DPM are known carcinogens. Because of that, it is possible that DPM as a whole can be a carcinogen at some level of exposure [8]. Excessive exposure to gases can also adversely affect the human body, as described below [5, 7].

- Carbon monoxide reduces the capacity of blood to carry oxygen, which can result in loss of consciousness and possibly death. There is also a possible link between long-term exposure and the development of heart disease.
- Carbon dioxide can affect sensory perceptions, and cause disturbed judgment, mood changes and, in extreme situations, death.
- Nitrogen dioxide can produce severe respiratory irritation. Severe lung problems such as emphysema and chronic bronchitis can occur immediately or after a delay of several days.

Other emitted gases can irritate sensitive parts of the body, such as the nasal passages, throat, lungs and parts of the eyes. As early as 1988, NIOSH issued a report which stated that diesel exhaust as a whole is a suspected occupational carcinogen. In 2002, the U.S Environmental Protection Agency (EPA) classified diesel exhaust as "likely to be carcinogenic". In June, 2012, IARC classified diesel exhaust including DPM as a known human carcinogen (Group 1) based on sufficient evidence that this exposure is associated with an increased risk for lung cancer [10]. A positive association, with limited evidence, of an increased risk of bladder cancer was also found. The IARC was careful to state that the classification of diesel emissions as a carcinogen was dependent on the duration, frequency and concentration of exposure required to produce an actual risk. As with many exposures, the probability of harm increases with the level of exposure, and this was an important aspect of the IARC's findings [11].

## 5  Sampling and Analysis Methods for DPM

Diesel particulate matter has a median diameter of 0.1 μm, with 90% of the particles being <1.0 μm in diameter. It is composed primarily of organic carbon, elemental carbon, adsorbed and condenses hydrocarbons, and sulphate. The ratio of organic carbon to elemental carbon varies depending on factors such as fuel type, engine type, duty cycle, engine maintenance, operator habits, use of emission control devices, and oil consumption. Mass measurements of DPM are prone to interferences from other sources of aerosols (mineral dusts, cigarette smoke, etc.) in the mining environment and are not sensitive enough for the low concentrations below 200 μg/m$^3$. Therefore, EC was used as a surrogate to determine DPM exposure [12].

Two sampling methods are routinely used in underground mines to collect DPM samples for analysis: respirable dust sampling and size selective sampling. Three analytical methods are used to quantify DPM in collected samples; these are gravimetric analysis, respirable combustible dust analysis and elemental carbon analysis. Combining the sampling and analytical methods yields three methods to quantify DPM, (1) respirable dust sampling with respirable dust analysis, (2) size selective sampling with gravimetric or elemental carbon analysis, and (3) respirable dust sampling with elemental carbon analysis [13].

- The respirable combustible dust method (RCD) was developed in Canada to estimate diesel particulates in non-coalmines [7]. RCD is composed of all combustible substances collected on a sample filter including drill oil mist, the soluble fraction of the particulate matter, elemental carbon and other combustible material such as carbonaceous material found in the ore dust.
- Size selective (SS) sampling is based on the demonstration that sub-micrometer aerosols found in coalmines are primarily diesel in origin. The difference in the aerodynamic diameter particle size between combustion and mechanically generated aerosols can be used to separate diesel particulates from non-combustion aerosols. The SS sampler can be used in conjunction with the method for determining elemental carbon for quantification of diesel particulates in coalmines.
- NIOSH (1998) has developed a sensitive measure of the elemental carbon (EC) portion of diesel particulate matter (Method 5040). The method also determines organic carbon (OC) and by summation of the EC and OC the total carbon can be determined. In general, elemental carbon accounts for about 50 per cent of the mass of diesel particulate matter, but this varies as discussed above. Since EC is a product of combustion and is composed of inert graphitic carbon it is a specific marker of diesel exhaust aerosol where other combustion aerosols are not present. The OC portion, on the other hand, is subject to interferences from other organic aerosols not associated with diesel exhaust.
- Gravimetric-based methods (e.g. RCD, RCD in combination with SS sampling and SS sampling on its own) are inadequate at moderately low workplace concentrations because so little mass is collected that the weighing error becomes very large. RCD has further limitations because all combustible substances are measured, also those of non-diesel origin. Methods based on the NIOSH Method 5040 are much more sensitive to diesel particulate matter and reasonably strong correlation

between EC and diesel particulate matter. Because of the presence of both organic and elemental carbon in coalmine dust, a sub-micron impactor can be used to separate the larger coal dust particles from the diesel particles [14].

## 5.1 Real Time Ddiesel Particulate Matter Monitors

The NIOSH 5040 method involves taking samples from work site and analysing at laboratory. Although this procedure may be the most accurate method for collecting and measuring compliance samples of DPM, the time and cost involved in the process make it an impractical method for mines that are looking to monitor the effectiveness of DPM controls. In addition, the NIOSH 5040 method is a one-dimensional measurement, meaning that it simply provides an average DPM exposure measurement over a given time period without recording critical information pertaining to the cause of the overexposure [15]. Because of these drawbacks portable instrument that is capable of measuring concentrations of elemental carbon (EC) in near real-time are introduced for DPM monitoring. Using Elemental Carbon as a surrogate for Total carbon, these instruments can provide DPM measurements quickly and continuously in an underground mine. In addition, they also provide charted outputs of DPM concentration changes over time. Because these concentrations are often transient in nature, understanding this data will help mine operators obtain a clearer picture of how DPM levels are affected by mining activity and how well they respond to control strategies. This data can provide valuable information on the effectiveness of ventilation, vehicle-specific emissions, diesel particulate files ilters failures, miner-specific exposures, and the effectiveness of cab filtration systems [12, 16].

## 6  International Stipulation Concerning the Operation of Diesel—Powered Equipment in Underground MINES

### 6.1  Chronology of Statues in Various Countries

- In 1990 the Canadian ad hoc Diesel Committee published a guideline suggesting that exposure to diesel particulate matter should be measured using the respirable Combustible Dust (RCD) method and be limited to 1.5 mg/m$^3$ over a normal eight-hour shift [7]. This exposure limit has thereafter been adopted by most mining provinces in Canada.
- In January 2001, the US Mine Safety and Health Administration (MSHA) issued a final ruling for US metal and non-metal mines. In this ruling, MSHA requires that mines meet a limit of exposure of 0.40 mg/m$^3$ within eighteen months. Mines would thereafter be expected to reduce exposure in order to meet a 0.16 mg/m$^3$ limit of exposure by January 2006 (NIOSH 2002). This limit of exposure is based on the measurement of total carbon using the NIOSH 5040 Method.
- The American Conference of Governmental Industrial Hygienists (ACGIH) is the organisation that publishes the well-known Threshold Limit Value (TLV) guidelines on an annual basis. The ACGIH guidelines do not have any legal standing, but are being used in many parts of the world as legal exposure limits by regulators.

In 1996, the ACGIH Published a notice of intended change in which a diesel particulate matter TLV of 0.15 mg/m$^3$ was suggested. In 1998 the ACGIH further reduced this proposed TLV to 0.05 mg/m$^3$. Both of these limits were based on the measurement of total carbon similar to the MSHA rule. In 2001, the ACGIH suggested a limit of 0.02 mg/m$^3$ based on the measurement of elemental carbon only [7].

- European mines and tunnel construction projects are also subject to diesel particulate matter limits of exposure. In Europe, a method similar to the NIOSH 5040 is being used to measure elemental and organic carbon. Countries have adopted different limits of exposure depending on whether elemental or total carbon is measured for compliance purposes.
- Until 1996 Germany applied an eight-hour threshold limit value of 0.2 mg/m$^3$ in the general workplace and for non-coalmines, a limit of 0.6 mg/m$^3$, measured as total carbon. These exposure limits have subsequently been revised in 1997 as 0.3 mg/m$^3$ for elemental carbon in non-coal mines and 0.1 mg/m$^3$ for other work places. Exposure in coalmines has not been addressed specifically [7, 18].
- In road tunnels in Switzerland the limit of exposure is 0.2 mg/m3 expressed as total carbon [18].
- Elemental Carbon levels in Australian underground metalliferous mines have been measured at 0.01–0.42 mg/m$^3$. Investigations in 2005 by SIMTARS also found elevated exposures in Queensland underground metalliferous mines. For surface mining operations, forklift operators have been found to be the highest exposed group. Levels for forklift operators have ranged from 0.007 to 0.40 mg/m$^3$, with a median of 0.075 mg/m$^3$ as EC [17].
- Ambient air concentrations of elemental or total carbon are at present not regulated in UK, South Africa and India (Table 2).

**Table 2.** The limits of DPM at different countries are tabulated below

| Country | Limits in mg/m$^3$ | Limiting parameter | Remarks |
|---|---|---|---|
| USA | 0.16 | Total carbon | |
| Canada | 0.4 to 1.5 | Total carbon | |
| Germany | 0.3<br>0.1 | Elemental carbon | U/g non coal mines general |
| Switzerland | 0.2 | Elemental | For tunnels |
| Australia | 0.1 | Elemental carbon | |

## 7   National Standard for DPM and Diesel Exhaust

There is no such regulatory provision regarding the exposure limit for diesel exhaust and DPM in existing mine safety regulations in India. However vide DGMS Tech Circular 30/1973 following provisions are provided. "Adequate arrangements should be made to circulate required air quantity of air reaching the site of blasting as to ensure, after every round of blast, dilution of carbon monoxide and oxides of nitrogen in the blasting fumes to less than 50 PPM and 5 PPM, respectively, within a period of

5 min". Regarding the exposure limits of DPM no such statutory limits are prescribed in existing mine safety regulations. However, considering the increasing population of diesel operated equipment in underground mines and the serious health impacts due to such exposures, statutory limits should be framed based on the international experiences and control values for implementation in Indian mines. Monitoring of diesel particulate matter is being done at some of the metalliferous mines in India. The elemental carbon part of the DPM was monitored by using a real time monitor, Airtec manufactured by FLIR. The Airtec DPM displays elemental carbon levels in real time using the technology developed by the diesel particulate group at the NIOSH Pittsburgh Research Laboratory and has been determined to replicate results from their method 5040 test. Spot values as well as the TWA values of DPM were measured while different diesel equipment were being operated. TWA values were found in the range of 90–150 µg of EC however, Spot values up to 600 µg were observed at many readings taken. The TWA values of countries USA, Australia, etc. were derived considering time weighted averages for exposure during an 8 h workday for a total of 40 h per week [19]. However in Indian conditions most of the mines are being worked in eight hour shift for 6 days. Considering this elevated weekly working hours the TWA values should be reduced proportionately. Further limiting values for the overages of the TWA should also be framed to avoid short term exposure to high DPM values.

## 8 Control Measures

Engineering controls are the most effective strategy for minimizing worker exposure to DPM. A combination of controls is often required [20]. Examples include (a) performing routine preventive maintenance of diesel engines to minimize emissions, (b) Installing engine exhaust filters, (c) Installing cleaner burning engines, (d) Installing diesel oxidation catalysts, (e) Using special fuels or fuel additives (e.g., biodiesel), (f) Providing equipment cabs with filtered air, and (g) Installing or upgrading main or auxiliary ventilation systems, exhaust ventilation arrangements, etc.

Administrative controls refer to changes in the way of performing a task to reduce or eliminate the hazard [23]. For examples (a) Prohibiting and/or restricting unnecessary idling or lugging of engines, (b) Restricting the amount of diesel-powered equipment and total engine horsepower operating in a given area and ensure that the number of vehicles operating in an area does not exceed the capacity of the ventilation system, (c) Designate areas that are off-limits for diesel engine operation and/or personnel travel.

## 9 Conclusion

The health hazards due to toxic gases from the diesel exhaust and the DPM are having very high risk due to such exposures. Indian mining industry is poised for quantum jump in production of minerals using different level of mechanisation in underground including diesel power operated equipment. It is expected that the extent of the problem

will be quite significant in the near future. A national standard limiting the exposure of the toxic exhaust gases and DPM is very much essential. Further it is important to develop guidelines for controlling the emissions, dilution, monitoring and mitigation of such toxic gases and DPM to help the industry in introducing such technologies safely.

# References

1. McGinn, S.: Controlling diesel emissions in underground mining within an evolving regulatory structure in Canada and the United States of America. p. 11
2. Bugarski, A.D., Janisko, S.J., Cauda, E.G., Noll, J.D., Mischler S.E.: Office of mine safety and health research national institute for occupational safety and health: diesel aerosols and gases in underground mines. Guide to exposure assessment and control (2011)
3. NIOHS.: Carcinogenic effect of exposure to diesel exhaust. CurrIntell Bull 50 U.S. (1988)
4. Silverman, D.T., Samanic, C.M., Lubin, J.H., Blair, A.E., Stewart, P.A., Vermeulen, R., Coble, J.B., Rothman, N. Schleiff, P.L., Ravis, W.D., Ziegler, R.G. Wacholder, S. Attfield M.D.: The diesel exhaust in miners study: a nested case—control study of lung cancer and diesel exhaust
5. MSHA Report, MSHA diesel inventor (2014)
6. Prasad, R., Bella, V.R.: A review on diesel soot emission, its effect and control
7. Diesel emissions evaluation program (DEEP) Report.: Sampling for diesel particulate matter in mines, p. 26 (2001)
8. Chang, P., Xu, G.: A review of the health effects and exposure-responsible relationship of diesel particulate matter for underground mines
9. Draft GUIDELINE for Managing diesel emissions in underground metalliferous mines in Western Australia, Ministry of Mines and Petroleum Resources Safety
10. WHO, IARC Press Release No 213, 12 (2012)
11. Australian institute of occupational hygienists diesel particulate matter & occupational health issues (AIOH), Exposure Standards Committee, p. 13 (2013)
12. Noll, J.D., Mischler, S.E., Schnakenberg, Jr. G.H., Bugarski, A.D.: Measuring diesel particulate matter in underground mines using submicron elemental carbon as a surrogate
13. Watts, W., Ramachandran, G.: Diesel particulate matter sampling methods—statistical comparison. report of investigation submitted to the diesel emissions evaluation program (DEEP) technical committee; Août (2000)
14. Gillies, S, Wu, H.W.: Mine real time personal respirable dust and diesel particulate matter monitoring. In: Proceedings, Queensland mining industry health and safety conference, Townsville, pp. 407–416 (2007)
15. Nolland, J.D., Janisko, S.: Evaluation of a wearable monitor for measuring real-time diesel particulate matter concentrations in several underground mines
16. Watts, W.F., Kittelson, D.B., Kogut, J.M.S.: Diesel particulate matter sampling methods statistical comparison
17. Australian institute of occupational hygienists diesel particulate matter & occupational health issues (AIOH), Exposure Standards Committee, pp. 13 (2013)
18. Gangal, M.: Summary of worldwide underground mine diesel regulations NRCan, CANMET MINING, 18th MDEC Conference Toronto. Ontario, Canada (2012)
19. IARC. Diesel and gasoline engine exhausts and some nitroarenes? (1989)
20. Schnakenberg, G.H., Bugarski, A.D.: Review of technology available to the underground mining industry for control of diesel emission, NIOSH (2002)

# DPM Variation Analysis Over Multiple LHD Work Cycles with the Use of CFD

Hongbin Zhang[1,2]([✉]), Lorrie Fava[1,2], Ming Cai[1,2], Nick Vayenas[1], and Enrique Acuña[3]

[1] Laurentian University, Sudbury, ON P3E 2C6, Canada
hzhang@mirarco.org
[2] MIRARCO Mining Innovation, Sudbury, ON P3E 2C6, Canada
[3] Escuela de Minas, Facultad de Ingeniería, Universidad del Desarrollo, Santiago 7620001, Chile

**Abstract.** Computational fluid dynamics (CFD) is used to study the diesel particulate matter (DPM) variation over multiple work cycles of diesel-powered load-haul-dump (LHD) equipment in an underground mine. The LHD's work cycle considered consisted of three parts: tramming into the heading, mucking, and tramming out of the heading to the drop point. For the study, DPM data was collected from an underground gold mine in the western U.S. For the CFD model, a DPM source was created close to the working face to mimic the DPM released over the work cycles of the LHD. The DPM source was modeled as a cube mounted on the floor of the drift. The species transport model with transient simulation was applied to simulate the DPM concentration distribution over 1.5 h in the heading. Monitoring points were created in the CFD model to record the DPM data over time. After comparing the results of the CFD model to those of the experiment, it is concluded that the DPM concentration can be correctly modeled with the proposed CFD approach. This CFD approach could be helpful to improve the operation of a mine's ventilation system.

**Keywords:** Diesel particulate matter (DPM) · Computational fluid dynamics (CFD) · Mine ventilation

## 1 Introduction

Achieving production targets while ensuring health and safety of the workforce is paramount for mines all over the world. Mine ventilation, which dilutes and removes contaminants and provides fresh air to personnel and equipment, plays a significant role in health and safety in underground mines.

For metal and non-metal mines, a main health and safety concern arises from the diesel particulate matter (DPM) concentration due to the fact that it is carcinogenic after long-term exposure [1–3]. DPM mainly comes from heavy-duty diesel equipment such as mine trucks and load-haul-dumps (LHDs). DPM consists of very small particles emitted in diesel exhaust [4], mainly organic carbon and elemental carbon. The sum of organic carbon and elemental carbon is called total carbon, which is commonly referred as DPM [5]. Practically, elemental carbon is measured according to the NIOSH 5040 method [6].

Mines have employed various methods to protect personnel from exposure to high-DPM exhaust. These methods include installation of environmental cabs on mine trucks, applying diesel particulate filters to tailpipes, and the use of personal particulate filters (or respirators) [7]. In addition, a well-designed and controlled ventilation system helps to efficiently dilute DPM.

This paper proposes a computational fluid dynamics (CFD) approach to study the DPM concentration behavior after multiple work cycles of an LHD in a heading of an underground mine.

## 2   Prior DPM Modeling Methods Using CFD

Zheng et al. [8] conducted a validation study for a CFD model using the species transport model to predict DPM concentrations at various locations. The study confirmed that the CFD approach could assess options for DPM reduction. Furthermore, Zheng et al. [9] used the species transport model available in ANSYS Fluent to investigate the DPM behavior over a period of 200s for four alternative auxiliary ventilation systems. It was found that the CFD approach could be used to select the best DPM control strategy. Kurnia et al. [10] evaluated different ventilation strategies for efficient and economical control of hazardous gas released by diesel equipment with the species transport model in ANSYS Fluent.

However, none of the literature previously mentioned provides specific methods for a longer-term DPM simulation in the CFD model, which would reflect the actual underground operation of diesel equipment in a heading. Most of the approaches proposed would be prohibitively computationally expensive and would require the use of high performance computing (HPC), which is not usually available at a mine site. A new approach is proposed in the following section to improve the performance of CFD modeling.

## 3   Proposed DPM Modeling Approach

In this study, a new CFD approach was introduced to efficiently simulate the DPM concentration over 1.5 h. A single diesel source was created in the CFD model to release DPM in order to mimic the exhaust emissions of diesel equipment (in this case, an LHD) over multiple work cycles.

One work cycle of an LHD consists of three parts: tramming into the heading, mucking at the working face, and tramming out of the heading. The DPM emissions from the tailpipe of the LHD vary over the work cycle. The concentration is highest when the LHD is mucking and lowest when the LHD is tramming into the heading. Due to the long duration of the period simulated, an averaged DPM concentration was used to represent the DPM concentration over each work cycle of the LHD. The averaged DPM concentration was obtained through trial-and-error in the CFD model.

DPM was simulated as octane ($C_8H_{18}$) [11]. The species transport model was employed to simulate DPM concentration in the fluid domain.

# 4 Validation of the DPM Modeling Approach

## 4.1 Experiment Setup

Four Flir Airtec DPM monitoring [12] units were installed at four different locations A, C, D, and E, on the back of a heading. An example of the location of a DPM monitor in the cross-sectional area is shown in Fig. 1. Each DPM monitor was set to collect data every minute. The raw DPM data was expressed as weight of elemental carbon and the one-minute DPM concentration data was then manually calculated according to [13].

A ventilation survey was performed at locations A, B, C, D, and E using the traverse methodology [14] to obtain the dimensions of the experiment area and velocities to calculate the airflow volumes. The plan view of the experiment area is shown in Fig. 2. Arrows in the figure indicate the airflow direction.
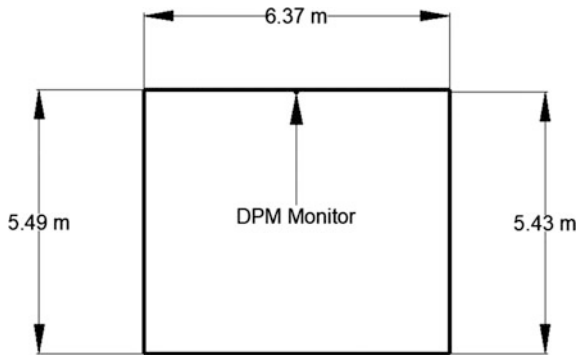


**Fig. 1.** Cross-section of the heading, showing the location of a DPM monitor at location C
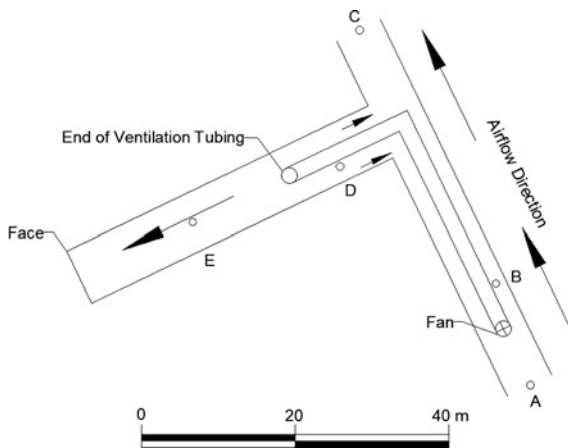


**Fig. 2.** Plan view of the experiment area

## 4.2  CFD Model

A 3D view of the CFD model is shown in Fig. 3. The ventilation tubing, shown in green, has a diameter of 1.067 m. The dimensions of the DPM source are 0.3 m by 0.3 m by 0.3 m. The source was placed 7.5 m away from the working face.
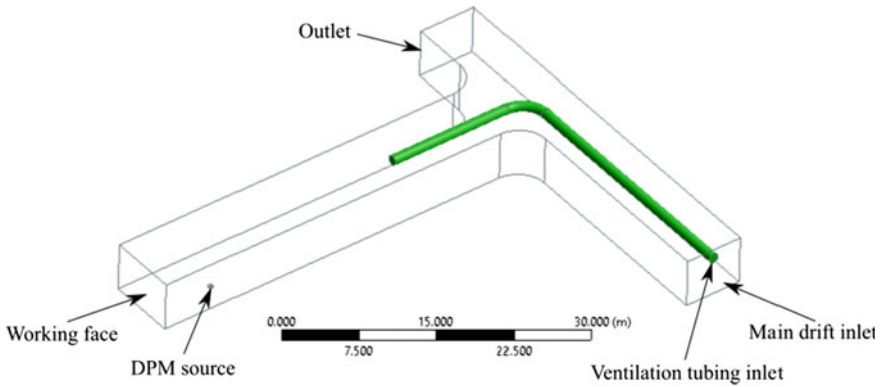


**Fig. 3.**  3D view of the CFD model

The CFD model was created with ANSYS Workbench 17.2. The geometry of the CFD model was established in DesignModeler, and the mesh was built in Meshing. The mesh has a total of 221,855 elements. Inflation layers were created to take care of the low-airflow zone near the wall [15]. Governing equations including mass, momentum, energy, species transport equations are solved in the CFD model. ANSYS Fluent was used as the CFD solver. The standard k-epsilon turbulence model was used to simulate the turbulent flow in the flow domain. The transient simulation was conducted to simulate the airflow and DPM concentration over time. Monitoring points were created at locations C, D, and E in the CFD model to record the DPM concentration distribution over time. These results were compared with the experimental data.

Boundary conditions used in the CFD model are presented in Table 1. The temperature of the diesel plume from the DPM source was set to 594 K [11]. The rest of the data shown in Table 1 were obtained from the ventilation survey. It was assumed that the DPM concentration and velocity magnitude of the diesel exhaust plume are constant when the diesel equipment is working. The velocity profile and the DPM concentration profile over time for the DPM source are shown in Figs. 4 and 5, respectively. DPM concentrations were applied to the CFD model as mass fractions. The DPM concentration shown in Fig. 4 has been converted from mass fraction to show concentration in $\mu g/m^3$.

**Table 1.** Boundary conditions

|  | Area (m²) | Velocity (m/s) | DPM mass fraction | Temperature (K) |
|---|---|---|---|---|
| Ventilation tubing inlet | 0.89 | 35.97 | 0 | 300 |
| Main drift inlet | 34.08 | 1.61 | 0 | 300 |
| Outlet | Outflow boundary condition | | | |
| DPM source inlet | DPM and velocity profiles are shown in Figs. 4 and 5 respectively | | | 594 |
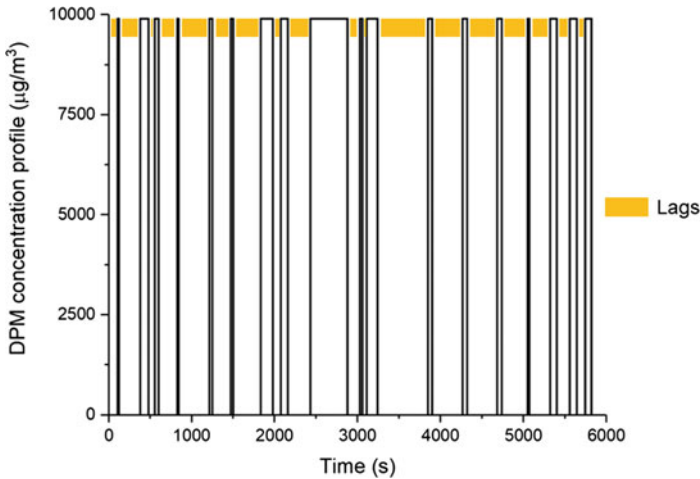


**Fig. 4.** DPM concentration (µg/m³) profile over time at the DPM. *Source* In the CFD model. The DPM concentration in the diesel exhaust plume toggles between a constant value and 0. The lags, highlighted in orange, are periods when no DPM is released

The equipment timeline report provided by the mine indicated that both the LHD and the truck were in the experiment area to carry out the mucking and dumping tasks. Based on the data collected by the DPM monitors, neither the LHD nor the truck was always working in the experiment area, and there were lags when neither of them was operating, or they were out of the experiment area. Here, a lag refers to a period of time when there is no DPM released into the heading. In the CFD model, the lags were modeled by the DPM source not releasing DPM for a period of time. The lags, determined through trial-and-error in the CFD model, are indicated in Figs. 4 and 5. The simulation time is 99 min. The magnitude of the averaged DPM concentrations is indicated in Fig. 4. This DPM profile from the source was set up in Fluent by means of a user-defined function (UDF) [16], and was used to define boundary conditions.

The velocity profile over time is shown in Fig. 5. The velocity magnitude is 24.1 m/s [11]. It is assumed that the velocity of the diesel exhaust plume from the DPM source stays constant over time. The velocity profile is also programmed to a UDF. The UDF of velocity magnitude over time was loaded to ANSYS Fluent solver to define boundary conditions.
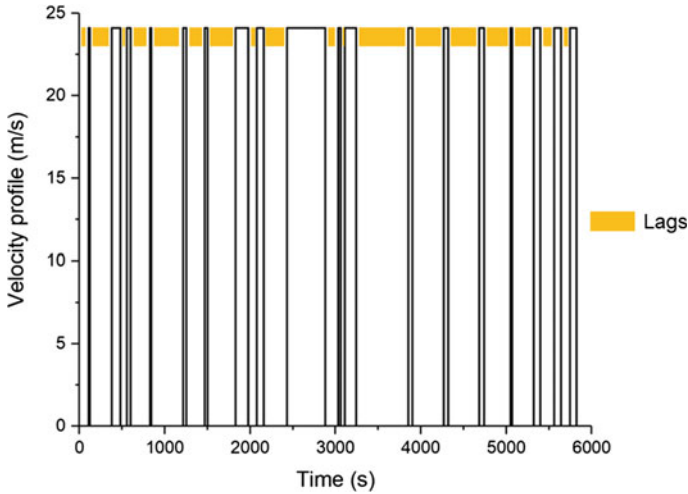
**Fig. 5.** Velocity (m/s) profile over time at the DPM. *Source* The modeled velocity of the diesel exhaust plume toggles between a constant value and zero. The lags, highlighted in orange, are periods when no DPM is released

## 5   Results

The results from the CFD model are shown in the following figures. This simulation could have been conducted on a desktop computer, but to save time HPC was used by means of SHARCNET (the Shared Hierarchical Academic Research Computing Network) [17], and it took 2.9 h to obtain the results.

Figures 6, 7, and 8 present the DPM concentration comparisons between the Experiment and the CFD model at locations D (behind the end of the ventilation tubing), C (the outlet), and E (close to the working face), respectively.

It is seen from Fig. 6 that the results at location D from the CFD model match the experimental data well. To statistically compare the two data sets, the differences of the two data sets were first calculated and a t-test [18] was then conducted on the differences. The p-value [18] was calculated as 0.021. The mean of the samples' differences is not significantly different from the test mean (0) under the significance level of 0.01.

The DPM concentration data from the experiment consists of the discrete values 0, 140, 280, 420, 560 $\mu g/m^3$. Unlike the experimental data, in the CFD model the DPM concentration is not restricted to discrete values and never falls to 0. It is also obvious that the DPM concentration would not change sharply in the heading; the DPM is gradually diluted. The data indicate that the DPM concentrations in the experiment could have errors in the range of 70 $\mu g/m^3$.
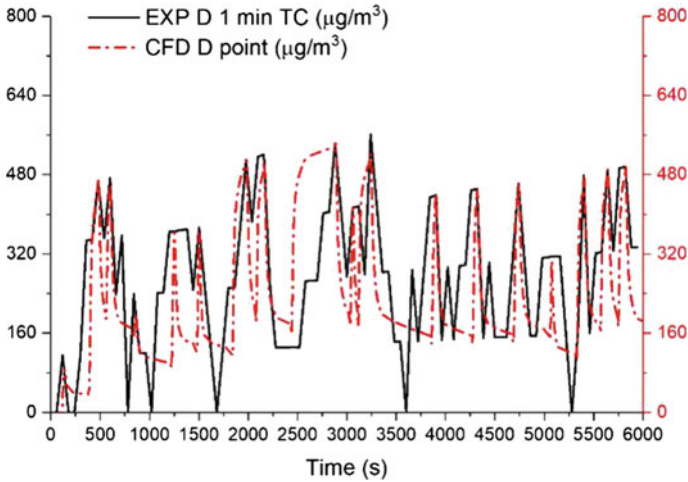
**Fig. 6.** Comparison of DPM concentrations over time at location D, between the CFD model and the experiment. The DPM concentration profile from the CFD model matches well with the experiment
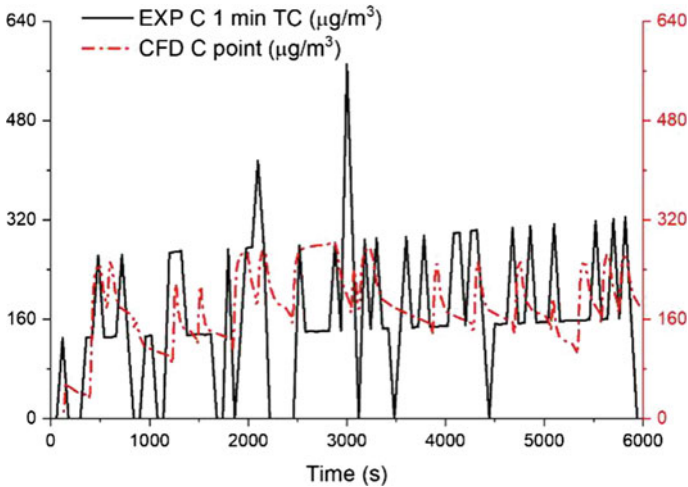


**Fig. 7.** Comparison of DPM concentration distributions over time at location C between the CFD model and the experiment. The main trend of the DPM concentration over time is captured by the CFD model

Similarly, the DPM concentration trend at location C in the CFD model matches that from the experiment as shown in Fig. 7. Considering the long duration of the period simulated, the results from the CFD model have a good agreement with that from the experiment. To statistically compare the two data sets, the differences of the two data sets were first calculated and a t-test was then conducted on the differences.
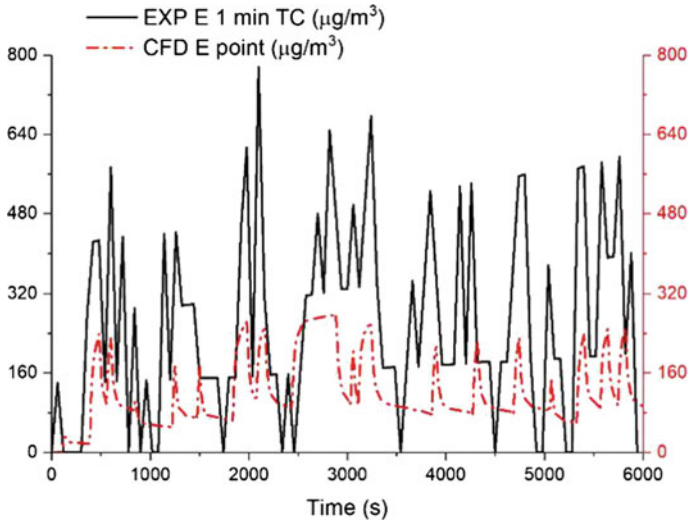
**Fig. 8.** Comparison of DPM concentration distributions over time at location E between the CFD model and the experiment. Magnitudes of the DPM concentration over time do not match well, but the trend matches

The p-value was calculated as 0.094. The mean of the samples' differences is not significantly different from the test mean (0) under the significance level of 0.01. There are two DPM concentration spikes over 400 µg/m$^3$ in the experiment, while the DPM concentration is always below 320 µg/m$^3$ in the CFD model.

For both the experiment and the CFD modeling, the DPM concentration at location C is lower than that at location D. This is expected because location C is near the outlet and there is fresh air coming from the inlet (location A in Fig. 2) to dilute the DPM.

As can be seen in Fig. 8, the trend of the DPM concentration at location E in the CFD model has a good agreement with that from the experiment. To statistically compare the two data sets, the differences of the two data sets were first calculated and a t-test was then conducted on the differences. The p-value was calculated as 7.583E-13. The mean of the samples' differences is significantly different from the test mean (0) under the significance level of 0.01. The DPM concentration peaks in the CFD model are far below those in the experiment. This may occur due to the turbulence at location E. Also, in the experiment, the DPM concentrations at location E are higher than that at locations C and D, however, in the CFD model the DPM concentrations at location E are lower than those at locations C and D.

## 6    Conclusion

A 99-min DPM simulation was presented. According to the literature review, this is the first time that a DPM simulation with that length has been attempted. Based on the results, the proposed CFD approach successfully models the DPM concentration over

the defined period of time (99 min). The DPM profile over time, which is an essential input to the CFD model, was estimated based on the experimental data. For the same heading with the same equipment fleet and the same auxiliary fan speed, the calibrated CFD model can be used to predict the DPM accumulation over time to assist the mine in preventing the formation of a high-DPM zone in the heading.

Compared with the approaches reported in Sect. 2, this approach is more efficient, especially with a larger experimental area and a longer period simulated. The advantage will be more apparent when there are multiple mining areas with various diesel equipment. This CFD approach is a part of an on-going hybrid CFD-network methodology, which aims to find the optimum airflow quantity to dilute contaminants in one or multiple headings to under the regulatory limit. This study makes an important step to achieving the hybrid methodology and determining the adequate airflow volume for a heading.

More experiments are needed to test the repeatability of this approach. Of course, the lags in DPM and velocity profiles will need to be recalculated for each experiment. In addition, the application of statistical analysis will be required in the future to quantify the confidence level of the CFD results compared to the experimental data.

# References

1. Anon.: Threshold limit values for chemical substances and physical agents and biological exposure indices. american conference of governmental industrial hygienists (ACGIH) (2001)
2. Anon.: Health Assessment Document for Diesel Exhaust. U.S. Environmental Protection Agency (EPA). Report EPA/600/8-90/057E (2000)
3. Anon.: Carcinogenic effects of exposure to diesel exhaust. In: National Institute for Occupational Safety and Health (NIOSH), Department of Health and Human Services, Publication, pp. 88–116 (1988)
4. Twigg, M.V., Phillips, P.R.: Cleaning the air we breathe—controlling diesel particulate emissions from passenger cars. Platin. Met. Rev. **53**(1), 27–34 (2009)
5. Grenier, M.G.: Reducing miners' exposure to diesel particulate matter using real-time measurement. In: CIM conference and exhibition (2010)
6. Birch, M.E.: NIOSH manual of analytical methods
7. Bugarski, A.: Integrated approach to reducing exposure of underground miners to diesel particulate matter and gases. In: DPM Workshop. Elko, Nevada, p. 36 (2007)
8. Zheng, Y., Lan, H., Thiruvengadam, M., Tien, J.C.: DPM dissipation experiment at MST's experimental mine and comparison with CFD simulation. J. Coal Sci. Eng. **17**(3), 285–289 (2011)
9. Zheng, Y., Thiruvengadam, M., Lan, H., Tien, C.J.: Effect of auxiliary ventilations on diesel particulate matter dispersion inside a dead-end entry. Int. J. Min. Sci. Technol. **25**(6), 927–932 (2015)

10. Kurnia, J.C., Sasmito, A.P., Wong, W.Y., Mujumdar, A.S.: Prediction and innovative control strategies for oxygen and hazardous gases from diesel emission in underground mines. Sci. Total Environ. **481**, 317–334 (2014)
11. Zheng, Y.: Diesel particulate matter dispersion analysis in underground metal/nonmetal mines using computational fluid dynamics (2011)
12. Flir Systems. Airtec diesel particulate monitor operators manual. Albuquerque, NM, USA
13. Flir systems.: Airtec measurement calculations. Albuquerque, NM, USA
14. McPherson, M.J.: Subsurface ventilation and environmental engineering. Mine Ventilation Services, Inc., Fresno, CA, USA
15. Feroze, T., Genc, B.: Estimating the effects of line brattice ventilation system variables in an empty heading in room and pillar mining using CFD. J. South. African Inst. Min. Metall. **116**(7), 1143–1152 (2016)
16. ANSYS Inc. ANSYS Fluent 12.0 UDF Manual. Canonsburg, PA
17. Bauer, M.A.: High performance computing: The Software Challenges. In: Proceedings of the 2007 International Workshop on Parallel Symbolic Computation—PASCO '07. ACM Press, London, Ontario, Canada, pp. 11–12 (2007)
18. Ross, A., Willson, V.L.: ONE-SAMPLE T-TEST. In: Basic and advanced statistical tests. SensePublishers, Rotterdam, pp. 9–12 (2017)

# Part IX
# Spontaneous Combustion I

# Risk Evaluation of the Spontaneous Combustion of Coal for Underground Coal Mining

Zhang Yutao[1(✉)], Liu Yurui[1], Jerry C. Tien[2], Li Yaqing[1], and Shi Xueqiang[1]

[1] Xi'an University of Science & Technology, Xi'an, Shaanxi, People's Republic of China
ytzhang@xust.edu.cn
[2] Monash University, Clayton, VIC 3800, Australia

**Abstract.** In underground coal mining, one of the biggest challenges is spontaneous combustion, which can often result in huge economic losses, serious environmental problems, safety hazards and fatalities. The occurrence of spontaneous combustion depends on many factors, primarily including coal properties, mining methods, the advance rate of working face, ventilation, and surrounding geological conditions. Consequently, a comprehensive evaluation to systematically assess all these factors is necessary during mine planning to control the spontaneous combustion hazard. The main contributing factors to the spontaneous combustion of coal were collected, optimized, and then categorized into four groups, which were further subdivided into thirty eight subfactors. Analytic Hierarchy Process (AHP) was utilized to evaluate all contributing factors and help build a comprehensive evaluating system. The factors in the hierarchy structure were then weighed and integrated with the help of ten experts in spontaneous combustion. The results indicate that coal rank plays the most significant role in the risk of spontaneous combustion, followed by the inhibiting agent injection and the monitoring system. The risk of spontaneous combustion for a mine was classified according to the comprehensive evaluation index proposed. Four coal mines were then selected to illustrate the application of this evaluation system. The results indicate that a mine with low-rank coal may still have a low risk of spontaneous combustion, if effective precautions are used.

**Keywords:** Spontaneous combustion · Underground coal mining Risk evaluation

## 1 Introduction

In most countries, coal has always been the leading energy source in the energy structure. In the United States between 1978 and 1988, approximately 15% of underground coal mine fires were caused by the spontaneous combustion of coal. More than 17% of reported underground coal mine fires for the period 1990–1999 were caused by spontaneous combustion [1]. Another 10 underground spontaneous

combustion events were reported for the period 2000–2006 [2]. When methane is present, a spontaneous combustion may even become the trigger of a catastrophic explosion.

Numerous studies on the mechanism of coal spontaneous combustion have been conducted for the prevention and suppression of coal fires. The effects of volatile matter, moisture content, ash content, inorganic components, particle size and petrographic composition of coals were extensively studied [3–6]. In addition, various evaluation indices for evaluating the propensity of spontaneous combustion have been developed, such as minimum self-heating temperature, initial rate of heating and total temperature rise, R70 self-heating rate, oxygen absorption by gas chromatography, U Index, crossing point temperature, oxidation kinetics, activation energy [7–10]. However, these indexes were only proposed from the aspects of coal properties.

Field studies proved that the occurrence of spontaneous combustion is dependent on not only coal properties, but also multiple factors such as ventilation, geological conditions, mining methods, prevention measures, and so forth [11, 12]. Consequently, a unilateral indicator is not able to represent the real hazard of coal spontaneous combustion. Instead, a comprehensive evaluation system that can handle multi-factors is necessary to systematically assess the spontaneous combustion hazard.

To handle the multi-factors affecting spontaneous combustion, a neural network model [13] and a non-parametric discriminant analysis model [14] were utilized to predict the incubation period of spontaneous combustion. However, a large number of learning samples were needed to train the models. NIOSH has developed an application program to evaluate the hazard of spontaneous combustion. Nevertheless, a quantitative evaluating result could not be obtained from the program.

In the field, besides the hazard of spontaneous combustion, it is desirable that the individual contribution of each factor to spontaneous combustion be known so that mine operators can design effective measures to efficiently prevent and control coal spontaneous combustion. Analytic Hierarchy Process (AHP) was employed in this study to judge the significance of each factor and to evaluate the hazard of spontaneous combustion in a mine.

## 2    The Evaluation System for the Hazard of Spontaneous Combustion

AHP, developed by Saaty [15], is a structured technique for organizing and analyzing complex decisions. When using AHP, factors must be successively collected, optimized, categorized, weighted and synthesized.

### 2.1    Hierarchical Structure of the Factors

The factors impacting the spontaneous combustion of coal were collected by both reviewing available literature and conducting field investigations. The factors in the hierarchical structure needed to be representative, explicit, and independent. During the process of classification, some factors or subfactors were eliminated, such as inorganic salt content, elevation of the coalfield, and so forth. Their impacts are not quantified

and require further investigation [9, 13, 16]. Four main factors and thirty eight sub-factors were ultimately determined in the hierarchical structure.

The final hierarchical structure is shown in Fig. 1. The "Coal Spontaneous Combustion Hazard" is set to be the goal, under which the factors include coal properties, geological conditions, mining conditions and fire prevention measures. There are also subfactors subordinate to each factor.
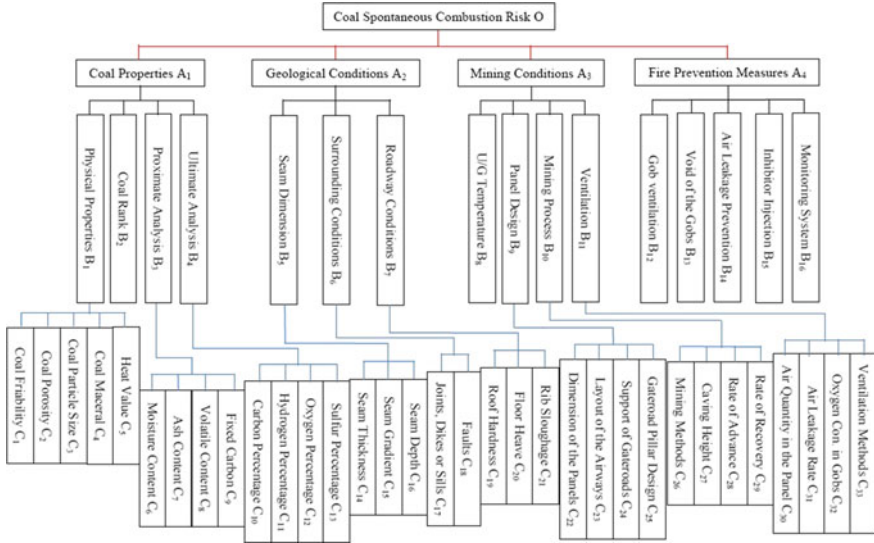


**Fig. 1.** Hierarchy structure of the factors impacting spontaneous combustion

## 2.2 Weighting of the Factors

Relative weights among the factors/subfactors of the hierarchy should be established by making a series of judgments based on pairwise comparisons. Numbers from 1 to 9 are used to express the relative importance of one factor/subfactor over another (Table 1).

**Table 1.** Principle of pairwise comparisons in AHP (readjust table to stay out of margin)

| Pairwise comparison | 1 | 3 | 5 | 7 | 9 | 2, 4, 6, 8 |
|---|---|---|---|---|---|---|
| Relative importance | Equal | Moderate | Strong | Very Strong | Extreme | Intermediate values |

Judgment matrices in the form of $(a_{ij})_{n \times n}$ can be constructed based on the pairwise comparison results. The value $a_{ij}$ represents the relative importance of $a_i$ over $a_j$ and $n$ is the number of the factors or subfactors.

Ten experts in the spontaneous combustion of coal were invited to weigh the factors to reduce any bias. The experts' opinions were assumed to have identical

authority and thus were weighted equally. The ultimate judgment matrix was listed in Tables 2, 3 and 4 by geometrically averaging the ten experts' judgments.

**Table 2.** Judgment matrix for weights of factors under O

| O | $A_1$ | $A_2$ | $A_3$ | $A_4$ |
|---|---|---|---|---|
| $A_1$ | 1 | 3 | 4 | 2 |
| $A_2$ | 1/3 | 1 | 2 | 1/2 |
| $A_3$ | 1/4 | 1/2 | 1 | 1/2 |
| $A_4$ | 1/2 | 2 | 2 | 1 |

**Table 3.** Judgment matrix for weights of factors under $A_1$–$A_4$

| $A_1$ | $B_1$ | $B_2$ | $B_3$ | $B_4$ | $A_3$ | $B_8$ | $B_9$ | $B_{10}$ | $B_{11}$ |
|---|---|---|---|---|---|---|---|---|---|
| $B_1$ | 1 | 1/5 | 1/3 | 1/3 | $B_8$ | 1 | 1/3 | 1/4 | 1/6 |
| $B_2$ | 5 | 1 | 1 | 1 | $B_9$ | 3 | 1 | 1 | 1/2 |
| $B_3$ | 3 | 1 | 1 | 1 | $B_{10}$ | 4 | 1 | 1 | 1/2 |
| $B_4$ | 3 | 1 | 1 | 1 | $B_{11}$ | 6 | 2 | 2 | 1 |
| $A_2$ | $B_5$ | $B_6$ | $B_7$ | $A_4$ | $B_{12}$ | $B_{13}$ | $B_{14}$ | $B_{15}$ | $B_{16}$ |
| $B_5$ | 1 | 1/2 | 1 | $B_{12}$ | 1 | 2 | 2 | 1/6 | 1/4 |
| | | | | $B_{13}$ | 1/2 | 1 | 1 | 1/9 | 1/7 |
| $B_6$ | 2 | 1 | 2 | $B_{14}$ | 1/2 | 1 | 1 | 1/9 | 1/7 |
| $B_7$ | 1 | 1/2 | 1 | $B_{15}$ | 6 | 9 | 9 | 1 | 1 |
| | | | | $B_{16}$ | 4 | 7 | 7 | 1 | 1 |

**Table 4.** Judgment Matrix for Weights of Factors under $B_1$–$B_{11}$

| $B_1$ | $C_1$ | $C_2$ | $C_3$ | $C_4$ | $C_5$ | $B_3$ | $C_6$ | $C_7$ | $C_8$ | $C_9$ | $B_4$ | $C_{10}$ | $C_{11}$ | $C_{12}$ | $C_{13}$ |
|---|---|---|---|---|---|---|---|---|---|---|---|---|---|---|---|
| $C_1$ | 1 | 1/8 | 1/7 | 1/4 | 1/3 | $C_6$ | 1 | 3 | 1 | 3 | $C_{10}$ | 1 | 1 | 1/2 | 1/6 |
| $C_2$ | 8 | 1 | 1 | 3 | 4 | $C_7$ | 1/3 | 1 | 1/3 | 1 | $C_{11}$ | 1 | 1 | 1/2 | 1/6 |
| $C_3$ | 7 | 1 | 1 | 2 | 3 | $C_8$ | 1 | 3 | 1 | 3 | $C_{12}$ | 2 | 2 | 1 | 1/3 |
| $C_4$ | 4 | 1/3 | 1/2 | 1 | 1 | $C_9$ | 1/3 | 1 | 1/3 | 1 | $C_{13}$ | 6 | 6 | 3 | 1 |
| $C_5$ | 3 | 1/4 | 1/3 | 1 | 1 | | | | | | | | | | |
| $B_5$ | $C_{14}$ | $C_{15}$ | $C_{16}$ | | | $B_6$ | $C_{17}$ | | $C_{18}$ | | $B_7$ | | $C_{19}$ | $C_{20}$ | $C_{21}$ |
| $C_{14}$ | 1 | 1 | 2 | | | $C_{17}$ | 1 | | 1/2 | | $C_{19}$ | | 1 | 2 | 2 |
| $C_{15}$ | 1 | 1 | 2 | | | $C_{18}$ | 2 | | 1 | | $C_{20}$ | | 1/2 | 1 | 1 |
| $C_{16}$ | 1/2 | 1/2 | 1 | | | | | | | | $C_{21}$ | | 1/2 | 1 | 1 |
| $B_9$ | $C_{22}$ | $C_{23}$ | $C_{24}$ | $C_{25}$ | | $B_{10}$ | $C_{26}$ | $C_{27}$ | $C_{28}$ | $C_{29}$ | $B_{11}$ | $C_{30}$ | $C_{31}$ | $C_{32}$ | $C_{33}$ |
| $C_{22}$ | 1 | 1 | 1 | 1 | | $C_{26}$ | 1 | 1 | 1/2 | 1/3 | $C_{30}$ | 1 | 1/4 | 1/4 | 1/3 |
| $C_{23}$ | 1 | 1 | 1 | 1 | | $C_{27}$ | 1 | 1 | 1/2 | 1/3 | $C_{31}$ | 4 | 1 | 1 | 2 |
| $C_{24}$ | 1 | 1 | 1 | 1 | | $C_{28}$ | 2 | 2 | 1 | 1/2 | $C_{32}$ | 4 | 1 | 1 | 2 |
| $C_{25}$ | 1 | 1 | 1 | 1 | | $C_{29}$ | 3 | 3 | 2 | 1 | $C_{33}$ | 3 | 1/2 | 1/2 | 1 |

## 2.3    Calculation of the Overall Weights

A set of overall weights for the hierarchy can be obtained by synthesizing these judgments using following equations.

$$W_i' = \sqrt[n]{a_{i1} \cdot a_{i2} \cdots a_{in}} \tag{1}$$

$$W_i = W_i' / \sum_{i=1}^{m} W_i' \tag{2}$$

where, $W_i'$ is the original weight of factor $i$; $W_i$ is the normalized weight of factor $i$ in this group. Based on Eqs. (1) and (2), the weight for each factor/subfactor in its group can be calculated. The importance of every factor/subfactor within its group can then be indicated.

## 2.4    Consistency Check of the Judgments

The purpose of a Consistency Check is to see whether the judgment matrix is reliable and acceptable. This can be done using Eq. (3) as follows:

$$CI = \frac{\lambda_{\max} - n}{n - 1} \tag{3}$$

where, $CI$ is the consistency index, $\lambda_{\max}$ is the maximum eigenvalue of the judgment matrix. The maximum eigenvalue can be calculated using Eq. (4):

$$\lambda_{\max} = \sum_{i=1}^{n} \lambda_i / n \tag{4}$$

where, $\lambda_i$ is the eigenvalue of the pairwise comparisons judgment matrix. This matrix can be obtained with

$$\lambda_i = \sum_{j=1}^{n} a_{ij} W_j / W_i \tag{5}$$

When the judgment matrix has absolute consistency, $CI = 0$. A large CI value represents a poor consistency. The ratio of consistency index and the random index can be employed to check whether or not the consistency is satisfactory.

$$CR = \frac{CI}{RI} \tag{6}$$

where, $CR$ is the ratio of consistency index to random index. $RI$ is the random index that can be read from Table 5.

**Table 5.** The value of random index given by Saaty [17]

| n | 1 | 2 | 3 | 4 | 5 | 6 | 7 | 8 | 9 |
|---|---|---|---|---|---|---|---|---|---|
| RI | 0 | 0 | 0.58 | 0.90 | 1.12 | 1.24 | 1.32 | 1.41 | 1.45 |

If the value of the CR is smaller than 0.10, the consistency of the judgment matrix is thought to be acceptable. Otherwise, the judgment matrix needs to be revised.

According to Eq. (3)–(6), the parameters related to the consistency check were calculated. All of the CR values were less than 0.10. The small CR values indicated that all of the judgment matrices are consistent and the results are reliable as well.

## 2.5   The Weight of Each Subfactor to the Goal

In practice, the subfactors are more specific than the factors. They can be directly obtained by measurements or tests. Thus it is necessary and useful to know the direct impact of every subfactor on the risk of spontaneous combustion. The weight of each subfactor can be calculated by Eq. (7),

$$W_{oi} = \varepsilon W_{A,i} \cdot W_{B,i} \cdot W_{C,i} \tag{7}$$

where, $W_{Oi}$ is the impact of the $i$th subfactor on the goal, $W_{C,i}$ is the weight of $C_i$ within the group, $W_{A,i}$ and $W_{B,i}$ are the weights of the factors that $C_i$ belongs to, $\varepsilon$ is the correction factor.

The correction factor is produced to prevent the extreme disparity generated in the multilayer judgment along the subfactors' weights. For an evaluation system with a small number of layers (like this case), the correction factor can be considered one. Table 6 lists the impact of each subfactor on spontaneous combustion ordered by weighting importance.

Coal rank plays the most important role in affecting the risk of spontaneous combustion. Consequently, people will take precautions to avoid spontaneous combustion based on coal rank in the absence of any propensity rating data. However, coal rank is an intrinsic property of coal. For the coal in a certain panel, the coal rank is almost unchanged and therefore uncontrolled.

The second important subfactor, "inhibiting agent injection", is completely controllable. A regular injection of inhibiting agent, such as foam, slurry, and an inert colloid, can effectively reduce or even eradicate the occurrence of spontaneous combustion.

A monitoring system is necessary for early detection and tracking of spontaneous combustion status. Monitoring is the prerequisite to perform the early forecast of spontaneous combustion and the incipient firefighting. The impacts of other subfactors will not be elaborated here due to the limiting length of this dissertation.

**Table 6.** Impact of each subfactor on spontaneous combustion (readjust table to stay out of margin)

| Subfactor | Weight (%) | Subfactor | Weight (%) | Subfactor | Weight (%) |
|---|---|---|---|---|---|
| Coal rank | 13.25 | Oxygen concentration in gobs | 1.82 | Ventilation methods | 0.84 |
| Inhibiting agent injection | 11.88 | Air leakage rate | 1.74 | Seam gradient | 0.76 |
| Monitoring system | 9.25 | Carbon percentage | 1.65 | Seam depth | 0.76 |
| Volatile content | 6.10 | Fixed carbon | 1.54 | Air Quantity in the panel | 0.69 |
| Moisture content | 5.61 | Seam thickness | 1.52 | Layout of the airways | 0.64 |
| Oxygen percentage | 4.30 | Average particle size | 1.52 | Coal maceral | 0.53 |
| Faults | 4.03 | Rate of advance | 1.30 | Coal friability | 0.49 |
| Sulfur percentage | 3.76 | Joints, dikes, sills | 1.23 | Gateroad pillar design | 0.45 |
| Rate of recovery | 3.64 | Void of the gobs | 1.12 | Heat value | 0.43 |
| U/G temperature | 3.60 | Hydrogen percentage | 1.00 | Mining methods | 0.40 |
| Gob ventilation | 2.92 | Roof hardness | 0.96 | Dimension of the panels | 0.38 |
| Air leakage prevention | 2.67 | Floor heave | 0.96 | Support of the gateroads | 0.38 |
| Coal porosity | 2.21 | Ash content | 0.91 | | |
| Rib sloughage | 1.92 | Caving height | 0.85 | | |

## 2.6    Comprehensive Evaluation of the Spontaneous Combustion Risk

The comprehensive evaluation index (CEI) of spontaneous combustion can be calculated with Eq. (8),

$$CEI = \Psi \sum_{i=1}^{m} C_i \cdot P_i \tag{8}$$

where, CEI is the comprehensive evaluation index, $\Psi$ is the modification factor, $C_i$ is the combined weight of the ith factor, $P_i$ is the actual value of the ith factor, m is the number of the factors.

A comprehensive evaluation requires the integration of multiple factors. All of these factors should be quantified when applying Eq. (8). Only a few, however, can be feasibly measured quantitatively, including sulfur percentage, moisture content, seam thickness, and so forth. Some, like monitoring system, ventilation methods and mining methods, are difficult to measure. They are even more difficult to quantify.

In this study, an experts grading method was used. The rating of each factor was between −3 and 3. The rating value depends upon the impact on spontaneous combustion. A positive value represents a promotion effect; a negative value indicates an inhibitory effect.

To simplify the evaluating system, only the top ten subfactors (i.e. the ones above "U/G Temperature") were selected as representatives. These subfactors comprise almost 70% of effects. The detailed rating of each subfactor is listed in Table 7.

**Table 7.** Rating criteria of the top ten subfactors

| Subfactor | Rating criteria | Rating | Notes |
|---|---|---|---|
| Coal rank | Anthracite | 0 | |
| | Bituminous | 1 | |
| | Subbituminous | 2 | |
| | Lignite | 3 | |
| Inhibiting agent injection | Yes | −3 to −1 | Dependent on both the execution conditions and the effects |
| | No | 0 | |
| Monitoring system | Yes | −3 to −1 | Dependent on the layout of the detectors |
| | No | 0 | |
| Volatile content | 0–10% | 0 | |
| | 10–20% | 1 | |
| | 20–37% | 2 | |
| | >37% | 3 | |
| Moisture content | 0–1.5% | 1 | |
| | 1.5–5 % | 2 | |
| | >5 % | −1 to −3 | The larger the moisture content is, the smaller the grade will be |
| Oxygen percentage | 0–5% | 1 | |
| | 5–10% | 2 | |
| | >10% | 3 | |
| Faults | Yes | 1–3 | Dependent on both their sizes and their impacts on spontaneous combustion |
| | No | 0 | |
| Sulfur percentage | 0–1% | 1 | |
| | 1–3% | 2 | |
| | >3% | 3 | |
| Rate of recovery | >90% | 1 | |
| | 75–90% | 2 | |
| | <75% | 3 | |
| U/G temperature | <15 °C | 0 | |
| | 15–20 °C | 1 | |
| | 20–26 °C | 2 | |
| | >26  °C | 3 | |

Some ratings in Table 7 can be specifically determined according to the evaluating system, such as coal rank, sulfur percentage, and rate of recovery. With respect to ratings, including inhibiting agent injection, monitoring system, and faults, experts can decide their ratings depending on real situations. The flexibility makes the evaluating system more flexible and helps increase the accuracy. For example, if the faults are located in the rock strata and have few effects on the coal seam, a small rating such as one can be given. If the faults are located in or near to the coal seam leading to a serious air leakage, a high rating such as 3 can be given.

For the rating criteria of sulfur percentage, moisture content, volatile content, oxygen percentage, and rate of recovery, experts' opinions and corresponding references were obtained from to Singh and Demirbilek [18], Singh et al. [19], Luppens et al. [20], and Deng [21]. The value $\Psi$ in Eq. (9) is set to be 78.6. Thus, the calculated *CEI* is between −54 and 100.

$$CEI = 78.6 \sum_{i=1}^{m} C_i \cdot P_i \qquad (9)$$

The evaluation system was applied to a number of coal mines for trialing. The risk classification listed in Table 8 was adopted.

**Table 8.** Risk classification of spontaneous combustion in coal mines

| CEI | <0 | 0–30 | 31–55 | >55 |
|-----|-----|------|-------|------|
| Risk | No | Low | Medium | High |

The risk was classified into four levels. If the calculated *CEI* is less than zero, the mine is completely free of spontaneous combustion issues. Generally, coal mines with zero risk have relatively high-rank coal and are equipped with adequate prevention measures as well. If a mine has high-rank coal or low-rank coal with excellent prevention measures of spontaneous combustion, *CEI* may fall between 0 and 30. This coal mine has a low risk of spontaneous combustion. Medium risk of spontaneous combustion generally applies to a coal mine with low-rank coal and fair prevention measures of spontaneous combustion. A coal mine with low-rank coal and bad prevention measures at the same time may suffer high risk of spontaneous combustion.

## 3    Case Studies

Three coal mines were selected to test the application of the evaluating system. The information obtained from the mines and their risk evaluation results are given in Table 10. Mine C and Mine C' are the same mine but at different stages of development. In detail, Mine A was built in the 1990s and is located in the Powder River Basin in southeast Montana and northeast Wyoming, USA. The mine produces anthracite coal with a coal production of 3 megatons. The currently active working face is 218 m under the ground with a recovery rate of 85%. Retreating longwall mining method is used in this working face. The sulfur content, moisture content and volatile content of the coal are pretty low. Mine B was built in 1989, located in Illinois Basin, USA. The mine has a total coal production of 3.8 megatons with a mining depth of 250 m. Approximate 85% of the coal was recovered and the coal rank of this mine is subbituminous coal. Mine C is located in West Virginia, USA and the mine produces lignite. The coal production of this mine is about 3 megatons. The mine has a high recovery rate, but suffered serious spontaneous combustion problem.

The risk of spontaneous combustion for the three coal mines can be obtained from the CEI in Table 9. The rank among them, from low to high, is Mine A < Mine C ' < Mine B < Mine C. The low risk in Mine A is a result of both its high coal rank (anthracite) and low sulfur percentage (0.7%). Essentially, the coal in Mine A has a low spontaneous combustion propensity. Therefore, strict precautions are not indispensable and a regular inhibiting agent injection is not required.

Mine B has the highest spontaneous combustion risk, primarily because of the spontaneous combustion propensity and the surrounding geological conditions, like faults. Both a poor execution of the inhibiting agent injection and a defective monitoring system further add the possibility of spontaneous combustion.

Due to the low coal rank and bad prevention measures, Mine C has a high risk of spontaneous combustion. Spontaneous combustion in Mine C used to occur once a week. Then, Mine C started to upgrade monitoring system and conduct regular inhibitor injection from January, 2009. Only one sign of spontaneous combustion has been observed since then. The mine currently has a low risk of spontaneous combustion (Mine C' in Table 9b).

**Table 9.** **a** Risk evaluation for mines A and B, **b** Risk Evaluation for Mines C (readjust table to stay out of margin)

| Subfactor | Mine A | | Mine B | |
|---|---|---|---|---|
| | Grade | Note | Grade | Note |
| **(a)** | | | | |
| Coal rank | 0 | Anthracite | 2 | Subbituminous |
| Inhibiting agent injection | 0 | No | −1 | Inject only when sponcom signs appear |
| Monitoring system | −1 | Only monitors return airway | −2 | Monitors neutral and return airway |
| Volatile content | 0 | 7.8% | 2 | 24.3% |
| Moisture content | 2 | 1.8% | 2 | 2.3% |
| Oxygen percentage | 1 | 3.2% | 2 | 6.3% |
| Faults | 1 | Small ones and have only a little affect | 3 | Two big ones and near to the coal seam |
| Sulfur percentage | 1 | 0.7% | 2 | 1.5% |
| Rate of recovery | 2 | 85% | 2 | 85% |
| U/G temperature | 1 | 18 | 1 | 20 |
| *CEI* | 20 | | 46 | |
| Risk | Low | | Medium | |

| Subfactor | Mine C | | Mine C′ | |
|---|---|---|---|---|
| | Grade | Note | Grade | Note |
| **(b)** | | | | |
| Coal rank | 3 | Lignite | 3 | Lignite |
| Inhibiting agent injection | −1 | Inject only when sponcom occurs | −3 | Inject regularly and frequently |
| Monitoring system | −1 | Only monitors return airway | −3 | Tube bundle monitoring system |
| Volatile content | 3 | 39.0% | 3 | 39.0% |
| Moisture content | 2 | 3.9% | 2 | 3.9% |
| Oxygen percentage | 2 | 8.7% | 2 | 8.7% |
| Faults | 1 | A small one with few air leakage | 1 | One small one with few air leakage |
| Sulfur percentage | 2 | 1.8% | 2 | 1.8% |
| Rate of recovery | 2 | 91% | 1 | 91% |
| U/G temperature | 1 | 18 | 1 | 18 |
| *CEI* | 62 | | 26 | |
| Hazard | High | | Low | |

## 4    Conclusions

Evaluation of the spontaneous combustion hazard provides significant guidelines during the prevention and suppression of coal fires. The following conclusions can be drawn based on the study in this paper.

(1) AHP is applicable to handle the multi-factors and help build the comprehensive evaluating system of spontaneous combustion of coal for the entire mine.

(2) Coal rank plays the most significant role in the hazard of spontaneous combustion, followed by the inhibiting agent injection and the monitoring system. So the spontaneous combustion problem can be well addressed as long as the primary contributive factors are handled.

(3) The built evaluation system can be used to assess the risk of spontaneous combustion for an entire mine. Case studies proved the effectiveness of the system. The results also indicate that a mine with high-rank coal may still have a low risk of spontaneous combustion, if effective precautions are utilized.

## References

1. De Rosa, M.I.: Analysis of mine fires for all U.S. underground and surface coal mining categories: 1990–1999. Information Circular 9470 (2004)
2. Yuan, L., Smith, A.C.: Simulating sponcom—looking at CFD modeling of spontaneous heating in longwall gob areas. Coal USA Magazine, (8)32–33 (2009)
3. Chandra, D., Prasad, Y.V.S.: Effect of coalification on spontaneous combustion of coals. Int. J. Coal Geol. **16**(1–3), 225–229 (1990)
4. Cornelia, A.B., Marc, A.R., Nikos, E.M., Carmen, A.B., Corina, C.B., Andreea, C.J.: Addressing the impact of environmental xenobiotics in coal-fired flue gas. Sustainability **7** (3), 2678–2694 (2015)
5. Sujanti, W., Zhang, D.: A laboratory study of spontaneous combustion of coal: the influence of inorganic matter and reactor size. Fuel **78**(5), 549–556 (1999)
6. Zhang, Y., Wang, D.: Study on influence of water on low-temperature oxidation of coal. Saf. Coal Mines **11**, 1–4 (2007)
7. Banerjee, S.C.: Prevention and combating mine fires. A.A. Balkema Publishers, pp. 376 (2000)
8. Qi, Y., Qian, G.: Method for identifying tendency of coal to spontaneous combustion by oxygen absorption with chromatograph. Coal **2**, 5–9 (1996)
9. Sensogut, C., Cinar, I.: A research on the tendency of ermenek district coals to spontaneous combustion. Mineral Resour. Eng. **9**(4), 421–427 (2000)
10. Smith, A.C., Lazzara, C.P.: Spontaneous Combustion Studies of U.S. Coals, USBM RI 9079, pp. 28 (1987)
11. Beamish, B.B., Lau, A.G., Moodie, A.L., Vallance, T.A.: Assessing the self-heating behavior of Callide coal using a 2-metre column. J. Loss Prev. Process Ind. **15**(5), 385–390 (2002)

12. Zhou, F., Wang, D.: Directory of recent testing methods for the propensity of coal to spontaneous combustion. J. Fire Sci. **22**(2), 91–96 (2004)
13. Wang, G., Zhang, X., Xiao, Y.: Prediction of self-ignition duration of coal with feed-forward multi-layer artificial neural network. J. Hum. Univ. Sci. Technol. **27**, 21–22 (2008)
14. Chen, J.: Numerical simulation of a pulverized coal combustion two-phase flow. J. Xi'an Univ. Sci. Technol. **28**, 293–294 (2008)
15. Saaty, T.L.: A scaling method for priorities in hierarchical structures. J. Math. Psychol. **15**(3), 234–281 (1977)
16. Xu, J.: Determination theory of coal spontaneous combustion zone. Coal Industry Press, pp. 288 (2001)
17. Saaty, T.L.: Axiomatic foundation of the analytic hierarchy process. Manage. Sci. **32**(7), 841–855 (1986)
18. Singh, R.N., Demirbilek, S.: Statistical appraisal of intrinsic factors affecting spontaneous combustion of coal. Mining Sci. Technol. **4**, 155–165 (1987)
19. Singh, R.N., Shonhardt, J.A., Terezopoulosa, N.: A new dimension to studies of spontaneous combustion of coal. Mineral. Resour. Eng. **11**, 147–163 (2002)
20. Luppens, J.A., Rohrbacher, T.J., Osmonson, L.M.: Coal resource availability, recoverability, and economic evaluations in the united states—a summary. U.S. Department of the Interior, pp. 21 (2009)
21. Deng J.: Coal chemistry. pp. 167. Metallurgical Industry Press, Beijing (2011)

# The Effect of Moisture in Air
# on the Spontaneous Combustion
# Characteristics of Coal

Ma Dong[1,2,3] and Qin Botao[1,2,3(✉)]

[1] Key Laboratory of Coal Methane and Fire Control, Ministry of Education,
China University of Mining and Technology, Xuzhou 221116, China
{madongcumt, qbt2003}@l63.com
[2] Faculty of Safety Engineering, China University of Mining and Technology,
Xuzhou, Jiangsu 221116, China
[3] State Key Laboratory of Coal Resources and Mine Safety, China University
of Mining and Technology, Xuzhou Jiangsu 221008, China

**Abstract.** This study evaluated the effects of moisture in air on spontaneous combustion characteristics of coal. Air with four relative humidities (dry air, 30, 60 and 100%) were used in the study. The crossing point temperature (CPT) and oxidation products were measured using a customized spontaneous combustion system. The results showed that the CPT values were determined to be 153, 151, 150 and 148 °C under four humidities, respectively. The concentration of oxidation productions increased with the increase of air humidity. The thermal characteristics of coal were also studied using thermogravimetry and differential scanning calorimeter (TG-DSC) methods. It was found that the second peak of heat flow appeared to be 417.28, 411.25, 402.64 and 385.68 °C, respectively under four different humidities. As a consequence, the water adsorbed had expedited the coal oxidation to the next stage.

**Keywords:** Coal spontaneous combustion · Humidity · Oxidation products
TG-DSC

## 1   Introduction

Air humidity is one of the important factors causing spontaneous combustion of coal, which have been researched over a long period [1]). Because of the influence of underground water, earth's surface water and rainfall, ordinary air can have high and can fluctuate depending on the surrounding environment. In China, the underground air humidity of some mines could reach as high as 95%, such as Xin'an Coal Mine, where spontaneous combustion can occur frequently.

Many investigators have researched on the effects of air humidity on spontaneous combustion of coal and a number of works have been published. Scott studied the effects of moisture on spontaneous heating of sub-bituminous. The experiments results demonstrated the importance of humidity in spontaneous heating of coal [2]. Bhat and Agarwal [3] took a single isothermal particle as a research object, to simulate the effect

of relative humidity of air on spontaneous combustion of coal. The results showed that higher relative humidities favor spontaneous combustion.

The water vapor in the atmosphere is absorbed by coal particles from ambient atmosphere and release heat in the process of condensation under appropriate conditions [4]. The rate and amount of heat release by sorption of water vapor is much more than by coal oxidation [5], which can raise the temperature of coal particles and contribute to the process of coal self-heating [6]. However, A. Küçük et al. attained the contradictory experimental results, which stated that with the reduction of air humidity, the liability of spontaneous combustion of lignite was increased [7].

In general, the effects of humidity on coal spontaneous combustion characteristics is not completely understood. Most previous investigations state the sorption of water vapor can affect the propensity of coal spontaneous combustion, although the extent of which is unclear, especially when the humidities in the environment change. In this paper the crossing point temperature, oxidation products, and thermal characteristics of coal under different humidities are measured, and their effects on coal spontaneous combustion characteristics are evaluated.

## 2  Experimental

### 2.1  Materials Preparation

A gas-fat coal sample was collected from Xin'an Coal Mine in China, then sealed it and sent to the laboratory. According to the ASTM standards (ASTM D2013-72), the coal sample was stored in an oxygen-free vacuum box after stripping the oxidation layer. Next, the sizes of coal particles in the ranges of 0.18–0.38 mm and 0.096–0.15 mm were sieved and dried at 40 °C for 48 h to remove the moisture of coal sample. After that, coal samples were placed in a vacuum bag at room temperature to be used in the experiment. Table 1 lists the proximate and ultimate analysis of coal samples used. Dry air and humid air with 30, 60, 100% relative humidities (RH) supplied by Huazhong Gas Co., Ltd. were stored in the bottle at room temperature ready to be used in the study.

**Table 1.**  Analyses of coal sample used

| Coal sample | Proximate analysis, wt% (air-dry basis) | | | | Ultimate analysis, wt% (air-dry basis) | | | | |
|---|---|---|---|---|---|---|---|---|---|
| | Moisture | Ash | VM | FC | C | H | N | S | O |
| Xin'an gas-fat coal | 2.31 | 13.10 | 31.01 | 53.59 | 78.41 | 4.99 | 1.31 | 0.83 | 14.46 |

### 2.2  Measurement of Crossing Point Temperature(CPT)and Oxidation Products

The CPT and oxidation products were measured by a customize-designed spontaneous combustion system, which consists of preheating tube, coal reaction vessel,

temperature logger, programed temperature enclosure and gas chromatograph (Fig. 1). The gas chromatograph was used to measure the oxidation products such as CO, $CO_2$, $C_2H_4$, $C_2H_6$, etc.
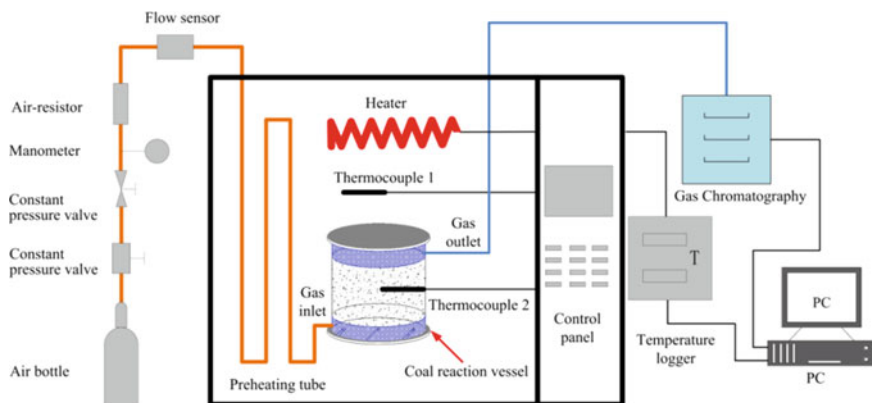


**Fig. 1.**  Schematic diagram of the self-designed spontaneous combustion system

Before the experiment, 50 g ($\pm$0.01 g) of coal sample in the range of 0.18–0.38 mm was weighted by electronic balance and placed in the coal reaction vessel. Then the programed temperature enclosure was turned on and run at a constant ambient temperature for 1 h. Next, the programed temperature enclosure was set to run at 0.8 °C/min and the dry air or moist air prepared was flowing into the coal reaction at a flow rate of 100 mL/min. During the early experimental period, the oxidation products were analyzed by gas chromatography at every 10 °C rise of the coal temperature. During the later experimental period, the oxidation products were analyzed after the last analysis.

## 2.3    Measurement of Thermal Characteristics

TG-DSC is used to measure the weight change, heat of reaction and the rate of heat release during the process of coal oxidation. This experiment is conducted by a SDT-Q600 simultaneous TG-DSC instrument made in America.

Before the experiment, 10 mg of coal sample in the range of 0.096–0.15 mm was weighted by electronic balance and put into the crucible. Then the dry air or moist air was flowing into the crucible as a flow rate of 100 mL/min and the coal sample was heated at a constant heating rate of 2 °C/min from ambient temperature to 800 °C.

# 3    Results and Discussion

## 3.1    Effects on CPT

The effects of humidity on CPT were investigated during coal oxidation process, as shown in Fig. 2.
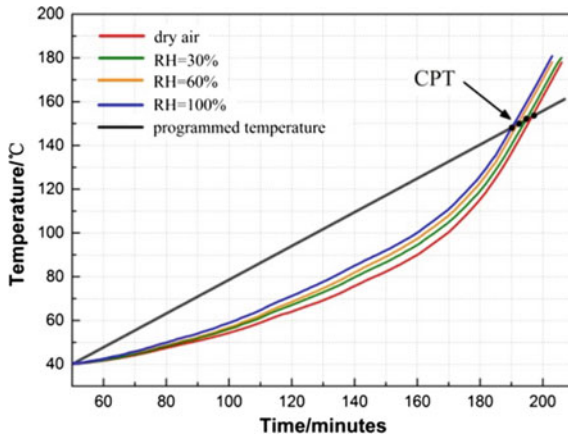


**Fig. 2.** Crossing point temperature (CPT) during coal oxidation with dry air and air of 30, 60 and 100% relative humidity

As can be seen from Table 2, the CPT values were determined to be 153 °C with dry air. While with the air of 30, 60 and 100% relative humidity, the CPT values were 151, 150 and 148 °C respectively. These results showed that the value of CPT decreased with the increase of air humidity, which indicated that air humidity had a positive effect on spontaneous combustion of coal. This result can be explained as follows: The water molecules in air were attached to coal particles gradually as the moist air flowing through the coal, which can release amounts of heat due to the process of condensation. This part of heat was much more than the heat generated by coal oxidation in the early stage [5], and can accelerate the increase of coal temperature as the temperature-rise curves shown in Fig. 2.

**Table 2.** Summary of measured CPT values

| Air humidity (%) | Dry | 30 | 60 | 100 |
|---|---|---|---|---|
| CPT value (°C) | 153 | 151 | 150 | 148 |

In general, the coal is capable of holding a certain amount of water under given pressure and temperature, which can generate vapor pressure in coal. When the partial pressure of water vapor in the air is higher than vapor pressure in coal, there would be a sorption of water from the air and condensation heat is generated. With the ongoing

sorption process vapor pressure in the coal increases rapidly. When the vapor pressure is equal to the partial pressure of water vapor in the air, the equilibrium is established. The higher the air humidity, the higher the vapor pressure established by the equilibrium, the greater the heat release. Then due to the increase of temperature, the water desorbs from coal during the process of evaporation and cause heat loss. However, the coal temperature still continues to rise evidenced by the coal temperature curves, showing heat loss only has a slight effect on coal oxidation at this stage.

## 3.2   Effects on Oxidation Products During Low-Temperature Oxidation

CO is usually regarded as the indicator gas of spontaneous combustion of coal in coal mine. Besides, $C_2H_4$ emerges at a higher temperature, which can be used to be a prediction index when coal oxidation run into the accelerated oxidation stage [8]. For this reason, we studied the effects of air humidity on emission of CO and $C_2H_4$ during low-temperature oxidation.

As shown in Fig. 3, the CO concentration differs from each other as a result of air humidity. With the increase in temperature, the higher the air humidity, the higher the CO concentration. Figure 3 also shows that when temperatures rises from 30 to 100 °C, water sorption also occurs, as shown by the CO emission-temperature curves, indicating that water adsorbed from air will enhance CO emission. For example, when temperature reaches 70 °C, the CO concentration is 27 ppm with dry air while it is 114 ppm when air is fully saturated (100% relative humidity). The results also shows that humidity can significantly enhance coal oxidation, a critical index for predicting and preventing coal spontaneous combustion.
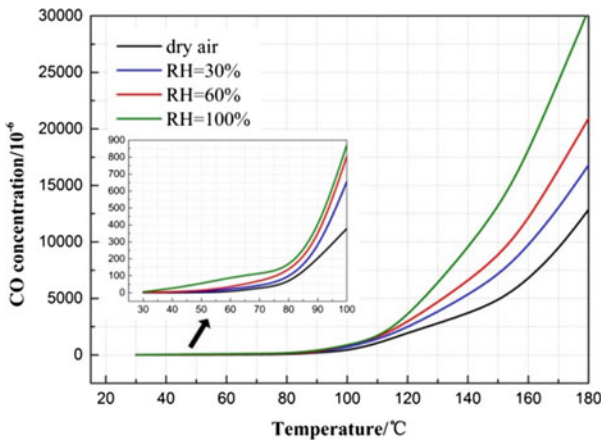


**Fig. 3.** CO emission-temperature curves with dry air and air of 30, 60 and 100% relative humidity

The experiment results of $C_2H_4$ emission-temperature curves as shown in Fig. 4 has also verify the conclusion above. The $C_2H_4$ concentration increases with the increase of

air humidity. With an air relative humidity of 100%, $C_2H_4$ emerges at 80 °C and the concentration is 0.35 ppm. With an air relative humidity of 60%, $C_2H_4$ also emerges at 80 °C but the concentration drops to 0.12 ppm. However, the $C_2H_4$ havn't been found when it is 30% RH or dry air at 80 °C. The results demonstration the air humidity can lead to the emergence of $C_2H_4$ earlier, which is important for increasing the efficiency of predicting the coal fire.
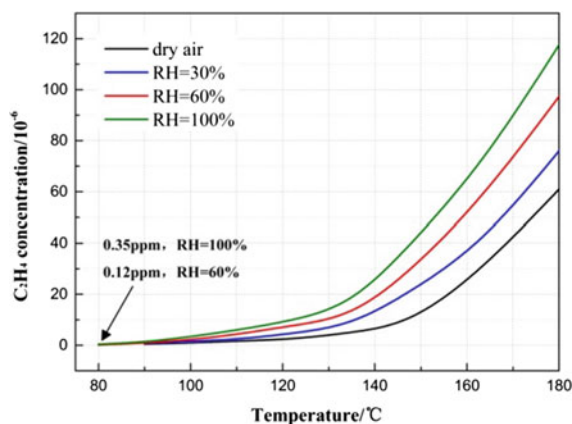


**Fig. 4.** $C_2H_4$ emission-temperature curves with dry air and air of 30, 60 and 100% relative humidity

## 3.3    Effects on Thermal Characteristics

The thermal characteristics of coal under different air humidity conditions were studied by TG-DSC tests. The experiment results were shown in Fig. 5. Two different reaction regions were observed in TG-DTG curves of coal samples under four types of air humidities. The reaction region, peak and burn-out temperature and mass loss data of coal samples were listed in Table 3. The TG-DSC curve of coal with dry air was obtained as shown in Fig. 5a. In the first region, the TG curve showed a downward trend, which was mainly caused by desorption of air-dried moisture and gases absorbed of the coal [9]. Then with the temperature rising, the reaction of coal-oxygen started and accelerated gradually. In the second region (260–500 °C), the mass of coal decreased obviously and entered the stage of rapid weightlessness, which indicated the complicated chemical reactions occurred and produced oxidation products. During this stage, the heat flow formed a peak as shown in DSC curve. This peak represented that the rate of heat release by reaction of coal-oxygen reached the maximum with the value of 75.68 mW. Next, the reaction rate of coal-oxygen decreased and the heat release tend to drop off.

(a) Dry air  (b) RH=30%

(c) RH=60%  (d) RH=100%
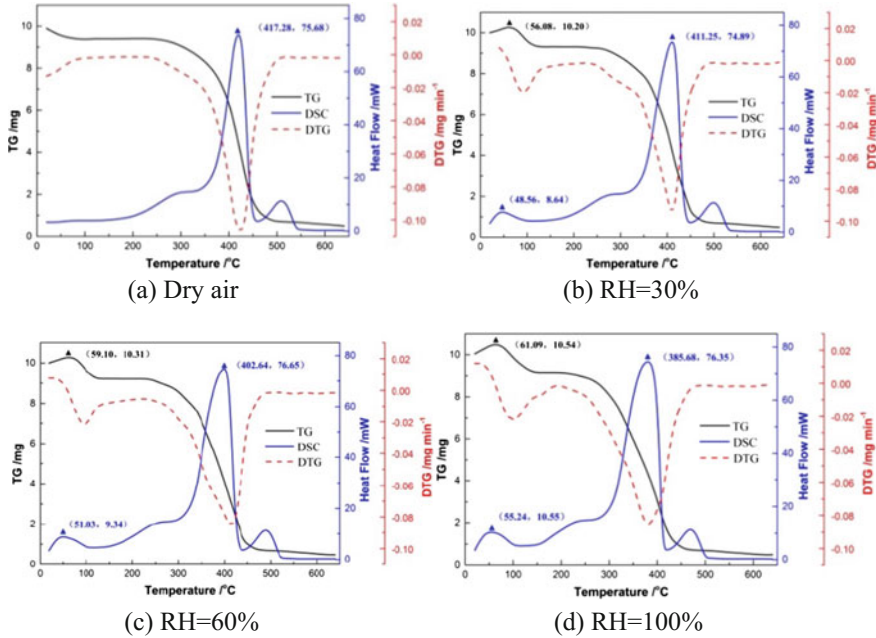
**Fig. 5.** TG-DSC curves of coal with dry air and air of 30, 60 and 100% relative humidity (this needs to be on the previous page)

**Table 3.** Reaction region, peak temperature and mass loss data of coal samples (TG-DTG) with dry air and air of 30, 60 and 100% relative humidity

| Air relative humidity (%) | Reaction region-I (°C) | Peak temp.I (°C) | Mass loss-I (%) | Reaction region-II (°C) | Peak temp. II (°C) | Mass loss-II (%) | Burn-out temp. (°C) |
|---|---|---|---|---|---|---|---|
| 0 (dry air) | 25–260 | 102 | 8.12 | 260–500 | 420 | 81.88 | 648 |
| 30% | 25–250 | 100 | 8.58 | 250–485 | 410 | 80.42 | 642 |
| 60 | 25–235 | 101 | 9.15 | 235–475 | 405 | 78.85 | 635 |
| 100 | 25–215 | 100 | 10.11 | 215–468 | 390 | 76.902 | 624 |

Figure 5b, c, d were obtained with air relative humidity of 30, 60 and 100%, respectively. As shown in the first region of TG-DTG curves, the mass of coal increased rapidly in the initial stage and a mass peak formed, then the mass of coal began to decline. This process can be divided to four stages as shown in Fig. 6. A coal particle was seen as an object of study. Firstly, the water molecules were adsorbed by coal particle, which led to the mass of coal increased rapidly; Then because of the equilibrium established between coal particle and moist air mentioned in Chap. 3.1 of this work, the water molecules desorbed with the temperature rising. In the third stage,

the desorption of water molecules in the pores was the main action. The pores in the coal had a capacity of water retention, where the water molecules existed by physical and chemical sorption [10, 11]. When the coal temperature reached to the critical value, those water molecules run into the process of desorption. Finally, water molecules in the pores fully desorbed, coal mass is reduced.
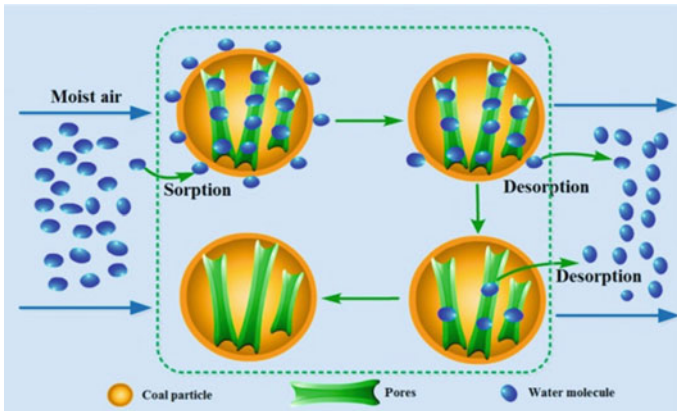


**Fig. 6.** The process of water molecule migration in the coal particle

As shown in Fig. 5, three different reaction regions were observed in DSC curves of coal samples under four kinds of air humidities. Table 4 lists Reaction region, peak temperature and maximum heat flow data of coal samples (DSC) with dry air and air with 30, 60 and 100% relative humidity. When the temperature reached nearly 400 °C, the peak of Region II will be shown in DCS curve. At this point, the rate of reaction of coal-oxygen reached the maximum value. As shown in Table 4, the peak temperature II decreases with the increase of humidity. When air saturated or has a relative humidity 100%, the coal-oxygen reaction will be at its maximum and temperature will be at 385.68 °C. The results showed that the maximum coal-oxygen is obtained at a lower temperature when moisture is present, oxidation is accelerated due to the presence of water.

**Table 4.** Reaction region, peak temperature and maximum heat flow data of coal samples (DSC) with dry air and air of 30, 60 and 100% relative humidity

| Air relative humidity (%) | Reaction region-I (°C) | Peak temp. I (°C) | Reaction region-II (°C) | Peak temp.II (°C) | Reaction region-III (°C) | Peak temp. III (°C) | Max. heat flow (mW) |
|---|---|---|---|---|---|---|---|
| 0 (dry air) | n.a. | n.a. | 130–455 | 417.28 | 455–540 | 510 | 75.68 |
| 30% | 25–140 | 48.56 | 25–445 | 411.25 | 445–530 | 505 | 76.35 |
| 60 | 25–130 | 51.03 | 130–430 | 402.64 | 430–525 | 490 | 76.65 |
| 100 | 25–125 | 55.24 | 125–415 | 385.68 | 415–500 | 475 | 76.35 |

n.a.—not available

## 4    Conclusion

The CPT and oxidation products at different humidities during coal spontaneous combustion were investigated. The experimental results indicated that humidity can significantly accelerate coal oxidation process by decreasing CPT and increasing CO and $C_2H_4$ emission. Then, the TG-DSC experiments were conducted to study the effects of air humidity on the thermal characteristics of coal. The results illustrated the maximum rate of coal-oxygen reaction were likely to be reached at a lower temperature because of the presence of water vapor, the water adsorbed will accelerate coal oxidation.

In conclusion, humidity can significantly accelerate coal oxidation, which is an important discovery that can be used to fight coal mine fires.

## References

1. Schmal, L.D., Duyzer, J.H., van Heuven, J.W.: A model for the spontaneous heating of coal. Fuel **64**, 963–972 (1985)
2. Stott, J.B.: Influence of moisture on the spontaneous heating of coal. Nature **188**(4744), 54–54 (1960)
3. Bhat, S., Agarwal, P.K.: The effect of moisture condensation on the spontaneous combustibility of coal. Fuel **75**(13), 1523–1532 (1996)
4. Bhattacharyya, K.K.: The role of sorption of water vapour in the spontaneous heating of coal. Fuel **50**(4), 367–380 (1971)
5. Miura, K.: Adsorption of water vapor from ambient atmosphere onto coal fines leading to spontaneous heating of coal stockpile. Energy Fuels **30**(1), 219–229 (2015)
6. Ren, T.X., Edwards, J.S., Clarke, D.: Adiabatic oxidation study on the propensy of pulverised coals to spontaneous combustion. Fuel **78**(14), 1611–1620 (1999)
7. Küçük, A., Kadıoğlu, Y., Gülaboğlu, M.Ş.: A study of spontaneous combustion characteristics of a Turkish lignite: particle size, moisture of coal, humidity of air. Combust. Flame **133**(3), 255–261 (2003)
8. Liang, Z., Wang, J.R.: The technology of forecasting and predicting the hidden danger of underground coal spontaneous combustion. Procedia Eng. **26**, 2301–2305 (2011)
9. Kok, M.V.: Simultaneous thermogravimetry–calorimetry study on the combustion of coal samples: effect of heating rate. Energy Convers. Manag. **53**(1), 40–44 (2012)
10. Pastor-Villegas, J., Rodríguez, J.M.M., Pastor-Valle, J.F., Rouquerol, J., Denoyel, R., García, M.G.: Adsorption–desorption of water vapour on chars prepared from commercial wood charcoals, in relation to their chemical composition, surface chemistry and pore structure. J. Anal. Appl. Pyrol. **88**(2), 124–133 (2010)

11. Hayashi, J., Norinaga, K., Kudo, N., Chiba, T.: Estimation of size and shape of pores in moist coal utilizing sorbed water as a molecular probe. Energy Fuels **15**(4), 903–909 (2001)
12. Lu, P., Liao, G.X., Sun, J.H., Li, P.D.: Experimental research on index gas of the coal spontaneous at low temperature stage. J. Loss Prev. Process Ind. **17**(3), 243–247 (2004)
13. Wang, H., Dlugogorski, B.Z., Kennedy, E.M.: Role of inherent water in low-temperature oxidation of coal. Combust. Sci. Technol. **175**(2), 253–270 (2003)

# Numerical Simulation of the Coal Spontaneous Combustion Dangerous Area in Multi-seam Longwall Gobs

Zhi-jin Yu$^{(\boxtimes)}$, Hu Wen, and Chao Wang

College of Safety Science and Engineering, Xi'an University of Science
and Technology, 710054 Xi'an, China
`yuzj0927@163.com`

**Abstract.** A comprehensive hazard evaluation for coal self-heating in composite longwall gobs is heavily dependent on computational simulation. In this study, the spatial distributions of cracks which caused significant air leakage were simulated by universal distinct element code (UDEC) simulation. Based on the main paths of air leakage and characteristics of coal self-heating, a computational fluid dynamics (CFD) modeling was conducted to model the coal spontaneous combustion dangerous area in multi-seam longwall gobs. The results included the oxygen concentration distributions and temperature profiles showed that the numerical approach is validated by comparison with the test data. Furthermore, major locations where control measures for extinguishing and preventing longwall gob fires are necessary were also examined.

**Keywords:** Computational simulation · Coal self-heating · CFD modeling
Long-wall gobs

## 1 Introduction

Spontaneous combustion is an important attribute of coal in terms of loss prevention. All the major coal producing countries in the world are concerned with the possible danger associated with coal spontaneous combustion [1, 2]. China's coal deposit is susceptible to spontaneous combustion, accounting for roughly 60% of underground coal fires [3]. However, because of the large space in longwall gobs and roof falling, it is very difficult to detect spontaneous combustion in the field. Numerical modeling can be helpful in forecasting spontaneous combustion susceptibility and provide insights for prevention and controlling spontaneous combustion fires.

Numerous numerical models have been used to simulate the process of coal self-heating in longwall gobs [4–7]. These studies always represented the mechanisms of spontaneous combustion in natural surroundings, and made full use of the experimental results. However, few modeling have been constructed based on specific engineering conditions. Especially, lacking both actual ventilation system and geological characteristics, resulted in a low agreement with field condition. Some investigators conducted modeling studies of longwall gobs to develop coal spontaneous combustion control strategies [6, 8], but the study was only for a single coal seam. For composite

longwall gobs, because of the influence of multi-seam mining and the smaller space between the two coal seams, the coal left in gobs are more prone to spontaneous combustion. At present, related simulation about composite longwall gobs has not been found.

In this paper, as a background of 22,305 longwall working face in Bulianta coal mine of China, the main air leakage paths in composite longwall gobs were investigated by UDEC simulation. The CFD model was then used to simulate the areas with possible spontaneous combustion for accurate detection of the locations of self-heating with an actual ventilation system. This study also presented the comparison of simulations and test data.

## 2   Background

In Fig. 1, the gob area of 22,305 longwall working face in 2# coal seam is 300 m long, 50 m wide, and 7 m high starting from the bottom of the coal seam. The 12,306 longwall working face in 1# coal seam is above the 22,305 longwall working face, and their average vertical spacing between two seams is 43 m. Furthermore, the depth from the surface of 1# coal seam is 115 m. When the 22,305 longwall working face was excavating, the 12,306 working face had already mined-out and sealed, the gob area of 12,306 is 300 m long, 4.6 m high, and 500 m wide. Taking into account the roof caving, the total area of composite longwall gobs reaches 156,000 $m^2$, the affected space exceeds 18 million $m^3$. Fresh air enters the 22,305 longwall working face by intake airway to supply workers breathing. Undoubtedly, parts of air will enter into the 12,306 gobs via vertical cracks.
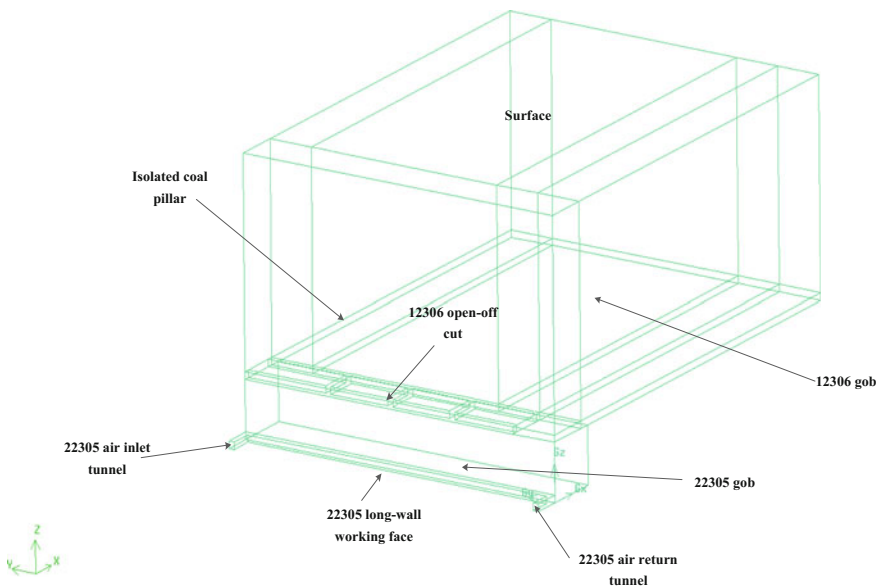


**Fig. 1.** Layout of longwall working faces and composite gobs

From the distribution of working faces, once spontaneous fires occurred somewhere in the longwall gobs, toxic gases such as CO will threaten the safety of workers. Therefore, in order to prevent the occurrence of spontaneous combustion of coal, identifying spontaneous combustion dangerous area in advance is necessary.

## 3    Modeling of Air Leakage Channel

### 3.1    Methods

Based on actual layout of the working face and the Mohr–Coulomb plastic constitutive relation, the characteristics of stress distribution of composite longwall gobs were simulated by software UDEC. Firstly, the 1# coal seam was excavated for 190 m in the width direction and 300 m in the length direction simultaneously. After that the 2# coal seam would be excavated with the same sequence. Geometric model in the process of excavation was shown in Fig. 2.
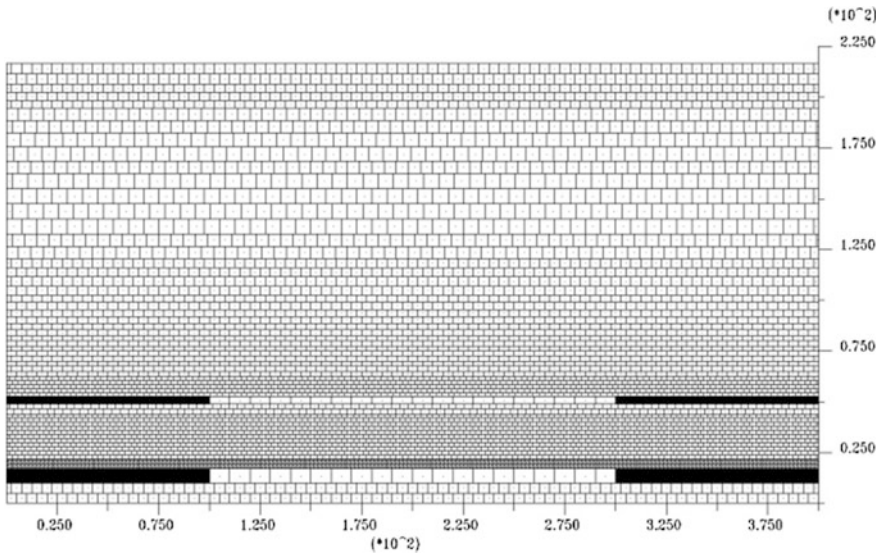


**Fig. 2.**  Geometric model

In Fig. 2, the model is 400 m long, 170 m high, and 400 m wide. The condition of top pressure was the result of gravity, which is determined by the height of overburden; others were set as fixed boundaries. The main parameters of materials in the model were similar as those used in the field.

## 3.2 Results and Discussion

After both coal seams finished mining, the simulated results of vertical stress were shown in Figs. 3 and 4.

Figure 3 shows that there are obvious stress concentration regions at the top of not only the stopping line and open-off cut, also the coal pillars at each side of the mining space. Both 1# coal seam and 2# coal seam, the vertical stress of borders were more than the middle part of gobs. Another characteristic is the stress concentration region that extended to the surface after the excavation of 2# coal seam. This means the main cracks may connect to the ground and had a significant amount of air leakage. Figure 4 indicates the specific vertical stress at various heights. In the vertical direction, with the increase of height, the vertical stress has a slight decrease at the middle of composite gobs. The main cracks caused by mining were always formed in the stress concentration regions [9]. In other words, due to the influence of repeated mining, it formed a fissure zone of double hump shape on both sides of the mining space which was the main path of air leakage.
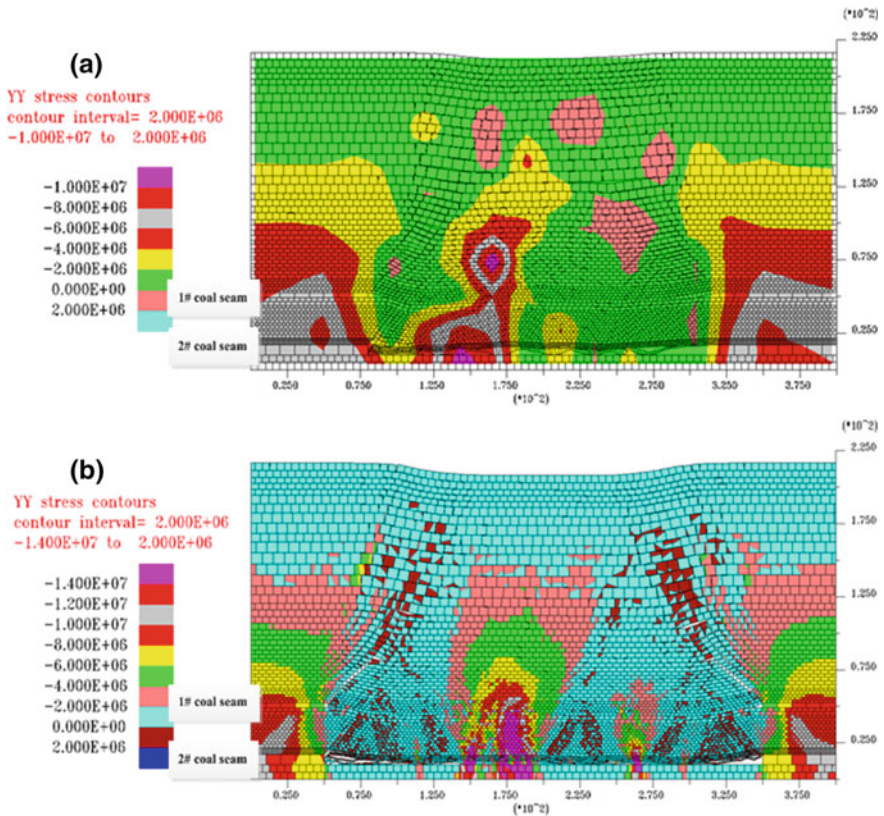


**Fig. 3.** Vertical stress distributions: **a** in the length direction, **b** in the width direction
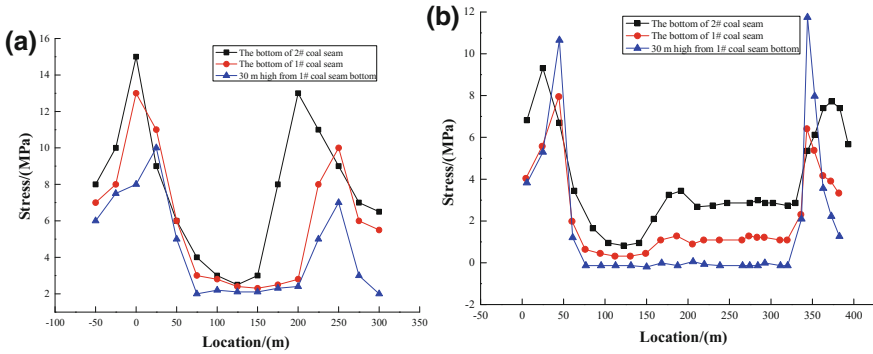
**Fig. 4.** Vertical stress at various heights: **a** in the length direction, **b** in the width direction

## 4 Modeling of Spontaneous Combustion Dangerous Area

### 4.1 Theoretical Model

The spontaneous combustion of coal refers to a range of complex physico-chemical processes, which is caused by the exothermic reaction between coal and oxygen. Meanwhile, the heat generated from oxidation is dissipated by conduction and convection [10]. To describe the above processes, the basic theoretical models can be defined as follow,

(1) For gas flow in porous medium

$$\frac{\rho_g}{\varepsilon}\left[\frac{\partial U}{\partial t} + (U\nabla)U\right] = \frac{\mu\nabla^2 U}{\varepsilon} - \nabla p - \frac{\rho_g \varepsilon f(U)U}{\sqrt{k_p}} - \frac{\mu U}{k_p} \tag{1}$$

where $\varepsilon$ is the porosity of coal. $U$ is velocity, $\rho_g$ is gas density. $k_p$ is the permeability of coal. $\mu$ is the dynamic viscosity of gas. $f$ is form-drag constant.

(2) For species transport

$$\varepsilon\frac{\partial c}{\partial t} + U\nabla c + \nabla(D\nabla c) = -(1-\varepsilon)r \tag{2}$$

where D is the diffusion coefficient. $c$ is gas concentration. r is the oxygen-consumption rate in coal spontaneous combustion process.

(3) For energy conservation

$$\begin{aligned}\left[(\varepsilon\rho_g C_g) + (1-\varepsilon)\rho_s C_s\right]\frac{\partial T}{\partial t} + \rho_g C_g U\nabla T = \\ \left(\varepsilon\lambda_g + (1-\varepsilon)\lambda_s\right)\nabla^2 T + (1-\varepsilon)rQ\end{aligned} \tag{3}$$

where the source term $(1 - \varepsilon)rQ$ denotes the heat flux released by oxidation reaction between oxygen and coal. $\rho_s$ is coal density. $C_s$, $C_g$ is of heat capacity of the coal particles and gas, respectively. $\lambda_s$, $\lambda_g$ is thermal conductivity of the coal particles and gas, respectively.

To simulate gobs in a multi-seam longwall operation, the boundary conditions needs to be defined. Based on the conclusions of Sect. 3.2, four cracks within 160 m high above the 2# coal seam which connected surface above the gobs were assumed. Other ventilation conditions were also used as boundary conditions in the simulation. The flow rate at intake of 22,305 longwall working face was 20 m$^3$/s. The pressures of air return gateroad and cracks were assumed to be at the barometric pressure. The initial temperature was 17 °C and the initial concentration of oxygen was 21%. The longwall face is assumed to be stationary. Meanwhile, the permeability and porosity distributions of the gobs were based on geotechnical features of longwall mining and the associated stress-strain changes shown in Fig. 3. Other parameters in the model were derived from the laboratory tests [11]. Fluent, a commercial CFD program, was used in this study to simulate the gas flow and spontaneous heating in the composite longwall gobs.

## 4.2 Results and Discussion

### 4.2.1 Oxygen Concentration Distribution

Simulations were first conducted for stationary longwall panel in Fig. 5 to study the oxygen concentration distribution at various heights in the multi-seam longwall gobs. There is no doubt that gas flow is a principal factor influencing the distribution of oxygen. As shown in Fig. 5, the oxygen concentration in the longwall gobs is very high beside the gateroad intake. In the 12,306 longwall working face, the volume fraction of oxygen remains >12% until 100 m behind the workface. However, beside the air return tunnel, 30 m from the workface, the volume fraction of oxygen drop to <8%. The trends in the reduction of oxygen in the longwall gobs are very similar at various heights.

Meanwhile, with the increase of height, the area of high oxygen concentration turns larger. This verifies that the vertical cracks above the gobs have been connected to the ground. This leads to lots of fresh air leaking into the gobs. Furthermore, by comparing oxygen concentration distributions $z = 30$ m versus $z = 70$ m, it indicates, for air leakage, the air volume from the ground is far more than it from 22,305 longwall working face, as shown on Fig. 5.
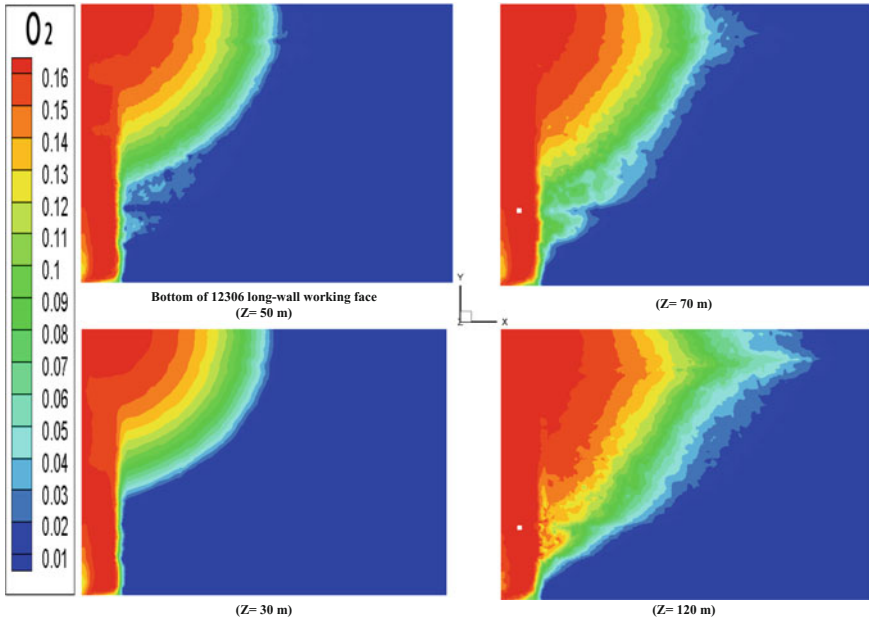
**Fig. 5.** Oxygen concentration distributions in parallel within coal seams

## 4.2.2 Temperature Profiles

Temperature profiles at various heights (z = 30, 50, 70 and 120 m) for stationary longwall panel are represented in Fig. 6. Please note that the high temperature zone is dependent on both heat dissipation and accumulation. Despite there is a high oxygen concentration around the air inlet tunnel, the rate of air leakage is also great. As a result, the high temperature zone is located at the side of return air close to the workface where there is plenty of oxygen to sustain coal oxidation. In addition, the most predominant characteristics in Fig. 6 is that the maximum temperature for the level of 12,306 workface is approximately 110 °C higher than other levels. Above the 12,306 work-face, with an increase of height, the area of high temperature zone decreases gradually. Below the 12,306 workface, despite the area of high temperature zone remains unchanged, the temperature of coal appears to have dropped.
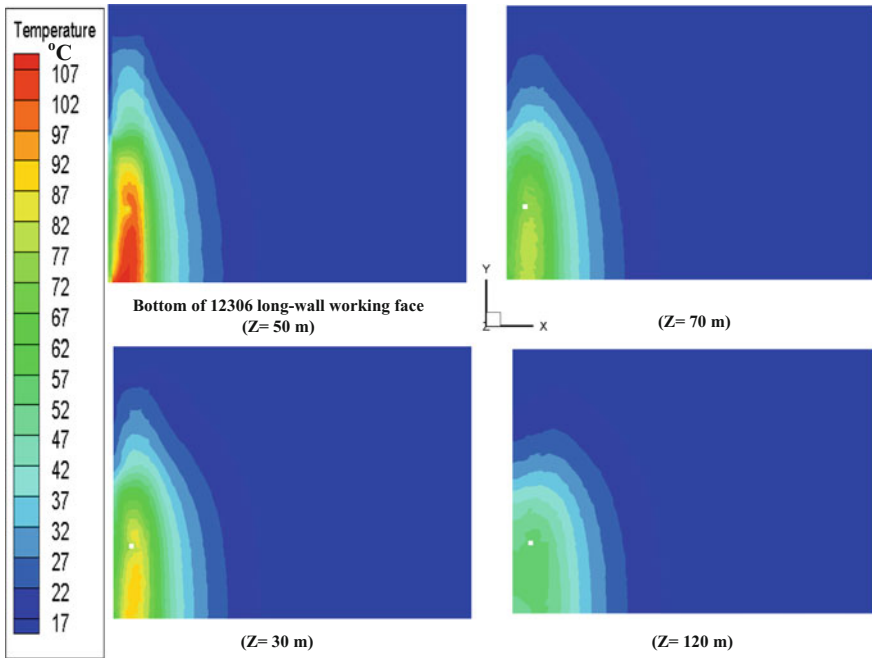
Fig. 6.　Temperature profiles in parallel with coal seams

### 4.2.3　Definition of Dangerous Area with Spontaneous Combustion

Based on the above analysis of the oxygen concentration distributions characteristics and temperature profiles, we can identify a semi-elliptical dangerous area with spontaneous combustion in the longwall gobs. As presented in Fig. 7, the center of this area is located at the return corner of the 12,306 longwall working face. Its major axis is 150 and 50 m for minor axis. In this region, adequate oxygen is available, which significantly intensifies spontaneous coal combustion. Besides, because it is far away from the source of leakage, heat dissipation in this region will increase of temperature. This is a critical region where coal spontaneous combustion will likely occur and effective measures must be taken to prevent such incidents from happening.

### 4.2.4　Model Validation

To validate the simulated results, mixed gas samples were collected by boreholes from the longwall gobs in Bulianta coal mine and analyzed by gas chromatography to obtain the oxygen concentration. Figure 8 shows the locations of gas collection points.

In Fig. 8, the collection tubes were placed in the gob near the return, air intake, and the middle of workface. The results were then comparing with the simulated oxygen concentration at same position in Fig. 9.
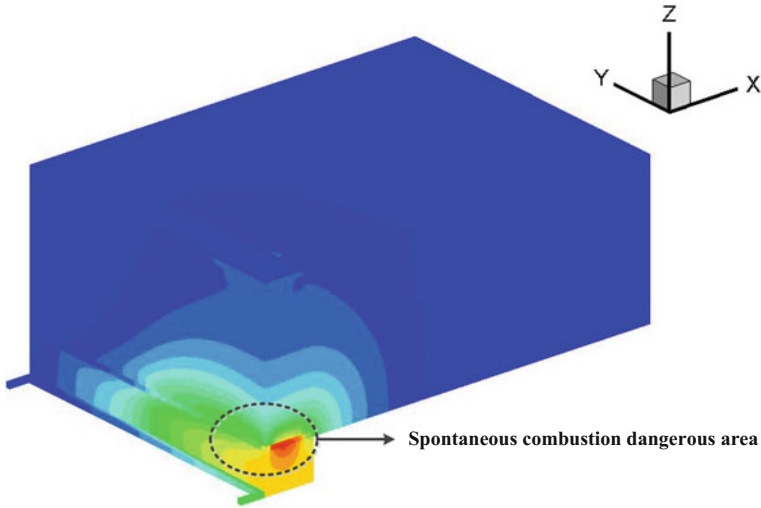
**Fig. 7.** The spatial temperature profiles in the model
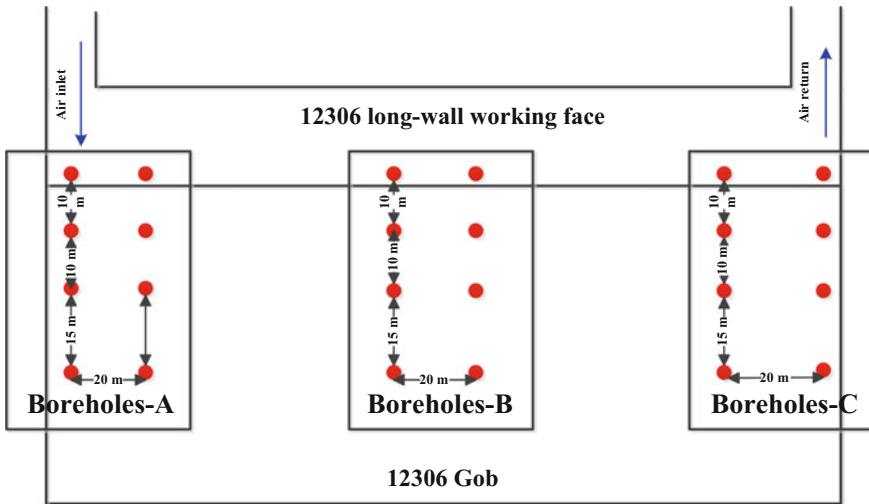


**Fig. 8.** Gas collection points in Bulianta coal mine

It can be found that the measured oxygen concentration show a fairly good agreement with the modeled results. The agreement is better in the boreholes B and boreholes A while there is slightly discrepancy in the boreholes C. However, the maximum error is no more than 2%. Taking into account that some factors may not have been considered in the simulations, simulation results are acceptable and the model based on the actual conditions of air leakage is able to predict the spontaneous combustion dangerous area in the multi-seam longwall gobs.
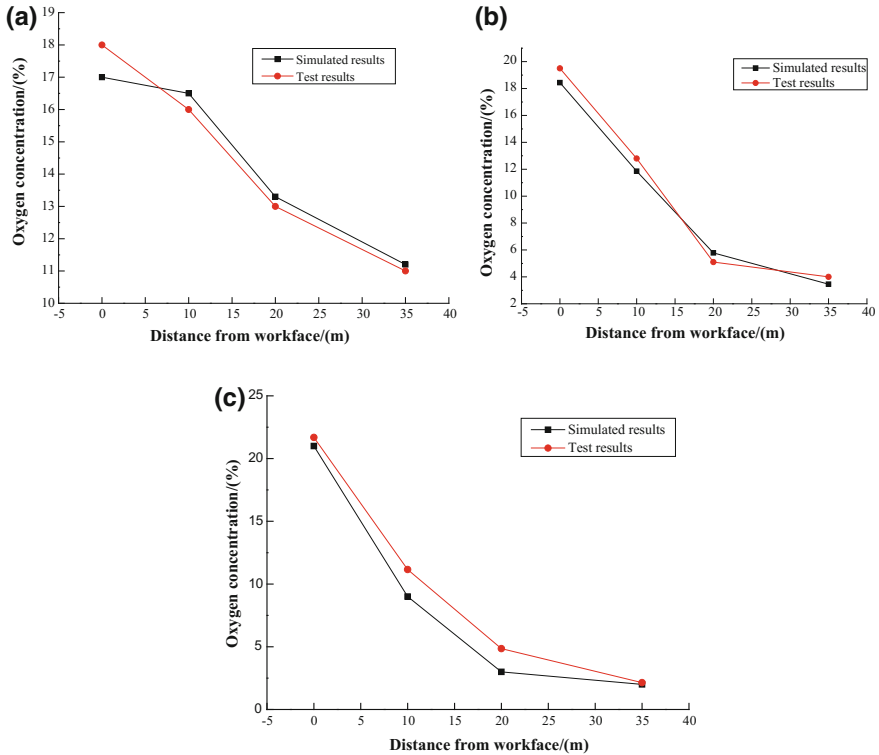
**Fig. 9.** Comparison of observation and simulation of oxygen concentration: **a** boreholes A, **b** boreholes B, **c** boreholes C

# 5   Conclusions

The stress distribution of overlying strata in the multi-seam longwall gobs was simulated with UDEC. The results using CFD simulations show the main cracks at the boundaries of mining space generated as a result of subsidence are connected to the surface which can cause air to leak to the underground workings. Comparing the oxygen concentration distributions and temperature fields to simulation show that there is a semi-elliptical shaped area adjacent to the return airway of shallower workface spontaneous combustion does occur (in this paper, it is 12,306 longwall working face). A average discrepancy of less than 2% between observed and simulated oxygen concentration at twelve boreholes at various monitoring locations indicates a good agreement between observation and simulation. The method of numerical simulation is available to investigate various complex situations of spontaneous combustion and provide a means for preventing spontaneous heating fires, especially in the longwall gobs. This study also indicates that leakage from the surface is greater when the coal seams are at shallower depth.

# References

1. Bowman, M., Debray, S.K., Peterson, L.L.: Reasoning about naming systems. ACM Trans. Program. Lang. Syst. **15**(5), 795–825 (1993).http://doi.acm.org/10.1145/161468.16147
2. Ding, W., Marchionini, G.: A study on video browsing strategies. Technical Report. University of Maryland at College Park (1997)
3. Fröhlich, B., Plate, J.: The cubic mouse: a new device for three-dimensional input. In: Proceedings of the SIGCHI Conference on Human Factors in Computing Systems (The Hague, The Netherlands, April 01–06, 2000). CHI '00. ACM, New York, NY, 526–531. (2000). http://doi.acm.org/10.1145/332040.332491
4. Tavel, P.: Modeling and simulation design. AK Peters Ltd., Natick, MA (2007)
5. Sannella, M.J.: Constraint satisfaction and debugging for interactive user interfaces. Doctoral Thesis. UMI Order Number: UMI Order No. GAX95-09398., University of Washington (1994)
6. Forman, G.: An extensive empirical study of feature selection metrics for text classification. J. Mach. Learn. Res. **3**, 1289–1305 (2003)
7. Brown, L.D., Hua, H., Gao, C.: A widget framework for augmented interaction in SCAPE. In: Proceedings of the 16th Annual ACM Symposium on User Interface Software and Technology (Vancouver, Canada, November 02–05, 2003). UIST '03. ACM, New York, NY, 1–10. (2003). http://doi.acm.org/10.1145/964696.964697
8. Yu, Y.T., Lau, M.F.: A comparison of MC/DC, MUMCUT and several other coverage criteria for logical decisions. J. Syst. Softw. **79**(5), 577–590 (2006). http://dx.doi.org/10.1016/j.jss.2005.05.030
9. Spector, A.Z.: Achieving application requirements. In: Mullender, S. (eds.) Distributed Systems, pp. 19–33. ACM Press Frontier Series. ACM, New York, NY. (1989). http://doi.acm.org/10.1145/90417.90738
10. Hooman, K., Maas, U.: Theoretical analysis of coal stockpile self-heating. Fire Saf. J. **67**, 107–112 (2014)
11. Liu, Leizheng: Dangerous Region Judgment of Spontaneous Combustion in Overlying Goaf of Excavation in Shallow Depth Contiguous Seams Group. China University of Mining and Technology, Xu Zhou, China (2015)

# The Effect of High Geo-Temperature Environment on Coal Spontaneous Combustion: An Experimental Study

Jun Deng[1,2], Changkui Lei[1(✉)], Yang Xiao[1,2], Li Ma[1,2],
Kai Wang[1,2], and Chimin Shu[3]

[1] School of Safety Science and Engineering, Xi'an University
of Science and Technology, 58, Yanta Mid. Rd, Xi'an, Shaanxi 710054,
People's Republic of China
lchangkui@l26.com

[2] Shaanxi Key Laboratory of Prevention and Control of Coal Fire,
Xi'an University of Science and Technology, 58, Yanta Mid. Rd, Xi'an,
Shaanxi 710054, People's Republic of China

[3] Graduate School of Engineering Science and Technology, Yunlin University
of Science and Technology (YunTech), Yunlin 64002 Taiwan, China

**Abstract.** To investigate the effect on coal spontaneous combustion due to high geo-temperature, an experimental apparatus was developed to measure parameters for two kinds of coal samples under different temperatures: one was pretreated at constant temperature of 40 °C (G coal sample), and the other was a rising temperature from room temperature (20 °C, Sample C). Based on the relationship between CO concentration and the temperature variation, a calculation model of the apparent activation energy of coal was established. The results indicated that the oxygen consumption rate, generation rates of CO and $CO_2$, and heat release intensity of Sample G were higher than C coal sample. This trend was more and more obvious as the temperature is increased. Furthermore, the apparent activation energy of G coal sample was smaller than sample C, especially at low temperatures, which demonstrated that the oxidation ability and reactivity of sample G was enhanced, and less energy was required to break the barrier of oxidation reaction. Under the same condition, the speed of oxidation reaction was faster for the coal in the high geo-temperature environment, which was more susceptible to spontaneous combustion.

**Keywords:** Spontaneous combustion · High Geo-temperature
Gas concentration · Apparent activation energy · Oxidation reaction

## 1 Introduction

Coal spontaneous combustion is one of the major cause of disasters in underground coal mining [1–3]. With increased mechanization in coal mining and the gradual reduction of shallow coal resources, the depth of underground mining is increasing, and the problem of high geo-temperature has been an increasing concern [4]. The temperature of No. 1 well in Amandelbult, Africa [5] reaches 55 °C at 3300 m. Due to the

impact of geothermal water, the temperature of the Fengyu lead–zinc ore mine in Japan [6] reaches 80 °C at 500 m. According to preliminary data, roughly 53% of Chinese coal reserves are below 1000 m, the temperature are 32–36 °C at 700 m, and up to 40–45 °C at 1000 m [6]. Due to the high temperatures, the initiation temperature of coal spontaneous combustion is high and the incubation period is shortened, which makes coal spontaneous combustion in mines with high temperatures a serious concern, presenting challenges to safety production in these mines [7].

There have been efforts to harvest heat sources in deep underground coal mines through a HEMS (High Temperature Exchange Machinery Systems) technology, in a stepwise manner, which obtained acceptable results [6, 8]. Guo et al. [9] used Zhang Shuanglou coal mine through the field test, to investigate the technology of utilizing mine water as coolant for underground mine cooling system and transferring underground geothermal energy to ground surface through mine drainage systems. Further, Guo et al. [10] presented a geothermal recycling system for mines (GRSM) for parallel mine cooling and surface heating. Chen et al. [5] proposed the split-type vapor compression refrigerator (SVCR) system for heat hazard control in deep mines.

At present, the research on geo-temperature in deep mine mainly focused on the technologies of prevention, control, and utilization of heat [11–13]. However, the theoretical research, such as the effect and the main features of high temperature on coal spontaneous combustion is lacking. In terms of coal spontaneous combustion, activation energy is a vital kinetic parameter in the low temperature oxidation of coal, which determines the rate of oxidation reaction and characterizes the energy required for coal combustion [14–16]. Nevertheless, owing to the oxidation reaction of coal at low temperatures is very complicated [17–19], the activation energy obtained is just apparent. Activation energy refers to the lowest energy requires for coal to oxidize, usually, the smaller activation energy is, the less energy demands for oxidation reaction of coal, the easier the reaction proceeds [20–22]. Therefore, it is necessary to ascertain the apparent activation energy of coal in high temperature environment and analyze the impact of high temperature environment on the risk of coal spontaneous combustion.

In this study, the temperature-programmed experimental system was developed to study the spontaneous combustion characteristics of two types of coal samples: One was pretreated at the constant temperature of 40 °C to simulate the high temperature environment in deep mines, and the other was employed temperature-programmed test from room temperature of 20 °C. Our aim was to analyse the variation laws of oxygen consumption rate, gas generation rates, and heat release intensity, to determine the change of apparent activation energy at different temperature stages based on the relationship between CO concentration and the temperature variation, to provide a theoretical basis for the prevention of coal spontaneous combustion in high temperature coalmines.

## 2   Experimental Methods

A self-designed XK-I temperature-programmed experimental system was used to study the oxidation characteristics of the coal samples in low-temperature oxidation. Numerous characteristic parameters could be obtained from the experimental system,

which would produce theoretic parameters for understanding the effect in a high temperature environment on coal spontaneous combustion.

The experimental system consists of five parts: An experimental oven; coal sample tank; temperature control system; gas collection device and gas chromatograph analysis system (Fig. 1). The experimental oven measures 50 cm high, 40 cm wide and 30 cm long. The 9.5-cm circular coal sample tank mounted vertically in the middle of the oven, is 25.0 cm in length, and the coal loading capacity can be up to 1.1 kg, with approximately 2 cm of free space remaining at both the upper and lower ends of the coal sample tank. The free space at the bottom was necessary to hold the coal using copper wire mesh to allow air current to blow through, as shown in Fig. 2.
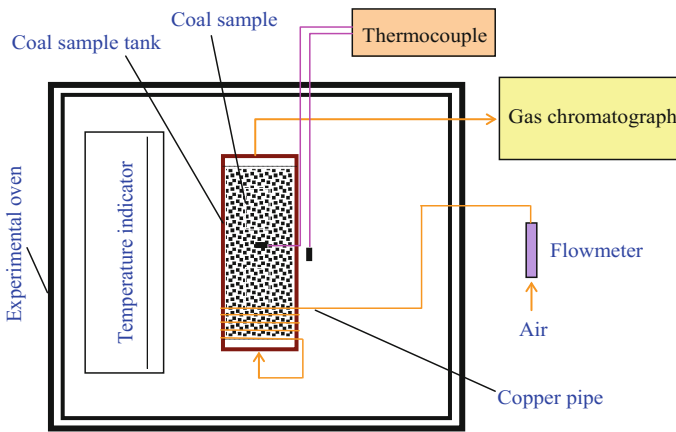


**Fig. 1.** XK-I temperature-programmed experimental system

The fresh coal samples obtained from Jianxin coalmine in (northwestern?) Shaanxi province, _____ from Xi'an. The samples were prepared as follows:

Sample G: A fresh sample was selected, pulverized, and screened. Next, 1000 g coal sample of mixed grain sizes, 0–0.9, 0.9–3, 3–5, 5–7 and 7–10 mm per 200 g, were mixed together evenly. Then the mixed coal sample was filled in the coal sample tank and aired for 30 min. After this Sample G was oxidized at a constant temperature of 40 °C in the oven and the temperature and gas composition remained unchanged. When temperature-programmed test started, the temperature was raised to 170 °C at a rate of 0.3 °C min$^{-1}$, and 120 mL min$^{-1}$ airflow was provided as the reaction gas during the whole experiment. To assist with the coal oxidation.

Sample C: the test was started with the room temperature of 20 °C, with other conditions remaining the same as for the Sample G. Gas samples were analysed by SP-2120 gas chromatograph at every 10 °C temperature increment. The temperature of coal in the tank was monitored by the thermocouple at the center of the tank where the coal sample was placed. Other test conditions are shown in Table 1.
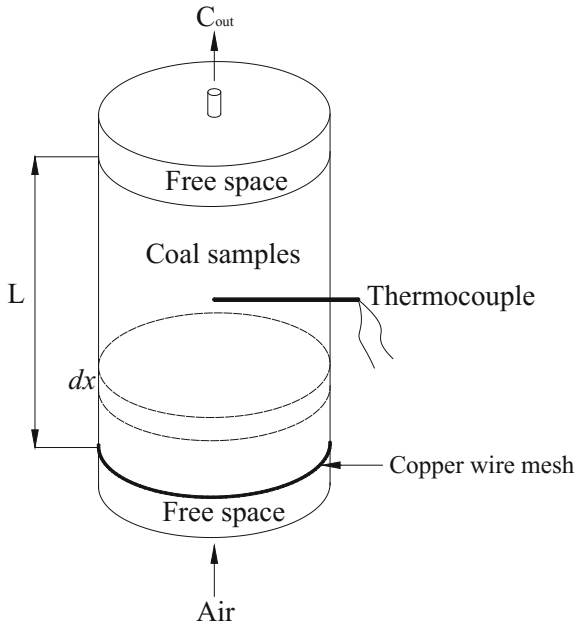
**Fig. 2.** The schematic diagram of coal sample tank

**Table 1.** Experimental conditions for samples C and G

| Coal sample | Mass of coal sample/g | Average particle size/mm | Voidage/ % | Air flow/mL min$^{-1}$ | Heating rate/°C min$^{-1}$ | Pretreatment conditions |
|---|---|---|---|---|---|---|
| C coal sample | 1000 | 4.18 | 0.545 | 120 | 0.3 | Room temperature of 20 °C |
| G coal sample | 1000 | 4.18 | 0.545 | 120 | 0.3 | Constant temperature of 40 °C |

## 3    Results and Discussion

### 3.1    Oxygen Consumption Rate

The oxygen consumption rate of the coal sample can be calculated using the oxygen concentration at the inlet and outlet of the coal sample, as follows [23]:

$$V_{O_2}(T) = \frac{Q \times C_{O_2}^1}{S \times L} \times \ln \frac{C_{O_2}^1}{C_{O_2}^2} \tag{1}$$

where $V_{O_2}(T)$ is the oxygen consumption rate when the coal temperature is $T$, mol cm$^{-3}$ s$^{-1}$; $Q$ is the air flow, mL min$^{-1}$; $S$ is the cross-sectional area of the coal sample tank, cm$^2$; $L$ is the coal length in the coal sample tank, cm; $C_{O_2}^1, C_{O_2}^2$ are oxygen concentration in inlet and outlet of the coal sample tank, respectively, vol.%, and air was the reaction gas, $C_{O_2}^1 = 21$ vol.%.

Substituting the oxygen concentration $C_{O_2}^2$ measured by gas chromatograph and other parameters into Eq. (1), the relationship between temperature and oxygen consumption rate $V_{O_2}(T)$ are shown in Fig. 3.
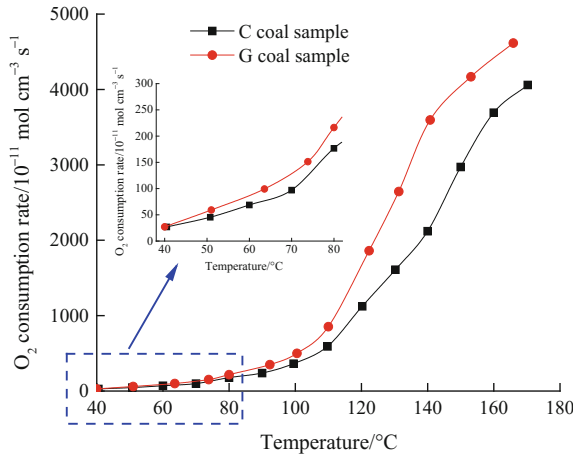


**Fig. 3.** Variation between oxygen consumption rate and coal temperature for Samples C and G

## 3.2 CO and CO₂ Generation Rates

The CO and CO$_2$ generation rates in the coal body are proportional to the oxygen consumption rate during the coal oxidation process, they are important parameters of coal spontaneous combustion [24]. According to the fluid flow and mass transfer theory, the equations of CO and CO$_2$ generation rates can be derived from Eq. (1) [23]:

$$V_{CO}(T) = \frac{V_{O_2}(T) \cdot (C_{CO}^2 - C_{CO}^1)}{C_{O_2}^1 \cdot [1 - \exp\frac{-V_{O_2}(T) \cdot S \cdot L}{Q \cdot C_{O_2}^1}]} \tag{2}$$

$$V_{CO_2}(T) = \frac{V_{O_2}(T) \cdot (C_{CO_2}^2 - C_{CO_2}^1)}{C_{O_2}^1 \cdot [1 - \exp\frac{-V_{O_2}(T) \cdot S \cdot L}{Q \cdot C_{O_2}^1}]} \tag{3}$$

where $V_{CO}(T)$ and $V_{CO_2}(T)$ are the CO and CO$_2$ generation rates when the coal temperature is both at $T$, mol cm$^{-3}$ s$^{-1}$; $C_{CO}^1, C_{CO_2}^1$ and $C_{CO}^2, C_{CO_2}^2$ are CO and CO$_2$ concentration in inlet and outlet of the coal sample tank, at vol.%.

Based on Eqs. (2) and (3), CO and $CO_2$ generation rates can be calculated for different coal temperatures, as shown in Fig. 4.
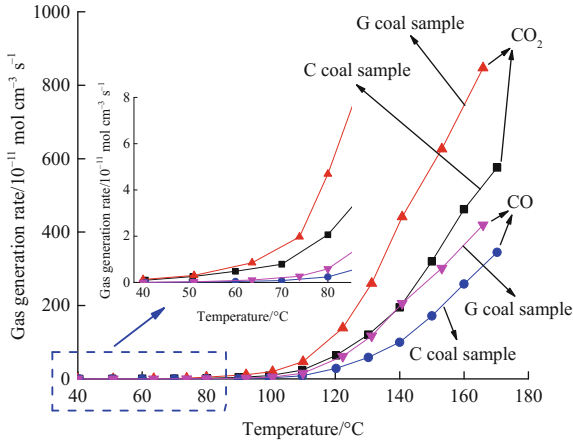


**Fig. 4.** CO and $CO_2$ generation rates for Samples C and G

## 3.3  Extreme Heat Release Intensity

The heat release intensity of coal is a crucial index to characterize the exothermicity of coal. Based on the bond energy estimation method, using the oxygen consumption rate, CO and $CO_2$ generation rates of coal at different temperatures, and the variation of bond energy during the coal-oxygen reaction, the extreme heat release intensity of coal can be calculated [23]. The actual heat release intensity is between maximum and minimum values [24].

$$q_{max}(T) = \frac{V_{CO}(T)}{V_{CO}(T) + V_{CO_2}(T)} V_{O_2}(T) \cdot \Delta H_{CO} + \frac{V_{CO_2}(T)}{V_{CO}(T) + V_{CO_2}(T)} V_{O_2}(T) \cdot \Delta H_{CO_2}$$

$$(4)$$

$$q_{min}(T) = \Delta H_s \cdot [V_{O_2}(T) - V_{CO}(T) - V_{CO_2}(T)] + \Delta H_{CO} \cdot V_{CO}(T) + \Delta H_{CO_2} \cdot V_{CO_2}(T)$$

$$(5)$$

where $q_{max}(T)$ and $q_{min}(T)$ are the maximum and minimum heat release intensity when the coal temperatures are at $T$, J cm$^{-3}$ s$^{-1}$; $\Delta H_s$ is chemical adsorption heat of coal-oxygen reaction, $\Delta H_s = 58.8$ kJ mol$^{-1}$; $\Delta H_{CO}$ and $\Delta H_{CO_2}$ are the average reaction heat of CO and $CO_2$, respectively, kJ mol$^{-1}$.

The oxygen consumption rate, CO and $CO_2$ generation rates and other parameters obtained by the Eqs. (1), (2), and (3) are substituted into the Eqs. (4) and (5), extreme heat release intensity can be calculated for different coal temperatures, as shown in Fig. 5.
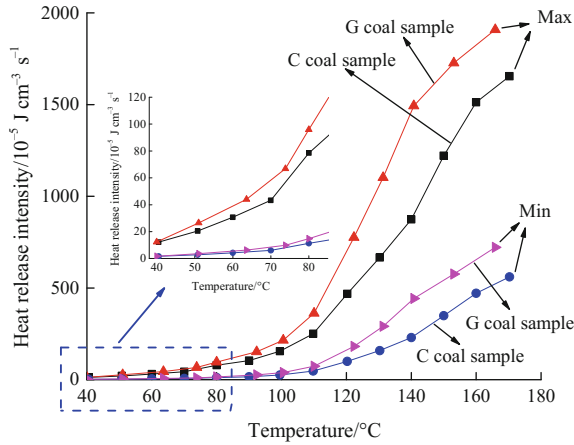
**Fig. 5.** Extreme heat release intensity for samples C and G

As can be seen from Figs. 3, 4 and 5, the oxygen consumption rate, CO generation rate, $CO_2$ generation rate, and extreme heat release intensity of the two types of coal samples increased with the rise of coal temperature with similar pattern, which is in agreement with the law of exponential growth. During the entire process, the oxygen consumption rate, CO generation rate, $CO_2$ generation rate, and extreme heat release intensity of Sample G were higher than those of Sample C. With the coal temperature below 120 °C, the growth rate for the above parameters was slow, and the two types of coal samples were similar. However, the rate increase sharply when coal temperature goes above 120 °C. The growth for Sample G was greater than Sample C. Tests show that the reaction intensity for coal oxidation was low when the coal temperature was lower than 120 °C, accelerated when the temperature exceeded 120 °C. The reason is that coal-oxygen reaction was mainly dominated by physical adsorption and chemical adsorption at lower temperatures (lower than 120 °C), and the heat release intensity mainly depended on physical adsorption heat and chemical adsorption heat [25–28]. With the increase in temperature, the adsorption reached equilibrium, coal-oxygen reaction mainly depended on the chemical reaction [23, 28], and the number of reactive functional groups increased, the heat release intensity mainly due to chemical reaction heat, which resulted in much more heat release, supporting a swift oxidation reaction when the temperature was over 120 °C.

Based on the above analysis, it is shown that the oxidability and exothermicity of Sample G which was pretreated at a constant temperature of 40 °C and then temperature-programmed test exceeded the Sample C. The oxidation and heat release capacity of coal were strengthened under the high temperature environment. Sample G was more susceptible to oxidation and heat storage under the same condition, which indicated that the coal in the high temperature environment had a greater risk of spontaneous combustion.

### 3.4 Apparent Activation Energy

**Calculation Model**. The reactive groups in the coal react with oxygen to produce CO, $CO_2$, and other products during coal oxidation, the oxidation equation of coal can be expressed as follows [29]:

Coal + $O_2 \rightarrow m$CO + $g$CO$_2$ + other products
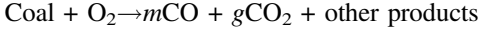
Based on the reaction rate formula and the Arrhenius equation, the following relationship can be obtained:

$$V_{O_2}(T) = V_{CO}(T)/m = Ac_{O_2}^n \exp(-E/RT_i) \tag{6}$$

where $m$ is the stoichiometric number of CO; $T_i$ is the thermodynamic temperature of coal, K; $A$ is the pre-exponential factor, $s^{-1}$; $c_{O_2}$ is the oxygen concentration in the reaction gas, mol m$^{-3}$; $n$ is the reaction order; $E_a$ is the apparent activation energy, J mol$^{-1}$; $R$ is the molar gas constant, 8.314 J mol$^{-1}$ K$^{-1}$.

During the test, it is assumed that the air flows uniformly along the vertical axial in the tank at a constant rate, the temperature distribution within the tank is also uniform, the mass variation of coal samples before and after the test can be negligible. The CO generation rate equation with the infinitesimal volume with the thickness $dx$ can be expressed as follows:

$$S \cdot V_{CO}(T)dx = kV_g dc \tag{7}$$

where k is unit conversion factor, $22.4 \times 10^9$; $V_g$ is air flow rate, m$^3$ s$^{-1}$; $dc$ is the generated CO concentration when air flows through the coal sample with the thickness $dx$ in the tank, vol.%.

Substituting Eq. (6) into Eq. (7) gives:

$$\int_0^L SmAc_{O_2}^n \exp(-E_a/RT_i)dx = \int_0^{C_{CO}^2} kV_g dc \tag{8}$$

Integrating on the both sides of Eq. (8) leads to Eq. (9):

$$SmAc_{O_2}^n \exp(-E_a/RT_i)L = kV_g C_{CO}^2 \tag{9}$$

Calculating the natural logarithm on both sides of Eq. (9):

$$\ln C_{CO}^2 = -\frac{E_a}{R} \cdot \frac{1}{T_i} + \ln\left(\frac{mSALc_{O_2}^n}{kV_g}\right) \tag{10}$$

Based on Eq. (10), plotting ($\ln C_{CO}^2 \sim \frac{1}{T_i}$), apparent activation energy of coal samples in different reaction stages can be obtained through the calculation of slope.

**Results Analysis**. Plotting the calculated model using $\ln C_{CO}^2$ as the ordinate, and $1/T_i$ as the abscissa, the linear fitting results of coal sample with the change of $1/T_i$ at different temperatures can be seen from Fig. 6. In this paper, coal temperature below 120 °C was defined as low temperature stage, above 120 °C was defined as high temperature stage. The correlation coefficients $R^2$ of linear fitting for the both coal samples were greater than 0.98, which indicated that the fitting degree was favourable and consistent with the actual results. On the basis of Eq. (10), the apparent activation energy $E_a$ of the two kinds of coal samples at different temperature stages can be obtained by the slope $(-E_a/R)$ of each fitting line in Fig. 6 and Table 2 summarizes the results of the apparent activation energy $E_a$, and a further comparison is presented in Fig. 7.



**(a)**
$$\ln C_{CO}^2 = -3976.7/T_i + 18.949$$
$$R^2 = 0.986$$
$$\ln C_{CO}^2 = -8326.73/T_i + 29.968$$
$$R^2 = 0.994$$

**(b)**
$$\ln C_{CO}^2 = -4106.53/T_i + 19.087$$
$$R^2 = 0.987$$
$$\ln C_{CO}^2 = -8829.62/T_i + 30.987$$
$$R^2 = 0.981$$
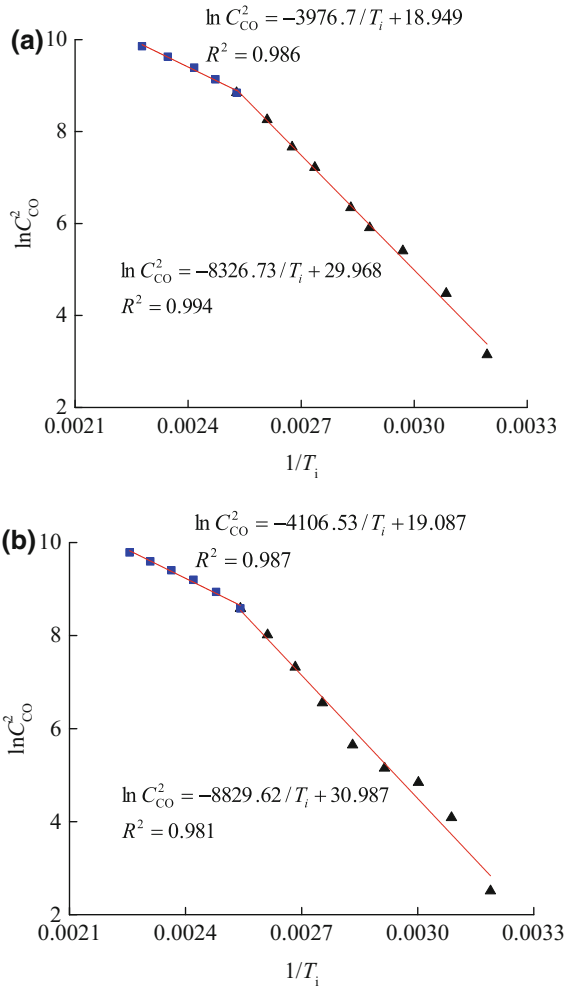
**Fig. 6.** Variation relation between $\ln C_{CO}^2$ of coal samples and $1/T_i$. **a** G coal sample; and **b** C coal sample

It can be seen from Fig. 7 and Table 2 that the apparent activation energy of coal-oxygen compound reaction was different at different temperature stages. The apparent activation energy of high temperature stage was much smaller than low temperature stage, the variation was more than half, which demonstrated that the coal was more prone to oxidation, and the reaction was faster at high temperatures. This further illustrated the reason why the oxygen consumption rate, CO generation rate, $CO_2$ generation rate, and extreme heat release intensity grown more rapidly at high temperatures. At the same time, it was shown from Table 2 that the apparent activation energy of the G coal sample was smaller than that of the C coal sample, especially the low temperature stage, the apparent activation energy of G coal sample was much smaller than that of C coal sample, the variation reached up to 4.18 kJ $mol^{-1}$. At the high temperature stage, the apparent activation energy of G coal sample and C coal sample did not show much difference, the variation was 1.08 kJ $mol^{-1}$. However the low temperature stage is the key of coal spontaneous combustion, because the emphasis on prevention and control of coal spontaneous combustion is focused on the low temperature stage [30–33]. According to the definition of apparent activation energy, the smaller activation energy means the less energy required for activating the reaction under the same conditions [34]. Namely, G coal sample had stronger oxidation ability and higher reactivity than C coal sample, especially in the low temperature stage, oxidation reaction of G coal sample would be easier and faster, the requirements of the thermal storage environment was lower, and it would be more liable to oxidize and bring about spontaneous combustion.

**Table 2.** Summary on apparent activation energy of coal samples C and G at low and high temperature stages

| Coal sample | Apparent activation energy $E_a$/kJ $mol^{-1}$ | | |
|---|---|---|---|
| | Low temperature stage | High temperature stage | Variation |
| C coal sample | 73.41 | 34.14 | 39.27 |
| G coal sample | 69.23 | 33.06 | 36.17 |
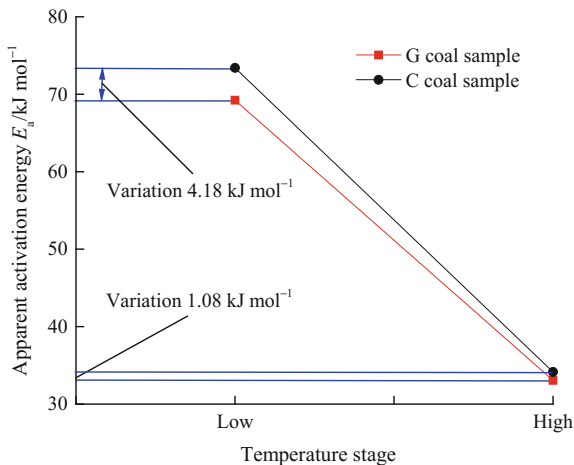


**Fig. 7.** Comparison on apparent activation energy of coal samples C and G

# 4   Conclusions

The oxygen consumption rate, CO and $CO_2$ generation rates, and extreme heat release intensity of the coal sample which was pretreated at the constant temperature of 40 °C were higher than those of the temperature rising from room temperature of 20 °C, and the phenomenon became increasingly obvious with the increase of temperature, which indicated that the high temperature environment made the oxidability and exothermicity of coal enhance.

The calculation model of apparent activation energy was established based on the relationship between CO concentration and temperature. The apparent activation energy of the G coal sample was smaller than that of the C coal sample, especially in the low temperature stage, the apparent activation energy was much smaller, which indicated that the G coal sample had stronger oxidation ability and higher reactivity than C coal sample. It was more easier to heat up, the risk of spontaneous combustion increased.

Due to pre-oxidation of the high temperature environment, the exothermic oxidization of the coal in the high geo-temperature environment was enhanced, and it was more likely to oxidize and warm up, eventually lead to spontaneous combustion. As for as safety, the high geo-temperature mine should strengthen the work of monitoring and forecasting for coal spontaneous combustion, and carry out the pre-control measures on cooling and air leakage to reduce the mine temperature and prevent spontaneous combustion of coal.

# References

1. Stracher, G.B.: Coal fires burning around the world: a global catastrophe. Int. J. Coal Geol. **59**(1–2), 1–6 (2004)
2. Xie, J., Xue, S., Cheng, W., Wang, G.: Early detection of spontaneous combustion of coal in underground coal mines with development of an ethylene enriching system. Int. J. Coal Geol. **85**(1), 123–127 (2011)
3. Xiao, Y., Li, Q., Deng, J., Shu, C., Wang, W.: Experimental study on the corresponding relationship between the index gases and critical temperature for coal spontaneous combustion. J. Therm. Anal. Calorim. **127**(1), 1009–1017 (2017)
4. Xie, H.P., Zhou, H.W., Xue, D.J., Wang, H.W., Zhang, R., Gao, F.: Research and consideration on deep coal mining and critical mining depth. J. China Coal Soc. **37**(37), 535–542 (2012)
5. Chen, W., Liang, S., Liu, J.: Proposed split-type vapor compression refrigerator for heat hazard control in deep mines. Appl. Therm. Eng. **105**, 425–435 (2016)
6. He, M.: Application of HEMS cooling technology in deep mine heat hazard control. Min. Sci. Technol. **19**(3), 269–275 (2009)

7. Qin, B., Sun, Q., Wang, D., Zhang, L., Xu, Q.: Analysis and key control technologies to prevent spontaneous coal combustion occurring at a fully mechanized caving face with large obliquity in deep mines. Min. Sci. Technol. **19**(4), 446–451 (2009)
8. He, M., Cao, X., Xie, Q., Yang, J., Qi, P., Yang, Q., et al.: Principles and technology for stepwise utilization of resources for mitigating deep mine heat hazards. Min. Sci. Technol. **20**(1), 20–27 (2010)
9. Guo, P., Qin, F.: Preventive measures against heat hazard and its utilization in Zhangshuanglou Coal Mine. J. China Coal Soc. **38**(S2), 393–398 (2013)
10. Guo, P., He, M., Zheng, L., Zhang, N.: A geothermal recycling system for cooling and heating in deep mines. Appl. Therm. Eng. **116**, 833–839 (2017)
11. Sasmito, A.P., Kurnia, J.C., Birgersson, E., Mujumdar, A.S.: Computational evaluation of thermal management strategies in an underground mine. Appl. Therm. Eng. **90**, 1144–1150 (2015)
12. Millar, D., Trapani, K., Romero, A.: Deep mine cooling, a case for Northern Ontario: Part I. Int. J. Min. Sci. Technol. **26**(4), 721–727 (2016)
13. Trapani, K., Romero, A., Millar, D.: Deep mine cooling, a case for Northern Ontario: Part II. Int. J. Min. Sci. Technol. **26**(6), 1033–1042 (2016)
14. Arisoy, A., Beamish, B.: Reaction kinetics of coal oxidation at low temperatures. Fuel **159**, 412–417 (2015)
15. Li, B., Chen, G., Zhang, H., Sheng, C.: Development of non-isothermal TGA–DSC for kinetics analysis of low temperature coal oxidation prior to ignition. Fuel **118**(8), 385–391 (2014)
16. Qi, G., Wang, D., Zheng, K., Xu, J., Qi, X., Zhong, X.: Kinetics characteristics of coal low-temperature oxidation in oxygen-depleted air. J. Loss Prev. Process Ind. **35**, 224–231 (2015)
17. Wang, D., Xin, H., Qi, X., Dou, G., Qi, G., Ma, L.: Reaction pathway of coal oxidation at low temperatures: a model of cyclic chain reactions and kinetic characteristics. Combust. Flame **163**, 447–460 (2016)
18. Zhang, Y., Wu, J., Chang, L., Wang, J., Xue, S., Li, Z.: Kinetic and thermodynamic studies on the mechanism of low-temperature oxidation of coal: A case study of Shendong coal (China). Int. J. Coal Geol. **120**, 41–49 (2013)
19. Ozbas, K.E., Kök, M.V., Hicyilmaz, C.: Comparative kinetic analysis of raw and cleaned coals. J. Therm. Anal. Calorim. **69**(2), 541–549 (2002)
20. Deng, J., Li, Q., Xiao, Y., Wen, H.: The effect of oxygen concentration on the non-isothermal combustion of coal. Thermochim. Acta **653**, 106–115 (2017)
21. Yu, L.Y., Li, P.S.: Thermogravimetric analysis of coal and sludge co-combustion with microwave radiation dehydration. J. Energy Inst. **87**(3), 220–226 (2014)
22. Chen, G., Ma, X., Lin, M., Lin, Y., Yu, Z.: Study on thermochemical kinetic characteristics and interaction during low temperature oxidation of blended coals. J. Energy Inst. **88**(3), 221–228 (2015)
23. Xu, J.: Determination theory of coal spontaneous combustion zone. China Coal Industry Publishing House, Beijing (PR China) (2001)
24. Deng, J., Zhao, J., Zhang, Y., Huang, A., Liu, X., Zhai, X., et al.: Thermal analysis of spontaneous combustion behavior of partially oxidized coal. Process Saf. Environ. Prot. **104**, 218–224 (2016)
25. Deng, J., Xiao, Y., Li, Q., Lu, J., Wen, H.: Experimental studies of spontaneous combustion and anaerobic cooling of coal. Fuel **157**, 261–269 (2015)
26. Wang, C., Yang, Y., Tsai, Y., Deng, J., Shu, C.: Spontaneous combustion in six types of coal by using the simultaneous thermal analysis-Fourier transform infrared spectroscopy technique. J. Therm. Anal. Calorim. **126**(3), 1591–1602 (2016)

27. Baris, K., Kizgut, S., Didari, V.: Low-temperature oxidation of some Turkish coals. Fuel **93**, 423–432 (2012)
28. Wang, H., Dlugogorski, B. Z., Kennedy, E. M.: Coal oxidation at low temperatures: oxygen consumption, oxidation products, reaction mechanism and kinetic modelling. Prog. Energ. Combust. Sci. **29**(6), 487–513 (2003)
29. Tang, Y., Xue, S.: Laboratory study on the spontaneous combustion propensity of lignite undergone heating treatment at low temperature in inert and low-oxygen environments. Energy Fuels **29**(8), 4683–4689 (2015)
30. Su, H., Zhou, F., Li, J., Qi, H.: Effects of oxygen supply on low-temperature oxidation of coal: a case study of Jurassic coal in Yima. China. Fuel **202**, 446–454 (2017)
31. Zhang, Y., Wang, J., Wu, J., Xue, S., Li, Z., Chang, L.: Modes and kinetics of $CO_2$ and CO production from low-temperature oxidation of coal. Int. J. Coal Geol. **140**, 1–8 (2015)
32. Zhou, C., Zhang, Y., Wang, J., Xue, S., Wu, J., Chang, L.: Study on the relationship between microscopic functional group and coal mass changes during low-temperature oxidation of coal. Int. J. Coal Geol. **171**, 212–222 (2017)
33. Song, Z., Kuenzer, C.: Coal fires in China over the last decade: A comprehensive review. Int. J. Coal Geol. **133**, 72–99 (2014)
34. Tang, Y.: Sources of underground CO: Crushing and ambient temperature oxidation of coal. J. Loss Prev. Process Ind. **38**, 50–57 (2015)

# Study on Thermal Effect of Coal Oxidation at Low-Temperature

Zhang Yanni[1,2], Chen Long[1,2(✉)], Jun Deng[1,2], and Zhao Jingyu[1,2]

[1] School of Safety Science and Engineering, Xi'an University of Science
and Technology, Xi'an 710054, Shaanxi, People's Republic of China
cl435425396@foxmail.com; 798850990@qq.com
[2] Shaanxi Key Laboratory of Prevention and Control of Coal Fire,
Xi'an University of Science and Technology, Xi'an 710054, Shaanxi,
People's Republic of China

**Abstract.** Spontaneous combustion of coal is one of the most severe hazards that affect the safety production. The most critical factor for the development and occurrence of coal spontaneous combustion is the heat produced by coal and oxygen at ambient temperature. Therefore, studying the exothermic property of coal is not only the understanding of the process, but also the mechanism of coal spontaneous combustion. In this paper, gassy coal and caking coal were used as the research objects, and the thermal reaction process of coal was studied by C80 microcalorimeter. The changes of heat release rate, initial exothermic temperature, reaction heat and the influence of heating rate were analyzed. Additionally, the low-temperature reaction process was divided into three stages: slow heat energy release, accelerated heat energy release, and rectilinear heat energy release. The variation and amount of reaction heat in the stages are compared. The results show that the initial exothermic temperature weakly caking coal is lower than that of gassy coal, while the reaction heat is large than that of gassy coal, which suggest the spontaneous combustion of weakly caking coal is greater than gassy coal from the perspective of thermal effect. The exothermic characteristics of coal have obvious stage characteristics. The duration of slow heat energy release is long and the heat release is small while rectilinear heat energy release is more than twice that of the sum of heat released in the first two stages. This study is of great theoretical significance to reveal the mechanism of spontaneous combustion of coal.

**Keywords:** Low-temperature oxidation · Thermal effect · Stage characteristics

## 1 Introduction

Coal is the most abundant and widely distributed fossil fuel in the world and is one of the main energy sources used by human beings since the 18th century. The spontaneous combustion of coal can occur during the mining, transportation, and utilization processes. It can endanger workers, waste resources, and pollute the environment [1, 2]. Usually at low-temperature, coal could be oxidized accompanied by heat release and accumulation, which could lead to spontaneous combustion. The spontaneous combustion of coal caused by low-temperature oxidation presents a great potential

safety hazard for daily coal production and storage. Thus, the study of thermal effect of coal oxidation at low-temperature has attracted widespread attention [3, 4].

At present, the most common thermal analysis methods used in coal oxidation, pyrolysis and combustion process are DTA (differential thermal analysis), TGA (thermogravimetry) and DSC (differential scanning calorimetry) [5–7]. The DSC is more accurate if the exothermic and endothermic characteristics of coal in the process of oxidation are studied and analyzed. Therefore, DSC has more applications in the studies of coal spontaneous combustion. Peng [8] studied the heat energy release of 70 samples of 8 kinds of coal within 600 °C and concluded that coal with low rank has more reaction heat and was more prone to spontaneous combustion than coal with high rank. Pilar Garcia et al. [9] examined the spontaneous combustion of three weathered coals within 600 °C by DSC experiments and divided the oxidation process into three stages according to the heat release rate. It was also proposed that the onset temperature was a better indicator of the propensity of coal. Based on previous studies, Mohalik [10] compared three different thermal analysis techniques and found that most of the researchers studied the temperature range above 500 °C, the highest close to 2000 °C, and proposed the development trend of thermal analysis techniques in the evaluation of coal spontaneous combustion. Xu et al. [11] simulated the exothermic characteristics of coal oxidation process by using the self-developed large-scale spontaneous combustion and temperature programmed experimental apparatus, and put forward that the exothermic intensity is an important parameter for characterizing the process of coal spontaneous combustion.

Last but not least, as previously mentioned many scholars have conducted thermal analysis of coal oxidation, however, most of them regarded the entire oxidation process of coal from ambient temperature to about 600 °C as the research object and focused on the high-temperature phase. Coal can react with oxygen at ambient temperature and produce large amounts of heat, which will lead to a temperature rise and thermal runaway described as spontaneous combustion if the heat cannot be timely dissipated. In this paper, weakly caking coal and gas coal were used as the research objects to study the thermal reaction process. The exothermic character was analyzed and the thermal effect of coal spontaneous combustion was mastered.

## 2 Experiments

### 2.1 Samples

Coal samples were collected from coalfields in China. Weakly caking coal was collected from the Chaoyuan coal mine in Yulin, Shaanxi province; gas coal was from the Zhangji coal mine in Huainan, Anhui province. The samples were not subjected to water injection, spraying, or other treatments and were, instead, sealed and packed with multilayer plastic and nylon bags before being transported to the laboratory. The results of proximate analysis are shown in Table 1. Using the international classification method, the weakly caking coal is ranked as high volatile-A bituminous while the gas coal is semi-anthracite.

**Table 1.**  Proximate analyses

| Sample | Moisture/% | Volatile/% | Ash/% | Fixed carbon/% |
|--------|-----------|-----------|-------|----------------|
| Weakly caking coal | 5.09 | 21.24 | 34.56 | 39.11 |
| Gas coal | 1.84 | 6.42 | 32.47 | 59.27 |

## 2.2  Experimental Apparatus and Conditions

According to the experimental requirements, in this study, DSC was adopted, and the DSC instrument used here was the C80 micro-calorimeter produced by SETARAM. The apparatus is shown in Fig. 1, mainly including C80 mainframe and gas circulating pool. The gas circulation pool is composed of two chambers of high thermal conductivity, which are identical in shape, size and material. One is used for loading samples and the other is used for loading reference. In addition, the 3D Calvet sensor is used to totally surround the sample and no matter how small the thermal transformation it can provides a complete picture of the event. Therefore, it can accurately test the heat generation during coal low-temperature oxidation even though only a minor amount of heat is generated. This feature is of great significance for studying the minor heat release in the low temperature stage.
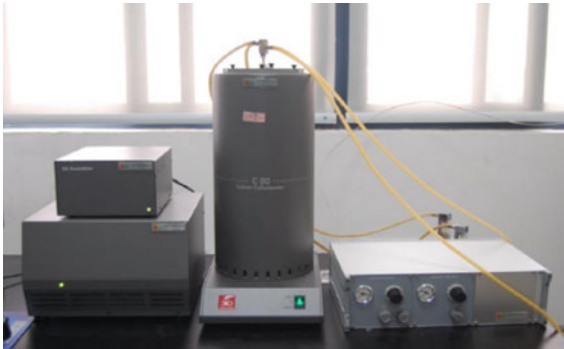


**Fig. 1.**  C80 micro-calorimeter

The samples were crushed and screened to 0.106 to 0.18 mm with 1600 mg for testing. The air flow rate is 100 mL/min, and the heating rates are 0.1, 0.2, 0.4 and 0.6 °C/min. The starting temperature is 30 °C and the termination temperature is 260 °C.

## 3    Experimental Results and Discussion

### 3.1    Heat Release Behavior of Coal Low-Temperature Oxidation

In measuring heat release characteristics of coal samples, the change in temperature due to the heat release induces the change of the resistivity of the thermocouple and further lead to the change of the voltage. Therefore, the read signal is voltage, that is, the heat flow of the coal sample is actually a signal converted from the voltage difference between the sample and the reference cell. In theory, if there is no endothermic or exothermic reaction, the voltage signal measured in the sample cell is the same as the reference cell, and the heat flow signal should be zero, while the exothermic or endothermic reaction occurs, the heat flow signal will change.

The measured heat flows versus temperature are shown in Fig. 2. The heat flow increases with the temperature, indicating that the exothermic trend strengthens. The heat flow of each coal sample is very small in the early stage. After 125 °C, the heat flow curve of weakly caking coal increases rapidly formed while the rapid increase for gas coal starts after 150 °C indicating that the higher rank coal is slower in heat release than the lower rank coal. Moreover, the maximum heat flow of weakly caking coal is close to 600 mw while that of gas coal is about 400 mw indicating that the exothermic property of weakly caking coal is greater than that of gas coal. It can be inferred that the reaction heat of weakly caking coal is greater than that of gas coal.
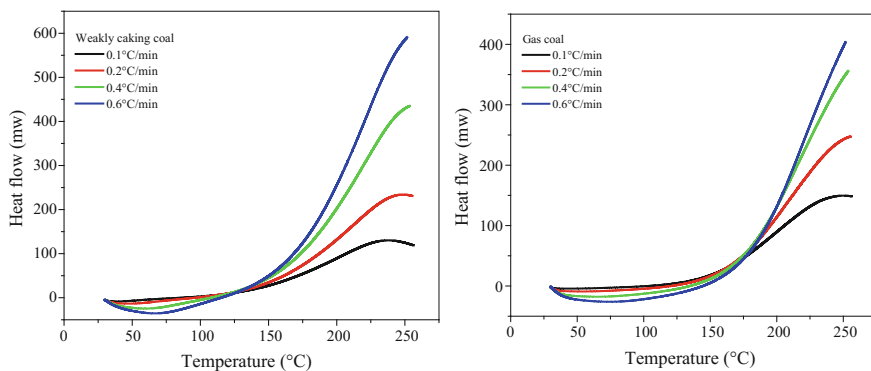


**Fig. 2.**  Curves of heat flow versus temperature with different heating rate

Figure 2 also shows that as the heating rate varies from 0.1 to 0.6 °C/min, the heat flow also shows certain patterns. The higher the heating rate, the greater the absolute value of the heat flow, which is due to the poor thermal conductivity of coal. When the heating rate is higher, the temperature rise of the reference pool is faster than sample pool, so the voltage difference between the sample pool and the reference cell is larger, and the heat flow value is larger. As the reaction progresses, the heat flow increases rapidly with the increase of the heating rate, which is due to the fact that the temperature of the coal increases fast when the heating rate is high, and the active groups in

coal molecule are higher activity at higher temperatures, so the reaction is more intense, and the heat flow is larger.

## 3.2    Initial Exothermic Temperature and Reaction Heat

Due to the difference in quality and air humidity between the sample cell and the reference cell, the heat flow signal fluctuates at the initial experimental stage. Therefore, in the analysis of the exothermic characteristics of coal sample, when a relatively stable heat flow signal is encountered, it is considered that the heat flow signal of the sample cell and the reference cell is in a state of equilibrium. If the heat flow signal is greater than the usual heat flow signal, it is an exothermic reaction. On the contrary, if the heat flow signal is less than normal heat flow signal, it is an endothermic reaction.

The initial exothermic temperature is inferred from the stable heat flow signal, and the initial exothermic temperature of the two coal samples is shown in Table 2. The initial exothermic temperature of at different heating rates gradually increased with the increase of heating rate, which indicates that the faster the heating rate, the higher the temperature at which the instrument can measure. This is due to the fact that the temperature rise rate is low, so the temperature gradient inside the coal sample is very small. On the contrary, if the temperature rise rate is too fast, because of the influence of the thermal conductivity and the thickness of the coal sample, the temperature difference is obvious, thus affecting the test results. At the same heating rate, the initial exothermic temperature of weakly caking coal is lower than that of gas coal, which indicates that the coal with low rank have stronger reactivity and can release heat at a lower temperature.

**Table 2.**  Initial exothermic temperature and reaction heat with different heating rate

| Sample | Heating rate/°C | Initial exothermic temperature/°C | Reaction heat J/g |
|---|---|---|---|
| Weakly caking coal | 0.1 | 37.90 | 4441.9 |
| | 0.2 | 46.21 | 3402.8 |
| | 0.4 | 58.07 | 2669.5 |
| | 0.6 | 65.08 | 2231.4 |
| Gas coal | 0.1 | 42.37 | 4111.6 |
| | 0.2 | 47.47 | 2842.1 |
| | 0.4 | 59.42 | 1778.8 |
| | 0.6 | 68.91 | 1261.2 |

The reaction heats of two coal samples, shown in Table 2, were obtained by integrating the respective heat flow curves. The reaction heat of weakly caking coal is between 2174.635 and 4141.079 J/g while the gas coal is between 1223.2 and 3710.531 J/g. At the same heating rate, the reaction heat of weakly caking coal is higher than that of gas coal, which indicates that the pyrophorisity of weakly caking coal is stronger. In addition, the reaction heat of two coal samples decreases as the

heating rate increases. The faster heating rate induces faster temperature rise, the coal sample cannot get fully reacted at a certain temperature and consequently produces less reaction heat.

### 3.3    Stage Characteristics of Reaction Heat

Usually, coal spontaneous combustion occurs under adiabatic conditions, so the small heating rate is closer to the real reaction. The stage characteristics of reaction heat using the heating rate of 0.1 °C/min are shown in Fig. 3. The curve of reaction heat and temperature is divided into three stages, defined as slow heat energy release, accelerated heat energy release, and rectilinear heat energy release. In the first stage, the reaction heat of the two coal samples increased slowly. After entering the second stage, the reaction heat increased rapidly with the increase of temperature, and in the last stage, the heat release increased exponentially. The reason for the phenomenon is that coal-oxygen reaction was mainly dominated by physical and chemical adsorptions when the temperature is low. The reaction heat mainly depends on the heats generated in physical and chemical adsorption processes. With the increase in temperature, the adsorption reached equilibrium, coal-oxygen reaction mainly depends on the chemical reaction, and the number of reactive functional groups increases. The reaction heat mainly focuses on the chemical reaction heat, which resulted in much more heat release.
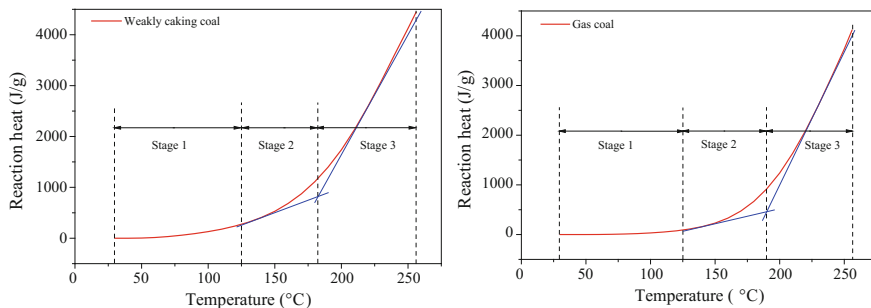


**Fig. 3.**  Stage characteristics of reaction heat versus temperature

The reaction heat of coal samples at each stage and its percentage is shown in Table 3. Although the first stage experiences a long temperature rise range, the amount of reaction heat during this period is very small. Weakly caking coal and gas coal account for 6.1 and 2.2% of the total reaction heat, respectively. In the second stage, the oxidation of coal samples produces more heat than that of the first stage, accounting for about 20% of the total reaction heat. In the last stage, reaction heat is more than twice as much as the sum of heat in the first two phases, accounting for about 75% of the total heat released. In addition, in each stage, the reaction heat of weakly caking coal is larger than that of gas coal, indicating a strong propensity to spontaneous combustion.

**Table 3.** Reaction heat in different stage

| Sample | Stage 1 | | Stage 2 | | Stage 3 | |
|---|---|---|---|---|---|---|
| | Reaction heat (J/g) | Percentage (%) | Reaction heat (J/g) | Percentage (%) | Reaction heat (J/g) | Percentage (%) |
| Weakly caking coal | 272.2 | 6.1 | 864.3 | 19.4 | 3305.4 | 74.5 |
| Gas coal | 91.7 | 2.2 | 828.3 | 20.1 | 3191.6 | 77.7 |

## 4  Conclusion

The initial exothermic temperature of the coal sample increases with the heating rate, while the reaction heat decreases as the heating rate increases. At the same heating rate, the initial exothermic temperature of weakly caking coal is lower than that of gas coal, but the reaction heat is higher than that of gas coal, which indicates that weak caking coal can react and release heat at lower temperature, so its pyrophorisity is stronger than gas coal.

The reaction heat has the stage characteristic. The first stage is very small, which is less than 10% of the total reaction heat, and the second stage accounts for about 20%. The reaction heat in the third stage is more than twice as much as the sum of the first two stages, accounting for about 75% of the total reaction heat.

## References

1. Stracher, G., Taylor, T.: Coal fires burning out of control around the world: thermodynamic recipe for environmental catastrophe. Int. J. Coal Geol. **59**, 7–17 (2004)
2. Zhang, J., Liang, Y., Ren, T.: Transient CFD modelling of low-temperature spontaneous heating behaviour in multiple coal stockpiles with wind forced convection. Fuel Process. Technol. **149**, 55–74 (2016)
3. Qi, G., Wang, D., Zheng K.: Kinetics characteristics of coal low-temperature oxidation in oxygen-depleted air. J. Loss Prev. Process Ind. **35**, 224–231 (2015)
4. Qi, G., et al.: The application of kinetics based simulation method in thermal risk prediction of coal. J. Loss Prev. Process Ind. **29**, 22–29 (2014)
5. Sorescu, M., Xu, T.: Particle size effects on the thermal behavior of hematite. J. Therm. Anal. Calorim. **107**, 463–469 (2012)
6. Zhou, Y., Liu, J., Liang, D., et al.: Effect of particle size and oxygen content on ignition and combustion of aluminum particles. Chin. J. Aeronaut. **30**, 1835–1843 (2017)
7. Duz, M., Tonbul, Y., Baysal, A., et al.: Pyrolysis kinetics and chemical composition of Hazro coal according to the particle size. J. Therm. Anal. Calorim. **81**, 395–398 (2005)
8. Peng, B.X.: Application of thermal analysis technology to study the oxidation and spontaneous combustion process of coal. Saf. Coal Mines **4**, 1–12 (1990)

9. Garcia, P., Hall, P.J., Mondragon, F.: The use of differential scanning calorimetry to identify coals susceptible to spontaneous combustion. Thermochim. Acta **336**(1–2), 41–46 (1999)
10. Mohalik, N.K., Panigrahi, D.C., Singh, V.K.: Application of thermal analysis techniques to assess proneness of coal to spontaneous heating. J. Therm. Anal. Calorim. **98**(2), 507–519 (2009)
11. Xu, J.C., et al.: Analysis on influential factors of thermal effect in coal oxidation. China Saf. Sci. J. **11**(2), 31–36 (2001)
12. Vyazovkin, S., Wight, C.A.: Isothermal and non-isothermal kinetics of thermally stimulated reactions of solids. Int. Rev. Phys. Chem. **17**, 407–433 (1998)

# Part X
# Spontaneous Combustion II

# Test and Analysis of Electromagnetic Radiation in the Process of Coal Oxidation and Spontaneous Combustion

Li Zenghua[1,2], Kong Biao[1,2(✉)], Wang Enyuan[1,2], and Xu Jun[1,2]

[1] Key Laboratory of Gas and Fire Control for Mines, Ministry of Education of China, China University of Mining and Technology, Xuzhou 221116, China
kongbiao8807@l63.com
[2] School of Safety Engineering, China University of Mining and Technology, Xuzhou 221116, China

**Abstract.** The detection of the spontaneous combustion of coal is restricted by the underground environment, and the existing fire detection methods have certain limitations. Efficient and quick detection of a concealed fire is of great importance to the prevention and control of coal spontaneous combustion fires. For this paper, an experimental test system for coal oxidation heating and combustion electromagnetic radiation (EMR) was constructed, the temperature-EMR of coal oxidation heating and combustion under a constant heat source was carried out and the EMR variation characteristics of coal during the oxidation process was studied. Coal can produce significant EMR signals during the process of coal oxidation heating and combustion, and these EMR signals have a significant correlation with the characteristic temperature. The micro-mechanism of free electron generation in the process of coal oxidation heating and combustion was analyzed, and the generation mechanism of EMR was obtained. Finally, the method of detecting spontaneous combustion of coal by EMR was used. The research results may be applied to the detection of spontaneous combustion of coal.

**Keywords:** Coal spontaneous combustion · Electromagnetic radiation Generating mechanism · Fire detection

## 1 Introduction

Coal spontaneous combustion has posed a serious problem not only in the coal mining industry, but also in the transportation and storage of coal. Coal spontaneous combustion seriously affects the normal production of coal; it can lead to fires, asphyxiation, explosions, loss of life, and result in high social, economic and environmental costs [1]. Coal fires have occurred in numerous countries, with the most affected being China, India, the USA, and South Africa [2]. Fifty-six percent of the coal seams in China have a spontaneous combustion tendency; the amount of burning coal exceeds 20 million tons annually because of coal fires. In the western coal areas of China, coal

spontaneous combustion occurs primarily in shallow seams with large air leakage. The XinJiang, Inner Mongolia, NingXia, and ShanXi provinces have a serious risk of coal fires [3].

Coal fires have a characteristically wide range and can cause serious damage. Coal fires are difficult to extinguish and can easily re-ignite. It is difficult to find the fire source in an underground coal field, such as a broken coal pillar or spontaneous combustion of the coal in the goaf [4]. Locating the origin of the fire is difficult even if there is a spontaneous cause or spontaneous combustion. The detection and location of hidden fire sources in a mine are difficult tasks that are nonetheless needed to prevent and control coal fires. It is necessary to efficiently and quickly confirm the occurrence of a fire and locate its source.

Magnetic and electromagnetic signals can be produced in the combustion process of a coal fire. The EMR signal is produced by the deformation and fracture of coal. EMR has the advantage of multi-direction cross-locating and has been widely used to monitor and provide early warnings for coal and rock disasters [5, 6]. Macroscopic deformation and fracture characteristics appear during coal and rock mass heating. The μCT225kVFCB-type high-precision micro CT test system was used to study the relationships between thermal cracking and temperature changes in brown coal and gas coal [7, 8].

Coal rock deformation and fracture can produce EMR signals. Therefore, in coal's thermal damage process, EMR signals are related to thermal deformation and thermal cracking [9]. The change laws of the EMR variation characteristics from coal heating can reveal the temperature effect on EMR signals that can be utilized for a new method to detect concealed fire in coal mines using EMR technology.

For this paper, an experimental test system for coal oxidation heating and combustion EMR was constructed, the temperature EMR of coal oxidation heating and combustion under the condition of constant heat source was carried out, and the EMR variation characteristics of coal during oxidation process were studied.

## 2    Experiment

### 2.1    Coal Samples

Large pieces of coal samples with good integrity were taken from the Da An Shan (DAS) coal mine, the San He Jian (SHJ) mine, the Tong Ting (TT) mine and the Bai Lu (BL) coal mine. The industrial analysis of the coal samples is shown in Table 1.

**Table 1.**  Industrial analysis of coal samples

| Coal sample | Moisture (%) | Volatile matter (%) | Ash (%) | Fixed carbon (%) |
|---|---|---|---|---|
| BL long flame | 3.72 | 26.42 | 11.53 | 59.66 |
| SHJ gas coal | 1.74 | 37.53 | 13.51 | 47.22 |
| TTkin cog coal | 0.51 | 25.23 | 9.85 | 64.41 |
| DAS anthracite | 1.03 | 10.19 | 12.84 | 75.95 |

## 2.2 Experimental System

The experimental EMR testing system for coal heating is shown in Fig. 1. It consists of four parts: a heating device, a temperature-measuring device, an EMR test and analysis device, and a shielding system.
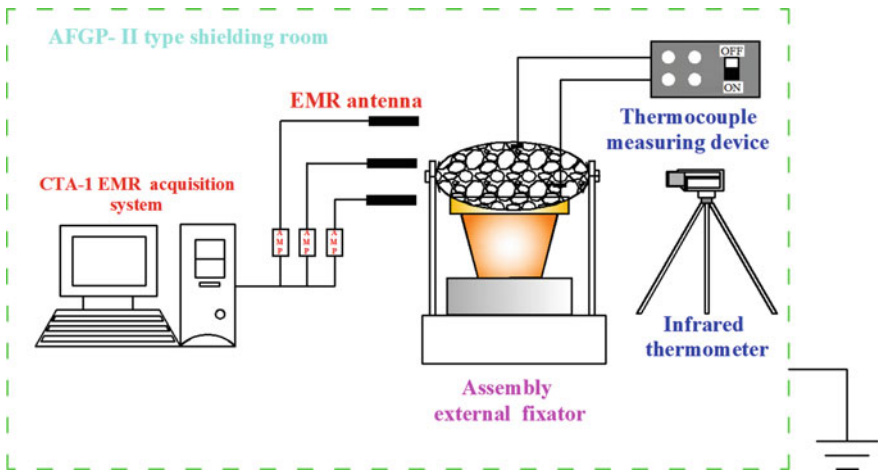


**Fig. 1.** Experimental EMR testing system diagram

EMR signals were acquired using the CTA-1-type electro-acoustic dynamic data acquisition system which can simultaneously collect and analyze data for 8 channels. The working mechanism of this system is as follows: first, the signals received by EMR sensors are amplified by the preamplifier and transmitted into the filter circuit through the coaxial shielded cable. After being filtered, the signals are transmitted into the 16-bit A/D conversion module. Next, the converted digital signal enters the parameter-forming circuit to form EMR parameters which are stored in the buffer and then transmitted to the computer through the PCI bus for further processing and display. An optris PI450 high-resolution infrared thermography testing instrument and thermal-couple measuring device were used to test the coal temperature. To reduce the interference of industrial electricity, radio broadcasts, and communication networks in the receipt of EMR signals, the experiment was performed in an AFGP-II type high-efficient shielding room.

The experimental procedures were as follows: first, the experimental EMR testing system for coal heating was established. Before the start of the experiment, the threshold value of the acquisition system was adjusted to make the threshold value of EMR signals higher than that of EMR signals generated by the machine and environment. In this way, the interference of the environment with the experiment could be effectively eliminated. Meanwhile, layouts of the experimental system and the data acquisition system were adjusted appropriately. The threshold value and sampling rate of the acquisition system were set at 45 dB and 1 MSPS, respectively. The EMR

preamplifier had a gain of 60 dB. The EMR signals were tested from different metamorphic-grade coals—DAS, SHJ, and TT—in the heating process. When the intensity of EMR signals exceeded the threshold value, the high-speed data acquisition system would record the EMR data.

## 3   Results

### 3.1   Changing Characteristics of EMR During Coal Oxidation Heating and Combustion

During coal oxidation heating and combustion, the magnitude of the EMR energy represents the intensity of the signal. The changing characteristics of the EMR signal time series is shown in Fig. 2.

In Fig. 2, it can be seen that the four kinds of metamorphic coal can produce significant EMR signals during the heating process, and there are great differences in the measurement of EMR signals. EMR signals are positively correlated with increase in temperature; as the temperature of the coal body gradually increased, the EMR signals did, too. Because EMR signal trends change at varying temperatures, EMR can reflect change in coal temperature to a certain extent.

### 3.2   Changing Characteristics of EMR Under Varying Distances

The time series characteristics of EMR were tested under different distances, and the relationship between the energy of EMR, the number of pulses and the temperature was obtained, as shown in Table 2.

From the table, it can be seen that the EMR and temperature show a polynomial relationship. The change curves of the EMR energy at different testing distances and different temperature ranges are shown in Fig. 3.

In Fig. 3, there is a significant change in the measurement of EMR under varying distances. A greater test distance corresponds to weaker EMR signals. According to the non-linear regression analysis, EMR signals show a negative exponential decay with an increase in testing distance. The EMR measurements at different distances indicate that EMR comes from the heated coal body. This further indicates that EMR can be applied to detect the hidden fires resulting from coal spontaneous combustion, providing a theoretical basis for the location of fire sources through EMR.
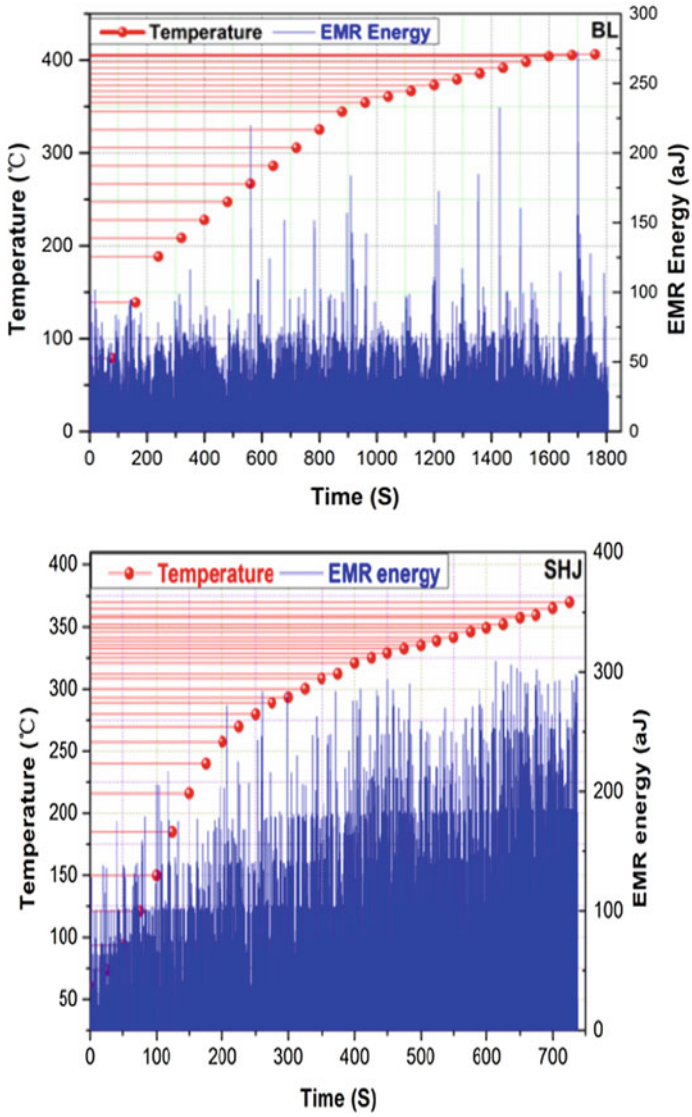
**Fig. 2.** Changing characteristics of EMR with change in temperature
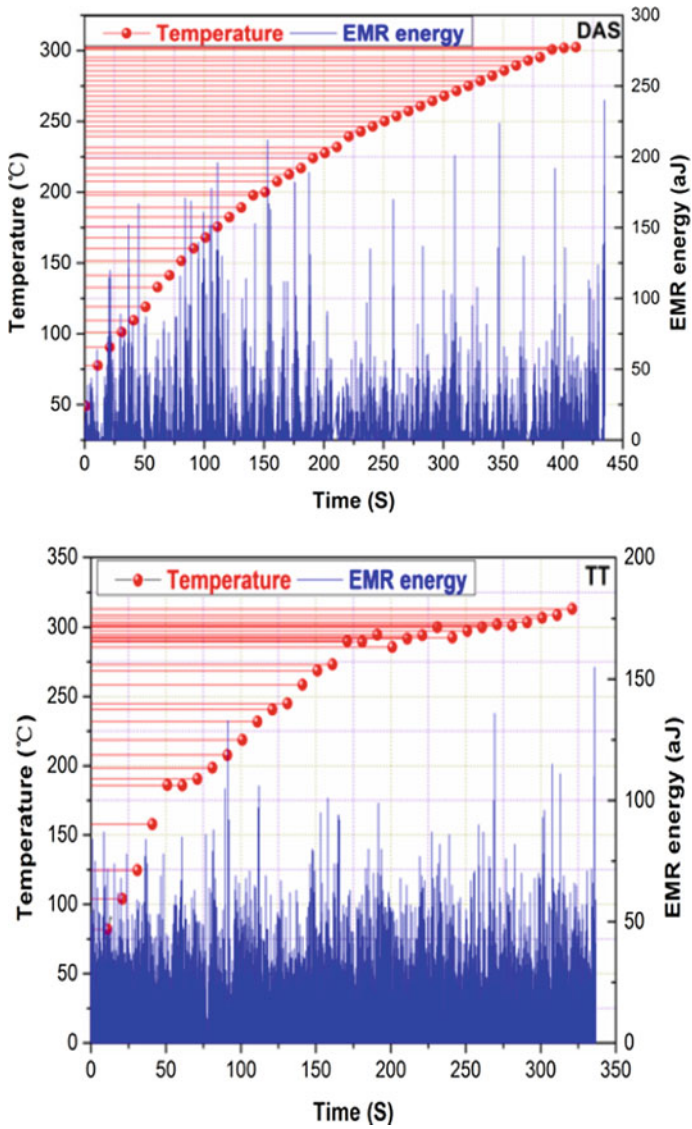
**Fig. 2.** (*continued*)

**Table 2.** Relationship between EMR and temperature

| # | Energy | R | Pulse | R |
|---|--------|---|-------|---|
| 1 | $E = -0.03T^2 + 36.83\,T + 750.4$ | 0.85 | $N = -0.003T^2 + 1.51\,T + 96.3$ | 0.87 |
| 2 | $E = 0.16T^2 + 7.69T + 496$ | 0.87 | $N = 0.003T^2 + 0.61\,T + 68.4$ | 0.93 |
| 3 | $E = 0.017\,T^2 + 7.37T + 254$ | 0.61 | $N = -0.0003T^2 + 0.7T + 43.2$ | 0.72 |
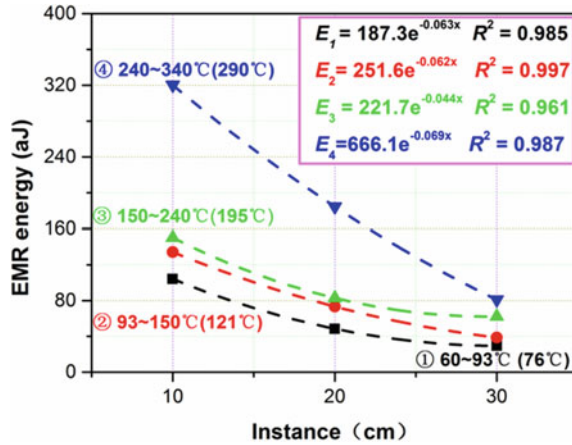
**Fig. 3.** The change curves of the EMR energy at different testing distances

## 3.3  Correlation Between EMR and Temperature During Coal Heating and Combustion

By testing EMR signals during the continuous heating of coal, the strength of the EMR signals at varying frequencies can be related to temperature. As shown in Fig. 4, EMR signals of different frequencies can be produced during the heating process of coal. EMR signals can be received at frequencies of 1, 15 and 50 kHz with a consistent trend; the frequency band of the EMR was wider during the coal-heating process. EMR signals of different frequencies increased with the increase in temperature during the heating process. Thus, EMR can reflect temperature changes as well as deformation and the failure process during coal heating.
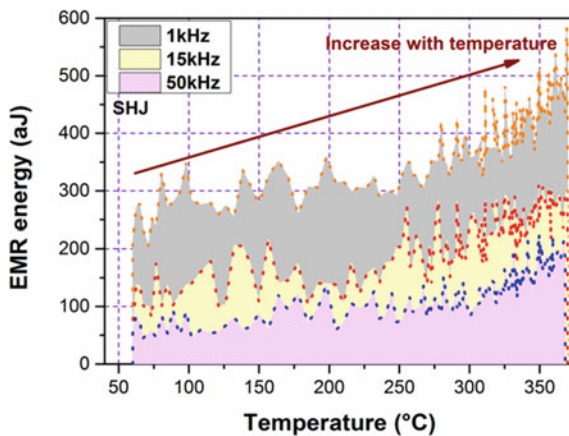


**Fig. 4.** Changing frequency of EMR

The correlation between EMR frequencies and temperature is shown in Fig. 5. EMR signals at different frequencies are strengthened with an increase in temperature. Comparison of the EMR signals at different frequencies at the same temperature shows that the 1 kHz EMR signal is the strongest of all tested frequency bands at most temperatures. In general, the strength of EMR signals increase with a decrease in frequency (see Fig. 4). The correlation between the 1 kHz EMR signal and temperature is the strongest.
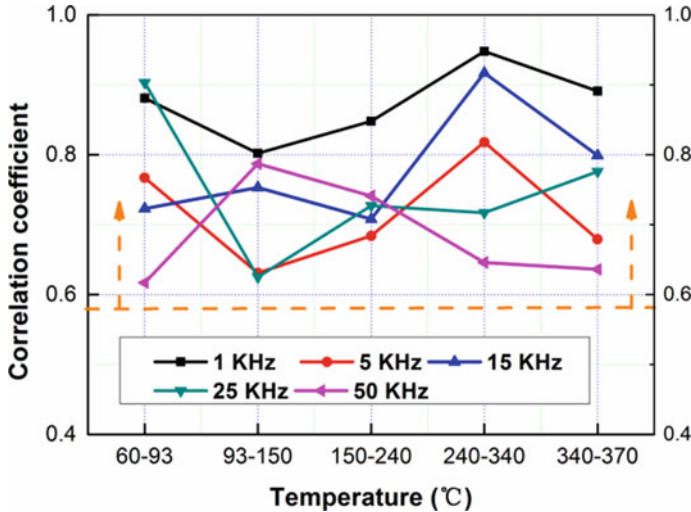


**Fig. 5.** Correlation between EMR and temperature

## 3.4 Microscopic Generate Mechanism of EMR Signals

The common minerals in coal are quartz, feldspar, kaolinite, illite, pyrite, siderite, and calcite. Among these, quartz is the most prevalent. In semi-dull and dull coal, quartz can comprise more than 5–10% of the total amount of organic and inorganic macerals. The X-ray diffraction pattern of the raw coal sample indicates the presence of inorganic minerals such as kaolinite and quartz in the coal samples [10].

Quartz produces a piezoelectric effect when compressed, and this triggers an EMR signal for the deformation of coal and rock under loading. EMR signals are generated by induction of a transient electric dipole, separation of the crack edge charge with crack propagation and relaxation of the separation charge of the crack wall [6]. Friction and slippage occur when the particles in the coal sample are destroyed. The micro-cracks emerge gradually, so the friction is more intense, and the EMR signals are more abundant.

Coal and rock-heating produces swelling deformation during the heating process; therefore, deformation and fracture can produce EMR signals. Coal will produce a large number of cracks in the low temperature stage. Lignite and anthracite produce large amounts of thermal cracking after a rise in temperature. The deformation degree

of coal also varies with temperature [7, 8]. At about 100 °C, the large fissures are in a dominate position; at about 200 °C, medium fissures are dominant; at 300 °C and above, micro-cracks are dominant.

When coal and rock masses are heated, they produce a thermal expansion crack, and an EMR signal is produced as a result. The swelling stress of coal rock increases with the increase in temperature, and the increase in thermal stress promotes the deformation and fracture of coal and rock. When the temperature is increased to a certain value, internal particles of the coal rock tensile strain exceed the ultimate tensile strain, which causes the mineral grain or cement interface to fracture; micro-cracks are produced and appear to continuously slip and expand [11, 12].

Coal and rock thermal fracture studies show that the generation and development of cracks and pores are mainly caused by the effect of thermal stress on the inhomogeneous minerals. When temperature increases, few micro-cracks can be observed, and the partial cracks coalescence to form larger cracks. In the process of crack initiation and propagation, the dipole groups move at the crack tip and emit electromagnetic waves outward. The thermal crack of the coal and rock mass can cause thermal damage, the parameters of which indicate the damage degree of the coal and rock mass in the heating process. The heterogeneity of the coal and rock mass creates varying strengths of each component of the coal and rock.

The relationship between the cumulative amount of EMR pulse $\sum N_T$ and temperature $T$ can be shown as [11]:

$$\frac{\sum N_T}{N_m} = aT^3 + a_1 T^2 + a_2 T + a_3 \tag{1}$$

Equation (1) is the relationship between the cumulative number of EMR pulses and temperature.

## 4 Electromagnetic Radiation Detection Method

The EMR method is a geophysical method that is used to predict dynamic disasters. It can meet the non-contact, no drill requirement. The sensors are not affected by the contact degree of coal and rock. Based on the study of the EMR method by the University of Mining and Technology of China to predict coal and rock dynamic disasters, a non-contact EMR-monitoring instrument for the coal rock dynamic disaster of KBD5 was developed [13]. The monitoring instruments and their arrangement in the working face or roadway are shown in Fig. 6.

As can be seen from Fig. 6, the EMR device was placed in the roadway; the antennas were moved toward the effective receiving area and the testing angle was 60°. Multiple points to test the coal goaf were used, labeled 1–3.

Coal and rock can produce clear EMR signals after thermal damage and EMR can reflect the deformation and fracturing of coal. When the coal or rock is deformed or cracks under pressure, EMR pulse and energy growth are accelerated. But before the crack or deformation, EMR energy and pulsing can serve as an early warning by predicting the trend toward coal and rock deformation and fracturing.
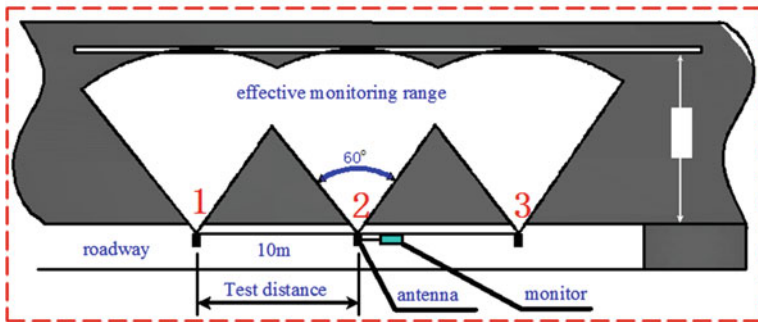
**Fig. 6.** Monitoring instruments and arrangement in the working face or roadway

Under the heating process, coal and rock will produce thermal deformation and rupture. Thermal deformation and rupture will produce EMR. A conceptual design of a method to detect concealed fires in underground mine is presented based on this process [11].

## 5   Conclusions

(1) EMR signals were clearly produced during different metamorphic grades of the coal-heating process. Different frequencies of EMR signals emerged during coal heating. The EMR test frequency signals and test distance affected the EMR signal intensity. EMR was positively correlated with increasing temperature.

(2) During the coal-heating process, thermal deformation and thermal cracking occurred in the coal body. EMR resulted from thermal swelling, deformation and heating fracturing. EMR can thus reflect temperature changes, deformation and the rock failure process during coal heating.

(3) Borrowing the changing characteristics of EMR during the coal-heating process, a conceptual design of a method to detect concealed fires in underground mines has been presented. The results have important significance in revealing temperature's effect on coal EMR and for a method of using EMR to predict mine fires.

# References

1. Li, Z., Kong, B., Wei, A., Yang, Y., Zhou, Y., Zhang, L.: Free radical reaction characteristics of coal low-temperature oxidation and its inhibition method. Environ. Sci. Pollut. Res. **23**(23), 23593–23605 (2016)
2. Song, Z., Kuenzer, C.: Coal fires in China over the last decade: A comprehensive review. J. Coal Geol. F. **133**, 72–99 (2014)
3. Kong, B., Li, Z., Yang, Y., Liu, Z., Yan, D.: A review on the mechanism, risk evaluation, and prevention of coal spontaneous combustion in China. Environ. Sci. Pollut. Res. **1**, 1–8 (2017)
4. Deng, J., Xiao, Y., Chen, X., Cheng, F., Wang, W.: Study on early warning method of multi-source information fusion for coal mine fire. J. Min. Safety Eng. **28**(4), 638–643 (2011)
5. Wang, E., He, X.: An experimental study of the electromagnetic emission during the deformation and fracture of coal or rock. Chin. J. Geophys. (In Chinese) **43**(1), 131–137 (2000)
6. Wang, E., Jia, H., Song, D.: Use of ultra-low-frequency electromagnetic emission to monitor stress and failure in coal mines. Int. J. Rock Mech. Min. Sci. **70**, 16–25 (2014)
7. Meng, Q., Zhao, Y., Yu, Y.: Micro-ct experimental study of crack evolution of lignite under different temperatures. Chin. J. Rock Mech. Eng. **29**(12), 2475–2483 (2010)
8. Feng, Z., Zhao, Y.: Pyrolytic cracking in coal: Meso-characteristics of pore and fissure evolution observed by micro-CT. J. China Coal Soc. **40**, 103–108 (2015)
9. Kong, B., Wang, E., Li, Z., Wang, X., Liu, X., Li, N., Yang, Y.: Electromagnetic radiation characteristics and mechanical properties of deformed and fractured sandstone after high temperature treatment. Eng. Geol. **209**, 82–92 (2016)
10. Zhang, L., Li, Z., Yang, Y., Zhou, Y., Kong, B., Li, J.: Effect of acid treatment on the characteristics and structures of high-sulfur bituminous coal. Fuel **184**, 418–429 (2016)
11. Kong, B., Wang, E., Li, Z., Niu, Y.: Time-varying characteristics of electromagnetic radiation during the coal-heating process. Int. J. Heat Mass Trans. **108**, 434–442 (2017)
12. Wang, E.Y., Kong, B., Liang, J.Y., Liu, X.F., Liu, Z.T.: Experimental study of electromagnetic radiation during coal heating. J. China Univ. Min. Technol. **45**(2), 205–210 (2016)
13. Wang, E., He, X., Liu, X.: A non-contact mine pressure evaluation method by EMR. J. Appl. Geophys. **75**, 338–344 (2011)

# Using CFD to Study Spontaneous Combustion of Coal in Power Plant Stockpile

Santosh Kumar Ray[(✉)], Niroj Kumar Mohalik, Asfar Mobin Khan,
Debashish Mishra, and Nageshwar Sahay

CSIR-Central Institute of Mining and Fuel Research (CSIR-CIMFR),
Barwa Road Campus, Dhanbad, Jharkhand 826015, India
Santoshray8@gmail.com

**Abstract.** Spontaneous combustion of coal in stockpiles depends on coal characteristics, stock geometry, ambient atmospheric condition, viz. wind speed, wind direction, and temperature. The study investigates the coal characteristics, using CFD simulation and field investigation to understand the spontaneous combustion phenomena of coal stockpiles; Fluent Ansys 16.2 was used in the study. 3D transient simulation with a time step of 86,400 s was carried out for thirty days. Three different cases, viz. one stockpile, two stockpiles side by side and four stockpiles were studied with ambient temperature at 27 °C, activation energy $4.8 * 10^7$ J/kg mole, wind speed at 4.5 m/s and wind direction along the length of the stockpile. The rise in temperature is noticed at the base of the coal stockpile and the intensity of the temperature was found to be reduced with the increase in stockpile height. Thermal survey of coal stockpiles using infrared gun reveals that the temperature at the base (120–300 °C) is high as compared to the ones at the top (45–60 °C). This high temperature may be due to the stock of coal for a period more than a month. CFD simulation study thus corroborates the field and laboratory investigation data.

**Keywords:** Spontaneous combustion · Stockpile · DSC study
CFD simulation

## 1 Introduction

Thermal power plant requires heat source for producing steam and coal is used to produce this heat. A large amount of coal is required to fire up the boiler. Depending on the size of the power plant, tens to hundreds of thousands of coal required for this purpose is typically stored openly in stockyards in the form of coal stockpile. There are numerous problems in open coal stockpile: spontaneous combustion of coal, dust generation leads to air pollution, reduction in calorific value leads to effect of coal quality, health hazards to workers as well as surrounding villagers. This paper deals with spontaneous combustion behavior of coal in the stockpile of a power plant.

There are different parameters affecting spontaneous heating of coal stockpiles which can be broadly divided into two categories, endogenous which depends on the nature of coal, and exogenous which depends on the storage conditions. Endogenous parameters include particle size, moisture content, volatility, thermal conductivity,

specific heat and carbon content, while exogenous parameter include atmospheric condition, wind velocity, dimensions of stockpile, moisture content, porosity and degree of compaction and stacking methods. Fine particle size will have greater coal surface area for oxidation reaction whereas in of larger particle reactivity is decreased due to limited accessibility of oxygen to the internal surfaces of coal [1, 2]. Some researchers [3, 4] studied that rate of oxidation increases with a decrease in particle diameter until a critical value is reached. This critical value was found to be 138–387 µm. The moisture content of coal either accelerates or prevents coal oxidation process. The stockpile is considered as a porous domain with a restricted flow of oxygen, where the auto-oxidation of coal from adsorption of atmospheric oxygen resulting formation of a peroxy complex as the source of heat generation.

The wind velocity normal to the stacking axis should be taken into consideration while designing the stockyard. A wind rose diagram should be constructed and direction of piles should be such that it is parallel to the direction of maximum velocity. The penetration of air also plays an important role in auto oxidation of stockpile. The rainfall after a period of dry season increases the risk of spontaneous fire which may be attributed to the release of heat of wetting of dried coal. Proper stacking can help prevent fires by providing heat loss mechanism to the coal stack, many stacking models have been proposed which provide optimum fire safety. Generally, it is observed that more consolidated stacks are less prone to heating than loose stacks. Therefore, care must be taken to ensure proper consolidation.

The study investigates the coal characteristics, CFD simulation and field investigation to understand the spontaneous combustion phenomenon of coal stockpiles. The paper also addresses laboratory investigations dealing with coal characteristics, field investigations comprising a thermal survey of coal stockpiles and CFD simulation involving input parameters like stock geometry, atmospheric condition, wind speed and, direction.

## 2 Laboratory Investigations

Laboratory investigations comprise of proximate analysis, critical oxidation temperature, gross calorific value, differential scanning calorimetry studies have been carried out in the laboratory. The proximate analysis of coal is used widely as the basis for coal characterization. It was developed as a simple means of determining the distribution of products obtained when the coal sample is heated under specified conditions. While moisture, ash, volatile matter are determined experimentally, fixed carbon is determined indirectly. The results of proximate analysis are depicted in Table 1. It can be clearly noticed that all the studies regarding the determination of crossing point temperature, a method widely used in India, involved heating the coal samples to high temperature exceeding 110 °C. For detection of early heating, some criteria involving heating of coal samples to near ambient temperature is required. For this purpose, a concept called critical oxidation temperature has been evolved. The aim of this study is, therefore, to assess the reactivity of coal with oxygen at an ambient temperature in terms of critical temperature. The layout of the experimental setup is shown in Fig. 1.

**Table 1.** Results of proximate analysis, critical oxidation temperature (COT), and GCV

| Sample code | M (%) | Ash (%) | VM (%) | FC (%) | COT (°C) | GCV (cal/g) |
|---|---|---|---|---|---|---|
| Yard-2 heap-202 (1) | 7.07 | 45.29 | 24.34 | 23.31 | 84.4 | 3349 |
| Yard-2 heap-202 (2) | 4.39 | 43.62 | 24.14 | 27.86 | 74.9 | 2924 |
| Yard-1 heap-211 (1) | 8.65 | 36.81 | 26.62 | 27.93 | 81.9 | 3610 |
| Yard-1 heap-211 (2) | 7.76 | 34.91 | 27.16 | 30.18 | 86.9 | 3779 |
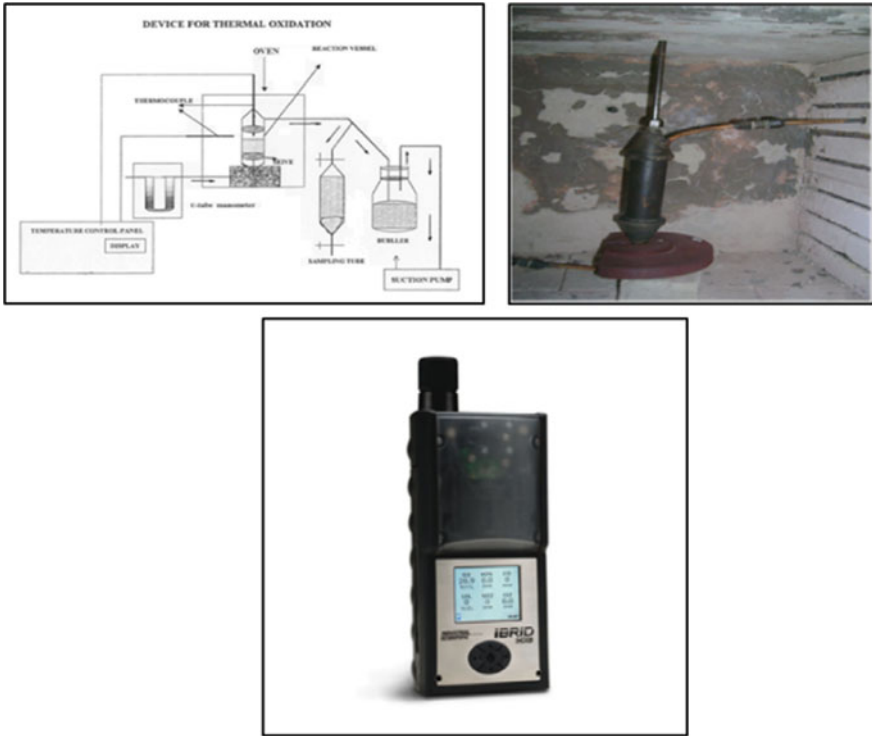


**Fig. 1.** Experimental set-up of thermal de-compositional study for fire ladder

The coal samples were isothermally heated in an air bath at 1 °C/min with a flow rate of 80 cc/min and gas samples from reaction vessel were collected at a different temperature. The gas samples were analysed using multi-gas analyser (CO sensor having accuracy of 1 ppm). The mathematical analysis of the trend of the rise of CO in ppm with temperature obtained from the experimental results revealed that the relationship between CO in ppm and temperature rise is exponential with boundary condition (0 °C < temperature < 130 °C) as given in Eq. 1.

$$y = Ae^{Bx}(when\ x\ is\ 0\ °C\ to\ 130\ °C) \tag{1}$$

Where, A and B are constants; y is the value of CO generated corresponding to x value i.e. temperature.

When x = 0, then y = A

The positive value of y signifies that CO evolved even at temperature 0 °C [10]. By differentiating Eq. 1 i.e. dy/dx = ABe$^{B.x}$, When dy/dx = 1 i.e. 1 = ABe$^{B.x}$

$$x = \frac{1}{B}\ln\frac{1}{AB}\ °C \tag{2}$$

Putting the value of A and B we get a value of temperature known as the critical temperature, the result indicates that emission of CO followed the exponential trend. The critical temperature calculated from experimental results is given in Table 1.

Gross calorific values (GCV) of coal samples were determined with the help of a Bomb Calorimeter using the standard test method ASTM D5865-13. Results are depicted in Table 1.

In present investigation a DSC-404 F3 Pegasus Differential scanning calorimeter of NETZSCH, Germany has been used. DSC experiments were carried out for taking coal sample for analysis in air atmosphere, temperature range from 30 to 930 °C with a heating rate of 10 K/min and flow rate of 100 ml/min. The DSC thermograms (i.e. temperature X-axis and time and heat flow in Y-axis) represent the various reactions of coal oxidation (Fig. 2). The onset temperature, peak temperature, endset temperature and area of the experiment are presented in Table 2.
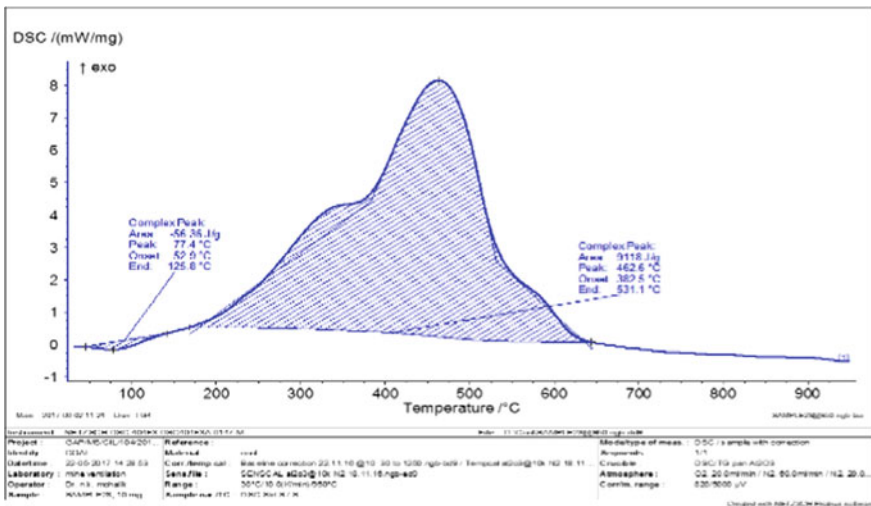


**Fig. 2.** DSC results of Yard-2 heap-201 (1)

**Table 2.** DSC results of coal samples

| Sample code | 1st endothermic peak | | | | 2nd exothermic peak | | | |
|---|---|---|---|---|---|---|---|---|
| | Onset (°C) | Peak (°C) | Endset (°C) | Area (J/g) | Onset (°C) | Peak (°C) | Endset (°C) | Area (J/g) |
| Yard-2 heap-202 (1) | 52.9 | 7.4 | 125.8 | −56.36 | 382.5 | 462.6 | 531.1 | 9118 |
| Yard-2 heap-202 (2) | 55.1 | 79 | 116.9 | −44.8 | 381.1 | 480.1 | 565.4 | 10196 |
| Yard-1 heap-211(1) | 49.1 | 77.7 | 116.7 | −87.77 | 368.6 | 476.7 | 557.7 | 9901 |
| Yard-1 heap-211(2) | 48.5 | 71.3 | 156.1 | −45.71 | 373.8 | 450.3 | 624 | 9043 |

## 3   Field Investigations

Thermal survey of coal yard has been carried out using an Infrared gun at different places of yard 1 and yard 2 (Fig. 3). The thermal survey results for all coal heaps in coal yard are shown in Table 3 for the month of May-June 2017. The temperature varies from 41 to 250 °C up to 12 m vertical height and 48–650 °C up to 4 m vertical height (Table 3). This clearly reveals that near the base temperature is higher as compared to top of the stockpile (Figs. 4, 5 and 6).



**Fig. 3.** Thermal survey using infrared gun at yard no 202

The temperature was high (650 °C) at bottom of the heap as well as some flames in top of yard in heap no. 211. The slope coal yard heap varies from 40° to 45° and stack dimension varies (length: 160–170 m, width: 30–35 m, height: 12–14 m).

**Table 3.** Thermal survey data for Heap 202 and 211

| Hz. | Range | | | | |
|-----|-------|---|---|---|---|
| Vt. ht. | 450–500 m | 500–550 m | 550–600 m | 600–650 m | 650–700 m |
| *Temperature in heap-202 yard #02 road side* (°C) | | | | | |
| 4 m | 48 | 51 | 55 | 50 | 55 |
| 8 m | 50 | 51, 81 | 60, 65 | 55 | 45 |
| 12 m | 100 | 60, 80 | 150, 45 | 48 | 60 |
| *Temperature in heap-202 yard #02 conveyor 7A side* (°C) | | | | | |
| 4 m | 75 | 300,250 | 100 | 65, 60 | 68 |
| 8 m | 50 | 45,52 | 207, 60 | 50, 60 | 70 |
| 12 m | 55 | 50,50 | 50 | 50, 55 | NA |
| *Temperature in heap-211 yard #01 conveyor 7A side* (°C) | | | | | |
| 4 m | 40, 39 | 42, 40 | 40 | 200, 150 | 400 |
| 8 m | 37, 40 | 40, 41 | 50, 48 | 170, 200 | 200, 70 |
| 12 m | 41 | 39, 40 | 50, 40 | 50, 250 | NA |
| *Temperature in heap-211 yard #01 road side* (°C) | | | | | |
| 4 m | 50 | 45, 120 | 53 | 50, 650 | 50 |
| 8 m | 60 | 140, 130 | 53, 50 | 100, 190 | 53, 52 |
| 12 m | 50 | 50, 50 | 50, 40, 50 | 50, 170, 50 | 50 |
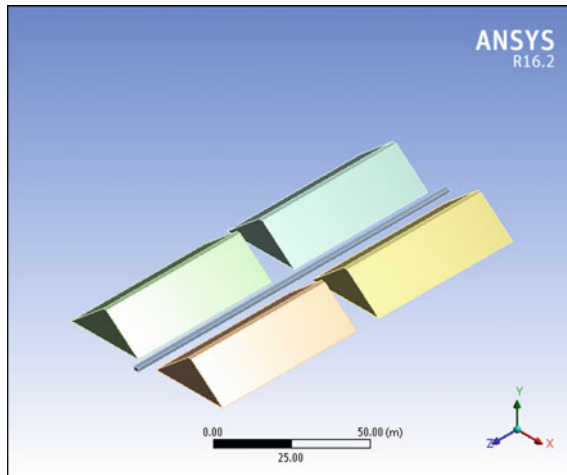


**Fig. 4.** Geometry of 4 coal stockpiles
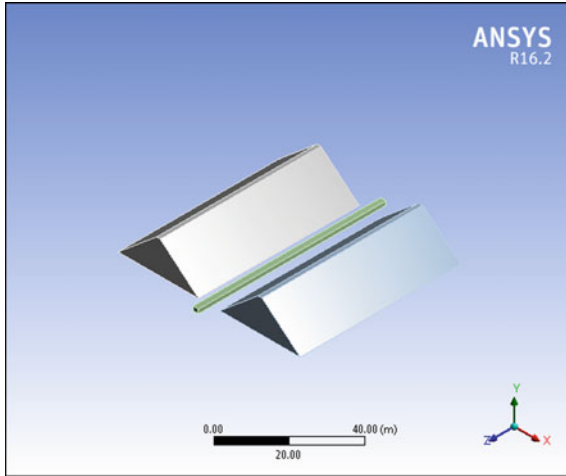
**Fig. 5.** Geometry of 2 coal stockpiles
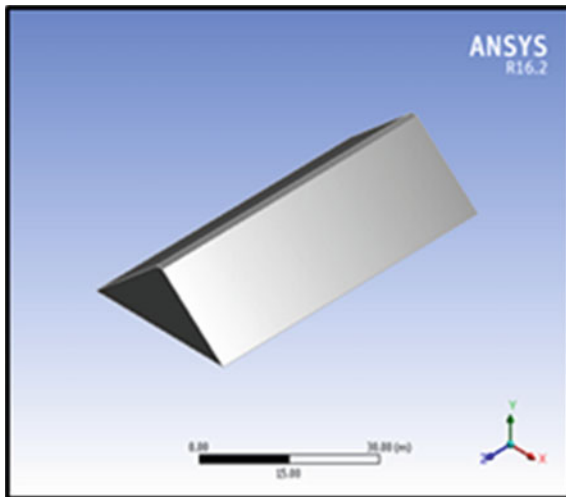


**Fig. 6.** Geometry of 1 coal stockpiles

## 4   Computational Fluid Dynamics (CFD) Simulation

For this study 3-D simulations was performed on Ansys-Fluent 16.2 CFD software. The k − ε turbulence model [5, 6] has been used to determine the flow behavior of the air near and around the coal stockpiles (CS). Three cases, viz. one stockpile (Case-1), two stock piles side by side (Case-2), and four stockpiles, two in each side (Case-3) were studied for a better prediction of the spontaneous combustion phenomenon. Inlet was taken as velocity inlet, outlet as pressure outlet. The inlet velocity was taken to be

4.5 m/s as collected from wind rose diagram. The wind direction was taken along the length of the stockpile as per wind rose diagram. The models were simulated for 30 days to monitor the effect of wind on spontaneous combustion in all three models. Transient model was used. The species model was used to implement spontaneous combustion in CFD modeling. Activation energy value was taken to be $4.8 * 10^7$ J/kg mole and pre-exponential factor was taken to be 890. Porosity was equal to 0.3. Table 4 presents dimensions of the model. The computational mesh was designed with the Hexa-dominant method with about a quarter million cells.

**Table 4.** Dimensions for geometry of coal stockpile

| Properties | Value (s) |
|---|---|
| Stack height | 12 m |
| Stack width bottom | 30 m |
| Stack width top | 2 m |
| Stack length | 60 m |
| Stack slope | 40° |
| Horizontal distance between stacks | 8 m |
| Longitudinal distance between coal stacks | 10 m |
| Width of conveyor | 2 m |

## 5 Results and Discussion

### 5.1 Case 1

The transient simulation was run for 30 days and the effect was observed. In Fig. 7 the temperature of the affected zone (shown in green colour) is around 330 K (57 °C). In Fig. 8 it is observed that the temperature contours are rising from base covering 50% of the slope area with some area in yellow zone i.e. around 335 K (62 °C).

Figure 9 shows a graph of maximum temperature versus time step, it can be observed that as the time increases there is a rise in maximum temperature of the coal stockpile which is around 353 K (80 °C). Figure 10 is a histogram which represents frequency (number of occurrence) versus static temperature. Figure 9 predicts that the maximum temperature zones lies between 300 and 350 K (27–77 °C).

Figures 11 and 12 show the section plane (sct. pl.) of coal stockpile for the front view and side view. It reveals that the major high temperature zones are near the base of the stockpile. From the side view, it can be clearly seen that the temperature decreases with height. All temperature affected areas are marked with red.

Figures 13 and 14 show the $O_2$ mass fraction of coal stockpile in side view and front view. The red zone shows the mass fraction $O_2$ to be 0.23 and the blue zone shows the $O_2$ concentration to be the least. At the boundary of the stockpile, it is observed that the $O_2$ mass fraction transient from red to blue which indicates consumption of $O_2$ at the boundary.
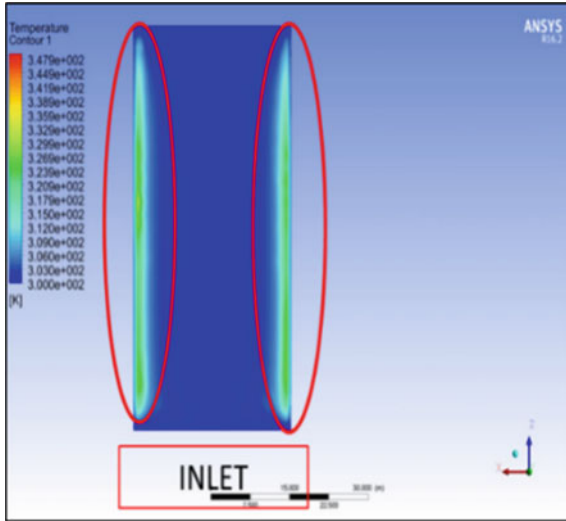
**Fig. 7.** Top view of temp contours of CS
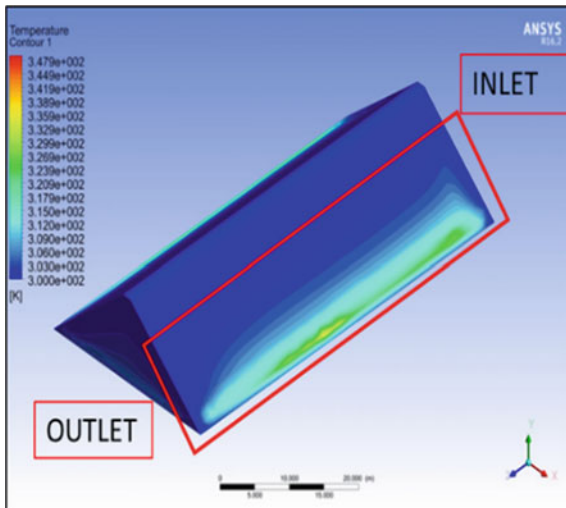


**Fig. 8.** Isometric view of temp contours of CS
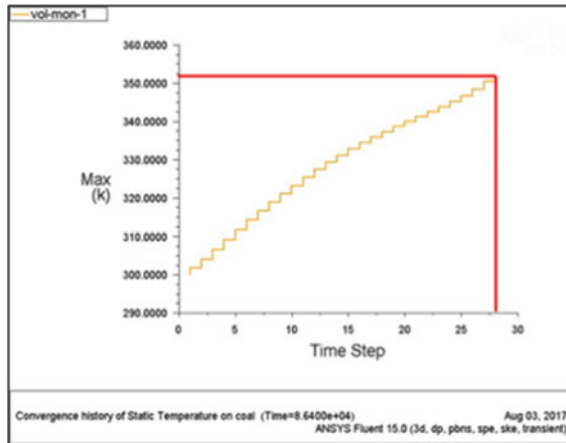
**Fig. 9.** Max temp (Vol. intgl.) versus time step
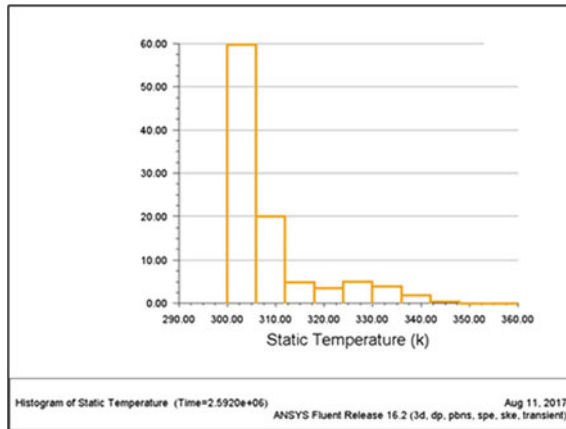


**Fig. 10.** Histogram of static temp

From all the referred figures of Case 1 (stockpile 1), it is observed that the temperature of the coal stockpile is around 330–335 K (57–62 °C) with a maximum of 353 K (80 °C). The normal air temperature is 330 K (27 °C) and the simulation was run for 30 days with a time step of 1 day i.e. 86,400 s. The rise in temperature is noticed at the base of the coal stockpile and the intensity of the temperature is reduced with the height of stockpile as observed from the contour. It can safely be judged that the base of the stockpile is mostly affected by the temperature rise and is more prone to spontaneous combustion and this proneness reduces with the height of the stockpile. It is also observed that the highest temperature region is not at the surface of the stockpile but it is within a vertical height of 2–4 m inside the stockpile at the base which can be clearly seen from the figure. This fact can be further proved by observing the $O_2$ mass fraction contour which shows decreasing gradient of $O_2$ from surface to a depth of 2–4 m.
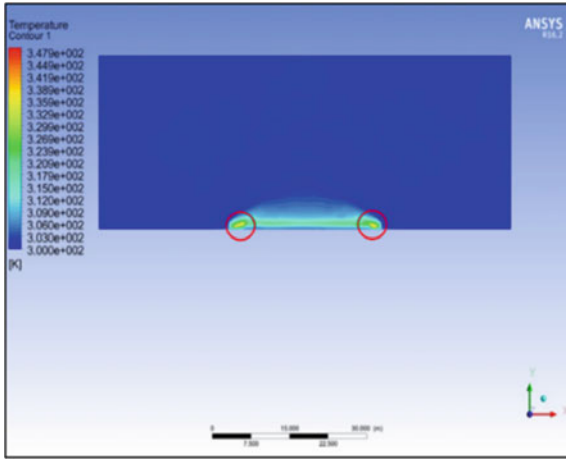
**Fig. 11.** Front view of sct. pl. for temp contour
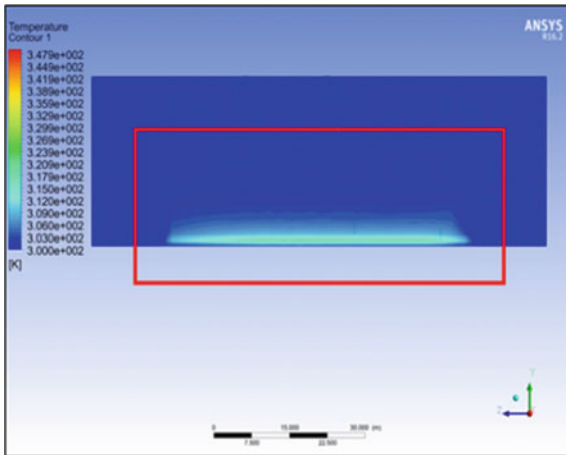


**Fig. 12.** Side view of sct. pl. for temp contour

## 5.2    Case 2

In this case, high temperature zone was found to be around 315 K (42 °C). The effect is witnessed in 30 days. In Figs. 15 and 16, it is observed that the temperature contours are rising from base covering 50% of the slope area with some area in the yellow zone i.e.

The maximum static temperature versus time graph for both the stockpiles is shown in Figs. 17 and 18. The maximum static temperature of stockpile 1 is around 325 K (52 °C) and for stockpile 2 is around 324 K (51 °C).
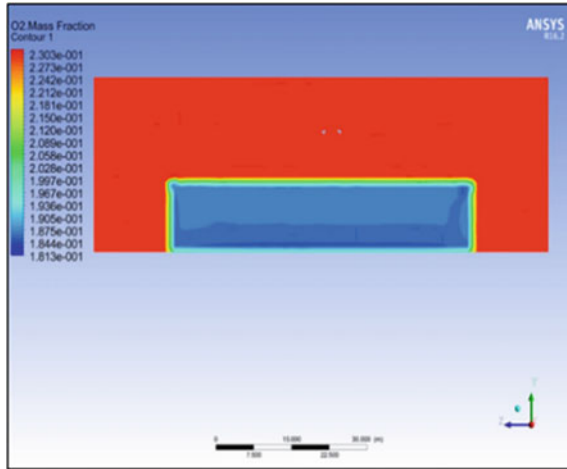
**Fig. 13.** Side view sct. pl. for $O_2$ mass fraction
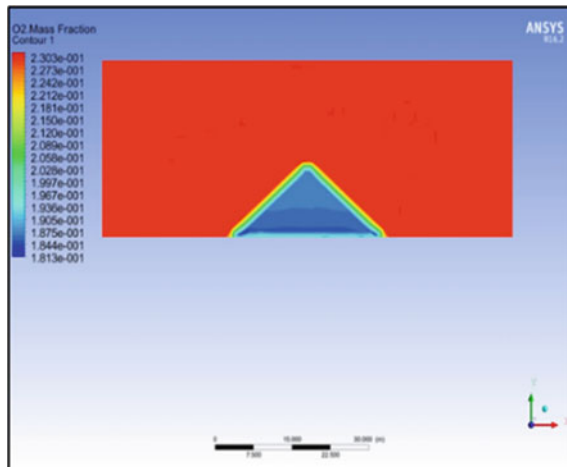


**Fig. 14.** Front view sct. pl. for $O_2$ mass fraction

Figure 19 shows Histogram of static temperatures which represent frequency (no. of occurrence) versus static temperature. The figure predicts that the maximum temperature zone lies between 300 and 325 K (27–52 °C). Figure 20 shows top view of coal stockpile for $O_2$ mass fraction which indicates lesser concentration of $O_2$ at the base of coal stockpile and comparatively more at the upper slope.

Figure 21 is a front view of a section plane for temperature, the maximum temperature at the base area was observed to be 320 K (47 °C).
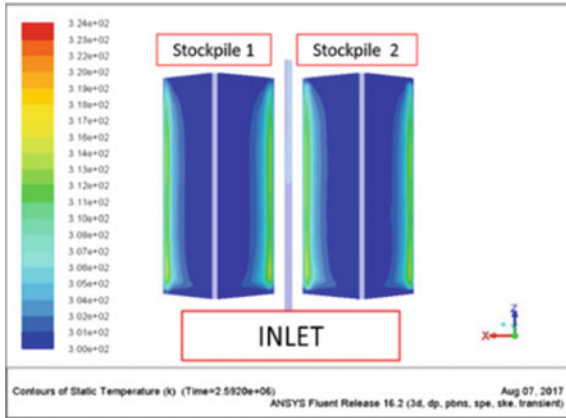
**Fig. 15.**  Top view of temp contours of CS
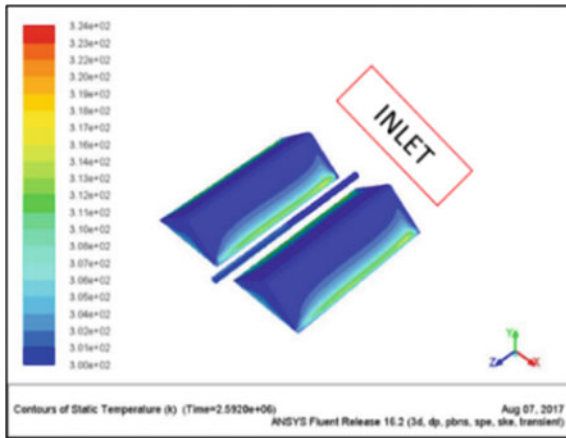


**Fig. 16.**  Isometric view of temp contours of CS

### 5.3    Case 3

Figure 22 shows four coal stockpiles, with a conveyor belt between the stockpiles. The conveyor belt is used to carry the coal from the site to power plant and is an integral part of the Coal Handling plant. It is observed the temperature of the affected zone is around 318 K (45 °C). The effect is witnessed in 30 days. In Fig. 23 it is observed that the temperature contours are rising from base covering 50% of the slope area with some area in yellow zone i.e. around 323 K (50 °C). In Case 3, temperature contours of stockpiles 1 and 2 are the same. Further, the temperature profiles of stockpile 3 and 4 are the same. It is also observed that the temperature contours of stockpile 1 and 2 are different than that of 3 and 4.
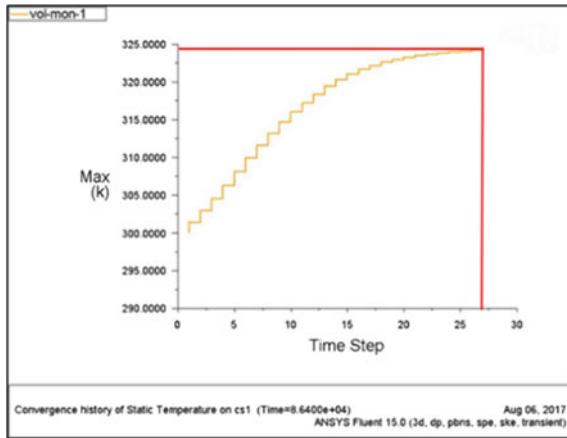
Fig. 17. Max temp of CS 1 versus time step
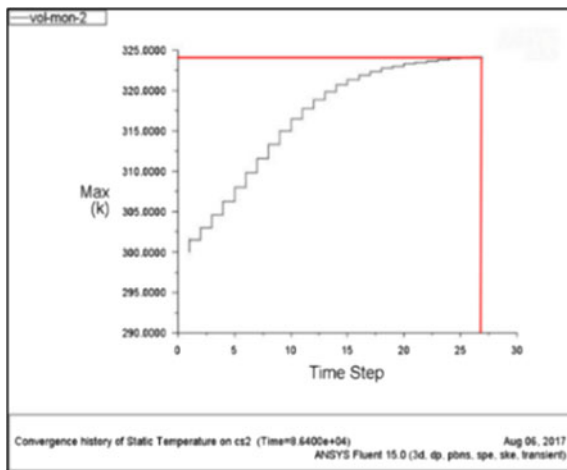


Fig. 18. Max temp of CS 2 versus Time step

Figure 24 shows maximum temperature of stockpile 2 versus time step, the maximum temperature observed is about 328 K (55 °C). Figure 25 shows maximum temperature of stockpile 4 versus time step, the max temperature observed is about 324 K (51 °C). Obviously, the maximum temperature of stock pile 2 is more than stockpile 4.

A similar pattern of results is observed in Case 2 and 3 except that the temperature values are of lesser value and that may be due to shielding effect from the other stockpile. The temperature range in Case 2 is around 315–318 K (42–45 °C) and the maximum value is around 325 K (52 °C) and the temperature range in Case 3 is around
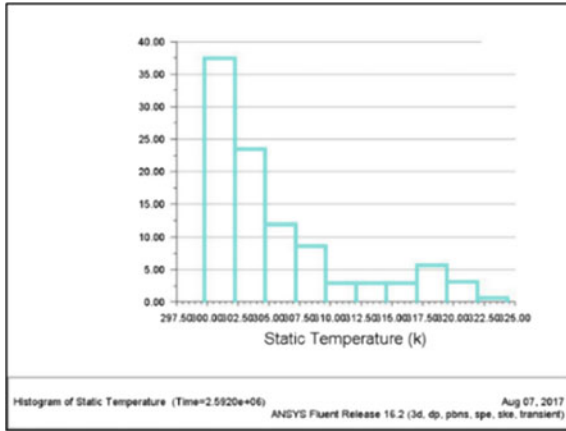
**Fig. 19.** Histogram of static temperature
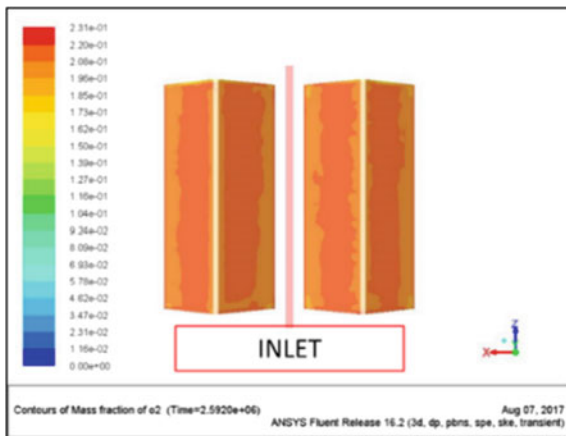


**Fig. 20.** Top view of a CS for $O_2$ mass fraction

318–323 K (45–50 °C) and the maximum value is around 328 K (55 °C). This effect may be due to shielding effect from other stockpiles.

In Case 3, temperature contours of stockpiles 1 and 2 are the same. Further, the temperature profiles of stockpile 3 and 4 are the same. It has also been observed that the temperature contours of stockpile 1 and 2 are different than that of 3 and 4. This also justifies the shielding effect of stockpiles.
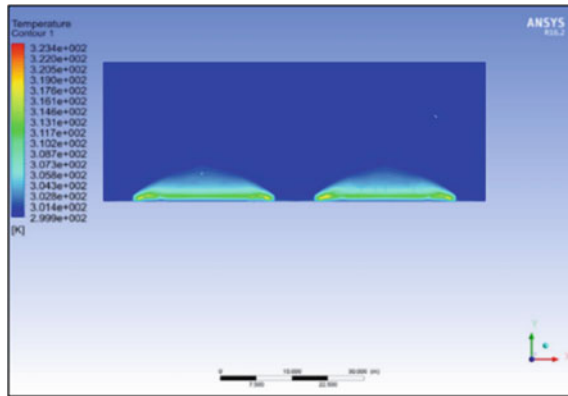
**Fig. 21.** Front view of a section plane for temperature
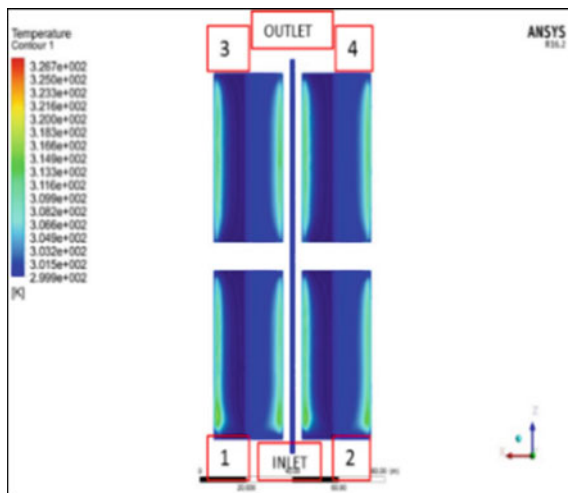


**Fig. 22.** Top view of temperature of four CS
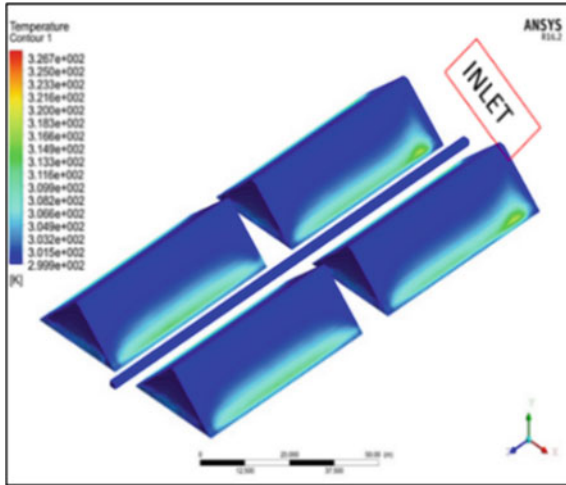
**Fig. 23.** Isometric view of temp of four CS
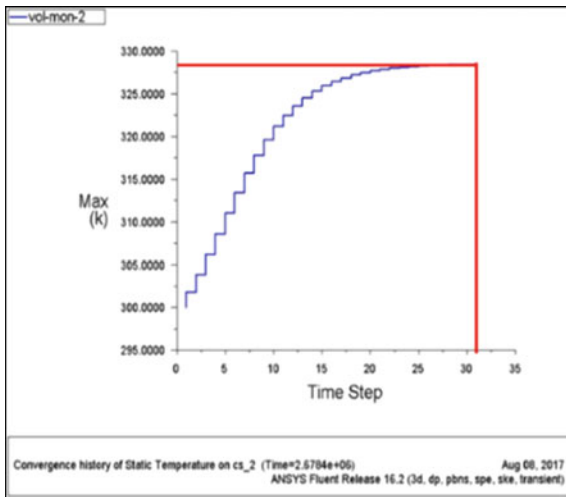


**Fig. 24.** Max temp. of cs 2 versus time step
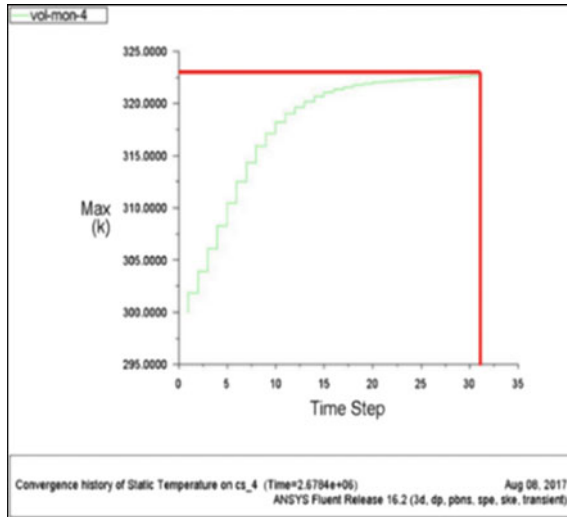
**Fig. 25.** Max temperature of cs 4 versus time step

## 6   Conclusions

The following conclusions are drown from the present study:

1. Laboratory results reveal that the coal is more liable to spontaneous heating having moisture content (4.39–8.65%), critical oxidation temperature (75–87 °C) and endothermic peak temperature (71.3–79.0 °C) from the DSC study.
2. The temperature varies from 41 to 250 °C up to 12 m vertical height and 48–650 °C up to 4 m vertical height. This clearly reveals that up to 4 m temperature is higher as compared to the top of the stockpile.
3. The simulation results reveal that the maximum rise of temperature is up to 80 °C near the base for one stockpile and the highest temperature region is within 2–4 m deep inside the stockpile.
4. It may be mentioned here that simulation for spontaneous combustion of coal stockpile has been done for 30 days whereas the coal stockpiles in the field was more than 2 months old. Simulation with 30 days establishes the same trend.
5. $O_2$ mass fraction contour shows decreasing gradient from the surface to a depth of 2–4 m. Similar observations were also found for cases with two stockpiles and four stockpiles. The rise in temperature is noticed at the base of the coal stockpile and the intensity of the temperature reduces with the increase in height.

## References

1. Akgun, F., Essenhigh, R.H.: Self ignition characteristics of coal stockpiles: theoretical prediction from a two-dimensional unsteady state model. Fuel **80**, 409–415 (2001)

2. Taraba, B., Michalec, Z., Michalcoava, V., Blejchar, T., Bojko, M., Kozubkova, M.: CFD simulations of the effect of wind on the spontaneous heating of coal stockpiles. Fuel **118**, 107–112 (2014)
3. Carpenter, D.L., Sergeant, G.D.: Fuel **45**, 311–327 (1966)
4. Akgun, F., Arisoy, A.: Effect of particle size on the spontaneous heating of a coal stockpile. Combust. Flame **99**, 137–146 (1994)
5. Launder, B.E., Spalding, D.B.: Lectures in Mathematical Models of Turbulence. Academic Press, London, England (1972)
6. Versteeg, H., Malalasekra, W.: An Introduction to Computational Fluid Dynamics, 2nd edn. Pearson, India (2016)

# Study of Structural Changes in Dried Bituminous Coal Soaked in Water and Its Effect on Spontaneous Combustion in Coal Mines

Xiaowei Zhai[1,2(✉)], Long He[1,2], Shibo Wu[1,2], Kai Wang[1,2], Jianchang Zhang[3], and Yongjun He[4]

[1] College of Safety Science and Engineering, Xi'an University of Science and Technology, Xi'an 710054, China
zhaixw@xust.edu.cn
[2] Key Laboratory of Western Mine Exploitation and Hazard Prevention Ministry of Education, Xi'an 710054, China
[3] College of Humanities and Foreign Languages, Xi'an University of Science and Technology, Xi'an 710054, China
[4] Sichuan Police College, Luzhou 646000, China

**Abstract.** This study examines the effects of changes in microphysical structure of dried bituminous coal soaked in water on its propensity to spontaneously combust. A scanning electron microscope (SEM) and low temperature liquid nitrogen adsorption experiments were used to determine the changes in specific surface area, total pore volume, average pore size, and approximate fracture dimensions in the coal samples. Experimental results show that compared with raw coal samples, pores and fractures on the surface of dried bituminous coal soaked in water are enlarged and the pores and fractures also increased in numbers. The results also show that, for dried bituminous coal soaked in water, specific surface area and total pore volume decrease, average pore size increases, and the connectivity of pores and fractures is improved. This contributes to increased oxygen adsorption and increases the risk of coal oxidation and spontaneous combustion of bituminous coal.

**Keywords:** Dried bituminous coal soaked in water · Surface structure
Pore structure · Specific surface area · Total pore volume · Spontaneous combustion of bituminous coal

## 1 Introduction

Because of the rich coal resources in its western regions, China has gradually refocused its coal mining activities to this region in recent years [1]. About 90% of the western coal is bituminous coal with a low degree of metamorphism and the vast majority of the coal seams mined are susceptive to spontaneous combustion [2]. During mining of the lower working face, residual coals in goaf often come in contact with or even immersed in water for long periods, resulting in coal swelling and the dissolution of organic and

inorganic matters on the coal's surface. Thus significant changes in the physical and chemical properties of the coal take place [3–6]. The water content in coal has an effect on the total oxygen absorption and heat release [7].

Analysis of the surface fractal structure of Australian Victorian brown coal in wetting and drying states has found that external moisture can break coal lumps, increase particle volume and porosity, and decrease particle size. After the moisture has evaporated, the specific surface area of the coal in contact with oxygen has increased and this will initiate spontaneous combustion [8]. In oxygen-fuel combustion mode, moisture evaporation significantly reduces the temperature of the gas generated by coal combustion and the ignition time for the coal particles increases in proportion to the extent of moisture evaporation [9]. Matrix moisture content can decrease the gas sorption rate and the coal's macro-diffusivity and cause coal swelling/shrinkage and mechanical property changes that can affect the coal's permeability under reservoir conditions [10].

During the Upgraded Brown Coal (UBC) process[1] in a nitrogen environment, the heating value of the coal is increased from 5448 to 6623 kcal/kg as the coal's moisture content decreases from 15.96 to 3.22% [11]. When the moisture content of the coal is 25%, the rate of heat release from coal oxidation is at its maximum, whereas heat release is lowest when the moisture content is 20% [12]. It has also been found that low-rank coal with 5–10 wt% moisture undergoes oxidation more quickly than does absolutely dry coal [13]. Meanwhile, the crossing point temperatures (The temperature at which the air curve crosses the oven curve is generally referred to as the crossing point temperature) for coal rise with an increase in its moisture content [14]. Using the R70 self-heating rate testing method, it has been shown that the self-heating rate can be tested when the moisture content of Callide coal[2] is ≈40–50%, but that natural oxidation is delayed if the moisture content is more than the critical value [15].

Coal, a porous media, has very complex surface and pore structures, and the microphysical structure of coal affects coal ignition, combustion, and burnout behaviour, and the main relevant parameters are particle size, microscopic internal and external surface area, and pore structure [16]. For fractured media (including coal), it is believed that permeability strongly depends on the fracture volume and (or) fracture aperture [17, 18]. Scanning electron microscopy is commonly used to analyse coal's surface and pore structure including surface morphology, the shape and size of the pores, pore distribution, and pore connectivity [19–21]. Low temperature liquid nitrogen adsorption experiments can also be used to study the coal's pores including specific surface area, pore connectivity, pore size, pore distribution, and other features [22, 23].

In summary, moisture has significant effect on coal's tendency to combust spontaneously. According to combustion theories [24], coal's surface structure affects the coal–oxygen reaction, examining the effect of moisture on coal's surface can help us understand how moisture influences coal's spontaneous combustion. This study uses

---

[1] UBC was developed by Kobe Steel of Japan in the 1990s, it is a method to upgrade low rank coal, such as lignite, using an economic dewatering process.

[2] Samples from Callide Coalfields in Queensland, Australia.

scanning electron microscopy and low temperature liquid nitrogen adsorption experiments to analyse the surface structure and pores of both raw coal samples and dry and wet coals, which will help us better under combustion behavior and device coal combustion resistance and effective combustion control technologies.

## 2 Coal Samples

Samples of bituminous coal of different rank were collected from seams in the Cangcun Coal Mine (the Cc Samples) in Shaanxi Province, the Selian Second Mine (Sl Samples) in Inner Mongolia Autonomous Region, and the Wangwa Second Mine (Ww Samples) located in Ningxia Hui Autonomous Region. The coal is from the Jurassic period, with aquifers above, so it is possible that the coal could have been impacted by water during mining. Proximate analyses of raw coal and dried coal soaked in water were carried out with a Proximate Analyzer[3] according to GB212-91 coal analytical standard [25], and results are shown in Table 1. The analyses show that after soaking and drying the raw coal, the Vdaf (Dry ash-free basis volatile), Ad (Ash content) and FCad (Fixed Carbon) decrease slightly, but generally less than 4%, and the Mad (Dry ash-free basis moisture) content increases fairly significantly, up to about 15%.

**Table 1.** Proximate analyses for coal samples from the Cangcun Coal (Cc), Selian Second (Sl) and Wangwa Second (Ww) mines

| Sample | Mad (%) | $V_{daf}$ (%) | $A_d$ (%) | $FC_{ad}$ (%) | Coal type |
|---|---|---|---|---|---|
| Cc-ym | 2.15 | 28.46 | 11.09 | 58.30 | Long flame coal |
| Cc-js | 2.45 | 28.32 | 10.74 | 58.11 | |
| Change rate (%) | 14.0 | −0.49 | −3.16 | −0.33 | |
| Sl-ym | 8.12 | 27.75 | 9.94 | 54.19 | Non-caking coal |
| Sl-js | 9.11 | 27.30 | 9.78 | 52.19 | |
| Change rate (%) | 12.2 | −1.62 | −1.61 | −3.69 | |
| Ww-ym | 4.75 | 22.82 | 9.38 | 63.05 | Weakly caking coal |
| Ww-js | 5.78 | 22.46 | 9.17 | 61.52 | |
| Change rate (%) | 21.5 | −1.58 | −2.2 | −2.43 | |

## 3 Experimental Methods

### 3.1 Low Temperature Liquid Nitrogen Adsorption

Low temperature liquid nitrogen adsorption was employed to test the specific surface area, total pore volume, and pore distribution of two types of coal samples and to investigate the pores of the dried bituminous coal samples soaked in water. To begin the immersion experiments, the oxidized layer on the surface of lumps of raw

---

[3] Model 5E-MAG6700; by Changsha Kaiyuan Instruments Co., Ltd. in Hunan Province

bituminous coal was first stripped off coal samples were then crushed and screened to obtain samples with 140–180 mesh size range. Three samples, one from each mine, were then soaked in water for 30 days in a constant-temperature, anaerobically sealed vessel. The samples were then removed and dried in vacuum at 30 °C for 72 h before being hermetically sealed in glass-stoppered bottles.

A fully-automatic physical/chemical adsorption analyzer[4]. was used for the adsorption experiments. An approximately 2 g coal sample (weighed using an analytical balance with 1-part-in-10,000 accuracy) was placed in the preconditioning position in the experimental chamber. Before the experiments are performed, the coal samples undergo desorption pre-treatment under vacuum. For pre-treatment, helium is introduced into the experimental chamber and the temperature is raised by 5 °C/min until the temperature reaches 100 °C. The sample is held at 100 °C for 100 min before the temperature is raised, again at 5 °C/min, to 110 °C. The temperature is held constant for 600 min, after which the sample is allowed to cool naturally to room temperature. To perform the nitrogen adsorption measurements, nitrogen is injected into a test tube with the coal sample. The amount of nitrogen adsorbed by the sample is measured under different pressure conditions at −196 °C [The LN2 boiling point is 77 K at room pressure (1 atm)].

## 3.2 Scanning Electron Microscopy

For the SEM investigations, the water-soaked samples were prepared using the same procedure above except the samples were not crushed. Instead, coal samples with large and smooth surfaces were selected for observation.

A JSM-5900 SEM[5] was used to acquire images of raw bituminous coal samples and dried bituminous coal samples that had previously been soaked in water. After the sample was placed in the sample chamber, the chamber was evacuated and the surface structure, pores, and fractures were observed at magnifications of 3000, 20,000, and 70,000 times. The SEM images acquired were used to analyse the samples surface structure, pores, pore filling material, and pore connectivity.

# 4 Results and Discussion

## 4.1 Low Temperature Liquid Nitrogen Adsorption Experiments

The specific surface area of a solid is defined as the total surface area per unit of mass, the surface area being the sum of the areas of the inner and outer surfaces. As described in Sect. 3, the surface area and pore size distribution of coal samples were measured by low temperature liquid nitrogen adsorption. When the temperature is constant, the adsorptive capacity of a test samples changes with changes in pressure. These changes define an isothermal adsorption curve.

---

[4] Model Autosorb-iQ-C produced by Quantachrome Instruments Co., Ltd, United States
[5] Manufactured by JEOL Ltd.

(1)  Analysis of Specific Surface Area

Because the structure of coal molecules is extremely complex, the BET (for Brunauer-Emmett-Teller) method is used to calculate the specific surface area for coal. The BET adsorption isotherm equation can be expressed by Eq. (1):

$$\frac{P}{V(P_0 - P)} = \frac{1}{V_m \cdot C} + \frac{C - 1}{V_m \cdot C} \cdot \frac{P}{P_0} \tag{1}$$

where P and $P_0$ refer to adsorbate (gas) pressure and adsorbate saturation vapor pressure respectively, and C refers to the BET constant. V and $V_m$ indicate gas adsorption capacity and monolayer saturated adsorption capacity, respectively.

Additional parameters used to define the BET line are defined by Eqs. (2), (3), (4), and (5):

$$Y = \frac{P/P_0}{V(1 - P/P_0)} \tag{2}$$

$$X = \frac{P}{P_0} \tag{3}$$

$$X = \frac{P}{P_0} \tag{3}$$

$$A = \frac{C - 1}{V_m \cdot C} \tag{4}$$

$$B = \frac{1}{V_m \cdot C} \tag{5}$$

The BET line is shown in Fig. 1.
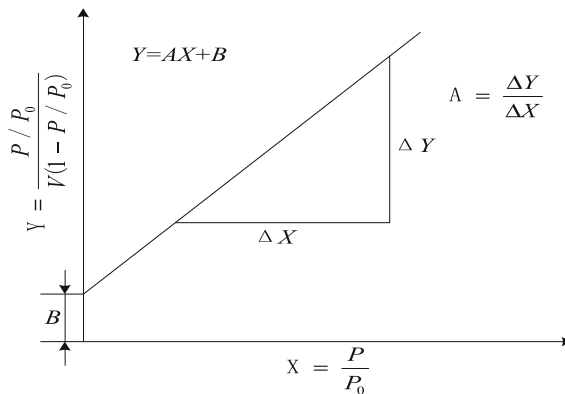


**Fig. 1.** $V_m = 1/(\text{intercept} + \text{slope})$ is obtained and substituted into Eq. (6) to obtain the specific surface area for the coal samples

$$S_g = \frac{4.36 \cdot V_m}{W} \qquad (6)$$

where W and $S_g$ are the sample weight and specific surface area, respectively.

The specific surface areas for the coal samples determined from the isothermal adsorption curves generated by the test results are listed in Table 2.

**Table 2.** Specific surface areas for coal samples determined from isothermal adsorption curves

| Sample | Specific surface area (m²/g) | | Difference of specific surface area (m²/g) | Change rate of specific surface area (%) |
|--------|------------------------------|----------------------------|----------------------------------------|------------------------------------------|
|        | Raw coal sample | Dried coal sample soaked in water |                                        |                                          |
| Cc     | 13.106 | 8.192 | −4.914 | 37.5 |
| Sl     | 8.592  | 5.398 | −3.194 | 37.2 |
| Ww     | 7.248  | 4.398 | −2.85  | 39.3 |

As shown in Table 2, the change in specific surface area between raw bituminous coal samples and dried bituminous coal samples soaked in water is relatively large. For the raw coal samples, the specific surface area of the Cc coal sample is the largest (more than 13 m²/g), and that of Ww coal sample is the smallest (about 7.2 m²/g).

The specific surface area of dried bituminous coal samples soaked in water is smaller than that of the raw bituminous coal samples, which corroborate with Ref. [26]. The change of specific surface area in the Cc samples is the largest and that in the Ww samples is the smallest, but the changes are close to 40% for all the samples. The reason for the changes in surface area may be changes in the internal pore structure of the coal caused by the soaking and drying of the samples. In general, the larger the specific surface area of coal, the larger the surface area of oxidation, and the oxidation of coal is more severe. However, it will reduce the concentration of oxygen in the coal particles and the oxidation rate of coal if the specific surface area is too large, so that the oxidation rate of coal reduce with the increase of specific surface area [26]. Therefore, the reduction of the specific surface area of coal has promoted the oxidation of coal and increased the risk of spontaneous combustion of dried bituminous coal samples soaked in water in this paper.

(2)  Analysis of pore size distribution

Coal pores can be divided into three size ranges, micropores (<2 nm), transitional pores (2–50 nm), and macropores (>50 nm). The amount of liquid nitrogen in pores as measured by the adsorption method can be considered equivalent to the volume of the micropores based on the theory of capillary condensation and the equivalent exchange principle [27].

The Kelvin equation is reproduced as Eq. (7):

$$\ln\frac{p}{p_0} = \frac{2\gamma\overline{V}}{rRT}\cos\theta \tag{7}$$

where, r and $\gamma$ represent the pore range and the surface tension of liquid nitrogen, respectively; T and R are absolute temperature and the universal gas constant; $\overline{V}$ denotes liquid molar volume, and $\theta$ refers to the adsorption dip which is 0° for liquid nitrogen.

The equation for calculating pore size can be written as Eq. (8):

$$\overline{d} = \frac{4V}{A} \tag{8}$$

where V is the total pore volume of the adsorbent and $\overline{d}$ represents the average pore size of the analysis section.

The pore size range for dried bituminous coal soaked in water was calculated by the BJH (for Barret, Joyner and Halenda) liquid-vapor equilibrium method and the pore size range is 5–180 nm. The results are shown in Fig. 2 along with the pore size ranges for the raw coal samples.

In Fig. 2, dv(r) denotes a density function for pore volume distribution corresponding to pore radius; cumulative pore volume is the cumulative total pore volume as the radius of the pores in the coal sample increases.

Figure 2 shows that total pore volume is obviously greater in raw coal samples than in dried coal sample soaked in water, but pore size and the proportion of transitional pores and macropores are smaller. Total pore volumes and average pore sizes for the six coal samples are listed in Table 3.

As shown in Table 3, total pore volume in Cc-ym is the largest (0.1870 cm³/g⁻¹) and that of Sl-js is the smallest (0.0736 cm³/g⁻¹). Average pore size of Sl-js is the largest (9.226 nm), and that of Cc-ym is the smallest (5.565 nm).

By comparing the total pore volumes and sizes in Table 3, it is clear that total pore volume of dried coal samples soaked in water is smaller than that of raw coal samples but that the average pore size is larger, which corroborate with Ref. [26]. The reason may be the internal structure of the coal is colloidallized due to swelling [28], which results in the total pore volume decreasing. The average pore size of dried coal samples soaked in water may be greater than that of raw coal samples because some of the organic and inorganic matter on the coal's surface is dissolved when the coal is soaked in water for a long period. The moving resistance of oxygen in coal pores is small because the pore size of transitional pores and macropores is large, then oxygen can be supplied quickly in the rapid oxidation period of coal, which increases the risk of spontaneous combustion of coal [29]. But micropores is the opposite. Reference [30] has proved that the oxidation of coal is mainly in the transitional pores and macropores. Therefore, the increase of average pore size adds to the risk of spontaneous combustion of dried coal samples soaked in water. Considering the changes in total pore volume and average pore size in the samples after soaking and drying, the pores in Ww are the largest and those on Sl are the smallest. The trend of the changes in total pore volume
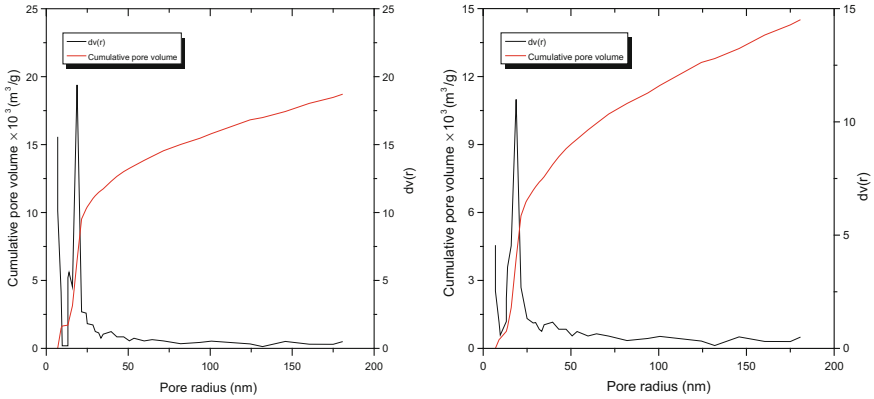
(a₁) Cc raw coal and (a₂) Cc dried coal soaked in water

(b₁) Sl raw coal
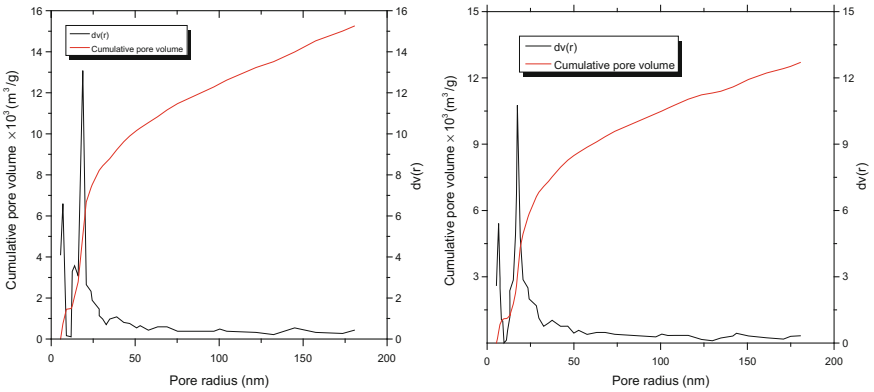
(b₂) Sl dried coal soaked in water
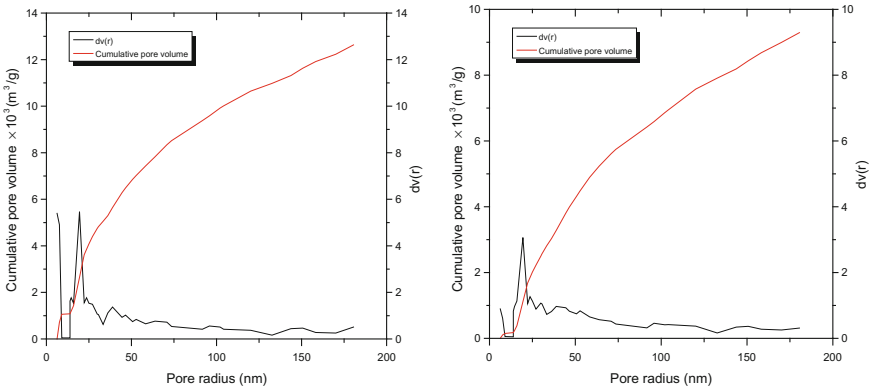
(c₁) Ww raw coal

(c₂) Ww dried coal soaked in water

**Fig. 2.** Pore size distributions of raw coal samples and dried coal samples soaked in water. dv(r) is a density function of pore volume distribution corresponding to pore radius

**Table 3.** Total pore volumes and average pore diameters for six coal samples from coal mines in China

| Sample | Cc-ym | Cc-js | Change rate (%) | Sl-ym | Sl-js | Change rate (%) | Ww-ym | Ww-js | Change rate (%) |
|---|---|---|---|---|---|---|---|---|---|
| Total pore volume $(cm^3/g^{-1})$ | 0.1870 | 0.1496 | 20 | 0.0866 | 0.0736 | 15.0 | 0.1263 | 0.0947 | 25.0 |
| Average pore size (nm) | 5.565 | 7.304 | 31.2 | 8.615 | 9.226 | 7.1 | 6.439 | 8.616 | 33.8 |

and average pore size are the same in the three samples. That is, the smaller the change in total pore volume is, the smaller the change in average pore size.

## 4.2 Scanning Electron Microscope Images

Coal micropores are mainly composed of stoma, pores generated from the residual tissue of a plant, intergranular pores, and moldic pores. Microfractures are either endogenetic fractures or structural fractures [31]. The descriptions and analysis of the six coal samples below are based on the categories just listed.

Figure 3 shows that the surface of the raw coal sample is relatively dense and a small amount of mineral matter has filled pores and fractures. The crack in the surface is large and flat with an imbricate shape and great toughness. It is probably a structural fracture. The fractures and pores in the dried coal sample soaked in water are better developed and more connected than the fractures and pores in the raw coal sample.

It can be seen in Fig. 4 that the micropores in the Sl raw coal samples are mainly pores generated from residual plant tissue. Layered fusinite and fusinite after xylem (fusinite showing remnants of xylem structure) can be observed in Fig. $4a_1$. A small number of intergranular pores accompanied by some mineral crystals can be seen in Fig. $4b_1$. Large and well-developed micropores are visible in Fig. $4c_1$. The number of micropores is larger and pore development is also more advanced in the dried coal sample soaked in water.

In Fig. $5a_1$, the extensive micropore distribution in the sample suggests that the micropores can be classified as pores generated by residual plant tissue; the pores are associated with a few mineral crystals. Different cell tissues with a fringe pattern can also be observed, including fusinite, xylem, and phloem. In Fig. $5b_1$, the development is more advanced, the connectivity is better, and a microfracture is fully developed. The fractures and pores are connected to each other. As can be seen in Fig. $5c_1$, the surface of raw coal sample Ww is rough and composed of particles. However, in the dried coal sample soaked in water, the pores and fractures are larger, and they are both more numerous and better connected. All these contribute to the coal's ability to adsorb oxygen.
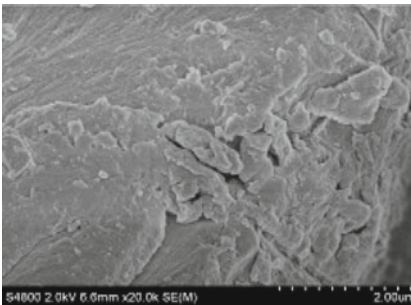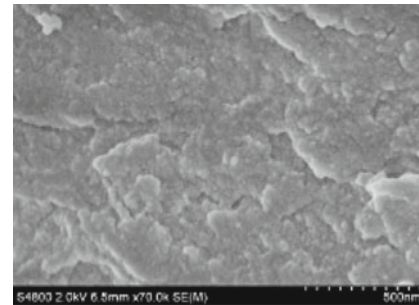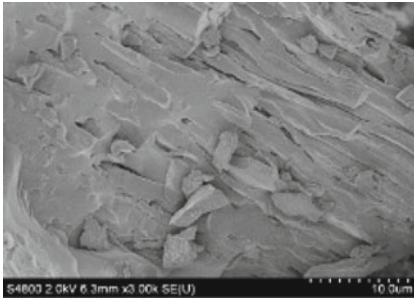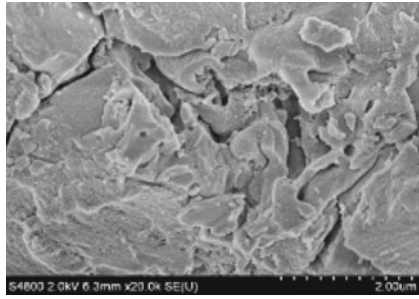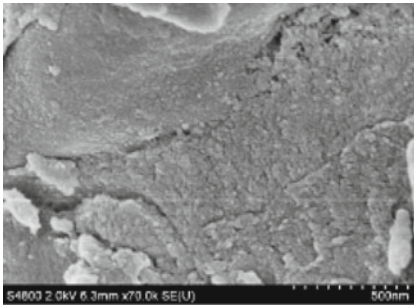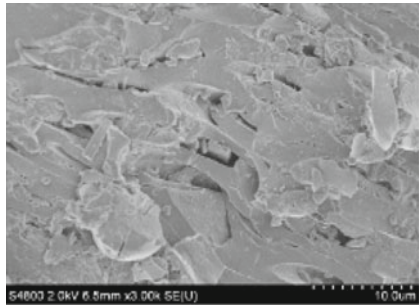
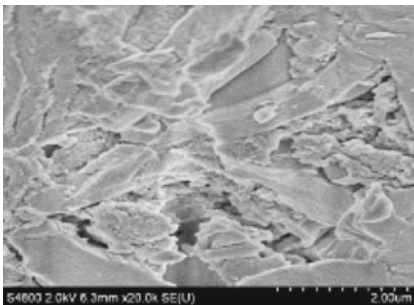(1) Cc coal samples



(a₁) 3,000 times

(b₁) 20,000 times
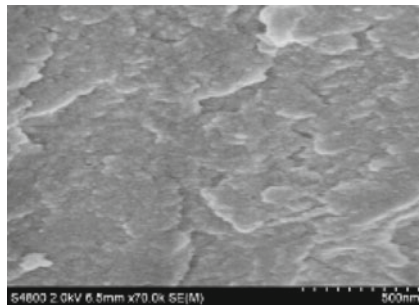
(c₁) 70,000 times

(a₂) 3,000 times

(b₂) 20,000 times

(c₂) 70,000 times
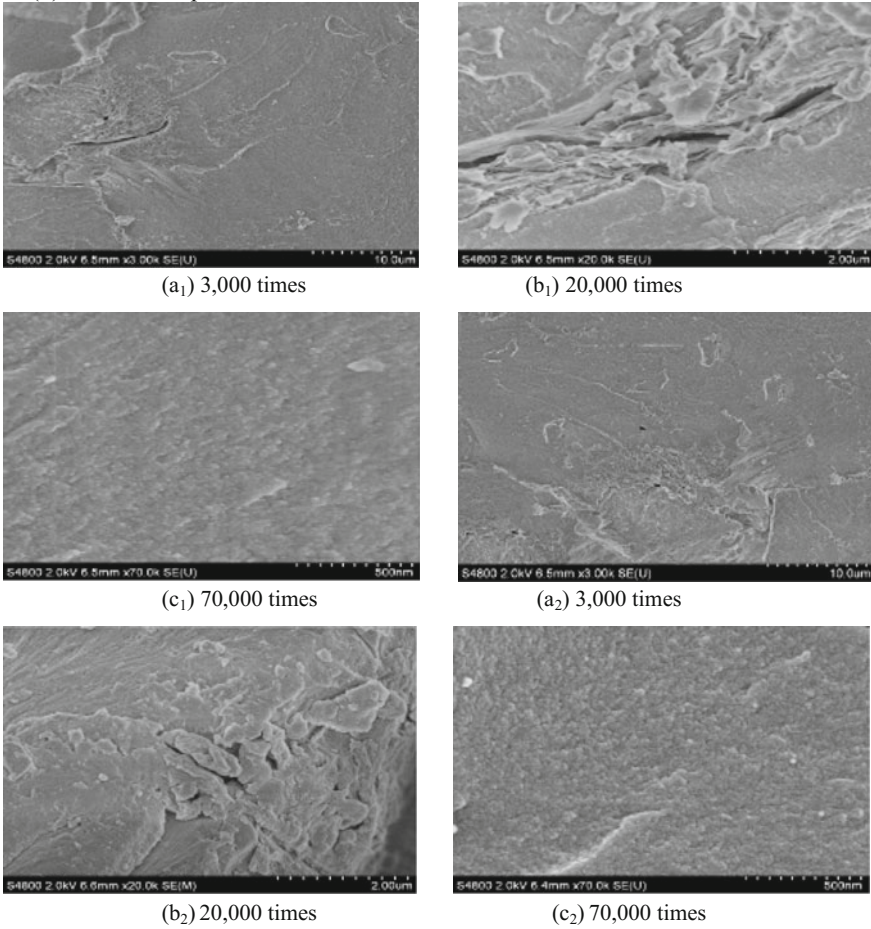
**Fig. 3.** SEM images of Cc coal samples at different magnifications. $a_1$, $b_1$, $c_1$ raw coal sample; $a_2$, $b_2$, $c_2$ dried coal sample soaked in water

Figures 3, 4, and 5 show that the number of pores and fractures on the surface of raw bituminous coal samples differs widely. The pore and fracture widths are at the micron level. Among the samples studied, fracture development is lowest in the Cc raw coal sample but highest in the Ww sample. On the surface of dried bituminous coal samples soaked in water, the pores and fractures are more developed; they are more numerous and the connectivity between the pores and fractures is better. The reason is the coal's degree of metamorphism. Because the degree of metamorphism of bituminous coal is low, there are large numbers of pores and fractures on the coal's surface. Organic and inorganic matter in those pores and fractures dissolves when the coal is soaked in water for a long period. This increases the contact area for coal and oxygen, contributes to the adsorption of oxygen, and results in a higher risk of spontaneous combustion for dried bituminous coal soaked in water.

(2) Sl coal samples
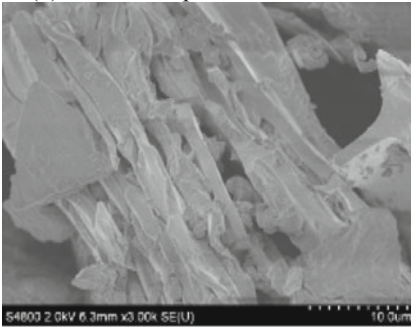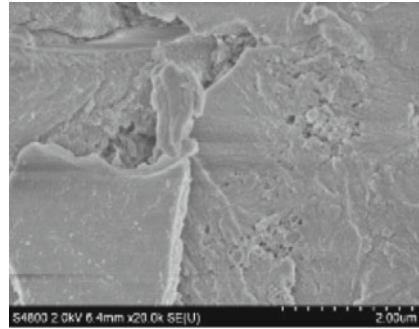


(a₁) 3,000 times
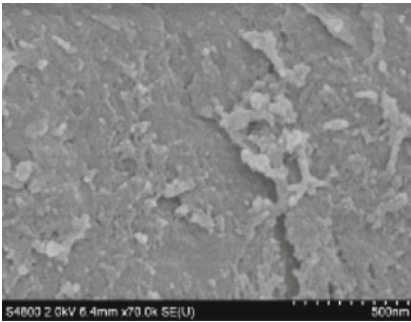
(b₁) 20,000 times
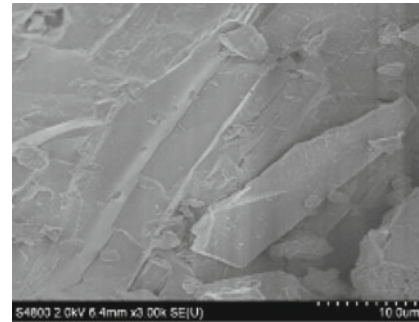
(c₁) 70,000 times

(a₂) 3,000 times

(b₂) 20,000 times

(c₂) 70,000 times

**Fig. 4.** SEM images of Sl coal samples at different magnifications. $a_1$, $b_1$, $c_1$ raw coal sample; $a_2$, $b_2$, $c_2$ dried coal sample soaked in water

(3) Ww coal samples



(a₁) 3,000 times

(b₁) 20,000 times

(c₁) 70,000 times

(a₂) 3,000 times

(b₂) 20,000 times

(c₂) 70,000 times

**Fig. 5.** SEM images of Ww coal samples at different magnifications. $\mathbf{a_1}$, $\mathbf{b_1}$, $\mathbf{c_1}$ raw coal sample; $\mathbf{a_2}$, $\mathbf{b_2}$, $\mathbf{c_2}$ dried coal sample soaked in water

## 5  Conclusions

Bituminous coal samples were from Western part of China, half of were soaked in water for 30 days and then dried. All samples for the liquid nitrogen adsorption experiments low temperature were examined using a scanning electron microscope to analyse the microphysical structure of raw coal, findings were s follows:

(1) Raw bituminous coal from this region in Western China, although varying in amount depending particular types of coal, have abundance of micron-scale pores and fracture on their surfaces. When coal were soaked in water, surface pores and fractures are more developed, number of pores and fractures increased, and the connectivity among the pores and fractures also increased. All these features aid oxygen adsorption, reduce the time to initiate spontaneous combustion and increase the risk of spontaneous combustion after coal having been soaked in water.

(2) The specific surface area of coal soaked in water is less than that of the raw bituminous coal by about 40% observed in all samples used. This reduction in specific surface area accelerated coal oxidation and increased the risk of spontaneous combustion.

(3) Total pore volume of these dried coal soaked in water is smaller than that of the raw coal, but the average pore size is larger for the former. The increase in average pore size adds to the risk of spontaneous combustion. The pattern of changes in total pore volume and average pore size in coal samples are the same. In other words, the smaller the change in total pore volume, the smaller in average pore size variations.

# References

1. Liu, X., Song, G., Li, X.: Classification of roof strata and calculation of powered support loads in shallow coal seams of China. J. South Afr. Inst. Min. Metall. **115**(11), 1113–1119 (2015)

2. Zhang, Y.N., Deng, J., Yang, H., Zhao, J.Y., Zhao, C.P.: Experimental study of the characteristic features of the microstructure of coal at different coal sorts. J. Saf. Environ. **14** (4), 67–71 (2014) (in Chinese)

3. Yu, J.L., Tahmasebi, A., Han, Y.N., Yu, F.K., Li, X.C.: A review on water in low rank coals: the existence, interaction with coal structure and effects on coal utilization. Fuel Process. Technol. **106**(2), 9–20 (2013)

4. Zou, Y.P., Lü, R.S., Yang, J.: Three-dimensional excitation emission matrix fluorescence spectroscopic characterization of dissolved organic matter in coal mine water. J. China Coal Soc. **37**(8), 1396–1400 (2012)

5. Nakagawa, H., Namba, A., Böhlmann, M., Miura, K.: Hydrothermal dewatering of brown coal and catalytic rothermal gasification of the organic compounds dissolving in the water using a novel Ni/carbon catalyst. Fuel **83**(6), 719–725 (2004)

6. Zubrik, A., Hredzák, S., Turčániová, L., Sepelak, V.: Distribution of inorganic and organic substances in the hydrocyclone separated Slovak sub-bituminous coal. Fuel **89**(8), 2126–2132 (2010)

7. He, Q.L., Wang, D.M.: Influence of moisture on absorbed oxygen and released heat of coal. Int. J. Min. Sci. Technol. **34**(3), 358–362 (2005)

8. Reich, M.H., Snook, I.K., Wagenfeld, H.K.: A fractal interpretation of the effect of drying on the pore structure of Victorian brown coal. Fuel **71**(6), 669–672 (1992)

9.  Prationo, W., Zhang, J., Cui, J.F., Wang, Y.T., Zhang, L.: Influence of inherent moisture on the ignition and combustion of wet Victorian brown coal in air-firing and oxy-fuel modes: Part 1: the volatile ignition and flame propagation. Fuel Process. Technol. **138**, 670–679 (2015)

10. Pan, Z., Connell, L.D., Camilleri, M., Connelly, L.: Effects of matrix moisture on gas diffusion and flow in coal. Fuel **89**(11), 3207–3217 (2010)

11. Choi, H., Thiruppathiraja, C., Kim, S., Rhim, Y., Lim, J., Lee, S.: Moisture readsorption and low temperature oxidation characteristics of upgraded low rank coal. Fuel Process. Technol. **92**(10), 2005 (2011)

12. Xu, T., Wang, D., He, Q.: The study of the critical moisture content at which coal has the most high tendency to spontaneous combustion. Int. J. Coal Prep. Utilization **33**(3), 117–127 (2013)

13. Clemens, A.H., Matheson, T.W.: The role of moisture in the self-heating of low-rank coals. Fuel **75**(7), 891–895 (1996)

14. Kadıoğlu, Y., Varamaz, M.: The effect of moisture content and air-drying on spontaneous combustion characteristics of two Turkish lignitesa. Fuel **82**, 1685–1693 (2003)

15. Beamish, B.B., Hamilton, G.R.: Effect of moisture content on the R70 self-heating rate of Callide coal. Int. J. Coal Geol. **64**, 133–138 (2005)

16. Jiang, X.M., Yang, H.P., Yan, C., Zhang, C.Q., Zheng, C.G., Liu, D.C.: Fractal characteristic of surface structure of micro-pulverized coal. Proc. CSEE **23**(12), 168–172 (2003) (in Chinese)

17. Meng, Z.P., Zhang, J.C., Wang, R.: In-situ stress, pore pressure and stress-dependent permeability in the Southern Qinshui Basin. Rock Mech. Min. Sci. **48**(1), 122–131 (2011)

18. Zhang, J.C., Standifird, W.B., Roegiers, J.C., Zhang, Y.: Stress-dependent fluid flow and permeability in fractured media: from lab experiments to engineering applications. Rock Mech. Rock Eng. **40**(1), 3–21 (2007)

19. Meng, Q.R., Zhao, Y.S., Hu, R.Q., Feng, Z.C., Yu, Y.M.: Experimental study on pore structure and pore shape of coking coal. J. China Coal Soc. **36**(3), 487–490 (2011) (in Chinese)

20. Zhang, Y.T., Wang, D.M., Zhong, X.X.: Features of fissure sharp in coal borehole and variation law with temperature. Coal Sci. Technol. **35**(11), 73–76 (2007) (in Chinese)

21. Jiang, W.P., Song, X.Z., Zhong, L.W.: Research on the pore properties of different coal body structure coals and the effects on gas outburst based on the low-temperature nitrogen adsorption method. J. China Coal Soc. **36**(4), 609–614 (2011) (in Chinese)

22. Deng, Y.B., Ma, X.W., Ge, S.C.: Experimental study on pore structure and distribution characteristics of long flame coal. J. Dalian Marit. Univ. **38**(2), 121–124 (2012) (in Chinese)

23. Liu, Z.: Research and Application of the Microscopic Pore Structure Characteristics of Low Permeability Coal Seam. Xi'an University of Science and Technology, Xi'an (2013) (in Chinese)

24. Miroshnichenko, D.A., Kaftan, Y.S., Desna, N.A., Nazarov, V.N., Nikolaichuk, Y.V.: Ignition temperature of coal. 1. Influence of the coal's composition, structure, and properties. Coke Chem. **59**(8), 277–282 (2016)

25. Lin, Y.J., Chen, K.Q., Hao, Y.J.: Proximate analysis of coal (GB212-91). Coal Anal. Utilization **4**, 20–27 (1992) (in Chinese)

26. Li, X.: Experimental Study on Characteristic Parameters of Spontaneous Combustion of Soaked and Air-Dried Coal. China University of Mining and Technology, Xuzhou (2014) (in Chinese)

27. Chen, J.M., Tan, P., Wang, J.Y.: Characterization of pore structure and specific surface area based on gas adsorption applied for porous materials. Powder Metall. Ind. **21**(2), 45–49 (2011) (in Chinese)

28. Qin, Z.H., Jiang, C., Hou, C.L., Li, X.S., Zhang, L.Y., Chen, J., Jiang, B.: Solubilization of small molecules from coal and the resulting effects on the pore structure distribution. Int. J. Min. Sci. Technol. **19**(6), 761–768 (2009)
29. Feng, X.S.: Correlation Research on Microscopic Pore Structure Characteristics and Combustion Characteristics of Coal. Taiyuan University of Technology, Taiyuan (2015) (in Chinese)
30. Wen, Y.R.: Study on Low-Temperature Oxidation Characteristics and Influencing Factors of Highly Active Pulverized Coal. China Coal Research Institute CCRI, China (2016) (in Chinese)
31. Hao, Q.: On morphological character and origin of micropores in coal. J. China Coal Soc. **4**(4), 51–56+97–101 (1987) (in Chinese)

# The Distribution and Change of Oxygen-Containing Functional Groups in Coal

Huang Zhian[1,2](✉), Yang Rui[1], Zhang Yinghua[1], Gao Yukun[1],
Wang Hui[1], and Liu Fangzhe[1]

[1] State Key Laboratory of High-Efficient Mining and Safety of Metal Mines,
Ministry of Education, University of Science and Technology Beijing,
Beijing 100083, China
huang_za@ustb.edu.cn
[2] Work Safety Key Lab on Prevention and Control of Gas and Roof Disasters
for Southern, Xiangtan, China

**Abstract.** Oxygen-containing functional groups are the most important active groups of coal and critical for heating. This paper collected five different coal samples and explored the distribution of main oxygen-containing functional groups (hydroxyl, carboxyl, methoxyl, carbonyl and inactive oxygen) and their changes after oxidation with chemical titration and Fourier Transform infrared (FT-IR) spectroscopy. The results show that there are mainly hydroxyl and no carboxyl in anthracites; in meagre coal, the hydroxyl- and carboxyl-based oxygen-containing group is more uniform, and coking coal has comparable hydroxyl, carboxyl, methoxyl and inactive oxygen, except carbonyl. After oxidization, the methoxyl and inactive oxygen decreases, as well as the total oxygen-containing functional groups. The ratios of hydroxyl, methoxyl, carbonyl and inactive oxygen decrease and the carboxyl rises in anthracites; the proportions of carboxyl, methoxyl and inactive oxygen decline and carbonyl goes up in coking and meagre coal from Tangshan Mine and Fan'gezhuang Mine. However, for the coking coal from Pingdingshan Mine, the ratios of hydroxyl and carbonyl rise and methoxyl, carbonyl, inactive oxygen decrease. The research about oxygen-containing functional groups could be a reference to further understand the mechanism of coal spontaneous combustion.

**Keywords:** Coal spontaneous combustion · Oxygen-containing functional group · Oxidation · FT-IR

## 1 Introduction

Complex mining conditions and the restriction of mining technologies make the coal industry suffer from disastrous fire accidents frequently, of which coal spontaneous combustions accounts for over 90% of the fires [1]. And in China, more than 53.1% major state-owned coal mines have a risk of spontaneous fire [2]. Up to now, direct oxidation of coal, double parallel reaction, self-reaction of active functional groups and free radical reaction have been proposed to characterize the microcosmic mechanism [3–6]. However, due to the undeveloped categories, distribution and variation of active function groups, detailed heating process is still quite unclear. Therefore, the studies of

active groups are critical to clarify the mechanism of spontaneous combustion. Among the active functional groups, oxygen-containing functional groups is the most important, which influences both the spontaneous combustion proneness and surface properties [5, 7]. Chemical method, Fourier transform infrared (FT-IR) spectrometry and other technologies have been widely used in active radicals, and the FT-IR is widely used in active functional groups of coal [8, 9]. Xu discussed the change of five main groups in coal with FT-IR and proposed the in-suit FT-IR is better [10]. Zhou obtained the formation and proportion of carboxyl, alcohol hydroxyl, phenol hydroxyl, methoxyl and carbonyl group in low-rank coal through chemical titration [11]. Others analyzed carboxyl group, coal aromaticity, aliphatic CH groups by Fourier transform [12, 13].

Although there have been plenty of researches on the radicals of coal, study of the ratio of all oxygen-containing functional groups in different coal and their variation after oxidation are scant. In this paper, the distribution of oxygen-containing groups including hydroxyl, carboxyl, methoxyl, carbonyl and inactive oxygen is investigated with chemical method and the FT-IR. Meanwhile, comparing the original FT-IR spectrum with the oxidized, the groups' variation after low temperature oxidation (80 °C) is analyzed. The fundamental study of oxygen-containing groups is essential towards the understanding of coal heating and fire-prevention technology.

## 2 Measurement of Oxygen-Containing Functional Groups

### 2.1 Sample Preparation

Coal samples were collected from the working faces of Guotou Baodi Mine #1 of Xinjiang Province, Yangquan Mine #2, Tangshan Mine and Fan'gezhuang Mine and Pingdingshan Mine, which are assigned as XJ, YQ, PDS, FGZ and TZ in this paper. The coal was ground to less than 120 mesh. One part of them was dried for more than 100 days in air-blower-driver drying closets that maintained a constant temperature of 80 °C, and finally sealed with multilayer plastic bag for use. The other part was dried in vacuum with a temperature of 80 °C and then saved in a container with nitrogen.

To figure out the ranks of coal samples, a proximate analysis was conducted for each sample with results are shown in Table 1.

**Table 1.** Proximate analysis results of coal samples

| Samples | $M_{ad}$ (%) | $V_{ad}$ (%) | $V_d$ (%) | $A_{ad}$ (%) | $A_d$ (%) | $FC_{ad}$ (%) |
|---------|---------|---------|---------|---------|---------|---------|
| XJ | 1.21 | 7.86 | 7.96 | 9.30 | 9.41 | 81.64 |
| FGZ | 0.70 | 22.00 | 22.15 | 3.49 | 3.51 | 73.82 |
| YQ | 1.06 | 8.31 | 8.40 | 12.21 | 12.34 | 78.43 |
| PDS | 0.98 | 18.67 | 18.86 | 9.41 | 9.51 | 70.94 |
| TS | 0.53 | 28.14 | 28.29 | 8.86 | 8.91 | 62.48 |

According to the China national standards of coal classification [14], the coal sampled from Xinjiang Province and Yangquan Mine #2 is anthracite, the coal collected from Pingdingshan Mine and Tangshan Mine is coking coal, and the coal sampled from Fan'gezhuang Mine is lean coal. The descending order of the five samples by metamorphic grade is: XJ > YQ > PDS > FGZ > TS.

## 2.2    Chemical Experiment

In this chapter, the FT-IR is used to measure the oxygen-containing functional groups in raw and oxidized coal, and an improved chemical method using ultrasonic water bath and constant-temperature water bath [15] is applied for the calculation of carboxyl and hydroxyl groups only in raw coal, which results serve as a complement to the FT-IR spectrum.

**Determination of overall acidic groups**. 0.2 g coal sample that dried in vacuum was infiltrated with 4 drops of anhydrous ethanol in text tube. The tube was sealed after adding 25 ml barium hydroxide solution of 0.125 mol/L, staying in ultrasonic cleaner with a temperature of 50 °C for 40 min and then in a 95 °C water bath for 4 h to react. Filter the reactants, wash the filtered solid to neutrality and collect the filtrate and washing liquor into a flask that already has 30 mL hydrochloric acid standard solution of 0.25 mol/L and 4 drops of phenolphthalein in it. Finally, the mixture was titrated with 0.1 mol/L sodium hydroxide standard solution to neutrality and a blank test was conducted for reference.

**Determination of carboxyl**. Altering the barium hydroxide solution with 50 ml calcium acetate solution of 0.25 ml/L and removing the hydrochloric acid used, repeat the above steps to obtain the carboxyl content,

**FT-IR experiments**. The FT-IR experiment used the 470 FT-IR spectrometer made in America. Two mg samples dried in vacuum and 600 mg potassium bromide powder were mixed and ground with a vibratory mill for 2–5 min. And 100–300 mg of ground mixture was pressed into a piece with mold and hydraulic press. The max pressure was 10 T for 2 min. Then the samples placed in the press clamp of potassium bromide were tested with a reference solution of pure potassium bromide after 30 min warm-up. Finally, alter the samples with these dried with ventilation and repeat the above operations to obtain the spectrums of oxidized coal samples.

# 3    Results and Analyses

## 3.1    Distribution of Oxygen-Containing Groups in Raw Coal

(1) Chemical experiments

After chemical experiments, all sodium hydroxide standard solution (0.1 mol/L) used were recorded. According to chemical mechanism and the dosage difference of sodium hydroxide between the experiments and the blank, quantity of hydroxyl and carboxyl can be obtained. The volume records and calculated results are listed in Table 2.

**Table 2.** Sodium hydroxide volumes used in experiments

| NaOH | Samples | | | | | |
|---|---|---|---|---|---|---|
| | XJ | YQ | PDS | FGZ | TS | Blank sample |
| Overall acidic radicals | 37.50 | 37.00 | 34.0 | 35.00 | 34.40 | 29.10 |
| Hydroxyl | 20.70 | 21.00 | 23.10 | 23.50 | 23.30 | 20.70 |
| Carboxyl (mmol/g) | 0 | 0.15 | 1.20 | 1.40 | 1.30 | – |
| Hydroxyl (mmol/g) | 4.20 | 3.80 | 1.25 | 1.55 | 1.35 | – |

Examining the data above, hydroxyl in samples from Xinjiang Province and Yangquan Mine #2 is significantly higher than carboxyl and the majority of acidic radicals. However, in the other samples, the contents of hydroxyl and carboxyl are comparable and the hydroxyl is a litter higher. Therefore, the acidic radicals are mainly contributed by hydroxyls in high-rank coal and in low-rank coal, the content of carboxyl and hydroxyl are comparable but the hydroxyl is litter more in general.

(2) FT-IR spectrum of raw coal samples

After infrared scans, corresponding FT-IR spectrums for the five raw coal samples were obtained. The functional groups in coal could be analyzed qualitatively when absorbing peaks are calibrated and identified with the bands assignment of FT-IR absorption peaks of coal, listed in Table 3.

**Table 3.** Bands assignment of FT-IR absorption peaks of coal [13, 16]

| Bands position/cm$^{-1}$ | Functional group | Bands position/cm$^{-1}$ | Functional group |
|---|---|---|---|
| 3697–3685 | –OH | 1770–1720 (1735) | C=O |
| 3684–3625 | | 1736–1722 | C=O, –CO–O– |
| 3610–3580 | | 1715–1690 | –COOH |
| 3624–3610 | | 1690–1650 | C=O |
| 3550–3200 | | 1650–1640 | –CO–N– |
| 3400 | | 1590–1560 | –COO– |
| 2780–2350 (2650) | –COOH | 1410 | –COO– |
| 1910–1900 | | 1060–1020 | Si–O |
| 1780–1765 | C=O | 979–921 | OH |
| | | 900–940 | OH |

To avoid the impact of deviation of peak positions that results from various internal and external factors, a peak-fitted method was applied in data process to separate interfered spectrum peaks. Original spectrums and corresponding fitted results that processed by Origin software package are shown in Fig. 1. All differences are less than 0.005, proving that the fitting results is reliable.
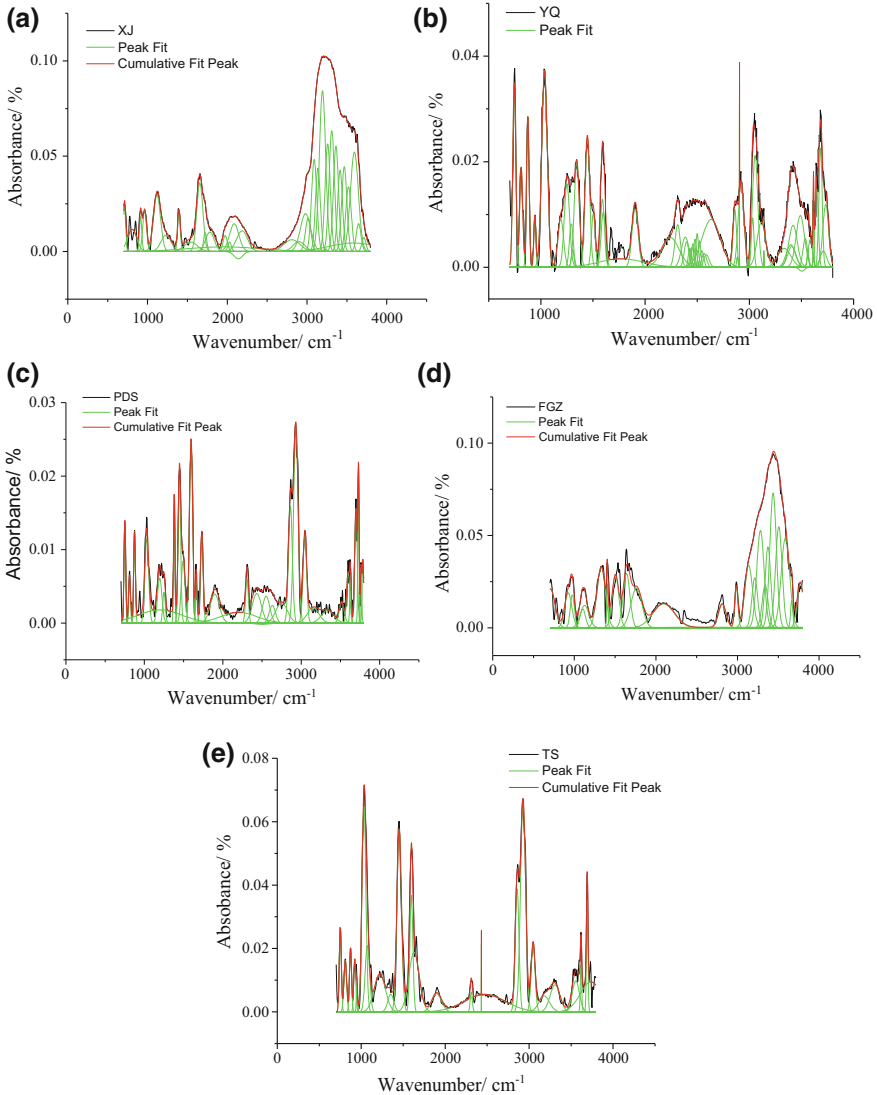
**Fig. 1.** Original and fitted spectrums of coal samples **a** Guotou Baodi mine #1, **b** Yangquan mine #2, **c** Pingdingshan mine, **d** Fan'gezhuagn mine, **e** Tangshan mine

From the spectra, there are five main oxygen-containing functional groups, including hydroxyl, carboxyl, methoxyl, carbonyl and inactive oxygen (mainly methyl bond), the amount of which is comparable with directly measured oxygen quality. Thus, in this part, all results and discussions are based on the five main radicals.

According to the processed figures and peak-fitting curves, the area of peaks representing the same functional group is cumulative and divided by overall peak area to obtain the proportion of the group in coal. The calculated results are listed in Table 4.

**Table 4.** Calibration results of main oxygen-containing groups

| Coal samples | | Radicals | | | | | | |
|---|---|---|---|---|---|---|---|---|
| | | OH | COOH | CH$_3$–O | C=O | C–O | Oxygen-containing group | Overall peak area |
| XJ | Peak area | 37.17 | 0 | 1.56 | 4.58 | 3.87 | 47.18 | 81.88 |
| | Proportion | 45% | 0 | 2% | 5% | 6% | 58% | |
| YQ | Peak area | 30.77 | 0 | 1.50 | 3.59 | 6.74 | 42.6 | 74.42 |
| | Proportion | 41% | 0 | 2% | 5% | 9% | 57% | |
| PDS | Peak area | 1.69 | 1.70 | 0.97 | 0 | 1.84 | 6.2 | 16.69 |
| | Proportion | 10% | 10% | 6% | 0 | 11% | 37% | |
| FGZ | Peak area | 5.57 | 4.27 | 0.47 | 0.86 | 2.10 | 13.27 | 30.22 |
| | Proportion | 18% | 14% | 2% | 3% | 7% | 44% | |
| TS | Peak area | 3.01 | 3.34 | 2.14 | 0 | 3.84 | 12.33 | 38.75 |
| | Proportion | 8% | 9% | 6% | 0 | 10% | 33% | |

As shown in Table 4, the sample with the highest metamorphism from Guotuo Baodi Mine #1 contains four types of oxygen-containing functional groups except carboxyl, of which the hydroxyl is the majority accounting for 45%, while methoxyl, carbonyl and inactive oxygen are relatively small. In the sample with second highest metamorphism from Yangquan Mine #2, the hydroxyl are also major oxygen-containing functional groups, which ratio is 41%. However, its inactive oxygen proportion is 9, 4% more than the ratio of coal from Guotuo Baodi Mine #1. For the sample of lean coal from Fan'gezhuang Mine, the coal is the third highest coal rank and unlike the former two samples, the carboxyl content is 14%, only 4% less than the hydroxyl of 18%. When it comes to the coking coal with the forth high coal rank from Pingdingshan Mine, the hydroxyl, carboxyl, methoxyl, and inactive oxygen proportion are 10, 10, 6 and 11%, respectively. The content of carbonyl is zero. The sample of Tangshan Mine is also coking coal, but with the lowest metamorphism in the samples. The distribution of oxygen-containing functional groups is similar with the Fan'gezhuang Mine, which also prove they have similar metamorphism grade.

We can see that the total proportion rises as the coal rank increases, the reason of which maybe due to new oxygen-containing groups generated in the process, although all functional groups decrease with higher degree of coalification,, which leads to higher ratio of oxygen-containing groups. Comparing the oxygen-containing functional groups distribution of the five samples, in the coal with higher rank like coal in Guotou Baodi Mine #1 and Yangquan Mine #2, the hydroxyl is a dominant radical while carbonyl is almost absent. The proportions of methoxyl, carbonyl and inactive oxygen are relatively small. The lean coal, such as coal from Fan'gezhuang Mine, with lower rank, has two major radicals-hydroxyl and carboxyl. Finally, regarding to the coking coal with lowest rank, the contents of hydroxyl, carboxyl, methoxyl, and inactive oxygen in the coal samples from Pingdingshan Mine and Tangshan Mine are comparable, but the carbonyl doesn't exist.

Besides the ratio of hydroxyl to carboxyl FT-IR experiments is basically coincided with the chemical experiments.

## 3.2    Distribution and Comparison of Oxygen-Containing Groups After Oxidation

In the process described in Sect. 3.1.2, the infrared spectra of oxidized coal samples are analyzed after peaks fitting and calibration, and the oxygen-containing group distribution of the five coal samples are shown in Table 5.

**Table 5.** Calibration results of main oxygen-containing groups for oxidized samples

| Coal samples | | Radicals | | | | | | |
|---|---|---|---|---|---|---|---|---|
| | | OH | COOH | CH$_3$–O | C=O | C–O | Oxygen-containing group | Overall peak area |
| XJ | Peak area | 30.98 | 0 | 0 | 7.87 | 0 | 38.85 | 104.45 |
| | Proportion | 30% | 0 | 0 | 8% | 0 | 38% | |
| YQ | Peak area | 25.88 | 9.28 | 0 | 1.65 | | 36.81 | 92.89 |
| | Proportion | 29% | 10% | 0 | 2% | 0 | 41% | |
| PDS | Peak area | 17.07 | 0 | 0 | 5.01 | 0 | 22.08 | 67.35 |
| | Proportion | 25% | 0 | 0 | 7% | 0 | 32% | |
| FGZ | Peak area | 19.31 | 6.97 | 0 | 8.56 | | 34.44 | 107.18 |
| | Proportion | 18% | 6% | 0 | 8% | 0 | 32% | |
| TS | Peak area | 8.00 | 0 | 0 | 6.50 | 0 | 14.5 | 97.40 |
| | Proportion | 8% | 0 | 0 | 7% | 0 | 15% | |

In Table 5, it could be found that after oxidation, there won't be any methoxyl or inactive oxygen in the five coal samples, which implies the two groups change first when oxidizing. To quantify the amount of variation of the main oxygen-containing groups, the differences between the data after oxidation and data of raw coal are calculated, of which the negative value means a decrease in the functional group and a positive value represents an increase. Histograms based on the proportion data of raw and oxidized coal are plotted in Fig. 2.

It can be seen in this histogram that the overall oxygen-containing functional groups decreases in all coal samples, this is a result of oxygen-containing functional groups reacting during heating. Regarding to concrete samples, the concrete radical changes have a relationship with the coal category. In the coal from Xinjiang Province, the hydroxyl, methoxyl and inactive oxygen decline and the carbonyl content rises. In the coal from Fan'gezhuang Mine, all the oxygen-containing functional groups decrease except the rising carbonyl and stable hydroxyl. In the coal from Yangquan Mine #2, the proportions of hydroxyl, carbonyl and methoxyl decrease and the carboxyl goes up. And in the coal from Pingdingshan Mine, the methoxyl and inactive oxygen decrease, but the hydroxyl and carbonyl rise. Finally, in the coal from
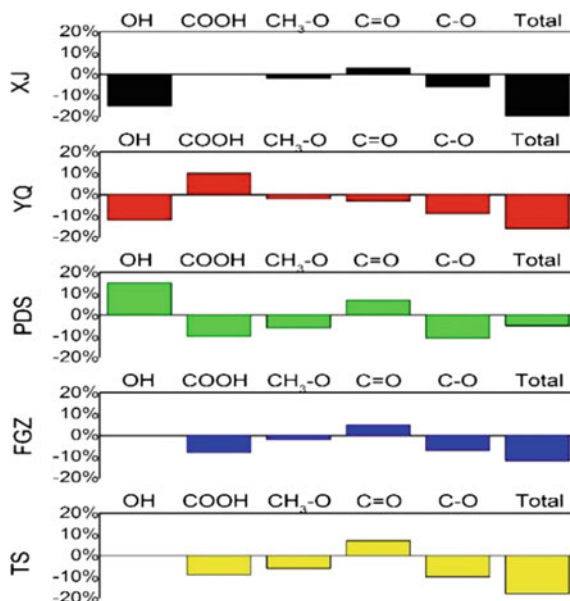
**Fig. 2.** Change of total oxygen-containing functional groups

Tangshan Mine, the carboxyl, methoxyl and inactive oxygen rise, and the carbonyl content rises. When the variations are analyzed from the coalification, it is found that the methoxyl and inactive oxygen decline in all the five coal samples, and the groups changes of the high-rank coal from Xinjiang Province and Yangquan Mine #2 have the same pattern and the low-rank coal from other three coalmines also shows the same variation. However, the change pattern of high- and low-rank coal is different and even opposite carbonyl group.

## 4   Conclusion

(1) The oxygen-containing functional groups mainly include hydroxyl, carboxyl, methoxyl, carbonyl and inactive oxygen (ether bond) and their content varies from coal to coal.

(2) In the anthracite, the hydroxyl is the dominant radical of oxygen-containing functional groups, the carbonyl content is almost non-existent. In the lean coal, the hydroxyl and carboxyl are two comparable major radicals. In the coking coal, there are average hydroxyl, carboxyl, methoxyl, and inactive oxygen, but the carbonyl is absent.

(3) The oxygen-containing functional groups generally decrease after oxidation. The methoxyl and inactive oxygen decline in all five samples, the hydroxyl proportion decreases in samples from Yangquan Mine #2 and Guotuo Baodi Mine #1, rises in samples from Pingdingshan Mine 2The carboxyl and carbonyl go up in Fan'gezhuang Mine, Pingdingshan Mine and Tangshan Mine.

# References

1. Melody, S.M., Johnston, F.H.: Coal mine fires and human health: What do we know? Int. J. Coal Geol. **152**, 1–14 (2015)
2. Deng, J., Ma, X.F., Zhang, Y.T., et al.: Effects of pyrite on the spontaneous combustion of coal. Int. J. Coal Sci. Technol. **4**(4), 306–311 (2015)
3. Nelson, C.R.: Chemistry of Coal Weathering. Elsevier Science Ltd. (1989)
4. Wang, H., Dlugogorski, B.Z., Kennedy, E.M.: Kinetic modeling of low-temperature oxidation of coal. Combust. Flame **131**(4), 452–464 (2002)
5. Qi, X.Y.: Oxidation and Self-Reaction of Active Groups in Coal. China University of Mining and Technology (2011)
6. Wei, A.Z.: Experimental Study on Free Radical Reaction Mechanism of Coal Spontaneous Combustion. China University of Mining and Technology, Xuzhou (2008)
7. Xiang, L.I., Qin, Z.H., Liang-Hui, B.U., et al.: Structural analysis of functional group and mechanism investigation of caking property of coking coal. J. Fuel Chem. Technol. **44**(4), 385–393 (2016)
8. Cui, Q., Yang, M., Zhang, X.X., et al.: Introduction to the analysis method of oxygen functional groups in coal. Chem. Bull. **75**(9), 808–814 (2012)
9. Balachandran, M.: Role of infrared spectroscopy in coal analysis—an investigation. Am. J. Anal. Chem. **5**(6), 367–372 (2014)
10. Xu, T., Wang, D.M., Xin, H.H., et al.: In-situ series diffuse reflection FT-IR used in studying the oxidation process of coal. Energy Sour. Part A: Recov. Utilization Environ. Eff. **36**(16), 1756–1763 (2014)
11. Zhou, J.L., Wang, Y.G., Huang, X., et al.: Determination of O-containing functional groups distribution in low-rank coals by chemical titration. J. Fuel Chem. Technol. **41**(2), 134–138 (2013)
12. Geng, W., Nakajima, T., Takanashi, H., et al.: Analysis of carboxyl group in coal and coal aromaticity by Fourier transform infrared (FT-IR) spectrometry. Fuel **88**(1), 139–144 (2009)
13. Riesser, B., Starsinic, M., Squires, E., et al.: Determination of aromatic and aliphatic CH groups in coal by FT-TR: 2. Studies of coals and vitrinite concentrates. Fuel **63**(9), 1253–1261 (1984)
14. Chen, M.S., Tao, Y.L., Zhang, X.Y., et al.: China national standards of coal classification (GB GB5751—86). Coal Anal. Utilization **01**, 92–101 (1986)
15. Liu, C.L., Xu, H.L., Wang, Z.C., et al.: Improvement of chemical determination method of acidic functional group containing oxygen in low rank coal. J. Anhui Univ. Technol. (Nat. Sci.) **26**(3), 275–277 (2009)
16. Cooke, N.E., Fuller, O.M., Gaikwad, R.P.: FT-IR spectroscopic analysis of coals and coal extracts. Fuel **65**(9), 1254–1260 (1986)

# Part XI
# Underground Fire Control I

# Research on Blockage Ratio Effects
# on Large-Profile Tunnel Fire Behaviors

Jian Li[1], Congling Shi[1(✉)], Changkun Chen[2], Li He[1],
Xuan Xu[1], and Binbin Wu[1]

[1] Beijing Key Laboratory of Metro Fire and Passenger Transportation Safety,
China Academy of Safety Science and Technology, Beijing 100012,
People's Republic of China
shicl@chinasafety.ac.cn
[2] Institute of Disaster Prevention Science and Safety Technology,
Central South University, Changsha, Hunan 410075, People's Republic of China

**Abstract.** In recent years, railway construction in China is in a rapid development stage. As a result, more and more long-profile large-distance tunnels are designed and constructed. To accommodate for rapid deployment of vehicular tunnels, it is necessary to enlarge its profile, namely, to reduce the tunnel blockage ratio since train cross-section remains unchanged. This study has analyzed the impact of blockage ratio on tunnel smoke controlling critical ventilation velocity (CVV) as well as the smoke flow behaviors around the train on fire and in its immediate surroundings, using CFD numerical simulation. The results show that in certain fires, CVV decreases as the blockage ratio increases, and the opposite is also true while CVV increases gradually accelerates, while, temperatures near the top of tunnel roof decrease gradually as the blockage ratio decreases. The smaller the blockage ratio, the smaller the critical high temperature area. As a train passes by, the peak ventilation velocity increases as the blockage ratio increases. Results of this study could provide a theoretical basis for safety design as well as operation of long-large interval tunnels to prevent possible disasters.

**Keywords:** Subway · Long-large interval tunnel · Fire · Blockage ratio

## 1   Introduction

Recent years the world has witnessed a great development in urban rail transit facilities, particular in China. With the progress of rail transit construction, construction of many urban rail transit facilities gradually extends from urban area to suburbs and country side. Since the population density in suburb is lower and the distance between stations is longer, long distance tunnels with larger files are on the rise in recent years, to meet high-speed train requirements, although these long and large tunnels present challenges such as smoke control in case of a tunnel fire.

Smoke control in tunnels has been one of the research priorities in recent years. Thomas [1] proposed the use of longitudinal ventilation for controlling the smoke reflux, and he proposed an equation for calculating the critical ventilation velocity (CVV).

Bettis et al. [2] have conducted a full-dimension tunnel fire experiment and discovered that the critical ventilation velocity varies at 1/3 of its power when the fire source heat release rate is low, and its critical ventilation velocity would basically remain unchanged even when heat release rate is increases to a certain level. This finding has been proven by an American full-dimension Memorial Tunnel fire experiment. There are other research results that show the above critical ventilation velocity values are on the high side [3–5] when the fire source heat release rate is very high.

Oka and Atkinson [6] conducted a small-dimension tunnel fire experiment to study the smoke controlling critical ventilation velocity in horizontal tunnel, and proposed a dimensionless critical ventilation velocity calculating formula with tunnel height as characteristic length. Furthermore, they also found that when the fire source conditions are the same, the critical ventilation velocity required by an uphill tunnel is smaller than horizontal tunnel. Wu et al. [7] discovered that the critical ventilation velocity calculation model developed by Oka et al. cannot be used for full consideration of the impact of most tunnel cross-sections on the critical ventilation velocity, and after experiment and simulation research of 5 different types of tunnels with the same height but different width, they came up with a dimensionless critical ventilation velocity calculation formula with hydraulic diameter as characteristic dimension. Li et al. [8] respectively conducted experiments by using single-span tunnel with rectangular cross-section and small-dimension tunnel model with arched cross-section to also obtain a dimensionless critical ventilation velocity calculation formula with tunnel height as the characteristic dimension, and they also pointed out the deficiencies of the experiments conducted by Oka et al. and Wu et al. Lee et al. [9] deemed that height/width ratio of tunnel cross-section was also an important factor affecting magnitude of critical ventilation velocity, and they thus designed five tunnels with basically the same hydraulic diameter but different cross-section height/width ratios to study the influence of such parameters, and discovered that Wu's model could not be used for good identification of the impact of such parameters. Then Lee et al. introduced cross-section height/width ratio to rectify the model of Wu et al. [10, 11].

Roh et al. [12] believed that fire source heat release rate was under the influence of controlled longitudinal ventilation velocity, but prior researches failed to take it into account, and they also conducted an experiment (oil sump fire) by using three kinds of fuel, namely, methanol, acetone and normal heptane, which showed that combustion heat release rate of methanol reduced as the longitudinal ventilation velocity increased, while the combustion ratio of acetone and normal heptane increased as the longitudinal ventilation velocity increased. Ko et al. [13] believed that Oka's experiment used propane as the fire source, and heat release rate during the experiment was constant, without being subject to the impact of ventilation velocity.

Yuan et al. [14] believed that the research results of Wu and Bakar were based on the condition under which the heat release rate basically remained unchanged, and since flame is susceptible to the impact of longitudinal airflow, thus, the credibility of their conclusions with regard to oils related fire needs further verification. Hu et al. [15] believed that the model predicted values of Wu and Bakar were lower than the actual critical ventilation velocity. Kunsch [16] came up with a simplified critical ventilation velocity calculation model by adopting a 2-dimension method. However, the applicability of such model is quite limited due to the complicated calculation. Through a

computational analysis of the said model, Vauquelin et al. [17] compared the predicted value of this model with the experiment data, and found that the predicted value of this CVV calculation model was on the high side.

In general, scholars around the world have done a lot of researches on smoke controlling in interval tunnels to date. However, most of the current researches, especially researches on smoke control in interval tunnels, are mainly directed to ordinary tunnels. A long-large interval tunnel is characterized by big length and higher running speed of the trains than in ordinary interval tunnels. A higher running speed requires an enlarged tunnel cross section, and thus, the cross-section blockage ratio of a long-large interval tunnel (the ratio of train cross-section to tunnel cross-section) decreases along with it. With small blockage ratio, the smoke spreading characteristics, smoke controlling critical ventilation velocity as well as the distribution of temperature and velocity, etc. surrounding the train in case of a train fire is somewhat different from ordinary tunnel. This paper conducts a research on a long-large interval tunnel in terms of the impact of blockage ratio on smoke controlling critical ventilation velocity as well as temperature and distribution of temperature and velocity, etc. surrounding the train.

## 2    Introduction of Long and Large-profile Subway Tunnel

The long and large-provide tunnel investigated in this paper is 5687 m long. To give a good consideration to the impact of train blockage on the diffusion of smoke in case of a tunnel fire, the study uses a Model B train with six cars parking in the middle of the tunnel with the fire source in the center of the train. Cross-sectional dimensions of the train are 2.8 m × 3.8 m (W × H), and the train 120 m long (see Fig. 1).
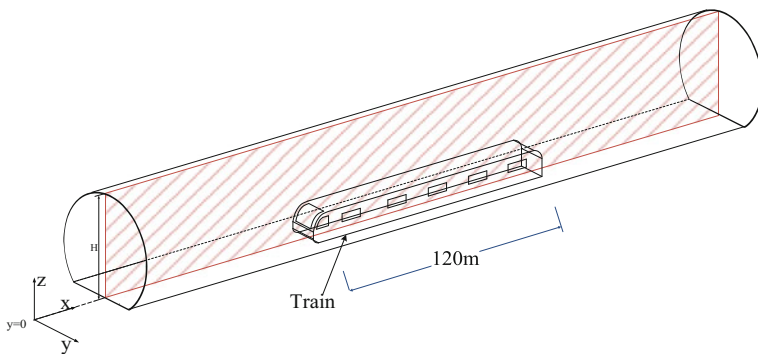


**Fig. 1.** Sketch showing a long-large interval tunnel

In this research, the blockage ratio is set as follows: cross-sectional area of the train remains unchanged, but the tunnel cross-sectional dimensions are varied. Dimensions of the tunnel model taken for the various blockage ratios are specifically shown in Table 1.

**Table 1.** Cross-sectional dimensions of long-large interval tunnel in correspondence with different blockage ratios

| Blockage ratio | Height H (m) | Radius r (m) |
|---|---|---|
| α = 0.4 | 5.8 | 3 |
| α = 0.3 | 6.1 | 3.3 |
| α = 0.2 | 6.8 | 4 |

Measuring points are provided on the vertical cross section at center of the tunnel, and their designations are respectively A1–A11; B1–B11…D1–D11, where A–D are designations of measuring point groups on the height of the tunnel (specific conditions to be determined according to different tunnel dimensions). See Fig. 2 for the specific distribution on height. 1–11 are designations on the length of the tunnel, beginning from the left end of the tunnel. One group of measuring points is set in every 30 m, and a total of 11 groups are provided. Each measuring point is named by using both the designations (A–D) on the height and the designations (1–26) on the width.
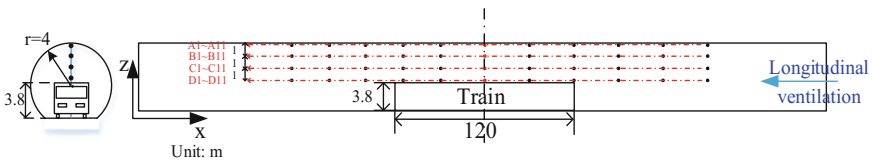


**Fig. 2.** Sketch showing distribution of measuring points (the blockage ratio is 0.2)

Critical ventilation velocity (CVV) and smoke flow behavior in case of fire is subject to FDS simulation. The set simulation duration is 1200 s, and fire source power is 10 MW and the heating curve uses quick fire heating curve. The initial temperature in the simulated area and the outdoor ambient temperature are both 20 °C and the pressure is 1 standard atmospheric pressure.

Distribution of smoke and air velocity surrounding the train is simulated by using Fluent, and the relevant dimensions are the same as FDS numerical simulation.

## 3    Impact of Blockage Ratio on Smoke Controlling Critical Ventilation Velocity

The example is based on a blockage ratio of 0.4. The ventilation velocity is respectively set at 1.8, 1.9 and 2.0 m/s. Longitudinal smoke spreading condition inside the tunnel during fire stabilization stage is as shown in Fig. 3. At a ventilation velocity of 1.8 m/s, smoke reflux occurs; at a ventilation velocity of 1.9 m/s, a little smoke reflux occurs; and at a ventilation velocity of 2.0 m/s, no smoke reflux occurs. Therefore, it can be judged that the smoke controlling critical ventilation velocity is 2.0 m/s or so at a blockage ratio of 0.4. By using the same approach, the smoke controlling critical

ventilation velocities (CVV) obtained for a blockage ratio of 0.3 and 0.2 are approximately 2.3 and 3.2 m/s, respectively.
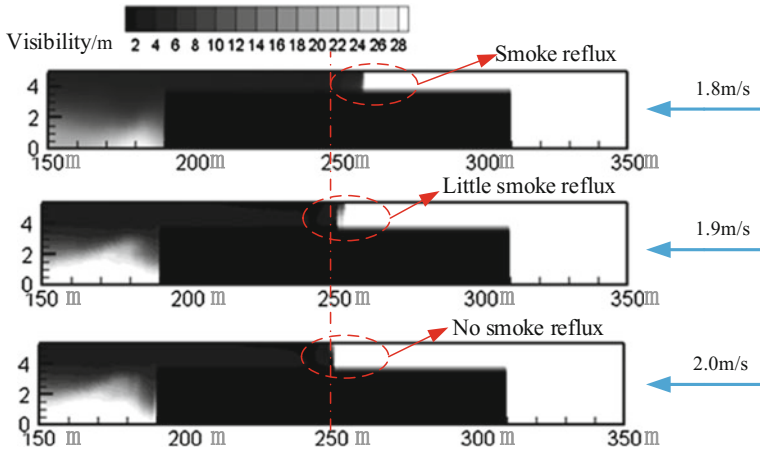


**Fig. 3.** Visibility inside tunnel during fire stabilization stage (200 s) with a blockage ratio of 0.4

The example is based on a blockage ratio of 0.4. The ventilation velocity is respectively set at 1.8, 1.9 and 2.0 m/s. Longitudinal smoke spreading condition inside the tunnel during fire stabilization stage is as shown in Fig. 3. At a ventilation velocity of 1.8 m/s, smoke reflux occurs; at a ventilation velocity of 1.9 m/s, a little smoke reflux occurs; and at a ventilation velocity of 2.0 m/s, no smoke reflux occurs. Therefore, it can be judged that the smoke controlling critical ventilation velocity is 2.0 m/s or so at a blockage ratio of 0.4. By using the same approach, the smoke controlling critical ventilation velocities (CVV) obtained for a blockage ratio of 0.3 and 0.2 are respectively approximately 2.3 and 3.2 m/s.

Basically, the CVV in the tunnel increases as the blockage ratio decreases under a certain fire source power. Meanwhile, it can also be seen that the critical ventilation velocity increase gradually accelerates as the blockage ratio decreases gradually. This poses even a bigger challenge on the smoke exhaust design of long large-profile tunnels. This is because it is necessary to enlarge the tunnel cross section in order to meet the requirements of high-speed operation of the trains in a long-large interval tunnel. Even if the CVV remains unchanged, there is still a necessity to increase the capacity of the exhaust fan. And as the tunnel cross-sectional area increases and the blockage ratio decreases, the increase of critical ventilation velocity is higher than the linear trend. This causes the increase of tunnel fan delivery to be higher than a percentage of quadratic function, posing even a greater challenge on tunnel fan specification and subway operation.

## 4   Impact of Blockage Ratio on Smoke Controlling Critical Ventilation Velocity

Considering that the smoke exhaust design of a subway interval tunnel shall prevent reflux of smoke from occurring, the design ventilation velocity shall generally bigger than the CVV. This paper studies the impact of blockage ratio on the high temperature areas in case of fire by using numerical simulation and by assuming that the smoke exhaust velocities inside the interval tunnel under the various blockage ratios equal to the smoke controlling critical ventilation velocity and the train fire curves are the same.

Figure 4 shows the distribution of high-temperature areas inside a tunnel with smoke exhaust at CVV under different blockage ratios. It can been seen that the fire development is fast at the time points of 50–100 s, and during 100–200 s, the distribution of high-temperature areas with the fire is basically stable. It can be seen from the figure that at a blockage ratio of 0.2, the high-temperature area (for example, 180 °C) surrounding the train is obviously smaller than in a tunnel with a blockage ratio of 0.3 and 0.4. One of the reasons is that the space in the tunnel above the train is bigger at a smaller blockage ratio (with a fixed train cross sectional area, a smaller blockage ratio means a bigger cross-sectional area of an interval tunnel), under which condition the heat cannot be easily gathered; the other reason is that the CVV is higher at a smaller blockage ratio (according to the results achieved in the previous chapter), and a higher smoke exhaust velocity can eliminate the heat resulted from the train fire at a faster speed. To sum up the above two points, under the same fire source power, the high-temperature area inside a tunnel with a smaller blockage ratio is smaller under the critical ventilation velocity.

## 5   Impact of Blockage Ratio on Ventilation Velocity Around Train

Use Fluent to simulate the impact of blockage ratio on the airflow velocity surrounding the train in operation. Tunnel dimensions are set the same as above, and the train cross-sectional dimensions are 2.8 m × 3.8 m. The train is located on the centerline at one end of the tunnel, the simulation duration is 18 s and the train traveling speed is 20 m/s.

Figure 5 shows the airflow velocities surrounding the train under different blockage ratios. In general, the peak airflow velocity increases as the blockage ratio increases, and the airflow velocity shows the same variation trend under three different blockage ratios. Specifically, as the train comes over, the maximum airflow velocity gradually increases with the increase of blockage ratio, and the time required to reach the maximum velocity is longer. This is because a tunnel with a bigger blockage ratio tends to have a smaller tunnel cross-sectional area. To make up the airflow eliminated by the train cross section after the train has passed by, bigger ventilation velocity is required.

(a)  A blockage ratio of 0.2



(b)  A blockage ratio of 0.3



(c) A blockage ratio of 0.4
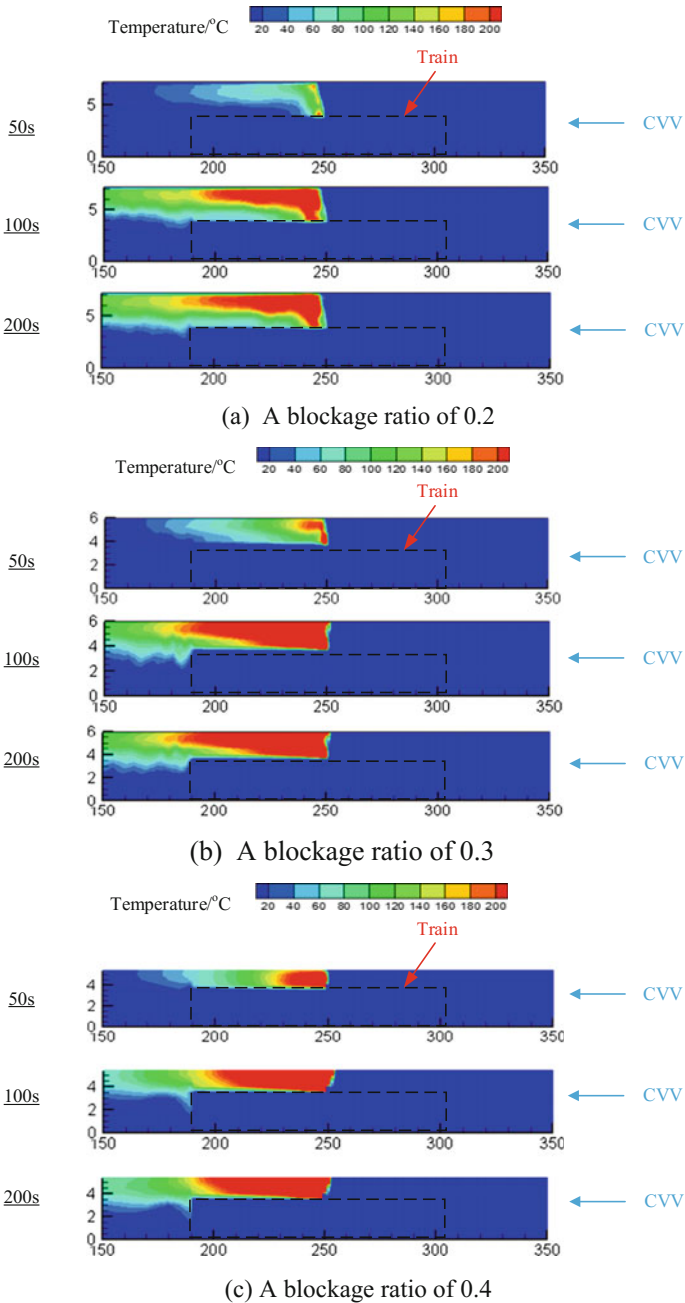
**Fig. 4.** Hot smoke distribution surrounding the train on fire under different blockage ratios
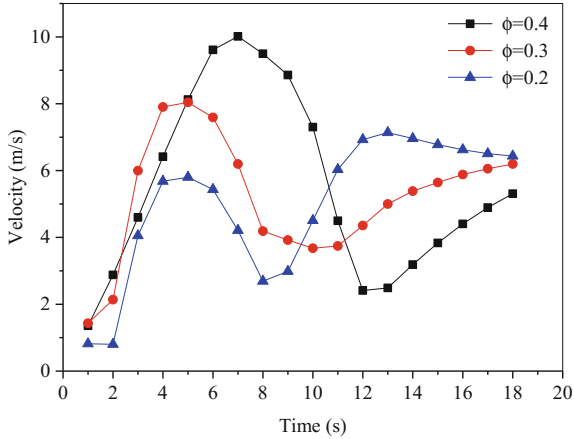
**Fig. 5.** Airflow velocities near an operating train under different blockage ratios

Figure 6 is a nephogram showing velocity at tunnel center cross section under different blockage ratios. It can be seen that under a small blockage ratio, the train squeezing action on the nearby airflow is clearly visible when distance of the train from the tunnel ceiling is bigger, which produces an obvious laminar airflow surrounding the train; when the distance of the train from the tunnel ceiling at a bigger blockage ratio, the train squeezes the surrounding airflow towards the tunnel, and the velocities at the tunnel surface are relatively concentrated.



(a) Blockage ratio =0.2     (b) Blockage ratio =0.3     (c) Blockage ratio =0.4
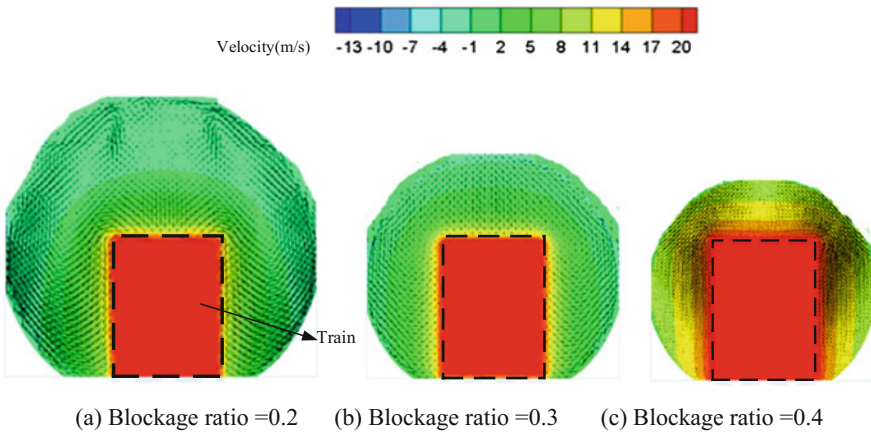
**Fig. 6.** Velocity nephogram at tunnel center cross section under different blockage ratios

## 6 Conclusions

To meet the requirements of high-speed train operation in a long large-file tunnel, it is necessary to enlarge the tunnel cross section, that is, to reduce the blockage ratio. This paper uses CFD numerical simulation software FDS and Fluent as tools to study the impact of the blockage ratio of long-large interval tunnel on smoke controlling critical ventilation velocity (CVV), and the behaviors of smoke flow surrounding the train on fire and the nearby areas as well as the velocity surrounding the train.

It is found that under a certain fire source power the tunnel smoke controlling critical ventilation velocity decreases as the blockage ratio increases, and as the blockage ratio further decreases, the CVV increasing trend gradually accelerates. Considering that a long-large interval tunnel needs an enlarged tunnel cross section, it is necessary to increase the fan delivery in the same proportion in order to keep the velocity the same; Meanwhile, the increase of tunnel cross-section area has reduced the blockage ratio, resulting in the increase of critical ventilation velocity to exceed the linear function, which causes the increase of tunnel fan delivery to be higher than a percentage of quadratic function, posing even a greater challenge on tunnel fan specification and subway operation.

This paper has studied the of high-temperature distribution inside a tunnel with smoke exhaust at CVV under different blockage ratios, and the results show that under the same fire, a tunnel with a smaller blockage ratio tends to have a smaller high temperature area at the CVV.

Under a small blockage ratio, the train squeezing action on the surrounding airflow is clearly visible when distance of the train from the tunnel ceiling is bigger, which produces an obvious laminar airflow surrounding the train; when the distance of the train from the tunnel ceiling at a bigger blockage ratio, the train squeezes the surrounding airflow towards the tunnel, and the velocities at the tunnel surface are relatively concentrated.

The research results of this paper can provide a theoretical reference for ventilation and smoke exhaust design and safety management of long-large intervals of urban rail transit facilities including subways, etc.

## References

1. The movement of smoke in horizontal passages against an air flow, Fire Research Note 723/1968. Fire Res Station (1968)
2. Bettis, R.J., Jagger, S.F., Macmillan, A.J.R., et al.: Interim Validation of Tunnel Fire Consequence Models; Summary of Phase 1 Tests. The Health and Safety Laboratory Report IR/L/FR/94/2. The Health and Safety Executive, UK (1994)

3. Zhang, S., Yao, Y., Zhu, K., et al.: Prediction of smoke back-layering length under different longitudinal ventilations in the subway tunnel with metro train. Tunn. Undergr. Space Technol. **53**, 13–21 (2016)
4. Chen, L.F., Hu, L.H., Tang, W., et al.: Studies on buoyancy driven two-directional smoke flow layering length with combination of point extraction and longitudinal ventilation in tunnel fires. Fire Saf. J. **59**, 94–101 (2013)
5. Mounesan, M., Talaee, M.R., Molatefi, H.: Investigation of effective parameters on critical ventilation velocity in underground tunnels. Mech. Eng. **48**(1) 2016
6. Oka, Y., Atkinson, G.T.: Control of smoke flow in tunnel fires. Fire Saf. J. **25**(4), 305–322 (1995)
7. Wu, Y., Bakar, M.Z.A.: Control of smoke flow in tunnel fires using longitudinal ventilation systems—a study of the critical velocity. Fire Safety J. **35**(4), 363–390
8. Li, Y.Z., Lei, B., Ingason, H.: Study of critical velocity and backlayering length in longitudinally ventilated tunnel fires. Fire Saf. J. **45**(6), 361–370 (2010)
9. Lee, S.R., Hong, S.R.: An experimental study of the effect of the aspect ratio on the critical velocity in longitudinal ventilation tunnel fires. J. Fire Sci. **23**(2), 119–138 (2005)
10. Tsai, K.C., Chen, H.H., Lee, S.K.: Critical ventilation velocity for multi-source tunnel fires. J. Wind Eng. Ind. Aerodyn. **98**(10–11), 650–660 (2010)
11. Lee, S.C., Kim, S.I.: The Effect of Grid Number and the Location and Size of the Fire Source on the Critical Velocity in a Road Tunnel Fire, vol. 14, issue 3 (2012)
12. Roh, J.S., Ryou, H.S., Kim, D.H.: Critical velocity and burning rate in pool fire during longitudinal ventilation. Tunn. Undergr. Space Technol. **22**(3), 262–271 (2007)
13. Ko, G.H., Kim, S.R., Hong, S.R., et al.: An experimental study on the effect of slope on the critical velocity in tunnel fires. J. Fire Sci. **28**(1), 27–47 (2010)
14. Jianping, Y., Zheng, F., Haifeng, H., et al.: Model of Critical Velocity for Fire Ventilation in Horizontal Tunnels, vol. 31, issue 6, pp. 66–70 (2009)
15. Longhua, Hu, Huo, Ran, Wang, Haobo, et al.: Experiment of fire smoke temperature and layer stratification height distribution characteristic along highway tunnel. China J. Highw. Trans. **19**(6), 79–82 (2006)
16. Kunsch, J.P.: Modelling of tunnel fires and experimental validation. PAMM **5**(1), 677–678 (2005)
17. Vauquelin, O., Wu, Y.: Influence of tunnel width on longitudinal smoke control. Fire Saf. J. **41**(6), 420–426 (2006)

# Fire Ladder Study to Assess Spontaneous Combustion Propensity of Indian Coal

N. K. Mohalik[1(✉)], E. Lester[2], and I. S. Lowndes[2]

[1] Mine Ventilation Division, CSIR-CIMFR, Barwa Road, Dhanbad, India
niroj.mohalik@gmail.com
[2] Faculty of Engineering, University of Nottingham, Nottingham NG7 2RD, UK

**Abstract.** Spontaneous combustion of Indian coals was investigated using sponcomb rig at University of Nottingham, UK to assess their susceptibility. In present study authors used eleven coal samples collected from the Jharia coalfield (JCF), India covering both fiery and non-fiery coal seams. Both thermal as well as gas profiles from sponcomb rig were studied critically to develop a fire ladder facilitating assessment of spontaneous combustion propensity of coal. The product of combustion gases ($CO$, $CO_2$, $CH_4$ and $H_2$) emitted from sponcomb rig within the temperature range between ambient and 300 °C of these coal samples were studied. It has been observed that in this study temperature of coal samples reached to 550 °C. The signature of gases released from heating reveal that the $CO$ releases in low temperature range i.e. 60–120 °C whereas $H_2$ in temperature range 80–140 °C. The emission of $CO_2$ initiates within the temperature range from 180 to 240 °C whereas $CH_4$ releases at higher temperature range i.e. 360–480 °C. The oxygen concentration of the product of combustion gases reduces as the $CO_2$ levels increase. The initial product of combustion gas i.e. $CO$ followed by $H_2$ indicates spontaneous combustion of coal in laboratory condition for Jharia coalfield. The temperatures at which $CO$ and $H_2$ release in the level of 50 ppm (i.e. $T_{CO50}$, $T_{H250}$) and modified crossing point temperature of coal ($CPT_{CT}$) determined from sponcomb rig categorises the coal as per their propensity to spontaneous combustion. The results of these methods have been compared with other standard method i.e. crossing point temperature method, which is widely adopted in India to verify the suitability of this method.

**Keywords:** Spontaneous combustion · Sponcomb rig · Fire ladder
Crossing point temperature

## 1 Introduction

Different countries have adopted different methods to assess the propensity of coals to spontaneous combustion in the laboratory. It may be broadly grouped under three headings: determination of the chemical constituents, the oxygen avidity studies and the thermal studies [3]. The uses of thermal analytical studies are widely used all over world. In thermal studies, researchers have employed a range of different methods, including: heat based measurement—crossing point temperature (CPT) and ignition point temperature (IPT), modified CPT, puff temperature (PT), basket heating test

method, Chen's method, Critical air blast method, Olpinski index; Calorimetric studies—adiabatic calorimetric (SHT—USA, R70—Australia), isothermal calorimetric; thermal analysis—differential thermal analysis (DTA), differential scanning calorimetric (DSC) and thermogravimetric analysis (TGA), to determine the susceptibility of coal towards spontaneous heating. Amongst these assessment techniques: the CPT method is widely used in India, South Africa, Poland, China and Turkey; the isothermal and adiabatic calorimetric methods are used in UK, USA and Australia and the puff temperature and Olpinski index methods are widely used in Russia. Subsequently a number of further modifications to CPT methods with respect to their experimental parameters and the apparatus design have been proposed [1–15]. The higher the determined CPT value, the less will be the susceptibility of coal to spontaneous combustion. The CPT and moisture content of coal data is required by mine planner to design the mine, mine operators and regulators for ensuring safety of miners and machines. These two techniques are simple, basic practices, user friendly and often time consuming process. The repeatability and reproducibility are sometime uncertain for their reliability to laboratory as well as field condition. However, it is conceded that the results of this laboratory analytical techniques may often be contradicted by actual mine conditions due to the influence of extraneous parameters such as mining, geological and environmental parameters. So, mine regulators and mine operators requires these tests to predict spontaneous combustion/fire risk to minimise hazards for ensuring safety of miners and machine for sustainable growth.

## 2 Materials and Methods

### 2.1 Sample Collection

Eleven different types of coals were sampled from the Jharia coalfield (JCF) containing both fiery and non-fiery coal seams. The classifications of coal seam fires were based on the history of fires as well as present condition of coal seams. About 2 kg of representative sample from different seams were collected and samples of different sizes were prepared as per requirement keeping aerial oxidation minimum. The locations of the eleven coal seams sampled are detailed in Table 1. Among these eleven samples five samples (sample numbers: 1, 2, 3, 4 and 5) are having present and past history of fires & spontaneous heating and rest of these have not had any observation of fire.

### 2.2 Basic Coal Characteristics Study

Proximate analysis, ultimate analysis and calorific value of all samples were carried out following the ASTM standard on a received basis. The maceral analysis [16] and rank analysis [17] of the prepared polished blocks were carried out using microscope. The macerals and rank of a coal sample require the preparation and analysis of representative blocks for each coal sample. The CPT of coal samples were determined as per the Directorate General Mine Safety (DGMS) circular, i.e. DGMS Cir. Tech.3/1975. The results of proximate analysis, ultimate analysis, calorific value, maceral, rank and CPT

**Table 1.** Proximate, ultimate, GCV and CPT analysis of the eleven coal samples

| Sample | Seam name | Mine name | Fire status | Moisture (%wt) | Ash (%wt) | Volatile matter (%wt dafb) | Fixed carbon (%wt dafb) | C (%wt dafb) | H (%wt dafb) |
|---|---|---|---|---|---|---|---|---|---|
| 1 | S–14 | Chasnala | Yes | 1.14 | 10.31 | 30.69 | 61.37 | 77.16 | 4.92 |
| 2 | S–14 | Jitpur | Yes | 1.18 | 10.84 | 29.54 | 61.99 | 79.77 | 4.81 |
| 3 | S–13 | Chasnala | Yes | 1.16 | 7.78 | 32.44 | 61.52 | 79.85 | 5.28 |
| 4 | S–16 | Jitpur | Yes | 1.30 | 9.34 | 30.06 | 62.50 | 79.12 | 4.91 |
| 5 | S-11 | Enna | Yes | 0.61 | 20.94 | 26.95 | 57.31 | 81.31 | 5.02 |
| 6 | S–11 | Bhalgora | Yes | 1.22 | 16.71 | 28.26 | 58.88 | 83.96 | 5.06 |
| 7 | S–11 | Simlabahal | No | 1.25 | 13.40 | 27.22 | 62.11 | 82.10 | 4.69 |
| 8 | S–12 | Simlabahal | No | 1.13 | 16.74 | 26.42 | 60.44 | 79.99 | 4.81 |
| 9 | S-10 | Bhalgora | No | 0.64 | 17.19 | 24.86 | 61.74 | 83.94 | 4.73 |
| 10 | S-10 | Simlabahal | No | 0.63 | 16.75 | 25.08 | 61.90 | 84.14 | 4.95 |
| 11 | S-09 | Simlabahal | No | 0.92 | 16.88 | 27.02 | 59.99 | 83.53 | 4.94 |

| Sample | SN (%wt dafb) | S (%wt dafb) | O (%wt dafb) | Calorific value (MJ/kg) | CPT (°C) | Vitrinite (Vm) | Liptinite (Lm) | Semi-fusinite (SFm) | Fusinite (Fm) | Vitrinite reflectance (VRm) |
|---|---|---|---|---|---|---|---|---|---|---|
| 1 | 1.52 | 0.28 | 16.10 | 29.64 | 145 | 67.2 | 2.4 | 21.6 | 3.6 | 0.74 |
| 2 | 1.58 | 0.27 | 13.57 | 28.86 | 142 | 69.2 | 1.6 | 18.8 | 3.6 | 0.76 |
| 3 | 1.57 | 0.31 | 12.98 | 29.29 | 136 | 62.4 | 1.6 | 10.4 | 9.2 | 0.87 |
| 4 | 1.43 | 0.32 | 14.21 | 28.68 | 152 | 72.0 | 2.8 | 23.6 | 6.8 | 0.97 |
| 5 | 1.62 | 0.00 | 12.06 | 25.59 | 169 | 40.4 | 0.8 | 27.2 | 6.0 | 1.00 |
| 6 | 1.88 | 0.54 | 8.57 | 27.42 | 171 | 74.4 | 3.2 | 26.4 | 4.0 | 1.02 |
| 7 | 1.73 | 0.41 | 11.07 | 28.34 | 159 | 55.2 | 1.2 | 27.2 | 8.8 | 1.15 |
| 8 | 1.64 | 0.50 | 13.05 | 27.24 | 152 | 74.8 | 5.6 | 36.0 | 7.6 | 1.08 |
| 9 | 1.90 | 0.35 | 9.08 | 26.72 | 165 | 68.4 | 1.2 | 46.0 | 12.8 | 1.04 |
| 10 | 1.90 | 0.39 | 8.63 | 27.46 | 168 | 57.2 | 1.2 | 32.0 | 9.6 | 1.05 |
| 11 | 2.00 | 0.50 | 9.04 | 26.77 | 162 | 64.8 | 2.0 | 25.2 | 4.0 | 1.09 |

*M* moisture, *A* Ash, *VM* Volatile matter, *FC* Fixed carbon, *C* Carbon, *H* Hydrogen, *N* Nitrogen, *S* Sulphur, *O* Oxygen, *CV* Calorific value, *CPT* Crosing point temperature of coal, $V_m$ Vitrinite, $L_m$ Liptinite, $SF_m$ Semi-Fusinite, $F_m$ Fusinite, $VR_m$ Vitrinite Reflectance

for all the samples were presented in Table 1. Five different prepared samples of each coal type were tested and the mean data of these tests are presented.

## 2.3 Experimental Setup and Procedure

A spontaneous combustion rig (sponcomb rig) was developed at the University of Nottingham (UoN) to determine the crossing point temperature of coal. This rig measured thermal profile inside (both vertical & radial) and outside of heated coal sample holder. The experimental rig comprises: a vertical furnace, sample holder, thermocouples with their attachment and configuration, a controlled gas exhaust system to collect the product gases, and a multi gas analyser (Fig. 1). The measurements were collected through a data interface to a personal computer. The coal sample holder is formed by a stainless steel cylinder (length—0.08 m and inner diameter—0.05 m, wall thickness—1 mm), with a capacity to hold 100 g of coal of −272 size micron. The detail of the sensor position (thirteen numbers of thermocouples—K type) inside the

sample holder are indicated on (Fig. 1). All of the heated coal samples were exposed to slow ramp rate to increases in temperature having following experimental parameters: 100 g of sample, heating rate of 1 °C min$^{-1}$, atmospheric air flow rate of 200 ml min$^{-1}$, under an oxidative atmosphere from 20 to 350 °C. Exhaust pump was fixed to exhaust inside atmospheric air and was controlled through rotameter to feed constant flow rate inside rig. The exhaust gases are passed through a multi gas analyser (MX6iBrid) continuously to determine the different gas species concentrations i.e. CO, H$_2$, CO$_2$, CH$_4$ and O$_2$. An analysis of the results of these experiments is subsequently conducted to identify coals that are prone to self-oxidation and less reactive coals at low temperatures.
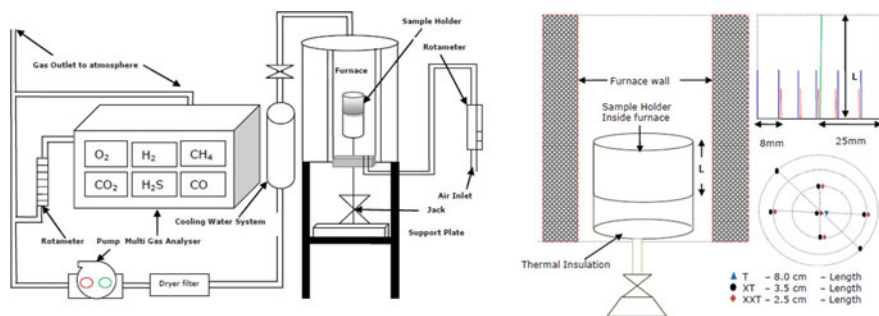


**Fig. 1.** Schematic of the UoN spontaneous combustion rig, sample holder and their sensor locations (not to scale)

## 3    Analysis of Results

### 3.1    Basic Coal Characteristics

The proximate analyses of coal samples reveals that M, VM and A content of the samples varies across a range from 0.61% (sample 5) to 1.30% (sample 4); 20.43% (sample 9) to 29.55% (sample 3); 7.78% (sample 3) to 20.94% (sample 5) respectively. Similarly the ultimate analysis results reveal that C, H, N, S & O of the tested coal samples vary from 63.78% (sample 5) to 72.72% (sample 2); 3.89% (sample 9) to 4.81% (sample 3); 1.27% (sample 5) to 1.64% (sample 11); 0.0% (sample 9) to 0.44% (sample 6), respectively. The gross calorific values (GCV) vary across a range from 25.59 MJ kg$^{-1}$ (sample 5) to 29.64 MJ kg$^{-1}$ (sample 1). The vitrinite, liptinite, semifusinite, fusinite percentages determined for all of the samples varies between 40.40 (sample 9) to 74.80% (sample 3); 0.80 (sample 9) to 5.60% (sample 3); 10.40 (sample 8) to 46.00% (sample 9) and 3.60 (sample 1) to 12.80% (sample 9) respectively. There were no significant pyrite content levels detected in the majority of the coal samples examined. The CPTs vary across a range from 136 °C with sample 3–171 °C with sample 6. The CPT values determined for samples 3 is low (<140 °C) which is categorised as highly prone to spontaneous combustion, whereas sample numbers 1, 2, 4, 7 and 8 are in the range of 140–160 °C which are moderately

susceptible and sample numbers 5, 6, 9, 10 and 11 are high (>160 °C), which denotes low susceptibility to spontaneous combustion.

## 3.2    Thermal Analysis

The result of thermal profile concludes that initially rise in coal bed temperature was less than of the air in the oven for all samples. One of the thermocouples located at the centre top (CT) of sample holder, achieves a maximum temperature very close to 550 °C during experiment from ambient to 350 °C. Other thermocouples achieve maximum temperatures of up to 300 °C for all samples. The stage at which both the coal bed and bath temperature (furnace programme temperature [FPT]) are equal is known as crossing point temperature. Following the achievement of the CPT, the coal sample temperatures are observed to increase at a much faster rate until the ignition temperature of the coal was reached. The rate of the temperature rise then slows down once the coal reaches its ignition point temperature. The thermal profile of the different thermocouples varied from the centre of sample holder to wall, depends upon the thermal conductivity of coal, the packing density of sample in sample holder and the distance between outer wall of sample holder and furnace wall. The evolution of the temperatures measured at the centre bottom, middle and centre top with respect to the FPT are shown in Figs. 2 and 3. An analysis of the data on these figures reveals there is no ignition after the hot spot in the centre middle and bottom sensor because of a lack of oxygen except centre top (presence of oxygen at top). So, the centre bottom and middle temperature cannot reach the crossing point temperature because it did not trigger to ignition of coal. A study of the data trends presented in Figs. 2 and 3 reveals that there are larger temperature differences recorded by the central vertical axis thermocouples as compare to those across the radial direction. This temperature differences recorded along the central vertical axis thermocouples (centre) occur due to the reactions that take place at the top of sample holder and not in the middle (4.5 mm vertical distance from top of sample holder) or bottom (5.5 mm vertical distance from top of sample holder) of the sample. Consequently, crossing point temperature of each coal sample were determined with respect to centre top i.e. $CPT_{CT}$. The computed values of the $CPT_{CT}$ are shown in Table 2. An analysis of the thermal profile data trends concludes that the $CPT_{CT}$ values vary across a range from between 196 °C (sample 8) to 231 °C (sample 5). The $CPT_{CT}$ values follow a similar trend mainly due to availability of oxygen at the top of the sample holder.
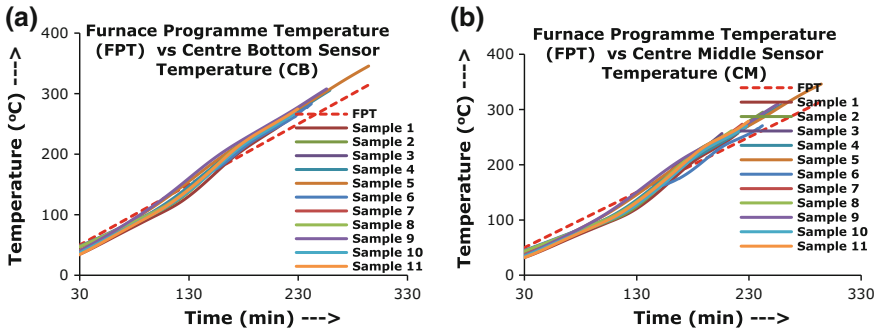
Fig. 2. CPT of coal samples FPT versus Centre Bottom and FPT-Centre Middle
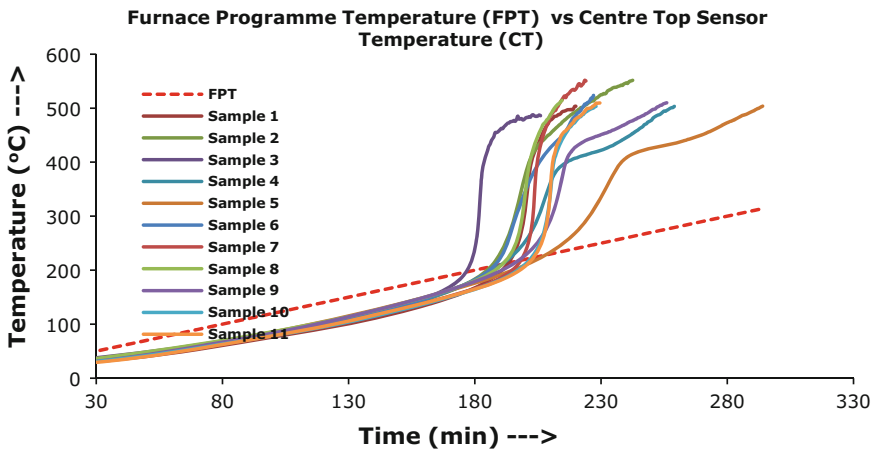


Fig. 3. CPT of coal samples (FPT-Centre Top)

**Table 2.** Temperatures at which CO and $H_2$ releases in the level of 50 ppm (i.e. $T_{CO50}$, $T_{H250}$)

| Sample No. | $CPT_{CT}$ | $T_{CO50}$ | $T_{H250}$ |
|---|---|---|---|
| 1 | 213 | 134 | 176.8 |
| 2 | 206 | 157 | 194.7 |
| 3 | 196 | 141 | 185.0 |
| 4 | 211 | 161 | 202.1 |
| 5 | 231 | 175 | 208.5 |
| 6 | 228 | 164 | 211.7 |
| 7 | 218 | 155 | 157.2 |
| 8 | 211 | 152 | 190.1 |
| 9 | 216 | 171 | 191.8 |
| 10 | 222 | 160 | 196.8 |
| 11 | 223 | 151 | 185.9 |

### 3.3 Gas Compositional Analysis

The MX6IBrid multi gas analysers was used to continuously measure and record the concentration of product of combustion gases i.e. CO, $H_2$, $CO_2$, $CH_4$ and $O_2$. During the execution of the experiments the product gases liberated on the heating of the coal samples were measured every 30 s and all this data were matched against the thermal data record to determine the product of combustion (POC) gases released at different temperatures. The results of all five gases for all samples with respect to time are given in Figs. 4, 5, 6, 7 and 8.
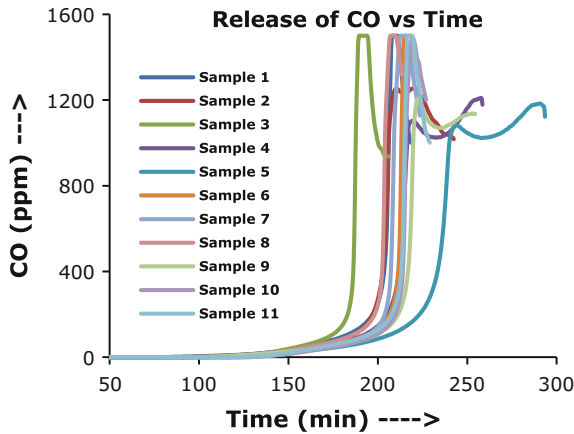


**Fig. 4.** Release of CO versus time
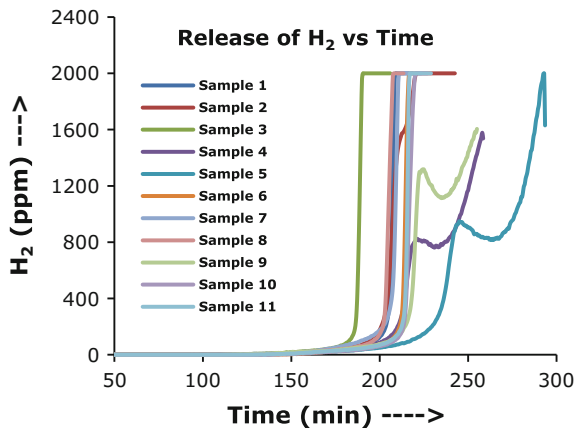


**Fig. 5.** Release of $H_2$ versus time
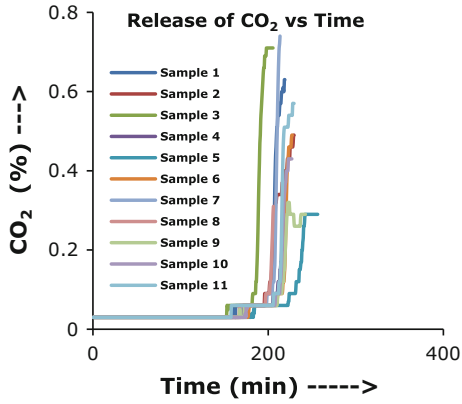
**Fig. 6.** Release of $CO_2$ versus time
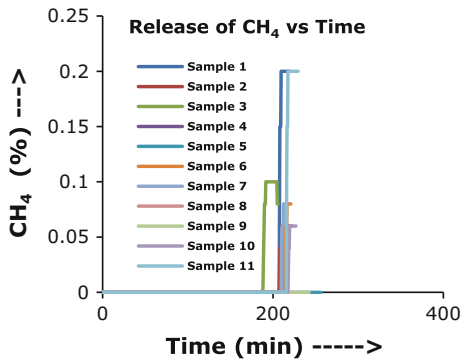


**Fig. 7.** Release of $CH_4$ versus time
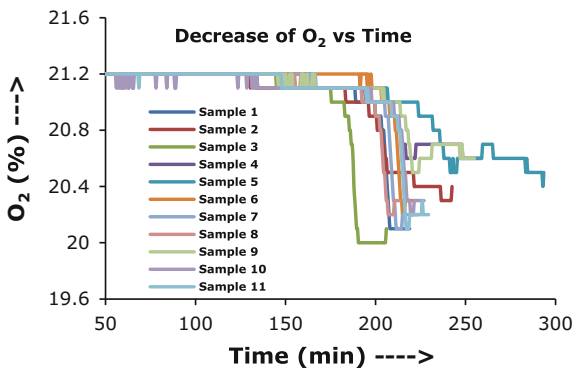


**Fig. 8.** Decrease of $O_2$ versus time

An analysis of the gas emission profile data measured from the heated samples reveals that the CO and $H_2$ releases are at low temperatures (<130 °C), whereas the $CO_2$ releases at temperatures above 150 °C and $CH_4$ releases at higher temperatures (>350 °C) [18, 19]. The oxygen content of the emissions reduces as the $CO_2$ levels increase. The production of CO and $H_2$ is more than 1500 and 2000 ppm for most of samples except sample number 4, 5 and 9. The maximum CO production could not be recorded as it exceeded the upper measurement capacity of the instrument. The maximum $CO_2$ and $CH_4$ production are 0.74 and 0.20% respectively. The lower limit of the oxygen level measured during combustion was 20.0%.

The production of combustion gases (CO, $H_2$, $CO_2$, and $CH_4$) is the function of time and temperature. A study from above figure reveals that in initial phase there was slow increase of combustion gases followed by immediate increases of combustion gases [20–22]. Then there is slow downfall of the gases because of availability of oxygen does not reach coal as air feeds to sample holder from top. In first phase the coal, oxygen, heat and chain reaction are there to produce the combustion gases. After first few layer of coal burns generates ash which does not allow the oxygen availability to coal surface. Another issue may be the flow rate and direction of flow is important for penetration of air and availability of oxygen in coal surface for fire tetrahedral. In reality after completion of each experiment it was observed that ash layer was present in few centimetres (i.e. 1.5–2.5 cm) which are approximately 15–25% of sample holder height. The thermal profiles of centre top sensor for all coal samples shows there are slow increase means the rate of reaction downtrends and Fig. 3 corroborate the same.

All of the coal samples heated under laboratory conditions initially released CO and $H_2$ gases, which may indicate the onset of spontaneous heating confirmed by previous studies [23]. Struminski and Madeja-struminska [24] reported the results of experiments conducted to investigate the gases released at given heating temperatures. Gas mixture risk indices (such as Graham's ratio [used to indicate $CO/O_2$ deficiency], $CO_2$/$O_2$ deficiency, C/H ratio and Willet's ratio, etc.,) are used to assess risk of the atmosphere present in the ventilating air in underground mines, as well as fire status of the atmosphere in within sealed off areas [23, 25, 26]. The potential emission of CO may endanger the health and safety of workers especially in underground mines. Consequently, the CMR 1957 of India, states that if the CO content of the ventilating air exiting a working is greater than 50 ppm then the mining activities should cease and the workers should be withdrawn. The thermal profiles (temperature of top centre thermocouple) were determined to maintain the gas emissions (CO and $H_2$) at 50 ppm which are known as $T_{CO50}$ and $T_{H250}$ (Fig. 9). The thermal profile results for above two are given in Table 2.

An analysis of the thermal profile data of the heated coal samples presented on Table 2 concludes that the samples 1, 2 and 3 are low thermal values. The sample number 5, 6, 9 and 10 are high for CO at 50 ppm, and $H_2$ at 50 ppm. The sample 1, 2 and 3 are more to spontaneous heating which verifies to CPT Indian method and thermal profiles from sponcomb rig.
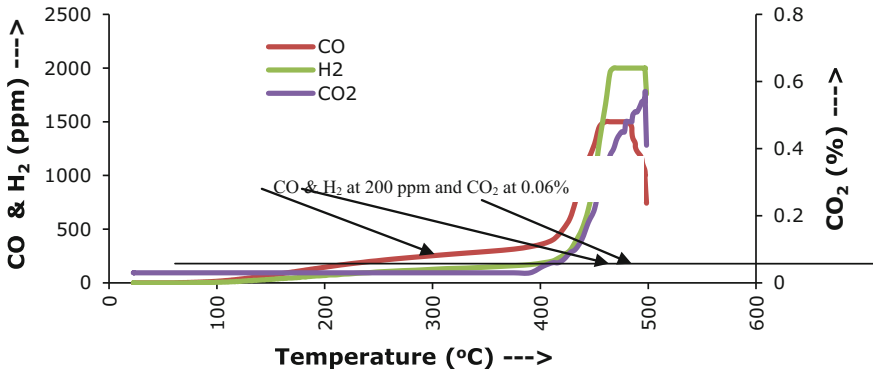
**Fig. 9.** Gas analysis result for all coal samples at CPT

## 3.4    Validation of Results with CPT

Correlation studies were carried out to classify and validate the results from fire ladders study with established potential methods of spontaneous heating susceptibility indices. The correlation coefficients derived for a $p < 0.05$ confidence interval for all the spontaneous heating susceptibility indices were given in Table 3 and Fig. 10. The results of Table 3 reveals that the CPT show the highest significance with the $CPT_{CT}$ ($R^2 = 0.93$) and $T_{CO50}$ ($R^2 = 0.73$) and has poor correlation with the $T_{H250}$. The $CPT_{CT}$ has poor correlation with both the indices $T_{CO50}$ and $T_{H250}$. Similarly, the $T_{CO50}$ has poor correlation with $T_{H250}$. Fire ladder study of all the coal samples is correlated with crossing point temperature, which is widely used in India. It has been observed that $CPT_{CT}$ and $T_{CO50}$ results are well corroborated with CPT.

**Table 3.** Correlation matrix of different spontaneous heating indices

|  | CPT | $CPT_{CT}$ | $T_{CO50}$ | $T_{H250}$ |
|---|---|---|---|---|
| CPT | 1.00 |  |  |  |
| $CPT_{CT}$ | 0.93 | 1.00 |  |  |
| $T_{CO50}$ | 0.73 | 0.59 | 1.00 |  |
| $T_{H250}$ | 0.37 | 0.34 | 0.58 | 1.00 |
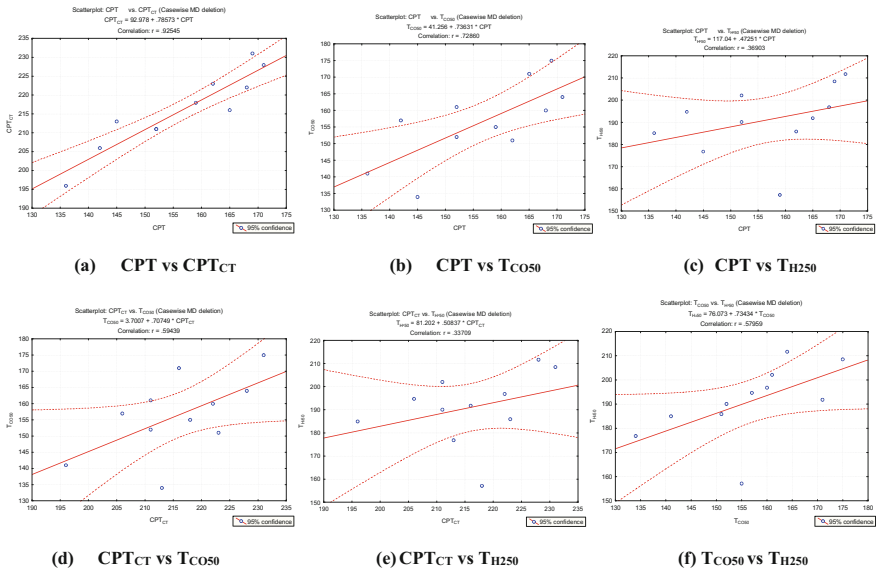
**Fig. 10.** Correlation plot of different spontaneous heating indices

## 4 Conclusions

The present study has the results of a series of analytical investigations to characterise the characteristic properties (proximate, ultimate, GCV), petrography (macerals, rank of fresh coal) and spontaneous combustion susceptibility indices (CPT, $T_{CO50}$ and $T_{H250}$) for eleven coal samples from a number of mines across the Jaharia Coalfield, India. The design and development concept of sponcomb rig at university of Nottingham has improved further. The product of combustion gases (CO, $CO_2$, $CH_4$ and $H_2$) emitted from sponcomb rig within the temperature range between ambient and 300 °C of these coal samples were studied. It has been observed that in this study temperature of coal samples reached to 550 °C. The signature of gases released from heating reveal that the CO releases in low temperature range i.e. 60–120 °C whereas $H_2$ in temperature range 80–140 °C. The emission of $CO_2$ initiates within the temperature range from 180 to 240 °C whereas $CH_4$ releases at higher temperature range i.e. 360–480 °C. The oxygen concentration of the product of combustion gases reduces as the $CO_2$ levels increase. The initial product of combustion gas i.e. CO followed by $H_2$ indicates spontaneous combustion of coal in laboratory condition for Jharia coalfield. The temperatures at which CO and $H_2$ releases in the level of 50 ppm (i.e. $T_{CO50}$, $T_{H250}$) and modified crossing point temperature of coal ($CPT_{CT}$) determined from sponcomb rig categorises the coal as per their propensity to spontaneous combustion. The results of these methods have been compared with other standard method i.e. crossing point temperature method, which is widely adopted in India to verify the suitability of this method.

# References

1. Tideswell, F.V., Wheeler, R.V.: LXXXVI.-The oxidation of the ingredients of banded bituminous coal. Studies in the composition of coal. J. Chem. Soc. Trans. **117**, 794–801 (1920)
2. Kreulen, D.J.W.: Elements of coal Chemistry. Nijgh and Van Ditmer N.V, Rotterdam (1948)
3. Parr, S.W., Coons, C.C.: Carbon dioxide as an index of the critical oxidation temperature for coal in storage. Ind. Eng. Chem. **17**(2), 118–120 (1925)
4. Chamberlain, E.A.C., Hall, D.A.: The practical early detection of spontaneous combustion. Colliery Guardian **221**(5), 190–194 (1973)
5. Feng, K.K., Chakravorty, R.N., Cochrane, T.S.: Spontaneous combustion—a coal mining hazard. Can. Min. Metall. Bull. **66**(738), 75–84 (1973)
6. Banerjee, S.C., Banerjee, B.D., Chakravorty, R.N.: Rate studies of aerial oxidation of coal at low temperatures (30–170 °C). Fuel **49**(3), 324–331 (1970)
7. Bagchi, S.: An investigation on some factors affecting the determination of crossing point of coals. J. Mine. Metall. Fuels **13**(8), 243–247 (1965)
8. Gouws, M., Wade, L.: The self-heating liability of coal: Predictions based on simple indices. Min. Sci. Technol. **9**, 75–80 (1989)
9. Gouws, M., Wade, L.: The self-heating liability of coal: predictions based on composite indices. Min. Sci. Technol. **9**, 81–85 (1989)
10. Panigrahi, D.C., Saxena, V.K, Udaybhanu, G.: A study of susceptibility of Indian coals to spontaneous combustion and its correlation with their intrinsic properties. In: Proceedings, 1st International Conference on Mine Environment and Ventilation, Dhanbad, India, pp. 347–353 (2000)
11. Panigrahi, D.C., Sahu, H.B.: Classification of coal seams with respect to their spontaneous heating susceptibility—a neural network approach. Geotech. Geol. Eng. **22**(4), 457–476 (2004)
12. Sahu, H.B., Padhee, S., Mahapatra, S.S.: Prediction of spontaneous heating susceptibility of Indian coals using fuzzy logic and artificial neural network models. Exp. Syst. Appl. **38**(3), 2271–2282 (2011)
13. Nimaje, D.S., Tripathy, D.P., Nanda, S.K.: Development of regression models for assessing fire risk of some Indian coals. Int. J. Intell. Syst. Appl. **2**, 52–58 (2013) (Published Online January 2013 in MECS)
14. Ganguli, M.K., Banerjee, N.G.: Critical oxidation and ignition temperature of coal. Indian Min. Mettalurgy Assoc. (IMMA) Rev. **2**, 1 (1953)
15. Chen, X.D., Chong, L.V.: Several important issues related to the crossing-point-temperature (CPT) method for measuring self-ignition kinetics of combustible solids. Trans. IChemE Part B Process Saf. Environ. Prot. **76**(B), 90–93 (1997)
16. BS-ISO-7404-3: Methods for the Petrographic Analysis of Coals—Method of Determining Maceral Group Composition. British Standards Institute, UK (2009)

17. BS-6127-5: Petrographic Analysis of Bituminous Coal and Anthracite—Part 5: Method of Determining Microscopically the Reflectance of Vitrinite. British Standards Institute, UK (1995)
18. Marinov (a), V.N.: Self-ignition and mechanisms of interaction of coal with oxygen at low temperatures. 1. Changes in the composition of coal heated at constant rate to 250 °C in air. Fuel **56**(2), 153–157 (1977)
19. Marinov (b), V.N.: Self-ignition and mechanisms of interaction of coal with oxygen at low temperatures. 2. Changes in weight and thermal effects on gradual heating of coal in air in the range 20–300 °C. Fuel **56**(2), 158–164 (1977)
20. Wang, H., Dlugogorski, B.Z., Kennedy, E.M.: Coal oxidation at low temperatures: oxygen consumption, oxidation products, reaction mechanism and kinetic modelling. Prog. Energy Combust. Sci. **29**(6), 487–513 (2003)
21. Xie, W., Pan, W.P.: Thermal characterization of materials using evolved gas analysis. J. Therm. Anal. Calorim. **65**(3), 669–685 (2001)
22. Trenczek, S.: Levels of possible self-heating of coal against current research. Arch. Min. Sci. **53**(2), 293–317 (2008)
23. Mohalik, N.K., et al.: Proper sampling of mine gases, analysis and interpretation—a pre requisite for assessment of sealed off fire area. J. Mines Metals Fuels **54**(10 & 11), 210–217 (2006)
24. Struminski, A., Madeja-Struminska, B.: Evaluation of arising spontaneous fire centre temperature and time of coal self-Ignition. In: Eighth International Mine Ventilation Congress, Brisbane Queensland, pp. 511–515, 6–8 July 2005
25. Ray, S.K., et al.: Assessing the status of sealed fire in underground coal mines. J. Sci. Ind. Res. **63**(7), 579–591 (2004)
26. Singh, A.K., et al.: Mine fire gas indices and their application to Indian underground coal mine fires. Int. J. Coal Geol. **69**(3), 192–204 (2007)

# Novel Paste Foam for Sealing and Cooling Coal and Rock Fractures with High Temperature

Lu Yi[1,2,3(✉)], Shi Shiliang[3], Wang Haiqiao[3], Tian Zhaojun[3], Ye Qing[3], and Pang Min[3]

[1] Work Safety Key Lab on Prevention and Control of Gas and Roof Disasters for Southern Coal Mines, Hunan University of Science and Technology, Xiangtan, Hunan 411201, China
luyijx@l63.com
[2] Hunan Province Key Laboratory of Safe Mining Techniques of Coal Mines, Hunan University of Science and Technology, Xiangtan, Hunan 411201, China
[3] School of Resource, Environment and Safety Engineering, Hunan University of Science and Technology, Xiangtan, Hunan 411201, China

**Abstract.** Coal and rock fractures formed at high temperatures due to heat are main causes for spreading coal fires. Existing materials used to prevent and control coal spontaneous combustion, a type of paste foam consist a mixture of polyacrylamide (A), composite surfactant (B), and mixed powder. Orthogonal test method was used to optimize the proportion of the paste foam ingredient with water retention rate, foaming ratio and inhibition rate, and the result is A4B4C4, with A at 70 g/l, B at 19.5 g/l, and C at 270 g/l. The micro morphology changes of paste foam under different temperatures were investigated, and the mechanism of water retention, heat absorption and heat stability was analyzed from water absorption of the liquid film, bubble size and distribution, particles distribution and hydration in the liquid film, and the kinetic energy of surfactant molecules. Finally, Fire spread at 302 working face at Anyuan Coal Mine was used to analyze and determine the extent of fire spread, paste foam was then injected to control high temperature fractures. The temperature and gas concentration such as CO, $O_2$, and $CH_4$ in the 1-5# drilling field and No. 3 cross-hole was monitored. What that all means, the paste foam can seal the air leakage and inhibit spontaneous combustion of coal effectively.

**Keywords:** Spontaneous combustion of coal · High temperature fracture Paste foam · Prevention and control

## 1 Introduction

Mine fire is one of the majors in underground coal mining, and the coal spontaneous combustion accidents caused by air leakage through coal and rock cracks account for more than 90% of the total number of mine fires [1]. According to preliminary statistics of the coal mine accident inquiry system of the State Administration of Work Safety (SAWS), of the 770 gas explosions in 2002–2016, more than 30% were caused by coal

spontaneous combustion [2]. There is a large area in Xinjiang, Ningxia, Inner Mongolia and other provinces in China where coal has been burning, and the economic loss is over 20 billion yuan [3]. Large coal bases such as Shendong (northern Shanxi) and Huanglong (east of Huangning), coal seams are shallow and near surface, spontaneous combustion caused by serious leakage is also very frequent [4]. In addition, the problem of spontaneous combustion of coal caused by the negative pressure in the gob caused by gas drainage operation [5] and the leakage through small coal pillars along the goaf [6] has also become very prominent. At home and abroad, fire prevention and extinguishing technologies such as grouting [7], nitrogen injection [8], foam [9], spraying inhibitor [10], gel grouting and composite colloid [11] are usually used. Grouting technology has a small coverage and difficult to achieve its effectiveness unless the entire space is filled with grouting material. Water and soil loss as a result of seepage also make conventional grouting difficult.

Nitrogen injection technology has the inserting effect and wide coverage, but with air leakage, cooling and extinguishing capacity is also reduced. Firefight measures also bring about other negative effects: retarding agent, corrosion inhibitors may corrode underground equipment and harm workers' physical and mental health, gel or compound colloid has the disadvantages of small flow, high cost and small discharging range. A typical foaming agent will remain stable for 5–6 h, and it is difficult to continuously plug the cracks of high temperature (250–300 °C) coal and rock after materials start to decompose [12].

Based on the above analysis, the key to prevent and control coal spontaneous combustion is to plug the cracks in coals and rocks. The foam material has good diffusion capacity, can easily be used to fill an entry. For this reason, a paste foam material is developed to seal coal and rock cracks, cool, to control coal spontaneous combustion. Through orthogonal test best formula for the composite can be determined, and then used in the mine site in case of a fire.

## 2 Experiment and Methods

### 2.1 Materials

Materials used in the field test include pure polyacrylamide, silica fume, calcium chloride dihydrate, magnesium chloride hexahydrate, lauryl sodium sulfate and twelve alcohol. while fly ash contain 60% $SiO_2$ and $Al_2O_3$ (what's the remaining material?. And 425# Portland cement, with a 5% fine materials..

### 2.2 Preparation Process

The basic preparation process can be grouped into four steps: (1) fly ash (65.4 wt%), 425# Portland cement (23.1 wt%), silica fume (10.5 wt%), magnesium chloride hexahydrate (0.4 wt%) and calcium chloride dihydrate (0.6 wt%) were mixed and formed the mixed powder; (2) using 2.5 wt% lauryl sodium sulfate and 2 wt% twelve alcohol to make composite surfactants compound; (3) polyacrylamide, mixed powder and composite surfactants are added in the water to form a compound paste; (4) compound

paste is foamed in the foaming device. The foaming device is a mixer with a hollow spiral rod and an outlet on the hollow screw rod. The air pressure is 0.3–0.4 Mpa, and the volume ratio of air supply and compound paste is 10:1. The compressed air is discharged from the inner of the hollow screw rod, and then mixed with the compound paste in the spiral channel (rotational speed of 150–200 r/min), and the formed vortex is transformed into turbulence, and vortex is generated at a certain frequency. The loss of kinetic energy acted on the compound paste and then paste foam was generated.

## 2.3     Analysis Method of Key Performance

(1) Water retention rate. The test device is KQ-1202 hot air circulation drying box (Kechang detection instruments Co. Ltd.). The sample of 1000 g ($m_0$) is put in the test box, and the test temperature is 150 °C. After heating for 10 h, the paste was recovered to normal temperature and removed from the thermostat. The quality of the paste ($m_1$) was measured by electronic balance, and the water retention rate ($\eta$) was calculated according to the formula (1).

$$\eta = \frac{m_1}{m_0} \times 100\%$$ (1)

(2) Foaming rate. The ratio of the foaming ratio is the ratio of the density of the compound paste ($\rho_0$) to the paste foam ($\rho_1$).

(3) Inhibition rate. The test system for the characteristic of coal spontaneous combustion (Fig. 1) is adopted and the inhibition rate of the paste foam is measured by measuring the CO concentration. The test coal samples are from the Anyuan coal mine. After crushing and screening, the coal sample is 50 g, and the size is 40–80 mesh. The coal sample is placed in the copper tank, the coal sample tank is placed in the box with program temperature control, and then the inlet gas path, the outlet gas path and the temperature probe (the probe is placed in the geometric center of the coal sample tank) are connected, and the tightness of the gas path is checked. In the test, the dry air of 50 ml/min is passed into the coal sample. When the specified test temperature is reached 100 °C, the gas composition and concentration are analyzed by gas sample after a constant temperature of 5 min. The difference of CO amount released from two groups of original coal samples ($h_0$, mg/m$^3$) and coal samples treated with paste foam ($h_1$, mg/m$^3$) is calculated, and the formula (2) for calculating the inhibition rate ($\varepsilon$, %) is calculated.

$$\varepsilon = \frac{\Delta h}{h_0} = \frac{h_0 - h_1}{h_1} \times 100\%$$ (2)
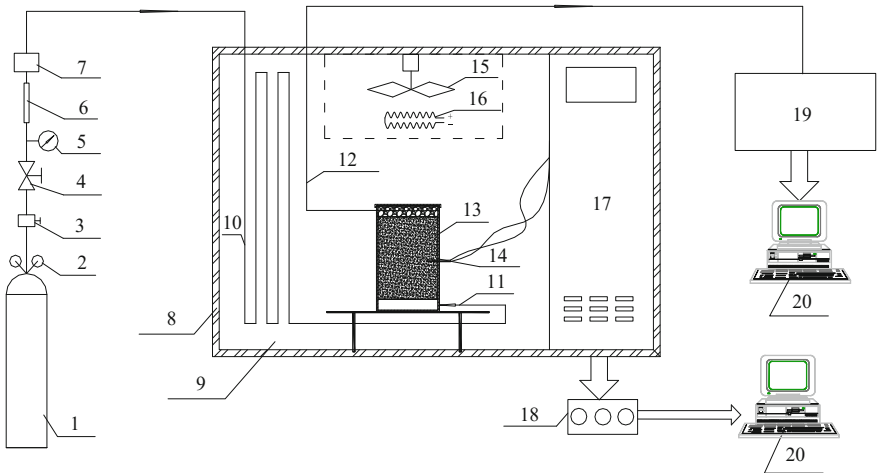
**Fig. 1.** Test system for the characteristic of coal spontaneous combustion

## 2.4 Design of Orthogonal Test

In order to study the optimum ratio of polyacrylamide, composite surface active agent and mixed powder, orthogonal experimental analysis was used to analyze. Taking water retention rate, foaming ratio and inhibition rate as indicators, we selected polyacrylamide concentration (A), composite surfactant concentration (B) and mixed powder concentration (C) as elements to study the relationship between these three elements and three indicators. Five levels were selected for each factor, and the orthogonal test level and element design were shown in Table 1.

**Table 1.** Level and element design of orthogonal test

| Element | Level | | | | |
|---|---|---|---|---|---|
| | 1 | 2 | 3 | 4 | 5 |
| Polyacrylamide concentration (g/l) | 40 | 50 | 60 | 70 | 80 |
| Composite surfactant concentration (g/l) | 3.5 | 8.5 | 13.3 | 19.5 | 24.1 |
| Mixed powder concentration (g/l) | 159 | 196 | 233 | 270 | 307 |

## 3 Results and Discussion

The experiment was carried out according to the orthogonal test (Table 1), and the results were shown in Table 2.

**Table 2.** Orthogonal test results

| Test number | A (g/l) | B (g/l) | C (g/l) | Water retention rate (%) | Foaming rate | Inhibition rate (%) |
|---|---|---|---|---|---|---|
| 1 | 40 | 3.5 | 159 | 50.18 | 3.00 | 27.13 |
| 2 | 40 | 8.5 | 196 | 51.29 | 5.80 | 40.12 |
| 3 | 40 | 13.3 | 233 | 51.99 | 7.70 | 54.12 |
| 4 | 40 | 19.5 | 270 | 60.02 | 7.90 | 57.23 |
| 5 | 40 | 24.1 | 307 | 52.62 | 8.10 | 43.25 |
| 6 | 50 | 3.5 | 196 | 60.41 | 310 | 41.25 |
| 7 | 50 | 8.5 | 233 | 61.23 | 6.00 | 57.78 |
| 8 | 50 | 13.3 | 270 | 64.21 | 8.50 | 59.32 |
| 9 | 50 | 19.5 | 307 | 65.54 | 8.70 | 32.14 |
| 10 | 50 | 24.1 | 159 | 62.98 | 7.30 | 25.69 |
| 11 | 60 | 3.5 | 233 | 77.63 | 3.80 | 60.98 |
| 12 | 60 | 8.5 | 270 | 78.21 | 6.90 | 62.21 |
| 13 | 60 | 13.3 | 307 | 80.63 | 9.45 | 43.65 |
| 14 | 60 | 19.5 | 159 | 79.65 | 9.05 | 28.23 |
| 15 | 60 | 24.1 | 196 | 77.12 | 9.10 | 44.96 |
| 16 | 70 | 3.5 | 270 | 79.21 | 5.10 | 73.02 |
| 17 | 70 | 8.5 | 307 | 81.14 | 7.20 | 43.11 |
| 18 | 70 | 13.3 | 159 | 84.75 | 8.90 | 26.17 |
| 19 | 70 | 19.5 | 196 | 85.96 | 9.40 | 51.22 |
| 20 | 70 | 24.1 | 233 | 79.56 | 9.45 | 72.77 |
| 21 | 80 | 3.5 | 307 | 70.32 | 4.30 | 41.96 |
| 22 | 80 | 8.5 | 159 | 71.87 | 6.25 | 23.61 |
| 23 | 80 | 13.3 | 196 | 78.69 | 9.15 | 47.26 |
| 24 | 80 | 19.5 | 233 | 76.22 | 9.35 | 69.95 |
| 25 | 80 | 24.1 | 270 | 73.01 | 8.70 | 69.12 |

According to the test results of Table 2 and the orthogonal test data analysis, the optimum formula was A4B4C4. When the concentration of polyacrylamide was 70 g/l, the compound surface active agent was 19.5 g/l, and the concentration of the mixed powder was 270 g/l, the comprehensive performance of the paste foam was the best. After testing, the water retention rate of the paste foam was 85.31%, the foaming rate was 9.62, and the inhibition rate was 70.31%. Paste foam as a foam fluid system, in the process of prevention in coal field, its flow and diffusion ability in high temperature coal and rock fracture, its heat absorption and cooling characteristics on high temperature wall, and its stability under heating condition were all related to its pore structure. Therefore, the BT-1600 image particle analysis system was used to characterize the foam of the paste. The distribution of the pore structure in the case of 10 times magnification was showed in Fig. 2, and the distribution of the liquid membrane and its attachment particles in the case of magnification of 100 times was showed in Fig. 3.
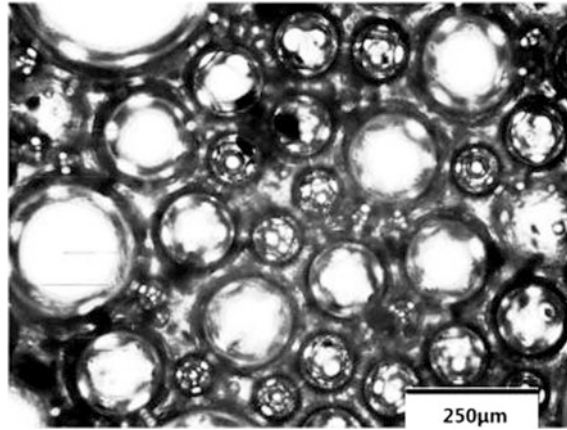
**Fig. 2.** Bubble size and distribution
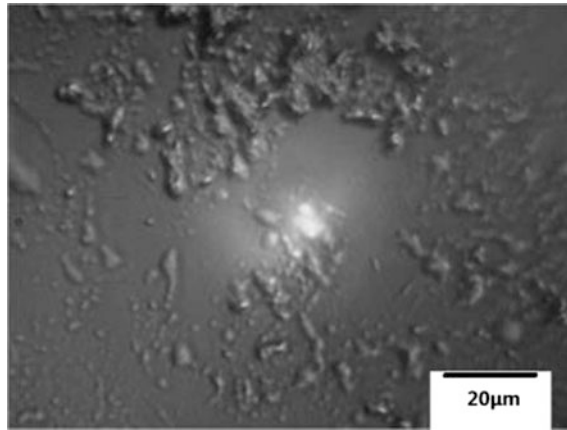


**Fig. 3.** Attached particles in bubble liquid membrane

As shown from Fig. 2, bubbles in the paste foam were evenly distributed and the size of the bubble size was between 100 and 300 μm. The average bubble diameter was about 165 μm and the thickness of the bubble wall was about 10.2 μm. Therefore, it could prevent high temperature heat source from spreading and diffusing in coal and rock fractures in a way of heat conduction and convection. Figure 3 shows that the mixed powder could be evenly distributed in the liquid film of the paste foam. Among them, fly ash, cement, silica fume and other particles had low thermal conductivity and large radiant absorption ratio [13], so when it covered the surface of high temperature coal and rock mass, it could play the role of heat rejection and thermal radiation suppression. This also increased the limiting environment temperature that the paste foam could bear. In addition, the mesh structure of the alveolar membrane carrier was also observed in Fig. 3. This was mainly because the carrier of the paste foam was

polyacrylamides (chemical formula is $-[CH_2CH]_nCONH_2-$). When it absorbed water, the ionic hydrophilic group began to dissociate under the action of water molecules. The anion was fixed on the polymer chain, and the cation was used as a movable ion to maintain electrical neutrality within the resin. Due to the elasticity of the network, a large number of water molecules could be accommodated [14]. When water entered into the reticulate structure, the free enthalpy of the whole membrane system would be reduced and the temperature of the high temperature coal could be cooled better. At the same time, only when the heat movement of the water molecules exceeded the binding force of the polymer network, the water volatilized and escaped [15]. So the paste foam had good thermal stability.

## 4    Field Application

### 4.1    Basic Situation of the Working Face

The coal seam of 302 working face in Anyuan Coal Mine is large trough with complex structure with varying coal seam thickness. It contains a 1–4 layer of pinch stone with the thickness of 0.2–1.5 m. Under the influence of the fault, the mine floor grade varies significantly, which has a big impact on mining. The large trough coal seam is susceptible to spontaneous combustion, and the incubation period is 3–6 months. The seam has an absolute gas emission rate of 1.2 $m^3$/min, and relative emission rate of 0.78 $m^3$/t. The coal seam is also susceptible to dust explosions with an explosion index of 43.98%. On January 1st 2016, CO concentrations was measured to more than 300 ppm at several locations: 302 working face, 302 air return roadway, as well as 3127 behind the goaf, and CO concentration reached 700 ppm The CO concentration in 3127 closed goaf was up to, the $C_2H_2$, $C_2H_4$ concentration was 150 ppm, and the strong smell of coal could be detected.

### 4.2    Fire Area Analysis

The area near the inlet side of the 302 working face has been mined when mining the 301 working face, due to the shortage of resources it has been exploited again, and the air leakage was serious. The area near the return air was solid coal. However, due to the construction of the floor gas drainage roadway below the working face and the construction of a large number of boreholes in the upper coal seam, the actual coal area was actually disturbed by the coal seam fractures, and there was a certain leakage. In order to further determine the fire area, the constructed 1# and 2# drilling field of gas drainage were utilized, and then the 3#, 4#, 5# drilling fields in working face were built.

Observation and analysis were carried out by collecting gas samples in the drill holes. From January 1st to January 4th, the average CO concentration in the 5 drill holes was 480 ppm (1#-1), 440 ppm (2#-1), 500 ppm (3#-1), 280 ppm (4#-1) and 260 ppm (5#-1), respectively. At the same time, there was CO concentration exceeding limit at the intersection of air intake roadway and No. 5 oblique roadway. Between January 1st and January 4th, there was a continuous abnormal gush of CO between 11:00 and 15:00, and the concentration was up to 150 ppm. After field monitoring and

analysis with on-site engineers and technicians, it was determined that the main fire zone was located in the area near the intersection of the air return roadway of original 301 working face and No. 3 cross-hole, as shown in Fig. 4.
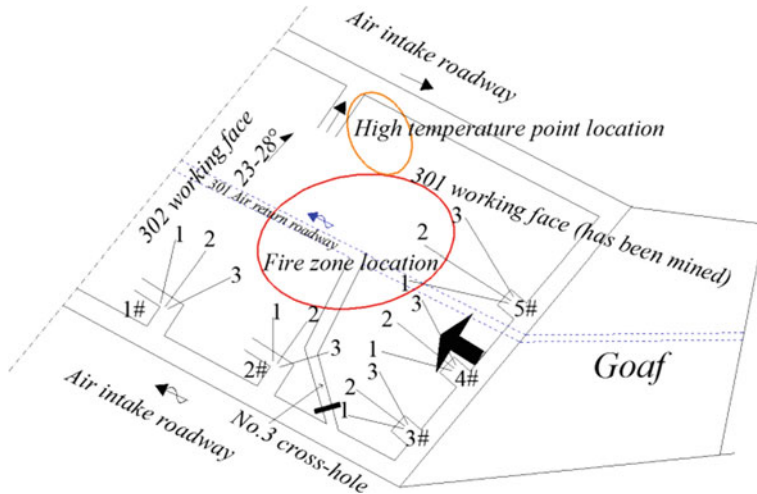


**Fig. 4.** Fire zones analysis and drilling layout in 302 working face

## 4.3   Injecting Paste Foam Through Drill Holes

From the above analysis, the coal seam in front of the working face was already in a high temperature environment. The most important way to control the fire zone was extinguishing and cooling the coal body with high temperature, and controlling the air leakage passageway in time. For this reason, two drills of No. 2 and No. 3 were re constructed on the 3#, 4# and 5# drilling fields in the evening of January 4th. At the beginning of the morning shift in January 5th (8:00), the paste foam was injected from the No. 2 and No. 3 drilling holes in five drilling fields, and the amount of foam was 300 m$^3$. The No. 1 drilling hole of five drilling fields was taken as the monitoring point for sampling analysis. The concentrations of CO in the main monitoring points of the working face were changed as shown in Fig. 5.

From Fig. 5 it can be seen that, before the morning shift in January 5th, the CO concentrations of all monitoring points had a steadily increased, but the increase range was not significant. This was mainly because the air volume of the working face has been reduced from 380 to 200 m$^3$ on January 3rd. However adjusting the ventilation system alone was not able to suppress the fire. After the injection of the paste foam from the borehole in the morning shift on January 5th, it could be seen that CO concentrations at each monitoring point began to decline rapidly by as much as 100 ppm. This was mainly because the layout of the boreholes was more, and the working face had a dip angle of 23°–28°, and the fracture of the coal seam was disturbed by a large scale. The paste foam itself had a good flow and diffusion capacity
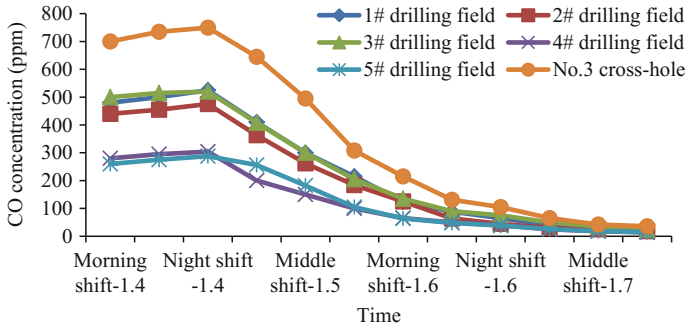
**Fig. 5.** Change of CO concentration in the main monitoring points before and after the injection of foam

for the fractures. So the paste foam could reach the predetermined fire and high temperature zone in a relatively short period of time. The high temperature coal rock mass was covered and cooled, and the fracture channel was blocked. It stopped the spread and development of the fire from the two aspects of temperature and air supply. In the night shift of January 6th, the concentration of CO in borehole monitoring point decreased to less than 80 ppm, and the CO in No. 3 cross-hole was reduced to 105 ppm. In the night shift of January 7th, the CO concentration in 1-5# drilling field was reduced to 22, 18, 23, 14 and 14 ppm, respectively. The CO concentration in No. 3 cross-hole was reduced to 36 ppm. Obviously, after injecting paste foam for 3 days, the fire situation of the working face was effectively controlled.

## 5    Conclusions

(1) Using the orthogonal test, the water retention rate, the foaming rate and the retarding rate are used as the indices, and polyacrylamide (A), composite surfactant (B) and mixed powder (C) are used as variables to form optimum firefighting materials. It is concluded that the optimum mixture ratio of the paste foam is the A4B4C4 compound with A at 70 g/l, B at 19.5 g/l and C at 270 g/l.

(2) Examining the microscopic composition of the paste foam showed that the average pore size was about 165 μm in diameter and 10.2 μm in thickness. The main ingredient is polyacrylamide which acts as a "carrier" of the liquid film, it would swell upon absorbing water. The particles were evenly distributed on the liquid film. The composition structure of the retardant material will absorb water and decrease the "free enthalpy" of the whole bubbling system, which could be able to better cool the high temperature coal and increased the binding force of the thermal movement of the water molecules. Adhered particles in liquid film could play the role of heat rejection and thermal radiation suppression, increased the limiting temperature of paste foam.

(3) The paste foam was applied at the 302 working face for controlling the fire zone. The CO concentrations in #1-5 drilling field and No. 3 cross hole were significantly reduced. It shows that it could block the "hot" cracks in coals and rocks, and then restrained coal spontaneous combustion.

# References

1. Shao, Z., Wang, D., Wang, Y., Zhong, X., Tang, X., Hu, X.: Controlling coal fires using the three-phase foam and water mist techniques in the Anjialing open pit mine, China. Nat. Hazards **75**(2), 1833–1852 (2015)
2. SAWS Homepage, http://media.chinasafety.gov.cn. Accessed 21 April 2017
3. Song, Z., Kuenzer, C.: Coal fires in china over the last decade: a comprehensive review. Int. J. Coal Geol. **133**, 72–99 (2014)
4. Wang, S., Li, X., Wang, D.: Mining-induced void distribution and application in the hydro-thermal investigation and control of an underground coal fire: a case study. Process Saf. Environ. Prot. **102**, 734–756 (2016)
5. Qin, B., Li, L., Ma, D., Lu, Y.: Control technology for the avoidance of the simultaneous occurrence of a methane explosion and spontaneous coal combustion in a coal mine: a case study. Process Saf. Environ. Prot. **103**, 203–211 (2016)
6. Lu, Y., Qin, B.: Identification and control of spontaneous combustion of coal pillars: a case study in the Qianyingzi Mine, China. Nat. Haz. **75**(3), 2683–2697 (2015)
7. Wang, W., Dai, G., Nie, S.: Research on performance of grouting plugging material for inhibition of coal spontaneous combustion. J. Safety Sci. Technol. **10**(11), 107–112 (2014)
8. Hu, X.: An intelligent gel designed to control the spontaneous combustion of coal: fire prevention and extinguishing properties. Fuel **210**, 826–835 (2017)
9. Zhou, F., Wang, D., Zhang, Y.: Practice of fighting fire and suppressing explosion for a super-large and highly gas mine. J. China Univ. Min. Technol. **17**(4), 459–463 (2007)
10. Quintero, J., Candela, S., Ríos, C.: Spontaneous combustion of the upper paleocene Cerrejón formation coal and generation of clinker in La Guajira Peninsula (Caribbean Region of Colombia). Int. J. Coal Geol. **80**(3–4), 196–210 (2009)
11. Deng, J., Xiao, Y., Lu, J.: Application of composite fly ash gel to extinguish outcrop coal fires in China. Nat. Haz. **79**(2), 881–898 (2015)
12. Lu, Y.: Laboratory study on the rising temperature of spontaneous combustion in coal stockpiles and a paste foam suppression technique. Energy Fuels **31**(7), 7290–7298 (2017)
13. Qin, B., Lu, Y., Li, Y.: Aqueous three-phase foam supported by fly ash for coal spontaneous combustion prevention and control. Adv. Powder Technol. **25**(5), 1527–1533 (2014)
14. Song, X., Zhang, Y.: Water absorption and fragmentation resistance of modified polyacrylamide absorbent resin. Mater. Rev. **30**(6), 56–60 (2016)
15. Ma, Y., Zhang, H., Yuan, S.: Hydration structure of partially hydrolyzed preformed particle gel. Chem. J. Chin. Univ. **36**(2), 386–394 (2015)

# Numerical Simulation of Smoke Variation During Fire in Intake Airways on a Coal Mining Face

Wang Jian-guo[1(✉)], Wu Rui-meng[1,2], Wang Yan-qiu[1,2], and Su Jun-kai[1,2]

[1] College of Safety Science and Engineering, Xi'an University of Science and Technology, Xi'an 710054, China
wjglll8@l26.com
[2] Key Laboratory of Western Mine Exploitation and Hazard Prevention of the Ministry of Education, Xi'an 710054, China

**Abstract.** In order to study the variation of smoke parameters during fire in the intake airway of coal mining face under the different fire source scales and wind speeds, the variation of the CO concentration, temperature and visibility were simulated by Pyrosim. The five fire sources scales are 1, 2, 5, 10 and 20 MW, respectively. The eight kinds of airflow velocity are in the range of 1.0–2.4 m/s. The results show that: (1) With the increasing size of the fire source, the concentration of CO and the time required for CO and temperature entering the stable phase are increased, and the speed of temperature drop is accelerated. (2) As the air velocity increases, the time required for CO entering the stable phase is shortened, and CO concentration in steady phase decreases. As the air velocity goes up, the temperature in return airways rises. With the air velocity decreases, the temperature at the fire source falls. (3) As the air velocity rises, the smoke spreads faster and the visible range at the exit narrows. (4) As the air velocity increases, CO concentration and temperature in the upper windward side of the fire source decrease, and the rollback distance of the smoke flow shortens. The smoke does not rollback after exceeding the critical wind speed.

**Keywords:** Intake airway fire · Carbon monoxide · Temperature field Visibility

## 1 Introduction

Mine fire not only damage mine equipment and burn coal resources, but also consumes oxygen in the wind airflow, so that the oxygen concentration in airflow reduces. At the same time, a large amount of heat, toxic and harmful gases and dusts will be generated and smoke spreads, which will cause reduced visibility, burning, poisoning or suffocation to those who work at the polluted area, and seriously threaten their safety.

In terms of the simplification degree of the fire and different modeling methods, numerical simulation of mine fire mainly includes regional simulation, field simulation (CFD simulation) and complex simulation of field network [1]. The CFD,

a computational fluid dynamics simulation software that emerged in the mid-1980s, is a mature and useful tool, and has been commonly used in simulating fluid behaviors, including fire research.

Hardy Cross method was first used to model mine ventilation network in the 1950s, gradually computers were introduced in the modeling work to be used in simulating more complex network with increased speed, and improved ease of use [2]. Fire modeling started by Greuer in the mid 1970s first through a steady state simulation of mine fire in 1973, and completed the program of transient simulation of mine fire (MTU) in 1979 [3]. In 1985, Dziurzynski and Trutwin introduced a mine fire transient simulation program (POZAR), based on unsteady air flow and unstable heat transfer between fire, air current and surrounding rocks [4].

In China, the earliest mine fire transient simulation program was proposed by China University of Mining and Technology in 1985, which was based on solving a set of linear equations of unstable compressible flow. Since then, the Mine Fire Rescue Decision Support System (MFRDSS) was developed, using object-oriented technology to overcome major shortcomings of existing programs. For example, the MFIRE lacks graphical display capabilities, and the POZAR does not provide the basic data and graphics interactive editing capabilities. In 1988, Chang developed the MFIRE under the guidance of Greuer and then completed the CFIRE system [5]. Qi et al. use C language to program a dynamic simulation software, which reflects the airflow, smoke flow and change of ventilation system structure during a mine fire [6]. In 1996, Wang et al. grouped existing mine fire simulation methods into three general types: steady-state simulation, one-dimensional transient simulation and multi-dimensional transient simulation [2]. Based on MFIRE, Xie et al. used the object-oriented method to develop a mine fire database and mine graphical interface system [7]. Ma et al. used multi-element area method to simulate mine fires, and analyze the differences of the results of three hypothetical physical models under different fire source scales, and then proved the applicability of CFAST in mine roadway fire simulation [8].

In this paper, an intake belt fire near a coal working face, with different fire sources, air velocities, CO concentration, temperature and visibility were simulated using Pyrosim. Pyrosim was developed on the basis of Fire Dynamics Simulations (FDS) and provides a graphical user interface for FDS [9–11]. It is helpful for coal mine fire rescue work.

## 2 Model

### 2.1 Basic Assumptions

It is very difficult to simulate the actual combustion process because of the complexity of the fire development. In order to simplify the process, the following assumptions are made:

(1) Before the disaster, the temperature of the airflow in the roadway was uniform and the turbulent flow was fully developed;

(2) The conditions of wall thermal boundary are set as the temperature of external wall, i.e., the temperature of the wall in the roadway does not change, which is equal to the temperature of the surrounding rock cooling zone;

(3) The mechanical flow of mine ventilation and the smoke flow generated by fire are approximately regarded as multi-component ideal gas, which follows the ideal gas equation of state;

(4) Ignoring the chemical changes that occur during the flow of high temperature flue gases in the roadways.

## 2.2   Physical Model

Figure 1 shows the fire physical model in the intake airway of working face. As shown in Fig. 1, the length of the intake airway is 200 m, and the length of the working face is 100 m. The roadway cross-sections are rectangles of 4 m × 4 m. The fire source is set in the intake airway, located in the middle of the roadway, 20 m away from the mining face, 0.5 m from the floor, and the fire source area is 1 m × 1 m.
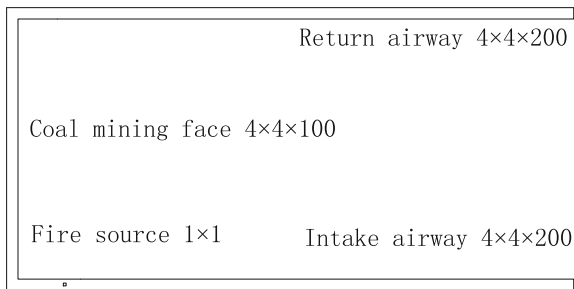


Fig. 1.   The fire physical model in the intake airway of the working face

## 2.3   Mesh

The structured grids with uniform grid size are used in the solution areas. The grid size is 0.5 m × 0.5 m × 0.5 m, and the number of grids is 62976.

## 2.4   Initial and Boundary Conditions

(1) Initial conditions

The flow of smoke during fire is an unsteady process. It is assumed that the initial temperature in the roadway is 20 °C, the initial velocity is 0 m/s, the initial pressure is 101,325 Pa and the relative pressure at the opening is 0 Pa.

(2) Inlet boundary conditions

The type of boundary conditions at the inlet of the intake airway is the speed-inlet. The material entered is air. The temperature is 20 °C, and the pressure is 101,325 Pa. The "Coal Mine Safety Regulations" stipulates that the minimum and the maximum allowable wind speed in the coal mining face are 0.15 and 4.0 m/s, respectively. During the actual production process of coal mine, the air volume of working face is generally 1000–2000 m³/min. Therefore, the inlet velocity of the wind varies from 1.0 to 2.4 m/s, with a 0.2 m/s step change.

(3) Outlet boundary conditions

The type of boundary conditions at the outlet of the return airway is outflow, and the initial temperature is 20 °C. As the fire simulation calculation proceeds, the outlet temperature is determined by the average temperature of the mesh near the innermost grid.

(4) Wall boundary conditions

The wall boundary conditions include the wall flow boundary and wall thermal boundary. For the wall flow boundary, the smoke is regarded as impermeable, and the wall velocity is zero. The wall thermal boundary is set as the temperature of the outer wall surface, i.e., the wall surface temperature is same as the temperature of the surrounding rock cooling zone.

## 2.5 Fire Definition

The premixed combustion model used by FDS simplifies the physical and chemical processes of complex combustion in real conditions, and the definition of the release of reactants, products, and heat from combustion follow a quantitative mathematical relationship. The fire which occurs in a working face is a fire of large space, thus the specific combustion process of the fire source can be ignored. Therefore, a surface is defined abstractly as a fire source by setting the heat release rate per unit area ($kW/m^2$). In the fire model, the reaction parameter is PVC, and the rate of smoke producing is selected to be 0.185 g/g. According to the study "Experimental Study on the Combustion Characteristics of Mine Fires" [12], the CO production rate is set as 0.1203 kg/kg.

$t^2$ fire is the most widely used unsteady fire source. The PVC tape is set to a fixed fire source which is developed by $t^2$ fire. The fire will not spread, although there are obvious limitations, it can meet the basic requirements of fire risk analysis. Fire growth rate is an important index to measure the risk of fire. The relationship between the fire heat release rate and the fire development time can be described by Eq. (1):

$$Q_f = \alpha(t - t_0)^2 \tag{1}$$

$Q_f$    Heat release rate of the fire source, kW;
$\alpha$    Fire growth factor, $kW/m^2$;
$t$    Burning time of the fire, s;
$t_0$    Smoldering time of the fire, s.

Since the smoldering stage of fire has little effect on the spread of fire, so $t_0 = 0$. Therefore, Eq. (1) can be simplified to Eq. (2):

$$Q_f = \alpha t^2 \tag{2}$$

Four types of standard fires are defined in the national standard ISO/TS16733:2006 [13]: slow fire, moderate fire, fast fire, and super-fast fire. Table 1 shows the fire growth factors of the four types of standard fires. The flame retardant in the PVC flame retardant conveyor belt slows down the combustion reaction and makes it difficult to ignite the reaction. Therefore, it is not considered to be a super-fast fire, and the type of fire is determined to be fast fire. The fire growth factor is taken as 0.04689 kW/s$^2$.

**Table 1.** Fire growth factors

| Fire types | Typical combustible material | Fire growth factor (kW/s$^2$) | The time of heat release rate up to 1 MW (s) |
|---|---|---|---|
| Slow fire | Hardwood | 0.00293 | 584 |
| Moderate fire | Cotton, polyester mat | 0.01172 | 292 |
| Fast fire | Cartons, woodpile, foam | 0.04689 | 146 |
| Super-fast fire | Pool fire, light curtains and other home textiles | 0.1875 | 73 |

## 3   Simulation Results

The effects of fire source scale on the smoke in the intake airway of the working face were investigated with the inlet wind speed 2.0 m/s and with the fire source scale 1, 2, 5, 10 and 20 MW, respectively. With the fire source scale 10 MW and the inlet air velocity varying from 1.0 to 2.4 m/s, the effects of the wind speed on the smoke in the intake airway of the working face were also analyzed.

### 3.1   Effect of Fire Source Scales on Smoke

Figures 2 and 3 show the CO concentration field and the temperature field at a distance of 1.6 m away from the floor of the working face, respectively, with a wind speed of 2.0 m/s and 1, 2, 5, 10 and 20 MW fire source scales.

It can be seen from Fig. 2 that, with the increasing of the fire source scale, the time required for CO concentration to enter the stable phase is prolonged. The CO concentration in the stable phase is increased, and proportional to the fire source scale.

As shown in Fig. 3, with the increasing of the fire source scale, the time required for the temperature to reach the stable phase is prolonged, and the temperature along the way is increased, and the temperature drop speed is accelerated.

(a) CO concentration in the middle
of return airway

(b) CO concentration at 900s
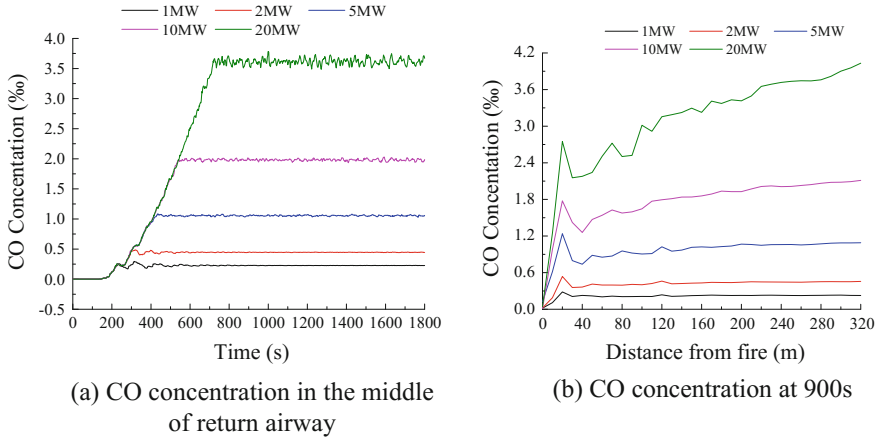
**Fig. 2.** CO concentration under different fire source scales



(a) Temperature in the middle
of return airway

(b) Temperature at 900s
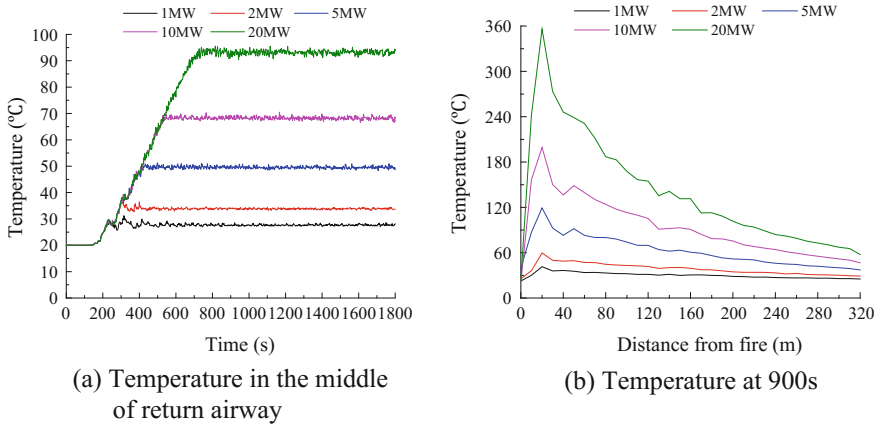
**Fig. 3.** Temperature under different fire source scales

### 3.2  Effect of Air Velocity on Smoke

Figure 4 shows the variation of CO concentration at a distance of 1.6 m away from floor on the downwind side of fire source in the working face under different wind speeds, with the fire source scale 10 MW.

It can be seen from Fig. 4 that the wind flow at the air inlet corner is more disordered and the CO concentration fluctuates, but there is a tendency to decrease with increasing wind speed. When the wind speed is 1.0, 1.2, 1.4, 1.6, 1.8, 2.0, 2.2 and 2.4 m/s, respectively, the CO concentration in the return airway corner is stable at 3.5‰ for 880 s, 2.8‰ for 620 s, 2.5‰ for 570 s, 2.2‰ for 550 s, 2.0‰ for 530 s, 1.8‰ for 510 s, 1.65‰ for 500 s, and 1.55‰ for 480 s, respectively; the CO concentrations at the middle of return airway is stable at 4.0‰ for 920 s, 3.3‰ for 800 s,

(a) in the intake airway corner

(b) in the return airway corner

(c) middle of the return airway

(d) in the working face at 900s
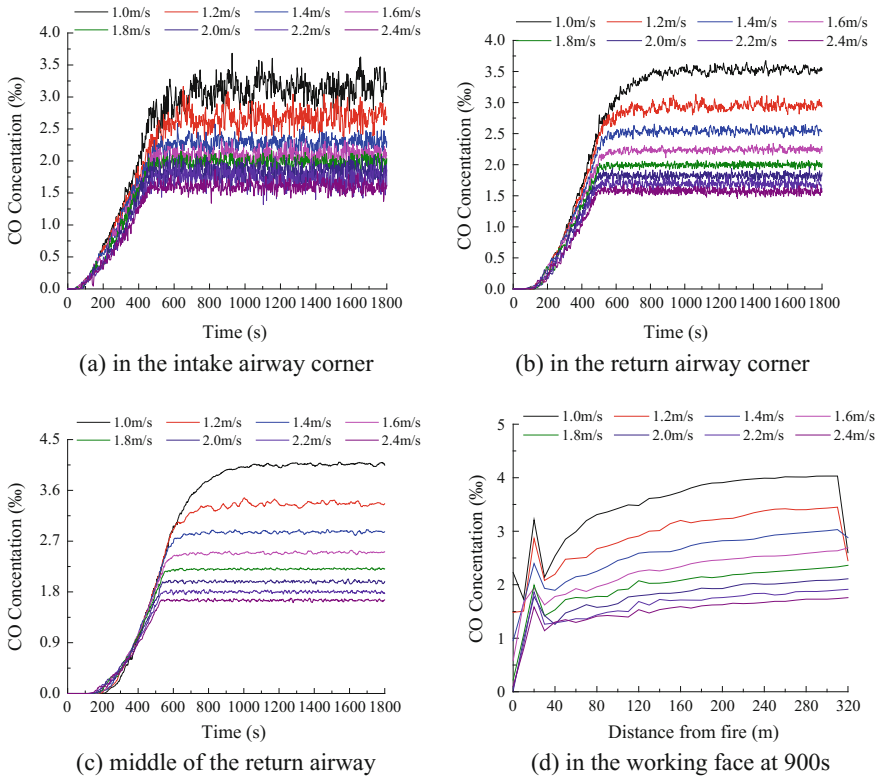
**Fig. 4.** CO concentrations under different wind speeds at different test points

2.85‰ for 700 s, 2.5‰ for 650 s, 2.2‰ for 590 s, 1.95‰ for 550 s, 1.75‰ for 530 s, and 1.65‰ for 520 s, respectively.

Therefore, with the increasing of wind speed, the time for the CO concentration to enter the stable phase is shortened, and the CO concentration in the stable phase is reduced, which means that the smoke mixes fully with the fresh air and the capability of smoke dilution is enhanced.

Figure 5 shows the variation of temperature at a distance of 1.6 m away from floor on the downwind side of fire source in the working face under different wind speeds, with the fire source scale 10 MW.

As shown in Fig. 5, due to the combined effects of convection and wall cooling, the temperature of the high-temperature flue gas gradually decreases. With the increase of wind speed, the air volume increases, and the amount of heat absorbed by the fresh air flow increases. As the wind speed decreases, the high-temperature flue gas is more in contact with the roadway wall surface, and the surrounding rock absorption heat increases. As shown in Fig. 5, the convection of hot and cold air plays a leading role near the fire source, so that the temperature of smoke at low wind speed is higher than that of smoke at high wind speed. For example, the air flow temperature is as high as 275 °C at a wind speed of 1.0 m/s at a distance of 1.6 m from the floor, and only 150 °C at 2.4 m/s.
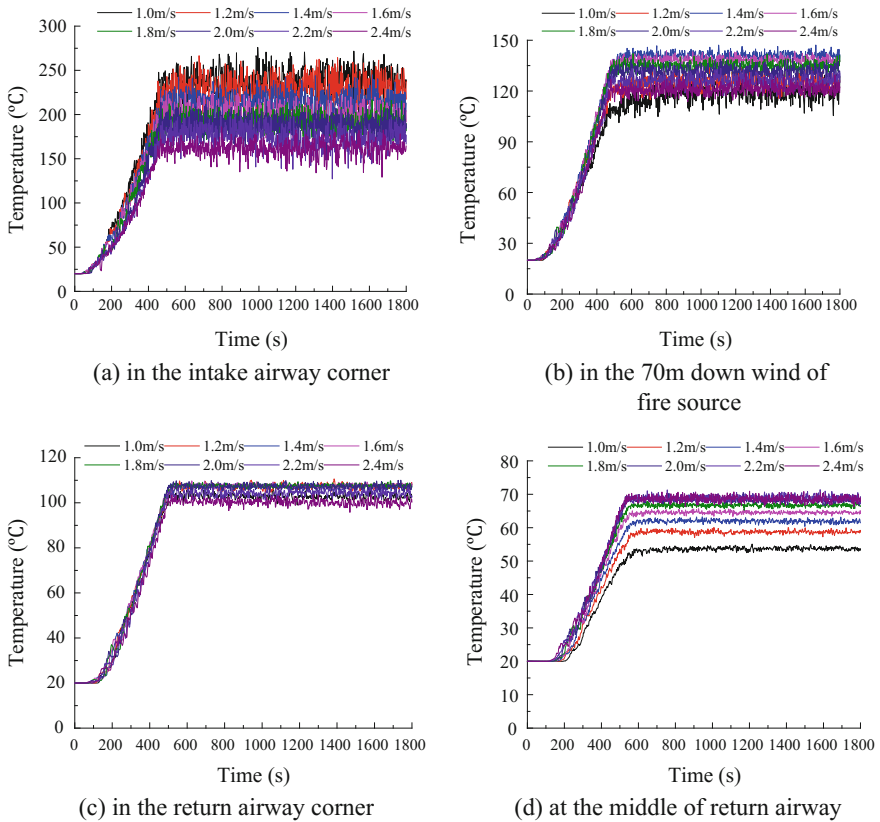
Fig. 5. Temperature under different wind speeds at different test points

It can be seen from Fig. 5b that, as the smoke spreads downstream, the effect of wall cooling becomes even more pronounced. After the wind flows through the intake airway corner, the temperature of the smoke at low wind speed rapidly decreases.

As seen from Fig. 5c, at the return airway corner, the smoke temperature under different wind speeds is not much different. As shown in Fig. 5d, the smoke temperature increases as the wind speed increases.

Figure 6 shows the visibility distribution of working face under different wind speeds when the fire source scale is 10 MW.

It can be seen from Fig. 6 that, under the same fire source scale, with the increase of wind speed, the smoke spreads faster. At 200 s, as the wind speed increases, the range of visibility at the outlet decreases. When the wind speed is 2.2 m/s, the visibility at the outlet is 9–12 m; when the wind speed is 2.4 m/s, the visibility at the outlet is 6–9 m. Therefore, when the wind speed is above 2.2 m/s, the high concentration smoke will lead to the visibility below 10 m, or even only 3–6 m, which will seriously affect the miner's escape speed.
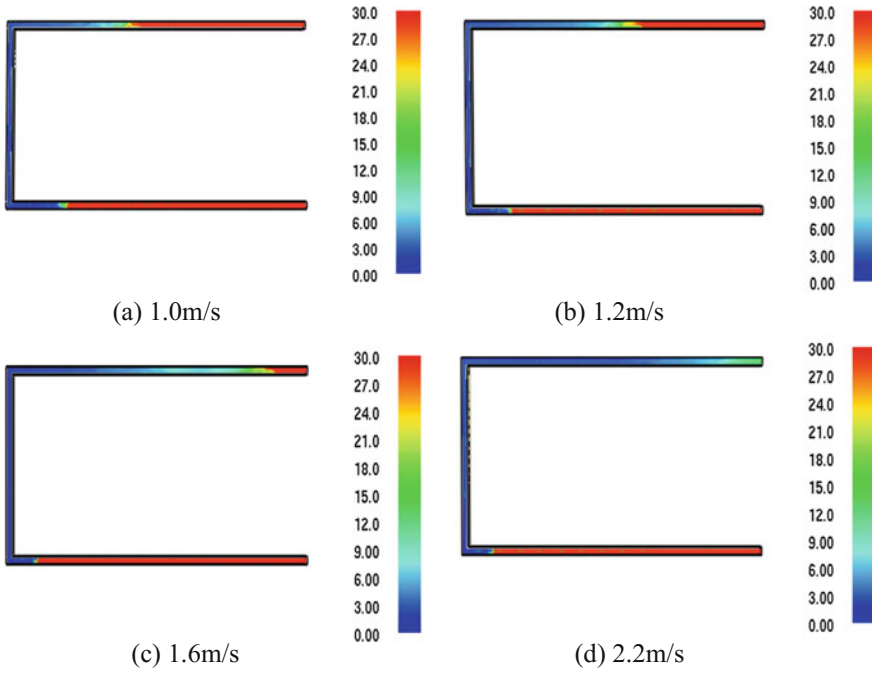
**Fig. 6.** Visibility distribution under different wind speeds at 200 s

## 3.3    The Critical Speed of Smoke Rollback

Figures 7 and 8 show the smoke rollback in the upper windward side of fire source under different wind speeds when the fire source scale is 10 MW at 1200 s. In Figs. 7 and 8, the abscissa represents the distance between the measuring point in the upper windward side and the fire source. Table 2 shows the CO rollback distance under different wind speeds at the 10 MW fire source scale.
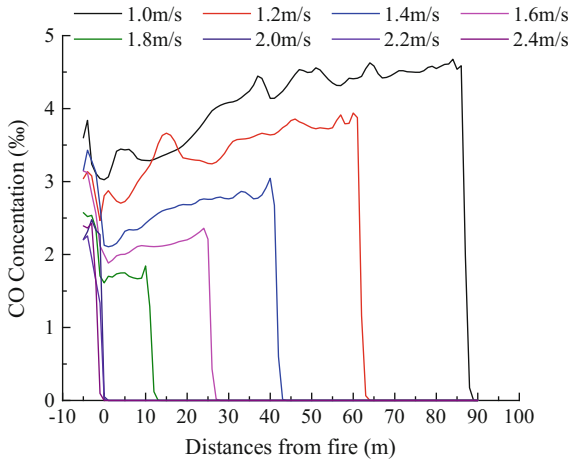


**Fig. 7.** CO concentration at 1200 s
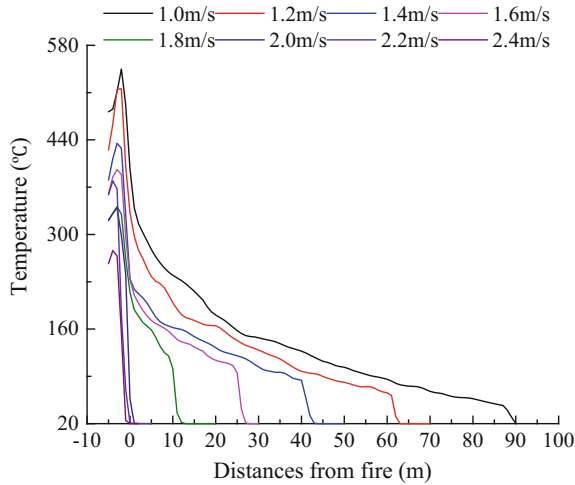
**Fig. 8.** Temperature at 1200 s

**Table 2.** CO rollback distance

| Wind speed (m/s) | 1.0 | 1.2 | 1.4 | 1.6 | 1.8 | 2.0 | 2.2 | 2.4 |
|---|---|---|---|---|---|---|---|---|
| Reverse distance (m) | 85–90 | 60–65 | 40–45 | 25–30 | 10–15 | 1–3 | 0 | 0 |

It can be seen from Figs. 7 and 8 that, the temperature distribution at the roof is basically the same as the distribution of CO concentrations at the roof. However, within 5 m in the windward side under the wind speed of 2.2 and 2.4 m/s, the temperature rises less than 20 °C. This phenomenon is not caused by the smoke rollback, but because the fresh air flow is affected by the heat radiation of the fire and hot smoke. As the wind speed increases, the CO concentration and temperature in the windward side of the fire source decrease, and the distance of the smoke rollback shortens. When the wind speed exceeds the critical wind speed, the smoke does not produce a smoke rollback phenomenon.

As shown in Table 2, the critical wind speed in mine working face fire with a fire source scale of 10 MW and a section of 4 m × 4 m is determined to be between 2.0 and 2.2 m/s.

## 4 Conclusions

Pyrosim was used to establish the fire model in working face to study the effects of fire source scale and wind speed on the distribution of CO concentration field, temperature field and visibility during the fire. The conclusions are as follows:

(1) When the wind speed is 2.0 m/s, with the increasing of the fire source scale, the time required for CO to enter the stable phase is prolonged, and the CO

concentration in the stable phase is increased, and it is proportional to the fire source scale; the time required for the temperature to reach the stable phase is prolonged, and the temperature along the way is increased, and the temperature drop speed is accelerated.

(2) When the fire source scale is 10 MW, with the increasing of wind speed, the time for the CO concentration to enter the stable phase is shortened, and the CO concentration in the stable phase is reduced, which means that the smoke mixes fully with the fresh air and the capability of smoke dilution is enhanced.

(3) When the fire source scale is 10 MW, with the increase of wind speed, the smoke spreads faster. At 200 s, as the wind speed increases, the visible range at the outlet decreases; when the wind speed is above 2.2 m/s, the high concentration smoke will lead to the visibility below 10 m, or even only 3 ∼ 6 m, which will seriously affect the miner's escape speed.

(4) When the wind speed exceeds the critical wind speed, the smoke does not produce a smoke rollback phenomenon; the critical wind speed in the mine working face fire with a fire source scale of 10 MW and a section of 4 m × 4 m is determined to be between 2.0 and 2.2 m/s.

# References

1. Quanlong, D.: The Numerical Simulation of the Smoke Flow During Fire and the Safety Zone Divide in Mine Roadways. Jiangxi University of Science and Technology (2015)
2. Deming, W., Xingshen, W., Qingguo, B.: The study of mine fire computer simulation. Chin. Saf. Sci. J. **6**(2), 1–4 (1996)
3. Greuer, R.E.: Transient state simulation of ventilation system in fires conditions. In: The 3rd International Mine Ventilation Congress, pp. 407–410 (1984)
4. Dziurzynski, W., Trutwin, W.: A simulation of mine fires. In: The 4th International Mine Ventilation Congress, pp. 276–281 (1985)
5. Xintan, C.: Simulation of mine fire ventilation. Coal Mine Saf. **04**, 22–29 (1991)
6. Qi, Y., Wang, X., Bao, Q.: Dynamic simulation of the flow of mine air and the change of ventilation systems during mine fire. J. China Univ. Min. Technol. **24**(3), 19–23 (1995)
7. Xuyang, X., Xuewen, Y., Hongbing, D., et. al.: Application of object-oriented technology in mine fire simulation. Coal Mine Saf. **8**, 41–42 (2001)
8. Hongliang, M., Xinquan, Z., Xuan, W.: Application of multi-element area method to mine fire disaster simulation. J. Coal Sci. Technol. **36**(1), 62–64+81 (2008)
9. Xinhui, L.: Smoke flow propagation simulation research of coal mine fires. Ind. Saf. Environ. Prot. **42**(6), 14–16 (2016)
10. Xiaotao, Z.: Numerical Simulation of Descensional Ventilation Fire, pp. 1–4. China University of, Geosciences (2014)

11. Yang, L.: Study of Numerical Simulation and Safety Evacuation for Building Fire Based on FDS. Liaoning Technical University, pp. 5–9 (2012)
12. Deming, W., Xingshen, W., Qingguo, B.: Study on the combustion characteristics of mine fires. J. China Univ. Min. Technol. **01**, 49–56 (1996)
13. ISO/TS 16733:2006, Fire Safety Engineering—Selection of Design Fire Scenarios and Design Fires

# Part XII
# Underground Fire Control II

# Experimental Investigation on Instability Characteristics of Heated Siltstone in the Coal Fire Area

Xiaoxing Zhong[1(✉)], Hongwei Ren[2], and Jie Zen[2]

[1] Key Laboratory of Gas and Fire Control for Coal Mines
(China University of Mining and Technology), Ministry of Education,
Xuzhou 221116, China
zhxxcumt@163.com
[2] School of Safety Engineering, China University of Mining and Technology,
Xuzhou 221116, China

**Abstract.** Fractures in the overlying rock is one of the main factors in the development of coal fires. Understanding the characteristics of heated overlying rock is of great significance to examine the combustion mechanism of a coal fire. In this paper, the stress-strain curves, peak stress and brittleness coefficient of siltstone specimens in the coal fire area at different temperatures were tested using an MTS810 experiment system. Meanwhile, the change in fractures caused by combustion was also explored. Results show that the peak stress of the siltstone first decreases, then increases before the secondary reduction as temperature increases. Similarly, the brittleness coefficient first increases, then decreases and increases again during this process. When the temperature is lower than 200 °C or higher than 700 °C, the decrease of the peak strength is the main factor influencing the siltstone breakage and the development of combustion fractures. As the temperature rises from 200 to 700 °C, the rock stability is dictated by compressive strength and loading structure. The higher the temperature, the greater the coal loss due to burning, and failure of the siltstone is more violent. Once the balance of rock forces is broken by the coal combustion and exceed the rock bearing capacity, severe brittle failure will occur, and a large number of combustion fractures will be generated.

**Keywords:** Siltstone · Thermal instability · Combustion fractures

## 1 Introduction

Coal fire is the common disaster facing world's major coal production countries. In addition to a loss of resource due to burning, the process also generates lots of toxic and harmful gases, causing serious damages to the ecological environment [1–3]. Combustion fractures are major air leakage that will provide oxygen to the gob area to sustain coal fires. Studying heated overlying rock in the coal fire area is of great significance to understand the fractures development due to coal combustion, and to control the coal fire.

In China, the major components of the overlying rock in the coal fire area are sandstone and siltstone. There have been some researches about the impact of temperature on mechanical properties of sandstone and siltstone, Refs. [4–11] described the mechanical parameters of sandstone and siltstone at different temperatures; Wu et al. [12] made a comparative analysis and found the mechanical parameters of sandstone in coal seam roof after high-temperature treatment and at high temperatures are different. To study the rock mechanics at high temperatures, Chen et al. [13] studied mechanical properties and failure mechanism of sandstone in coal roof at different temperatures within 600 °C; the variation of sandstone strength and deformation characteristics with temperature within 600 °C was researched by Jin et al. [14], Lu and Tang [15, 16] respectively studied the changing law of elastic modulus and peak stress of sandstone and siltstone in a underground coal gasification field when the temperature varied between 100 and 750 °C. It can be seen that, many studies now focus on the variation of mechanical properties of sandstone with temperature. However, few researches are involved in siltstone in real-time temperature. In view of this, based on the mechanical experiment of siltstone in different real-time temperatures, this paper explored the instability characteristics of heated overlying rock. Besides, the evolution law of combustion fractures of the coal fire area in temperature-rise period was also researched.

## 2  Experiment

### 2.1  Rock Sample

Siltstone samples were from a fire area in Xinjiang Province. The rock sample was processed to specimens with 20 mm in diameter and 50 mm in height. The processing precision of specimens meets the Chinese national standard of rock test method (GBT 50266-2013). The height and diameter of specimens were measured and numbered after processing. Then they were wrapped up in asbestos.

### 2.2  Experimental Process

The MTS810 experiment system was used in the experiment. Firstly, place specimens in the middle of the pressure head of the test machine. Then, uniaxial compression experiment at normal temperature was carried out with the loading rate of 0.002 mm/s. Secondly, the specimen temperature was heated up to the preset temperatures 100, 200, 300, 400, 500, 600, 700, 800, 850 and 900 °C at a rate of 2 °C/min. To ensure rock samples were heated evenly, when the sample temperatures reached a preset temperature, hold it for 20 min before loading. Thirdly, the axial load was applied at the same loading rate until the rock sample was destroyed. In the process of loading, the Teststar II program was used to record the axial strain and axial stress of each sample.

## 3 Result Analysis

### 3.1 Stress-Strain Curves of Siltstone Samples at Different Temperatures

Figure 1 is a typical stress-strain curve of rocks. It can be seen that rock deformation and failure experienced five stages [17]: (1) compression stage (OA), (2) linear elastic stage (AB), (3) stable fracture development stage (BC), (4) unstable fracture development stage (CD) and (5) strain softening stage (DE). Figure 2 is the stress-strain curves of the siltstone at different temperatures. Compare Fig. 1 with Fig. 2, we found that within the temperature range from normal temperature to 300 °C, the strain softening stage of the siltstone is obvious after reaching the peak stress. It indicates that the damage form of siltstone mainly shows ductile damage when the temperature is lower than 300 °C. When it is higher than 300 °C, due to the high temperature, the rock failure form is changed. Particularly after reaching the peak point, there is a sudden stress drop with no obvious strain softening stage, which illustrates that damage form of the siltstone in this temperature section primarily presents brittle damage.



**Fig. 1.** A typical stress-strain curve of rocks

(a) Normal temperature ~300 ℃          (b) 400 ℃~900 ℃
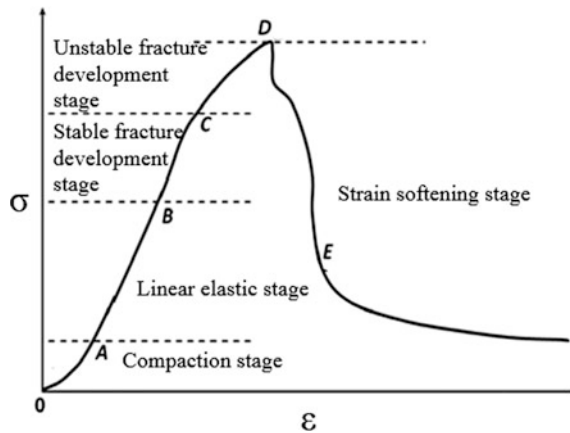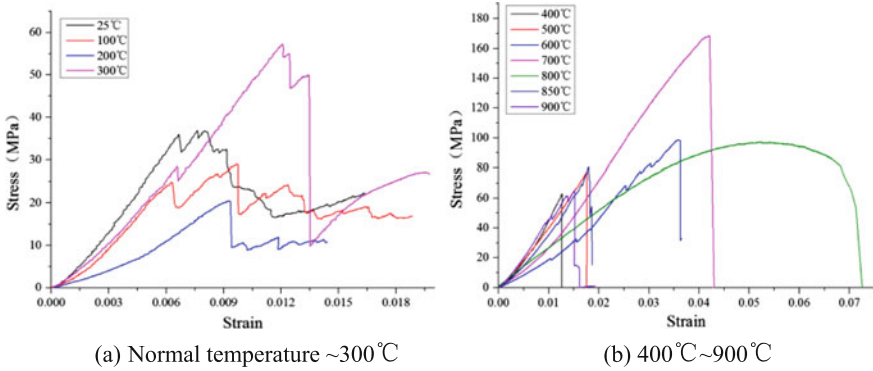
**Fig. 2.** Stress-strain curves of siltstone at different temperatures

## 3.2    Variation of Peak Stress and Brittleness Coefficient of Siltstone with Temperatures

The peak strength of rock is the maximum strength that it can resist under the compression load, which is calculated based on the peak on the stress-strain curves.

The brittleness coefficient is an index parameter to evaluate the characteristics of rock failure. The higher the rock brittleness coefficient, the more intense the brittle failure. The calculation formula is as follows [18]:

$$B = \frac{\sigma c - \sigma r}{\sigma c} \tag{1}$$

In Eq. (1), $B$ is the brittleness coefficient, the value range is 0–1; $\sigma c$ is the peak strength; $\sigma r$ is the residual strength.

Figure 3 is the variation of peak strength and brittleness coefficient of siltstone with temperatures.



(a) peak stress                    (b) brittleness coefficient
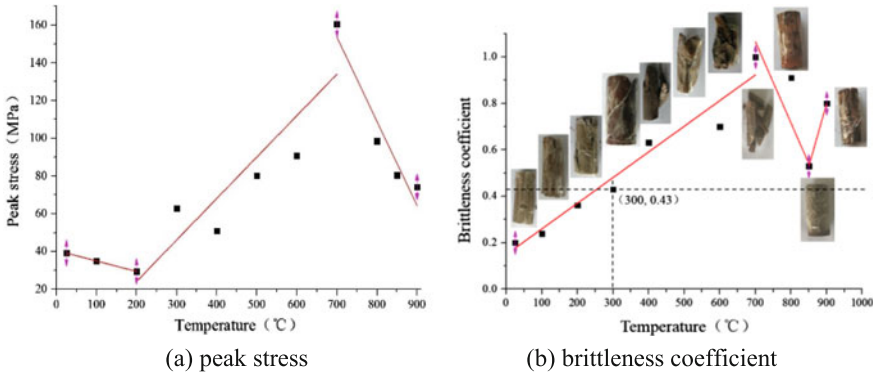
**Fig. 3.** The variation of peak stress and brittleness coefficient with temperatures

As can be seen from Fig. 3, peak stress of the siltstone first decreases and then increases before the secondary reduction with the increases of temperature. When the temperature is lower than 200 °C, the peak strength of siltstone decreases gradually with the increases of temperature. As the temperature rises from 200 to 700 °C, the peak strength of the siltstone linearly increases with the increases of temperature and reaches the maximum at 700 °C. when the temperature is higher than 700 °C, the peak intensity begins to decline.

Contrary to the change of peak stress, with the increase of temperature, the brittleness coefficient of siltstone increases first and then decreases and increases again. When the temperature is lower than 700 °C, the siltstone brittleness coefficient increases gradually with the temperature increase. The crushing degree of the specimens becomes severer. At 700 °C, the specimens are directly crushed into pieces. Between 700 and 850 °C, the siltstone brittleness coefficient begins to decrease with the increase of temperature. The fragmental morphology of siltstone is relatively complete, which indicates that the siltstone brittleness begins to weaken. Between 850 and 900 °C, as the temperature goes up, the siltstone brittleness coefficient begins to increase with the increase of temperature. Combined with the stress-strain curves of siltstone at different temperatures, it is possible to determine that 300 °C is the turning point from ductile failure to brittle failure.

## 4    Analysis of the Change Process of Combustion Fractures

The above study shows that both the peak stress and the brittleness coefficient of the siltstone are changed with temperatures. Generally, the coal seams in coal fire area in Xinjiang and Shanxi in China are shallow. For coal fire area caused by spontaneous combustion of coal in the gob, the mining of shallow coal seams makes the upper overlying rock in the gob break down in early stage of the fire. It would cause some cracks in the rock mass above that "communicate" with the surfaces as shown in Fig. 4. Take the rock mass above the gob as the research object and simplify the stress situation of the rock mass after rock mass caving, in the vertical direction, the rock mass is mainly affected by the axial pressure of upper rock strata, its own gravity G and the supporting force F of the caving coal and rocks in the gob.
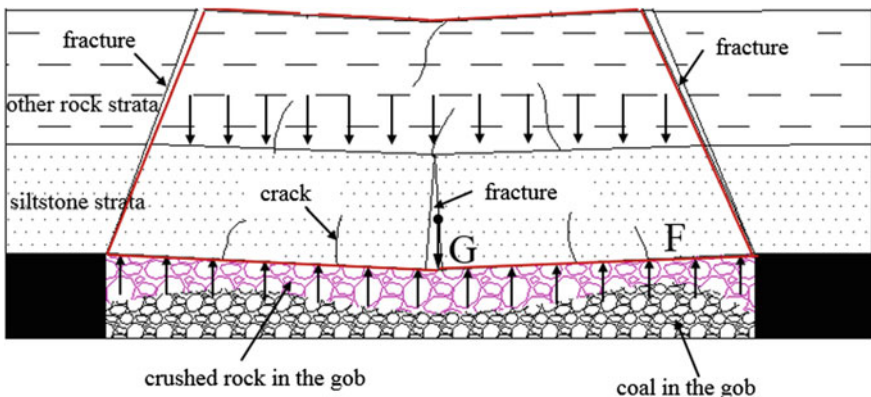


**Fig. 4.** Schematic diagram of stress on rock mass in coalfield

Meanwhile, with the temperature change of the fire area, the coal weight in the fire area also changes in the course of coal fire. Figure 5 is the weight variation of coal in a coalfield in Xinjiang by SDT-Q600 instrument (TA Instruments) which was used first to conduct TG and DSC experiments in this coal. It can be seen that in the low-temperature oxidation stage, the coal weight change is rather small. The coal weight decreases rapidly after entering the combustion stage. When the temperature rises to the burnout temperature (Td), the coal weight keeps stable again, which means the coal in the gob almost burns out.
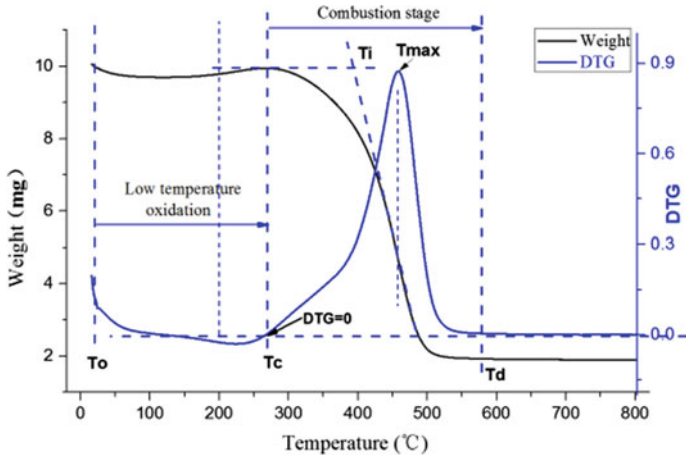


**Fig. 5.** The variation curve of coal weight in the gob with temperatures

As shown in Figs. 3 and 5, it can be seen that when the temperature is less than 200 °C, the coal weight change is small, and the overall force structure of the rock strata remains invariant. Nonetheless, the inner stress of rock strata would change to achieve new equilibrium state as its intensity reduces. In the process of stress change, some new fractures and cracks would be generated in the stress concentration area inside the rock strata. At this stage, the damage form of siltstone mainly manifests ductile damage. These are few combustion fractures, which is the initial stage of combustion fractures. At around 200 °C ~ initial temperature of volatile combustion (Tc), similarly, the coal weight change is small with little change of whole rock stress structure. Additionally, at this stage, as the peak stress of siltstone increases, the combustion fractures are in a relatively stable transition period.

As the temperature increases from Tc to Td, the burnout of a large amount of residual coal changes the mechanical structure of rock mass. The compressive strength of the siltstone increases gradually at this stage, but the support force F of the rock mass decreases suddenly, which breaks the original stress balance. Once the resultant force of the rock mass exceeds the maximum pressure that it can bear, the rock mass would suffer a strong brittle failure and produce a large number of combustion fractures, and this is the rapid development stage of combustion fractures; At Td ~ 700 °C, the

residual coal in the gob almost burns out, the overall force structure remains stable with the increasing compressive strength of siltstone, and combustion fractures development is relatively stable; when the temperature is higher than 700 °C, the compressive strength of siltstone decreases rapidly, and the bearing capacity of rock decreases again. Under the action of thermal stress generated by high temperature, the combustion fractures will develop again.

## 5 Conclusion

1. The peak stress of the siltstone first decreases and then increases before the secondary reduction as temperature increases, while the brittleness coefficient increases firstly and then decreases and increases again during this process.
2. The mechanical properties of the siltstone and the stress state change of the rock strata jointly influence the stability of the rock mass. With the increase of temperature, the combustion fractures experience five stages: initial development stage—stable stage—rapid development stage—stable stage—redevelopment stage.

## References

1. Jennifer, M.K.: Old Smokey coal fire, Floyd County, Kentucky: estimates of gaseous emission rates. Int. J. Coal Geol. **46**(87), 150–156 (2011)
2. Rai.: Causes of Subsidence potentiality above old abandoned underground coal mines workings at Karharbari formation, Giridih, Jharkhand. J. Mines Met. Fuels **61**(1–2), 37–42 (2013)
3. Taku Ide, S.: Fissure formation and subsurface subsidence in a coalbed fire. Int. J. Rock Mech. Min. Sci. **35**(47), 81–93 (2010)
4. Yin, G.: Experimental investigation on mechanical properties of coarse sandstone after high temperature under conventional triaxial compression. Chin. J. Rock Mech. Eng. **28**(3), 599–604 (2009)
5. Hassanzadegan, A.: Thermoporoelastic properties of Flechtinger sandstone. Int. J. Rock Mech. Min. Sci. **49**(9), 94–104 (2012)
6. Su, H.: Experimental investigation on loading rate effect of sandstone after high temperature under uniaxial compression. Chine. J. Geotech. Eng. **36**(6), 064–1071 (2014)
7. Jin, Y.: Experimental investigation on mechanical properties and permeability evolution of red sandstone after heat treatments. J. Zhejiang University-Science A (Applied Physics & Engineering) **16**(9), 749–759 (2015)
8. Gautam, P.K.: Thermomechanical analysis of different types of Sandstone at elevated temperature. Rock Mech. Rock Eng. **49**(7), 1985–1993 (2016)
9. Hassanzadegan, A.: The effects of temperature and pressure on the porosity evolution of Flechtinger Sandstone. Rock Mech. Rock Eng. **47**(2), 421–434 (2014)
10. Zuo, J.: Three-point bending test investigation of the fracture behavior of siltstone after thermal treatment. Int. J. Rock Mech. Min. Sci. **70**(8), 137–141 (2014)

11. Yin, T.: Study on mechanical properties of post-high-temperature Sandstone. Chin. J. Undergr. Space Eng. **3**(6), 1060–1063 (2007)
12. Wu, Z.: Experimental study on mechanical character of sandstone of the Upper Plank of coal bed under high temperature. Chin. J. Rock Mech. Eng. **24**(11), 1863–1867 (2005)
13. Chen, L.: Mechanical characteristics and cracking mechanism of coal roof Sandstone under high temperature. J. Chongqing Univ. **28**(5), 123–126 (2005)
14. Jin, Y.: Study on the thermo-dynamic destructive features via the experiments of the overburdened coal seam outcrop fire area. J. Saf. Environ. **14**(4), 76–79 (2014)
15. Lu, Y.: Fracture evolution of overlying strata over combustion cavity under thermal mechanical interaction during underground coal gasification. J. China Coal Soc. **37**(8), 1292–1298 (2012)
16. Tang, F.: Fracture Evolution and Breakage of Overlying Strata of Combustion Space Area in Underground Coal Gasification. China University of Mining and Technology, Xuzhou (2013)
17. Xie, H., Chen, Z.: Rock Mechanics. Science Press, Beijing (2004)
18. Zhou, H.: Quantitative evaluation of rock brittleness based on stress-strain curve. Chin. J. Rock Mech. Eng. **33**(6), 1114–1122 (2014)

# Experiences in Extracting Coal in the Longwall Face Affected by an Endogenous Fire in the OKD, a. s., Czech Republic

Václav Zubíček[1(✉)], Jindřich Šancer[1], Luboš Dúbravka[2], and Radka Matová[1]

[1] VŠB-TU Ostrava, 17. Listopadu 15, 708 33 Ostrava—Poruba, Czech Republic
`vaclav.zubicek@vsb.cz`
[2] OKD, a. s., Stonavská 2179, 735 06 Karviná, Czech Republic

**Abstract.** The issue of endogenous fires in deep mines still remains a concern. These emergencies often have an impact on the health and life of people, and/or the bottom line of the mine operation. Black coal mining was behind the dynamic development in the territory of Ostrava and Karviná, and it is still closely connected with these areas. The development of mining and safety technology has brought progress in this sector and the importance of developing analysers, means of signalling endogenous fires as well as means of preventing mine fires, especially the possibility of nitrogen inertization and the construction of more effective explosion-proof dams, cannot be overphasized, because a serious risk and frequent cause of endogenous fires of the Karviná part of the OKR (Ostrava-Karviná Coal District) is the self-ignition of the coal mass; the most frequent occurrence of spontaneous fires is at the longwall faces in the caved spaces with the presence of the residual coal fragments. The geological situation of the Longwall Face No. 40 903 at Mining Plant 1, locality Darkov will first be briefly described and evaluated, followed by a description of the laboratory test of the susceptibility of coal to self-ignition and the estimation of the self-ignition phase and the temperature of the endogenous fire outbreak in this longwall face based on the indicator gases. Then, a practical solution of the completion of extracting coal deposits in Longwall Face No. 40 903 is described.

**Keywords:** Endogenous fires · Coalface · OKR · Practical solution

## 1 Introduction

Despite the decreased coal mining activities in the OKR, more attention must be paid to the spontaneous combustion of coal mass at mining operations. Self-ignition of coal represents a serious problem with its safety and economic impacts on the operation. In spite of continuous efforts to minimize this risk, there are still several cases of self-ignition of coal every year, followed by a transition to an endogenous fire.

One of the many factors contributing to the development of an endogenous fire is the geological situation of the given longwall face and, above all, the very degree of susceptibility of the coal mass. From 1 January 2009, a mandatory requirement is to

determine the degree of self-ignition by the Pulse Calorimetry method prior to the block extraction. In order to combat the endogenous fire, it is important, from the point of view of safety of all workers involved in the combustion, to estimate the self-ignition phase and the temperature of the focal point on the basis of sampling indicator gases. The aim is to propose a variant of a possible method of completion of the extracting the coal reserves [1, 2].

## 2    Description of the Longwall Face no. 40 903

The concerned Longwall Face No. 40 903 is located at Darkov, Mining Plant No. 2 within the company OKD a. s. The longwall face was used to extract the Coal Seam No. 40, classified as the saddle sediment of the Karviná formation, which is one of the most important factors but also due to the complicated geological conditions, the most dangerous. Saddle sediments are problematic both from the point of view of the danger of rock bumps and the problem of increased methane emissions as well as the susceptibility to self-ignition of the coal mass.

The coal seam is about 1040–1210 m below surface. In the concerned area, the layers have a general inclination of about 12° in the north-east direction. The average thickness of the Seam No. 40 is 4.8 m and the overburden consists of alternating layers of sandstones and conglomerates with a total thickness of 33.2 m up to Seam No. 39 (with a real coal thickness of 1.48 m). This overburden can be classified as fixed with frequent caving delays. The immediate underlying rock of the Seam No. 40 is a layer of dust [1, 2].

The drift length of the Longwall Face No. 40 903 was 543 m and the width of the longwall face ranged between 193.5 and 195 m, and after the planned shortening it was supposed to range between 183 and 186 m. The width of the advance was 0.8 m, the mined thickness 440–550 cm. The slope of the gangway was 1° to 8°, the slope of the air gate 1° to 15°, and the breakthrough slope ranged from 7.5° to 14.5°. The longwall face was excavated uphill by means of a longwall working on a controlled caving from the field using mechanized support DBT 2.6/5.5 (113 pcs) and MEOS 22/22/46 (2 pcs.). Coal extraction was carried out by the narrow-bore two-cylinder Eickhoff SL 500 power loader, and small-scale blasting operations were used when extracting the main-gate stables, in fault, erosive and pressure zones. Longwall Face No. 40 903 is excavated under the deck and was ventilated by passing air [3].

Extracting Longwall Face No. 40 903 began in November 2015. Termination of mining was planned for April 2016. Although the longwall face was verified by a number of exploration boreholes, an erosive excavation of amplitude of 5 m, Fig. 1, was created after the commencement of the mining process, resulting in a time delays. Due to the necessity to carry out the blasting work in the longwall face, there was a daily reduction of advance to 1.2 m/working day [3].
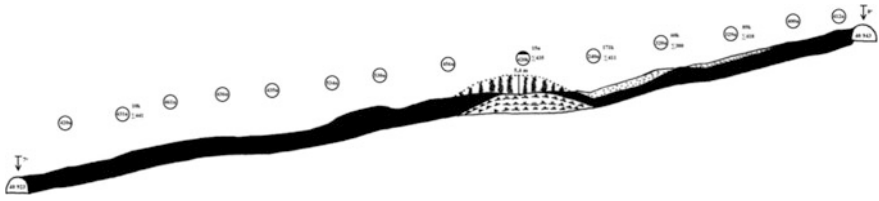
Fig. 1. Geological profile of extracting 40 903 at the site of the erosion pothole

## 2.1 Determination of the Degree of Coal Self-ignition Risk in the Longwall Face

As mentioned above, the extraction of saddle seams in the OKR involves, among other things, the issue of the spontaneous combustion of coal. For this reason, in the framework of the prevention of self-ignition, security measures imposed by the valid legislation are applied in the OKD (Ostrava-Karviná Mines). Under these regulations, it is necessary to take coal samples before starting each longwall face, to determine the susceptibility of coal to self-ignition, and to determine the degree of self-ignition risk for each longwall face using the "M-F" criterion.

Evaluation of the degree of susceptibility is conducted on the basis of a calorimetric test. The susceptibility of coal samples to oxidation is expressed by the pulse calorimetry method by determining the oxidation heat parameter $q^{30}$ (J g$^{-1}$). This parameter represents the heat value of the chemical interaction of $O_2$ developed over a thirty-minute exposure of a fresh coal sample to oxygen. According to the value of $q^{30}$, a coal sample is classified into one of three categories, Table 1 [4].

Table 1. The categories of coal susceptibility to self-ignition according to the pulse calorimetry method [5, 6]

| Category of susceptibility to self-ignition | $q^{30}$ (J g$^{-1}$) hard coal | $q^{30}$ (J g$^{-1}$) lignite |
|---|---|---|
| Low susceptibility to self-ignition | <0.35 | <3.5 |
| Medium susceptibility to self-ignition | 0.35–0.85 | 3.5–7.5 |
| High susceptibility to self-ignition | >0.85 | >7.5 |

The coal of the concerned Longwall Face No. 40 903 was classified under the following category I. Highly reactive coal.

Coal oxidation reactivity was also determined by the isothermal oxygen sorption method. This method monitors and evaluates the pressure drop in closed containers, but does not address the composition of the atmosphere itself. The evaluation criterion of the coal susceptibility to self-ignition is the value of the PT index, which is evaluated on the basis of the pressure drop in closed containers [8, 9]. Based on the PT index, the susceptibility of coal to self-ignition is classified according to Table 2. For the Longwall Face No. 40 903, this value was 49,651, which is at the very border between the medium and high coal susceptibility to self-ignition.

**Table 2.** Classification scale of coal susceptibility evaluation by the method of isothermal oxygen sorption [7]

| Category | Class of susceptibility to self-ignition | PT index value S |
|---|---|---|
| 1 | Low | <35,000 |
| 2 | Medium | 35,000–50,000 |
| 3 | High | >50,000 |

In order to determine the coal self-ignition risk in a longwall face, a special method called "M-F" criterion is developed for the OKD, which takes into account not only the susceptibility of coal to self-ignition but also the mining and technical conditions of the longwall face. The "M-F" criterion evaluates separately the individual phases of the longwall face, namely the stage of fitting and preparation of the longwall face, the stages of the mining operation, and the stage of liquidation and abandoning the longwall face. The parameters of each phase of the longwall face are evaluated, based on the degree of danger. Each evaluated parameter of a given phase is assigned points (the higher the value, the greater the risk, the negative impact on the endogenous fire), and the sum of all the points for the individual phases determines the susceptibility to self-ignition. If the total sum of M-F criteria points is higher than 35, the longwall face is classified as susceptible to self-ignition.

By this methodology, the level of self-ignition risk for the Longwall Face No. 40 903 was quantified for the individual phases: the start of the Longwall Face 28, the operation of the Longwall Face 45, and for the liquidation of the longwall face, the determined value was 43.

## 2.2   Preventive Measures Against Endogenous Fire in the Longwall Face

In view of the findings confirming the susceptibility of coal to self-ignition, a self-ignition prevention project with technical and safety measures and measures to prevent a spontaneous fire for the extraction of the Longwall Face No. 40 903 has been developed. The following technical measures have been established on the basis of this project.

The mining work should be carried out, where possible, with the maximum possible monthly advance of 84 m and regular recovery of the support of the initial class after the longwall face. In order to reduce the flow of airflow through the caved area, a start-up screen was always supposed to be installed when the class was recovered. This screen (area-wide) was to be extended up to the section of the longwall face support [9].

Always before the block of free or non-working days (two days and more), the insulation foam barriers must be built at the level of the blocking edges of the two longwall face galleries. At the site of the construction of the foam barriers, it was forbidden to carry out the recovery of the TH support. It was forbidden to dispose of these insulation foam barriers, they had to be left in the cave-in area.

From the introductory class, three drafts of the lost pipe for the $N_2$ inertization were placed into the caving spaces of the longwall face. The first draft of the lost pipeline was based on the initial breakthrough of the longwall face, the second after the direction

advance by 50 m, and the third draft after longwall face direction advance of 100 m. One draft of the lost pipe $CH_4$ degassing was placed on the outlet class from the initial breakthrough. In order to ensure the tightness of the gas pipelines, the pipeline was placed at the beginning of the mine workings only after the mining operations ended. The amount of nitrogen filled into the lost pipeline and the discharge points were decided by the mine manager depending on the concentration of CO and on the basis of the specific values of the minimum volume of winds in front of the workplace [9].

The amount of convergence was continuously monitored in the area of the longwall face. In addition, a sensor for continual airflow velocity measurement on the outlet system was installed.

The inspection work carried out for the extraction of the longwall face consisted of the continuous monitoring of CO, $CH_4$ concentrations by means of sensors located at the beginning of the separate ventilation department (SVD), at the outlet class No. 40 943, and at the end of SVD.

At least twice a month, wet air sampling (for chromatographic analysis) was also performed in the longwall face area. Dry air sampling (CO, $CO_2$, $CH_4$ and $O_2$ analysis) at sites designated for wet sampling as well was performed at least once a week, and when the shift concentration of 30 ppm CO on the exhaust class was exceeded, the mine manager always decided on possible further dry air sampling in the Longwall Face No. 40 903 area. The concentration of gases (CO, $CO_2$, $CH_4$ and $O_2$) were also analysed by the shift technician using the Dräger 5600 Xam Personal Analyser, at least twice per working shift [9].

## 3 Endogenous Fire—Emergency State

Despite all precautionary measures, an endogenous fire occurred. The suspected reason was mining went through a 5 m long erosion pothole as shown in Fig. 1. This resulted in a time lag due to blasting work, with the daytime advance reduced to 1.2 m/working day.

As a result of passing through this geological anomaly, a considerable amount of the broken coal was left behind in the caving space with progressive passage of the erosion pothole. In particular, the time lag and the remaining coal fragments were the main causes of the fire. This fire was discovered because of a subsequent increase in CO concentration in the return air behind the longwall face, when an increase in CO by 1–2 ppm per hour, it is evident that a fire is developing [10]. The gradual increase of CO in the return airflow occurred after 22 November 2016 (Fig. 2). Despite the measures taken to control the spontaneous fire, CO concentration continued to increase and on 4 December 2016, construction of explosion-proof seals to barricade the area began. On 6 December 2016, the mine manager announced that CO concentration has exceeded 130 ppm in the return air behind the longwall face. On the same day, the accident liquidation head (ALH) declared an emergency and the longwall face was operated in an emergency mode. Due to the increase in CO, and the occurrence of higher hydrocarbons in the air samples taken (see Table 3), the ALH decided to seal off the longwall face using explosion-proof seals.
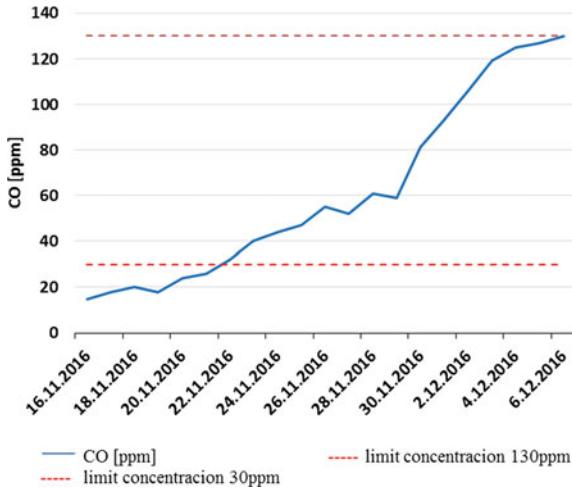
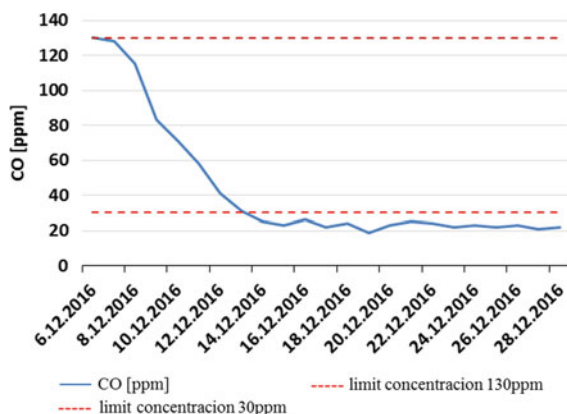**Fig. 2.** Development of CO value before explosion-proof closure by H1 and H2 dams

**Table 3.** Values evaluated by gas chromatograph from the Longwall Face 40 903 area

| Sampling | | CO | $C_2H_6$ | $C_3H_8$ | $C_4H_{10}$ | $C_2H_4$ | $C_3H_6$ | $H_2$ | $C_2H_2$ |
|---|---|---|---|---|---|---|---|---|---|
| Date | Place | From PW (l min$^{-1}$) | | | | | | | |
| 4.12.16 | Outlet 20 m | 123.25 | 7.00 | 3.94 | 1.57 | 1.28 | 0.59 | – | – |
| 4.12.16 | Section 67 | 123.25 | 2.66 | 1.77 | 0.99 | 0.69 | 0.29 | – | – |

The following work continued on seal construction, which ended on 8 December 2016, and then the air measurement was taken in front of the permanent seals and the sampling of the dry air samples from the permanent seals at intervals determined by the ALH order, Fig. 2.

Analysis of the mine air samples is used in the OKD not only for the early detection of endogenous fire, but also for the estimation of the temperature at the focal point of the fire. Both the absolute outputs of the individual indicator gases - in the case of sampling in the passage wind (PW) (Q in l/min) or the ratios of the indicator gases, the so-called binary indicators of the indicator gases (in the case of sampling of gas outside the passage wind, e.g. behind the seals).

By analysing the indicator gases, the temperature of the spontaneous fire at the time of the longwall face closure was estimated at 180 °C. The sampling of gas continued after the closure to monitor the temperature drop to re-open the fire site (Fig. 3).

On 11 February 2017, check sampling was carried out in the non-PW area across the seal, Table 4, the obtained values show that endogenous fire was extinguished, but the situation did not allow the exploration and access to the fire site because the gas concentrations still corresponded to a fire temperature of about 75 °C according to Table 5. Access to and subsequent introduction and increase of $O_2$ concentration could have disrupted the repressive state of the fire at this stage, and the spontaneous fire

could have rekindled again, and subsequently the fire site would have had to be re-closed. Table 4 values were evaluated by gas chromatograph from area 40 903 outside PW.



**Fig. 3.** Development of CO value after explosion-proof closure by H1 and H2 dams

**Table 4.** Values evaluated by *gas chromatograph* from the area of the Longwall Face No. 40 903 outside PW

| Sampling | | CO | $C_2H_6$ | $C_3H_8$ | $C_4H_{10}$ | $C_2H_4$ | $C_3H_6$ | $H_2$ | $C_2H_2$ |
|---|---|---|---|---|---|---|---|---|---|
| Date | Place | Outside PW (ppm) | | | | | | | |
| 11.2.17 | DamH1 | 23 | 5 | 1.1 | 0.3 | 0.2 | – | – | – |
| 11.2.17 | DamH2 | 21 | 6 | 0.9 | 0.2 | 0.2 | – | – | – |

**Table 5.** Dependence of the development of gaseous components on the stages of endogenous fire development at locations outside PW [11, 12]

| | Endogenous fire stages | | | | |
|---|---|---|---|---|---|
| | Incubation | Spontaneous fire | | Transition | |
| Point | Critical | Turning | Smoldering | Ignition | Setting fire |
| temperature | 30–60 °C | 60–100 °C | 100–150 °C | 150–230 °C | Above 230 °C |
| Development of the individual gaseous components (ppm) (at places outside PVP) | | | | | |
| CO | 4–20 | 20–40 | 50–100 | 100–400 | 400–700 |
| $C_2H_6$ | 2–5 | 5–6 | 6–12 | 12–30 | 30–100 |
| $C_3H_8$ | 0.2–0.8 | 0.8–2 | 1–4 | 2–16 | 6–30 |
| $C_4H_{10}$ | Traces | 0.2–0.4 | 0.4–1 | 1–7 | 4–13 |
| $C_2H_4$ | – | 0.2–0.6 | 1–2 | 1–10 | 2–20 |
| $C_3H_6$ | – | Traces | 0.2–0.8 | 0.6–4 | 2–8 |
| $H_2$ | – | Traces | Traces–200 | 100–700 | 700–1600 |
| $C_2H_2$ | – | – | – | – | Traces |

## 4    Enabling Access to the Fire Site

In the closed longwall face, all the mining machinery was in place, the mine owners decided to re-open the fire site to remove this machinery or to complete extraction of the coal reserves. Due to the fact that one of the main causes of the endogenous fire was the slowing of the process of the excavation due to passing a 5-m fault in the longwall face (erosion pothole), it was decided to excavate the new Longwall Face Gangway No. 40 943.7 and shorten the length of the longwall face, see Fig. 4.
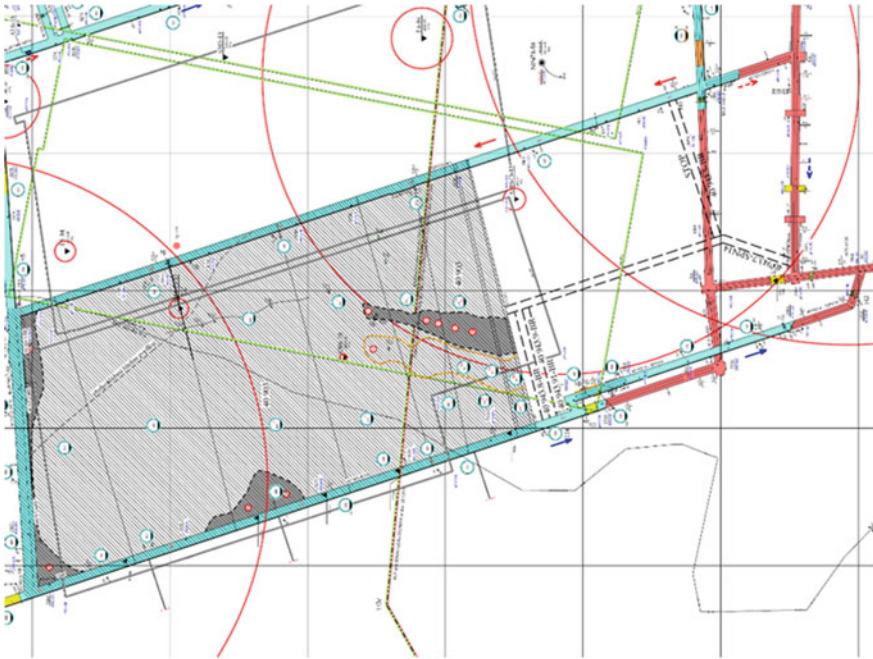


**Fig. 4.** Excavating the dividing class and shortening the Longwall Face No. 40 903

When the CO concentration is below 1%, the $CO_2$ is between 4 and 5%, the $O_2$ value is between 8 and 10%, and $N_2$ above 80% are considered to be of sufficient evidence of extinction of the endogenous fire. Opening and subsequent ventilating of a sealed off fire site depends on if acetylene ($C_2H_2$) is no longer present in the concerned area and that the amount of ethylene ($C_2H_4$) is reduced to 1 ppm [13]. These gas concentrations were measured at the end of June 2017. Prior to accessing the fire site, a plan for the opening of the closed fire site at the Longwall Face No. 40 903 was prepared.

Due to the fact that the difficult microclimatic conditions prevailed at the site of the fire, the workplace was made accessible by mine rescue team equipped with fire-resistant clothes, Dräger BG-4 breathing apparatuses and multifunctional measuring devices. The endangered area was first checked by rescue patrols [14].

The plan for the opening of the closed fire site was divided into six successive stages:

Phase I—excavation of the class No. 40 943.7 and preparation for driving through to the closed fire site of the Longwall Face No. 40 903

Phase II—exploration of the closed fire site of the Longwall Face No. 40 903

Phase III—ventilation of the fire site of the Longwall Face No. 40 903

Phase IV—disabling access to the fire site of the Longwall Face No. 40 903 behind the erosion pothole

Phase V—installation of the route for $N_2$ and sampling points in the fire site of the Longwall Face No. 40 903

Phase VI—commissioning of the gas mining laboratory

**Phase I**—excavation of the class No. 40 943.7 and preparation for driving through to the closed fire site of the Longwall Face No. 40 903

The excavation of the class No. 40 943.7, Fig. 5, was carried out and a solid block of coal (about 5 m) was left between the newly mined class and the closed fire site of the Longwall Face No. 40 903.

**Phase II**—exploration of the closed fire site of the Longwall Face No. 40 903

The exploration focused mainly on the passability of the closed area, the verification of the potential flooding of the excavation area, swelling up of the base, the state of the construction, the measurement of the concentrations of the gaseous pollutants, the temperature measurements, the mechanized support state and the sealing of the caving spaces of the longwall face. On the basis of the verified state of the fire, the situation was assessed positively and it was proceeded to the next stages.

**Phase III**—ventilation of the fire site of the Longwall Face No. 40 903

This was followed by the exhaust ventilation of the fire site at Longwall Face No. 40 903, which was carried out by connecting the separate exhausting ventilation and the gradual addition of flexible reinforced ventilating tubing until the air became breathable. After ventilating, samples were taken for chromatographic gas analysis, thermal imaging and measurement of parameters to determine microclimatic conditions. After venting, the residual coal was left between the longwall face and the new longwall face gangway.

**Phase IV**—disconnecting access to the fire site of the Longwall Face No. 40 903 behind the erosion pothole

After the rescue exploration, venting and driving through, the machinery was disconnected and access was disconnected to the part of the Longwall Face No. 40 903 (behind the fault) from the Breakthrough 40 903.4.

**Phase V**—installation of the route for N2 and sampling points in the fire site of the Longwall Face No. 40 903

After the ventilation of the roof, the sealing off the caving area was carried out using a gas-tight insulation foam barrier. Further, the installation of a lost pipe for the inertization of the caving spaces with $N_2$ was carried out, behind the mechanized

support sections, and the inertization of the longwall face with $N_2$ was started. Installation of sampling points for sampling indicator gases was carried out, as well as their connection by means of a tubing to the DPL gas laboratory in the longwall face (DPL). DPL has a measuring range for individual gases: $CH_4$ 0–100%, $H_2$ 0–10%, CO 0–5%, $CO_2$ 0–25%, $O_2$ 0–25%, temperature 0–60 °C, relative humidity 0–100%, wind speed 0–10 $ms^{-1}$.

**Phase VI**—commissioning of the gas mining laboratory

Gradually, a separate exhausting ventilation was disposed of. Following the works mentioned in the previous phases, a mining gas laboratory was put into operation, whereupon the longwall face was ready for completing the extraction.

The fire site was made accessible about seven months after the closure. Further work on completing the extraction of the Longwall Face No. 40 903 resumed its normal operation.

## 5   Completing the Extraction of the Longwall Face

Completing the extraction of the coal reserves resumed after opening the fire site. After the mining process started in a shortened length and with a regular advance without delays, the extraction of the newly formed coal block was completed up to the "stop line". The following measures to suppress possible self-ignitions were taken during extraction:

- Nitrogen inertization of the caved areas,
- Sealing off caved area with sealing barriers and nitrogen foam,
- Isolating old workings by sealing using explosion-proof seals and injecting water into the caved area
- Continuously check and analyze depression pressure drop reduction,
- Avoiding air leakage to the caved area,
- Rapid and efficient cooling of the area threatened by the self-ignition process using nitrogen foam, and
- injection of antipyrogenic substances into the coal pillar (GEOLITH®, ANTYPYROFIX®).

The GCA device was deployed during coal production. It is a special device that efficiently cools the gaseous nitrogen supplied to the caving space behind the longwall face. It can be used as a means of prevention spontaneous fire, or for the repression of the developing endogenous fire enclosed by a seal, when it is part of the preparation for subsequent access to the fire site. The device has a cooling chamber, which is hermetically sealed. Cooling water is taken from a mine fire-water duct and has an open circuit. The device can cool the supplied nitrogen by approximately 30 °C to the recommended minimum temperature of −1 °C [15].

# 6   Conclusion

Hard coal mining is currently underway in the Czech Republic only within the OKR. This is a deep mining, about 1000 m below the surface and under difficult geological conditions. Most currently mined seams are susceptible to coal spontaneous combustion. In addition, all mines in the OKR are classified as "gassy" where there is a risk of methane explosion. For this reason, the issue of self-ignition needs a great deal of attention, which mainly consists of prevention of spontaneous combustion.

This paper uses a practical case to demonstrate both the prevention against spontaneous fire and repressive measures that are applied in the case of a endogenous fire in the OKR. Thanks to the timely closure of the fire site and its subsequent successful re-open, it was possible to save the mining machinery and other equipment of the longwall face. Subsequently, a total of 548.6 kilotons of coal was safely extracted in the shortened longwall face, which saved considerable financial costs.

# References

 1. Interní materiály OKD, a. s. Dolu Darkov, 2014: POPD porubu č. 40 903, Stonava (2014)
 2. Interní materiály OKD, a. s. Dolu Darkov, 2015: Plán dobývání porubu 40 903, Stonava (2015)
 3. Interní materiály OKD, a. s. Dolu Darkov, 2015: Technologický postup porubu č. 40 903, Stonava (2015)
 4. MATOVÁ, Radka. Asanace záparu likvidovaného porubu č. 40 901 na lokalitě Důl Darkov. Ostrava (2015)
 5. Adamus, A.: Náchylnost slojí OKR k samovznícení. VŠB-TU Ostrava, Ostrava (2004). ISBN 80-248-0585-5
 6. Taraba, B., Pavelek, Z.: Investigation of the spontaneous combustion susceptibility of coal using the pulse flow calorimetric method: 25 years of experience. Fuel **125**, 101–105 (2014)
 7. Keler, R.: Klasifikace náchylnosti černých uhlí k samovznícení metodou izotermické sorpce kyslíku. Doktorská disertační práce VŠB-TUO, Ostrava (2005)
 8. Lazzara, C.P.: Overview of U.S. Bureau of Mines spontaneous combustion research. In: Session Papers—American Mining Congress Coal Convention, pp. 143–154 (1991)
 9. Interní materiály OKD, a. s. Dolu Darkov, 2015: Příkaz č. 279/2015, Stonava (2015)
10. Niu, H.-Y., Deng, X.-L., Li, S.-L., Cai, K.-X., Zhu, H., Li, F., Deng, J.: Experiment study of optimization on prediction index gases of coal spontaneous combustion. J. Central South Univ. **23**(9), 2321–2328 (2016)
11. Faster, P., Makarius, R., et al.: Báňské záchranářství I. Kompendium pro báňské záchranáře, MONTANEX a. s., ISBN: 80-7225-043-4 (2000)
12. Adamus, A., Šancer, J., Guřanová, P., Zubiček, V.: An investigation of the factors associated with interpretation of mine atmosphere for spontaneous combustion in coal mines. Fuel Process. Technol. **92**(3), 663–670 (2011)
13. Kubica, J., Kroul, J.: Geotechnika 1, Centrální vzdělávací středisko OKD, a.s., (2013)
14. OKD Služební řád, HBZS a. s., Ostrava (2002)
15. Provázek, J., Záchranář, Zařízení pro chlazení plynného dusíku GCA, OKD, HBZS a. s., (2017)

# A Mine Fire Evaluation System Based on Vulnerability

Shuicheng Tian[1,2] and Chengzhen Zhang[1,2(✉)]

[1] College of Safety Science and Engineering, Xi'an University of Science and Technology, Xi'an 710054, China
1848173964@qq.com
[2] Key Laboratory of Western Mines and Hazard Prevention, Ministry of Education of China, Xi'an 710054, China

**Abstract.** It is essential to have a sound mine fire evaluation system with accurate results. Based on the vulnerability theory, with the disturbance factor added to the three characteristic factors of vulnerability, a four-characteristic-factor of vulnerability is proposed (Disturbance, Expose, Susceptibility, Resilience). Vulnerability "Glass Heart" model, an index system and index formula are established. Study found that the four characteristic factors are not independent or having sequence relationships, in fact, they are cross-impacting, which can be well described by vulnerability "Glass Heart" model. The model can be used to test the vulnerability of the coal mine fires, and then to establish the vulnerability index system. By using vulnerability index formula to calculate the vulnerability degree of the fire, it can accurately reflect the vulnerability degree of a coal mine fire.

**Keywords:** Vulnerability · Mine fire · "glass heart" model · Index system Index formula

## 1 Introduction

In 1968, Margat J first proposed the concept of vulnerability in the study of groundwater pollution [1]. In recent years, there have been more and more attention to the study of vulnerability. In April 2001, Science magazine published a paper on "sustainable sciences", listing vulnerability research as the seven core issues of sustainable science [2]. Therefore, it would be helpful to combine mine fire characteristics with the above vulnerability to establish a vulnerability evaluation system to better characterize mine fires.

Over the last 10 years in the field of safety engineering, some scholars have studied theories of vulnerability. As the result of the comprehensive effect of the various factors in the system, the problem of safety is also based on the "man-machine-environment-management" system. Therefore, the theory of vulnerability applied to a mine fire can bring new perspective to the mine fire study. Based on GIS and other technologies, Wuqiang's team proposed vulnerability index of coal floor water inrush evaluation [3]. Liu Tiemin studied the identification and evaluation of system vulnerability based on safety issues [4, 5]. Based on the study of the vulnerability of underground traffic

system network [6], fire [7] and disturbance of heavy passenger flow [8], Song Shouxin team proposed a successive evaluation method of vulnerability characteristic factors [9], but the characteristic factors of vulnerability were not a simple sequential relationship, so further studies are required. In this paper, with in-depth study of vulnerability, a mine fire vulnerability evaluation system is established.

## 2  Vulnerability Characteristic Factors

Most scholars agree with the viewpoints of three factors of vulnerability. Those who hold the view of the three factors believe that the vulnerability is the relationship between the various components such as the external exposure, the system exposure, the susceptibility to disturbance and the adaptability [10, 11]. To address the system safety issues, the research object is the "man-machine-environment-management" system, and the disturbance comes from the intersection of the trajectory of potential hazard and energy release in the system, so for safety issues, the disturbance comes from within the system, and the system's vulnerability plays a crucial role [12]. Therefore, it is necessary to consider the disturbance as a characteristic factor of system safety vulnerability. Based on the three factors of vulnerability, this dissertation adds disturbance factor and proposes four factors of vulnerability: disturbance, exposure, susceptibility and resilience.

(1) **Disturbance**: It refers to the size of the system and the duration of the disturbance. The disturbance factor comes from the accidental release of energy within the system and the direct cause of the accident. The degree of disturbance depends on the size of the hidden danger in the system, the magnitude of accidental release of energy, and the probability of the orbital crossing of energy and hidden danger. The higher the disturbance is, the greater the system vulnerability is.

(2) **Exposure**: It refers to the extent of unsafe behaviors from human and an unsafe environment within the "man-machine-environment-management" system, which includes the degree of exposure and the length of exposure. The higher the exposure is, the greater the potential hazard is hidden in the system, which will directly lead to increase of the probability of system disturbance, and rise in the system vulnerability.

(3) **Susceptibility**: It is the degree to which the system deviates from its normal state under disturbances. This includes the speed of deviation and the degree. The susceptibility of the system depends on the nature of the system and the indirect causes of system accidents. The more sensitive is the system, the greater is the vulnerability of the system.

(4) **Resilience**: It refers to the recovery ability of the system after system state deviates from the normal state and accidents. The resilience factor includes the speed and degree of recovery. the greater the system's resilience, the lower chance the system exposes, the stronger the resilience when the system is out of state and after accidents, which means less system vulnerability.

# 3   The Construction of Mine Fire Evaluation System

## 3.1   The Construction of Vulnerability "Glass Heart" Model

Through in-depth analysis of the complex relationship between the various factors of the vulnerability of the "human-machine-environment-management" system, the "Glass Heart" secondary accident model is established, as shown in Fig. 1. The disturbances originate from the accidental release of energy and the hidden trajectories cross with each other. The disturbance generated by the system will cause the system state to deviate, and the system will recover actively then. When the deviation is within the critical line of the accident, it is a sign of danger that happens, not an incident. When the deviation exceeds the critical line of the accident, there will be an accident, at the same time the system will try to actively recover. Accident is also equivalent to a big disturbance, which will make the system again a major deviation from the state. That will lead to a sequential accident, while the system will also be active after the accident happens. For systems without secondary accidents, the vulnerability "Glass Heart" model is the first heart in Fig. 1.
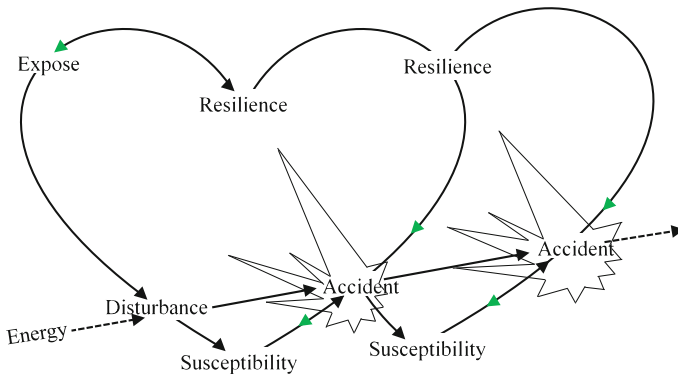


**Fig. 1.**  The vulnerability "Glass Heart" secondary accident model

## 3.2   Applications

The vulnerability "Glass Heart" model was used to analyze the "11.29" major gas explosion in Jingyou Coal Mine, Qitaihe City, Heilongjiang Province. High vulnerability is the root cause of the gas explosion. Disturbances are miner's illegal gunfire and hot work. The poor ventilation led to gas accumulation. Also, there are no effective gas and dust prevention measures. Susceptibility factor is illustrated as a lack of safety and technical management, no safety education and training in accordance with the law, failing to implement the main responsibility for safety production and failing to provide supervision. Resilience is shown as the inefficient ventilation system, no rescue team, and no emergency rescue plan. It is found that the "Glass Heart" model can well reflect the vulnerability of the coal mine fires.

## 3.3 The Index System for Vulnerability Evaluation

According to the four characteristic factors of vulnerability proposed in this paper, and as a second-level index, each of the first-level index was then broken down into a corresponding third-level index to establish the "man-machine-environment- management" system vulnerability evaluation system, as shown in Fig. 2.
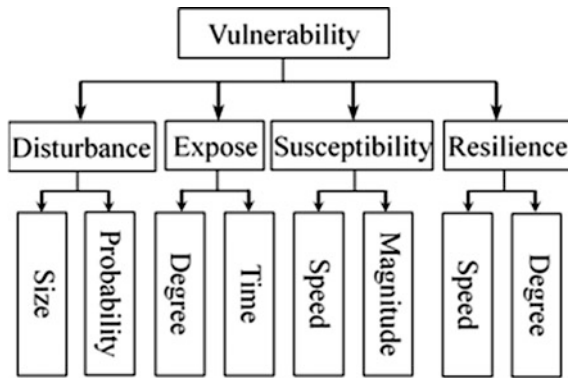


**Fig. 2.** Index system of vulnerability evaluation

## 3.4 Vulnerability Classification and System Status Changes

Considering the changes of the system states during the interaction of the four major characteristic factors of the system vulnerability, the magnitude of the vulnerability is divided into four levels respectively: Complete, Cracked, Broken, and Crushed.

Level I: Complete—means that there will be no casualties and large property losses in the system.
Level II: Cracked—means the system is likely to have injuries or large property losses.
Level III: Broken—means the system is likely to have personnel death and large property damage or system and property loss.
Level IV: Crushed—means the system is likely to see fatalities and total loss of property.

For different levels of system vulnerability, the system state changes under disturbances will also be different, as shown in Fig. 3. The left side of point A is the normal state of the system. Under disturbance, the system deviates from the normal state. At the same time, the system is actively recovering itself, and finally the system state will deviate from the limit state point B, at which point the disturbance is controlled and then the system will recover slowly. The system vulnerability is ranked according to the region where the limit state point B is located. For Level I, Level II and Level III vulnerabilities, the system states under disturbance are 1#, 2# and 3# curves, respectively, and finally the system can be restored to operational status. The change of IV Level vulnerability system state is curve 4#, which will cause the accident

under the disturbance. The resilience of the system itself can't help the system with this level of vulnerability, and the system will eventually be scrapped or replaced by a new system.
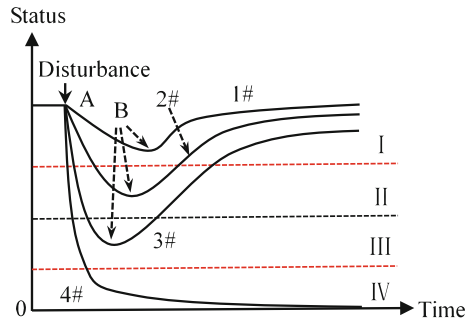


**Fig. 3.** System state change curve

Some Level II, Level III and Level IV vulnerability system accidents occurred under disturbance, which will lead to a big disturbance as a secondary accident, resulting in greater damage to the system. This will increase the system's vulnerability, so the system vulnerability grading also needs to be considered, as shown in Fig. 4. The system deviates from the normal state under disturbance, and at the same time, the system is actively recovering itself. When the state of the system deviates from below the critical line of the accident, an accident will occur in the system. When at point A*, the accident of the system triggers a second accident as a disturbance. The system state deviates more greatly. The curve of #5 shows that the limit point B deviating from the state of the system is not lower than the crushing threshold of the system. When the system state reaches point B, the accident is controlled and the system slowly returns to the running state. The secondary accident caused by system #6 curve exceeds the ability of the system's self-resilience, which directly diverts the state of the system below the crushing threshold and eventually damages the system or a new system will replace the current one.
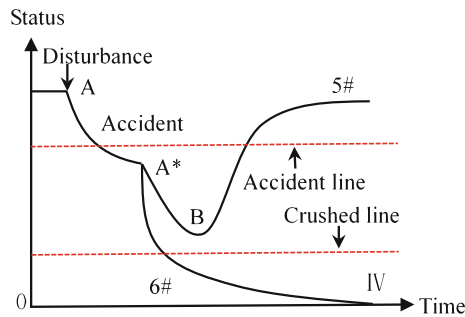


**Fig. 4.** System state change curve of a secondary accident

## 3.5    Vulnerability Index Formula

The disturbance come from the cross track between the accidental release of energy and the hidden dangers of exposure. The disturbance depends on the size of the hidden danger of the system, the magnitude of accidental release of energy, and the probability of cross track, so the degree of disturbance equation is:

$$D = \sum_{i=1}^{n} \left( \left( E_i + \sum_{y=1}^{q} E*_{iy} \right) \cdot P_i \right) \tag{1}$$

The system vulnerability index formula should reflect the degree of impact of each feature factor on the system vulnerability and the degree of interaction of each featured factor. Based on these principles, the system vulnerability index formula is obtained through further research and repeated verification [13]:

$$V = \frac{\sqrt{\sum_{i=1}^{n} \left( \left( E_i + \sum_{y=1}^{q} E*_{iy} \right) \cdot P_i \right) \cdot \sum_{j=1}^{m} S_j}}{\sum_{k=1}^{t} R_k} \tag{2}$$

where: $V$ is the degree of vulnerability, $D$ is the disturbance, $E_i$ is one of the third-level index of system expose, $n$ is the total number of third-level index of system expose, $E*_{iy}$ is one of the secondary accidents that one of the third-level index of the system expose may cause, $q$ is the total number of secondary accidents that a three-level indicator of system expose may cause, $P_i$ is the probability of cross track between one of the third-level index and accidental release of energy, $S_j$ is the degree of deviation of the system from the normal state due to disturbance caused by a hidden danger, $m$ is the total number of third-level index of system susceptibility, $R_k$ is one of the third-level index of system resilience, $t$ is the total number of third-level index of system resilience.

According to the system vulnerability value calculated according to the vulnerability index formula, the range of each vulnerability level is quantified according to the four levels of vulnerability: ① Level I ($V \leq 0.25$). ② Level II ($0.25 < V \leq 0.50$). ③ Level III ($0.50 < V \leq 0.75$). ④ Level IV ($0.75 < V$).

## 4    Coal Mine Fire Case Verification

In this paper, a coal mine fire incident in Yunnan Province is used as a case study, to verify the vulnerability "Glass Heart" model. According to the vulnerability index system and the actual situation of the coal mine, a vulnerability index system was established for this fire, as shown in Table 1. The probability of a fire incident is defined as the possibility of the cross between one of the third-level index and the accidental release of energy, as shown in Table 2. Six experienced safety managers of the coal mine were invited to rate the level of the coal mine fire vulnerability and the average of each index was used as the vulnerability score of the index, as shown in Table 3.

**Table 1.**  Vulnerability index system of coal mine fire

| Second-level | Third-level Index |
|---|---|
| Disturbance D | Coal spontaneous combustion D1; Open fire D2; Electric fire D3; Flammable fire D4 |
| Expose E | Spontaneous combustion of coal E1; Open fire work E2; Welding work E3; Electrical appliances E4; Wire/Cable E5; Transformer/Distribution electrical equipment E6; Shipping tape E7; Blasting E8; Gas E*1; Coal dust E*2 |
| Susceptibility S | Coal fire safety education S1; Staff safety awareness S2; Safety training S3; Safety input S4; Safety check S5; Safety organization and decision-making S6; Safety culture S7; Fire emergency plan S8 |
| Resilience R | Organization and coordination capacity R1; Fire Fighting System R2; fire alarm system R3; ventilation system R4; Anti-coal spontaneous combustion capacity R5; Refuge chamber R6; Escape equipment R7; Incident response ability R8; After-treatment capacity R9 |

**Table 2.**  Possibility of coal mine fire

| Level | $P$/(times/a) | Level | $P$/(times/a) |
|---|---|---|---|
| Very likely | 0.1 | Not often | 0.0001 |
| Easy | 0.01 | Almost not | 0.00001 |
| Occasionally | 0.001 | Difficult | 0.000001 |

**Table 3.**  Vulnerability index score of coal mine fire

| Index | Score/$P$ | Index | Score | Index | Score |
|---|---|---|---|---|---|
| E1 | 0.80/0.1 | S2 | 0.08 | R3 | 0.29 |
| E2 | 0.13/0.0001 | S3 | 0.60 | R4 | 0.66 |
| E3 | 0.28/0.001 | S4 | 0.63 | R5 | 0.75 |
| E4 | 0.30/0.001 | S5 | 0.83 | R6 | 0.68 |
| E5 | 0.29/0.001 | S6 | 0.15 | R7 | 0.92 |
| E6 | 0.29/0.001 | S7 | 0.40 | R8 | 0.95 |
| E7 | 0.61/0.01 | S8 | 0.50 | R9 | 1.00 |
| E8 | 0.83/0.01 | R1 | 0.41 | E*1 | 0.80 |
| S1 | 0.10 | R2 | 0.36 | E*2 | 0.70 |

Take the value of each index in Table 3 and the probability of occurrence of hidden danger fire into Eq. (2), calculate the vulnerability of the coal mine fire index, which is $V = 0.2896$. According to the range of vulnerability, the coal mine fire vulnerability is Level II, the system vulnerability is Cracked, and the risk of the coal mine fire is also reflected the same result, which is consistent with the evaluation result of fire hazard level of the coal mine [14]. Therefore, it proves that the evaluation results of the vulnerability "Glass Heart" model on coal mine fire vulnerability can reflect the real situation of the system, and also the vulnerability "Glass Heart" model has strong practicability.

## 5 Conclusion

(1) By adding the four characteristic factors of the vulnerability of the disturbance factor, the system safety features can be more reasonably reflected compared with the previous three factors of vulnerability.

(2) Based on the four characteristics of the system safety vulnerabilities proposed in this paper, the vulnerability "Glass Heart" model was first established, which can better represent the interaction between the characteristic factors compared to the previous evolutionary model of vulnerability.

(3) Based on the vulnerability "Glass Heart" model, the vulnerability index system and index formula for the model, a coal mine fire accident was used to verify this theory. Quantitative results were calculated, and the range of the vulnerability level was compared. Results show that the vulnerability level can accurately reflect the real situation of the vulnerability of the coal mine fire.

## References

1. Margat, J.: Vulnerability of Groundwater to Pollution, pp. 6–7. Orleans, France (1968)
2. Kates, R.W., Clark, W.C., Corell, R., et al.: Environment and development: sustainability science. Science **292**, 641–642 (2001)
3. Qiang, W., Bo, Z., Wende, Z., et al.: A new practical methodology of coal seam floor water burst evaluation V: the comparison study among ANN, the weight of evidence and the logistic regression vulnerable index method based on GIS. J. China Coal Soc. **38**(1), 21–26 (2013)
4. Tiemin, L.: Recognition of disaster causes: study of the vulnerability. J. Saf. Sci. Technol. **6**(5), 5–10 (2010)
5. Tiemin, L., Yongli, X., Hao, W.: The frequent serious accidents exposing the system vulnerability of work safety: reflection on several serious accidents in 2013. J. Saf. Sci. Technol. **10**(4), 5–12 (2014)
6. Jia, X., Shouxin, S., Pengwei, Y., et al.: Evaluation of network vulnerability of subway stations based on ANP. China Saf. Sci. J. **25**(12), 129–134 (2015)
7. Shouxin, S., Chuyang, X., Huaiyuan, Z., et al.: Influential factors for subway electrical fire based on vulnerability. J. Xi'an Univ. Sci. Technol. **36**(5), 691–696 (2016)
8. Shouxin, S., Dezhi, Y., Chuyang, X.: Research on subway vulnerability under large passenger flow disturbance based on multi-level extension evaluation method. Res. Urban Rail Transit **1**, 25–31 (2017)
9. Shouxin, S., Jia, X., Liming, C., et al.: The mechanism and evaluation of vulnerability factors progressive growth. J. Beijing Univ. **16**(2), 57–65 (2017). (Social Sciences Edition)
10. Smit, B., Wangdel, J.: Adaptation, adaptive capacity and vulnerability. Glob. Environ. Change **16**(3), 282–292 (2006)

11. Brooks, N., Adger, W.N., Kelly, P.M.: The determinants of vulnerability and adaptive capacity at the national level and the implications for adaptation. Glob. Environ. Change **15**(2), 151–163 (2005)
12. Shuicheng, T., Guoxun, J.: Safety Management. Mechanical Industry Press, Beijing (2016)
13. Xingkai, Z.: Index method of mine fire risk assessment. J. Saf. Environ. **6**(4), 89–92 (2006)
14. Chen, M.: A multilevel fuzzy comprehensive evaluation of coal mine fire hazard. Central South University, Changsha (2014)

# Application of ABT-Q High-Efficiency Composite Filling and Sealing Technology

Xinhai Zhang[✉], Zhen Feng, Tianci Zhang, Erjun Xing,
and Shanlin Zhou

College of Safety and Engineering, Xi'an University of Science and Technology,
Xi'an 710054, Shanxi, China
`zhangxinh@l26.com`

**Abstract.** The heat release reaction between loose coal and its surrounding air is the main reason of spontaneous combustion. By blocking air leaking channels, coal is isolated from oxygen, and coal seam spontaneous combustion can be prevented effectively. The ABT-Q high-efficiency composite is a newly-developed filling material, whose raw material is a one-component liquid that reacts with water more than 20 times of its weight to generate high-water content elastomer. This sticky material, harmless to the environment and can resist high-temperature. The material had been used in Xin'an Coal Mine successfully, where the fissures and other air leaking channels in the mine were effectively blocked by injecting ABT-Q high-efficiency composite filling material underground. In another case, temperature of coal fire zone was known to be lowered from ignition point to below 70 °C by injecting into the spontaneous combustion region. The material is proved to be effective and efficient in coal fire prevention and control.

**Keywords:** Filling material · Filling technology · Leakage blocking
Fire prevention and extinguishing

## 1 Introduction

Coal spontaneous combustion is chemical process with reaction between coal and oxygen that enters the loose coal along the fissures and air-leaking channels, which releases large amount of heat. Temperature of the coal rises automatically due to accumulation of the heat, and ultimately coal spontaneous combustion takes place [1]. Thus, by blocking the air leaking passage spontaneous combustion of coal seam can be prevented and controlled effectively. As to sealing materials, inorganic materials are generally high-temperature resistant but can't endure dynamic pressure and its foaming expansion time is low [2]. Existing solidifying and foaming organic materials, like polyurethane foam, are made from two fluid raw materials to fill the fissures and other air-leaking channels [3–5]. However, polymerization process to prepare foaming organic materials is generally an exothermic chemical reaction, which can easily raise the coal temperature in coal seam during sealing operation because of its active thermal insulation property. Therefore, it is not suitable for mine fire prevention and

extinguishing [6]. *Coal Mine Safety Code of China* stipulates that filling materials is not suitable for coal mine use if the materials generate large amount of heat. If the material has to be used in coal mine, possible risk must be evaluated, and preventive counter measures be formulated to avoid any possible risks.

In the present study, a serial of newly developed high-efficiency composite filling materials is developed, which can react with water to generate high-water elastomer and its temperature rises slightly during the filling process. The filling materials are used successfully in many coal mines, which proved that the materials are suitable for filling and blocking air-leaking passages in coal seam.

## 2    ABT-Q High-Efficiency Composite Filling Material

The main ingredient of ABT high-efficiency composite filling material is a light yellow viscous liquid which reacts with water to generate an elastomer. The proportion of water to raw material ranges from 1:1 to 20:1. When the ratio exceeds the maximum value (20:1) the excessive water will not enter the bulk phase of the elastomer, but wrapped into the solidified body. The heat released by the chemical reaction during mixing is largely absorbed by the reactant water. Since specific heat capacity of water is very high, temperature rises of the material during the filling process is so small and is usually negligible. The component water increases the electrical conductivity and flame retardancy on the surface of the material, so the material is not combustible and static electricity can't accumulate on the surface of the material. Therefore, the material possesses a good fissures and voids filling, and coal fire prevention and extinguishing property.

## 3    Filling Technology and Equipment

ABT-Q raw materials and water are mixed at the proportion of 1:1 ∼ 1:20 before injected into the filling area. The mixture penetrates into the interconnected fissures to tightly seal the air-leaking passages by forming elastomer in the curing reaction.

The equipment specifically designed to be ease of use and transport. It has an air intake pipeline and two feeding pipes for two raw materials' intake, two pneumatic reciprocating cylinders each being connected with two pistons in two injecting cylinders by connecting rods. Compressed air drives the connected pistons to move back and forth in their respective cylinders. On the both sides of an injecting cylinder, there are two check valves controlling the inhalation and drainage of the injecting component. Out of four injecting cylinders, three are connected with conversion valves respectively. Schematic structure of the device is shown below:

In the device, diameter of one pneumatic piston and the attached injection pistons (on the right side of the Fig. 1) are two times that of the other corresponding ones (left). Therefore, flow rate of the raw material through each injection cylinder on the right is four times that of the corresponding one on the left. The ratio of the diameter of the pneumatic cylinder to the connecting injection cylinder is 2:1, so the outflow pressure

is four times of air pressure. In general, the pressure of compressed air in mine is 0.7 MPa, so the injection pressure of this equipment can reach 2.8 MPa.
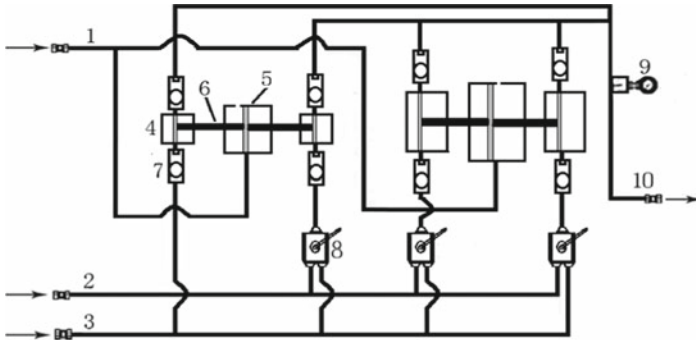


(1: Air intake pipe; 2: Material A feeding pipe; 3: Material B feeding pipe; 4: material cylinder; 5: Pneumatic cylinder; 6: connecting rod; 7: check valve; 8: steering valve; 9: Pressure gauge; 10: Discharge port)

**Fig. 1.** Schematic structure of ABT filling material perfusion equipment

By shifting the conversion valve, two types of raw materials can be mixed using this device according to the ratio of 1:1, 4:6, 1:4, or 1:9. The grouting in different proportion can also be realized by adjusting the flow rate of gas that passing through the two cylinders.

This pneumatic equipment can be moved underground through manual or mechanical transportation, being placed before the filling place 5–50 m to meet the needs of all filling locations flexibly, so it improved work efficiency and reduced workers' working intensity significantly. The whole equipment is driven by gas to meet the requirements of safe operation.

## 4   Application

### 4.1   Application in Xin'an Coal Mine

ABT-Q high-efficiency composite filling material was first applied in Xin'an Coal Mine in Shuangyashan Mining Area, Heilongjiang Province in northern China. Xin'an Mine is a modern coal operation mining four layers of close-distance coal seams. The goaf was sealed with a two-brick-wall sealing filled with fly ash in the middle after the whole panel was mined out. The outside surface of the sealing as well as its surrounding coal within 10 m were sealed and reinforced by guniting. However, air leakage through the sealing is still serious, which caused coal spontaneous combustion inside the closed area, as indicated by increased CO concentration on top of the closed wall.

In order to control coal spontaneous combustion in the closed area, ABT-Q high-efficiency composite filling material was used to seal air leakage cracks in March 2017. The filling technique is shown in Figs. 2 and 3.
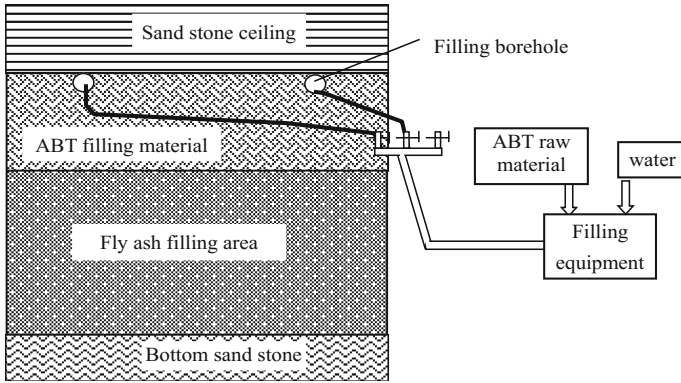


**Fig. 2.** Cutaway view of the arrangement of filling technology (vertical to the direction of tunnel)
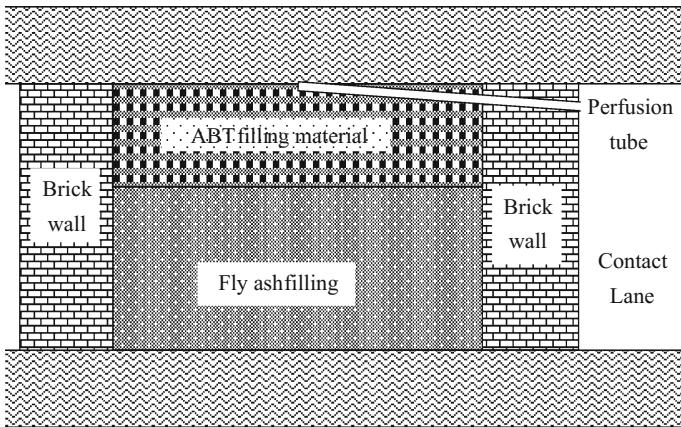


**Fig. 3.** Cutaway view of filling position of inorganic foam material (along the direction of tunnel)

The ABT raw material and water mixed on proportion (1:9) and then injected into the boreholes on the top of the closed wall through the pipeline using the pneumatic filling equipment. Only a small portion of filling material was seen to extruded from the surrounding fissures during the filing process. The filling body is high-water viscoelastic material that does not crack after being deformed by high pressure.

At the beginning of the filling process, there was water seepage through fissures in the lower part of sealing wall and its surrounding coal seam. There is no obvious temperature rise in the seeped water, which proved that the filling process does not release large amount of heat.

As the perfusion of the ABT material goes on, the fissures in the bottom of the wall were filled and water seepage level moved up gradually toward the roof of the tunnel. The perfusion stopped when pressure inside the infusion pipeline surpassed 2 MPa and no water leakage was seen on the surface of the sealing wall and its surrounding area.

It takes about 3 min for the mixture of filling raw material to solidify completely, so part of the mixture that was not fully reacted will leak out along the fissures. As the filling continues, all the fissures in the closed wall were sealed by generated elastomer so the seepage area disappeared. Therefore, water is both a reactant and an indicator of the leakage in the closed wall during the filling process.

The self-ignition indices such as CO on top of the sealing wall disappeared after the wall is filled with ABT-Q high-efficiency composite filling material. It proved that the air leaking fissures were completely sealed and the ABT high-efficiency composite meet the need of goaf spontaneous combustion prevention.

## 4.2 Application in Fire Extinguishing

ABT-Q high-efficiency composite filling material was used for fire extinguishing in a mine. Due to the heat release reaction between large amount of loose coal on top of the support and its surrounding air, the spontaneous combustion took place in the top coal falling region in the intersection of Auxiliary Shaft and working face tailgate. The spontaneous combustion position is shown in Fig. 4.
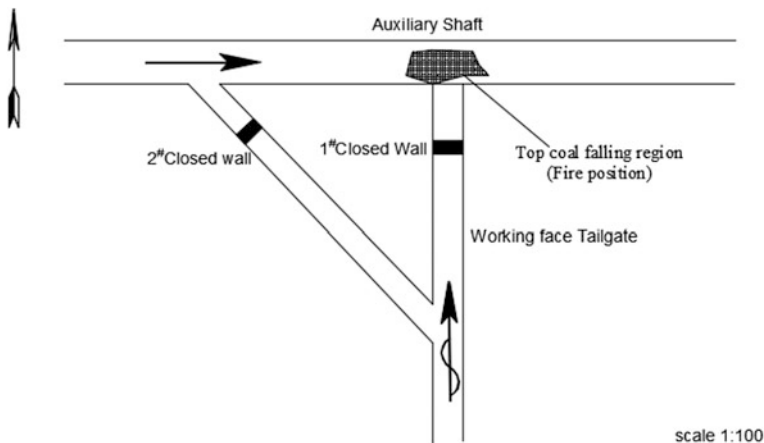


**Fig. 4.** Plan view of fire position

By applying gunite lining and nitrogen injection at the top coal fall region, kerosene smelling disappeared. But the concentration of CO was still very high (over

10,000 ppm) which indicated that there still exists air leaking passages and high temperature point. To control the fire, a plan was draw up to fill air leakage cracks with ABT-Q high-efficiency composite filling material through boreholes directly above the Auxiliary Shaft roadway. The boreholes were drilled every 2 m into the top coal fall region whose angle of tilt are among 45°–60°. ABT-Q high-efficiency composite filling material was injected into these drilling holes with a specially designed pneumatic device. It's raw material is fluid which reacts with more than 20 times of water to form high-water elasticity filling body, to cover the high temperature coal, seal air leaking channels, and cool the high-temperature coal. The filling technology is shown in Fig. 5.
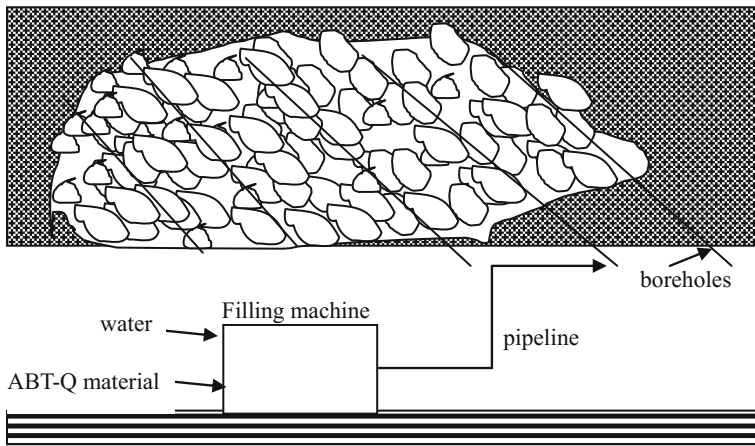


**Fig. 5.** Cutaway view of filling technology

The change of the CO concentration in the flow of the Auxiliary Shaft and Working face Tailgate during the perfusion process are shown in Figs. 6 and 7.

It can be seen that the curves of CO concentration have a regular zigzagged change after 5 through 10 h infusion of the ABT-Q high-efficiency composite filling material. After that the CO concentration dropped to less than 50 ppm. The CO concentration oscillations during infusion of ABT-Q high-efficiency composite filling materials shows that the material was in contact with fire. CO concentration declined obviously after filling the material indicates that fire was largely extinguished by injecting the ABT-Q high-efficiency composite filling material.
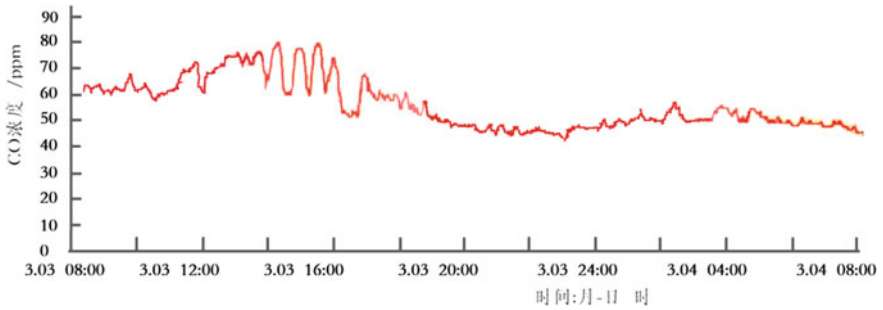
**Fig. 6.** CO Concentration variation in Auxiliary Shaft
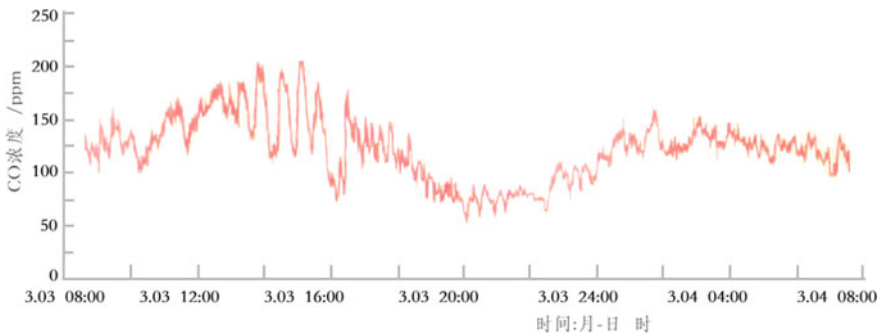


**Fig. 7.** CO Concentration variation in tailgate

## 5    Conclusions

(1)  Filling and sealing is an important way to prevent spontaneous combustion of coal seams. The elastomer generated by the reaction between ABT-Q material and water has good resistance to dynamic pressure, and it can fill the fissures and air leakage cracks in coal seams without heat releasing, meeting the needs of mine fire prevention.

(2)  Water is both one of raw materials for the reaction and an indicator in the filling process. The water seepage appeared in the early stage of filling process, then disappeared as the operation goes on, indicating that the air leaking channels were sealed. Therefore, to fill fissures and air leaking channels using ABT-Q material ensures the sealing effect.

(3)  ABT-Q material can be mixed with more than 20 times water to form high water elastomer which can cool the high temperature rapidly. As a use of filling material, ABT-Q high-efficiency composite can block air leakage to control fire quickly so that there is no rekindling after fire is extinguished.

# References

1. Feng, G., Ding, Y., Zhu, H., Bai, J.: Experimental research on a superhigh-water packing material mining and its micromorphology. J. China Univ. Min. Technol. **39**(6), 813–819 (2010)
2. Zhang, X., Guo, R., Bai, F., Guo, C.: Sealing technology of inorganic foam filling material. Saf. Coal Mines **46**(11), 74–76 (2015)
3. Song, Y.: Application of polyurethane in rock formation reinforcement and ventilation control. Coal Sci. Technol. (02), 25–28 + 31 + 57 (1998)
4. Qiu, C., Zhang, X.: Technology of Lukexiu foam product applied in Jining No. 2 mine. Coal Sci. Technol. **06**, 59–60 (2003)
5. Chu, F.: New Mali powder used in Liuqiao No.1 coal mine. Coal Technol. **01**, 99–100 (2007)
6. Hu, X., Wang, D.: Influence of curing agent on the curing behavior of mine filling foam. China Saf. Sci. J. **22**(11), 48–54 (2012)

# Part XIII
# Refrigeration and Cooling

# Evaluation of the Hydraulic Recovery Potential in a Lake-Sourced Underground Mine Refrigeration System

Jeffery Templeton[1], Leyla Amiri[1], Ali Kuyuk[2],
Seyed Ali Ghoreishi-Madiseh[2(✉)], Ferri P. Hassani[1],
and Agus P. Sasmito[1]

[1] McGill University, 3450 Rue University, Montreal, QC H3A 2A7, Canada
[2] Norman B. Keevil Institute of Mining Engineering, 511-6350 Stores Road,
Vancouver, BC V6T 1Z4, Canada
ali.madiseh@ubc.ca

**Abstract.** The foray of underground mines to ever deeper deposits has elevated mine refrigeration into an integral part of the operations. The air temperature limit, established through legislation, aims to ensure that workers in the mine are not exposed to temperatures extreme enough to cause heat stress. Because of the scale of refrigeration demanded by an underground mine, electricity/operating costs will constitute a significant portion of the budget. Using a lake for a cold-water source is a novel alternative to conventional refrigeration plants for subsurface cooling. The kinetic energy from the cold lake water flowing down the mineshaft can be harnessed with turbines, to reduce water pressure and produce usable energy. The scenarios examined includes ignoring the use of a turbine, using a turbine-generator combination, and using a turbine-pump combination. Considering the energy required to pump the return water from the bottom of the mine to the surface, the turbine-pump scenario is most economical. The scenario considering no turbine demonstrated the highest energy costs, while the turbine-generator combination was slightly less economical than the turbine-pump scenario.

**Keywords:** Underground mine · Cooling system · Hydraulic power
Hydraulic turbine

## 1 Introduction

According to mine regulations, every underground mine is required to implement appropriate ventilation systems in order to provide an adequate quantity of fresh air [1, 2]. The objective is to provide miners a safe, healthy, and comfortable atmosphere by reducing health hazards and enhancing the working conditions. For deep mines (depth greater than 1.5 km or 5000 ft) and ultra deep mines (depth greater than 2.5 km or 8200 ft) [3, 4], when the fresh air from the ventilation system is not enough to maintain satisfactory temperatures refrigeration becomes mandatory. Employing a refrigeration system within the existing ventilation system will increase the operating cost of the

mine as refrigeration systems are recognised as one of the most intensive electricity consumers in an underground mining operation [5, 6]. After a certain depth, surface refrigeration is incapable of providing enough cooling to overcome the impact of auto-compression and the miscellaneous heat sources within the mine, even with dedicated 'fridge shafts' [7]. Due to the cooling limit of surface refrigeration plants, secondary cooling will be required underground. As more ore bodies with immense potential are being exploited at increasing depths [8], more mines are encountering heat issues [9]. So, the number of deep underground mines equipped with cooling systems will increase in the future as deep mining becomes more prevalent. The mining industry can push to improve the energy efficiency of mine refrigeration systems to diminish the associated electricity demands and operational expenditures.

There are several ways of refrigerating fresh air in underground mines and there has been an international effort to further research on this subject [10–12]. So far, there are only two identified Canadian mines equipped with mechanical cooling plants; Kidd Creek [13] and LaRonde [14]. Their capital and operating costs make up an important portion of their mining cost, as Kidd Creek's 7.5 MW of underground cooling cost $3.75 M and LaRonde has 10.5 MW of underground refrigeration [15]. This paper evaluates the feasibility of an innovative mine cooling system which uses a lake in the vicinity of the mine as a heat sink. The cold lake water is sent to an underground bulk air cooler (BAC) to provide refrigeration. For deep/ultra-deep mines, the costs associated with pumping the water to the mine and out of the mine should be estimated and the potential for recovering the hydraulic energy of the down-flowing water has to be assessed. Accordingly, this paper studies the electricity costs associated with a lake-cooling system with and without a hydraulic-power recovery system. Mining companies operating deep/ultra-deep mines may be interested in adopting a lake sourced cooling system to outsource their refrigeration costs as well as to build their sustainability/environmental/social reputation. A lake source refrigeration system is especially applicable to deep mines in Canada, as there is a plethora of lakes scattered across the country and many mines that could profit from the advantages of such a refrigeration system.

## 2    Methodology

The kinetic energy of the down-flowing cold lake water could be recovered in a water turbine, so as to partially compensate for the pumping power demand as well as to control the pressure in the pipes [16]. Such an arrangement would have the further advantage of mitigating the increase in water temperature based on the pressure reduction, creating a considerable increase in the available cooling capacity of the water. The rise in temperature of down-flowing water evaluated by Whillier [17] can be used to support this idea. The conclusion given in some studies, most important of them [17, 18], confirm that the investment in hydraulic energy recovery systems for the water going down mine shafts would be well justified. A summarization of the influence of such hydropower energy recovery systems on the electricity consumption will be investigated.

Different parameters such as the distance between the surface water (heat sink) and underground galleries (heat source), as well as the number and capacity of the

hydropower plants (including turbines, generators and pumps) should be taken into account for an accurate assessment of the system. The distance between the cold source (i.e. lake) and the headframe of the mine, as well as the distance from the surface of the mine to where the BAC is situated underground, will influence the economics of cooling the mine with lake water.

This study focuses on some parameters of the lake cooling system, and calculates the recoverable hydropower for similar cooling systems. One of the main components of the lake cooling system is the hydropower equipment needed to recover the potential hydropower energy from the water going down the mineshaft. Its design will determine the pressure drop imposed on the turbines and pumps as well as the amount of heat energy exchanged between chilled lake water and underground air.

Whereas a closed loop system holds the water within the system to prevent exposure to the exterior, the cold lake water is contained in a system that is semi-closed loop, since the water is entirely contained except for its contact with the mine air in the underground BAC. As shown in Fig. 1, water is circulated in a semi-closed loop system in a deep mine to provide cooling to the underground mine air. Cold lake water, at a temperature of 5–7 °C, is supplied by the pipeline network from the lake to the underground workings. The system typically includes turbines, generators, and pumps (c.f. Fig. 1).
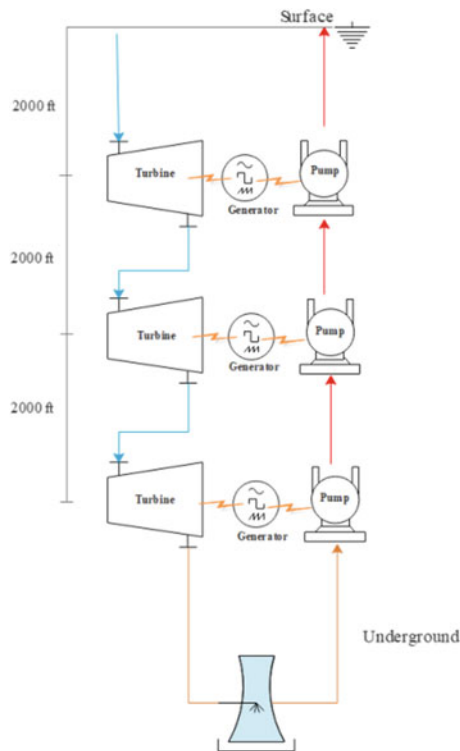


**Fig. 1.** Schematic design of hydropower energy recovery from the water going down mineshaft for cooling purposes

As shown in Fig. 1, the difference in depth between the turbine stations is assumed to be 2000 ft (610 m). It should be noted that the main stations in the mine shaft are also placed regularly at every 2000 ft (610 m). The amount of water that should be sent down to cool the underground openings and pumped back to the surface depends on the cooling demand of the mine. Consider Mine A, a deep mine in Ontario with an expected cooling capacity of 7100 kW, which can be provided by sending 250 l/s of chilled water underground (c.f. Fig. 1).

From an analytical point of view for the electricity cost calculation, Eqs. 1–3 are used.

$$SPR = (1 + \varepsilon)/(\eta_p \times \eta_m) - (1 - \varepsilon) \times (\eta_t \times \eta_g) \tag{1}$$

$$\text{Electric Power for bulk cooler (kW)} = CC/EER \tag{2}$$

$$\text{Hydraulic Power (kW)} = \sum_i \dot{m}_i g H_i \tag{3}$$

where
SPR     Supplementary Pumping Ratio
$\eta_g$       Generator efficiency
$\eta_t$        Turbine efficiency
$\eta_m$       Motor efficiency
$\eta_p$       Pump efficiency
$\varepsilon$         (friction losses + shock losses)/gravity head
CC      Cooling Capacity (kW)
EER     Energy Efficiency Ratio
$\dot{m}$       Water mass flow rate (kg/s)
H        Hydraulic head (m)

In order to point up the effect of a hydropower recovery system, an example will be given with the following assumptions (Table 1).

**Table 1.** The highlights of the assumptions for calculations

| | | |
|---|---|---|
| $\eta_g = 0.95$ | $\varepsilon = 0.10$ | EER of the bulk cooler = 10 |
| $\eta_t = 0.85$ | m = 250 kg/s | Availability = 8760 h/yr |
| $\eta_m = 0.90$ | g = 9.82 m$^2$/s | Electricity Price = 0.12 \$/kW hr |
| $\eta_p = 0.80$ | CC = 7100 kW | |

## 3   Results

Three different scenarios are considered and the electricity costs (i.e. operating costs) for each of them is calculated and shown in Table 2. The first scenario is comprised of; (I) turbines, (II) generators, and (III) pumps for pumping the water back to the surface after cooling the underground air. In the second scenario, the generators are eliminated and turbines are directly coupled to pumps to enhance the overall efficiency and reduce the capital and maintenance costs. Finally, the third scenario is investigated to show the electricity costs of the underground lake cooling system if the hydropower of the water is not captured. Table 2 shows the energy summary for the three potential scenarios, where the first scenario requires 4300 kW, the second scenario requires 3448 kW, and the third scenario requires 8827 kW.

## 4   Discussion

Incorporating a hydraulic recovery system within the delivery system for the cold lake water can theoretically reduce the operating cost of the lake cooling technology by about CAD$3.82 million per year. Without a hydraulic recovery system, the operating costs are twice as high when compared to the scenarios employing a hydraulic recovery system. The significant difference in operating costs is a solid justification for incorporating the turbines within a hydraulic recovery system due to the prohibitive operating costs of the third scenario. Additionally, the hydraulic recovery system will regulate the hydraulic pressure, and mitigate the water temperature rise as it flows to the underground BAC.

Table 2 demonstrates the superior energy efficiency of a turbine-pump combination in comparison to the turbine-generator combination. The difference in operating costs is due to the turbine-pump combination directly converting the water pressure head into pumping work, whereas the turbine-generator combination loses energy through converting the water pressure head into electricity and then back into pumping work. In other words, the turbine-generator scenario has the extra energy loss associated with generating electricity compared with the turbine-pump, all other energy losses being the same. Overall, the turbine-pump combination (second scenario) has the lowest operating costs compared to the turbine-generator combination (first scenario) and compared to ignoring hydraulic recovery (third scenario).

**Table 2.** Required electric power for water circulation and electricity costs for the different scenarios of underground cooling systems

| Items | Scenarios | | |
| --- | --- | --- | --- |
| | Turbine-generator | Turbine-pump | No hydraulic recovery |
| H (m) | 1828 | | |
| Hydraulic Power (kW) $= \sum_i \dot{m}_i g H_i$ | 4488 | | |
| SPR $= (1 + \varepsilon)/(\eta_p \times \eta_m) - (1 - \varepsilon) \times (\eta_t \times \eta_g)$ | 0.80 | 0.61 | 1.53 |
| A = Electric Power for water circulation (kW) = SPR × HP | 3590 | 2738 | 8117 |
| B = Electric Power for bulk cooler (kW) = CC/EER | 710 | 710 | 710 |
| C = A + B | 4300 | 3448 | 8827 |
| Total Required Electric Power for water circulation underground (kW) | | | |
| Electricity Costs (million $CAD/yr) | 4.52 | 3.63 | 7.50 |

## 5  Conclusion

Results indicated (as shown in Table 2) that an annual electricity cost of CAD\$4.52 million, CAD\$3.63 million and CAD\$7.50 million could be realised by implementing the turbine-generator combination (first scenario), turbine-pump combination (second scenario), and absence of hydraulic recovery system (third scenario), respectively. Results of this study highlight that implementation of such energy recovery systems could facilitate large savings along with certain operational advantages by mitigating pressure and temperature rise within the system. Furthermore, the turbine-generator combination (first scenario) is slightly less energy efficient than the turbine-pump combination (second scenario), which leads to the more efficient turbine-pump combination having the lowest operating costs from the three scenarios.

## References

1. Underground Mining: Ventilation. Ministry of Labour, Ontario, CA (2011)
2. Ghoreishi-Madiseh, S.A., Sasmito, A.P., Hassani, F.P., Amiri, L.: Performance evaluation of large scale rock-pit seasonal thermal energy storage for application in underground mine ventilation. Appl. Energy. **185**(Part 2), 1940–1947 (2017)
3. Schweitzer, J.K., Johnson, R.A.: Geotechnical classification of deep and ultra-deep Witwatersrand mining areas, South Africa. Miner. Deposita **32**, 335–348 (1997)
4. https://www.mindat.org/glossary/deep_mining
5. Vosloo, J., Liebenberg, L., Velleman, D.: Case study: energy savings for a deep-mine water reticulation system. Appl. Energy **92**, 328–335 (2012)
6. du Plessis, G.E., Liebenberg, L., Mathews, E.H.: Case study: the effects of a variable flow energy saving strategy on a deep-mine cooling system. Appl. Energy **102**, 700–709 (2013)
7. Mackay, L., Bluhm, S., Van Rensburg, J.: Refrigeration and Cooling Concepts for Ultra-deep Platinum Mining. The Southern African Institute of Mining and Metallurgy (2010)
8. Darling, P.: SME mining Engineering Handbook, 3rd edn. Society for Mining, Metallurgy, and Exploration (2011)
9. Ghoreishi-Madiseh, S.A., Sasmito, A.P., Hassani, F.P., Amiri, L.: Heat transfer analysis of large scale seasonal thermal energy storage for underground mine ventilation. Energy Procedia **75**, 2093–2098 (2015)
10. Xiaojie, Y., Qiaoyun, H., Jiewen, P., Xiaowei, S., Dinggui, H., Chao, L.: Progress of heat-hazard treatment in deep mines. Min. Sci. Technol. (China) **21**, 295–299 (2011)
11. He, M., Cao, X., Xie, Q., Yang, J., Qi, P., Yang, Q., et al.: Principles and technology for stepwise utilization of resources for mitigating deep mine heat hazards. Min. Sci. Technol. (China) **20**, 20–27 (2010)
12. Wagner, H.: The management of heat flow in deep mines (part 2). Geomech. Tunn. **4**, 157–163 (2011)
13. Howes, M.J., Hortin, K.: Surface Cooling at Kidd Creek Mine. Eighth International Mine Ventilation Congress, Brisbane, Australia (2005)

14. Moore, P.: Refrigeration Applications in Mining—Standing the Heat. Mining Magazine (2007)
15. Werniuk, J.: LaRonde Extension. http://www.canadianminingjournal.com/features/laronde-extension/ (2008)
16. McPherson, M.J.: Subsurface Ventilation Engineering (2008)
17. Whillier, A.: Recovery of energy from the water going down mine shafts. J. South Afr. Inst. Min. Metall. **77**, 183–186 (1977)
18. Stephenson, D.: Distribution of water in deep gold mines in South Africa. Int. J. Mine Water **2**, 21–30 (1983)

# Efficiency of Cooling Methods in Polish Underground Mines

Nikodem Szlązak [ID], Dariusz Obracaj[(✉)] [ID], Marek Korzec [ID], and Justyna Swolkień [ID]

AGH University of Science and Technology, Al. Mickiewicza 30, 30-059
Kraków, Poland
obracaj@agh.edu.pl

**Abstract.** This paper highlights the specificity of work in the underground mine. The cooling methods in Polish underground mines are characterised. Mine refrigerators, water chilling machines and spot air-coolers are described. Indirect and direct refrigerators are specified. The operation parameters of these devices are presented. In the Polish mining industry the classification of cooling systems depends on the location of the refrigeration equipment. Depending on that three types were used: local cooling including workplace cooling, group and central cooling systems. Practical information on the proper planning of these cooling systems are provided. The audit results of the cooling systems in selected coal mines are also presented. Attention was paid to the low efficiency of the tested cooling systems. The reasons for this state are specified and described.

**Keywords:** Mine cooling · Cooling systems · Cooling efficiency

## 1 Introduction

Please note that the first paragraph of a section or subsection is not indented. The first paragraphs that follows a table, figure, equation etc. does not have an indent, either. Underground mining is connected with the occurrence of many threats. Apart from technical threats also natural threats have the influence of the safety. Natural threats are connected with rock massive surrounding excavations (water, rock and gas outburst, gas and ash explosions, cramps, and hot microclimatic conditions). During the last few years in Polish underground mines microclimate conditions have become worse. Ensuring appropriate microclimate conditions using only ventilation methods are very difficult. It is related to increasing depth, the intensification of mining activities and the extent of mechanization. Considering these factors, it should be stated that the conditions of the microclimate in Polish mines will be even worse in the future.

There are natural and technological sources of heat in underground mines. The high temperatures of air occur as the result of heat transfer into the mine excavations. Also, high humidity makes that the microclimatic conditions are very bad. Bad microclimatic conditions have hot influence for miners underground causing reduction of perception, concentration, attention, and perceptiveness. They lead to serious heat-related health hazards such as heat exhaustion, heat syncope, and heat stroke other conditions [1, 2].

For ensuring safety working terms in underground excavations cooling systems are used. Sometimes underground mining activities are conducted in a very large area. Depending on the dispersion of mining areas in mines different types of cooling systems are used. Personal cooling systems are made use of, spot cooling system (known as a local cooling system), large underground or surface cooling systems known as centralized cooling systems). The effectiveness of these cooling systems depends on different factors. The precise design of such systems is necessary due to their subsequent expansion along with the expansion of future areas of mining in a mine.

## 2    Sources of Heat in Mine Excavations

Subsequent paragraphs, however, are indented. The level of the hot microclimatic condition depends on the parameters of air in mine excavations. The parameters of air are changing when the air flows through a mine excavation. Changes in air temperatures are the consequence of processes of air compressing in fields of gravitational forces as well as heat and moisture exchange between rock-mass and flowing air. The heat transfer process towards the mine excavation from exposed rock mass surfaces takes place by means of convection, radiation, and conduction. There is the latent heat transfer from fissure water or technological water towards to the ventilation air, too. Machinery and equipment, especially electric and diesel engines are extra sources of heat load. Airways from the surface to the mining districts in many cases are several kilometres long in Polish mines [3–5]. The intensity of heat and moisture exchange depends on many factors, but the biggest influence on this process has the thermal properties of rocks. These properties impact the rate at which virgin rock temperature varies with depth.

The relationship between Virgin Rock Temperature (VRT) and depth for different mining areas all over the world are presented in Fig. 1. In Polish conditions, there is high geothermal gradient compared to other countries. It causes that VRT is very high on the depth 800–1000 m below the surface. The surface level is about 250 m above sea level. The average depth of mining activities in Polish mines reached 800 m below the surface level in 2016 and rising about 8 meters every year. In the deepest Polish mines VRT is greater than 50 °C. The relationship between VRT and the depth for the Upper Silesia Coal Basin are presented in Fig. 2. High VRT on the deepest level and use of machines cause that in mines occur hot microclimatic conditions. Electric equipment of total power reaching 2–4 MW is located in the typical Polish longwall panel in a coal mine.

Apart from VRT and machines in excavations also other factors influence on shaping microclimate conditions in underground mines:

– thermophysical properties of rocks (thermal conductivity, thermal capacity, thermal diffusivity, density etc.),
– the temperature of flowing air and its changes,
– airflow velocity and time of existence excavations,
– pressure drop in mine excavation.
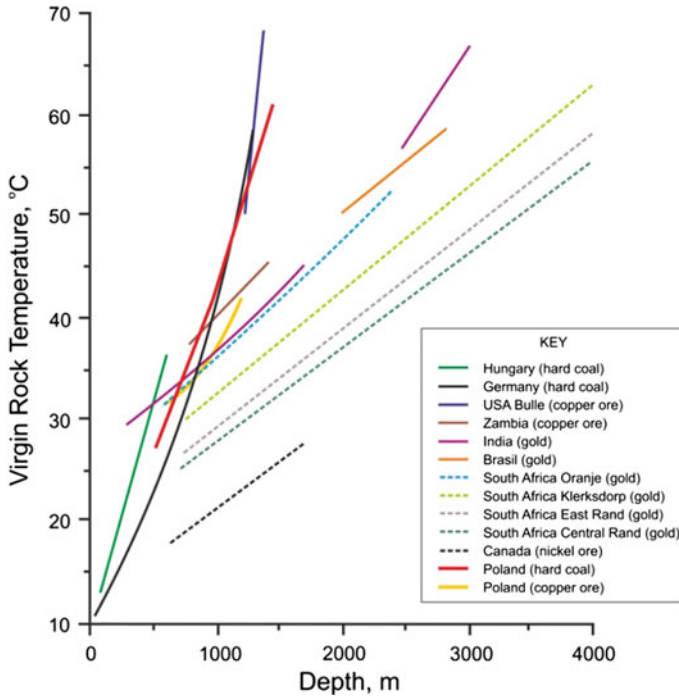
**Fig. 1.** Relationship between Virgin Rock Temperature and depth for different basins all over the world

For thermal working conditions in a hot mine, the environment also influences the proper planning of underground excavations, the organization of transport, localization of electric devices, and rational ventilation. Heating of fresh air flowing to the working areas should be avoided in the mine with hot microclimate problems.

In the near future, a further deterioration in thermal conditions in Polish coal mines can be expected as a result of an increased extraction concentration and mining at deeper and deeper levels. The design cooling systems is very important for ensuring the safety for miners working in hot mine microclimate.
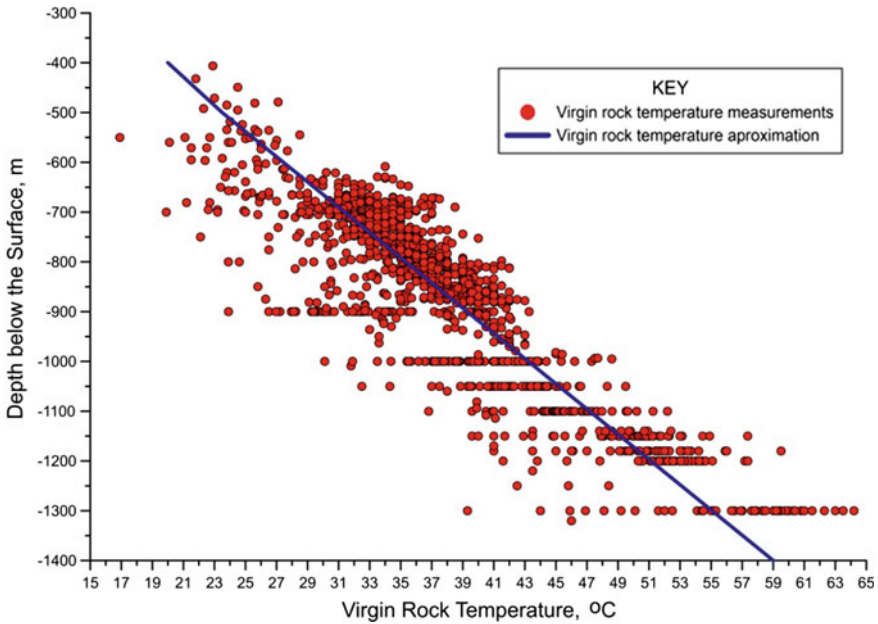
**Fig. 2.** Relationship between Virgin Rock Temperature and depth for Upper Silesia Coal Basin

## 3   Cooling Systems in Polish Mines

The primary, secondary, and tertiary cooling system is known in global mining [6–9]. Polish mines use systems that can be classified as tertiary (in-stope) cooling systems. In Polish mines, primary cooling systems based on bulk air cooling are not used. Only underground or surface refrigeration plants are used [10].

Cooling systems in the Polish mining industry is based on the use of the following refrigeration units.

- Refrigerating machines of little power of several hundred kW, which are direct or indirect air-cooling units in the tertiary cooling system. Individual movable vapour-compression machines are used in this system. Condensed heat can be directly transported by a water to mining wastes or through water pipes to an evaporative cooler of water (indirect-contact heat exchanger). This is a decentralized cooling system, which is known as spot cooling systems, or in-stope air cooling system [6]. The cooling system is called "local cooling system" in the Polish mining industry.
- Stationary cooling units of a few MW cooling power with chilled water in closed circuits, which cool the air in spot coolers placed close to workplaces. Movable cooling-coil heat exchangers as spot air-coolers are used in this system. A dozen or so spot air-coolers can be connected to a chiller several kilometres away. This is the centralized cooling system. The cooling system is called a "group cooling system" in the Polish mining industry.

- An underground refrigeration plant consisting of two or three water chilling machines (chillers) connected in parallel, which is placed close to the downcast shaft. The cooling duty of the refrigeration plant is from 2 to 5 MW of cooling power. Chilled water is transported to air spot air-coolers while water cooling a condenser is taken out through pipelines to the surface. The cooling system is called a "central cooling system" in the Polish mining industry.
- A surface refrigeration plant consisting of several chillers connected to a cascade system and chilling water or brine taken down through shafts or special holes. Chilled water is directly distributed to spot air-coolers in a mine. The cooling system is called a "central cooling system" in the Polish mining industry as well.

Three types of cooling systems are used in Polish underground mines taking account the above mentioned and are presented in Fig. 3. The individual cooling systems are applied in mines using diesel engine vehicles. The decision which cooling system should be used depends on the demand for cooling power in working areas. The possibility of locating a water chilling plant underground or on the surface is also an important factor influencing the decision on the choice of air cooling system. The next important issue is connected with the possibilities of rejecting condensed heat to mine excavations [11]. Some limitations of applying cooling systems could be the distance between working areas and place of localization refrigeration plants (chillers).
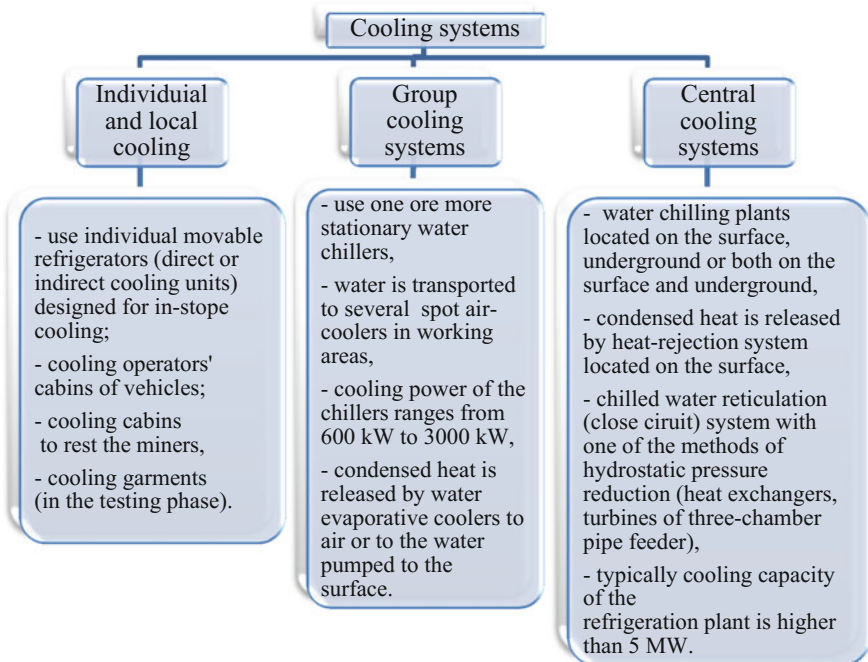


**Fig. 3.** Cooling systems in Polish underground mines

Hard coal, copper ore and salt are extracted using underground mining technology in the Polish mining industry Hot microclimate conditions occur only in some coal mines and copper ore mines. The localization of coal and copper ore basins are presented in Fig. 4. Nowadays, only one big coal mine (10 mln Mg coal output) is located in the Lubelskie Coal Basin. The 19 coal mines operate in the Upper Silesian Coal Basin, but some of them are complex mines (one mine is a combination of several mines). Three mines work on a copper ore basin.



**Fig. 4.** Localization of coal and copper ore deposits in Poland

The majority of Polish mines extract coal seams in the Upper Silesian Coal Basin. In this basin, the average geothermic gradient is about 33.2 m/°C, which means that the virgin rock temperature at the depth of 1000 m is approximately 40 °C. Locally, in some mines, the virgin temperature of rocks at this depth reaches 45 °C.

The average geothermic gradient in copper ore mines is even lower and is greater than 27.4 m/°C in the south-eastern part and 30.2 °C in the north-western part of the Lubin-Sieroszowice ore deposit. The result is that the virgin rock temperature at the depth of 1100 m, on which mining operations are currently carried out, is 45 °C.

There is a gradual increase of heat loads connected with localization working areas on deeper levels where VRT is higher in most of the Polish underground mines. Chillers located in plants on the surface or underground are typically used when the request for cooling power is high and there are many cooling places in mining districts. Localization refrigeration plant underground and rejecting condensed heat to ventilation air are limited. When the power of the refrigeration plant is relatively big or when condensed heat cannot be released underground then it has to be transferred to the surface. Different types of mining systems in mines are used, and this fact determines

types of different cooling systems are used. The longwall mining system is used in coal mines. In turn, the room and pillar mining system is made use of in copper ore mines.

The total cooling duty of refrigeration machines applied underground has risen for many years in the Polish mining industry. The total duty of installed refrigeration machines in all Polish mines achieved 193 MW in 2016. The changes of total cooling capacity in Polish underground mines are presented in Fig. 5.
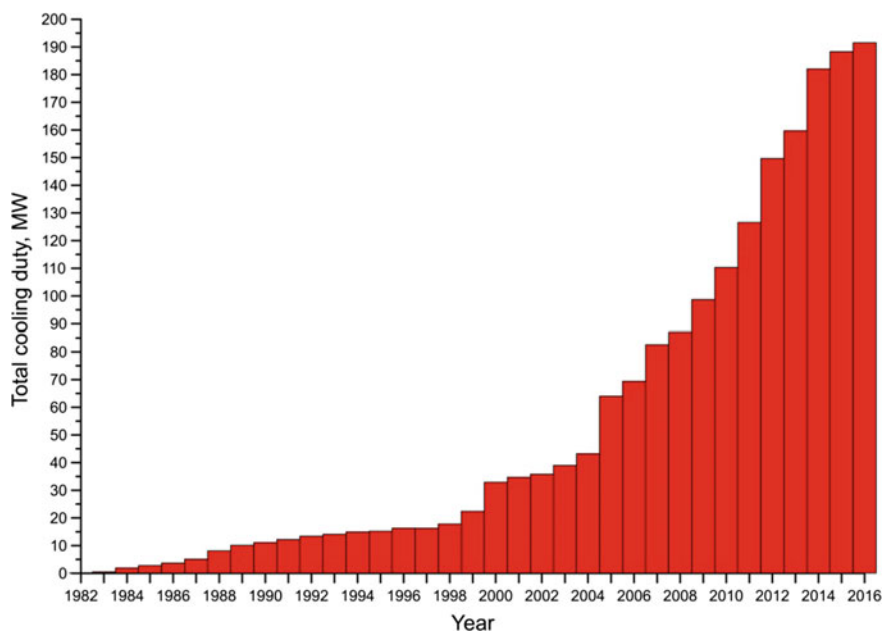


**Fig. 5.** Changes in total cooling duty in Polish underground mines

Different types of cooling systems are used in underground mines depending on the request for cooling power. The percentage of total cooling duty which is generated by refrigeration machines in three types of cooling systems in Polish coal mines in 2016 are presented in Fig. 6. The short characteristic of cooling systems installed in each Polish coal mine is listed in Table 1.

In 2017 took place restructuring in the Polish coal mining industry, and some cooling systems (especially local cooling systems) were shut down. Probably the total cooling capacity in 2018 will be 10% lower than in 2016. To ensure maximum efficiency of the cooling system it is very important to design it very properly. The issues related to designing cooling systems in Polish conditions are presented in the next part of the article, because there are many factors which have an influence on the design process. Those issues are related also to the extension and reconstruction of cooling systems in the life of a mining project.
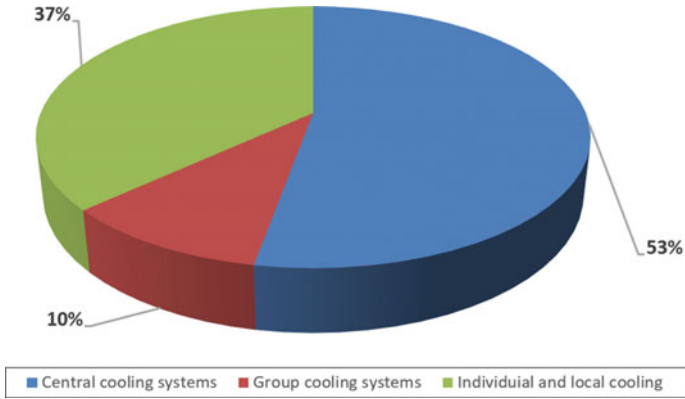
**Fig. 6.** Percentage of cooling duty in cooling systems in Polish coal mines in 2016

**Table 1.** Cooling systems in underground Polish mines in 2016

| No | Company | Coal Mine—Operation | Cooling system | Total cooling duty (MW) |
|---|---|---|---|---|
| 1 | PGG | ROW—O.Jankowice | Local | 2.5 |
| 2 | | ROW—O.Chwalowice | Local | 1.5 |
| 3 | | ROW—O.Marcel | Local | 3.0 |
| 4 | | ROW—O.Rydultowy | Group and local | 5.0 |
| 5 | | Ruda—O.Bielszowice | Group and local | 5.0 |
| 6 | | Ruda—O.Halemba | Local | 4.0 |
| 7 | | Ruda—O.Pokoj | Local | 1.0 |
| 8 | | Piast-Ziemowit—O.Piast | Local | 1.0 |
| 9 | | Piast-Ziemowit—O. Ziemowit | Local | 1.0 |
| 10 | | Boleslaw Smialy | Local | 2.5 |
| 11 | | Sosnica | Local | 3.0 |
| 12 | | Murcki-Staszic | Group and local | 6.0 |
| 13 | | Myslowice-Wesola | Group and local | 2.0 |
| 14 | | Wieczorek | Local | 1.0 |
| 15 | | Wujek | Group and local | 4.5 |

(*continued*)

**Table 1.** (*continued*)

| No | Company | Coal Mine—Operation | Cooling system | Total cooling duty (MW) |
|---|---|---|---|---|
| 16 | JSW S.A. | Pniowek | Central | 13.0 |
| 17 | | Borynia-Zofiowka-Jastrzebie—O.Borynia | Group and local | 4.0 |
| 18 | | Borynia-Zofiowka-Jastrzebie—O.Zofiowka | Group and local | 5.0 |
| 19 | | Borynia-Zofiowka-Jastrzebie—O.Jastrzebie | Group and local | 4.0 |
| 20 | | Knurow-Szczyglowice | Local | 4.0 |
| 21 | | Budryk | Group and local | 10.0 |
| 22 | TAURON | Brzeszcze | Local | 2.0 |
| 23 | | Janina | Local | 1.5 |
| 24 | | Sobieski | Local | 0.5 |
| 25 | Weglokoks | Bobrek-Piekary—O.Bobrek | Local | 2.0 |
| 26 | | Bobrek-Piekary—O. Piekary | Local | 2.0 |
| 27 | PG Silesia | PG Silesia | No cooling system | 0.0 |
| 28 | Kazimierz Juliusz Sp. z o.o. | Kazimierz Juliusz | No cooling system | 0.0 |
| 29 | LW Bogdanka S. A | LW Bogdanka | Central | 15.0 |
| 30 | KGHM | ZG Rudna | Central | 50.0 |
| 31 | | ZG Polkowice-Sieroszowice | Central | 20.0 |
| 32 | | ZG Lubin | Local | 2.0 |
| 33 | SRK | Mines in the restructuring process | Group and local | 15.0 |
| – | **Total** | – | – | **193.0** |

The appropriate design of air conditioning systems is very important to achieve maximum efficiency in the use of cooling duty. Due to the fact that many factors affect the subsequent operation of the air conditioning system. The next part of the article presents the issues concerning the design of air conditioning systems in underground mines, which are considered and analyzed in the conditions of Polish underground mines. These issues also concern the development and reconstruction of air conditioning systems.

## 4    Cooling Systems in Polish Mines

### 4.1    Factors Influencing the Design Process

Choosing a proper cooling system for the condition of a mine is a very complex issue and should be supported by an analysis including factors such as:

– predicting microclimate conditions in excavations according to the schedule of development headings and mining district,
– directions of development mining districts after start using the cooling system,
– predicted request for cooling power in mine,
– verification places for localization chillers underground or on the surface,
– technical and economic analysis.

In many cases, it is very difficult to decide which type of cooling system and devices localization will be the best for the specific condition of a mine. Various concepts design of the system should be developed and an analysis has to indicate the most convenient system. The concept design of the cooling system should take into account many issues that need to be solved. The most important ones are as follows:

– determination number and localization of spot air-coolers (coil heat exchangers) or other devices of the cooling system (according to the prediction of microclimate conditions in excavations),
– connections between chillers and spot air-coolers using water pipelines,
– the balance of water in cooling system pipelines (according to water flow through the air-coolers),
– selection parameters of pipelines (diameter of pipes, the material of pipes, insulation parameters, etc.),
– performing pressure drop calculations (in order to select water pumps for the cooling system),
– performing calculations of the cooling power lost in pipelines (predicting the temperature of cold water in places of air-coolers' localization),
– selection of additional devices and technical equipment in the cooling system (filters, valves, safety valves, vent valves, temperature sensors, pressure sensors, etc.),
– determination places and parameters of devices responsible for the proper water flow in the cooling system (regulation valves parameters, etc.).

### 4.2    Development of Mining Districts

Mining progress in underground mines causes the ongoing movement of working areas. Knowledge about planned changes in underground excavations is very important for the proper localization of chillers in mines. The long distance between chillers and spot air-coolers in a working district causes that the effectiveness of cooling systems is relatively low. The analysis of the planned movement of working areas should be done before the designing cooling system. Experiences in Polish mines shows that when the distance between chillers and coolers are longer than 5000 m there is a considerable

increase in the heat gain in cold water pipelines. Then, the effect of cooling air in the working areas is insufficient.

Research conducted by the authors in underground mines shows that for spot air-coolers located at a long distance from chillers the temperature of cold water is significantly higher than for air-coolers located nearer. Particularly high temperatures were registered in single air-coolers for which the volumetric of the water flow was relatively low.

**Predicting microclimate conditions**. Only two levels of headings should be numbered. Lower level headings remain unnumbered; they are formatted as run-in headings.

Predicting microclimate conditions is very important in designing a cooling system. According to Polish regulations [12] when the Virgin Rock Temperature is higher than 30 °C predicting microclimate parameters is obligatory. Then also methods for preventing hot microclimate conditions have to be designed. The SCT index is calculated as following formula:

$$SCT = 0.6 \cdot t_w + 0.4 \cdot t_d - v_a \tag{1}$$

where:

$SCT$    substitute climate temperature, °C;

$t_w$    wet-bulb temperature, °C;

$t_d$    dry-bulb temperature, °C;

$v_a$    mean air velocity in the mine excavation, in meters per second multiplied by the conversion factor equal to $1\,\frac{\text{s}\cdot°\text{C}}{\text{m}}$

The SCT index is used for the following parameter limits:

- the mine air temperature measured with a wet-bulb thermometer or determined on the basis of dry temperature measurements, with relative humidity and pressure is no more than 30 °C,
- the mine air temperature measured with a dry-bulb thermometer or measurement sensor is no more than 35 °C,
- air velocity amounts to no more than 4 m/s.

If the air velocity in the mine excavation is greater than 4 m/s, the calculation is assumed to be 4 m/s.

Preventing thermal condition is difficult because many parameters and processes have an influence on temperature and humidity underground. Both the VRT and devices located in mine excavations are the most important factors. In Polish underground coal mines electrical devices are used (the summary power of devices in longwall panel is about 3.5–5.0 MW). In cooper ore mines also Diesel engine machines are used. Designing cooling systems without performing prediction of microclimate condition may lead to incorrect assumptions of cooling power demand.

Predicting microclimate conditions should be conducted for several periods of time in the future, according to the appropriate methodology. In Poland, a few methods are used for predicting microclimate conditions in mining excavations [5]. Some of them

are used to longwall panels, others for development headings. Example results of predicting microclimate conditions for longwall panel are presented in Fig. 7.
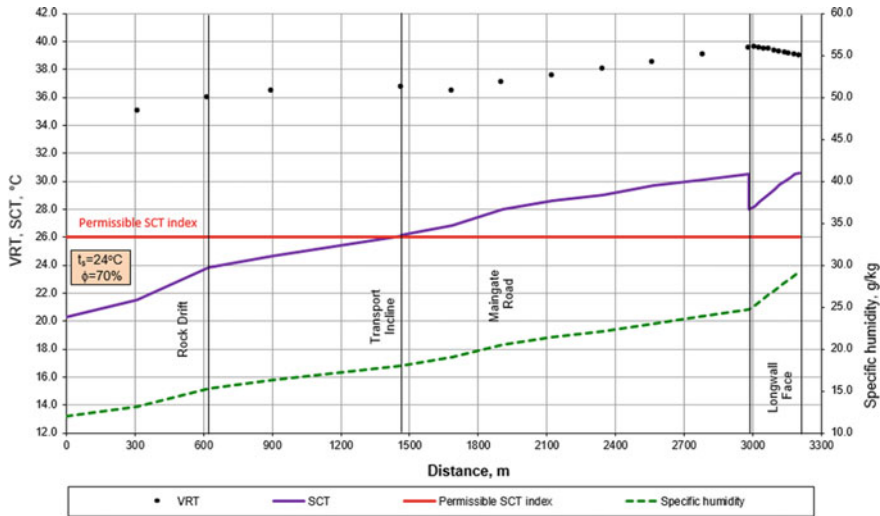


**Fig. 7.** Example of predicting microclimate condition in longwall panel

After predicting microclimate conditions should be taken a decision about the necessity of using the cooling system in a particular excavation. According to Polish regulations [12], a hot microclimate condition occurs in the excavation when the SCT index is above 26 °C. When the SCT index is not higher than 30 °C then the excavation belongs to the 1st category of hot microclimate condition. When the SCT index is not higher than 32 °C then the excavation belong to the 2nd category. A SCT index above 32 °C means 3rd category, and work in the excavation is forbidden.

In addition to temperature also humidity is very important during performing prediction of microclimate condition. The cooling capacity of air-coolers is provided by producers assuming that the relative humidity in the inlet to the air cooler is no higher than 70%. In many cases, air coolers are located in excavations where the relative humidity is higher than 80%. Then, despite providing other parameters (water volumetric flow and their temperature), cooling capacity is lower than theoretically possible to obtain. The high humidity of air makes reducing the temperature of the air difficult, because a big part of the cooling capacity is spent on reducing humidity. The percentage of distribution cooling capacity in air coolers in 6 mines (data from the measurements performed by the authors in the mines) is presented in Fig. 8. In those mines, 20–45% of the cooling capacity of the coolers is spent on cooling of drying air. The abovementioned shows that are very important to reduce unnecessary humidification of air in excavations, especially in mining districts where cooling systems have to be used.
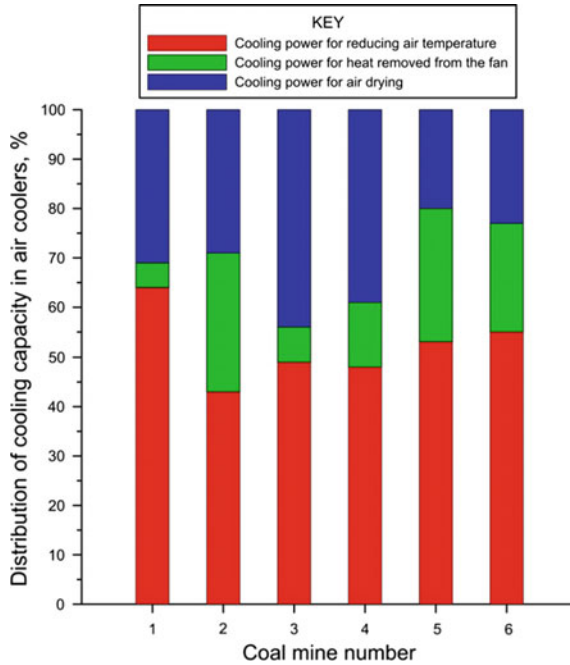
**Fig. 8.** Percentage of distribution cooling capacity in air coolers in 6 mines

**Request for cooling power in mine**. In Polish underground mines requests of cooling power is established according to the prediction of a microclimate condition. An example of establishing a request of cooling power in longwall panel is shown in Fig. 9. The authors conducted many measurements in most of the cooling systems in underground mines [13]. The results of the measurements show that the average efficiency of air coolers reaches 70% (for air coolers with accurate water volumetric flow and temperature). This fact should be included in establishing requests of cooling power in mines. An impact on the low effectiveness of air coolers has also the cleanliness of exchangers in coolers. The heat transfer from the coolers' fans to cooling air is very important, too.

The calculation results of the requirement cooling power, for the selected period of time, are characterised by fluctuations. An example of establishing the required cooling power in a mine for several years of mining activity is shown in Fig. 10. The cooling system should be designed for the period of time when those requirements are stable, and have to allow to reduce temperature in mining districts to acceptable limits.

Correctly made predictions of microclimate conditions and establishing the correct requirement of cooling power is very important for:

- choosing a proper cooling system,
- localization chillers in the group and central cooling systems,
- choosing a method for released condensed heat,
- choosing pipelines diameters,

– deciding where main pipelines should be installed,
– choosing control and measurements devices,
– choosing devices to regulate water flow in pipelines.
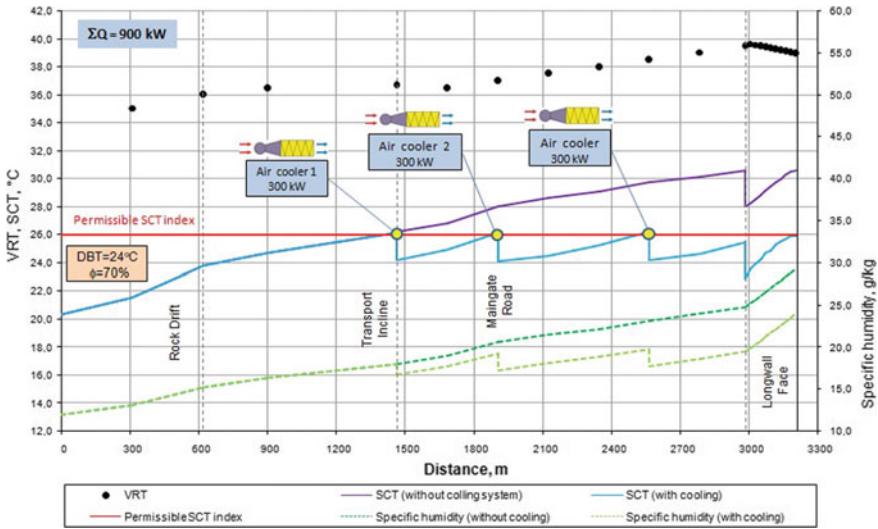


**Fig. 9.** Example of request for cooling power in longwall panel
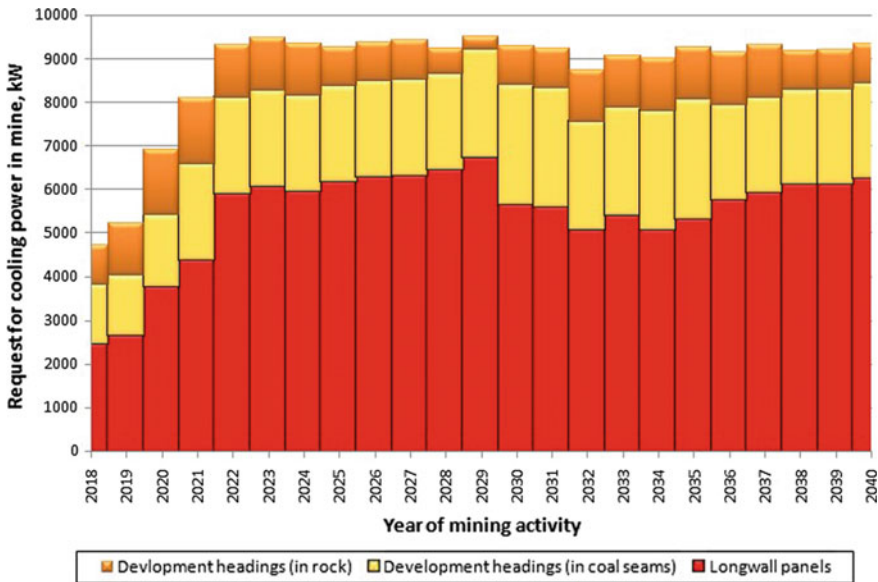


**Fig. 10.** Example of request for cooling power in mine

### 4.3   Choosing a Cooling System in Mine

Selecting a proper cooling system for an underground mine is difficult. Each mine has specific conditions and cooling systems have to match them. Very important are issues connected with the main parts of the system (like chiller types, chiller localization, pressure reducer or high-pressure heat exchanger, water pumps, water treatment stations, filters, heat exchangers, water tanks, air-coolers types, etc.). The cooling system needs free space underground (normally near a downcast shaft). Depending on the cooling system the excavation for the localization cooling system has to be 50–100 m length, have an appropriate cross-section area (of about 15–20 m$^2$) and air flow. Sometimes a new excavation has to be developed for the cooling system. In central cooling systems it is also very important to check the infrastructure on the surface. Moreover, the cross sectional area of the shaft has to be checked for installing water pipes. Pipes could be also installed in the boreholes.

In the case of group cooling systems it is very important to check for possibilities of released condensed heat underground. Condensed heat could be released into the air. Then the parameters and volumetric flow of air in the place of localization evaporative water coolers have to be appropriate. The temperature should be lower than 27 °C and relative humidity should not exceed 75%. There are also possibilities to release condensed heat to the water. In the Polish coal mining industry working two cooling system with released condensed heat to water underground (this water is pumped on the surface). Currently, one coal mine in the Upper Silesia Coal Basin considers also this solution. The most important for applying this solution is the flow rate of water pumped on the surface and its purity.

### 4.4   The Algorithm of Designing Cooling System in Mine

Designing a cooling system should be performed for the periods when the required cooling power and summary pipelines distance will be the biggest. During the design of the cooling system it is very important precisely to consider the main water pipeline route between the chiller and spot air-coolers. In practice in Polish mines use steel and PE pipes, which allow for 4 MPa pressure. During planning localization of chiller and air-coolers should be used the rule that the elevation difference between the deepest and the highest cooler should not be more than 250 m. Sometimes additional pumps or pressure reducers have to be used.

The block scheme of designing a cooling system in a mine is presented in Fig. 11. Polish coal mine experience shows that loss of heat between chillers and air-coolers is very important for the efficiency of the cooling system.

### 4.5   The Influence of Selected Technical Parameters for the Effectiveness of a Cooling System

Research conducted in Polish mines shows that in cooling systems with long distances of cold water distribution pipelines the occurred heat loss is because water is warmed by air flowing through the excavations. Loss of heat has a big influence on the effectiveness of the cooling system. It could be considered that heat is not lost because
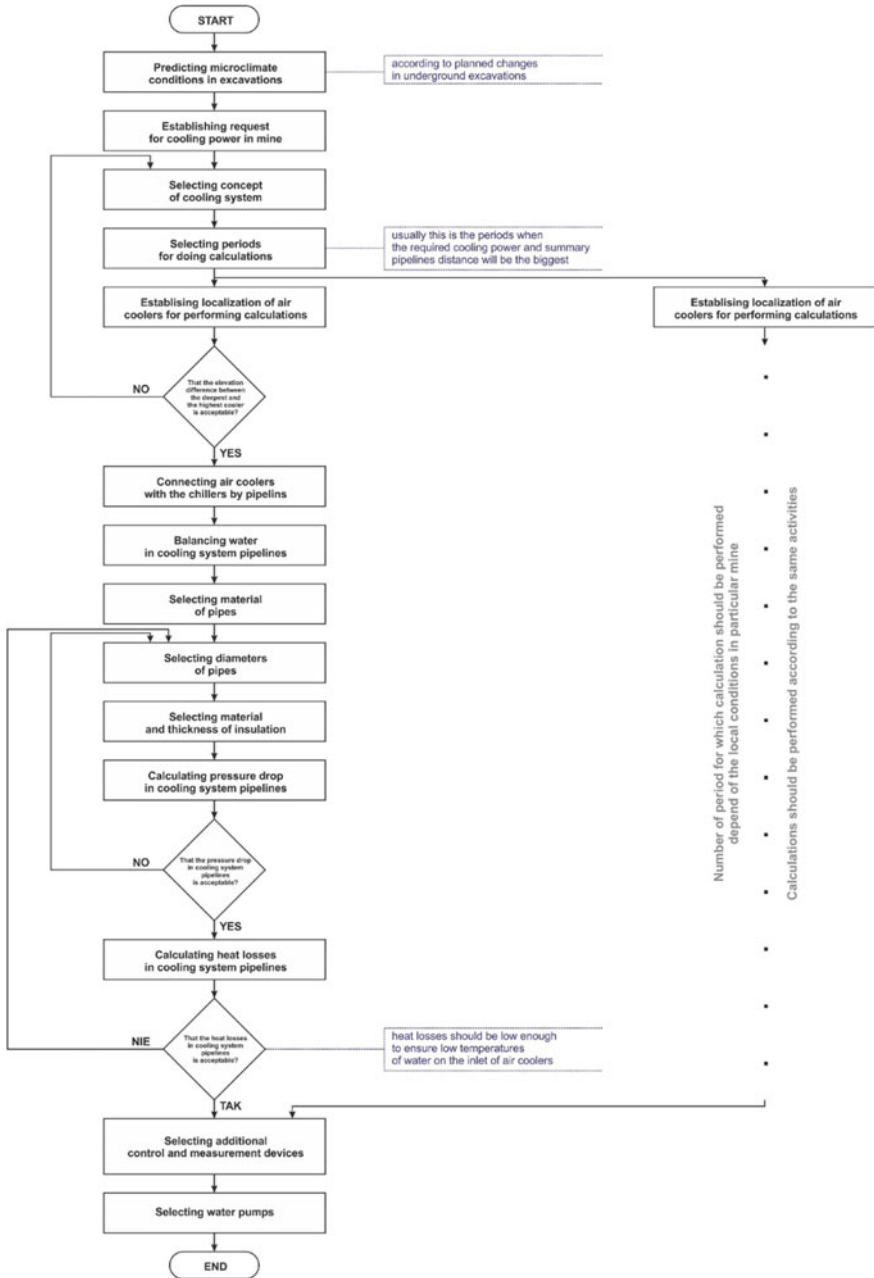
**Fig. 11.** Block scheme of designing cooling system in mine

there is warmed water cool air in excavations. The loss of heat caused that the water on the inlet of the air cooler is higher so the effectiveness of cooling in working areas is lower. Loss of heat depends on the water velocity in pipelines. Low velocity (lower than 0.5 m/s) causes the intensification of heat exchange between water in the pipes and air in the excavation. Water velocity should be within the range 0.5–2.0 m/s. High water velocity causes a high pressure drop in pipes. When the number of spot air-coolers in the mining district changes sometimes pipes have to be rebuild. Loses of cooling power in water pipelines for six mines are presented in Fig. 12.
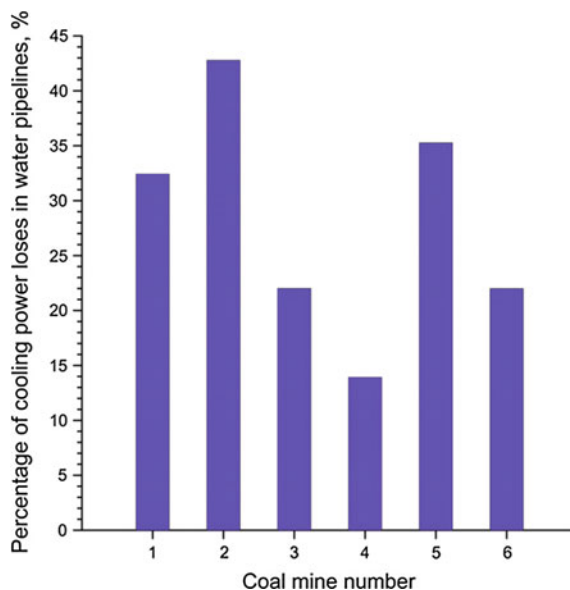


**Fig. 12.** Loses of cooling power in water pipelines for six mines

It needs to be highlighted that the loss of cooling power in many cases is not higher than had been assumed in the project of the cooling system. However, this fact should be noted during the cooling system design. The condition of pipelines isolation should be checked during the operation of the cooling system.

Measurements conducted in mines show that ongoing support of cooling systems in mines is very important. Caring about proper water flow in pipelines is one of the most important issues for achieving the high effectiveness of air cooling. In particular cases, it was found that the air cooling effect by air-coolers was very low. The reasons for the low cooling are presented below.

- Too small volumetric water flow in air coolers (no flow control and regulation of water flow, too much resistances, no rebuild of main pipelines). In Fig. 13 the relationship between cooling power and cold water volumetric flow is shown.
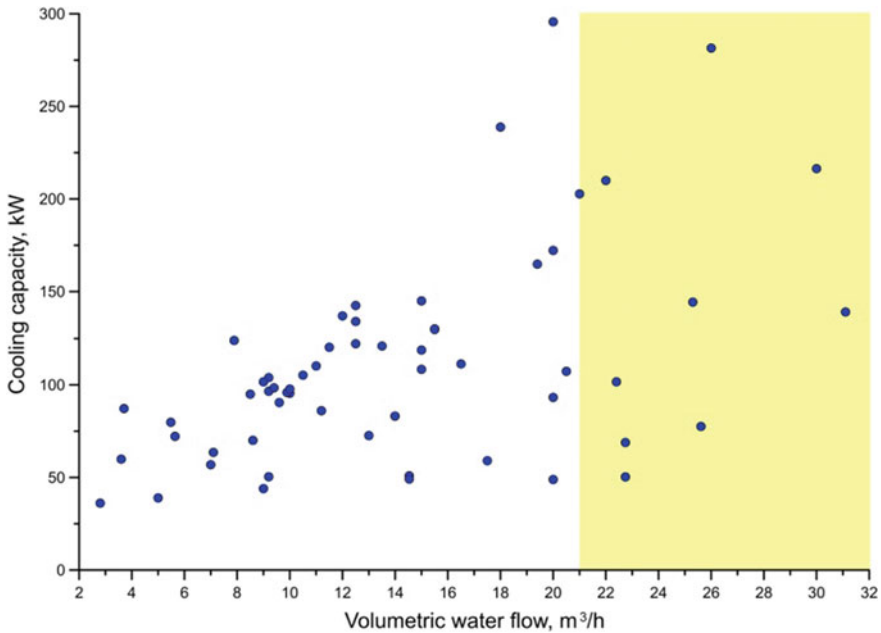
**Fig. 13.** Relationship between cooling power and cold water volumetric flow

- Too high temperature of water in air cooler inlet (no flow control and regulation of water flow). In Fig. 14 the relationship between cooling power and cold water temperature is shown.
- Too low temperature of air in the place of localization air coolers (wrong location of air coolers). In Fig. 15 the relationship between cooling power and air temperature before the cooler is shown.

There are marked the areas of required water and air parameters in Figs. 13, 14 and 15. For achieving the required cooling power of air-coolers, both water and air before the coolers have to be within these ranges. Moreover, very important is caring for the cleanliness of the heat exchangers of the air-coolers.

## 4.6 Expansion and Rebuilding Cooling Systems

Apart from designing new cooling systems very often systems working in mines have to be expanded. Then the same rules should be applied that are presented in the article. The next issue connected with cooling systems is current rebuilding. Mining progress in underground mines causes the ongoing movement of working areas and new pipelines have to be built. Those pipelines should have a proper diameter that does not exceed water pump parameters (maximum pressure drop). The diameters of the pipelines should also allow achieving a low temperature of water on the inlet of the spot air-coolers.
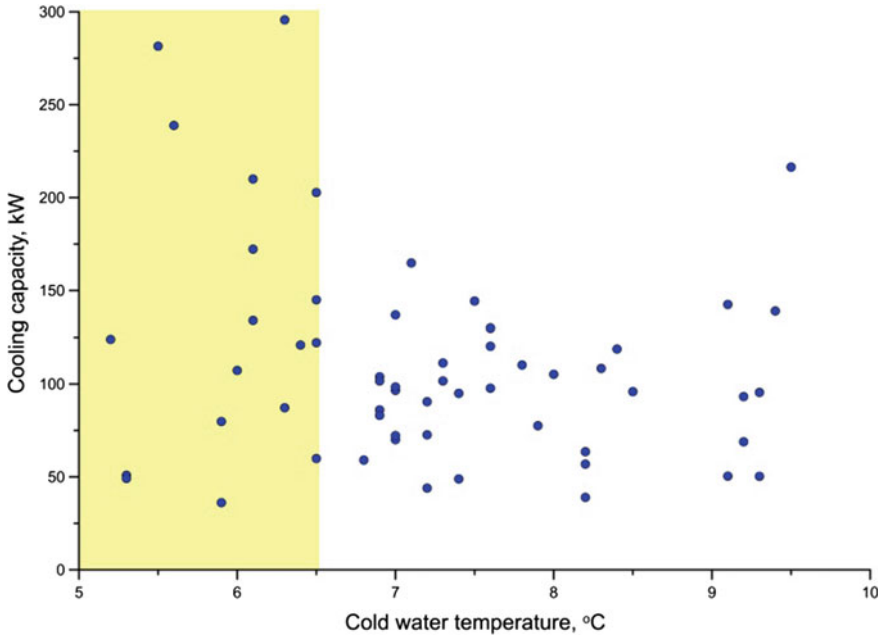
**Fig. 14.** Relationship between cooling power and cold water temperature
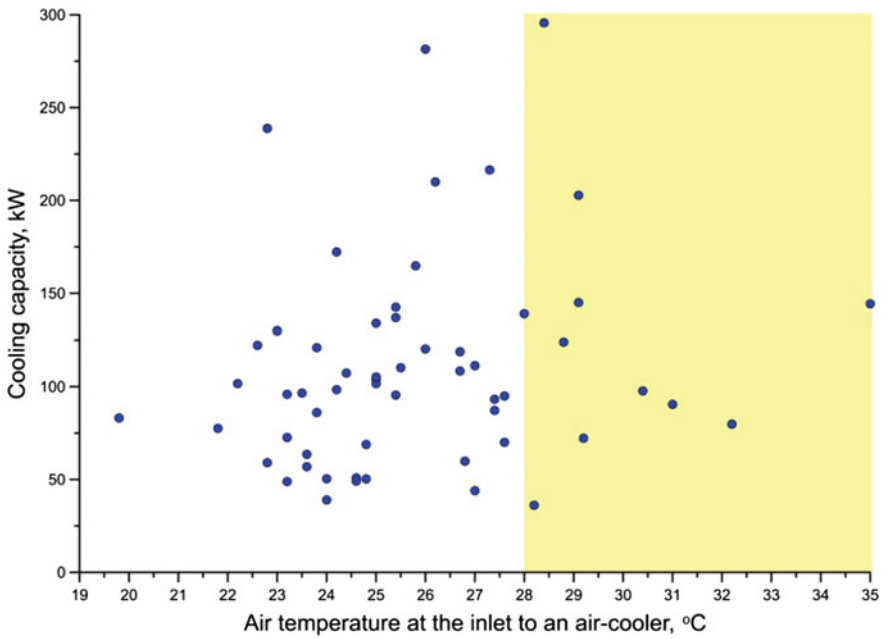


**Fig. 15.** Relationship between air temperature before an air-cooler

Because the issues related to designing cooling systems are very complicated computer software is very helpful to perform calculations. In Poland for this purpose could be used KlimaSystem software. The program can be used not only to design new cooling systems, but it also can be helpful in rebuilding and expanding working systems. The program can also be adapted for cooperation with control and measurement devices in cooling systems and for example used to the controlled distribution of chilled water.

## 5    Conclusions

The parameters of air change when air flows through mine excavations. The level of hot microclimate depends on the parameters of air flowing through mines, both in coal and copper ore mines. In Polish conditions, there is a high geothermal gradient of the strata. It causes that in underground excavations there occurs high VRT. High VRT on the deepest levels and the use of machines causes that in mines occurs hard thermal conditions.

Increasing ventilation intensity and eliminating heat sources from intake airways are the basic ways of improving thermal work conditions in Polish coal mines. However, if an increase in air flow rate results in an increase in heat transfer coefficient as well as an increase in heat flux rock walls, it is necessary to use cooling systems. Different types of cooling systems may be used in mines. Choosing a proper cooling system for the condition of a mine is a very complex issue and should be supported by an analysis including many factors.

The appropriate design of air conditioning systems is very important to achieve maximum efficiency in the use of cooling duty. Measurements carried out by the authors on most of the Polish cooling systems in underground mines confirmed that proper designing and current service is important for achieving high efficiency of cooling. The methodology presented in this article could be useful for designing new cooling systems or the expansion and rebuilding of existing ones.

## References

1. Kocsis, K.C., Sunkpal, M.: Identifying and controlling heat-induced health and safety problems in underground mines. Min. Eng. **69**(9), 53–60 (2017)
2. Maurya, T., Kailash, K., Vardhan, H., Aruna, M., Raj, G.M.: Potential sources of heat in underground mines—a review. Procedia Earth Planet. Sci. **11**, 463–468 (2015)
3. Szlązak, N., Nawrat, S., Jakubów, A.: Pierwsza klimatyzacja centralna w KWK "Pniowek" Jastrzębskiej Spółki Węglowej S.A. Przeglad Gorniczy no. 10 (2000) (*in Polish*)
4. Szlązak, N., Obracaj, D., Borowski, M., Swolkień, J.: Methods for improving thermal work conditions in Polish coal mines. In: Panigrahi, D.C. (eds.) Mine Ventilation, vol. 2—Proceedings of the Ninth International Mine Ventilation Congress, pp. 253–262. Oxford & IBH Publishing Co. Pvt. LTd, New Delhi (2009)

5. Wacławik, J., Cygankiewicz, J., Knechtel, J.: Warunki klimatyczne w kopalniach głębokich. Biblioteka Szkoly Eksploatacji Podziemnej. Wyd. PAN CPPGSMiE, Krakow (1995) (book —in Polish)

6. McPherson, M.J.: Subsurface Ventilation and Environmental Engineering. Springer Science & Business Media, New Delhi (2012)

7. du Plessis, J.J.L. (ed.): Ventilation and Occupational Environment Engineering in Mines, 3rd edn, revised and expanded. Mine Ventilation Society of South Africa, Johannesburg (2014)

8. Hartman, H.L., Mutmansky, J.M., Ramani, R.V., Wang Y.J.: Mine Ventilation and Air Conditioning, 3rd edn. Wiley, New York, USA (1997)

9. Ramsden, R., Branch, A.R., Wilson, R.: Factors influencing the choice of cooling and refrigeration systems for mines. Journal of the Mine Ventilation Society of South Africa **60** (3), 92–98 (2007)

10. Szlązak, N., Obracaj, D., Swolkień, J., Piergies, K.: Controlling the distribution of cold water in air cooling systems of underground mines. Arch. Min. Sci. **61**(4), 793–807 (2016)

11. Szlązak, N., Obracaj, D., Borowski, M.: Free-cooling in central air-conditioning systems of underground mines. Gornictwo i Geologia **4**(3), 122–131 (2009)

12. Regulation of the Minister of Energy of November 23, 2016 on Detailed Requirements for the Operation of Underground Mining Facilities (Dz. U. 2017 poz. 1118 z dnia 09.06.2017r.) —(Mining Law & Regulations in Poland)

13. Szlązak, N., Obracaj, D.: Methods of air-conditioning in mine excavations of underground mines. In: Szlązak, N. (ed.) Aktualny stan zagrozen aerologicznych w kopalniach podziemnych—Proceedings of the 9th School of Mining Aerology (ed. by), pp. 19–36. Art-Tekst Pub., Krakow (2017) (in Polish)

# Easy and Rapid In Situ Measurement
# of Thermal Conductivity of Rock

Masahiro Inoue[1(✉)], Bing-rui Li[2], and Akitaka Higuma[1]

[1] Kyushu University, Fukuoka, Japan
inoue@mine.kyushu-u.ac.jp
[2] Shandong University of Science and Technology, Qingdao,
People's Republic of China

**Abstract.** Thermal conductivity of rock is a basic characteristic concerning the safety and thermal environment in mines. However, considerable preparation work and time are necessary for the measurement by a typical measuring method. Although, a new measuring method based on heat conduction theory of spherical heat source was developed, an easy and rapid measuring method to measure in situ thermal conductivity has yet to be developed. The method was first theoretically examined by a computer simulation and several measuring devices were made based on the result for verification. The test using the devices was conducted for various materials in a laboratory. Comparative measurement using another device based on line heat source currently used was also conducted. In addition, thermal conductivities of rock in a mine were measured. As a result, it has been found that the in situ measurement by the new method can be done easily and rapidly with acceptable accuracy.

**Keywords:** Thermal conductivity of rock · Spherical heat source
In Situ measurement

## 1 Introduction

Thermal conductivity of rock is necessary for thermal environment simulation and fire safety evaluation of an underground space [1, 2]. Many researches on the measurement have been reported up to now [3–5]. However, a lot of preparation work and measurement time are required in current methods. The authors conducted studies of a method of measuring the thermal conductivity rapidly and easily in situ based on the heat conduction theory of spherical heat source and found it practical for the measurement with acceptable accuracies.

## 2 Theory

### 2.1 Spherical Heat Source Method

The following equation describes a steady state heat conduction by the spherical heat source [6].

$$Q = 2\pi di \cdot \lambda(\theta i - \theta e) \cdot de/(de - di) \tag{1}$$

Where, Q; heat supply (W), di; inside diameter (m), de; outside diameter, $\theta i$; inside temperature (K), $\theta e$; outside temperature, $\lambda$; thermal conductivity [W/(m · K)]. The next equation is derived when an outside diameter is considerably larger than the inside diameter.

$$Q = 2\pi di \cdot \lambda(\theta i - \theta e) \tag{2}$$

The thermal conductivity is obtained by the next equation.

$$\lambda = Q/(2\pi di(\theta i - \theta e)) \tag{3}$$

Here, it is necessary to confirm the steady state condition and good contact between the measuring probe and the rock.

## 2.2 Line Heat Source Method

Line heat source method is one of the major methods to measure the thermal conductivity of rock. The following equation is obtained when the line heat source is in a medium with uniform initial temperature distribution [7].

$$(\theta 2 - \theta 1)/\ln(t2/t1) = q / (4\pi\lambda) \tag{4}$$

where, t; time (s), $\theta$; temperature (K) and q; heat supply per length (W/m). The thermal conductivity is obtained by the following equation.

$$\lambda = q/(4\pi) \cdot \ln(t2/t1)/\theta 2 - \theta 1 \tag{5}$$

The above two equations took totally different approach, with the line heat source method using the temperature change with time while the spherical heat source method uses the steady state temperature independent of time. Since the line heat source method can obtain the value with high reliability, the value obtained can be used to calibrate the thermal conductivity obtained using the spherical heat source method in this research.

However, it is necessary to make a large and a small diameter hole in the rock for the measurement to achieve the analytical condition of the line heat source. The minimum length of the hole must be more than 30 times of the diameter. When the material is soft, this drilling is not so difficult, however it is considerably difficult when the material is as hard as rock. The drilling in rock in situ is more difficult.

## 3   Examination by Computer Simulation

The heat conduction simulation program for the temperature change by the spherical heat source and the line heat source using finite difference method was made and the calculations were done. The program adopted three dimensional orthogonal coordinate cells to be able to correspond to both the line heat source and the spherical heat source and to consider various boundary condition.

A 100-mm cubic sample is used as an analytical model for the simulation. A typical value of rock [density 2300 kg/m$^3$, thermal capacity 840 J/(kg K), and thermal conductivity 2 W/(mK)] are used for the cubic material. The spherical heat source with 5 mm diameter was set to the center of the cube.

Figure 1 shows the surface temperature change of the spherical heat source. The heat supply is 1 W. The steady state temperature of the heat source by the Eq. (2) is about 15 K when the boundary temperature is 0 K. The temperature rises by 12 K at 200 s after the beginning of the heating. It increases up to 80% of the steady state temperature in a short time.
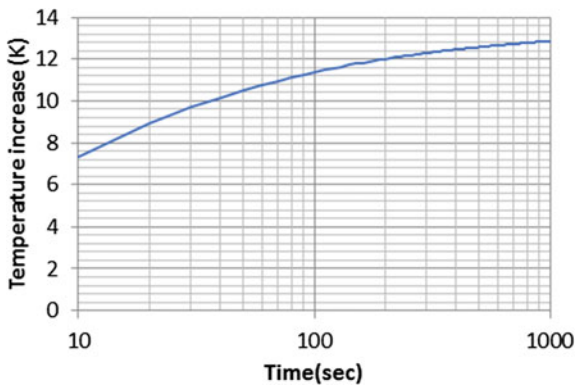


**Fig. 1.** Surface temperature change of the spherical heat source

## 4   Probes for Measurement

Two kinds of measurement probes were made, that is, probes for the spherical heat source method and probes for the line heat source method as shown in Fig. 2. Accurate thermal conductivity values can be obtained by the line heat source method as long as the measurement is properly conducted. So, the thermal conductivities obtained by the spherical heat source method are corrected by the values obtained by the line heat source method. The probe of the line heat source is 1 mm diameter and 50 mm in length. A nichrome heater (0.2 mm diameter, 34.4 Ω/m resistance) and thermistor are built into the probe. Two types of probes were made for the spherical heat source method. A probe uses a very small lamp (3 mm diameter) as the heat source and a

thermistor is used to measure the temperature. Another probe is coiling the nichrome wire heater around a thermistor. Both sizes are about 4 mm diameter and about 40 mm in length.
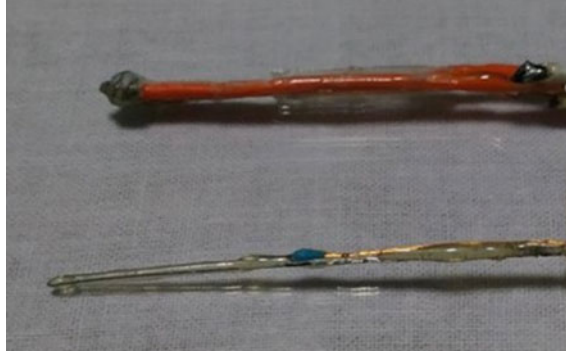


**Fig. 2.** Probes for the measurement by the spherical heat source method (up) and by the line heat source method (bottom)

## 5    Measurement in a Laboratory

Same material (filling material) was measured by the spherical heat source method and the line heat source method to confirm the accuracy of the spherical heat source method. As the result, the thermal conductivity was 1.18 on average by the spherical heat source method and 1.30 on average by the line heat source method.

The ratio of the values (line heat source method/spherical heat source method) is 1.10. It is thought to be reasonable to multiply 1.1 to the value obtained by the spherical heat source method to correct the thermal conductivity because the result of the line heat source method is more accurate than that of the spherical heat source method. Figure 3 shows an example of the surface temperature change of the spherical heat source obtained by the experiment.
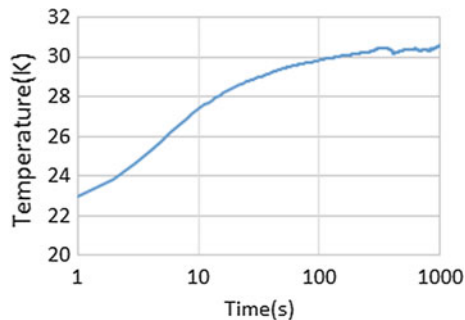


**Fig. 3.** Surface temperature change of the spherical heat source in the laboratory

## 6    Measurement in a Mine

An in situ measurement was conducted in a mine by the spherical heat source method. The measurement was done in a short time, and ended within 30 min for each measuring point including the preparation work. An example of the measured temperature change is shown in Fig. 4. The thermal conductivities were estimated as the following values. The data are corrected by multiplying 1.1 on the raw data as previously explained.
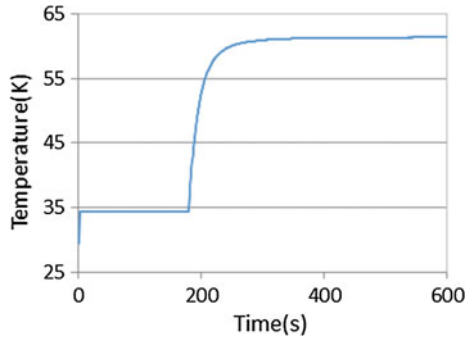


**Fig. 4.** Surface temperature change of the heat source during the measurement in a mine

(1)  Tuff; 0.79, the difference among four measurements is within 10%.
(2)  Sandstone; 1.23, the difference between two measurements is about 20%.

According to the obtained data about the mine up to present are, 1.4 to 2.5 for tuff and 2.6 to 3.6 for sandstone. The measurement result is small compared to these values.

## 7    Re-measurement in the Laboratory

It seemed that the measured thermal conductivities in situ were too small as described in the previous session. The following problems were found through the examination of the measured data. That is, temperature increase is too high and the time required to reach the steady sate is considerably shorter than that required in the previous simulation. It was thought that these phenomena were mainly caused by the poor contact of the sensor and the rock. Therefore, the thermal conductivities were measured again in the laboratory by using the rock taken from the mine and measurements taken under three conditions.

(1)  The probe was only inserted into the measurement hole.
(2)  The entrance of the measurement hole is closed with the filling material.
(3)  A paste is put into the measurement hole to make the good contact.

Figure 5 shows the result. Results for (1) and (2) showed sharp temperature increase in a very short time ($\approx$50 s) to reach the steady sate, and too small thermal

conductivity were also obtained. As for (3), the temperature increases were gradual and appropriate value was obtained. The values were 1.65 for tuff and 2.21 for sandstone. These values are thought to be small compared with the previous data.
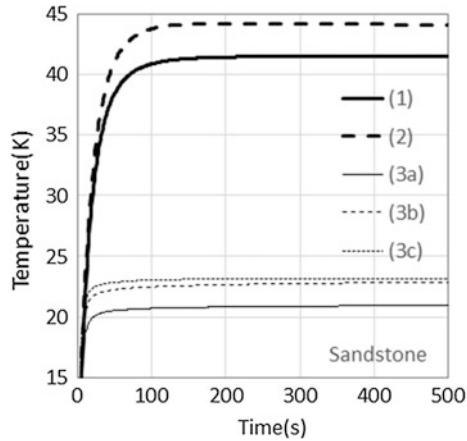


**Fig. 5.** Surface temperature change of the heat source during re-measurement

## 8 Temperature Distribution by Spherical Heat Source Method

It is necessary to know the steady state temperature by the spherical heat source in this thermal conductivity measurement. In general, a long duration is necessary to reach the steady state in the heat conduction. Figure 6 shows the surface temperature change of the spherical heat source with time obtained by the simulation up to 3600 s after the heating begins. The size of the heat source is almost 6 mm and several conditions were tested until the steady state temperature becomes 1.0 K. Other thermal conditions are the same as the case shown in Fig. 1. The simulation temperature is about 0.95 at 3600 s after the heating, and it has not reached the steady state temperature yet.

Figure 7 shows the relationship between the temperature change and time shown in Fig. 6 by the double logarithmic plot. The result shows a nearly straight line and the temperature change can be estimated by the Eq. (6) below.

$$\Theta = -1.54/\mathrm{sqrt(t)} + 0.98 \tag{6}$$

The equation was derived using temperature change from 60 to 150 s.

The equation means that the steady state temperature is 0.98 which is very near to the correct steady state temperature 1.0 K. On the other hand, the highest temperature which is most nearly in a steady state temperature was 0.95 by the simulation at 3600 s as shown in Fig. 6. The value by Eq. (6) demonstrated by the broken line in Fig. 6. The
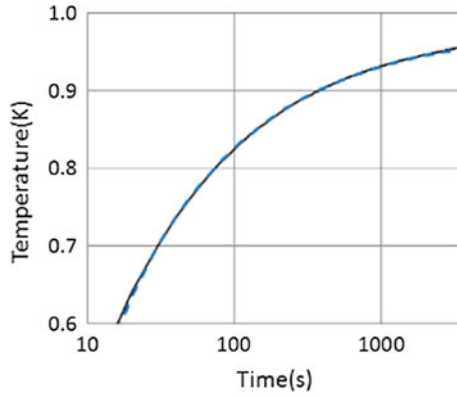
**Fig. 6.** Partial figure showing surface temperature change of the spherical heat source by the simulation and estimated temperature by Eq. (6)
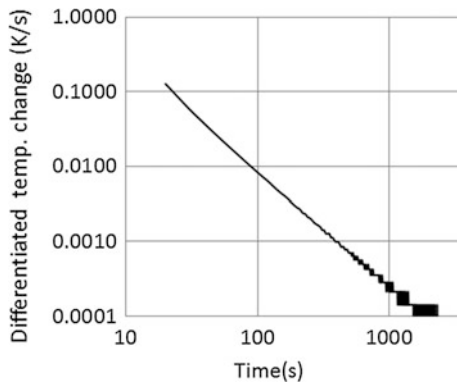


**Fig. 7.** The relation between the differentiated temperature change and time

difference between the simulated temperature and the estimated temperature by Eq. (6) is very small and it is difficult to distinguish between two curves. The shows that the accuracy of this estimation method is acceptable.

The estimation method was applied to the measured data of the "re-measurement in the laboratory". The steady state temperatures were estimated by the accuracy within 2% for 3a, 3b, and 3c by using the temperature data from 10 to 20 s. The relation between the differentiated temperature change and the time of these temperature changes are shown in Fig. 8 by the double logarithmic plot. The relations of (3a, 3b, 3c) are almost straight line from which the reliable thermal conductivity can be obtained, and the relations of (1, 2) are not obviously a straight line from which the reliable thermal conductivity cannot be obtained. That is, the reliability of the measurement can be evaluated whether the relation is straight line or not.
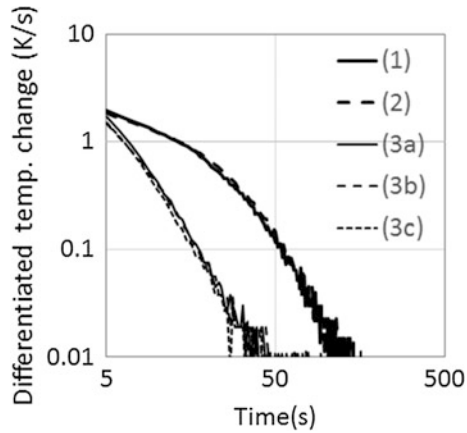
**Fig. 8.** The relation between the differentiated temperature change and time

## 9 Conclusion

A new method to measure in situ thermal conductivity was developed in this research. It was first theoretically examined by the computer simulation, actual measurements using custom-made probes were taken to measure the thermal conductivity in the laboratory. Results show that test results using either a spherical heat source method ore the line heat source method are almost the same.

The in situ thermal conductivity of the rock was then measured in a mine relatively quickly and easily. Since data collected underground show large discrepancies due to uncontrolled field conditions, measurement was repeated again in the laboratory using rock sample taken underground with proper probe boundary conditions carefully duplicated. It was confirmed that an appropriate value can be obtained by filling the measurement hole with a paste. Finally it was concluded that the new method was appropriate to measure the thermal conductivity in situ.

## References

1. Crossley, A., Lowndes, I.: Climatic and thermodynamic modelling of rapid development drivages. In: 7th international mine ventilation congress, Poland, pp. 57–61 (2001)
2. McPherson, M.: Subsurface ventilation and environmental engineering. Chapman & Hall, London (1993)
3. Beck, A.: The use of thermal resistivity logs in stratigraphic correlation. Geophysics **41**(2), 300–309 (1976)
4. Yanagimoto, T., Uchino, K.: J. Min. Metall. Jpn. **1028**, 645–650 (1989)
5. Imai, T., Yamaguti, S., Kamosida, N., Sugimoto, F.: Jour. Japan Soc. Eng. Geol. **45**(4), 174–182 (2004)
6. Nishikawa, K., Fujita, N.: Heat transfer, p. 19, Rikogakusha (1982)
7. Woodside, W., Messmer, J.: Thermal conductivity of porous media. J. Appl. Phys. **32**(9), 1688–1706 (1961)

# Experimental Study on the Effect of Air Cooling Garment on Skin Temperature and Microclimate

Liu Heqing[(⊠)], Gao Liying, You Bo, Liu Tianyu, and Ou Congying

School of Resource, Environment and Safety Engineering, Hunan University of
Science and Technology, Xiangtan 411201, Hunan, China
hqliu8222638@l63.com

**Abstract.** The Air Cooling Garment (ACG) was employed to study skin temperature and Clothing Inner Microclimate (CIMC) Regulation, which provides theoretical basis for further optimization of aerodynamic layout of AGG towards human thermal comfort improving. 15 male postgraduates served as subjects in the experiment, each runs at 5 km/h (to simulate Moderate Work, MW) or 7.5 km/h (Heavy Work, HW) on the treadmill in an artificial climate chamber with or without the Air Cooling Garment (ACG) for 40 min respectively. The temperature of the artificial climate chamber changed from 24 to 34 °C. The skin temperature of upper body, clothing inner Wind Velocity (WV), Relative Humidity (RH) and temperature were measured. Results showed that the skin temperature decreased much more significantly with the ACG than without when the ambient temperature is over 26 °C, especially when engaged in HW. The WV and RH in clothes changed with the labor intensity, rather than the ambient temperature. The variation of clothing inner temperature field was different, with the front and back sides decreased with labor intensity, while the left and right sides were not affected. It proved that the ACG can improve CIMC and enhance human thermal comfort effectively.

**Keywords:** Air cooling garment · Skin temperature · Clothing inner microclimate · Labor intensity

## 1 Introduction

Miners working in the high-temperature environment, in deep buried mine will possibly develop a series of symptoms such as thermal fatigue, heat cramp sand heat exhaustion. These symptoms may pose serious health risk and reduced production efficiency [1]. High temperature personal protective equipment, with the advantage of a very good cooling effect low cost and high security, is widely used in fire, mining, and metallurgical industries [2–4].

High-temperature personal protective equipment mainly refers to the cooling clothes used by personal. According to the cooling principle and characteristics of cooling medium, it can be divided into liquid cooling clothes, phase-change cooling clothes and ACG [5]. By heat conduction, the liquid cooling clothes mainly use cool liquid to reduce the body temperature [6–8]. Solid liquefaction is an endothermic

process, in which phase-change cooling clothes play a better role on local cooling [9–11]. Furthermore, ACG is more applicable in mine environment, which is characterized by economy, lightweight, comfort, and so on [12]. Both the fan-type and ventilated ACG can reduce skin temperature, sweat, heat stress, increase heat dissipation, maintain heat balance and improve human comfort effectively [13–16]. In comfortable condition, local heating or cooling on the subject may enhance human thermal comfort. A strong local thermal sensation determines the overall thermal sensation [17, 18]. The human physiological indexes change remarkably with environmental temperature and humidity. Skin temperature is a good index of local thermal sensation, and CIMC determines the degree of thermal comfort [19, 20]. Therefore, reducing the clothing inner temperature can improve thermal comfort effectively.

Deep underground mines, characterized by high temperature and humidity, have great harm to miners' mental and physical health. Reducing the ambient temperature or improving the CIMC is a good way to enhance the thermal comfort of workers, which can create a safe and comfortable working environment for miner. The research used a self-developed ACG to study its cooling effects on skin temperature of upper body and clothing inner microclimate at different labor intensity and ambient temperature. The study provided theoretical basis for further optimization of ACG aerodynamic layout and thermal comfort improving.

## 2 Methods

### 2.1 Equipment

The experimental simulation environment was in the artificial climate chamber with an internal dimension 3 m $\times$ 2.5 m $\times$ 2.2 m, which could simulate the required stable experimental environment. The grade 1 standard thermometer (minimum scale value: 0.05 °C) and JT-IAQ indoor thermal environment comfort tester (accuracy: $\pm 1.5\%$) were used to calibrate ambient temperature and RH respectively in the experiment. Skin temperature was measured by the thermocouple temperature sensor DS1922L (MAXIM, US, resolution 0.0625 °C), breathable medical tapes were used to stick on the skin surface. CIMC was measured by HD29 sensor (Delta, Italy), in addition, the date stored and read by Agilent Workstation.

The ACG adopted supporting structure, with air compressed through main and branch pipeline, the airflow channels were formed between the body surface and clothing. The air supply branch pipe was evenly symmetrically distributed over the inner surface of ACG. The compressed air blew to the human body surface though the holes in the gas branch pipe at a controlled speed. The ACG makes full use of the endothermic process of compressed air expansion, the enhanced human skin sweat decalescence and thermal convection, reinforces the cooling effect, and thereby is effective and efficient in microclimate control.

## 2.2    Experimental

15 male postgraduates whose age averages 24, height $171 \pm 3.6$ cm, weight $62.4 \pm 6.4$ kg were employed for the study. They were all healthy and with no bad habits. During the experiment, the subjects' upper body were either naked or wore ACG, and wearing long trousers. The wind speed in climate chamber was less than 0.05 m/s. According to the symmetry of temperature distribution on human body from literature [21], we selected ten points of human upper body to stick the temperature sensors. The five measuring points in front of the body were at left chest, right chest, middle, left abdomen and right abdomen respectively, the other five points in the back were left scapula, right scapula, middle, left waist, right waist respectively, as shown in Fig. 1. Each one was tested for 45 min, including 5 min for pre-adaptation in the chamber and 40 min running on treadmill.
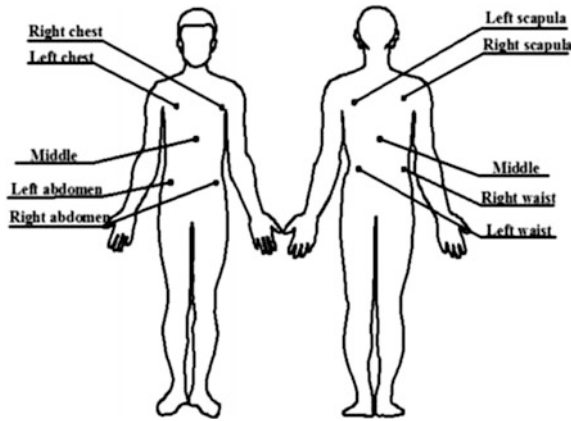


**Fig. 1.** Distribution of the ten measuring points

Microclimate measuring instruments were at four positions (front, back, left, right) of inner clothing. As shown in Fig. 2, subjects wearing ACG in the experiment.

According to West Germany labor intensity classification, MW was 232 W and HW was 348 W. Metabolic was calculated as follows [22]:

$$M_w = 1.5W + 2(W + L)(L/W)^2 + \eta(W + L)(1.5V^2 + 0.35VG) \qquad (1)$$

Where $M_w$ = metabolic rate, W; W = naked weight, kg; L = load carried, kg; V = speed of walking, m/s; G = grade, %; $\eta$ = terrain factor ($\eta$ = 1.0 for treadmill). Due to the required labor intensity, we chose running speed as 5, 7.5 km/h, the value of other parameters were: W = 62.4 kg, L = 0.8 kg, $\eta$ = 1, G = 0, so metabolic rate were 276.5, 505.1 W.

According to "Coal Mine Safety Regulations" (China), the air temperature should not exceed 26 °C in the working place, the workers must stop working when temperature over 30 °C. So the experimental conditions were set as follows (Table 1).

**Fig. 2.** Subjects in experiment wearing ACG

**Table 1.** Experimental conditions

|  | Air supply rate (m$^3$/h) | Temperature (°C) | Humidity (%) | Labor intensity |
|---|---|---|---|---|
| No ACG | 0 | 24, 26, 28, 30, 32, 34 | 90 | MW, HW |
| Wearing ACG | 10 | | | |

The ACG air temperature was 29–31 °C, pressure was 0.8 MPa

## 2.3 Statistical Analysis

The data of skin temperature, clothing inner WV, RH and temperature were expressed by mean and standard deviation (SD). The mean skin temperature was the average of ten parts of skin temperature. The graphs were drawn with Origin, the Person correlation test and *t*-test for significant analyses were calculated by SPSS.

# 3   Results

## 3.1   Skin Temperature

The skin temperature with or without wearing ACG in MW and HW were measured by the temperature sensor as shown in Fig. 3. Two groups of data before and after dressing were analyzed by T paired test.
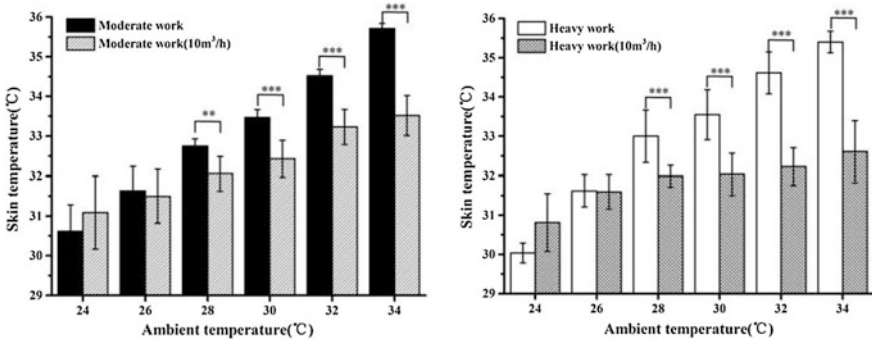


**Fig. 3.** The skin temperature of ten parts of 12 subjects during 40 min running at 5 or 7 km/h with wearing ACG or not

As shown in Fig. 3, in MW and HW, the skin temperature of upper torso was significantly affected by ambient temperature (P < 0.05). Skin temperature increased obviously, which was not related to the clothes. After wearing ACG, the correlation between the ambient temperature and skin temperature decreased (n = 15, $r^2$ = 0.998, 0.988; $r^2_{wear}$ = 0.994, 0.946).

When the ambient temperature was higher than 26 °C, the skin temperature decreased (P < 0.01) significantly, and the maximum decrease of skin temperature is 2.789 °C. When the ambient temperature arrived at 28 °C, the skin temperature with wearing ACG in HW was lower than that in MW condition. However, there was no significant difference of skin temperature in different working conditions without wearing cold clothing. It showed that the ACG would be better used in HW.

The SD decreased with the increasing of ambient temperature with no ACG, but there was no significant difference with wearing ACG.

## 3.2   Microclimate

Through the microclimate measuring instrument, the changes of wind speed and relative humidity in each part of the garment under moderate and severe working conditions are shown in Tables 2 and 3.

According to Tables 2 and 3, it is found that the change of wind speed and relative humidity in different parts of the garment is independent of the ambient temperature. But the state of labor has great influence on the microclimate inside the clothing.

**Table 2.** The values of WV and RH were measured in MW when subjects were wearing ACG, each part has different WV and RH in different temperature

| Part | Microclimate | Ambient temperature (°C) | | | | | |
|---|---|---|---|---|---|---|---|
| | | 24 | 26 | 28 | 30 | 32 | 34 |
| Front | Velocity (m/s) | 0.31 ± 0.01 | 0.34 ± 0.03 | 0.32 ± 0.00 | 0.34 ± 0.02 | 0.37 ± 0.02 | 0.32 ± 0.01 |
| | Humidity (%) | 58.64 ± 1.22 | 54.74 ± 1.65 | 57.61 ± 0.94 | 57.72 ± 0.80 | 51.74 ± 1.75 | 62.78 ± 1.93 |
| Back | Velocity (m/s) | 0.16 ± 0.00 | 0.15 ± 0.01 | 0.12 ± 0.00 | 0.16 ± 0.03 | 0.14 ± 0.03 | 0.17 ± 0.02 |
| | Humidity (%) | 65.54 ± 1.32 | 65.43 ± 1.75 | 67.04 ± 1.68 | 65.20 ± 1.39 | 64.16 ± 0.56 | 75.78 ± 2.37 |
| Left | Velocity (m/s) | 0.45 ± 0.06 | 0.37 ± 0.02 | 0.35 ± 0.03 | 0.36 ± 0.00 | 0.39 ± 0.04 | 0.38 ± 0.03 |
| | Humidity (%) | 54.50 ± 0.90 | 54.12 ± 0.46 | 54.39 ± 1.02 | 63.24 ± 1.73 | 58.64 ± 1.27 | 53.53 ± 1.35 |
| Right | Velocity (m/s) | 0.35 ± 0.00 | 0.37 ± 0.02 | 0.41 ± 0.04 | 0.46 ± 0.07 | 0.39 ± 0.01 | 0.45 ± 0.03 |
| | Humidity (%) | 52.32 ± 1.48 | 49.79 ± 2.83 | 55.96 ± 1.23 | 50.36 ± 1.48 | 53.12 ± 0.67 | 48.06 ± 1.04 |

**Table 3.** The values of WV and RH were measured in HW when subjects were wearing ACG, each part has different WV and RH in different temperature

| Part | Microclimate | Ambient temperature (°C) | | | | | |
|---|---|---|---|---|---|---|---|
| | | 24 | 26 | 28 | 30 | 32 | 34 |
| Front | Velocity (m/s) | 0.38 ± 0.02 | 0.36 ± 0.01 | 0.38 ± 0.00 | 0.34 ± 0.02 | 0.39 ± 0.01 | 0.41 ± 0.02 |
| | Humidity (%) | 68.32 ± 1.56 | 66.69 ± 1.92 | 72.09 ± 2.45 | 76.12 ± 2.75 | 80.26 ± 2.90 | 79.07 ± 3.58 |
| Back | Velocity (m/s) | 0.20 ± 0.00 | 0.22 ± 0.01 | 0.26 ± 0.02 | 0.23 ± 0.00 | 0.19 ± 0.01 | 0.18 ± 0.01 |
| | Humidity (%) | 100 | 100 | 100 | 100 | 100 | 100 |
| Left | Velocity (m/s) | 0.37 ± 0.02 | 0.37 ± 0.01 | 0.36 ± 0.00 | 0.40 ± 0.04 | 0.41 ± 0.02 | 0.42 ± 0.03 |
| | Humidity (%) | 70.14 ± 0.98 | 62.21 ± 1.67 | 70.03 ± 1.26 | 71.13 ± 2.37 | 63.24 ± 2.48 | 76.65 ± 3.35 |
| Right | Velocity (m/s) | 0.45 ± 0.02 | 0.38 ± 0.00 | 0.35 ± 0.01 | 0.49 ± 0.03 | 0.46 ± 0.02 | 0.39 ± 0.01 |
| | Humidity (%) | 73.59 ± 1.05 | 73.48 ± 1.96 | 69.22 ± 2.05 | 67.15 ± 1.90 | 68.78 ± 3.27 | 73.01 ± 2.39 |

During the experiment, the clothing inner RH maintained at a steady state, indicating that the ACG could be discharge of sweat to the outside timely. So we could get the Fig. 4.
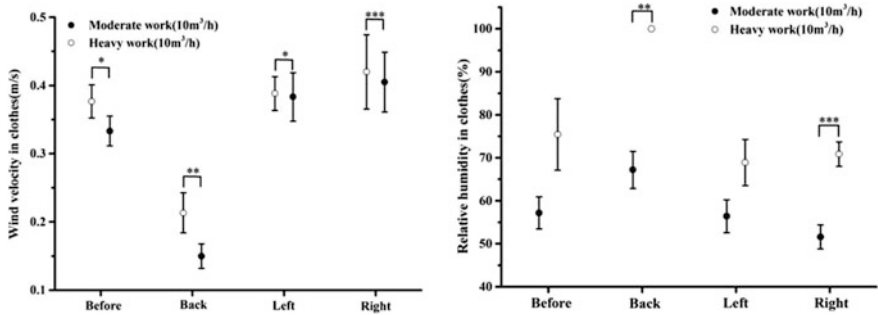


**Fig. 4.** Mean ± SD WV and Mean ± SD RH in different parts of the garment, in MW or HW condition, the significance was also shown

As shown in Fig. 4, the WV and RH were higher in HW than those in MW. The WV in back was the lowest, but the RH was the highest. The effect of WV on the body was stronger in HW than that in MW ($P < 0.05$), the evaporation and convection was the main heat dissipation mode. The intensity of labor only had a significant effect on the relative humidity of the back and right side ($P < 0.01$), and had no significant effect on the front and left side ($P > 0.05$).

**Clothing Inner Temperature**. The temperature in the clothing has a great influence on the thermal comfort of the human body. By discussing the changes in the temperature of the clothes under different labor intensity and ambient temperature, the effectiveness of the air cooling clothes is judged. Through experiments, it is found that the temperature inside the four parts of the front, rear, left and right can reach a stable state at a certain ambient temperature. The temperature of each part of the garment varies with the ambient temperature under different working conditions as shown in Fig. 5.

As shown in Fig. 5, the increase of labor intensity could significantly reduce the temperature in front and back sides thus improved comfort. The temperature inside and outside the clothing is not affected by the labor intensity, and the temperature inside the two sides of the subject is almost symmetrical. In MW, when the ambient temperature reached 34 °C, the temperatures in both back and front sides were lower than ambient temperature. When the ambient temperature reached 32 °C, temperatures in the both front and back sides were lower than ambient temperature in HW. That is to say that WV and RH played a leading role on the improvement of human thermal comfort. It can be seen that the temperature in front and back sides had greater impact on thermal comfort and skin temperature than the left and right sides.
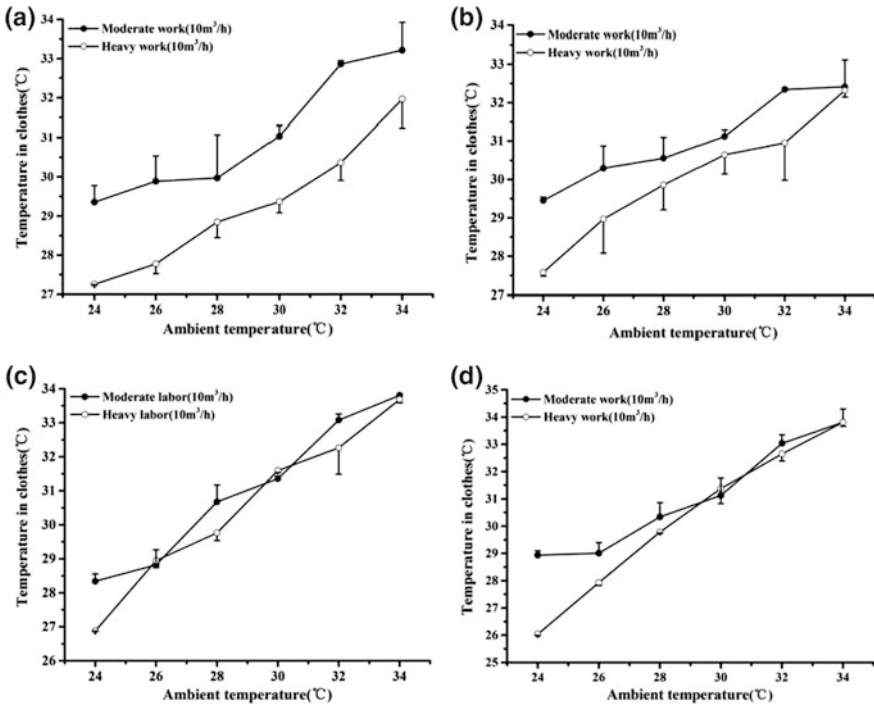
**Fig. 5.** Temperature of front (**a**), back (**b**), left (**c**), right (**d**) changing with ambient

## 4   Conclusions

(1) The ACG could effectively reduce skin temperature, enhance microclimate, and improve human thermal comfort under different working conditions, in particular, to meet the requirement of heavy physical work.

(2) The temperature distribution in the ACG clothing is very uneven. The temperatures in front and back sides are relatively low, which has great influence on the human body. The temperatures on both sides are high, but it has little influence on the human body.

(3) When ambient temperature reaches 28 °C and above, the ACG has a good cooling effect on skin temperature and the greater the labor intensity, the better the cooling effect.

(4) The wind speed and relative humidity have more influence on human comfort than in condition of heavy working than moderate labor.

# References

1. Yang, D.: Thermal environment in mine and its control. Metallurgical Industry Press, Beijing (2009)
2. Taylor, N.A.: Challenges to temperature regulation when working in hot environments. Ind. Health **44**, 331–344 (2006)
3. Langø, T., Nesbakken, R., Faerevik, H., et al.: Cooling vest for improving surgeons' thermal comfort: a multidisciplinary design project. Minim. Invasive Ther. Allied Technol. Mitat Official J. Soc. Minim. Invasive Ther. **18**, 1–10 (2009)
4. Teunissen, L.P.J., Wang, L., Chou, S., et al.: Evaluation of two cooling systems under a firefighter coverall. Appl. Ergon. **45**, 1433–1438 (2014)
5. Liu, H., Gao, L., Li, Y.: Review of cooling garment development situation. Min. Eng. Res. **4**, 75–80 (2015)
6. Bishop, P.A., Sarah, A., et al.: Comparisons of air and liquid personal cooling for intermittent HW in moderate temperatures. Am. Ind. Hyg. Assoc. Q. **52**, 393–397 (1991)
7. Labat, K.: Design process for developing a liquid cooling garment hood. Ergonomics **53**, 818–828 (2010)
8. Yang, K., Jiao, M.L., Liu, Z., et al.: A heat dissipating model for water cooling garments. Therm. Sci. **17**, 1431–1436 (2013)
9. Gao, C., Kuklane, K., Holmér, I.: Cooling vests with phase change materials: the effects of melting temperature on heat strain alleviation in an extremely hot environment. Eur. J. Appl. Physiol. **111**, 1207–1216 (2011)
10. Zhou, M., Feng, L., Liang, Z.: Test of performance of mine thermal protective vest. J. Anhui Univ. Sci. Technol. (Nat. Sci.) **32**, 29–34 (2012)
11. Jovanović, D., Karkalić, R., Zeba, S., et al.: Physiological tolerance to uncompensated heat stress in soldiers: effects of various types of body cooling systems. Vojnosanitetski pregled. Mil. Med. Pharm. Rev. **71**, 259–264 (2014)
12. Liu, Y., Chen, N., Wang, L., et al.: Design and development of mine personal cooling protective clothing. Coal Eng. **7**, 120–121 (2011)
13. Hadid, A., Yanovich, R., Erlich, T., et al.: Effect of a personal ambient ventilation system on physiological strain during heat stress wearing a ballistic vest. Eur. J. Appl. Physiol. **104**, 311–319 (2008)
14. Xu, X., Gonzalez, J.: Determination of the cooling capacity for body ventilation system. Eur. J. Appl. Physiol. **111**(12), 3155–3160 (2011)
15. Zhao, M., Gao, C., Wang, F., et al.: A study on local cooling of garments with ventilation fans and openings placed at different torso sites. Int. J. Ind. Ergon. **43**, 232–237 (2013)
16. Chan, A.P., Song, W., Yang, Y.: Meta-analysis of the effects of microclimate cooling systems on human performance under thermal stressful environments: potential applications to occupational workers. J. Therm. Biol **49–50**, 16–32 (2015)
17. Arens, E., Zhang, H., Huizenga, C.: Partial- and whole-body thermal sensation and comfort —part II: non-uniform environmental conditions. J. Therm. Biol **31**, 53–59 (2006)
18. Zhang, H., Arens, E., Huizenga, C., et al.: Thermal sensation and comfort models for non-uniform and transient environments, part III: whole-body sensation and comfort. Build. Environ. **45**, 399–410 (2010)
19. Tian, X., Zhang, D., Wang, Z., et al.: Simulation research on the human comfortableness during wear. J. Qingdao Univ. (Eng. Technol. Ed.) **20**, 64–67 (2005)
20. Liu, W., Lian, Z., Deng, Q.: Evaluation model of individual thermal comfort based on mean skin temperature. J. Southeast Univ. **26**, 254–257 (2010)

21. Liu, W., Lian, Z., Deng, Q., et al.: Evaluation of calculation methods of mean skin temperature for use in thermal comfort study. Fuel Energy Abstr. **46**, 478–488 (2011)
22. Pandolf, K.B., Givoni, B., Goldman, R.F.: Predicting energy expenditure with loads while standing or walking very slowly. J. Appl. Physiol. Respir. Envir. Exerc. Physiol. **43**, 577–581 (1977)
23. Vallerand, A.L., Michas, R.D., Frim, J., et al.: Heat balance of subjects wearing protective clothing with a liquid-or air-cooled vest. Aviat. Space Environ. Med. **62**, 383–391 (1991)
24. Mclellan, T.M., Frim, J., Bell, D.G.: Efficacy of air and liquid cooling during light and heavy exercise while wearing NBC clothing. Aviat. Space Environ. Med. **70**, 802–811 (1999)
25. Yang, H.: Exploration of human skin temperature during exercise. Dissertation, Suzhou University (2014)
26. Guo, X., Yuan, X.: Influencing factors analysis of cooling power of air cooling personal thermal protective equipment. J. Astronaut. **31**, 276–281 (2010)
27. Zhu, Y.: Building environment. China Building Industry Press, Beijing (2010)
28. Han, Z., Tang, S., Lai, J.: The experimental evaluation studies of circulating air cooling garment. China Pers. Prot. Equip. **3**, 11–14 (2010)

# Part XIV
# Climatic Control

# Achieving Nitrogen Dioxide Reductions in Mechanized Underground Mining

Darryl Witow[1], Melissa Brown[2], Roki Fukuzawa[2], Simon Arsenault[2], and Wendy Harris[3(✉)]

[1] Hatch Ltd, Sudbury, ON P3C 1S8, Canada
darryl.witow@hatch.com
[2] Hatch Ltd, Mississauga, ON L5K 2R7, Canada
[3] Hatch Ltd, Brisbane, QLD 4000, Australia
wendy.harris@hatch.com

**Abstract.** Nitrogen dioxide is a notable workplace contaminant in many types of underground mines, both due to its production in fossil fuel combustion and blasting, as well as for its human health effects. In some jurisdictions, permissible limits have reduced by over 90%. Although it is recognized that non-diesel technologies such as battery electric equipment are shaping to eventually dominate in underground ore haulage, in the near-term many mines face the challenge of achieving safe and healthy workplace conditions while still using diesel engines. Where initially deemed unattainable, Hatch have demonstrated that order of magnitude reductions in underground nitrogen dioxide levels can be achieved through: emission control technologies initially designed for surface industries, improvements in burners for mine heating, and selection of lower emission explosives.

**Keywords:** Nitrogen dioxide · Tier 4 final (Stage IV) · Selective catalytic reduction · Underground mining · Ventilation · Workplace hygiene

## 1 Introduction

Nitrogen dioxide levels are an important consideration in the ventilation design of underground mines because of their human health impacts; specifically, acute and/or chronic exposure has been observed to impact the respiratory system. Allowable limits are regulated by jurisdiction, with some areas having seen a 90% reduction in recent years.

There are three main sources of nitrogen dioxide in underground mining: direct fired heaters, blasting operations, and diesel engines. Each source has a different contribution to the nitrogen dioxide level in the workplace in terms of when, where, and how much is produced. The three sources are summarized in Table 1.

Although direct fired heaters and blasting operations contribute to overall workplace nitrogen dioxide levels, their impact, as shown above, is typically far less significant than that of diesel engine operation. As such, the control of nitrogen dioxide from all three sources will be discussed; however, the opportunity to most significantly reduce nitrogen dioxide levels comes from emissions related to diesel engines.

**Table 1.** Summary of nitrogen dioxide contributions to the mine workplace by source

| Source | Timing of generation | Means of workplace contamination | Typical impact on workplace concentration relative to diesel engines | Factors influencing workplace concentration level |
|---|---|---|---|---|
| Direct fired intake air heating | Winter months | Combustion products directly in fresh air supply | <30% of diesel engine contribution | Burner performance; heater duty |
| Blasting | Between shifts | Residual blasting fume in airways and residual gas in blasted material | <50% of diesel engine contribution | Explosive type and emission characteristics; ventilation rate |
| Diesel Engines | On-shift at the workplace | Direct exhaust into workplace | – | Engine emission characteristic; ventilation rate |

Combustion of diesel in a diesel engine, as with many industrial combustion processes, produces oxides of nitrogen (NOx), composed of nitric oxide (NO) and nitrogen dioxide ($NO_2$). The main component of NOx is NO, which is slowly (but continuously) oxidized by oxygen to produce $NO_2$ at ambient conditions. NOx is a concern for public health and air quality; consequently, diesel engines operating on surface have undergone government-mandated reductions in allowable NOx emissions through the phased Tier (or Stage) system since 1996. The latest and current engine regulation in North America, Tier 4 Final (Stage IV in Europe), required a significant reduction in allowable NOx emissions. To achieve this reduction, selective catalytic reduction (SCR) technology was implemented in the exhaust after-treatment system. Although not enforced for use in underground mines, this technology presents an opportunity to achieve order of magnitude reductions in $NO_2$ levels. Implementation in underground mines does present challenges, such as the need for an additional engine fluid storage and distribution system; however, the potential advantages outweigh the implementation challenges, which can be alleviated through well-planned mine design and by providing the mining industry with information on these types of systems.

## 2 Diesel Engine Emission Control

### 2.1 Emission Regulations

Regulated exhaust emissions for surface vehicles have undergone reductions based on the Tier or Stage system since 1996, with the purpose of improving air quality and public health, particularly in urban areas in North America and Europe (EU). Increasingly advanced technologies have been required to meet each new level. Tier 4 Final (Tier 4F), or EU Stage IV, was the latest phase to come into effect for surface compression-ignition engines, and was an upgrade from Tier 4 Interim (Tier 4I) or EU

Stage IIIB. A major difference between the two Tier 4 levels is a significant NOx reduction (i.e., 80% reduction for nonroad engines rated 175–750 hp), that was recognized as only achievable through the implementation of selective catalytic reduction (SCR) technology in the exhaust after-treatment system. Chinese nonroad surface exhaust emission regulations have largely followed the European standards, except for the most recent European Stage IV limit, which has not been adopted at this point. The reduction in allowable NOx emissions for nonroad surface engines through the phased Tier/Stage system is shown in Fig. 1.
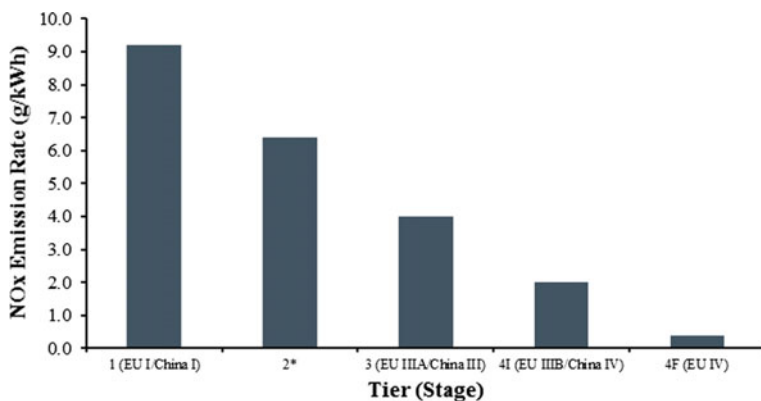


**Fig. 1.** Reduction in allowable NOx emissions through the Tier/Stage system for nonroad compression-ignition engines rated 300–750 hp [1–5]. Tier 2 and 3 (EU Stage IIIA and China Stage III) emission standards represent the sum of NOx and nonmethane hydrocarbons. *EU and China Stage II max NOx emission of 6.0 g/kWh

The use of Tier 4 Final (EU Stage IV) engine technology provides an opportunity to significantly reduce nitrogen dioxide levels in underground mining applications. This can be seen in Fig. 2, which plots the resulting workplace $NO_2$ concentration with different Tier/Stage rated engines operating at varied load factors (i.e., percent of the load seen by the motor during operation compared to the total rated power). It is evident that Tier 4 Final (EU Stage IV) engines have the potential to provide significantly lower $NO_2$ concentrations compared to those achievable with previous engine ratings.

## 2.2 Engine Technologies

Engine original equipment manufacturers developed increasingly advanced engine technologies to meet stricter emission regulations enforced in surface compression-ignition engines. A variety of in-cylinder and exhaust after-treatment technologies have been implemented to help meet NOx regulations, as well as regulations controlling other diesel combustion products. The selection of individual control technologies is dependent on the engine manufacturer and the desired emission levels for diesel
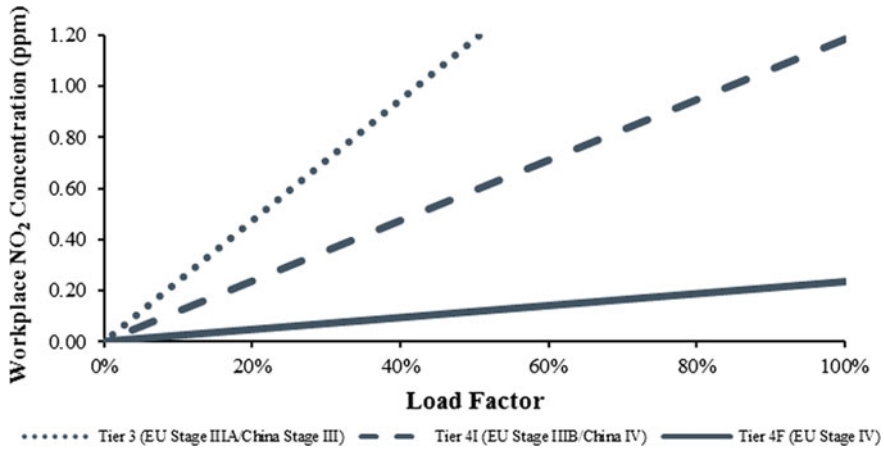
**Fig. 2.** Comparison of resulting workplace $NO_2$ concentration with different Tier/Stage rated engines operating at various load factors (applicable for engines sized 175–750 hp). Assumes a NOx emission rate equivalent to the maximum allowable based on the Tier/Stage rating, ventilation rate of 74 cfm/bhp, ambient conditions of 20 °C and 1.2 kg/m$^3$, 10% (mol) $NO_2$/NOx ratio in the undiluted engine exhaust, and 10% (mol) conversion of NO to $NO_2$ in the ambient air

particulate matter, unburnt hydrocarbons, and NOx. It is also important to note that some technologies may address the issue of one contaminant but can exacerbate the issue of another. Available technologies are discussed in more detail below, along with considerations regarding their use in underground mining applications and specifically their impact on workplace $NO_2$.

**Diesel Oxidation Catalyst**. Diesel oxidation catalysts (DOCs) are used to oxidize carbon monoxide (CO) to carbon dioxide. There are many catalyst types available, and the catalyst activity is highly dependent on exhaust temperature. In addition, low sulphur content fuel must be used to prevent sulphate formation and subsequent catalyst deactivation. NO can also be oxidized to $NO_2$ in the DOC, which is not helpful for workplace hygiene, as $NO_2$ is noxious at lower levels and thus has a lower workplace contaminant threshold. The conversion is impacted by the catalyst type; for example, high NO to $NO_2$ conversion potential is seen with platinum formulation catalysts.

DOCs are also effective at lowering levels of other un-burned hydrocarbons such as diesel particulate; however, as with typical high temperature gas processes involving air, the high temperatures associated with DOC operation increase NOx generation. This limits their potential to be used in systems that have low NOx emission limits, and are not capable of removing this NOx prior to release to the atmosphere.

DOCs offer an effective means of controlling CO; however, in underground mining applications with low $NO_2$ requirements, catalyst types must be selected carefully to limit NO to $NO_2$ conversion. In addition, it is likely another NOx removal technology would be required downstream of the DOC to reduce emissions to the mine workings.

**Diesel Particulate Filter**. Diesel particulate filters (DPFs) physically capture diesel particulate matter (DPM) from the engine exhaust. The exhaust gas passes through

while particulates are trapped in the filter walls. The filter must be cleaned periodically or continuously (a process known as regeneration) to remove the collected soot and prevent high engine back-pressure. The removal process involves the oxidation of filter particulates into gaseous products.

Regeneration has been a challenge in some underground applications where exhaust temperatures high enough to support DPF regeneration may not be reached with sufficient frequency and duration, particularly for secondary equipment that are limited to short tramming distances. As such, the exhaust gas and filter may need to be heated by an external source, often relying on the injection of fuel into the exhaust stream to achieve the required oxidation temperature. Catalyst coatings can also be used to support DPF regeneration at lower temperatures.

Some engine manufacturers install a DOC upstream of the DPF, with the purpose of helping promote DPF regeneration. At typical low exhaust temperatures, $NO_2$ has a higher oxidative potential than oxygen, and can be used to support oxidation of the DPM. However, the typical low concentration of $NO_2$ in diesel exhaust is normally inadequate to promote DPF regeneration. Installation of a DOC upstream of the DPF will increase the $NO_2$ concentration in the exhaust gas and support DPF regeneration, as seen in Fig. 3. When combined with oxidation of diesel particulates in the DOC, a "passive regeneration" can be achieved where buildup never exceeds capacity and no regeneration cycles are required.
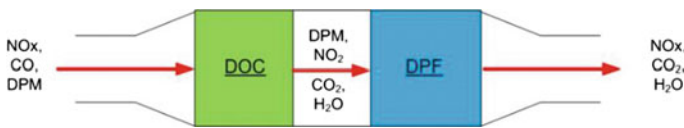


**Fig. 3.** Contaminant removal with a DOC installed upstream of a DPF

DPFs require maintenance in underground mining applications; as such, engines with a reduced strain on the DPF would be advantageous from a maintenance interval perspective.

**Exhaust Gas Recirculation**. Exhaust gas recirculation (EGR) is a technology used to reduce NOx formation. Higher temperatures promote NOx generation; therefore, EGR works to lower the peak combustion temperature.

With EGR, a valve is used to control the amount of exhaust gas to be recirculated to the intake manifold. The exhaust gas typically must be sent through a cooler to reduce its temperature prior to recirculation to effectively reduce combustion temperatures. Furthermore, the recirculated exhaust gas dilutes the air/fuel mixture in the combustion chamber, thus reducing the peak combustion chamber temperature and inhibiting the formation of NOx.

By lowering the peak combustion temperature, EGR decreases the engine's thermodynamic efficiency. This results in a lower fuel efficiency and increased diesel fuel costs, along with related climate change impacts. In addition, more DPM is generated at these lower combustion temperatures. Consequently, EGR puts a greater strain on

the DPF and increases the need for filter regeneration and maintenance. Both factors make EGR less than desirable for underground mining applications; however, the need for low NOx emission rates has resulted in fairly widespread adoption of this technology underground.

**Selective Catalytic Reduction**. Selective catalytic reduction (SCR) is a technology used in Tier 4 Final (EU Stage IV) engines to reduce NOx. Diesel engine combustion is considered lean (i.e., large amount of excess oxygen), which drives the formation of NOx; therefore, SCR uses a specific reducing agent, known as diesel exhaust fluid (DEF), to convert NO and $NO_2$ back to nitrogen gas. The main components of the SCR system, as seen in Fig. 4, are the: hydrolysis catalyst (converts urea to ammonia), main SCR catalyst (uses ammonia to convert NOx to nitrogen and water) and an ammonia oxidation catalyst (prevents ammonia "slip" through its conversion to nitrogen and water). The use of ammonia for NOx scrubbing is widespread in industry, including applications in thermal power generation off-gas treatment since the 1970s.
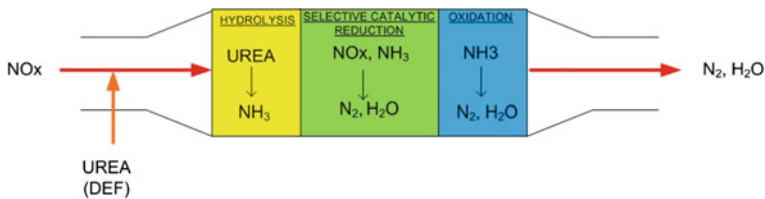


**Fig. 4.** Components of the selective catalytic reduction system

SCR has significant indirect impacts on engine performance. It reduces or eliminates the need for EGR, which enables improved engine performance and increased fuel efficiency. In addition, less DPM is formed with a more efficient combustion process, which reduces the strain on the DPF.

Some SCR systems will have an oxidation catalyst upstream of the main SCR catalyst to modify the NOx ratio in support of a particular chemical reaction. The conversion potential of NO to $NO_2$ will depend on the specific catalyst formulation. As such, the exact removal of each species in the SCR system will be dependent on a variety of factors (e.g., $NO_2$/NOx ratio, exhaust temperature, catalyst formulation). For underground mining applications, the resulting $NO_2$/NOx ratio from the SCR system will be critical to ensure compliance with occupational exposure limits, depending on the jurisdiction.

Overall, SCR presents many advantages for underground mining applications; however, as a new technology, it could present some implementation challenges and risks, which are discussed further in Sect. 3.5.

**Summary**. The effects on contaminant levels and engine efficiency with technologies discussed in the previous sections are summarized in Table 2.

The exact combination of engine technologies utilized is dependent on the manufacturer; an example configuration is shown in Fig. 5.

**Table 2.** Summary of engine emission reduction technologies

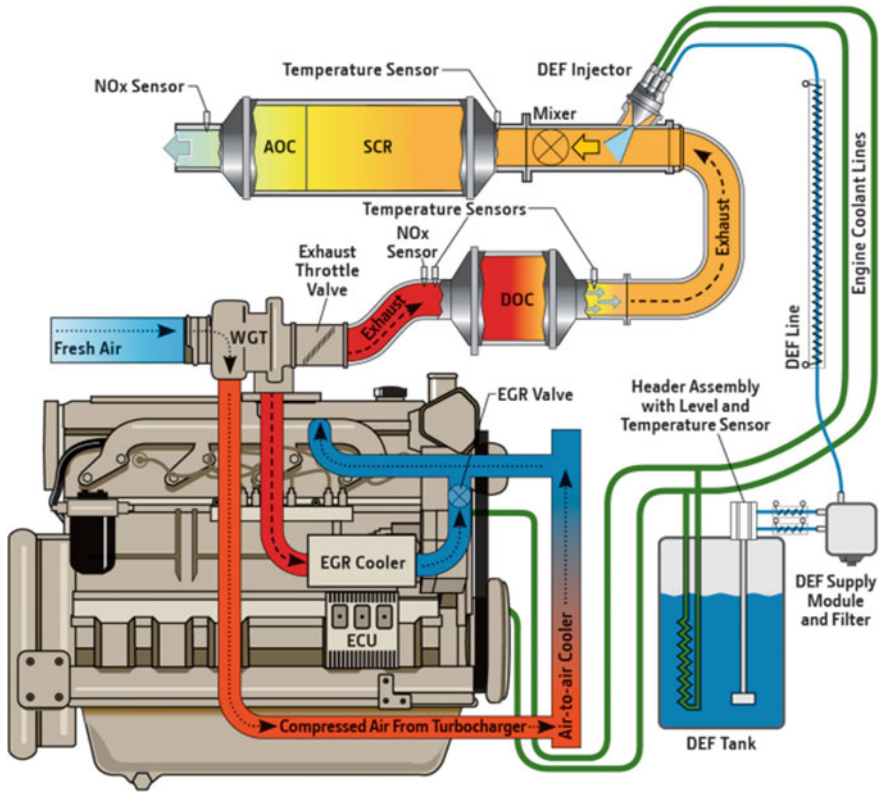| Technology | NOx | CO | DPM | Engine efficiency |
|---|---|---|---|---|
| DOC | NO converted to NO$_2$ | Reduction | Reduction in soluble organic fraction | – |
| DPF | – | – | Reduction | – |
| EGR | Reduction | – | Generation | Decreased |
| SCR | Reduction | – | – | Increased |



**Fig. 5.** John Deere engine using a variety of in-cylinder and after-treatment technologies [6]

# 3 Underground Mine Case Study

## 3.1 Background

Hatch was recently presented with a challenge during the detailed ventilation design of an underground Canadian mine: to meet the strict occupational exposure limit for nitrogen dioxide in a jurisdiction that had recently seen a reduction in the allowable

limit by over 90% to 0.2 ppm. Although previously deemed unattainable, working with the client, Hatch undertook a thorough investigation to address this issue. As the use of battery electric equipment was not feasible for this mine, Hatch identified another solution to reduce the nitrogen dioxide levels: the use of engine technologies in Tier 4 Final (EU Stage IV) equipment. As demonstrated in Sect. 2.1, these technologies can enable significant reductions in the workplace $NO_2$ concentration. Although not enforced for use in underground mining, these technologies provide an opportunity to meet strict exposure limits and improve the overall air quality for miners.

## 3.2    Engine Performance Specification Development

Hatch developed a diesel engine specification for the project to define the specific performance required to meet the desired $NO_2$ limit. An important aspect of the specification was to highlight that an engine being Tier 4 Final (EU Stage IV) certified did not necessarily guarantee compliance. Engines are regulated on a total NOx emission basis, which is composed of both NO and $NO_2$. For this mine, a low $NO_2$/NOx ratio at the engine tailpipe was required in order the meet the jurisdictions' $NO_2$ limit. Therefore, instead of simply specifying a Tier 4 Final (EU Stage IV) rated engine, the specification dictated the requirement for SCR as part of the exhaust after-treatment system, as well as maximum mass emission rates of NO and $NO_2$ in the undiluted engine exhaust. The maximum allowable emission rates were calculated based on a variety of factors including the: $NO_2$ occupational exposure limit, fresh air ventilation rate and expected equipment utilization.

Another important aspect of the specification was the requirement for an ammonia oxidation catalyst in the exhaust after-treatment system. Preventing ammonia "slip" from the engine is critical in underground mining applications to protect the health and safety of the workers. As such, the specification also prescribed a maximum allowable ammonia emission rate in the undiluted exhaust, again based on factors such as the ammonia occupational exposure limit and fresh air ventilation rate.

The specification also outlined requirements for the SCR and DEF system, including proper instrumentation and controls to improve system reliability. Design aspects to prevent component damage due to DEF freezing were also stipulated based on the mine location and fluid storage location during certain ventilation phases.

## 3.3    Engine Manufacturer Consultation

Following the development of the diesel engine performance requirements, Hatch consulted with engine manufacturers to analyze engine data and determine compliance with the specification. It was critical to consult with the manufacturer directly to quantify the $NO_2$/NOx ratio at the tailpipe and the resulting workplace $NO_2$ concentration.

Analysis of engine data showed both the concentration and mass emission of $NO_2$ in the undiluted engine exhaust could vary quite significantly over different engine operating modes. The results for one engine analyzed over eight different test modes can be seen in Fig. 6. While emissions from some test levels were so low they were

virtually undetectable, high $NO_2$ concentrations and mass emissions were seen when the engine was operating under low torque and power, and high RPM.
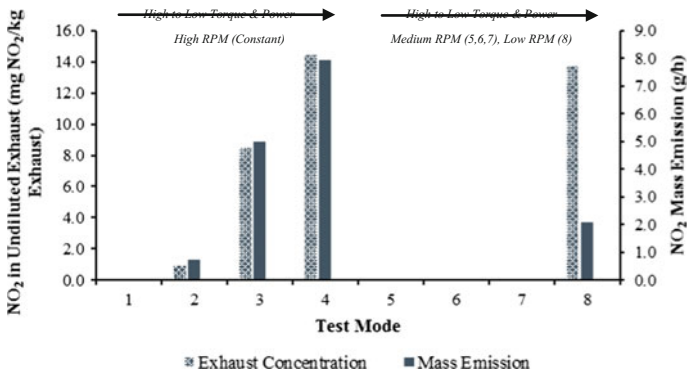


**Fig. 6.** Comparison of $NO_2$ concentration and mass emission rate showing markedly different levels at different engine operating modes, with some modes having negligible $NO_2$ emissions

The $NO_2$ undiluted exhaust concentration does not necessarily correlate to the resulting ambient $NO_2$ concentration. For example, if the engine is operating in a mode with a low exhaust flow rate, it could have a high tailpipe concentration based on the mass emission of $NO_2$; however, dilution with the mine fresh air ventilation system could significantly reduce the resulting workplace concentration. In addition, conversion of NO to $NO_2$ in the air over time will also impact the resulting ambient concentration. These effects are illustrated in Fig. 7, which shows the calculated workplace $NO_2$ concentration for the same engine (and operating modes) as discussed above.
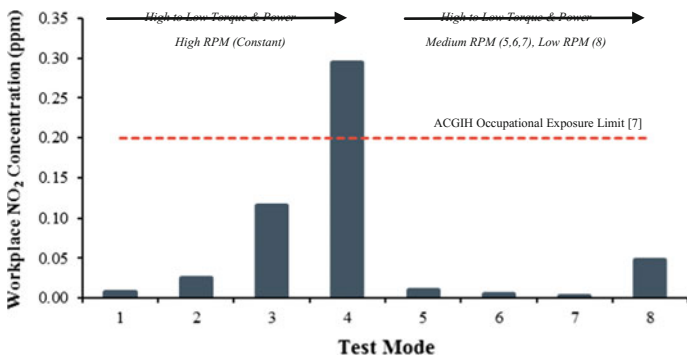


**Fig. 7.** Comparison of workplace $NO_2$ concentration for different engine operating modes, assuming: ventilation rate of 74 cfm/bhp, ambient conditions of 20 °C and 1.2 kg/m$^3$, and 10% (mol) conversion of NO to $NO_2$ in the ambient air (based on NO mass emission in the exhaust as provided by the engine vendor for the different test modes)

Despite engine test modes 3 and 8 having high $NO_2$ concentrations at the tailpipe, fairly low workplace concentrations are achieved once diluted with fresh air. Meanwhile, the highest $NO_2$ concentration is observed at the tailpipe and the workplace with test mode 4. Also, engine test modes that had virtually undetectable $NO_2$ concentrations at the tail pipe (i.e., 1, 5, 6 and 7) can still contribute to workplace $NO_2$ levels through the conversion of NO to $NO_2$ in the ambient air. Thus, the exhaust $NO_2$ concentration cannot be used alone, and instead must be fully analyzed with the ventilation air and exhaust NO level, to understand the engine's impact on the workplace $NO_2$ concentration. The impact of additional equipment using the same ventilation air would also need to be considered when quantifying the overall workplace $NO_2$ concentration.

## 3.4  Benefits to Underground Mining Applications

Technologies associated with Tier 4 Final (EU Stage IV) engines, such as SCR, provide many advantages in underground mining applications. Firstly, as discussed in previous sections, order of magnitude reductions in nitrogen dioxide levels can be achieved. Not only does this improve air quality for miners and help comply with occupational exposure limit regulations, it also enables economic ventilation air quantities. In some jurisdictions, air flow requirements are dictated specifically based on the engine (and corresponding Tier/Stage rating). For example, the Canadian CANMET organization prescribes roughly 30% lower air flow for Tier 4 engines than earlier engine ratings. Ventilation power is one of the largest contributors to a mine's operating costs; thus, any reduction in required air flow volume is beneficial from an economic perspective. Alternatively, keeping the same ventilation volume could drive productivity improvements.

Tier 4 Final (EU Stage IV) engines also help address operability issues associated with previous engine ratings. For example, SCR reduces or eliminates the need for EGR, which improves engine performance and increases fuel efficiency. SCR also reduces the strain on the DPF, as less DPM is formed in a higher temperature and more efficient combustion process. As DPFs can be a persistent maintenance issue, this is an important advantage with SCR-equipped engines. Regeneration of the DPF can also be troublesome in underground mining, with exhaust temperatures often not high enough to support active regeneration of the filter. Thus, as mentioned in Sect. 2.2, some engine manufacturers install a DOC upstream of the DPF to increase the $NO_2$ concentration to support DPF regeneration at lower temperatures. Depending on the jurisdiction, without SCR as part of the exhaust after-treatment system, this extra $NO_2$ could be problematic in terms of achieving regulated occupational exposure limits. However, with an SCR-equipped engine, the DOC can be used to support DPF regeneration, and any extra $NO_2$ should be sufficiently removed in the SCR system prior to release to the workplace.

## 3.5  Challenges

Despite the advantages of Tier 4 Final (EU Stage IV) engines outlined in Sect. 3.4, their implementation in underground mining also presents many challenges. A main

motivation for their implementation is to meet $NO_2$ occupational exposure limits, which have decreased dramatically in some jurisdictions over the past few years. Although Tier 4 Final (EU Stage IV) engines have much lower NOx emissions compared to previous engine ratings, they may not necessarily guarantee compliance in certain jurisdictions with low $NO_2$ requirements, and hence, also require low $NO_2$/NOx ratios at the tailpipe. The readiness of engine vendors to bias SCR to $NO_2$ conversion is uncertain at this point. Tier 4 Final (EU Stage IV) engines were originally designed for surface applications, which do not have the same focus on $NO_2$ emissions (versus overall NOx) as underground mining; consequently, engine vendors have not yet been faced with this specific request.

In addition, as seen in Sect. 3.3, the $NO_2$ emissions from an engine can vary greatly across different operating modes. During certain test modes (e.g., during start-up when there is a lag in efficiency as the SCR system comes to the proper temperature), the $NO_2$ emissions could be high enough to exceed regulated limits. Alleviating these high $NO_2$ excursions and preventing high workplace concentrations during certain engine operating modes requires further investigation.

Ammonia slip protection is also critical in applying SCR-equipped engines underground. SCR systems are employed with an ammonia oxidation catalyst to prevent slip; however, the amount of ammonia released to the atmosphere needs to be minimized to the maximum extent possible to protect the health and safety of the workers.

Lastly, SCR systems introduce an additional fluid to the diesel engine system called diesel exhaust fluid (DEF). It is a solution made simply of urea in deionized water. DEF is non-toxic, non-hazardous and non-flammable, which makes it a relatively benign substance being introduced into the underground workplace; however, urea is a common nitrogen-based fertilizer which could be a concern for water treatment systems if a spill occurs and therefore, containment must be included as appropriate. Its use also requires storage and dispensing infrastructure, which must be purchased, installed and requires space in the equipment fueling areas. DEF has very specific storage and handling requirements to prevent contamination; thus, thoughtful planning is required for such a system, especially in an underground mine environment. Preventing component damage due to DEF freezing should also be considered depending on the mine location and fluid storage location.

## 3.6 Operations Feedback

Although utilizing the SCR technology typically employed in Tier 4 Final (EU Stage IV) engines for surface compression-ignition engines offers advantages in terms of improved air quality and the potential for reduced air flow volumes, there remains some hesitation regarding their implementation in underground mining applications. These engines are new to many mine operators, leading to uncertainties surrounding reliability and maintenance. Despite the concerns, in the absence of battery electric equipment, mines are limited in terms of equipment options when needing to meet strict nitrogen dioxide limits, and thus, may have no choice but to embrace SCR-equipped engine technology.

Hatch obtained feedback from a Canadian mine operation who retrofitted one of their 50T trucks with an engine utilizing SCR technology. With the previous engine, the operators had complained about the strong odour from NOx. Following the switch to the SCR-equipped engine, they noted that the odour in the environment improved significantly. They also saw an improvement in the required maintenance interval, increasing from 12,000 to 20,000 h. The new engine also eliminated the need for a DPF, which eliminated the 4000-h regular maintenance interval associated with the filter. Overall, the new engine was highly appreciated by the operators and was found to be reliable and perform well in the environment. Based on the results, the mine plans on retrofitting the remainder of the primary fleet with SCR-equipped engines.

## 4    Secondary Emission Sources and Controls

### 4.1    Direct Fired Heaters

Depending on the location, surface heaters may be required for underground mines to heat the intake air to a minimum temperature to prevent freezing in the fresh air shaft. Unlike indirect fired heaters which have no emissions to the mine, direct fired heaters can contribute $NO_2$ to the workplace. High flame temperatures (i.e., >800 °C) or "dwell" lead to $NO_2$ formation, with the $NO_2$ then supplied directly to the workplace via the mine fresh air stream.

In North America, burner emission requirements are according to CSA Standard 3.7/ANSI Z83.4, which dictates an $NO_2$ level of less than 0.5 ppm in the airstream [8]. Although this is a low concentration, it could still represent a significant contribution to the total mine $NO_2$ level depending on the jurisdiction. Vendors have reported some improvements in burner product lines, with $NO_2$ regularly measured and reported as below detection limits in heated air streams.

For mines with strict $NO_2$ occupational exposure limits, indirect fired heaters are preferred; however, premium direct burner technology is improving and will likely regularly achieve $NO_2$ levels below the CSA standard in the future.

### 4.2    Blasting Operations

Blasting operations can also contribute $NO_2$ to the mine workings, both through the immediate smoke plume and in residual gases in the interstitial spaces of blasted rock that are released during mucking. $NO_2$ levels in the plume are significant and can exceed 150 ppm. Although the plume is removed through a blast clearing ventilation mode, residual blasting gases in the workplace on-shift remain a concern.

Testing was undertaken at a northern Canadian mine to quantify blast clearing times associated with different explosive types [9]. Two types of ammonium nitrate fuel oil (ANFO) and two types of emulsion explosives were tested. The $NO_2$ concentrations exceeded 100 ppm with the ANFO explosives, while $NO_2$ levels were below the detection limit with the emulsion types over multiple tests in the same

heading. Overall, emulsion explosives are very promising for underground mines requiring a reduction in $NO_2$ levels, both from the initial blast and residual gases in the muck; however, their use comes at a cost premium in comparison to other explosive types.

## 5 Conclusions

Nitrogen dioxide levels in underground mining remain a concern for human health and safety, as well as regulatory compliance. While reductions are achievable from secondary nitrogen dioxide sources with indirect fired heaters, high efficiency direct fired burners and emulsion explosives, the most significant potential reductions come from diesel engine controls. For mines where the use of battery electric equipment is not feasible, exhaust after-treatment technologies used in Tier 4 Final (EU Stage IV) compression-ignition engines operating on surface provide an opportunity to achieve order of magnitude reductions in underground nitrogen dioxide levels. Not only do these technologies offer improvements in air quality for miners, they can offer economic advantages in terms of reduced ventilation air flow volumes and corresponding power requirements, more efficient diesel fuel usage and lower maintenance costs. Challenges in implementation do exist, including: hesitation to adopt new technologies, high NOx emissions during engine startup and DPF regeneration modes, ammonia slip protection, and DEF storage and distribution infrastructure; however, they can be alleviated through well-planned mine design and providing information on these types of systems to the mining industry.

## References

1. Nonroad compression-ignition engines: exhaust emission standards EPA-420-B-16-022. United States Environmental Protection Agency Office of Transportation and Air Quality (2016)
2. Final regulatory analysis: control of emissions from nonroad diesel engines EPA420-R-04-007. United States Environmental Protection Agency Office of Transportation and Air Quality (2004)
3. Directive 97/68/EC of the European Parliament and of the Council (2012)
4. Limits and measurement methods for exhaust pollutants from diesel engines of non-road mobile machinery (I, II). GB 20891-2007 (2007)
5. Limits and measurement methods for exhaust pollutants from diesel engines of non-road mobile machinery (China III, IV). GB 20891-2014 (2014)
6. John Deere: https://www.deere.com/en_US/corporate/our_company/news_and_media/press_releases/2013/engines_drivetrain/2013apr17_power_ft4.page. Last accessed 2018
7. American conference of governmental industrial hygienists threshold limit values and biological exposure indices. ACGIH Signature Publications (2017)
8. American national standard/CSA standard for non-recirculating direct gas-fired industrial air heaters. ANSI Z83.4-2003/CSA 3.7-2003 (2003)
9. Thorslund, K.: Estimating blast clearing times for different types of explosives. Undergraduate Thesis, Queen's University, Kingston, ON (2017)

# Determination of Climatic Work Conditions—Thermal Discomfort Index

Jan Drenda[(✉)]

Silesian University of Technology, ul. Akademicka 2A, 44-100 Gliwice, Poland
RRl@polsl.pl

**Abstract.** Climatic conditions in underground mines and other plants depend on climate, kind and intensity of work (metabolic rate), clothing and acclimatization. The thermal discomfort index "δ" is the parameter which evaluates these conditions. The paper presents its definition and tables including metabolic ratios and thermal insulation of miners' clothing determined from in situ measurements. The nomograms specified for estimation of the index have also been presented in the paper. Five nomograms are included in the text concerning different values of relative humidity: 20, 40, 60, 80 and 100%. Each nomogram includes the results for a non-clothed man (thermal insulation of clothes $I_{cl}$ = 0) and for a fully-clothed man ($I_{cl}$ = 1 clo). The nomograms also consist of isolines of air velocity and metabolic rate for workers who are acclimated and for those who are not acclimated. Results for different values of relative humidity can be interpolated. The value of "δ" does not have a unit. When δ = 0, it is understood as thermal comfort; when δ $\geq$ 1, it is understood as a dangerous discomfort. However, when 0 < δ < 1, the value denotes acceptable discomfort conditions.

**Keywords:** Climate · Climatic conditions · Thermal comfort · Thermal discomfort

## 1 Introduction

Polish coal mines can be characterized as having difficult to very difficult climatic work conditions. The reason for this is their great depth of operation and the use of high-power mining machines. The climatic work conditions of miners are influenced by climate parameters such as air temperature, humidity and airflow velocity, and factors related to humans such as metabolic rate, clothing and acclimatization. Metabolic rate is a stream of metabolic heat produced by the human body to maintain a constant internal temperature of 37 °C. A person's metabolic rate depends on the difficulty of the work that they are performing. Heat transfer between a human being and the environment takes place through convection, thermal radiation, and evaporation of sweat; these are the three basic ways to exchange heat that determine a person's internal temperature. Through convection and thermal radiation, a person can emit and receive heat. By evaporating sweat, a person can only emit heat. In hot environments this plays a fundamental role. The emission of heat by evaporation of sweat ceases when the partial pressure of water vapor in the air equals the partial pressure of water

vapor saturated at the surface temperature of human skin, which in conditions that are safe for health should not exceed 35 °C [1–4].

## 2  The Thermal Discomfort Index, "δ"

Thermal discomfort index is a parameter defining climatic working conditions. It can be determined as a function of climate parameters and human parameters [1, 5–7].

$$\delta = f(M, t_d, \varphi, t_r, W, I_{cl}, A) \tag{1}$$

Where:
M    metabolic rate, $W/m^2$
$t_d$    dry temperature, °C
$\varphi$    relative humidity,
$t_r$    average radiant temperature, °C
w    air velocity, m/s
$I_{cl}$    thermal insulation of clothes, clo
A    acclimatization, (acclimated or not acclimated).

In mine environments it can be assumed that the average temperature of radiation is equal to the air temperature ($t_a = t_r$).

On the basis of research conducted in coal mines, average energy expenditure was determined for miners performing various mining functions (see Table 1) and thermal resistance values of different sets of mining clothing (see Table 2) [8, 9].

**Table 1.** Categories of work and average metabolic rates of the miners at work in underground mines [8, 9]

| Workplace | | Average metabolic rate ($W/m^2$) | Work intensity |
|---|---|---|---|
| Longwalls | Cutter-loader men | 170 | Moderate work |
| | Section men | 172 | Moderate work |
| | Supervisors | 148 | Moderate work |
| | Mechanics, electricians | 169 | Moderate work |
| | Helpers | 154 | Moderate work |
| Headings | Cutter-loader men | 191 | Moderate work/hard work |
| | Miners in blind end | 214 | Hard work |
| | Supervisors | 197 | Moderate work/hard work |
| | Mechanics, electricians | 192 | Moderate work/hard work |
| Transport | Transport, conveyor transfer stations | 174 | Moderate work |

**Table 2.** Thermal insulation of dry and wet miners' clothes (principle static insulation) [8, 9]

| Clothing sets | Clothing items | Dry clothes $I_{cl}$; clo | Wet clothes $I_{cl}$; clo |
|---|---|---|---|
| E1 | Helmet, rubber boots, mining lamp cover, shorts | 0.12 | – |
| E2 | Helmet, rubber boots, mining lamp cover, shorts, t-shirt | 0.28 | 0.022 |
| E3 | Helmet, rubber boots, mining lamp cover, pants | 0.32 | – |
| E4 | Helmet, rubber boots, mining lamp cover, pants, t-shirt | 0.50 | 0.16 |
| E5 | Helmet, rubber boots, mining lamp cover, pants, flannel shirt with long sleeves | 0.77 | 0.33 |
| E6 | Helmet, rubber boots, mining lamp cover, pants, flannel shirt with long sleeves, work blouse | 0.97 | 0.47 |

The acclimatization of the worker should be specified in determining the thermal discomfort index. It is assumed that a person is acclimated if they work in a warm environment for at least 2 weeks.

The thermal discomfort index was determined on the basis of Fanger's thermal comfort equation and graphs, as well as the WBGT reference values, which were compared to the value of the effective temperature of the ET [1, 6, 7, 10].

Figure 1 and Eq. 2 display the definition of thermal discomfort index "δ". For the given climate parameters, metabolic rate, clothing, and acclimatization of the workers shown in Fig. 1, Fanger's thermal comfort isoline [2] has been determined (Line k) as well as the reference value of the ET index according to the standard [4] (Line g). Figure 1 shows the areas that determine the climatic conditions of work to be safe [between the comfort curve (k) and ET (g)]; hazardous [right of ET (g)]; and cool [left from the comfort curve (k)]. Assuming any points A, B, C and created BA and BC vectors on the graph (see Fig. 1), the thermal discomfort index is the coordinate ratio of BA to BC vectors.
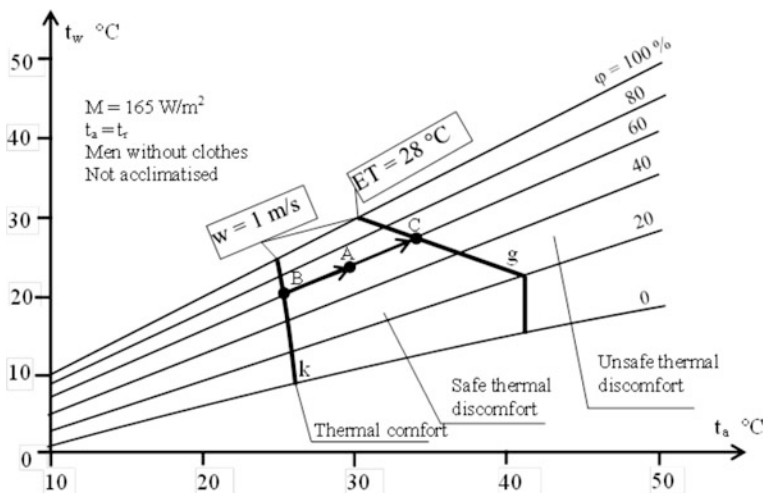


**Fig. 1.** Vectors of the thermal discomfort index "δ"

$$\delta = \frac{BA}{BC} = \frac{t_{aA} - t_{aB}}{t_{ac} - t_{aB}} \tag{2}$$

Depending on the value of the thermal discomfort index $\delta$, the climatic working conditions are divided into:

| | |
|---|---|
| $\delta = 0$ | thermal comfort |
| $\delta < 0$ | cold environment |
| $\delta > 0$ | warm environment |
| $\delta = 1$ | border of safe thermal comfort |
| $0 < \delta < 1$ | acceptable thermal discomfort |
| $\delta \geq 1$ | dangerous thermal discomfort. |

A breakdown of climate conditions in the range of $0 < \delta < 1$ is provided in Table 3.

**Table 3.** Division of climatic conditions safe for health

| Climate conditions | | |
|---|---|---|
| $0 < \delta < 1$ | $0 < \delta < 0.2$ | Favorable |
| | $0.2 \leq \delta < 0.5$ | Satisfactory |
| | $0.5 \leq \delta < 0.8$ | Difficult |
| | $0.8 \leq \delta < 1$ | Very difficult |

## 3 Nomograms for Determining Thermal Discomfort Index

The heat discomfort index "$\delta$" can be determined from nomograms. Five nomograms for five air humidity values of 20, 40, 60, 80, and 100% have been presented. Each nomogram describes a man without clothes with thermal resistance of clothing $I_{cl} = 0$ (left side of the nomogram) and a man with clothes $I_{cl} = 1clo$ (right side of the nomogram). There are isolines on the nomograms depicting air velocity and metabolic rate for acclimated workers and for workers who are not acclimated [7–10] (Figs. 2, 3, 4, 5 and 6).

The method for reading the thermal discomfort index from nomograms is shown in Fig. 5 for air humidity $\varphi = 80\%$. The following parameters have been assumed: air temperature $t_d = 25\ °C$ (Point A), flow velocity $w = 0.5$ m/s (Point B), energy expenditure $M = 165\ W/m^2$, and acclimated person (Point C). By going through points A, B, and C in succession on the nomogram, the value of the "$\delta$" index can be read. A thermal discomfort index for people wearing clothes is determined in the same way, using points B′, C′, and D′.

For other air humidity and thermal insulation of clothes values, the thermal discomfort index can be interpolated from the nomograms provided.
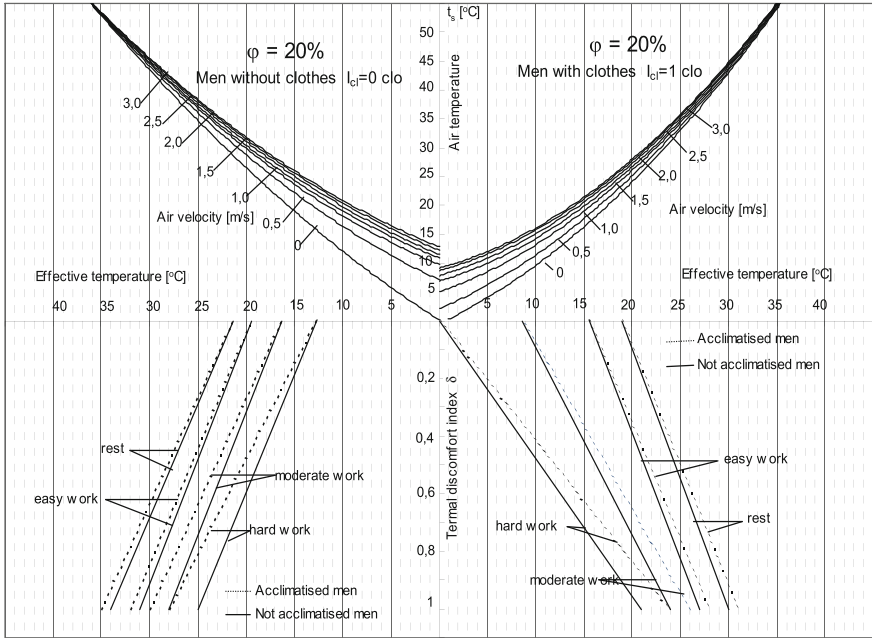
**Fig. 2.** Nomogram for evaluating thermal discomfort indeks for relative humidity $\varphi = 20\%$
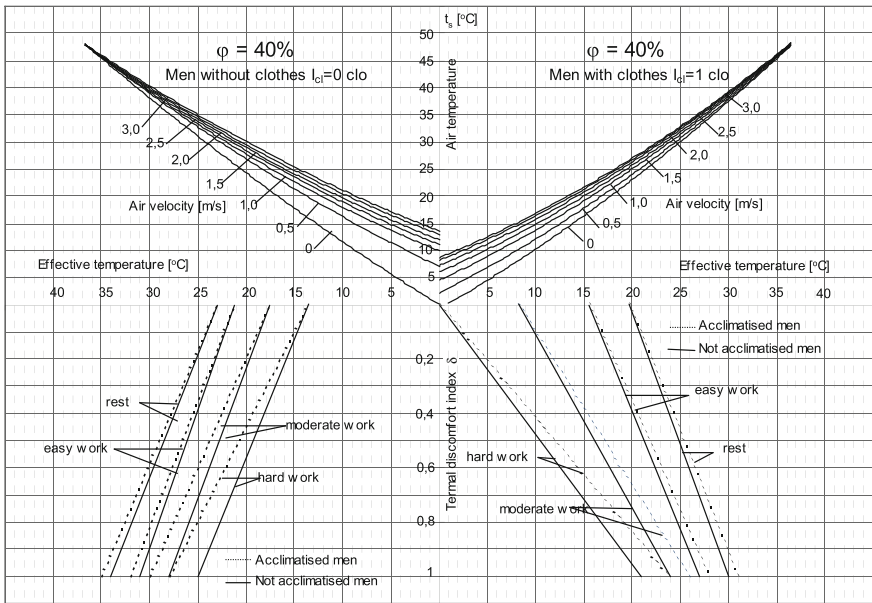


**Fig. 3.** Nomogram for evaluating thermal discomfort indeks for relative humidity $\varphi = 40\%$
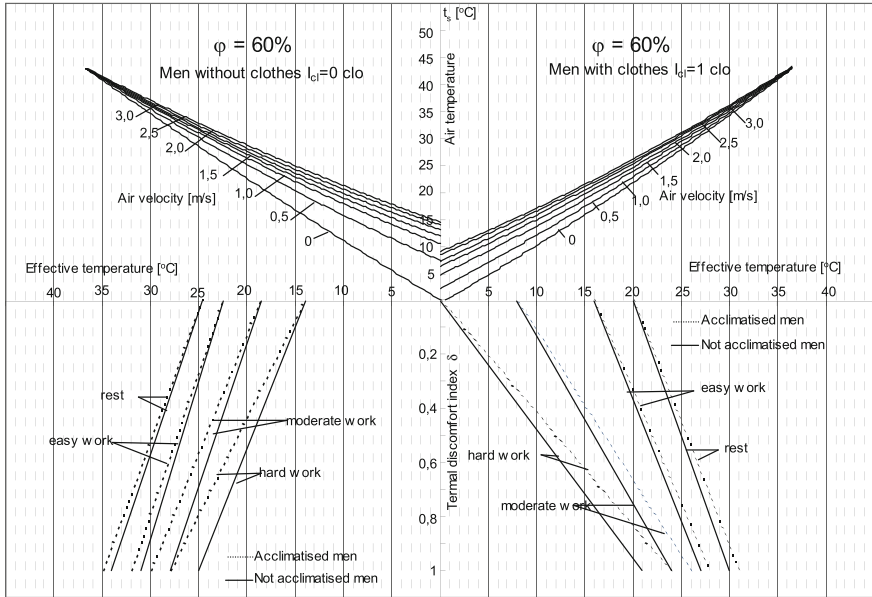
**Fig. 4.** Nomogram for evaluating thermal discomfort indeks for relative humidity $\varphi = 60\%$
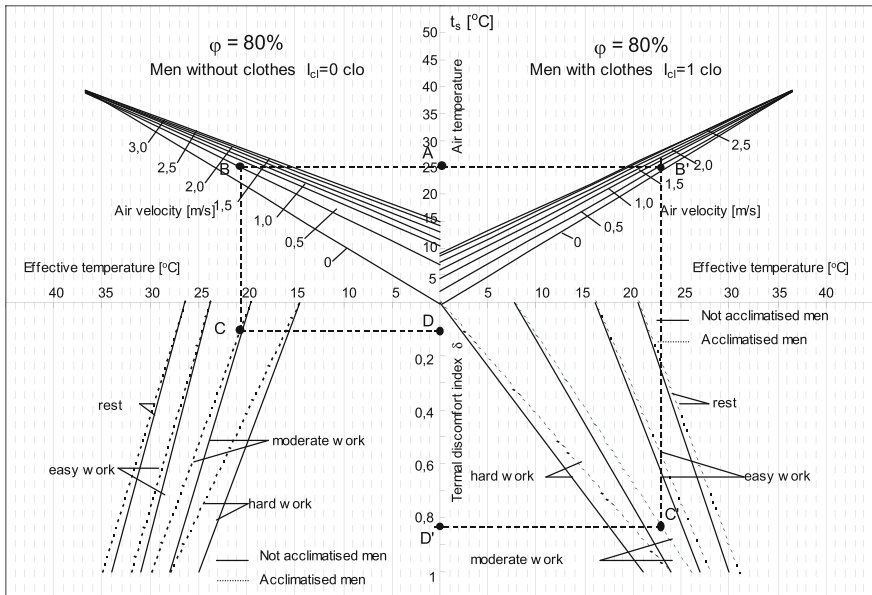


**Fig. 5.** Nomogram for evaluating thermal discomfort indeks for relative humidity $\varphi = 80\%$
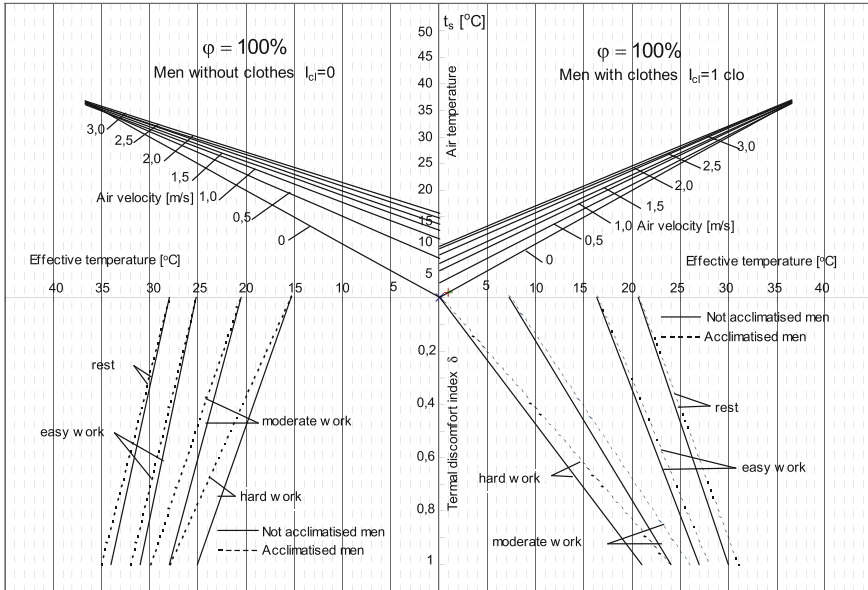
**Fig. 6.** Nomogram for evaluating thermal discomfort indeks for relative humidity $\varphi = 100\%$

## 4    Conclusions

The thermal discomfort index is a parameter that fully evaluates the climatic conditions of a person or a group of people in warm environments, taking into account parameters related to both climate and the human. Thermal discomfort values between 0 and 1 are easy to memorize and analyze. The Thermal discomfort index, when greater than 1, indicates a climatic hazard for workers.

The monograph "*Monograph catalogue used for establishing discomfort coefficient for persons working in different environments above the ground and underground without sunlight*" (in Polish) includes 53 nomograms in which the air humidity changes in increments of 10%, and the thermal resistance of clothing every 0.1 clo [9].

## References

1. Drenda, J.: Thermal discomfort in working environments of deep mines. Zeszyty Naukowe, Politechnika Śląska, z. 213, Wydawnictwo Politechniki Śląskiej, p. 131 (in Polish) (1993)
2. Fanger P.O.: Thermal comfort. Analysis and Applications in Environmental Engineering. Copenhagen (1970)
3. Wenzel H.G., Piekarski C.: Klima und Arbeit. Bayerisches Staats-ministerium für Arbeit und Sozialordnung. 4 Aufl. München (1984)
4. PN-85/N-08011: (ISO 7243-1982), Hot environments-Estimation of the heat stress on working man, based on the WBGT-index (wet bulb globe temperature) (1982)

5. Drenda, J., Sułkowski, J., Pach, G., Różański, Z., Wrona, P.: Two stage assessment of thermal hazard in an underground minearch. Arch. Min. Sci. **61**(2), 313–326 (2016)
6. Drenda, J.: Geometrical interpretation of the index of thermal discomfort. Zeszyty Naukowe, Politechnika Śląska, z. 227, Wydawnictwo Politechniki Śląskiej, p. 50 (in Polish) (1996)
7. Drenda, J.: Thermal safety of workers in warm and hot work conditions. In: Proceedings of the 5th international conference on air distribution in rooms roomvent-96, Yokohama, Japan (1996)
8. Drenda, J., Kułagowskam, E., Różański, Z., Pach, G., Wrona, P., Karolak, I.: Determination of the metabolic rate and work arduousness class for workers in coal mines—the results of in situ research. Arch. Mining Sci. **62**(2), 313–326 (2017)
9. Drenda, J.: i inni: Katalog nomogramów do wyznaczenia wskaźnika dyskomfortu cieplnego, "δ" (WDC) dla osób przebywających w różnych środowiskach na powierzchni i pod ziemią bez nasłonecznienia. Wydawnictwo Politechniki Śląskiej, p. 64 (in Polish) (2017)
10. Drenda, J.: Evaluation of efficiency of means adopted to improve the climatic conditions in deep mines. In: Proceedings of the 7th international mine ventilation congress, Cracov, Poland, pp. 157–162 (2001)

# Wireless Sensor Network Based Underground Coal Mine Environmental Monitoring Using Machine Learning Approach

Lalatendu Muduli[1(✉)], Devi Prasad Mishra[2], and Prasanta K. Jana[1]

[1] Department of Computer Science & Engineering, Indian Institute of
Technology (Indian School of Mines), Dhanbad, India
lalatendu.bapil23@gmail.com, prasantajana@yahoo.com
[2] Department of Mining Engineering, Indian Institute of Technology
(Indian School of Mines), Dhanbad, India
dpmishra@iitism.ac.in

**Abstract.** Underground coal mines are associated with environmental problems and serious hazards resulting in the loss of coal resources and valuable lives. Wireless sensor network (WSN), nowadays, is widely adopted for continuous monitoring of environmental parameters and other aspects of underground coal mines. Sensor nodes deployed in underground coal mines are meant for sensing the environmental parameters and transferring the data to ground monitoring station for processing. Since the monitoring data are imprecise and vague in nature, it is imperative to analyze the data for taking precautionary measures. In this paper, we applied data mining or Machine Learning (ML) technique to predict the occurrence of mine fire hazard in underground coal mines. Machine learning concept is inherited from Artificial Intelligence (AI) which has an ability to learn from the past experiences. We applied supervised learning method on the collected data set which partitioned into training and testing data sets. The purpose of training data set is to train the model, whereas the testing data set is meant for evaluation of the trained model. Learning method is implemented at the base stations or sinks instead of monitoring station for taking immediate real-time decision on sensed data in case of any hazard. Learning method for monitoring of different hazard conditions are simulated using WEKA (data mining and machine learning) Tool. This system is more reliable and responsive to any kind of hazards as compared to offline monitoring system used in underground coal mines.

**Keywords:** Underground coal mine · Wireless sensor network
Machine learning · Fire hazard · Environmental monitoring

## 1 Introduction

### 1.1 Background

Underground coal mines are vulnerable to various hazards like roof fall, explosion, mine fire, etc. [1]. However, mine fire constitutes the major hazard which leads to the loss of valuable human lives and damage of mining machinery and infrastructure.

There are various prime factors, such as blasting, welding, mine explosion, open flame, frictional spark from drilling and cutting operations, electrical sparking and arcing, spontaneous combustion of coal, etc., leading to mine fires. Among these, spontaneous combustion of coal contributes 75–90% of coal mine fires. Spontaneous combustion of coal is the process of auto-oxidation of coal and other carbonaceous matter which leads to generation of different poisonous and inflammable gases like carbon dioxide ($CO_2$), carbon monoxide (CO), and heat. The heat so generated goes on accumulating due to improper dissipation, and that leads to mine fire. Hence, continuous monitoring of spontaneous combustion at its early stage can prevent the occurrence of coal mine fires and ensure a safe working environment for the miners.

## 1.2 Motivation

Nowadays, wireless underground sensor network (WUSN) [2–4] is used for continuous monitoring of environmental parameters of underground coal mines. WUSN can be realized by deploying sensor nodes in the wall and roof of underground coal mines galleries. These sensor nodes are meant for sensing the environmental parameters and sending the sensed data to the ground monitoring station through base station (sink). Thereafter, ground monitoring station takes decisions from the monitoring data. However, it is somewhat difficult to predict the chances of occurrence of any events from these monitoring data. Hence, some prediction technique like machine learning should be applied on these monitoring data to increase the efficiency and efficacy of underground coal mine monitoring system.

In this paper, we propose a WSN-based early fire prediction system for underground coal mines using machine learning approach. The sensor nodes in WUSN collect different monitoring parameters like temperature, CO, $CO_2$ and $O_2$, and send these parameters to ground monitoring station for prediction of fire hazards [5]. The fire prediction system using machine learning approach uses aforementioned parameters as feature input data and predicts the target value. The main contributions of the paper are given below.

- Deployment of sensor nodes for sensing the environmental and other parameters in underground coal mines.
- Propose a machine learning approach based early fire prediction system in coal mines.
- Perform the simulation of proposed method and discuss various performance parameters related to mine fire prediction.

The rest of the works are organized as follows. In Sect. 2, we discuss the literatures emphasizing the wireless sensor network based underground coal mines monitoring using machine learning approach. The detailed system model used is explained in Sect. 3. The proposed machine learning based fire prediction system is presented in Sect. 4 followed by the simulation results in Sect. 5. Finally, Sect. 6 concludes the paper.

## 2    Literature Review

This section presents the pioneering research works done on the application of machine learning in underground coal mines as our proposed work is based on it. Jiang et al. [6] proposed a support vector machine (SVM) based risk prediction system for assessing the rock bolts failure in underground coal mines. The SVM method is applied on the data collected from underground coal mines. Bogucki et al. [7] presented an early responsive system for prediction of seismic hazard in coal mines. This system helps in providing a safe workplace environment in underground coal mines. Kabiesz et al. [8] proposed induction or rule based seismic hazard prediction system for longwall mine. This machine learning method outperformed the other techniques used in mines in terms sensitivity and specificity of prediction. Kačur et al. [9] proposed a support vector machine based UCG data prediction in coal mines.

None of the above applications of machine learning method describes the prediction of fire in underground coal mines. Keeping this in view, we propose a machine learning based early fire prediction system in wireless underground sensor network.

## 3    System Model

This section briefly discusses about the Naïve Bayes Classification as our proposed classification algorithm is based on it.

### 3.1    Naive Bayes Classification

It is a supervised leaning method based on Bayes' theorem with a naïve assumption that every feature pairs are independent. For example, let us consider a class variable "$y$" and a set of dependent features "$x_i$", then the relationship among these variables using Bayes' theorem can be represented as

$$P(y|x_1,\ldots,x_n) = \frac{P(y)P(x_1,\ldots,x_n|y)}{P(x_1,\ldots,x_n)} \tag{1}$$

By using naïve independence assumption, Eq. (1) is represented by

$$P(y|x_1,\ldots,x_n) = \frac{P(y)\prod_{i=1}^{n}P(x_i|y)}{P(x_1,\ldots,x_n)} \tag{2}$$

As $P(x_1,\ldots,x_n)$ is constant for a given input data, Eq. (2) can be written as follows:

$$P(y|x_1,\ldots,x_n) \propto P(y)\prod_{i=1}^{n}P(x_i|y) \tag{3}$$

Now, the Naïve Bayes classifier model can be implemented from Eq. (3). For this, the probability of feature input dataset $\{x_1, \ldots, x_n\}$ are calculated with respect to each

possible value of Target set ($y$) and the probability with maximum value are chosen as output which is represented as follows:

$$y = argmax_y P(y) \prod_{i=1}^{n} P(x_i|y) \tag{4}$$

where $P(y)$ and $P(x_i| y)$ are the class and conditional probability, respectively.

## 4 Proposed Work

Sensor nodes are deployed in the wall and roof of the intake and return airways of underground coal mines, which coordinate among themself and form the WUSN. The deployment of WUSN in longwall and bord and pillar mining are schematically shown in Fig. 1. These sensor nodes are meant for sensing the environmental parameters and other aspects of underground mines and send the data to the base station for processing. The base station transmits these processed data to the ground monitoring station. The monitoring station takes the decision on the data and provides preventive measures in case of any hazard. Therefore, some decision or prediction methods should be incorporated on the monitoring data for increasing the accuracy and reliability of WUSN.

Different fire indices, such as Graham's ratio, Young's ratio, etc. are commonly used for early detection of fire in underground coal mines caused due to spontaneous combustion. During the combustion process, different combustible gases like CO and $CO_2$ are produces with depletion of $O_2$ and liberation of heat, which increases the temperature (T) of underground coal mine environment. The generation of T, CO, and $CO_2$ above usual values and depletion of $O_2$ give clear indication of fire in underground coal mines. However, detection of fire in coal mines utilizing the aforementioned fire indices is done offline and does not provide high temporal and spatial resolutions to the system. Hence, we propose an online fire prediction system based on machine learning approach in which we used T, CO, $CO_2$ and $O_2$ as the feature matrix of input parameters for early detection of fire in underground coal mines. The machine learning approach based fire prediction in underground coal mines is presented in Algorithm 1 and its stepwise descriptions are given below.
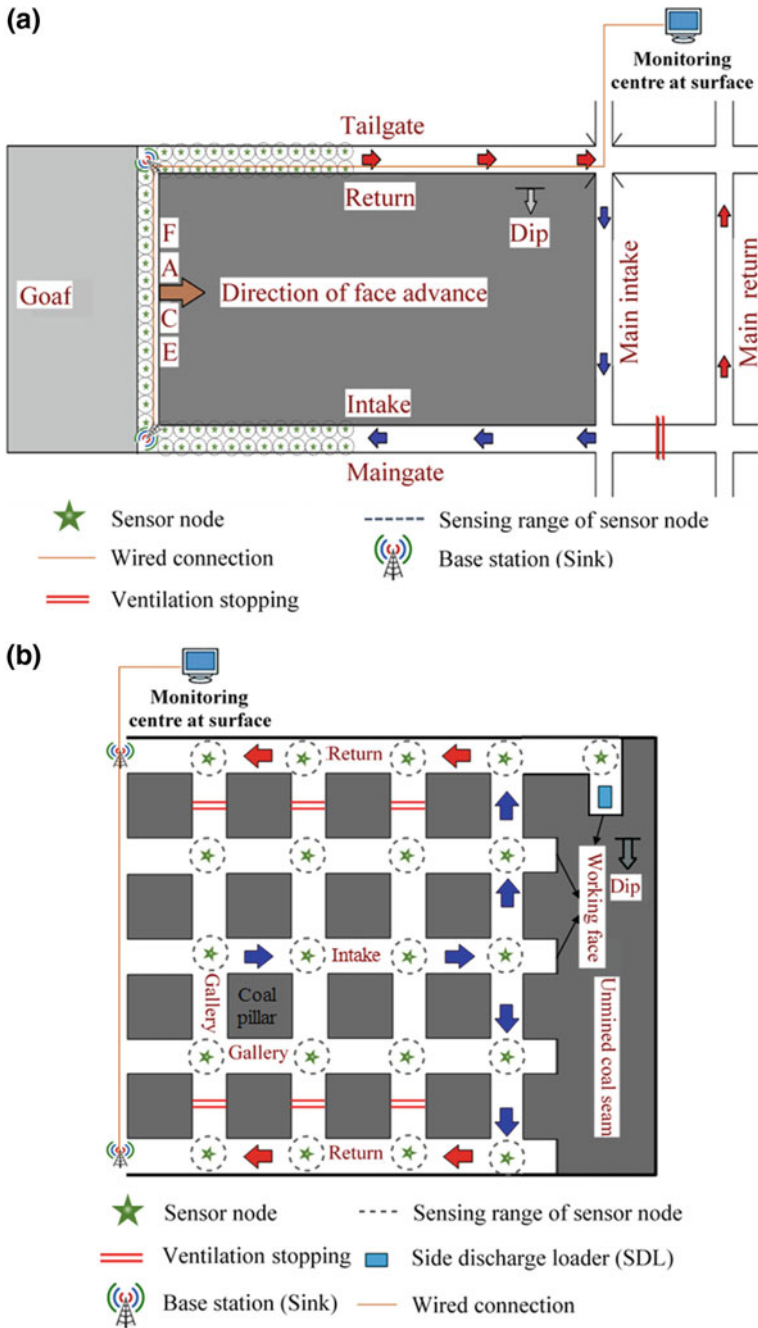
**Fig. 1.** Deployment of WUSN in underground coal mines: **a** longwall mining, **b** bord and pillar mining

```
Algorithm 1: Machine Learning based Fire Prediction in Under-
ground Coal Mines

INPUTS: [Temperature (T), Carbon monoxide (CO), Carbon dioxide
(CO₂), Oxygen (O₂)]: feature matrix; F: target vector; n: number
of instances/samples in dataset
OUTPUTS: Classification into the set Fire (F) or Not-Fire (NF)
1. Load the fire dataset
2. Store the feature matrix and target vector
3. Split the feature matrix and target vector into Training and
Testing sets
4. Train the model using Training dataset
5. Make predictions on Test dataset
6. Compare actual target values with predicted target values and
calculates different metrics
```

**Step 1**    The fire dataset having n instances of [T, CO, $CO_2$, $O_2$, F] is loaded into the classifier.

**Step 2**    The fire dataset [T, CO, $CO_2$, $O_2$, F] is stored separately as feature matrix [T, CO, $CO_2$, $O_2$] and target vector (F).

**Step 3**    The feature matrix [T, CO, $CO_2$, $O_2$] and target vector (F) are split into training sets, i.e. Train ([T, CO, $CO_2$, $O_2$]) and Train (F), and testing sets, i.e., Test ([T, CO, $CO_2$, $O_2$]) and Test(F) using 10-fold cross-validation. The 10-fold cross-validation means the total sample dataset is divided into 10 number of random subsamples in which a single subsample is used as a Testing set for testing or validating the model, whereas remaining 9 subsamples are used as Training set to train the model.

**Step 4**    The 9 random subsamples of training set are now used to train the model using Naïve Bayes classifier as in Eq. (4).

**Step 5**    The single random subsamples of testing set are now used to validate or test the model and generates the output (Predicted (F)) using Naïve Bayes classifier.

**Step 6**    The actual target value (Test (F)) and the predicted target value (Predicted (F)) calculated from Step-5 are now being compared and calculation of several metrics like sensitivity, recall, precision, Accuracy, F-measure, etc. have been performed which are discuss hereafter.

**True Positive (TP)**    Number of instances whose target value are predicted as positive, however, its actual target value is positive.

**False Positive (FP)**    Number of instances whose target value are predicted as positive, however, its actual target value is negative.

**True Negative (TN)**    Number of instances whose target value are predicted as negative, however, its actual target value is negative.

**False Negative (FN)**    Number of instances whose target value are predicted as negative, however, its actual target value is positive.

These aforementioned four parameters are used in the confusion matrix as presented in Table 1.

**Table 1.** Confusion matrix

|  | Not-Fire (NF) | Fire (F) |
|---|---|---|
| Not-Fire (NF) | True Positive (TP) | False Positive (FP) |
| Fire (F) | False Negative (FN) | True Negative (TN) |

**TP Rate**: It is the rate at which instances classified correctly into a particular class. It is also known as *Recall* or *Sensitivity*.

$$Recall = TP/(TP + FN) \tag{5}$$

**FP Rate**: It is the rate at which instances classified incorrectly into a particular class.

**Precision**: It is the proportion of instances that are positively classified to a given class by the total number of instances that are predicted positively to that class.

$$Precision = TP/(TP + FP) \tag{6}$$

**Accuracy**: It is the rate at which instances predicted correctly to a particular class with respect to the total number of instances in the dataset.

$$Accuracy = (TP + TN)/(TP + TN + FP + FN) \tag{7}$$

**Error Rate**: It is the negation of Accuracy.

$$Error\,Rate = 1 - Accuracy \tag{8}$$

**F-Measure**: It is the combined measure of Recall and Precision which is calculated as follows:

$$F - Measure = (2 * Precision * Recall)/(Precision + Recall) \tag{9}$$

## 5    Simulation Results

The proposed algorithm was simulated using a Data Mining and Machine Learning Tool, namely Waikato Environment for Knowledge Analysis (WEKA) [10] on a system with an Intel Core i7-4770 processor, 3.40 GHz CPU and 4 GB RAM running on Microsoft Windows 10 platform. The collected monitoring data from underground coal mine are input to the WEKA tool in which temperature, CO, $CO_2$ and $O_2$ are taken as feature input data as shown in Fig. 1a–d and Class which consists of Non-Fire

(NF) and Fire (F) sets are considered as target set. The figure shows a rising trend in Temperature, CO and $CO_2$ concentrations and falling trend in $O_2$ concentration. This might be due to the occurrence of spontaneous combustion of coal. The simulation results for input dataset are presented in Table 2 (Fig. 2).

**Table 2.** Simulation results of fire prediction in underground coal mines using data mining and machine learning tool (WEKA)

```
=====================Run Information =====================

  Scheme:      weka.classifiers.bayes.NaiveBayes
  Relation:    Dataset-weka.filters.unsupervised
  Number of Instances in Dataset:   1065
  Number of Attributes: 5 (Temperature (deg C), O2 (%), CO (%), CO2 (%), Class)
  Test mode:   10-fold cross-validation

  ================Classifier Model (full training set) ================

  Name of Classifier: Naive Bayes Classifier

               Class
  Attribute      NF      F
             (0.65)  (0.35)

  Time taken to build model: 0 seconds

  ===================Summary of Results====================

  Correctly Classified Instances:   1048          98.4038 %
  Incorrectly Classified Instances: 17            1.5962 %
  Kappa statistic:                  0.9651
  Mean absolute error:              0.0156
  Root mean squared error:          0.1204
  Relative absolute error:          3.4535 %
  Root relative squared error:      25.3158 %
  Total Number of Instances:        1065

  =================Detailed Accuracy By Class ==================
          TP Rate FP Rate Precision Recall F-Measure MCC ROC Area Class
          0.976   0.000   1.000   0.976   0.988   0.966   1.000   NF
          1.000   0.024   0.956   1.000   0.977   0.966   1.000   F
  Weighted
  Average 0.984   0.008   0.985   0.984   0.984   0.966   1.000

  ====================Confusion Matrix====================

                      a     b   ← classified as
                    680   17  |  a = NF
                      0  368  |  b = F
```

From Table 2, it is observed that out of the five attributes used in the simulation, four, such as Temperature, CO, $CO_2$ and $O_2$ are selected for feature input data and one,
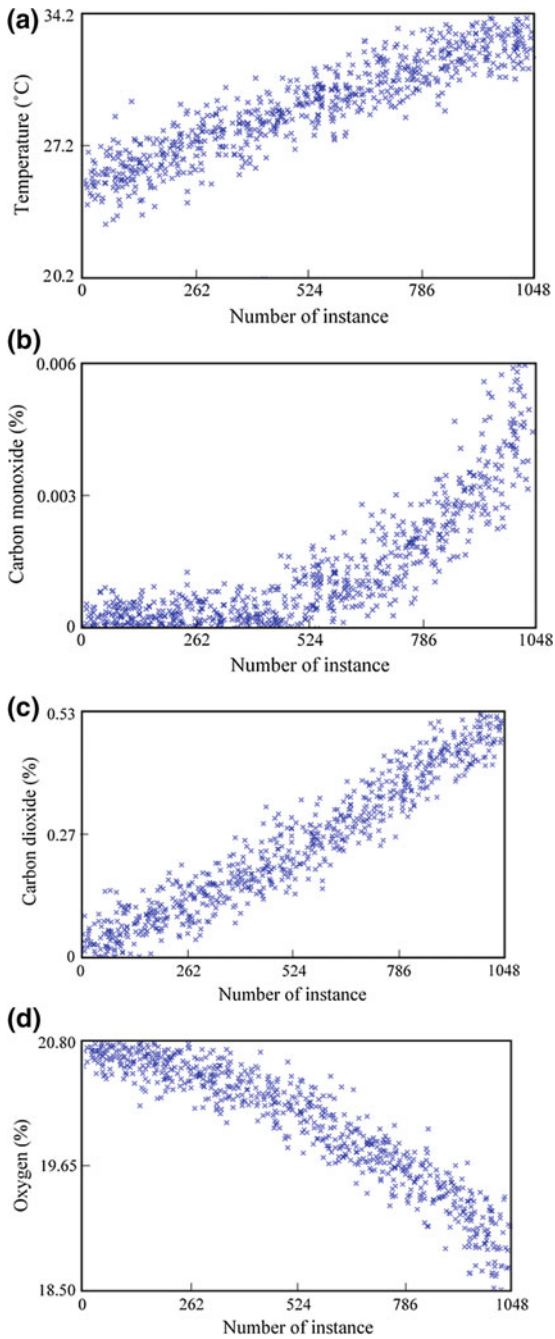
**Fig. 2.** Monitoring dataset: **a** temperature, **b** carbon monoxide, **c** carbon dioxide, **d** oxygen

i.e., Class is selected for target set. 10-fold cross validation is used to divide the entire dataset having 1065 instances into training and test sets. Out of these 1065 instances, 1048 are correctly classified into its appropriate class, whereas 17 instances are wrongly classified. Results of different errors and classification accuracy parameters as discussed in Sect. 4 are presented in summary of results and detailed accuracy by class are presented in Table 2. Finally, confusion matrix section which gives TP = 680, FP = 17, FN = 0 and TN = 368 are presented in Table 2.

## 6 Conclusions and Future Work

This paper proposed a wireless sensor network based fire prediction system for underground coal mines using machine learning approach. Sensor nodes were deployed in the wall and roof of the intake and return airways of underground coal mine for sensing/detecting environmental parameters and transfer these collected data to the ground monitoring station through base station for decision-making. As these sensor data are vague and imprecise in nature, it is very much difficult to analyze the patterns of monitoring data for taking preventative measures. Therefore, in this study, a prediction technique, named as machine learning (Naïve Bayes Classification) has been incorporated with the WUSN system for monitoring the environmental parameters and detecting the occurrence of fire hazard in underground coal mines. The Naïve Bayes Classification uses the concept of Artificial Intelligence and trained itself from the characteristic input data. The proposed classification technique is simulated using a Data Mining and Machine Learning Tool, namely Waikato Environment for Knowledge Analysis (WEKA). The simulation results revealed that the machine learning based monitoring system is reliable and more accurate than the offline monitoring system used in practice. In future, the work will be extended to measure the accuracy of underground coal mine monitoring system with respect to different classifiers used in the machine learning approach.

## References

1. Ramlu, M.A.: Mine Disasters and Mine Rescue. Balkema, The Netherlands (1991)
2. Akyildiz, I.F., Stuntebeck, E.P.: Wireless underground sensor networks: research challenges. Ad Hoc Netw. **4**(6), 669–686 (2006)
3. Muduli, L., Jana, P.K., Mishra, D.P.: A novel wireless sensor network deployment scheme for environmental monitoring in longwall coal mines. Process Saf. Environ. Prot. **109**, 564–576 (2017)
4. Muduli, L., Mishra, D.P., Jana, P.K.: Application of wireless sensor network for environmental monitoring in underground coal mines: a systematic review. J. Netw. Comput. Appl. **106**, 48–67 (2018)
5. Muduli, L., Jana, P.K., Mishra, D.P.: Wireless sensor network based fire monitoring in underground coal mines: a fuzzy logic approach. Process Saf. Environ. Prot. **113**, 435–447 (2018)

6. Jiang, P., Craig, P., Crosky, A., Maghrebi, M., Canbulat, I., Saydam, S.: Risk assessment of failure of rock bolts in underground coal mines using support vector machines. Appl. Stochast. Models Bus. Ind. (2017)
7. Bogucki, R., Lasek, J., Milczek, J.K., Tadeusiak, M.: Early warning system for seismic events in coal mines using machine learning. In: IEEE Federated Conference on Computer Science and Information Systems (FedCSIS), pp. 213–220 (2016)
8. Kabiesz, J., Sikora, B., Sikora, M., Wróbel, Ł.: Application of rule-based models for seismic hazard prediction in coal mines. Acta Montanist. Slovaca **18**(4) (2013)
9. Kačur, J., Laciak, M., Durdán, M., Flegner, P.: Utilization of machine learning method in prediction of UCG data. In: IEEE 18th International Carpathian Control Conference (ICCC), pp. 278–283 (2017)
10. Weka 3: Data mining with open source machine learning software. https://www.cs.waikato.ac.nz/ml/weka/. Last accessed 2018/02/15

# Evaluation of Microclimate Conditions
# in Polish Underground Mines

Nikodem Szlązak and Dariusz Obracaj[(✉)]

AGH University of Science and Technology, al. Mickiewicza 30,
30-059 Kraków, Poland
`obracaj@agh.edu.pl`

**Abstract.** This paper presents the current and previous legal status of the assessment of thermal working conditions in the Polish mining industry. There was a change of mining law and regulations in the field of heat stress control in Polish mines in 2017. The genesis and extent of the use of new "substitute climate temperature" (SCT) index according to regulations in force are outlined. This heat index was compared to the index valid in previous mining regulations. Both indices were compared on the basis of the PHS model included in the International Standard ISO 7933: 2004. Differences in the heat hazard for the critical values of both indicators covering employee working time were demonstrated. The disadvantage of direct indicators based on direct measurements of environmental parameters is the lack of consideration of behavioural parameters. These parameters are necessary to the evaluation of safe work and setting exposure limits in deep mines. Particular attention was paid to the need to take into account the metabolic rate of miners and thermal insulation of clothing in assessing hot microclimate in the workplace.

**Keywords:** Mine microclimate · Heat load · Heat stress · Heat stress indices

## 1 Introduction

Mining raw materials are obtained from deeper and deeper deposits because the dynamic development of technology allows for their safe exploitation. The increase in depth is of particular importance in forming the conditions of the microclimate in underground workplaces. The trend of coal extraction from deeper coal seams is also observed in the Polish mining industry. Workplaces located in such an environment pose a threat to exposing an employee to the impact of dangerous, harmful and onerous factors [1].

In 2016, 13 underground coal mines and 3 copper mines, employees were employed in hot working conditions. In 2016, about 6000 employees were employed in coal mines at 353 workplaces where the permissible working time had to be limited in a 24 h period. Respectively, in three copper mines, the number of miners was around 6400 for 143 such workplaces.

The air flowing through mine excavations changes its thermodynamic parameters as a result of the heat transfer from the surrounding strata and from other sources depending on the mining activities in excavations. These heat sources affect the

increase in temperature and moisture content in the air. In addition, microclimate conditions at workplaces deteriorate.

The majority of Polish mines extract coal seams in the Upper Silesian Coal Basin. In this basin, the average geothermic gradient is about 33.2 m/°C, which means that the virgin rock temperature at the depth of 1000 m is approximately 40 °C. Locally, in some mines, the virgin temperature of rocks at this depth reaches 45 °C.

The average geothermic gradient in copper ore mines is even lower and is greater than 27.4 m/°C in the south-eastern part and 30.2 °C in the north-western part of the Lubin-Sieroszowice ore deposit. The result is that the virgin rock temperature at the depth of 1100 m, on which mining operations are currently carried out, is 45 °C.

Such geothermal conditions in Polish mines make it impossible to ensure microclimate conditions with only ventilation means. Therefore, to lower the air temperature it is necessary to cool the air, what will ensure that the required thermal conditions are maintained.

In hot work areas this often results in a thermal imbalance between the employee and the environment. The effect of this can be thermal stress. If the human body is in an environment at a high temperature of the air and performs work with a large energy expenditure, the main mechanism of heat dissipation is sweat evaporation. According to Fanger [2, 3], to maintain thermal comfort, the worker's sweat rate must be within the comfort limits; the worker must be in heat balance; the mean temperature of the employee's skin must fall within the comfort limits. To achieve this, seven factors (air temperature, relative humidity, barometric pressure, radiant temperature, air velocity, metabolic rate, and clothing properties as insulation and water vapour permeability) must be met, which can be divided into both environmental and personal [3, 4]. On the basis of the resultant influence of these factors, heat indices are determined. Furthermore, the imbalance between the environment and the individual can lead to thermal stress resulting in serious heat-related health hazards such as heat stroke, heat exhaustion, heat syncope and other conditions. Heat stroke is the most severe condition and it can even lead to death [5–7]. Heat stress indices can be divided into 3 groups: indices that are based on calculations involving the heat balance equation ("rational indices"), indices that are based on objective and subjective strain ("empirical indices"), and indices based on direct measurements of environmental variables ("direct indices") [3].

Indices of the first two groups are more difficult to implement in workplaces, since they involve many variables and some of them require invasive measurements.

The third group of indices is more friendly and applicable since these indices are based on monitoring environmental variables [8].

## 2   Control of Microclimate Conditions in Polish Mines

Thermal working conditions in Polish underground mines are subject to the law. Occupational hazards include, among others, heat stroke and thermal exhaustion with their consequences. The employer is obliged to systematically carry out tests and measurements of harmful factors. The Polish regulations impose, inter alia, the measurement of microclimate indices in the case of a hot microclimate [9].

The assessment of the thermal load of an employee in a hot microclimate in all industrial plants in Poland is determined using the WBGT index. The method of assessing the microclimate conditions on the basis of the WBGT index can be found in the ISO 7243:2017 standard [10].

However, as is known, this index is beneficial when the environmental heat load is mainly caused by high dry-bulb temperature and radiation temperature with the air humidity being relatively low. That is why the Polish underground mining WBGT index is not used and the environmental thermal load is determined differently. In Poland, various indices of heat stress used in global mining have been known for a long time. There are different views on the usefulness of various direct indices based on direct measurements of environmental variables among Polish researchers.

Until 2017, the Polish mining regulations required the measurement of cooling power of the environment using a wet kata thermometer [11]. The wet kata reading proves to be of limited value as an index of heat stress because environments with equal wet kata do not necessarily have the same cooling power. Therefore, this index was also considered once with the dry-bulb temperature. Time limitations during work in hot environments determined, respectively, the dry-bulb temperature and specific cooling power based on the wet kata thermometer's result. Shift duration was not limited if a dry-bulb thermometer did not exceed 28 °C or cooling power was not less than 11 wet-kata degree. If any of these parameters were exceeded, working time had to be reduced to a 6 h working day. If the dry-bulb temperature exceeded 33 °C work was forbidden [11].

The debate on the need to change regulations begun in the Polish mining environment following the heat-related death of six mine rescuers during an accident in the Niwka-Modrzejow Coal Mine in Sosnowiec in 1998. At the same time, Polish mines reached increasingly deep levels of extraction of natural resources. The increase in the problem of hiring people in difficult microclimatic conditions resulted in the development of new regulations only in 2017 [12]. The concept of "climate hazard" was introduced then. This concept is identical with the hazard of heat stress. In addition to the concept of heat hazard introduced in the law, it is extremely important to develop rules for the control and assessment of this threat in mining excavations [6, 12].

The basic criterion for assessing the heat stress hazard is an occurrence in the mine excavation, hereinafter referred to as "workstation", the "substitute climate temperature" being higher than 26 °C.

The "substitute climate temperature" SCT is an empirical index, which is given by the formula:

$$SCT = 0.6 \cdot t_w + 0.4 \cdot t_d - v_a \tag{1}$$

where:

SCT    substitute climate temperature, °C;

$t_w$    wet-bulb temperature, °C;

$t_d$    dry-bulb temperature, °C;

$v_a$    mean air velocity in the mine excavation, in meters per second multiplied by the conversion factor equal to $1 \frac{s \, °C}{m}$

SCT is used for the following parameter limits:

- the mine air temperature measured with a wet-bulb thermometer or determined on the basis of dry temperature measurements, with relative humidity and pressure is no more than 30 °C;
- the mine air temperature measured with a dry-bulb thermometer or measurement sensor is no more than 35 °C;
- air velocity amounts up to 4 m/s.

If the air velocity in the mine excavation is greater than 4 m/s, the calculation is assumed to be 4 m/s.

The measurements of the substitute climate temperature or parameters of mine microclimate and calculations of substitute temperatures of climate at workstations are taken no less frequently than once a month [12].

The SCT index at workstations located in air-conditioned chambers or cooled excavations is determined on the basis of the results of measurements of the parameters of the mine air made during operation of cooling devices.

The results of the measurements of the SCT index or parameters of the mine microclimate, used to determine this index, are documented in the book of "climate hazard" control.

Three levels of risk for work in a hot mine environment were introduced in Polish underground mines. Individual work positions are classified to a given degree of heat hazards according to the following criteria:

- the first stage of heat hazard at a work location is defined for a SCT not higher than 30 °C;
- the 2nd stage of heat hazard at a work location is if SCT is higher than 30 °C but is not higher than 32 °C;
- to the third stage of heat hazard at the work location is
  - SCT is higher than 32 °C or
  - mine wet-bulb temperature is higher than 34 °C, or
  - the mine air temperature measured with a dry-bulb or a measuring sensor is higher than 35 °C.

At workplaces classified to the first and second degree of the heat hazard, technical solutions are applied to lower the temperature or the working time is limited to 6 h a day. If the working time is longer than 2 h in the workplace with hot environment, employees may work for a maximum of 4 h within a six-hour work shift including time for ingress and egress. These employees are subject to the obligation to train in the scope of hazards resulting from working at elevated temperatures. Only both, employees who were not previously employed in the workplace with hot environment and employees who return to work after a break longer than 14 days caused by the disease may be employed in workplaces classified to the second degree of the heat hazard after additional medical tests. However, at workplaces classified to the third degree of the heat hazard, employees may only be employed while carrying out rescue operations [12].

According to the regulations, documentation should be kept on the basis of which a given workplace is attributed to the appropriate degree of heat hazard.

In the majority of Polish underground mines, hot discomfort is experienced. With exploitation to increasingly lower levels, increased concentration of deposit extraction and the mechanization of mining processes, there are increasing difficulties in maintaining satisfactory thermal work conditions. Therefore, devices that provide intensive ventilation or air conditioning are used. In recent decades, very heavy and hard physical work has been effectively reduced in the mines. Most of the activities performed by miners are a moderate effort [1].

The following section describes the influence of the severity of work and thermal insulation of clothing on the border physiological parameters of humans in relation to the developed temperature range of the substitute.

# 3 Control of Microclimate Conditions in Polish Mines

## 3.1 Research Method

The new heat stress index has not been studied in detail so far in the Polish mining industry, despite the fact that in copper mines it was previously applied by way of derogation from general mining regulations. The PHS model was selected for the assessment of this index as well as comparisons to the indices used in previous mining regulations.

The "Predicted Heat Strain" (PHS) model is the most advanced method of assessing thermal comfort and the method of analytical determination and interpretation of heat stress experienced by workers in a hot environment. This method was introduced in the ISO Standard 7933 in 2005 [13].

The model was physiologically valid by 8 research institutions that performed 747 laboratory experiments and 336 field experiments, covering the whole range of hot working Conditions [14–16]. It is based on the heat balance of the human body and enables the prediction of sweat rate, skin temperature and rectal temperature respectively, as the response of the human body to the working environment.

The PHS model allows:

– assessment of heat stress in conditions with an excessive increase in core temperature or loss of water from the body due to a specific working environment, or,
– determining the maximum allowable exposure duration in a hot environment, which from the physiologists' point of view is acceptable (expected no real damage to the body) and to optimise the working environment.

Using the PHS model, a comparison of different heat stress indices was carried out. The results are presented in monograph [6]. For various values of the indices, water losses from the body and rectal temperatures were calculated with the same both environment and personal parameters. The assumption of a standard employee with known both metabolic rate and thermal insulation of clothing was assumed. Each time, values of a given index for three values of air velocity (0.5, 1.0, 3.0 m/s), three relative humidity values (60, 80, 90%) and two exposure times: 450 and 360 min were calculated. According to Polish mining regulations, the working time of man shift is 7.5 h. In a hot environments (1° or 2° of climate risk) the working shift length is reduced to

six hours including travel time in/out of the mine. The results of the comparison of the indices with the PHS model are presented in graphical form. Both water loss and rectal temperature are given as a function of a given index. The analysis of other indices can be found in the work [6].

Figures 1, 2, 3 and 4 present a comparison of changes in the rectal temperature and water loss for heat stress indices defined in both old and new mining regulations.
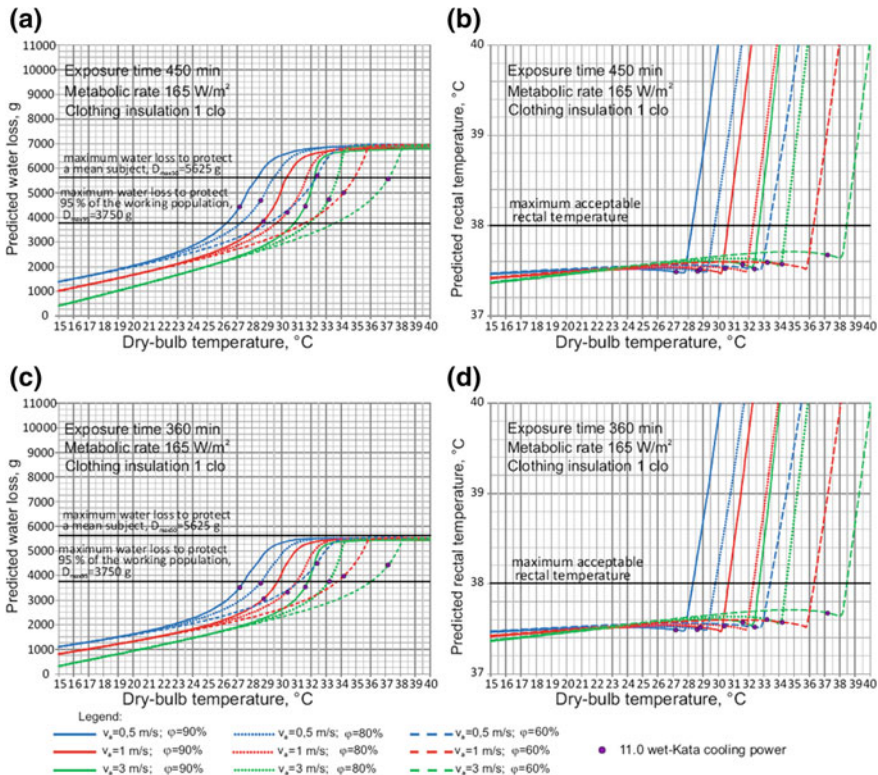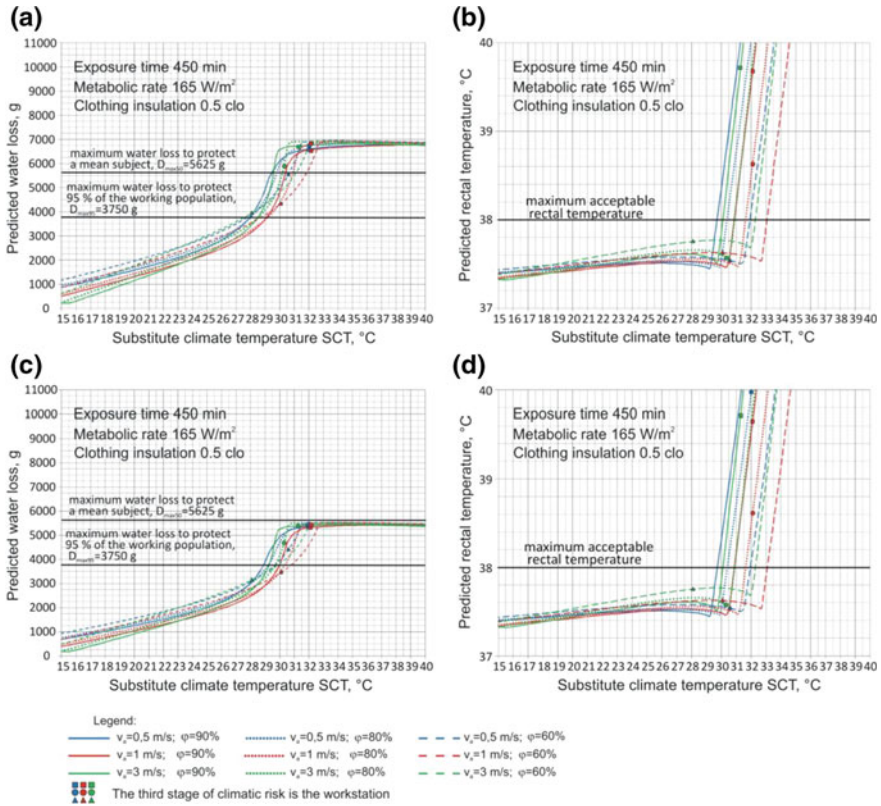


**Fig. 1.** Change in the value of physiological parameters of the employee as a function of dry-bulb temperature for thermal insulation of clothing 1.0 clo: **a** loss of water from the body—calculation results for exposure 450 min, **b** rectal temperature—calculation results for exposure 450 min, **c** water loss from the body—calculation results for 360-min exposure, **d** rectal temperature—calculation results for 360-min exposure

## 3.2  Results

According to the Polish Labor Code [9], the employer is responsible for providing protective clothing and decides about the quality of this clothing. Thermal insulation of clothing is very important in determining the worker's exposure to the impact of the hot
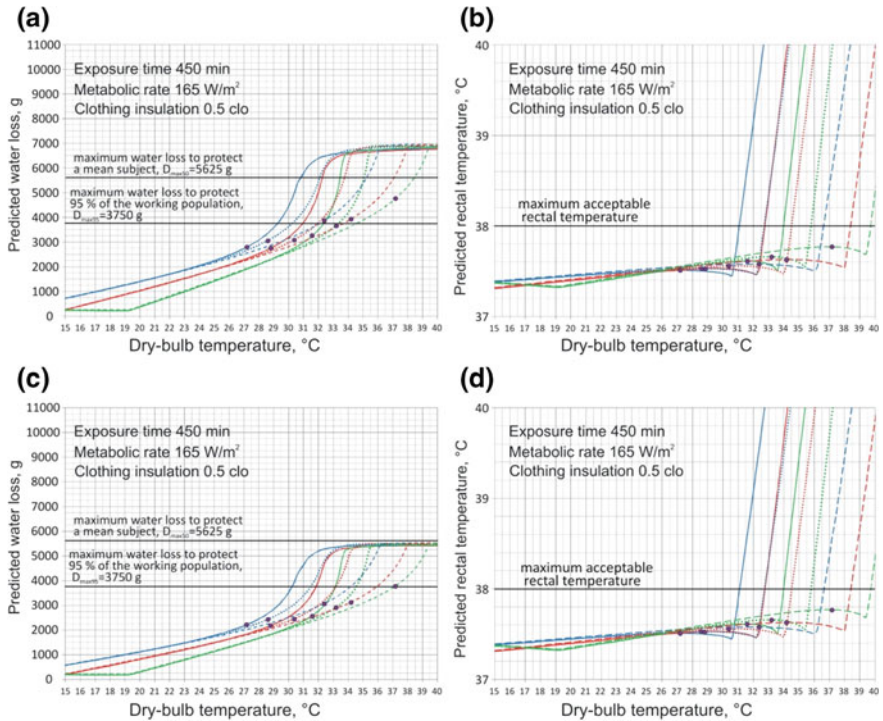
**Fig. 2.** Change in the value of physiological parameters of the employee as a function of dry-bulb temperature for thermal insulation of clothing 0.5 clo: **a** loss of water from the body—calculation results for exposure 450 min, **b** rectal temperature—calculation results for exposure 450 min, **c** water loss from the body—calculation results for 360-min exposure, **d** rectal temperature—calculation results for 360-min exposure

environment. The calculation includes the standard clothing of the employee, whose thermal insulation is 1.0 clo [6]. A common practice in the mining industry shows that employees often take off part of their clothing in hot conditions. Therefore, calculations were also made for the clothing insulation of 0.5 clo.

The results of the calculations of the changes in the physiological parameters of the worker for the old regulations are shown in Figs. 1 and 2. Changes in both the rectal temperature and water loss according to the dry temperature and cooling power for clothing insulation 1 clo are shown in Fig. 1, and for 0.5 clo in Fig. 2. The results of calculations for the new SCT index are presented in Figs. 3 and 4, respectively.

Four graphs are shown in each Figure. Two graphs show the rectal temperature and the water loss for 450 min of the miner's work. The next two graphs refer to a 360-min working time. Only one value of metabolic rate was considered during the calculations. Studies on the metabolic rates in the Polish coal mining show that currently the average metabolic rate of the miner at 165 W/m$^2$ can be assumed in most workplaces.

The calculations assume water replenishment in the body through unrestricted access to beverages.
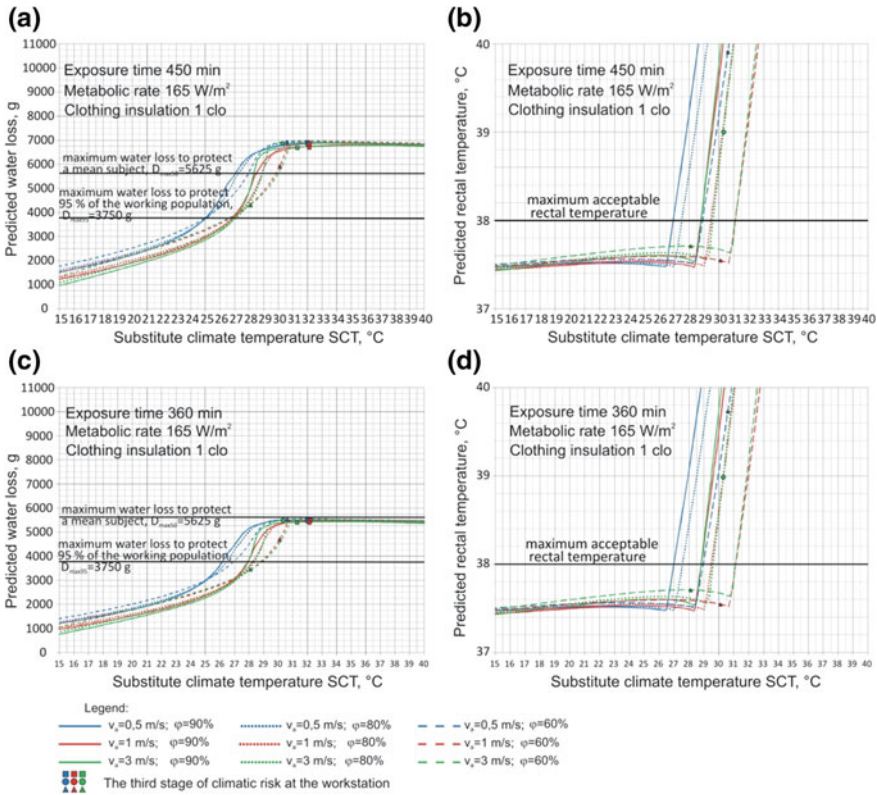
**Fig. 3.** Change in the value of physiological parameters of the employee as a function of SCT index for thermal insulation of clothing 1.0 clo: **a** loss of water from the body—calculation results for exposure 450 min, **b** rectal temperature—calculation results for exposure 450 min, **c** water loss from the body—calculation results for 360-min exposure, **d** rectal temperature—calculation results for 360-min exposure

The analysis of changes in physiological parameters of employees working for 7.5 h as well as for 6 h working shift length was performed. The courses of changes in physiological parameters in Figs. 2 and 3 are marked with different colours and types of lines depending on the relative humidity and air velocity. Limit values of physiological parameters are marked in each graph with black horizontal lines. For the assumed thermodynamic model of the miner, the limit of water loss from the body is 3750 g, while the limit value of the rectal temperature is 38 °C. There are also marked a higher limit value of the weight loss of water from the body in the graphs if workers are allowed to work in a hot environment based on specialist medical tests. Maximum body water loss is equal to 5625 g $H_2O$, which corresponds to the water loss of 7.5% of the body mass.

**Fig. 4.** Change in the value of physiological parameters of the employee as a function of SCT index for thermal insulation of clothing 0.5 clo: **a** loss of water from the body—calculation results for exposure 450 min, **b** rectal temperature—calculation results for exposure 450 min, **c** water loss from the body—calculation results for 360-min exposure, **d** rectal temperature—calculation results for 360-min exposure

## 3.3 Discussion

The presented curves in Figs. 1, 2, 3 and 4 show the final results of calculations of the physiological parameters of the standard employee for the assumed time of his work. The calculations were made for air parameters corresponding to the values of the heat stress indices according to old and new mining regulations in Poland. Each colour, as well as each style of the curve, corresponds to different values of humidity and air velocity. The point corresponding to the limit of full and shortened working time according to the old regulations (11.0 wet-Kata cooling power) is marked in the curves shown in Figs. 1 and 2. The curve to the right of this point indicates the values of extreme thermal work conditions. The curve to the left of this point indicates the normal working environment.

This point was compared to the loss of water from the body or to the rectal temperature. Regardless of whether the thermal insulation of clothing is 1.0 clo (see

Fig. 1b, d) or 0.5 clo (see Fig. 2b, d). The rectal temperature 38 °C is in no case higher than the calculated temperature for this point. Old regulations well limited overheating of the body of miners. However, the graphs (see Figs. 1a, c and 2a, c) show that the permissible water loss from the body has been exceeded.

The calculated value of $D_{max50}$ is greater than 5625 g for the data: v = 0.5 m/s, $\varphi$ = 90% and 1.0 clo. This means the risk of whole-body dehydration may occur because the index indicates the allowable working environment under such conditions (see Fig. 1a). Such a risk occurs already at a temperature of 26.5 °C. During a shortened working time (see Fig. 1c), i.e. in the dry-bulb temperature range 28–33 °C, the limiting value of water loss can be exceeded even at air velocities of 1 m/s and 80% relative humidity (see Fig. 2c).

The data also suggests that the set limits for the application of short-time work or work ban could create a risk of dehydration of the individual with 1.0 clo clothing. Employees were secured when the working time was reduced to 360 min and the thermal insulation of clothing value 0.5 clo was included.

Summing up, it can be stated that the old Polish mining regulations protected against exceeding the physiological limit values for a 7.5-h shift, when air velocities were above 1 m/s and the dry-bulb temperature was up to 28 °C. Similar results of calculations for SCT values according to the new mining regulations in Poland are presented in Figs. 3 and 4. The point corresponding to the third degree of heat hazard is marked on the presented curves. The curve running to the right of this graph illustrates the prohibition of work.

Figure 3 shows that under normal operating conditions (SCT < 26 °C) exceeding the limit of water loss occurs only at air velocities below 0.5 m/s.

In the case of the first and second degree of heat hazard (26 °C < SCT ≤ 32 °C) with a 6-h work shift, the temperature limit may be exceeded for all analyzed air parameters at the rate of 1.0 clo except for v > 3 m/s and <60%. Shortening the working time reduces the loss of water from the body, but the limit value of 3750 g of water loss from the body.

The results of the calculations presented in Fig. 4 indicate that reducing the thermal insulation of clothing to 0.5 clo reduces the level of heat load. This means that index SCT < 26 protects against exceeding the limiting rectal temperature and the maximal value of 3750 g of water loss from the body for a 7.5-h working time with thermal insulation 0.5 clo and metabolic rate of 165 W/m$^2$. On the other hand, in the temperature range 26 °C < SCT ≤ 32 °C, even for the reduced working time, the limit value of rectal temperature and the limit value of 3750 g of water loss from the individual may be exceeded.

An analysis of this case shows that the value of the SCT index is undervalued both at low values of air velocity and high humidity. The SCT index included in the new Polish mining regulations does not well define the working environment conditions for low air velocities and high relative air humidity. The airflows in excavations are rather high. Therefore, special attention should be paid to the moisture content and to maintain the lowest relative humidity of the air.

The SCT index provided in the Polish mining industry is an empirical indicator and refers only to the air parameters that flow around the employee. It does not take into account either the metabolic rate or thermal insulation of the employee's clothing.

Although this index is better than the indices applicable in Polish mining, it does not give satisfactory results at low airflows and high relative air humidity.

## 4   Conclusions

There are many heat stress indices of exposure of employees to the impact of hot environment, which consider only certain ranges of parameters of the surrounding environment (air velocity and relative humidity). Heat stress indices in the mining industry are often used to assess the safe work environment. Heat stress indices in the mining industry are often used to assure and assess the safe work environment.

The selection of the heat stress indices for setting the maximum exposure time or safety limits under a wide range of environmental conditions should be referred to the indices taking into account the physiological parameters of the miners in the form of metabolic rate and clothing, and not the indicators resulting only from air parameters.

In a hot environment that can occur in an underground mine, the maximum working time without loss of injury to an employee's health should be determined for a specific job, including an estimate of the employee's metabolic rate. It also seems necessary to determine the thermal parameters of the protective clothing of a miner working in a hot environment.

It is also important to pay attention to the actual time of miners stay at the workplace with heat load during the work shift. In most cases, miners work much less than 450 min in a hot environment, and in the remaining time allocated for access to and exit from workplaces (including ingress and egress) they stay in much more favourable thermal conditions. The above aspects should be taken into account when developing guidelines for hiring workers in a hot environment in underground mines.

## References

1. Szlazak, N., Obracaj, D., Gluch, B.: Estimation of microclimate conditions at longwall excavations in hard coal mines. AGH J. Min. Geoeng. **37**(1), 117–128 (2013)
2. Fanger, P.O.: Thermal comfort. Analysis and applications in environmental engineering. Copenhagen, Denmark: Danish Technical Press (1970)
3. Roghanchi, P., Kocsis, K.C.: Challenges in selecting an appropriate heat stress index to protect workers in hot and humid underground mines. Saf. Health Work 17 April 2017. https://doi.org/10.1016/j.shaw.2017.04.002. Last accessed 25 Jan 2015
4. Maurya, T., Kailash, K., Vardhan, H., Aruna, M., Raj, G.M.: Effect of heat on underground mine workers. Procedia Earth Planet. Sci. **11**, 491–498 (2015)
5. Maurya, T., Kailash, K., Vardhan, H., Aruna, M., Raj, G.M.: Potential sources of heat in underground mines—A review. Procedia Earth Planet. Sci. **11**, 463–468 (2015)
6. Szlazak, N., Głuch, B.: Methods of evaluation of microclimate conditions in underground excavations. Arch. Min. Sci. ISSN: 0860-7001. Monograph No. 16, Krakow, p. 168 (in Polish) (2016)

7. Waclawik, J., Branny, M., Borodulin-Nadzieja, L.: Numerical modelling of heat exchange between a human body and the environment in hot mines, AGH Press, Krakow (book in Polish) (2004)
8. Epstein, Y., Moran, D.S.: Thermal comfort and the heat stress indices. Ind. Health **44**, 388–398 (2006)
9. The Act of June 26, 1974. The Polish labor code (Polish act)
10. ISO 7243:2017: Ergonomics of the thermal environment—assessment of heat stress using the WBGT (wet bulb globe temperature) index (2017)
11. Regulation of the Minister of Economy of 28 June 2002 on occupational health and safety, operation and specialized fire protection in underground mining facilities (Dz.U.Nr 139, poz.1169 oraz z 2006 r. Nr 124, poz.863) (old mining law and regulations in Poland)
12. Regulation of the Minister of Energy of 23 November 2016 on detailed requirements for the operation of underground mining facilities (Dz. U. 2017 poz. 1118 z dnia 09.06.2017r.) (the latest mining law and regulations in Poland)
13. UNI Standard EN ISO 7933: 2005. Ergonomics of the thermal environment—Analytical determination and interpretation of heat stress using calculation of the predicted heat strain (2005)
14. Malchaire, J.: Evaluation and control of warm working conditions. In: Proceedings of the BIOMED "Heat Stress" conference, 14–15 June, Barcelona, Spain (1999)
15. Mehnert, P., Malchaire, J., Kampmann, B., Piette, A., Griefahn, B., Gebhardt, H.: Prediction of the average skin temperature in warm and hot environments. Eur. J. Appl. Physiol. **82**(1–2), 52–60 (2000)
16. Malchaire, J., Piette, A., Kampmann, B., Mehnert, P., Gebhardt, H., Havenith, G., Den Hartog, E., Holmer, I., Parsons, K., Alfano, G., Griefahn, B.: Development and validation of the predicted heat strain model. Ann. Occup. Hyg. **45**(2), 123–135 (2001)

# Management of Occupational Exposure Limits: A Guide for Mine Ventilation Engineers

Derrick J. (Rick) Brake[1,2(✉)]

[1] Mine Ventilation Australia, Brisbane, QLD, Australia
`rick.brake@mvaust.com.au`
[2] Monash University, Melbourne, VIC, Australia

**Abstract.** Many underground mines do not have a qualified or dedicated occupational (industrial) hygienist on site, or even available as a resource. Many mine ventilation engineers do not even consider occupational exposure monitoring to be relevant to their role as an engineer. In many cases where occupational exposure monitoring is conducted, the mine ventilation engineer is not informed about the results of the monitoring, or if he is, cannot interpret correctly what these results mean. This bunker mentality separating occupational hygiene and ventilation engineering reduces the range of tools available to the ventilation engineer to actively adjust or tune the ventilation system to keep the underground environment healthy, or as healthy as it could otherwise be. This paper sets out the principles and practices that the mine ventilation engineer needs to know to be able to understand how to interpret occupational hygiene monitoring results, and the implications for the mine primary and secondary ventilation systems.

**Keywords:** Occupational · Industrial · Hygiene · Monitoring
Underground · Ventilation

## 1 Introduction

In most countries, occupational (or industrial) hygiene is managed by professional hygienists—quite a different field of specialty to engineers; mine ventilation engineers have only been peripherally involved if at all. The exception is probably South Africa where the role of ventilation engineers now tends to encompass at least basic occupational hygiene management. There are arguments for and against combining the roles of hygienist and engineer, but the dual-role system has not been adopted elsewhere to date. Therefore in most of the world, ventilation engineers and hygienists need to do their separate jobs well and then share their information to get a high-quality result for the workforce. For example, an external (consulting) hygienist may find that a particular group of underground workers has high respirable crystalline silica dust doses, but it is probably the ventilation engineer who is best able to identify where this dust is coming from and assess the range of changes available, taking into account their

engineering, operational and cost implications, to either eliminate the dust or dilute it, in accordance with the hierarchy of controls. This paper therefore approaches the topic from the perspective of what a ventilation engineer needs to know to support achievement of the overall occupational hygiene outcomes at their mine.

## 2   Reasons for Managing Exposures to Atmospheric Contaminants

There are important ethical and moral reasons to monitor and manage the doses of airborne (and other) environmental contaminants that workers are being exposed to such as toxic gases, flammable gases, toxic dusts, explosive dusts, diesel particulate matter (DPM), noise, radiation, heat stress and other human environmental hazards.

In addition, there are also legal regulations with criminal penalties and the more general "Duty of Care" as well as "ALARA/P" (as low as reasonably achievable/practicable) is also frequently a legal requirement. Monitoring *changes* in exposures over time is also important as one of the principles of proving ALARA is to demonstrate that doses are reducing over time, i.e. the operation is achieving "continuous improvement" and this requires an ongoing, rather than one-off, monitoring program.

There are also sound economic reasons for monitoring occupational exposures. Firstly, in some jurisdictions, it may be allowable to reduce airflows in part or all of the mine (saving capital and operating costs) below some otherwise prescriptive value (such as 0.06 $m^3$/s per kW diesel) providing a monitoring program demonstrates (i.e. proves) contaminant doses are safe. Secondly, the legally allowed dose limits of many contaminants have been lowered in the past and will further reduce with time as more medical research is completed, and in some cases, legal claims (e.g. for lung disease), including large class action cases have been initiated many years after exposure, so that monitoring doses and keeping sound records is good business.

## 3   The Different Roles of Key Professional Groups

The measurement and management of environmental exposures to hazards is the practice of occupational (or industrial) hygiene. The clinical detection and treatment of occupational disease is the practice of occupational medicine (physicians). The prevention of occupational disease is achieved by occupational hygiene monitoring programs (conducted by hygienists) and health surveillance programs (conducted by physicians).

The ventilation department in an underground mine should have a critically important role to play in occupational hygiene management. However, the ventilation department must also measure and manage other hazards (or assist with this process) that are not considered to be within the role of the occupational hygiene such as explosive gases and dusts. The safety department may have input into these areas and also the maintenance department (e.g. in terms of measuring tailpipe (raw) engine gas and diesel particulate emissions).

An important issue is that the ventilation officers should be underground daily assessing and managing the ventilation circuits, and are therefore often the most informed personnel on site about underground airborne environmental conditions, the sources of the contaminants and the reasons for the concentrations, as occupational hygienists or physicians will be underground much less frequently.

## 4   Types of Monitoring Programs

It is important to understand and "risk assess" the full range of potential sources of environmental contaminants in the workplace, both those produced as part of the normal work process and those produced in "upset" conditions such as mine fires or the failure of seals into old areas of the mine.

Various types of monitoring programs will be used to manage these risks. Examples include:

- Measuring raw or undiluted tailpipe emissions of gas or DPM from diesel vehicles on a regular basis. Vehicles with high values are then monitored more regularly, or sent off for engine or emissions systems' servicing, rebuild or replacement.
- Measuring "general body" gas or dust concentrations (or temperature, radiation, etc.) where persons are working. This includes both:
  – Spot checks at single points in time
  – Time-averaged "fixed location" measurements or area sampling
  – Real-time continuous "fixed location" measurements or area sampling.


- Measuring doses of dust or DPM for individuals and groups over full working shifts using personal samplers
- Re-entry (clearance) gas checks after blasting
- Procedures to measure and manage toxic or explosive gases including behind seals or in unventilated or worked-out areas
- Confined space procedures
- Health surveillance programs utilising lung function tests, chest x-rays or audiometry (hearing loss) tests, etc.

Note that the overall dose of a contaminant to an individual may not be solely via breathing, and in such cases cannot be controlled purely by managing the atmosphere and the ventilation circuits. Such examples would be:

- Blood lead levels, which are also affected by biting fingernails, eating with unwashed hands, smoking, etc.
- Radiation doses which are also affected by direct gamma ray irradiation
- Heat stress which is affected by a combination of many factors.

For these reasons, every mine should have an approved overall Occupational Hygiene Management Plan for the operation.

It is also important to note that allowable *occupational* doses are usually much higher than allowable doses for the *general public*. There are many reasons for this, but

one is that workers are only exposed to occupational doses for an average of about 40 h per week or about 2000 h per year, whereas the public, if exposed by virtue of where they live, can be subject to $365 \times 24$ or 8760 h exposure per year. Also the general public includes babies, the elderly and the sick—all of whom often have lower tolerance than healthy workers.

Regarding the legal standing of exposure limits (ES) for respirable hazards, the following points should be noted:

- The laws relate to *personal* measurements, i.e. not "static" or fixed location concentration.
- In most cases the personal measurement is the *dose* over some period of time.
- The sampling location should always be in the "breathing zone" of the person, the exact definition depends on the jurisdiction.
- The law is generally silent on the statistical treatment of exposure measurements. The law deals in absolutes which implies that even a single over-exposure to a single worker at a single day would be a breech.[1] However, this would mean that virtually all workplaces would be non-compliant. Therefore some form of statistical analysis appears both valid and necessary, even if there is no legal provision for same.
- Similarly, the law is couched in terms of exposures of individual persons not exposures of similarly exposed sample groups of workers.

## 5   Making the Information Available

Reputable mining companies will often make their key safety and health policies public (e.g. [4]) and often publish their overall performance, and future targets, to the public. At the very least, measured occupational doses should be advised to the individuals concerned after every set of measurements, and aggregated data for groups of workers provided to key stakeholders such as that group of workers, the individuals' line management and the ventilation engineer.

## 6   Limits for Exposures, Sample Size and Sampling Strategy

There are in practice many types of exposure standards (ES), often called "threshold limit values" or TLVs, a term owned and copyrighted by the American Conference of Government Industrial Hygienists. These include time weighted average

---

[1] OSHA in 1978: "OSHA recognizes that there will be day-to-day variability in airborne lead exposure experienced by a single employee. The permissible exposure limit is a maximum allowable value which is not to be exceeded: hence exposure must be controlled to an average value well below the permissible exposure limit in order to remain in compliance" [5].

(TLV-TWA[2,3]), short-term exposure limits (TLV-STEL[4]) and Ceiling[5] (or Peak) limits (TLV-C). There are also "Immediate danger to life and health" (IDLH) limits which relate to emergency conditions rather than normal operating conditions. Ceiling limits are, in effect, instantaneous airborne concentration limits rather than time-weighted doses.

Note that some legislation mandates "maximum allowable concentrations" (MACs) or similar, and these are ceiling limit concentrations not time-weighted dose limits. The ventilation engineer needs to be familiar with both concentration and dose limits.

The limits for gases are usually volume by volume concentrations (e.g. ppm), particulates are mass by volume concentrations (e.g. mg/m$^3$), fibres such as asbestos are fibres per milliliter of air and biological agents such as Legionella (found sometimes in underground cooling towers) are colony-forming units per litre (CFU/litre of water).

It should also be remembered that some concentration limits (especially $O_2$, $CO_2$ and CO) will be affected by altitude. Specialist advise should be sought in such cases.

The choice of the numerical limit will depend on a variety of factors, but good practice would be to use the lower (i.e. more conservative) of either the value stipulated by law in the local jurisdiction, or some global value chosen by the mining company based on first-world standards. In many cases, the mine may voluntarily choose an Internal Limit (IL) that is lower than the legal requirement. This is particularly the case

---

[2] An ACGIH term: "The concentration for a conventional 8-h workday and a 40-h workweek, to which it is believed that nearly all workers may be repeatedly exposed, day after day, for a working lifetime without adverse effect. Although calculating the average concentration for a workweek, rather than a workday, may be appropriate in some instances, ACGIH does not offer guidance regarding such exposures".

[3] And also "Occupational exposure limits" (OELs), "Permissible exposure limits" (PELs), "Recommended exposure limits" (RELs) and "Workplace exposure limits" (WELs). There can be subtle differences in the definitions of these terms and the ventilation engineer should be certain which applies to his mine.

[4] An ACGIH term: "A 15-min TWA exposure that should not be exceeded at any time during a workday, even if the 8-h TWA is within the TLV–TWA. The TLV–STEL is the concentration to which it is believed that workers can be exposed continuously for a short period of time without suffering from (1) irritation, (2) chronic or irreversible tissue damage, (3) dose-rate-dependent toxic effects, or (4) narcosis of sufficient degree to increase the likelihood of accidental injury, impaired self-rescue, or materially reduced work efficiency. The TLV–STEL will not necessarily protect against these effects if the daily TLV–TWA is exceeded. The TLV–STEL usually supplements the TLV–TWA where there are recognized acute effects from a substance whose toxic effects are primarily of a chronic nature; however, the TLV–STEL may be a separate, independent exposure guideline. Exposures above the TLV–TWA up to the TLV–STEL should be less than 15 min, should occur less than four times per day, and there should be at least 60 min between successive exposures in this range. An averaging period other than 15 min may be recommended when this is warranted by observed biological effects".

[5] An ACGIH term: "The concentration that should not be exceeded during any part of the working exposure. If instantaneous measurements are not available, sampling should be conducted for the minimum period of time sufficient to detect exposures at or above the ceiling value. ACGIH believes that TLVs based on physical irritation should be considered no less binding than those based on physical impairment. There is increasing evidence that physical irritation may initiate, promote, or accelerate adverse health effects through interaction with other chemical or biological agents or through other mechanisms".

if achieving the IL is relatively easy (and is therefore targeting a lower limit is entirely in accordance with the ALARA principle).

It is also important to note that a legal limit should never be viewed as a clear demarcation line between a "safe" and an "unsafe" level; hence the need to apply ALARA. As an example, if the TWA for ammonia is 25 ppm, this does not mean that 25 ppm is "safe" and 26 ppm is "unsafe".

Almost all ESs are based on a traditional work roster of $5 \times 8$ h shifts per week. Where workers are on other rosters (e.g. 12-h shifts) then an adjustment must be made to these 8-h values. The recommended guideline in Australian mining is from WA Resources Safety [14], mainly because it specifically addresses the "fly-in, fly-out" non-standard rosters commonly used in the Australian mining industry. However, other guidelines are also available [2, 6]. Where synergistic effects may occur due to exposure to two or more contaminants, ESs may need further adjustment using an approved procedure as ESs only apply for exposure to one substance at a time.

Any contaminant listed in a document such as the ACGIH TLVs [1], or Safe Work Australia [12], requires monitoring. However, non-toxic but otherwise hazardous substances may also require monitoring. These include explosive gases such as methane, simple asphyxiants such as nitrogen or non-toxic dusts often called "Particles not otherwise classified" (PNOC[6]). In terms of knowing what contaminants to monitor, a thorough, systematic and documented analysis of the environment and each workplace and work activity is needed, typically a *qualitative* occupational hygiene survey followed up by a more targeted *quantitative* occupational hygiene survey. For example, if a qualitative survey finds that diesel equipment is in use, then diesel exhaust gases and DPM will be present and probably need to be measured in the quantitative survey. If some of the minerals being mined are sulphides, then there is the potential (depending on the exact mineralogy) for $SO_2$, $H_2S$, sulphide dust explosions or spontaneous combustion hazards to be present. Silica is often present in mines and can result in crystalline silica dust of respirable size entering the air. Metals in the minerals such as lead or mercury are also toxic with one of the pathways into the body being via inhalation. Certain strata may result in $CH_4$, $H_2$, $CO_2$ or other gases being released. Contaminants can also be introduced via chemicals in use, or other parts of the mining cycle such as cement used in ground support. Where exploration drilling notes "bubbles of gas" being produced in the drilling fluid, samples of such gas should be collected in suitable bags and analysed in a gas chromatograph.

Any monitoring program and the choice of exposure or dose levels should be tailored to and prioritised by the toxicity or hazard of the contaminant and the number of persons exposed. In addition, the internal response of the organisation should usually be progressive, i.e. using "action levels" or a Trigger Action Response Plan (TARP) so that detection of low levels of a contaminant triggers an initial response involving more frequent monitoring, whilst detecting higher levels triggers more profound and rigorous responses. Management interventions should comply with the Hierarchy of Controls.

---

[6] Particles not otherwise classified (PNOC) are also referred to by alternate authorities as Particles not otherwise specified (PNOS) or Particles not otherwise regulated (PNOR).

A typical requirement would be for an ES management plan to be implemented where particulates exceed 1/10th of the ES or gases exceed ½ the ES [10].

Where the technology exists, some occupational doses can be continuously measured *individually* for each person. An example is gamma radiation. However, in most cases of airborne respirable contaminants, continuous personal measurement is impractical and the statistically appropriate way of managing occupational exposures is to divide the workforce into groups of workers who do the same or very similar jobs and who will all therefore be exposed to the same dose of airborne contaminants. Such groups are called "Similarly (or Homogenous) Exposed Groups" (SEGs or HEGs).

A statistically valid sample of workers from each SEG is monitored regularly. To avoid any bias, this sample is chosen randomly for each new sampling program so that some individuals are not always being monitored and others never being monitored.

The division of the workforce (including contractors) into SEGs and the choice of sample size within each SEG for routine measurement, the measurement intervals, techniques and equipment must all comply with a recognised standard and good practice. In general, the sample size should be such that at least one worker from each SEG will be within the top 10% of exposures of that SEG population to a 95% confidence limit. Note that for small SEG sizes, this may mean sampling all or almost all persons in the SEG each sampling interval. Guidance on sample sizes can be found in many documents [7–11, 13]. It is certainly not good enough to merely do what is expedient.

The South African Codebook [11] describes a way of separating the workforce into HEGs in which a HEG is only correctly populated if both the average and 90th percentile of the HEG fall in the same classification band. If this is not the case, then the workers in the HEG must be sub-divided or reclassified. However, it is difficult to see any justification for this practice and to this author's knowledge it is not applied elsewhere.

The actual sampling device and sampling procedures must also conform to an accepted standard such as AS2985-2009 [3]. In the case of respirable dust, the samplers ensure only the respirable fraction of the dust is sampled.[7] The sampling period should

---

[7] Quoting from AS 2985-2009: "Occupational hygiene practice commonly differentiates between two size fractions of airborne dust, namely respirable and inhalable dust. Where particles may have toxic effects if absorbed in the nasopharyngeal (nose and throat) region or may have toxic effects if ingested after deposition in this region, it is appropriate to measure the mass concentration of inhalable particles in the atmosphere. It may also be apt to measure this size fraction for particles that exhibit no specific toxic effects, namely 'particulates/dusts not otherwise classified.' … Respirable particles can be measured when the nature of these particles is such that they exhibit toxic effects primarily when deposited in the alveolar region (deepest reserve) of the lungs. This usually applies to toxic insoluble particles that accumulate in the lungs such as crystalline silica, coal dust and cadmium oxide fume…

Respirable dust: The proportion of airborne particulate matter that penetrates to the unciliated airways when inhaled. This fraction is further described in ISO 7708 as the percentage of inhalable matter collected by a device conforming to a sampling efficiency curve that passes through the points shown in Table 1. Alternatively, it can be described by a cumulative log-normal distribution with a median EAD of 4.25 μm and a geometric standard deviation of 1.5 μm.

be "as long as possible", with a minimum of 4 working hours, but preferably a full working shift. *Sampling strategies must never be chosen to deliberately under-report the doses*.

In theory, where workers are required to wear respiratory protective equipment (RPE) during parts of their work activity, it is acceptable to calculate their respirable doses taking into account the reduction achieved by the RPE. For example, if a worker is wearing RPE with a minimum protection factor of 10, then the respirable dust (say) measured by the sampling device (which does not have RPE on its air inlet, unlike the worker) for that period of time can be reduced by 10. However, good practice is to *not* do this for many reasons. Firstly it requires very detailed observation of the worker during the shift (assuming RPE must not be worn all shift by the worker). Secondly it requires the dust doses to be measured separately when RPE is being worn versus when it is not. Thirdly, it assumes the RPE is worn "as required" at other times (when sampling is not being undertaken and therefore the worker is not being observed). And fourthly, it assumes the RPE is achieving its rated protection factor (which may not be the case, e.g. if there is any facial hair or even minor stubble).

Good practice is generally for a medical surveillance program to be adopted for all workers in any SEG that exceeds 50% of the allowable ES. This adds extra costs and complexity to having workers subject to more than 50% of the ES allowable doses and would be an incentive to keep SEGs below 50% of the ES.

# 7 Statistical Analysis and Interpretation of the Sampling Data

A correct and auditable statistical analysis of the sample data is very important. Some important points to understand in interpreting the data are:

- Most occupational exposure doses follow a log-normal distribution[8] (Fig. 1). Note the arithmetic and geometric means are different values as is the mode (most common value). The geometric mean is usually taken to be the best indicator of the average of the sample, especially small samples. In a true log-normal distribution, the geometric mean and median are identical. However, in some cases the geometric mean (median) is not the best estimator of the average. In such cases it is usual to use either the maximum likelihood estimator (MLE) or the minimum variance unbiased estimator (MVUE) to assess the SEG position.[9] Suitably competent persons should make this statistical assessment in accordance with recognised guidelines.

---

[8] Where exposures are *very tightly controlled*, the types of factors that lead to a log-normal distribution may not be present, and the distribution may be "normal". This should be checked.

[9] Where the "test" is to ensure the sample population is *below* an exposure standard, then a "one-tailed" test is sufficient, i.e. the UCL is effectively set at the 95% on its own.
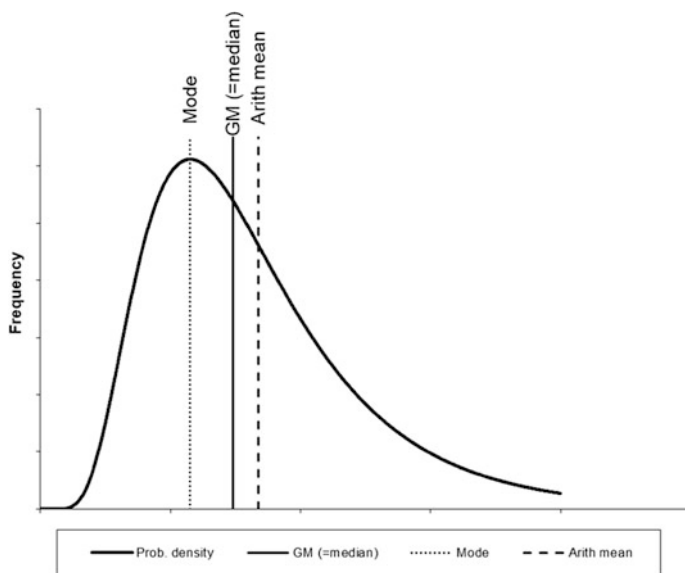
**Fig. 1.** Log-normal distribution showing the mode, geometric mean (median) and the arithmetic mean

- The true average (or MVUE) for a SEG is unknown and unknowable. Correct statistical treatment means that the true average lies somewhere (unknown) between the Lower and Upper Control Limits (LCL and the UCL). Effectively, since 95% of the population is expected to lie between the LCL and the UCL, this means 2.5% of the population of the SEG is expected to be above the UCL and hence above the ES. To be suitably "confident" (in the statistical sense) that the average is *lower* than the ES, the UCL for the sample must be lower than the ES (Fig. 2). In most cases, the average of the sample must be very much less than the UCL to comply, and in fact it is possible that almost all the individual measurements can comply but the sample as a whole still "fail".
- Conversely, if the LCL is above the ES, then the SEG has certainly "failed" (Fig. 4).
- Where the ES lies between the LCL and the UCL, then the SEG "may" have passed or "may" have failed (Fig. 3). This should be treated as a "fail" or "exceedance".
- Therefore if legislation states that exposures "must not be above" the limit, then regulators cannot (technically) require exposures to be "below" the limit.[10] Hence whilst Fig. 3 may have some or even most measurements above the ES, because the LCL is still lower than the ES, this sample still "is not above the exposure limit"

---

[10] The Safe Work Australia requirement is "no employee is exposed at levels *above* the appropriate exposure standards" (this author's italics). Exposure *at* the exposure limit is acceptable.
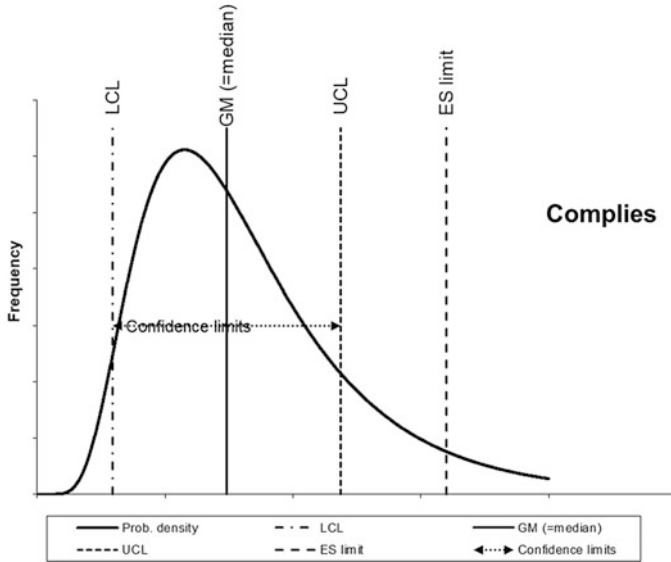
**Fig. 2.** This SEG does comply with the exposure standard (ES)
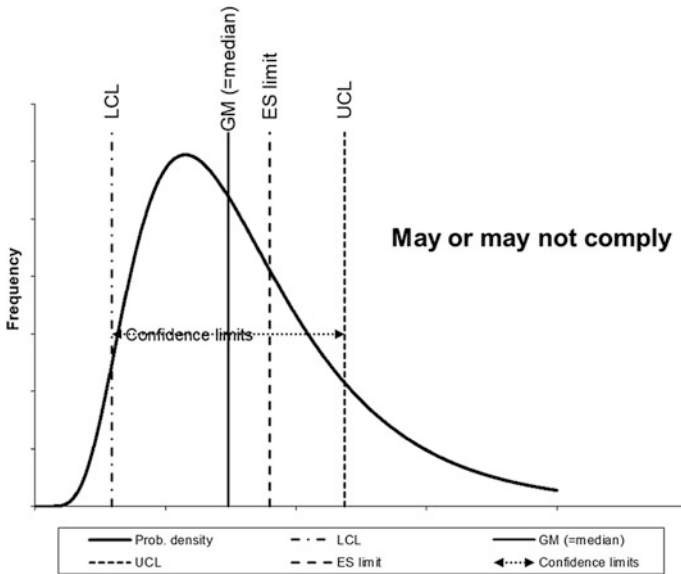
**Fig. 3.** This SEG may or may not comply with the exposure standard

(from a statistical standpoint). However, it is important to emphasise that most reputable employers will seek to manage exposures so that they are below the ES, i.e. the UCL is below the ES (Fig. 2) and not merely that the LCL is not above the ES (Fig. 4).
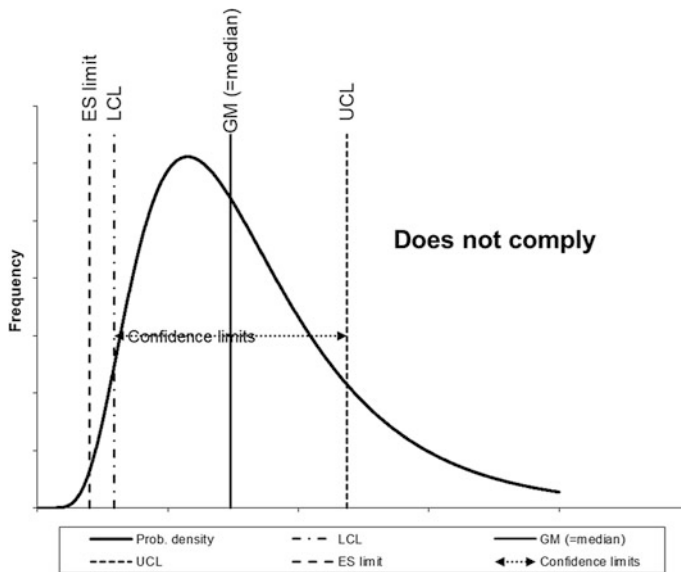
**Fig. 4.** This SEG does not comply with the exposure standard

- In effect, this means the number of "exceedances" (for any contaminant) is not the number of persons measured that failed, but the total population of each SEG that failed. It further means that only "2 or 3 more" failed results in a testing program can push the entire SEG population into the "fail" (exceedances) criteria.
- The sampling interval will depend on how close the measured values are to the ES. Note that where exposures are either very low or much above the ES, then sampling interval is extended (conducted less frequently). For high exposures, this reflects the fact that RPE (respiratory protection equipment) will be required and in use. For very high exposures, sampling is required to audit the protection being provided by the RPE. For example, if the UCL for a SEG is under 25% of the ES, then infrequent sampling may be reasonable. If the UCL is more than 100% of the SEG, then again, only infrequent sampling is needed assuming no efforts are made to reduce the dose exposures. Where the UCL is between 25 and 50% then more frequent monitoring may be required to avoid triggering a medical surveillance program. Where the UCL is between 50 and 100%, then more frequent monitoring may be required to take action to avoid exceeding the ES. SEGs with UCLs falling between 25 and 100% of the ES are the most critical in terms of monitoring.

Note also that there will not be a linear relationship between the average concentrations in the air and the number of exceedances.

## 8  Case Example

A lead-zinc mine conducted sampling for blood lead levels and obtained the values shown in Fig. 5. The UCL for the SEG for the "UG Crusher operators" exceeds the ES, and therefore *all* workers in this SEG are considered to exceed the ES (i.e. are "exceedances") even though testing of this group may show only a few actually do. For example, if there were 20 "UG Crusher operators" in the mine and 10 were sampled from this SEG and 8 of those 10 were below the ES ("passed"), but the UCL was above the ES, then all *20 UG Crusher operators should be treated as "fails" (exceedances) even though only 2 actually "failed"*.



| | UG - Service Crews (45) | UG - Dev Charge Crew (8) | UG - Prod Charge Crew (12) | UG - Mag Keeper (4) | UG - Loader Operators (28) | UG - Truck Operators (38) | UG - Nippers / Supervisors (23) | UG - Drillers (44) | UG - Fibrecreters (10) | UG - Crusher Operators (8) |
|---|---|---|---|---|---|---|---|---|---|---|
| – LCL95% Lands Exact | 52% | 41% | 41% | 28% | 26% | 13% | 26% | 29% | 36% | 58% |
| ● MVUE | 67% | 53% | 53% | 36% | 31% | 18% | 36% | 39% | 52% | 74% |
| – UCL95% Lands Exact | 96% | 75% | 74% | 52% | 40% | 28% | 61% | 61% | 96% | 107% |
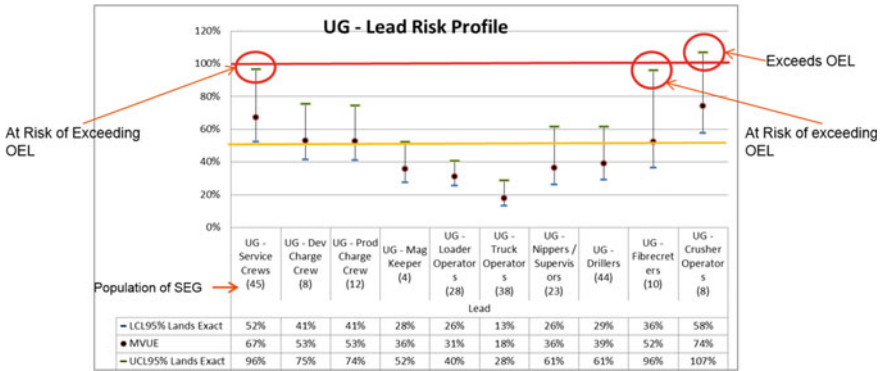
**Fig. 5.** The blood lead levels for a number of SEGs at one underground mine

A similar situation exists in Fig. 6 with respect to diesel particulate matter results. All but one of the SEGs had average values below the ES, but the UCL for most SEGs is above the ES, so all workers in that SEG (whether sampled or not, and whether they individually passed or not) are treated as "fails" (exceedances).

As discussed earlier, not only should exceedances be "nil", but the *trend* in exposures should show a decrease with time. Therefore examining the trend of exposures for each SEG is important as it will allow the ventilation engineer to see which ones are trending either towards non-compliance or compliance.
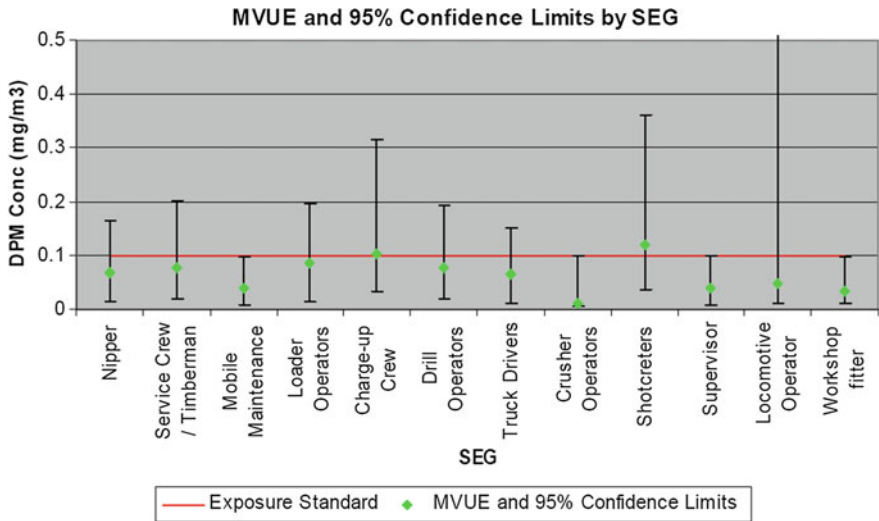
**Fig. 6.** DPM hygiene monitoring results

## 9    Conclusions

Occupational hygiene monitoring is rarely the responsibility of the mine ventilation engineer and ventilation engineers, if ever, have sufficient training to taken on the role of a professional hygienist. However, it is essential that occupational hygiene monitoring is being completed on all mine sites according to an approved Management plan and an informed ventilation engineer is in a better position to help ensure this is being done and is being done properly. It is equally important that the data obtained under this hygiene management plan is then shared with a ventilation engineer who can understand what it means, and its limitations, and who should then be charged with reviewing the range of controls for particular groups of workers, and the performance of the ventilation system in certain locations of the mine or at certain periods of time or activity. When accompanied by other measurements, including routine hand-held sampling and "fixed location" sampling for dusts, DPM and gases, the interpretation of the data provides a powerful way to not only ensure compliance with legislation and good practice, but also to assess the effectiveness of various controls, including the primary and secondary ventilation systems themselves.

## References

1. ACGIH: Documentation of the Threshold Limit Values and Biological Exposure Indices, 7th edn (2017)
2. AIOH: Adjustment of Workplace Exposure Standards for Extended Work Shifts Position Paper, 2nd edn. Australian Institute of Occupational Hygienists (2016)

3. Australian Standard AS2985-2009: Workplace Atmospheres—Method for Sampling and Gravimetric Determination of Respirable Dust (2009)
4. BHP Billiton: Health Our Requirements. Available from: https://www.bhp.com/-/media/bhp/documents/aboutus/ourcompany/governance/160404_gld_health.pdf?la=en. Accessed 3 Feb 2018 (2016)
5. Bullock, W.H., Ignacio, J.S.: A Strategy for Assessing and Managing Occupational Exposures, 3rd edn. American Industrial Hygiene Association (2006)
6. Drolet, D.: Guide for the Adjustment of Permissible Exposure Values (PEVs) for Unusual Work Schedules, 4th edn. Technical guide T22. Institut de recherche Robert-Sauvé en santé et en sécurité du travail (IRSST) (2015)
7. Grantham, D.: Simplified Monitoring Strategies—A Guidebook on How to Apply NOHSC's Exposure Standards for Atmospheric Contaminants in the Occupational Environment to Australian Hazardous Substance Legislation. Australian Institute of Occupational Hygienists (AIOH) (2001)
8. Leidel, N., Busch, K., Lynch, J.: Occupational Exposure Sampling Strategy Manual, pp. 77–173. NIOSH (1977)
9. Nevada Mining Association Industrial Hygiene Sub-committee (NMA): Industrial Hygiene Sampling Manual (2008)
10. SA Department of Mines and Energy (SA DME): South African Mines Guideline for the Compilation of a Mandatory Code of Practice for an Occupational Health Programme on Personal Exposures to Airborne Pollutants. DME Mine Health and Safety Inspectorate (2002a)
11. SA Department of Mines and Energy (SA DME): South African Mines Occupational Hygiene Programme Codebook. DME Occupational Hygiene Directorate (2002b)
12. Safe Work Australia: Workplace Exposure Standards for Airborne Contaminants (2011)
13. WA Resources Safety: Risk-Based Hygiene Management Planning and CONTAM System Procedures. Government of Western Australia (2015)
14. WA Resources Safety: Adjustment of Atmospheric Contaminant Exposure Standards—Guide. Government of Western Australia (2016)

# Part XV
# Metal and Non-metal Mining

# Monitoring Methane in Gassy Salt Mines

Albert E. Ketler P. E.[(✉)], Lauren E. Sargent, Craig D. Mattock,
Thayananthan Narayanan, and Brian A. Dale

Rel-Tek Corporation, 4185 Old William Penn Highway, Monroeville,
PA 15146-1619, USA
engineering@rel-tek.com

**Abstract.** Over the past two decades Rel-Tek developed and supplied permissible gas detection systems (GDS) for two large salt mines—Morton Salt, Weeks Island Facility, New Iberia, Louisiana, USA and Compass Minerals (formerly North American Salt) Franklin, Louisiana, USA. Both underground mines were deemed hazardous (i.e. containing methane gas) by MSHA (US Dept of Labor, Mine Safety and Health Administration) so all of the electrical gas detection equipment required protection against methane gas ignitions throughout the mine. This required a combination of MSHA-approved Explosion Proof (XP) and Intrinsically Safe (IS) products. A two-stage Blast Timer software feature was included to aid in production management. Data and alarm logging provides historical records, printable off line. Multiple Touch screen display terminals distribute information throughout the operation. The GDS is modularly expandable to suit virtually any mine configuration, and is particularly applicable to Chinese coal mines where they are fully hazardous, from the portable to the face.

**Keywords:** Permissible · Methane gas · Data acquisition · Intrinsically safe
Sensors

Classified environment—The two salt mines were MSHA (US Mine Safety and Health Administration) classified under US-CFR30, Part 57 as Class IIA mines. Originally, before the introduction of the Rel-Tek gas detection system, the mines deployed intrinsically safe methane sensors connected to the surface with long, heavy gage cables extending thousands of feet ($\times 1.6$ m) from the underground locations to the surface, where intrinsically safe barriers, power supplies and 4–20 ma signal detection systems monitored the mine for methane. Eventually the connecting cables grew so long that this concept became unwieldy, unreliable, and subject to unacceptable voltage losses over the cable lengths. Rel-Tek Corp. was called on to provide an electronic replacement for the long cable concepts, employing high speed digital telemetry combined with permissible (MSHA-approved) underground equipment.

Modular arrangement—Fig. 1 shows a typical equipment arrangement, with each mine having variations to suit their particular needs. Confidential details of each mine are not shown. The equipment arrangement shown is illustrative of the principles only. Both mines had underground shop areas which required separate on-line video

displays. One mine also had six remote display terminals, consisting of 21″ (534 mm) touch screen video monitors stationed in fresh air supervisory offices. Remote terminals were connected to the primary gas monitoring computer over this client's existing Ethernet LAN.
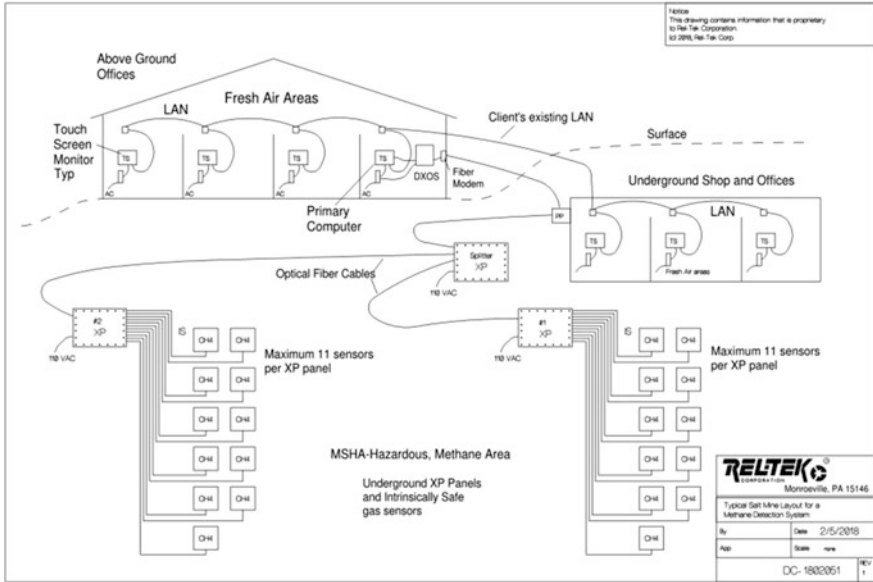


**Fig. 1.** A typical salt mine equipment arrangement

XP outstations and optical fiber cable—Rel-Tek supplied its explosion proof (XP) outstation boxes or panels that can be placed at AC-powered sites underground, near the working faces where blasting can uncover pockets of methane gas. Figure 2a, b show these XP outstation boxes. Each contains 12 intrinsic safety barriers capable of accessing as many as 11 methane sensors and one alarm unit per panel. Sensors were connected with reasonably short cable lengths, i.e. less than 200 ft (61 m) of 18 AWG, three-conductor, shielded. High-speed telemetry (19.2 kb, with 120 sensors per second processing rate) was provided over a mix of multi-mode and single mode optical fiber cables among the boxes and the surface monitoring stations. Some of these fiber cables were 2500 ft (762 m) long.

Figure 3 shows the internal view of the XP outstation used in both installations. These outstations were steel, with aluminum lids. Each measured about 29″ long × 21″ wide × 11″ high (737 × 533 × 279 mm), weighed about 350 lbs (159 kg), and had 14 cable glands. Active components inside included: a 6.5A 110-24VDC power supply, 12 Intrinsic Safety barriers; 12 current regulators; one DX4404 I/O card (with 4AI, 4DI, 4DO), one DX8000 I/O card; (with 8 AI); 2, 3 or 4 optical fiber drivers; 2 12VDC/4AH rechargeable batteries, a battery charge management module, and a hydrogen sensor to detect any battery emissions.
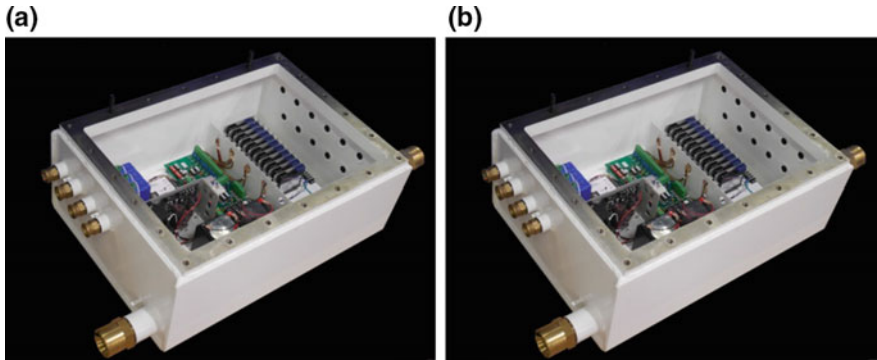
**Fig. 2.** Explosion proof outstation, two views
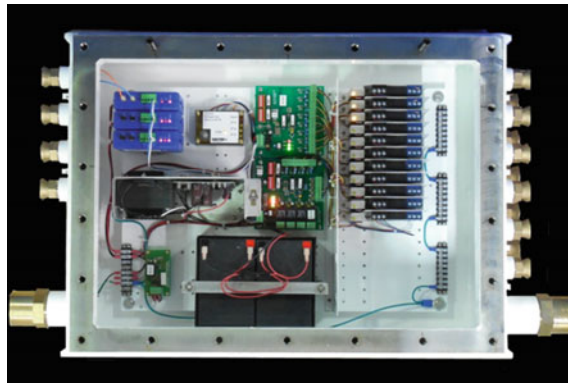


**Fig. 3.** Internal view of an XP outstation

The IS barriers are a Rel-Tek product, having a unique dual-circuit design, with an aluminum back plate heat sink to permit close packing, without concern for over-heating. One barrier completely serves one GasBoss methane sensor.

Intrinsically Safe Methane Sensors—Fig. 4 shows Rel-Tek's MSHA-approved "GasBoss" LEL-range methane sensor used in both salt mines. One mine had 16 sensors, the other had 12. This is a catalytic bead (CB) technology that is widely used in US coal mines. Note that CB sensing heads avoid optical technology (IR) that is susceptible to the "ethane catastrophe" phenomenon, wherein 1% ethane (present in most natural gas) reads out as 20% methane [1, 2]. The epoxy-sealed electronics is housed in a gasketed fiberglass NEMA-4x enclosure. All hardware is non-corrosive plastic or stainless steel. This is a workhorse sensor, with thousands in operation in US mines, demonstrating an average life expectancy of 8–10 years. It operates from 12-30VDC, drawing about 80 ma full scale, while producing a 4–20 ma linear output signal. Sensors in the salt mines are manually calibrated monthly using a portable calibration kit supplied by Rel-Tek.

**Fig. 4.** GasBoss methane sensor

Monitoring software—Rel-Tek's Millennia-FT SW has been constantly evolving for 30 years to its present world-class status with features and capabilities that excel in simplicity, speed, and reliability. Unique features include data and alarm logging, automatic file management, visual Boolean control logic, automatic graphic report printing by shift, day and week. Visual diagnostics, statistical telemetry analysis, and data offload to Excel for offline analysis. Figure 5a, b illustrate typical interactive HMI screens available at the two salt mines.
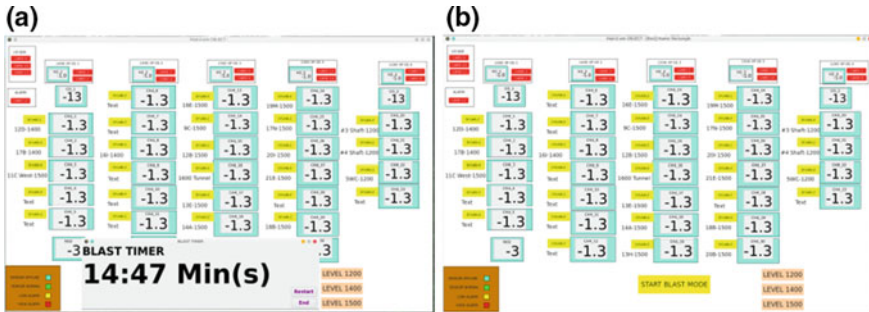


**Fig. 5.** Video screens showing normal and also with blast timer operating

Blast timer—Typical for US salt mines, the ore recovery process involves blasting, waiting for atmosphere to clear, and then gathering, crushing and loading the salt into conveyors and trucks. After blasting the atmosphere contains gases from blasting, as well as methane from any gas pockets that were uncovered by the blast. Therefore the computer configured to disconnect alarms and high-gas shutdown controls prior to the blast. After 15 min, the atmosphere is generally clear. A count-down display on the

primary computer aids the mine management in planning re-entry of personnel. But, if the sensors show that the air is not sufficiently clear, than a second 15-min backup timer is activated by clicking on an icon, for added safety.

Permissible audio/visual alarms—Fig. 6 Permissible alarms were supplied by Rel-Tek, but were not installed because of the remoteness of the locations where no personnel were present. All alarms were on the surface, in fresh air.



**Fig. 6.** Permissible audio-visual alarm unit

High speed telemetry—Rel-Tek's unique high speed "Flash Telemetry" was employed at both mines, wherein sensor gas levels can be acquired and transmitted over the fiber cables to the primary computer at the rate of 120 sensors per second. The alarm reaction time is therefore less than 0.36 s, indeed, indeed real-time response. Telemetry errors are very infrequent, usually less than 10–7%, and any errors are immediately discovered and corrected. The Flash Telemetry data highway is fast and accurate.

Successful salt mine installations—Problems were experienced and overcome. Intermittent fiber cable terminations occurred at the outset, which had to be overcome by personnel training and careful cleaning measures. Torn fiber cables occurred from time to time. Power line surges from the main power centers inside the mine caused damage to the GDS communication circuits. This was corrected by adjusting the power centers, or, in one case, by replacing a power center completely. In one case, the irregularity of the client's LAN caused remote display terminals to go off line, requiring

manual resetting, a nuisance. Rel-Tek engineers changed in the remote terminal software to add an automatic refresh feature, thus eliminating terminal downtime.

Best methane sensor technology—Rel-Tek's GasBoss methane sensors employs a catalytic beat (augmented pellister) technology, which has proven to be accurate, reliable and long lasting in underground coal and salt mines for half a century. It is important to recognize that optical (NDIR) sensors are not to be used in situations where the natural gas mixture includes both methane and ethane. Indeed, in virtually all underground mines and natural gas operations. The reason for this is that the optical footprint for methane lies directly on top of that of ethane, and NDIR sensors overly react to the ethane, corrupting the lower explosive limit (LEL) determinations. The US National Institute of Occupational Safety and Health (NIOSH) (1), Rel-Tek [3] and others [1, 4] have confirmed that 1% ethane reads out as about 20% methane on an optical sensor calibrated with methane gas. Calibrating NDIR sensors with a methane mixture biases the sensor to read methane in natural gas improperly high (e.g. readings of 150% methane are possible) in the presence of even at small percentage of ethane. The British have known this for decades, dubbing it the "ethane catastrophe." For this reason, optical sensor technology seldom used in British and US underground coal mines for reckoning the LEL flammable safety conditions, relegating, instead, methane and LEL determinations to the tried and true catalytic bead (augmented Pellister) technology.

Future expansion options—Having modular architecture, the salt mine systems can be readily expanded to add 50 or more XP outstations and hundreds more of sensors. Sensor types can include methane, carbon monoxide, nitrous oxide and oxygen, as well as air velocity, smoke, temperature, humidity, pressure, air velocity, vibration, water level, RPM, and so on. Rel-Tek has to its credit over 120 MSHA and NRTL approval actions covering use of all of these sensor types in hazardous areas of underground mines, whether salt, coal or other.

AwAir is a new land-mark product recently developed by Rel-Tek and approved by MSHA (Fig. 7). It is an XP gas extraction system for sampling up to five gases (CO, $CH_4$, $CO_2$, $H_2$ and $O_2$) through four gas tubes routed to key locations. AwAir was designed to support underground emergency shelters (refuge alternatives,) but the electrical approval enables the system to be used for monitoring virtually anywhere in aside a coal or salt mine, particularly in gob areas where access for sensor inspection and calibration is difficult or dangerous. Unique to this system is a fully automatic sensor calibration utility that maintains the accuracy and calibration documentation for all five gases for five years, without human interaction. High-speed telemetry via fiber to a surface location is standard. A 96-h battery backup is available for emergency shelter applications. Stationing these AwAir units near blasting areas would be of immediate benefit.

Rel-Tek has pioneered in the development of products to enhance the safety of underground mining, tunneling, gas/oil operations and alternative fueled vehicles. Figure 8 shows Rel-Tek's Safety Technology Center in Monroeville, Pennsylvania, USA, designed to pursue new technologies and methods to save lives and costs, through the innovation of new products for mines, tunnels and industry. An article describing some of these next-generation safety products is available on request to Rel-Tek.
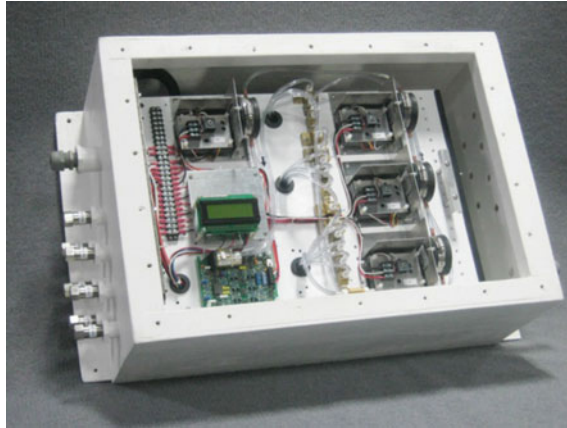
**Fig. 7.** AwAir gas extraction system



**Fig. 8.** Rel-Tek safety technology center

# References

1. Ketler, P.E., A.E., Rel-Tek Corporation: Personal conversations and data from E. J. Chilton, Ph.D. (gas monitoring specialist, NIOSH) regarding "ethane catastrophe," i.e. ethane interference on infrared (NDIR) sensors when monitoring for methane (2002)
2. Taylor, C.D., Chilton, J.E., Martikainen, A.L.: National Institute for Occupational Safety and Health, Use of Infrared Sensors for Monitoring Methane in Underground Mines. Pittsburgh Research Laboratory, Pittsburgh, PA USA (2008)
3. Ketler, P.E., A.E., Rel-Tek Corporation, et al.: Research report, CNG Monitoring Issues for A&E Firms. 4185 Old William Penn Highway, Monroeville, PA, USA 15146, 22 Oct 2015. Copies available on request to author
4. Goodman, G.V.R., Karacan, C.O., Schatzel, S.J., Krog, R.B., Taylor, C.D., Thimons, E.D.: National Institute for Occupational Safety and Health, research for monitoring and

controlling methane at U.S underground coal mining operations. Pittsburgh Research Laboratory, Pittsburgh, PA, USA (2009)

5. International Sensor, Hazardous Gas Monitors: A practical guide for selection, operation and applications (1999). http://www.intlsensor.com

6. Ketler, P.E., A.E., Rel-Tek Corporation, Monroeville, PA, USA: Monitoring system innovations benefit mine ventilation. In: De Sousa, E. (ed.) Proceedings of the North American/Ninth US Mine Ventilation Symposium, Kingston, ON, Canada, Mine Ventilation, June 2002. ISBN 90 5809 387 5

7. Ketler, P.E., A.E., Rel-Tek Corporation, Monroeville, PA, USA: Atmospheric monitoring systems for very large mines. In: Wallace, K.G. (ed.) 12th U.S./North American Mine Symposium, Reno, NV, USA (2008). ISBN 078-0-615-20009-5

8. A.E. Ketler, Rel-Tek Corporation, Monroeville, PA, USA: Monitoring system innovations benefit mine ventilation. In: De Sousa, E. (ed.) Proceedings of the North American/Ninth US Mine Ventilation Symposium, Kingston, ON, Canada, Mine Ventilation, June 2002. ISBN 90 5809 387 5

9. A.E. Ketler, Rel-Tek Corporation, Monroeville, PA, USA: Atmospheric monitoring systems for very large mines. In: Wallace Jr., K.G. (ed.) 12th U.S./North American Mine Symposium, Reno, NV, USA (2008). ISBN 078-0-615-20009-5

10. Ketler, A.E., Rel-Tek Corporation, et al.: Research report, CNG Monitoring Issues for A&E Firms. 4185 Old William Penn Highway, Monroeville, PA, USA 15146, 22 Oct 2015. Copies available on request to author

11. Gas Quality, Navigates, 12/4/2011-12/6-2011: Analyses of natural gas from 15 Marcellus gas wells in NW Pennsylvania, USA

12. Rel-Tek Corporation: Next Generation Ventilation Safety Products

# Ventilation Characteristics of Underground Metal Mines in Turkey

Alper Gönen[✉] and Ercüment Yalçın

Dokuz Eylul University, 35390 Izmir, Turkey
alper.gonen@deu.edu.tr

**Abstract.** In many underground mines, ventilation systems represents a significant percentage of the power used. In fully mechanized metal mines, diesel equipment is used extensively. In the last decades, the demand for ventilation has also increased because of the increased use of diesel equipment to achieve high production. The paper contains a survey conducted in underground metal mines in Turkey. For this purpose, total diesel power, total airflow quantity, daily production capacity and current mining depth of each mine has been documented. Airflow requirement depending on the operating characteristics in different mines was investigated.

**Keywords:** Diesel equipment · Mine ventilation · Airflow requirement

## 1 Introduction

As part of the Tethyan-Eurasian Metallogenic Belt and with its complex geology, Turkey has great mining potential with diverse mineral deposits [1]. Turkey holds 2.5% of the world's industrial mineral reserves, 1% of coal, 0.8% of geothermal and 0.4% of the metallic mineral reserves and produces some 50 different metals and minerals that are suitable for exploitation [2]. In 2016, the mining sector in Turkey exported 47% of its natural stone and metal ores (such as chrome, zinc and copper). After new arrangements made to improve laws to entrepreneurs with foreign partners in 2005 and 2010, Turkey has become more attractive to foreign investors. Today, the private sector dominates Turkey's industrial minerals and metals sectors. This resulted in an increase in mining and in mineral exploration activity in the country with especially on copper, gold, nickel and zinc production. The aim of this survey was to collect some basic information from participated mines in Turkey and evaluate the ventilation requirements. For this purpose, diesel equipment fleet of each mine is examined and total installed diesel power and other basic mining features are obtained from each mine.

## 2 Airflow Requirement in Underground Metal Mines

In fully mechanized metal mines, diesel equipment is used extensively. Here the ventilation requirements depend on the power capacity of the diesel equipment fleet [3]. The basic rule is that there should be sufficient ventilation to dilute the exhaust gases and particulates to quantities below their threshold or limiting values [4].

For design, many ventilation engineers assume a requirement of 0.06–0.08 $m^3$/s of airflow for each kW of diesel power, with all equipment total discharge cumulative in any one air split [5]. Metal mines in Turkey, just like their counterparts in other countries, are now seeing increased levels of equipment automation and diesel equipment usage. Therefore, the demand for extensive ventilation is also increasing. There are many factors that influence the ventilation requirement for underground mines (like mining method, production rate, depth, number of production stopes, diesel fleet, contaminants and their types, etc.).

Table 1 lists data collected from participating nine mines such as, total diesel power, total supplied airflow quantity, daily production capacity and current mining depth. To ensure confidentiality, in this study, each mine is identified by a number and real names of the mines are not given here. The names Mine A, Mine B, Mine C, etc. are used to present the results of this study. In Mines A, B, E, F cut & fill mining method is used to extract ore. In Mines C, D and G longhole stoping, in Mines H and Mine I, shrinkage stoping is used as mining method. Two of them are gold mine, three copper mine, two zinc-lead and two chromite mines. Mining depth varies from 210 to 720 m with an average of 390 m. Production rates vary from 560 to 4500 tonnes per day with an average of 2100 tonnes per day.

**Table 1.** Summary of data collected from mines

| Mine | Production (tonnes/day) | Mining depth (m) | Total airflow ($m^3$/s) | Total diesel power (kW) | Quantity ($m^3$/s/tonne) | ($m^3$/s/kW) |
|------|------|------|------|------|------|------|
| Mine A | 1300 | 280 | 160 | 3060 | 0.123 | 0.052 |
| Mine B | 4500 | 720 | 195 | 6350 | 0.043 | 0.031 |
| Mine C | 3750 | 500 | 180 | 5520 | 0.048 | 0.033 |
| Mine D | 3300 | 550 | 190 | 4350 | 0.058 | 0.044 |
| Mine E | 1200 | 225 | 110 | 2700 | 0.092 | 0.041 |
| Mine F | 1800 | 340 | 90 | 2480 | 0.050 | 0.036 |
| Mine G | 1750 | 280 | 105 | 1470 | 0.060 | 0.071 |
| Mine H | 560 | 430 | 75 | 1080 | 0.134 | 0.069 |
| Mine I | 750 | 210 | 65 | 1550 | 0.087 | 0.042 |

Figure 1 shows airflow quantity needed to extract a tonne of ore for each mine participated in the survey. Mine H has highest ventilation rate per tonne with 0.134 $m^3$/s/tonne due to high air leakage and mining depth. Mine A has high ventilation rate compared to other mines with 0.123 $m^3$/s/tonne, where production is conducted from multiple levels and stopes in mine.

In Mines D, E and I, ventilation rate per tonne changes from 0.087 to 0.94 $m^3$/s/tonne. Mines E and Mine I have long spiral mine ramps without shaft. Mines (B, C, F, G, J) have similar ventilation rates changing from 0.041 to 0.063 $m^3$/s/tonne. In this study, average ventilation rate per tonne of mined ore is found to be 0.077 $m^3$/s/tonne, which has similar results with previous research studies [6].
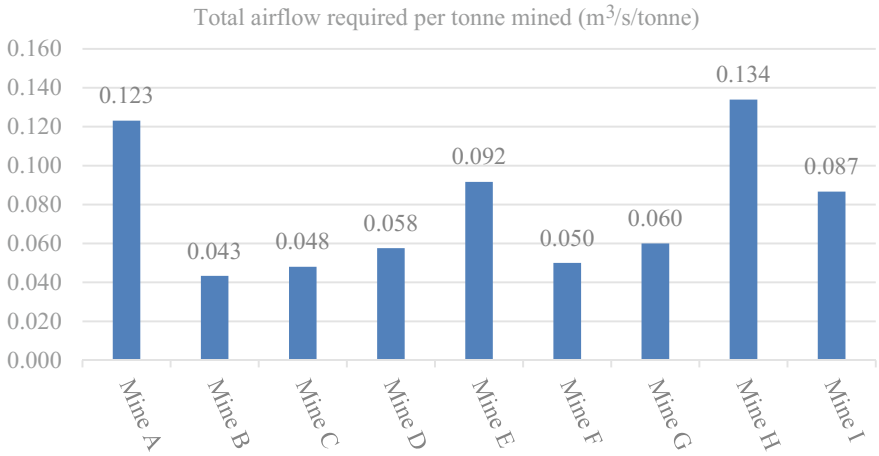
Fig. 1. Histogram of total airflow required per tonne mined

Figure 2 presents total airflow quantities and daily production capacities of participated mines. Results show that, there is a good correlation between airflow quantity and production rate. Correlation coefficient is 74.4% and connection between the variables is strong.
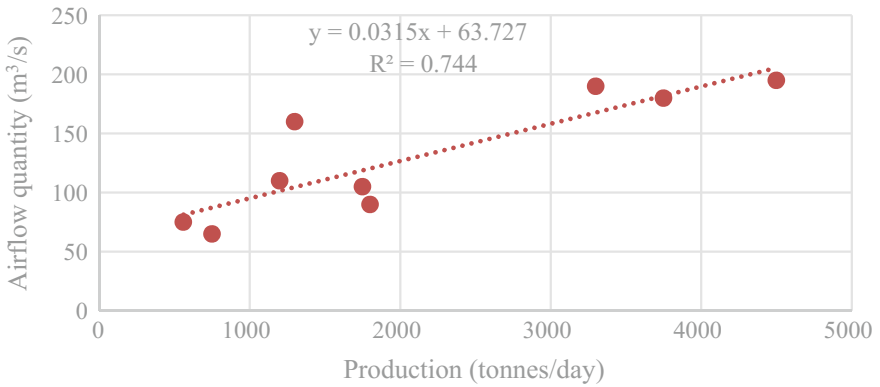


Fig. 2. Total airflow quantities of mines in terms of production capacity

Figure 3 shows total diesel power per tonne mined ore in participated mines. Mine A has highest value (2.35 kW/tonne) due to its high mechanization degree and mining method (cut & fill mining). The second highest diesel power per tonne mined is in Mine E with 2.25 kW/tonne. Mines (B, C, D, F and H) use similar diesel power per tonne mined. Mine G has lowest diesel power with 0.84 kW/tonne and the average value for all mines is 1.67 kW/tonne.

Total diesel power per tonne mined (kW/tonne)
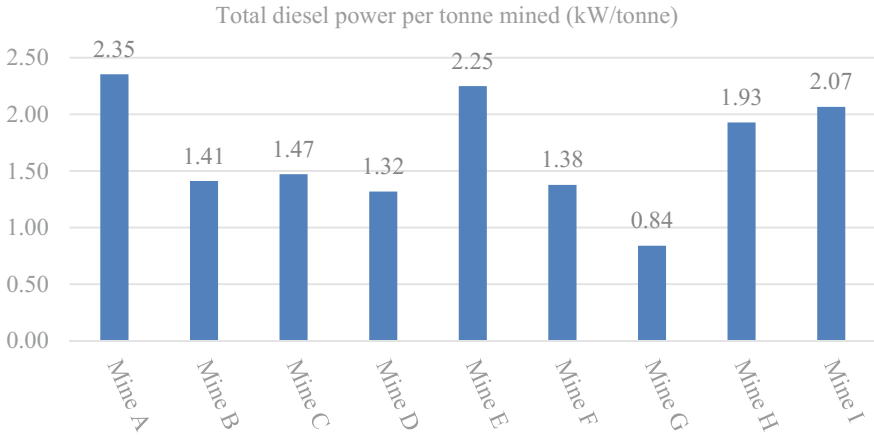


**Fig. 3.** Histogram of total diesel power required per tonne mined

Figure 4 presents the ventilation rates related to the power capacity of the diesel equipment fleet of each mine. Each mine has its own total ventilation rate calculation criteria depending on diesel engine's type and their emissions. Mine G has the highest ventilation rate with 0.071 m³/s/kW. Although it has moderate diesel power, due to air leakages in old working areas, total airflow quantity provided is relatively high. Mine B has the lowest ventilation rate per kW despite it is the deepest mine in survey (0.071 m³/s/kW). In Mine B, most of diesel engines are suited to Stage III (Tier 4) emission standards. Mines (C, D, E, F, I) have modest ventilation rates (0.033–0.042 m³/s/kW). Average ventilation rate is 0.047 m³/s/kW for this survey.

Total diesel power per tonne mined (m³/s/kW)
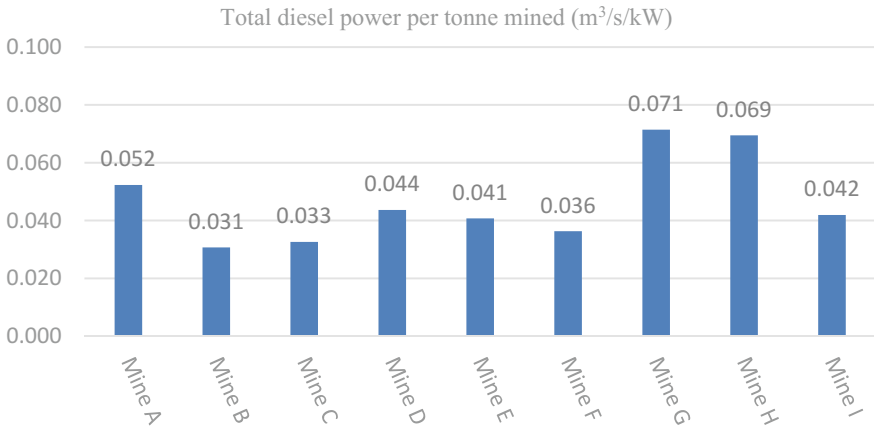


**Fig. 4.** Histogram of total airflow per kW per tonne mined

Figure 5 presents total airflow supplied to mines and total power for diesel fleets. Results show that, there is very strong 82% relationship between total airflow and total diesel power used.
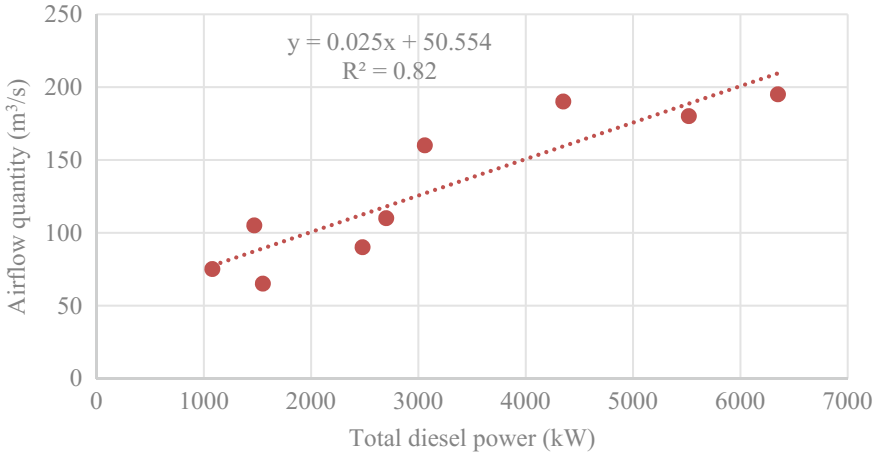


**Fig. 5.** Total airflow quantities of mines in terms of total diesel power

Figure 6 shows relation between total airflow and current mining depth for several participating mines in the study. As seen in Fig. 6, relation is very weak between these variables. Correlation coefficient is 52.1%, which means there is no meaningful relation between total airflow and mining depth.
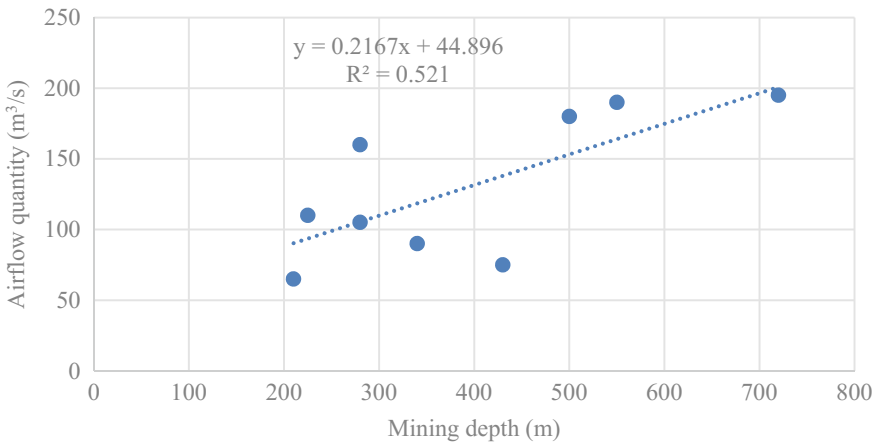


**Fig. 6.** Relation between total airflow quantity and mining depth

## 3    Results and Conclusion

This survey is conducted in nine participating underground metal mines in Turkey and ventilation characteristics of each mine have been collected and analyzed. Results show that, there is a strong correlationship among ventilation rate, diesel power and production capacity. Average value is found to be 0.077 m$^3$/s per tonne mined and 0.047 m$^3$/s per kW of diesel power, which show similar results when compared to previous research studies [6, 7]. On the other hand, mining depth in surveyed mines does not show any significant relation with ventilation rate. Diesel power use mines is further increased and proper ventilation design in mechanized underground mines is getting more important. Optimization of ventilation costs while creating a healthier environment for the underground workforce is getting more complex. Therefore, restrictive regulations of diesel emissions and developments in diesel motor technology will continue to be decisive when the total air quantity is determined.

## References

1. Yigit, O.: A prospective sector in the tethyan metallogenic belt: geology and geochronology of mineral deposits in the Biga Peninsula, NW Turkey. Ore Geol. Rev. **46**(2012), 1118–1148 (2012)
2. Yörükoglu, A., Delibas, A.: Mineral potential of Turkey. Mining Turkey Mag., 18–23 (2012). http://miningturkeymag.com/pdfler/mak-1411047215.pdf, Last Accessed 10 Mar 2018
3. Stinnette, D.: Establishing total airflow requirements for underground metal/nonmetal mines based on the diesel equipment fleet. M.Sc. thesis, Queen's University, Kingston Ontario (May 2013)
4. Gonen, A.: Ventilation requirements for today's mechanized underground metal mines. Int. J. Adv. Res. Eng. **4**(1), 7–10 (2018)
5. Tuck, M.A.: Mine ventilation. In: Darling, P. (ed.) SME mining engineering handbook society for mining. Metall. Explor. Inc., Colorado, USA (2011)
6. Mafuta, R.K., Fytas, K., Paraszczak, J., Laflamme, M.: Impact of diesel equipment on ventilation in quebec underground mines. In: Proceedings of the 22nd MPES Conference, pp. 571–579, Dresden, Germany (2013)
7. Wallace, K.: General operation characteristic and industry practices of mine ventilation systems. In: Proceedings of the 7th International Mine Ventilation Congress, pp. 229–234, Krakow, Poland (2001)

# Ventilation System Design for the Prestea Underground Mine

K. G. Wallace[1(✉)], B. S. Prosser[1], S. Ampiah[2], and E. Gyawu[2]

[1] SRK Consulting, (U.S.), Inc., Clovis, CA, USA
kwallace@srk.com
[2] Golden Star (Bogoso/Prestea), Ltd., Accra, Ghana

**Abstract.** This paper describes a ventilation project to support the development of a new mining zone within an existing mine. The project included installing a new booster fan for initial development and a new surface exhaust fan. An additional booster fan will be commissioned once ventilation raises are completed. Sealing old workings from the new ventilation system has proven to be difficult. This paper describes the challenges in developing a new ventilation system in a complex, old existing mine with small airways.

**Keywords:** Case studies · Ventilation design

## 1 Introduction

The Prestea Underground Mine (PUG) is in the Ashanti Gold Belt in Ghana, West Africa. Golden Star Resources Ltd. (GSR) purchased the mineral concession to the property in 2002. The Prestea Mine was originally known as the New Century Mine (NCM) after a joint venture (JV) was established between Golden Star Bogoso/Prestea Ltd (GSBPL), Prestea Gold resources (PGR) and the Government of Ghana in March 2002. Golden Star later bought the shares of PGR. The Primary Mandate of the JV was to put the mine under care and maintenance and to conduct exploration and feasibility studies to determine the economic viability of re-opening the underground mine for commercial purposes. The mine has operated for over 100 years and was mined to 34 Level with a strike length of over 6 km. The original mine developed the main reef that extended between a series of shafts. This main reef has namely been mined out except for some zones about half way between the Central and Bondaye shafts. The original mining methods were non-mechanized shrinkage stoping, conventional cut and fill and rill mining along the narrow gold bearing vein. Ore was transported via narrow gauge rail to the Central Shaft for hoisting to surface.

Whilst on care and maintenance the mine was partially flooded. GSR dewatered the mine to put the water table between 25 and 26 Level and rehabilitated shafts and airways. During this time, exploration teams identified a high-grade ore zone in the West Reef. This reef is approximately 200 m west of the main reef and mining areas. Figures 1 and 2 show the approximate location of the West Reef (into the page) in relation to the strike of the main reef. Subsequent improvements to the mine included
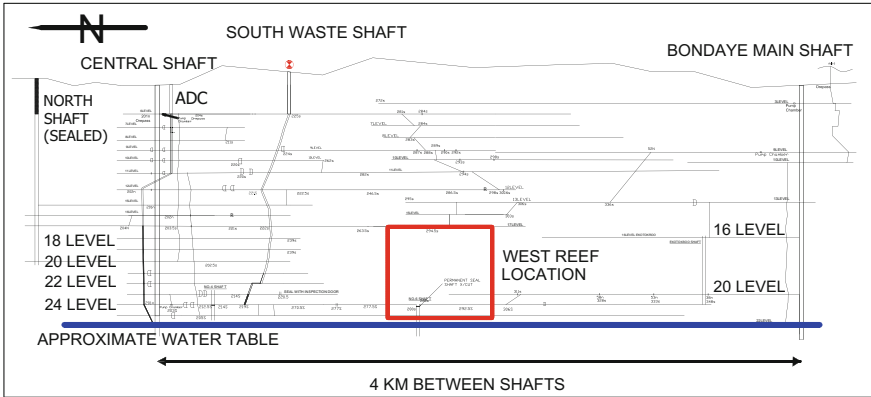
**Fig. 1.** PUG original mine with west reef location (24 Level)
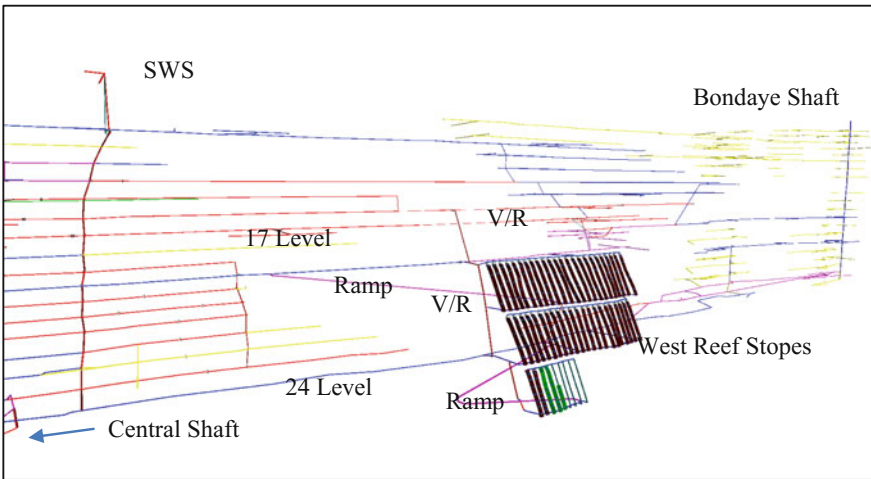


**Fig. 2.** Long range stope arrangement for west reef zone

upgrading the rail system on 24 Level from the West Reef to the Central Shaft and upgrades to the Central Shaft hoisting system.

The ore zone is between two of the access shafts, the Central Shaft and the Bondaye Shaft. The distance between the two shafts is approximately 4 km. The Central Shaft is the primary hoisting shaft and is 2 km from the West Reef orebody.

The ore zone is between 17 and 27 levels with initial production beginning on 24 Level. This level is approximately 900 m below the Central Shaft collar. The West Reef location is shown on Fig. 2. The West Reef narrow vein orebody will be mined using a mechanized shrinkage method called Alimak Stoping. Small Load Haul Dump vehicles will transfer the ore to rail cars for transport to the Central Shaft.

Initially there was very limited airflow to 24 Level. Only a small booster fan was positioned on 24 Level pulling air from the Bondaye shaft towards the Central shaft. This fan provided approximately 4–5 m³/s for initial exploration. Two small surface exhaust fans operated on the top of the South Waste shaft to provide the primary exhaust for the mine. The surface concrete tunnels that connect the SWS with the old primary fan are shown on Fig. 5.

The ventilation system was enhanced by a series of ventilation modifications. First, an interim booster fan was installed on 23 Level to push air up from 24 Level and into the South Waste Shaft to two double stage exhaust fans. The next improvement was to replace the surface fans with a single larger exhaust fan. Future ventilation enhancements will include driving exhaust raises to 17 Level, installing a new exhaust booster fan on this level and removing the interim booster fan on 23 Level.

## 2 PUG Mining Method

The West reef is a narrow vein orebody that will be mined with Alimak raises. The concept is to drive an Alimak raise then drill along the strike of the orebody. Pillars are left between the Alimak stopes along with a crown pillar left for ground stability between vertical stopes. Figure 3 shows the basic concept for the mining system. The figure shows the various stages of stope development, that is one stope near completion, one full of broken ore to be removed from the base of the stope, two being blasted, two being drilled to prepare for blasting and two under construction. The pattern is repeated across the strike length. Mining was initiated on 24 Level from the north working to the south.

Figure 3 also shows the airflow design values for the stopes. Each Alimak will initially be ventilated by compressed air lines. When the Alimak is complete, the open raise is designed for 2.5 m³/s. Once the stopes are blasted closed, ventilation will again
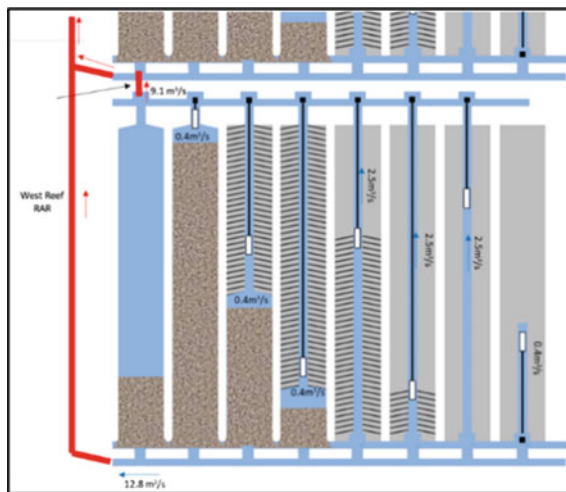


**Fig. 3.** West reef mining method with ventilation design values

use compressed air for ventilation. Calculations have been performed to verify blasting smoke clearance times after the stopes have been blasted with compressed air ventilation.

## 3   Development of the Ventilation System

This section describes the staged upgrades to the PUG mine system from exploration to life of mine production of the West Reef.

### 3.1   Exploration Ventilation System

The exploration ventilation system consisted of a small booster fan on 24 Level pulling air from the Bondaye Shaft towards the Central and South Waste Shafts. Figure 4 shows the approximate airflows for this system. This system supported limited activity, but allowed for exploration of the West Reef to be completed. On 24 Level, temperatures were high with wet bulb temperatures approaching 30 °C (Fig. 5).
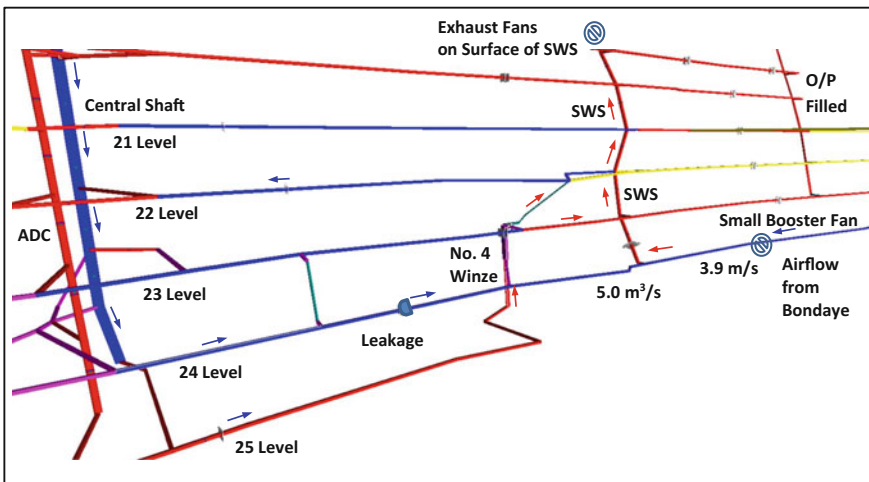


**Fig. 4.**  Exploration ventilation system



**Fig. 5.**  Surface concrete tunnel with temporary fans shown

### 3.2 Installation of Interim Booster Fan

To provide sufficient airflow to support mining of the West Reef, a ventilation study was performed that evaluated bringing intake air from the Bondaye Shaft across 24 Level to the No. 4 Shaft through a booster fan on top of this raise, then into the SWS to exhaust to surface. For this option to be successful, it was necessary to replace the door on 24 Level with airlock doors between the Central Shaft and the No. 4 Shaft and to seal old stopes along the 3.5 km strike between the Bondaye shaft and the No. 4 Shaft. The ventilation analysis showed an interim booster fan located on 23 Level capable of 35 $m^3$/s at a pressure of 2.15 kPa will provide approximately 20 $m^3$/s across 24 Level.

After a competitive bid process, GSR selected a ClemCorp vane axial fan model CC1800Mk1. This fan was installed in mid-2016. Figure 6 shows the location and photo of the booster fan on 23 Level, Fig. 7 shows the initial airflow readings across 24 Level along with a drawing of 24 Level. Initial field testing showed there was significant leakage from 25 Level up to 24 Level in the No. 4 Shaft. In addition, there was significant leakage in the rock filled SWS on 24 Level. GSR personnel built a solid, brick wall/bulkhead to contain the leakage or recirculated air coming off the SWS onto 24 Level. A second door was added on Level 23 from the Central Shaft to the Booster fan location. The circles on Fig. 7 show the leakage points that were corrected as well as the numerous stope accesses along the 4-km strike length from the Bondaye to Central Shafts.

The preliminary sealing program resulted in increasing flow across 24 Level from 8.9 to 15.1 $m^3$/s. Further sealing resulted in 19.5 $m^3$/s coming from the Bondaye Shaft on 24 Level.
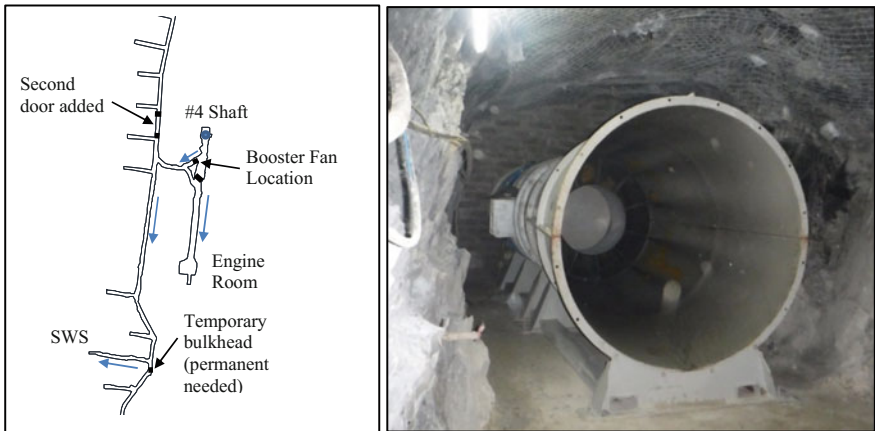


**Fig. 6.** 23 Level booster fan location and photo
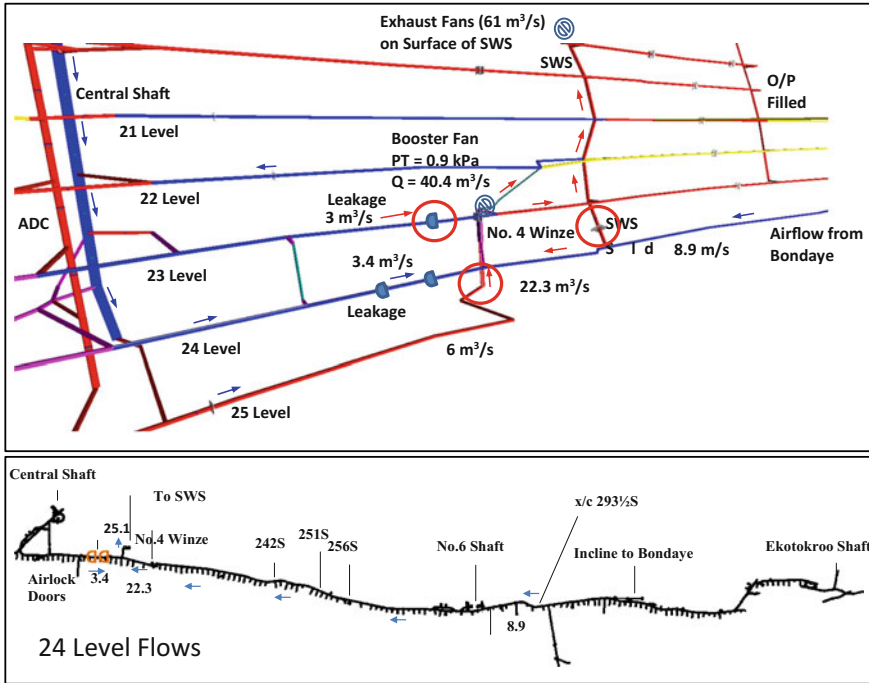
**Fig. 7.** Initial airflow readings with 23 Level booster fan in operation

## 3.3  Installation of New Surface Fan

To achieve the design flows to support the upper West Reef development, a new surface exhaust fan is required. Ventilation analyses showed that upon completion of an internal raise system from the West Reef to 17 Level and the SWS, added exhaust capacity is required above the current 60 m³/s the two small surface fans can deliver. Long range ventilation planning resulted in quantifying the exhaust fan at 93 m³/s at 1.4 kPa. GSR selected a ClemCorp Model CC1800 with a 250 kW motor and variable speed drive. This vane axial fan was installed in the surface concrete tunnel leading to the original surface fan. To minimize impact on operating the temporary fan in this tunnel, a hole was constructed in the side of the tunnel allowing for air to exhaust from the operating fan while installing the new fan. Figure 8 shows how the fan was installed without interrupting the operating exhaust fan. With this configuration the new exhaust fan could be installed until the final fan commissioning when Fan 1 would be removed through the open hole and the hole sealed. Figure 9 shows photos of the main fan.

Fan start-up testing showed a volume of 95 m³/s at a fan pressure of 1.7 kPa. De-livered pressure to the mine was measured at 1.2 kPa. Because the West Reef exhaust ventilation raise was not installed at the time of the new fan commissioning, no increase in flow on 24 Level was observed. Airflow on level 17 was increased to the SWS. This allowed for ramp development to the West Reef off of this level (Fig. 3).
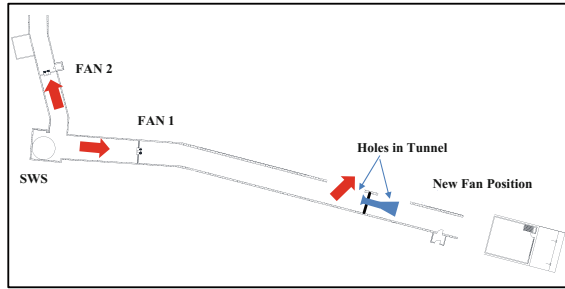
**Fig. 8.** Installation sketch for new surface fan



**Fig. 9.** Photos of main fan installation

## 3.4  Final Ventilation System Upgrades

The final ventilation upgrades to support the West Reef include construction of a primary exhaust ventilation raise from 24 Level to 17 Level. On 17 Level a new booster fan will be installed and the booster fan on 23 Level will be decommissioned. The final system will intake air from the Central shaft on 17 and 24 Levels and from the Bondaye shaft on 24 Level. Intake air will course in the ramp from 17 to 24 and across 24 to the ramp location. Air will intake the ramp to the stopes and exhaust through the internal ventilation raise. On 17 Level a booster fan will pull the air up from the lower
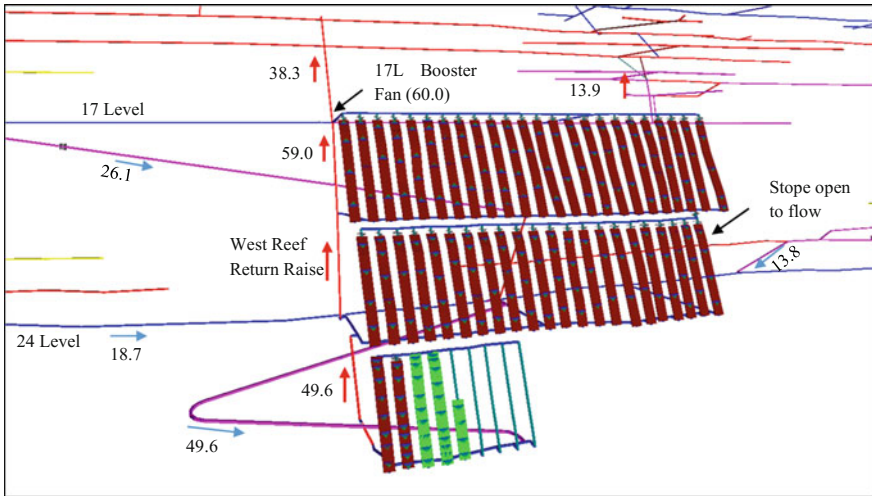
**Fig. 10.** Ventilation model with west reef near full development

**Table 1.** Predicted fan duties during west reef development

| Date | Main SWS exhaust fan | | | 17 level booster fan | | |
|------|---------------------|--|--|---------------------|--|--|
| | Pressure (kPa) | Quantity (m³/s) | Motor power (kW)[a] | Pressure (kPa) | Quantity (m³/s) | Motor power (kW)[a] |
| Q8 | 1.38 | 93 | 184 | 0.93 | 45 | 186 |
| Q10 | 1.40 | 93 | 186 | 0.65 | 45 | 42 |
| Q16 | 1.11 | 93 | 147 | 2.89 | 66 | 273 |
| Q20 | 1.18 | 93 | 157 | 2.19 | 60 | 188 |

[a]Assume 70% fan efficiency

stopes and exhaust up to 12 and 11 Levels. From these levels the air will pass to the SWS and up to the primary surface exhaust fan. Figure 10 shows the ventilation system when the West Reef is nearly mined out. Table 1 shows the predicted fan duties during various stages of the mine development.

## 4    Conclusion

One of the major challenges in establishing a new ventilation system is controlling air leakage. In this mine it the leakage through the numerous old stopes. Not all stopes are sealed from existing airways and air can communicate from upper or lower levels to an exhaust airway even if the stopes appear to have been filled. GSR continues to construct bulkheads to seal off old stopes to optimize the ventilation system performance. Another challenge for the ventilation system is heat in the underground. After the mine was placed on care and maintenance, the lower portion of the mine was flooded.

Although the lower levels have been pumped out, much of strata remained wet/saturated. The primary heat source in the underground is rock (estimated at 30–31 °C) and small diesel and electric systems. Measured wet bulb temperatures approach a nearly saturated condition of 30 °C. This temperature is likely the result of long travel times for the air to reach the West Reef, high moisture content of the rock and the surface subtropical environment. Air cooling may be a consideration as the West Reef is developed.

The results of this study showed that with proper engineering it is feasible to design a ventilation system to support a modern mining/extraction technique in an old, existing mine.

# CFD Analysis of the Effect of Porosity, Quantity and Emanating Power Variation on Gas Emissions in Block/Panel Cave Mines

Rahul Bhargava[1], Purushotham Tukkaraja[1(✉)], Khosro Shahbazi[1], Kurt Katzenstein[1], and David Loring[2]

[1] South Dakota School of Mines and Technology, Rapid City, SD 57701, USA
PT@sdsmt.edu
[2] Freeport-McMoRan Inc., Phoenix, USA

**Abstract.** Block/panel caving is an underground mining method that uses the gravity for mining massive, deep ore deposits. Since caving is a dynamic process, the design of a ventilation system for block/panel cave mines is a challenging task, especially when the ore body contains uranium-bearing mineralization, where radon gas is a major concern for mining operations. This study utilizes a continuum-based computational fluid dynamics (CFD) approach to investigate the effect of changing cave porosity (Ø), air quantity (Q), and radon emanating power (B) on radon daughter emissions from a cave in a block/panel cave mine. The aim of the study is to predict radon daughter concentrations in the production drifts based on the quantity supplied to the drift, emanating power of ore and porosity of the cave. The predicted radon daughter concentrations can be useful data for mine ventilation engineers in designing an effective ventilation system for block/panel cave mines.

**Keywords:** Porosity · Radon daughter · Radon emanating power

## 1 Introduction

Block/Panel Caving is an underground mining method that utilizes gravity to exploit massive, deep ore deposits, which are too deep to be mined economically by conventional surface mining methods. There are numerous variations of the block caving technique that use different layouts and extraction patterns. Panel caving is one of the variants. The fundamental difference between block and panel caving is that block caving produces from the full ore body footprint while in panel caving the active caving zone moves across the panel i.e. while one end is being undercut, the other end is producing [1].

Ventilation is one of the key elements in caving mining methods especially in production drifts of a panel cave mine where majority of personnel and machinery are concentrated. This study investigates the effect of changing the porosity of the broken ore in the cave, air quantity supplied to the production drifts, and radon emanating

power of the broken ore on the radon daughter concentrations in the production drifts. A continuum based computational fluid dynamics (CFD) approach is used for this study. Figure 1 shows the decay chain of uranium to a relatively long-lived radon daughter $Pb^{210}$ (RaD).
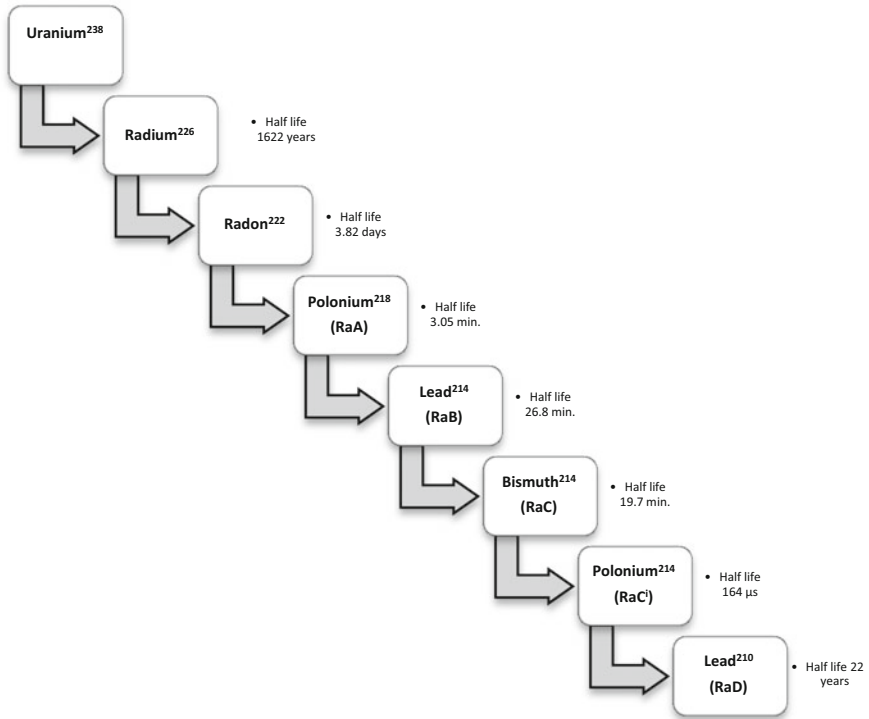


**Fig. 1.** Uranium decay chain

## 2 Background

In the United States, radon has been listed as the second leading cause of lung cancer after tobacco [2]. Considering the short half-life of radon gas and its daughter products, monitoring of their concentrations in the underground environment becomes very important.

According to Code of Federal Regulations (CFR), 30 CFR 57.5038, no person should be subjected to a radon cumulative exposure of 4 Working Level Months (WLM) in one year with an upper limit of 2 WLM in two months. At a constant rate of emission, the rise in the concentration of non-radioactive gases is inversely proportional to the rate of through-flow of fresh air. This is not the case for radon daughters

because of the ongoing effects of radioactive decay [3]. In order to control the working level of radon in a mine, McPherson developed a relationship (Eq. 1) to determine the quantity of air needed to achieve the desired radon working level at the exit of an airway supplied with uncontaminated air with constant radon emanation. This equation predicts the radon level at the exit of an airway [3]. However, prediction of radon daughter concentration with respect to space and time is not fully explored. This research is focused on developing a CFD model that can be used to predict radon daughter concentration in a panel cave mine with respect to the emanating power of ore, quantity supplied in the production drifts, and porosity of the cave.

$$\frac{WL_1}{WL_2} = \left(\frac{Q_2}{Q_1}\right)^{1.8} \tag{1}$$

where $WL_1$ is the working level corresponding to $Q_1$ (Airflow rate in m$^3$/s) and $WL_2$ corresponding to $Q_2$ (Airflow rate in m$^3$/s).

## 3   Methodology and Research Approach

The basic steps involved in the study can be summarized in Fig. 2.
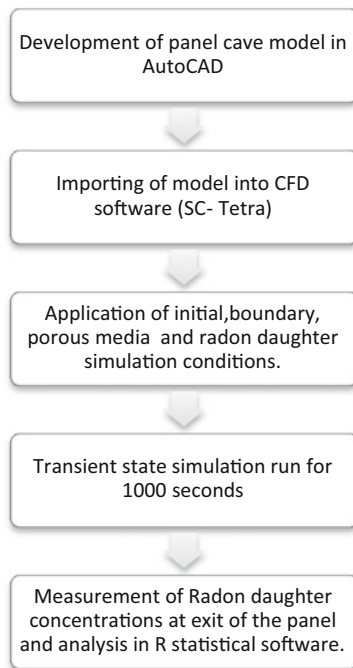


**Fig. 2.** Flowchart describing steps involved in this study

### 3.1 Cave Layout

For the CFD analysis, this study considered a panel cave continuum model of 375 m × 256 m × 356 m (height × length × width) with nine production and three undercut inlets and nine production, eight undercut, and eight exhaust outlets. The cave region was divided into eighteen different regions diagonally and each region was divided into 3 sub-regions laterally. Particle sizes and porosity values were assigned to each region. From field studies, it was observed that particles at the boundary of the panel were having coarser size along with higher porosity as compared to particles in mid region. The CFD model also incorporates this phenomenon. Keeping the computational time in mind, only two cave zones, namely broken rock and uncaved in situ rock zone, are modelled in this study. Porosity change inside the cave has been modelled with the caving starting from the rightmost zone and propagating towards the left. The production drifts, undercut drifts and exhaust drifts have dimensions of 4.3 m × 4.3 m. There is an undercut inlet duct (inside the undercut drifts) having dimensions of 1 m × 1 m providing fresh air to the cave. The exhaust drifts represent the connections of the cave to the older depleted workings and finally to exhaust shaft as part of mitigation of radon/other harmful gases produced inside the cave. The dimensions and other important details of the model are shown in Figs. 3, 4 and 5.
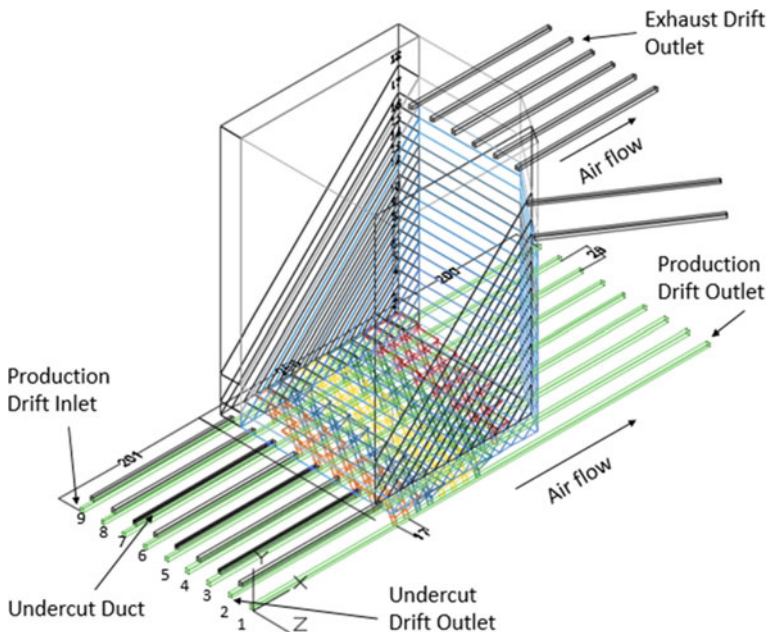


**Fig. 3.** Isometric view of the panel cave model
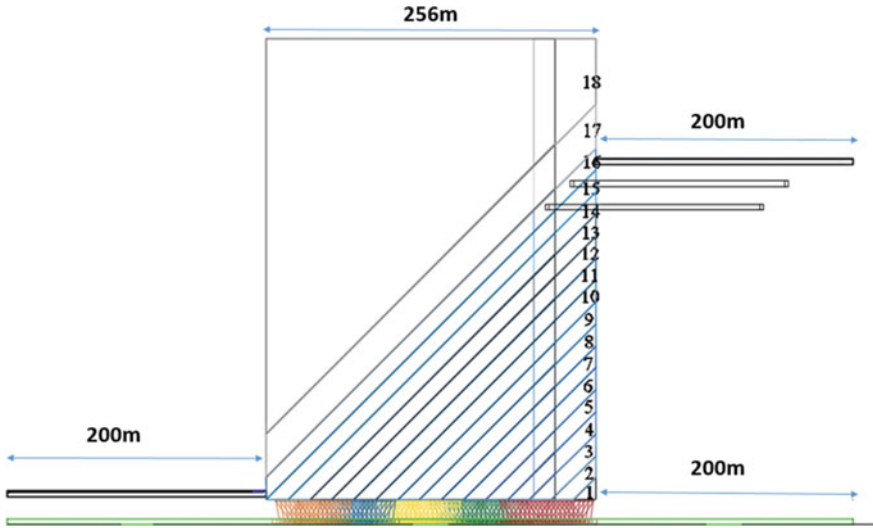
**Fig. 4.** Front view of the panel cave model
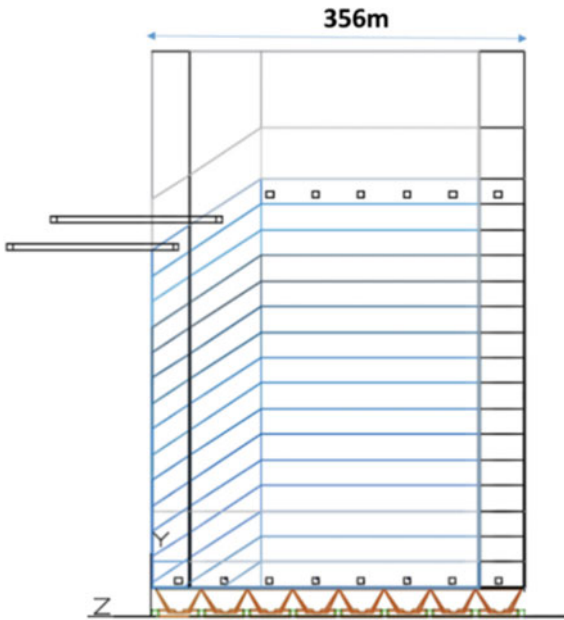


**Fig. 5.** Side view of the panel cave model

As shown in Fig. 4, broken rock is represented by regions 1 through 16 where region 16 represents the top layer of broken rock while number 1 represents the bottom layer. The higher numbers (regions 1 through 16) indicate the zones with larger particles and higher porosity values. However, region 17 represents the yield zone having a very low porosity (0.01% was assumed) and an assumed thickness of 34 m. Region 18 represents undisturbed intact rock that has the highest volume in the cave model. Similar to the yield zone, its porosity is low (0.00001% was assumed to represent the elastic zone with some fractures) and has an assumed thickness of 51 m.

### 3.2  Porous Media

SC/Tetra has a model for the porous media whereby the porosity of the given volume can be specified. The model has different types of porous media, however, the porous media packed bed filled with solid particles is used for this simulation. SC/Tetra does not consider the flow path in porous calculation configuration; an external force is applied in opposite direction to flow in order to induce pressure loss. Total porosity of the porous media is given as the ratio of fluid region volume over total volume. Characterization of particle type within the porous media model requires three different inputs; porosity, diameter of the particle, and the shape factor. In this study, bulk cave porosity values range from 21 to 56%, diameters of particles range from 6 to 30 cm and shape factor value is assigned as 1.

### 3.3  Boundary Conditions

Obtaining a reliable result from a CFD model is highly dependent on the boundary conditions. The boundary condition used for the inlet is the velocity condition with different values based on the quantity of airflow. The inlet temperature of the airflow is set as 20 °C with no concentration of radon. Natural inflow/outflow is used for the outlet conditions of both drifts; this condition assumes that velocity and pressure do not change in the normal direction [4]. Therefore, the condition can be used if the flow does not really change near the boundary. It is used because the flow is assumed to continue into other sections of the mine. The boundary conditions used for this study are summarized in Table 1.

**Table 1.** Boundary conditions

| Region | Base boundary conditions |
|---|---|
| Production drifts (9 nos.) | Inlet air velocity—1, 1.25, 1.5 and 1.75 m/s<br>Outlet—natural inflow/outflow |
| Undercut inlet drift duct (3 nos.) | Inlet air velocity—17 m/s |
| Undercut drift (8 nos.) | Outlet—natural inflow/outflow |
| Exhaust drift (8 nos.) | Outlet—natural inflow/outflow |
| Roof top | Natural inflow/outflow |

### 3.4    Radon Emanation, Diffusion, and Decay

Radon emanation is defined as the escape of a radon atom from a radium bearing grain into the pore space [5]. The actual emanation of radon from a rock surface can be measured or calculated from Eq. 2 [6].

$$J = C_\infty \sqrt{\lambda D \phi} \qquad (2)$$

where $J$ is the radon gas emanation from rock surface (pCi/m$^2$s), $\emptyset$ is the rock porosity (fraction), $C_\infty$ is the radon concentration at infinite distance into rock (pCi/m$^3$) calculated as ($B/\lambda\emptyset$), B is the radon gas emanation from fragmented rock (pCi/m$^3$s); usually called emanating power, $\lambda$ is radon decay constant ($2.1 \times 10^{-6}$ Bq), and D is the diffusion coefficient for rock (m$^2$s).

To study the migration of radon in a mine, the emanating rate from an exposed surface J (pCi/m$^2$s) and emanating power B (pCi/m$^3$s) from drill cores or the samples must first be measured. In the past, several experiments and surveys have been conducted to determine the emanating powers of different samples. It is important to note that several factors such as radium distribution, grain size, moisture content, and temperature affect the emanation power of a given sample [3]. In panel caving, it is complex to predict the emanation power because caving is a dynamic process. The rock surfaces in the drifts have the potential to emanate some quantity of radon gas into the mine environment. As the cave continues to propagate, the geometry of the cave changes. This change in geometry affects the porosity, which is another useful variable to predict the gas emanation. The extraction of ore from the draw points also changes the porosity of the cave. This dynamic nature of the cave complicates the study of radon gas migration in a block cave mine [4]. In this CFD modeling study, a fully developed cave has been assumed and radon emanation from the broken ore muck pile inside the cave and the draw bells has only been considered with no emissions from the wall surfaces.

Grinding increases the emanating power up to a limit, after which no significant increase occurs. The ore crystal grains are fractured during fine grinding, and micro-fracturing increases with crushing. Both fine grinding and crushing contribute to an increased rate of radon gas release [7]. Previous work suggests that the emanating power of ore samples having Uraninite ($U_3O_8$) (trace to 0.075%) varies from 6 to 187 pCi/m$^3$s depending on whether it is a coarsely or finely ground sample [7]. Considering the above factors, scenarios of three different (6, 90, 180 pCi/m$^3$s) emanating powers of ore were simulated. For a given emanating power of the ore, four different cave porosities (21, 28, 42 and 56%) were modeled and for a given porosity, four different air quantities (18.5, 23.1, 27.7 and 32.3 m$^3$/s) were modelled for the production drifts. Therefore, the total number of simulations run was 36.

Diffusion is one of the major factors that should be considered in the analysis of radon transport. The concentration of each diffusion species is treated as the ratio of the mass of a specific species to the total mass of all species present in the volume as depicted in Eq. 3.

$$C_i = \frac{m_i}{M} \qquad (3)$$

where $m_i$ is the mass of a specific species and M is the total mass of all species. Important parameters for simulation of radon diffusion are diffusive coefficient or mass diffusivity, molar mass, specific heat at constant pressure and thermal conductivity [4]. Radon$^{222}$, Po$^{218}$ and Pb$^{214}$ diffusivities were set to $1.1 \times 10^{-5}$, $5.5 \times 10^{-6}$, and $5.0 \times 10^{-6}$ m$^2$/s respectively [3, 8]. The zones were modeled as volume sources for radon gas. Radon emanation from the volume of broken ore was assumed as 6, 90, and 180 pCi/m$^3$s.

Radioactive decay is considered in the analysis of radon transport and the model included the effect of radon decay on radon migration. Since the simulation of the decay process is computationally expensive, the decay of Rn$^{222}$ (Radon) up to Pb$^{210}$ (RaD) was only simulated in this study. The half-life of Pb$^{210}$ (RaD) is 22 years and it is relatively a stable element in the uranium decay chain. In this case, alpha, beta, gamma were defined elements to balance the mass equation as shown below. The reaction rate is defined as the decay constant of radon ($2.1 \times 10^{-6}$ Bq). Similarly for the other radon daughters also, the decay constant was defined and entered during the simulation run as given by the Eqs. 4, 5, 6, 7 and 8.

$$\ce{^{222}_{86}Rn} \rightarrow \ce{^{218}_{84}Po} + \ce{^{4}_{2}\alpha} \qquad (4)$$

$$\ce{^{218}_{84}Po} \rightarrow \ce{^{214}_{82}Pb} + \ce{^{4}_{2}\alpha} \qquad (5)$$

$$\ce{^{214}_{82}Pb} \rightarrow \ce{^{214}_{83}Bi} + \ce{^{0}_{-1}\beta} + \ce{^{0}_{0}\gamma} \qquad (6)$$

$$\ce{^{214}_{83}Bi} \rightarrow \ce{^{214}_{84}Po} + \ce{^{0}_{-1}\beta} + \ce{^{0}_{0}\gamma} \qquad (7)$$

$$\ce{^{214}_{84}Po} \rightarrow \ce{^{210}_{82}Pb} + \ce{^{4}_{2}\alpha} \qquad (8)$$
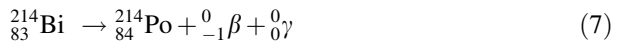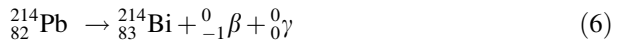
## 3.5 Solver Settings

Airflow through the mine was assumed as incompressible and turbulent. A time step of 1 s was used in this study and convergence criteria of $10^{-5}$ was considered for the radon daughters, pressure, and velocity. Standard $k - \varepsilon$ model was used for this simulation [9]. In summary, the conservation of energy, momentum, mass, turbulence model, diffusion, and porous media equations were solved for analyzing radon daughter concentrations in the production drifts of a panel cave mine.

## 3.6 Grid Independence Study

In order to insure that the simulation provides reliable results, it is very important that the simulation results are grid independent. Due to the complex geometry of the cave, a

reliable mesh size was determined by conducting the grid independent study. From the analysis of the results with mesh elements ranging from 5.55 to 15.83 million, it was observed that further increase in the mesh elements from 11.83 million did not have much effect on the result. Hence, 11.83 million mesh elements were used for this study.

## 4   Results

The concentration of radon daughters was measured at the exit of the panel cave (458 m from the inlet) for production drifts 1, 3, 5, 7 and 9. Figures 6, 7 and 8 show sample average radon daughter concentration in drift 5 for 18.5 m$^3$/s air quantity and a cave porosity of 21%. A summary of average radon concentration in Drift 5 (458 m from the inlet) was summarized in Table 2 and similar data was collected for the other drifts also. The results were analyzed in R statistical software to develop the relationships between radon daughter concentration (WL), porosity, emanating power, and quantity supplied to the production drifts. The relationships were summarized in Table 3 where B represents the emanating power, Q is the quantity supplied and Ø represents the porosity of the cave.
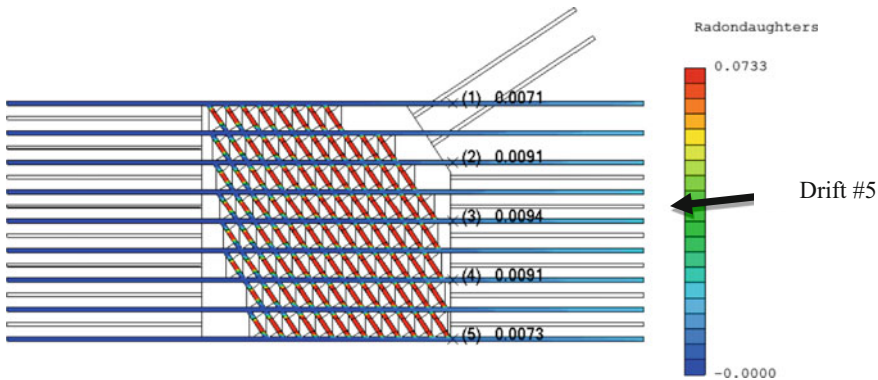


**Fig. 6.** Radon daughter concentration (WL) in production drifts with simulation time of 1000 s at Q = 18.5 m$^3$/s, B = 6 pCi/m$^3$s, Ø = 21%
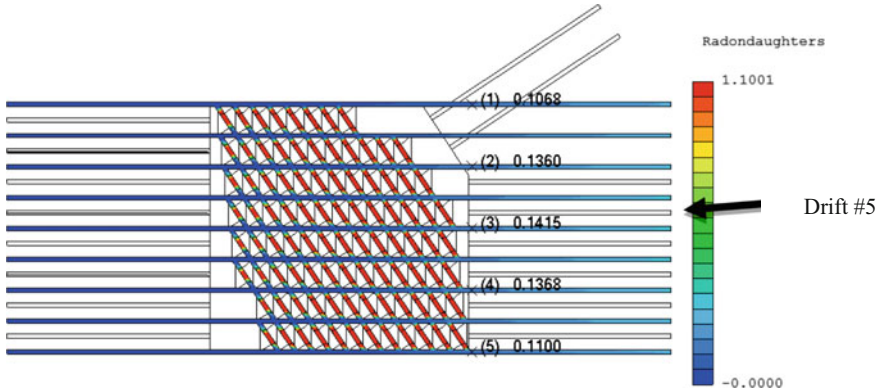
**Fig. 7.** Radon daughter concentration (WL) in production drifts with simulation time of 1000 s at $Q = 18.5$ m$^3$/s, $B = 90$ pCi/m$^3$s, $\emptyset = 21\%$
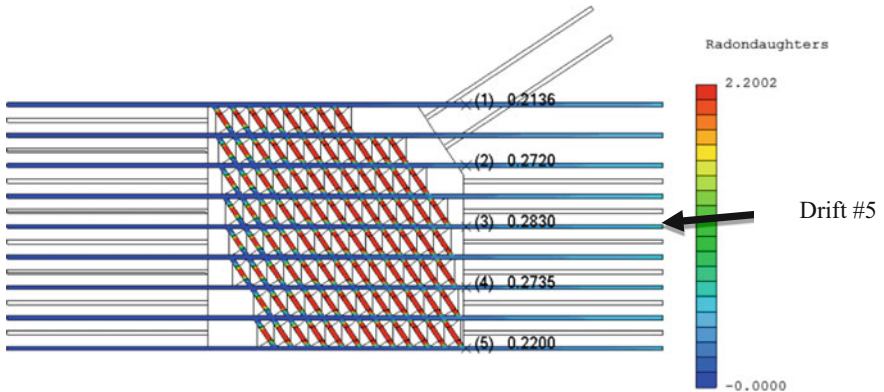


**Fig. 8.** Radon daughter concentration (WL) in production drifts with simulation time of 1000 s at $Q = 18.5$ m$^3$/s, $B = 180$ pCi/m$^3$s, $\emptyset = 21\%$

**Table 2.** Summary of average radon daughter concentration in drift #5

| Q (m$^3$/s) | Ø (%) | WL (B = 6 pCi/m$^3$s) | WL (B = 90 pCi/m$^3$s) | WL (B = 180 pCi/m$^3$s) |
|---|---|---|---|---|
| 18.5 | 21 | 0.009 | 0.142 | 0.283 |
| 23.1 | 21 | 0.007 | 0.097 | 0.194 |
| 27.7 | 21 | 0.005 | 0.071 | 0.142 |
| 32.3 | 21 | 0.004 | 0.055 | 0.100 |
| 18.5 | 28 | 0.010 | 0.153 | 0.306 |
| 23.1 | 28 | 0.007 | 0.105 | 0.211 |
| 27.7 | 28 | 0.005 | 0.078 | 0.155 |

(*continued*)

**Table 2.** (*continued*)

| Q (m$^3$/s) | Ø (%) | WL (B = 6 pCi/m$^3$s) | WL (B = 90 pCi/m$^3$s) | WL (B = 180 pCi/m$^3$s) |
|---|---|---|---|---|
| 32.3 | 28 | 0.004 | 0.060 | 0.120 |
| 18.5 | 42 | 0.013 | 0.197 | 0.394 |
| 23.1 | 42 | 0.009 | 0.138 | 0.276 |
| 27.7 | 42 | 0.007 | 0.104 | 0.207 |
| 32.3 | 42 | 0.005 | 0.082 | 0.163 |
| 18.5 | 56 | 0.018 | 0.270 | 0.540 |
| 23.1 | 56 | 0.013 | 0.193 | 0.387 |
| 27.7 | 56 | 0.010 | 0.148 | 0.310 |
| 32.3 | 56 | 0.008 | 0.119 | 0.237 |

**Table 3.** Radon daughter concentration

| Production drift | Radon daughter concentration (WL) |
|---|---|
| Drift #1 | $WL = e^{-1.12}Q^{-1.86}\emptyset^{0.13}B^{0.99}$ |
| Drift #3 | $WL = e^{-0.71}Q^{-1.64}\emptyset^{0.69}B^{1.00}$ |
| Drift #5 | $WL = e^{-0.68}Q^{-1.62}\emptyset^{0.73}B^{0.99}$ |
| Drift #7 | $WL = e^{-0.78}Q^{-1.67}\emptyset^{0.59}B^{1.00}$ |
| Drift #9 | $WL = e^{-1.28}Q^{-1.83}\emptyset^{0.05}B^{0.99}$ |

# 5   Conclusions

The simulation results show that the radon daughter concentration in the production drifts of the panel cave mine is inversely proportional to the airflow quantity to the power of 1.6–1.8, and directly proportional to the emanating power of the broken rock in the cave. The simulation results also indicate that the porosity of the cave plays a very important role and does have a profound effect on the radon daughter concentrations in the production drifts. It should be noted that the results reported in this study are yet to be validated.

# 6   Future Work

Future work will be focused on improving the model by incorporating additional parameters that affect the radon daughter concentration and validating the model results with the field data. The additional parameters include rock size, cave height, temperature, pressure, number of draw bells and their orientation.

# References

1. Keeping up with caving. Min. Mag., 46–64 (June 2012)
2. Miller, K.J., Coffey, M.A.: Radon and you: promoting public awareness of radon in Montana's air and ground water. Montana Bureau Min. Geol. (1998)
3. McPherson, M.J.: Subsurface ventilation and environmental engineering. Springer Science & Business Media (2012)
4. Kayode Ajayi, P.T., Shahbazi, K., Katzenstein, K., Loring, D.: Computational fluid dynamics study of radon gas migration in a block caving mine. In: 15th North American Mine Ventilation Symposium, 341–348 (2015)
5. Sakoda, A., Ishimori, Y., Yamaoka, K.: A comprehensive review of radon emanation measurements for mineral, rock, soil, mill tailing and fly ash. Appl. Radiat. Isot. **69**(10), 1422–1435 (2011)
6. Bates, R., Edwards, J.: Mathematical modeling of time dependent radon flux problems. In: International Mine Ventilation Congress, 2nd edn (1980)
7. Sengupta, M.: Mine Environ. Eng. **1**. CRC Press (1989)
8. Malet, J., et al.: Mass transfer of diffusive species with nonconstant in-flight formation and removal in laminar tube flow. Application to unattached short-lived radon daughters. Aerosol. Sci. Technol. **32**(3), 168–183 (2000)
9. Hurtado, J.P., et al.: Shock losses characterization of ventilation circuits for block caving production levels. Tunn. Undergr. Space Technol. **41**, 88–94 (2014)

# Design and Construction of High Capacity Fixed Refuge Chambers at PT Freeport Indonesia's Underground Operations

E. Paul Meisburger IV[1(✉)], D. Iryanto[1], D. Quinn[2], A. Widyastutie[1], and A. Mone[1]

[1] PT Freeport Indonesia, Jakarta, Indonesia
pmeisbur@fmi.com
[2] Minearc Systems PTY Ltd., Welshpool, Australia

**Abstract.** PT Freeport Indonesia's Ertsberg mining complex in Indonesia's Papua Province consists of some of the largest underground mining operations in the world with thousands of employees underground each shift. This presents extraordinary challenges in underground emergency refuge chamber design and construction. PT Freeport Indonesia has approached this challenge by designing and building some of the largest fixed refuge chambers in the world. This paper describes the design and construction of several fixed refuge chambers with capacities of 70–600 persons each.

**Keywords:** Refuge chambers · Emergency response · Emergency management

## 1 Introduction

A complex of four underground mining operations under development and production exists within PT Freeport Indonesia's (PTFI) Block A Contract of Work area in the Western Ertsberg district of Papua, Indonesia, located about 100 km north of the southwest coast of Papua between 2500 and 4000 m above sea level. The underground mining complex consists of the following planned and operating mines and the anticipated or achieved maximum production rates; the Grasberg Block Cave (GBC) mine (160,000 tpd), the Deep Mill Level Zone (DMLZ) panel cave (80,000 tpd), the Deep Ore Zone (DOZ) panel cave (80,000 tpd), and the Big Gossan open stoping mine (7000 tpd) (Fig. 1).

## 2 Background

The risk of an underground fire is present in all underground mining operations. While the occurrence of serious underground fires is low, the consequences of such events can be severe. In large, modern mechanized mining operations, fuel loads due to mechanized equipment, fuel and lubrication storages, electrical distribution networks and warehouses can be sizeable. In these operations, care is required to minimize all possible sources of fire ignition. While mining operations strive to eliminate all
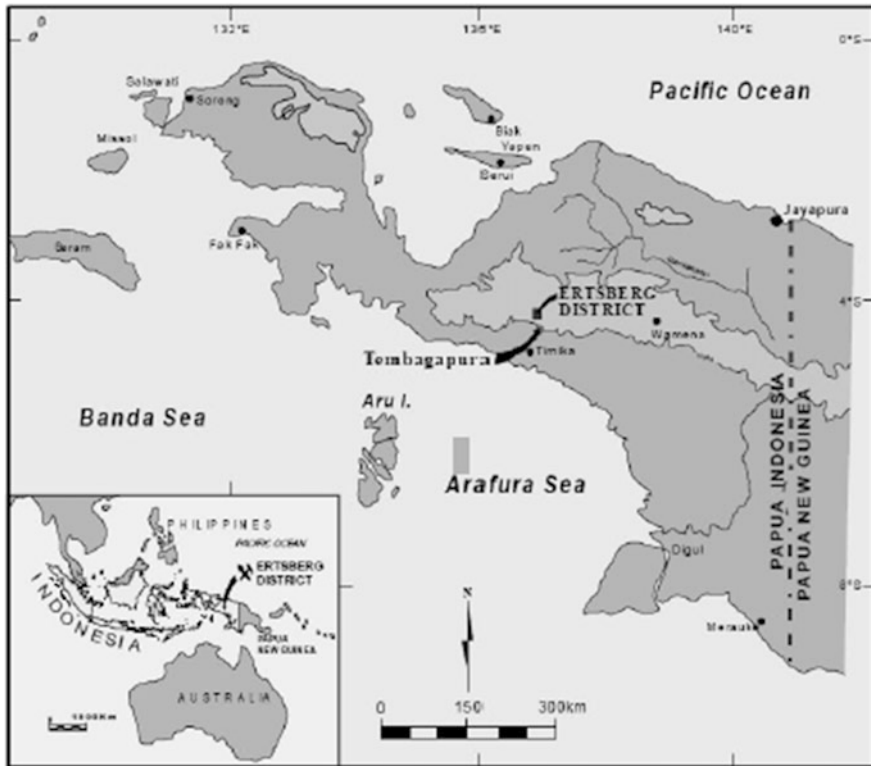
**Fig. 1.** Ertsberg District Location, Papua, Indonesia

potential sources of ignition, there must be an equal application of effort to the mitigation of a fire event should prevention controls fail. One of these mitigation efforts is the provision for escape or a safe location of refuge from fire for underground miners.

The majority of deaths arising from mine fires and explosions are caused not by burning or blasting effects, but by the inhalation of toxic gasses, in particular, carbon monoxide [1]. A primary mitigation control for the inhalation of toxic gasses in most underground operations is the provision of a self-rescue device which will allow the wearer to escape to the surface. Where distances to surface are substantial, a self-rescue device may not provide the duration to allow a wearer to escape to the surface, so alternative refuge locations within the underground mine must be considered.

As is typical for a modern underground mine, PTFI installs refuge chambers within the underground operation in order to address the risk identified above. Refuge chambers are portable or fixed locations that provide safe refuge from toxic gas by having an independent source of fresh breathing air that can be sealed off from the outside mine air environment. Due to the layout of a typical caving style mine operation, the majority of the workforce is concentrated within a small geographical area. Therefore, larger fixed refuge chambers, supplemented by smaller portable refuge chambers in remote or development areas, are the typical practice applied at PTFI.

While being a standard practice at PTFI, large fixed refuge chambers do create several non-traditional challenges, specifically: mass ingress, multi-story construction, the requirement for multi-purpose spaces, and personal sanitation (Fig. 2).
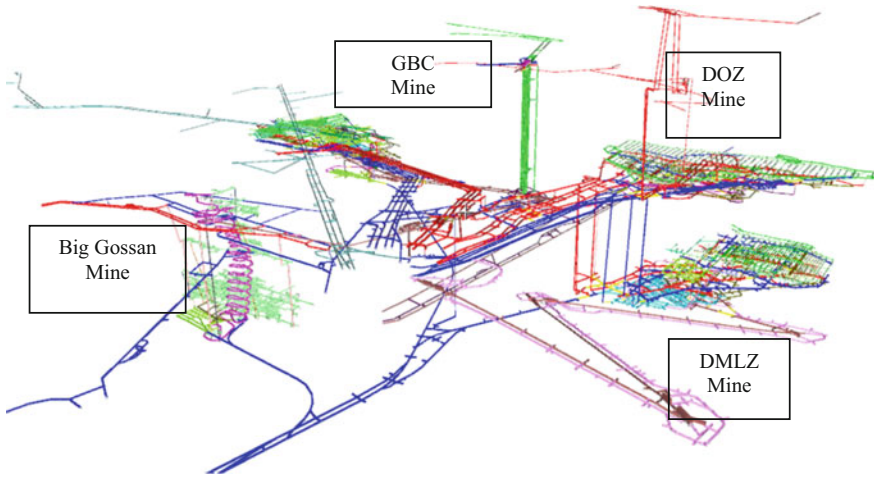


**Fig. 2.** Underground Operations at PT Freeport Indonesia

## 3  Design Criteria

### 3.1  General Design Requirements

PTFI's general refuge chamber design requirements are based upon standards set by the Government of Indonesia [2], supplemented by guidelines from Western Australia [3], refuge chamber equipment vendors [4], and consulting engineers [5]. A summary of PTFI's refuge chamber design requirement is provided in Table 1.

**Table 1.**  Summary of PTFI general refuge chamber design criteria

| |
|---|
| *Spacing* |
| Intervals not to exceed distance achievable with the normal underground occupant's self-rescuer duration |
| *Capacity* |
| Large enough to accept the normal number of people expected to be working within walking distance plus an additional factor for people such as visitors, management, engineers, and other non-regular visitors to the area |
| *Location restrictions* |
| Safe distance away from hazards such as large transformers, fueling bays, parking areas, combustible materials, stopes/blasting areas, and flooding areas |

(*continued*)

**Table 1.**  (*continued*)

| |
|---|
| *Physical size requirement* |
| Government of Indonesia requirement of 2 m$^3$ (volumetric) and 0.6 m$^2$ (floor area) per person, but for fixed refuge vendor requirement of 1.5 m$^2$ per person is used to account for machinery floor space requirements |
| *Occupancy duration* |
| 36 h of self-contained continuous operation at rated capacity |
| *Life support systems* |
| Primary—compressed air 85 l/min/person |
| Secondary—medical oxygen 0.5 l/min/person for 36 h with appropriate CO/$CO_2$ scrubbing system |
| Tertiary—oxygen candles |
| *Air quality monitoring* |
| Digital and manual (gas tube) monitoring equipment for appropriate gasses ($O_2$, CO, $CO_2$) plus others as required |
| *Temperature control* |
| Air conditioning system capable of maintaining temperature below 32 °C WB and 65% RH for rated duration at rated capacity |
| *Sanitation* |
| Toilet facilities with provisions for privacy designed to accommodate rated capacity for rated duration |
| *Drainage* |
| Trapped waste water drainage |
| *Lighting* |
| Lighting provided for rated duration |
| *Communications* |
| Telephone and two-way radio |
| *Others* |
| Provisions for first aid and psychological needs |

While PTFI's general refuge chamber design criteria is quite typical of a modern underground mining operation, the size and complexity of PTFI's refuge chambers require additional considerations discussed in the following sections.

## 3.2    Mass Ingress Requirements

Maintaining an adequate positive pressure is key to preventing the entry of contaminants to the refuge chamber from the mine atmosphere. This is generally achievable with most portable, custom built, steel fabricated refuge chambers; however, in large permanent rooms that becomes more difficult. The larger the occupancy, the more difficult meeting that constant overpressure becomes. This is due to the emergency ingress period where large numbers of occupants begin to enter the room. A large volume can be pressurized, however once the door is opened and the occupants begin to enter, the aperture of the leak point is large enough and open long enough for the

pressure in the room to equalize and allow contaminants to enter the occupied refuge space. For these purposes, an air lock is required, as well as the ability purge or to chemically remove contaminants that may pass the air lock if it is not used correctly. Unfortunately, with a large occupancy comes a long entry time. For example, a refuge chamber for 600 persons, assuming orderly and proper use of an air locked entry system, could take 30 min to accept its rated capacity. Since these persons may be arriving at the location having already utilized their self-rescue device, this would not be acceptable.

The proposed solution for this problem was to develop a high flow air lock system using air curtains. This solution still requires doors, however the entry process is to open the first door, automatically start the air curtain system and continue through to the second door to enter the refuge chamber. From there until the end of the occupant ingress, the doors will remain open and only finally closed at the end of the refuge entry process. It was shown in application that the use of an air curtain on entry into a refuge chamber would provide sufficient protection against breathing contaminant ingress. With the size of large refuge chambers, any entrained smoke on entry will not contaminate the chamber to a point where chemical scrubbing is required. This solution has been successfully installed and demonstrated on a 250 person refuge chamber at PTFI and is currently being installed on a 300, 360, and 500 person refuge chamber at PTFI (Fig. 3).



**Fig. 3.** Air curtain installation arrangement in a 250-person refuge chamber at the GBC mine

### 3.3 Multi-level Requirements

For the largest currently planned refuge chamber at PTFI (600 persons), the option of using a two-story refuge chamber design to reduce overall area footprint is being planned. For this to be effective, the second floor will need to be constructed in a way that allows for the entire space to behave like a single volume of air. This dictates that the second floor be constructed using an open flooring material such as expanded metal

grating. The requirement to scrub and cool the air over the complete volume of this large chamber is considered complex enough to require computational fluid dynamics (CFD) analysis in order to aid the equipment placement designs.

The primary flow componentry of the CFD model were 9 scrubbing systems ($\sim$4.6 m$^3$/min), 9 $\times$ 8 kW air conditioning units ($\sim$800 Lpm), and outlet flow via 4 check valve exits overpressured to $\sim$200 Pascals. Due to the excessive size of the CFD model, the system is only calculated over the first minute of scrubbing to give indicative flow paths as well as to identify dead air spaces (Figs. 4 and 5).
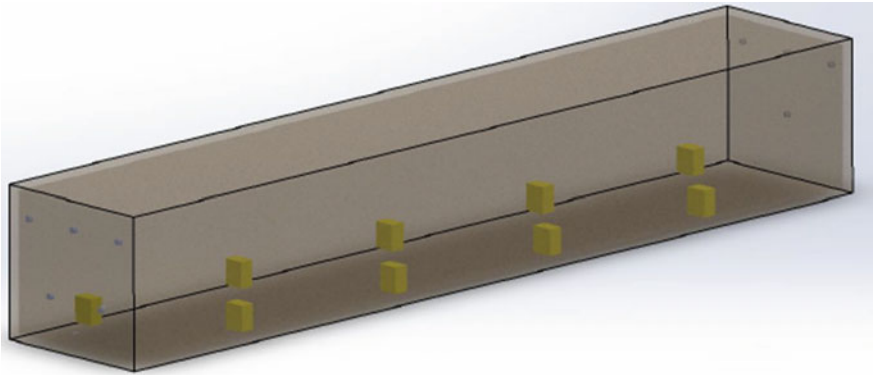


**Fig. 4.** Initial configuration of CFD model for a multi-level refuge chamber
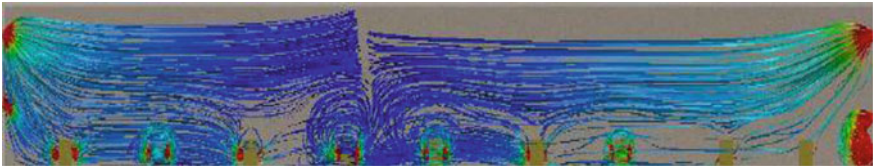


**Fig. 5.** Flow trajectories (Y plane) from CFD modeling for a multi-level refuge chamber

Flow results from the CFD model show that the system will mix correctly, however the center of the second level will likely require some small mixing fans be installed to ensure complete air circulation.

### 3.4 Multi-purpose Requirements

Some of the large refuge chambers at PTFI serve dual purposes as everyday lunchroom and office locations. In this configuration, it is important to consider several additional factors such as how to secure refuge chamber emergency medical, food and water supplies from casual usage as well as how to ensure life support systems are not damaged. At PTFI, emergency medical, food, and water supplies are kept either within

a locked room or locked cabinets which can be unlocked by using a key within a breakable key box. Life support equipment is protected from unintentional damage by using specially designed waterproof covers that protect the equipment when not being used. Additionally, multi-purpose refuge chambers are fitted with a filtered HVAC system to provide ventilation during non-refuge chamber operations. All components of the HVAC system are contained within the refuge chamber so that they can be isolated from the outside atmosphere by simply closing the refuge chamber doors. A centralized disconnect button is installed to de-energize the HVAC system when used as a refuge chamber. The multipurpose concept has been executed on a 250-person refuge chamber at PTFI and is currently under construction in a 300 and 500-person refuge chamber at PTFI (Figs. 6, 7 and 8).



**Fig. 6.** Dual-purpose 250-person lunchroom/refuge chamber at the GBC mine



**Fig. 7.** Protective covers for life support equipment in a 250-person dual purpose lunch room/refuge chamber

**Fig. 8.** Emergency food and drinking water storage room in a dual-purpose lunchroom/refuge chamber

## 3.5 Sanitary Requirements

Lastly, the issue of toilet sanitation is very important when it comes to a large refuge chamber. It is important that an appropriate number of chemical or other type of self-contained toilets are available to accommodate the rated capacity for the rated duration of the refuge chamber. At PTFI, chemical toilets are used for this purpose. For dual purpose refuge chambers, these chemical toilets are kept locked during normal operations and every-day toilets are provided outside of the refuge chamber space. Chemical toilets are a part of all currently installed and under construction refuge chambers at PTFI (Fig. 9).



**Fig. 9.** Chemical toilets in a 300-person refuge chamber at PTFI's DMLZ mine

## 4 Refuge Installation

Large fixed refuge chambers at PTFI are typically installed in a location with multiple accesses to allow for multiple points of ingress during an emergency. Prior to refuge chamber construction, the ground condition is evaluated and appropriate permanent ground support is installed. Next, the construction of concrete floors and concrete block door bulkheads follow. After the basic refuge chamber structure is complete, electrical cabling and installation of the refuge chamber equipment follows and is completed with the vendor onsite for the commissioning process. At PTFI, this construction work is handled internally by Central Services Construction or the mine's Underground Construction team (Figs. 10 and 11).
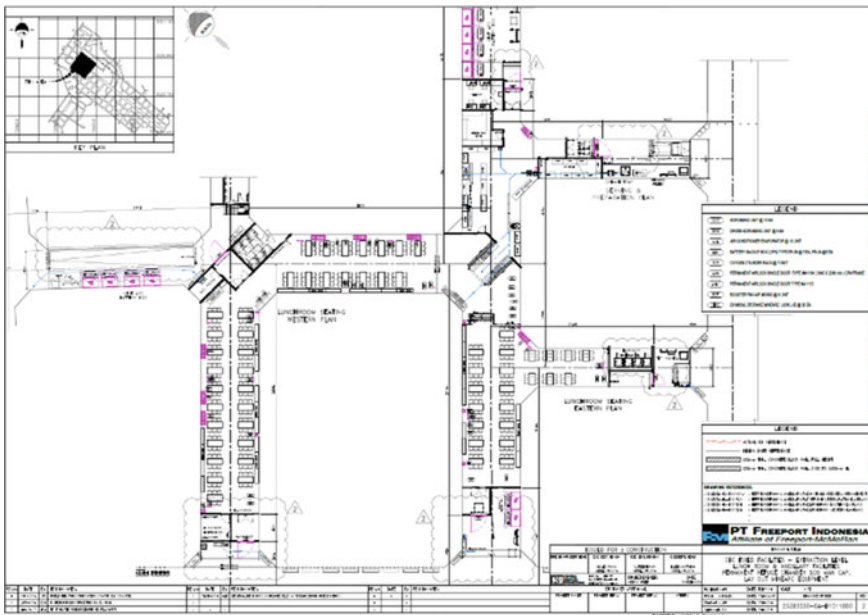


**Fig. 10.** Layout drawing for a 500-person dual-purpose lunchroom/refuge chamber in the GBC mine

## 5 Conclusions

To date, following the design criteria discussed in this paper, PTFI have installed a 250 and 300-person fixed refuge chamber. As of May 2018, ongoing construction activities on a 300, a 360, and a 500-person refuge chamber were underway. Additionally, in the design stage are a 70-person refuge chamber, a 175-person refuge chamber, a 300-person refuge chamber, and a 600-person refuge chamber. Large fixed refuge chambers are an integral part of PTFI's underground fire risk control and response management and plan can be successfully designed and installed in similar mining operations (Fig. 12).

**Fig. 11.** Bulkhead under construction at a 500-person dual-purpose lunchroom/refuge in the GBC mine



**Fig. 12.** 300 person refuge chamber in the DMLZ mine

# References

1. McPherson, M.: Subsurface Ventilation Engineering, 2nd edn. Mine Ventilation Services, Inc., Fresno, California, USA (2009)
2. Indonesian Minster of Mines and Energy: Decree of the Minister of Mines and Energy Number 555.K/26/M.PE.1995 on General Mining Occupational Safety and Health (1995)
3. Department of Mines and Petroleum: Refuge Chambers in Underground Mines—Guideline. Department of Mines and Petroleum, Western Australia, Australia (2013)
4. Minearc Systems PTY, Ltd.: Internal reports for PT Freeport Indonesia. Tembagapura, Papua, Indonesia
5. Brake Ph.D., D.: Internal reports for PT Freeport Indonesia. Tembagapura, Papua, Indonesia

# Part XVI
## Ventilation Modeling

# Incorporating Ventilation Network Simulation into CFD Modeling to Analyze Airflow Distribution Around Longwall Panels

Aditya Juganda[(⊠)], Jürgen Brune, and Gregory Bogin Jr.

Colorado School of Mines, Golden, CO, USA
ajuganda@mines.edu

**Abstract.** Understanding the airflow patterns in and around the longwall panel can help to identify poorly ventilated areas that may be prone to methane accumulation. Ventilation network modeling provides quick simulation time, and flexibility in adjusting airway parameters and ventilation controls. Such modeling is effective for analyzing linear ventilation networks in underground mines but not suitable for modeling flows in caved areas of hard rock mines or longwall gobs. The use of Computational Fluid Dynamics (CFD) enables a more detailed investigation of the interaction between the airflows in these caved areas but requires much longer computational times. Airway friction factors and ventilation controls are simple to implement in a network model but can be difficult to model and adjust in CFD. This paper will focus on using mine ventilation network simulation to identify and analyze key parameters that are affecting airflow distribution in and around the longwall panels, which then can be used to inform a more detailed analysis obtained with CFD modeling.

**Keywords:** Longwall mine · Ventilation · Network modeling
CFD modeling

## 1 Introduction

In longwall coal mine ventilation systems common in the U.S., the main purpose of bleeder ventilation is to dilute methane gas and prevent the formation of explosive gas mixtures in the caved, poorly ventilated gob areas and adjacent mine workings. In longwall operation, these critical areas include the development headings in by the longwall face, and the gob. Methane-air explosions in these areas may be ignited by spontaneous combustion, rock-on-rock friction and other sources. Although rare, ignitions due to rock-on-rock friction caused by roof falls caving into the longwall gob are possible and were suspected in the Willow Creek mine explosions in 1998 [1] and 2000 [2]. Rock-on-rock frictional ignitions are difficult to prevent, as they occur in inaccessible areas. Therefore, rendering the gob area inert is essential to prevent the formation of explosive mixtures. Research by Gilmore et al. [3] and Brune et al. [4] has shown that gob inertization can be a difficult or impossible when using bleeder systems, since the flow of gases through the gob depends on the gob permeability and the amount of fresh air leaking from the face and the immediate roof caving conditions

cannot be controlled by the mine operator. Having the ability to predict the location where explosive gas zones (EGZs) form inside the gob will be helpful for designing the best ventilation setup to minimize explosion and fire risks.

The use of Computational Fluid Dynamics (CFD) modeling enables detailed investigation of the interaction between the airflows in the longwall face and gob areas. However, CFD analysis requires significantly longer computational times. Modelers must determine a variety of modeling parameters values used to specify boundary conditions that are not readily comparable with the data obtained from mine ventilation field study, such as airway friction factors and leakages through ventilation controls. Linear ventilation network simulation models provide faster simulation times and adjustment to the airway parameters and utilize units commonly used in mining industry, such as Atkinson's friction factor. Yet, linear models are limited to solving one-dimensional flow problems. This paper will focus on incorporating ventilation network software into CFD modeling of the longwall ventilation system and compare the two modeling techniques side-by-side.

## 2   Linear Ventilation Network Modeling

Ventilation engineers commonly use network simulation as a predictive tool for planning and monitoring. Ventilation models predict air quantities, pressure drops, regulator settings, temperatures and contaminant levels throughout the mine. Programs are also frequently used to estimate refrigeration needs. Air qualities and gas concentrations can be easily tracked in open entries but linear network tools are rarely used to determine air flow through caved areas such as longwall gobs or hard rock caving operations.

The ability to incorporate actual fan performance curves, easy adjustment of airways parameters, regulators, stoppings and other ventilation controls and relatively short simulation times (a few seconds for steady state simulation) make network modeling practical to be used by mine engineers on a daily basis. Airway friction factors representing wall roughness and obstructions can vary significantly for each airway. McElroy [5], Kingery [6], Kharkar et al. [7], Prosser and Wallace [8] have conducted experimental studies to measure friction factors values typically found in underground mine airways. While these values can be used as an early estimation for planning purposes, site specific parameters may need to be adjusted based on ventilation surveys. Using the correct friction factors is crucial for ventilation modeling. Ventilation network models typically allow the use of pressure-quantity survey data as input values to represent realistic mine conditions and the resulting equivalent resistances should have better accuracy compared to the estimated resistance based on friction factor input. Most current network modeling software packages also have a built-in database for typical ventilation control parameters, such as resistances for doors, seal, and stoppings.

Most linear network models do not automatically include the effect of shock losses when an airway changes direction in the simulation. Equivalent shock loss values must be estimated and entered manually into the model to provide correct results. For example, if a given airflow splits into two airways of identical resistance, one

continuing straight and the other branching off 90°, the quantity is split into two equal amounts following Kirchoff's first law and the momentum of the airflow "wanting" to continue straight is typically ignored unless corrections are made to properly account for shock losses.

In this study, the software package VentSim Visual v. 4.8 [9] by Chasm Consulting was used. Use of this software does not imply endorsement by the authors, Colorado School of Mines or the research sponsor, CDC NIOSH.

## 3   Computational Fluid Dynamic Modeling

CFD models allow detailed modeling of airflow distribution and gas mixing in three-dimensional spaces. The models can simulate the flow distribution inside individual mine drifts, including the longwall face area. CFD can also be used to model flow through caved areas and permeable rock strata. CFD models are built by discretizing the flow space into small segments for which the computer will iteratively solve the 3-D Navier-Stokes equations, turbulent flow, gas mixing, heat transfer, and, if desired, chemical reactions.

CFD models allow for great detail in modeling flow geometry but generally do not have the same flexibility as linear network models in terms of adjusting airways and ventilation control parameters, such as regulators, ventilation curtains, and stoppings. In a linear network model, one Atkinson friction factor along with the cross sectional area and length is used to represent friction losses for each airway. CFD software requires much more detailed representation of surface roughness, cross sectional opening and obstacle shapes. Thus, it is not easy to directly apply the quantity and pressure loss data obtained from a mine ventilation survey in a CFD analysis. CFD models must capture mesh-size detail of the airways to accurately represent the effects of wall roughness and any obstacles to accurately capture boundary layers effects and turbulent flow conditions which can impact the flow through the mine entries.

Modeling a regulator with a small opening area can also be problematic in CFD, considering the requirement to represent the geometry with a minimum number of mesh cells to resolve the flow across the regulator. Modeling a regulator as an opening that can be adjusted based on the required air quantity is not practical in CFD. Instead, a porous medium with adjustable viscous resistance is typically used to simulate the airflow through regulators.

A major constraint with CFD modeling is the computing power and time required to run the simulation. Depending on the number of cells used in the model, a large CFD model may require several days to achieve convergence. In comparison, an equivalent linear ventilation network model only takes seconds to run, however with possibly reduced accuracy due to the lower fidelity of the model.

## 4    Longwall Bleeder Modeling

### 4.1    CFD Model

A CFD model for a bleeder-ventilated longwall gob was developed using the ANSYS®, Inc., Fluent® v. 16 software [10]. Use of this software does not imply endorsement by the authors, Colorado School of Mines or the research sponsor, CDC NIOSH.

The modeled longwall panel is 1000 m long and 300 m wide, and the coal seam is 2.2 m high. The coal chain pillar dimensions are 60 m long by 18 m wide. The gateroad dimensions are 6 m by 2.2 m, consisting of two headgate entries, a belt entry and two tailgate entries. Figure 1 shows a plan and cross-section view of the longwall model geometry.
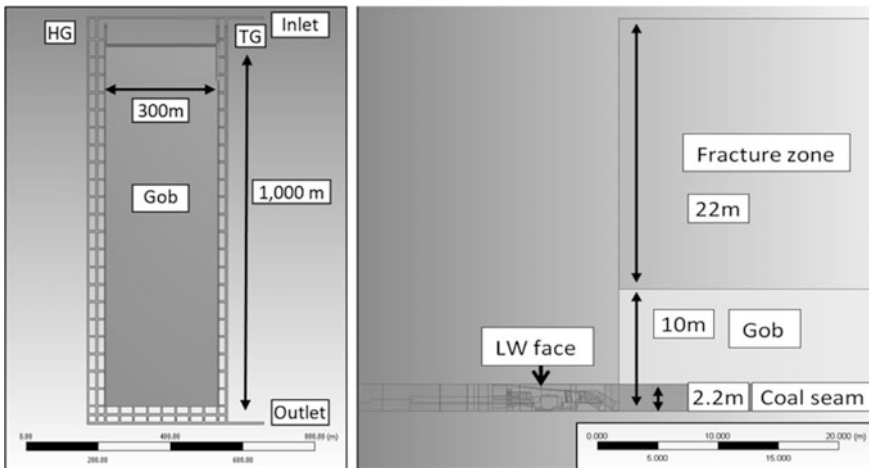


**Fig. 1.** Plan (left) and cross-section view (right) of CFD longwall model. HG = headgate and TG = tailgate

The gob and fracture zone heights are 10 and 22 m, respectively. It is assumed that the immediate roof behind the shields has fully caved. The face includes the operational components typically found in a longwall, such as a shearer, stage loader, face conveyor, shield supports, face curtain, gob plate and the headgate and tailgate drives. For this study, a wall roughness constant of 1 was used to represent a non-uniform, rough wall condition, while roughness heights of 0.3 and 0.4 m were chosen to represent the wall roughness conditions for the bleeder entries on the headgate and tailgate sides, respectively.

The longwall face is supported by 176 hydraulic shields. Each shield is 7 m long, 1.75 m wide and 2.2 m high. On the back of each shield, there is a 0.28 m$^2$ opening that allows air exchange between the face and the gob. On the headgate side, a ventilation curtain extends from the rib of the chain pillar to shield No. 6 to reduce face air

leakage into the gob. The shearer was assumed to be cutting the tailgate corner of the coal face. The shearer body is 1.1 m in height, with cutting drum diameters of 1.5 m and a cutting depth of 1 m. The model geometry of the longwall shields and shearer are shown in Fig. 2.
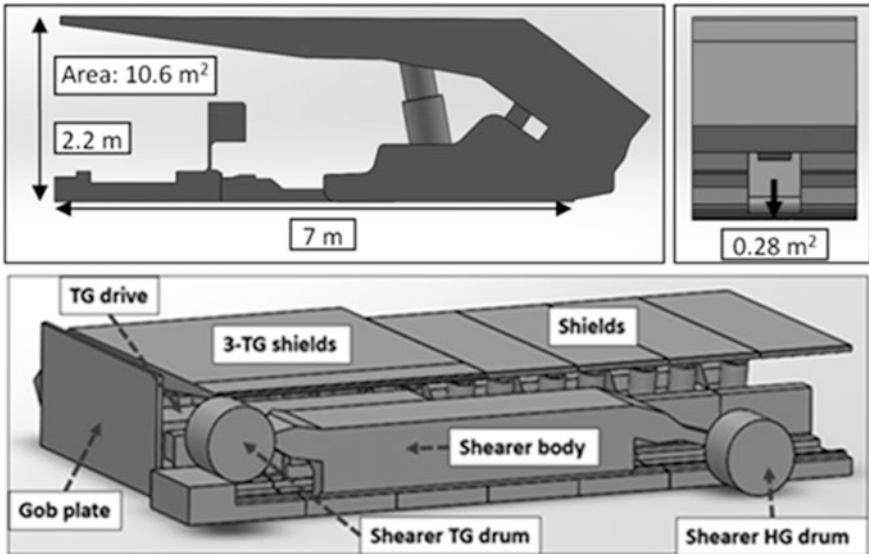


**Fig. 2.** Side and back view of shield model (top) and simplified shearer model (bottom)

Figure 3 show the ventilation setup for the CFD longwall model. For face ventilation, 52 $m^3$/s of fresh air is delivered from the two headgate entries; 14 $m^3$/s is assumed to leak through the headgate curtains and 4.7 $m^3$/s of air is returned through the belt entry, resulting in 33 $m^3$/s of air delivered to the longwall face. The two tailgate entries are set as intakes that supply 4.7 $m^3$/s of fresh air from each entry.

On the back of the panel, 4.7 $m^3$/s were allowed to pass through regulator R4 (see Fig. 3). Regulator R5 is adjusted as a part of this study, while regulator R6 was fully open.

The gob characteristics used in this study were based on a geotechnical model developed by Marts et al. [11] and validated with subsidence data observed in the field. Gob porosity ranged from 14% in the gob center to 40% around the gob edge, while gob permeability ranged from $2 \times 10^{-8}$ $m^2$ in the gob center to $7 \times 10^{-7}$ $m^2$ around the edge. In FLUENT, porous media permeability is assigned as flow resistance, which is the inverse value of permeability. Figure 4 shows the gob resistance and porosity distribution for the CFD model based on Marts' model.

In this study, it is assumed that a rider seam above the mined coalbed supplies methane from an infinitely large reservoir above the fracture zone in an evenly distributed manner. The methane flow was set up to produce a methane concentration of 1.97% $CH_4$ by volume at the outlet, shown in Fig. 3.
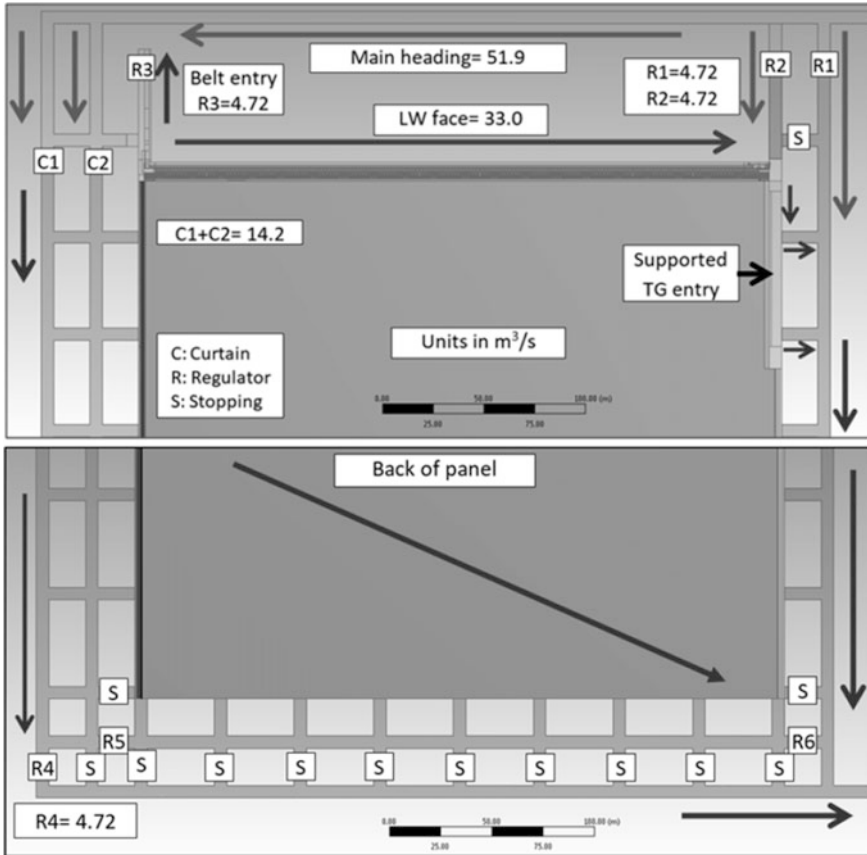
**Fig. 3.** Ventilation network air quantity in a bleeder-ventilated gob

## 4.2   Linear Ventilation Network Model

The ventilation network model was built using VentSim Visual$^{TM}$ v. 4.8 software [9] by Chasm Consulting. The model parameters, such as the panel and airway geometry, follow the same dimensions used in the CFD model and shown in Figs. 1 and 3. The longwall face is modeled as a series of 10-m-long airway segments with cross sectional areas of 10.6 m$^2$. The last airway segment in the tailgate corner has a reduced cross section of 6.6 m$^2$ to represent the obstructions by shearer and gob plate. At the junctions between face segments, there are 0.5-m-long airways with 0.28 m$^2$ opening that allow air exchange between face and gob. For the airway friction factor, 0.020 and 0.023 kg/m$^3$ were used for the bleeder entries on the headgate and tailgate side, respectively. These values represent the equivalent wall roughness heights of 0.3 and 0.4 m used in the CFD model. Figure 5 shows a plan view of the network model.

The longwall gob is modeled as a mesh of three layers of 10-m-long airways interconnected in both the horizontal and vertical directions. Each individual airway branch represents a 10-m-wide and 3-m-high gob zone equivalent to the CFD model.
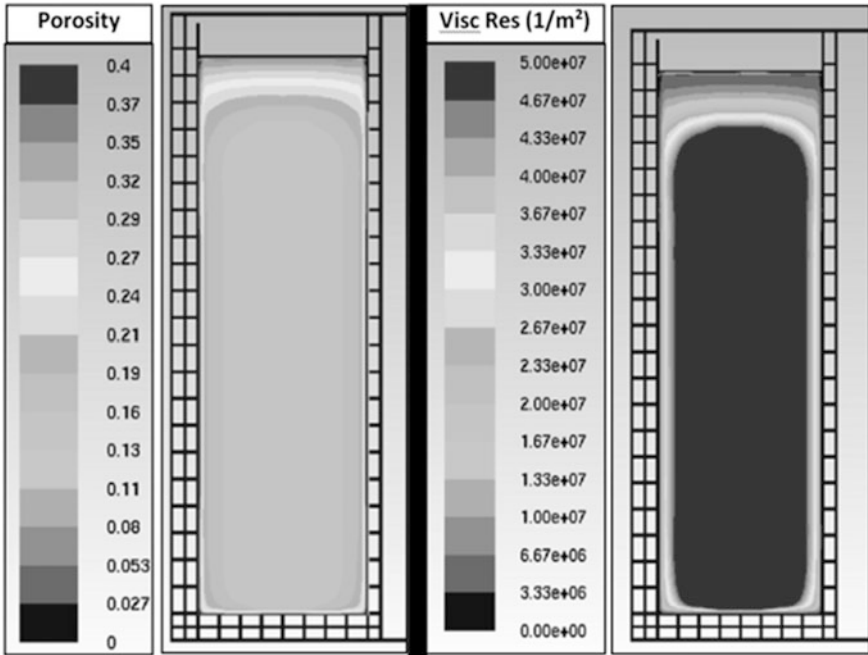
**Fig. 4.** Base case gob porosity and viscous resistance

The gob is further divided into three zones to represent the change in gob permeability; zones A, B and C, as shown in Fig. 5. Air pressures and flow quantities are assigned to each branch based on values obtained from the CFD model.

Figure 6 represents a cross section through the VentSim model showing the three layers of airways. The methane source is represented as a series of branches injecting from the top of the gob. Figure 7 also shows methane injection branches feeding gas from a single source directly into the third gob layer that represents the fracture zone.

### 4.3 Comparison of Longwall Face Leakage

A key parameter for the comparison and validation of the two ventilation models is the leakage flow from the face into the gob. The results of the simulations for airflow distribution across the face are shown in Fig. 7.

The simulation results for the airflow distribution across the face using the CFD and network model show similar trends and magnitudes, indicating that 11–12 m$^3$/s or about 1/3 of the face airflow will leak into the gob over the length of the face. Both models indicate major air leakage close to the headgate corner. Figure 8 (left) shows the flow pathlines for this leakage in the CFD model, while Fig. 8 (right) shows the equivalent leakages in the VentSim model, with the arrows representing the airflow direction.

The formation and permeability characteristics of the gob govern the leakage occurring in this area. Fresh air leaks through the high permeability area along the
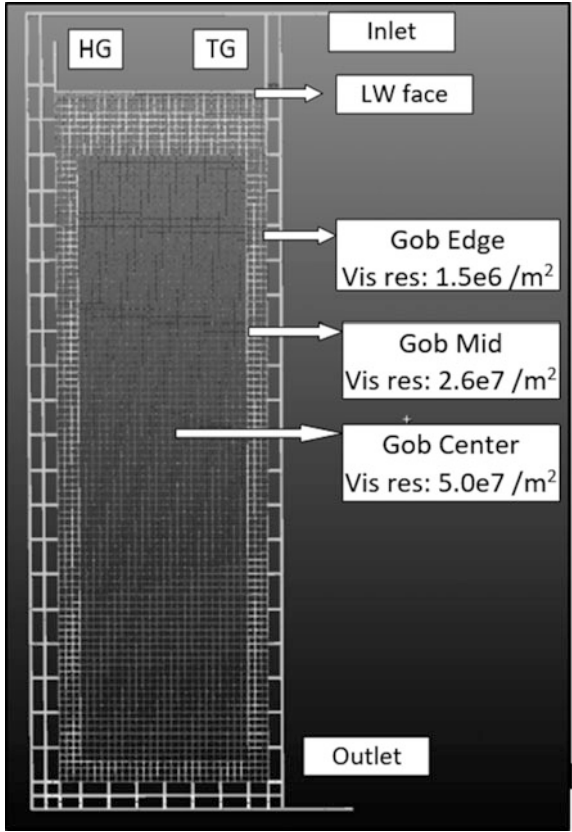
**Fig. 5.** Plan view of VentSim longwall model
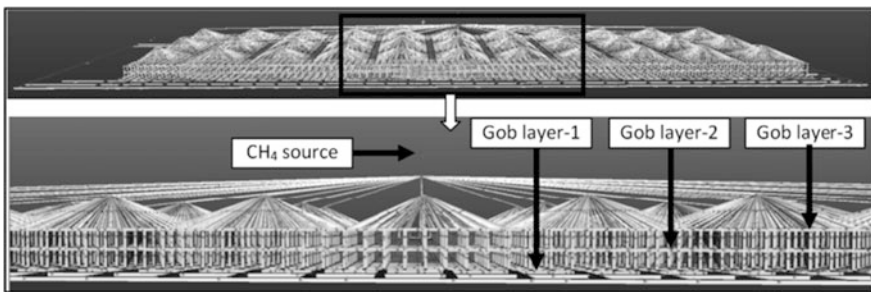


**Fig. 6.** Cross-section view of VentSim model

gob's headgate side, enters back into the headgate entry and then mixes with the fresh air that leaked though the headgate curtain. The remainder of supplied fresh air continues to flow towards the tailgate corner. Gangrade [12] observed similar leakage flow patterns in a 1:30 scale physical model of a longwall section. The CFD model
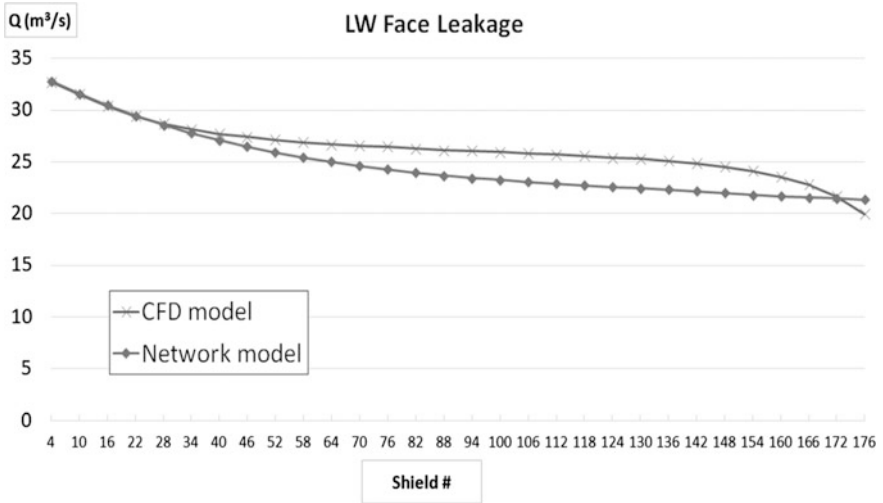
**Fig. 7.** Comparison of longwall face airflow leakage rate
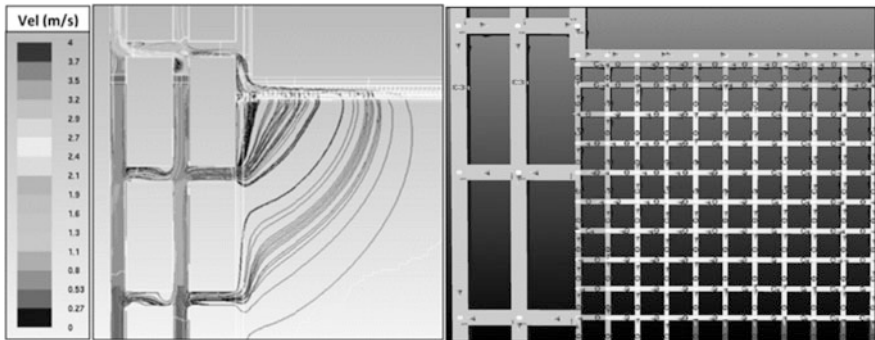


**Fig. 8.** Comparison of headgate corner leakage in CFD (left) and network (right) model

captures the effect of the shearer and gob plate obstructions near the tailgate. These obstructions cause increased leakage from the face to the gob over the last 30 shields towards the tailgate, as shown in Fig. 9 (left). The linear network model shows similar results as the CFD model, shown in Fig. 9 (right).

## 5 Methane Distribution Inside Gob

Researchers have developed a coding and coloring scheme to document the extent of explosive gas zones (EGZs) inside longwall gobs, based on the molar concentrations of methane and oxygen evaluated in Coward's Triangle shown in Fig. 10 [3]. The EGZs are shown for a horizontal plane 1.5 m above the mine floor.
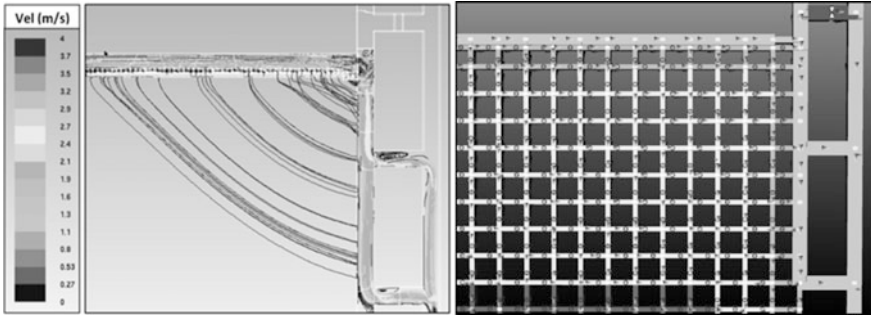
**Fig. 9.** Comparison of tailgate corner leakage in CFD (left) and network (right) model
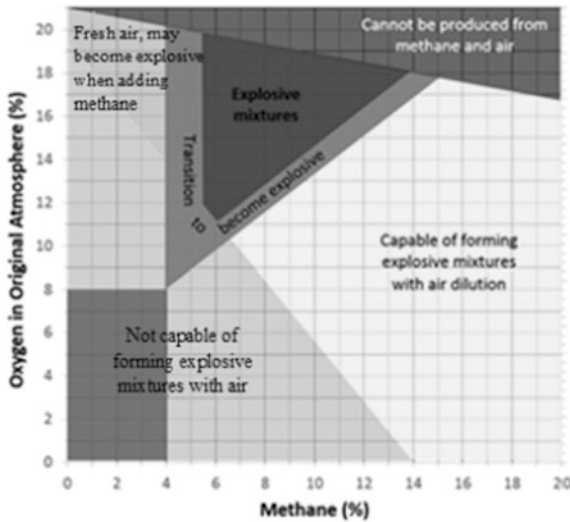


**Fig. 10.** Explosibility diagram of methane and air mixtures [3]

Two back regulator setups were tested in this study. Regulator locations are marked in Fig. 3.

- Case 1 represents the condition when R5 is blocked off, R4 is restricted and R6 is fully open
- Case 2 represents the condition when R5 is fully opened, keeping R4 at 4.7 m³/s and R6 wide open.

The results of the simulations show EGZs forming inside the gob. Case 1 is shown in Fig. 11 while Fig. 12 displays Case 2. The linear network model, using VentSim, shows a stunning similarity with the CFD solution when the effects of gravity have been turned off. This comparison is shown in Figs. 11 and 12 in the left versus the center image.
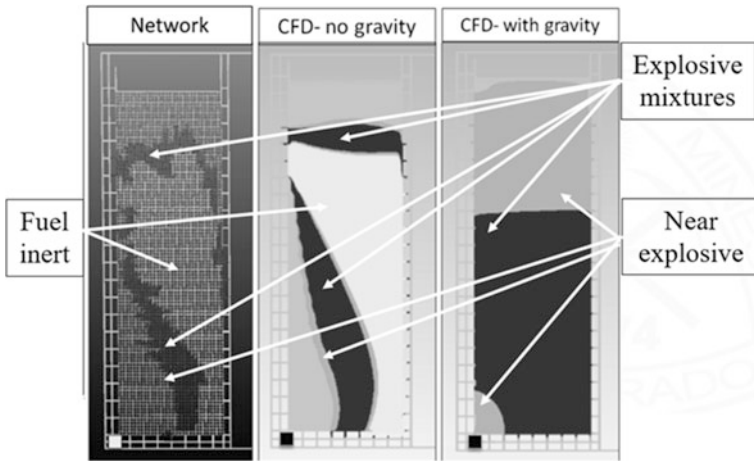
**Fig. 11.** Comparison of EGZ formation inside gob—back regulator completely closed
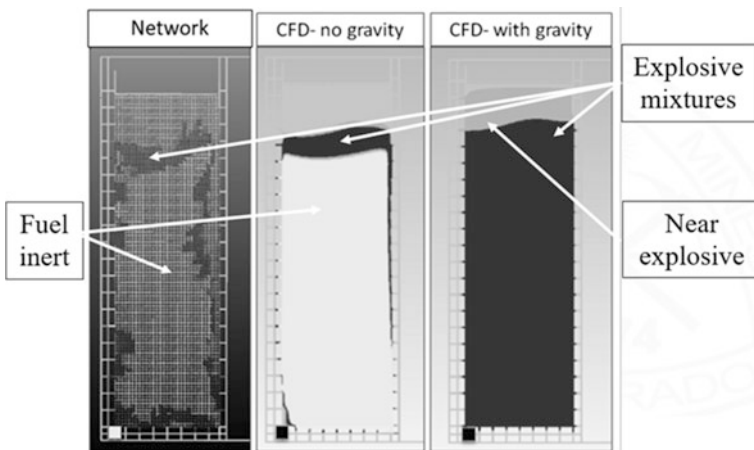


**Fig. 12.** Comparison of EGZ formation inside gob—back regulator completely opened

The VentSim model has limitations in its degree of discretization especially in the vertical dimension where only three layers of model branches were considered. As a result, the VentSim network model fails to fully capture the methane layering and buoyancy effects inside the gob and thus overpredicts the methane concentration inside the gob at the working section elevation, 1.5 m above the mine floor. The CFD images with gravity effects turned on show different, more realistic scenarios (see the right images in Figs. 11 and 12). Due to its buoyancy, more methane will remain in the upper regions of the rubble zone of the gob. This causes large areas of the gob to transition from fuel-rich inert to explosive. The methane-air mixture is near the explosive range in the gob area directly behind the face.

Comparing Cases 1 and 2 shows the impact of regulator settings at the back end of the panel; both models show that the regulators will significantly impact EGZ formation. Closing R5 (Case 1) forces air from the headgate entries to sweep the back end of the longwall panel and move the EGZ towards the center of the gob, as shown in Fig. 11.

Opening R5 (Case 2) creates a leakage path for the air from headgate entry to reach the bleeder fan. It should be noted that this is a common practice in the U.S. mining industry where headgate air is used to dilute methane or "sweeten" the air quality recorded at the bleeder evaluation point, usually Regulator R6 (Fig. 3). Regulation 30 CFR §75.323(e) limits the allowable methane concentration at this point to 2%.

As a result, most of the air from the headgate entry flows through R5, bypassing the gob, while only a smaller percentage of headgate air sweeps the gob area. This will increase the overall methane concentration inside the gob. Methane may accumulate in the crosscuts connecting the headgate entries and the gob area, which is a potential explosion risk considering these crosscuts are prone to roof falls. Since these entries must be inspected weekly, this also presents a direct explosion and asphyxiation hazard to mine examiners.

Researchers note that the gob gas distributions, concentrations and EGZ formation may vary depending on the gob air flow characteristic, ventilation patterns, regulator setup, and the amount of methane flowing into the gob from remnant coal and coalbeds above or below the mined seam. The VentSim linear network model can be used to quickly capture and demonstrate the effects of changing regulators and ventilation patterns around the gob.

## 6   Physical Scaled Model

In a new NIOSH sponsored project, researchers at the Colorado School of Mines are designing a 1/40th scale model version of a longwall panel. The design will allow for flexibility to simulate various mine ventilation types. Furthermore, it will include moving parts such as the shearer, shields, and the gob following the advance of the face. The model will be used to study the airflow and gas mixing pattern in and around the gob and will have the capability to simulate methane gas explosion at various locations, such as at the coal face or inside the gob. The model will then contribute to validating work of previous developed longwall CFD models.

## 7   Conclusions

Linear ventilation network modeling has a wide range of applications in mine ventilation design. Researchers at the Colorado School of Mines have demonstrated ventilation models, such as VentSim Visual, also offer practical used to model airflow distributions in caved areas of a mine, in this case, a longwall gob. A VentSim model can incorporate the result of mine ventilation surveys into the model and can then be used to study important parameters affecting the ventilation in caved areas. Although the VentSim model does not have the level of detail required for simulating gas

distribution inside the gob, it has the capability to quickly analyze the airflow patterns and effects of changing ventilation controls in and around the longwall panel. Vent-Sim's flexibility and short simulation times make it suitable for preliminary studies to determine the effect of the ventilation control setup on the gas distribution inside the gob, before going into detail with CFD modeling.

# References

1. Elkins, D.W., Luzik, S.J., Lemon, J.O.D.: Report of investigation, underground coal mine fire, November 25, 1998. Willow Creek mine, Cyprus Plateau Mining Corporation, Helper, Carbon County, Utah, ID. No. 42–02113. U.S. Department of Labor, Mine Safety and Health Administration, Arlington, VA (2001)
2. McKinney, R., Crocco, W., Tortorea, J.S., Wirth, G.J., Weaver, C.A., Urosek, J.E., Beiter, D.A., Stephan, C.R.: Report of investigation, underground coal mine explosions, July 31–August 1, 2000. Willow Creek mine, MSHA ID No. 42–02113. Plateau Mining Corporation, Helper, Carbon County, Utah (2001)
3. Gilmore, R.C., Marts, J.A., Brune, J.F., Saki, S., Bogin Jr., G.E., Grubb, J.W.: Impact of regulator settings on the formation of explosive gas zones in bleeder ventilated gobs. In: SME Annual Meeting and Exhibit. Pre-prints, Denver (2015)
4. Brune, J.F., Grubb, J.W., Bogin Jr., G.E., Marts, J.A., Gilmore, R.C., Saki, S.A.: Lessons learned from research about methane explosive gas zones in coal mine gobs. Int. J. Min. Mineral Eng. **7**(2), 155–169, 2016 (2015)
5. McElroy, G.E.: Engineering Factors in the Ventilation of Metal Mines. Bureau of Mines Bull. 385, 1935, 196 pp (1935)
6. Kingery, D.S.: Introduction to Mine Ventilating Principles and Practices. Bureau of Mines, Washington (1960)
7. Kharkar, R., Stefanko, R., Ramani, R.V.: Analysis of leakage and friction factors in coal mine ventilation systems. Special Research Report Number SR-99, Pennsylvania Department of Commerce (1974)
8. Prosser, B., Wallace, K.: Practical values of friction factors. In: Proceedings of the 8th US Mine Ventilation Symposium. University of Missouri, Rolla (2002)
9. Consulting, Chasm: Ventsim Visual User Guide. Ventsim Visual, Queensland (2017)
10. ANSYS: ANSYS FLUENT, 16.2 edn. SAS IP, Inc., Canonsburg, PA (2014)
11. Marts, J., Gilmore, R., Brune, J., Bogin, G., Grubb, J., and Saki, S.: Dynamic gob response and reservoir properties for active longwall coal mines. SME Min. Eng. J., 41–48 (Dec, 2014)
12. Gangarde, V., Harteis, S.P., Addis, J.D.: Development and applications of a scaled aerodynamic model for simulations of airflows in a longwall panel. In: Proceedings of the Sixteen North American Mine Ventilation Symposium. Golden, CO (2017)

# Numerical Modeling of Flow Phenomena in Mine Drift Using Laser Scan Results

Jakub Janus[✉] and Jerzy Krzwczyk

Strata Mechanics Research Institute of Polish Academy of Sciences, 30-059 Krakow, Poland
kjanus@interia.pl

**Abstract.** Currently CFD numerical simulations are an important part of the research on the airflow in mining drift. One of the first steps throughout the simulation process is to build a geometric model that will reflect the geometry in which the problem is being investigated. In the case of numerical calculations for underground mine workings, due to the very complicated shape of the mine drift, simplification of the geometric model is required. One of the most common simplifications is to set a constant geometry of the model over its entire length. This results in a significant workload reduction in the geometric modeling process as well as a shortening of the numerical calculation time. However, knowledge of the impact of such simplifications is needed to assess the accuracy of the results obtained. For this purpose, accurate data on the geometry of the mine pavement were obtained using a laser scanning technique that was used to analyze the variability of the area in particular cross-sections of the examined fragment of the gallery. Geometric models have been constructed with a precise reflection of the geometry of mine drift and geometry with a constant cross section assuming a standard shape of the arch-yielding supports. For all geometries the flow calculations were performed assuming the same boundary conditions. The results of the studies and analyzes show the influence of the introduced geometric simplifications in numerical model geometries on numerical simulation results.

**Keywords:** Laser scanning · TLS · CFD · Numerical model geometry

## 1 Introduction

Proper mine ventilation system operation is one of the necessary conditions for the safety and mine work efficiency. Ventilation systems are designed to provide state of the atmosphere that allows their normal use as well as to minimalize the effects of possible failures and disasters. This task needs to be executed at the expense of the smallest possible outlay. However, due to the enormous size of such ventilation systems and their complex structure, consisting often the hundreds kilometers of mine drifts, in this area there are many problems that have not been solved in a satisfactory manner, or may be better resolved. Therefore, it was necessary to use innovative tools for the purposes of cognitive occurring in this environment flow phenomena. Opportunities for development of this branch of science was given to be computer techniques

in the form of numerical simulations using the finite elements methods in solving the equations of fluid mechanics. While the development of flow simulation methods was mainly associated for technical applications, such as: aerodynamics, metrology, hydrology and urban planning, this method is more often use to imaging flow in the mine drifts. With help of this method, velocity vectors, development of velocity profile or schedule pressure and dynamic response as a result of changes in the geometry of the numerical model and the model of turbulence, can be shown in a graphical way.

Several comparisons of simulation and measurement data indicate, that for a given class of problems must be chosen optimal methodology for modeling (best practice). For many problems, there are sets of instructions regarding the whole process of modeling—building model geometry (best practice guidelines), build computational meshes, choice of turbulence models. But so far there was not developed a universal method of solving the numerical simulations for mine drift. The process of formulating appropriate recommendations to carry out numerical simulations in the mine environment, which guarantee god results compared to measured data is still expand.

In the process of carrying out numerical calculations, one of the most important stages it the pre-processing stage. First, the geometry of the calculation area should be designed, and then a numerical net covering this area should be generated. Subsequently, the type of boundary conditions for the calculation area should be determined, together with the physical parameters of the airflow.

As far as airflow problems in underground conditions are concerned, first obstacle preventing determination of proper guidelines for numerical simulations is creating a geometrical model that would correspond with the geometry of mine drift in a reliable way. The geometry of mine drift poses a lot of problems in the process of creating numerical models. With some standard measurement techniques at our disposal (a meter-stick, a laser rangefinder), it is really difficult to map such elements as: mine drifts intersections, floor uplifts, mine drifts convergence, deformation of arch-yielding supports, uneven placing of arch-yielding supports, presence of mining equipment, such as band conveyors, mining combines, stone-dust barriers, hydraulic installations, or pipelines.

Thus, at present, previous research of the airflow problems in underground conditions using the CFD methods, are carried out on geometries of the model of mine drifts, which are not accurate projection of the object in question, but it is rough representation. Results of such works cast doubt on the accuracy calculation results due to the "freedom" of building geometric models and the lack of any guidance to process of building these models.

Is necessary to make some simplifications during the mapping the geometry model. Such simplifications are often necessary if we want to obtain a clear image of the investigated phenomenon and shorten the duration of numerical calculations. Still, we need to know in what way such simplifications will influence the accuracy of the obtained calculation results. One of the conditions essential for obtaining this knowledge is getting detailed information about the geometry of the mine drift. Classic measurement methods require a huge investment of time and effort of many people, who frequently work in conditions that pose a threat to their health and lives. Therefore it is needed to search advanced measurement techniques that will be able to fulfill the needs of obtaining large amounts of information concerning the geometry of object

with high accuracy in difficult conditions, while reducing the maximum time consuming. One of such measurement techniques is Terrestrial Laser Scanning, which, due to the increasing availability of equipment and its prices, becomes one of the basic measurement technologies. Area of application the laser scanners are very wide, and with the spread of the measurement technology appear more and more new areas, in which it applies. In Poland, due to its recent implementation, this method is relatively unknown. However, conducting scientific work to enable the implementation of scanning applications in research and business, seems to be necessary to improve the competitiveness of the economy and modernization of methods and technologies used by it. One of the area in which scanning can be extremely useful measurement technique is mining. The implementation of laser scanning technology to underground mining made it possible to quickly obtain information about the geometry of the measured object for the purpose of cataloguing and geodesy, while maintaining the required accuracy [2–4]. However, this information has never been used for the constructing the numerical model of mine drifts! The accuracy of measurements results lead to the conclusion that the information needed for mapping the various types mine objects, which are complex in shape, and where measurements using conventional methods are extremely difficult and sometimes impossible, sufficiently can be obtained with help of laser scanning.

## 2   Measurements of the Mines Drift Geometry Using Terrestrial Laser Scanning

In measuring of the geometry of a gallery in mine drift, one of the commercially available 3D scanners was used, i.e. the FARO Focus 3D laser scanner. It is a most compact instrument, whose dimensions are mere $0.24 \times 0.20 \times 0.10$ m, and whose total weight is 5 kg. The range of the instrument is 0.6–120 m; the laser beam falls—at the angle of 90°—on the surface whose reflectance is 90%. The scanner is characterized by a high speed of the measurement—from 120,000 points per second to 976,000 points per second, depending on the scan resolution. The measurement error is $\pm0.002$ m. The visual field of the instrument is 360° in the horizontal plane and 305° in the vertical plane. The laser power is 20 mW, the wave length—905 nm, and the typical value of the beam divergence is 0.16 mrad. During measurements, all the data is recorded on an SD card, and therefore it can be transferred to a computer safely and easily.

Measurements of a 3D scanner were carried out in the ZG Sobieski mine, in the Grodzisko cross-cut gallery, level 300. As the measurement site, the neighborhood of a turn was chosen, which gave the researchers vast measurement possibilities [8].

Due to the complex structure of the mine drift (floor uplifts, clamps in the lining, the arch—yielding supports, a turn), it was necessary to choose proper sites for measurements performed with a 3D scanner. In order to map the geometry of the gallery in the best possible way, a double scanning site in the cross-section of the mine drift was established. One of the elements in the cross-sections were pipelines running underneath the roof. Performing measurements in one site only would result in emergence of the so-called dead spaces—areas in the shadow of the pipelines where laser has no

access. The scanning sites were placed at the left and the right sidewall, which made it possible to minimize the areas where no scanning was performed [9, 10]. Subsequently, the researchers had to determine the measurement cross-sections and place the proper number of markers, which link the scans from consecutive sites and place them in a chosen set of coordinates. In order to obtain a full spatial model of the mine drift, the whole section of the gallery was divided into 11 scanning cross-sections, which resulted in 22 measurement sites. First scanning cross-section was 23 m before turn, last scanning cross-section 56 m after turn (as illustrated in Fig. 1).
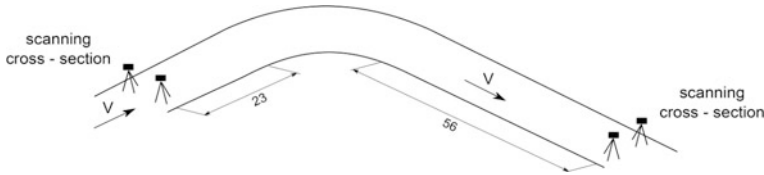


**Fig. 1.** Schematic layout of the scanning cross-sections

As a result of laser scanning in the Grodzisko cross-cut gallery, pre-processing of the obtained point cloud and reduction number of point [1], a very accurate, digital representation of the whole mine drift area consisting of 152 million points was obtained [5].

## 3 Measurements of Airflow in the Drift

One of the research methods of air flow distribution through the mine drifts cross-section is measuring the local air flow velocity by the sensors placed in this cross-section. The number of sensors used is a compromise between the required accuracy of determining the distribution and the least possible interference in the flow itself. The multi-spot flow velocity field measurement system (SWPPP), developed at the Strata Mechanic Research Institute of the Polish Academy of Sciences, was used to measure the volume flow of air in the mine drift [6]. In order to locate vane anemometer at selected cross-sectional point of the mine drift, it was necessary to use a suitable supporting structure consisting of four vertical beams and one or two horizontal stiffening beams are fixed. The anemometers are mounted on vertical beams, depending on the size of the cross-section, it is possible to adjust the number of sensors to the mine drift.

The main measurement tools used in the SWPPP system were 16 vane anemometers [7]. The basic metrological parameters of the air flow rate sensor are given below:

– measuring range: $\pm(0.2–20$ m/s),
– uncertainty: $\pm(0.5\%$ rdg $+ 0.02$ m/s),
– resolution: 0.01 m/s,
– sampling frequency 1 Hz.

Prior to the measurements, each of 16 anemometers used in SWPPP system was subjected to the calibration process in the wind tunnel of the Calibration Laboratory for Ventilation Measuring Instruments, accredited by the Polish Accreditation Center.

Measurements using the SWPPP system were carried out in the same place as geometry measurements. The mine drift cross-section near the turn was chosen as a place of measurement, giving great measurement possibilities. From the inflow side, the turn was preceded by a straight section of a mine drift, approximately 500 m long. The cross-section was 3 m before the turn inlet. Measured dimensions of the cross-section: 4.78 m wide and 3.25 m high. The arch-yielding supports were spaced apart by 1 m (Fig. 2).

## Measuring cross-section
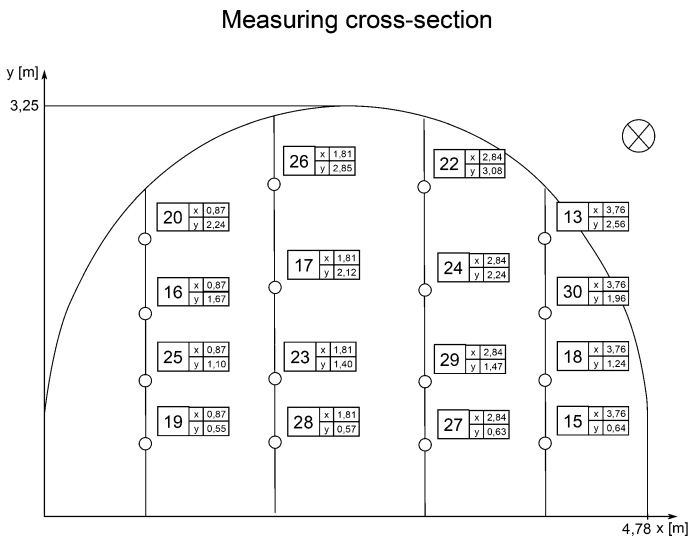


**Fig. 2.** The location of anemometers sensors on the measuring cross-section

Figure 3 presents the record of flow velocity and average velocity field calculated as a quotient of the estimated flow rate and cross-section area.

In the measurement cross-section, the highest velocity were recorded on sensors no. 23 and 29, placed approximately 1.43 m above the floor. The values indicated the sensor no. 15 are close to the average flow velocity, amounting to 1.49 m/s. Sensors no. 13, 20, 22 and 26 located under the roof, indicate significantly lower speed.

To make visualization of air flow in cross-section easier, it was decided to present the average measured air velocity in the form of iso-lines (Fig. 4). The iso-lines of velocity distribution were made with the gridding estimation, using the triangulation method together with the linear interpolation. Analyzing the visualization of the flow in the cross-section, an expanded profile of the airflow was observed. Obtaining such shaped velocity profile was possible through a 500 m straight section of a mine drift,
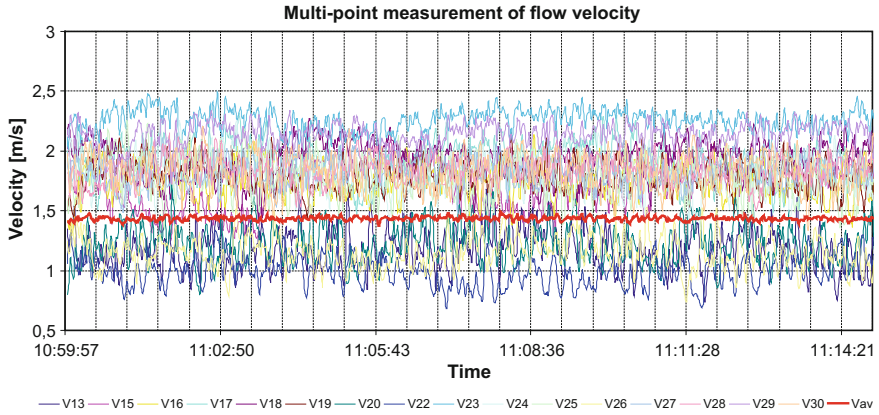
**Fig. 3.** Multi-point measurement of flow velocity
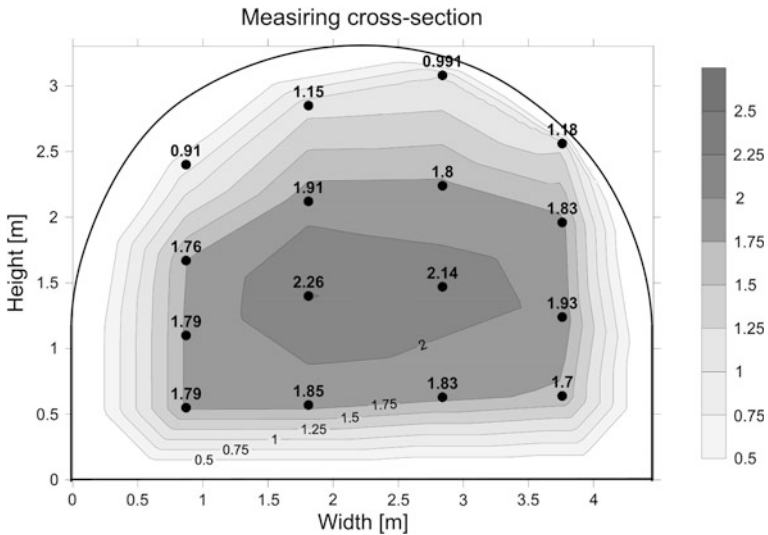


**Fig. 4.** Velocity iso-lines in the measurement cross-section

preceding the measurement cross-section. At the inlet to the mine drift section due to the intersection, the profile was disturbed, and only alone this straight section, due to the tangential forces originating from the fluid layers located in the immediate vicinity of arch-yielding supports, transferred to layers closer to the mine drift axis, the velocity profile was formed.

# 4    Numerical Calculations

## 4.1    Computational Geometry

Due to the size of the numerical model geometry obtained from laser scanning, the computational area was divided. For calculation purposes only the use of model fragments from inlet to half-turn was used. This area included a 35 m section of a straight pavement, and a part of the turn with a 35 m turning radius and 26° turning angle (Fig. 5). The initial section of the mine drift was straight axis, there were only changes in the cross-section. In the further part, the mine drift turned slightly to the left with 63 m radius, which then went through a sharper turn to the right with a 35 m radius.
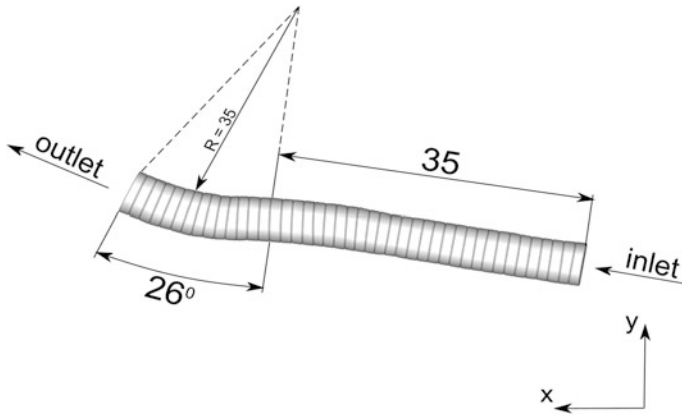


**Fig. 5.**  Dimensioning of the numerical model geometry

In order to investigate the sensitivity of numerical calculations to the accuracy of mapping the numerical model geometry, it was decided to design another computational geometry. The authors decided to create a geometrical model, containing simplifications that the use during the geometry construction, having data about the cross-sections area and the arc dimension of the arc-yielding support in which measurements of air flow velocity were made. In connection with this, the second geometric model had simplifications in the form of flat floor and the same shape of arch yielding support. The cross-section area corresponded to the cross-section area in the measuring cross-section and was 13.20 m$^2$. The presence of a pipeline and hydraulic hose was omitted. The shape of the turn has been preserved.

## 4.2    Numerical Mesh

Geometry of the calculated area and the unpredictable layout of flow distributions in the entire numerical model justified the imposition of a dense computing mesh. It was decided to use the size function mesh control, which allowed to control the size of a

mesh around a selected point, edge or surface. Numerical models have been digitized with the unstructured tetrahedral mesh, which then, due to the large size of model and selection of a dense computing mesh, was converted into a polyhedral mesh. The scanning model consisted of 13 mln tetrahedral cells, 2.8 mln polyhedral cells were obtained after conversion (Figs. 6 and 7). Simplified model consisted of 9 mln tetrahedral cells, 1.9 mln polyhedral cells were obtained after conversion.
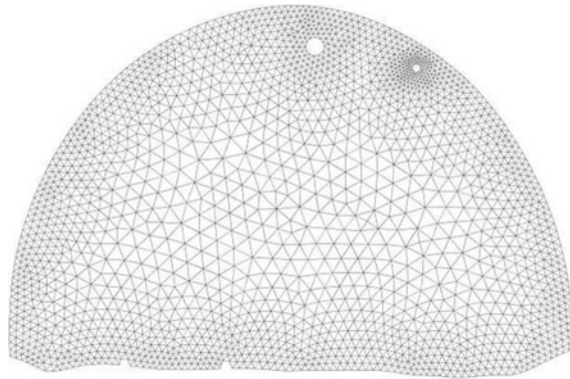


**Fig. 6.** Tetrahedral mesh at the measuring cross-section
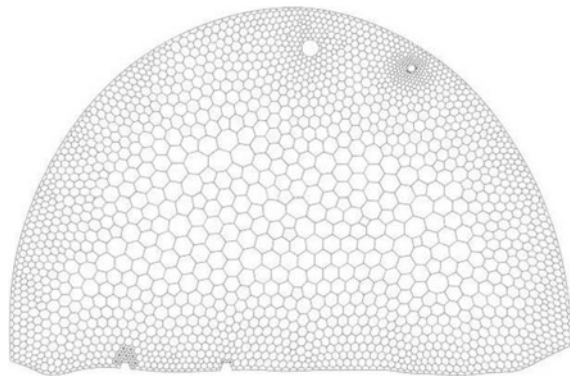


**Fig. 7.** Polyhedral mesh at the measuring cross-section

### 4.3  Boundary Conditions

Data from the SWPPP system allowed us to use them as a boundary condition at the inlet. In addition, the defined profile was compacted with points between the measured points, consisting o3 31 points. Velocity values at additional points were obtained using the triangulation method with linear interpolation. After importing the defined
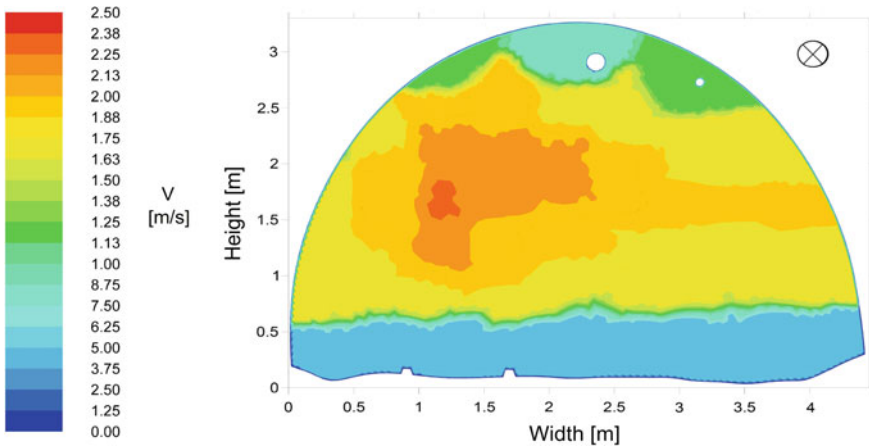
**Fig. 8.** Velocity profile from measurement data and additional points

profile from SWPPP system and additional points to the numerical program, using the zero-order interpolation process, the inlet profile was received (Fig. 8)

The remaining parameters at the inlet were defined as

- turbulence intensity 10.0%
- hydraulic diameter 3.54 m.

In all cases, the outlet has been defined as outflow, corresponding to the outflow model in which it does not define the velocity or pressure conditions. The floor, arches, rails and pipelines were defined as wall surfaces. Inequalities of the floor in the model were treated as roughness with a height of 0.05 m, and in the case of arches, rails and pipelines a roughness height of 0.001 m.

### 4.4    Calculation Results

Obtained results of air distributions numerical calculations in geometries with accurate mapping and simplified geometry, were presented in the form of a tabular comparison of registered flow velocities with calculated values (Table 1) and in the form of velocity contours. Measured values correspond to the average values of the air velocity calculated from entire period of SWPPP system registration in measurement cross-section. The calculated velocities correspond to the averaged values of air flow velocities from the moment where flow was stable.

Velocity contours obtained from the numerical calculations are made in the measuring cross-section of the geometry, located 32.0 m after the numerical model inlet. Contours were made in the same scale (Fig. 9).

In order to present a quantitative evaluation of the numerical simulations accuracy, it was decided to use the approximation error. The average approximation error for the entire measuring cross-section was calculated as a sum of the approximation errors in the individual measurement points divided by the number of measurement points.

**Table 1.** Comparison of measured flow velocities with numerical calculation values from different geometries

| Anemometer number | V (m/s) | | |
|---|---|---|---|
| | SWPPP | Accurate mapping geometry | Simplified geometry |
| 13 | 1.18 | 0.58 | 0.57 |
| 15 | 1.70 | 1.60 | 1.68 |
| 16 | 1.76 | 1.80 | 1.77 |
| 17 | 1.91 | 2.00 | 1.97 |
| 18 | 1.93 | 1.66 | 1.79 |
| 19 | 1.79 | 1.66 | 1.77 |
| 20 | 1.22 | 0.91 | 0.91 |
| 22 | 0.99 | 1.01 | 0.49 |
| 23 | 2.26 | 2.09 | 2.18 |
| 24 | 1.80 | 1.90 | 1.70 |
| 25 | 1.79 | 1.82 | 1.96 |
| 26 | 1.15 | 1.00 | 0.94 |
| 27 | 1.83 | 1.54 | 1.69 |
| 28 | 1.85 | 1.63 | 1.79 |
| 29 | 2.14 | 1.96 | 2.04 |
| 30 | 1.83 | 1.12 | 1.36 |

Compatibility of the measurement results with the calculation results for both geometries are at a similar level and amounts to about 88% (Table 3). Analyzing the results for individual measurement points, it can be seen that the highest consensus was obtained from points no. 13 and 30, located at the right side of the mine drift (Table 2).

**Table 2.** Approximation errors for all measuring points

| Anemometer number | δ (%) | |
|---|---|---|
| | Accurate mapping geometry | Simplified geometry |
| 13 | 50.51 | 51.33 |
| 15 | 6.19 | 1.27 |
| 16 | 2.43 | 0.41 |
| 17 | 4.72 | 2.92 |
| 18 | 14.03 | 7.10 |
| 19 | 7.45 | 1.38 |
| 20 | 0.00 | 0.05 |
| 22 | 1.60 | 50.27 |
| 23 | 7.43 | 3.71 |
| 24 | 5.39 | 5.75 |
| 25 | 1.75 | 9.14 |

**Table 2.**  (*continued*)

| Anemometer number | δ (%) | |
| --- | --- | --- |
| | Accurate mapping geometry | Simplified geometry |
| 26 | 12.98 | 18.55 |
| 27 | 15.74 | 7.52 |
| 28 | 11.89 | 2.97 |
| 29 | 8.34 | 4.68 |
| 30 | 38.96 | 25.65 |

**Table 3.**  Average approximation errors for different geometries

| $\delta_{av}$ (%) | |
| --- | --- |
| Accurate mapping geometry | Simplified geometry |
| 11.86 | 12.04 |



Accurate mapping geometry                    Simplified geometry
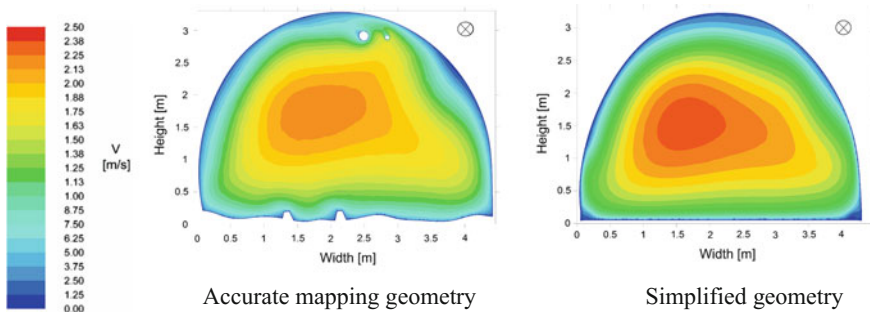
**Fig. 9.**  Velocity contours for different geometries

The comparison of the obtained results shows small influence of the introduced simplification on the numerical model geometry for obtained results. After simplifying the geometry, the accuracy of the obtained results decreased by 0.18%, which, with the accuracy of the vane anemometer, is negligible. The differences in the velocity profile shape are also small. Calculation results for simplified geometry show higher velocity in the central part of the cross-section, which is caused by the faster formation of boundary layer, which is caused by the same geometry of arch-yielding support.

## 5 Summary

The article presents an innovative way of using the results of laser scanning method to build the numerical models geometry. Terrestrial Laser Scanning allows fast acquisition of sufficiently precise information needed for mapping the various types mine objects, which are complex in shape, and where measurements using conventional methods are extremely difficult and sometimes impossible. Classic measurement methods require a huge investment of time and effort of many people, who frequently work in conditions that pose a threat to their health and lives.

Subsequently, the results of the numerical simulations variability for the simplifications on the numerical geometry were presented. Two geometrical models were designed, first accurate mapping geometry and second simplified geometry. For both geometric model, the same boundary conditions were assumed.

The obtained results of calculation show small effect of simplification on the changes of obtained results. Simplifications of the geometry model in the form of not taking into account pipelines with a diameter of 7 and 16 cm, floor unevenness reaching up to several centimeters and tightening arch-yielding support in air flow simulations for straight axial section of mine drift, cause deterioration of obtained results by about 0.2%.

## References

1. Baścik, M.: 3D Laser Scanning in Underground Mines—Practical Experience. School of Underground Mining 2013, The Mineral and Energy Economy Research Institute of Polish Academy of Sciences, Poland (2013)
2. Janus, J.: The application of laser scanning in the process of constructing a mine drift numerical model. In: 24th World Mining Congress Proceedings—Underground Mining, Brazilian Mining Association, Rio de Janeiro, s. 440–449, Brazil (2016)
3. Janus, J.: Zastosowanie skaningu laserowego do budowy modelu numerycznego wyrobiska górniczego, vol. 18, no. 3, s. 27–34. Prace Instytutu Mechaniki Górotworu PAN, Kraków (2016)
4. Janus, J.: Ocena możliwości wykorzystania skaningu laserowego do budowy modeli numerycznych, vol. 17, no. 1–2. Prace Instytutu Mechaniki Górotworu PAN, Poland (2015)
5. Janus, J,: Construction the numerical models geometry by using terrestrial laser scanning. In: Selected Issues Related to Mining and Clean Coal Technology, AGH, Kraków (2016)
6. Krach, A., Krawczyk, J., Kruczkowski, J., Pałka, T.: Zmienność pola prędkości i strumienia objętości powietrza w wyrobiskach kopalń głębinowych. Archives of Mining Sciences, Kraków (2006)
7. Kruczkowski, J., Ostrogórski, P.: Metanoanemometr SOM 2303. Nowoczesne metody zwalczania zagrożeń aerologicznych w podziemnych wyrobiskach górniczych, GIG, Katowice (2015)
8. Lipecki, T.: Kompleksowa ocena stanu geometrycznego obiektów i urządzeń szybowych z zastosowaniem skaningu laserowego. Rozprawy i Monografie 2013, Poland (2013)
9. Lipecki, T.: Laser scanning measurement of mining equipments geometry and deformation. Pol. Min. Rev. (7–8). Poland (2010)
10. Sokoła-Szewioła, V., Wiatr, J.: Application of laser scanning method for the elaboration of digital spatial representation of the shape of underground mining excavation. Pol. Min. Rev. (8). Poland (2013)

# A Mine Ventilation Program Integrated with Gob Flow Field Simulation

Fengliang Wu[✉], Xintan Chang, and Zhuo Dan

College of Safety Science and Engineering, Xi'an University of Science and
Technology, Xi'an 710054, China
15038537@qq.com

**Abstract.** In order to implement an integration simulation of mine ventilation
network and gob flow field, a program named iMVS (integrated Mine
Ventilation System) was developed based on the technology of ObjectARX. The
integration model of mine ventilation network and gob flow field was intro-
duced. The node pressure method of ventilation network calculation and the
finite element method for gob flow field were used to establish the governing
equations. The ObjectARX technique was used to make iMVS a visual inter-
face. The custom class method in ObjectARX was used to create the data
structures and operations for iMVS. A sample based on iMVS was analyzed,
which shows the software simplify the simulation process and use.

**Keywords:** Gob flow field · Mine ventilation network · Mine ventilation
software · ObjectARX

## 1 Introduction

Ventilation system provides a safe workable environment where harmful gas mixtures
are in compliance with the law. Mine ventilation system is complicated and many
simulation programs have been developed in the past decades to provide engineers an
useful tool for ventilation planning. The use of such simulation software is beneficial in
the initial design of a particular ventilation and accident control system to test different
scenarios. Simulation models with various scenarios also enhance decision-making
with alternative designs to address the various issues such as gas or fires control
problems underground.

There are mainly three kinds of such software. The first kind of classical simulation
programs, for instance VnetPC, MineVent with one dimensional network modeling and
solution algorithms, are widely available for mine ventilation system design [1, 2]. The
second not only contains the basic function such as pressures, fan effects, and flow
rates, but also can model the spread of fumes on a real time basis, such as MFIRE
[3, 4]. The third software with CFD or grid technology help engineers "see" the
"unseen" areas of the mine gob through visualization of the data and ultimately help
improve worker safety [5–8]. The first two kinds of programs are professional mine
ventilation software and have been a powerful planning and management tool, while
CFD software require a thorough understanding how airflow behaves in gobs and
knowledge of mathematics and flow mechanics in order to simulate gob flow field

underground. But most commonly used CFD programs are commercial software designed for mechanical engineering applications, to make the grid technology a practical tool in mine ventilation planning lots of work still remain to be done. Authors of this research have also developed a ventilation network calculation program based on ObjectARX [9, 10]. This research will add the gob flow field simulation into the software to make the gob simulation more user-friendly and accepted by the industry.

## 2   The Integrated Model for Mine Ventilation System

### 2.1   Integrated Model of Network and Gob Based on Shared Nodes

A typical working face and gob is shown in Fig. 1. The gob flow can be solved using finite element method which divides the gob into mesh with enough triangular elements and nodes (in dash lines) and airways in solid lines (Fig. 2b). The nodes with the numbers from 3 to 8 are defined as shared nodes for the network and gob. The following work will show the governing equations for pressures of all nodes, boundary conditions in gob flow simulation are simulated at the same time.



(a) Gob layout          (b) shared node model
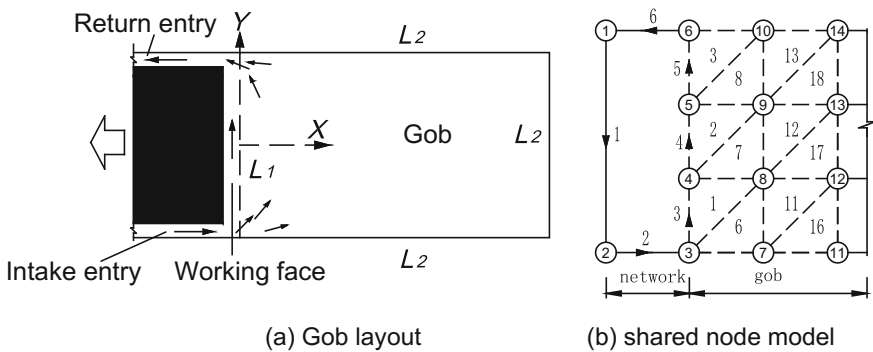
**Fig. 1.** Integrated model of working face and gob in a U-ventilation system
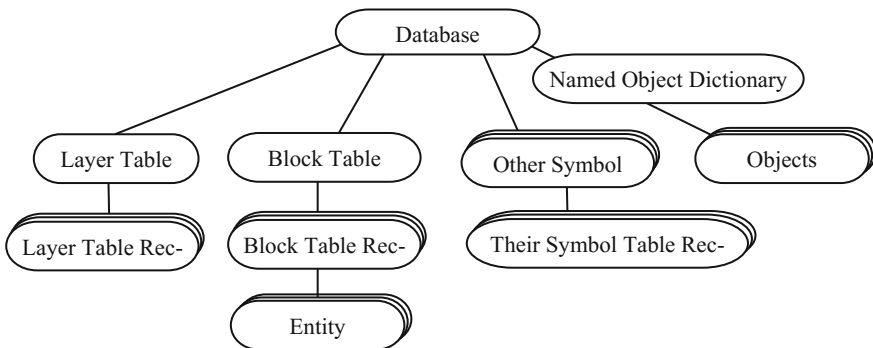


**Fig. 2.** The structure of a database in AutoCAD

## 2.2    Governing Equations

**Governing Equations in Gob Flow**. Airflow in the gob can be firstly assumed to be an isotropic steady linear seepage and obeys the Darcy law and the continuity equation, and can be expressed with the differential equation:

$$\begin{cases} \frac{\partial}{\partial x}\left(T\frac{\partial P}{\partial x}\right) + \frac{\partial}{\partial y}\left(T\frac{\partial P}{\partial y}\right) = 0 & (x,y) \in G \\ P = p_0 & (\text{on } L_1) \\ T\frac{\partial P}{\partial x}n_x + T\frac{\partial P}{\partial y}n_y = 0 & (\text{on } L_2) \end{cases} \tag{1}$$

where $T$ represents the hydraulic conductivity; $p_0$ represents the known pressure values on $L_1$ and can be calculated from the network boundary nodes (Fig. 2); pressure of node 9 should equal to the average value of node 3 and node 4; $n_x$, $n_y$ respectively represent the components of outer unit normal vector of $L_2$, which are the boundaries of no air leakage; $P$ is the pressure function of gob.

By finite method for Eq. (1), it has been proved for each node not on the boundary $L_1$ there exists an equation [11]

$$\sum_{\Delta i} \frac{T_\Delta}{4A_\Delta}\left[(b_ib_i + c_ic_i)p_i + (b_ib_j + c_ic_j)p_j + (b_ib_k + c_ic_k)p_k\right] = 0, \quad i = 1,2,\ldots,S \tag{2}$$

where $S$ is the count of the nodes not on boundary $L_1$; $\sum_{\Delta i}$ represents a sum operation to all of the elements which are connected with the node $i$; $A_\Delta$ is the area of each triangular element with the unit of $m^2$. $T_\Delta$ represents the hydraulic conductivity of each triangular element; $p_i$, $p_j$ and $p_k$ are pressures of each triangular elements nodes which are counter-clockwise around the triangle; the coefficients $a$, $b$, $c$ can be calculated through the coordinates of each triangular element, which are: $a_i = x_jy_k - x_ky_j$, $b_i= y_j - y_k$, $c_i = x_k - x_j$, $a_j = x_ky_i - x_iy_k$, $b_j = y_k - y_i$, $c_j = x_i - x_k$, $a_k = x_iy_j - x_jy_i$, $b_k = y_i - y_j$, $c_k = x_j - x_i$. Equations (2) is a linear system of equations about $p_i$ ($i = 1, 2,\ldots$, $S$) as the governing equations of steady linear seepage model in gob. When all nodes pressures are known, the airflow velocity $V_\Delta$ and its components in each element can by calculated by Darcy law.

In fact the airflow in the gob area, especially in the area nearby the working face, is not linear seepage. Li et al. researched a method to solve the nonlinear seepage based on the linear model with a correction to the hydraulic conductivity of $T$, which was used in this research [12].

**The Network Governing Equations**. If there are $M$ nodes in the network, anyone can be taken as a base node and the pressure is set to zero, the rest $M - 1$ nodes pressures are in relative to the base node pressure. There should be an airflow rate balance control equation for each of the rest of $M - 1$ nodes in the network:

$$\sum_{j=1, j\neq i}^{M} q_{ij} = 0, \quad i = 1,2,\ldots,M - 1 \tag{3}$$

where $c_{ij}$ equals 1 when air flows out from node $i$ to element $j$ and equals $-1$ when flowing into node $i$ from element $j$, otherwise it is zero; $q_{ij}$, with the unit of m³/s, is the airflow rate of the branch between the node $i$ and node $j$. $q_{ij}$ can be expressed in:

$$q_{ij} = b_{ij} \frac{1}{\sqrt{R_{ij}}} \cdot \sqrt{|p_i - p_j|} \cdot \frac{p_i - p_j}{|p_i - p_j|}$$

where $p_i$, $p_j$ with the unit of Pa, respectively represent the pressure of node $i$ and node $j$ based on zero pressure node; $R_{ij}$, with the unit of Ns²/m⁸, is the resistance of the branch between node $i$ and node $j$; $b_{ij}$ equals 1 when a branch exists between node $i$ and node $j$, otherwise $b_{ij}$ is zero.

## 3 Implementation of the Models Based on ObjectARX

The program was named iMVS (integrated Mine Ventilation Simulation) and designed as a CAD system based on ObjectARX.

### 3.1 ObjectARX Technology

AutoCAD has excellent drawing and editing functions, widely applied in engineering drawing [13]. It provides four interfaces for developers: ObjectARX, LISP, COM and .Net. The ObjectARX SDK (Software Development Kit) provides an object-oriented C++ API. AutoCAD can be customized and extended, and the database and graphics system can be accessed directly through the ObjectARX API. ARX programs provide user interface functions, such as customizing commands, creating graphics, define a custom entity with drawing and storing ability. An AutoCAD drawing is a collection of objects stored in a database as shown in Fig. 2. Some of the basic database objects are entities, symbol tables, and dictionaries. Entities which a user can see on the screen and manipulate are a special kind of database object that have a graphical representation within an AutoCAD drawing, such as lines, circles, text. Symbol tables and dictionaries are containers used to store database objects. Both container objects map a symbol name (a text string) to a database object. An AutoCAD database includes a fixed set of symbol tables, each of which contains instances of a particular class of symbol table record. No other symbol table can be added to the database. Examples of symbol tables are the layer table (AcDbLayerTable), which contains layer table records, and the block table (AcDbBlockTable), which contains block table records. All AutoCAD entities are owned by block table records.

### 3.2 Definition of Custom Entity in iMVS

Adding custom entity data structure into the class hierarchy of database objects in AutoCAD is the main work of this study. As Fig. 3 shows, AcDbObject is the base class for all objects that reside in database of AutoCAD. AcDbEntity derived from
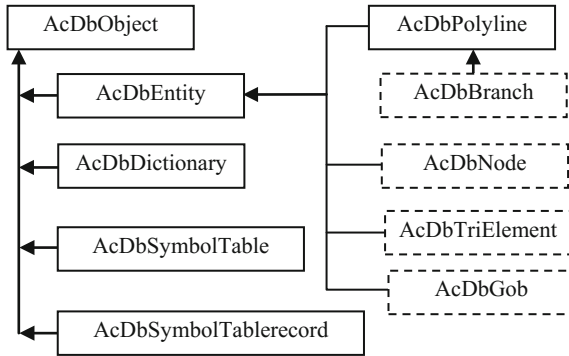
**Fig. 3.** The hierarchy of iMVS's custom entity in ObjectARX

AcDbObject is the abstract base class for all database objects which have a graphical representation. Three custom classes named AcDbNode, AcDbGob, AcDBTriElement were derived from AcDbEntity to respectively represent node, gob and triangular element in this research. The class of AcDbBranch representing branch in this research was derived from AcDbPolyline which has enough geometric characteristics for representing a branch. The four custom classes are shown with dash lines in Fig. 5. AcDbEntity and AcDbPolyline share the base class functions to the four classes, such as layer, color, line type, line weight, highlight. The essential interfaces listed in Table 1 were implemented in the four classes. Graphics are plotted by drawing primitives in AutoCAD. In the function of "subWorldDraw", the geometric graphics interface class AcGiGeometry will provides enough primitive drawing functions to draw a complicated entity with these base functions in 3D space. The functions of "dwgInFields" and "dwgOutFields" must be overridden for reading and writing DWG files. The same order must be kept when reading and writing data which are in DWG files. In addition, the geometric operation classes AcGePoint2d, AcGeVector2d, and AcGeMatrix2d provide various operations for point, vector and matrix, respectively. Only the features of mine ventilation or gob flow need to be concerned in developing, which reduces the developing workload greatly.

**Table 1.** Interface for an AcDbEntity

| Functions overridden | Description |
|---|---|
| subWorldDraw | Draw the entity for itself |
| subGetGeomExtents | Calculate the corner points of a box that encloses the entity |
| subTransformBy | Make the transformation matrix created by AutoCAD to the entity so that this custom entity can be moved, copied or other operations |
| dwgOutFields | Allow the object to write out its data to a ".dwg" file |
| dwgInFields | Allow the object to read in its data from a ".dwg" file |

## 4 Sample Analysis Using iMVS

### 4.1 Modeling of Network and Meshing of Gob in iMVS

The iMVS provides enough commands for drawing network and for pre and post-processing of gob grids. The input data needed in iMVS mainly include resistances of branches and hydraulic conductivity distributions in the gob. Figure 4 is a screenshot of iMVS when modeling of network and meshing of gob for the following sample. The other abilities of iMVS can also be roughly illustrated in the following sample.
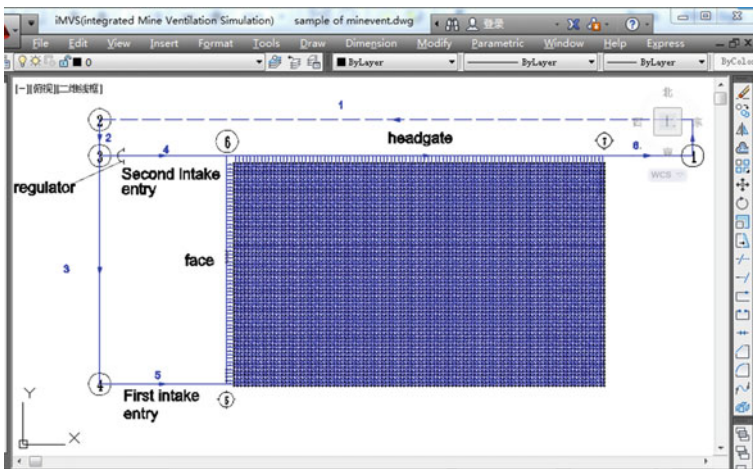


**Fig. 4.** Interface of iMVS

The sample is a Y-ventilation system as shown in Fig. 5. The whole panel is 2000 m long, 300 m wide, 6 m high from the bottom of the coal seam and the active gob is 500 m long. Figure 4 shows the geometric model of the face and gob and branch 1 is in the fixed airflow rate of 40 m³/s. The working face was designed with 30 m³/s of
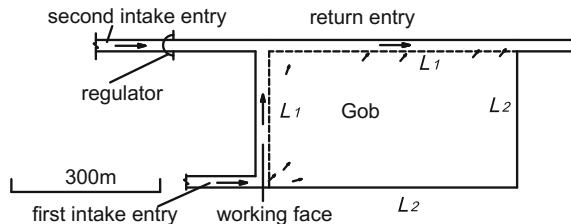


**Fig. 5.** Layout of working face and gob in a Y-ventilation system

airflow rate so a regulator was set at the second intake entry. The branches resistances are listed in the Table 2 and the distribution of hydraulic conductivity in the gob is shown in Fig. 6. The working face and the headgate were totally divided into 157 branches and 158 nodes were shared for the network and gob. And the gob was discretized into 12,000 elements and 6161 nodes.

**Table 2.** Resistance of branches

| Branches | Resistance ($Ns^2/m^8$) |
|---|---|
| $R_{23}$ | 0.002 |
| $R_{34}$ | 0.0128 |
| $R_{45}$ | 0.0781 |
| $R_{36}$ | 0.0625 |
| $R_{71}$ | 0.0005 |
| Per hundred meter resistance of working face | 0.0208 |
| Per hundred meter resistance of headgate | 0.0104 |
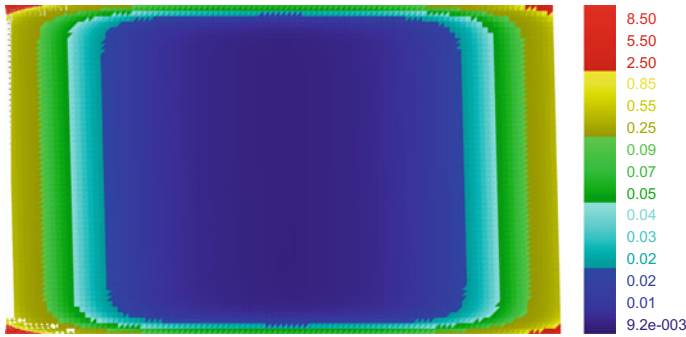


**Fig. 6.** Hydraulic conductivity distributions in the gob areas

## 4.2 Results Analysis

Results of simulation can be illustrated in various ways in iMVS. Figure 7 shows the airflow rate of each branch and that the gob is highlighted by three colors in different magnitude by velocity for spontaneous combustion management. The red area velocity is from 0.0017 to 0.004 m/s which has been generally thought in favor of heat accumulation. Gob's flow lines colored by velocity magnitude is shown in Fig. 8 where any two adjacent flow lines contain the same flow rate in an unit thick. Figure 9 gives the
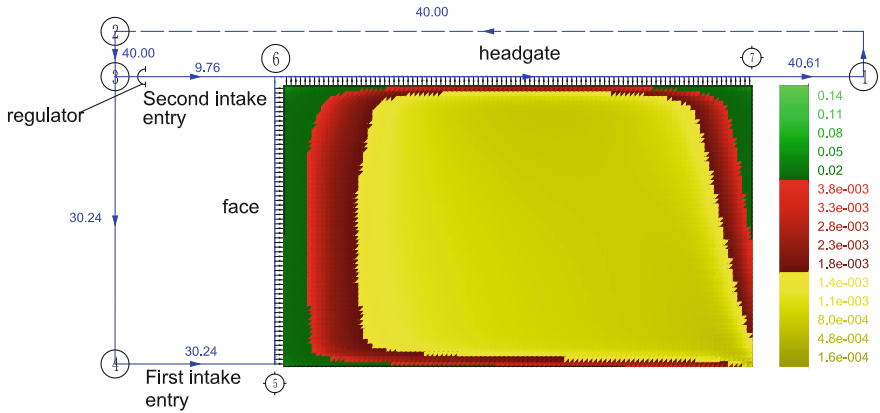
**Fig. 7.** Branch air rate and velocity (m/s) cloud chart of gob
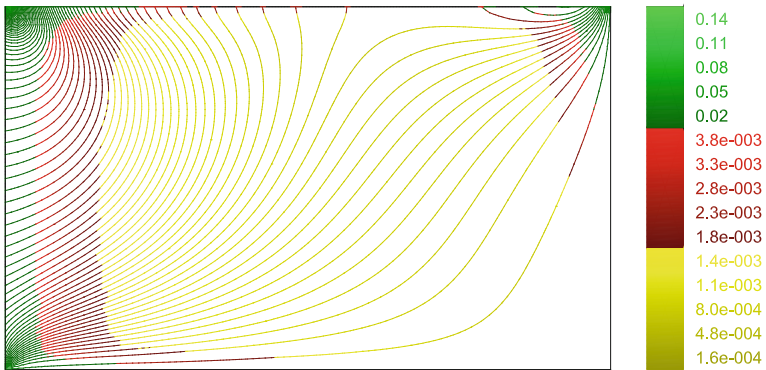


**Fig. 8.** Flow lines colored by velocity magnitude (m/s) in gob areas

information of accumulation rate of airflow entering into the gob along working face and headgate. Both of Figs. 8 and 9 show air always flows into the gob along the whole working face and flows out from gob at almost along the whole headgate. Figure 10 shows each branch's pressure drop and the pressure lines in gob.
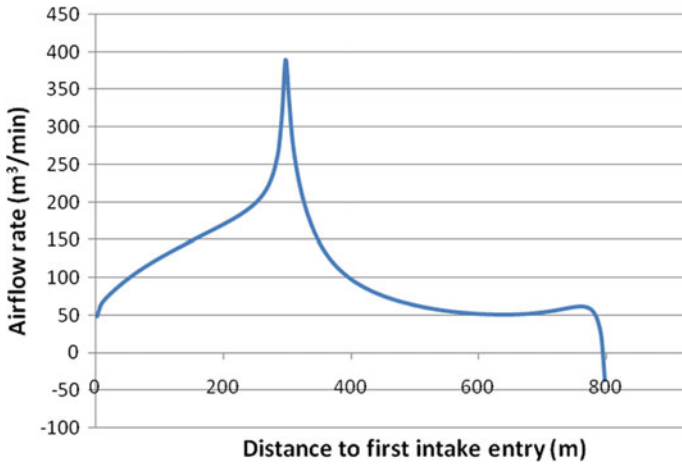
**Fig. 9.** Accumulation rate of airflow flowing into gob along working face and headgate
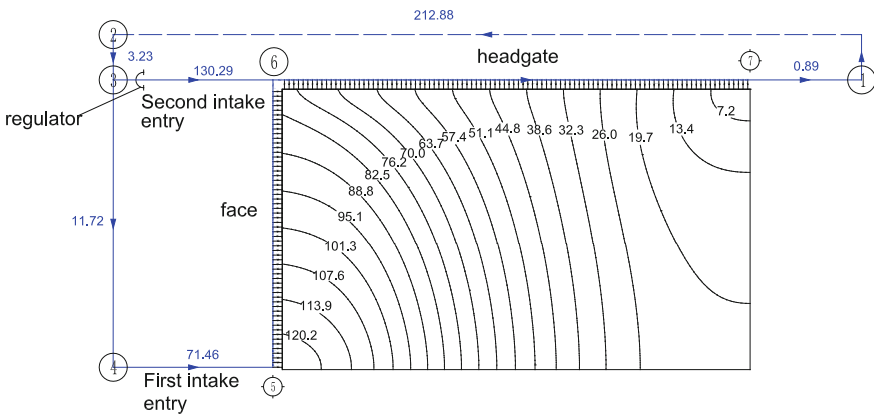


**Fig. 10.** Branch pressure drop and pressure lines in gob

Figure 11 gives a scenario that the regulator is damaged by some accidents. Results show the airflow rate of working face decreases greatly and the gob flow field changes greatly too.
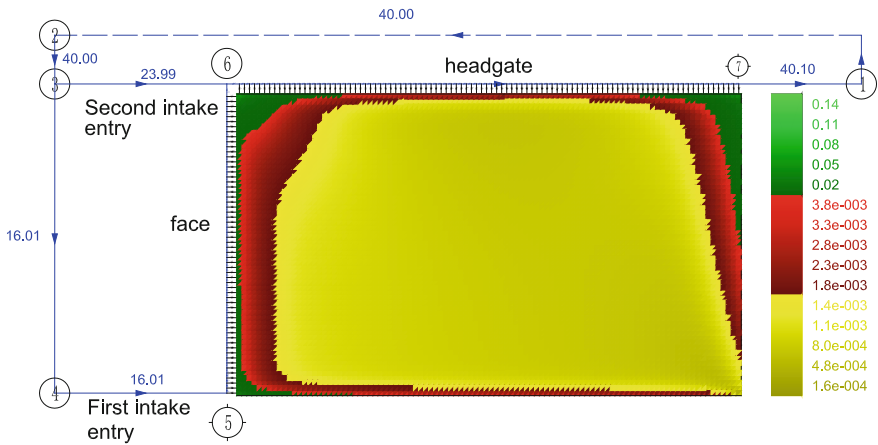
**Fig. 11.** Branch air rates and velocity (m/s) cloud chart of gob when regulator damaged

## 5    Conclusions

A program of iMVS was developed based on the technology of ObjectARX to make the gob flow field can be simulated with the ventilation network. The shared nodes integrate the ventilation network and gob flow field as a whole. Four custom classes of AcDbBranch, AcDbNode, AcDbGob, AcDBTriElement were defined to represent the branch, node, gob and element in this research. The key functions inherited from base class of AcDbEnity were implemented in the four class.

The iMVS with sufficient pre and post-processing functions provides a more precise result of mine ventilation simulation. The iMVS runs with input data mainly including branch resistances and hydraulic conductivity distributions in gob with no boundary conditions. Airflow rate, velocity and pressure can be viewed by isoline, cloud chart.

## References

1. Hardy, R.J., Heasley, K.A.: Ventilation simulation programs MineVent and MFIRE: updates to advance the technology of simulation programming. In: 11th U.S. North American Mine Ventilation Conference, State College, PA
2. Deming, W., Jun, W., Fubao, Z.: Developed mine ventilation graphics system based on the object-oriented technologies. J. China Coal Soc. **25**(5), 510–513 (2000)
3. Zhou, L., Smith, A.C., Yuan, L.: New improvements to MFIRE to enhance fire-modeling capabilities. Min. Eng. **68**(6), 45–50 (2016)

4. Chang, X.: Digital Simulation of Transient Mine Ventilation, 162 pp. Ph.D. Dissertation, Michigan Technological University, Houghton, MI (1987)
5. Yuan, L., Smith, A.C.: Numerical study on effects of coal properties on spontaneous heating in longwall gob areas. Fuel **87**, 3409–3419 (2008)
6. Qin, Y., Liu, W., Yang, X.: Numerical simulation of impact of non-Darcy seepage on spontaneous combustion in goaf. J. China Coal Soc. **37**(7), 1177–1183 (2012)
7. Yuan, L., Smith, A.C., Brune, J.F.: Computational fluid dynamics study on the ventilation flow paths in longwall gobs. In: 11th U.S./North American Mine Ventilation Symposium, pp. 591–597, Taylor & Francis Group, London (2006)
8. Yuan, L., Smith, A.C.: Computational fluid dynamics modeling of spontaneous heating in longwall gob areas. SME Annual Meeting, Denver, CO (2007)
9. Wu, F., Gao, J., Chang, X., Li, L.: Symmetry property of Jacobian matrix of mine ventilation network and its parallel calculation model. J. China Coal Soc. **41**(6), 1454–1459 (2016)
10. Wu, F., Zhou, P., Li, H.: Research on the model of mine ventilation CAD based on the intelligent object. Coal Sci. Technol. **37**(5), 54–57 (2009)
11. Zhao, Y.S.: Finite Element Method and its Application in Mining Engineering. Beijing: Coal Industry Press, (1994) (in Chinese)
12. Li, Z., Liu, Y., Wu, Q.: Improved iterative algorithm for nonlinear seepage in flow field of caving goaf. J. Chongqing Univ. **31**(2), 186–190 (2008) (in Chinese)
13. Yang, B., Yu, G., Wang, D.: Hydraulic calculation software development of water supply networks based on AutoCAD. In: Proceedings of the International Conference on Pipelines and Trenchless Technology, Beijing, China, pp. 1571–1580 (2011)

# Study on a Method for the Prediction of Thermal Environment Parameters of Mine Roadways Under a Overall Ventilation Network

Xin Yi[1(✉)], Fengliang Wu[1], Zhenping Wang[2], Zhenbao Li[1], and Li Ma[1]

[1] Xi'an University of Science and Technology, Xi'an 710054, Shaanxi, China
20661918@qq.com
[2] Yankuang Group Limited Company, Zoucheng 273500, Shandong, China

**Abstract.** Accurate mine air temperature prediction is essential for work areas with high temperatures. It provides the basis for understanding high temperature thermal disaster and the design of a cooling system underground. The air volume for a single tunnel air temperature prediction model is known. However, the air flow distribution in fact can be affected by natural airflow pressure, which is due to temperature difference in the mine ventilation network. So the relationship between the air temperature and airflow are determined. It also puts forward a forecasting method of air temperature based on an overall mine ventilation network solution. Through iterative calculation of air volume and air temperature, the prediction of them is achieved in a balanced equilibrium. The software is developed for calculating the temperature of airflow and humidity in the mine roadway based on an ObjectARX platform. Through the simulation of Zhaolou coal mine ventilation network calculation results and the measured value, the air temperature and the natural wind pressure are predicted accurately in the mine ventilation network. The measured and calculated data agree well, indicating that the forecasting method is useful in ventilation planning. It can also determine basic parameters for thermal environment and thermal comfort analysis.

**Keywords:** Thermal environment parameter · Thermal comfort
Overall ventilation network prediction method

## 1 Introduction

The gradual depletion of accessible coal resources has led to mining at increasing depths, which has highlighted the problem of mine heat [1, 2]. It has become necessary to accurately predict the air temperature of deep mines when designing ventilation systems and design a mine cooling system. As part of this effort, Huang [3, 4] conducted studies on methods for predicting mine air temperatures. Hou et al. [5–7] analyzed the heat exchange between the air and the surrounding rock, and they determined a method for the calculation of the heat adjustment circle of wall rock. They also established a prediction model for measuring roadway temperature and humidity,

based on known roadway air quality and known air temperature and humidity at the inlet, which has been proposed as a baseline for accurate predictions of air temperature. Moreover, Jeppe [8] performed predictions of air temperature in deep mines, which have formed the basis for the prediction and calculation of air temperatures in modern mines. Additional prediction methods include the Scherban prediction method for one-dimensional roadway air temperature, and the Foss and Hiramatsu methods [9]. Tian [10] established a mathematical model for the thermal environment of a mine and developed a calculation program. Uchino [11, 12] corrected a calculation for the air temperature and humidity in a mine by considering complex boundary conditions. Kertikou [13] studied the distribution characteristics of temperature and humidity in a single-end roadway. Moloney [14] used computational fluid dynamics to obtain the distribution law of airflow within mines.

The model used for the calculation of humidity has considerable influence on predictions of air temperature, and such models can be grouped into two categories: those based on the concept introduced in the SHR model, and those based on moisture content introduced at the starting and end points of an airway. Realizing the interaction between air volume and temperature in an airway, the combination of single tunnel air temperature prediction and mine ventilation network is considered effective. Zhang [15] applied the single tunnel wind temperature model to the wind net, and introduced the moisture content of the beginning and ending points into the model. The impact of wind flow humidification on wind temperature can be further improved. Existing models for predicting air temperatures are complex and have to be performed considering all factors involved and interactions between local heat source and its interaction with the entire ventilation system. From the description above, it can be concluded that existing models for predicting air temperatures are complex and have to be performed considering all factors involved in each kind of roadway and interactions. The prediction model of wind temperature can be further improved and applied conveniently. Therefore, the airflow temperature prediction models under the action of various heat sources is analyzed in this paper. Combined with the coupling relationship between air temperature and air volume, the air temperature prediction method based on an overall mine ventilation network solution is put forward, which can accurately predict the temperature and humidity of mine air flow. At the same time, it provides an important basis for geothermal disaster analysis and the design of cooling system of mine.

## 2    Model for Predicting Air Temperature in a Dead-End Roadway

### 2.1    Heat Source Analysis Underground

The main heat sources in a mine include the heat dissipation of surrounding rock, oxidation heat dissipation, heat dissipation of electromechanical devices, heat dissipation of hot water, heat dissipation of humans, and heat dissipation (heat absorption) of air compression/expansion. The overall heat dissipation can be calculated as follows:

**Heat Dissipation of Surrounding Rocks**

$$q_{ck} = K_\tau \cdot (t_y - t_k) \cdot U \cdot L = \frac{\lambda}{R_0} K \cdot (t_y - t_k) \cdot U \cdot L \qquad (1)$$

where $t_y$ is the original rock temperature, $t_k$ is the original air temperature, $U$ is the perimeter, $\lambda$ is the thermal conductivity of the rock (W/m K), $R_0$ is the equivalent radius of the roadway, and $K_\tau$ is the unsteady heat transfer coefficient, i.e., the heat dissipation/absorption of the roadway wall per unit area per unit time with a temperature difference of 1 K between the original rock and the air (i.e., $K_\tau = \lambda K/R_0$). Here, $K$ is a function of $B_i$ and $F_0$, i.e., $K = f(B_i, F_0)$, where $B_i = aR_0/\lambda$, for which $a$ is the heat transfer coefficient between the surrounding rock and the air (W/m² K), and $F_0 = \lambda\tau/(c\rho R_0^2)$, where $c$ and $\rho$ are the specific heat capacity (kJ/kg °C) and the density (kg/m³) of the rock, respectively, and $\tau$ is the ventilation time (s). The analytic solution of $K_\tau$ is highly complex; therefore, the regression formula proposed by Cen et al. (with accuracy of 99%) is used here:

$$K = \exp[(A + B \ln F_0 + C \ln^2 F_0) + \frac{A' + B' \ln F_0 + C' \ln F_0}{B_i + 0.375} \qquad (2)$$

where under the condition $\infty > F_0 \geq 1$, the parameters are defined as $A = 0.02001$, $A' = -1.061628$, $B = -0.2998413$, $B' = 0.1366794$, $C = 1.59764 \times 10^{-2}$, and $C' = -9.702536 \times 10^{-3}$, and under the condition $1 > F_0 > 0$, the parameters are defined as $A = 2.409134 \times 10^{-2}$, $A' = -1.063224$, $B = -0.3142634$, $B' = 0.151002$, $C = 1.469856 \times 10^{-2}$, and $C' = -1.625136 \times 10^{-2}$.

**Oxidation Heat Dissipation**

$$Q_{ox} = q_0 \cdot U \cdot L \cdot W^{0.8}, \quad \text{(kW)} \qquad (3)$$

where $q_0$ is the equivalent oxidation heat dissipation coefficient (kW/m²), which is within the range $0.12$–$0.87 \times 10^{-3}$ for the rock roadway and within the range $1.5$–$6.7 \times 10^{-3}$ for the preparation roadway. The value of $q_0$ is set as $6 \times 10^{-3}$ for the mining roadway.

**Heat Dissipation of Electromechanical Devices**

$$Q_m = N_m K_m, \quad \text{(kW)} \qquad (4)$$

where $N_m$ is the rated power of the device, kW, and $K_m$ is a comprehensive coefficient.

**Heat Dissipation of Hot Water**. The heat dissipation of a covered ditch has little effect on air temperature and so it can be ignored. However, there are exchanges of both heat and quality between the air and the hot water in an uncovered ditch. This heat exchange can be calculated as shown in Eqs. (5) and (6):

$$Q_{WX} = \alpha_W F(t_W - t_k), \quad (\text{kW}) \tag{5}$$

$$Q_{WQ} = \beta F(P(t_{sw}) - \phi P(t_k)), \quad (\text{kW}) \tag{6}$$

where $a_w$ is the heat transfer coefficient between the water and the air (kW/m$^2$ °C), $t_w$ is the water temperature (°C), $F$ is the area of contact between the water and the air (m$^2$), $\beta$ is the mass and heat exchange coefficient that is within the range 0.0097–0.0125 (kW/m$^2$ Pa), $P$(t) is the saturated vapor pressure for a temperature of $t$ (Pa), and $\varphi$ is the relative humidity of the air. The increased vapor due to the mass exchange can be expressed as follows:

$$M_1 = Q_{WQ}/r, \quad \text{kg/s} \tag{7}$$

**Heat Dissipation of Humans**. The average heat dissipation ($q_r$) is 0.4 kW, and the total heat dissipation in relation to the number of humans ($n$) can be calculated as follows:

$$Q_r = q_r \times n, \quad \text{kW} \tag{8}$$

**Heat Dissipation due to Air Compression**. In a leveled roadway, heat is released in the downstream airflow and heat is absorbed in the upstream airflow, which can be expressed as follows:

$$Q_F = 9.81 \times 10^{-3} G(Z_1 - Z_2), \quad \text{kW} \tag{9}$$

where $G$ is the mass flow rate in the roadway (kg/s), and $Z_1$ and $Z_2$ are the center levels of the beginning and end cross sections (m).

## 2.2    Prediction of Air Temperature and Humidity in a Roadway

In addition to the dissipations of heat via the surrounding rock and hot water, other heat sources can be regarded as point heat sources within the mine. When calculating the humidity of the air flow, the spot heat source humidification is not taken into consideration. That is, the point heat source is treated as sensible heat. The effects of increasing temperature and humidification of a ditch on the air are expressed in Eqs. (5) and (6). Therefore, the calculation models of increasing temperature and humidification between the surrounding rock and the air can be conducted in terms of the sensible heat ratio and the humidity coefficient.

**Sensible Heat Ratio**. The total heat released from the surrounding rock ($q_{ch}$) can be divided into the sensible heat of a dry wall ($q_x$) and the latent heat of water vaporization ($q_q$), i.e., $q_{ch} = q_x + q_q$. The sensible heat ratio is the ratio of $q_x$ and $q_q$. Here, $c_{pk}$ is the specific heat capacity of air, $\Delta t_k$ and $\Delta i$ represent the differences in the temperature and enthalpy of air, respectively, and $G$ is the mass flow rate. The sensible heat ratio can be calculated based on measurements of $\Delta t_k$ and $\Delta i$:

$$\varepsilon = \frac{q_x}{q_{ch}} = \frac{G c_{pk} \Delta t_k}{G \Delta i} = \frac{c_{pk} \Delta t_k}{\Delta i} \tag{10}$$

**Roadway humidity ratio**. The humidity ratio [16] is the evaporation quality of water in a wall with certain humidity and the evaporation quality of water in a wall that is completely covered by water. The heat dissipation from the surrounding rock to the air can be expressed using the humidity ratio ($f$):

$$q_{ck} = \alpha(t_b - t_k) + \frac{f \beta r}{R_{sh} T}[P(t_b) - \varphi P(t_k)] \tag{11}$$

where $f$ is the humidity ratio of the roadway, $\beta = a/(c_{pk}\rho_k)$ (m/s), $R_{sh}$ is the gas constant of water vapor (kg m/kg K), $T$ is the absolute temperature of the air (K), and $P(t_b)$ and $P(t_k)$ are the saturated vapor pressure with air temperatures of $t_b$ and $t_k$, respectively (Pa).

The expression of the first degree ($P(t_b) = b_0 + b_1 t$) represents the saturated vapor pressure in the range of normal temperature (the values of $b_0$ and $b_1$ can be found in Ref. [3]). Here, $A = r/(c_{pk}\rho R_{sh} T)$ and Eq. (11) can be transformed to $q_{ck} = a(t_b - t_k^*)$. The heat dissipation of the surrounding rock (Eq. 1) by means of the unsteady heat transfer coefficient can be transformed to the following expression:

$$q_{ck} = \frac{\lambda}{R_0}(t_y - t_k^*)ULK^* \tag{12}$$

where, $t_k^* = \{tk - fA[b_0 - \phi P(t)]\}/(1 + fAb_1)$, and $K^*$ is the modified dimensionless unsteady heat transfer coefficient ($K^* = f(B_i^*, F_0)$, where $B_i^* = a^* R_0/\lambda$), $\alpha^* = (1 + fAb_1)\alpha$. Here, $B_i$ can be replaced by $B_i^*$ in Eq. (2) and thus $K^*$ can be obtained.

The sensible heat ratio ($\varepsilon$) and the humidity rate ($f$) are two different concepts representing roadway humidity. The conversion relationship between them is as follows:

$$\varepsilon = \frac{1}{1 + fAb_1} - \frac{\alpha(t_k - t_k^*)}{q_{ck}} \tag{13}$$

Because of the air temperature, humidity, and humidity rate constant, the sensible heat ratio is proportional to the heat dissipation of the surrounding rock. As the release of heat from surrounding rock ($q_{ch}$) decreases with time, $q_{ck}$ is large at the beginning of ventilation and the sensible heat ratio is positive. As $q_{ck}$ decreases to a certain value, the sensible heat ratio becomes negative, which indicates that water evaporation can absorb heat from the air and thus the air temperature decreases. Research has shown that the sensible heat ratio changes obviously with time during a ventilation process; therefore, the sensible heat ratio determined for a specific mine is a non-transferable engineering statistic. Although the humidity ratio is not the ratio of a wet wall to a dry wall, it is easy to establish a perceptual understanding of the variation of humidity in different

roadways. For example, the humidity ratio ($f$) of a roadway with accumulated water on the floor can be selected as 0.1; otherwise, $f$ is within the range 0.05–0.08.

**Prediction of air temperature and humidity**. In this instance, the roadway entrance is considered as point 0 and the roadway exit is considered as point 1. As for the known humidity ratio, the sensible heat ratio ($\varepsilon$) can be calculated using Eq. (10). Therefore, the total latent heat can be expressed as $Q_q = (1 - \varepsilon)q_{ck}$, and the absorbed vapor quality of the air can be derived as follows:

$$M_2 = Q_q/r, \tag{14}$$

where $r$ is the latent heat of water vaporization (kJ/kg). The air temperature in the roadway entrance is represented by $t_{k0}$, and the humidity at point 0 can be expressed as follows:

$$d_0 = 0.622 \frac{\varphi_0 P(t_{k0})}{P - \varphi_0 P(t_{k0})} \tag{15}$$

The humidity at point 1 can be expressed as follows:

$$d_1 = d_0 + \frac{M_1 + M_2}{G} \tag{16}$$

Therefore, the air temperature at point 1 can be calculated as follows:

$$t_{k1} = t_{k0} + \frac{\varepsilon q_{ck} + Q_{WX} + Q_r + Q_F + Q_{OX} + Q_m}{G(c_{Pk} + 0.5(d_0 + d_1)c_{Psh})} \tag{17}$$

where $c_{pk}$ is the specific heat capacity of dry air (kJ/kg K) and $c_{psh}$ is the specific heat capacity of wet air (kJ/kg K). The absolute static pressure is $P$; thus, the humidity at point 1 can be derived as follows:

$$\varphi_1 = \frac{Pd_1}{P(t_0) \cdot (d_1 + 0.622)} \tag{18}$$

# 3   Prediction of Air Temperature for an Entire Mine

The air quality in the prediction model of air temperature for a single roadway is known. Meanwhile, the prediction of air temperature for the branch ends is conducted along the upstream to downstream of the airflow in the network map to determine the air temperatures of all the roadways. The depth of a high-temperature mine is considerable and the temperature difference between roadways is substantial. Therefore, the natural air pressure can be exploited in a ventilation circuit. There can be many natural flows of air within a ventilation network, and the natural variations of air pressure can affect the airflow distribution of the branches, which has an impact on the calculation of the inlet air temperature at the main points. The relationship between the

calculation of air temperature and air quality is considered fully in the model for the prediction of air temperature. For an airflow network with $N$ edges and $J$ nodes, the mathematical model with the network solution of natural air pressure is shown as Eqs. (19) and (20):

$$\sum_{j=1}^{N} c_{ij} R_j Q_j^2 - \sum_{j=1}^{N} c_{ij}(H_{fj} + H_{zj}) = 0, \quad (i = 1, 2, \ldots, N - J + 1) \tag{19}$$

$$\sum_{j=1}^{N} b_{ij} Q_j = 0, \quad (i = 1, 2, \ldots, J - 1) \tag{20}$$

where $c_{ji} = 1$ means the same direction of branch $j$ and loop $i$; $c_{ji} = -1$ means the reverse direction of branch $j$ and loop $i$; $c_{ji} = 0$ means no branch $j$ exists in loop $i$; $b_{ji} = 0$ means branch $j$ is not connected to node $i$; $b_{ji} = 1$ means the air of branch $j$ flows into node $i$; $b_{ji} = -1$ means the air of branch $j$ flows out of node $i$; $R_j$ and $Q_j$ are the resistance and flow rate of the air, respectively; $H_{fj}$ is the fan discharge pressure of branch $j$; and $H_{zj}$ is the natural air pressure, which can be selected as 0 if there is no corresponding term. As for branch $j$, the beginning and end nodes are $m$ and $k$, respectively. Here, $Z_m$ and $Z_k$ are the elevations of these two nodes, and the natural air pressure can be expressed as $H_{zj} = \tilde{n}_j \times (Z_m - Z_k)$. The absolute static pressure of the airflow is $B$, and the average air density can be obtained by means of the average air temperature and humidity of the branch.

According to the solution of Eqs. (12) and (13), the distribution of air temperature, under the action of natural air pressure and mechanical pressure, within a mine ventilation network can be obtained. Moreover, the above model and the model for the prediction of air temperature of a single roadway can be iterated as shown in Fig. 1, allowing the air temperature and quality in the equilibrium state to be obtained. As the prediction of air temperature includes a prediction of humidity, the model actually realizes a comprehensive prediction of the climatic conditions of a mine.

## 4 Air Temperature Prediction Software Based on ObjectARX

A large number of mine maps are saved in the dwg format, which illustrates the practicability of AutoCAD as a development platform for air temperature prediction. ObjectARX is a powerful tool for the secondary development of AutoCAD. According to the development protocol of ObjectARX, roadways, nodes, and other entities can be embedded in AutoCAD for the visualization of a mine ventilation network based on existing network calculation software [17]. According to these entities, the parameters of the ventilation network solution and the air temperature prediction can be obtained. Figure 2 presents an example of the main graphical user interface of the software, displaying the current ventilation network of the Zhaolou mine in China.
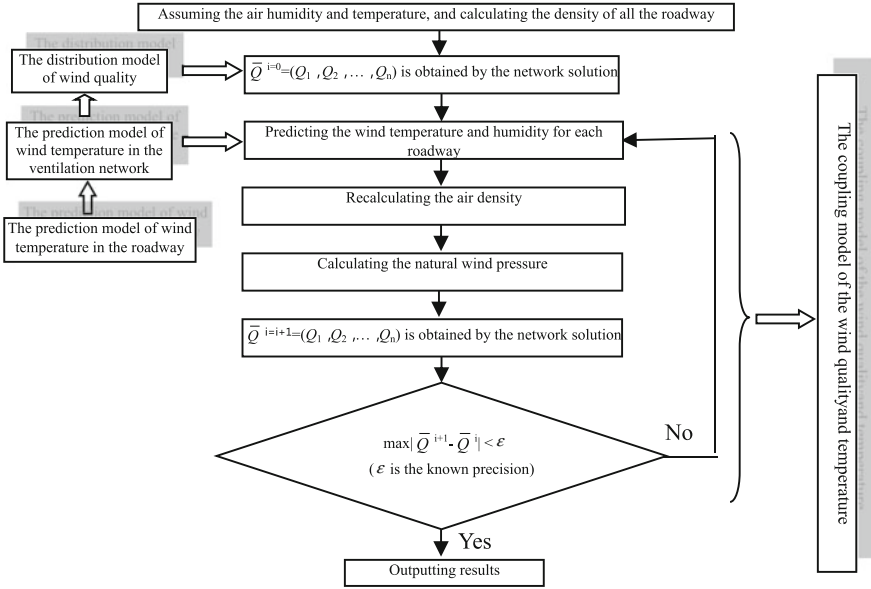
**Fig. 1.** Solution flow chart for predicting the air temperature and quality within the ventilation network of a mine
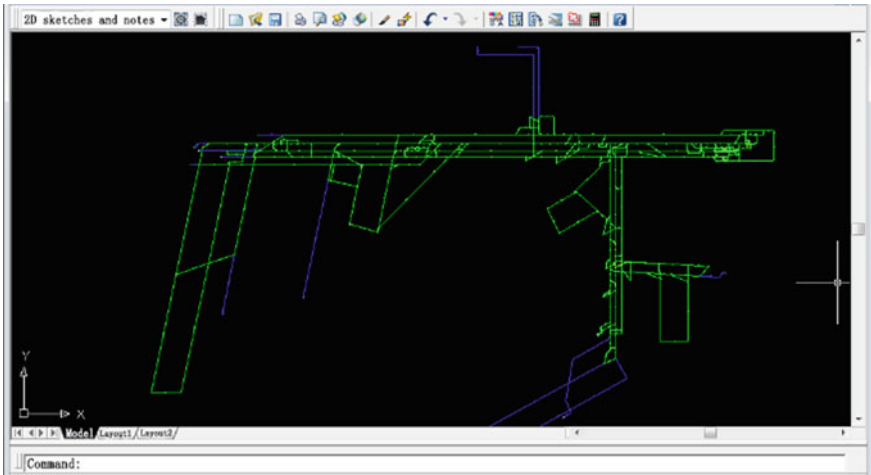


**Fig. 2.** Main graphical user interface displaying an example of the ventilation network of the Zhaolou mine in China

# 5   Prediction and Verification of Air Temperature in a Mine

With different depths of mining, the diurnal air temperature variation has different effect on the air flow temperature of the underground working site, the deeper the mining depth, the higher the temperature of the surrounding rock. The mining depth of the Zhaolou coal mine exceeds 1000 m. Therefore, the inlet temperature is selected as the local mean daily air temperature (inlet air temperature of 14 °C). To verify the efficacy of the model, the quality, temperature, and pressure of air within a ventilation network were predicted for the Zhaolou mine. The predicted air temperature for two main air channels are shown Fig. 3. The corresponding measurement points were arranged on the ventilation line of the working face, and the parameters of the air state at each point were tested. The comparison of the predicted and measured air temperatures for the auxiliary mine and roadway to working faces 3303 and 1307 is shown in Fig. 4.
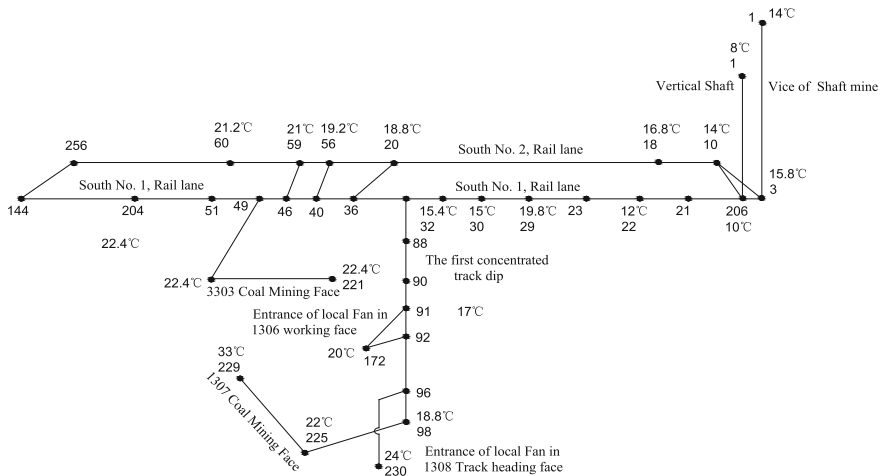


**Fig. 3.** Diagram of air flow from the auxiliary mine and roadway to working faces 3303 and 1307 of the Zhaolou mine

As shown in Fig. 4, the predicted and measured results are in good agreement. The temperature amplification of the auxiliary roadway from the ground to the working face is small, but the temperature amplification of the auxiliary roadway from the air inlet to the working face is large. The results show that the underground heat source is concentrated mainly at the working face, but that the heat dissipation of the transportation roadway is small. In some sections, the transportation roadway absorbs heat from the air, reducing the air temperature, which means roadway walls can play a role in the adjustment of air temperature.
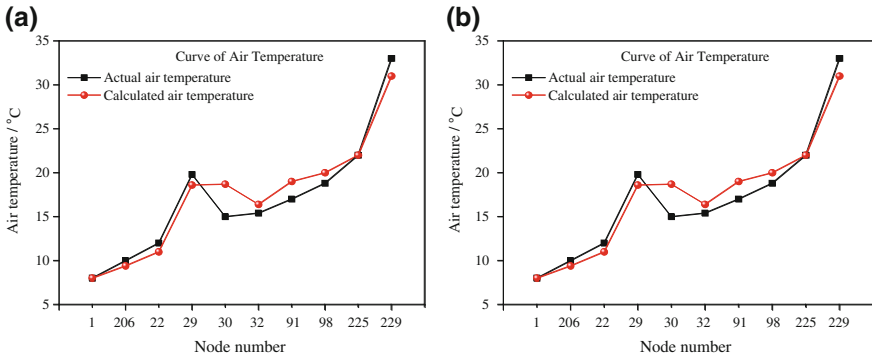
**Fig. 4.** Comparisons of predicted and measured air temperatures in Zhaolou mine: **a** working face 3303 and **b** working face 1307

## 6 Conclusions

(1) Based on analysis of the prediction model for air temperature with consideration of various heat sources, a coupling relationship between the predictions of air temperature and quality was obtained. It was demonstrated that consideration of the combination of air temperature predictions for a single roadway and a ventilation network is effective for predicting air temperature within a mine.

(2) According to the coupling relationship between the air temperature and quality under the action of natural air pressure, prediction models for air temperature and humidity were established based on a complete ventilation network solution. Moreover, software for the calculation of the state parameters of the air was developed using ObjectARX. The roadways, nodes, and other entities were embedded in AutoCAD, and the parameters of the ventilation network solution and the air temperature predictions could be obtained.

(3) It was demonstrated that the predictions and measurements for the ventilation system of Zhaolou mine were in reasonable agreement. Thus, the methods proposed for the prediction of air temperature and quality can be considered capable of accurate simulation of the air temperature and pressure in different periods of the mine.

## References

1. He, M., Guo, P.: Deep rock mass thermodynamic effect and temperature control measures. Chin. J. Rock Mechan. Eng. **12**, 2377–2393 (2013)
2. Li, H., Fu, K.: Some major technical problems and countermeasures for deep mining. J. Min. Saf. Eng. **23**(4), 468–471 (2006)

3. Huang, H.: Discussion on prediction of mine air temperature. Saf. Coal Min. **8**, 7–16 (1980)
4. Huang, H.: Statistical study on prognostication of mine air temperature. J. China Coal Soc. **3**, 51–58 (1981)
5. Hou, Q., Shen, B.: The prediction model of temperature and moisture transfer between tunnel periphery rock and air. J. Wuhan Univ. Technol. **19**(3), 123–127 (1997)
6. Yang, D.: Mine air heat exchange. Saf. Coal Min. **34**(9), 94–97 (2003)
7. Zhou, X., Shan, Y., Wang, J.: The unsteady thermal exchange between wall rock and airflow of roadway. J. Liaoning Tech. Univ. (Natural Science) **21**(3), 264–266 (2002)
8. Jeppe, C.W.B.: The estimation of ventilation and temperatures in deep mines. J. Chem. Metall. Min. Soc. S Afr. (1939)
9. 平松良雄,気流冷却坑内の研究, 日本鉱業会誌. **71**(803) (1955)
10. 天野勲三,マイクロ機の坑内通気設計システムの開発を利用する, 日本鉱業会誌. **102**(1185) (1986)
11. Uchino, K., Inoue, M.: New practical method for calculation of air temperature and humidity along wet roadway—the influence of moisture on the underground environment in mines (2nd report). J. Min. Metall. Inst. Jpn. **102**(6), 353–357 (1986)
12. Uchino, K., Inoue, M.: Improved practical method for calculation of air temperature and humidity along wet roadway-The influence of moisture on the underground environment in mines (3rd report). J. Min. Mater. Process. Inst. Jpn. **106**(1), 7–12 (1990)
13. Kertikou, V.: Air temperature and humidity in dead-end headings with auxiliary ventilation. In: Proceedings of 6th International Mine Ventilation Congress, Society for Mining, Metallurgy, and Exploration, Inc., Pittsburgh, pp. 269–275 (1997)
14. Moloney, K.W., Lowndes, I.S., Stockes, M.R., Hargrave, G.: Studies on alternative methods of ventilation using computational fluid dynamics, scale and full scale gallery tests. In: Proceedings of the 6th International Mine Ventilation Congress, Pittsburgh, pp. 497–503 (1997)
15. Zhang, S., Ke, J., Qin, Y.: Study on the prediction of air temperature distribution in overall mine ventilation network and a computer program for this purpose. J. China Univ. Min. Technol. **21**(3), 34–42 (1992)
16. Cen, Y., Hou, Q.: Mine Thermal Environment Engineering. Wuhan University of Technology Press, China, pp. 94–96 (1989)
17. Li, L., Wu, F.: Study on organization parameters method in ventilation design. J. China Coal Soc. **29**(5): 576–580 (2006)

# Part XVII
# Mine Emergency Planning

# Critical Review of Present Rescue Practices in Indian Mines: Suggestions for Effecting a Qualitative Improvement in the Existing Scenario

Aftab Ahmad[1](✉), A. K. Dash[2], A. K. Sinha[1], and
R. M. Bhattacharjee[2]

[1] Directorate General of Mines Safety, Dhanbad 826001, India
ahmadaftabdgms@gmail.com
[2] Indian Institute Technology (ISM), Dhanbad 826004, India

**Abstract.** In response to recent mine disasters and role of mine rescue services in Indian mines, Inspectorate at Directorate General of Mines Safety (DGMS, Dhanbad) conducted national workshop with mine emergency experts to investigate current needs and issues. Some of the issues include emergency response preparedness, Competency of persons selected in rescue services, Courses of Instruction and Practices prescribed for rescue trained person, Fitness of persons selected for rescue training, Scope of recue and recovery in surface and opencast operations, Rescue and Recovery operation in case of persons engulfed in underground strata failure, caught between extremities, sudden influx of smoke and gases etc.—Rapid transportation of injured miners to the surface, Basic and Advance firefighting skills in open and confined spaces, Training for Exploration and navigation in poor visibility and water hazards, First Aid Training and certification—refresher training in first aid and their periodicity, Still water diving training, Working over heights and training in dealing with huge boulders and debris, Mine Emergency response development drill programme for managers, control room members and rescue team members, Establishment of safe haven in Underground and Mine rescue contests (Zonal and All India). This paper undertakes a systematic review of the present rescue practices in India, in order to strengthen mine emergency rescue capabilities.

**Keywords:** Emergency preparedness · Emergency plan · Employee training

## 1 Introduction

When lives are in danger, mine emergency response systems must function rapidly and competently [1]. The orders of precedence of response actions in any mine emergency begins with the doctrine of self-escape than with first responder and finally the mine rescue team (aided rescue). Mining industry is one of the high risk based industry due to its dynamic nature. If there is a breakdown in self-escape and first responders are not successful, then the deployment of mine rescue teams under the control of joint

consultative committee on the surface is necessary for a safe rescue to be accomplished. An emergency preparedness, including developing crisis/disaster plans and training employees is essential for workplaces nowadays [2]. The mine rescue services in Indian mines play a very important role in management of emergency in a mine arising out of a disaster or a condition which is potentially disastrous. The rescuers are engaged during such emergencies for rescue of the person trapped belowground, emergency sealing of a mine or part thereof, locating problem site to control the situation and ascertaining causes, circumstances resulting in the accident/incident/unsafe condition and recovery of the mine or part thereof. The dilemma over the decision of deployment of rescuers and formation of a rescue team from amongst the rescue trained persons summoned at the surface of a mine, after a disaster is a difficult task for the officer- in charge of the rescue operation. Aging work force in Indian rescue services and its associated complications demands for review of the existing system in vogue. The discussion and deliberation supported by the safety perception survey during the workshop has provided motivation for evolving and framing suitable code(s) of assessment for rescue team emergency preparedness.

## 2    Mine Emergency Plan—Legal Issues

In exercise of the powers, conferred by clause (r) to (w) and clause (v) and (w) of section 58 of The Mines Act 1952, the Central government made The Mines Rescue Rules, 1985. Regulation 199A of the Coal Mines Regulations 1957 and Regulation 190A of the Metalliferous Mines Regulations' 1961 stipulates of an emergency plan for every mine having worked belowground for use in time of emergency. The emergency plan shall incorporate provision for mock rehearsals at regular intervals. Recently, a DGMS (Tech.) (S&T) circular no. 05 dated 2nd April; was also issued, detailing an integrated approach for development of Safety Management Plan for coal and metalliferous mines and also underlining the concept of emergency exercise.

## 3    Mine Rescue Services in Indian Mines: Issues and Concern

No amount of technological advancement in emergency preparedness will pay dividend, unless we trained our emergency response experts, in standardized skills training for a wide range of mine emergency response and prepare individuals who are in good health and have adequate level of fitness. After reviewing to the recent mining disasters and the existing mine rescue legislation, a national workshop was conducted with all the stake holder (representing Inspectors from DGMS, Head Safety, Rescue, Rescue Superintendents, Active rescue trained persons from fields, Researchers and Academicians from IIT-ISM and CIMFR, Dhanbad) of the mining company on 22.04.2016 under the ages of Directorate General of Mines safety, Science and Technology Division, DGMS, Dhanbad to investigate current needs and issues. Seventy-eight participants of the workshop discussed and deliberated on some of the issues which includes amongst others emergency response preparedness, real-life training capabilities and training facilities, medical fitness standards of the rescue trained persons,

Training in first-aid, Mine Rescue contests etc. Some of the critical areas requiring immediate interventions are:

- There is a need to develop a structured protocol for conducting mine rescue practices.
- There is a general requirement for more emergency response preparedness training, mobilization of emergency assets.
- There is a need to develop protocol for selection and training of rescue personnel in Indian mines.
- There is a lack of communication between control room and rescue teams.
- Standardization of rescue skills and practices needs to be done.
- There is overall shortage of mine rescue training facilities.
- Fitness and medical standards of rescue team needs to be relooked at, as their work is unpredictable, occurring at extremely short notice, usually physically and psychologically demanding.
- There has to be a real-time triggering of information to incident management team. (Emergency initiation protocol, Duties of manager and other competent persons in emergency to be re-defined).

## 4 Agenda for Future—Discussion and Deliberation

- Competency of persons selected for emergency Preparedness and response management.
- Courses of Instruction and Practices prescribed for rescue trained person.
- Fitness of persons selected for rescue training.
- Scope of Recue and Recovery in Surface and Opencast Operations e.g. slope failure, dump failure, fire- fighting, Machine related emergencies, caught between extremities etc.
- Rescue and Recovery operation in case of persons engulfed in underground strata failure, caught between extremities, sudden influx of smoke and gases etc.—Rapid transportation of injured miners to the surface before arrival of aided rescue from surface (confined space rescue).
- Basic and Advance firefighting skills in open and confined spaces (in fire gallery and outdoor burn pad).
- Training for Exploration and navigation in poor visibility and water hazards.
- First Aid Training and certification—refresher training in first aid and their periodicity.
- Still water diving is an important area of training to be considered for cases of drowning (dredging and pontoon operations).
- Working over heights and training in dealing with huge boulders and debris.
- Mine Emergency response development drill programme for managers, control room members and rescue team members (Managers duty in emergency).
- Establishment of safe haven in Underground.
- Mine rescue contests (Zonal and All India) should be made realistic (Practical Simulated Exercise).

| Sl. no | Parameters | Present criteria | International standards |
|--------|-----------|------------------|------------------------|
| 1. | Entry age | 21–30 yrs.—No exit ages (extension given up to 35 yrs. by special order) | There is a definite entry and exit age for a mine rescuer (20–45 yrs.) |
| 2. | Underground experience | Sufficient as certified by manager (1 yr., 2 yrs., 3yrs.) | Minimum underground experience specified |
| 3. | Medical fitness | As per standards laid down in schedule VI, certified by a Doctor | Elaborate and exhaustive medical standard of fitness prescribed |
| 4. | Suitability for rescue work with breathing apparatus | After examination and interview by superintendent of rescue station | After physical and psychological testing of person |

### 4.1 With This Backdrops Following Are the Comparative Statement Regarding Competency of the Persons Selected for Rescue Training

.

### 4.2 Courses of Instruction and Practices Given to a Rescue Trained Person

- 14 days of initial training [12 days with SCBA + 2 days with smoke helmet needs review to make a confident Rescue Trained Person (RTP)].
- Skills requirement for specific jobs needs to be prescribed (keeping in view application of rescue rule to surface and opencast operations).
- The training facilities shall have state-of-the art technology with projectors and animated films, videos, case studies of disasters/accidents/incidents etc.

### 4.3 Fitness of Persons Selected for Rescue Training

- In selecting members for a mine rescue team each individual should, amongst other requirements, be: (a) In good health and physically fit (b) Have good vision and Hearing
- Capable of performing long and arduous physical labor.

It is therefore important that each member is medically examined by a physician prior to commencing mine rescue training and annually thereafter (methodology to be developed) (Fig. 1).

Technical and tactical component of the fitness may be covered by developed Protocol

- There has to be developed a comprehensive protocol for medical examination of rescue personnel that may include amongst others: (a) Health Assessment (Assessment of cardiovascular variables, Respiratory variables, Gastrointestinal
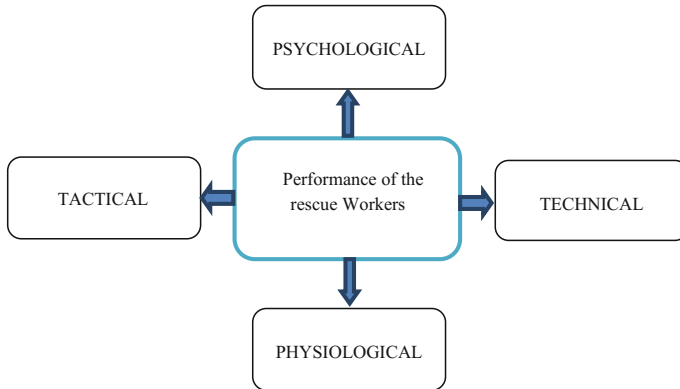
Fig. 1. The fitness component—mines rescue personnel [3]

variables, renal variables, Neurological variables, Hearing, Vision, Hematological indicators, Endocrine indicators, Musculoskeletal indicators, Behavioral indicators) [4]. (b) Physical Fitness Assessment (Aerobic fitness, Musculoskeletal fitness—To check both, exercise protocol may be developed).

### 4.4  Scope of Recue in Surface and Opencast Operations

- Scope of establishing fire gallery and fire suppression gallery to teach basic and advance fire-fighting skills in confined spaces, where mine rescue team can learn how to extinguish gaseous, liquid and solid fuel fire, evaluate firefighting tactics and handle fire extinguishers may be explored.
- Utilization of rescue training in the field of heavy object lifting and removal, vertical rope rescue training, rescue in confined space shall also be explored.

### 4.5  Rescue and Recovery Operation in Case of Persons Engulfed in Underground Strata Failure, Caught Between Extremities, Sudden Influx of Smoke and Gases Etc.—Rapid Transportation of Injured Miners to the Surface Before Arrival of Aided Rescue from Surface (Confined Space Rescue)

- Scope of training multiple task force (MTF) (selected mine personnel) (Other than RTP'S) in the field of navigation and working under apparatus, with tools and tackles for short duration and in reduced visibility in cases of engulfment of mine personnel during strata failure, drowning, smoke/dust/gas, their first aid and rapid transportation to surface may be explored. Issues relating to identification of MTF and compensation etc. may suitably be addressed.

## 4.6 First Aid Training and Certification—Refresher Training in First Aid, Training of the Trainers Etc.

- Initial training in rescue work should include courses for first aid training (covering courses as prescribed by St. Jones Ambulance Association).
- There has to be schedule for refresher training in first aid for all first aiders, so as to update their knowledge and skill in tune with the latest developments.
- Rescue trained personnel should be imparted specialized medical training (in the field of CPR, Bleeding, and Musculoskeletal injuries) and training in transportation of the injured miners. Training of the trainer in first-aid is also an important component of the first aid training programme.

## 4.7 Still Water Diving Is an Important Area of Training to Be Considered for Cases of Drowning (Dredging, Pontoon Operations and Similar Type of Operations Involving Risk of Drowning)

- Dredging and Pontoon operations involving risk of drowning, needs personnel with water diving skills also cases of inundation requiring services of rescue trained persons needs to be trained in water diving.
- There has to be made provision for still water training at the rescue stations (water pools with gallery situations).

## 4.8 Mine Emergency Response Development Drill Programme for Managers, Control Room Members and Rescue Team Members (Managers Duty in Emergency)

- Mine emergency response development exercise serves a vital role in achieving the purpose of improvement and better understanding of the skill and knowledge needed for decision making and the mobilization of mine rescue team. These drills at regular intervals improve their performance during actual emergency situations.

## 4.9 Application of Refuge Chamber or Safe Havens in Underground Coal Mines

- The basic principles of any emergency escape plan in an underground coal mine must be to seek to evacuate the mine with minimum complication and delay.
- As a part of above strategies use of safe havens (refuge stations/bays) and self-rescuers may be put in place (Mustering point $\Longrightarrow$ Refuge chamber $\Longrightarrow$ easy access to surface as the case may be) [5].
- It is the need of the hour to establish a robust emergency survival strategy for use in large hot and gassy mines or where there are significant gradients impeding passage out of the mine.

### 4.10 Mine Rescue Contests (Zonal and All India Mine Rescue Competition)

- Mine rescue contests serve a vital role in achieving the purpose of improvement of safety and health of miners.
- These competitions have served to assure that mine rescue teams are well trained and capable of responding to mine emergencies.
- The competitions may be made a practical simulation exercise such as a fire or explosion drill in a model underground mines earmarked for the purpose.

## 5 Safety Perception Survey

A safety perception survey was conducted amongst the various participants of the workshop. The survey consists of two sets of questionnaires. First set of fifty one questions consists of questionnaires about current needs and issues of the rescue team emergency preparedness and the second set consists of 15 questionnaires asking views of the participants on the emergency preparedness based on risk management logic. The questionnaires were a set of liker-type scales multiple choice items (Tables 1 and 2) and were distributed to the participants individually. The result of the perception survey was broadly categorized into 15 different heads highlighting awareness and perception of the participants on the following fields.

**Table 1.** Percentage respondents' distribution on emergency response preparedness and safety management plan

| Heads | n | TD (%) | D (%) | NS (%) | A (%) | TA (%) |
|---|---|---|---|---|---|---|
| 1. Present rescue services need change | 72 | 1.5 | 3.6 | 4 | 25.9 | 65 |
| 2. There is a need to standardized rescue skills and practices | 72 | 3.4 | 12.2 | 17.2 | 22.4 | 44.8 |
| 3. There is a requirement for training of members of emergency control room | 72 | 4.1 | 9.3 | 5.1 | 32.5 | 49.0 |
| 4. There has to be developed and structured protocol for conducting mine rescue practice | 72 | 3.3 | 8.3 | 6.1 | 37.5 | 44.8 |
| 5. There has to be developed and structured protocol for selection and training of rescue personnel | 72 | 0 | 3.4 | 5.1 | 12.5 | 79.0 |
| 6. There has to be developed and structured protocol for fitness and medical standards of rescue team members | 72 | 0 | 0 | 0 | 14.7 | 85.3 |
| 7. There has to be developed and structured protocol for Training in first aid, refresher training and training of trainers in first aid | 72 | 0 | 0 | 2.3 | 32.5 | 65.2 |
| 8. There has to be specialized training in the field of fire-fighting, ventilation effect of fire, vertical rope rescue, exploration in poor visibility, rapid transportation of injured, still water diving etc. | 72 | 4.0 | 5.3 | 5.1 | 32.5 | 53.1 |

**Table 1.** (*continued*)

| Heads | n | TD (%) | D (%) | NS (%) | A (%) | TA (%) |
|---|---|---|---|---|---|---|
| 9. Risk assessment and scenario planning may be the basic criteria for emergency response | 72 | 0 | 1.9 | 3.1 | 22.5 | 72.5 |
| 10. Every mine should have incident management team to deal with emergency situation | 72 | 0 | 0 | 0 | 7.4 | 92.6 |
| 11. Every district should have adequate arrangement for first responder like trauma kits, airbags, wire nut cutters, small hydraulic jacks, power hammers, emergency medicines etc. | 72 | 0 | 2.6 | 9.3 | 32.5 | 59.0 |
| 12. Incident management team should include incident controller, logistic controller, operation controller and technical service controller | 72 | 0 | 3.3 | 2.7 | 15.0 | 79.0 |
| 13. Safe havens/Refuge chambers should be established in each underground mine for self-escape | 72 | 4.1 | 9.3 | 5.1 | 32.5 | 49.0 |
| 14. There is a scope of recue and recovery in surface and opencast operations | 72 | 0 | 0 | 5.1 | 22.5 | 72.4 |
| 15. A comprehensive guideline should be developed to deal with emergency situation in a mine | 72 | 0 | 0 | 4.7 | 14.5 | 80.8 |

**Table 2.** Characteristic of the sample

| Characteristic | Category | Frequency | Percentage |
|---|---|---|---|
| Rescue trained persons | 1. Active | 52 | 72.2 |
| | 2. Non active | 20 | 27.8 |
| Age | 20–30 | 03 | 4.1 |
| | 31–40 | 17 | 23.6 |
| | 41–50 | 33 | 45.8 |
| | >50 | 19 | 26.5 |
| Education | Field candidates | 16 | 22.2 |
| | Diploma | 25 | 34.7 |
| | Degree | 31 | 43.1 |
| Position | Workers | 09 | 12.5 |
| | Supervisors | 07 | 9.7 |
| | Managers and assistant managers | 43 | 59.8 |
| | Agents and general managers | 13 | 18.0 |

# 6   Result and Discussions

Analysis made on the perception towards present day mine rescue services in Indian mines and current needs and issues reveals that most of them are agreed that there is a general requirement to strengthen mine emergency rescue capabilities and a

comprehensive guideline should be developed to deal with emergency situation by mine rescuers after summoned at the mine to avoid exposing rescuers to unacceptable levels of risk.

## 7    Conclusion and Recommendations

Mine operators often rely on mine rescue teams to save lives and property during an underground/aboveground emergency such as an underground fire, explosion or roof fall and other eventualities. It is extremely important that team members are provided with adequate exploration equipment and that training simulations are conducted in a realistic manner [5, 6]. Preliminary findings suggest that defining active rescue trained persons by restricting their entry and exist age and increasing their capabilities may help mine rescue teams be better prepared for mine emergencies. Our rescue stations may develop some of the discussed training facilities to provide skills training. These facilities are structured to be systematic, efficient; self- contained and designed to provide realistic training. Fitness standards of mine emergency experts need review as no two rescues are same. Performance limitations of the rescue workers affected by the biomechanical loads placed upon the body, high physiological costs (oxygen uptake in comparison to type of walking), reduced strength, decreased stability or balance and fatigue [4, 7]. Thus, rescue personnel should be selected with the physiological demands of the task in mind. Aging work force in rescue services and its associated complications, demands for review of the entry and exist age limits. Medical and Physical fitness assessment protocols are the need of the hours, that may be suitably incorporated at the later stage in the statute. Further studies are needed to more clearly define the mine rescue training; medical, physiological and psychological fitness needs and develop recommendations for improvement. An introspection of the present emergency management practices in Indian mines reveals that recommendations made as above, if incorporated, would be instrumental in effecting a qualitative improvement in the current system in vogue.

## References

1. Bealko, S.B., Aliexander, D.W., Chasko, L.L.: Mine Rescue Training Facility Inventory—Compendium of Ideas to Improve US Coal Mine Rescue Training. NIOSH, Pennsylvania (2010)
2. Rahman, N.A.A., Rasdan, I.A., Arifpin, M.M.: Analysis of the perception of occupational accident in mining and quarry sector towards safe and healthy working environment. Int. J. Curr. Res. Acad. Rev. (IJCRAR) (Special Issue-1), 95–102 (2014)
3. Department of Industry and Resources Document No ZMR002BF Fitness of Mine Rescue Personnel Guideline
4. Mine Safety Technology and Training Commission: Improving Mine Safety Technology and Training: Establishing U.S Global Leadership, pp. 55–77 (2006)
5. Margolis, A., Westerman, C.Y.K.: Underground mine refuge chamber expectations training: program development and evaluation. Saf. Sci. **49**(3), 522–530

6. Conti, R.S., Chasko, L.L., Stowinsky, L.D.: Mine rescue training simulations and technology. In: Proceedings of the Fifth Annual Conference of the International Emergency Management Society, pp. 453–464
7. Mott, M.L., Snyder, M.P.: Mine emergency responsiveness development program procedures. Min. Eng. **45**(10), 1258–1261 (1993)

# Risk Identification and Disaster Prevention and Control Techniques for Mines

Yong Feng Liu[1,2(✉)]

[1] China Academy of Safe Science and Technology, Beijing 100012, China
liuyf@chinasafety.ac.cn.com
[2] State Administration of Work Safety Supervision Key Laboratory of Mine
Goaf Disaster Prevention and Control, Beijing 100012, China

**Abstract.** By summing up the basic conditions and production safety procedures in Chinese mines, the paper conducts an in-depth analysis of major types of disasters caused by gas, roof falls, fires, flooding, outbursts, dust, thermal harm, ground subsidence, and slope instability and blowouts in mines. From the perspective of prevention and control of coal and gas outbursts, rock outbursts, gob fires, and tailings pond failures and water inrush disasters, it addresses outcomes from the latest research in risk identification and disaster prevention and control techniques in Chinese mines. Finally, with respect to existing problems, the paper proposes risk identification, measures for disaster prevention and control in country's mines and its development during the 13th Five-Year Plan period (2016–2020).

**Keywords:** Mine · Safety status · Risk identification · Disaster prevention and control · Development trends

## 1 Mine Risk Status and Features

### 1.1 Conditions of Mines in China

According to available statistics, by the end of 2015, there were 10,800 coal mines in the country, of which 1050 were large coal mines with an annual production of at least 1.2 million tons, an increase of 400 large mines since 2010. The proportion of overall output from large mines increased from 58 to 68% of the total. Small coal mines in 2015 numbered around 7000, at least 4000 fewer than in 2010. The proportion of output from small mines dropped from 21.6% down to about 10% of the total. Despite accounting for less than 20% of the output, these mines accounted for more than 70% of all accidents. More than from underground mines accounts for 95% of the total output of coal. Underground mines are distributed in 1260 counties in 26 provinces (municipalities and autonomous regions) across the country. Open-pit mines account for only 0.3% of total output, with production capacity accounting for about 5%. The proportion of open pit coal mines in the United States is 67%, and 80% in India.

By the end of 2015, there were 58,562 non-coal mines in China, of which 3787 were licensed and 6819 were under construction. Among the certificate holders, there were 34,035 metal and nonmetal mines. Of these, 2793 were non-ferrous metal mines,

2275 ferrous metal mines, and 28,967 non-metallic mines. According to mining statistics: 3748 of the metal and nonmetal mines are underground mines, and 28,287 are open pit mines. According to the construction scale statistics, there are 1119 large-scale mines (226 underground mines and 893 open mines), 2100 medium-sized mines (595 underground mines and 1505 open mines), 30,063 small mines (4927 underground mines, 25,889 open mines seat) and 8869 tailings dams. According to the storage capacity, there are 7 first class libraries, 207 second class libraries, 764 third class libraries, 2207 fourth class libraries, 5679 fifth class libraries, and 88.9% of the fourth and fifth class tailings banks. According to the degree of safety, the disease storehouse is 403, and the normal library is 8466. There are no dangerous depot and dangerous libraries.

## 1.2    Chinese Mine Safety Conditions

Since the "11th Five-Year Plan," with the continual expansion of national security science and technology investment, the continuous improvement of mine safety supervision and production safety situation, the number of accidents and the number of deaths have both dropped for 10 consecutive years. Among them, the non-coal mine "Eleven Five" to "Twelve Five" deaths fell 57.3%, as shown in Fig. 1.
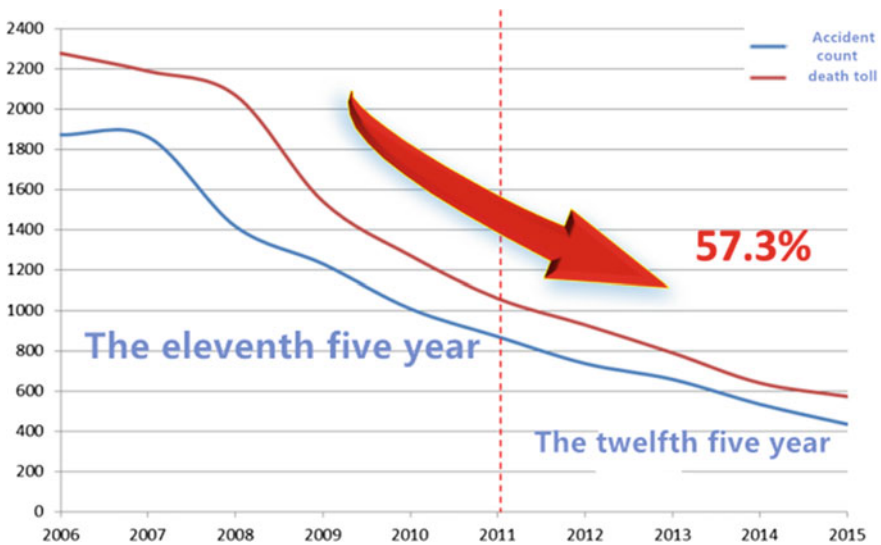


**Fig. 1.**  "Second five" non-coal mine safety conditions

Safety conditions in coal mines is the most serious concern among the industrial enterprises in China. The death toll is the highest among the major coal mining countries in the world. For a long time, the death toll from coal mines in China has accounted for 80% of the death toll in the world's coal mines. In 2015, there were 352 coal mine accidents in China with a death toll of 598, a decrease of 168 and 348,

respectively, from the previous year, representing a decrease of 32.3 and 36.8%, respectively. There were 35 major accidents with 157 deaths, down 13 cases and 42 deaths from the same period of the previous year, representing drops of 27.1 and 21.1%, respectively. There were 5 major accidents with 85 deaths, down 9 accidents and 144 deaths; 64.3 and 62.9%, respectively. No particularly serious accident occurred. The death rate per million tons was 0.162, down 36.5% on a year-by-year basis. During the "12th Five-Year Plan", the number of coal mine accidents in the country hit an average of 1197 with an average of 14 major accidents each year, down 64.4 and 53.3%, respectively, from the "Eleventh Five-Year" period.

Approximately 91% of China's coal mines are underground mines, and the underground mining conditions are the most complicated of the major coal-producing countries in the world. The average depth of coal mining in China increases by more than 20 m per year. With the increase in mining depth and production rates, the relative gas emissions increase by an average of 1 m$^3$ per ton per year, and the number of high-gas mines increases by 4% per year. The number of coal and gas outburst mines increases by 3% per year. Prominent mine disasters due to water inundations, fires, rock-bursts, and thermal hazards are increasingly serious, making the need for disaster prevention and relief more urgent.

In 2015, a total of 435 industrial accidents occurred and 573 people died in non-coal mines across the country, a year-to-year decrease of 99 and 67, respectively, and 18.5 and 10.5%, respectively. Among them, there were 20 fatal accidents with 89 fatalities, marking a decrease of 5 cases and 1 death, respectively, down 20.0 and 1.1%, respectively, over the same period of the previous year. The following year, there were 2 accidents and 31 fatalities, an increase of 2 from the previous year and 31 deaths, with no major accidents. The overall non-coal mine safety conditions in China maintained stable and improving development trends, but major accidents occurred in an upward trend, and safety conditions were still quite poor. Major accidents have occurred from time to time in non-coal mining enterprises, of which there were two serious accidents in Shanxi in 2008, accounting for a total of 326 deaths.

From 2001 to 2011, Chinese tailings dam accidents have trended upward, with a total of 67. Among these 67, 15 were fatal accidents and 360 deaths occurred.

## 1.3 Types and Causes of Mine Accidents in China

Coal mine disasters in China consist of gas disasters, roof disasters, mine fires, water damage, rock-bursts, dust damage, heat damage, etc., as shown in Fig. 2.

Gas accidents are the biggest danger. China's coal mines have the most serious coal and gas outbursts in the world. Mines with high rates of gas outbursts account for about 49.5% of China's total mines, and have the lowest initial protrusion depth and high gas pressure (13.8 MPa), accounting for about 40% of the world's total. An average of 3.30 people were killed in each accident. Among the 24 major accidents with more than 100 deaths, 21 were gas accidents, accounting for 90% of the deaths. In the past 10 years, there were 8 gas and coal dust incidents in 12 accidents involving 100 people. Among them, there were 6 incidents of over one hundred miners in 15 months from October 2004 to December 2005, as shown in Fig. 3.
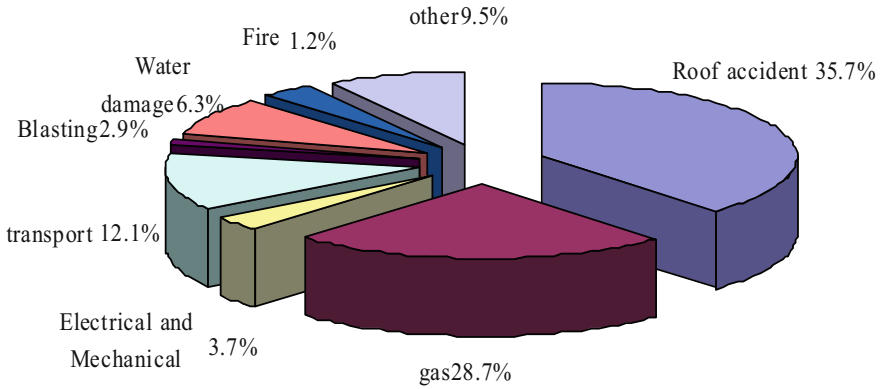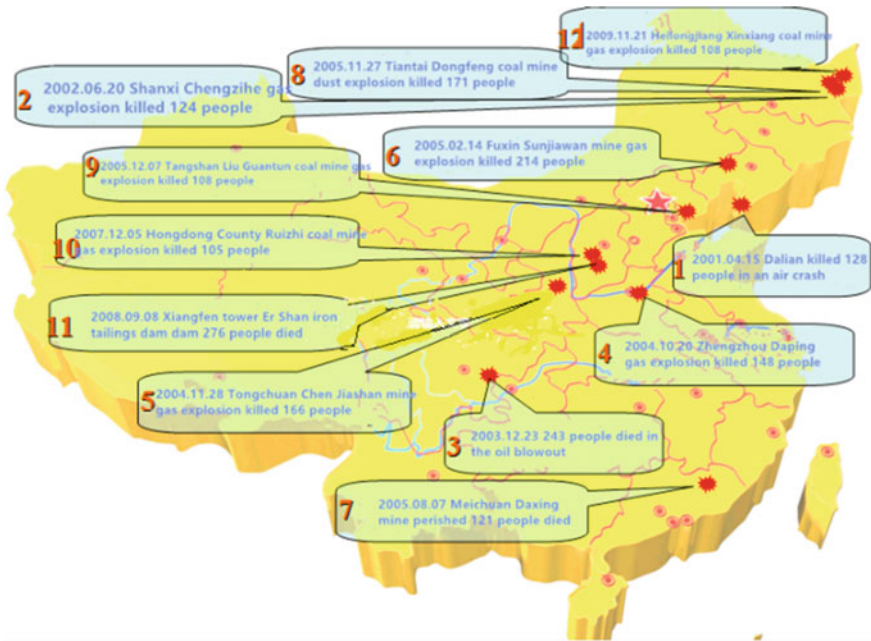
**Fig. 2.** Coal mine deaths by type of accident



**Fig. 3.** 12 accidents in the past 10 years

Roof accidents are the most widespread. These accounted for 55% of the total number of accidents, with the death toll accounting for 43% of the total number of deaths.

Most accidents occur in the mining face. The number of roof accidents and deaths accounted for more than 75% of total deaths. At the same time. the most serious damage from dust occurs in the mining face, where dust intensity is at a maximum.

Miners' pneumoconiosis is a serious condition, accounting for about 50% of pneumoconiosis cases nationwide.

Natural fire hazards are also a serious concern. All coal-producing areas are at risk for naturally occurring fires, with 72% of coal mine spontaneous combustion fires considered "more serious," and 51.3% of coal mine spontaneous combustion fires considered "serious." Fire problems are prominent in northern coalfields.

Coal dust explosions are widespread and seriously harmful. There are 532 coal mine dust explosion incidents annually in key state-owned coal mines, accounting for 87.4% of total incidents. Coal dust in small coal mines also poses a danger of explosion, of which up to 57.71% are highly explosive.

Water problems are complicated. In China's large and medium-sized coal mines, 25.04% of the coal mines with hydrogeological conditions belonging to complex or extremely complex types are threatened by ores of orogenic limestone in 80% of the coal fields in North China. The flooding accidents in the goafs and old kilns are on the rise, causing deaths and major accidents.

Impact pressure and thermal damage are also becoming prevalent in China's mines. The average mining depth of China's coal mines is 460 m, and is increasing by 10–20 m per year. There are 102 coal mines with different degrees of impact pressure; the maximum magnitude has reached 4.3. Thermal damage is becoming a major new disaster in coal mines with increase in mining depth, increase in temperature of surrounding rock.

China's non-coal mines face six major types of catastrophes: ground subsidence, downhole roof tiles, underground permeable water, deep rock-bursts, and slope instability and blowout, as shown in Fig. 4. Ground subsidence and collapse are common land-destruction problems in underground mining, and 80% of non-coal underground mines have serious surface subsidence problems.
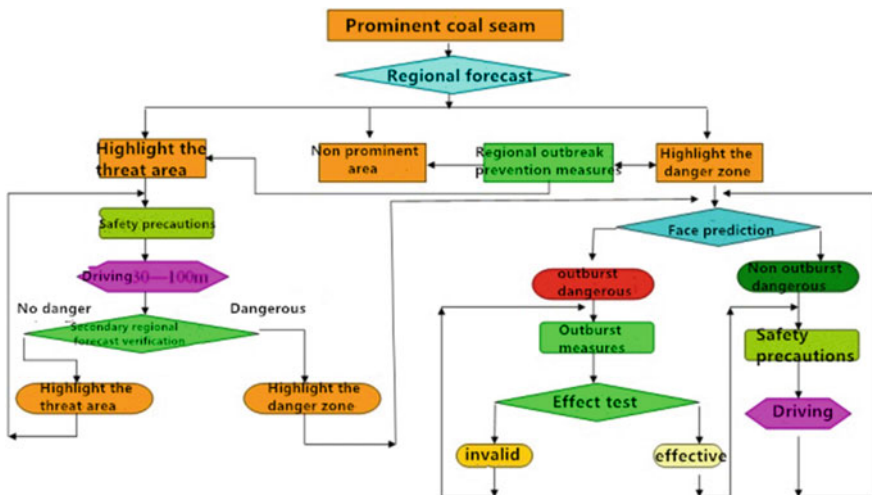


**Fig. 4.** Integrated outburst measures process flow diagram

Downhole roof tiles and collapses are the most frequent and widespread types of disasters in non-coal mines, resulting in the largest number of deaths. Collapses and the death tolls at the top of the mountain account for 44% of deaths occurring in non-coal mines.

The groundwater disaster in China's mines is also serious. The main manifestations of this are the inundation of water inrush, seawater intrusion, debris flow in the underground and the collapse of the ground. Water damage is the main type of damage in the goaf.

Non-coal mines are dominated by open-pit mines, and landslide hazards in slope and dump sites are serious. Many non-coal surface mines in China have varying degrees of open-slope stability problems. Firstly, dump sites in China conform to the Soviet Union's design pattern. Without any stable safety and evaluation procedures, the environment is exposed to various dangers; secondly, a large number of dumps are located in residential areas, forming a threat; thirdly, dumping in China is generally higher than in most countries, and as a result there are a large number of landslides and debris flow hazards.

50% of China's proven natural gas fields are high in sulfur, posing serious potential for the leakage of hydrogen sulfide and making exploitation difficult.

66% of the other mining accidents in China are a result of objects being hit or falling from above. The major accidents in China take place in underground mines. The types of accidents common vary by the type of mine; while collapse is the most common type of accident in open-pit mines, common to underground mines are poisoning and asphyxiation, permeation, poisoning and suffocation, tailings dam accidents, and dam-breaking events.

## 2   Mine Risk Identification and Disaster Prevention Technology Status Quo

### 2.1   Coal and Gas Outburst Disaster Prevention and Treatment

China's anti-collision technology can be roughly divided into three stages of development. The first phase was prior to 1950, when the main safety precaution to avoid casualties was shocking blasting. During the second stage, from the 1950s to the 1970s, the main measures to prevent outbreaks were regional and local preventative measures, which were supplemented by safety precautions. By the third stage, comprehensive outbreak prevention measures were added to highlight the forecast and the results of the test of the effect of the measures have resulted in the formation of a "four in one" integrated anti-outburst measure that highlights the prediction of the danger, the prevention of sudden impacts, the inspection of the effectiveness of measures, and the safety precautionary measures as shown in Fig. 4.

**Prediction Methods and Indicators for Coal and Gas Bursts**. Contact Prediction (Traditional Prediction): individual or comprehensive indicators such as gas analysis index (K1, $\Delta h2$), drilling dust volume, initial rate of gas emission from borehole and its attenuation and dusting temperature are determined by drilling holes. Though these

methods are currently widely used, they occupy a great deal of time and engineering to use and cannot forecast continuously. They also have an unpredictable delay.

**Non-Contact Prediction**. Various information generated in the excavation process is processed by sensors and hosts installed on the back of the working face, and the real-time continuous prediction is performed according to the processing result. The main methods are the gas emission dynamic index method, the acoustic emission detection method, the electromagnetic radiation method, and the three-dimensional seismic method, shown in Fig. 5.
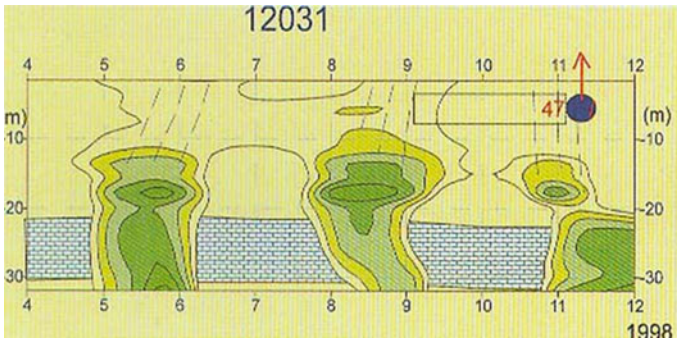


**Fig. 5.** Three-dimensional seismic structure detection

## 2.2 Rock-Burst Prevention and Control

Rock-burst is a sudden disaster caused by the dynamic evolution process of the deformation and fracture of coal and rock mass. The premise of effective control is accurate prediction. Real-time monitoring of the evolution of coal-rock impact is an important way to predict the disaster effectively. Rock-burst monitoring methods are divided into mining methods and geophysical methods, shown in Fig. 6.

During the deformation and rupture of coal rock, not only acoustic emission but also electromagnetic radiation is generated. The advantages of electromagnetic radiation monitoring and warning of coal rock impact are non-contact directional reception, small transmission by the coal rock fracture structure, ease of shield interference, the large amount of information obtained, and the coal and rock rupture process can be continuously monitored.

Using portable electromagnetic radiation monitors to identify key monitoring areas of mining faces, two or three receivers are arranged in the high-impact danger and concentration areas of the mining face, and the antenna faces the monitored area and moves forward with the working face. The results of real-time and early-warning monitors are transmitted to the ground-based center, shown in Fig. 7. When there is a risk of shock being detected, a timely warning should be issued and measures to deal with the danger should be taken.

The intensity of electromagnetic radiation or the number of pulses is a sensitive indicator of rock burst pressure, and when its size and rate of change exceed the critical
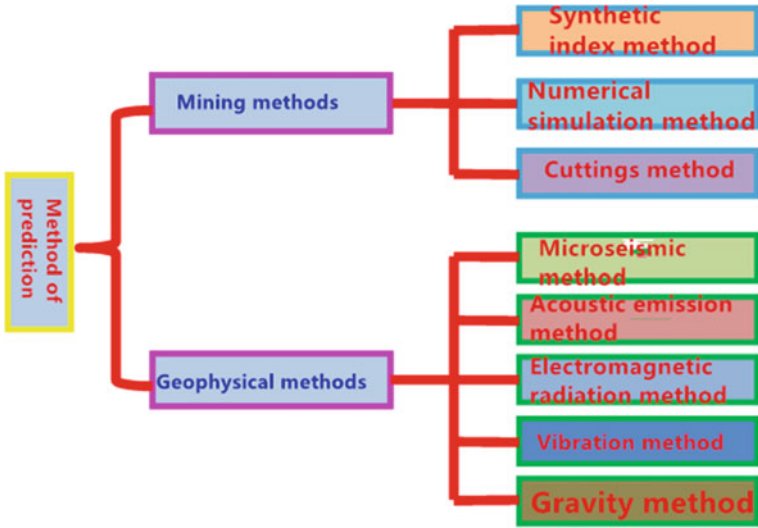
**Fig. 6.** Impact pressure prediction method
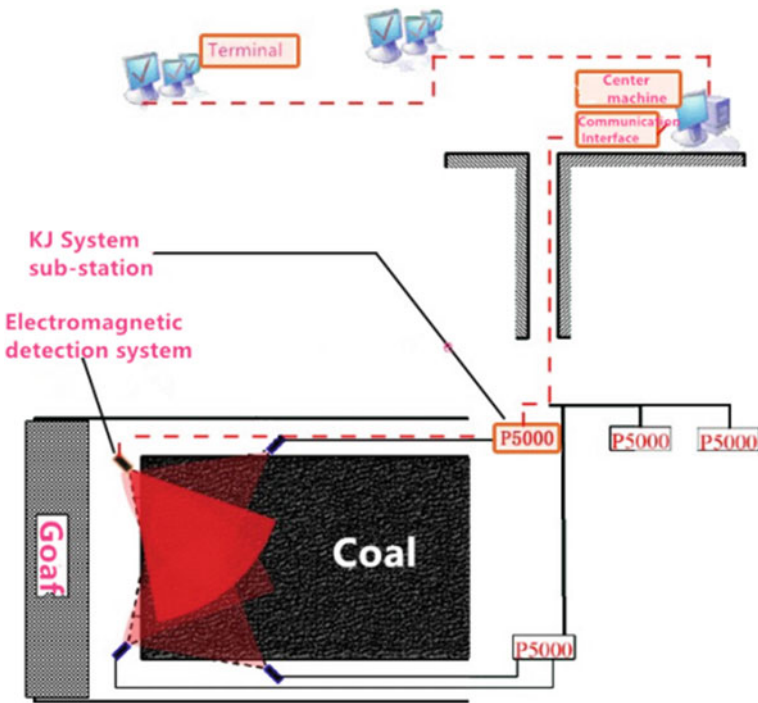


**Fig. 7.** Electromagnetic radiation monitor of the structure of rock burst

value, there is the risk of rock burst. According to the prediction criteria and a large number of experiments, the prediction method combining the critical value and the dynamic trend is determined to realize the classification pre-warning, as shown in Figs. 8 and 9 (Table 1).
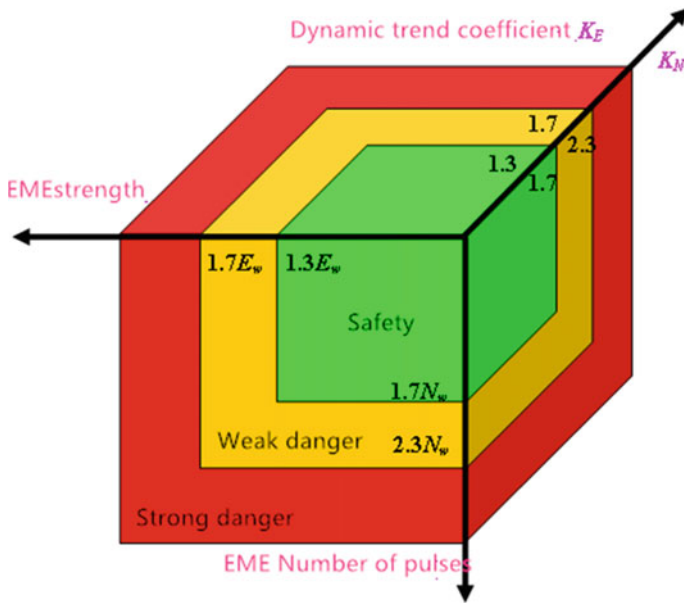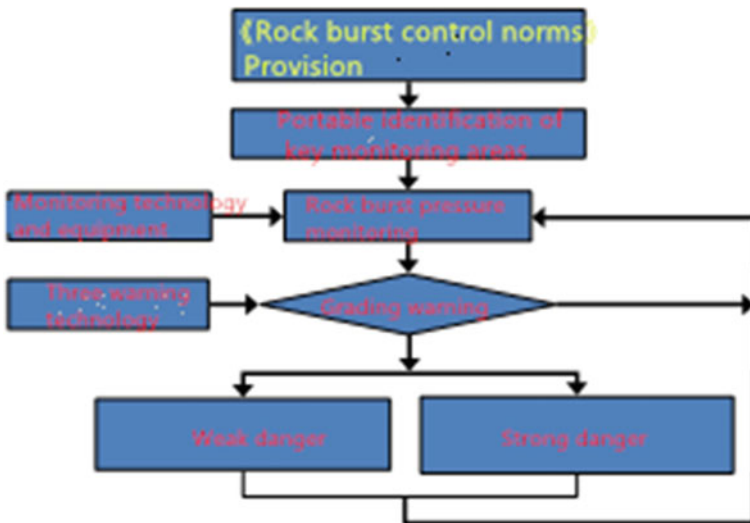


**Fig. 8.** Blasting grading warning



**Fig. 9.** Blasting grading warning process

**Table 1.** Blasting grading warning value

|  | No danger | Minimal danger | Strong danger |
|---|---|---|---|
| Threshold | E < 1.3Ew<br>N < 1.7Nw | E $\geq$ 1.3Ew<br>Or N $\geq$ 1.7Nw | E $\geq$ 1.7Ew<br>Or N $\geq$ 2.3Nw |
| Dynamic trend | KE < 1.3 KN < 1.7 | Or KE $\geq$ 1.3<br>Or KN $\geq$ 1.7 | Or KE $\geq$ 1.7<br>Or KN $\geq$ 2.3 |
| Measures | No need to adopt measures | Need to adopt measures | Dismiss or immediate action |

When the impact of pressure is dangerous, appropriate control measures should be taken: first, blasting pressure relief refers to the formation of the impact of the risk of coal, with a blasting method to reduce the degree of stress concentration of a solution to dangerous measures. Second, the induced blasting is under the condition of the danger of shock being detected; the blast with a higher dose is used to induce the rock-burst by manpower and force the rock-burst to occur at a particular time and place, so as to avoid more damage. The third and final step is to alter the physical and mechanical properties of coal seams, among them water injection, relaxation artillery and drilling tank relief pressure.

## 2.3    Goaf Disaster Prevention and Treatment

The key to the comprehensive management of hidden dangers in goaf is to correctly evaluate the stability of goaf, and the key to this is to find the shape of goaf. First, according to the limitations and working requirements of the survey area, a borehole is designed using transient electromagnetism, the high-density electricity method, the geologic radar and the delineation of the goaf through the geological tomography advanced prediction system in the downhole (Fig. 11). Then, the space-based 3D laser scanner is used to obtain the spatial shape of the goaf (Fig. 12) and to detect and identify hidden dangers in the unknown goaf in the research area (Fig. 10).

In order to strengthen the safe management of the goaf in the mine and prevent the occurrence of safety accidents caused by the instability of the goaf, it is necessary to implement the goaf-classified management method. According to their different levels, different goaf management requirements are proposed separately. Space risk classifications III and IV should be carried out for stability monitoring.

Site monitoring of goaf stability includes rock displacement monitoring, stress-change monitoring, acoustic-testing, acoustic emission-monitoring, and micro-seismic monitoring. Displacement is a very intuitive deformation parameter of rock mass; it can be obtained through accurate measurement methods, but also by simple measurement methods, such as the commonly used multi-point displacement meter, level gauge, extensometer, slide and so on. The displacement of hard rock mass is small, therefore requiring long-term monitoring. The rock mass is evaluated and predicted according to the measured displacement value and displacement velocity.

At present, the more advanced technology of the stability monitoring of the mined-out area in our country is the online monitoring technology for surrounding rock deformation supporting structures around the goaf, as shown in Fig. 13.
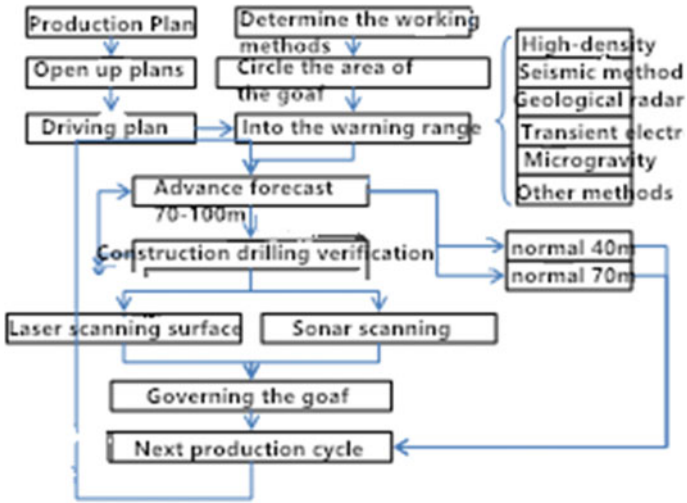
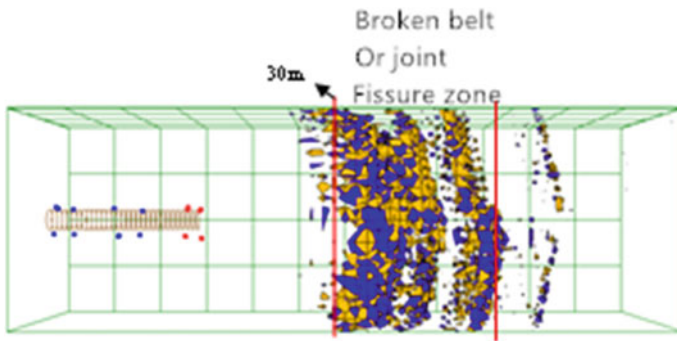**Fig. 10.** Mogong hidden dangers of the integrated detection process



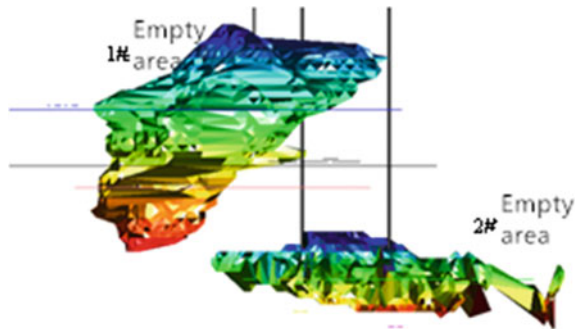**Fig. 11.** Geological forecast results



**Fig. 12.** Cals laser scanning space morphology, front view
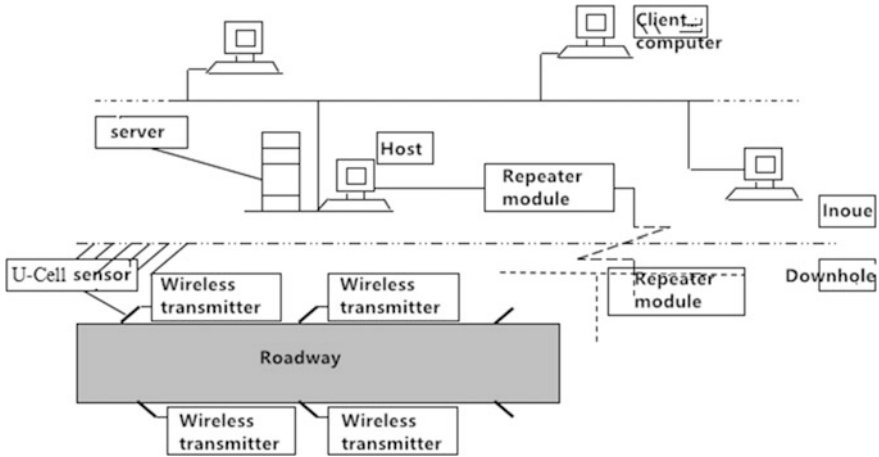
**Fig. 13.** Gobang stability monitoring system overall layout

## 2.4    Tailings Dam Disaster Prevention and Treatment

The key to the integrated treatment of hidden dangers in tailings lies in the correct evaluation of the stability of tailings reservoirs. The key to the correct evaluation of the stability of tailings reservoirs lies in the detection of tailings dam damage.

Tailings Reservoir Hidden Damage Diagnosis Technology is based on the high-density electrical method, methods that use geological radar and nuclear magnetic resonance to find the water, and other integrated geophysical methods to diagnose the distribution of tailings' hidden dangers and the parameters of the technology and methods. Based on the comprehensive geophysical exploration method, this paper puts forward the technology of rapidly diagnosing the hidden troubles of the tailings pond based on the comprehensive geophysical prospecting method, and determines the distribution scope, scale and depth of the loose sandstone and other hidden troubles and the position of the immersion line, as shown in Fig. 14.

Based on the analysis of the causes of dam break in tailings dams, the dam break mode and dam-break path of tailings dam are proposed. This is based on the preliminary determination, preliminary screening and fine screening of the dam-break risk indicator, the risk index system of tailings dam break. The risk assessment for tailing dam failure can be calculated based on the dam failure area (Fig. 15).

According to AQ 2030-2010 "Technical Specifications for Safety Monitoring of Tailings Reserves", the third-class tailings reservoirs should be installed using an online monitoring system. The tailings ponds online monitoring system can establish a comprehensive regulatory platform. When relying on this intelligent software system, when the monitoring data is abnormal, a timely warning shall be made to remind the enterprise to adopt the corresponding treatment measures and plans to ensure the safe operation of the tailings pond. The system structure consists of a dam surface displacement monitoring subsystem, a saturation line monitoring subsystem, a reservoir
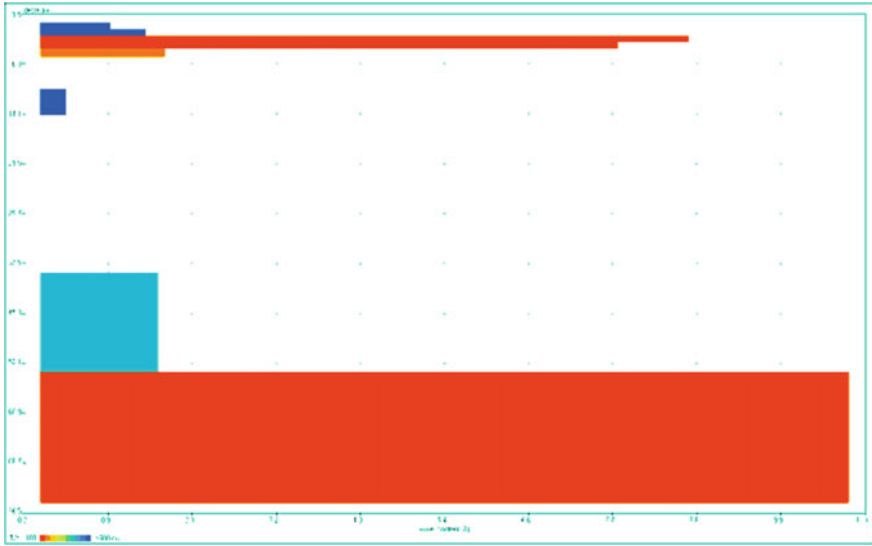
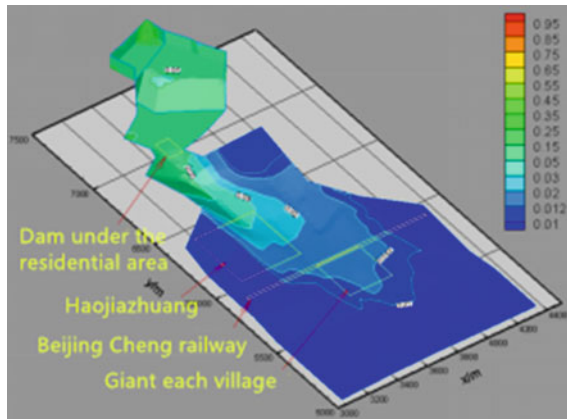**Fig. 14.** NMR water detector of tailings sinkline



**Fig. 15.** Tailings dam failure range

water level monitoring subsystem, and rainfall and other different sensing networks. The basic structure of the topology is shown in Fig. 16.

## 2.5 Water Damage Control

Through the analysis of the characteristics and causes of mine water hazards, the main ways to reduce mine water hazards are to strengthen the scientific detection of mine water hazards and comprehensive prevention and control during mining. While
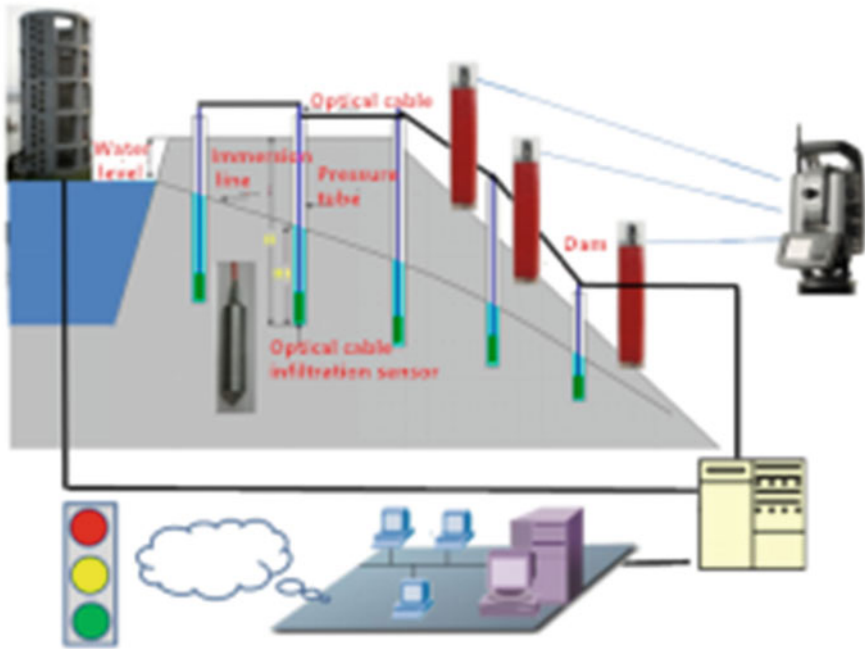
**Fig. 16.** Tailings dam disaster monitoring and early warning system diagram

exploration is the foundation, comprehensive prevention and control is the main node to avoid mine water damage.

Aqueduct and empty water zone, and fracture detection and analysis techniques make use of hydrophobic aquifers and aqueducts, which are probed with an electro-acoustic transmissometer; geologic structures are probed with a seismic prospecting tool and a combination logging tool; water levels are monitored through geological formations; energy spectra of environmental isotopes 3H, 14C in mines are measured using isotope mass spectrometry. The launch age was analyzed using ion and high-pressure liquid chromatography. The geologic tomographic imaging advanced prediction system and geological radar were used to predict the water damage in front of the tunnel face, as shown in Fig. 17.

In the process of mine production, we must adhere to the principle of "doubtful exploration, exploration first and then excavation", and formulate measures for water diversion after finding sources of water. Common mine water control technologies are shown in Fig. 18.

Hydrophobic step-down prevention and the control of mine technology is achieved through special engineering and technical measures under the conditions of artificial controlled advancement ahead of pre-dewatering or dredging pressure, thus reducing or eliminating the water body in the tunneling and production that is a threat to the mine, as shown in Fig. 19.
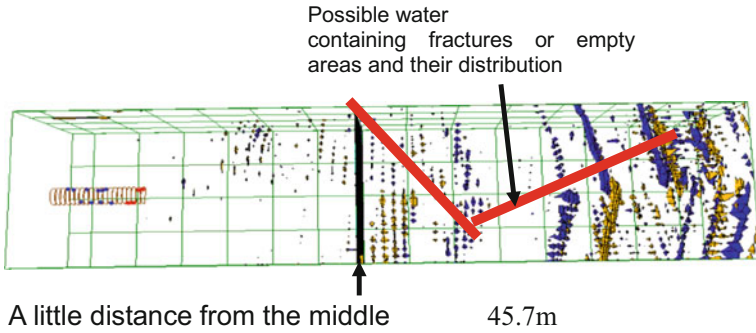
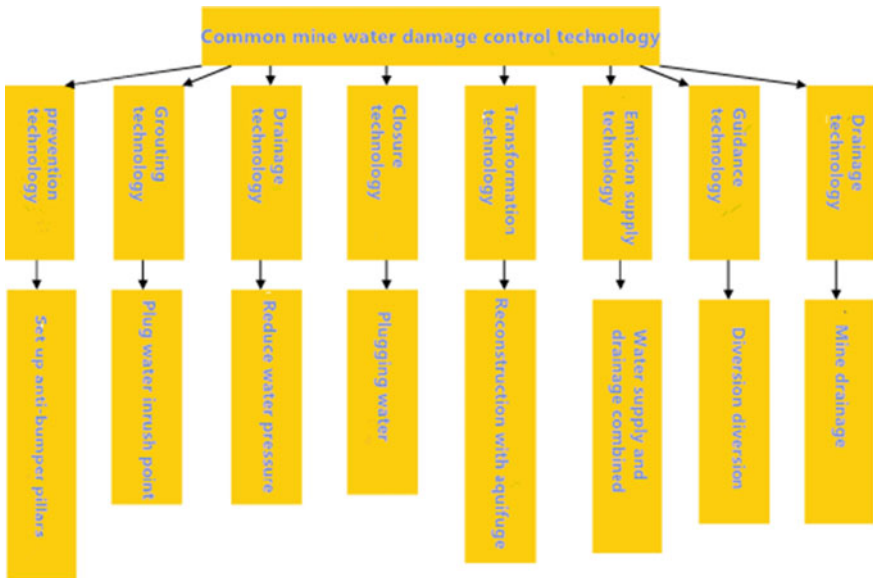**Fig. 17.** Advanced forecast system results



**Fig. 18.** Common mine water damage prevention and control technology
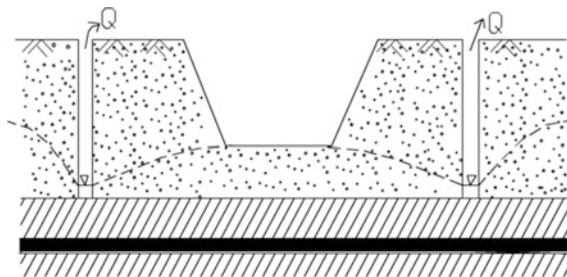


**Fig. 19.** Dry decompression scheme

Grouting water-blocking prevention and technology to control mine water damage is based on the particular types of hydrological and water hazards and characteristics of the low permeability slurry or aggregate into aquifers. The water-resisting layer in the gaps and fault zones render the rock impermeable, with the passage of water blocked. Water-containing voids reduce rock permeability and increase rock strength to achieve the purpose of water flow, as shown in Fig. 20.
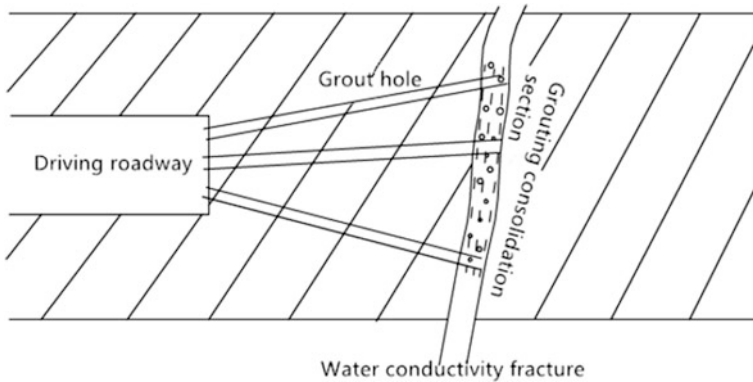


**Fig. 20.** Grouting plugging scheme

# 3   Questions and Outlook

## 3.1   Problem

In China, the average degree of mining mechanization is less than 50%. Accidents with at mines with a low degree of mining mechanization account for more than 70% of total accidents and more than 80% of deaths, with less than 5% due to mechanical and electrical accidents.

**Gas Prevention and Treatment**. Firstly, due to poor permeability of coal seams in China, pre-drainage of gas is difficult and there has been a lack of effective drainage technology. Secondly, soft and prominent coal seam drilling is difficult and there is a lack of advanced drilling technology and equipment, including long-hole directional drilling (1000 m). Thirdly, if "first pumping after mining" is not fully achieved, there is a mining pumping ratio imbalance, mining deployment adjustment is difficult, and there is also gas drainage, the use of higher costs, and the need for policy support. Fourth, there is a lack of safeguard technology for low concentration gas utilization.

**Coal and Gas Outburst**s. Firstly, there is not sufficient research on basic problems such as tectonic coal, gas geology and in situ stress, and the mechanism of coal and gas outburst is not completely understood; secondly, the number of postponed prominence of coal mines in China increases with the lack of effective technical countermeasures.

The accuracy of the value and the reliability of the indicator is not high. Thirdly, because the protective layer mining technology harsh conditions, the scope of application is limited.

**Mine Fires**. Firstly, technologies that detect hidden causes of spontaneous fire disasters and coal and sulfur spontaneous combustion have not yet been fully implemented, nor have indicators of fires and explosions. There is a lack of relevant control measures in the environmental conditions for auto-ignition.

**Dust and explosion prevention**. Firstly, high-efficiency dust removal technology and dust online monitoring technology and equipment need to be improved. Secondly, the correct application of passive flameproof sheds and solving the scaffolding quickly and easily move the method are finished. Thirdly, anti-jamming equipment, anti-interference ability and lag time should be improved.

**Mine water damage**. Firstly, the formation mechanism of mine water damage is not clear. Secondly, the old kiln water, limestone karst water distribution and rich water need to be mastered. Thirdly, there is a lack of effective detection and prediction of mine water damage technology.

## 3.2   The Thirteenth Five-Year Plan Development and Prospects

The period of the 13th Five-Year Plan is a crucial period for China to build a prosperous society and accelerate the transformation of economic development. It is also a crucial period for realizing the goal of "striving to achieve a fundamental improvement in our work safety by 2020" as set by the State Council. The following is the proposed development of mine risk identification and disaster prevention technology during the Thirteenth Five-year Plan Period:

1. Major coal mine safety hazard diagnosis, evaluation and treatment technology and equipment research and development are carried out. This mainly includes gas disaster research; coal mine gas dynamic disaster monitoring and early warning technology; gas coal dust explosion prevention and control technology; CBM drilling technology and equipment; CBM development technology; technology research and development; deep mine thermal harm control technology and equipment; underground disaster accident rescue and emergency evacuation key technologies and equipment; a new generation of mine emergency rescue respiratory protection technology and equipment; disaster accident simulation and simulation-testing technology and equipment; disaster relief communication technology research; coal mine underground environment-related equipment reliability testing technology.

2. Non-coal mine major security risk diagnosis, evaluation and management technology, and equipment research and development are carried out. This mainly includes research and development of key technologies and equipment for exploration; evaluation and treatment of large-area goafs; research and development of mine water source detection and prevention technologies and equipment; rapid diagnosis of tailings dam structures; risk assessment and hidden danger management technologies and equipment development; field landslide and induced debris-flow disaster prevention and control technology, and equipment research and

development; open-pit mine landslide detection methods, diagnosis and treatment technology and equipment research and development; early warning and control technologies for rock-burst in deep metal mining.

3. Carry out major hazard identification and evaluation, monitoring technology and equipment research and development. This mainly includes major mine-hazard identification technology; risk analysis and grading standards for major mine-hazard sources; monitoring indicator systems and early warning models for major mine-hazard sources; key technologies and equipment for monitoring systems for major mine-hazard sources.

4. Application of Information Technology in Mines: This mainly includes IOT technology in mine safety production and the application of key technologies and equipment; virtual reality in mine safety management and the application of key technologies and system development.

5. Drilling process geology, stratigraphic parameters detection technology, sulfur-based gas exploration and development of key technologies and equipment, emergency management and disposal technologies for sulfur-containing gas wells and other high-risk gas field development safety technology.

6. The theory and method of mine risk management, the theories and methods of emergency management of dangerous events and accidents, and other modern safety management theories and techniques.

## 3.3    Conclusions

The mines in China are great in number and distributed widely, occupying an important position in the development of the national economy. After combining data on the conditions of the mines in China and drawing on and introducing advanced technologies, the following suggestions are made to strengthen supervision and work safety procedures and ensure mine risk identification and the use of disaster prevention and treatment technologies:

Firstly, mining safety science and technology should be increased. China should improve safety and science and technology policies and input mechanisms, promote a technological innovation system that integrates production, education and research with the enterprise as the mainstay, and implement the project of "rejuvenating the science and technology" to address major mine hazards such as gas, water, fire, roof, rock-burst and other occupational hazards. Measures for prevention and control of these hazards should be taken, and basic research as well as the development of key technologies and major equipment should be undertaken. China should strive to make breakthroughs in disaster mechanisms and key technology research, and an integrative system for mine disaster prevention and control should be improved and perfected.

Secondly, the use of advanced and applicable technologies and equipment should be promoted. There should also be increased effort to eliminate outdated equipment and processes that do not comply with current safety standards. Technology and equipment are included in the national directory of industrial restructuring.

Thirdly, production safety professional technical services should be strengthened. Innovating and improving upon the management of safety production professional service agencies and establishing a comprehensive assessment system for classification

regulation and technical service quality is important. It is also important to invest in the professional and technical support functions of professional technical service agencies so that they can provide safety assessments, testing, inspections, safety signs, and training and consulting. The safety equipment industry should be developed to enhance the level of technology and equipment for prevention and control of major accidents such as gas control in coal mines and the technical level of safety equipment such as avoidance, safety monitoring and personal protection, and to cultivate safety equipment manufacturing enterprises with strong technical capabilities.

# References

1. "13th Five-Year Plan" for Coal Mine Safety (Draft for Comment)
2. Non-coal Mine Safety Production "13th Five-Year Plan" (Draft for Comment)
3. Xie, X., Tian, W., Wang, Y., Zhang, X.: The safety analysis of current situation and management counter measure on tailing reservoir in China. J. Saf. Sci. Technol. **5**(2), 5–9 (2009)
4. Jiao, Y., Duan, Y., Zhou, X., Kang Y.: The law of methane explosion induced by spontaneous combustion process in closed fire zone of coal mines. J. China Coal Soc. **05**, 850–856 (2012)
5. Xu, J., Zhang, F., Gui, H., Zhang, T.: Characteristics and experimental study of water conduction caused by fault activation due to mining. J. China Univ. Min. Technol. **41**(3), 415–419 (2012)
6. He N., Wang, G., Duan, M., et al.: Concept of medium-depth pipeline transportation in deepwater. Oil Gas Fields Dev. Pet. Eng. Constr. **36**(3), 33–38 (2010)

# Application and Development Trend of Radar Detection Technology in Mine Rescue

Hu Wen[1,2,3], Wen-qing Wu[1(✉)], Xue-zhao Zheng[1,2,3], and Jun Guo[1,2,3]

[1] School of Safety Science and Engineering, Xi'an University of Science and Technology, Xi'an 710054, China
1250806541@qq.com
[2] State Mine Emergency Rescue (Xi'an) Research Center, Xi'an University of Science and Technology, Xi'an 710054, China
[3] Key Laboratory for Prevention and Control of Coal Fires in Shaanxi Province, Xi'an 710054, China

**Abstract.** Compared with optical life detection, audio detection and infrared detection, radar detection can penetrate obstacles without any influence from external noise, light and other environmental factors and has much broader applications and brighter prospects. In this paper, through elaborating the principle of radar detection technology and application situation of radar detection system in detail, the advantages and disadvantages of the present radar detection system are analyzed, and the future development trend of radar detection technology is also discussed. This paper summarized the mine emergency rescue technologies and equipment. Hopefully, this can guide the future system development for mine disaster rescue.

**Keywords:** Emergency rescue · Radar detection · Life information detection Development tendency

## 1 Introduction

China is rich in mineral resources. As a critical sector of China's national economy, coal production accounts for 76% of the total primary energy production [1]. By the end of 2013, the proven reserves of available coal amounted to about 1.48 trillion tons, which accounted for 11.6% of the world's total reserves [2]. How to produce coal safely has always been the focus of scientific research on coal mine safety in the current scale of the coal industry. In recent years, accidents have still caused a great deal of casualties and loss of resources. Although there are some effective policies to control small and medium-sized incidents in coal mines with the joint efforts of China's government and mining enterprises, the situation of mine safety in production is still unacceptable. According to the statistics, there were about 198 people killed in mine accidents with more than 3 deaths from January 1st to December 3rd in 2016, of which 145 were killed from September to December, accounting for 73% of the year [3]. After the accident, the key to reducing casualties often depends on whether the rescue can be carried out quickly and effectively. However, the rescue process is often

restricted by the rescue equipment and technology. For example, the current mine emergency rescue equipment cannot fully satisfy the requirements of safe production need. There are still some gaps compared to foreign countries in mine rescue distress signals for the long-distance remote sensing, ultra-long-distance and ultra-penetrating ability of life detection technology and positioning technology [4]. Solving the above problems will make the future rescue work carried out more effectively.

Through the inspection of domestic and foreign mine rescue technology and equipment information, the authors compared and analyzed characteristics and shortcomings of these life detection equipment based on the status of their application. Among them, the radar detection technology based on the principle of electromagnetic wave reflection is taken as an example to summarize its characteristics of high resolution, strong penetration, low interception rate and strong anti-interference. The technique is based on the electromagnetic wave Doppler effect [5]. It can be determined whether there are trapped persons in the surveyed area [6] by analyzing the waveform displayed in the terminal, which makes it widely used in mine emergency rescue. Finally, through the application of radar detection technology in rescue, the authors analyzed the shortcomings of the existing radar detection system and discussed the future development trend of radar detection technology, which showed that it's still necessary to study and explore its application in mine rescue and continuously improve its effective detection range in active life detectors. It will provide valuable theoretical support and reliable practice basis for the research and development of mining radar life detector [7]. With the gradual development of high-precision positioning technology of miners, this will also provide effective information support for the mine emergency workers.

## 2 Rescue Features of Mine Disaster

It has been known that fire, flood, gas accident, roof accident and coal dust accident are the five major disasters in coal mine production operations, which seriously threatens the lives and safety of underground workers. When an accident happens in a mine, jam of the roadways and destruction of the original communication facilities in the mine usually occurs, which prevents the rescue workers from entering the disaster-stricken areas. The rescue headquarters cannot grasp the situation of the disaster areas and spot the trapped people in the mine timely and accurately, affecting the search and rescue of underground trapped personnel and scientific setup of rational program.

Underground emergency rescue generally has the characteristics of time-critical, decision-making based on fuzzy information and complex disaster state. The key to mine disaster rescue is the accurate positioning of personnel and timely search and rescue [8]. Therefore, emergency rescue decision-making needs the support of scientific and effective technical equipment. Developing various appropriate and effective mine life detection equipment will win valuable time for the rescue and trapped personnel according to different accident characteristics.

## 3   Existing Life Detection Equipment

Current life detectors generally include optical, audio, infrared, human body bioelectric field sensing and radar type [9, 10]. In the field of detector application and technology research, some countries have mastered comparatively comprehensive and mature technologies, such as the life detector of DKL company in the United States. It is based on the ultra-low frequency conduction technology, combined with advanced biochemical and DNA technology. The detector detection range in the open area can reach 500 m, while also ensuring a high detection accuracy. In China, with the improvement of science and technology, it has developed rapidly in the field of life detection technology, although it starts relatively late in the field of audio and video integration. A series of comparative studies have also been made to improve the technical theory and advanced equipment. Some common life detectors can be seen below the Table 1.

Analysis above Table 1 shows that, although the life detectors currently equipped in various countries contain different combinations, life detectors still have some limitations under the conditions of varying underground accidents. As one of the most advanced life detectors in the world at present, radar life detector can effectively enhance the capability of regional detection under adverse environmental conditions such as high temperature, high humidity and noise, and has played an important role in emergency rescue.

Among all the mine accident detection rescue systems, the application of China's life information drilling detection system has created the first successful case of the large-caliber drilling rescue in mine rescue history and also becomes the third successful drilling in the world rescue cases. The life information drilling detection system can be used for mine disaster areas and it was fully developed by the team of mine emergency rescue of Xi'an University of Science and Technology. It can transmit the detected information to ground command center through twisted pair and its transmission distance is 4 km away with the function of intake, detection, storage, display and playback of image, voice, temperature parameters and other multimedia signals. This team successfully applied "Life Information Drilling Detection System" to the rescue of the Pingyi gypsum mine collapse accident in Shandong province in December 2015 and provided visualized accurate information for the rescue process after the successful findings of 4 trapped miners [11]. The great progress in the rescue work was highly praised by all the societies in the country including the National Rescue Command Center and the Shandong provincial government [12].

After the analysis of the existing life detectors, it can be found that although the related technologies and equipment are relatively advanced in research and development, they still have limitations under various conditions:

1. Optical life detector: based on the principle of using light reflection for life detecting, its imaging is susceptible to smoke and other substances. The usage can be greatly affected if the environment filled with smoke and coal dust or the place the optical probe cannot reach.
2. Audio detector: the detector detects the life signal through a special sensor that senses subtle vibrations, such as the shouts of trapped persons and the sounds of beating objects like rocks, to determine and display the positions of the trapped

**Table 1.**  Comparison of life detectors

| Country | Name and model | Detection principle | Scope |
|---|---|---|---|
| China | Low-frequency secondary radar life detector | Radar scanning and sensing electric field | There is a body's respiratory motion |
| | Mine ultra-wide band intrinsically safe radar life detector | | |
| | YSR15 mine flameproof radar life detector | | |
| | LSJ-007 radar life detector | | |
| | Explosion-proof s-y-250 infrared life detector | Thermal radiation detection and imaging | There is also a heat radiation source |
| United States | Multi-listen audio life detector | Audio/video awareness | Audio and video from the human body can be heard or seen |
| | "Hawkeye" video life detector | | |
| | DELSAR video life detector | | |
| | SEARCHAM video life detector | | |
| | Mine intrinsically safe thermal imaging camera | Thermal radiation detection and imaging of human body | There is also a heat radiation source |
| | SC-HH5-T infrared thermal imaging life detector | | |
| | ISI3500 thermal imager | | |
| | ST01 human body search system | Crystal resonance | Chemical composition analysis of human cadaver |
| | DKL radar life detector | radar scanning and sensing electric field | There is also a body's respiratory movement |
| France | LifeHunter thermal imager | Thermal radiation detection and imaging | There are also thermal radiation sources in the human body |
| | All-in-one video life detector | Audio/video awareness | Audible and visual audio from human beings can be heard or seen |

persons. However, sound waves decay rapidly in coal and rock. They are sometimes not ideal for detection of people buried in rubble when they penetrate the underground ruins. Meanwhile, sound waves are also easily disturbed by noise.

3. Infrared detector: according to the infrared radiation principle of objects, it uses "infrared light" radiation around the environment and then captures the trapped persons' body heat radiation to determine the location of trapped persons. But the

infrared life detector cannot penetrate underground ruins and the detection results are not accurate enough in high temperature environment [8].

Compared with the above technologies, radar detection, as a technique of transmitting and receiving high frequency electromagnetic waves, can penetrate many kinds of obstacles without any influence from external noise, light and other environmental factors and has much broader applications and brighter prospects.

## 4   Applications of Radar Detection Technology

### 4.1   The Principle of Radar Detection

Ground penetrating radar transmits high-frequency electromagnetic waves ($10^6$–$10^{9\ Hz}$) in the form of wide-band and short pulses to the ground through the ground transmitting antenna [13]. When penetrating underground media, it encounters electric stratums and targets that have different electric potentials, part of the energy returns to the ground and is received by another antenna [14].

Ground penetrating radar, as an advanced geophysical equipment, has been widely applied in the field of engineering and rescue. According to the principle of geometric optical reflection, ground penetrating radar (GPR) is used to reflect and position the target by electromagnetic waves with judging and analyzing the physical characteristics of the target [15]. The detection method is based on the differences of the electrical properties of the medium to explore the internal invisible target body and different media interface to accurately determine and locate the target [16]. When the GPR is working, the pulse source generates a periodic nanosecond signal under the control of the radar host. It is coupled to the object under investigation by the transmitting antenna in a direction that is as nondestructive as possible. After the signal hits the non-uniform body or surface of the medium in the propagation path, it generates reflected signals and is received by the receiving antenna. Due to propagation paths of electromagnetic waves in the medium and the strength of electromagnetic fields varies with geometric forms and sizes of the medium, the echo amplitude and shape that receiver has received also change with it. Then the signal needs to be shaped and enlarged and go through other processing in the receiver. After that it's transmitted to the computer, the computer digitizes these waveform signals and records and stores them in the form of images. Finally, the characteristics and parameters of underground target body can be determined by studying the propagation characteristics of electromagnetic waves and analysis of the images, such as shape, size, orientation and others. The detection principle is shown in Fig. 1.

Radar life detector as a new type of life detection equipment, is based on the principle of reflection of electromagnetic waves. It combines radar detection technology and biomedical engineering technology. It's different from the traditional safety rescue detectors because it cannot be affected by ambient temperatures, hot objects and sound interference. It even can penetrate obstacles (such as reinforced concrete brick walls and debris flow strata, etc.) to detect the breath, body movement and other life characteristics of the buried life, and accurately measure the depth of buried life distance. It detects all kinds of fretting (such as movement and tremble) caused by human
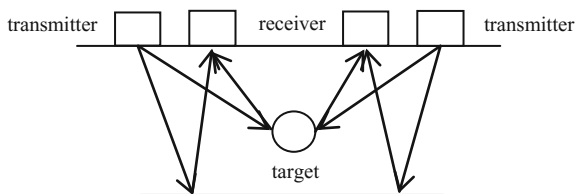
**Fig. 1.** GPR detection principle diagram

life activities and obtains the information about respiration and heartbeat from these fretting to identify whether there is life or not.

## 4.2    Applications of Radar Life Detectors

**Low-frequency secondary radar life detector**. Considering the high humidity in the coal mine, the conductivity of coal and rock will increase with humidity increasing. Therefore, the receiving coefficient of the receiver will be affected. The application of low-frequency secondary radar life detector will be able to solve this problem and detect the deep trapped. The system principle is shown in Fig. 2.
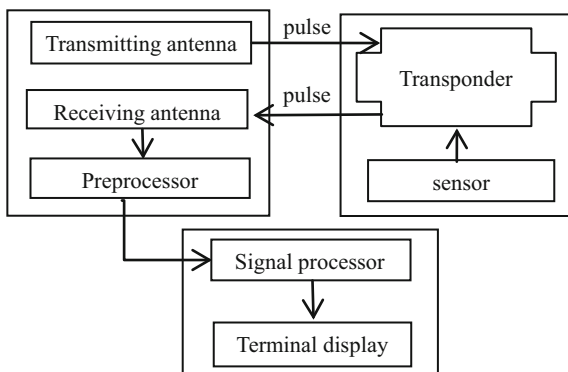


**Fig. 2.** System schematic of low-frequency secondary radar life detector

The secondary radar can track the active targets and its emission wavelength can be easily detected. During the operation, the signal of the radar is triggered by the interrogation signal, and then the radio transponder loads the data. After delaying for a fixed period, the transmitted response signal from the transponder is accepted by the radar as an echo signal. Compared to the one-way transmission of primary radar, the transmitting signal or response signal of secondary radar life detector radar is transmitted back to the receiver after a two-way transmission, so the transmission power and size of antenna can be reduced [8]. If the power is fixed, the corresponding detection

distance can be doubled theoretically, thereby it ensures the exploration of the trapped people and gains valuable time for rescue work.

**Ultra-wide band radar life detector in mine**. Ultra-wide band (UWB) radar refers to a radar whose working bandwidth is accounted for at least 25% of the total system center frequency. The typical UWB radar usually has a minimum central frequency of 500 MHz.

The UWB radar life detector, which utilizes the characteristics of nanosecond electromagnetic pulse with wide spectrum, strong penetrating ability, high resolving power and strong anti-interference ability, transmits nanosecond narrow-pulse electromagnetic waves from the ruin surface to the ruins to detect the remote sensing of human life activities (such as breathing, heartbeat, bowel movements, etc.). According to the repeated cycle changes of the echo pulse sequence after the wave is reflected by human body, the detector performs demodulation, integration, amplification, filtration and other procession to echo pulse sequence. Then, the detector puts the signal into the computer for data processing and analysis. After that, the corresponding life characteristics of the measured parameters can be obtained.

Intrinsically safe mine detector is commonly used today, which is based on the principle of UWB radar. The life detector system consists of intrinsically safe power, signal processing and control circuit, transmitter, receiver and hand-held terminal. The usage of intrinsically safe power is to prevent the discharge energy reaching the ignition energy in extreme cases. As a processing and control core of entire system algorithm, the integrated sampling output signal of receiver takes AD conversion in signal processing and control circuit. After becoming discrete digital signals, the in-phase and quadrature digital signals I(n) and Q(n) are output to the digital signal processor (DSP) for signal processing after digital orthogonal phase discrimination (I/Q separation). Then it can get the target distance and orientation information. DSP can send the target distance and orientation information to the hand-held terminal for display through the WIFI interface. In the meantime, in order to guarantee the synchronization control of the clock of the transmitter and receiver, the field programmable gate array (FPGA) sends out the high-speed logic time sequence control signal.

Actually, the transmitter of the system is composed of a triggering signal, an UWB pulse source and a transmitting antenna. The working process is as follows: the signal processing and control circuit generates a controllable digital trigger signal of the same frequency as an input signal of the UWB pulse source. Under the action, the UWB pulse source uses the avalanche effect of the avalanche triode to produce the nanosecond pulse, and finally it emits the pulse through the transmitting antenna. The receiver filters and amplifies the echo signal and performs integral sampling, and then sends it to the signal processing and control circuit. The system obtains the target distance and position information by processing the echo of the pulse signal. The system has the advantages of long detection range, high positioning accuracy, strong penetrating performance and good anti-interference ability. Therefore, the system can be widely used in emergency rescue of disaster areas in mines.

### 4.3 The Existing Problems and Development Direction

As most mine-based life detectors currently available are usually based on the radar detection of modulated linear frequency modulation continuous wave (LFMCW) and the usage of a computer as a terminal for signal analyzing, processing, and displaying. These often lead to the following problems:

1. Detection range is limited; speed and distance are prone to coupling [8] and the signal is susceptible to interference.
2. Using a computer as a terminal objectively increases the cost of the system, and causes the system to be too large and inconvenient to carry. At the same time, most of the analog signals are collected by the USB data acquisition card, which is a module. It can make some troubles to system structure optimization.
3. In mine accidents, the detection and extraction of life signals are still very difficult. On-site personnel and the environment may still interfere with signals, resulting in the detection effect of the existing radar life detectors very vague.

Of course, with the continuous development of positioning technology, high-precision development has been studied more and more. Some foreign companies have developed different high-precision positioning systems. The Ubisense UK developed a real-time location system (RTLS) combined TDOA (Time Difference of Arrival) with AOA (Angle of Arrival). It applies UWB technology to achieve high positioning accuracy in the challenging disaster-hit environments, and the high stability allows accuracy to 0.15 m. The positioning system is mainly used for indoor and outdoor environment. But the system cost is high, and the structure is more complicated. The nano RTL, a real-time positioning system from Nanotron in Germany, offers a maximum positioning accuracy of 0.6 m and a 3 m positioning accuracy even in complex environments.

In China, the high-precision positioning technology for miners still need to be further studied. In the special and complicated underground environment, the high-precision positioning technology on the ground cannot be directly applied to down-hole positioning. Faced with the urgent need of upgrading and updating of the existing down-hole positioning system, it is more urgent to carry out high-precision research on the orientation of underground miners [17–21].

## 5 Conclusion

Although the mine emergency rescue system is greatly improved, there are still urgent needs to conscientiously learn from the successful experiences and improve the emergency rescue technology and the performance of the equipment. Based on current situation of mine emergency rescue, it will need further integrate high and new technologies in various fields, integrate technology and equipment resources of various industries, build actual combat capabilities and strive to build a more efficient emergency rescue system.

# References

1. Zheng, X.: The Research of Mine-Visualizing Rescue Commanding Instrument. Xi'an University of Science and Technology, Shaanxi, pp. 1–6 (2005)
2. Wen, H., Guo, J., Jin, Y., et al.: Progress and trend of evaluation study on coal mine thermodynamic disasters in china. Saf. Coal Min. **47**(3), 172–174 (2016)
3. China Coal Education Network: 2015, 2016 coal mine accident statistics table [EB/OL]. http://www.xn–fiqs8sdpmo5ke0ah52dugc.cn/cinfocontent.php?id=4029 (2016)
4. Zhao, P., Hu, J.: Status analysis on rescue technology and equipment for personnel in difficulty in underground mine. Coal Sci. Technol. **37**(8), 38–45 (2009)
5. Zhao, W.: The Research on the Technology of Radar Life-Detection. National University of Defense Technology Graduate School, Hunan, pp. 7–28 (2009)
6. Xue, C., Liu, P., Song, W.: Design of radar life detecting for coal mine. Coal Mine Mach. **36**(4), 56–58 (2015)
7. Zhan, Q.: Exploration and Design of Active Life Detection Instrument for Coal Mine. Chongqing University, Chongqing, pp. 18–55 (2014)
8. Guo, J.: Safety Evaluation and Dynamic Prediction for the Rescue Operation After Mine Thermo Dynamic Disasters. Xi'an University of Science and Technology, Shaanxi, pp. 16–35 (2016)
9. Li, X.: Study of mine ultra wideband radar life detector. Coal Mine Mach. **36**(6), 96–99 (2015)
10. Tang, J., Gao, G., Zhao, J.: Radar life detecting system for coal mine rescue. Colliery Mech. Electr. Technol. **2**, 47–49 (2008)
11. Wen, H., Deng, J., Wu, J., et al.: Life information drilling detection system. Chinese Patent: CN201120005791.9, 2011-8-3
12. Lv, Y.: The life detection system of Xi'an University of Science and Technology: providing information security in Pingyi gypsum mine rescue. Shaanxi Daily, 2016-2-1(01)
13. Willett, D.A.: Accuracy of ground-penetrating radar for pavement-layer thickness analysis. J. Transp. Eng. **132**(1), 96–103 (2006) (ISSN 0733-947X)
14. Wang, J., Lv, J.: Technical application of applying ground penetrating radar to the detection of obstruction. Geol. Explor. **39**(3), 84–86 (2003)
15. Li, H., Li, X., Guo, L.: Application of ground penetrating radar in advanced forecast of mine tunnel. Chin. J. Undergr. Space Eng. **7**(2), 1742–1752 (2011)
16. Liu, C.: Research on the mechanism of probing cavity with ground penetrating radar and analysis on application examples. Chin. J. Rock Mech. Eng. **19**(2), 238–241 (2000)
17. Zhang, F.: UWB radar life detector system design and test. Fire Sci. Technol. **35**(7), 967–969 (2016)
18. Yang, X., Chang, J., Liu, T., et al.: The key technology research on a new radar life detector. Fire Forum **5**, 46–47 (2016)
19. Zhou, X., Chang, W.: Coal Mine Emergency Disaster Rescue Technology. China University of Mining and Technology Press, Xuzhou, pp. 155–183 (2007)
20. Yuan, Z.: Automatic Target Detection Technology of Ultra-Wideband Through Walls Radar. National University of Defense Technology Graduate School, Hunan, pp. 27–38 (2012)
21. Ke, B.: Study on High Accuracy Personal Positioning Technology in Mine Tunnel. University of Electronic Science and Technology of China, Sichuan, pp. 15–30 (2014)

# Response Characteristics and Monitoring-Warning of Acoustic-Electromagnetic Signals in Coal Roadway Heading

Enyuan Wang[1,2,3(✉)], Zhonghui Li[1,2,3,4], Liming Qiu[1,2,3], and Xiaojun Feng[1,2,3]

[1] State Key Laboratory of Coal Resources and Safety Mining, China University of Mining and Technology, Xuzhou 221116, China
`weytop@263.net`
[2] Key Laboratory of Gas and Fire Control for Coal Mines, China University of Mining and Technology, Xuzhou 221116, China
[3] School of Safety Engineering, China University of Mining and Technology, Ministry of Education, Xuzhou 221116, China
[4] National Engineering Research Center for Gas Control, China University of Mining and Technology, Xuzhou 221116, China

**Abstract.** Accurate prediction of coal and gas outburst risk is essential for outburst prevention and control. In this paper, the evolution law of electromagnetic radiation (EMR) and acoustic emission (AE) in the process of deformation and rupture of coal and rock are analyzed. Then, the characteristic laws of EMR and AE signals in coal roadway during the driving process of Jiulishan Coal Mine are studied. The critical values of acoustic and electromagnetic monitoring and warning is solved using the fuzzy pattern recognition method. Results show that: (1) The change trending of AE and EMR signals is consistent with stress level. However, there are abrupt changes in the acoustic and electromagnetic signals before the stress peak. The degree of signal fluctuation is significant. (2) EMR is mainly produced by rheological and frictional deformation after coal body ruptures, while AE is mainly caused by the rupture of coal and rock. The intensity and pulse of EMR can better respond and early-warn the danger of coal and gas outburst during tunneling. (3) By using fuzzy pattern recognition method, the critical values of acoustic and electromagnetic monitoring and warning can be solved. It is more reliable to predict the outburst danger when the membership degree $\mu_A(x_0)$ is 0.6–0.8.

**Keywords:** Roadway · Heading · AE · EMR · Monitoring · Warning

## 1 Introduction

Coal and gas outburst (referred to as the outburst) is a sudden occurrence of coal and gas from the coal ribs to the mining space during mining [1, 2]. Coal and rock mass containing high-pressure gas rapidly lose its stability when accumulated energy reach a critical extent. This process leads to roadway collapse and release of huge energy, due to complex nonlinear dynamics [3, 4].

In monitoring, early-warning, prevention and control of coal and gas outburst, there have been positive developments resulting in forecasting indicators. Among them, the traditional forecasting indeices include gas desorption index $\Delta h2$, drill cuttings amount S, borehole gas emission initial velocity q with comprehensive index R and other static indices. The disadvantage of drilling method is its complex operation, heavy workload, affecting advance speed, and the real-time regionalized monitoring cannot be realized. It can only display the coal body static information throughout the entire drilling process, a non-continuous static information that is difficult to reflect the entire picture. The amount of information obtained is limited with low prediction accuracy, which is proven by low index outburst and delay outburst. With the development of technology, the dynamic continuous monitoring method (e.g., EMR and AE) is applied in the monitoring and prediction of coal and gas outburst [5–8].

According to the characteristics of coal and gas outbursts during coal roadway excavation, it is essential that an integrated, real-time, automatic, positioning and quantitative monitoring and warning of coal and gas outburst be developed. At present, there is a big gap between the demand and present technologies [9]. During the coal and gas outburst in coal tunneling process, the corresponding EMR and characteristics of AE signals are still not clear. The models used for the acoustic-electromagnetic warning of coal and gas outburst are still less than ideal. Based on this, the acoustic-electromagnetic monitoring experiments of coal and rock are carried out in the laboratory. The evolution laws of EMR and AE in the process of deformation and rupture of coal and rock are analyzed [10] and EMR and AE signals characteristics in coal tunneling process are studied through statistic research at Jiulishan Coal Mine. Finally, based on experimental research and field applications, critical value of acoustic and electromagnetic monitoring and warning are solved by using fuzzy pattern recognition method. It is of great practical significance to further develop the predictive method of acoustic-electromagnetic monitoring and warning, and to improve the accuracy of predictions and ensure the safety and efficient production of coal mines.

## 2 Experimental Study on Acoustic and Electromagnetic Characteristics of Coal Samples

### 2.1 Experimental System

The experimental system is shown in Fig. 1. Loading system uses YAW electro-hydraulic servo pressure testing machine system. The system can achieve constant loading, with an acceptable accuracy for loading control and data analysis. The maximum load stress can be up to 3000 kN. The acoustic-electromagnetic data acquisition system uses a CTA-1 multi-channel data acquisition system from Physical Acoustics Company. The system consists of preamplifier, filter circuit, A/D conversion module, waveform processing module, computer and other components. It enables parameter setting, signal acquisition, signal A/D conversion, data storage, graphics display and other functions. Based on its high-speed sampling capability, spectrum analysis of AE and EMR waveform acquisition and post-processing data processing can be achieved.
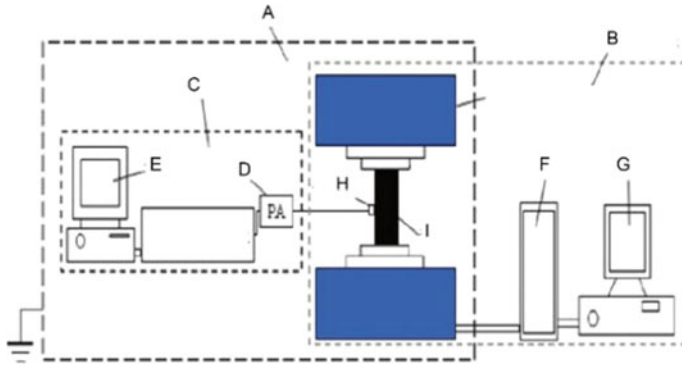
**Fig. 1.** Experimental system diagram. A = shielding room; B = YAW loading system; C = acoustic-electromagnetic data acquisition system; D = preamplifier; E = PC; F = control device; G = control host; H = sensor; I = specimen

## 2.2 Experimental Results Analysis

**Uniaxial Compression Process**. The standard sample of raw coal in Jiulishan Coal Mine is used for uniaxial compression test with a loading rate of 50 N/s. The experimental results are shown in Figs. 2 and 3.
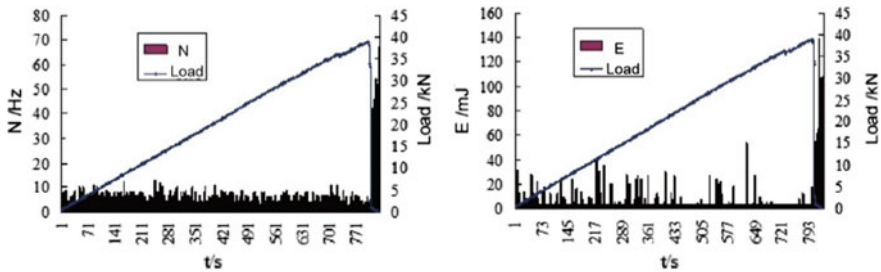


**Fig. 2.** EMR-stress curves under uniaxial compression
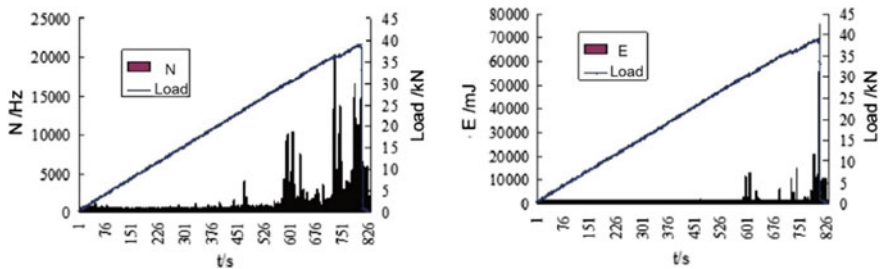


**Fig. 3.** AE-stress curves under uniaxial compression

The EMR and AE signals generated during deformation and rupture of the coal body increase with the increasing loading, showing a good correspondence with the stress. Before the sample is loaded near the load peak, the EMR and AE signals have abnormal enlargement, and the signal fluctuations are more intense. EMR and AE signals are very rich during the entire loading process. AE and electromagnetic signals respond well to micro-cracks or large ruptures in coal, even during the deformation process, and have obvious rheological characteristics.

**Hierarchical Loading Process**. The experiment of grading and loading raw coal samples from Jiulishan Coal Mine was simulated. Force control is applied with a loading rate of 50 N/s. When the load rises to 10 kN, the stress is maintained for 5 min. After that, it continues to load at a rate of 50 N/s until the specimen is destroyed. The results are shown in Figs. 4 and 5.
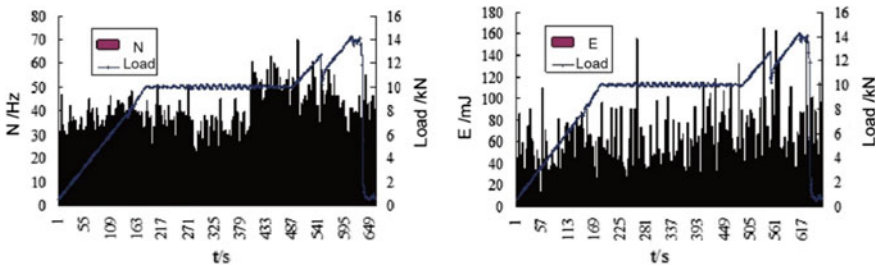


**Fig. 4.** EMR-stress curves during grading loading
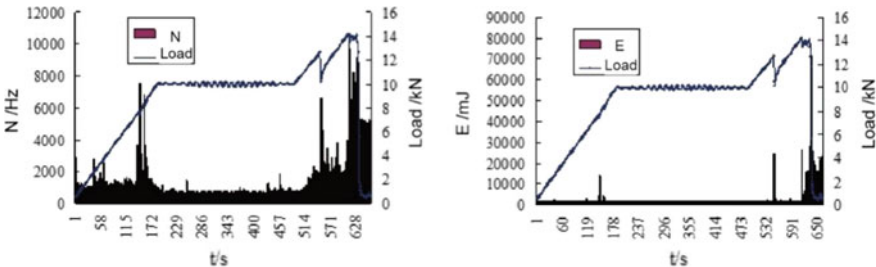


**Fig. 5.** AE-stress curves during grading loading

From Fig. 4, the EMR of coal samples generally increases with the increasing stress. The EMR signal has a sudden change before the peak load, and fluctuates unevenly. During the first stage of loading, the EMR basically increases with the increasing load, and it also has a good response to the expansion of tiny cracks. The value of EMR rapidly increases in the later period, indicating that the coal body creeps under constant stress condition. Therefore, coal and gas outburst are affected by coal stress, physical and mechanical properties of gas and coal, as well as the time factor. After the constant loading stage, the deformation and rupture of coal samples gradually

aggravate with the increase of loading. The EMR signal responds well until the coal body is unstably broken.

AE also shows a good response to staging loading. The AE signal counts and energy positively correlated with the loading level. However, regarding the constant loading stage, there are more EMR signals and fewer AE signals, which proves the correlation between AE and rupture of coal sample again.

## 3 Response of EMR When Coal Outburst

Figure 6 shows the results of the EMR test conducted during the excavation of the No. 16 Seam Downhill Transportation Lane from June 27 to August 11 (between 35 m → 62.8 m). During this period, we conducted a total of 15 tests, in which 7 tests (or 46.67%.) exceeded the standard level. The result ($\Delta h2 = 340$ Pa) shows that the coal seam is in significant danger. The intensity of EMR is 61 mV, and the value of EMR is significantly increased, which is completely consistent with the danger of coal. On 3rd July, we constructed 45 emission bored holes in the roadways, the result shows that the outburst danger has not been eliminated. Until 12th July, the forecast value returned to normal. In the meantime, the value of EMR dropped to a minimum on the 5th July but increased again on 8th July, indicating that the coal body was still not stable with regard to stresses. On 12th July, the value of EMR was still relatively large, which is inconsistent with the forecast result of the conventional index.
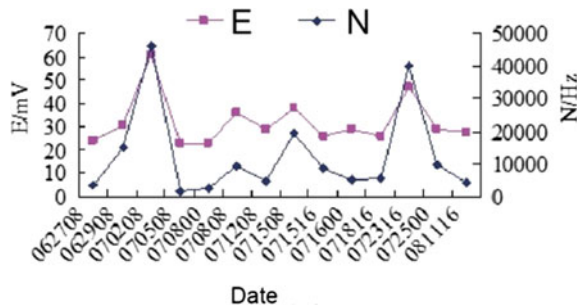


**Fig. 6.** The 16th coal seam EMR signal

On 15th, 18th, 20th and 23rd July, there was a continuous overhang for the conventional indicators, indicating that the zone is still in obvious danger. The intensity of EMR remained above 26 mV and reached the maximum on 23rd July, indicating that the EMR is very sensitive to the slightest change in stress. Despite the intensification of local outbreak prevention measures, the conventional forecasting indicators declined in a short time after the measures, but the EMR values remained high, which proved that the outburst danger of coal still remained. The reason for the discrepancy between the prediction result and the conventional index may be that the monitoring range of the

EMR is far away from the drilling method. The received signal includes all the information of the stress relief and concentration zones.

## 4    Discussion on the Critical Thresholds of AE and EMR

The current prediction of the critical value of coal and gas outburst is determined by statistical method. EMR and AE prediction of coal and gas outburst should eventually be used in the critical value form. Due to the difference in physical properties and geological conditions of coal and rock in coal mines, the level of acoustic and electromagnetic signals would also be different. In addition, the complicated factors affecting the coal and gas outburst lead to the critical value determination unpredictable. The critical value was determined on the basis of at least 50 datasets and solved by the fuzzy pattern recognition method.

According to the fuzzy set theory, when the membership degree takes 0 or 1, the fuzzy set will appear as a common set, and the prediction result has fuzziness no longer. There are only two situations: no outstanding danger at all or inevitably occur prominently. Only when the degree of membership is in the interval of (0, 1), the prediction result will be uncertain. As the membership degree increases, the prominent risk increases. In general, when the membership degree is taken as 0.5, the forecast result is between the prominent danger and no prominent danger. At this time, the forecast result is the most ambiguous, and the critical value is not reliable completely. According to the field experience, when the membership degree is between 0.6 and 0.8, the prominent danger is more reliable. Taking 0.65 as an example, the critical value of EMR intensity of coal and gas outburst for the 14141-transport roadway is calculated to be 26 mV. The critical value of the pulse number is 4874 Hz. Using the same method, the critical AE intensity for the 14141-transport roadway is 38 mV and the pulse threshold is 276 Hz.

Therefore, the critical value of EMR intensity for the 16th coal descending roadway is 26 mV, and the critical value of the number of pulses is 2906 Hz. Using the same method, the critical value of AE intensity of 16th coal descending roadway is 43 mV and the pulse threshold is 225 Hz.

## 5    Conclusion

(1) The AE and EMR signals have a same trending for stress in the whole process of deformation and rupture of coal samples. It increases with the increasing stress basically; before the stress peak, the acoustic signal has varying degrees of mutation, the signal fluctuates significantly. After the main rupture, the EMR increased firstly and then decreased with the decrease in stress sometimes. The corresponding relationship between AE and rupture will decrease rapidly after the main rupture. (2) EMR of coal body is mainly caused by coal body's rheological behavior during tunneling. Compared to conventional indicators, EMR intensity and pulse can better respond and warn the dangers of coal and gas outbursts. (3) The fuzzy pattern recognition method can solve the critical value of the acoustic-electromagnetic monitoring and early-warning.

When the membership degree is in the range of 0.6–0.8, the prominent of risk is more reliable.

# References

 1. Chen, Z., A-Meng, X. U.: Prediction of gas flow-rate from boreholes based on grey Markov model. China Saf. Sci. J. **22**(3), 79–85 (2012)
 2. Wang, E.Y., Zhong-Hui, L.I., Xue-Qiu, H.E., et al.: Application and pre-warning technology of coal and gas outburst by electromagnetic radiation. Coal Sci. Technol. (2014)
 3. Frid, V.: Electromagnetic radiation method for rock and gas outburst forecast. J. Appl. Geophys. **38**(38), 97–104 (1997)
 4. Kulakov, G.L., Yakovitskaya, G.E., Markov, V.A., et al.: Apparatus modernization for electromagnetic emission recording under in-situ conditions. Fiziko-Tekhnicheskie Problemy Razrabotki Poleznykh Lskopaemykh n2 Mar–Apr 1994, pp. 150–152
 5. Frid, V.: Electromagnetic radiation method water-infusion control in rockburst-prone strata. J. Appl. Geophys. **43**(1), 5–13 (2000)
 6. Liu, M., Xu, K., He, X., Ding, W.: Probing into rheologically electromagnetic radiation theory of coal and gas outburst. Ming Saf. Environ. Prot. **05**, 30–32 (2001)
 7. Wang, E.Y., Xue-Qiu, H.E., Nie, B.S., et al.: Principle of predicting coal and gas outburst using electromagnetic emission. J. China Univ. Min. Technol. **29**(3), 225–229 (2000)
 8. Hu, S., Wang, E., Li, Z., et al.: Nonlinear dynamic characteristics of electromagnetic radiation during loading coal. J. China Univ. Min. Technol. **43**(3), 380–387 (2014)
 9. Xiao, H., He, X.: Research on temporal-spatial distribution laws of electromagnetic emission during tunnel excavation of coal rock. Chin. J. Rock Mech. Eng. **28**, 2868–2874 (2009)
10. Song, D., Wang, E., Song, X., et al.: Changes in frequency of electromagnetic radiation from loaded coal rock. Rock Mech. Rock Eng. **49**(1), 291–302 (2016)

# Part XVIII
## Regulations

# Comprehensive Evaluation of Safety Training Effect of Non-coal Mines Based on Combinational Empowerment Extension Model

Fuliang Jiang$^{(\boxtimes)}$, Guan Chen, Xiangyang Li, Jintao Guo, Xiaoli Wang, Wenchao Yang, Shuai Zhang, and Ming Li

University of South China, Hengyang 421001, China
jfljfd@l63.com

**Abstract.** The effect of safety training in non-coal mines is closely related to the production of non-coal mines. Therefore, study the safety training system of non-coal mines is of positive significance to the safety of non-coal operations. Based on the survey conducted in the Safety Training Center of Hengyang City, the statistical analysis shows that the primary factors that affect the training effect are the basic conditions of trainees, the safety awareness of trainees, the safety behaviors of trainees and the objective conditions of training. Based on the above, an Extension Model of Comprehensive Evaluation of safety training effect is established, and the subjective and objective weights of the above indicators were respectively obtained by using the Variation Coefficient Method and the Analytic Hierarchy Process, and the above weights were integrated by using Game Theory. The comprehensive evaluation of the safety training effect of non-coal mines have been done by using the optimized weight. According to the results of the analysis and evaluation of this model, the safety awareness of trainees had the greatest influence on the training effect. According to the results of the study, some suggestions were provided to improve the safety training system of non-coal mines.

**Keywords:** Non-coal mine · Safety training effect · The extension model
Combination weighting method · Comprehensive evaluation

## 1 Introduction

Safety production in mines has always been a sensitive issue in China. After many years' research and continuous effort, Chinese safety conditions have been greatly improved. However, the safety production situation is still very harsh. According to the statistics, a total of 659 production safety accidents occurred in non-coal mines across the country in 2013, with 852 deaths [1]. Many scholars have used mathematical methods to study the safety problems for years.

In 1983, Cai Wen founded Extenics [2], which has grown rapidly in recent years. The introduction of correlation functions in extension sets and the related weight assignment methods can be used to evaluate qualitative and quantitatively. It is very

important to obtain the weights in the safety assessment, and related scholars have done a lot of research in this area. There are mainly three kinds of methods: (1) Subjective weighting method (including Analytic Hierarchy Process (AHP) [3], Fuzzy Mathematical Method [4], Gray Clustering Evaluation Method [5], and Unascertained Measurement Theory [6]). (2) Objective weighting method (including the Entropy Method [7] and the Coefficient of Variation Method (CV) [8], etc.). (3) Combination Weighting Method (including the Integrated Assigned Weighting Method based on unitization constraint [9], Multiplication and Normalization Combination Weighting Method [10] and Game Theory Combination Weighting Method [11], etc.).

This paper divides the influence factors of the non-coal mine safety training into four aspects, which are general background, safety awareness, safety behavior and objective condition of training. It may affect the accuracy of the evaluation results if using one single assigned weight method, so the combination of weights was put forward. First of all, the assignment scores of 4 influencing factors were done by AHP and CV method, the corresponding weights were calculated, and then the comprehensive weights were made by using the Game Theory. Finally, the combination weights obtained were applied to the Extension Model, and the safety training system for non-coal mines has been evaluated.

## 2   The Matter-Element Extension Model for the Evaluation of Non-coal Mine Safety Training Effect

### 2.1   Establishing a Matter-Element to Be Evaluated

Matter-element is the set of characteristics of the research object, which $P$ is the effect of training in non-coal mines, $C$ is the index that affects the training effect and $X$ is the value corresponding to each index. Then the ordered triples $R =[P, C, X]$ is the objective element. Usually the research object has multiple indicators, so $C$ and $X$ can be described by $C_1, C_2, \ldots, C_n$ and $X_1, X_2, \ldots, X_n$.

$$R = \begin{bmatrix} P & C_1 & X_1 \\ & C_2 & X_2 \\ & \vdots & \vdots \\ & C_n & X_n \end{bmatrix} \tag{1}$$

Combined with the definition of Matter-element, the Matter-element to be evaluated for the effect of non-coal mine safety training is the set of the $R$ actual scores data of the factors which affected non-coal mine safety training.

### 2.2   Determine the Classic Domain and Section Domain

The classical domain is a matter element matrix composed of the features $C$ of the research object $P$ and the standard range of values of $C$. The classical domain can be written as $R_j$ for different rank $J$:

$$R_j = [J_j, C, X_{ji}] = \begin{bmatrix} J_i & C_1 & X_{j1} \\ & C_2 & X_{j2} \\ & \vdots & \vdots \\ & C_n & X_{jn} \end{bmatrix} = \begin{bmatrix} J_i & C_1 & (a_{j1}, b_{j1}) \\ & C_2 & (a_{j2}, b_{j2}) \\ & \vdots & \vdots \\ & C_n & (a_{jn}, b_{jn}) \end{bmatrix} \qquad (2)$$

In the Formula (2), $X_{ji}$ is the magnitude limit specified by $J_i$ for the indicator $C$, and $a_{ji}$ and $b_{ji}$ are respectively the lower limit and the upper limit of $X_{ji}$.

The section domain can be obtained by extending the range of the eigenvalues of the classical domain.

$$R_0 = [P_0, C, X_{pi}] = \begin{bmatrix} P_0 & C_1 & X_{p1} \\ & C_2 & X_{p2} \\ & \vdots & \vdots \\ & C_n & X_{pn} \end{bmatrix} = \begin{bmatrix} P_0 & C_1 & (a_{p1}, b_{p2}) \\ & C_2 & (a_{p2}, b_{p2}) \\ & \vdots & \vdots \\ & C_n & (a_{pn}, b_{pn}) \end{bmatrix} \qquad (3)$$

In the Formula (3), $P_0$ is the safety training effect of non-coal mines. $X_{pi}$ is the range of values taken by $P_0$ about evaluation index $C$. $a_{pi}$ and $b_{pi}$ are respectively the lower limit and the upper limit of $X_{pi}$.

## 2.3 Determine the Various Indicators and the Level of Relevance

Define the correlation function according to the extension set:

$$H_{ij}(x_j) = \begin{cases} \dfrac{-\rho[x_i, (a_{ji}, b_{ji})]}{|(a_{ji}, b_{ji})|}, & x_j \in (a_{ji}, b_{ji}) \\ \dfrac{\rho[x_j, (a_{ji}, b_{ji})]}{\rho[x_j, (a_{jD}, b_{jD})] - \rho[x_j, (a_{ji}, b_{ji})]}, & x_j \notin (a_{ji}, b_{ji}) \end{cases} \qquad (4)$$

In the Formula (4):

$$|(a_{ji}, b_{ji})| = b_{ji} - a_{ji}$$

$$\rho[x_{ji}, (a_{ji}, b_{ji})] = |x_j - 0.5(a_{ji} + b_{ji})| - 0.5(b_{ji} - a_{ji})$$

$$\rho[x_j, (a_{jD}, b_{jD})] = |x_j - 0.5(a_{jD} + b_{jD})| - 0.5(b_{jD} - a_{jD})$$

In the above formula, $\rho[x_j, (a_{ji}, b_{ji})]$ is the distance from $x_j$ to the rank interval $(a_{ji}, b_{ji})$. $\rho[x_j, (a_{jD}, b_{jD})]$ is the distance between $x_j$ and the domain $(a_{jD}, b_{jD})$.

Therefore, the correlation matrix between each evaluation index and each evaluation level is obtained by:

$$G = \begin{bmatrix} g_{11} & g_{12} & \cdots & g_{1m} \\ g_{21} & g_{22} & \cdots & g_{2m} \\ \vdots & \vdots & \cdots & \vdots \\ g_{n1} & g_{n2} & \cdots & g_{nm} \end{bmatrix} \tag{5}$$

As there is still $g_{ij} \leq 0$, the coefficient of variation cannot be used, and we transform the above matrix into:

$$r_{ij} = \frac{1 + g_{ij}}{\sum_{i=1}^{n}(1 + g_{ij})} \tag{6}$$

### 2.4  Determine the Evaluation Object and Evaluation Level Comprehensive Relevance

Assuming $u^*$ is the weight, and the comprehensive relevance of the element $p$ to be evaluated on the safety training effectiveness level D is:

$$M_i(P) = \sum_{j=1}^{m} u^* h_{ij}(x_j), \quad i = 1, 2, \ldots, n \tag{7}$$

Compared with the calculated degree of correlation and taken $M_i = \max[M_i(P)]$, the rank of $M_i$ is the non-coal mine safety training effect level.

## 3  Optimizing of the Compounded Weight

Weight is an important parameter in the comprehensive evaluation method, which determines the importance of an index in the whole evaluation system. From the Formula (7), we can see that the value of indicator weight $u^*$ directly depends on the reliability of evaluation results of Matter-element extension model. The commonly used methods of weight determination are Expert Investigation, AHP, Entropy Method, Simplified Correlation Function Method, and Coefficient of Variation Method [12]. In the method of comprehensive integrated weighting based on the unitization constraints, the comprehensive weight is determined by maximizing the evaluation object. Each index proportion of the comprehensive weight can be calculated. The linear combination weighting method is judged by the distribution coefficient according to the subjective practical experience or optimized by the degree of difference between different weighting values to find the assigned weighting coefficient with different weights. The comprehensive weight obtained by the game-theoretic weighting method keeps all the weights in a coordinated and balanced manner as a whole. In order to improve the scientific value of weight assignment, we choose the coefficient of variation and AHP respectively to calculate the weights and came up with the idea of combinatorial empowerment of game theory to optimize the weight of two kinds of weighting methods. We combine the game theory with the matter-element extension

model to evaluate safety training effects comprehensively in order to improve the rationality of the evaluation result.

## 3.1 The Comprehensive Weight Based on the Game Theory

Supposed the non-coal mine safety training system weights of each indicator with $L$ (in this paper $L = 2$) kinds of methods to calculate the weight, the set is obtained as:

$$u_k = [u_{k1}, u_{k2}, \ldots, u_{km}], \quad (k = 1, 2, \ldots, L)$$

Linear combination coefficient is:

$$\alpha = (\alpha_1, \alpha_2, \ldots, \alpha_L)$$

The combination of $L$ vectors is:

$$u = \sum_{k=1}^{L} \alpha_k u_k^{\mathrm{T}}, \quad \alpha_k > 0 \tag{8}$$

The solution of the coefficient $\alpha_k$ in the Formula (8) is optimized, and the deviation of the $u$ and $u_k$ is minimized, which can be obtained as follows:

$$\min \left\| \sum_{k=1}^{L} \alpha_k u_k^{\mathrm{T}} - u_k \right\|, \quad k = 1, 2, \ldots, L \tag{9}$$

The Formula (9) can be altered to the linear system of the Eq. (10):

$$
\begin{bmatrix}
u_1 \cdot u_1^{\mathrm{T}} & u_1 \cdot u_2^{\mathrm{T}} & \cdots & u_1 \cdot u_L^{\mathrm{T}} \\
u_2 \cdot u_1^{\mathrm{T}} & u_2 \cdot u_2^{\mathrm{T}} & \cdots & u_2 \cdot u_L^{\mathrm{T}} \\
\vdots & \vdots & \cdots & \vdots \\
u_L \cdot u_1^{\mathrm{T}} & u_L \cdot u_2^{\mathrm{T}} & \cdots & u_L \cdot u_L^{\mathrm{T}}
\end{bmatrix}
\begin{bmatrix}
\alpha_1 \\
\alpha_2 \\
\vdots \\
\alpha_L
\end{bmatrix}
=
\begin{bmatrix}
u_1 \cdot u_1^{\mathrm{T}} \\
u_2 \cdot u_2^{\mathrm{T}} \\
\vdots \\
u_L \cdot u_L^{\mathrm{T}}
\end{bmatrix}
\tag{10}
$$

## 3.2 Simplification of Weight Coefficient Based on the Game-Theory

$(\alpha_1, \alpha_2, \ldots, \alpha_L)$ can be calculated through the Formula (10). In the last part of the study, we compared the comprehensive degree of correlation obtained for each level. Whether the coefficients are normalized, it will not affect the final conclusion. Omitting the normalized steps, the direct weight of the evaluation index is:

$$u^* = \sum_{k=1}^{L} \alpha_k^* u_k^{\mathrm{T}} \tag{11}$$

$$\alpha^* = \alpha_k / \sum_{k=1}^{L} \alpha_k \tag{12}$$

In the Formula (11), $u^*$ is the comprehensive weight, and substituting $u^*$ into Formula (7) can get the comprehensive evaluation result of the effect grade of non-coal mine safety training.

## 4   The Case Study

In this paper, the students participating in the non-coal mine safety training are taken as the research objects. Based on the survey results, the impact index that affect the safety training of non-coal mines can be divided into four factors, as shown in Fig. 1.
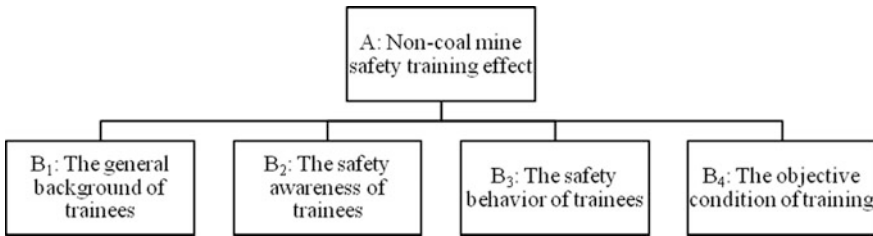


**Fig. 1.** The evaluation index system for safety training effect of non-coal mine

### 4.1   Specific Score of the Impact Index

According to the data provided by the Safety Training Center of Hengyang City, the corresponding score can be drawn (Table 1).

**Table 1.** The specific score of impact indicators for non-coal mine safety training effect

| Index | Actual score |
|---|---|
| $B_1$: The general background of trainees | 64 |
| $B_2$: The safety awareness of trainees | 98 |
| $B_3$: The safety behavior of trainees | 82 |
| $B_4$: The objective condition of training | 79 |

### 4.2   The Classical Domain and Section Domain

In this paper, the training effectiveness indicators on the safety training questionnaire are divided into five levels (The evaluation set), which are level one (Excellent), level two (Better), level three (General), level four (Poor), and level five (Poorer). According

to the statistical data of the questionnaire, each indicator is analyzed and scored, and the indexes that affect the non-coal mines are ranked, and then the classical domain and the section domain of each indicator are determined as shown in Table 2.

**Table 2.** The classical and section domain that affect the effectiveness of non-coal mine safety training results

| Category | $B_1$ | $B_2$ | $B_3$ | $B_4$ |
|---|---|---|---|---|
| Excellent (classic domain) | 90–100 | 96–100 | 90–100 | 90–100 |
| Better (classic domain) | 75–90 | 92–96 | 80–90 | 75–90 |
| General (classic domain) | 60–75 | 88–92 | 70–80 | 60–75 |
| Poor (classic domain) | 50–60 | 84–88 | 60–70 | 50–60 |
| Poorer (classic domain) | 40–50 | 80–84 | 50–60 | 40–50 |
| Section domain | 40–100 | 80–100 | 50–100 | 40–100 |

### 4.3 The Correlation Between Evaluation Index and Evaluation Grade

According to the Formula (4) and the actual findings of the safety training center, determining the correlation degree of each index affects the safety training effect of non-coal mines on each evaluation level. According to the Formula (5) to determine the evaluation index and the level of evaluation of the degree of decision-making composed of the decision matrix, be listed here in the form of a table, and such as shown in Table 3.

Table 3 can be converted into Table 4 by the Formula (6), as shown below.

**Table 3.** The correlation between evaluation grade and evaluation index

| Category | $B_1$ | $B_2$ | $B_3$ | $B_4$ |
|---|---|---|---|---|
| Excellent (classic domain) | −0.520 | 0.500 | −0.308 | −0.375 |
| Better (classic domain) | −0.111 | −0.500 | 0.200 | 0.267 |
| General (classic domain) | 0.267 | −0.750 | −0.100 | −0.160 |
| Poor (classic domain) | −0.143 | −0.833 | −0.400 | −0.475 |
| Poorer (classic domain) | −0.368 | −0.875 | −0.550 | −0.580 |

**Table 4.** The correlation degree between the evaluated grade and the evaluation index after transformation

| Category | $B_1$ | $B_2$ | $B_3$ | $B_4$ |
|---|---|---|---|---|
| Excellent (classic domain) | 0.116 | 0.590 | 0.180 | 0.170 |
| Better (classic domain) | 0.216 | 0.197 | 0.312 | 0.345 |
| General (classic domain) | 0.307 | 0.098 | 0.234 | 0.229 |
| Poor (classic domain) | 0.208 | 0.066 | 0.156 | 0.143 |
| Poorer (classic domain) | 0.153 | 0.049 | 0.117 | 0.114 |

## 4.4   Determining the Index Weight

From the data of Table 4, the weight of each indicator $U_1$ can be obtained by using the coefficient of variation method:

$$U_1 = \begin{bmatrix} 0.1798 & 0.4708 & 0.1583 & 0.1910 \end{bmatrix}$$

The weight of each index obtained by Analytic Hierarchy Process is $U_2$:

$$U_2 = \begin{bmatrix} 0.0463 & 0.5656 & 0.2652 & 0.1229 \end{bmatrix}$$

Put $U_1$ and $U_2$ into the Formulas (8)–(12) gives the values of $\alpha_1$ and $\alpha_2$ as follows:

$$\alpha_1 = 0.6043, \ \alpha_2 = 0.395$$

And the Table 5 is contained comprehensive weight $u^*$.

**Table 5.** The comprehensive weights of influence indicators for non-coal mine safety training effect

| Index | Coefficient of variation method | Analytic hierarchy process | Comprehensive weight |
|-------|-------------------------------|----------------------------|----------------------|
| $B_1$ | 0.1798 | 0.0463 | 0.127 |
| $B_2$ | 0.4708 | 0.5656 | 0.509 |
| $B_3$ | 0.1583 | 0.2652 | 0.201 |
| $B_4$ | 0.1910 | 0.1229 | 0.163 |

## 4.5   Final Determination of the Grade

According to the Formula (7), we can get the comprehensive relation degree between the evaluation object and each level:

$$M_i(P) = \{-0.066, -0.185, -0.394, -0.599, -0.698\}$$

$$M_i = \max M_i(P) = -0.066$$

Therefore, the safety training system's comprehensive evaluation result of the Safety Training Center of Hengyang City on non-coal mine is 'Excellent'.

# 5   Conclusions

(1) Based on the data provided by the Safety Training Center of Hengyang City and the corresponding references, the non-coal mine safety training evaluation system is divided into the basic information of trainees, the safety awareness of trainees, the safety behaviors of trainees and the objective conditions of training. An

Extension Evaluation Model of non-coal mine safety training system was established.

(2) Analytic Hierarchy Process (AHP) and Coefficient of Variation (CVA) were used respectively to obtain the weight values of the above four factors on the comprehensive performance of the non-coal mine safety training system. The weight of the evaluation index of non-coal mine safety training system was obtained by the Game Theory. It combines two ways advantages to ensure the reasonable weighing vector.

(3) Based on game theory comprehensive empowerment and extension safety evaluation model applied to the non-coal mine safety training system of the Safety Training Center of Hengyang City, the training effect of non-coal mine safety training system is 'Excellent'.

(4) The selection of classical domains and section domains in the extension model of non-coal mine safety training system is based on the relevant rules and experience, and there may be some deviation. Therefore, the selection of classical domains and section domains needs to be further improved.

# References

1. The First Department of State Administration of Work Safety. 2013 National Non-coal Mine Production Safety Accident Analysis Report. The First Department of State Administration of Work Safety, Beijing (2014)

2. Cai, W., Yang, C.: Basic theory and methodology on extenics. Chin. Sci. Bull. **58**(13), 1190–1199 (2013)

3. Gong, J., Hu, N., Zhang, Y., et al.: Optimization of mining methods in high-altitude areas based on AHP-FCE. Metal Mines **9**, 1–5 (2013)

4. Niu, X., Lv, L., Lin, J., et al.: Study on mine ventilation system evaluation method based on fuzzy mathematics. Min. Metall. **22**(2), 19–23 (2013)

5. Li, C., Chen, R., Su, H.: Grey clustering evaluation model and its application in mine ventilation system. Coal Technol. **29**(3), 120–122 (2010)

6. Li, S., Ma, C., Wang, G.: Colliery ventilation safety evaluation on the basis of the unascertained measure. J. Beijing Univ. Sci. Technol. **28**(2), 101–103 (2006)

7. Liu, B., Wang, J., Guo, K., et al.: Mineral resources security based on the geological survey and assessment—taking a copper mine in central Tibet as a case. Metal Mines **8**, 87–90 (2014)

8. He, Y., Xie, M., Long, D.: Application of gray correlation model for the optimization of hydro-power project investment based on the variation coefficient method. J. Water Resour. Water Eng. **20**(2), 127–129 (2009)

9. Wang, S., Fei, L., Lei, Y., et al.: Comparative study of two combination weighting method applied to benefit evaluation of water saving and improvement in irrigation district. Bull. Soil Water Conserv. **29**(4), 138–142 (2009)
10. Jiang, Q., Fang, K., Zhang, G.: Assessment of geo-hazards risk based on new combined weight method. J. Nat. Disasters **24**(3), 28–36 (2015)
11. Gan, R., Xuan, H., Liu, G., et al.: Application of weighted matter-element extension based game theory in groundwater quality evaluation. Water Resour. Power **33**(1), 39–42 (2015)
12. Chen, Y., Hu, S., Xuan, S., et al.: Model for evaluating the effectiveness of shipping company safety management based on combination weight. China Saf. Sci. J. **22**(8), 78–84 (2012)

# Education Is the Key to Ventilation Safety

Duncan Chalmers[(⊠)] and Guangyao Si

University of New South Wales, Kensington, NSW 2052, Australia
d.chalmers@unsw.edu.au

**Abstract.** Maintaining a safe working environment requires several key elements. These are the effective use of technology, the provision of air and management of its distribution throughout the mine and the supervision and planning of ventilation requirements. Additionally, the culture pervading the mining operation plays a significant role in the way that these elements are managed and controlled. The technology, air distribution and planning are well understood and their effectiveness can easily be measured. When it comes to supervision and management, issues can arise that can compromise the best plan, system or technology. Having highly educated, trained and empowered personnel managing the ventilation system is crucial to the safe operation of an underground mine. Over the course of history the mining industry has left a trail of graves. The unfortunate miners that have been killed, have led Governments to change the laws to prevent further loss of life. Successive disasters have prompted additions to the law to the point where it is an onerous task to comply. By using case studies and contrasting them with the change in attitudes and safety culture, making the Australian mining industry one of the safest in the world is highlighted.

**Keywords:** Education and training · Disasters · Management plans

## 1 Introduction

Mining, especially for coal, has been considered a dangerous occupation. Methane and/or coal dust explosions have occurred even into the 21st Century. Notably, Sago and Upper Big Branch, USA, Pike River New Zealand, Tunlan, China, Halemba, Poland, and Ulyanovskaya Mine, Russia, all involved multiple fatalities as a result of an underground explosion. The causes of each of these explosions can be attributed to three things, sufficient fuel, sufficient oxygen and an ignition source that has ignited/triggered the explosion. The circumstances that brought these things together are different, however each explosion is preventable. Rather than exploring these incidents in detail, this paper looks at the role that education and the change in culture can have in making explosions in mines a tragic thing of mining's past.

## 2    Methane and Coal Dust Explosions

The requirements for an explosion to occur require three things to be present, and conversely the presence of less than these three will prevent an explosion from occurring. However the isolation of all three will increase the level of safety. This works by ensuring that the sudden introduction of one of these factors will not result in an explosion.

### 2.1    Sago Mine

The inquiry into Sago focused on the ignition source, the effectiveness of the seals constructed to contain the goaf/gob and the effectiveness of self- contained breathing apparatus [7]. This report for the West Virginia Office of Miners' Health, Safety and Training, suggests that the likely cause of the explosion was a lightning strike. The inference being that it is acceptable to have an explosive mixture present in a sealed area, thus providing two of the three requirements for an explosion to occur.

### 2.2    Upper Big Branch Mine

Upper big Branch is more complex in that there were two inter-related events that caused the subsequent disaster. The Report of Investigation, Mine Safety and Health Administration (MSHA), details a small methane ignition that then triggered a massive coal dust explosion. Additionally, this report describes that PCC/Massey kept two sets of books with respect to safety and health hazards, of an established practice of relaying advanced notice of health and safety inspections and suggested intimidatory practices by management of the mine that raising safety concerns would jeopardize jobs [3].

This explosion was a tragedy waiting to happen. The MSHA report concludes from the specific accident investigation that the flagrant violations committed by PCC/Massey were:

1. "illegally providing advance notice to miners of MSHA inspections (a violation of section 103(a) of the Mine Act);
2. failing to properly conduct required examinations and to identify, record, and correct hazards (4 flagrants for violations of 30 CFR sections 75.360, 75.362, 75.363(a), and 75.364);
3. allowing hazardous levels of loose coal, coal dust, and float coal dust to accumulate (violation of 30 CFR section 75.400);
4. failing to adequately apply rock dust to the mine (violation of 30 CFR section 75.403);
5. failing to comply with the approved ventilation plan by operating the shearer with missing and clogged water sprays (violation of 30 CFR section 75.370(a)(1)); and
6. failing to adequately train its miners (violation of 30 CFR part 48.3).

PCC/Massey also committed three contributory violations that were not flagrant:

1. failing to maintain the longwall shearer (worn bits) in safe operating condition (violation of 30 CFR 75.1725(a));

2. failing to comply with its approved roof control plan in the 1 North Panel tailgate entry, as required by the approved roof control plan (violation of 30 CFR 75.220(a)(1)); and

3. failing to maintain the volume and velocity of the air current in the areas where persons work or travel at a sufficient volume and velocity to dilute, render harmless, and carry away flammable, explosive, noxious, and harmful gases, dusts, smoke, and fumes (violation of 30 CFR 75.321(a)(1))."

A flagrant violation is one where the violator exercises knowing conduct to flaunt the law.

Having inadequate ventilation to dilute flammable gas allowed an explosive mixture to exist, blunt picks and blocked water sprays provided two of the three requirements, floor breaks releasing sufficient methane into the environment completed the elements. Additionally, the resultant ignition raised coal dust into suspension mixing it with the ventilation air completing the set conditions for a coal dust explosion.

These conclusions on Upper Big Branch report highlight the role that culture and lack of education played in contribution to this disaster.

## 2.3  Pike River Mine

Pike River disaster was another methane explosion resulting in the loss of 29 people. The Royal Commission report was comprehensive and stated that the mine had not completed the systems and the infrastructure to produce coal safely. The Commission found that there had been 21 reports of methane-air mixtures reaching explosive levels in the 48 days preceding the disaster. These reports included the day of the event [4].

Delays in establishing the mine, cost over runs contributed to the pressure on management to provide a cash flow to continue installation of the gas detection system.

The Commission describes the incident as "an unintended escape of methane followed by an explosion in the mine. It occurred during a drive to achieve coal production in a mine with leadership, operational systems and cultural problems." [4].

The placement of the main fan underground at the bottom of the exhausting shaft was a major error [4]. Despite objections from ventilation consultants and some of Pike River's Staff the decision to place the main fan in an underground gassy coal mine was not reviewed. Panckhurst, Bell and Henry further state that "The decision was neither adequately risk assessed nor did it receive adequate board consideration." Although this would increase the flow of air through the mine, its location would provide the opportunity for leakage from the exhaust stream into the main intakes. This main fan and its electrical equipment were not explosion protected and were destroyed in the explosion.

Additionally, this event highlighted the inadequacies of the legal framework for health and safety in New Zealand.

### 2.4    Soma Mine

Soma Mine disaster was another example of a tragic loss of life. Duzgun and Yaylaci [2] suggest that there was a fire that started in the roof of the main road and that methane ignited in the belt roadway. Ventilation in the mine was limited due to the risk of spontaneous combustion and the mine was ventilated by series ventilation. Additionally, the quantity of air provided was calculated on a per person basis rather than controlling the gases in the mine [1]. This per person determination for air was based on the legislation that was in place in Turkey.

Duzgun and Yaylaci [2] also comment on changes in legislation that occurred prior to this incident and state that requirements in the old legislation were removed without developing appropriate protocols allowed risks to be take easily. They further state that legislation that is designed to improve safety needs to be supported by standards and protocols for it to be effective, and that these were not in place at the time of the fire.

The likely cause of this fire would have been spontaneous combustion, Canubulat [1] and Duzgun and Yaylaci [2] report that the conveyor systems that were installed were not fire resistant nor anti-static (FRAS). As a consequence once the conveyor was on fire copious amounts of carbon monoxide would be produced. Eylül (2014) reports that the cause of death for the majority of 301 mine workers that died was carbon monoxide asphyxia.

### 2.5    Tunlan Coal Mine

Tunlan Coal Mine is situated in Shanxi Province. A faulty flame proof enclosure in crosscut no. 1 of Longwall 12,403 allowed the propagation of an explosion into the surrounding atmosphere. This continued to propagate to the face of the longwall via the transport road, the return airway and the belt roadway on the other side of the block [5, 9].

What was unclear in both the discussions of Zhou et al. and Sun were the reasons for the fan in No 1 cut through, and the reasons for an accumulation of methane in one of the two intakes. Further to that the propagation of the shock wave on the other side of the longwall to the face suggests that the explosion propagated in both roadways from this one ignition source.

Irrespective of the source of ignition it is clear that there was a flammable mixture present and all that was required was the third element to be brought into action.

### 2.6    Halemba, Poland, and Ulyanovskaya Mine, Russia

News reports for both these disasters suggested that there was a methane explosion that may have involved coal dust. Without documentation into the cause of these two disasters the only conclusions that can be drawn is that at the time all three elements were present. However it is likely that there were flammable mixtures present waiting for an ignition source.

## 3 Discussion

It is evident that changing legislation, having a good safety record, reliance on technology has not prevented mine explosions. Australian coal mines mine coal that has high gas contents, has ranging propensity to spontaneous combustion, uses gas drainage, has goaves where there is an explosive fringe and has seams/roof strata that can produce incendive sparks.

Australian mines prior to September 1994 had explosions that took lives, so what has changed? Moura No 2 Disaster that occurred 7th August 1994 was the last mine explosion where there was a loss of life. The warden's inquiry into this disaster made many recommendations as did the previous inquiries. The change here was that it occurred during an ongoing cultural change process.

This led to changes in legislation and the adoption of a substantial number of the recommendations made by the Wardens.

These significant and ongoing changes occurred as a result of several disasters in Australia. These were the adoption of a cultural shift within the coal mining industry, improvement in safety training and education, appointment of a new statutory position of ventilation officer, development of principal hazard management plans, risk assessments and trigger action response plans (TARP). Complementing this was the advancements in technology, legislation, standards, codes of practice, audits and review processes.

The cultural shift that was supported by management, employees, contractors and visitors was that there is no such thing as an accident, these are events that can be foreseen and can be controlled. This included the reporting of near miss events, incidents and breaches in protocols, standards and equipment. The concept that management was interested in hearing from "whistleblowers", that if something is wrong then the operation must be stopped until it is fixed, Management also saw that operating safely made good business sense providing a continuous revenue stream rather than having a peak followed by the results of a disaster on the bottom line.

The Warden's report also recommended that Mine Safety Management Plans are to be put in place and that they be audited regularly by both internal and external auditors. It also outlined key risk areas that these plans should address should include:

- Ventilation
- Spontaneous Combustion
- Gas Management
- Methane Drainage
- Emergency Evacuation
- Strata Control

The plans should include:

- standards to be adopted at the mine for the prevention, management, and control of risks which have been identified by the risk analysis;
- action plans in the event of an identified risk occurring;
- appropriate training programmes for the identification and prevention of risks; and
- procedures which are consistent with the intent of Quality Assurance Standards [6].

The implementation of Mine Safety Management Plans (also called Principal Hazard Management Plans) and their underpinning TARPs provide the framework to respond to alarms and potential incidents well before the situation could develop into a disaster.

An example format for a TARP may consist of four levels

- Green, sensor showing above normal reading, however it is within the dynamic range of fluctuations. Continue working and monitor level more frequently.
- Yellow, Sensor showing above normal reading and is above the dynamic range of fluctuations. Take additional readings, send competent, authorised person to investigate, inform senior management. Initiate remedial actions.
- Orange, sensor trending towards dangerous level, apply remedial actions, monitor and inform senior management, advise other sections that there is a worsening situation.
- Red, orderly evacuation of mine and implement emergency procedures to deal with event. Inform senior management, establish incident management team, involve mines inspectorate, rescue station, etc.

Windridge et al. also recommended the establishment of the Ventilation Officer who was subordinate only to the mine manager. This was implemented as a statutory position requiring the person to demonstrate evidence that they had met the required competency standards. To this end, the School of Mining Engineering at University of New South Wales has provided education and training of Ventilation Officers in both NSW and Queensland since 1998. Over 500 people have attended this course and over 400 certificates have been awarded. In context, this is about an average of 11 qualified persons per mine. Additionally, there are other providers to the Qld mines that have deemed people competent. However, despite this number of people with qualifications, retirement and promotion to other roles has there is still a shortage of qualified people.

The benefits other than having competent people whose function is to maintain the safety and welfare of the ventilation system, they are supported by Managers, and other statutory officials that are also qualified to hold the Ventilation Officer's position.

Mines also introduced "toolbox talks" where issues specific to the safe operation of the mines would be raised and the solutions and controls that were being implemented to manage them would be conveyed to the work force. If the matters only related to the mine then a separate "toolbox" talk would be conducted before the crew started work in their section of the mine.

# 4   Conclusions

To keep doing something and expecting a different outcome, is madness. The history of mining is littered with fatalities, yet the outlined examples suggest that the industry is continuing to do those things that lead to explosions.

Wherever there is methane in a mine that is in contact with the ventilation air there will be an explosive fringe. Diligence in monitoring and controlling this fringe is essential.

Reducing the volume of this explosive fringe is achievable and should be a priority.

The use of inert gas in goaf areas to remove the explosion risk is a must.

Having competent people with the authority to make informed decisions about the mine with respect to ventilation, spontaneous combustion, gas drainage and management is crucial to safe operations.

The ventilation office needs to be well informed, so a robust and comprehensive monitoring system needs to be in place.

All of these things need to be supported by an appropriate legislative framework, underpinned by standards and codes of practice.

A cultural change needs to take place so that the reporting of incidents, near misses and damaged equipment, devices and services takes place without fear or favour. And that management see this as an appropriate pursuit.

A safe mine can be a productive one after all the sharpening of the sickle does not delay the reaping.

# References

1. Canubulat, I.: Personal Communication (2018)
2. Duzgun, S., Yaylaci, E.: An evaluation of Soma underground coal mine disaster with respect to risk acceptance and risk perception. In: Mitri, H., Shnorhokian, S., Kumral, M., Sasmito, A., Sainoki, A. (eds.) 3rd International Symposium on Mine Safety Science and Engineering, Montreal, pp. 368–374, August 13–19. McGill University, Montreal (2016)
3. Page, N., Caudill, S., Godsey, J.F., Moore, A., Phillipson, S., Steffey, D., Stolz, R., Watkins, T., Cripps, D., Maggard, C., Morley, T., Sherer, H., Stephan, C., Vance J., Brown, A.: Report of Investigation. Fatal Underground Mine Explosion April 5, 2010, Upper Big Branch Mine-South, Performance Coal Company Montcoal, Raleigh County, West Virginia, ID No. 46-08436. Mine Safety and Health Administration Office of the Administrator Coal Mine Safety and Health 1100 Wilson Boulevard Arlington, Virginia 22209 (2010)
4. Panckhurst, G., Bell, S., Henry, D.: Report of Royal Commission on the Pike River Coal Mine Tragedy (2012)
5. Sun, J.: The causes and lessons of "2·22"gas explosion disaster at Tunlan Coal Mine. J. China Coal Soc. **35**(1) (2010)
6. Windridge, F., Parkin, R., Neilson, P., Roxborough, F., Ellicott, C.: Wardens inquiry conducted pursuant to Section 74 of "The Coal Mining Act 1925" Report on an Accident at Moura No 2 Underground Mine on Sunday, 7 August 1994 Queensland, Australia (2014)
7. Wooten, R.: Report of Investigation into the Sago Mine Explosion which Occurred January 2, 2006, Upshur Co. West Virginia. West Virginia Office of Miners' Health, Safety, And Training (11 Dec 2006)
8. Yalcin, E., Akpinar, E., Onur, A., Erturk A.: Expert report on the mining accident in the coal mine in Eynez village on 13 May 2014 (2014)
9. Zhou, F., Wei, L., Chen, K., and Cheng, J.: Analyses of cascading failure in mine ventilation system and its effects in a serious mine gas explosion disaster. J. Fail. Anal. Preven. https://doi.org/10.1007/s11668-013-9726-x (2013). ISSN 1547-7029

# Part XIX
# Miscellaneous Topics

# Study on the Practice of Concealed Goaf Detection in Metal Mine Based on Geophysical Prospecting Technology

Xianfeng Shi[(✉)], Yongfeng Liu, Jiaguol Hu, Shigenl Fu, Zhentaol Li, and Zhipengl Liu

China Academy of Safety Science and Technology, Beijing 100012, China
`sxianfeng@l26.com`

**Abstract.** In the 1970s, the exploitation of mineral resources in China experienced a period of dangerous growth while the civil mining situation became chaotic. This led to a large number of mined-out areas being left in underground mines. With this increase in exposure time, the stability of goaf is getting worse, causing geological disasters such as rock collapses, landslides and ground subsidence, and endangering the life safety of miners. Due to the complexity of geological engineering and mining technology, it is difficult for traditional technology to accurately determine the location and shape of goaf. The adaptability of surface and underground detection methods and technologies is analyzed in this paper according to the characteristics of goaf in metal mines, and the technology needed for precise exploration of concealed goaf in metal mines, based on 3D seismic technology, is put forward. By extracting the electrical and seismic response characteristics of metal mine goaf, the 3D seismic method can be used to detect the distribution of the goaf. The number, volume and filling condition of metal mine goaf are identified, which have guiding significance for mine safety.

**Keywords:** Metal mine · Concealed goaf · 3D seismic technology
Detection

## 1 Introduction

The open stope method has accounted for about 53.5% of underground metal mining in China, and as a result of this long-term exploitation, a large number of untreated goaf has been formed. Ground subsidence and collapses are common problems in underground mining, with the total area of surface subsidence having reached 1150 km$^2$. More than 30 cities have been affected by mining collapse disasters in China, and the losses caused by ground collapse are more than 400 million yuan each year. New buildings built over hidden goaf with no historical records will begin to crack due to the slow settling of the empty area below. This situation is common in more than 200 mining cities in China, intensifying the criticism of the local miners, affecting normal production of enterprises and destroying the harmonious development of the society. If the surrounding rock is unstable in the empty area, it is likely to cause serious collapses resulting in loss of life and property [1–6]. On November 6, 2005, a massive collapse

of the goaf in the gypsum mine in Xingtai, Hebei, resulted in the death of 37 people underground and above ground. Many mining cities have undertaken house relocation and housing repair projects to alleviate complaints from residents, but a vicious cycle of "subsidence, relocation, re-subsidence and re-relocation" has been formed, which cannot rectify the fundamental problem.

The goaf has become one of the main sources of the hazards compromising efficient production as well as the safety of the mining environment. The existence of a large number of goafs leads to the deterioration of mining conditions and the increase of hidden hazards which in turn leads to disasters such as rock migration, surface subsidence and water inrush in the underground area. When the goaf is below the groundwater level, it forms stagnant water. Once newly mined drifts are connected with the mined out areas, a serious breach results that instantly drowns the mine. Due to the complexity of geological engineering and mining technology, it is difficult for traditional technology to accurately identify the location and shape of metal mine goaf, and most detection methods fail to meet production safety requirements. Surrounding rock collapses and goaf water accumulation occurs after mining, so personnel cannot directly enter the goaf to measure its parameters. It is difficult to delineate the goaf boundaries which are limited by the shape of the ore deposit. Data on many historical closures of small metal mine goaf is nonexistent.

The frequent accidents resulting from the goaf have greatly strengthened research attention on the goaf. A variety of technologies have been used to detect the goaf: Liu [7] used ground-penetrating radar; Wang [8–10] used the transient electromagnetic method; Xu [11, 12] used the seismic wave method; Xue [13, 14] used the high density electrical method; Guo [15] used the integrated electric method; Li Ming [16] used the DC method. In order to accurately grasp the shape of the goaf, some scholars have adopted the laser detection method in recent years, and have achieved good results [17–23]. Due to the characteristics of metal mine goaf, there are some limitations to the application of various detection technologies in the mined-out area of metal mines.

Based on research of the adaptability of surface and underground detection methods for goaf in metal mines, this paper puts forward the application of 3D seismic technology for more precise exploration of concealed goaf. The electrical and seismic response characteristics of metal mine goaf are extracted, and the number, volume and filling situation of metal mine goaf are identified.

## 2    Characteristics of 3D Seismic Data in Goaf of Metal Mines

### 2.1    Characteristics of 3D Seismic Data in Goaf of Metal Mines on Single Shot Record

From the 3D seismic data presented in Fig. 1 of a single shot record of a metal mine goaf, it can be noted that the boundary of the goaf has obvious diffraction waves, the frequency is reduced and the phase axis is interrupted and then disappears. As shown in Fig. 2, according to the spectrum analysis of the goaf, the dominant frequency of the seismic reflection waves in the outer strata of the goaf is above 70 Hz.
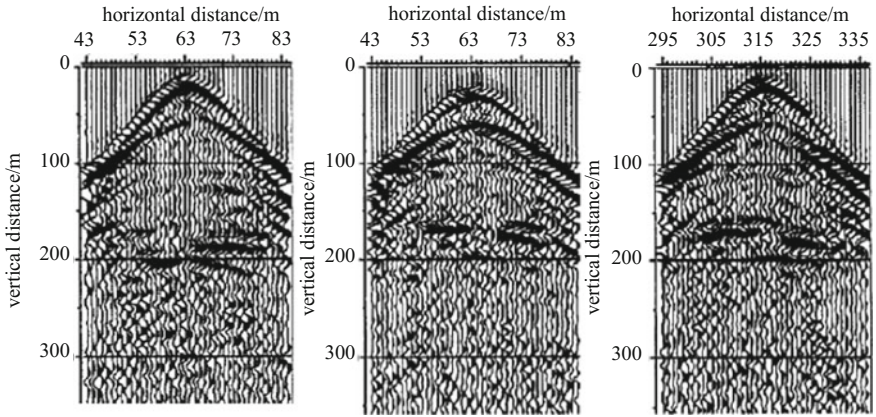
**Fig. 1.** Single shot record of metal mine goaf
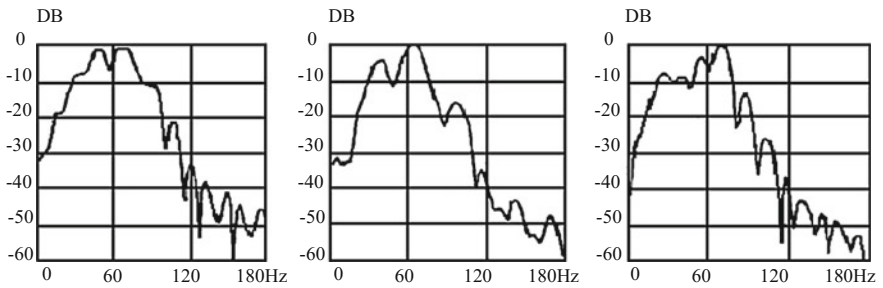


**Fig. 2.** Spectrum of reflection wave in outer strata of goaf

As shown in Fig. 3, the dominant frequency of seismic reflection waves in the inner strata of the goaf is below 60 Hz. It can be seen that the existence of goaf causes the dynamic variation of seismic reflection waves, which is manifested as amplitude weakening, frequency reduction, phase inversion and waveform distortion. Therefore, in the process of 3D seismic exploration and interpretation, the dynamic characteristics of the above goaf can be used as a model.
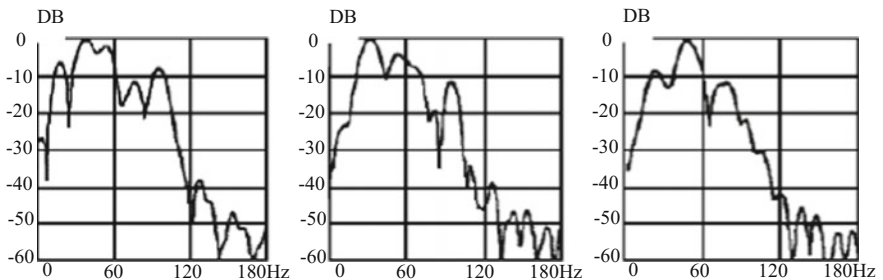


**Fig. 3.** Spectrum of reflection waves in the inner strata of the goaf

## 2.2    Characteristics of the Time Section of 3D Seismic Data in Metal Mine Goaf

**The Disappearance of the Waveform of the Reflected Wave or the Blurring of the Seismic Waveform**. On the seismic waveform, the goaf makes the reflection wave of the top and bottom difference; the reflected energy is weak on one side and the position of the phase axis has no reflection wave.

**The Change of The Frequency Band of The Reflected Wave in the Seismic Waveform Diagram**. In seismic waveforms, the difference in physical properties on both sides of the goaf boundary will cause sudden changes in the frequency band of the wave, such as the narrowing of the frequency band and decreasing wave value.

**Distortion Mutation of the Reflection Event**. A reflection event will pull down at the goaf, distorting the waveform on the inside. The beginning and end of the distortion of the waveform is the boundary of the empty area.

**The Emergence of Invalid Waves**. In the course of seismic wave propagation, due to the uncoupling of the strata, diffraction will occur at the boundary of the goaf or other unfavorable geological body responsible for producing the diffraction wave.

# 3    Spatial Velocity Field Analysis of Goaf in Metal Mines

Before the 3D seismic exploration, surface lithology is obtained through a surface lithology survey, propagation velocity of the seismic wave is obtained through a rock sample test, propagation velocity of the seismic wave in the deep rock is obtained through the micro-logging method, and the spatial velocity distribution of the study area is established.

In a theoretical analysis, the data are iterated through the migration-scanning method and the geological model is constantly revised. According to actual engineering needs, the constraint conditions are loaded and the formation medium model is simplified. Depending on the requirements of the model, different calculation methods are adopted and a relatively accurate velocity field is obtained.

## 3.1    Tracing Reflection Horizon

Although an offset error is generated by the conventional migration method, all kinds of seismic waves on the offset time profile can return to their true values, and the relationship between the stratigraphic position and the geological structure can be clearly visible. This makes it convenient for seismic data interpretation on the velocity spectrum and easier to track speed changes and pick speed inflection points.

## 3.2    Velocity Analysis Along a Formation

The interpolation calculation method is used to increase the numerical density of the velocity map in the longitudinal direction. In the calculation process, the abnormal speed points are identified and the abnormal speed value is deleted so that there is an

appropriate speed ratio between the vertical and horizontal speed, thus showing a clear superposition velocity field, as shown in Fig. 4.
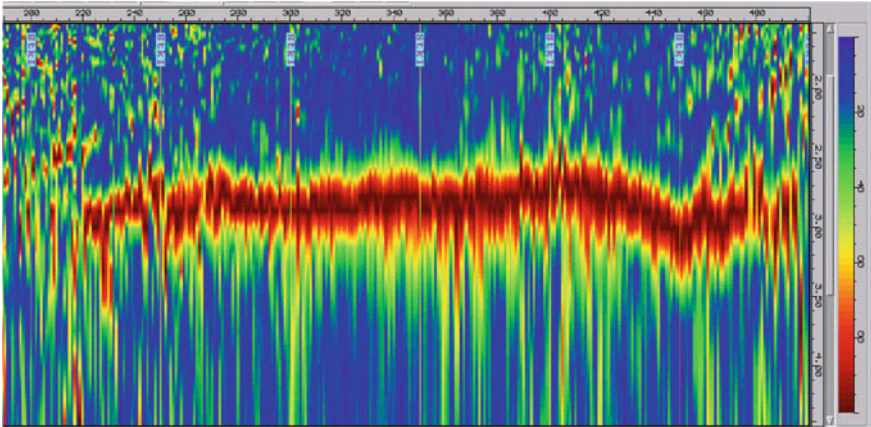


**Fig. 4.** The superposition velocity spectrum at the bottom of the quaternary system in the study area

### 3.3 Speed Angle Correction

The correction of the velocity dip is required because the root mean square velocity cannot be converted from the superposition velocity under the inclined bottom layer. Therefore, the inclination of the superposition velocity field must be corrected. In this way, the exact mean square root speed can be obtained by the conversion of the superposition velocity on the basis of the velocity spectrum.

### 3.4 Calculating Interval Velocity

Micro-logging and acoustic logging can obtain more accurate data on formation velocity, but they cannot represent the change in the formation velocity of the whole area. To obtain the velocity field of the whole work area, the Dix formula can be used, which is converted from the root mean square velocity to the interval velocity.

$$v_n = \sqrt{\frac{t_{0,n} v_{r,n}^2 - t_{0,n-1} v_{r,n-1}^2}{t_{0,n} - t_{0,n-1}}} \tag{1}$$

where

$v_n$      interval velocity, m/s;
$t_{0,n}$      the $t_0$ time of the $n$ layer, $s$;
$t_{0,n-1}$      the $t_0$ time of the $n-1$ layer, $s$;

$v_{0,n}$     root mean square velocity of the $n$ layer, $m/s$;
$v_{0,n-1}$  root mean square velocity of the $n-1$ layer, $m/s$.

### 3.5   Time-Depth Conversion

The depth value of the interpretation layer can be obtained by multiplying the horizon time value and the corresponding mean velocity by the seismic data interpretation. Using this depth value, we can easily compare with the borehole and analyze accuracy and error.

According to the stratigraphic characteristics of the study area and the known borehole data, the time and depth conversion results of the iron mine goaf within the metamorphic rocks are compared with the velocity obtained from the superposition velocity transformation and the calculation from the boreholes in the study and surrounding areas. Results of high accuracy are obtained by this comparison. Figure 5 is the superposition velocity and energy mass display in the study area.



*Vel=2000m/s  Vel=2200m/s  Vel=2400m/s  Vel=2600m/s  Vel=2800m/s*
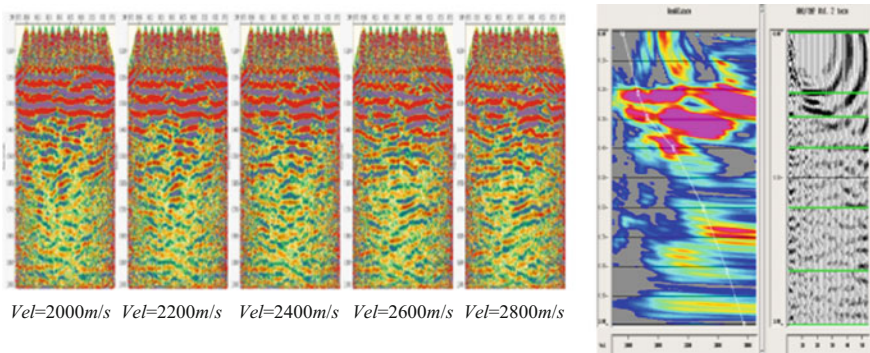
**Fig. 5.** Superposition velocity and energy mass display in the study area

## 4   Establishment and Analysis of Seismic Model of Goaf in Metal Mines

According to the state of the goaf, three models are established, such as unmined, unfilled and filled, then the seismic response characteristics of different models are analyzed.

1. As can be seen from the forward section of Fig. 6, the Quaternary loess and metamorphic strata form a strong reflection peak interface. The iron ore surrounded by metamorphic rock has a relatively small impedance difference. In the seismic section, the reflection interface of the peaks and the bottom trough is formed, and the shape and scale of the iron ore can be clearly depicted. At the same time, the

high velocity of the seismic wave through the iron ore causes the reflection interface below the iron ore to stretch upward slightly. Metamorphic rocks comprising the underlain strata form a weak reflection wave trough.
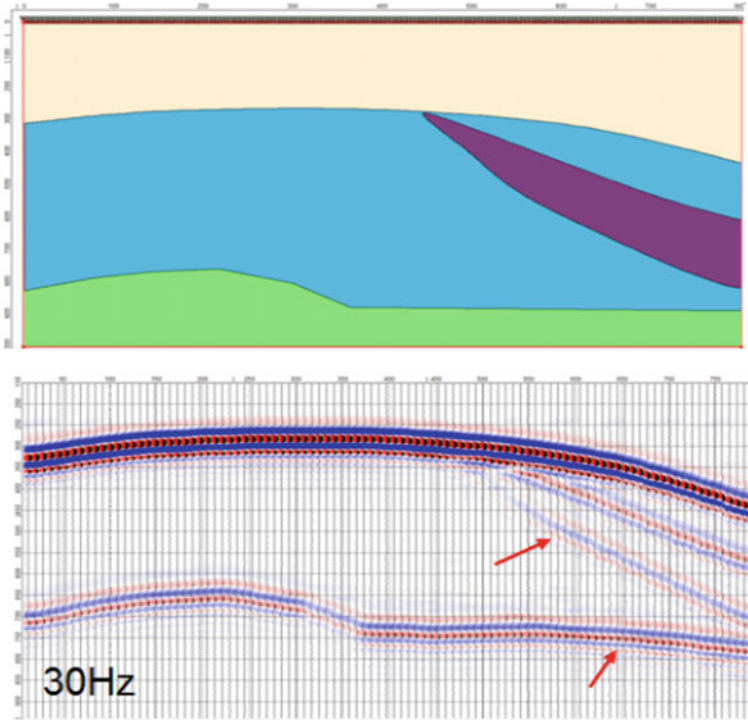


**Fig. 6.** Geological section forward of unmined iron ore

2. As can be seen from the forward section in Fig. 7, the Quaternary loess and metamorphic strata form a strong reflection peak interface. After the iron ore with metamorphic rock as the surrounding rock is mined, the goaf space fills with air. The upper part of the goaf has a large impedance difference with the top of the metamorphic rock, and there is also a large impedance difference between the lower part of the goaf and the iron ore itself, which leads to the strong seismic reflection of the top of the ore body, and the false reflection of multiple waves at the bottom.
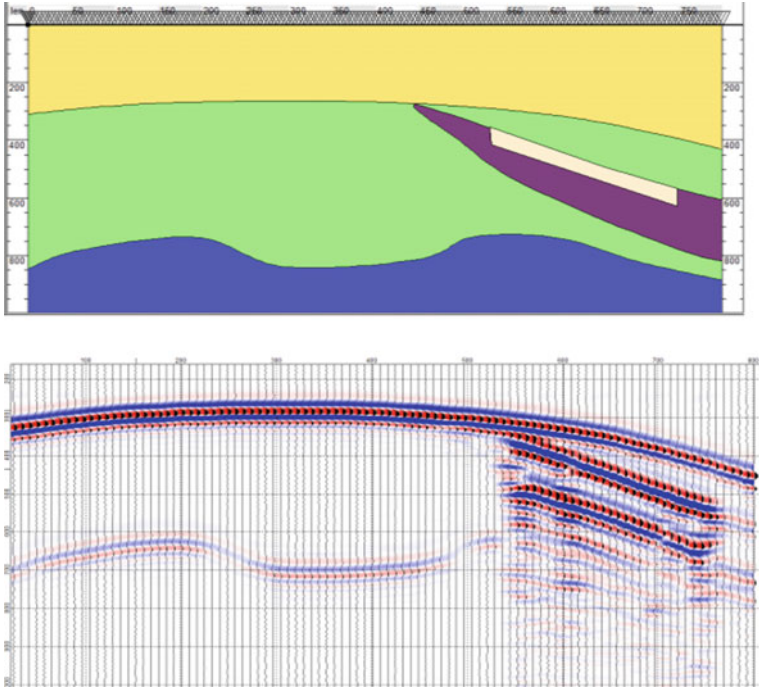
**Fig. 7.** Geological section forward of unfilled mined-out areas

3. As can be seen from the forward section in Fig. 8, the iron ore goaf has been filled. The Quaternary loess and metamorphic strata still form a strong reflection peak interface, but the cemented fill in the goaf reduces the impedance difference between the top of the goaf and the surrounding rock and weakens the reflection at the top of the goaf. Therefore, the reflection of the lower part of the filled iron ore goaf is mainly caused by the sudden weakening of the phase axis, the phase difference of the phase axis, the fault and the torsion.
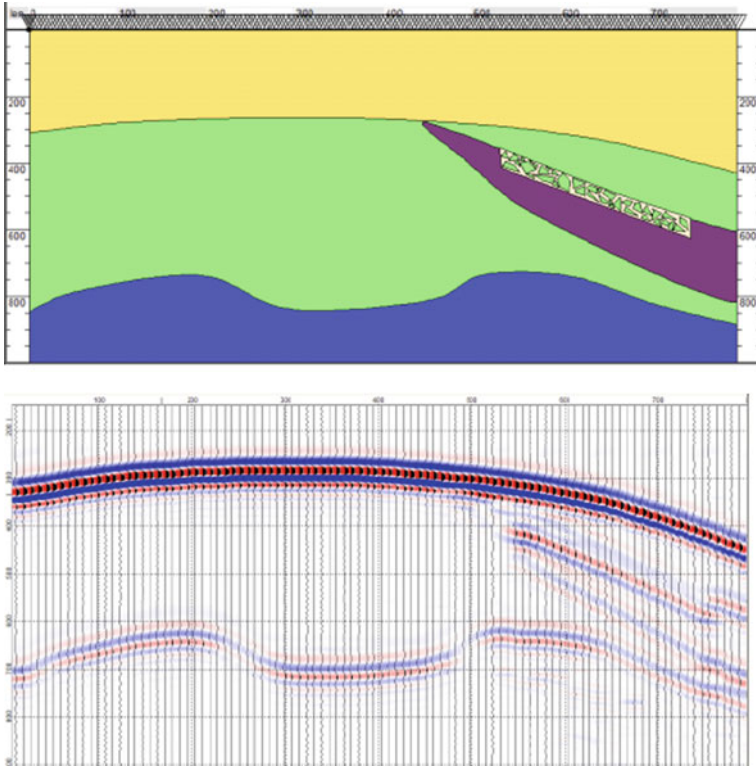
**Fig. 8.** Geological section forward of filled mined-out areas

## 5 Conclusions

For the first time, three-dimensional seismic technology has been applied to the exploration of metal mine goaf. A technique for accurate detection of concealed goaf in metal mines based on 3D seismic technology has been proposed. The physical basis and seismic wave characteristics of using seismic reflection waves to detect the metal mine goaf have been summarized. According to the characteristics of the goaf in the metal mine, the 3D seismic data acquisition scheme is optimized, and the electrical and seismic response characteristics of metal mine goaf are extracted. Finally, the seismic model of goaf in metal mines is established and tested in the study area, with good results having been obtained.

## References

1. State Administration of Work Safety: Safety Evaluation. China Coal Industry Publishing House, Beijing (2002)

2. Research Group of Continuous Development Institute of Chinese Academy of Science: China Sustainable Development Report 2015. Science Press, Beijing (2015)
3. State Administration of Work Safety (State Administration of Coal Mine Safety): National Safety Production Technology Development Plan (2004–2010) (2003)
4. Research Center of State Administration of Work Safety: Study on the Collapse and Hazard Prevention and Cure in Coal Cities in China (2004)
5. Liu, Z., Ji, H.: Prediction of impact disaster caused by roof collapse in goaf. West China Explor. Eng. **3**, 101–105 (2007)
6. Wang, C., Xing, Y., He, Jin., et al.: Mechansim analysis and the stability evaluation of the landslide at Dahu gold ore area in henan province. J. Geol. Hazards Environ. Preserv. **18**(2), 70–74 (2007)
7. Liu, D.: Study on Detecting and Control of Potential Hazards in Underground Rock Mass Engineering. Central South University, Changsha (2001)
8. Wang, J., Zhang, J., Xu, B.: The application of time domain electromagnetic methods to the detection of mined-out area under highway. Geophys. Geochem. Explor. **31**(4), 358–364 (2007)
9. Jiang, B.: Transient Electromagnetic Exploration. Geological Publishing House, Beijing (1998)
10. Zhang, K., Han, Z., Zhou, T.: Application of transient electromagnetic method in coal mine gob. Chin. J. Eng. Geophys. **4**(4), 341–344 (2007)
11. Xu, B., Wang, E., Tian, G.: Detecting underground water-bearing caves by seismic transverse wave reflection method. J. Northeast. Univ. (Nat. Sci.) **27**(1), 84–87 (2006)
12. Liu, D., Xu, G., Huang, R.: A new technique for prospecting exhausted areas in metal mines. China Min. Mag. **9**(4), 34–37 (2000)
13. Gao, J., Chai, Z.: The application of high definition electricity method in coal mine empty area. J. Anyang Teach. Coll. **2**, 137–139 (2007)
14. Derald, G.S., Harry, M.J.: Ground penetrating radar: antenna frequencies and maximum probable depths of penetration in quaternary sediments. J. Appl. Geophys. **33**(1–3), 93–100 (1995)
15. Guo, C., Liu, J.: Application of comprehensive electric method in the detection of the work-out section. SCI/TECH Inf. Develop. Econ. **14**(2), 142–144 (2004)
16. Zeng, R., Yao, J.: Application of D.C. electric method on surveying old mine area. Coal Geol. China **13**(4), 53–54 (2001)
17. Liu, X., Li, X., Li, F., et al.: 3D cavity detection technique and its application based on cavity auto scanning laser system. J. Cent. S. Univ. Technol. (English Edition) **15**(2), 285–288 (2008)
18. Guo, J., Gu, D., Luo, Z.: A new technique of 3D laser survey of finished stopes in metal mines. Min. Metall. Eng. **26**(5), 16–19 (2006)
19. Stuttle, M.C.: Combined probe drilling and laser surveying for complex underground mapping. Can. Min. J. **119**(6), 21–23 (1998)
20. Stuttle, M.C.: Laser scanning aids underground mine mapping. Min. Eng. **51**(3), 45–46 (1999)
21. Park, D.W., David, A.: Model studies of subsidence and ground movement using laser holographic interferometer. Int. J. Rock Mech. Min. Sci. Geomech. Abstr. **14**(4–6), 235–245
22. Brooker, G.M., Scheding, S., Bishop, M.V.: Development and application of millimeter wave radar sensors for underground mining. IEEE Sens. J. **5**(6), 1270–1280 (2005)
23. Grandjean, G., Gourry, J.C.: GPR data processing for 3d fracture mapping a marble quarry (Thassos, Greece). J. Appl. Geophys. **36**(1), 19–30 (1996)

# Oxidation Activity Evaluation of Sulfide Ores Based on Weight Gain Rate Fusion Under Different Oxidation Conditions

Wei Pan[⊠], Chao Wu, Zi-jun Li, and Zhi-wei Wu

School of Resources and Safety Engineering, Central South University,
Changsha 410083, China
panwei2012@csu.edu.cn

**Abstract.** This article describe a low temperature oxidation experiment and nine different sulfide ore samples to investigate a new evaluation method of oxidation activity of sulfide ores. The measured weight gain rate was studied by integrating wavelet de-noising and fuzzy comprehensive evaluation. The results show that mass variation trend of ore samples during the low temperature oxidation process consists of three stages: rapidly increasing, slowly increasing and unchanged. Content of water-soluble iron ion and sulfate ion of ore samples increase after oxidation. The surface of ore samples is relatively smooth and the particles are uniform before oxidation. After oxidation, ore samples surface is loose and porous, and there is obvious agglomeration of ore samples on the surface. The order ore samples oxidation activity is: Samples #2, #8, #5, #4, #9, #7, #1, #6 and #3.

**Keywords:** Sulfide ores · Oxidation activity · Low temperature oxidation
Weight gain rate · Comprehensive evaluation

## 1 Introduction

Spontaneous combustion of sulfide ores is a conversion of the chemical energy to heat owing to oxidation [1, 2]. When sulfide ores are exposed to air, the exothermic reactions between ore particles and oxygen will occur [3, 4]. If the reaction heat is entirely dissipated by external conditions, only low temperature oxidation will take place. If the heat is accumulated, spontaneous fires of sulfide ores will eventually happen. This disaster not only leads to serious economic losses, but also brings about lots of safety and environmental problems for further production in high-sulfur mines [5–7]. Therefore, researches on spontaneous combustion of sulfide ores are essential to ensure safe and efficient mining for high-sulfur mines.

Based on the relevant literature, reports on spontaneous combustion of sulfide ores can be groups into oxidation mechanism study, spontaneous combustion tendency evaluation, fire prevention and fire control technology. Payant et al. tested the hypothesis that galvanic interaction between some sulfides can promote self-heating [8]. Barnabe et al. determined the activation energy of four sulfide-bearing materials by using a custom-designed self-heating apparatus and procedure [9]. Li et al. analyzed the

main factors of infrared thermography method, including emissivity, distance, angle and dust concentration that affect the temperature measurement precision [10]. Liu et al. proposed a fire source locating method which can determine the point where the highest temperature on the surface of igniting ores occurs [11]. Wang et al. studied the effectiveness of using thermophile oxidation to reduce the risk of spontaneous combustion in mining high-sulfur content ores [12].
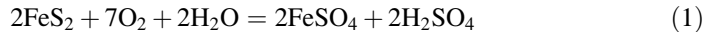
Sulfide ore heap has a strong ability to absorb oxygen due to its different types of pore structure and massive internal surface area. Under low temperatures, slow oxidation is accompanied by the dynamic change of adsorbed oxygen, which is a prerequisite for sulfide ores spontaneous combustion. Currently, research on low temperature oxidation process is mainly concentrating on the measurement of weight gain rate through laboratory experiment because it is a common evaluation index for sulfide ores spontaneous combustion [13, 14]. However, oxidation activity of the same ore under different oxidation conditions is significantly different. Therefore, it is necessary to carry out low temperature oxidation experiments under different oxidation conditions to explore a new evaluation method of oxidation activities.

In this work, nine typical sulfide ore samples from a pyrite mine in China were taken and their low temperature oxidation processes were simulated in laboratory. Combined with wavelet de-noising and fuzzy comprehensive evaluation, the comprehensive evaluation index for oxidation activity of sulfide ores under different oxidation conditions was proposed.

## 2 Experiment

### 2.1 Basic Principle

For the pyrite, the related reaction equations are as follows:

$$2FeS_2 + 7O_2 + 2H_2O = 2FeSO_4 + 2H_2SO_4 \tag{1}$$

$$4FeSO_4 + 2H_2SO_4 + O_2 = 2Fe_2(SO_4)_3 + 2H_2O \tag{2}$$

$$12FeSO_4 + 3O_2 + 6H_2O = 4Fe_2(SO_4)_3 + 4Fe(OH)_3 \tag{3}$$
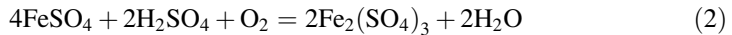
### 2.2 Samples Analysis

Nine sulfide ore samples were collected from a pyrite mine in China using multi-point sampling. Main chemical composition of the ore sample 1 is listed in Table 1.

**Table 1.** The main chemical composition of ore sample 1 (mass fraction, %)

| Water-soluble iron ion | Total sulfur | Monomer sulfur | Sulfate ion |
|---|---|---|---|
| 0.0016 | 35.27 | 0.044 | 1.57 |

Ore sample 1 is a pyrite with two-stage mineralization. The largest size of early-stage pyrite particles is about 5 mm and their average size is about 2 mm. They are fragmented as a result of the stress action. Unlike the early-stage pyrite particles, the late-stage pyrite particles are fine-grained aggregates with the average size of about 5 μm. The micrograph of the ore sample 1 is shown in Fig. 1.
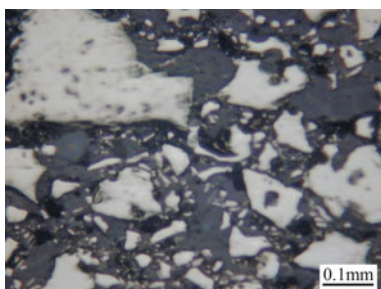


**Fig. 1.** Micrograph of ore sample 1

## 2.3 Experimental Scheme

The experiment is of low temperature oxidation of sulfide ores in natural environment at constant temperature and humidity environment (with temperature of 40 °C and humidity greater than 95%). Since moisture has an influence on the oxidation of sulfide ores, four kinds of experimental conditions were adopted in this experiment including samples with various levels of moisture content: 0%, (ConditionI), ≈5% (ConditionII), 0 and 5% under constant temperature and humidity environment (Conditions III and IV).

In the experiment, ore sample particles were ground to less than 180 μm in diameter. Each sample with mass of about 40 g was put into the glass dish on test bed under these four oxidation conditions. During the experiment, samples were weighed with electronic balance every 3–4 days until their mass remained stable. Weight gain rate can be expressed as

$$P = \frac{\Delta W}{W_0} = \frac{W - W_0}{W_0} \times 100\% \tag{4}$$

where $P$ is the weight gain rate, $\Delta W$ is the mass increase due to oxidation, $W_0$ is the initial mass and $W$ is the final mass after oxidation.

In order to study the changes of chemical composition content and apparent characteristics of samples, contents of water-soluble iron ion and sulfate ion were measured periodically, and surface conditions of several typical samples before and after oxidation was observed with a scanning electron microscopy.

Ore samples and combustion chamber used in the experiment are shown in Fig. 2.
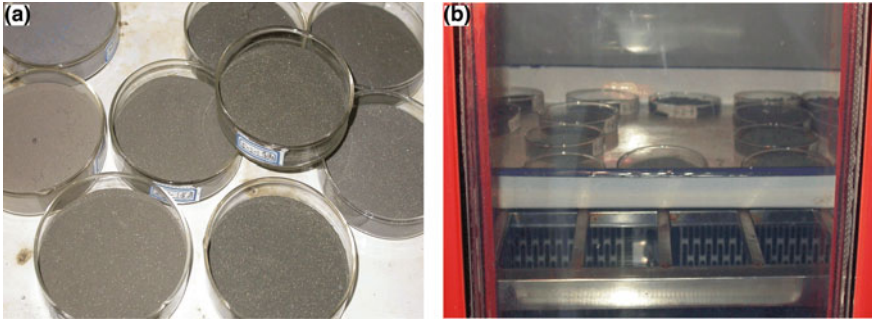
**Fig. 2.** Part of experimental photos: **a** Natural environment; **b** constant temperature and humidity

## 3   Experimental Results

### 3.1   Mass Variation Trend of Samples

During the experiment, it can be found that mass trend of ore samples under different oxidation conditions consists three stages: rapidly increasing (stage I), slowly increasing (stage II) and basically unchanged (stage III). At stage I), the oxidation products cover the ore particles surface so that the surface increases. Therefore, oxygen molecules are adsorbed more easily on the ore particles surface and react with the intermediate products, which cause sample mass to increase rapidly. At stage II, the ore particle surface is gradually oxidized and generates agglomeration. Oxygen absorption (especially chemical adsorption) reduces so that samples mass increases slowly at this stage. At stage III, ore particles surface is completely oxidized and oxygen absorption is mainly physical adsorption. Thus samples mass basically tends to be stable at this stage. Figure 3 depicts mass trend of partial ore samples under different oxidation conditions.

### 3.2   Trend of Chemical Composition Content of Samples

The experimental results show that content of water-soluble iron ion and sulfate ion of ore samples increase with the increase of oxidation time under different oxidation conditions. The reason is that water and oxygen are involved in the reaction during the low temperature sulfide ores oxidation, and the oxidation products contain water-soluble iron and sulfate ions. In general, when the oxidation activity is strong, content of these ions will be greater. Therefore, oxidation pattern under low temperature oxidation can be indirectly analyzed according to the trend of these chemical composition content (Fig. 4, Condition).
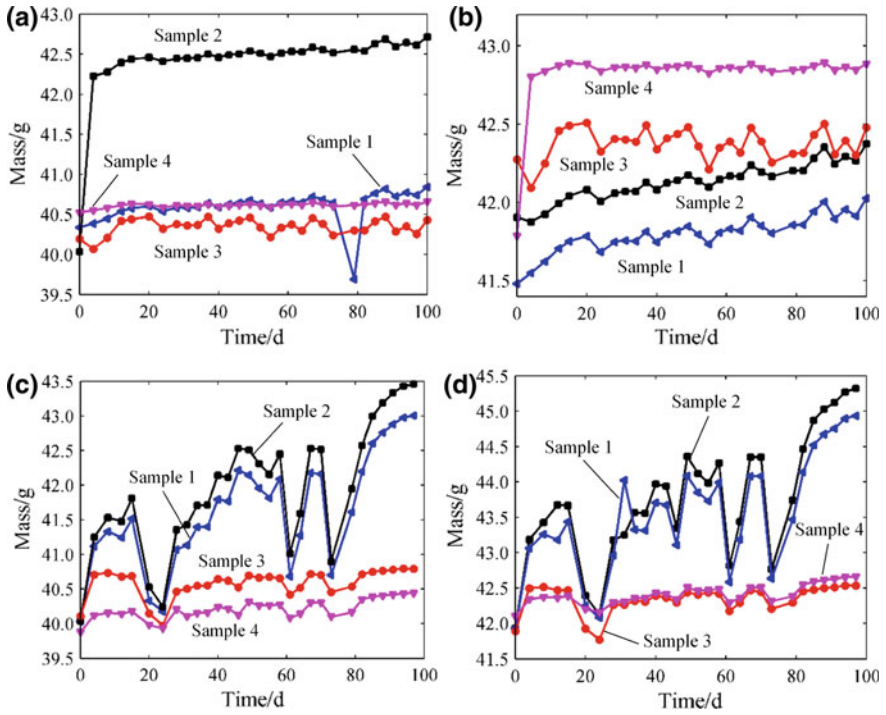
**Fig. 3.** Mass trend of partial ore samples under different oxidation conditions: **a** Oxidation condition I; **b** oxidation condition II; **c** oxidation condition III; **d** oxidation condition IV
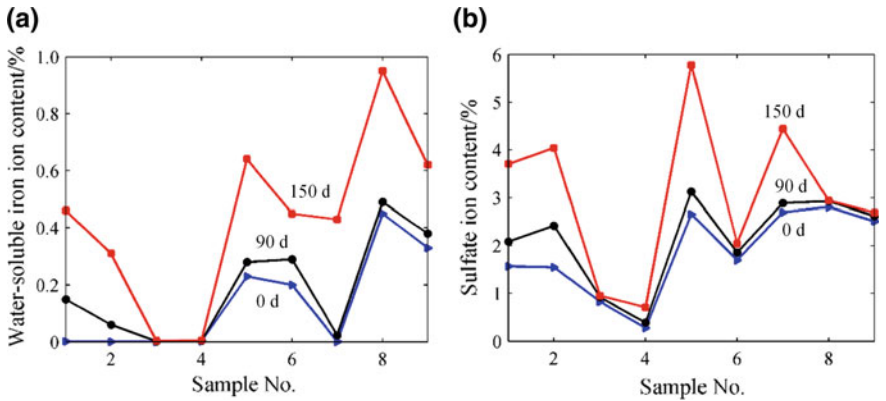


**Fig. 4.** Trend of chemical composition content under the oxidation condition I: **a** Water-soluble iron ion; **b** sulfate ion

### 3.3    Apparent Characteristics Change of Samples Before and After Oxidation

Before oxidation, the surface of ore samples is relatively smooth and the particles are uniform. After oxidation, the surface of ore samples is loose and porous, and moreover, there is obvious agglomeration on the surface of ore samples. This agglomeration is caused by chemical reaction and dissolution process. During the oxidation process of sulfide ores, variable valence elements of ore (such as Fe and S) cause its composition and crystal form to change. With the change of composition and crystal form, its specific gravity and specific volume also change, which is an important reason for agglomeration. Moreover, when ore particles absorb moisture from the air, or water inside the ore particles diffuses to its surface, solution film will generate on the surface. If the water of solution film is dried, solution film will become saturated solution to lead to the crystallization. With the passage of time, crystalline bridges will form owing to the crystal polymerization. Gradually, ore particles will be bonded together by crystalline bridges to produce agglomeration.

SEM photographs of Sample #2 before and after oxidation are shown in Fig. 5.
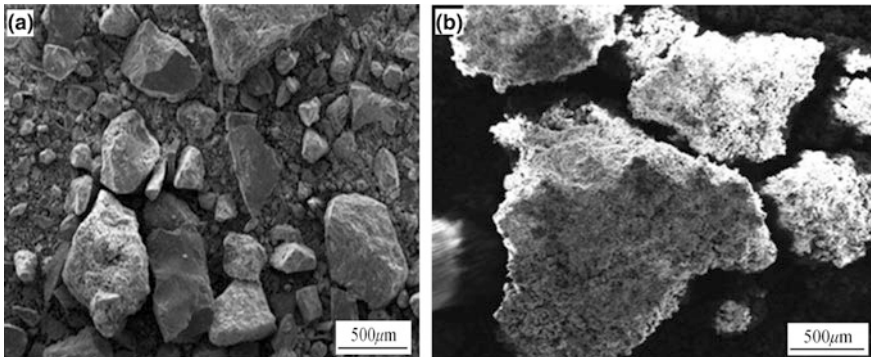


**Fig. 5.** SEM photographs of the ore sample 2: **a** Before oxidation; **b** after oxidation

## 4    Evaluation of Oxidation Activity of Sulfide Ores

### 4.1    Evaluation Index Optimization

Weight gain rate, content variation trend of water-soluble iron ion and sulfate ion and agglomeration properties can be used to roughly characterize the sulfide ores oxidation activities. According to reaction Eqs. (1)–(3), there is no gas emission during the low temperature sulfide ores oxidation. The main cause for sample mass increase is the absorbed oxygen from air based on the law of mass conservation. Therefore, weight gain rate can be used to evaluate the level of oxidation activities. At the early stage of low temperature oxidation, $Fe^{2+}$ will be produced. Then it will be further oxidized to $Fe^{3+}$ (such as $Fe_2(SO_4)_3$ and $Fe(OH)_3$). $Fe_2(SO_4)_3$ is with low solubility in water and $Fe(OH)_3$ is insoluble in water. Thus the measured chemical composition content will

not be to reflect the actual situation of oxidation reaction. Agglomeration is caused by the physical, chemical and other factors. Furthermore, it is difficult to analyze quantitatively. In this work, the rate of weight gain was selected as an evaluation index for oxidation activity based on the preceding analysis.

## 4.2 Wavelet De-noising of Weight Gain Rate Series

During the experimental process, the measured results of weight gain rate could be affected by many factors, such as humidity, dust floating in the air, moisture content variation of ore samples and measurement error of electronic balance. These factors could make the measured data contain some outliers. Therefore, in order to obtain accurate evaluation results, noise in the measured data need to be removed before evaluation model building. Because the wavelet technology has different de-noising combinations according to the different choice of wavelet base, decomposition scale and threshold value, it is very suitable for the weight gain rate series with unknown spectrum.

For the continuous case, the wavelet can be expressed as [15]

$$\psi_{a,b}(t) = |a|^{-1/2}\psi((t-b)/a) \quad a, b \in R;\ a \neq 0 \tag{5}$$

where $\psi_{a,b}(t)$ is a basic wavelet function or mother wavelet function, $a$ is the dilation (scale) factor, $b$ is the displacement factor.

Given a function $f(t) \in L^2(R)$, its continuous wavelet transform formulas and reconstruction formulas (inverse transform) are as follows:

$$W_f(a,b) = <f, \quad \psi_{a,b}> = |a|^{-1/2}\int_R f(t)\overline{\psi\left(\frac{t-b}{a}\right)}\,\mathrm{d}t \tag{6}$$

$$f(t) = \frac{1}{C_\psi}\int_{R^+}\int_R \frac{1}{a^2}W_f(a,b)\psi\left(\frac{t-b}{a}\right)\mathrm{d}a\mathrm{d}b \tag{7}$$

For the discrete case, the wavelet can be expressed as [16]

$$\psi_{j,k}(t) = |a|^{-1/2}\psi(2^{-j}t - k) \tag{8}$$

Correspondingly, the discrete wavelet transform coefficients and reconstruction formula are as follows:

$$C_{j,k} = \int_{-\infty}^{\infty} f(t)\overline{\psi_{j,k}(t)}\,\mathrm{d}t \tag{9}$$

$$f(t) = C\sum_{-\infty}^{\infty}\sum_{-\infty}^{\infty} C_{j,k}\psi_{j,k}(t) \tag{10}$$

where $C$ is a constant irrelative to the signal. Noise can be removed from the signal by the following steps:

(1) Select a suitable wavelet and determine the level of decomposition, and then decompose.
(2) Select the appropriate threshold value, and process the detailed coefficients.
(3) Reconstruct based on the detailed coefficients and approximate coefficients of wavelet decomposition.

It is very important for wavelet de-noising to select the appropriate wavelet function, decomposition level and threshold value. According to the fluctuation characteristics of weight gain rate, coifN or dbN with orthogonality, compactness and low vanishing moment were selected as the wavelet function. Because the high frequency components also contain massive real information, such as the weak fluctuation caused by dynamic oxygen adsorption process, decomposition level is not greater than 4 to avoid the useful information loss. In this work, decomposition level was determined with the value of 3 based on the trial calculation results. Default threshold method was selected as the estimation method of threshold value owing to its good universality for most of noise. Signal-to-noise ratio (SNR) was adopted to measure the de-noising effect.

Owing to the irregular measurement during the experimental process, the measured weight gain rate series were extended to equal time series with cubic spline interpolation method. Then, fifteen wavelet functions of wavelet series coifN and dbN were selected and the wavelet function with the maximum SNR was adopted as the optimum wavelet function. Optimum wavelet function and the de-noising effect of weight gain rate series under different oxidation conditions are listed in Table 2.

**Table 2.** Optimum wavelet function and the de-noising effect of weight gain rate series under different oxidation conditions

| Sample No. | Oxidation condition I | | Oxidation condition II | | Oxidation condition III | | Oxidation condition IV | |
|---|---|---|---|---|---|---|---|---|
| | Wavelet function | SNR | Wavelet function | SNR | Wavelet function | SNR | Wavelet function | SNR |
| 1 | coif4 | 23.9144 | db6 | 25.6013 | coif4 | 24.6371 | coif4 | 21.6543 |
| 2 | db7 | 45.5135 | db6 | 25.1605 | coif4 | 25.4155 | coif4 | 24.0467 |
| 3 | db6 | 15.8222 | db6 | 12.8779 | coif4 | 24.9288 | db8 | 25.3775 |
| 4 | db6 | 23.6281 | db6 | 43.9712 | coif4 | 22.3837 | coif4 | 23.8217 |
| 5 | coif5 | 38.1017 | coif5 | 38.9917 | coif4 | 34.5334 | coif4 | 34.5871 |
| 6 | db6 | 34.2041 | db6 | 29.5609 | db5 | 26.0123 | coif4 | 24.7743 |
| 7 | db5 | 31.1321 | db9 | 29.9399 | coif4 | 25.4637 | coif4 | 27.1654 |
| 8 | coif4 | 37.9392 | db6 | 33.6213 | coif4 | 24.5902 | coif4 | 24.9072 |
| 9 | db6 | 34.8232 | db6 | 27.3208 | coif4 | 25.8605 | coif4 | 25.6745 |

## 4.3 Evaluation of Sulfide Ore Oxidation Activity

Since oxidation activity of the same ore under different oxidation conditions is significantly different. If the rate of weight gain under a same oxidation condition is applied as the evaluation index of oxidation activity, although results could be inaccurate. Therefore, low temperature oxidation experiment of multi-sample under the four common oxidation conditions were carried out in the laboratory, and rate of weight gain was selected as an evaluation index for oxidation activity. On this basis, weight gain rate under the four common oxidation conditions were fused, and the integration value was defined as oxidation activity degree to be used in measuring the reaction ability of sulfide ores under different oxidation conditions.

According to the degree of oxidation activity, define the vector of oxidation activity degree under low temperature condition as $U = (u_1, u_2, u_3, u_4)$, where $u_1, u_2, u_3, u_4$ are weight gain rate under oxidation conditionsI-IV. To eliminate their difference of order of magnitude, $u_i$ ($i = 1, 2, 3, 4$) need to be normalized, namely $u_i \in U$, $U = (0, 1)$. Meanwhile, define the evaluation set as $V = (v_1, v_2, v_3, v_4, v_5, v_6, v_7, v_8, v_9)$, where $v_1$, $v_2, v_3, v_4, v_5, v_6, v_7, v_8$ and $v_9$ are corresponding to the ore sample 1–9. The experimental results show that fluctuation range of weight gain rate under oxidation condition I-IV decrease after 90 d. So the weight gain rate after wavelet de-noising of day 97 was selected as evaluation index.

Given the factors set $U$ and evaluation set $V$, $\alpha: U \to V$ is univariate evaluation function, so $f(\alpha(u_1), \alpha(u_2), \alpha(u_3), \alpha(u_4))$ is the comprehensive evaluation of $U$. Generally, comprehensive evaluation function involves two weight vectors, namely normalized weight vector and regularization weight vector.

In this work, the normalized weight vector was obtained with the value of (0.3730, 0.2616, 0.1806, 0.1848), and the univariate evaluation matrix $R = (r_{ij})_{4 \times 9}$ was established as

$$R = \begin{bmatrix} 0.1632 & 1 & 0.0400 & 0.0392 & 0.2604 & 0.2066 & 0.1075 & 0.3543 & 0.2375 \\ 0.4286 & 0.3569 & 0.0720 & 1 & 0.6864 & 0.2003 & 0.2717 & 0.2326 & 0.1738 \\ 0.5077 & 0.5840 & 0.1177 & 0.0956 & 0.5062 & 0.6261 & 0.7187 & 1 & 0.6340 \\ 0.5826 & 0.6585 & 0.1243 & 0.1079 & 0.3610 & 0.5967 & 0.7684 & 1 & 0.7138 \end{bmatrix}$$

(11)

Four kinds of evaluation functions were utilized to assess the oxidation activity of these nine samples.

When using the weighted average model, namely,

$$p_{1j} = \sum_{i=1}^{4} w_i r_{ij}$$

(12)

where $w_i$ is the weight vector elements and $r_{ij}$ is the scalar of normalized factors.

The evaluation value is $P_1 = (p_{11}, p_{12}, p_{13}, p_{14}, p_{15}, p_{16}, p_{17}, p_{18}, p_{19}) = (0.3723, 0.6935, 0.0780, 0.3134, 0.4348, 0.3528, 0.3830, 0.5584, 0.3805)$.

When using the geometric mean model, namely,

$$p_{2j} = \prod_{i=1}^{4} r_{ij}^{w_i} \tag{13}$$

The evaluation value is $P_2 = (p_{21}, p_{22}, p_{23}, p_{24}, p_{25}, p_{26}, p_{27}, p_{28}, p_{29}) = (0.3263, 0.6415, 0.0699, 0.1295, 0.4019, 0.3046, 0.2778, 0.4637, 0.3203)$.

When using the univariate decision model, namely,

$$p_{3j} = \bigvee_{i=1}^{4} (w_i \wedge r_{ij}) \tag{14}$$

The evaluation value is $P_3 = (p_{31}, p_{32}, p_{33}, p_{34}, p_{35}, p_{36}, p_{37}, p_{38}, p_{39}) = (0.4954, 1, 0.1243, 0.7013, 0.6864, 0.4954, 0.4954, 0.4954, 0.4954)$.

When using the main factors prominent model, namely,

$$p_{4j} = \bigvee_{i=1}^{4} (w_i \top r_{ij}) \tag{15}$$

The evaluation value is $P_4 = (p_{41}, p_{42}, p_{43}, p_{44}, p_{45}, p_{46}, p_{47}, p_{48}, p_{49}) = (0.3006, 1, 0.0616, 0.7013, 0.4814, 0.3032, 0.3807, 0.4954, 0.3536)$.

The above four kinds of evaluation values were taken as the initial evaluation, and then all of the initial evaluation were further evaluated. The final evaluation matrix $R_p$ was constructed based on the initial evaluation $P_i$ ($i$ = 1, 2, 3, 4), namely,

$$Rp = (P1, P2, P3, P4)T \tag{16}$$

According to the weighted average function, the formula of oxidation activity degree can be written as

$$\alpha = \sum_{i=1}^{4} \gamma_i \eta_{ij} \tag{17}$$

where $\alpha$ is oxidation activity degree, $\gamma_i$ is weight coefficient with the value of 0.25 and $\eta_1 - \eta_4$ are the column vectors of $R_p$.

Degrees of ore sample oxidation activity are listed in Table 3. From Table 3, it is found that the oxidation activity order of ore samples is: Samples #2, #8, #5, #4, #9, #7, #1, #6 and #3. Based on the degree of oxidation activities, self-heating initiative

Table 3. Sort of oxidation activity degree of ore samples

| Sample No. | 1 | 2 | 3 | 4 | 5 | 6 | 7 | 8 | 9 |
|---|---|---|---|---|---|---|---|---|---|
| Oxidation activity degree | 0.3737 | 0.8338 | 0.0834 | 0.4614 | 0.5012 | 0.3640 | 0.3842 | 0.5032 | 0.3875 |
| Sort | 7 | 1 | 9 | 4 | 3 | 8 | 6 | 2 | 5 |

temperature and ignition point, spontaneous combustion tendency of sulfide ores could be evaluated more accurately.

Currently, the common experimental conditions of low temperature oxidation of sulfide ores are in the natural environment under constant temperature and humidity. Usually rate of weight gain in a certain period under the same oxidation condition is measured and utilized as the evaluation index of oxidation activity. According to the massive experimental results, rate of weight gain under different oxidation conditions are not consistent. Thus, evaluation results might be questionable by using the traditional evaluation method.

The oxidation activity degree proposed in this work is the integration value based on the experimental results under different oxidation conditions, and the effect of noise is eliminated with the wavelet technology before evaluation model building. The evaluation results could be more accurate and objective with oxidation activity degree. Moreover, this is a new evaluation method for oxidation activity of sulfide ores.

## 5    Conclusions

(1) Ore samples mass variation trend during low temperature oxidation process consists of three stages: rapidly increasing, slowly increasing and basically unchanged.
(2) Content of water-soluble iron ion and sulfate ion of ore samples increase after oxidation. Oxidation pattern of low temperature oxidation can be indirectly analyzed according to the trend of chemical composition content of samples.
(3) The surface of ore samples is relatively smooth and particles are uniform before oxidation. After oxidation, the surface of ore samples is loose and porous, and there is obvious agglomeration on ore samples surface.
(4) The oxidation activity order of ore samples according to comprehensive evaluation results is: Samples #2, #8, #5, #4, #9, #7, #1, #6 and #3. The evaluation results are more accurate and objective with the oxidation activity degree method.

## References

1. Wu, C., Li, Z.J., Li, M.: Chemical thermodynamic mechanism of sulfide ores during oxidation and self-heating process. In: Proceedings of the 2007 International Symposium on Mining Safety Science and Technology, pp. 2435–2439. Science Press, Beijing (2007)
2. Li, Z.: Investigation on the Mechanism of Spontaneous Combustion of Sulfide Ores and the Key Technologies for Preventing Fire, pp. 1–3. Central South University, Changsha (2007)
3. Somot, S., Finch, J.A.: Possible role of hydrogen sulphide gas in self-heating of pyrrhotite-rich materials. Miner. Eng. **23**, 104–110 (2010)
4. Yang, F., Wu, C., Li, Z.: Spontaneous combustion tendency of fresh and pre-oxidized sulfide ores. J. Cent. S. Univ. **21**(2), 715–719 (2014)

5. Gunawan, R., Zhang, D.K.: Thermal stability and kinetics of decomposition of ammonium nitrate in the presence of pyrite. J. Hazard. Mater. **165**, 751–758 (2009)
6. Wu, C., Meng, T.: Theory and Technology for Control of the Mine Spontaneous Combustion of Sulphide Ores, pp. 1–4. Metallurgical Industry Press, Beijing (1995)
7. Pan, W., Wu, C., Li, Z., Yang, Y.: Self-heating tendency evaluation of sulfide ores based on nonlinear multi-parameters fusion. Trans. Nonferrous Met. Soc. China **25**(2), 582–589 (2015)
8. Payant, R., Rosenblum, F., Nesset, J.E., Finch, J.A.: The self-heating of sulfides: galvanic effects. Miner. Eng. **26**, 57–63 (2012)
9. Arnabe, N., Edwin, J., James, A.F.: Estimating activation energy from a sulfide self-heating test. Miner. Eng. **24**, 1645–1650 (2011)
10. Li, Z., Shi, D., Wu, C., Wang, X.: Infrared thermography for prediction of spontaneous combustion of sulfide ores. Trans. Nonferrous Met. Soc. China **22**(12), 3095–3102 (2012)
11. Liu, H., Wu, C., Shi, Y.: Locating method of fire source for spontaneous combustion of sulfide ores. J. Cent. S. Univ. Technol. **18**(4), 1034–1040 (2011)
12. Wang, H.J., Xu, C.S., Wu, A.X., Ai, C.M., Li, X.W., Miao, X.X.: Inhibition of spontaneous combustion of sulfide ores by thermopile sulfide oxidation. Miner. Eng. **49**, 61–67 (2013)
13. Deng, Y.: Research on Caking Mechanism of Sulfide Ores and its Detection Technology, pp. 40–41. School of Resources and Safety Engineering, Central South University, Changsha (2010)
14. Li, Z., Xu, Z., Deng, Y.: Parameter optimization of oxidation weight increase method for oxidability detection of sulfide ores at low temperature. China Saf. Sci. J. **22**(6), 54–59 (2012)
15. Mallat, S., Hwang, W.L.: Singularity detection and processing with wavelet. IEEE Trans. Inf. Theor. **38**(2), 617–643 (1992)
16. Donoho, D.L.: De-noising by soft-thresholding. IEEE Trans. Inf. Theor. **41**(3), 613–627 (1995)

# Investigation of Water Build-up in Vertical Upcast Shafts Through CFD Analysis

Joeline Viljoen and F. H. von Glehn[✉]

BBE Consulting, 24 Sloane St, Bryanston 2060, South Africa
{joeline, fvonglehn}@bbe.co.za

**Abstract.** Air that passes through mine workings generally accumulates moisture and is often saturated with water vapor when it reaches shaft bottom. As air rises up the shaft the barometric pressure reduces, thus decreasing the temperature. With this decrease in temperature, water condenses out of the air as very small droplets. As the air rises, more water will condense which will cause the small droplets to grow into larger drops. In deep shafts carrying large volumes of air, significant quantities of water can be condensed every hour. Previous studies found that the most common velocity at which water build-up occurs is ≈8 m/s, which is referred to as the critical velocity. With various factors influencing this figure, the critical air speed can range between 7 and 12 m/s. A study was recently conducted to investigate an incident at a mine that experienced structural damage to the main surface fan station. The incident was suspected to be a result of water build-up in the upcast shaft. A theoretical investigation was conducted using Computational Fluid Dynamics (CFD) analysis to investigate the possibility of water build-up in the shaft at the given operating conditions. This paper presents the theory behind water build-up and discusses the CFD model set up to simulate water build-up in a vertical upcast shaft. The results from the CFD analysis show at what critical velocity range water build-up occurred in this specific case.

**Keywords:** CFD · Water build-up · Upcast shaft

## 1 Introduction

An underground mine upcast shaft top bend experienced structural damage from an incident which sheared holding bolts, resulting in steel panels imploding in the shaft top bend. An incident investigation concluded that the most probable cause for the incident was water blanket formation in the shaft. These types of failures are not common and additional scientific analysis through Computational Fluid Dynamics (CFD) modelling was required to validate investigation findings.

Historically it has been found that the most common velocity at which water build-up occurs is 8.0 m/s (I presume these are measured/approximate numbers, using decimal points imply measurement accuracy, I wonder if we should just drop the decimal point?), which is referred to as the critical velocity. With various factors influencing this value, the theoretical critical air speed can range between 7.0 and 12.0 m/s.

This particular upcast shaft has a step-up in the diameter just below surface, resulting in a decrease in the air speed, as the air enters this section with a sudden expansion in the diameter. The air speed in the lower section of the shaft, with a smaller diameter, can be high enough to fall outside the critical velocity range but as soon as the air enters the larger diameter section, it is possible for the air speed to drop to within the critical range.

The upcast air speed in the lower section of shaft was known at the time of the incident and the CFD analysis had to firstly establish if water build-up would occur in the upper section of shaft at this air speed. Secondly, the critical air speed range for this particular shaft was determined and compared to currently available literature.

## 2  Literature Review

The main keyword phrases (combinations and individual) used in the literature search included the following (but not limited to): "upcast shaft velocity", "terminal velocity", "critical velocity range", "water droplet condensation", "water droplet size distribution", "fluid film" and "water blanket formation".

The first work done on the subject was by J. de V. Lambrechts [1] in the 1950s, when suspicions were raised that water droplet formation was contributing to higher than expected airflow resistances at a number of ventilation shafts. Empirical observations were made at twelve shafts, where the fan pressure increased over a period of time and the airflow rate decreased.

Air passing through working areas of an underground mine can become fully saturated with water by the time it reaches the bottom of the upcast shaft. As the air rises up the shaft, the barometric pressure reduces and subsequently the air temperature is reduced. The reduction in air temperature causes water to condense out of the air as small water droplets (foggy appearance) and as it rises further, more water condenses onto these droplets, causing them to grow even larger.

Different size droplets have different terminal velocities; thus, if the air velocity up the shaft is less than the droplet terminal velocity, the droplet will fall out and if more than the droplet terminal velocity, the droplet will be carried out of the shaft. If the air velocity is similar to the droplet terminal velocity, the droplet will remain suspended until either colliding with other droplets (growing larger) or colliding with the sidewall, breaking up into smaller droplets or forming part of the fluid film attached to the sidewall.

In his paper: 'The Value of Water Drainage in Upcast Mine Shafts and Fan Drifts', Lambrechts [1] recommended that an upcast velocity of 10.2 m/s (2000 fpm) should be avoided as this can lead to formation of a 'solid blanket of water' and it was termed the 'critical carrying velocity'. Depending on the shaft conditions, he recommended that upcast shaft velocities should be lower than 7.0 m/s or higher than 12.0 m/s.

Grave [2] stated the critical upcast velocity range as 7.5–12.5 m/s and that the source of water was due to condensation of water droplets in the air because of the drop in air temperature as it rises up the shaft.

Le Roux [3], in Note 3.7, stated a critical velocity of 8.0 m/s but with a caution that this was not an exact figure as it is affected by various factors. Due to the density

variation in deep shafts, the air velocity at the top of the shaft might be 10.0 m/s while it may be 8.0 m/s at the shaft bottom. Therefore, upcast shafts should be designed to not operate in the range of 7.0–12.0 m/s, so that water can either fall down or be carried out by the airstream.

McPherson [4] in Chap. 9 also refers to designing upcast shaft by avoiding velocities in the range of 7.0–12.0 m/s. Many authors have subsequently also referred to the recommended air speed range but mainly refer back to the original work done [for example, 5, 6].

In determining the dynamics of water drops in upcast shafts, knowledge of the drop size distribution is required. The literature search did not discover any meaningful studies done on the droplet size distribution in mine shafts and thus typical reference values in work relating to rain drops and nozzle-produced droplet sizes were used.

There are different processes by which droplets grow in moist air and the growth of drop population is discussed in literature relating to rainfall studies by Mason [7, 8] and Dufour [9]. In 2002 Babinsky and Sojka [10] reviewed three available methods for modelling drop size distribution. Water droplets with a diameter greater than 6 mm are rarely observed in natural rainfall, as they usually break up into smaller droplets. A typical drop size distribution was adopted for this study from Chen and Trezek [11] shown in Table 1.

**Table 1.** Water drop size distribution

| Drop size (mm) | Reference size (mm) | Probability of existence (% of volume) |
| --- | --- | --- |
| <1 | 0.5 | 8 |
| 1–2 | 1.5 | 30 |
| 2–3 | 2.5 | 27 |
| 3–4 | 3.5 | 21 |
| 4–5 | 4.5 | 12 |
| >5 | 5.5 | 2 |

## 3   Software and Computing Power

The analysis was conducted using the commercial CFD software StarCCM+ with an Intel® Core™ i7-4790K CPU @ 4.00 GHz processor with 32.0 GB RAM.

## 4   CFD Process Description

The CFD process, in short, consists of the following main steps:

- Import surface geometry from CAD model
- Assign Boundary Types
- Generate a Region-Based Mesh
- Define Physics
- Create reports, monitors and plots of required data to be analysed

- Simulate and monitor
- Post process data
- Evaluate results.

## 5    CAD Model Setup and Inputs

The main area of concern was the zone where the shaft diameter steps up to the larger diameter and hence it was deemed unnecessary to model the full length of the shaft. For this analysis, the following components were included in the model to capture the aerodynamic behaviour of the air and water in the shaft:

- Smaller diameter lower shaft section of 60 m
- Step in shaft diameter
- Large diameter upper shaft section of 55 m
- Shaft top bend
- Fan drift up to the fan inlet.

The total length of shaft modelled to capture the flow behaviour was 115 m. The quantity of water in suspension was calculated from information obtained from calibrated VUMA3D models (mine ventilation simulation software). The moisture content at the bottom of the shaft was approximately 0.0216 kg water per 1 kg of air (kg/kg) and at the inlet boundary of the lower shaft model 0.0203 kg/kg. This results in 0.0013 kg/kg of condensate in the shaft. At the airflow rate of 244 kg/s, the rate of water droplets in suspension was 0.3172 kg/s.

The typical drop size distribution varied from a minimum of 0.5 mm to a maximum of 5.5 mm [11], with a mean of 2.55 mm and a standard deviation of 1.7613 mm. The modelled airflow entering the shaft allowed for some moisture content, modelled with a volume fraction of water of 0.00006 (air volume fraction of 0.99994).

## 6    Meshing

Two meshing models were used for this study:

- Polyhedral Mesher
- Prism Layer Mesher.

A polyhedral cell mesh is used as the core volume mesh as it provides a balanced solution for complex mesh generation problems [12]. This mesh is relatively easy and efficient to build. The polyhedral meshing model utilizes an arbitrary polyhedral cell shape in order to build the core mesh; refer to Fig. 1 for the volume mesh.

The prism layer mesh model is used with the core volume mesh to generate orthogonal prismatic cells next to the wall surfaces and boundaries, refer to Fig. 2. Prism layers allow the solver to resolve near-wall flow accurately, which is critical in determining not only the forces and heat transfer on walls, but also flow features such as separation. Separation in turn affects integral results such as drag or pressure

**Fig. 1.** Volume mesh



Prism layer mesh
consisting of two layers
at the boundaries
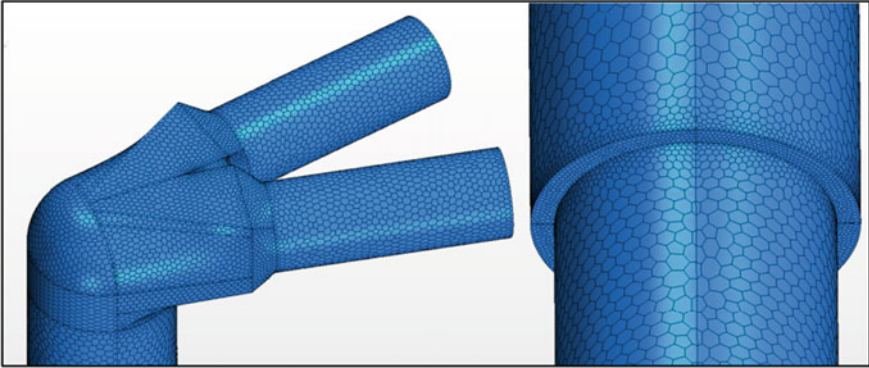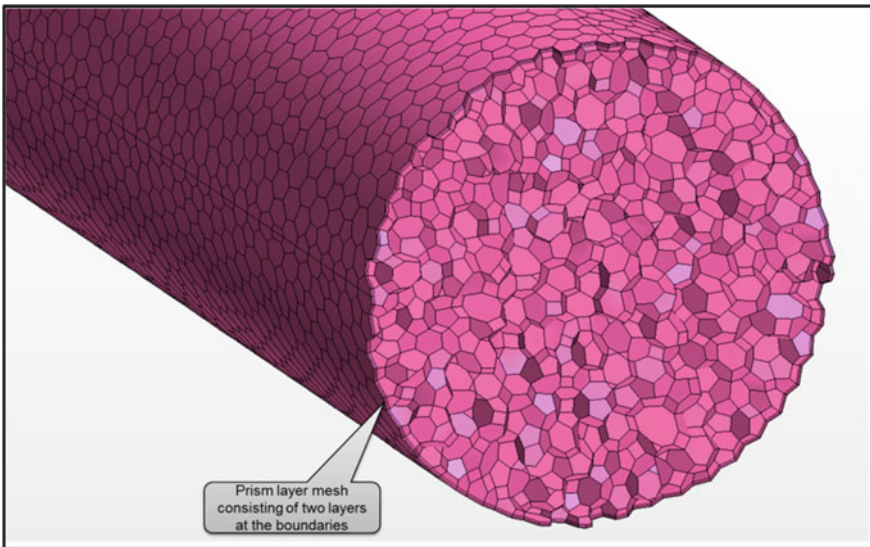
**Fig. 2.** Prism layer with volume mesh

drop. Accurate prediction of these flow features depends on resolving the velocity and temperature gradients normal to the wall. Table 2 indicates all of the mesh values defined for the model.

## 7    Setting up Physics Models

STAR-CCM+ contains a wide range of physics models and methods for the simulation of multi-phase fluid flow and turbulence [12]. To capture the dynamic behaviour and interaction of the airflow and water, the analysis was conducted in the transient domain.

**Table 2.** Mesh values

| Description | Reference values |
|---|---|
| Cell base size (mm) | 350 |
| Number of prism layers | 2 |
| Prism layer stretching (factor) | 1.5 |
| Prism layer thickness (mm) | 40 |
| Surface growth rate (factor) | 1.3 |
| Surface size relative to base size: minimum (mm), target (mm) | 87.5 (25%), 350 (100%) |

The physics models selected to capture the behaviour of the water in the air and the interaction between air and water are listed in Table 3.

**Table 3.** Physics models

| Model | Description/reason required |
|---|---|
| Space: three dimensional | |
| Time: transient | Time varying solution requiring unsteady model |
| Material: Eulerian multiphase | Two materials present; air and water. On selecting this model, an interaction model is automatically activated, allowing interaction between water and air |
| Eulerian multiphase model: volume of fluids (VOF) | To allow transition of the fluid film into water, allowing volumes of water to form within the airflow stream |
| Viscous regime: turbulent | Flow in the shaft is expected to be turbulent |
| Reynolds-averaged Navier-Stokes turbulence: K-epsilon turbulence | Solves transport equations for turbulent kinetic energy (k) and turbulent dissipation rate (epsilon) |
| Lagrangian multiphase | To model water droplets in suspension this model is used with an injector at the inlet boundary, coupled with the fluid film model |
| Fluid film | To allow for fluid film formation on the sidewall boundaries |
| Gravity | Accounts for gravitational acceleration |
| Segregated multiphase temperature | Allows for the control of thermal effects; solving the total energy equation with temperature as the solved variable. Enthalpy is computed according to the equation of state |

# 8    Boundary Conditions

Figure 3 indicates the CFD model inlet and outlet boundaries.
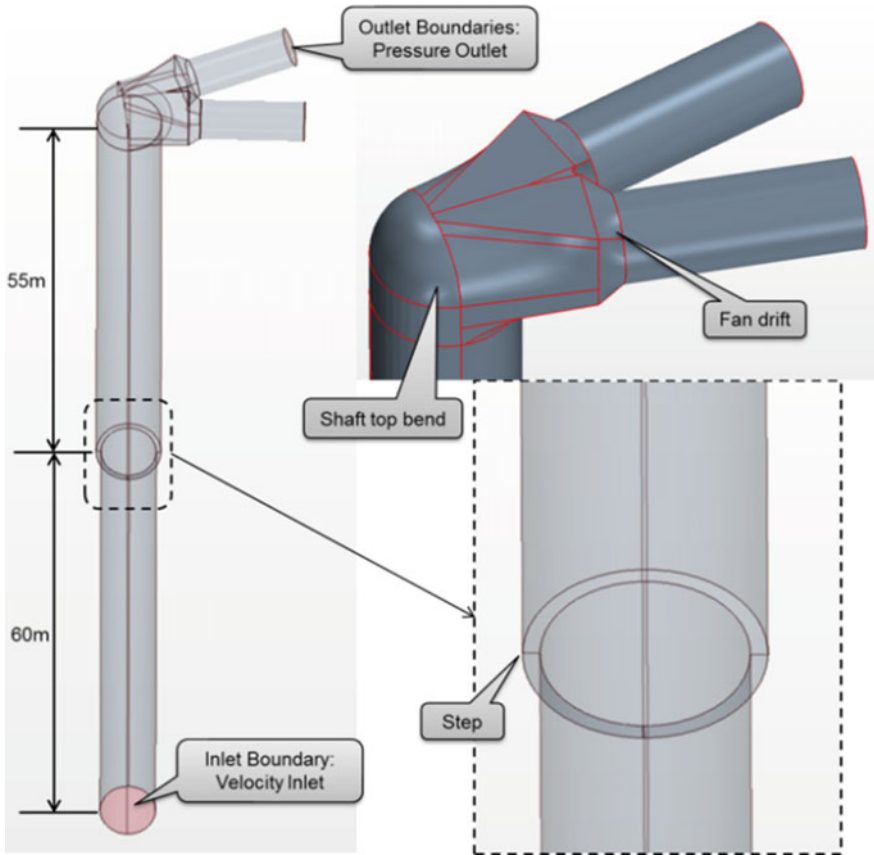
**Fig. 3.** Indication of model boundaries

## 8.1 Inlet Boundary

The shaft inlet boundary was modelled as a velocity inlet boundary. The following values were assigned to the inlet boundary:

- Static temperature: 23.3 °C
- Velocity magnitude: 13.3 m/s
- Volume fraction (Water, Air): 0.00006, 0.99994 (accounts for moisture in air).

Only the top section of the shaft was modelled, thus the inlet boundary of the shaft model had to take into account the water droplet formation that has already occurred in the lower portion of the shaft. As stated above, the inlet boundary was set up to allow for both water droplets and moisture in the air.

A Lagrangian phase injector was set up at the inlet boundary, to allow water droplets to enter the fluid region, with values assigned to the phase injector as discussed above.

## 8.2    Outlet Boundaries

The shaft outlet boundary was modelled as a pressure outlet boundary. The following values were assigned to the outlet boundary:

- Pressure: 0 Pa (relative to reference pressure*)
- Static temperature: 22.6 °C

  *Reference values: pressure of 85.8 kPa and density of 0.98 kg/m$^3$.

# 9    Monitoring

To determine if water build-up occurs in the shaft, certain parameters had to be monitored. This was done by setting up reports at both the inlet and outlet boundaries. The following parameters were monitored and plotted at both the inlet and outlet boundaries: droplet mass flow (kg/s), droplet velocity (m/s), air mass flow (kg/s), air velocity (m/s), air density (kg/m$^3$), air pressure (Pa) and total water mass flow (kg/s).

# 10    Method Statement—Base Case

Water build-up in upcast shafts usually occurs over several days. To simulate this real-time water build-up over days with a transient CFD simulation is not impossible but highly impractical. This would require excessive solving time and processing power due to the small time-steps required and the number of iterations per time-step. The actual time to solve one iteration is further complicated by the number of Physics Models required to capture the behaviour of air-water and water-water interaction, thus simulations were limited to approximately 15 min of operation in real-time; thus the difference between mass flow in and out of the system was expected to be very small.

   Several scenario simulations were completed, starting with the base case model with the flow conditions at the inlet of the shaft as given in Table 4. A constant inlet profile was assumed at the inlet of the shaft. The 60 m length of shaft is greater than the entrance length for airflow at 13.3 m/s, ensuring a developed airflow profile before the air reaches the step in the shaft.

Table 4.  Flow conditions at the inlet of the lower shaft section—base case

| Condition | Value |
| --- | --- |
| Barometric pressure (kPa) | 87.2 |
| Inlet density (kg/m$^3$) | 0.99 |
| Inlet flow (kg/s) | 244 |
| Shaft diameter (m) | 4.8 |
| Lower shaft section inlet velocity (m/s) | 13.3 m/s |

The main tracking parameters are the droplet mass flow and the evaporated water in the air at both the shaft inlet and the fan inlet (fan inlet boundary simulated as a drift outlet boundary). By plotting the variation of the water mass flow into the system and the mass flow out of the system, the water mass build-up over time can be determined.

## 11 Results and Analysis

The main purpose of the study was to evaluate the aerodynamic behaviour of the airflow in the shaft and thus the aerodynamic behaviour of the water in suspension; to determine if water is building up in the shaft over time and at what velocity water build-up will no longer occur. In this section, the results and findings from the simulations are discussed and evaluated.

### 11.1 Base Case—Lower Shaft Velocity of 13.3 m/s (10.1 m/s in Upper Section)

An inlet velocity of 13.3 m/s in the lower shaft section results in an average velocity of approximately 10.1 m/s in the upper shaft section; from experience and theory it is thus expected that water build-up will occur in the upper shaft section.

Figure 4 shows the mass flow of all forms of water (droplets in suspension and moisture in air) into the system (blue line) and out of the system (red data dots) over time. A linear trendline of the mass flow out of the system (red line) is plotted to show the actual trend of the mass flow out of the system. It can be seen that the mass flow of water out of the system decreases over time with a constant water inlet; the mass flow out trendline has a very slight downward slope, indicating that water mass gradually builds-up over time in the larger upper section of shaft.
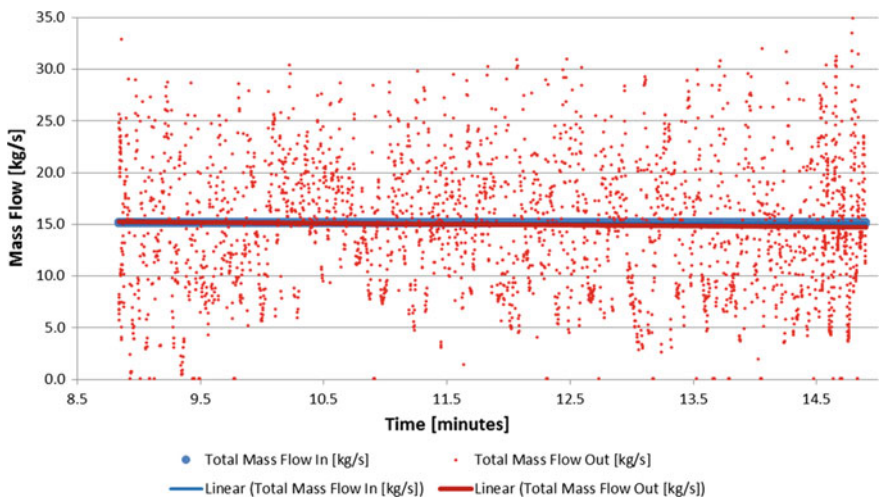


**Fig. 4.** Total mass flow over time—13.3 m/s in lower section

Isosurfaces were set up to indicate the volume fraction of water in the cells. The light blue/silver colour (as seen in Fig. 5) represents a volume fraction of water of 0.001. The slightly darker blue colour represents a water volume fraction of 0.015 and dark blue represents a volume fraction of 0.2.
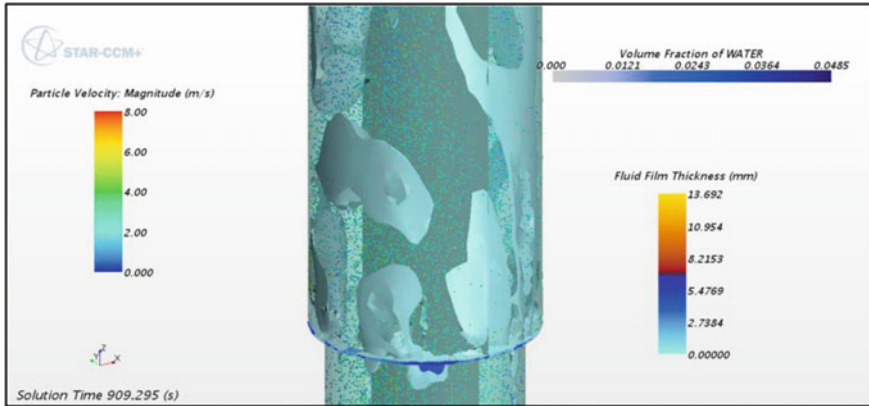


**Fig. 5.** Snapshot at step of 13.3 m/s scenario after 15 min

## 11.2 High Velocities—Lower Section Velocity of 18.0 m/s (13.2 m/s in Upper Section)

At a lower shaft section velocity of 18.0 m/s, the upper shaft section average velocity is approximately 13.2 m/s; at this velocity no water build-up is expected. The results from the CFD simulations are plotted in Fig. 6. It can be seen that the mass flow out of the system is more than the mass flow into the system (red line gives the linear trend of mass flow data out of the system), resulting in no water build-up in the shaft.

Figure 7 shows snapshots of the step in the shaft at about 10 min of operation. It is evident from these visual images that more water is exiting the system compared to the base case and with no water build-up in the shaft.

## 11.3 Determining the Inlet Velocity at Which Water Build-up No Longer Occurs

It is expected that at approximately 12 m/s, no water build-up should occur in the larger upper shaft section. At a small lower shaft section velocity of 16.0 m/s, the upper shaft average velocity is approximately 11.8 m/s, which is close to 12 m/s.

A number of simulations were carried out to determine at which velocity water build-up would no longer occur; the first scenario simulated was at a lower shaft velocity of 16.0 m/s (11.8 m/s in upper shaft). The CFD simulation results indicated that there would still be a gradual water build-up over time at these upcast velocities.

With the 16.0 m/s velocity in the lower shaft system still resulting in water build-up, the next velocity that was evaluated was 17.0 m/s, which results in an upper
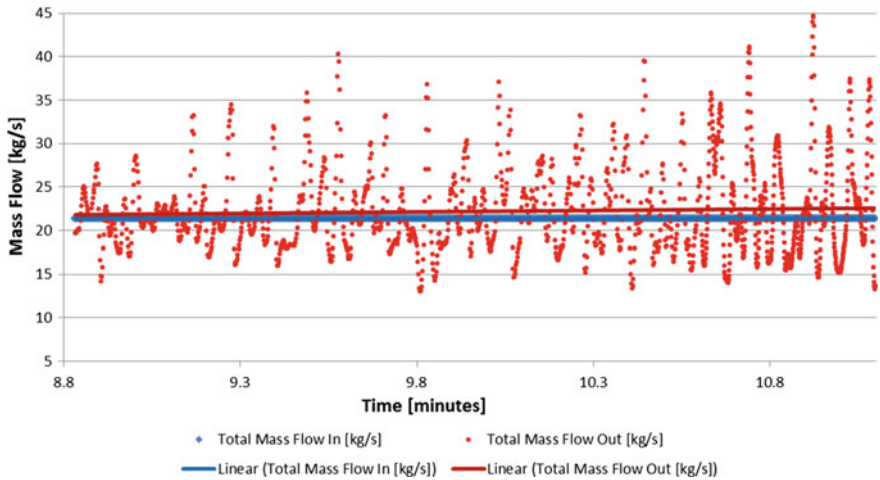
**Fig. 6.** Total water mass flow over time—18.0 m/s in lower section
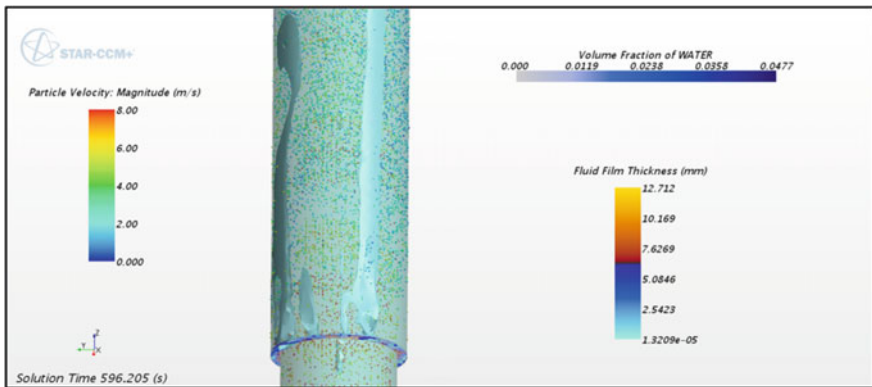


**Fig. 7.** Snapshot at step of 18.0 m/s scenario after 10 min

shaft section velocity of approximately 12.5 m/s. The results from the CFD simulation showed that the mass flow out of the system is constant and approximately equal to the mass flow into the system, which indicates no water build-up in the system.

## 12  Conclusion and Recommendations

The main purpose of this CFD study was to determine if water build-up would occur in the upcast shaft, causing water blanket formation, at the given operating conditions and to investigate possible solutions. The results indicated that at the given operating conditions (an air speed of 13.3 m/s in the lower shaft section), water build-up will occur in the system, which will lead to water blanket formation.

More simulations were conducted to determine at what air speed water build-up would no longer occur. From literature and previous studies, it is known that in upcast shafts in which significant condensation occurs, the air speed range of 7.0–12.0 m/s should be avoided to avoid the suspension of water droplets. From the CFD analysis of this particular case, it was found that to avoid formation of a water blanket, the air speed in the lower shaft section should be a minimum of 17.0 m/s, resulting in an upper shaft section velocity of 12.5 m/s; a result which can be achieved by changing the inlet guide vane settings on the main surface fans.

In addition to the above, the study also proved that the theoretical critical air speed range of 7.0–12.0 m/s is a valid range to avoid when doing mine ventilation planning and upcast shaft design for a system where significant moisture buildup in the upcast shaft is expected.

# References

1. Lambrechts de, V.J.: The value of water drainage in upcast mine shafts and fan drifts. J. Chem. Metall. Min. Soc. S. Afr., 307–324 (March 1956)
2. Grave, D.F.H.: Main and auxiliary practice in South African gold mines. The mine ventilation society of South Africa (1974)
3. Le Roux, W.L.: Le Roux's notes on environmental control, 4th edn. The mine ventilation society of South Africa (1990)
4. McPherson, M.J.: Subsurface ventilation engineering, pp. 9–13. MVS, California (2009)
5. Derrington, A.S.: Ventilation rules of thumb—friend or foe? Focusing on design upcast air velocities for shafts and raise bores. In: The Australian mine ventilation conference, Brisbane (August 2017)
6. De Souza, E.: The mystery of the ventilation raises. In: Brune, J (ed) Proceedings 16th North American mine ventilation symposium. Colorado school of mines, Golden Co (2017)
7. Mason, B.J.: Clouds, rain and rainmaking. University of Cambridge Press, Cambridge (1962)
8. Mason, B.J.: Physics of clouds. Academic Press, Cambridge (1963)
9. Dufour, L.: Thermodynamics of clouds. Academic Press, Cambridge (1963)
10. Babinsky, E., Sojka, P.E.: Modelling drop size distribution. Prog. Energy Combust. Sci. **28**, 303–329 (2002)
11. Chen, K.H., Trezek, G.J.: The effect of heat transfer coefficient, local wet bulb temperature and droplet size distribution on the thermal performance of sprays. ASME J. Heat Transf. **99** (August 1977)
12. CD-adapco. STAR-CCM+ Version 10.06 User Guide (2015)

# Evaluating the "Unknown" Risks of Vehicular Tunnel Fires Through the Rubric and Matrix Method

Kirk H. McDaniel$^{(\boxtimes)}$ and Jürgen F. Brune

Colorado School of Mines, Golden, CO 80401, USA
kirkhmcdaniel@outlook.com

**Abstract.** Major tunnel fires are rare, unpredictable, and often devastating. History provides examples of major tunnel operations that had incorporated various elements of Fire Life Safety (FLS) and Emergency Preparation and Management (EPM) into the design, infrastructure, operations, and emergency response capability. Yet, tunnel operators have often found out in hindsight that their preparations were not sufficient. Factors that may either minimize or worsen a catastrophic event can be estimated and evaluated. Risk analysis is used extensively in various industries for both quantitative and qualitative applications. Formal, quantitative risk analysis uses "known-unknowns" and enables the use of quantitative analysis of probabilities and consequences. Uncertainty analysis deals with "unknown-unknowns" and is restricted to qualitative analysis. Researchers at the Colorado School of Mines have created a unique process to evaluate qualitative risks through an Emergency Preparedness Rubric and an Event Consequence Matrix method. The process was applied cross the functional areas of FLS-EPM and the tunnel's functional components that are important to safety. The method is universally adaptable and enables stakeholders involved in tunnel design, operations, management, and emergency response to identify and communicate areas where the systems and components are insufficient. This paper will address the approach, methodology, and results for a representative focus case.

**Keywords:** Tunnel · Fire · Preparation

## 1 Introduction

Tunnel fires are rare events, and major tunnel fires that cause extensive loss of life and destruction of property are even less frequent. History has also shown that some tunnel operators, such as those at Mont Blanc Tunnel between France and Italy [1] and Caldecott Third Bore in California, USA [2], have discovered that their preparations were insufficient in the face of a major fire event. Presumably, operators and emergency responders thought they were prepared but found that they were not. In many cases, the FLS design was not comprehensive or the response strategy and technology were inadequate. In some cases, tunnel operators or responders had a myopic view of the potential for disaster at their facility. Other tunnel operators including those at the

Burnley Tunnel in Melbourne, Australia [3] were well prepared and prevented a greater catastrophe even though seven people lost their lives.

Predicting when a tunnel fire might occur is nearly impossible. Predicting circumstances that may trigger or aggravate the event is even more difficult. In the face of such unpredictability or uncertainty designers, engineers and operators need a robust FLS-EPM system to ensure that the FLS-EPM system of a tunnel does not have any fatal flaws or gaps.

Researchers that the Colorado School of Mines (CSM) have created a unique process to address the strength and viability of tunnel fire FLS-EPM systems through an Emergency Preparedness Rubric and an Event Consequence Matrix method. This method examines all functional areas of FLS-EPM and those functional components important to safety. This paper represents a summary of a larger body of research funded by the State of Colorado Department of Transportation.

## 2    Development of the EPR-ECM Method

The designers and operators of larger or complex vehicular tunnels with high traffic volumes typically incorporate FLS-EPM systems. Voeltzel and Dix [4] show these for the Mont Blanc, Tauern, and Gotthard Tunnels in the Alps. A review of the case study on the Caldecott Bore Three [2] fire showed similarities to those identified by Voeltzel and Dix [4]. Each of these Fire Life Safety components plays an important part in the overall effectiveness of the FLS-EPM systems to prevent the event from occurring, detect the event as soon as it occurs, respond to an event efficiently, and mitigate the consequences of an event.

From published investigation reports and through stakeholder and Subject Matter Experts on code enforcement [5], researchers at the Colorado School of Mines found that vehicular tunnel operators may not:

- Have a consistent perspective on the possibility of an event at their facility,
- Understand the severity of an event, including the growth rate and spread of the fire, understand the steps, facilities and equipment necessary to prevent an event,
- Know how well the facility is prepared to deal with an event, should it occur,
- Know how best to mitigate or reduce the consequences of an event,
- Understand the limitations of various elements of FLS,
- Understand the limitations of trained emergency personnel to fight a tunnel fire, or
- Have an effective tool to use to identify and evaluate short comings within the FLS-EPM system.

## 3    Uncertainty Versus Risk

Risk analysis is used extensively in various industries in both quantitative and qualitative studies. Formal, quantitative risk analysis uses "known-unknowns" and required the use of probabilities for events and consequences. Lack of statistically meaningful data on the probability of major tunnel fire events, and on the outcomes of applying

FLS-EPM components precludes the application of quantitative analysis for tunnel fires. Uncertainty analysis examines "unknown-unknowns" and is restricted to qualitative analysis [6]. This type of analysis, the "risk matrix," often consists of a qualitative likelihood rubric combined with a consequence rubric. Items that rank above a pre-determined threshold are deemed unsatisfactory and subjected to risk mitigation. When examining the FLS-EPM components of vehicular tunnels, the term "uncertainty" [7] is more appropriate than the term "risk." Tunnel fires occur randomly, and contributing factors are largely unpredictable.

## 4 The Emergency Preparedness Rubric and Event Consequence Matrix Method

The Emergency Preparedness Rubric (EPR) combined with an Event Consequence Matrix (ECM) permits researchers, tunnel operators and emergency managers to examine FLS-EPM systems and components and to identify problematic FLS-EPM areas so that corrective action can be implemented in advance of an emergency. EPR and ECM enable stakeholders to communicate, evaluate, and identify areas where the FLS-EPM components and systems are marginal or deficient. The spreadsheet-based process guides the user to identify, categorize, and evaluate FLS-EPM components and to determine how these components may affect the performance of the FLS-EPM system.

The process identified nine Functional Areas (FA) of vehicular tunnel safety along with their representative Functional Components (FC). In this iterative process, Components were added, combined, or modified as the development matured. Some FAs may only have a single Component while other may have as many as 10 FCs. The FAs are:

1. Vehicles and Traffic Control: The ability to control vehicles in the tunnel.
2. Tunnel Monitoring and Control: The ability to monitor conditions and activities inside the tunnel and on approach, and to facilitate effective action in an emergency.
3. Ventilation Capacity and Equipment: The type and capacity of installed ventilation and support equipment, and the ability to facilitate corrective action in an emergency.
4. Tunnel Communications and Signage for Users: The use of communications systems to notify tunnel users of changing traffic conditions or emergency action.
5. Safety Equipment and Facilities for Users: The installed safety equipment and facilities that are available for tunnel users.
6. Emergency Response Capability: The ability to respond to an emergency.
7. Emergency Training and Qualification: The extent of training received by personnel that respond to the tunnel in an emergency.
8. Operational Policies and Procedures: The operational policies and procedures related to safety in the tunnel.
9. Facility Users and Education: The extent to which tunnel users are educated on the dangers of tunnel and on effective self-rescue alternatives.

Table 1 presents a representative list of FLS-EPM Functional Areas and Components for a two FAs associated with a typical road tunnel. Other FAs follow suit.

**Table 1.**  Representative FLS-EPM functional areas and components

| Functional area | Description | Functional components |
|---|---|---|
| Tunnel monitoring and control | Describes the ability to monitor conditions and activities inside the tunnel and on approach, and to facilitate effective action in the event of an emergency | 1. Tunnel monitoring center 2. Fire detection tunnel interior 3. Fire detection tunnel approach 4. Visual monitoring of tunnel interior 5. Visual monitoring of tunnel approach 6. Over height or dangerous vehicle detection 7. Tunnel monitoring center emergency support |
| Ventilation capacity and equipment | Describes the type and capacity of installed ventilation and support equipment, and the ability to facilitate corrective action in the event of an emergency | 1. Ventilation capacity —supply 2. Ventilation capacity —exhaust 3. Ventilation zone control—supply 4. Ventilation zone control—exhaust 5. Ventilation capacity ramp up/power system 6. Ventilation, duct and fan design 7. Ventilation control system 8. System redundancy |

## 5    The Emergency Preparedness Rubric

Based on the FAs and FCs, researchers developed an Emergency Preparedness Rubric for each Functional Component in the FLS-EPM System. It examines all FCs, both those installed as well as those *not* implemented, and rank them against pre-determined criteria. Researchers chose a five-level rubric with the following categories and corresponding numerical rating: Leading Industry or Best Practice, Good, OK, Marginal, Deficient. These corresponded to a 5-4-3-2-1 numerical scale to create simple intuitive

scale to use with the EPR-ECM method. Figure 1 represents a typical Emergency Preparedness Rubric for the Functional Component: Visual Monitoring of Tunnel Interior:

| Emergency Preparedness Rubric | | | | |
|---|---|---|---|---|
| 5 | 4 | 3 | 2 | 1 |
| LIP/Best | Good | OK | Marginal | Deficient |
| Criteria | | | | |
| System is fully operational and enables full visual coverage of tunnel interior including pan/tilt with no blind spots in accordance with accepted standards and leading industry practices | System is fully operational and enables full visual coverage of tunnel interior including pan/tilt and has thermal capability but has potential for blind spots | System is fully operational but does not enable full visual coverage of tunnel interior, does not including pan/tilt and has potential for blind spots | System is not completely operational/subject to breakdown or uses technology that is inaccurate | System is not installed or is functionally obsolete |

**Fig. 1.** Typical emergency preparedness rubric

## 6 Event Descriptions

The project defined six different emergency events that are used to rank FCs in the Event Consequence Matrix sufficient to challenge for full spectrum of FLS-EPM requirements for each FC for the credible conditions a typical tunnel will encounter.

1. Small Fire (1–4 Passenger Vehicles): A fire involving a multiple (1–4) passenger vehicles, light duty trucks, panel vans or similar. Heat Release Rate is 7.5–10 MW.
2. Medium Fire (Light Duty Cargo Truck): A fire involving a light fuel load truck such as a pickup with a cargo in the rear bed or a cargo truck with an integrated cargo area. Heat Release Rate is 10–70 MW.
3. Large Fire (Single HGV): A fire involving a single Heavy Goods Vehicle with non-hazardous mixed goods load. Heat Release Rate 150 MW.
4. Major Fire (Multiple HGVs): A fire involving a 2 or more Heavy Goods Vehicles with non-hazardous mixed goods loads. Might also involve a Dangerous Goods Vehicle carrying hazardous materials. Heat Release Rate is 150 MW each.
5. Multiple Fires (Different Vehicles and Locations): An event where there are separate fires ongoing in non-contiguous sections of the tunnel.
6. Vehicular Accidents (Any Combination of Vehicles): An event where there are vehicle accidents that do not result in fire but require response of FLS-EPM functional components.

## 7 Event Consequence Matrix and Key

Developing the Event Consequence Matrix requires two steps. The first was developing an Event Consequence Rubric (ECR). The second was developing the Event Consequence Matrix (ECM) and imbedding the Emergency Preparedness Rubric and Event Consequence Rubric into it. The ECR is used to judge the relative benefit or consequence of all FC's performance against one of the six fire events. Like the Emergency Preparedness Rubric, it utilizes a 5(best)-4-3-2-1(worst) scale. Combining the EPR

scale and ECR scale forms a 5 by 5 Event Consequence Matrix. Numerical scores from 25 to 1 are obtained by multiplying ECR and EPR scores. An ECM score of 25 is considered "best" in terms of emergency preparedness and indicates that the FC that is Leading Industry Practice, significantly benefits the facility and the outcome of an event. A score of 1 is considered "deficient", indicating that the FC could significantly jeopardize the facility or the outcome of an event. The key is used as a guide for discussion purposes has been adjusted compared to the ECM scale for continuity. Table 2 indicates the Event Consequence Matrix Key.

**Table 2.**  Event consequence matric key

| ECM rating | Description |
|---|---|
| 1–2 | Component represents a significant deficiency to the overall tunnel FLS-EPM system and should be addressed on an urgent basis |
| 3–4 | Component represents a deficiency to the overall tunnel FLS-EPM system and should be addressed |
| 5–7 | Component represents a possible deficiency to the overall tunnel FLS-EPM system and should be addressed |
| 8–11 | Component represents a benefit to the tunnel FLS-EPM system but warrants attention |
| 12–19 | Component represents a benefit to the tunnel FLS-EPM system but could be improved |
| 20–25 | Component represents a significant benefit to the tunnel FLS-EPM system |

## 8   Vehicular Tunnel Case Study and Validation

The project applied the previous steps to a representative tunnel case as a means of demonstrating the process and to assist in adjusting and validating it. The tunnel is an existing operational twin-bore vehicular facility in the western United States. Each bore is approximately 2700 m (9000 ft.) long with only slight downhill grade from east to west of less than 2%. Each bore provides for two lanes of uni-directional traffic. The facility is characterized by a long and isolated approach of an estimated 10 miles from either east or west, with grades of approximately 6–8% to reach the portals at 3400 m (11,000 ft.) above sea level. The tunnels handle approximately 12 million vehicles, passenger cars, light duty, and heavy goods trucks. The tunnels were built in the 1960s to 1970s. Researchers visited the facility, reviewed documentation and interviewed facility personnel to compile data.

Based on the EPR-ECM analysis, more than half of the tunnels' Functional Components rated poorly, while only a quarter of FCs rated as beneficial. The results are presented in the Table 3.

**Table 3.** Results of case study facility

| ECM rating | Number of occurrences | Occurrences (%) |
|---|---|---|
| 20–25 | 10 | 18 |
| 12–19 | 4 | 7 |
| 8–11 | 3 | 5 |
| 5–7 | 7 | 13 |
| 3–4 | 12 | 21 |
| 1–2 | 20 | 36 |
| Total | 56 | 100 |

Tunnel Monitoring and Control is the only Functional Area that ranked predominantly beneficial. Functional Areas that rated the lowest overall include Vehicles and Traffic Control, Emergency Response Capability and Emergency Qualifications and Training. Some of the problematic areas are an inherent part of the design, and resolving some issues would require major modifications to the tunnel infrastructure or support facilities to correct.

Researchers validated the EPR-ECM method by examining several historic tunnel fires as well as different tunnels at various stages in their design and operational lives. Validation steps included:

1. A review of select historical tunnel fire case studies to show that the resolution of contributing factors could be increased. The Caldecott [2], Mont Blanc [1] and Gotthard [8] tunnel fires were analyzed for this purpose. The analysis yielded significantly increased resolution of contributing factors compared to the published literature.
2. Applying the EPR-ECM method to a historical tunnel fire not previously included in the research researched: Dix's [9] analysis of the Burnley tunnel fire was analyzed for this purpose. This analysis indicated that the published information correlated to 97% with to the expect results of the EPR-ECM analysis.
3. Applying the EPR-ECM method to a new tunnel in operation gave an assessment of the level of preparedness and identified gaps and flaws in the FLS-EPM. The Caldecott Bore 4 Tunnel in California, USA, was used for this purpose given that it has been in operation for only a few years. Researchers obtained information on the tunnel operation by visiting the facility, interviewing tunnel operations personnel, and by reviewing the tunnel Emergency Response Plan [10]. The project team expected to see a high number of beneficial components for this facility given that it is relatively new construction. This analysis indicated that the tunnel FLS-EPM correlated to 88% compared to the EPR-ECM scale.

# 9   Discussion and Conclusions

The EPR-ECM method focuses on promoting safety through a systematic evaluation of components and an assessment of the possible consequences during a series of discrete events. The process can improve safety through systematic identification and evaluation of individual components that may require attention, and that collectively comprise the various FAs of the FLS-EPM. The research distinguished between a "safe component" and a "safe tunnel". Future work in this area might include appropriate weighting factors for various components, and thus develop an "expert system" that provides a better indication of the degree of safety. In conclusion, the EPR-ECM method:

(1)  Creates a road map so tunnel stakeholders can better communicate on FLS-EPM issues
(2)  Is universally applicable to different road tunnels
(3)  Captures all relevant FA and FCs of the FLS-EPM system, and can accommodate changes
(4)  Gauges where a tunnel's FLS-EPM systems falls in comparison to LIPs and standards
(5)  Identifies gaps and fatal flaws in the FLS-EPM system, which can then be resolved
(6)  Does not depend on the assumption of quantitative measures of risk
(7)  Can examine different sizes and types of emergency events
(8)  Can be used to review tunnel projects at different functional stages
(9)  Promotes evaluation involving a representative cross-section of tunnel stakeholders.

# References

1. Luchian, S.F.: Minister of the interior, and ministry of equipment, task force for technical investigation of the 24 March 1999 fire in The Mont Blanc Vehicular Tunnel. Report of 30 June 1999 (English translation). Minister of interior, Minister of equipment, transportation and housing (1999)
2. National Transportation Safety Board: Highway accident report multiple vehicle collision and Fire, Caldecott Tunnel, Near Oakland, California, April 7, 1982 (NTSB/HAR-83/1). National Transportation Safety Board, Washington DC (1983)
3. Dix, A.: Operational management of fire suppression systems. In: 13th Australian tunneling conference. AusIMM, Melbourne, 5 (2008)
4. Voeltzel, A., Dix, A.: A comparative analysis of the Mont Blanc, Tauern and Gotthard Tunnel Fires. Routes-Roads (No. 324), 19 October (2004)
5. English, Gary, interview by Kirk H. McDaniel. 2016. Chief, Assistant Fire Marshal, Seattle Fire Department, Seattle, Washington, 4 August (2016)
6. Kerzner, H.: Project management, a systems approach to planning, scheduling and controlling. Wiley, New York (1998)

7. World Road Association: PIARC. Road tunnels manual, Chap. 2: Safety (2007)
8. Henke, A., Gagliardi, M.: The 2001 Gotthard fire: response of the system, behavior of the users. How was the fast reopening of the tunnel possible? In: 5th international conference safety in road and rail tunnels. Marseille, Tunnel Management International, France, 10 (2003)
9. Dix, A.: Expert report for the victorian coroner: the fatal burnley tunnel crashes, Melbourne, Victoria, Australia (2011)
10. California Department of Transportation District 4: Caldecott tunnel bore 3/bore 4 emergency response plan. 15 November (2013)

# A Set Pair Analysis Approach for Dynamic Risk Assessment of Tailings Dam Failure

Xin Zheng[1]([⊠]), Kaili Xu[1], and Quanming Li[2]

[1] College of Resources and Civil Engineering, Northeastern University, Shenyang, China
zhengxin@mail.neu.edu.cn
[2] China Academy of Safety Science & Technology, Beijing, China

**Abstract.** Tailings ponds are a critical and essential facility for mines and play a major role in protecting the environment of the mines and surrounding areas. But tailings ponds also present the potential hazard of mud flow, and the failure of a tailings dam may result in property damage and human casualties. It is therefore imperative to identify and analyze the hazardous and harmful risks present in tailings dams in a timely fashion and evaluate their safety levels accurately. In this paper, the safety of tailings dams is analyzed using a Set Pair Analysis (SPA) method, which combines a safety status assessment with trend analysis. A safety assessment index system is firstly established for safety analysis by searching for and analyzing the existing hidden dangers in the tailings dam. A case study is then conducted using the SPA method to evaluate the safety level of a selected tailings dam in China. It is concluded that the safety status of the tailings dam can be reflected by the status figures, and the development trend of the safety status of the tailings dam can be judged through the trend analysis.

**Keywords:** Set pair analysis · Tailings dam · Dynamic risk assessment
Trend forecast · Hazards

## 1 Introduction

The primary purpose of a tailings pond is to contain the tailings, and a secondary purpose is to conserve the water used in the mine and mill [1]. The tailings pond is a necessary facility for maintaining normal production of a mine, although it also presents a high potential threat of man-made debris flow hazards [2, 3]. According to statistics concerning major disasters in the world [4], tailings dam failure is the 18th most severe disaster after earthquake, cholera, floods and bomb blast. Many serious tailings dam failure accidents have occurred around the world [5–7]. These accidents reflect the deficiency of tailings dam management and the need for further study. Hazard analysis and risk assessment methods of tailings dams are highly valued in Canada, Australia, the European Union and other countries and territories.

Risk-assessment methods of tailings dams can be divided into quantitative and qualitative assessments. Qualitative risk assessment is primarily an analysis method, making judgments based on the nature, characteristics and development variation of the

dam and surrounding areas. This method is based on the intuition and experience of the analysts as well as the analysis of the past and present situations of the dam, using the latest information. The quantitative risk assessment is based on statistical data and uses mathematical models to establish a methodology to calculate the index values. This method requires accurate data and accurate descriptions of system uncertainties, sound judgment and assumptions, and full and complete analysis. Currently, data collection in many countries is not conducted sufficiently, which presents a fundamental obstacle for the use of this method.

In the last decade, a new assessment method called the Set Pair Analysis (SPA) method was proposed by Zhao [8] to deal with uncertainty problems. The SPA method can not only determine the safety state of the tailings dam system under certain conditions, but also predict the development trend of the safety state in the tailings dam system. The SPA method studies the links between two sets of information on the basis of three aspects: identity, discrepancy, and contrary degrees between the two sets. At present, the SPA method is widely used in many fields in China such as social sciences, economics, technology, and engineering [9–13], but its application has not been widely adopted internationally. The objectives of this study are to: (1) establish an evaluation indexing system through identifying and analyzing hazards during the operation of tailings dams; (2) study the grading standard of each evaluation index in the established evaluation indexing system in order to obtain a more scientific evaluation system and minimize the influence of subjective factors on the evaluation results; (3) calculate the weight of each index for a tailings dam to be used in a case study; and (4) assess the safety level of the tailings dam using the SPA method to obtain the safety level and the safety status development trend of the tailings dam. From this study, it is concluded that the SPA method is able to offer new insights on the failure prevention of tailings dams and provides an alternative scientific method for tailings dam safety assessment and management.

## 2 The Set Pair Analysis (SPA) Approach

The core idea of the SPA theory is to deal with both certainties and uncertainties within one uncertain system. The set pair refers to two interrelated sets of information. Under a specific background, the set pair analysis can be characterized by identity, discrepancy and contrary, in which the identity means the same features of the two sets, the contrary means the opposite features of the two sets, and the discrepancy means the features of the two sets are uncertain, not the same or opposite. For a problem W, if its set pair H is constructed by the sets A and B, the N features of the set pair H can be obtained by the following analysis: Assuming there are S identity features and P contrary features between Sets A and B, and there are F (F = N − S − P) features of uncertain relation, the connection degree of the two sets can be expressed as Eq. 1 if the weight of each feature is not considered [8]:

$$\mu(W) = \frac{S}{N} + \frac{F}{N}i + \frac{P}{N}j = a + bi + cj \tag{1}$$

where *S/N* is the identity degree, abbreviated as a; *F/N* is the discrepancy degree, abbreviated as b; and P/N is the contrary degree, abbreviated as c; *i* is the coefficient of the discrepancy degree with a range of $[-1, 1]$; *j* is the coefficient of the contrary degree with a value of $-1$; and μ is the connection degree with a range of $[-1, 1]$. The expression is linked to the certainty and uncertainty of the system, and reflects the relationship between the certainty and uncertainty, and that between mutual influence, mutual constraint and mutual conversion, while the uncertainty factors of the fuzziness, the randomness, the grey and the incompleteness are determined by the uncertainty *bi*.

Equation 1 is the connection degree expression for three elements, which can be expanded to multi-elements. During the safety assessment process, there are different safety evaluation levels in different safety evaluation methods, and the multi-element connection degree model can be used to evaluate all kinds of systems which have different evaluation levels. The numbers of the connection degree element and the levels of the safety evaluation should be the same.

## 3   Indexing System of Tailings Dam Safety Evaluation

To evaluate the tailings dam using the SPA method, the first step is to establish the set pair. One set of the set pair is made up of information on the tailings dam safety evaluation indexing system, and the other set of the set pair is made up of information on the selected tailings dam. Thus, the development of a scientific and reasonable evaluation indexing system is the key to the accurate evaluation of tailings dam safety.

These factors and their design indexes are classified according to the analysis of the main factors influencing the tailings dam failure, and a safety evaluation indexing system is then established, as shown in Table 1. In order to reduce the influence of subjective factors in the evaluation process, the evaluation criteria of each index should be given in Table 1. The safety evaluation index for studying the tailings dam stability can be divided into four grades, as also listed in Table 1.

In the safety evaluation indexing assessment system, the weight of each index should be exact and logical. The more important the index is, the greater the weight. In the field of risk assessment of the tailings dam, the amount of data is often very limited, and it is typical that there are insufficient data. Thus, it is often ineffective to use mathematical statistical methods. The Analytic Hierarchy Process (AHP) can compensate for the defects of the mathematical statistics [14]. Therefore, this paper adopts AHP to determine the weight of the evaluation index. The weights of the evaluation indexes are determined by the Analytic Hierarchy Process, as shown in Table 2.

## 4   Case Study on Using SPA to Evaluate the Stability of a Tailings Dam

### 4.1   Safety Evaluation Index of the Tailings Dam

In this section, the set pair analysis method introduced above is used to study the stability of the Heshangyu tailings dam located in the Shouyun iron mine in Beijing,

**Table 1.** Grading criteria of the safety evaluation index of the tailings dam

| Evaluation index | A | B | C | D |
|---|---|---|---|---|
| Flood control standard (once in no. of years) | >500 | 100–500 | 50–100 | <50 |
| Drainage capacity | The design capacity of drainage facilities meets the drainage requirements. When the 24-hour flood volume is regulating less than reservoir capacity for flooding, flood discharge time is less than 50 h | The design capacity of drainage facilities meets the basic drainage requirements. When the 24-hour flood volume is regulating less than reservoir capacity for flooding, flood discharge time is less than 72 h | The design capacity of drainage facilities is slightly insufficient. When the 24-hour flood volume is regulating less than reservoir capacity for flooding, flood discharge time is not more than 76 h | The design capacity of drainage facilities has serious inadequacies. When the 24-hour flood volume is regulating less than reservoir capacity for flooding, flood discharge time is not more than 76 h |
| Height difference between reservoir water level and tailings dry beach top (m) | >1.5 | 1.0–1.5 | 0.5–1.0 | <0.5 |
| Average grain diameter (mm) | >0.50 | 0.20–0.50 | 0.05–0.20 | <0.05 |
| Ratio of downstream slope (1:n) | >5.0 | 3.0–5.0 | 1.0–3.0 | <1.0 |
| Height of dam (m) | <20 | 20–50 | 50–80 | >80 |
| Seismic intensity design (°) | >8.0 | 6.5–8.0 | 5.0–6.5 | <5.0 |
| Unit weight (t/m³) | >2.0 | 1.7–2.0 | 1.4–1.7 | <1.4 |
| Height of saturation line (m) | >8.0 | 6.0–8.0 | 5.0–6.0 | <5.0 |
| Transverse crack | There is no visible horizontal crack in the tailings dam | The number of cracks in the tailings dam is less than 3, the width of the main transverse crack is less than 10 cm, and the crack depth is less than 0.5 m | The number of cracks in the tailings dam is less than 8, the width of the main transverse crack is less than 20 cm, and the crack depth is less than 1 m | Tailings dam cracks number greater than 8, or main transverse crack is through longitudinal cracks, which may cause piping or soil deformation |
| Longitudinal crack | There is no visible longitudinal crack in the tailings dam | The number of cracks in the tailings dam is less than 3, the width of the main longitudinal crack is less than 10 cm, and the crack depth is less than 0.5 m | The number of cracks in the tailings dam is less than 8, the width of the main longitudinal crack is less than 20 cm, and the crack depth is less than 1 m | Tailings dam cracks number greater than 8, or the main longitudinal crack is through transverse cracks, which may lead to the partial or global collapse of the tailing dam |
| Horizontal crack | After investigation, there is no horizontal | After investigation, there is a horizontal weak layer in the | After investigation, there is a horizontal weak layer in the | After investigation, there is a through horizontal weak |

**Table 1.**  (*continued*)

| Evaluation index | A | B | C | D |
|---|---|---|---|---|
| | interlayer in the tailings dam | tailings dam, but not through the dam, and the minimum depth of the downstream slope of the interlayer is not less than 4 m. Saturation line does not indicate obvious rise in the horizontal weak layer | tailings dam, but not through the dam, and the minimum depth of the downstream slope of the interlayer is not less than 2 m. Saturation line indicates obvious rise in the horizontal weak layer | interlayer in the tailings dam, and the leakage is serious |
| Operational state of drainage facilities | The facilities of the drainage system work properly | The drainage can be used safely, despite the presence of cracks, corrosion or wear | Drainage system is partial blockage or collapse, and drainage capacity decreases, which not meet the design requirements | The drainage system is blocked or collapse, cannot drain or drainage capacity decreased sharply |
| Safety management | Uniform ore drawing; established and improved safety management system of tailings facilities; miners are trained in special operations; system of personal responsibility at all levels implemented; hidden danger investigation institutionalized; clear responsibility investigation and rectification responsibility | Daily safety management of tailings facilities meets the basic safety needs of production | Uneven discharge; safety management document not implemented; personal responsibility at all levels is not perfect | Uneven discharge; safety management turmoil; no safety management document; responsibility is not clear; miners are not trained in special operations |
| Emergency | Sound emergency response agencies; responsibility is clear; sound emergency communications; rescue personnel, funds and materials to prepare; local government and residents regularly drilled on emergency rescue plan | Emergency management basically meets the safety needs of production | There are emergency measures, but no drill | There are no emergency measures; responsibility is not clear; no rescue personnel or emergency communications |
| Monitoring facilities | Saturation line-monitoring facilities and reservoir level-monitoring facilities operating normally, perfect means of monitoring, and early warning program | Despite the failure of individual monitoring holes, the monitoring facilities run normally. Early warning program is basically sound | There are saturation line-monitoring facilities, but no early waring program | There are no monitoring facilities or daily inspection systems |

China. The total capacity of the tailings pond is $1350 \times 104$ m$^3$, the total length of the tailings dam is about 900 m and the top elevation is 212 m. The tailings dam is used as an example and each safety evaluation index of the tailings dam is evaluated according to the grading standards of the indexes listed in Table 1. The corresponding evaluation results are summarized in Table 2.

**Table 2.** Weight of the safety evaluation index of the tailings dam and evaluation results

| The first level index | The second level index | Weight of the second level index | The third level index | Weight of the third level index | Evaluation results |
|---|---|---|---|---|---|
| Stability of tailings dam (T) | Flood overtopping (T$_1$) | 0.1088 | Flood control standard (T$_{11}$) | 0.33 | A |
| | | | Drainage capacity (T$_{12}$) | 0.34 | A |
| | | | Height difference between reservoir water level and tailings dry beach top (T$_{13}$) | 0.33 | B |
| | Slope instability (T$_2$) | 0.1147 | Average grain diameter (T$_{21}$) | 0.29 | C |
| | | | Ratio of downstream slope (T$_{22}$) | 0.24 | B |
| | | | Height of dam (T$_{23}$) | 0.22 | D |
| | | | Seismic intensity design (T$_{24}$) | 0.25 | A |
| | Seepage (T$_3$) | 0.1199 | Unit weight (T$_{31}$) | 0.17 | D |
| | | | Height of saturation line (T$_{32}$) | 0.83 | C |
| | Construction failure (T$_4$) | 0.1286 | Transverse crack (T$_{41}$) | 0.20 | A |
| | | | Longitudinal crack (T$_{42}$) | 0.25 | A |
| | | | Horizontal crack (T$_{43}$) | 0.21 | A |
| | | | Operation state of drainage facilities (T$_{44}$) | 0.34 | B |
| | Other factors (T$_5$) | 0.5279 | Safety management (T$_{51}$) | 0.42 | B |
| | | | Emergency (T$_{52}$) | 0.27 | A |
| | | | Monitoring facilities(T$_{53}$) | 0.31 | A |

## 4.2 Set Pair Analysis and Results

The safety grade of the tailings dam is the same as that of the evaluation index, and it can be divided into four grades. According to the "sharing principle," the range of the connection degree (μ) is divided into four sub-intervals corresponding to the four safety levels, which are shown in Table 3. If the number of the evaluation levels is four, the four-element connection degree is to be used, as formulated in Eq. 2:

$$\mu = a + b_1 i_1 + b_2 i_2 + cj = \sum_{k=1}^{A} \omega_K + \sum_{k=A+1}^{A+B} \varpi_k i_1 + \sum_{k=A+B+1}^{A+B+C} \varpi_k i_2 + \sum_{k=A+B+C+1}^{N} \omega_k j$$

(2)

According to Eq. 2, the safety evaluation indexes for the factors affecting the stability of the tailings dam considered in the case study can be calculated using Eqs. 3–7 and the tailings dam safety level can be computed using Eq. 8. In Eq. 8, the term $0.33i_1 + 0.13i_2$ represents the uncertain factors in the tailings dam system, where the values of $i_1$ and $i_2$ vary between $[-1, 1]$ under different conditions. Thus, due to the variations, the connection degree is uncertain while it is certain once the values of $i_1$ and $i_2$ are determined, which is why it is said that the connection degree shows the characteristics of both certainty and uncertainty. In order to calculate the safety level of tailings dams at a certain time using the SPA method, similar to that using the quantitative evaluation methods such as fuzzy mathematics, the values of $i_1$ and $i_2$ should be selected scientifically. The value of i has to be selected through conducting various analyses, according to different situations. Thus, the selection of a reasonable value of i for different situations is actually the main challenge of using the SPA method.

Currently, the valuing methods of $i_1$ and $i_2$ are: analysis valuing method, proportional valuing method, random valuing method, and special valuing method [8, 15]. In this paper, the analysis valuing method is adopted. According to the "sharing principle," $i_1 = 0.33$ and $i_2 = -0.33$. Thus, in this valuing method, the uncertain characteristics, i.e., the discrepancy features, are actually allocated in proportion to the identity and contrary features. The term of 0.05j in Eq. 8 represents the contrary factors in the tailings dam system. Thus, j = −1 and the connection degree is converted into a static value, which reflects the current safety state of the tailings dam system. If $i_1 = 0.33$, $i_2 = -0.33$ and $j = -1$, the safety level of the tailings dam is then $\mu_T = 0.51$, which indicates that this tailings dam is "very safe" according to Table 3. Li et al. [16] evaluated the safety level of the Heshangyu tailings dam using the fuzzy comprehensive evaluation method. Their evaluation result is the same as that from this paper, i.e., the safety level of Heshangyu tailings dam is deemed to be "very safe," which indicates the evaluation result from the SPA method in this paper is accurate.

Moreover, the term $0.33i_1 + 0.13i_2$ in Eq. 8 is the discrepancy degree, which changes with the change in time. If the hidden dangers of this tailings dam, such as the height of the saturation line and the ratio of downstream slope are rectified, the discrepancy degree may become the identity degree, which reveals that the stability of the tailings dam is improved. However, if no attention is paid to these hidden dangers, the discrepancy degree may be changed to the contrary degree. If the Set Pair Pessimistic Situation is considered, all discrepancy characters are transformed into the contrary characters, i.e., $i_1 = -1$ and $i_2 = -1$. Then, $\mu_T = -0.02$, which reveals that the safety level of this tailings dam will be changed to "dangerous," according to Table 3. The extreme values of $i_1$ and $i_2$ reflect the changing range of the safety level of the tailings dam. As it can be seen, the tailings dam safety grade crosses a great level of safety values, which indicates that the system is unstable. Thus, in order to maintain and

improve the stability of tailings dams, it is important to strengthen the safety management of hidden dangers and rectify them once identified.

**Table 3.** Tailings dam safety level

| Very dangerous | Dangerous | Safe | Very safe |
|---|---|---|---|
| The tailings dam collapse accidents may occur at any time. Production must be stopped and emergency measures must be taken | There are serious hidden dangers of safety facilities, which if not timely treatment will lead to a collapse accident | Safety facilities do not fully meet the design requirements, but ensure basic production safety | Normal operation condition and perfect safety management |
| $-1 \leq \mu \leq -0.5$ | $-0.5 < \mu \leq 0$ | $0 < \mu \leq 0.5$ | $0.5 < \mu \leq 1$ |

The dynamic evaluation of the tailings dam system should consider not only the safety level of the system, but also the evolution of the system. In order to make an objective and correct evaluation, the safety status and the development trend of the tailings dam should be comprehensively analyzed. If $c \neq 0$ in the connection number $\mu = a + bi + cj$, the value of $a/c$ is called the Set Pair Situation (*SPS*) in a specified problem, which is denoted as *SHI* $(H) = a/c$ [17]. The SPS can reflect the contact trend of the two sets. *SHI* $(H) > 1$ is called the identity situation, *SHI* $(H) = 1$ is called the balance situation, and *SHI* $(H) < 1$ is called the contrary situation.

For the tailings dam considered in the case study, the safety evaluation level is calculated using Eq. 8, i.e., $\mu T = 0.49 + 0.33i_1 + 0.13i_2 + 0.05j$. The comparison of this equation with Eq. 1 finds that $a = 0.49$, $b = 0.46$ and $c = 0.05$. The values of both $a$ and $b$ ($b1 + b2$) are much greater than that of $c$, which indicates that there are a few hazardous and harmful factors in this tailings dam and that the "uncertain" factors of this tailings dam are prominent. Correspondingly, the safety level of this tailings dam is unstable. Therefore, although the current safety level of the tailings dam is deemed "very safe," the daily safety inspection cannot be relaxed and the "uncertain" items should be checked thoroughly. The enterprises should carry out safety education and improve the safety awareness of employees, too. Otherwise, the safety level of the tailings dam is likely to change to "dangerous."

The safety assessment of the tailings dam is carried out once every three months starting with $i_1 = 0.33$ and $i_2 = -0.33$. The results of the assessment for one whole year are summarized in Table 4 and the corresponding trend analysis graph is shown in Fig. 1.

From the connection degrees, we can determine whether the certain items (i.e., the identity and/or contrary items) or the uncertain items (i.e., the discrepancy items) will change over time, which shows that the tailings dam is actually a complex and uncertain system. Thus, the evaluation results obtained by the SPA method are not merely a fixed value but also display the evolution of the items in the tailings dam. From the connection degrees $\mu_1 - \mu_4$ summarized in Table 4, we also know that the safety state of this tailings dam has been maintained at "very safe." The connection

**Table 4.** Assessment results for one year

| Month | Connection degree | SHI (H) | μ | Safety state |
|-------|-------------------|---------|---|--------------|
| March | $\mu_1 = 0.49 + 0.33i_1 + 0.13i_2 + 0.05j$ | 9.8 | 0.51 | Very safe |
| June | $\mu_2 = 0.48 + 0.4i_1 + 0.03i_2 + 0.09j$ | 5.33 | 0.51 | Very safe |
| September | $\mu_3 = 0.54 + 0.34i_1 + 0.12j$ | 4.5 | 0.53 | Very safe |
| December | $\mu_4 = 0.57 + 0.3i_1 + 0.09i_2 + 0.04j$ | 14.25 | 0.6 | Very safe |
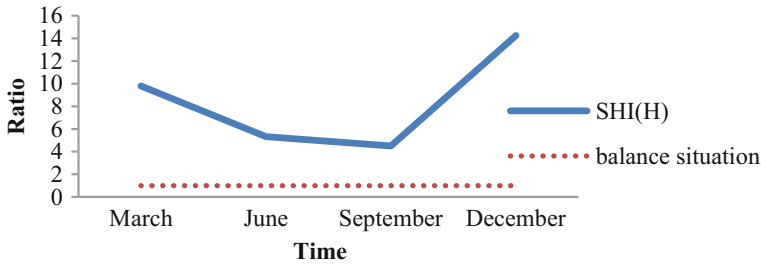


**Fig. 1.** State development trend of the selected tailings dam

degree number in June was 0.51, and 0.53 in September. If the value of μ were the sole indicator of the safety level of this tailing dam, we would be happy with the evaluation results since the tailing dam is regarded to be very safe. However, it can be seen from Fig. 1 that the development of the safety status of this tailings dam is worrisome. The value of *SHI(H)* is reduced from March to September. Finally, from September to December, the values of *SHI(H)* and μ are both increased, which reveals that both the current state of the tailing dam is very safe and that the development trend of the state of the tailing dam is very safe.

$$\mu_{T_1} = |0.33 \quad 0.34 \quad 0.33| \begin{vmatrix} 1 & 0 & 0 & 0 \\ 1 & 0 & 0 & 0 \\ 0 & 1 & 0 & 0 \end{vmatrix} \begin{vmatrix} 1 \\ i_1 \\ i_2 \\ j \end{vmatrix} \tag{3}$$

$$= 0.67 + 0.33i_1$$

$$\mu_{T_2} = |0.29 \quad 0.24 \quad 0.22 \quad 0.25| \begin{vmatrix} 0 & 0 & 1 & 0 \\ 0 & 1 & 0 & 0 \\ 0 & 0 & 0 & 1 \\ 1 & 0 & 0 & 0 \end{vmatrix} \begin{vmatrix} 1 \\ i_1 \\ i_2 \\ j \end{vmatrix} \tag{4}$$

$$= 0.25 + 0.24i_1 + 0.29i_2 + 0.22j$$

$$\mu_{T_3} = |0.17 \quad 0.83| \begin{vmatrix} 0 & 0 & 0 & 1 \\ 1 & 0 & 0 & 0 \end{vmatrix} \begin{vmatrix} 1 \\ i_1 \\ i_2 \\ j \end{vmatrix} \tag{5}$$

$$= 0.83 + 0.17j$$

$$\mu_{T_4} = |0.20 \quad 0.25 \quad 0.21 \quad 0.34| \begin{vmatrix} 1 & 0 & 0 & 0 \\ 1 & 0 & 0 & 0 \\ 1 & 0 & 0 & 0 \\ 0 & 1 & 0 & 0 \end{vmatrix} \begin{vmatrix} 1 \\ i_1 \\ i_2 \\ j \end{vmatrix} \tag{6}$$

$$= 0.66 + 0.34i_1$$

$$\mu_{T_5} = |0.42 \quad 0.27 \quad 0.31| \begin{vmatrix} 0 & 1 & 0 & 0 \\ 1 & 0 & 0 & 0 \\ 1 & 0 & 0 & 0 \end{vmatrix} \begin{vmatrix} 1 \\ i_1 \\ i_2 \\ j \end{vmatrix} \tag{7}$$

$$= 0.58 + 0.42i_1$$

$$\mu_T = |0.11 \quad 0.12 \quad 0.12 \quad 0.13 \quad 0.52| \begin{vmatrix} 0.67 & 0.33 & 0 & 0 \\ 0.25 & 0.24 & 0.29 & 0.22 \\ 0.83 & 0 & 0 & 0.17 \\ 0.66 & 0.34 & 0 & 0 \\ 0.58 & 0.42 & 0 & 0 \end{vmatrix} \begin{vmatrix} 1 \\ i_1 \\ i_2 \\ j \end{vmatrix} \tag{8}$$

$$= 0.49 + 0.33i_1 + 0.13i_2 + 0.05j$$

## 5 Conclusions

The safety assessment of the tailings dam is an important way to prevent tailings dam failure accidents and reduce property damage and human casualties if an accident occurs. This paper implemented the Set Pair Analysis (SPA) method to evaluate the stability of the tailings dam. From this study, the following conclusions can be drawn:

(1) A safety evaluation indexing system is firstly developed for studying the tailings dam failure risk by analyzing the factors which may lead to the tailings dam failure. Sixteen (16) indexes are identified in the safety evaluation indexing system and the analytic hierarchy process (AHP) method is then adopted to determine the weight of each evaluation index. After that, the grading criteria are developed for the safety evaluation indexing system to make the evaluation more objective and scientific.

(2) The SPA provides a new method for assessing tailings dam stability. The SPA method deals with certainty and uncertainty in one uncertain system and conquers the deficiency of using a single theory to solve a single uncertain problem. Through the so-called connection degree function, the SPA method can derive a static evaluation level for tailings dam stability. Through the transformation of determination and uncertainty, the SPA method can reflect the risk trends of tailings dam stability. Thus, the SPA method can fully take into account the fuzzy property of the grading standards and may provide a new alternative other than the fuzzy comprehensive evaluation and grey analytic hierarchy process.

(3) The case study of evaluating the stability of a tailings dam using the SPA method indicates that the SPA method is convenient in calculation and feasible in application. In order to make an objective and correct evaluation, the safety status and the development trend of the tailings dam should be comprehensively analyzed. Moreover, the case study highlights the importance of safety management in the risk assessment of tailings dam stability.

(4) Set pair analysis theory has obvious advantages; for example, it is useful in determining the development trend of the safety state, but there are some drawbacks, too, one of which is the difficulty in selecting a reasonable value for i. Further studies should be conducted to select the value of i more scientifically.

# References

1. Nazli, T.O., Resat, U., Nihat, S.I.: A study on geotechnical characterization and stability of downstream slope of a tailings dam to improve its storage capacity (Turkey). Environ. Earth Sci. **69**, 1871–1890 (2013)
2. Strachan, C.: Tailings dam performance from USCOLD incident-survey data. Min. Eng. **53**(3), 49–53 (2001)
3. Sharma, R.S., Al-Busaidii, T.S.: Groundwater pollution due to a tailings dam. Eng. Geol. **60**(1), 235–244 (2001)
4. Tian, W.Q., Xue, J.G.: Tailings pond safety technology and management. Coal Industry Press, Beijing (2008)
5. Tranca, M.J., Gezero, L., Ferreira, R.M.L., Amaral, S., Montenegro, H.D.B.: The failure of the Fonte Santa mine tailing dam. River, Coastal and Estuarine Morphodynamics: RCEM, 1153–1160 (2007)
6. Gipson, A.H.: Tailing dam failures-the human factor. In: 10th International Conference on Tailings and Mine Waste, pp. 451–456 (2003)
7. Rico, M., Benito, G., Salguerio, A.R., Diez-Herrero, A., Pereira, H.G.: Reported tailings dam failures: a review of the European incidents in the worldwide context. Hazard. Mater. **152**(2), 846–852 (2008)
8. Zhao, K.Q.: Set Pair Analysis and its Preliminary Application, pp. 1–200. Zhejiang Science and Technology Press, Hangzhou (2000)

9. Jiang, Y.L.: An analysis on the states in student studies by SPA. Appl. Stat. Manage. **22**(6), 5–8 (2003) (in Chinese)
10. Zhou, J.H., Xu, K.L., Xiu, S.J.: Study on the risk evaluation with logistics system of hazardous goods. J. Saf. Environ. **7**(1), 150–115 (2007) (in Chinese)
11. Zhang, X.Y.: The application of the set pair analysis and consultative method on the teaching evaluation. J. Technol. Coll. Educ. **23**(5), 43–46 (2004) (in Chinese)
12. Zhang, R.L., Geng J.M.: The research on comprehensive assessment method of government performance based on dynamic set pair analysis. Math. Pract. Theor. **36**(4), 84–90 (2006) (in Chinese)
13. Wang, F.Q., Guo, D.M.: Application of uncertainty set pair analysis for sandstorm forecast. J. Desert Res. **26**(2) (2006) (in Chinese)
14. Saty, T.L., Vargas, L.G.: Models, Methods, Concepts & Application of the Analytic Hierarchy Process. Kluwer Academic Publishers, Boston (2001)
15. Yu, G.X.: Study on the uncertainty number i of connection number. J. Liaoning Normal Univ. **25**(4), 349–352 (2002) (Social Science Edition) (in Chinese)
16. Li, Q.M., Zhang, X.K., Wang, Y.H., Zhang, B.Y.: Risk index system and evaluation model for tailings dam. J. Hydraul. Eng. **40**(8), 989–994 (2009) (in Chinese)
17. Ye, Y.C., Ke, H.L., Huang, D.Y.: Comprehensive Evaluation Technology and its Application. Metallurgical Industry Press, Beijing (2006). (in Chinese)

# Experimental Study on Influence of Low-Frequency Vibration on Radon Exhalation From Thermal Porous Medium

Zi-qi Cai[1,2], Xiang-yang Li[1,2(✉)], Lei Bo[1], Chang-shou Hong[1,2], Li Ming[1], and Wu Qiong[1]

[1] School of Environment and Safety Engineering, University of South China, Hengyang, China
+86-13786480277lcczclxy@l26.com
[2] Hunan Province Engineering Technology Research Center of Uranium Tailings Decommission Treatment, Hengyang, Hunan, China

**Abstract.** The purpose of the research is to study the effect of low-frequency vibration of thermal uranium mining operations on the radon exhalation of uranium ore. Uranium tailing sand from certain uranium mines in southern China, quartz sand and other materials are selected to produce the uranium-like rocks. Measure the cumulative radon concentration at different frequency and temperature conditions such as 40–50 and 10–40 Hz on the uranium-like rocks by designing independent simulated radon exhalation excitation and test system, the data correction and analysis of the measurement results were also constructed a mathematical prediction model of variation regularity of radon exhalation rate by uranium-like rock. At the same time, the damage degree of uranium-like rock mass is detected by the rock damage detection module. Testing results show that: under the condition of a single factor measurement within certain time range, low frequency vibration and high temperature heating have a positive effect on the radon exhalation rate of the test rock. Under low-frequency vibration and high-temperature content, based on the mathematical model, radon exhalation rate varied in three-dimensional surface. Experimental rules provide a theoretical suggestion for radon protection in the process of uranium mining.

**Keywords:** Uranium-like rock · Low-frequency vibration · Degree of rock damage · Radon exhalation rate

## 1 Introduction

Before the rock burst, a large number of micro-cracks exist among the mineral lattices, and radon exhalation increased significantly [1]. The relationship between radon exhalation and microfracture in the rock mass has been studied at China and abroad. Tuccimei [2] first explored the changing characteristics of radon during rock destruction, it is confirmed that the radon anomaly of the rock is related to the micro-cracks produced under mechanical vibration. Mollo [3] carried out a study on the radon exhalation rate of ruptured rock, and found that the radon exhalation before the rock

rupture has some effect on the crustal vibrations caused by earthquakes and volcanic activity. Lu [4] conducted a study on the characteristics of radon gas in the process of rock material damaged process, the experimental results show that ultrasonic vibration can promote the increase of radon precipitation before rock fracture.

In the present study, there are few studies on the influence of low frequency vibration on the radon exhalation of uranium ore, however, during the process of uranium mining operations, mechanical vibration and change of geological structure may result in the rupture of the uranium ore and the abnormal increase of the radon exhalation of uranium ore. In order to study the influence of low frequency perturbation load on the radon exhalation of uranium ore, the self-developed low frequency vibration radon exhalation test simulator was used to study the mechanism of radon exhalation mechanism of uranium-like rocks sample under low frequency vibration.

## 2 Materials and Methods

### 2.1 Preparation of Materials

Through the collation and analysis of the proportion of rock-like materials in recent years in China [5], it has been found that quartz sand, cement, calcium carbonate, gypsum, barite powder, water and additives are mostly used for the preparation of raw materials. The object of this paper is granite-type uranium ore rock. Through comprehensive analysis of the functions and characteristics of various raw materials, the raw materials selected including: Uranium tailings (aggregates) with particle size less than 4.75 mm, quartz sand (aggregate) with 0.60–4.75 mm, cement (cementitious material), micro silica fume (admixture and reducing mortar porosity), fine iron powder (admixture, increase the sample weight), admixture (early strength agent, water reducer) and distilled water. By consulting the relevant literature, the final three kinds of matching ratio are shown in Table 1.

**Table 1.** 3 kinds of sample materials ratio

| Test plan | A (water: cement) | B (aggregate: cement) | C (silica fume: cement) | D (refined iron powder: cement) |
|---|---|---|---|---|
| Sample 1 | 0.28 | 1 | 0.09 | 0.2 |
| Sample 2 | 0.28 | 1.2 | 0.12 | 0.25 |
| Sample 3 | 0.3 | 1.2 | 0.06 | 0.2 |

According to the above ratio, weighed good aggregate, cementing materials, additives and water and other raw materials added to the mixer, Stir well and pour into the prepared PVC mold and place it on the shaking table so that the air in the tube will be shocked to send out finally obtaining $70.7 \times 70.7 \times 70.7$ mm cube type uranium-like rock sample, the granite samples were obtained through on-site sampling and indoor processing. Next, we tested the physical and mechanical properties of the

uranium-like rocks and prototypes that were being cured, and obtained corresponding physical-mechanical and radioactive parameters, which showed in Table 2.

According to the research results of similar theory and the relevant experience of Jiang et al. [6] the uranium-like rock samples and prototype materials (granite uranium ore rock) not only fit the similar physical properties, but also through the mechanical parameters of the test to restore the similarities between the two kind of rocks. In the process of actual sample preparation, seven physical and mechanical parameters such as compressive strength, tensile strength, particle density, cohesion, internal friction angle, dry density and saturation density were selected as the indices to measure whether the orthogonal test blocks could restore the prototype simulated material testing standards.

## 2.2    Experimental Device

The experimental device consists of RAD-7 radon detector (which was demarcated by Radon the Laboratory of USC), excitation system, external track adsorption device (radon exhalation jar, slide rail) and signal acquisition and processing system, the experimental device shown as Fig. 1.

# 3    Experimental Principle and Experimental Procedure

## 3.1    Experimental Methods

Radon exhalation rate measurement from porous media containing radium commonly used electrostatic collection method, the experiment also uses this measurement method. Radon is precipitated from the surface of the uranium-like rock and enters the radon space, as the same time, $^{226}$Ra element in the solid lattice of the uranium-like rock emits $\alpha$ particles which in turn decay into radon atoms. Because of the back-attack action, uranium tailing sand of the rock forms mobile radon atoms in the interlinked micro-cracks, so as to molecular diffusion in the form of micro-cracks in the rock surface migration and eventually enter the radon space, as the result, the radon concentration in the radon space is increased on the based of the initial radon concentration and finally reaches the equilibrium state as the measurement time increases. The radon exhalation rate can be calculated based on the volume of radon space, accumulated radon concentration, the surface area of porous media and the sampling interval, and it can be determined using Eq. (1).

$$J = \frac{(C - C_0)V}{St} \tag{1}$$

where $J$ is the radon exhalation rate (Bq/(m$^2$s)), $S$ is the measured area of the uranium-like rock (m$^2$), $V$ is the volume of the radon space (m$^3$), $C$ is the radon concentration by accumulated t time in radon space (Bq/m$^3$), $C_0$ is the initial radon concentration (Bq/m$^3$), $t$ is represented testing time (s).

**Table 2.** Physical and mechanical properties of orthogonal test specimens

| Test plan | Compressive strength/MPa | Tensile strength/MPa | Particle density/ (g cm$^{-3}$) | Cohesion/MPa | Internal friction angle/° | Dry density/ (g cm$^{-3}$) | Saturation density/ (g cm$^{-3}$) | Radium content/Bq g$^{-1}$ |
|---|---|---|---|---|---|---|---|---|
| Sample 1 | 62.9 | 3.67 | 2.42 | 16.03 | 51.36 | 2.301 | 2.348 | 1.73 |
| Sample 2 | 71.2 | 4.12 | 2.49 | 15.91 | 50.44 | 2.365 | 2.402 | 1.88 |
| Sample 3 | 53.4 | 3.53 | 2.46 | 14.55 | 54.21 | 2.290 | 2.341 | 1.77 |
| The original sample of granite | 206.86 | 13.23 | 2.62 | 49.52 | 48.60 | 2.415 | 2.465 | 0.073 |
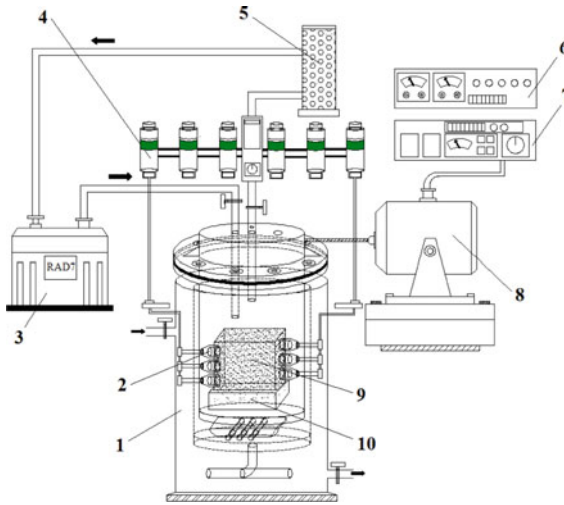
1、Water bath heating module 2、Piezoelectric transducer sensors(PZT) 3、RAD-7 radon detector 4、Rock damage detection module 5、Desiccant 6、Power amplifier 7、Sweep signal generator 8、JZK-20 Electric mode exciter 9、Uranium-like rock sample 10、Base module

**Fig. 1.** The experimental device

## 3.2    Experimental Procedure

Low-frequency perturbation vibration is one of the factors that induce radon and its progeny to abnormally exhalation in the uranium-like rocks. Different low-frequency frequencies have different effects on radon exhalation, the common induced exhalation is the perturbation effect of mining and blasting [7] and excavation on the roof and floor of the working face. Seismic and geological disasters [8] will cause abnormal exhalation. Specific inducing factors Vibration frequency range shown in Table 3, we can see that most of the vibration frequency is between 0 and 40 Hz, so set it to test excitation frequency range.

**Table 3.** Common uranium mining involves factor-related vibration frequencies (Hz)

| Mining relating factors | Deep-hole production blasting | Shallow-hole production blasting | Seismic wavelet | | | Hydraulic drilling jumbo boom | Shovel car |
|---|---|---|---|---|---|---|---|
| | | | Wenchuan seismic wave | Darui seismic wave | Kobe seismic wave | | |
| Vibration frequency | 10–60 | 9–48 | 5 –27 | 4–12 | 1 –25 | 10 –50 | 50 |

Specific test steps are as follows: (1) In the uranium-like wrapped in test foil, so as to keep one or both sides of the test block radon exhalation, check the device's airtightness; (2) Set the water bath heating The temperature range of the module is: 30°,

35°, 40°, 45°, and 50°. A total of five sets of radon exhalation experiments were conducted on the medium surface at different temperatures. (3) According to the requirements of the experiment, (4) First open the RAD-7 radon detector, purify 20 min, radon residue left within the instrument and the instrument to reduce the air humidity below 10%; the RAD-7 Set to "sniff" mode, set the time for each measurement to 5 min and the number of measurement cycles to 60.

## 4    Results and Discussion

Under the experimental conditions of keeping the blank control group (without applying low-frequency vibration), the radon exhalation changes of the uranium-like rock of different temperature were measured, and the corrected radon concentration was substituted into the Eq. (1) to obtain the corresponding radon exhalation rate, the radon exhalation rate and temperature were fitted as shown in Fig. 2 curve. According to the analysis of Fig. 2, with the increase of temperature, the curve shows a polynomial change, and the radon exhalation rate keeps a steady growth trend. The physical and chemical properties of the surrounding rock changed significantly when the temperature of the outer wall of the test block was in the range of 30° –50°. The temperature difference between the porous emanium medium and the air in the model cavity gradually increased, resulting in an increase of temperature and pressure gradient, forming a place and channel for radioactive elements to gather easily. During the migration of radon channels, air seepage easily occurs inside the porous emanium medium. As the temperature rises, the thermal motion of radon molecules in the media is accelerated. Aggregation of the heat causes the pore diameter and shape of the medium to change, thereby increasing the radon diffusion coefficient of the porous emanium medium and eventually increasing the radon exhalation rate.



The graph shows radon exhalation data with fitted curves:

$Y_1 = 0.09647 - 0.00434x + 9.70857 \times 10^{-5}x^2$
$R^2 = 0.99738$

$Y_2 = 0.00918 + 1.2185 \times 10^{-4}x + 2.2978 \times 10^{-5}x^2$
$R^2 = 0.97338$

Single-side data points: 0.05353, 0.06429, 0.07683, 0.09893, 0.1219
Double-side data points: 0.03479, 0.03857, 0.05224, 0.06232, 0.07192

■ Single-side
● Double-side
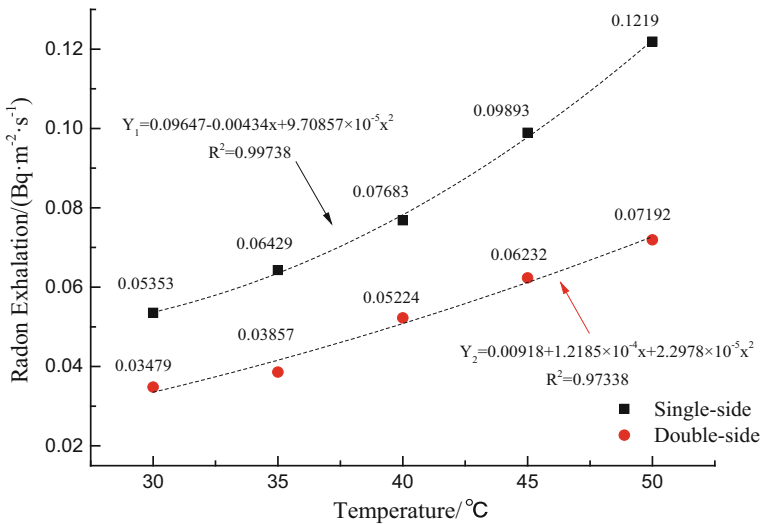
**Fig. 2.** The curve of radon exhalation of uranium-like rock with different temperature by blank control group (0 Hz)

From the test results, the radon exhalation rate of the Double-side test rock ranged from 60 to 65% of the single-side. The radon exhalation rate and vibration frequency were fitted as shown in Fig. 3 curve. Within the range of 0 to 30 Hz, under the action of 10 Hz, the cumulative amount of radon concentration is the least, the rate of radon exhalation is the slowest with the shortest stable time; Under the action of 30 Hz, the cumulative amount of radon concentration is the largest, the rate of radon exhalation is the fastest the longest stable time. However, when the test frequency reached 40 Hz, the radon exhalation rate was lower than that of the 0 –30 Hz test group, but there was still a significant effect of radon exhalation enhancement compared with the blank control group. The experimental results show that when the vibration frequency reaches a certain level, the effect of low frequency vibration on radon exhalation rate is not obvious. The experimental results show that the low-frequency disturbance can promote the radon exhalation of uranium-like rocks. One of the reasons is that the vibration changes the pore distribution of uranium-like test rocks and increases the number of micro-fissure, the diffusion resistance of radon in the test rocks is reduced. When the vibration frequency of the exciter is faster, the pore distribution of the test rock changes faster and the micro-fissure becomes larger, so the diffusion resistance is smaller.
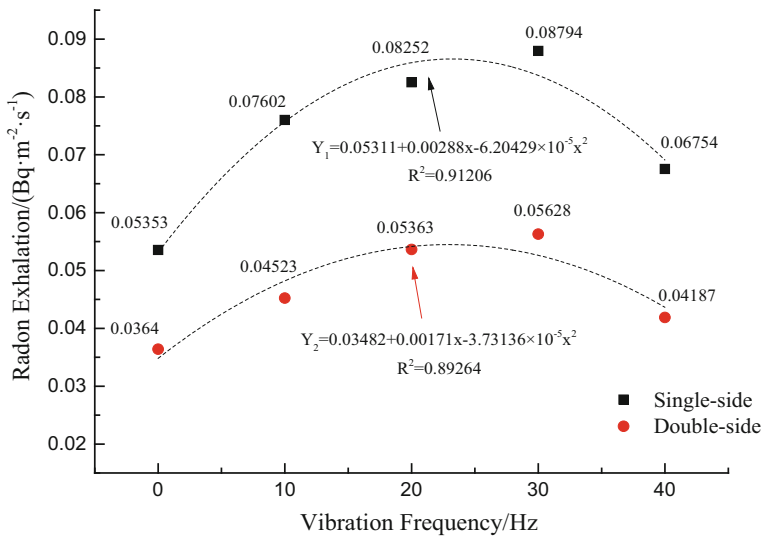


**Fig. 3.** The curves of radon exhalation of uranium-like rock with different frequency by test temperature is 30 °C

According to the results of orthogonal test, the single-side radon exhalation rate of different samples under different vibration frequency and temperatures can be calculated according to Eq. (1). Through MATLAB software toolbox for data processing to
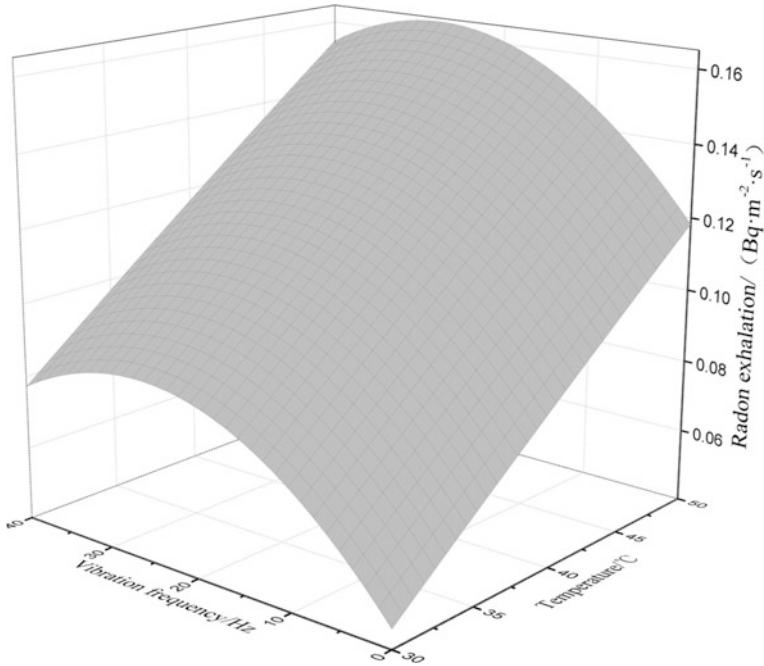
**Fig. 4.** The image of radon exhalation rate surface change under temperature and vibration by sample

get the mathematical model by the changes of radon exhalation rate under vibration frequency and temperature, as shown in Fig. 4.

$$Y_1 = -0.07586 + 0.004269x_1 + 0.00308x_2 \\ - 7.714 \times 10^{-6}x_1^2 + 5.08 \times 10^{-6}x_1x_2 - 6.081 \times 10^{-5}x_2^2 \tag{1}$$

According to the fitting mathematical model to obtain the corresponding relationship between different factors shows that the effect by low-frequency vibration and temperature to the radon exhalation rate is generally a polynomial relationship. However, the influence of these two factors on the radon exhalation rate is not superposed, but there is an interaction process. It can be conduct from the image that the radon exhalation rate of the uranium-like medium is the lowest at 30 °C, and reaches the maximum at 30 Hz and 50 °C with the increase of the depth of mining and the ground temperature.

In order to further study the relationship between the degree of sample rock damage and the radon exhalation rate under low-frequency disturbance. Based on the related literature [9, 10], the relationship between the degree of rock damage (*D*), rock-mass integrity index (*K*) and reduced rate of sonic velocity ($\mu$) was established based on acoustic method, the following relation shown in Eq. (2).

$$D = 1 - \frac{E}{E_0} = 1 - \left(\frac{v}{v_0}\right)^2 = 1 - K = 1 - (1 - \mu)^2 \qquad (2)$$

Where $E_0$ is the elastic modulus of the test rocks before low-frequency vibration, and $E$ is the equivalent elastic modulus of the test rocks after vibration. This defines $v_0$ is the acoustic velocity of the test rock before vibration, then the $v$ is the acoustic velocity of the test rock after vibration.

Figure 5, 6 and 7 shows the relationship between the damage degree of rock masses and the excitation time of different samples in the range of 0–40 Hz. It can be found that the degree of rock damage in the test section shows a monotonically increasing trend with the increase of excitation test time, as the same time, the images show that the rock damage of sample 2 and sample 3 is higher than that of sample 1. Analysis of the reasons shows that because of the lower amount of cement used as cementing material in the ratio of sample 2 and sample 3, the amount of water used in the preparation process is also lower, resulting in the rock sample pore structure being more likely to change during the vibration. With the excitation of the passage of time, the effect of low-frequency disturbance on the damage degree of the rock is getting smaller and smaller in the late stage of experiment. Combined with the previous radon exhalation rate test results, we can find that the low-frequency disturbance does not essentially change the rock mass structure and radon exhalation capacity of the uranium-like test rock.
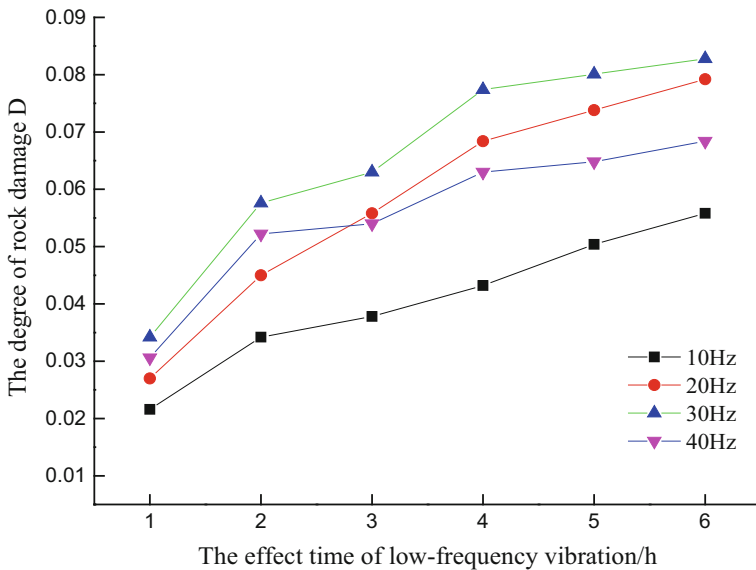


**Fig. 5.** The curve of relation between rock damaged degree and time of vibration in sample 1
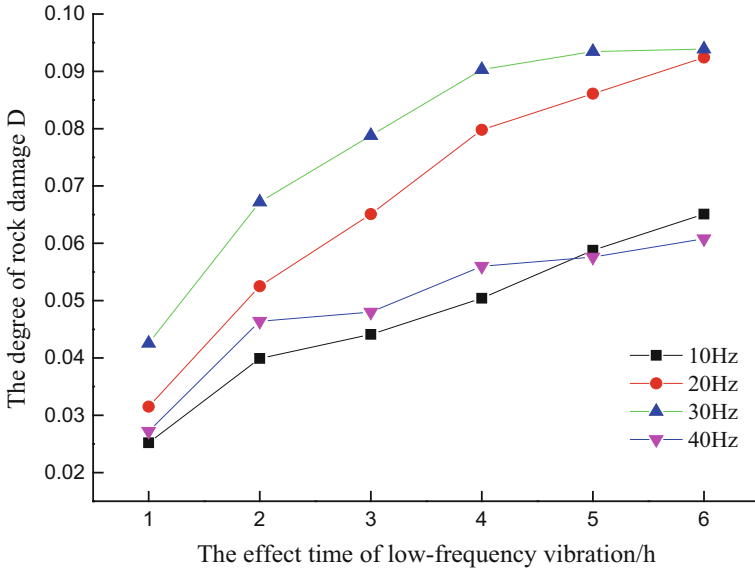
**Fig. 6.** The curve of relation between rock damaged degree and time of vibration in sample 2
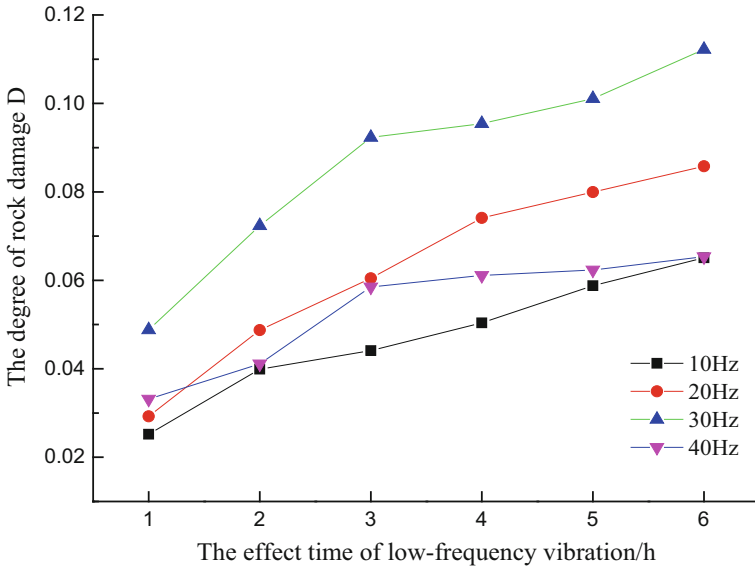


**Fig. 7.** The curve of relation between rock damaged degree and time of vibration in sample 3

## 5    Conclusion

(1)  The test group by radon exhalation rate of uranium-like samples in the range of 30°–50° showed a quadratic increase, indicating that the increase of temperature gradient can promote the radon exhalation of uranium-like rock; the radon exhalation rate of the uranium-like rock shows a quadratic trend of increasing first and then decreasing in the frequency range of 0–40 Hz, indicating that the low-frequency disturbance does not change the radon exhalation ability of the test block essentially.

(2)  Rock damage detection module is used to detect the degree of rock damage (D) of the uranium-like rock sample subjected to low-frequency vibration. The results show that the low-frequency disturbance can cause some rock damage to the sample, but with the increase of excitation frequency, rock mass damage caused by vibration is not obvious.

(3)  Based on matlab2014b software, the results of 25 orthogonal experiments on three different samples were processed and finally the mathematical model of radon exhalation rate surface under the combined effect of temperature and low frequency vibration was obtained. It is the next research focus to improve and the experimental equipment to simulate the roadway and carry out on-site measurement of radon migration in the frontline of uranium mine production.

## References

1.  Guangwei, L.: An experimental study of the relation between rock rupture and variation of radon(Rn) content. Chin. J. Geophys. **20**(04), 277–282 (1977)
2.  Tuccimei, P., Mollo, S., Vinciguerra, S., et al.: Radon and thoron emission from lithophysae ich tuff under increasing deformation: an experimental study **37**(5), 5305 (2010)
3.  Mollo, S., Tuccimei, P., Heap, M.J., et al.: Increase in radon emission due to rock failure: an experimental study. Geophys. Res. Lett. **38**(14), 130–137 (2011)
4.  Hanjiang, L.: Rn variation characteristics of rock material along rock failure progress. J. Basic Sci. Eng. **22**(01), 45–52 (2014)
5.  Dong Jinyu, Y.A.N.G., Jihong, Y.A.N.G.Guoxiang, et al.: Research on similar material proportioning test of model test based on orthogonal design. J. China Coal Soc. **37**(1), 44–49 (2012)
6.  Jiang, K., Fan, P., Xing, H., et al.: Preparation and mechanical properties of resin-based equivalent material for Jingping marbles. J. PLA Univ. Sci. Technol. (Natural Science Edition) **17**(01), 56–61 (2016)
7.  Yin, L.: Research on the blast vibration in an underground Uranium mined based on Ls-Dyna. Jiangxi University of Science and Technology (2015)

8. Yu, W.: Lightweight design and vibration characteristic analysis of hydraulic drilling Junbo boom. Central South University (2014)
9. Chang-bin, Y.: Measurement of sound waves to study cumulative damage effect on surrounding rock under blasting load. Chin. J. Geotech. Eng. **29**(04), 88–93 (2007)
10. Chang-bin, Y.: Amended expressions of Hoek-Brown criterion based on blasting cumulative damage effects of rock mass. Rock Soil Mech. **32**(10), 2951–2956 (2011)

# The Mechanism of Gas Storage and Transportation in the Elliptic Paraboloid Zone of Mining-Induced Fracture and Simultaneous Extraction of Coal and Gas

Shugang Li[✉], Haifei Lin, Pengxiang Zhao, Haiqing Shuang, Min Yan, and Yang Bai

School of Safety Science & Engineering, Xi'an University of Science & Technology, Xi'an 710054, Shaanxi, China

**Abstract.** The safety simultaneous extraction of coal and gas can meet the multiple effects of coalmine safety production, new energy supply and environmental protection. The key scientific problems of the safety simultaneous extraction of coal and gas are the law of rock movement, fracture evolution and pressure unloading gas migration. At home and abroad, there is a lack of three-dimensional experimental system to study these laws, so this paper develops a comprehensive experimental platform for coal and gas production. Through the simulation results of the experimental system, it is found that the fracture morphology of mining overburden in coal seam can be characterized by ellipsoid. Based on the key stratum theory of rock formation control, the dynamic evolution mathematical model of the mining-induced fracture elliptic paraboloid zone with the interval between the key layer and the roof of the coal seam is established. Applying the theory of fluid mechanics, mass transfer, seepage mechanics and mining mechanics, the gas seepage equation, the gas lift equation in the longitudinal fracture zone and the gas diffusion equation in the transverse fissure zone are obtained. This paper constructs a comprehensive control model of gas lift, diffusion and seepage in the elliptic paraboloid zone of mining-induced fracture. In this paper, the mechanism of gas migration is analyzed, and a reasonable extraction method of discharged gas is put forward. The effect of the gas extraction in Tianchi coalmine and Liyazhuang coalmine show that the mining-induced fracture ellipsoid is the main storage and transportation area of the unloaded gas. The arrangement of high drainage roadway and high-level borehole can effectively control gas, which provide scientific basis for simultaneous extraction of coal and gas.

**Keywords:** Elliptical paraboloid zone · Simultaneous extraction of coal and gas · Gas seepage-rising float-diffusion · High drainage roadway
High-level borehole

# 1    Introduction

Gas is the associated product in the evolution of coal seam. The main component of gas is methane, which is mainly adsorbed in the coal surface and pores [1]. Methane threatens mine safety, but it is a clean, efficient resource [2, 3]. The development and utilization of coal-bed methane can reduce the occurrence of mine gas accidents, optimize the energy structure and develop the national economy [4, 5]. The gas occurrence of coal seam in most mining areas in China has the characteristics of "three high and three low" [4, 6]. The low permeability of coal seam makes the gas pre-pumping effect worse. Therefore, the field is mainly extract gas from mining process. After coal seam mining, the migration and storage of gas depends on the evolution law and morphology of the fracture development. Academician Qian minggao and professor Xu jialin proposed the "O" ring model [7], academician yuan liang proposed the high crack ring shape model [8]. Yang and Xie [9–11] pointed out that the overlying mining-induced fracture has the characteristics of "∩". The author has proposed the dynamic evolution form of mining overburden fracture elliptic paraboloid zone [12]. All these results have laid a foundation for the establishment and improvement of the theory and technology system of coal and methane.

At present, the research methods and methods for the evolution of overburden fractures and the accumulation of pressure gas migration are mainly simulated by field measurement, numerical simulation and physical analogue. In the field of coalmine production, the research institute needs a long period of time, which consumes a lot of manpower and material resources, and is severely restricted by the field conditions. It is difficult to test the gas concentration and pressure change in the rock mass inside and in the mining fracture, so far it is still a problem that can't be solved well. Numerical simulation is difficult to accurately describe the mining-induced rock stress distribution and deformation of rock mass movement after damage, risk behind the changes in physical properties, and fracture of rock mass, the seepage and diffusion of pressure relief gas in evolution. Physical similar material simulation experiment is an effective research method, however there is still lack of synchronization study the movement of overburden rock, crack evolution and pressure relief gas migration rule of physical simulation experiment system [13, 14].

Based on the previous research, this paper has developed a three-dimensional physical analogue material simulation experiment platform, which is based on the principle of synchronous study of overlying strata movement, fracture evolution and unloaded gas migration. The experimental platform includes three dimensional physical simulation experiment platform for coal and gas, and the similarity criterion for the evolution of overburden and gas migration in three dimensional conditions. In this paper, the evolution law and mathematical model of the elliptic paraboloid zone of mining-induced fracture are studied by combining experimental system and physical numerical simulation. Applying the theory of fluid mechanics, mass transfer, seepage mechanics and mining mechanics, this paper constructs a comprehensive control model of gas lift, diffusion and seepage in the elliptic paraboloid zone of mining-induced fracture. In this paper, the mechanism of gas migration is analyzed, and a reasonable extraction method of discharged gas is put forward. Finally, the practice of gas

extraction was carried out in Tianchi coalmine and Liyazhuang coalmine in Shanxi Province, which achieved good results and ensured the safe and efficient production of the work surface.

## 2 Comprehensive Experimental Platform for Simultaneous Extraction of Coal and Gas

The experimental platform of simultaneous extraction of coal and gas mainly includes three dimensional physical simulation experiment platform, the evolution of overburden fracture and gas migration coupling similarity criterion and corresponding similar material.

### 2.1 Three Dimensional Physical Simulation Experiment Platform

Using modular design method, the high strength rigid framework, mining system, ventilation system, gas injection system, the gas extraction system, loading system, acoustic electric monitoring system, data acquisition control system are integrated, research and develop the coal and gas mining three-dimensional physical simulation experiment platform. (Length × width × height = 3000 mm × 2500 mm × 2000 mm) (as shown in Fig. 1). The platform integrates machine, electricity, liquid and gas, and has the characteristics of three-dimensional large-scale, multi-physical field coupling and multi-disciplinary intersection. It realizes the study on the law of overlying strata movement, the distribution of mining pressure, the law of gas migration and the law of gas extraction. It provides an experimental platform for the study of simultaneous extraction of coal and gas.
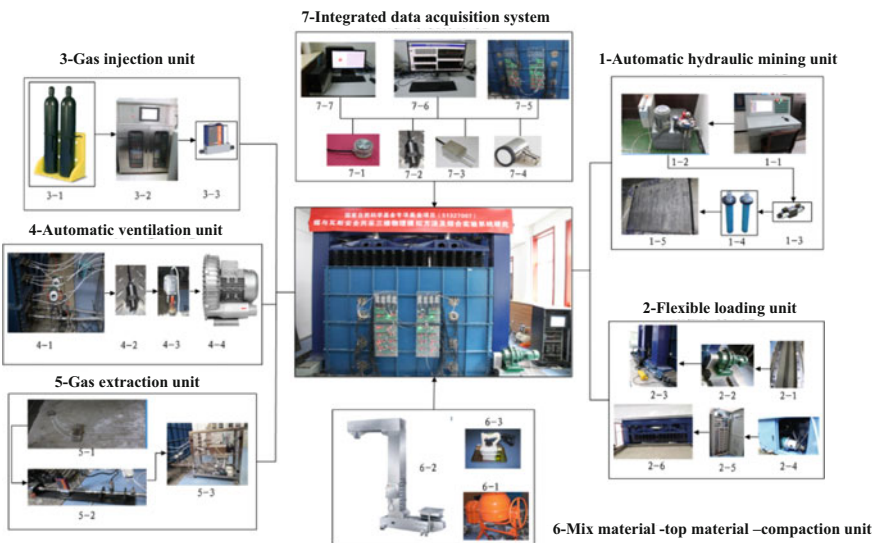


**Fig. 1.** Integrated experimental system of three-dimensional physical simulation

**Automatic hydraulic mining unit**: the unit consists of a hydraulic station, 80 hydraulic cylinders and 40 steel bars, with a range of 0–12 cm, which can simulate coal seams with different thickness, as shown in Fig. 1-1.

**Flexible loading unit**: the unit consists of a hydraulic station, a hydraulic cylinder, a multi-stage spring rubber plate and a moving frame, with a maximum capacity of 300 tons, which is used to simulate the load of the overburden strata, as shown in Fig. 1-2.

**Gas injection unit**: this unit is composed of a high-pressure cylinder, a multi-channel gas tank and a 40 pipe line, and its inflating pressure is 0–0.5 MPa, which provides a gas source for the experimental platform, as shown in Fig. 1-3.

**Automatic ventilation unit**: this unit is composed of variable frequency ventilator, ventilated pipe and strip steel, and can be used as a roadway, which can be used to simulate various ventilation modes such as U type, U + L type and Y type, as shown in Fig. 1-4.

**Gas extraction unit**: the unit is composed of pumping pump, pumping line, gas concentration sensor, negative pressure sensor and flow sensor. It can simulate the gas extraction method of upper corner, high-level borehole, as shown in Fig. 1-5.

**Mix material—top material—compaction unit**: this unit consists of plate machine, feeding machine and tamping machine, which can realize semi-automation in the process of model building, as shown in Fig. 1-6.

**Integrated data acquisition system**: this unit is composed of various kinds of sensors, data acquisition instrument and computer. It mainly tests the gas concentration and pressure, the top floor and overburden stress, and the fracture range of coal rock mass, as shown in Fig. 1-7.

## 2.2 The Similarity Criterion for the Evolution of Overburden Fracture and Gas Migration Coupling Under Three-Dimensional Conditions

The similarity between the field and the experiment refers to the constant proportion of the physical quantity of all the representational phenomena in the corresponding points and time. The similarity criterion is the key link between the field application and the laboratory test. Therefore, the accurate establishment of the similarity criterion will affect the phenomenon reproduction in the field practice. Based on previous research [15–18], using analysis methods of rock mechanics, fracture mechanics, seepage mechanics and similar principles, a coupled mathematical model for the evolution of mining overburden fractures and unloaded gas migration in three dimensional conditions is established. The similarity criterion of physical conditions, geometrical proportions, gravity, stress, pore pressure, time, permeability coefficient and gas storage coefficient of three-dimensional physical similarity simulation experiment are derived (as shown in formula 1). It provides a theoretical basis for the simulation experiment of fracture evolution and gas migration.

$$\begin{cases} C_G = C_\lambda = C_\varepsilon \ \textit{Physical similarity} \\ C_v = C_\varepsilon C_l \ \textit{Geometric similarity} \\ C_G C_\varepsilon = C_f C_l \ \textit{Gravity similarity} \\ C_\sigma = C_f C_l \ \textit{Stress similarity} \\ C_\alpha C_p = C_f C_l \ \textit{Pore pressure similarity} \\ C_t = \sqrt{C_l} \ \textit{Time similarity} \\ C_w = 1/\sqrt{C_l} \ \textit{Gas source term similarity} \\ C_S = 1/\left(C_y \sqrt{C_l}\right) \ \textit{Storage coefficient similarity} \\ C_K = \sqrt{C_l}/\sqrt{C_\lambda} \ \textit{Permeability similarity} \end{cases} \tag{1}$$

## 2.3    Similar Materials for Three-Dimensional Physical Simulation Experiments

The similar material is reasonable mix sand, nature calcium carbonate, cement, starch and other material, in order to make its mechanical property and the field overburden the stress, the permeability change law similar. Based on previous research [19–21], using methods of orthogonal test, extreme difference analysis and multiple regression analysis, in order to carry out experimental study on the dynamics, permeability, energy dissipation characteristics and influencing factors of similar materials under different proportions. In combination with the similarity criterion, suitable similar materials and their proportion were developed.

## 3    The Formation of the Elliptic Paraboloid Zone of Mining-Induced Fracture

### 3.1    Construction of Three-Dimensional Physical Model

In order to better combine with the previous test results, the experimental prototype is consistent with the 302 working face of a mine in Shanxi Province. The working face is arranged in a direction of 181 m and the length is 2025 m, and the surface is hilly. The ground elevation is +1483 to +1663 m, and the underground elevation is +1152 to +1224 m. The coal seam of 302 working face is Taiyuan Group 15#, coal thickness is 4.35–5.24 m, coal seam dip angle is 3°–14°, the average is 8.5°. Adopt the comprehensive mechanized coal mining method, and use fully caving coal mining method to manage the roof.

Considering the field and experimental conditions, according to the similarity criterion, the geometric similarity ratio is 1:10, and the wind speed similarity ratio is 1:1. In the process of model excavation, the data acquisition system is used to monitor the overburden mining stress, mining-induced fracture and gas concentration. Limited to the length of the article, the distribution characteristics of micro seismic events are analyzed in this paper (Table 1).

**Table 1.** Similarity ratio

| Simulation parameters | Prototype | Similar model | Similar ratio |
|---|---|---|---|
| Inlet air roadway section/m | 4.5 × 3.5 | 0.045 × 0.035 | 100 |
| ventilation roadway section/m | 4.0 × 3.2 | 0.04 × 0.032 | 100 |
| Wind speed/(m s$^{-1}$) | 3.17 | 3.17 | 1 |
| Time/s | 24 | 2.4 | 10 |
| Air volume/(m$^3$ min$^{-1}$) | 3000 | 0.3 | 10,000 |
| The amount of gas injected/(m$^3$ min$^{-1}$) | 18 | 0.0018 | 10,000 |

### 3.2 Analysis of Working Face Simulation Process

In the process of advancing the working face, the overburden of different layers will break, and the energy will be released during the process. The high frequency micro seismic system was used to detect the energy changes, and the high definition industrial peep instrument was used for the verification and analysis. Before the model excavation, the acoustic emission event evolution characteristics of similar materials in the process of mining are mastered through a large number of basic experiments, so the accuracy of monitoring is guaranteed [22].

(1) **The Evolution of Overburden Mining Fracture**

With the continuous advancement of the working face, the concentrated area of micro seismic events continues to develop along the direction and height. For every 20 m, the distribution form of micro seismic events in space is basically elliptical parabolic shape. The distribution height of micro seismic events in goaf is increasing along the strike and dip. When the working face is pushed to 180 m, the maximum distribution height is about 65 m. When the working face is pushed to 200 m, the concentration distribution height of the event is about 65 m, and the maximum distribution height is around 113 m. There are a lot of micro seismic events in the coal rocks around the goaf. With the advance of the working surface, the micro seismic events affected by the critical layers no longer evolve to higher strata (as shown in Figs. 2 and 3).

When the working face is pushed up to 200 m, a high definition borehole peep instrument is used to analyse the characteristics of borehole damage in different areas near the ellipse. The internal and external borehole stability of elliptical parabolic shape is analysed. According to statistical analysis, the characteristics of borehole fractures in A, B and C in Fig. 3 are shown in Fig. 4.

It can be seen from Fig. 4 that there is a distinct difference between the internal and external borehole cracks of the elliptical parabolic shape. The stability of borehole wall is better when it is not affected by mining, as shown in Fig. 4, area A. In the area of $B_1$ and $B_2$, the overburden fracture is large and the communication between cracks is better. In the C region, the fracture is the ionospheric fissure, and the fracture will be gradually compacted after the influence of the mining stress. Through the above analysis, the communication of the overburden cracks in the elliptic paraboloid zone is better, which can provide a better migration path and storage location for the pressure relief gas.
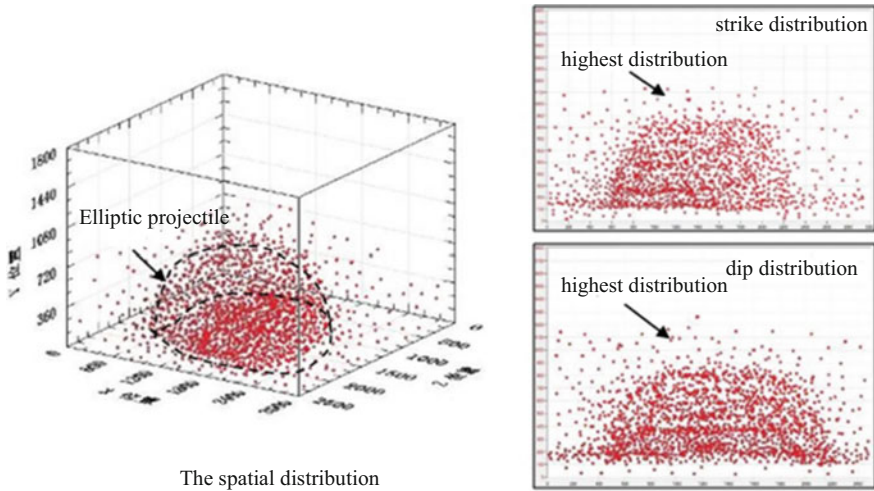
**Fig. 2.** The distribution characteristics of micro seismic events in the working face of 180 m
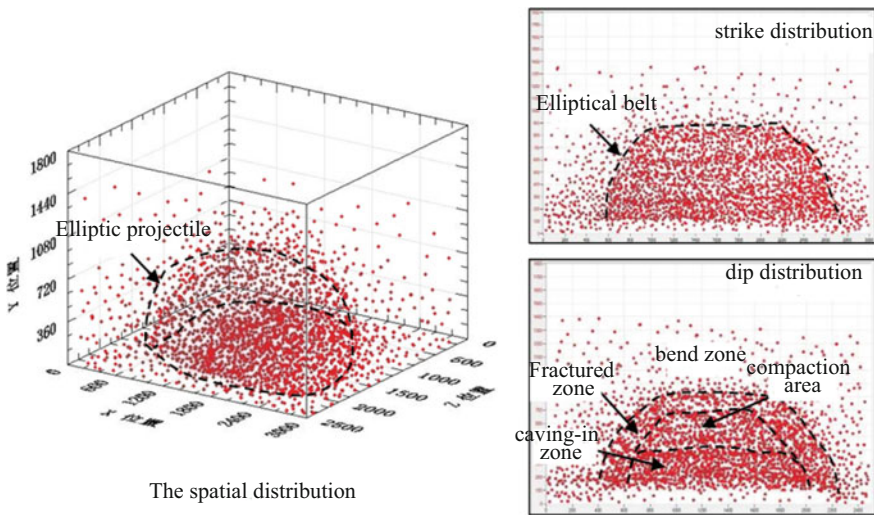


**Fig. 3.** The distribution characteristics of micro seismic events in the working face of 200 m

(2) **The Migration Law of Relieved Gas**

According to the actual situation of the working face, after promoting 200 m in the working face, the air volume is 3000 $m^3$ $min^{-1}$ when using U-type ventilation mode. The distribution of gas concentration along the working face and the distribution of gas concentration in the height direction is shown in Fig. 5.
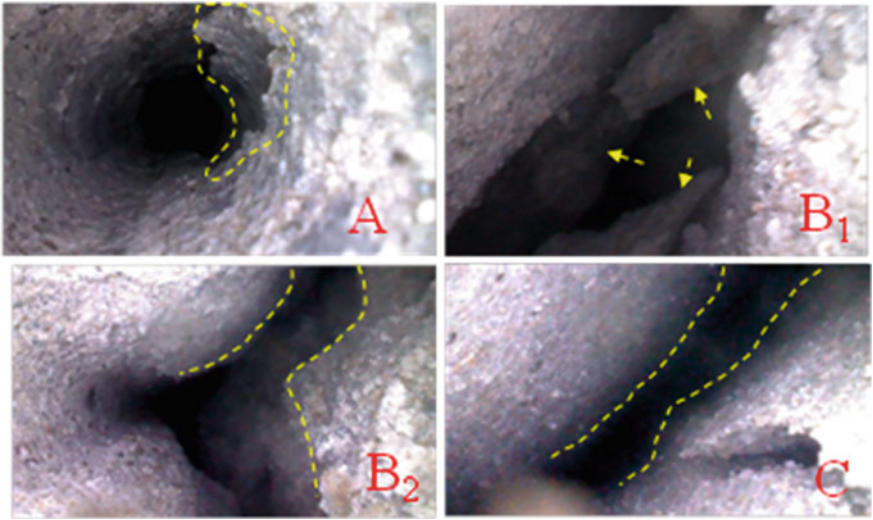
**Fig. 4.** The characteristics of the rock borehole fracture with the influence of mining
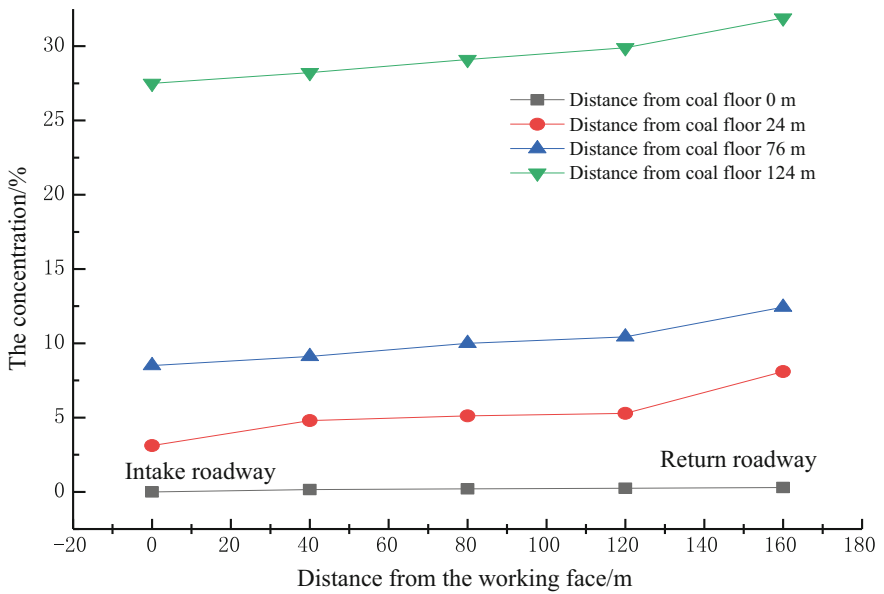


**Fig. 5.** The distribution of gas concentration at different distances in the working face

It can be seen from Fig. 2 that the compaction degree of different positions in the goaf will change the distribution characteristics of the gas concentration at different distances from the working face. In the working face, the gas concentration from the inlet side to the return airway increases successively, mainly because the gas

flow from the wind side to the back wind side of the air flow, so that the gas concentration on the return airway becomes higher. The gas concentration in the return air side of the goaf at 26 m from the working face is higher than the inlet side. And the gradient of gas concentration in the middle is obviously lower than that of the two sides. It is because the middle of the goaf is recompacted, the fracture density is lower, and the two sides are the flow channel of gas. The gas concentration at the inlet side of 76 and 124 m from the working face is slightly lower than the return airway. And the gas concentration on both sides is basically consistent, which is because the fracture network in the goaf is complex and the air leakage is less affected.

It can be seen from the Fig. 6 that the variation of gas concentration in the intake airflow roadway is same as it in return airway, but the gas concentration in the return airway is even higher. Due to the distance of 5 and 24 m from the coal seam, the relieved gas is in the lower part of the elliptic paraboloid zone, while the gas is mainly in the upward migration state, and the gas concentration is low. With the advance of the working face, the overburden mining fracture has less influence on the deep part of the goaf, so the change of gas concentration is small. At 60 m from the coal seam (the top of the elliptic paraboloid zone), the relieved gas was gathered in the area after the seepage—rise and float—diffusion movement, and the concentrations on both sides of the return airway and the intake airflow roadway are basically the same.

### 3.3    Analysis of Simulation Results

Through physical similarity simulation, it is found that after 2–3 cycles of periodic weighting, there is a connection between the mining-induced fracture ionosphere and fracture crack. As the working face advancing, the key stratum and rock affected by mining disturbance is different There will be an obvious gap between the working face and the cutting hole, and the compaction area will be formed in the middle of the goaf. The outer boundary of the overlying strata in the goaf is shaped like an elliptic paraboloid, as shown in Fig. 2, called the outer ellipsoidal surface. The mining-induced fracture in the middle of the goaf is called the inner ellipsoid. In the overlying strata of the whole goaf, a cap-shaped mining-induced fracture zone is formed between the ellipsoid, called Elliptic Paraboloid Zone (EPZ).

Based on previous research [1, 12], the width of the fissure area near the cut eye is equal to the initial pressure step distance. The crack area near the working face has a period of 1–2 times the initial pressure step distance. The width of the fissure zone in the inlet and back wind chute is about 0.8 times the initial pressure step distance. The distance between the height of the elliptical belt and the working face is shown in Figs. 2 and 3.

The study also found that the contours of the mining-induced fractures were different before and after the primary key stratum touched the gangue. When the main key stratum before touch the gangue, the movement of overburden rock formation of the parabolic profile is continuous, the lower the critical layer after first articulated structures, overburden to the mined-out area in central pressure, compacted zone and fracture zone, thus form a paraboloid. After the primary key stratum contacts the
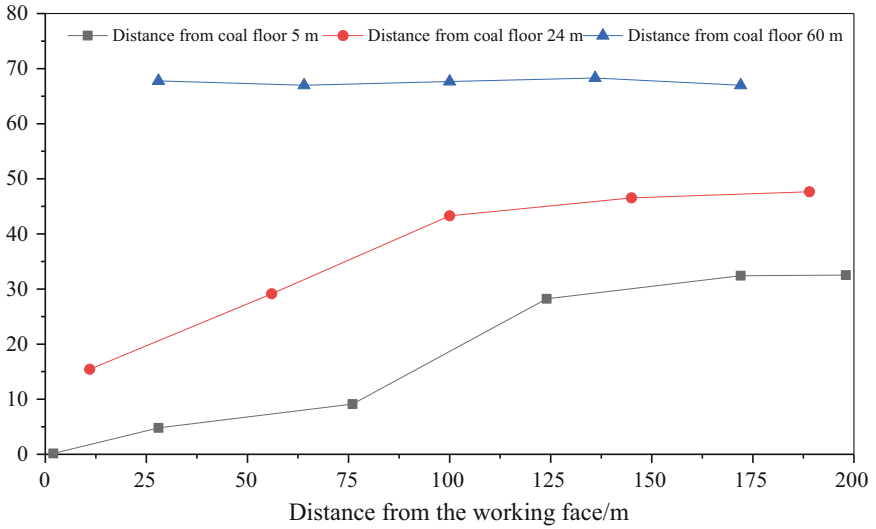
**(a) on the inlet side**
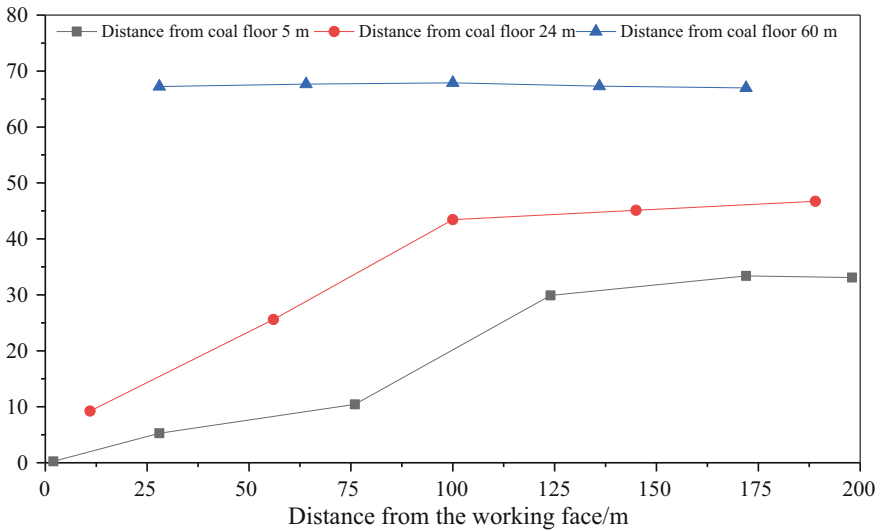


**(b) on the return air side**

**Fig. 6.** The gas concentration of different heights

gangue, the outside paraboloid stops developing, the inner paraboloid gradually develops to the main key layer as the working surface progresses. The middle of the goaf under the main key layer is compacted, but the fissures in the vicinity of the goaf can be maintained, and the continuous mining-induced fracture development will no

longer exist. The fissure region which can be transported by gas reservoir is formed between the inside and outside paraboloid, which is an approximate ellipse region.

## 4    The Mathematical Model of Elliptic Paraboloid Zone and the Migration Mechanism of Relieved Gas

### 4.1    The Mathematical Model of the Mining-Induced Fracture Elliptic Paraboloid Zone

Based on the experiment, the model of elliptical strip space is established as shown in Fig. 7. The different positions of the coal seam roof with different height and first substratum are analyzed, and the ratio of the height of the inner ellipsoid to the height is $F_1$, and the height of the outer elliptic paraboloid zone is $F_2$. This paper established cast mining fissure elliptic equation, Eq. (2) to consider under the influence of mining height are broken, mining fissure elliptic with mathematical models, Eq. (3) to consider the first and the key strata under the influence of mining fissure elliptic with mathematical model, as shown in Fig. 7.
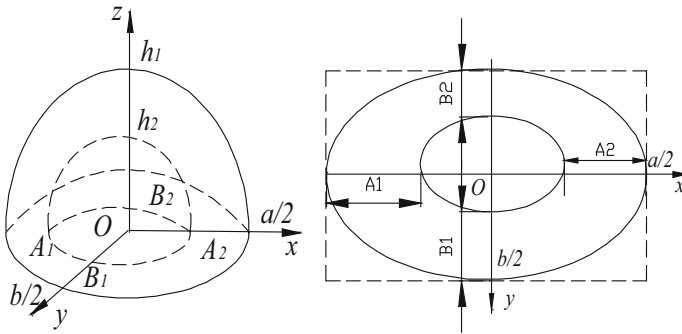


**Fig. 7.** The mathematical model of the mining-induced fracture elliptic paraboloid zone

$$\begin{cases} \dfrac{(2x-b)^2}{b^2} + \dfrac{4y^2}{a^2} = -\dfrac{z-m\cdot F_1}{c_1 m\cdot F_1} \\ \dfrac{\left(2by-a\sqrt{b^2-(A_1-A_2)^2}-bB_1+bB_2+ab\right)^2}{\left(a\sqrt{b^2-(A_1-A_2)^2}-bB_1-bB_2\right)^2} \\ + \dfrac{(2x-b-A_1+A_2)^2}{(b-A_1-A_2)^2} = -\dfrac{z-m\cdot F_2}{c_2 m\cdot F_2} \end{cases} \qquad (2)$$

$$\begin{cases} \dfrac{(2x-b)^2}{b^2} + \dfrac{4y^2}{a^2} = -\dfrac{z-H\cdot G_1}{c_1 H\cdot G_1} \\[2ex] \dfrac{\left(2by - a\sqrt{b^2-(A_1-A_2)^2} - bB_1 + bB_2 + ab\right)^2}{\left(a\sqrt{b^2-(A_1-A_2)^2} - bB_1 - bB_2\right)^2} \\[2ex] \quad + \dfrac{(2x-b-A_1+A_2)^2}{(b-A_1-A_2)^2} = -\dfrac{z-H\cdot G_2}{c_2 H\cdot G_2} \end{cases} \tag{3}$$

where $a$ is the working face width, m; $b$ is the distance promoted by the working face, m; $c_1$, $c_2$ is the rupture and swelling coefficient of the rock strata surrounded by outer and inner ellipsoidal surfaces; $A_1$, $A_2$ is the elliptical band width of the goaf at the upper part of the cutting hole and working face, m; $B_1$, $B_2$ is the elliptical band width at the entrance and return airway, m; $m$ is for height, m; $F_1$, $F_2$ is the ratio of the inner and outer ellipsoidal height and the height of the mining height; $H$ is the distance between the first sub-key layer and the roof of the coal seam, m; $G_1$, $G_2$ is the ratio of the interior and outer ellipsoidal height to the height of height under the influence of the first subcritical strata.

The ratio of interior and outer ellipsoidal height to mining height is determined by Eq. (4). The ratio of inner and outer ellipsoidal height to mining height of the first subcritical layer is determined by Eq. (5).

$$\begin{cases} F_1 = p_1 \ln m + q_1 \\ F_2 = v_1 \ln m + w_1 \end{cases} \tag{4}$$

$$\begin{cases} G_1 = p_2 H + q_2 \\ G_2 = v_2 H + w_2 \end{cases} \tag{5}$$

where $p_i$, $q_i$, $v_i$, $w_i$ (i = 1, 2) are coefficients, which can be obtained by experiment.

## 4.2 An Integrated Control Model for the Seepage—Rise and Float—Diffusion of an Elliptical Strip with Relieved Gas

(1) The seepage equation of relieved gas in the elliptic paraboloid zone

Generally, the gas seepage in the elliptic paraboloid zone conforms to the gas content, gas movement and gas state equation. Because the permeability coefficient is a function of the stress state and pore pressure of gas coal body [23], the coupling relationship between the permeability and stress of coal is obtained, and the control model of gas seepage is obtained:

$$\sum_{i=1}^{3} \frac{\partial}{\partial x_i}\left(K_{ij}\left(\sigma_{ii}^*, p\right)\frac{\partial p^2}{2\partial x_i}\right) = \frac{n}{2p}\frac{\partial p^2}{\partial t} \\ + p\frac{\partial n}{\partial t} + \frac{abp}{2p(1+bp)}\frac{\partial p^2}{\partial t} \tag{6}$$

where $K_{ij}$ (i, j = 1, 2, 3) is the permeability coefficient of coal seam, d; $\sigma_{ii}\left(\sigma_{xx}, \sigma_{yy}, \sigma_{zz}\right)$ is the volume stress of the coal, MPa; $a$ is the maximum gas adsorption capacity of

coal, m$^3$/t; $b$ is the adsorption constant, MPa$^{-1}$; $p$ is the gas pressure of adsorption equilibrium, MPa; $n$ is the porosity of the coal body; $t$ is time, s.

(2)   The lift equation of gas in the elliptic paraboloid zone

With the advance of the working surface, the gas emitted from the elliptic paraboloid zone rises and floats due to the density difference with the surrounding air (the gas density is 0.554 times the air) [13]. There are two kinds of buoyancy sources, namely instantaneous buoyancy sources and stationary buoyancy sources. This paper mainly discusses the gas lift movement in stationary environment under the action of constant buoyancy.

Generally, the floating form of the material under constant buoyancy is like an umbrella, which is called an umbrella flow. The basic equations governing material migration are: continuity equation, momentum equation, conservation equation of matter and state equation. Under the condition of boundary condition and the principle of mass conservation, the buoyancy control equation under constant buoyancy source is obtained. The passage of gas in the mining-induced fracture elliptical belt is mainly the longitudinal fracture crack. When there are hard and thick strata in the overlying strata in the stope, the gas lift will be impeded. According to the condition of producing the longitudinal fracture crack, the floating equation of gas in the mining-induced fracture elliptical belt can be obtained:

$$\frac{\Delta\rho_m}{\rho_a}g = \frac{1+\lambda^2}{\pi\lambda^2} \cdot \left(1.2k_s\sqrt{2\pi}\right)^{-1}(0.225A)^{-1/3}\frac{\lambda^2\Delta\rho_m}{\left(1+\lambda^2\right)\rho_a}$$
$$\pi V_m gb^2\left\{\left[h_i + L_i\cdot\sin\frac{\xi_i\varepsilon_{\tau i}\rho_{si}}{(1-\chi_i)\cdot\left(a_i+\sqrt[3]{12I_i}\right)d_i}\right]\right\}^{-5/3} \tag{7}$$

In the formula, $\Delta\rho_m$ is the density of floating umbrella flow center; $\rho_a$ is the density of surrounding gas, kg/m$^3$; $\lambda$ is the undetermined coefficient; $k_s$ is the sweep coefficient; $A$ is the area of floating umbrella flow, m$^2$; $V_m$ is the flow velocity of floating umbrella, m/s; $b$ is the half thickness of the flow section of the floating umbrella, m; $h_i$ is the spacing between the key layer $i$ and the roof of the coal seam, m; $L_i$ is the period breaking distance of the key layer $i$, m; $\xi_i$ is the opening displacement of the crack tip, m; $\varepsilon_{\tau i}$ is the ultimate tensile strain of key layer $i$; $\rho_{si}$ is the density of key layer $i$, kg/m$^3$; $a_i$ is the length of the longitudinal break fracture in the layer thickness of the key layer $i$, m; $\chi_i$ is the penetration degree of key layer $i$; $I_i$ is the moment of inertia bending at the key layer $i$; $d_i$ is the thickness of key layer $i$, m.

(3)   The diffusion equation of gas in the elliptic paraboloid zone

The gas diffuses in the elliptic paraboloid zone. Due to the continuous deformation of the strata caused by coal seam mining [24], the zone of ionosphere forming gas diffusion is formed between the strata. The equivalent area can be calculated with the following formula [25]:

$$\widetilde{S_t} = 2 \sum_{i=1}^{n-1} \int_0^A \theta_{\max i}\left(e^{-\frac{x}{2l_{i+1}}} - e^{-\frac{x}{2l_i}}\right) dx \tag{8}$$

$$l_i = h_i \sqrt{\frac{\sigma_\tau}{3q}} \tag{9}$$

where $\widetilde{S_t}$ is the equivalent area of the total ionosphere in the overburden, m$^2$; $A$ is the width of mining-induced fracture, m; $\theta_{\max i}$ is the maximum ionosphere, m; $l_{i+1}$, $l_i$ is the length of the fault block of the key layer of the $i + 1$ and the $i$ layer, m; $h_i$ is the thickness of the $i$ key layer, m; $\sigma_\tau$ is the tensile strength of the $i$ key layer, MPa; $q$ is the weight of the key layer and its control layer, kg; $x$ is the advance length of the working face, m.

For the stable state in the stationary air containing the gas, a stationary air column containing gas is set. In the diffusion equilibrium state, there is a calculation formula:

$$-\rho_z D \frac{d}{dz}\left(\frac{\rho_g}{\rho_z}\right) - D \frac{\rho_g \rho_a (m_a - m_g)}{\rho_z^2 RT} \frac{dp}{dz} = 0 \tag{10}$$

where, z is the vertical coordinate.

Because of the small amount of gas in the air, the partial pressure in the mixed gas is relatively low. So $\rho_a$ is approximately equal to $\rho_z$, and $\frac{dp}{dz}$, $T$ can also be considered a constant, so there are:

$$-\frac{d\rho_g}{dz} - D \frac{(m_a - m_g)}{\rho_a RT} \rho_g \frac{dp}{dz} = 0 \tag{11}$$

Take $\rho_g = c - \frac{(m_a - m_g)dp}{\rho_a RT dz} = a$ into Eq. (10) and integrate it:

$$c = e^{rz + s} \tag{12}$$

where $r$, $s$ are fitting constants.

Because $dp/dz < 0$, so $a > 0$, and $c = e^{az+b}$ as the index of monotone increasing function. Therefore, the greater the height of the fissure development is, the greater the corresponding $c$ value is. It can be concluded that the gas concentration increases with the increase of height in the stationary air. The diffusion of gas in the equivalent area of the overburden caused by mining is pure diffusion. Combined Eqs. (8) and (11) can form the gas diffusion equation in the ionosphere fissure.

### 4.3 The Mechanism of Extraction with Relieved Gas in the Elliptic Paraboloid Zone

The coal contains a large number of pore fissures, which are full of free gas and adsorption gas. When the mining fracture elliptic paraboloid zone is formed, the gas

adsorption balance condition is broken, and the gas is transformed from the adsorption state to the free state. Then, under the effect of concentration and pressure, the relieved gas is transported by seepage-rising-float-diffusion.

The main channel of gas migration is the fissure system. The layer fissure is the main migration path of gas, and the ionosphere fissure is the reservoir of gas. The development of fracture is affected by stress, which is mainly reflected in the change of permeability coefficient of coal/rock in the elliptic paraboloid zone. Therefore, the Eq. (6) considers the coupling relation between the permeability coefficient and the gas pressure, can better reflect the seepage characteristics of the coal/rock in the elliptic paraboloid zone. Under the action of buoyancy, the gas is transported by the vertical crack to the upper lift of the elliptic paraboloid zone, so formula (6) further clarifies the path of gas lift. When the gas rises to the ionosphere fissure, the diffusion occurs, (8) and (11) describe the migration process of gas in the ionosphere fissure.

In conclusion, by Eqs. (6), (7), (8) and (11) constructed elliptic cast with gas seepage-floating-diffusion integrated control model, theoretically explains the upper part of mining fissure elliptic paraboloid zone gathered large amounts of gas, as well as the phenomenon of neighboring fracture zone gathered large amounts of free gas.

If the high drainage roadway is arranged in the upper part of the elliptic paraboloid zone and the lower part of the fissure belt, it is not conducive to the gas flow to the working face, and it is not conducive to the gas removal from the upper part of the elliptic paraboloid zone. Due to the gradual increase of the gas accumulation area in the evolution of the elliptic paraboloid zone, the high bore holes should be arranged in different layers of the elliptic paraboloid zone in order to extract the gas at different stages. Part of high-level borehole should be arranged at the top for the gas can be pumped efficiently. In the early stage, the low level borehole was used to extract the gas in the enriched area, and the gas was transported in the later stage, and the distribution characteristics of the flow field in the working face were changed. This can prevent gas concentration exceeding limits in working face and ensure safe production of working face.

## 5    Engineering Practice of Simultaneous Extraction of Coal and Gas

### 5.1    The Technique of Extracting Gas from the High Drainage Roadway in the Elliptic Paraboloid Zone

In the process of gas control in 103 caving face of Shanxi tianchi coalmine, the height of the inner elliptic paraboloid zone is about 22 m, the height of the outer elliptic paraboloid zone is 34 m, and the width of the fissure zone near the return airway is about 24 m. In 103 working face, the high drainage roadway is arranged at a distance of 30 m from the roof of the coal seam and the return airway, to extraction with the gas. This effectively controls the gas concentration in the working face and the return airway, as shown in Figs. 8 and 9.

The average concentration of the gas extracted from the high drainage roadway reached 50.4%. The average extraction pure volume reached 67.3 $m^3$/min. The
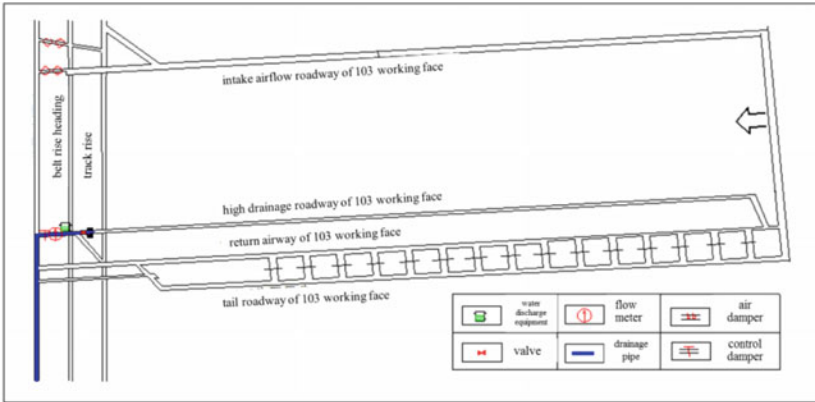
(a) The layout of the extraction system
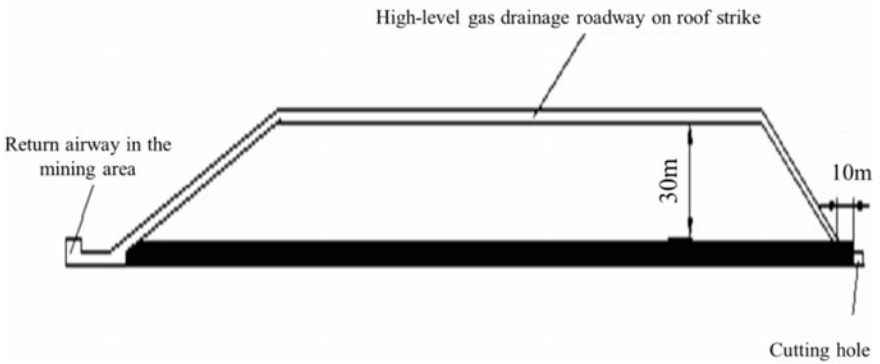


(b) The layout of high-level gas drainage roadway on roof strike

**Fig. 8.** The layout of gas extraction system of 103 fully mechanized face

extraction volume accounted for about 76.7% of the gas emission. In the process, the working face was pushed 251 m, producing 360,000 tons of coal. The maximum gas concentration is controlled within 1%, and the safe and efficient production of the work surface is realized.

## 5.2    The Gas Extraction Technology of the High-Level Borehole in the Elliptic Paraboloid Zone

The permeability coefficient of 2-603 working surface of Liyazhuang coalmine in Shanxi Province is low, and the pre-pumping effect is not obvious. In the recovery process, the gas concentration in upper corner is often exceeded. Combined with the evolution characteristics of the elliptic paraboloid zone of overburden mining fracture, the high drainage roadway is arranged in the elliptic paraboloid zone of adjacent working surfaces. It can improve the utilization rate of high suction lane, and Increase the flexibility of the placement of high bore holes. The specific layout of the lateral high
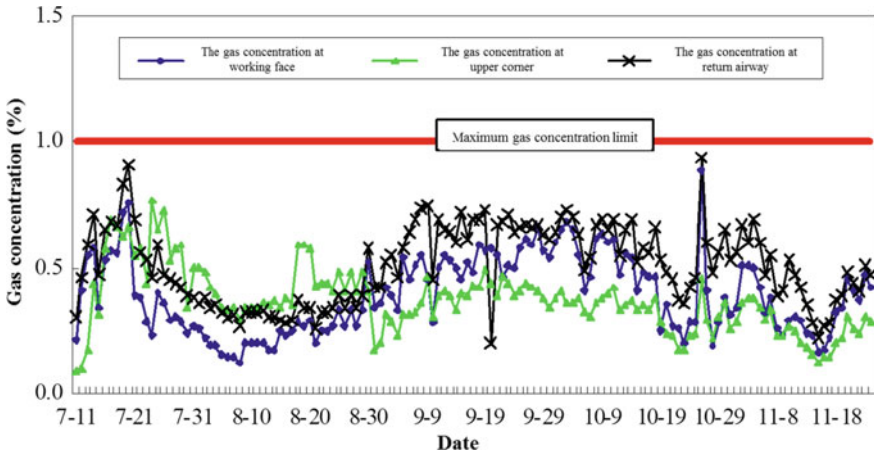
**Fig. 9.** The relationship between working face, upper corner and return airway and time
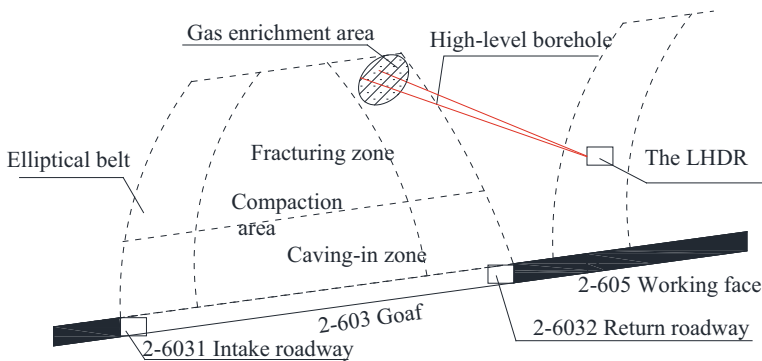


**Fig. 10.** The arrangement of mining fracture elliptical belt and extraction method

drainage roadway is shown in Fig. 8. Combined with physical analogue simulation and numerical simulation [26, 27], the mining-induced fracture zone is 44 m away from the roof of the coal seam, and the high-level borehole is arranged in the lateral high drainage roadway. The layout parameters are shown in Figs. 10 and 11. After 40 days' continuous monitoring, the gas concentration of each borehole is shown in Fig. 12.

It can be seen from Fig. 11 that the position of the high-level borehole directly determines the concentration and time of the extraction gas. When 1-1# borehole was arranged at the top of the elliptic paraboloid zone, the effective drainage days were 42 and 39 days respectively, and the average gas volume fraction was 52.4 and 43.0% respectively. The extraction concentration was greater than 80%, which were 12 and 13 days respectively, obviously higher than that in the lower part of the elliptic paraboloid zone. The low level borehole's exhausting and mining time is long and the concentration is low, which indicates that the lower part of the elliptical belt is not the main reservoir. It is proved that the relieved gas is mainly concentrated in the upper
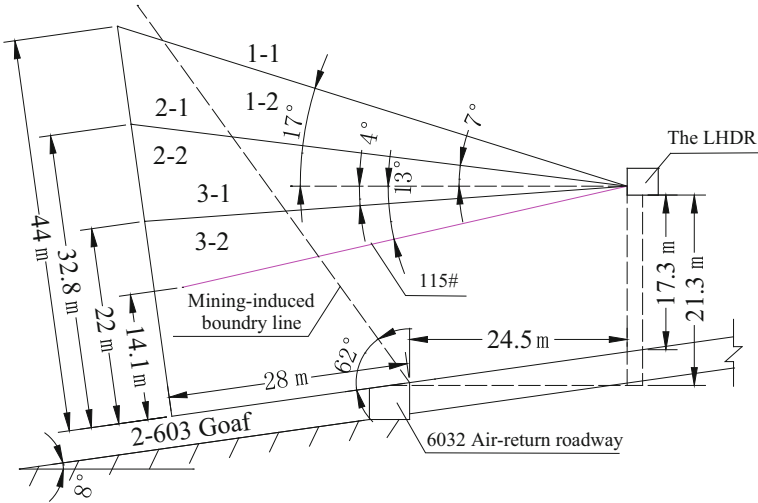
**Fig. 11.** Specific parameters of borehole
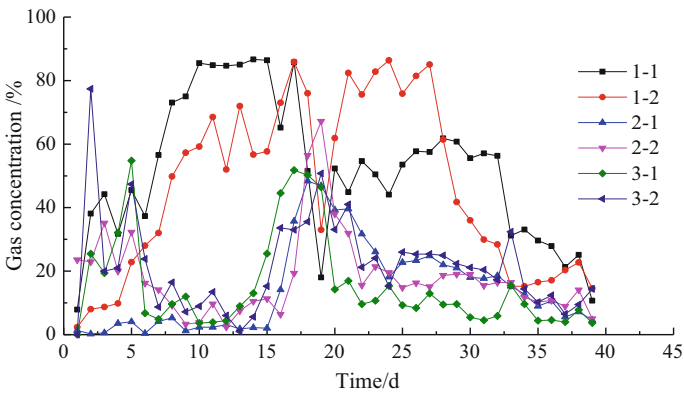


**Fig. 12.** The variation of gas concentration in the high-level borehole

middle part of the elliptic paraboloid zone. After long-term monitoring, the gas concentration in the upper corner of the production class was 0.50–0.95%, and the maintenance class was 0.47–0.89%. There was no gas exceeding the limit, and the coal production reached 230,000 t, which realized the safe and efficient production of the fully mechanized working face.

## 6    Conclusion

(1)    The integrated experimental system of coal and gas was developed independently. It realizes the study on the law of overlying strata movement, the distribution of mining pressure, the law of gas migration and the law of gas extraction. It provides an experimental platform for the study simultaneous extraction of coal and gas.

(2)    Combining three-dimensional physical simulation experiment and previous research results, this paper analyzes the formation process of mining fissure elliptic paraboloid zone, established the mathematical model, provides a mathematical basis for study of gas migration in elliptic paraboloid zone.

(3)    In this paper, a comprehensive control model of gas seepage—uplift—diffusion is established. The dynamic evolution relation between the gas migration and the longitudinal crack and the transverse fissure is obtained. According to this model, the gas migration mechanism in the mining-induced fracture elliptic paraboloid zone is clarified, which provides a theoretical basis for the extraction and unloading of gas.

(4)    Through the analysis of the characteristics of mining fracture elliptic paraboloid zone in the working face of 103 fully mechanized working face of Tianchi coalmine and 2-603 of Liyazhuang coalmine, the main storage and transportation channel of the unloading gas was verified. The high level roadway is arranged in the middle and lower part of the elliptic paraboloid zone, and the high-level borehole is arranged on the top of the elliptic paraboloid zone, which can effectively control the gas concentration of the working face and ensure the safe and efficient recovery of the working face.

## References

1.    Li, S., Qian, M., Shi, P.: Methane migration and accumulation state sfter seam mining. Coal Geol. Explor. **28**(5), 31–33 (2000)
2.    Yuan, L.: Key technique of safe mining in low permeability and methane-rich seam group. Chin. J. Rock Mech. Eng. **27**(7), 1370–1379 (2008)
3.    Li, S., Qian, M.: Simultaneous safety extraction of coal and coal-bed methane in China. Sci. Technol. Rev. **6**, 39–41 (2000)
4.    Li, S., Li, S., Lin, H., et al.: Technique of drawing relieved methane and simultaneous extraction of coal and coakbed methane. J. Xi'an Univ. Sci. Technol. **22**(3), 247–249 (2002)
5.    Xu, J., Qian, M., Jin, H.: Study on "coal and coal-bed methane simultaneous extraction" technique on the basis of strata movement. J. China Coal Soc. **29**(2), 129–132 (2004)
6.    Yuan, L.: Theory of pressure-relieved gas extraction and technique system of integrated coal production and gas extraction. J. China Coal Soc. **34**(1), 1–8 (2009)
7.    Qian, M., Xu, J.: Study on the "O-SHAPE" circle distribution characteristics of mining-induced fractures in the overlaying strata. J. China Coal Soc. **23**(5), 466–469 (1998)

8. Yuan, L., Guo, H., Shen, B., et al.: Circular overlying zone at longwall panel for efficient methane capture of multiple coal seams with low permeability. J. China Coal Soc. **36**(3), 357–365 (2011)
9. Yang, K., Xie, G.: Caving thickness effects on distribution and evolution characteristics of mining induced fracture. J. China Coal Soc. **33**(10), 1092–1096 (2008)
10. Karacan, C.Ö., Goodman, G.: Hydraulic conductivity changes and influencing factors in longwall Overburden determined by slug tests in gob gas vent holes. Int. J. Rock Mech. Min. Sci. **46**, 1162–1174 (2009)
11. Palchik, V.: Influence of physical characteristics of weak rock mass on height of caved zone over abandoned subsurface coal mines. Environ. Geol. **42**(1), 92–101 (2002)
12. Li, S., Shi, P., Qian, M.: Study on the dynamic distribution features of mining fissure elliptic paraboloid zone. Ground Press. Strata Control (3–4), 44–46 (1999)
13. Kan, W.U., Cheng, G., Zhou, D.: Experimental research on dynamic movement in strata overlying coal mines using similar material modeling. Arab. J. Geosci. **8**(9), 6521–6534 (2015)
14. Yang, K., Xie, G., Tan, G.: Experimental investigation on behaviors of bolt-supported rock strata surrounding an entry in large dip coal seam. J. Rock Mech. Geotech. Eng. **03**(s1), 445–449 (2011)
15. Li, S.: Movement of the Surrounding Rock and Gas Delivery in Fully-Mechanized Top Coal Caving. China University of Mining and Technology press, Beijing (2000)
16. Lin, H.: Study on the Law of Mining-Induced Fracture Evolution of Overlying Strata and Relieved Methane Delivery and Its Engineering Application in Fully-Mechanized Top Coal Caving. Xi'an university of science and technology, Xi'an (2009)
17. Li, S., Bie, C., Zhao, P., et al.: Study on influence factors of new solid-gas coupling simulation material. J. Min. Saf. Eng. **34**(5), 981–986 (2017)
18. Li, S., Zhao, P., Lin, H., et al.: Study on character of physical simulation similar material of coal-rock and gas solid-gas coupling. J. China Coal Soc. **40**(1), 80–86 (2015)
19. Lin, H., Zhai, Y., Li, S., et al.: Research on mechanics and permeability characteristics of similar material of solid-gas coupling based on orthogonal design. J. China Coal Soc. **41**(3), 672–679 (2016)
20. Li, S., Cheng, X., Liu, C., et al.: Damage characteristics and space-time evolution law of rock similar material under uniaxial compression. J. China Coal Soc. **42**(s1), 104–111 (2017)
21. Li, S., Cheng, X., Liu, C.: Effect law of damage characteristics of rock similar material with pre-existing cracks. In: Materials Science and Engineering Conference Series (2017)
22. Liu, C., Li, S., Xue, J., et al.: Identification method of high fractured body for overlying strata in goaf based on microseismic monitoring technology. J. China Univ. Min. Technol. **45**(4), 709–716 (2016)
23. Biot, M.A.: General theory of three-dimensional consolidation. J. Appl. Phys. **12**, 155–164 (1941)
24. Zhang, J., Liao, G.: Investigation on formation mechanism of separated layer of rock covering and calculation-method of separated layer. Undergr. Space **21**(5), 407–413 (2001)
25. Li, S., Qian, M., Shi, P.: Study on bed-separated fissures of overlying stratum and interstice permeability in fully-mechanized top coal caving. Chin. J. Rock Mech. Eng. **19**(5), 604–607 (2000)
26. Li, S., Shuang, H., Wang, H.: Determining the rational layout parameters of the lateral high drainage roadway serving for two adjacent working faces. International J. Min. Sci. Technol. **26**(5), 795–801 (2016)
27. Li, S., Shuang, H., Wang, H., et al.: Extraction of pressurized gas in low air-conductivity coal seam using drainage roadway. Sustainability **9**(2), 223 (2017)

# Author Index